THE PHYSICAL REVIEW

VOLUME 92 Second Series NUMBER 2

OCTOBER 15, 1953

Published for the

AMERICAN PHYSICAL SOCIETY

by the

AMERICAN INSTITUTE OF PHYSICS

LANCASTER, PA., AND NEW YORK, N. Y.

REVIEW

A journal

Published by the American Institute
for the

AMERICAN PHYSICAL

Officers

President

Serge Pease
Institute for Nuclear Studies
University of Chicago
Chicago 37, Illinois

Vice-President

H. A. Bethe
Cornell University
Ithaca, New York

Secretary

S. K. Allison
Bell Telephone Laboratories
Office:
Columbia University
New York 27, New York

Treasurer

G. B. Pegram
Columbia University
New York 27, New York

Local Secretary
for the Pacific Coast

J. Kaplan
University of California
Los Angeles
Los Angeles, California

Managing Editor

S. A. Goudsmit
Brookhaven National Laboratory
Upton, Long Island
New York

The Physical Review
Entered as second-class matter
Acceptance for mailing at special rate

REVIEW

Published by the

BOARD OF EDITORS

Associate Editors

1939–1941

W. F. Arnold
J. G. Beckerley
J. M. Cassel
Charles Hastman
R. W. Lawson
Jerome Rosenberg

1940–1942

E. L. Hill
Y. T. Wu

Communications to contributors and
Physical Review, Upton, Long Island,
Communications to any A publication
Physical Review in the Bell System

Communications concerning papers in the process
Publication Manager, American
New York, N. Y.

Subscription Rates

Foreign Postage

Single Numbers

Back Numbers

Changes in Address

Claims for Missing Numbers will be allowed
(3 months for foreign and Canada)

Subscriptions to the Physical Review, Reviews of Modern Physics and Rev
Institute of Physics, 57 East 55th Street, New York, N. Y.

Entered as second-class matter at the post office at Concord, New Hampshire, under the act of
Authorized January 21, 1925.

Publication office, 175 Main Street, Ithaca, New York.

Editorial and executive offices, Brown University, Providence, Rhode Island.

Printed by the Rumford Press, Concord, New Hampshire.

THE
PHYSICAL REVIEW

A journal of experimental and theoretical physics established by E. L. Nichols in 1893

SECOND SERIES, VOL. 92, NO. 2 OCTOBER, 15, 1953

Sensitive Hall Measurements on NaCl and on Photoconductive PbTe†

JOHN L. LEVY
Physics Department, University of Michigan, Ann Arbor, Michigan
(Received March 6, 1953; revised manuscript received July 6, 1953)

Sensitive Hall equipment was built according to a cross-modulation method with 60-cps magnetic field, 85-cps driving current, and 25-cps selective detection. An attempt was made to measure the Hall effect of ionic conduction in sodium chloride. Theoretically its Hall mobility is expected to be of the order of 10^{-7} m²/volt-sec (10^{-3} cm²/volt-sec). However, excessive current noise, of the order of 10 microvolt per cps, in the sample subjected to electric and magnetic fields of the order of 10^4 volt/m and 1 weber/m² at temperatures between 650°C and 800°C, prevented the observation of any Hall signal, yielding only an experimental upper limit of 10^{-7} m²/volt-sec (10^{-3} cm²/volt-sec) for the mobility.

Measurements of the Hall effect in photoconductive films of lead telluride at 30°C and −190°C are also reported. The results support Simpson's theory that the increase in photoconductivity is primarily due to an increase in carrier density and only secondarily to a change of mobility.

INTRODUCTION

WHILE the Hall effect for electronic conduction both in metals and semiconductors is measured relatively easily, the Hall effect of ionic conduction has never been detected. The main purpose for building the sensitive Hall apparatus described here was to detect the Hall effect for ionic conduction in alkali halides at elevated temperatures, near the melting point (about 800°C for sodium chloride).

The requirements for such an attempt were estimated as follows. The mobility of sodium ion vacancies in sodium chloride has been obtained by Etzel and Maurer[1] and ranges from 10^{-8} to 10^{-6} m²/volt-sec for the alkali halides in the structure-insensitive range of temperatures. This is about 10^{-3} times the lowest value of electronic mobilities in metals and semiconductors, which range from 10^{-5} to 2 m²/volt-sec. For an ionic crystal with linear dimensions of the order of 10^{-2} m, a magnetic field of the order of 1 weber/m², and an ionic mobility of 10^{-7} m²/volt-sec (or 10^{-3} cm²/volt-sec), the ratio of the Hall emf to the primary voltage is then of the order 10^{-7} and thus requires in conventional schemes of measurement the compensation of any potential difference present between the Hall electrodes with a precision of one part in ten million with respect to the primary voltage. This difficulty can be avoided at the high temperatures used, only by certain ac methods. These also minimize effects of electrolytic polarization in the sample. We adopted the cross-modulation method used first by Russel and Wahlig.[2] Accordingly, we built equipment capable of measuring Hall mobilities of the order of 10^{-8} m²/volt-sec, provided the noise generated by the sample is not excessive.

In addition to the primary purpose, the equipment was also used for the measurement of the Hall effect of photo conducting films of lead telluride. Since Hall mobility values were available only for the bulk material which is not photoconductive, the values for thin films should provide significant information regarding the mechanism of photoconductivity in such materials. According to Simpson's[3] theory the photoconductivity in lead telluride films results essentially from an increased density of carriers, excited into the conduction band by the incident radiation. The carrier mobility is assumed to be a slowly varying function of temperature and irradiation. We intended to verify this assumption experimentally by measuring the Hall mobility at room temperature and as a function of the irradiation at liquid air temperature.

† Supported by the U. S. Office of Naval Research. Part of a dissertation submitted to the University of Michigan for the degree of Doctor of Philosophy.

[1] H. W. Etzel and R. J. Maurer, J. Chem. Phys. **18**, 1003 (1950).

[2] B. R. Russell and C. Wahlig, Rev. Sci. Instr. **21**, 1028 (1950).

[3] O. Simpson, Trans. Roy. Soc. (London) **A243**, 578 (1951).

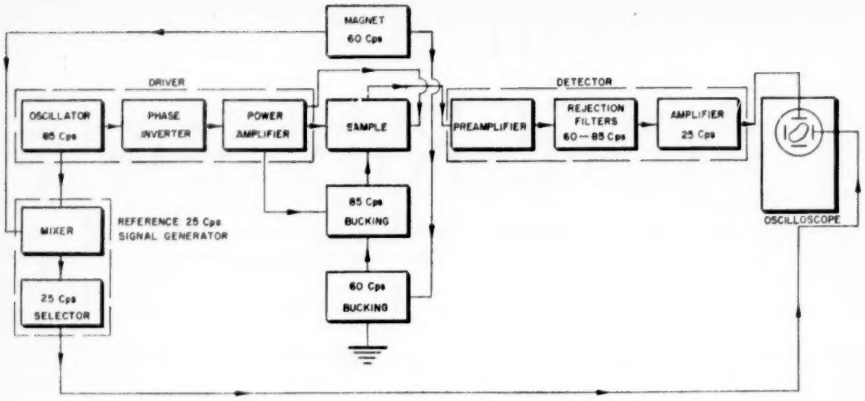

FIG. 1. Block diagram of the apparatus.

APPARATUS

a. Electronic Apparatus and Magnet

The apparatus, designed according to a cross-modulation method similar to that of Russell and Wahlig,[2] is represented by the block diagram in Fig. 1.

The driver, producing the 85-cps primary electric field applied to the sample, is capable of delivering 20 watts with negligible distortion, and its output can be matched to the sample impedance within a large range. In order to avoid spurious mixing of 85-cps and 60-cps signals, for instance through 60-cps magnetic pickup by transformers, R–C coupling and R–C filters in feedback circuits were used exclusively.

The laminated silicon steel magnet produced a 60-cps alternating field, essentially uniform within a 3×6 cm area. The ellipse of $0.95B_{max}$ has axes of 3.4 and 5.4 cm. The air gap width was 3.5 cm. The maximum peak field produced without distortion was about 1.5 weber/m^2. The power requirements of the magnet made the choice of 60 cps almost imperative.

The Hall signal was measured at the difference frequency of 25 cps. This frequency was chosen as a compromise between various tendencies. The high-input impedance required by the samples favored a low frequency. The frequency drift in the line voltage and a reasonable response time, combined with a good signal-to-noise ratio favored a not too low frequency. Finally, a frequency that could not be produced by combinations of overtones of the magnet and driver frequencies was desirable. These and other considerations led to the adopting of the frequencies of 60, 85, and 25 cps.

The Hall signal was amplified by the detector. Its sensitivity and bandwidth were about 1 microvolt and 1 cps, respectively. The selective part of the detector could also be tuned to 60 cps or 85 cps to guide and check the balancing out of the corresponding voltages in the Hall-probes circuit. For this purpose, two bucking sections provided signals of 60 and 85 cps, adjustable with a relative precision of 10^{-4}. In each section a Helipot potential divider provided the amplitude adjustment, while the phase was set by a sine-cosine resolver loaded with a suitable R–C circuit. All sensitive parts of the detector were carefully shielded against electric, magnetic, and mechanical disturbances.

The Hall mobility sign was determined by observing on an oscilloscope the phase of the detector output relative to a reference signal. The calibration of the apparatus was checked by measuring the Hall mobility of a Ge sample, kindly measured independently and put at our disposal by W. C. Dunlap of the General Electric Research Laboratory.

b. Sample Holders and Samples

For the measurements on sodium chloride which were taken between 650°C and 800°C, 2.5×20×20 mm synthetic optical grade single crystal samples of high purity, manufactured by the Harshaw Chemical Company, were placed in a lavite oven, shaped like a cigar box with two dc heating coils imbedded in the large faces. Approximately 400 watts, derived from storage batteries, were required to heat the box to the melting point of sodium chloride. The temperature of the sample was monitored by a chromel-alumel thermocouple, whose emf was calibrated in situ against melting points of several alkali halides in this temperature range. It was found that the most accurate and convenient determination of the sample temperature was by measurement of its electric conductivity.

The current electrodes consisted of 0.001-inch thick platinum foils pressed against the crystal by an assembly of quartz rods, plates, and springs. We observed no improvement in the electrical behavior of the sample when a platinum film was first deposited on the electrode areas of the sample by applying a coat of "liquid bright platinum." The Hall electrodes were made with 2×2 mm tongues of the same material. The ends of the quartz rods pressing them against the crystal were shaped into 1×2 mm rectangular areas, so that the Hall electrodes had approximately the same extension. After the crystal had been kept above 700°C

for a few minutes, the platinum foils adhered firmly to the sample.

For the measurements on lead telluride films, which were taken at 30°C and under controlled illumination at −190°C, photoconductive cells were especially prepared. The graphite electrodes were first painted on the Pyrex support of the cell with a coat of Aquadag. The distance between primary electrodes was about 10 mm, while the Hall electrodes were 1 mm apart. The cell envelope was then sealed to a vacuum system and the films were deposited according to Simpson's evaporation procedure.[3] The finished cell was placed in a light shielded cryostat. A glass tube sealed to the cell served as a light pipe to bring controlled amounts of irradiation onto the film from a light source outside the cryostat.

The results scattered, partly because the current noise between Hall probes was an appreciable fraction of the Hall signal at liquid air temperature, and partly because the cells were not stable, i.e., did not exhibit a definite and reproducible resistance when kept at −190°C under constant illumination. However, the measurements still permitted drawing significant conclusions.

RESULTS AND CONCLUSION FOR SODIUM CHLORIDE

A number of measurements were taken for various samples of sodium chloride at $B=0.86$ weber/m² rms. Excessive current noise of about 10 microvolt per cps in the sample when subjected to the electric and magnetic fields prevented the detection of any Hall emf. Consequently, only an experimental upper limit for the Hall mobility could be determined. The results are summarized in Table I.

The primary voltage of about 200 volts represented an electric field of 10^4 volt/m. The primary current ranged between 1.6 and 26 milliamperes, generally increasing with higher temperature T, which ran from 650°C to 795°C, as determined from the conductivity. The resulting rms noise V across the Hall electrodes in microvolts set a lower limit to the mobility that could be measured, or an upper limit $\mu_{\max}$ for mobilities that escape measurement. This upper limit for the Hall mobility was of the order of 10^{-7} m²/volt-sec.

Since electrons are expected to exhibit a considerably higher mobility, this suggests that, even near the melting point, no appreciable electronic conduction takes place. Furthermore, this experimental limit does not conflict with the estimates of the difference between mobilities of positive and negative vacancies that can be derived from Etzel's data on the mobility of sodium vacancies[1] and on Tubandt's measurements of transport numbers[4] at lower temperatures. This estimate was obtained as follows. According to Etzel the mobility of positive carriers is given by

$$\mu_+ = (1.96/T)e^{-9860/T} \text{ m}^2/\text{volt-sec}.$$

[4] C. Tubandt, *Handbuch der Experimental Physik* (Julius Springer, Berlin, 1932), Vol. 12, p. 402.

For the algebraic sum of the mobilities we have

$$\mu_+ - |\mu_-| = \mu_+(1-r),$$

where

$$r = |\mu_-/\mu_+|.$$

The temperature dependence of μ_- is assumed to have the same forms as μ_+. Thus, r has the form:

$$r = Ae^{-B/T}.$$

Since only Schottky defects are assumed to be present in NaCl, the densities of carriers of opposite sign are equal, and r equals the ratio of the transference numbers. Thus, Tubandt's data can be used to find the constants A and B, and this leads to

$$r = 1900e^{-9100/T}.$$

Tubandt's data lie in the range of 560–625°C. The constants A and B are assumed to be unchanged up to the temperature range of our experiments (650–800°C). The over-all rms error in $\mu_+ - |\mu_-|$ was estimated and was found to be 10 percent. The resulting values for $\mu_+ - |\mu_-|$ were 0.45×10^{-7} m²/volt-sec at 650°C and 1.3×10^{-7} m²/volt-sec at 795°C. These are seen to be of the same order of magnitude as the limit set by the noise.

While the precise cause of this noise is at present not known, the following information may be helpful in its interpretation. The noise is definitely a current noise and is more than a factor of 10 higher than the Johnson noise of the crystal and the entire detecting system combined. It is proportional to the crystal current and independent of the magnetic field. The values given are obtained after a few minutes of current; immediately after the current is switched on the noise is greater. The noise may have been connected with some plastic deformation in the crystal near the Hall electrodes. This deformation could not be avoided at the high temperatures used, without causing a poor contact between electrodes and crystal. Sufficient tests have been

TABLE I. Measurements on single crystals of sodium chloride.

V_A[a] volt	I_A ma	V microvolt	$\sigma\times10^{-5}$ ohm^{-1} cm^{-1}	T °C	$\mu_{\max}\times10^7$ m²/volt-sec
240	1.6	31	2.7	650	3
240	1.6	7.5	2.7	650	0.8
240	3.4	12.5	5.7	680	1.3
240	5.4	11	9	705	1.1
225	11.7	10	21	745	1.3
270	21	7.5	31	765	0.68
175	15	22.5	34	770	3.1
240	21	10	35	775	1
220	19	15	35	775	1.7
240	21	10	35	775	1
240	26	14	43	785	1.4
220	25	10	45	785	1.1
200	22	4.5	44	785	0.55
180	22	8.5	49	795	1.2

[a] V_A = primary voltage; I_A = primary current; V = rms noise between Hall electrodes; σ = conductivity of sample; T = temperature; and $\mu_{\max}$ = experimental upper limit of Hall mobility (1 m²/volt-sec = 10^4 cm²/volt-sec).

TABLE II. Measurements of the Hall effect in a photoconductive lead telluride film.

B[a] weber/m²	V_A volt	$V\times10^4$ volt	$R_p\times10^{-6}$ ohm	$R_H\times10^{-4}$ ohm	$\mu\times10^4$ m²/volt-sec	T °C	Remarks
0.43	24.5	11.8	2	6.2	1.5	30	
0.22	24.5	5.25			1.34	30	
0.22	102	25			1.53	30	
0.43	100	43.8			1.37	30	
0.43	150	69			1.44	30	
0.22	150	35			1.46	30	
			$>10^6$	$>10^6$		−190	dark
			5000	2800		−190	illuminated
0.43	100	37.5	1.9	6	1.17	30	
0.65	100	56.1			1.17	30	
0.65	24.5	10.6			0.9	30	
0.43	24.5	9			1.15	30	
0.43	12	5			1.3	30	
0.32	11.5	5	1.7	5	1.8	30	
0.32	19.5	6.25			1.34	30	
0.32	234	1		2000	1.78	−190	dark
0.32	210	37.5		800	1.12	−190	illuminated[b]
0.65	210	62.5		800	0.93	−190	illuminated[b]
0.32	195	62.5		5	1.33	30	
0.43	234	31	9	17	4.1	30	cell leaks

[a] B = rms magnetic field, V_A = primary voltage, V = Hall signal, R_p = sample resistance between primary electrodes, R_H = sample resistance between Hall electrodes, μ = Hall mobility (1 m²/volt-sec = 10^4 cm²/volt sec), and T = temperature of the sample.
[b] Rms input noise $2\cdot10^{-3}$ volt at 25 cps.

made to ascertain that the noise originates in the crystal. Its spectrum has not been determined. Investigations aimed at lowering the noise level are being carried on.

RESULTS AND CONCLUSIONS FOR LEAD TELLURIDE FILMS

A typical series of consecutive measurements on a lead-excess film is presented in Table II. The film was N type, as determined by the sign of its thermoelectric power, measured between primary electrodes. The sample conductivity, measured both between primary and between Hall electrodes depended on aging and thermal history of the cell. Also it drifted appreciably during illumination. The noise level between Hall electrodes was in general an appreciable fraction of the Hall signal. Nevertheless, examination of Table III, in which the average values of measurements on a group of five cells are presented, brings out the following features of physical interest.

(a) The Hall mobility at room temperature is of the order of 10^{-4} m²/volt-sec if the cell is photoconductive at low temperature; and its sign is the same as that of the thermoelectric power. It is positive for tellurium excess and negative for lead excess cells.

(b) At liquid air temperature the Hall mobility is of the order of 10^{-5} m²/volt-sec, whether the film is irradiated or not. At the most it changes by a factor of two, while the conductivity changes by a factor up to 25. Its sign is the same as at room temperature.

The order of magnitude of the Hall mobility in our samples is the same as in PbS and PbSe cells used by Lothrop[5] and Halvorsen.[6] This suggests that our films might have been activated by traces of oxygen, which were absent in Simpson's samples.

Since the Hall mobility change was small compared to the concurrent conductivity change, the increase in carrier density seemed to be mainly responsible for the photoconductivity, as was assumed by Simpson.

On the other hand, the Hall mobility in our films was much smaller than in the bulk material.[7] This could be explained by the presence of potential barriers in the films or by the granular structure of such evaporated layers.

TABLE III. Summary of measurements on films of lead telluride.[a]

Cell	T °C	R_H kilo-ohms	R_p kilo-ohms	$\mu\times10^4$ m²/volt-sec	Remarks
1	25	12	32	+21.5	Te-excess, P-type, large drift
1	−190	60	270	+2.2	dark
1	−190	59	240	+1.9	light
2	25	1.8	2.2	−104	large Pb-excess, N-type
2	−190	1.5	1.6	−124	no photo conductivity
3	30	50	200	−1.28	Pb-excess, N-type, small drift
3	−190	20 000	$>10^6$	−1.78	dark
3	−190	8000		−1.12	light
4	30	20	53	−2	Pb-excess, N-type, large change after first cooling
4	−190	5000		+0.07	dark
4	−190	50		+0.15	light
5	30	40	100	−1.4	Pb-excess, N-type
5	−190	10 000	$>10^6$	−2	dark
5	−190	1200	2300	−1.5	light

[a] Symbols as in Table II.

ACKNOWLEDGMENTS

We wish to thank Dr. E. Katz for suggesting the problem and for his guidance during the research, R. W. Terhune for the preparation of the cells used in the experiments, A. G. Dockrill for technical assistance, and Dr. W. C. Dunlap of the General Electric Company for furnishing a calibrated sample of Ge.

[5] E. W. Lothrop, Jr., Thesis, Northwestern University, 1949 (unpublished).
[6] K. G. Halvorsen, Thesis, Northwestern University, 1951 (unpublished).
[7] R. P. Chasmar and E. H. Putley, Conference on semiconducting materials, University of Reading, 1950 (unpublished).

Measurement of the Thermoelectric Power of Germanium at Temperatures above 78°K†*

A. E. MIDDLETON‡ AND W. W. SCANLON§
Department of Physics, Purdue University, Lafayette, Indiana

(Received July 13, 1953)

A systematic investigation of the thermoelectric power of germanium samples has been made in the temperature range between 78°K and about 925°K. The general method of measurement is the determination, through thermocouple readings, of the ratio $\Delta E/\Delta T$, where ΔE is the thermal emf (relative to chromel) measured between two points in the sample having a temperature difference ΔT. At first, difficulty was experienced in obtaining reliable and reproducible thermoelectric power data at the lower temperatures (78°K to about 350°K). A detailed discussion is given of the steps taken to eliminate this difficulty by reducing or removing the effects of thermal conduction by the thermocouple wires, convection currents around the the sample, poor contacts between thermocouple junctions and the sample, and inhomogeneities in the thermocouple wires. In the impurity range the sign of the thermoelectric power is the sign of the Hall coefficient, and the magnitudes of thermoelectric power, resistivity, and Hall coefficient increase with decreasing impurity content. With rising temperature the thermoelectric power increases in magnitude and passes through an extremum at a temperature somewhat lower than that corresponding to the end of the exhaustion range or flat portion of the Hall curve. The thermoelectric power of a p-type sample passes through zero at a temperature higher than that at which the Hall coefficient of the same sample becomes zero. The thermoelectric power curves of both p-type and n-type samples approach a common curve, having negative values, in the intrinsic range.

I. INTRODUCTION

EARLY investigations[1–4] of the electrical properties of the elements silicon, germanium, and tellurium showed them to be quite different from the metals and to belong in the category now referred to as semiconductors. Occasional studies of thermoelectric power were included in the general search for information about the electrical properties of these semiconductors.

Wick[5] measured the resistivity, Hall coefficient and thermoelectric power of two different silicon samples and found negative[6] values for both the Hall coefficient and the thermoelectric power, measured with respect to copper. Zimmerman[7] observed that silicon may show either positive or negative thermoelectric power with respect to copper. Smith[8] found that silicon samples having positive Hall coefficients have positive thermoelectric powers and that negative thermoelectric powers accompany negative Hall coefficients. Buckley[9] measured several electrical properties of each of four silicon samples as the temperature varied between 0°C and 100°C. He pointed out the variation from one silicon sample to another, even when cut from the same melt, is such that correlation between different electrical properties should be expected only when the properties are measured for the same sample.

Bidwell[10] studied the temperature variation of resistivity and thermoelectric power of a sample of 99.9 percent pure germanium. Haken[11] investigated several properties of tellurium including thermoelectric power and the variation of thermoelectric power with known additions of tin and antimony to the tellurium. Wold[12] made a rather complete investigation of the electrical properties, including thermoelectric power, of tellurium samples at temperatures between 0°C and the melting point.

The experiments reported by the authors in this paper were undertaken, starting in 1942, because, with the preparation of germanium samples with controlled amounts of various impurity additions at the Purdue laboratories, it became possible to investigate systematically over a wide temperature range the dependence of thermoelectric power upon the impurity content of the sample and to correlate these data with other electrical properties, especially the Hall coefficient and resistivity.[13]

II. METHOD OF MEASUREMENT

A. General Method

The general method of measuring thermoelectric power may be described as follows. A temperature

† The early part of this work was assisted by a National Defense Research Corporation contract with Purdue University and the later part by a Signal Corps contract with Purdue University.

* The investigations reported here are based in part upon doctoral theses submitted to the Faculty of Purdue University by A. E. Middleton and W. W. Scanlon.

‡ Now at Battelle Memorial Institute, Columbus, Ohio.

§ Now at Naval Ordnance Laboratory, Silver Spring, Maryland.

[1] J. Konigsberger and K. Schilling, Ann. Physik **32**, 179 (1910).

[2] K. Baedeker, *Die Elektrischen Erscheinungen in metallischen Leitern* (F. Vieweg und Sohn, Braunschweig, 1911).

[3] J. Konigsberger and G. Gottstein, Physik. Z. **14**, 232 (1913).

[4] J. Konigsberger and G. Gottstein, Ann. Physik **47**, 566 (1915).

[5] F. G. Wick, Phys. Rev. **25**, 382 (1907); **27**, 76 (1908).

[6] The thermoelectric power is defined to be positive if conventional current flows from the semiconductor to the reference metal at the cold junction. This convention produces agreement between the sign of the thermoelectric power and the sign of the charge carriers in an impurity semiconductor.

[7] C. I. Zimmerman, Trans. Am. Electrochem. Soc. **15**, 395 (1909).

[8] A. W. Smith, Phys. Rev. **30**, 1 (1910).

[9] O. E. Buckley, Phys. Rev. **4**, 482 (1914).

[10] C. C. Bidwell, Phys. Rev. **19**, 452 (1922).

[11] W. Haken, Ann. Physik **32**, 291 (1910).

[12] P. I. Wold, Phys. Rev. **7**, 169 (1916).

[13] Preliminary measurements were carried out by E. P. Miller, I. Walerstein, and K. Lark-Horovitz.

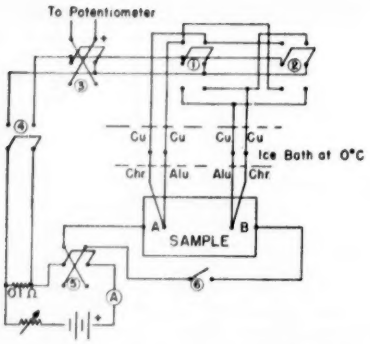

FIG. 1. Electrical circuit for measuring thermoelectric power and resistivity. Switches 4 and 6 are left open while measuring thermoelectric power; closing swith 2 upward with switch 1 open permits potentiometer measurement of the thermal emf in the germanium-chromel circuit. With switch 2 open, closing switch 1 upward and then downward gives the two emf's of chromel-alumel couples, the difference of which determines the temperature difference between points A and B. For resistivity determination, the PD between points A and B is measured with switches 2 and 6 closed; the PD is measured for both directions of current flow so that any thermal PD may be eliminated by subtraction. The current is found by measuring the PD across a 0.1-ohm standard resistor.

gradient is established in a sample so that the points A and B have the different temperatures T_1 and T_2, respectively. Thermocouples (e.g., chromel and alumel) placed at these points are used to measure the temperatures. By use of suitable switching systems (Fig. 1) the thermal emf of the sample with respect to one or the other of the thermocouple wires and the thermal emf of each thermocouple can be measured on a potentiometer. The four thermocouple wires are joined to copper wires leading to the switching system, and the copper-chromel and copper-alumel reference junctions are electrically insulated from one another and placed in an ice-water bath maintained at a uniform temperature of 0°C with the aid of a mechanical stirrer.

The thermoelectric power is found from the relation

$$Q=\Delta E/\Delta T, \tag{1}$$

where ΔE represents the thermal emf produced in the germanium chromel circuit by the temperature difference ΔT between the junctions and $\Delta T=T_1-T_2$.

One of the switching arrangements indicated in Fig. 1 permits the direct potentiometer reading of the emf ΔE. Other switching arrangements allow the potentiometric measurement of the thermal emf E_1 in the chromel-alumel couple with junctions at T_1 and 0°C and likewise the measurement of the thermal emf E_2 in the other chromel-alumel couple with junctions at T_2 and 0°C. From the values E_1 and E_2 one can determine, with the aid of National Bureau of Standards calibration data for chromel-alumel thermocouples, the average temperature $T_a=(T_1+T_2)/2$ and thence q_a, the thermoelectric power of a chromel-alumel thermocouple at T_a. This information permits determination of the temperature difference ΔT by the relation

$$\Delta T=(E_1-E_2)/q_a. \tag{2}$$

Thus, the thermoelectric power of the germanium sample, relative to chromel, at the temperature T_a is computed from the equation

$$Q(T_a)=(q_a\Delta E)/(E_1-E_2), \tag{3}$$

a quantity determined by three potentiometer readings and the quantity q_a taken from appropriate calibration tables. When advance-manganin, copper-constantan, or platinum-platinum rhodium thermocouples were substituted for the chromel-alumel couples, the same technique was employed and the $Q(T_a)$ values obtained from Eq. (3) were corrected to give readings relative to chromel.

For measurements above room temperature the samples were placed in a cylindrical electric heater which was closed at both ends to reduce convection currents. Because of the relative ease of establishing parallel isothermal planes in the sample and its surrounding medium at high temperatures, reproducible values of Q as a function of temperature were readily obtained independently of sample size, temperature gradient, or method of mounting the thermocouples on the sample.

At low temperatures, however, since the thermal gradient above the surface of liquid air in a Dewar flask was used to provide a variable range of sample temperatures, considerable difficulty was encountered in the earlier stages of this work in obtaining reliable thermoelectric power values. These difficulties called for careful consideration of certain aspects of the experimental procedure.

B. Problems of Measurement at Low Temperatures

The principal source of error in the measurement of Q occurs in the measurement of the difference in temperature between the points A and B on the surface of germanium. This difference is usually about 2°C so that the temperature difference should be known to within 0.1°C to determine Q to within five percent.

Investigations of the problems of precision thermometry with thermocouples[14] have indicated the following conditions that must be met in measurements of surface temperatures: (1) since the emf of a thermocouple measures the temperature of the junction at A or B, the junction should have the same temperature as the germanium surface at the point of contact; (2) the thermocouples should not distort the established isotherms in the vicinity; and (3) the thermocouple wires should be uniform in composition and reproducible in calibration.

In the earlier low temperature experiments large thermal gradients due to convection currents occurred

[14] American Institute of Physics Symposium, *Temperature, Its Measurement and Control in Science and Industry* (Reinhold Publishing Corporation, New York, 1941), pp. 180–316, 855–861.

near the sample surfaces. The resulting heat conduction in the thermocouple wires caused the junctions to assume temperatures intermediate between the surface temperature of the sample and the temperature of the surrounding medium a short distance away. This produced errors in the values of ΔT. The emf of a thermocouple is governed by the temperature of the junction at the point where the two wires leave it; for a large junction this temperature may be several tenths of a degree different from the temperature at the point where the junction contacts the sample. Thus the ideal junction is very small, and one aims at maximum heat conduction between the junction and sample and minimum heat conduction between the junction and its leads. These conditions can be approached by using thermocouple wires of very small cross section and by use of thermal insulation placed around the sample junction and a short section of lead wires.

The use of fine wires may introduce errors due to non-uniformity of the thermocouple wires. Samples of wire were tested for uniformity by moving a hot soldering iron along its length and measuring the emf developed; a discontinuity in emf appears when the iron touches a "junction" due to an inhomogeneity in the wire. This test led to the rejection of No. 40 chromel-alumel wires as too inhomogeneous, the acceptance of No. 36 chromel-alumel wires and No. 36 copper-constantan wires as sufficiently uniform, and also the acceptance of a special lot of one mil and two mil advance-manganin wires.

Sets of "matched" thermocouples were made to avoid errors due to non-uniformity between the two couples. The two junctions to be placed in contact with the sample were formed from as nearly identical material as possible by taking a long, homogeneous piece of each kind of thermocouple wire to be used, cutting them, and welding these freshly cut ends to form the junctions contacting the sample. The four free ends were soldered to copper leads from the switchboard, insulated from one another, bound together with wire, and submerged in the ice-water bath.

The effect of the method of mounting and size of temperature gradient upon the measurement of thermoelectric power may be shown by direct experiment. A germanium sample, ground to the customary shape of a rectangular parallelepiped 0.4 cm$\times$0.5 cm $\times$2.0 cm, was mounted vertically in the air column above liquid air in a Dewar flask. Two matched thermocouples of No. 36 chromel-alumel were soldered to the germanium surface near the ends of the sample with a minimum amount of solder. Wires of this size were chosen to emphasize the effects observed. An electric heater at the top was used to control the temperature gradient in the sample. The soldered junctions provided excellent electrical contacts and would not slip mechanically as might be the case with pressure contacts. Figure 2 shows the thermoelectric power curves obtained for this sample for different values of the temperature difference between the contact points. The thermoelectric power curves tend to converge at the higher temperatures, indicating that the measured thermoelectric power above 100°C is not sensitive to the size of the temperature gradient, in marked contrast to the behavior at the lower temperatures. Consideration of heat transfer by convection yields an explanation for the results of Fig. 2 on the basis that convection currents in the air above the liquid air bath cause the thermocouple junctions to have a temperature difference which is at marked variance with the temperature difference between the points of the sample contacted by the thermocouples. The error from this source is dependent on the temperature gradient.

Next, the same sample was mounted in a horizontal position so that it lay on an isothermal plane in the Dewar flask and thus convection currents were reduced. The sample was held in position between two graphite blocks by spring pressure; one of the blocks was wound with several turns of No. 36 nichrome wire, insulated from the graphite by asbestos tape, to serve as a heater to produce a temperature gradient in the sample (Fig. 3). With this arrangement there was much less dependence of the thermoelectric power curve upon the temperature gradient. However, errors appeared whenever the heater held the sample temperature 20° or 30° higher than that of the surrounding air; these errors were eliminated by thermally insulating the sample and short sections of thermocouple wires leaving the sample.

The difficulty of thermally insulating the sample was reduced by substituting smaller diameter wires for

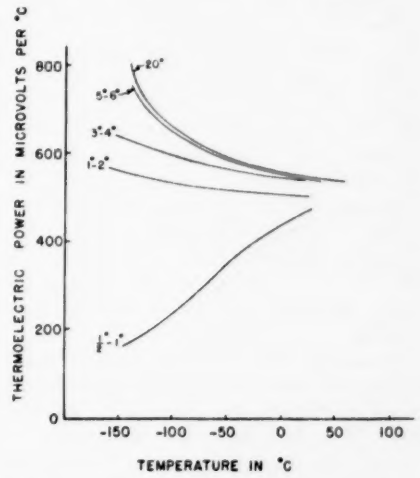

FIG. 2. Measured thermoelectric power for a germanium sample held vertically above the liquid air level in a Dewar flask. Numbers on the curves denote the approximate temperature difference maintained between ends of the sample during measurement.

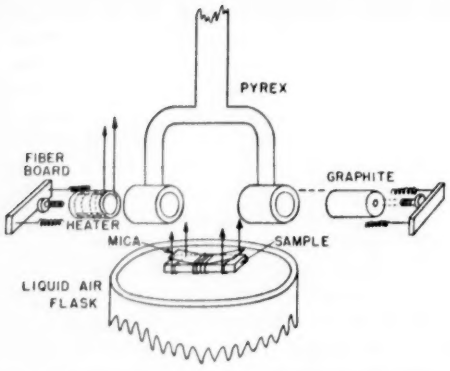

FIG. 3. Low temperature thermoelectric power apparatus. The mica strip bound to the sample is used with silicon, but not with germanium. One- or two-mil advance-manganin thermocouples are used.

the No. 36 thermocouple wires. A special lot of one- and two-mil advance and manganin wires were calibrated and used because this two-mil wire, considering its size and thermal conductivity, conducted about 1/2500 of the amount of heat that would be conducted by No. 36 chromel-alumel wires under the same temperature gradient. The junction for these fine wires was a flattened bead of silver solder, about 2 mm² in area, which held the junction to the sample. With this arrangement thermoelectric power values were independent of temperature gradients within the sample and between the sample and the surrounding air. The high electrical resistance of the fine wires produced difficulty in balancing the potentiometer and consequent random errors in thermoelectric power values.

Another example of the importance of the foregoing precautions is found in thermoelectric power measurements on a group of p-type samples with 3×10^{15}, 2×10^{16}, 2×10^{17}, and 5×10^{18} carriers per cm³ at 300°K. A family of curves was obtained similar to those shown in Sec. 3 (Fig. 5), but the magnitudes of the thermoelectric powers in the impurity range did not agree with the values calculated[15] from the Hall curves of these samples. After introducing the techniques described, the thermoelectric power curves of two of these samples were remeasured, the magnitudes were found to be increased considerably in the impurity range, and agreement between theory and experiment was obtained.

The foregoing discussion can be summarized by saying that the sample holding arrangement (Fig. 3) finally adopted for the low temperature measurements satisfied the requirements of (1) excellent thermal contact between each junction and the sample, (2) horizontal mounting of the sample to reduce convection current error, (3) smallest feasible values for the cross sections and thermal conductivities of the thermocouple wires, and (4) insulation of the thermocouple junctions from the surrounding air.

[15] V. A. Johnson and K. Lark-Horovitz, Phys. Rev. **69**, 259 (1946).

C. High Temperature Measurements

Thermoelectric power values at high temperatures (above 100°C) were readily measured. The sample was inserted vertically into a cylindrical electric furnace; the uniformity of the temperature inside this furnace made it unimportant whether the sample was held vertically or horizontally. Both ends of the furnace were closed off to reduce drafts. A small electric heater pressed against one end of the sample provided the necessary temperature gradient. Figure 4 shows the sample holder for high temperature measurements of thermoelectric power.

Holes were ground into the sample near each end, to a depth of about 3 mm, with a $\frac{1}{16}$-inch nickel tube for a drill and a mixture of No. 600 carborundum and water as an abrasive. Platinum foil was pounded into the bottom of the hole so that good electrical and thermal contact could be obtained between junction and sample. No. 36 chromel-alumel wires were used for the thermocouples. The junctions were welded together and filed off smoothly. Small lavite plugs were used to press the junctions tightly against the platinum in the holes, and the plugs were bound in position by fine wire. The thermocouple wires were wound around the sample several times and insulated with asbestos string. The sample was then placed inside a glass tube with a graphite contact on one end and a heater wound around a graphite core at the other end. Springs outside the furnace pressed the contacts against the sample.

By attaching current leads to the graphite it was possible to make simultaneous determinations of

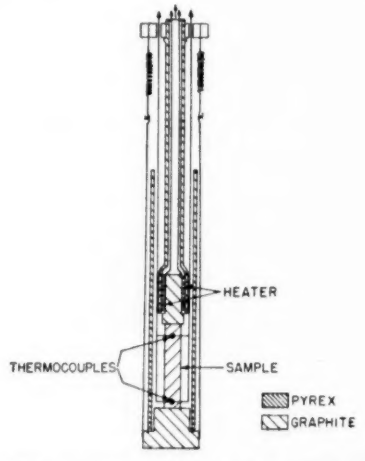

FIG. 4. High temperarure thermoelectric power apparatus.

thermoelectric power and resistivity. Since no thermal contact problem is involved, the resistivity data obtained with this arrangement were reliable and reproducible over the entire range from −190°C to above 600°C, whereas reliable thermoelectric power data were obtained only at temperatures above 50° or 100°C.

III. RESULTS

Thermoelectric power curves are presented here for those germanium samples for which the precaution described in Sec. 2B were employed in making the low temperature measurements. Figure 5 shows the thermoelectric power curves of four aluminum-doped, p-type, polycrystalline germanium samples; the carrier concentration at 300°K ranges from 5×10^{15} per cm³ to

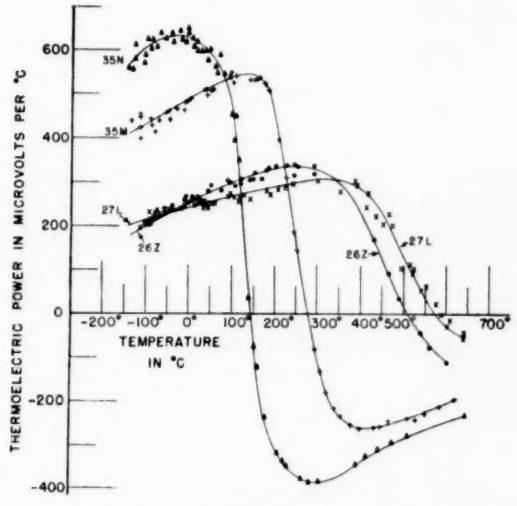

FIG. 5. Thermoelectric power curves for four polycrystalline, aluminum-doped germanium samples. The number of holes per cm³, at exhaustion, is 5.6×10^{15} for sample $35N$, 1.5×10^{17} for $35M$, 4.1×10^{18} for $26Z$, and 7.0×10^{18} for $27L$.

7×10^{18} per cm³. So that the thermoelectric power behavior of these samples may be correlated with their other electrical properties, their Hall curves are given in Fig. 6 and their resistivity curves in Fig. 7. Figure 8 presents the thermoelectric power curves of five antimony-doped, n-type, polycrystalline germanium samples with conduction electron concentrations ranging from 3×10^{15} per cm³ to 7×10^{17} per cm³. The Hall coefficients of these samples are given in Fig. 9 and the resistivities in Fig. 7.

Figure 10 shows the effect upon thermoelectric power of a heat treatment used to convert a germanium sample from n-type to p-type and then back to n-type. Sample $21V_a$ was originally prepared[16] by melting

[16] This sample was prepared by R. M. Whaley of Purdue University and was heat treated by the method recommended by him.

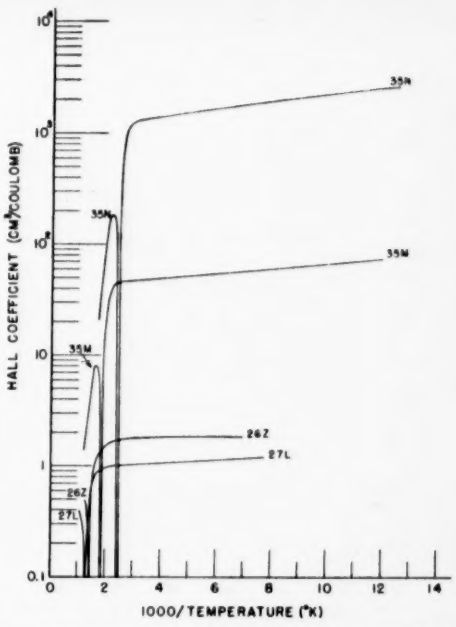

FIG. 6. Hall curves for the four p-type germanium samples for which thermoelectric power is given in Fig. 5. Hall values to the right of the zero point of each curve are positive, to the left negative.

spectroscopically pure germanium powder in a commerical helium atmosphere; a polycrystalline n-type sample was obtained. This sample could be converted

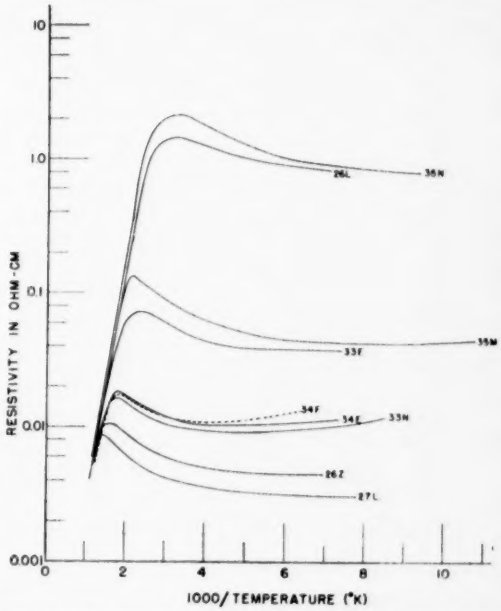

FIG. 7. Resistivity curves for the nine germanium samples for which thermoelectric power curves are given in Figs. 5 and 8.

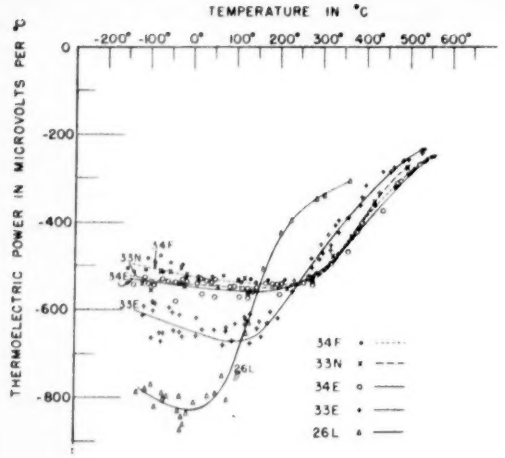

FIG. 8. Thermoelectric power curves for five polycrystalline, antimony-doped germanium samples. The number of conduction electrons per cm³, at exhaustion, is 3.4×10^{15} for sample $26L$, 9.6×10^{16} for $33E$, 5.8×10^{17} for $34E$, 7.1×10^{17} for $34F$, and 7.4×10^{17} for $33N$.

to p type by holding it at 800°C in a high vacuum furnace for four hours. It was converted back to n type by holding it at 500°C in a high vacuum furnace for eighteen hours. Hall coefficient, resistivity, and thermoelectric power curves were measured for this sample (1) in an initial n-type state, (2) after conversion to p type, and (3) after conversion back to n type. Figure 11 gives the resistivity and Hall curves corresponding to the thermoelectric power curves of Fig. 10; the third Hall curve was not obtained because of the accidental destruction of the sample.

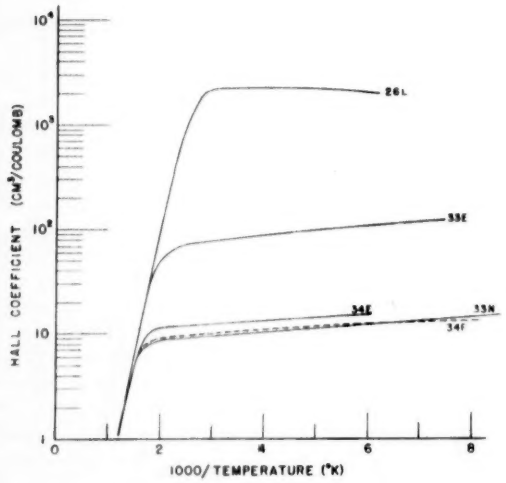

FIG. 9. Hall curves for the five n-type germanium samples for which thermoelectric power curves are given in Fig. 8. All Hall values in this figure are negative.

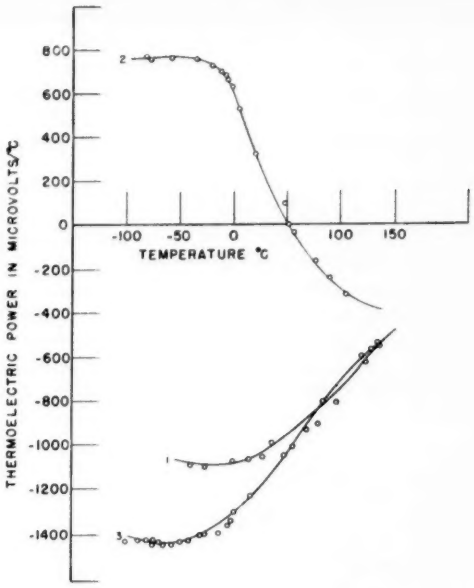

FIG. 10. The effect of heat treatment upon the thermoelectric power of germanium sample $21V_a$. Curve 1 was taken in the initial condition, curve 2 after holding the sample at 800°C in vacuum for 4 hours, and curve 3 after holding the sample an additional 18 hours in vacuum at 500°C.

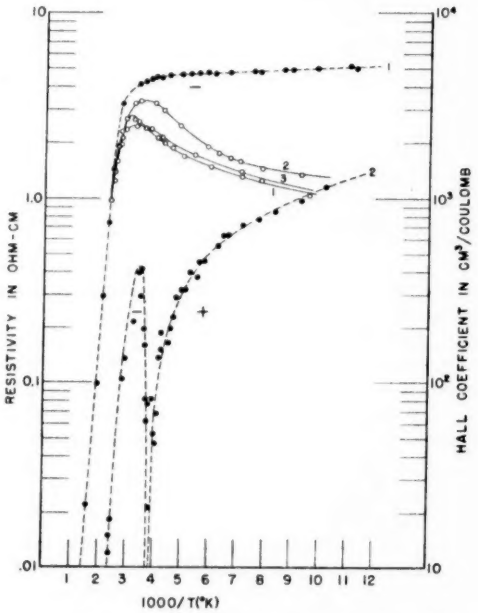

FIG. 11. The resistivity and Hall curves of heat-treated germanium sample $21V_a$. Curves 1, 2, and 3 correspond to the conditions given for Fig. 10. (The solid lines are resistivity curves and the broken lines Hall curves.)

Two silicon samples, obtained from Bell Telephone Laboratories, were studied. Both were p type and polycrystalline, but sample 112 was aluminum-doped and sample 26 G was boron-doped. The high temperature thermoelectric power was measured with an arrangement similar to that of Fig. 4, with quartz replacing glass and with No. 36 platinum-platinum, rhodium thermocouple wires being used. The low temperature thermoelectric power (200°C down to about −100°C) was obtained with the use of one-mil advance-manganin thermocouples and a holder arrangement similar to that of Fig. 3. The thermocouple junctions were pressed against nickel spots electroplated on the silicon to improve electrical contact. Figure 12 shows the thermoelectric power curves obtained for these samples, and Fig. 13 gives the corresponding Hall and resistivity curves.

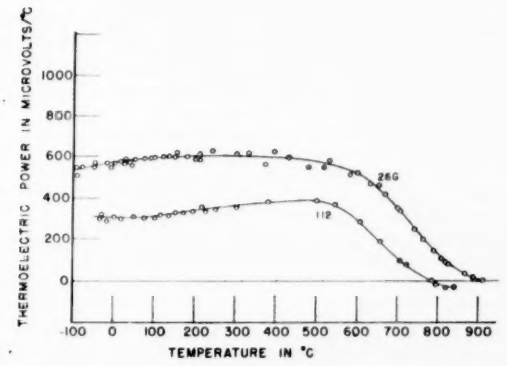

FIG. 12. Thermoelectric power curves for two silicon samples. Both are p type; sample 26 G was boron-doped and 112 aluminum-doped.

On the basis of the results presented in Figs. 5 through 13, one can draw the following qualitative conclusions about thermoelectric power behavior:

1. The sign of the thermoelectric power in the low temperature range, where conduction is due to impurity-introduced carriers (impurity range), is the sign of the carrier, i.e., p-type samples have positive thermoelectric powers and n-type samples negative thermoelectric power. Thus the signs of the Hall coefficient and the thermoelectric power are the same in the impurity range.

2. In the impurity range the magnitudes of thermoelectric power, resistivity, and Hall coefficient increase together with decreasing impurity content and decrease together with increasing impurity content.

3. The thermoelectric power of an n-type sample remains negative throughout. Beginning at the low temperature end of the curve, thermoelectric power slowly increases in magnitude with rising temperature and passes through an extremum at a temparature lower by about 50°K than the temperature at which

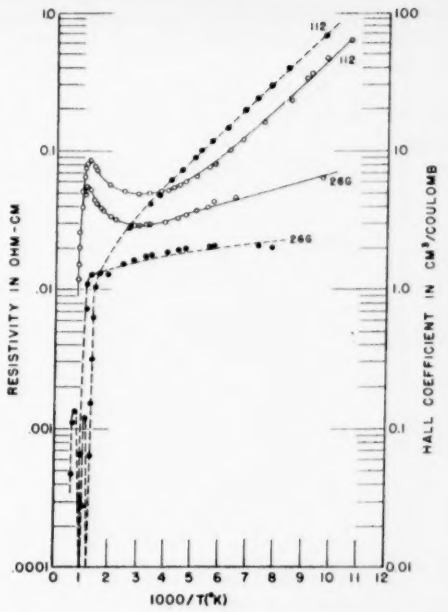

FIG. 13. Resistivity and Hall curves for the two silicon samples for which thermoelectric power curves are given in Fig. 12. (The solid lines are resistivity curves and the broken lines Hall curves.)

the Hall curve of the same sample breaks away from the flat portion characteristic of the exhaustion range. As the temperature continues to rise, the thermoelectric power decreases in magnitude and eventually approaches a curve common to all samples because it is determined by the properties of the intrinsic semiconductor. The magnitude of the extremum thermoelectric power value is roughly proportional to the logarithm of the Hall coefficient in the impurity range, when one compares various n-type germanium samples with one another.

4. Beginning at the low temperature end for a p-type sample, the thermoelectric power is positive and rises slowly to a maximum as the temperature becomes comparable with the temperature at which the Hall curve leaves the exhaustion range. Then, with rising temperature, the thermoelectric power decreases rapidly and, like the Hall coefficient of a p-type sample, changes sign from + to − because of the thermal release of intrinsic electrons and holes and the fact that electron mobility exceeds hole mobility. The thermoelectric power passes through zero at a temperature somewhat above that at which the Hall coefficient becomes zero for the same sample. Then the thermoelectric power passes through a minimum at a temperature considerably higher (by 50° to 150°) than the temperature of the minimum in the Hall curve. Finally, if the temperature range is extended far enough, the thermoelectric power approaches the common curve characteristic of intrinsic germanium. In comparing different

p-type samples with one another, one finds the heights of the maxima roughly proportional to the logarithms of the Hall coefficients in the impurity range and the depths of the minima roughly proportional to the logarithms of the Hall coefficients at the negative maxima.

The authors wish to thank K. Lark-Horovitz for suggesting this problem and for his continued interest and encouragement during the course of this investigation. They also wish to thank E. P. Miller and I. Walerstein for the use of their preliminary results and equipment and V. A. Johnson for helpful discussions during the progress of the work and for assistance in preparing this material for publication.

PHYSICAL REVIEW VOLUME 92, NUMBER 2 OCTOBER 15, 1953

Theory of Thermoelectric Power in Semiconductors with Applications to Germanium*

V. A. JOHNSON AND K. LARK-HOROVITZ
Department of Physics, Purdue University, Lafayette, Indiana

(Received July 13, 1953)

The thermoelectric power Q of a semiconductor is found by calculating the Thomson coefficient σ_T from electrical and thermal current density expressions and then integrating the relation $\sigma_T = T\,dQ/dT$. This procedure yields a general expression for Q in terms of the Fermi level, forbidden band width, temperature, ratio of electron to hole mobility, and effective electron and hole masses. In the impurity range the general formula for Q reduces to a simple dependence on the Hall coefficient and temperature if carrier scattering is largely due to the lattice of the semiconductor; the same expression may be used with the addition of a correction term when carrier scattering by impurity ions becomes important at the lower temperatures. When both holes and electrons must be considered as carriers, Q can be evaluated at any temperature from the resistivity and Hall coefficient at that temperature. An expression is also obtained for the thermoelectric power of an intrinsic semiconductor in a form depending on the mobility ratio, forbidden band width at 0°K, and the temperature rate of change of this band width. Hall and resistivity data measured for six polycrystalline germanium samples and two silicon samples have been inserted into the theoretical expressions derived in this paper. The thermoelectric power curves so calculated are found to give generally good agreement with the measured curves.

I. INTRODUCTION

LARK-HOROVITZ, Middleton, Miller, Scanlon, and Walerstein[1,2] have measured the thermoelectric power curves of a number of aluminum-doped and antimony-doped polycrystalline germanium samples, with carrier densities ranging from 10^{15} per cm^3 to 7×10^{18} per cm^3. The resistivity and Hall coefficient, as well as thermoelectric power, were measured over a temperature range as wide as 78°K to 925°K for some samples.[2] The calculations described in this paper were carried out in an attempt to explain the behavior of the thermoelectric power of a semiconducting sample on the basis of its Hall curve and resistivity.

Early theoretical work on the behavior of semiconductors contains references to thermoelectric power.[3–5] However, the results of these authors are not given in form suitable for comparison with experiment or for prediction of thermoelectric power behavior from measured Hall and resistivity data.

For use in comparison with experiment, a theoretical thermoelectric power expression must be adaptable for application in the impurity, transition, and intrinsic ranges. In the impurity range of temperatures the numbers of intrinsic electrons and holes due to thermal excitation of electrons from the filled band to the conduction band are negligible compared to the number of conduction electrons excited from impurity donor levels (n type) or the number of holes formed by ionization of acceptor levels (p type). Thus, one need consider, in the impurity range, only one sign of carriers. Many samples show "exhaustion" in the impurity range, i.e., all of the donors or acceptors become ionized and the number of carriers per cm^3 remains effectively constant with temperature rise until intrinsic conduction becomes important. Low resistivity samples may show "degeneracy" at low temperatures,[6] hence a general theory of the thermoelectric power of semiconductors must provide for the use of Fermi-Dirac statistics where appropriate.

"Transition range" is a suitable term to apply to those temperatures at which one must consider both

* This work was assisted first by a National Defense Research Committee contract with the Purdue Research Foundation and later by a Signal Corps Contract, and was reported in part to American Physical Society meetings at New York in January, 1946 and at Durham, North Carolina in March, 1953.

[1] Lark-Horovitz, Middleton, Miller, Scanlon, and Walerstein, Phys. Rev. **69**, 259 (1946).

[2] A. E. Middleton and W. W. Scanlon, preceding article [Phys. Rev. **92**, 219 (1953)].

[3] M. Bronstein, Physik. Z. Sowjetunion **2**, 28 (1932).

[4] R. H. Fowler, Proc. Roy. Soc. (London) **A140**, 505 (1933).

[5] A. H. Wilson, *Theory of Metals* (Cambridge University Press, Cambridge, England, 1936), p. 181.

[6] V. A. Johnson and K. Lark-Horovitz, Phys. Rev. **71**, 374, 909 (1947).

the intrinsic carriers and the carriers released from impurity levels. In this range one allows for the presence of carriers of both signs, but one cannot take the electron density to be equal to the hole density. The term "intrinsic range" is reserved for those temperatures at which the intrinsic electrons and holes completely swamp the carriers from impurity levels. Under this condition the electron density equals the hole density.

The general thermoelectric power expression, which is now obtained, can be put into special forms applicable to the various temperature ranges. These results are then used to calculate thermoelectric power curves to be compared with measured values.

II. GENERAL EXPRESSION FOR THE THERMOELECTRIC POWER

The thermoelectric power is found by obtaining the Thomson coefficient from the thermal and electrical current densities and then integrating the appropriate Thomson relation.[7] When both holes and electrons are present, the electrical (j_x) and thermal (w_x) current densities may be written:

$$j_x=\frac{4\pi e}{3}\int_0^\infty v_1{}^3 l_1\left(\frac{\partial f_1{}^0}{\partial x}-eE_x\frac{\partial f_1{}^0}{\partial \epsilon_1}\right)dv_1 - \frac{4\pi e}{3}\int_0^\infty v_2{}^3 l_2\left(\frac{\partial f_2{}^0}{\partial x}+eE_x\frac{\partial f_2{}^0}{\partial \epsilon_2}\right)dv_2, \quad (1)$$

and

$$w_x=-\frac{4\pi m_1}{6}\int_0^\infty v_1{}^5 l_1\left(\frac{\partial f_1{}^0}{\partial x}-eE_x\frac{\partial f_1{}^0}{\partial \epsilon_1}\right)dv_1 - \frac{4\pi m_2}{6}\int_0^\infty v_2{}^5 l_2\left(\frac{\partial f_2{}^0}{\partial x}+eE_x\frac{\partial f_2{}^0}{\partial \epsilon_2}\right)dv_2, \quad (2)$$

where subscript 1 refers to electrons and subscript 2 to holes. Furthermore, no magnetic field is applied, the electric field intensity and temperature gradient possess only X components, l denotes mean free path, f^0 the unperturbed distribution function, v the carrier velocity, ϵ the carrier kinetic energy ($mv^2/2$), and m the effective mass.

The unperturbed distribution functions are

$$f_1{}^0=2m_1{}^3h^{-3}\left\{1+\exp\left(\frac{\epsilon_1-\zeta_1}{kT}\right)\right\}^{-1}, \quad (3a)$$

and

$$f_2{}^0=2m_2{}^3h^{-3}\left\{1+\exp\left(\frac{\epsilon_2-\zeta_2}{kT}\right)\right\}^{-1}, \quad (3b)$$

where ζ_1 and ζ_2 are the "partial" Fermi levels. The quantities ϵ_1 and ζ_1 are zero at the bottom of the conduction band and have positive values in the conduction band, negative in the forbidden band. The zeros of ϵ_2 and ζ_2 are at the top of the filled band with positive values in the filled band, negative in the forbidden band. The condition for thermal equilibrium requires that the partial Fermi levels be related to ζ, the Fermi level of the sample, by

$$\zeta_1=\zeta \quad \text{and} \quad \zeta_2=-E_G-\zeta, \quad (4)$$

where E_G is the width of the forbidden band.

The integrals in Eqs. (1) and (2) are simplified by use of the relations

$$\frac{\partial f_1{}^0}{\partial x}=-\frac{\partial f_1{}^0}{\partial \epsilon_1}\frac{dT}{dx}\left\{\frac{\epsilon_1}{T}+T\frac{d}{dT}\left(\frac{\zeta}{T}\right)\right\} \quad (5a)$$

and

$$\frac{\partial f_2{}^0}{\partial x}=-\frac{\partial f_2{}^0}{\partial \epsilon_2}\frac{dT}{dx}\left\{\frac{\epsilon_2}{T}-T\frac{d}{dT}\left(\frac{E_G+\zeta}{T}\right)\right\}. \quad (5b)$$

Now Eqs. (1) and (2) may be rewritten as

$$j_x=-\frac{8\pi e}{3m_1{}^2}\left[\left\{eE_x+T\frac{d}{dT}\left(\frac{\zeta}{T}\right)\frac{dT}{dx}\right\}L_1(1) + \frac{1}{T}\frac{dT}{dx}L_2(1)\right]+\frac{8\pi e}{3m_2{}^2}\left[\left\{-eE_x - T\frac{d}{dT}\left(\frac{E_G+\zeta}{T}\right)\frac{dT}{dx}\right\}L_1(2)+\frac{1}{T}\frac{dT}{dx}L_2(2)\right] \quad (6)$$

and

$$w_x=\frac{8\pi}{3m_1{}^2}\left[\left\{eE_x+T\frac{d}{dT}\left(\frac{\zeta}{T}\right)\frac{dT}{dx}\right\}L_2(1) + \frac{1}{T}\frac{dT}{dx}L_3(1)\right]+\frac{8\pi}{3m_2{}^2}\left[\left\{-eE_x - T\frac{d}{dT}\left(\frac{E_G+\zeta}{T}\right)\frac{dT}{dx}\right\}L_2(2)+\frac{1}{T}\frac{dT}{dx}L_3(2)\right], \quad (7)$$

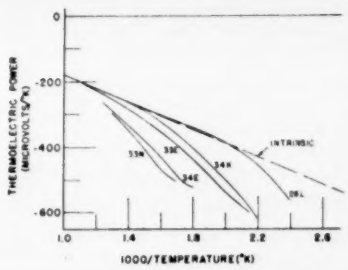

FIG. 1. Thermoelectric power as a function of reciprocal temperature for five n-type, antimony-doped polycrystalline germanium samples. The dashed line is drawn in to approximate the common line approached by all samples as they become intrinsic. The number of conduction electrons per cm³ at exhaustion is 3.3×10^{16} for $26L$, 7.7×10^{16} for $34K$, 1.1×10^{17} for $33E$, 6.2×10^{17} for $34E$, and 8.2×10^{17} for $33N$. The three purer samples become intrinsic within the range of investigation and so empirically determine the curve for intrinsic germanium as

$$Q=-86.3(2430°/T-0.34) \text{ microvolts/°K}.$$

[7] See, e.g., F. Seitz, *The Modern Theory of Solids* (McGraw-Hill Book Company, Inc., New York, 1940), p. 174.

TABLE I. Values of electron mobility to hole mobility ratio (c) and temperature variation of forbidden band width (a) found from the measured thermoelectric power curve of intrinsic germanium.

E_0(ev)	$c=\mu_1/\mu_2$	a(ev/°K)
0.70	3.98	-4.43×10^{-4}
0.72	3.80	-4.45×10^{-4}
0.74	3.62	-4.48×10^{-4}
0.76	3.47	-4.52×10^{-4}

where

$$L_j(1)=\int^{\infty}\epsilon^j l_1\frac{\partial f_1^0}{\partial\epsilon}d\epsilon \tag{8}$$

and $L_j(2)$ is the corresponding integral containing l_2 and f_2^0.

These current density equations are used to find the Thomson coefficient σ_T from the expression for the rate of heat development per unit volume:[7]

$$dH/dt=E_x j_x-\partial w_x/\partial x$$

$$=\rho j_x^2-\sigma_T j_x\frac{dT}{dx}+\frac{d}{dx}\left(\kappa_{el}\frac{dT}{dx}\right), \tag{9}$$

where ρ is the electrical resistivity and κ_{el} the portion of the thermal conductivity due to electron transport. The development of dH/dt yields the result

$$\sigma_T=-\frac{T}{e}\frac{d}{dT}\left(\frac{1}{T}\frac{g_1}{g_2}\right)+\frac{T}{e}\left(\frac{g_3}{g_2}\right), \tag{10}$$

where the functions g_1, g_2, and g_3 are defined by

$$g_1=L_2(1)/m_1^2-L_2(2)/m_2^2,$$
$$g_2=L_1(1)/m_1^2+L_1(2)/m_2^2,$$

and

$$g_3=\frac{L_1(1)}{m_1^2}\frac{d}{dT}\left(\frac{\zeta}{T}\right)+\frac{L_1(2)}{m_2^2}\frac{d}{dT}\left(\frac{E_G+\zeta}{T}\right).$$

One of the Thomson relations states that, if Q is the thermoelectric power in a semiconductor-metal circuit with junctions at temperatures T and $T+dT$, the product $T\,dQ/dT$ equals the difference between the Thomson coefficients of the semiconductor and metal. In this derivation, the Thomson coefficient of the metal is taken as zero, and so

$$\sigma_T=T\,dQ/dT \tag{11}$$

is the equation for determining thermoelectric power. Although the following thermoelectric power values are thus found for the semiconductor relative to a metal of zero Thomson coefficient, the values are approximately applicable relative to any metal because metals have σ_T values very much smaller than those of most semiconducting samples. The sign of Eq. (11) is consistent with the convention that the thermoelectric power is positive if conventional current flows from the semiconductor to the reference metal at the cold junction.

III. THE INTRINSIC RANGE

At temperatures high enough that the effects of impurity atoms may be neglected and only intrinsic carriers considered, one can assume that:

(A) Classical statistics apply and the distribution functions of Eqs. (3a) and (3b) may be replaced by

$$f_1^0=2m_1^3h^{-3}\exp\{(-\epsilon_1+\zeta)/kT\}, \tag{12a}$$

$$f_2^0=2m_2^3h^{-3}\exp\{(-\epsilon_2-E_G-\zeta)/kT\}. \tag{12b}$$

(B) The only important scattering of carriers is due to the lattice,[8] and hence the mean free paths l_1 and l_2 are independent of the energies ϵ_1 and ϵ_2.

(C) The conduction electron and hole densities are equal, i.e., $n_1=n_2$. Thence,

$$\zeta=-\tfrac{1}{2}E_G-\tfrac{3}{4}kT\ln(m_1/m_2). \tag{13}$$

Assumptions A and B lead to the following values for the integrals appearing in Eq. (10):

$$\begin{aligned}
&L_1(1)=-2l_1m_1^3h^{-3}kT\exp(\zeta/kT);\\
&L_1(2)=-2l_2m_2^3h^{-3}kT\exp\{-(E_G+\zeta)/kT\};\\
&L_2(1)=-4l_1m_1^3h^{-3}(kT)^2\exp(\zeta/kT);\\
&L_2(2)=-4l_2m_2^3h^{-3}(kT)^2\exp\{-(E_G+\zeta)/kT\}.
\end{aligned} \tag{14}$$

Also, when assumptions A and B are valid, the mean free paths can be expressed in terms of the electron and hole mobilities, μ_1 and μ_2, respectively:

$$l_{1,2}=\tfrac{3}{4}\mu_{1,2}(2\pi m_{1,2}kT)^{\frac{1}{2}}/e. \tag{15}$$

Insertion of expressions (14) and (15) into Eq. (10) and simplification yields a Thomson coefficient expression valid at high temperatures:[9]

$$\sigma_T=-\frac{T}{e}\frac{d}{dT}(2k\tanh z)$$
$$+\frac{T}{e}\left\{-\frac{1}{2}\tanh z\frac{d}{dT}\left(\frac{E_G}{T}\right)+k\frac{dz}{dT}\right\}, \tag{16}$$

where z is defined by

$$z=\frac{\zeta}{kT}+\frac{E_G}{2kT}+\frac{1}{2}\ln\left(\frac{cm_1^{\frac{3}{2}}}{m_2^{\frac{3}{2}}}\right), \tag{17}$$

in which c denotes the mobility ratio μ_1/μ_2.

[8] A. Sommerfeld and H. Bethe, *Handbuch der Physik* (Verlag. Julius Springer, Berlin, Germany, 1933), Vol. 24, No. 2, pp. 509–521, 558–560.

[9] A similar expression is given in a discussion of the thermoelectric power of tellurium samples by T. Fukuroi and S. Tanuma, Science Repts. Research Insts., Tôhoku Univ., 4, 353 (1952).

For an intrinsic semiconductor, one introduces Eq. (13) into Eq. (17) to obtain $z=\frac{1}{2}\ln c$ and thence

$$\sigma_T=-\frac{T}{e}\frac{d}{dT}\left\{\frac{2k(c-1)}{c+1}\right\}+\frac{T}{e}\frac{k(c-1)}{(c+1)}\frac{d}{dT}\left(\frac{-E_G}{2kT}\right). \quad (18)$$

Now Eq. (11) may be readily integrated to yield for the thermoelectric power

$$Q=-\frac{k(c-1)}{e(c+1)}\left(\frac{E_G}{2kT}+2\right). \quad (19)$$

Both experimental and theoretical considerations[10–14] indicate that E_G varies with temperature in an approximately linear manner:

$$E_G=E_0+aT. \quad (20)$$

Thence Eq. (19) becomes

$$Q=-\frac{k}{e}\frac{(c-1)}{(c+1)}\left(\frac{E_0}{2kT}+2+\frac{a}{2k}\right). \quad (21)$$

This predicts that a plot of Q as a function of the reciprocal of the temperature, in the intrinsic range, should be a straight line with parameters determined by E_0, a and c. Figure 1 shows a plot of Q *vs* $1/T$, at high temperatures, for several of the n-type germanium samples investigated by Middleton and Scanlon.[2] The approach of these curves to a common straight line may be seen; the empirical equation of this line is

$$Q=-\frac{k}{e}\left(\frac{2430^\circ}{T}-0.34\right). \quad (22)$$

One can determine a and c for germanium by comparing Eqs. (21) and (22) and inserting an experimentally determined value[1,12,13,15] of E_0. The results are shown in Table I.

The value of a obtained in this manner is in good agreement with the value obtained for germanium from optical data,[12] but higher than the value found from other data.[11–13] The c values of Table I are much larger than values found by methods[16–18] which employ data taken at lower temperatures (usually 300°K) and which give c between 1.5 and 2.1. Such a temperature difference in c values is to be anticipated if the electron mobility follows the expected $T^{-1.5}$ law[8] while the hole mobility varies with temperature about as $T^{-2.2}$, as has been indicated by recent experiments.[18,19]

[10] J. Bardeen, Phys. Rev. **75**, 1777 (1949).
[11] W. Shockley and J. Bardeen, Phys. Rev. **77**, 407 (1950).
[12] H. Y. Fan, Phys. Rev. **78**, 808 (1950).
[13] V. A. Johnson and H. Y. Fan, Phys. Rev. **79**, 899 (1950).
[14] T. S. Moss, Phys. Rev. **79**, 1011 (1950).
[15] J. R. Haynes and H. B. Briggs, Phys. Rev. **86**, 647 (1952).
[16] G. L. Pearson, Phys. Rev. **76**, 179 (1949).
[17] L. P. Hunter, Phys. Rev. **91**, 207 (1953).
[18] M. B. Prince, Phys. Rev. **91**, 208 (1953).
[19] W. C. Dunlap, Phys. Rev. **79**, 286 (1950).

IV. THE TRANSITION RANGE

In the transition range, both holes and electrons are present as carriers, but the carriers released by impurities are comparable with those due to intrinsic conduction; thus one cannot take n_1 equal to n_2. However, the temperature is high enough that assumptions A and B and, hence, Eq. (16) are still valid. When Eq. (16) is inserted into Eq. (11) and the integration performed, one obtains

$$Q=-\frac{2k}{e}\tanh z+\frac{k}{e}z-\frac{k}{e}\int\tanh z\frac{d}{dT}\left(\frac{E_G}{2kT}\right)dT$$

$$\approx-\frac{2k}{e}\tanh z+\frac{1}{eT}\left(\zeta+\frac{E_G}{2}\right)-\frac{E_G}{2eT}\tanh z. \quad (23)$$

The approximation made in evaluating the integral above is that of taking $\tanh z$ as a slowly varying function of T in comparison with $(d/dt)(E_G/2kT)$. The error from this approximation vanishes at the low temperature end of the transition range, but increases to $\frac{3}{4}(k/e)\ln(m_2/m_1)$ as the sample becomes intrinsic. The measurements of Benedict and Shockley[20] indicate that m_2/m_1 is probably less than 1.6 for germanium. Hence the maximum difference between the exact and approximate forms of Eq. (23) is probably less than 30 microvolts/°C.

Equations (12a) and (12b) can be used to convert Eq. (23) into an expression for calculating the thermoelectric power from the electron and hole densities:

$$Q=-\frac{k}{e(n_1c+n_2)}\left[2(n_1c-n_2)-n_1c\ln\left\{\frac{n_1h^3}{2(2\pi m_1kT)^{\frac{3}{2}}}\right\}\right.$$

$$\left.+n_2\ln\left\{\frac{n_2h^3}{2(2\pi m_2kT)^{\frac{3}{2}}}\right\}\right]. \quad (24)$$

The comparison of measured thermoelectric power with values calculated from Eq. (24) is discussed in Sec. 6.

TABLE II. Dependence of the Hall coefficient factor r, defined as $ne|R|$, and thermoelectric power upon relative proportions of lattice and impurity scattering.

$\frac{\rho_I}{\rho_I+\rho_L}$	$\frac{\rho_I}{\rho_L}$	r	$q=\frac{L_2}{kTL_1}$
0.0	0	1.1781	2.000
0.1	1/9	1.0289	2.379
0.2	1/4	1.0411	2.558
0.3	3/7	1.0650	2.698
0.4	2/3	1.0962	2.809
0.5	1	1.1348	2.947
0.6	3/2	1.1833	3.065
0.7	7/3	1.2475	3.199
0.8	4	1.3399	3.380
0.9	9	1.4963	3.639
1.0	∞	1.9328	4.000

[20] T. S. Benedict and W. Shockley, Phys. Rev. **91**, 207 (1953).

V. THE IMPURITY RANGE

At the lower temperatures the number of intrinsic carriers is negligible compared to the number of carriers released by impurities. When the terms pertaining to hole conduction are dropped from Eq. (10), one obtains

$$\sigma_T(n\text{-type})=-\frac{T}{e}\frac{d}{dT}\left\{\frac{1}{T}\frac{L_2(1)}{L_1(1)}\right\}+\frac{T}{e}\frac{d}{dT}\left(\frac{\zeta}{T}\right), \quad (25a)$$

and dropping out the electron-conduction terms in Eq. (10) leaves:

$$\sigma_T(p\text{-type})=\frac{T}{e}\frac{d}{dT}\left\{\frac{1}{T}\frac{L_2(2)}{L_1(2)}\right\}+\frac{T}{e}\frac{d}{dT}\left(\frac{E_G+\zeta}{T}\right). \quad (25b)$$

Equation (11) may be integrated to yield the results,

$$Q(n\text{-type})=-\frac{1}{eT}\frac{L_2(1)}{L_1(1)}+\frac{\zeta}{eT}, \quad (26a)$$

and

$$Q(p\text{-type})=\frac{1}{eT}\frac{L_2(2)}{L_1(2)}+\frac{E_G+\zeta}{eT}. \quad (26b)$$

For most germanium, silicon, and tellurium samples, the carriers obey classical statistics above liquid air temperature. In this case the distribution functions are given by Eqs. (12a) and (12b), and the Fermi level may be related to the carrier density by the equation:

$$\zeta=kT\ln\left\{\frac{n_1h^3}{2(2\pi m_1kT)^{\frac{3}{2}}}\right\}. \quad (27)$$

If most of the carrier scattering is due to the lattice, the mean free path is independent of the carrier kinetic energy, and Eqs. (14) and (27) may be used to obtain

$$L_2(1)/L_1(1)=L_2(2)/L_1(2)=2kT. \quad (28)$$

Inserting this result into Eqs. (26a) and (26b) produces the expression:

$$Q=\pm\frac{k}{e}\left[2-\ln\left\{\frac{n_{1,2}h^3}{2(2\pi m_{1,2}kT)^{\frac{3}{2}}}\right\}\right], \quad (29)$$

where the sign of Q is the sign of the carrier. Equation (24), when either n_1 or n_2 is set equal to zero, reduces to Eq. (29).

Under the conditions assumed in deriving Eq. (29), the carrier density is related to the Hall coefficient of the sample, R, by the relation:[21]

$$n=3\pi/(8e|R|), \quad (30)$$

where R is measured in cm³/coulomb, e in coulomb, and n per cm³. When Eq. (30) is substituted into Eq. (29) along with the values of the various quantities, including the free electron mass for $m_{1,2}$, a simple thermoelectric power expression is obtained:

$$Q=\pm(k/e)[\ln(|R|T^{\frac{3}{2}})-5.32]. \quad (31)$$

When this expression is valid, the thermoelectric power as a function of temperature may be found from a measured Hall curve which gives R as a function of T; and, conversely, measurement of the thermoelectric power curve gives an approximate determination of the Hall curve and carrier density curve of the same sample.

The assumption of predominant lattice scattering is best satisfied for relatively high purity samples at the higher temperature end of the impurity range. It has been found, especially in germanium, that, with decreasing temperature and increasing impurity content, a substantial portion of the carrier scattering is caused by the randomly distributed impurity ions.[22,23] An approximate correction for the effect of impurity scattering upon the thermoelectric power is based upon the result of Conwell and Weisskopf[22] that the mean free path due to impurity scattering is about proportional to the square of the kinetic energy, whereas Sommerfeld and Bethe[8] have found the mean free path due to lattice scattering (l_L) to be independent of energy. When both kinds of scattering are present, the mean free path l is given by

$$1/l=1/l_L+1/l_I. \quad (32)$$

If $l_I=a\epsilon^2$, the energy dependence of l is given by

$$l=\frac{al_L\epsilon^2}{l_L+a\epsilon^2}. \quad (33)$$

This expression enters into the determination of the Hall coefficient so that Eq. (30) should be replaced by

$$n=r/e|R|, \quad (34)$$

where r depends[24,25] on the ratio a/l_L (or ρ_L/ρ_I) in the manner given in Table II.[26]

The quantity $q=L_2(1)/\{kTL_1(1)\}=L_2(2)/\{kTL_1(2)\}$ also depends upon the relative amounts of lattice and impurity scattering in a manner found by inserting Eq. (33) into Eq. (8); the results of this computation are also given in Table II. When the corrections due to impurity scattering are considered and allowance is made for the difference between free electron mass m_0 effective mass, Eq. (31) is replaced by

$$Q=\pm(k/e)[\ln(|R|T^{\frac{3}{2}})-\ln r-7.16+q+\tfrac{3}{2}\ln(m_{1,2}/m_0)]. \quad (35)$$

[21] R. Gans, Ann. Physik **20**, 293 (1906).

[22] E. Conwell and V. F. Weisskopf, Phys. Rev. **69**, 258 (1946); **77**, 388 (1950).

[23] K. Lark-Horovitz and V. A. Johnson, Phys. Rev. **69**, 258 (1946).

[24] H. Jones, Phys. Rev. **81**, 149 (1951).

[25] V. A. Johnson and K. Lark-Horovitz, Phys. Rev. **82**, 977 (1951).

[26] A later paper will describe corrections required in resistivity, thermoelectric power, and Hall effect by the deviation of l_I from a simple ϵ^2 energy dependence.

Since modifications due to using Fermi-Dirac statistics in place of Boltzmann statistics are usually not important above liquid air temperature, thermoelectric power is degenerate semiconductors is not discussed here but will be presented in a later paper.

VI. COMPARISON WITH EXPERIMENT

The theoretical expressions developed in the preceding sections have been compared with the thermoelectric power curves measured by Middleton and Scanlon.[2]

The thermoelectric power curves in the impurity range are calculated by applying Eq. (31), or Eq. (35)

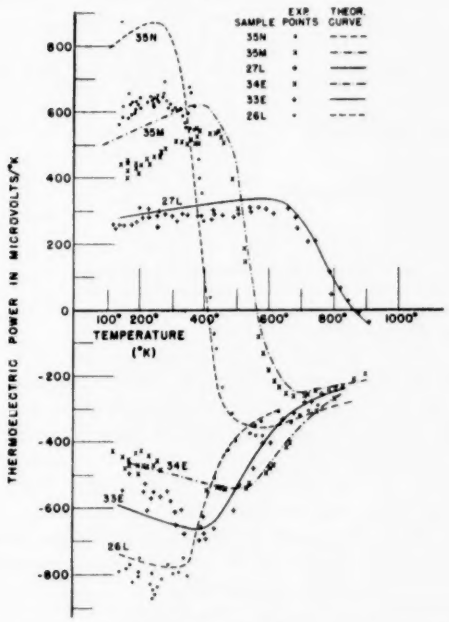

FIG. 2. Comparison of calculated and measured thermoelectric power curves for polycrystalline germanium samples. The smooth curves are calculated, and experimental points are indicated by dots and crosses. The number of holes per cm³ at exhaustion is 5.7×10^{15} for $35N$, 1.7×10^{17} for $35M$, and 7.2×10^{18} for $27L$; the number of electrons per cm³ at exhaustion is 3.3×10^{15} for $26L$, 1.1×10^{17} for $33E$, and 6.2×10^{17} for $34E$.

where required, to the measured Hall curves of the samples.[2] Equation (35) is used for quite impure samples at relatively low temperatures; m_1 and m_2 are taken equal to m_0, but proper values of r and q are inserted on the basis of analysis[27] of the resistivity curves of the samples.

The theoretical curves in the transition range are computed by putting into Eq. (24) values obtained

[27] K. Lark-Horovitz, National Defense Research Committee Report 14-585, pp. 36, Nov. 1945 (unpublished); K. Lark-Horovitz and V. A. Johnson, Phys. Rev. **69**, 258 (1946); K. Lark-Horovitz, Elec. Eng. **68**, 1047 (1949); H. C. Torrey and C. A. Whitmer, *Crystal Rectifiers* (McGraw-Hill Book Company, Inc., New York, 1948), pp. 58–61 and Figs. 3–7.

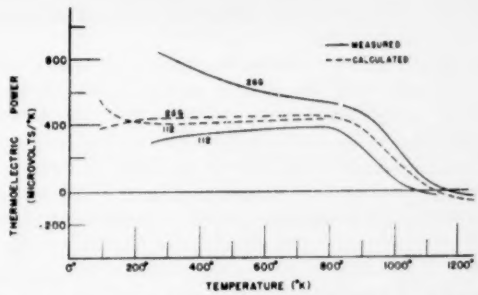

FIG. 3. Comparison of calculated and measured thermoelectric power curves for two p-type silicon samples, aluminum-doped 112 and boron-doped $26G$.

from measured Hall and resistivity curves.[2] The carrier densities n_1 and n_2 are found, for a given temperature, from the values of R and σ (electrical conductivity) at that temperature by using the equations:

$$R=-\frac{3\pi}{8e}\frac{n_1c^2-n_2}{(n_1c+n_2)^2}, \tag{36}$$

$$\sigma=n_1e\mu_1+n_2e\mu_2=1/\rho, \tag{37}$$

and

$$n_2-n_1=\pm N, \tag{38}$$

where N is the number of carriers per cm³ in the exhaustion range (the + sign applies to p-type samples, the − sign to n type). Algebraic elimination of n_1 and n_2 yields expressions for the mobility ratio c:

$$(n\text{-type})\quad 1-\frac{1}{c}=-\left\{\frac{8R}{3\pi e}\left(\frac{\sigma}{\mu_1}\right)^2+N\right\}\left(\frac{\sigma}{\mu_1 e}-N\right)^{-1}, \tag{39a}$$

and

$$(p\text{-type})\quad c-1=\left\{N-\frac{8R}{3\pi e}\left(\frac{\sigma}{\mu_2}\right)^2\right\}\left(\frac{\sigma}{\mu_2 e}-N\right)^{-1}. \tag{39b}$$

Only lattice scattering is important in the transition range, and so the electron mobility as a function of temperature[8] is given by

$$\mu_1=BT^{-\frac{3}{2}}, \tag{40}$$

where B is about 1.8×10^7 °K$^{\frac{3}{2}}$ cm²/volt-sec for electrons in single crystal germanium and less for the polycrystalline samples investigated by Middleton and Scanlon. For these polycrystalline samples mobility was extrapolated, following Eq. (40), from values at the high temperature end of the impurity range. The extrapolated mobility and measured R and σ at a chosen T are put into Eq. (39a) or (39b) to determine c at that temperature for the chosen sample. This process yielded c values for germanium, at temperatures in the 600°-900°K range, that averaged to about 3.0. No systematic variation of c with temperature or impurity content was observed. When c has been found, n_1 and n_2 may be evaluated from Eqs. (37) and (38), thus completing

the data required for evaluation of thermoelectric power from Eq. (24).

Figure 2 shows a comparison between the measured and calculated thermoelectirc power curves for three n-type, antimony-doped polycrystalline germanium samples and three p-type, aluminum-doped polycrystalline germanium samples. It is apparent that consistently good agreement exists in the transition range, where there is little scatter of the experimental points, and also quite good agreement in the impurity range in view of the rather wide scatter of the experimental points at these lower temperatures.

Figure 3 shows a similar comparison between theory and experiment for two polycrystalline silicon samples, both p type, one (26G) boron-doped and the other (112) aluminum-doped. While there is a fair degree of agreement between theory and experiment, it is not as good as for the germanium samples, perhaps because all measurements on silicon were more difficult than on germanium because pressure contacts were used instead of soldered ones.

The authors wish to thank A. E. Middleton, W. W. Scanlon, E. P. Miller, and I. Walterstein for their courtesy and cooperation in making available all of their experimental results continuously throughout the progress of this investigation.

PHYSICAL REVIEW VOLUME 92, NUMBER 2 OCTOBER 15, 1953

Luminescence Studies of KI-TlI

BERNARD SMALLER AND EUGENE AVERY
Chemistry Division, Argonne National Laboratory, Lemont, Illinois
(Received May 4, 1953)

The characteristics of the electron traps present in the KI-TlI phosphor have been investigated. Determination of trapping depth and frequency factor yields evidence for representation as a reaction rate process with a division into two distinct trapping systems, while absorption and emission studies indicate a common excited state. Evaluation of concentration and cross section of traps substantiates the above hypothesis.

A. INTRODUCTION

CRYSTALS composed of alkali-halides with small percentages of added thallium-halide have been studied extensively as model impurity-activated phosphors. The original work of Pohl's school[1] and Bünger[2] has been supplemented more recently by that of Garlick[3] and Randall[4] who have also extended studies of the thermoluminescence phenomenon originally investigated by Urbach.[5] The theoretical aspects of the problem, first treated by Seitz,[6] have been advanced quantitatively by Williams.[7] The specific system, potassium iodide-thallium iodide, had been investigated earlier at this laboratory[8] and also by Bonanomi.[9]

A complete analysis of a complex electron-trapping system requires a knowledge of the kinetics involved. For a monomolecular process, the activation energy and frequency factor are required constants for the various trapping levels, as well as the concentration and cross section for trapping under given excitation. Absorption and emission characteristics indicate the processes involved while knowledge of intertrap and nonradiative transitions are necessary to estimate the efficiency of the phosphorescent processes. We have attempted in this investigation to extend the preliminary results previously reported and to discuss certain quantitative aspects of a long-lived phosphorescent system hitherto not mentioned.

B. THERMOLUMINESCENCE STUDIES

If a phosphor is irradiated at a temperature T, the phosphorescent intensity I will be determined by the rate of release of trapped electrons, $-(dn/dt)$, and can be described, for a monomolecular process, by

$$I \propto -(dn/dt)=n/\tau, \tag{1}$$

where the decay time τ is given by

$$\tau=s^{-1}\exp(E/kT). \tag{2}$$

E is the activation energy required to raise the electron from trapped to emitting state, and s is defined as the frequency factor. If the irradiation is stopped after n_0 electrons are trapped and the temperature increased at a rate $\beta=dT/dt$, the emission will continue at a rate

$$dn/dt=-sn_0\exp\left[-\int_0^T \frac{s}{\beta}e^{-E/kT}dT\right]e^{-E/kT}. \tag{3}$$

[1] See R. Hilsch, Proc. Phys. Soc. (London) **49** (extra part), 40 (1937).
[2] W. Bünger, Z. Physik **66**, 311 (1930); W. Bünger and W. Z. Flechsig, Z. Physik **67**, 421 (1931) and **69**, 627 (1932).
[3] G. F. J. Garlick and M. H. F. Wilkins, Proc. Roy. Soc. (London) **A185**, 408 (1945).
[4] J. T. Randall and M. H. F. Wilkins, Proc. Roy. Soc. (London) **A184**, 347 (1945).
[5] F. Urbach, Wien. Ber. IIa. **139**, 353, 364, 483 (1930).
[6] F. Seitz, J. Chem. Phys. **6**, 150 (1938).
[7] F. E. Williams, J. Chem. Phys. **19**, 457 (1951).
[8] Smaller, May, and Freedman, Phys. Rev. **79**, 940 (1950).
[9] J. Bonanomi and J. Rossel, Helv. Phys. Acta. **24**, 310 (1951); Physica **18**, 486 (1952).

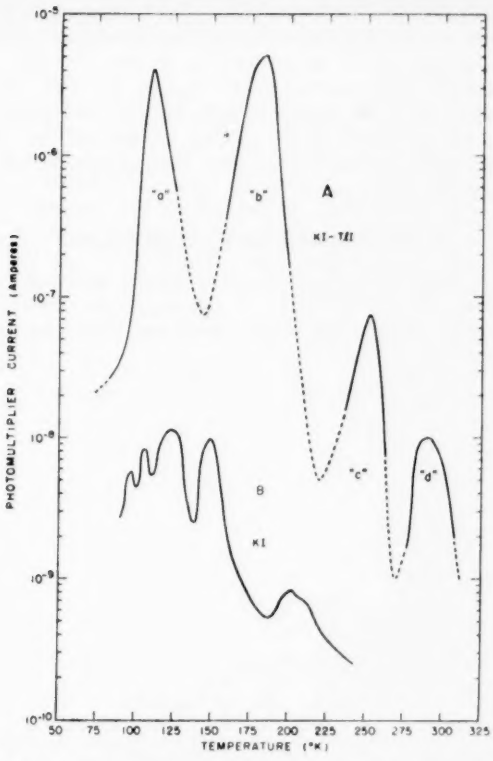

FIG. 1. Glow curves for thallium-activated and pure potassium iodide. A. Glow curve for a crystal containing 0.05 percent of thallium after being subjected to 50-kev x-radiation at 80°K. B. Curve for a control crystal containing less than 3×10^{-7} Tl/K. Heating rate, $\beta=0.22$ deg/sec^{-1}.

The dependence of I on T can be easily seen from the derivative relationship

$$\frac{d\ln I}{d(1/T)}=\frac{s}{\beta}T^2e^{-E/kT}-\frac{E}{k}. \tag{4}$$

Thus, the value of E can be determined from the behavior at low temperature and s then determined from the temperature T_G, where I passes through its maximum.

A representative glow curve for a crystal containing 0.05 percent of thallium (atomic percent of thallium relative to potassium), after being subjected to 50-kev x-radiation at 80°K is shown in Curve *A* of Fig. 1. The identification of the glow peaks with the thallium impurity can be made by comparison with a glow curve from a control crystal containing less than 3×10^{-7} Tl/K (Curve *B*, Fig. 1). The residual thermoluminescence may be presumed to be the result of lattice defects and/or *F* centers formed during irradiation. The heating rate was maintained at 0.22 deg/sec except over the high-temperature peak where an increase in rate was necessary to provide sufficient intensity. The thallium concentration in the crystals was measured by the radioactivity assaying technique[10] which in sensitivity and reliability is superior to spectrographic analysis. Similar results were obtained using the γ-radiation from a 3-millicurie Co^{60} source for the excitation and the single photon counting techniques developed previously for the detection of the luminescence.[8] The photomultiplier used was a cooled RCA 5819 tube. The use of the single photon technique made it possible to test and verify the assumption that saturation effects did not occur.

The absorption and emission spectra of the KI-Tl phosphor have been measured extensively; the correlation of these spectra with the various traps is thus of considerable interest. For these studies ultraviolet light from a monochromator having a 20A band width was used as the exciting agent. The thermoluminescent peaks, "*a*," "*b*," and "*c*," were again reproduced, although the peak intensities for which a saturation condition became evident were much lower than in the experiments using x- or γ-ray excitation. Sensitivity limitations of the recording equipment precluded the verification of Peak "*d*." The spectral dependence of the light-sum (i.e., integrated intensity across the peak) of each trap is shown in Fig. 2. The maximum response at 2310A for all three traps is consistent with the prominent spectral absorption peak at 2330A[11] and thus indicates that the excitation band is a common level for all subsequently trapped electrons. The reverse process, emission following the release of the trapped electrons, was also investigated. With the aid of a Hilger Raman spectrograph and Eastman 103-F emulsion the emission spectra of γ-ray-induced thermoluminescence

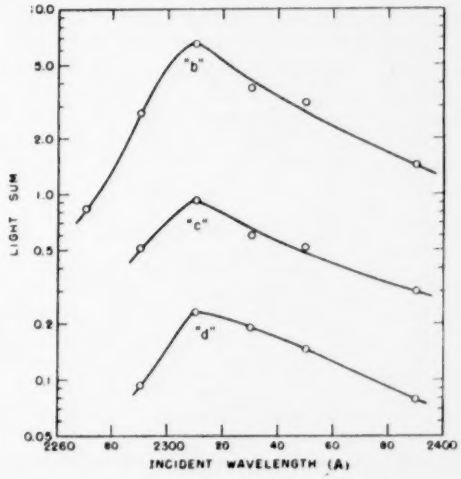

FIG. 2. Glow curve integrated intensity *vs* incident wavelength showing similar dependence of emission of glow peaks "*b*," "*c*," and "*d*" on wavelength of exciting radiation.

[10] Delbecq, Glendenin, and Yuster, Anal. Chem. **25**, 350 (1953).
[11] P. H. Yuster and C. J. Delbecq, Anal. Chem. **25**, 350 (1953).

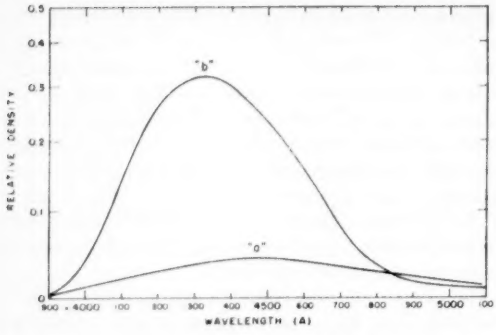

FIG. 3. Densitometer traces of the spectra of glow peaks "*a*" and "*b*" of KI-TlI excited by Co^{60} γ rays.

for the two most prominent peaks "*a*" and "*b*" were observed and are shown in Fig. 3. The other traps, too weak to record photographically, were observed with a pocket spectroscope and showed substantially the same response. The results are in good agreement with those previously reported on the luminescence of KI-TlI following excitation by ultraviolet light by Von Meyeren[12] and x-rays by Chatterjee.[13] The faint band reported at longer wavelengths by the latter may be related to the usual observation of a green-white emission during thermoluminescence too weak to record on the spectrograph. Thus, the evidence indicates that the photon absorption and emission process is identical for all participating electrons and is independent of the character of the trap.

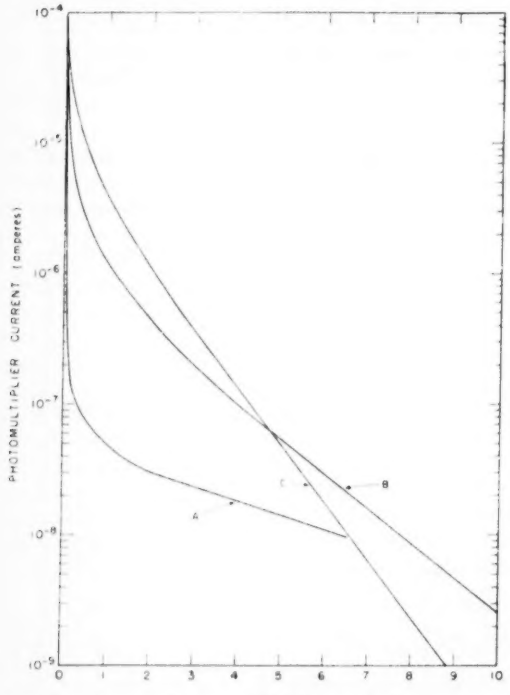

FIG. 4. Phosphorescence decay of KI-TlI for various temperatures.

Curve	T°C	Abscissa scale
A	−16	1 div = 180 min
B	+24	1 div = 300 sec
C	+58	1 div = 2.5 sec.

[12] W. Von Meyeren, Z. Physik **61**, 321 (1930).

C. PHOSPHORESCENT DECAY CURVES

A detailed study of the complete phosphorescence permitted the resolution of the composite electron-trapping system into a short-lived and long-lived set.

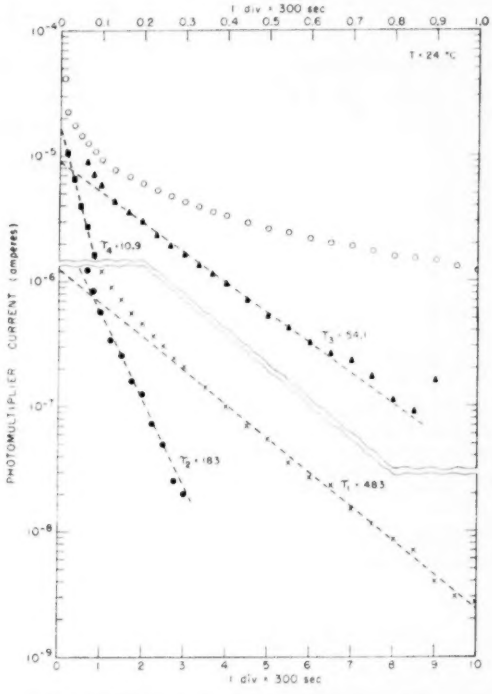

FIG. 5. Resolution of complex decay curve into exponential components.

The long-lived phosphorescence studies were conducted using a 390-curie Co^{60} gamma source as the exciting agent. The KI-TlI crystal, a 10-cc parallelepiped, was secured to the face of a 5819 photomultiplier tube and the excitation source lowered to a position near the opposite face of the crystal. After a given irradiation the source was removed, the photomultiplier high voltage applied and the photocurrent output connected through a direct current amplifier to a recording chart. The entire system was capable of being cooled to −20°C or heated to 100°C. The resultant phosphorescence for typical runs at various temperatures is shown in Fig. 4.

[13] A. Chatterjee, Indian J. Phys. **24**, 331 (1950).

The long stretches of logarithmic response with time indicated that the total response could be resolved into a sum of exponentials. This interpretation as a sum of monomolecular processes involving a set of independent trapping levels, rather than a (diffusion limited) higher order process, was verified by other criteria. A typical resolution into a set of exponentials is shown in Fig. 5 with the indicated decay times τ_i in seconds. From the dependence of the various τ_i's on temperature, as shown in Fig. 6, and using Eq. (2) the activation energy E and frequency factor s were derived. The results are shown in Table I. The traps were arbitrarily

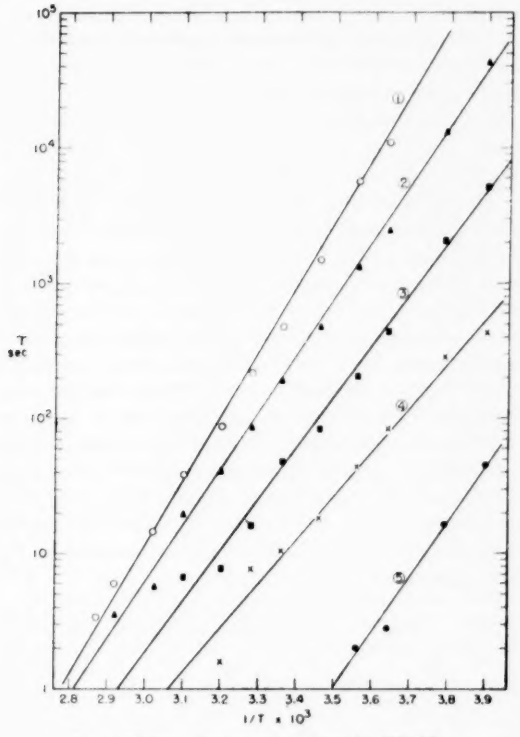

FIG. 6. Decay time *vs* temperature for KI-TII.

designated 1 to 8 in decreasing decay time while the correspondence with the glow peak designation was derived from further evidence to be presented later. The data for the short-lived set were derived from more indirect investigations. Although the E and s can be determined from the glow curve [Eq. (4)], more reliable values can be secured from phosphorescent studies. Thus for Trap No. 6 the values of Bonanomi have been inserted; while for Trap No. 7, where other data are unavailable, the glow curve values have been used. For Trap No. 8, corresponding to the shortest decay time in KI-TII of about 0.2 μsec, the values of E and s shown were determined from direct visual observation of the temperature dependence of pulse

TABLE I. Values of the frequency factor and activation energy derived from the temperature dependence of phosphorescence decay times (Fig. 5) and using Eq. (2), $\tau = s^{-1}e^{E/kT}$.

Set	Trap designation	Glow peak designation	Frequency factor $\log_{10}s$	Activation energy, E (ev)
Long-lived	1	*d*	12.81	0.92
	2	*d*	11.83	0.83
	3	*d*	11.25	0.76
	4	*d*	10.01	0.65
Short-lived	5	*c*	14.40	0.82
	6	*b*	12.41[a]	0.535[a]
	7	*a*	10.30[b]	0.26[b]
	8		7.91	0.065

[a] See reference 9.
[b] From glow curve data using Eq. (4).

decay. Substantiating evidence for the monomolecular nature of the electron-trapping process was revealed by the independence of the decay times on intensity or duration of excitation. Also, a recycling of the radiation showed that the phosphorescent intensity from each trap depended only on its own decay time and transitions between traps did not occur.

The distinction between long-lived and short-lived traps was based on the following empirical evidence. The frequency factor has, for chemical processes, been correlated with the entropy of activation, S. From Eyring's[14] Absolute Rate Theory, the decay time

$$\frac{1}{\tau} = \kappa \frac{kT}{h} \exp[\Delta S/R] \exp[-\Delta H/RT], \qquad (5)$$

where $\kappa \equiv$ transmission coefficient for activation and $\Delta H =$ heat of activation. Assigning a value of unity for κ and assuming, through lack of other evidence, that the zero point energies for metastable and excited states are equal, one can assign an entropy change for each trapping level. Thus for Trap No. 1 the given value of s corresponds to $\Delta S = 0$ while for Traps Nos. 2, 3, and 4, $\Delta S < 0$. Quantitative interpretation of these

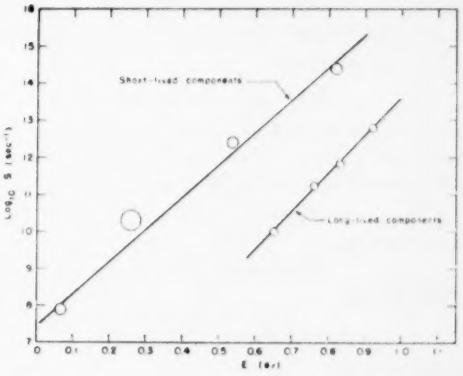

FIG. 7. Showing the separation of the traps of KI-TII into two sets.

[14] F. E. Williams and H. Eyring, J. Chem. Phys. **15**, 289 (1947).

TABLE II. Concentration and cross section of various traps.

Trap number	Cross section $\times 10^{17}$ cm^2	Concentration $\times 10^{-13}$/cc		
		Phosphorescence	Glow data	
			γ ray	x-ray
1	1.8	1.1	$\Sigma = 4.0$	$\Sigma = 2.0$
2	1.7	1.8		
3	2.4	1.5		
4	1.0	1.0		
5	1.4	11.0	11[a]	11.0[a]
6	1.4[a]	114	785	380
7				171

[a] Indicates assumed value.

values must await a more complete theoretical presentation. Also of interest is the dependence of ΔS on the level depth. From Fig. 7 of log$s$ *vs* E there exists for Traps 1 to 4 and for Traps 5 to 8 an empirical linear relation between ΔS and E. On the basis of these data along with the evidence on the trap concentration and cross section one is led to the division of the trapping system into two sets.

D. TRAP CONCENTRATION AND CROSS SECTION

The rate of filling of the ith kind of trap can be expressed in terms of the concentration of filled traps n_i, its cross section σ_i, and the intensity of excitation I_r by

$$dn_i/dt = I_r\sigma_i(N_i - n_i) - (n_i/\tau_i), \tag{4}$$

where N_i is the concentration of empty traps at the onset of irradiation ($t=0$). It is assumed that I_r is sufficiently low to preclude any significant emptying of traps by the exciting flux. After a time t the number of electrons in the traps will be

$$n_i = I_r\sigma_i N_i \tau_i'[1-\exp(-t/\tau_i')], \tag{5}$$

where τ_i', defined by

$$1/\tau_i' \equiv [(1/\tau_i) + I_r\sigma_i], \tag{6}$$

is the excitation-induced time constant. If one neglects nonradiative transitions, upon removal of excitation the traps will empty with a resultant phosphorescence the intensity of which

$$I \equiv -\alpha dn_i/dt = \alpha n_i/\tau_i. \tag{7}$$

The constants N_i and σ_i can be independently determined from a set of two runs. Thus for the extreme cases of duration of excitation given by a $t=t_a \gg \tau_i'$,

$$I_a \equiv -\alpha(dn_i/dt)_{t=t_a}, \tag{8}$$

and a $t=t_b \ll \tau_i'$,

$$I_b \equiv -\alpha(dn_i/dt)_{t=t_b}. \tag{9}$$

Having defined

$$I_i \equiv I_r[(I_b/I_a) - (t_b/\tau_i)]^{-1}, \tag{10}$$

one can solve for

$$\sigma_i = 1/I_i t_b, \tag{11}$$

$$N_i = (I_b/I_r)(I_i\tau_i/\alpha). \tag{12}$$

The cross section could thus be determined from a knowledge of only the excitation flux. It was assumed that the gamma radiation absorbed was converted to a secondary electron flux with an efficiency corresponding to 30 ev per secondary. To determine the trap concentration requires a knowledge of the light geometry and photomultiplier conversion efficiency. The gamma-ray intensity corresponded to an $(I_r\sigma_i)^{-1} = 20$ seconds for the long-lived traps, and thus the values of t_b and t_a used were three seconds and 60 seconds, respectively.

The results are shown in Table II. While the absolute values for σ_i and N_i may be in error by as much as 100 percent, the relative values indicate the interrelationships among the various traps. The results are the mean over the temperature range encountered and for Traps 1 to 4 were substantially independent of temperature. One must then assume that nonradiative transitions, involving a different temperature dependence, apparently play no important role. For Trap No. 5 the results were too meager to verify this assumption.

The approximate equality of the N and σ values for the long-lived traps implies that the *a priori* probability for electrons to fall in any given traps is the same for each of the four traps, if nonradiative processes can be neglected. An equivalent statement to $N\sigma = \text{constant}$ is that $I_0\tau = \text{constant}$, where I_0 is the initial intensity of luminescence from a trap of cross section σ, and the decay time τ is assumed much longer than the radiation time. In addition to the long-lived set of traps in KI-Tl, a corresponding analysis of the complex decay of thallium activated potassium chloride[15] yields three components having equal $I_0\tau$ values. These long-lived traps thus appear to form a unique set of levels the concentration of which, however, is considerably less than that of the thallium impurity.

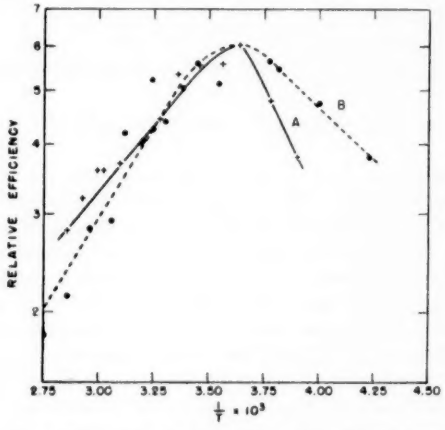

FIG. 8. Temperature dependence of phosphor efficiency.

[15] From decay curves reported by E. H. Hutten and P. Pringsheim, J. Chem. Phys. **16**, 241 (1948).

In a study of the trapping states of KCl-Tl, Johnson and Williams[16] report a low ratio of trap-to-impurity concentration and propose an excitation process in which competition between trapping and de-excitation of traps by the incident radiation accounts for the observed low value of trap concentration.

The characteristics for the short-lived traps can also be evaluated from the intensity of phosphorescence during excitation. For a single (or in our case, very prominent) trap after a time $t \gg \tau_i$ and for $1/\tau_i \gg I_r \sigma_i$ the conditions of dynamic equilibrium yield an emptying rate

$$dn_i/dt = I_r \sigma_i N_i. \tag{13}$$

Assuming the entire process is that of phosphorescence and assuming a value of σ_i as indicated, N_i can be computed. For the short-lived traps, however, dissipative processes cannot be ignored as indicated by the dependence of phosphorescent intensity on temperature. Curve *A* of Fig. 8 shows the gross phosphorescence during excitation, which may be attributed mainly to Trap No. 6 while in Curve *B* of Fig. 8 the results are shown for the very short-lived Trap No. 8. A comparison of the relative efficiencies (or $N_i \sigma_i$) of the various traps can be made with the glow-curve results of the light sum. Since only the product $N_i \sigma_i$ can be assigned to each trap, where σ_i could not be directly determined the assumption that $\sigma_i = 1.4 \times 10^{-17}$ cm^2 was made and the relative number N_i calculated. Thus from the γ-ray glow data, peak "*c*" corresponding to Trap No. 5 was used as a fiducial value and the values of N_i computed for the composite peak "*d*" (Traps 1 to 4) and peak "*b*." A similar assumption was made for the x-ray glow data. Since peak "*d*" consisting of Traps 1 to 4 remains unresolved, the total N_i for all four traps is indicated.

A check on the consistency of the values derived from the phosphorescence experiments may be made by using these values to compute a theoretical glow curve using Eq. (3) for the contribution to the total intensity from each trap. Comparison between the experimental glow curve of Curve *A*, Fig. 1 with a computed glow curve for peaks "*b*," "*c*," and "*d*," using the phosphorescent values for *E*, *s*, *N*, and σ, given in Tables I and II, is shown in Fig. 9. Since the dependence of σ on *T* is not well known, the agreement between results can be considered adequate.

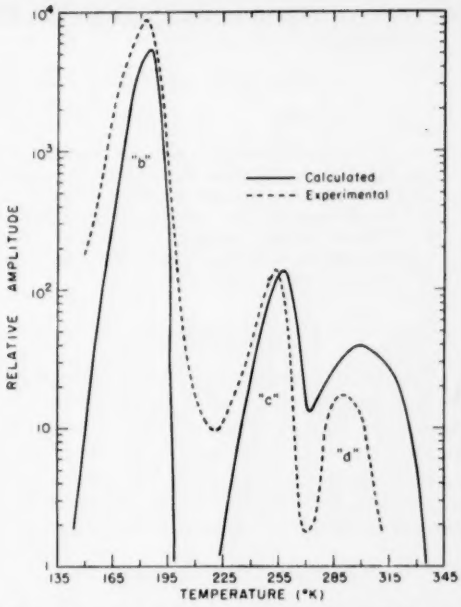

FIG. 9. Comparison of calculated and experimental glow curves for KI-TII. $\beta = 0.22$ deg/sec^{-1} (normalized at "*c*" peak).

ACKNOWLEDGMENTS

We are greatly indebted to P. H. Yuster for his invaluable cooperation in much of the thermoluminescence work. The spectrographic results were achieved through the assistance of J. K. Brody.

[16] P. D. Johnson and F. E. Williams, J. Chem. Phys. **21**, 125 (1953).

Superconductivity in Tin-Bismuth and Tin-Antimony Alloys*

W. F. Love
Randal Morgan Laboratory of Physics, University of Pennsylvania, Philadelphia, Pennsylvania
(Received April 27, 1953)

The Meissner effect in a series of spherically shaped solid solution alloys of tin with bismuth and antimony has been investigated. Magnetization curves have been obtained as a function of temperature and composition, from which critical field curves and transition temperatures have been derived. Increasing breadth of the magnetization curves and frozen in moment have been observed with increasing solute concentration. Thermodynamic analysis of the critical field data has shown an interesting variation of the electronic specific heat coefficient γ with solute concentration, which has been interpreted in terms of the overlapping band structure of tin.

I. INTRODUCTION

A STUDY of superconductivity in tin-bismuth and tin-antimony alloys is of interest because the electron-atom ratio can be increased by alloying bismuth and antimony, which have a valence of five, with tin, whose valence is four. In this manner, one can hope to obtain the influence of electron concentration on the superconductive properties of these alloys.

II. PREPARATION OF SAMPLES

Although bismuth and antimony are not soluble in tin to any appreciable extent at room temperature, the limits of solubility are increased considerably at higher temperatures.[1] Consequently, the samples studied must be kept in an annealing oven at temperatures sufficient to keep them in solid solution and must be rapidly quenched in a low temperature bath just prior to taking any measurements on them.

The samples were prepared from spectroscopically pure metals supplied by Johnson-Mathey, Ltd. The component metals were weighed in an analytical balance and melted over a Bunsen burner in a closed graphite crucible. The crucible was shaken vigorously to homogenize the melt and was quenched in running water. The resulting slug was remelted into a graphite mold made in two halves so that spherical specimens could be obtained. The mold was placed in a shallow pan of cool water so that the melt cooled from the bottom. This technique gives single crystals of pure tin most of the time, but results only in a large-grained polycrystalline sample for the alloys.

The tin-bismuth samples were kept in an annealing oven at 135°C where the limit of solid solubility is 12 atomic percent. Most of the samples were annealed for several weeks before any measurements were taken. The tin-antimony alloys were annealed at 225°C for 24 hours. At this temperature, antimony is soluble in tin up to 10 atomic percent. The tin-bismuth samples were quenched in liquid air just prior to taking the measurements. The tin-antimony samples were quenched in a bath of dry ice and acetone.

* This research has been carried out with the support of the U. S. Atomic Energy Commission.

[1] *Metals Handbook* (American Society for Metals, Cleveland, 1948), pp. 1180 and 1239.

III. EXPERIMENTAL TECHNIQUE

The method of taking measurements is the same as reported in an earlier paper.[2] The sample is displaced from the center of one pick-up coil to the center of another wound in opposition to the first, both coils located in a bath of liquid helium along the axis of an external solenoid surrounding the liquid helium dewar. When the sample acquires a magnetic moment in the field of the external solenoid and is displaced from one pick-up coil to the other, the flux changes in the coils add up to produce a deflection of an external galvanometer in series with the coils proportional to the magnetic moment of the sample.

IV. EXPERIMENTAL RESULTS

A set of typical magnetization curves for different alloys of tin-bismuth are shown in Figs. 1–3. The ratio of the galvanometer deflection to the maximum deflection at any field (D/D_{max}) is plotted against H/H_{c2}, where H_{c2} is taken to be the value of the external field at which penetration by that field is complete. H_{c1} will denote the field which first penetrates the specimen and is obtained by multiplying the field corresponding to the maximum in the magnetization curve by $\frac{3}{2}$ to account for the enhancement of the field at the equator of a sphere. Although H_{c1} and H_{c2} are the same for a pure metal, H_{c2} can be much greater than H_{c1} for an alloy. This fact, together with the much larger frozen in flux (irreversibility in the magnetization curve), constitutes the main difference in behavior between alloys and pure metals. The spread in the magnetic transition, as evidenced by the degree of "tailing" in the magnetization curves, increases with increasing bismuth content. The frozen in flux in general increases, but it also depends on the grain structure in the specimen. It is felt that the field H_{c1} is more indicative of the critical field characterizing the bulk of the sample and that H_{c2} is a measure of the inhomogeneity of composition or internal strain in the material. This supposition is given support by the influence of annealing on the magnetization curve of a tin+5 atomic percent bismuth alloy, as shown in Fig. 4. In this

[2] Love, Callen, and Nix, Phys. Rev. 87, 844 (1952).

figure, two magnetization curves are shown, corresponding to annealing times of 1 day and 45 days. Although the value of H_{c1} is uninfluenced by the prolonged annealing, H_{c2} and the frozen in moment are reduced considerably by this process. This shows that inhomogeneity of composition, which is removed by annealing, has a considerable effect on the breadth of transition, as one would expect. However, any further annealing no longer affects the magnetization curve even though some spread in the transition remains. This would indicate that even the most homogeneous alloy still has a considerable breadth of transition. This "inherent" breadth of transition could be due to internal strains caused by size differences between tin and bismuth atoms. Such effects have been observed by Wexler and Corak[3] who found that the breadth of transition in the hard superconductor vanadium was due to internal strains caused by dissolved interstitial impurity atoms of oxygen and nitrogen.

By taking magnetization curves at different temperatures, critical field data for alloys up to 10 atomic percent of Bi has been obtained. Critical field curves

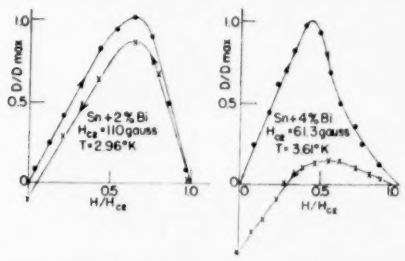

FIG. 1. Typical magnetization curves for Sn+2 atomic percent B and Sn+4 atomic percent Bi.

for alloys containing 2, 4, 6, and 8 atomic percent Bi are shown in Fig. 5, where both H_{c1} and H_{c2} are plotted against T^2. As can be seen from these curves, both of these fields can be represented fairly closely by a straight line.

The temperature breadth of transition of these alloys is represented in Fig. 6, where the galvanometer deflection in a small field (usually 2 gauss) is plotted as a function of temperature. There is a fair amount of breadth to these transitions as one would expect from the magnetization curves. However, the greater part of the transition takes place within one-tenth of a degree, indicating that the bulk of the material has a fairly well defined transition temperature.

The transition temperature T_c, obtained from the transition curves, is plotted as a function of the atomic percent of bismuth in Fig. 7.[4] T_c was obtained from the transition curves by extrapolating the linear portion

[3] A. Wexler and W. S. Corak, Phys. Rev. **85**, 85 (1952).

[4] In a private communication to the author, B. Serin has pointed out that T_c actually passes through a minimum around 0.1 atomic percent bismuth.

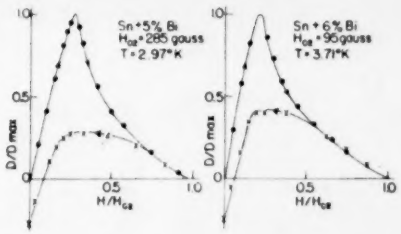

FIG. 2. Typical magnetization curves for Sn+5 atomic percent Bi and Sn+6 atomic percent Bi.

of the curves to zero deflection, and thus corresponds to the temperature at which the first appreciable sign of superconductivity appears. The behavior is in accordance with the known behavior of bismuth, that of raising the transition temperature when alloyed

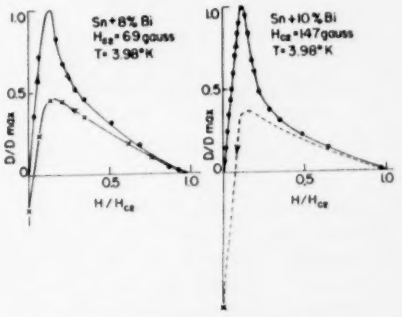

FIG. 3. Typical magnetization curves for Sn+8 atomic percent Bi and Sn+10 atomic percent Bi.

with other superconducting elements. It behaves as if bismuth would be a superconductor with a high transition temperature if it were to crystallize into the tetragonal white tin structure.

A less extensive survey of tin-antimony has been carried out in order to see what similarities exist

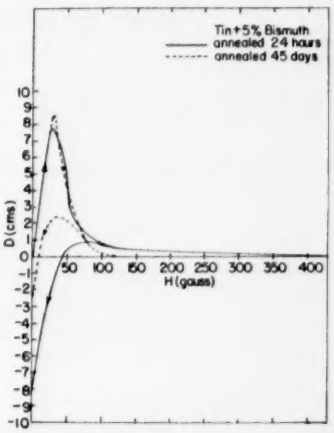

FIG. 4. Effect of annealing on the magnetization curve for Sn+5 atomic percent Bi.

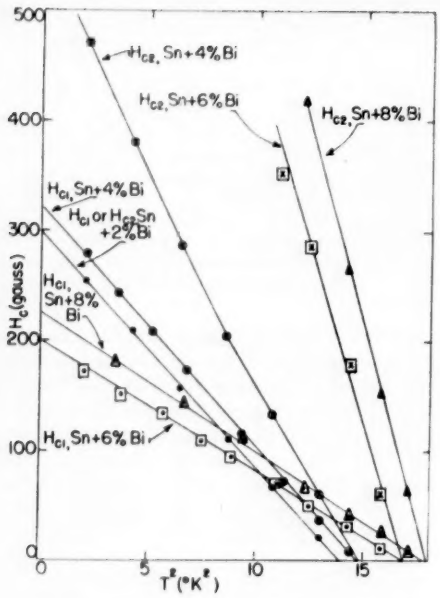

FIG. 5 Critical field curves for Sn-Bi alloys.

between tin-antimony and tin-bismuth alloys. Since both antimony and bismuth have the same valence, one can reasonably suppose that any similarities in behavior would be caused by the concentration of valency electrons, which is the same for alloys of the two systems having the same composition.

Similar measurements on the tin-antimony alloys were carried out and the results of these measurements are shown in Figs. 8 to 12. Figures 8 and 9 show typical

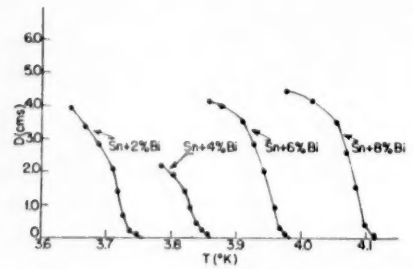

FIG. 6. Temperature transition curves for Sn-Bi alloys.

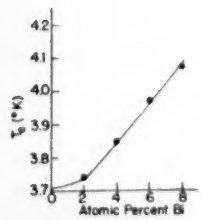

FIG. 7. Transition temperature as a function of atomic percent composition for Sn-Bi alloys.

magnetization curves for the alloys studied. The behavior is quite similar to the tin-bismuth alloys in that the breadth of transition and frozen in moment increase with increasing antimony content. However, for corresponding compositions, the tin-antimony alloys show somewhat sharper transitions. Figure 10 shows the critical field curves observed for these alloys. Figure 11 shows the transition temperature curves, and Fig. 12 shows the T_c *versus* composition curve obtained from the temperature transition curves by the same method as was used on the tin-bismuth alloys. It should be noted that the transition temperature for the tin-antimony alloys behaves diffently from that for the tin-bismuth alloys. In particular, the peak at around 6

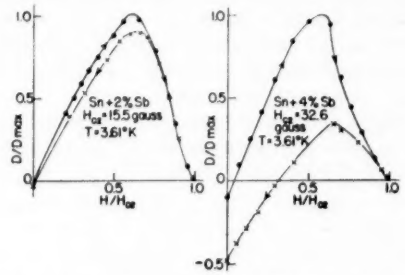

FIG. 8. Typical magnetization curves for Sn+2 atomic percent Sb and Sn+4 atomic percent Sb.

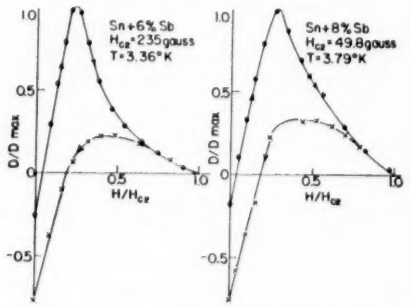

FIG. 9. Typical magnetization curves for Sn+6 atomic percent Sb and Sn+8 atomic percent Sb.

atomic percent antimony does not exist in the tin-bismuth alloys.

V. ANALYSIS OF EXPERIMENTAL RESULTS

An important parameter which can be derived from the critical field data is the Sommerfeld electronic specific heat coefficient γ, which gives the linear term γT in the specific heat of the normal state. Provided that there is no linear term in the specific heat of the superconducting state, one can then assume that the linear term in the formula for the difference in specific heats of the normal and superconducting states, as derived from the application of thermodynamics to the threshold field curve, represents the true electronic

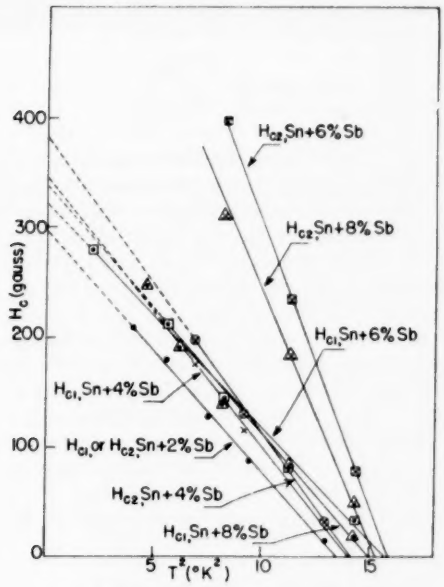

FIG. 10. Critical field curves for Sn-Sb alloys.

specific heat. If the threshold field is a parabola, as given by the formula

$$H_c = H_0[1-(T/T_c)^2],$$

then one can obtain[5]

$$\gamma = \tfrac{1}{2} V_m H_0^2/T_c^2, \text{ where } V_m = \text{molar volume.}$$

The validity of this relation is also based on the perfect reversibility of the superconducting-normal transition (Meissner effect). This, of course, is not the case in the alloys studied in this investigation. However, it seems reasonable to assume that H_{c1} represents the "true" critical field for these alloys. By "true" critical field, we mean that the greatest part of the sample has this value for its critical field and that if it were possible to remove the small volume of material responsible for the observed broadening of the transition and frozen in moment, the remaining part would show a sharp reversible transition at the "true" critical field. Some strong evidence in support of this assertion is obtained by comparing the predicted difference in specific heats at the transition temperature for the tin plus 4 atomic percent bismuth alloy with the actual value as observed by Mendelssohn and Moore.[6] They measured a $\Delta C_v = 3.42\times10^{-3}$ cal/mole deg, whereas the ΔC_v predicted from the H_{c1} threshold curve for this alloy is 3.39×10^{-3} cal/mole deg. The H_{c2} threshold curve predicts a value of 7.11×10^{-3} cal/mole deg. It would thus seem that the thermodynamic properties are more accurately predicted by the H_{c1} curve. However, one can only ascribe qualitative significance to any thermodynamic parameters derived from H_{c1}.

TABLE I. Critical field data for tin-bismuth and tin-antimony alloys.

Composition (atomic percent)	Sn-Bi T_c (°K)	Sn-Bi H_{c1} (gauss)	Sn-Bi $\gamma\times10^4$ cal per mole deg^2	Sn-Sb T_c (°K)	Sn-Sb H_{c1} (gauss)	Sn-Sb $\gamma\times10^4$ cal per mole deg^2
2	3.85	297	3.90	2.64	304	4.32
4	3.86	325	4.39	3.76	345	5.23
4.5	3.88	310	3.95	...	...	...
5	3.93	282	3.19	...	...	...
5.5	3.94	274	3.00	...	...	...
6	4.10	200	1.47	3.96	321	4.06
8	4.15	228	1.87	3.89	330	4.47
10	4.18	251	2.22	...	...	...

A summary of all the significant data on the two alloy systems is shown in Table I. This table gives the values of the parameters which best fit the observed data on the threshold fields by means of the relation $H_c = H_0[1-(T/T_c)^2]$. H_0 represents the critical field at 0°K and the subscripts 1 and 2 correspond to the fields at which penetration begins and is complete, respectively. The γ values given were derived from H_{c1}.

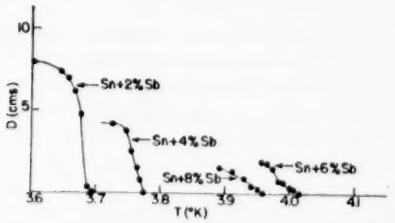

FIG. 11. Temperature transition curves for Sn-Sb alloys.

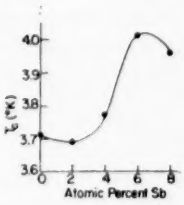

FIG. 12. Transition temperature as a function of composition for Sn-Sb alloys.

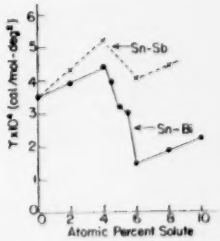

FIG. 13. γ vs atomic percent composition for Sn-Bi and Sn-Sb alloys.

[5] See F. London, *Superfluids* (John Wiley & Sons, New York, 1950), Vol. 1, p. 22.

[6] K. Mendelssohn and J. R. Moore, Proc. Roy. Soc. (London) **A152**, 34 (1935).

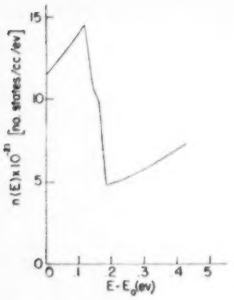

FIG. 14. Density of states curve derived from the Sn-Bi data.

A plot of γ *versus* atomic percent of solute is shown in Fig. 13 for the two alloy systems. There is a strong similarity in the two curves. In both cases, there is a linear rise in γ up to around 4 atomic percent of solute followed by a sharp drop between 4 and 6 atomic percent solute, and then a linear rise beyond this point. The shape of these curves has a natural explanation according to the band theory of metals. γ is proportional to the density of states at the surface of the Fermi distribution, and since the value of the Fermi surface is increased by adding bismuth or antimony atoms to the tin lattice, one should expect γ to vary in a manner closely related to the density of states curve for tin. Since tin is known to conduct by virtue of a small overlapping of energy bands, which leaves an incompletely filled Brillouin zone, one might expect that, on adding more electrons to the system, the first zone would be filled and the next outer zone would start to fill. Since the density of states is high at the top of a filled band and low at the bottom of the next higher band, one would expect a fairly sharp drop in the value of γ upon the completion of the filling of the lower band, and this is observed to be the case. One can obtain the density of states curve by integrating the observed data to get the change in Fermi energy. This can be done in the following way: we have $V=\frac{2}{3}\pi^2k^2V_mn(E)$ (cal/mole deg^2),[7] where k = Boltzmann's constant, V_m = molar volume, $n(E)$ = density of states per unit volume at the Fermi level E. Let $C=\frac{2}{3}\pi^2k^2V_m$, so that $\gamma=Cn(E)$. Let N = total number of electrons per mole in the alloy. Then $N=(4+f_B)A$, where f_B = fraction of bismuth atoms in the alloy, and A = Avogadro's number. Hence, $dN=Adf_B$. We can also write $dN=V_mn(E)dE$. Here dN denotes the number of electrons per mole added to the system to change the Fermi level by an amount dE. Combining these two results, we have

$$dE=dN/V_mn(E)=Adf_B/V_mn(E).$$

Hence,

$$E=E_0+\int_0^{f_B}\frac{Adf_B}{V_mn(E)},$$

where E_0 = Fermi level in pure tin. Since $n(E)=\gamma/C$, we have

$$E=E_0+\int_0^{f_B}\frac{CAdf_B}{V_m\gamma(f_B)},$$

where $\gamma(f_B)$ is the experimentally determined value of γ as a function of f_B. The two preceding formulas allow one to obtain $n(E)$ *versus* $(E-E_0)$. This integration has been carried out for the Sn-Bi alloys, and the resulting curve is plotted in Fig. 14. This curve cannot be assumed to represent the true density of states curve for pure tin for two reasons: (1) The γ values are subject to the uncertainty of the validity of the thermodynamic theory as applied to alloys; (2) The values of $n(E)$ were obtained from the alloys of tin and should be corrected for the effects of alloying on the $n(E)$ curve for pure tin. However, it seems reasonable to assume that qualitatively the shape of the curve resembles the shape of the true $n(E)$ curve. The fact that the curves of γ *versus* atomic percent solute in the Sn-Bi and Sn-Sb systems are different quantitatively indicates that bismuth and antimony have different effects on the electronic energy spectrum of tin.

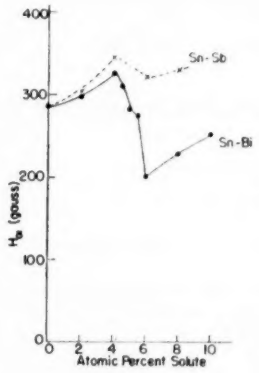

FIG. 15. H_{01} *vs* atomic percent composition for Sn-Bi and Sn-Sb alloys.

In Fig. 15, we show a plot of H_{01}, the critical field at absolute zero, for the Sn-Bi and Sn-Sb alloys as a function of atomic percent composition. The fact that H_{c1} behaves so similarly to $n(E)$, whereas there seems to be no corresponding behavior regarding T_c, indicates that H_{01} is determined to a large extent by the density of states. Of course, since $n(E)\propto H_{01}^2/T_c^2$ under the assumption made previously, then either H_{01} or T_c or both depend on $n(E)$. The observed behavior indicates that it is H_{01} which contains the dependency on $n(E)$, and that whatever other factors affect H_{01}, such as the magnitude of the interaction between electrons and lattice vibrations, also affect T_c in the same manner. This latter statement is supported by the isotope effect[8] which shows experimentally that H_{01} and T_c

[7] N. F. Mott and H. Jones, *The Theory of the Properties of Metals and Alloys* (Oxford University Press, London, 1936), p. 179.

[8] Reynolds, Serin, and Nesbitt, Phys. Rev. **84**, 691 (1951).

depend on isotopic mass in the same manner. This dependency of H_{01} on the density of states appears quite logical if one assumes that only the electrons in a narrow band of width ΔE at the surface of the Fermi distribution are involved in the superconductive transition. Then at absolute zero the energy difference between the normal and superconducting states will be $\bar{\epsilon}n(E)\Delta E$, where $\bar{\epsilon}$ = average energy difference per electron. Since this energy difference is also $H_{01}^2/8\pi$, it follows that $H_{01} \propto [n(E)]^{\frac{1}{2}}$, which is in accordance with the observed behavior of H_{01}.

VI. ACKNOWLEDGMENTS

The author is indebted to Professor F. C. Nix, whose interest and valuable advice have helped considerably in the execution of this research. He would also like to express his thanks to Messrs. W. B. Teutsch and F. Witt for much help in taking the necessary data.

PHYSICAL REVIEW VOLUME 92, NUMBER 2 OCTOBER 15, 1953

Superconductivity of Titanium

M. C. Steele and R. A. Hein
Naval Research Laboratory, Washington, D. C.
(Received May 4, 1953)

Critical magnetic fields of two specimens of titanium have been measured down to 0.23°K. The first specimen was a cold worked Ti wire having a purity of 99.98 percent. It was found to be superconducting at 0.37°K in zero magnetic field and the initial slope of the critical field curve was 465 gauss per degree. The second specimen was a Ti crystal bar with a purity greater than 99.99 percent. Its transition temperature was 0.49°K, and the initial slope of the critical field curve was 400 gauss per degree.

INTRODUCTION

THE superconductivity of titanium is of particular interest because of the large spread in reported transition temperatures. Meissner[1] first reported titanium to be superconducting at 1.13°K. Several subsequent investigations[2] on this metal have yielded transition temperatures from 0.53°K to 1.72°K.[3] The reported magnetic threshold values have also differed[3] by factors of two or more. In light of these circumstances, it was felt that additional data on the superconductivity of titanium would perhaps serve to clarify the situation. Before undertaking these measurements we sought to obtain titanium samples of the highest purity, since it is known that the properties of hard superconductors are very sensitive to even small amounts of impurity.

EXPERIMENTAL DETAILS

(A) Specimens

Two specimens of titanium were made available to us by E. J. Chapin of the Metallurgy Division, Naval Research Laboratory. Both were prepared by deposition from the iodide onto a titanium core.

(1) The first specimen was Ti wire with a diameter of 0.6 mm. The wire was prepared by cold swaging the original crystal bar (diameter 1.6 mm). No annealing followed this reduction in size. This wire was divided into lengths of 3–5 mm, and the pieces were then mixed with powdered chrome potassium alum. The mixture was compressed into a cylindrical pill having a diameter of 10 mm and a length of 12 mm. Spectrographic analysis showed that the Ti wire was 99.98 percent pure. The major impurities were oxygen and chromium, each of which appeared to the extent of 0.01 percent. The original crystal bar had a hardness of 70 on the Vickers scale.

(2) The second specimen was a Ti crystal bar with a diameter of 13 mm and a length of 13 mm. The purity of this sample exceeded 99.99 percent. The major impurity was oxygen which comprised ~0.005 percent of the total. Faint traces of silicon were also detected (~0.0001 percent). The hardness of this crystal bar was also ~70 on the Vickers scale. It was not annealed.

(B) Methods of Measurement

Because of the differences in the dimensions of the two specimens, we employed two distinct experimental arrangements for measuring the superconducting properties.

Ti Wire

For the Ti wire, thermal contact between the salt and metal was achieved by forming the pill described above. Temperatures below 1°K were obtained by the magnetic method, using a Bitter type solenoid to supply

[1] W. Meissner, Z. Physik **60**, 181 (1930).
[2] Meissner, Franz, and Westerhoft, Ann. Physik **13**, 555 (1932); W. J. de Haas and P. M. van Alphen, Proc. Amsterdam Akad. Sci. **34**, 70 (1931); R. T. Webber and J. M. Reynolds, Phys. Rev. **73**, 640 (1948); D. Shoenberg, Proc. Cambridge Phil. Soc. **36**, 84 (1940); J. G. Daunt and C. V. Heer, Phys. Rev. **76**, 715 (1949).
[3] This was the status at the time the present work was undertaken. Since then two additional papers have reported transition temperatures of 0.56°K and 0.39°K, respectively, for titanium; T. S. Smith and J. G. Daunt, Phys. Rev. **88**, 1172 (1952); Smith, Gager, and Daunt, Phys. Rev. **89**, 654 (1953).

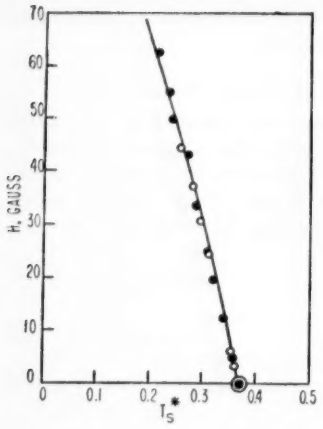

FIG. 1. Critical magnetic field of Ti wire as a function of T_s^*. ○—Oct. 23, 1952; ●—Nov. 6, 1952.

the magnetic fields. The temperature was determined from the magnetic susceptibility of the salt as measured by the ballistic mutual inductance technique.[4]

In order to obtain the extrapolated temperatures, T_s^*, based on Curie's law for a spherical salt specimen, we had to correct for the shape and filling factor of the salt. The value of Δ, obtained from $\Delta = cf(4\pi/3 - N)$, where c is the Curie constant, N is the demagnetization factor of the specimen, and f is the filling factor of the specimen, was found to be 0.01 degree. The occurrence of superconductivity in the titanium was also detected from these susceptibility measurements. Details of this procedure have already been given.[5]

Ti Crystal Bar

The existing apparatus was not large enough to allow us to press the salt around the Ti crystal bar. Further, it was thought advisable to avoid straining this specimen in order to be able to compare the results with those of the wire. Therefore, we achieved thermal contact in this case by suspending the crystal bar from the salt pill by means of a copper rod. The paramagnetic salt (again chrome potassium alum) was pressed onto an assembly consisting of a brass base to which a copper fin is silver soldered. Then a copper screw was threaded into tight fitting threads in the brass base of the salt pill. The Ti specimen was then tapped to accommodate the lower end of the copper screw.[6]

The copper screw was about 35 mm in length and 3 mm in diameter. Halfway between the salt pill and the Ti metal, we attached a thermometer holder to the copper rod. The holder consisted of a flat piece of copper, silver soldered to the rod, and then wrapped around a carbon composition resistor. The thermometer was cemented into this copper sleeve so formed with GE 7031 adhesive. This adhesive was also used in connecting the copper rod to both the salt pill and the metal sample. The thermal contact obtained with this arrangement seemed to be very satisfactory for the first time the apparatus was brought to liquid helium temperatures.

Our experience has shown that the thermal contact deteriorates to some extent once the apparatus is allowed to warm up from liquid helium temperatures to room temperature. It seems most likely that this difficulty is due to the salt's breaking away from the copper fin, although macroscopic examination did not reveal any cracks in the pill. In order to circumvent the possibility of having a poor thermal contact, we prepared new pills each time for the data to be reported here. On several occasions we did reuse an assembly, and found that the results for the transition temperature and critical field values were not reproducible. When new assemblies were used, the results were quite reproducible. In general, we found that poor thermal contact resulted in too low an apparent transition temperature and too flat a critical field curve. Independent magnetic measurements were made on the salt and metal in this arrangement. After demagnetization, we observed the susceptibility of both the salt and the metal as a function of time. The ballistic mutual inductance method was again employed here.

The superconductivity of Ti was evidenced by a large deflection of the galvanometer, indicating a diamagnetic susceptibility. By noting the time at which the metal returned to essentially zero susceptibility, we obtained the required transition temperature from the susceptibility of the salt. The value of Δ for these pills, needed to obtain T_s^*, was again 0.01 degree. Repeating this procedure with externally applied magnetic fields present during the warmup gave the critical field as a function of temperature.

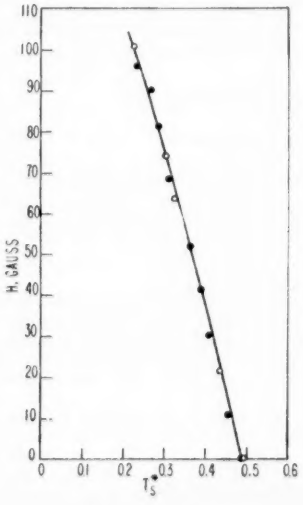

FIG. 2. Critical magnetic field of Ti crystal bar as a function of T_s^*. ○—Feb. 5, 1953; ●—Feb. 12, 1953.

[4] N. Kurti and F. Simon, Proc. Roy. Soc. (London) **A149**, 152 (1935).
[5] J. G. Daunt and C. V. Heer, Phys. Rev. **76**, 1324 (1949).
[6] This arrangement is similar to that employed by B. B. Goodman and E. Mendoza, Phil. Mag. **42**, 594 (1951).

The carbon resistance thermometer served to indicate the goodness of the thermal connection between the salt and metal. Thus, by calibrating the carbon thermometer previously and ascertaining its reproducibility to about 1 percent, we could be reasonably sure of good thermal contact if the carbon thermometer agreed with the temperature of the salt. On those occasions when we reused a given assembly it was observed that the carbon thermometer always read a higher temperature than the salt.

We used a gold ring seal to obtain vacuum tightness in the can containing the sample. This type of seal has proved to be most reliable and convenient for adiabatic demagnetization work. Vacuum tightness is maintained even after allowing the apparatus to warm up to room temperature. The coil system which surrounded the vacuum can consisted of three secondary coils and one primary coil. There was a secondary coil around the salt, another for the Ti metal, and a third one which was empty and could be connected in series opposition to either of the other two. The primary coil extended over all the secondaries. With this arrangement, we could switch either the salt system or the metal system to the ballistic galvanometer.

RESULTS

(A) Ti Wire

The critical magnetic field as a function of T_s^* for the Ti wire is shown in Fig. 1. We found a zero field transition temperature of 0.37 ± 0.01°K for both runs on the same specimen. The slope of the critical field curve at the transition temperature,

$$(dH/dT)_{T=T_c}=465 \text{ gauss/degree.}$$

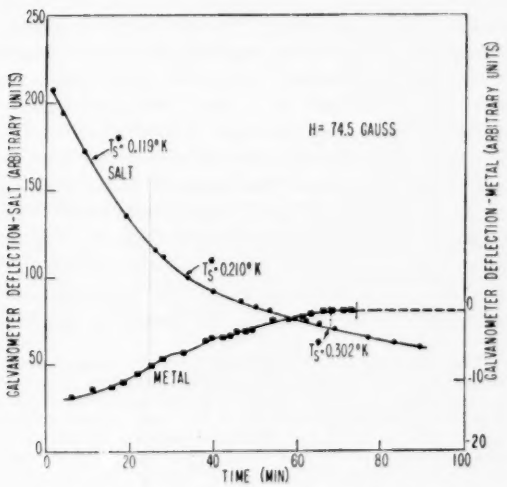

FIG. 3. Portion of a typical run with the Ti crystal bar.

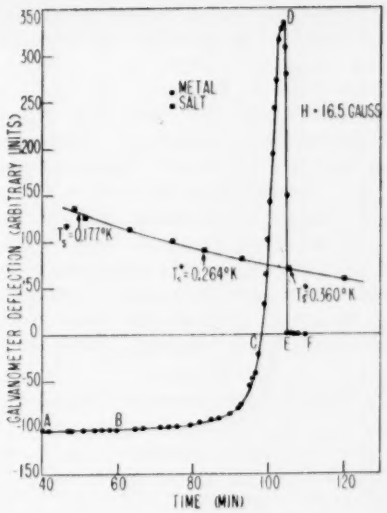

FIG. 4. Typical run with Cd rod, showing the "apparent" paramagnetism.

The curve in Fig. 1 could be represented adequately by the parabolic equation

$$H=H_0[1-(T/T_c)^2], \quad (1)$$

where H_0, the critical field at $T=0$°K, is 86 gauss and T_c, the zero field transition temperature, is 0.37°K. It took about two hours for the specimen to warm from 0.1°K to 0.5°K. From this it is estimated that the heat influx was less than 1 erg per second. The relatively slow warmup probably meant that the salt and metal were in good thermal contact. This supposition is made more plausible by the good reproducibility of the two runs on the same specimen.

(B) Ti Crystal Bar

The results for the Ti crystal bar are shown in Fig. 2, where the critical magnetic field is plotted as a function of T_s^*. Here the zero field transition temperature was found to be 0.49 ± 0.01°K. The slope of the curve,

$$(dH/dT)_{T=T_c}=400 \text{ gauss/degree.}$$

The curve in Fig. 2 could not be represented by the parabolic relation given in Eq. (1).

The warm-up times for these experiments were again of order two hours in going from 0.1°K to 0.5°K. The measurements in zero magnetic field can be used to estimate the percent of the Ti which actually is superconducting. Within experimental limits (±10 percent) this was found to be 100 percent. A portion of a typical run, with an applied field of 74.5 gauss, is depicted in Fig. 3, where the galvanometer deflections (in arbitrary units) of both the salt system and the metal system are plotted as functions of time after demagnetization. The deflections for the metal are adjusted so that zero

indicates the normal state. The time corresponding to the return to zero for the metal system deflection gives the desired temperature from the synchronous salt system deflection. For the applied field of 74.5 gauss this temperature was 0.302°K. The curve for the metal in Fig. 3 does not show the "apparent" paramagnetism which has been observed for soft superconductors such as zinc.[6] The Ti wire also failed to show this characteristic. The absence of this feature probably indicates that the magnetization curves for both Ti specimens are quite different from that of an ideal superconductor. This supposition is based on the explanation previously given by one of us.[7] We do not know if previous workers[2,3] observed the "apparent" paramagnetism in their experiments with Ti. Actually, the presence of this effect may be a good measure of how close the sample comes to being an ideal superconductor. In order to ascertain that our experimental arrangement was not responsible for the absence of this effect, we decided to conduct an experiment with a cadmium rod (Johnson Matthey Lab. No. 4753, 7 mm diam×20 mm long). The Cd was suspended from the salt pill by the same technique described for the Ti crystal bar. Figure 4 gives the results obtained for Cd in an applied field of 16.5 gauss. The galvanometer deflection (for the metal) is again adjusted so that zero indicates the normal state. From *A* to *B* the Cd had a constant differential diamagnetic susceptibility corresponding to the superconducting state. From *B* to *C* the diamagnetic susceptibility gradually decreased to zero as the Cd approached the intermediate state. In the portion *CDE* the Cd shows a paramagnetic *differential* susceptibility. Finally, the line *EF* represents the normal state again. The steepness of the line *DE* permits a very accurate determination of the temperature at which the Cd becomes normal in the particular applied field. The shape of the entire curve is consistent with the particular geometry of the sample and the previous analysis.[7] Complete results for Cd will be given in a subsequent paper. A comparison of Figs. 3 and 4 serves to confirm our belief that the Ti specimens differ appreciably from an ideal superconductor. Because of this, no attempt will be made to compute the thermodynamic properties of Ti from the critical field data.

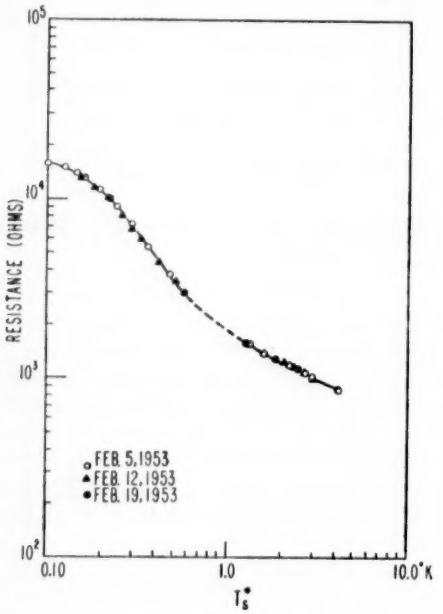

FIG. 5. Resistance-temperature curve for the carbon composition thermometer. Data from three separate experiments are shown.

A measure of the goodness of the thermal contact between the salt and the metal can be obtained from the carbon thermometer readings taken during a particular experiment. If the superconducting transition temperatures obtained from the salt's susceptibility and the carbon resistance agree from one run to another, we probably had good thermal contact on each occasion. Figure 5 gives the resistance *versus* temperature plot for the carbon thermometer.[8] Three sets of data are shown, of which two were obtained during the same runs that gave the critical field values for the Ti crystal bar. The reproducibility of results in both Figs. 2 and 5 indicates that the thermal contact was good. When the thermal contact between the salt and metal is poor, the values for both T_c and the critical field curve will be erroneous. In fact, for three experiments with poor contact we found results which varied from apparently no superconductivity for Ti (down to 0.20°K) to a T_c having a value of 0.37°K and 0.42°K, respectively. The apparent lowering of the transition temperature when the thermal contact is poor can be explained by the following argument. Immediately after the demagnetization has been completed, the salt will be at a lower temperature, T_s, than the metal, T_m. This direction for the thermal gradient, $\Delta T = T_m - T_s$, results from two factors. First, the salt is the agent which is cooled by demagnetization, and secondly, the metal is actually heated by eddy currents induced during the time the field is being removed. The behavior of the gradient ΔT as a function of time is then determined by the nature of the thermal connection between the salt and metal. For good contact we believe that in the order of minutes after demagnetization ΔT becomes essentially zero[9] (more specifically ΔT would be less than

[7] M. C. Steele, Phys. Rev. **87**, 1137 (1952).

[8] This particular thermometer had a nominal room temperature resistance of 270 ohms. Although we do not know the manufacturer of this resistor, we believe that they are no longer being made. The characteristic feature of this type of resistor is the white ceramic covering. This resistance thermometer is *not* of the same composition as the type described in detail by J. Clement and E. Quinnell, Rev. Sci. Instr. **23**, 213 (1952).

[9] This estimate is in agreement with the results of Goodman and Mendoza (reference 6).

0.01°K). However, for very poor thermal contact ΔT could be (and was found to be) as large as 0.5°K even an hour after demagnetization. With such a situation one would find the superconducting transition at too low a temperature. By exactly the same argument the critical field curve would be too flat, since in the presence of a field the time after demagnetization at which the metal becomes normal would be less and hence ΔT would be larger (assuming that ΔT decays toward zero with increasing time). It then follows that if the thermal contact for a particular assembly deteriorates between two runs, the two sets of data would not be in agreement. In fact, with this arrangement the most reliable results for a *given metal specimen* would be the highest reproducible transition temperature and the steepest reproducible critical field curve. The data shown in Fig. 2 met both these conditions within experimental limits.

(C) Discussion and Comparison with Previous Results

The comparison to previous work will be restricted to those measurements which found T_c for Ti to be below 1°K. In general, the agreement between different laboratories on measurements relating to hard superconductors has been poor. This is due, in large measure, to the sensitivity of the results to the characteristics peculiar to the particular specimen available. However, the measurements of Daunt and Heer[2] on unannealed Ti pieces (linear dimensions of about 2–3 mm) can be compared to our results for the Ti wire. Whereas their value of $T_c=0.53$°K differs considerably from ours, they found $(dH/dT)_{T=T_c}=470$ gauss/degree, which is in good agreement with the present results. The difference in T_c may easily be due to the fact that our Ti wire had been made by cold swaging without further annealing. Subsequent measurements by Smith and Daunt[3] on the same Ti (as used by Daunt and Heer[2]) in the annealed state did not reveal any significant differences from their earlier work. Both of these previous experiments used an experimental arrangement similar to that described in the present paper for the Ti wire; i.e., the metal (in the form of small pieces) was mixed with the paramagnetic salt and the mixture compressed into a pill. Kurti and Simon[10] have given arguments to show that such an arrangement probably gave better thermal contact between the metal and salt than other techniques. To our knowledge there are no experimental data to prove conclusively that the thermal contact is good at these temperatures.

Our results for the Ti crystal bar are in serious disagreement with the recent work of Smith, Gager, and Daunt.[3] They have reported $T_c=0.39$°K and $(dH/dT)_{T=T_c}=89.5$ gauss/degree for a very pure Ti crystal bar. Although their specimen was annealed subsequent to production, a comparison of the chemical purity and measured hardness shows that our specimen (unannealed) was similar to theirs. Therefore, it seems unlikely that the large differences, particularly in $(dH/dT)_{T=T_c}$, can be attributed to the specimens. It should be emphasized that our experimental technique for the Ti crystal bar was different from that of Smith *et al.*[3] It would appear that they pressed the paramagnetic salt around the Ti crystal bar to form an ellipsoidal pill,[11] whereas our specimen was suspended from the salt by the technique described above. Kurti and Simon[10] had considered the technique of Smith *et al.*[3] and had concluded that due to the thermal expansion coefficient of the salt being larger than that of the metal, there is danger that the salt will crack. This danger becomes greater as the size of the enclosed metal becomes larger. Whether or not these considerations can explain the difference between the two results would depend upon the reproducibility of each specimen from run to run.

Results from the two specimens used in the present experiments probably indicate that cold working the Ti has the effect of lowering T_c and making $(dH/dT)_{T=T_c}$ larger. The difference in making thermal contact between metal and salt may also be responsible in some way for this effect. In any event the observed trend is similar to other hard superconductors.[12] Finally, there is the question of the effect of annealing. Wexler and Corak[12] have pointed out that vacuum heat treatment of the hard superconductors only removes the internal strains due to cold work, and leaves unchanged the effects of the interstitially located foreign atoms such as oxygen and nitrogen. Even small amounts of such impurities can have appreciable effects upon the properties of the superconductor. Thus, although our Ti crystal bar contained only 0.005 percent oxygen, it is clear from the results obtained that the specimen is still far from being an ideal superconductor.

[10] N. Kurti and F. Simon, Proc. Roy. Soc. (London) **A151**, 610 (1935).

[11] The letter by Smith *et al.* (reference 3) does not give explicitly the technique used. However, their statement, "by methods previously reported," led us to believe that the salt was pressed around the metal.

[12] See, for example, the work of A. Wexler and W. S. Corak, Phys. Rev. **85**, 85 (1952) which contains a detailed discussion of the properties of hard superconductors.

Thermoelectric Power of Germanium below Room Temperature*

H. P. R. FREDERIKSE
Department of Physics, Purdue University, Lafayette, Indiana
(Received June 12, 1953)

The thermoelectric power of germanium single crystals has been measured in the temperature range 10 to 300°K. *N*-type samples of various impurity content have been investigated. Results show that the thermoelectric power Q decreases with increasing concentration of carriers. A few values of the heat conductivity are also reported.

The conventional theory predicts a relation between the thermal emf and the Hall coefficient. The temperature dependence of the thermoelectric power is in good agreement with this relation at temperatures higher than 200°K. Below this temperature Q rises sharply above the value given by this expression, reaches a maximum of several millivolts per degree near 15°K and decreases again at lower temperatures.

Large deviations may be expected at low temperatures due to the disturbance of the phonon equilibrium. The phonon current has a strong influence on the interaction with electrons and may lead to a maximum in the thermoelectric power at low temperatures. The contribution due to the non-equilibrium of the lattice is proportional to the ratio of phonon and electron mean free path. The former is related to the thermal conductivity while the latter can be derived from electrical data.

I. INTRODUCTION

THE thermoelectric power of germanium was measured several years ago by Scanlon and Middleton.[1] These authors investigated both *N*- and *P*-type material between 150 and 900°K. The results show within the experimental error good agreement with the theoretical treatment of Johnson and Lark-Horovitz.[2]

The purpose of this investigation was to extend these measurements to single crystals and to lower temperatures. The main problem was: to what extent is the above theory valid at low temperatures?

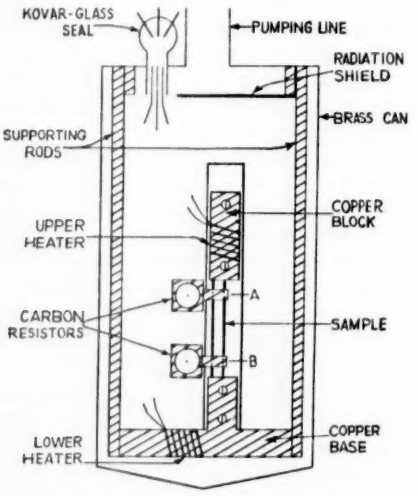

FIG. 1. Apparatus.

The results have led to a re-examination of the present theory of thermoelectric power in semiconductors. This theory contains the same assumption that Bloch[3] made for the case of metals, namely, that the lattice is in equilibrium. Peierls[4] has first questioned the general validity of this assumption. A few years later this problem was investigated in detail by Makinson[5] for the case of thermal conductivity in metals. This author shows that the non-equilibrium of the lattice has an important influence in Bi between 10 and 30°K. Gurevich[6] has made similar calculations for the thermoelectric power in metals. He describes the influence of the phonon current on the electrons as a carrying of the electrons by the lattice waves. In insulators and semiconductors where most of the heat is transported by the lattice vibrations, this effect is even larger.

It will be shown that the disturbance of the lattice vibrations leads to an additional term in the expression for the thermoelectric power of semiconductors, which plays an important role at low temperatures.

II. SAMPLES

The six samples studied are antimony-doped (*N*-type) germanium single crystals with different impurity content. All samples were cut from large crystals which were prepared by L. Roth of this department. The resistivities at room temperature for the six samples are indicated in Fig. 2. The surfaces of the samples were ground; the cross section is about 1×2.5 mm, while the length varies between 15 and 25 mm.

* Work assisted by contract between the U. S. Signal Corps and the Purdue Research Foundation.

[1] Lark-Horovitz, Middleton, Miller, Scanlon, and Walerstein, Phys. Rev. **69**, 259 (1946); W. W. Scanlon, Thesis, Purdue University, 1948 (unpublished).

[2] V. A. Johnson and K. Lark-Horovitz, Phys. Rev. **69**, 259 (1946); National Defense Research Council Report No. 14—585, 1946 (unpublished).

[3] F. Bloch, Z. Physik **52**, 555, 1928; **59**, 208 (1930).

[4] R. Peierls, Ann. Physik **4**, 121 (1930).

[5] R. E. B. Makinson, Proc. Cambridge Phil. Soc. **34**, 474 (1938).

[6] L. Gurevich, J. Phys. (U.S.S.R.) **9**, 477 (1945).

III. APPARATUS

A. Temperature Region 10–85°K

The thermoelectric power is measured with the potential method as used in thermal and electrical conductivity experiments. Figure 1 shows the apparatus.

The sample is soldered vertically between a copper base and a rectangular copper block, which are both mounted on a piece of lavite. Both block and base are provided with a nichrome heater. The upper heater enables the establishment of a temperature gradient along the sample, while the lower heater makes it possible to reach temperatures somewhat higher than the boiling point of the refrigerant. The copper base is suspended by means of two copper rods. This entire arrangement is enclosed in a brass can which can be evacuated through a monel pumping tube.

The temperature difference is determined with thermometers at two points (A and B) about 2 mm from the ends of the sample. In the temperature region 10–85°K Ohmite carbon thermistors (room temperature resistance=570Ω) were used. After removal of the insulation the resistors were embedded in small copper blocks (4×4×10 mm) and electrically insulated by means of cigarette paper and glyptal. The connection with the sample consists of 1-mm copper strips, which are soldered around the germanium specimen at the points A and B. The solder used is low melting cerroseal.

A copper shield prevents radiation through the pumping line from entering the brass can. All leads leave the can through a kovar-glass seal, except the copper wires leading to A and B. The thermoelectric power is measured between the latter ones, which are brought out through the pumping line in order to avoid additional thermal emf's.

The vacuum can is immersed in a refrigerant bath. Nitrogen is used for temperatures between 48 and 90°K, hydrogen between 10 and 25°K, and helium below 10°K.

During measurement of the thermoelectric power, the vacuum jacket is evacuated to pressures smaller than 10^{-4} mm of mercury. In order to calibrate the thermometers, a small amount of helium gas is admitted into the can. The temperature of the bath is determined by measuring the vapor pressure.[7]

The resistance of the carbon thermistors is compared with a standard resistance by means of a Leeds and Northrup K-2 potentiometer. The corresponding temperature T can be obtained from the calibration curves (log resistance against $1/T$). For the measurement of the thermal emf, a Rubicon thermofree six-dial potentiometer has been employed.

The thermoelectric power has been measured under steady state conditions. The time required to reach this state is of the order of 30 sec at liquid hydrogen temperatures, while it never exceeds 30 min in the liquid nitrogen region.

[7] Westinghouse Research Report R-94433-2A-1950 (unpublished).

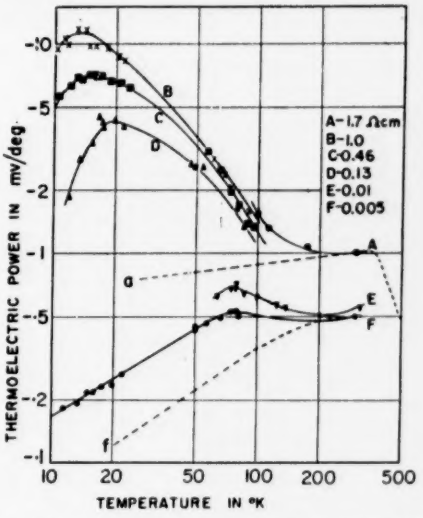

FIG. 2. Thermoelectric power of N-type germanium against copper as a function of temperature.

Heat Losses and Errors

The use of 5-mil advance wire to the resistors and 3-mil copper wire to the heater and to the sample makes the heat lost by conduction negligible. The heat leak through the wires is calculated to be 10^{-5} cal/sec, while the heat flow through the sample always exceeds 10^{-2} cal/sec.

The measuring current in the carbon resistors is kept very small ($\sim 10^{-4}$ amp). Taking into account the thermal conductivities of glyptal and copper, the temperature difference between thermometer and sample will be smaller than 10^{-3} degree.

Appreciable temperature gradients across the sample are difficult to obtain at low temperatures due to the high thermal conductivity of germanium (comparable with copper). Around 20°K the thermal resistance of the soldered contacts is much higher than that of the sample. The smallest temperature difference between A and B is 0.1 degree for which the accuracy of the thermoelectric power is estimated at 10 percent.

B. Temperature Region 78–300°K

The apparatus is essentially the same as the one shown in Fig. 1. Carbon resistors, however, are unsuitable at these temperatures and are therefore replaced by thermocouples. The combination of 5-mil manganin and 5-mil advance wire has been selected. Calibration points have been taken in the liquid nitrogen range, at 90.1°K (boiling point of oxygen), at 194.6°K (sublimation point of CO_2), and at room temperature. Agreement was found with the data of Scanlon,[8] who calibrated these thermocouples between 150 and 900°K.

[8] W. W. Scanlon, reference 1, p. 36.

IV. RESULTS

Figure 2 shows the results for the 6 samples *A–F*. Above 200°K these curves fit in very well with the measurements of Scanlon[1] on polycrystalline germanium which cover the temperature range 150–900°K.

Although the apparatus described in this paper was not designed to measure the thermal conductivity with a high degree of accuracy, it is nevertheless possible to estimate the magnitude of this quantity. A few values are given in Table I. The data in the liquid nitrogen range agree fairly well with the very accurate results of thermal conductivity measurements carried out by Goff.[9]

V. DISCUSSION

For a nondegenerate semiconductor (*N*-type), the conventional theory[2] predicts the following relation between the thermoelectric power Q and the Hall coefficient R in the impurity range:

$$\text{(I)} \quad Q=-\frac{1}{e}\left(\text{const}-\frac{\zeta}{T}\right)=-\frac{\kappa}{e}(\ln RT^{\frac{3}{2}}-\text{const}),$$

in which κ = Boltzmann constant and ζ = chemical potential. In order to check this formula, Hall measurements were carried out on the samples *A*, *D* and *F*.[10] The values of Q for sample *A* as calculated from (I) are indicated by the dashed line *a*. The other samples give similar results. It is clear that good agreement is obtained at temperatures higher than 200°K. Below this temperature all samples show larger values of Q than theoretically predicted, depending on the impurity content.

TABLE I. Resistivity and thermal conductivity of *N*-type germanium.

Samples	Resistivity at room temperature (Ω-cm)	Thermal conductivity (watts/cm °C) 20°K	50°K	60°K	70°K	80°K
B	1.0	11.5	7.5	5.1	4.2	3.5
C	0.46	10.5	—	5.1	3.5	2.9
D	0.13	10.5	—	4.7	3.3	2.7
F	0.005	4.7	4.2	3.3	3.0	2.3

Sample *F* has a degeneracy temperature of 55°K. The above formula therefore cannot be applied in this case at low temperatures. Johnson[11] has calculated the thermal emf using Fermi-Dirac statistics taking both impurity and lattice scattering of the electrons into account. The dashed line *f* represents the results.

An attempt has been made to explain the large values of the thermoelectric power at low temperatures. In the next section an expression for Q will be derived taking into account the deviation of the phonon distribution from its equilibrium value.

[9] J. F. Goff, Thesis, Purdue University, 1953 (unpublished).
[10] I want to thank Dr. Finlayson and Mr. Fritzsche for performing these measurements.
[11] V. A. Johnson and K. Lark-Horovitz, Bull. Am. Phys. Soc. **28**, No. 2, 32 (1953).

Electron-Phonon Interaction

Let us consider the semiconductor under the influence of a temperature gradient (in the x direction) and an electric field. A dynamic equilibrium is established through the interaction of electrons and phonons.

The following scattering mechanisms can occur:

I. *a.* electron—phonon
   b. electron—impurities;
II. *a.* phonon—phonon
   b. phonon—impurities
   c. phonon—electrons
   d. phonon—boundaries.

Under equilibrium conditions, the classical distribution function for the electrons is given by

$$f_0=\exp[-(E-\zeta)/\kappa T], \tag{1}$$

where E = kinetic energy of the electron ($\epsilon=E/\kappa T$).

The phonon distribution is represented by

$$N_0=1/(e^z-1), \tag{2}$$

where $z=h\nu/\kappa T$ and $h\nu$ = energy of the phonons.

Under the influence of the external forces, f and N will deviate from their equilibrium values and can be developed according to Fröhlich in spherical harmonics:

$$f=f_0+f_1=f_0+c(k)\frac{k_x}{\kappa T}\frac{\partial f_0}{\partial \epsilon}; \tag{3}$$

$$N=N_0+N_1=N_0+b(q)\frac{q_z}{\kappa T}\frac{\partial N_0}{\partial z}, \tag{4}$$

where $\mathbf{k}$ = electron wave vector and $\mathbf{q}$ = phonon wave vector.

The conditions for a steady state are given by the Boltzmann equations:

$$(\partial f/\partial t)_{\text{coll}}=-(\partial f/\partial t)_{\text{drift}}, \tag{5a}$$

$$(\partial N/\partial t)_{\text{coll}}=-(\partial N/\partial t)_{\text{drift}}. \tag{5b}$$

The solutions f and N can be substituted into the formulas for the electric current density and the heat current density of the electrons which are respectively given by:

$$J=-\frac{e}{4\pi^3}\int v_x f d^3k; \tag{6}$$

$$W=\frac{1}{4\pi^3}\int v_x E f d^3k. \tag{7}$$

From (6) and (7) expressions for the electrical conductivity σ, the thermal conductivity of the electrons λ_e, and the thermoelectric power Q can be derived.

We now proceed to the solution of Eqs. (5a) and (5b). In treating the perturbations of N_0, we will limit ourselves to the case of rather pure crystals, so that the

scattering of phonons by electrons and impurities may be neglected.

It will be assumed that the phonon-phonon processes (IIa) can be described by a mean free path $l_{ph}(q)$ which is defined by

$$(\partial N/\partial t)_{\text{coll}} = -sN_1/l_{ph}(q), \tag{8}$$

where s = velocity of sound.

When the external force is a temperature gradient, the parameter $b(q)$ can be calculated from (5b) with the result[12]

$$b(q) = -\frac{\hbar s}{T} l_{ph}(q) \frac{dT}{dx}. \tag{9}$$

The collisions of electrons and phonons (Ia) result in transitions in the state of the electron gas under absorption or emission of lattice quanta. These processes can be represented by

$$\mathbf{k}' = \mathbf{k} + \mathbf{q}_a, \quad E(\mathbf{k}') = E(\mathbf{k}) + h\nu; \tag{10a}$$

$$\mathbf{k}'' = \mathbf{k} + \mathbf{q}_e, \quad E(\mathbf{k}'') = E(\mathbf{k}) - h\nu. \tag{10b}$$

The change of the number of electrons $f(\mathbf{k})$ due to collisions with phonons becomes in the case of semiconductors:

$$\left(\frac{\partial f}{\partial t}\right)_{e\varphi} = \Phi_k \sum_q [(1+N_q) f(\mathbf{k}+\mathbf{q}_a) - N_q f(\mathbf{k}) + N_q f(\mathbf{k}+\mathbf{q}_e) - (1+N_q) f(\mathbf{k})], \tag{11}$$

where Φ_k = transition probability $= C/NMsk$,[13] C = constant, M = atom mass, and N = number of atoms. Substitution of (3) and (4) in (11) gives the result

$$\left(\frac{\partial f}{\partial t}\right)_{e\varphi} = \frac{C}{NMsk\kappa T} \sum_q \frac{1}{e^z - 1} \frac{\partial f_0}{\partial \epsilon} q(\cos\beta_a + \cos\beta_e)(c-b),$$

where β_a and β_e are respectively the angles between $\mathbf{q}_a$ and the x axis, and $\mathbf{q}_e$ and the x axis. We can now introduce polar coordinates with the polar axis in the direction of $\mathbf{k}$ and transform the sum over q to an integral. Integration over the aximuth ϕ yields

$$q\int_0^{2\pi} \cos\beta_a d\phi + q\int_0^{2\pi} \cos\beta_e d\phi = -2\pi k_x \frac{q^2}{k^2}. \tag{13}$$

The upper limit for the integration over q is in the case of semiconductors equal to $2k$.[14] Furthermore, $e^z - 1$ can be approximated by $z = h\nu/\kappa T = \hbar sq/\kappa T$. We will also assume for the time being that l_{ph}—and therefore b—is energy independent. Then,

$$\left(\frac{\partial f}{\partial t}\right)_{e\varphi} = -C'kTc\frac{k_x}{\kappa T}\frac{\partial f_0}{\partial \epsilon} + C'kTb\frac{k_x}{\kappa T}\frac{\partial f_0}{\partial \epsilon}, \tag{14}$$

where $C' = 4CV/\kappa\pi NMs^2h$ and V = volume of sample.

When $b = 0$ ($N = N_0$), a mean free path can be defined for the electron-phonon interaction. Thus,

$$\left(\frac{\partial f}{\partial t}\right)_{e\varphi} = -\frac{\hbar k}{m l_{e\varphi}} f_1 + C'kTb\frac{k_x}{\kappa T}\frac{\partial f_0}{\partial \epsilon}, \tag{15}$$

where

$$l_{e\varphi} = h/C'mT. \tag{16}$$

The scattering of electrons by impurities (Ib) has been treated by Conwell and Weisskopf.[15] The mean free path for this interaction l_{ei}, is energy dependent. The change of $f(\mathbf{k})$ due to electron-impurity scattering is given by

$$(\partial f/\partial t)_{ei} = -(hk/ml_{ei}) f_1. \tag{17}$$

The change of the electron distribution function caused by an electric field F and a temperature gradient dT/dx is

$$\left(\frac{\partial f}{\partial t}\right)_{\text{drift}} = \frac{\hbar}{m}\frac{k_x}{\kappa T}\frac{\partial f_0}{\partial \epsilon}\left\{-eF - T\frac{\partial}{\partial x}\left(\frac{\zeta}{T}\right) - \frac{E}{T}\frac{dT}{dx}\right\}. \tag{18}$$

From Eqs. (5a), (14), (17), and (18) it now follows that:

$$\left(\frac{1}{l_{e\varphi}} + \frac{1}{l_{ei}}\right)kc + \frac{1}{l_{e\varphi}}kb = \left\{-eF - T\frac{\partial}{\partial x}\left(\frac{\zeta}{T}\right) - \frac{E}{T}\frac{dT}{dx}\right\}. \tag{19}$$

$1/l_{e\varphi} + 1/l_{ei}$ can be replaced by $1/l_e$, where l_e is the electron mean free path for the case $N_1 = 0$ (Bloch approximation[3]). l_e can be determined experimentally when the only external force is an electric field.

Equation (19) determines c and therefore f_1. The expression for the electrical and heat current densities are then obtained from Eqs. (6) and (7):

$$J = -\mathcal{K}_1\left\{e^2F + eT\frac{\partial}{\partial x}\left(\frac{\zeta}{T}\right)\right\} - \mathcal{K}_2\frac{e}{T}\frac{dT}{dx} - \mathcal{K}'e\frac{dT}{dx}; \tag{20}$$

$$W = \mathcal{K}_2\left\{eF + T\frac{\partial}{\partial x}\left(\frac{\zeta}{T}\right)\right\} + \mathcal{K}_3\frac{1}{T}\frac{dT}{dx} + \mathcal{K}''\frac{dT}{dx}, \tag{21}$$

where

$$\mathcal{K}_i = \frac{16\pi m}{3h^3}\int E^i l_e \frac{\partial f}{\partial E} dE; \tag{22a}$$

$$\mathcal{K}' = \frac{16\pi m}{3h^3}\int E\frac{l_e}{l_{e\varphi}}\frac{\hbar s}{T}\left(\frac{2mE}{\hbar^2}\right)^{\frac{1}{2}} l_{ph}\frac{\partial f}{\partial E} dE; \tag{22b}$$

$$\mathcal{K}'' = \frac{16\pi m}{3h^3}\int E^2\frac{l_e}{l_{e\varphi}}\frac{\hbar s}{T}\left(\frac{2mE}{\hbar^2}\right)^{\frac{1}{2}} l_{ph}\frac{\partial f}{\partial E} dE. \tag{22c}$$

[12] A. Sommerfeld and H. Bethe, *Handbuch der Physik* (Julius Springer Berlin, 1933), Vol. 24, No. 2, p. 547.
[13] H. Fröhlich, *Elektronen Theorie der Metalle* (Julius Springer, Berlin, 1936).
[14] H. Fröhlich, reference 13, p. 234.
[15] E. Conwell and V. F. Weisskopf, Phys. Rev. **77**, 388 (1950).

The thermoelectric power may be derived from (20) and (21). The result is:

$$Q=-\frac{1}{e}\left(\frac{\mathcal{K}_2}{\mathcal{K}_1 T}-\frac{\zeta}{T}+\frac{\mathcal{K}'}{\mathcal{K}}\right). \tag{23}$$

It follows from (22a) that the first term is a constant. Comparison of this formula with the expression (I) shows that the non-equilibrium of the lattice ($N\neq N_0$) leads to an additional term $\mathcal{K}'/\mathcal{K}_1$.

In the analysis of Q we will begin with the second term. Using the classical chemical potential we find:

$$\frac{\zeta}{T}=\kappa \ln\frac{nh^3}{2(2\pi m\kappa T)^{\frac{3}{2}}}. \tag{24}$$

Hung and Gliessman[16] have shown that in many germanium samples the number of carriers n—as calculated from the Hall coefficient—changes little between 20 and 300°K. The temperature dependence of ζ/T in this region is therefore $(3/2)\ln T$.

Johnson[11] has evaluated the term $\mathcal{K}_2/\mathcal{K}_1 T$ for the two cases where either lattice scattering or impurity scattering predominates, and finds values ranging from 2κ to 4κ.

At very low temperatures Fermi-Dirac statistics has to be used; the first two terms will then be proportional to T.

It is readily seen from (22a) and (22b) that the scattering mechanism for the electrons has its influence also on the third term. When the electrons are mainly scattered by the lattice, $l_e\simeq l_{e\varphi}$ and

$$\frac{\mathcal{K}'}{\mathcal{K}_1}=\tfrac{3}{4}\pi^{\frac{1}{2}}\frac{l_{ph}}{l_{e\varphi}}\left(\frac{2ms^2}{\kappa T}\right)^{\frac{1}{2}}\kappa. \tag{25a}$$

On the other hand, when $l_{e\varphi}\gg l_{ei}$, then $l_e\simeq l_{ei}$ and

$$\frac{\mathcal{K}'}{\mathcal{K}_1}=\frac{35}{32}\pi^{\frac{1}{2}}\frac{l_{ph}}{l_{ep}}\left(\frac{2ms^2}{\kappa T}\right)^{\frac{1}{2}}\kappa. \tag{25b}$$

The essential factor in both expressions is the ratio of phonon and electron mean free paths. Taking $s=5\times10^5$ cm/sec, the factor $(2ms^2/\kappa T)^{\frac{1}{2}}$ is of the order 1 at $T=1$°K.

The evaluation of l_{ph} is a very complicated problem. Klemens[17] has discussed the different interactions of phonons in a paper concerning the thermal conductivity of dielectrics. Both he and Peierls[18] have shown that the Umklapp processes play a major role at low temperatures. The mean free path for these interactions $l_u(q)$, is inversely proportional to q^2 and contains the factor $e^{\theta/2T}$ (θ=Debye temperature). The quantity l_{ph} is related to l_u. The electrons interact mainly with phonons of low energy; Klemens has shown that for low energy phonons $l_{ph}\sim l_u(q_0)$ where $q_0=\kappa T/hs$. To obtain a value for l_{ph} however, requires extensive data on the thermal conductivity which are still lacking at the moment. A rough estimate shows, nevertheless, that already at 100°K the phonon mean free path l_{ph} is larger than $l_{e\varphi}$, and rises more rapidly than the electron mean free path when the temperature decreases. Thus $\mathcal{K}'/\mathcal{K}_1$ increases with decreasing temperature.

At very low temperatures boundary scattering will become important. The phonon mean free path for this type of scattering is constant and of the order of the crystal size. The electron mean free path, on the other hand, will continue to rise as $1/T$ with decreasing temperature and $\mathcal{K}'/\mathcal{K}_1$ will decrease.

From these considerations the conclusions may be drawn that the third term in the expression for Q(23) will offer an important contribution to the thermoelectric power at low temperatures. The thermal emf will increase with decreasing temperature, then reach a maximum at very low temperature, and tend to zero for $T\to0$. This temperature dependence agrees qualitatively with the experimental results.

ACKNOWLEDGMENTS

The author wants to thank Dr. K. Lark-Horovitz for his continued interest and helpful criticism. He also wishes to express his gratitude to Dr. H. Fröhlich, Dr. P. Feuer, Dr. H. Y. Fan, and Dr. P. H. Keesom for valuable discussions and to V. Bolyard for technical assistance.

[16] C. Hung and J. H. Gliessman, Phys. Rev. **79**, 726 (1950).

[17] P. G. Klemens, Proc. Roy. Soc. (London) **208**, 108 (1951).

[18] R. Peierls, Ann. Physik **3**, 1055 (1929).

PHYSICAL REVIEW VOLUME 92, NUMBER 2 OCTOBER 15, 1953

Energy of Trapped Electrons in Ionic Solids

KURT LEHOVEC
Sprague Electric Company, North Adams, Massachusetts
(Received April 23, 1953)

The calculations of Simpson, on the energy of an electron localized in a crystal at an impurity carrying a single positive charge, have been extended to impurities carrying a multiple positive charge. The thermal and optical activation energies corresponding to the transition of the electron from the 1*s*-orbit to the conduction band are derived. The various contributions to the polarization energy of the lattice near the impurity are analyzed in detail, which leads to an expression differing from that used by Simpson. The results are applied to a tentative interpretation of activation energies of SiC crystals as observed by Busch.

I. INTRODUCTION

AN electron in a crystal near an impurity carrying an extra positive charge moves in the periodic crystal potential with a superimposed potential V resulting from the extra charge of the impurity and the polarization of its surroundings. At large distances from the impurity (as compared to interatomic spacing), the potential V is a slowly varying function of position. The wave function of the electron in this region may be written as a sum of "atomic" functions (strictly "Wannier functions") localized at the various atoms with coefficients derived from a wave function $\psi(r)$, satisfying a Schrödinger equation which contains the potential $V(r)$ but not the periodic lattice potential.[1-3] In this Schrödinger equation the mass of the electron is to be replaced by an effective mass, and the energy is obtained relative to the conduction band of the crystal.

Simpson[4] has derived the wave function ψ and energy for an electron moving in an ionic crystal near an extra positive charge. The polarization in the crystal was approximated by that of a continuous dielectric with static dielectric constant s and high-frequency dielectric constant w. The wave function was derived from hydrogen-like trial functions, using the variational principle.

In what follows the calculations of Simpson[4] are extended to impurities carrying an extra charge ze. We shall consider four cases in detail:[5]

(1) the electron moves in the conduction band at large distance from the impurity;
(2) the electron is suddenly attached to the impurity;
(3) the electron stays long enough at the impurity so that equilibrium of the surrounding lattice can occur;
(4) the electron is suddenly removed from the impurity into the conduction band.

The energy of a configuration involving the electron, the extra charge, and the lattice polarization introduced by them, contains the following terms: kinetic energy of the electron, potential energy between electron and extra charge, interaction between induced dipoles and electron or extra charge, interaction among dipoles, and quasi-elastic energy of the dipoles. These energy terms will be treated in detail. The results do not agree fully with the simple procedure used by Simpson[4] to calculate the change in polarization energy when proceeding from case (4) to case (1).

II. FIELD ACTING ON THE ELECTRON; IONIC AND ELECTRONIC POLARIZATION

The extra charge ze, the electron, and the polarization caused by them introduce in the crystal an extra field $\mathbf{F}$. The extra field consists of two parts. One part, $\mathbf{F}_e$, of the extra field does not vary with the position of the electron in its orbit. $\mathbf{F}_e$ comprises the field due to (*a*) ze; (*b*) the ionic polarization $\mathbf{P}^i$ (displacement of ions); and (*c*) the electronic polarization $\mathbf{P}_e^e$ (displacement of electron shells), due to (*a*) and (*b*). The other part of the extra field $\mathbf{F}_t$ varies as the electron moves in its orbit. $\mathbf{F}_t$ is the field due to the electron and to the electronic polarization $\mathbf{P}_t^e$ caused by it. Since the field $\mathbf{F}_t$ is present also if the electron moves in the conduction band, it is not to be included in the extra field due to the impurity.[6] Hence the extra field due to the impurity, which gives rise to the potential V, is $\mathbf{F}_e$. We have[7]

$$\mathbf{F}_e = -(ze/r^3)\mathbf{r} - 4\pi\mathbf{P}^i - 4\pi\mathbf{P}_e^e \tag{1}$$

and

$$\mathbf{F}_t(\mathbf{r}) = -(e/w\rho^3)\boldsymbol{\rho}, \tag{2}$$

where $\boldsymbol{\rho}$ is the vector pointing from the position of the electron to the point $\mathbf{r}$ (Fig. 1). The electronic polariza-

[1] F. Peckar, J. Phys. (U.S.S.R.) **10**, 431 (1946).
[2] J. C. Slater, Phys. Rev. **76**, 1592 (1949).
[3] H. M. James, Phys. Rev. **76**, 1611 (1949).
[4] J. H. Simpson, Proc. Roy. Soc. (London) **A197**, 269 (1949).
[5] The physical meaning of these cases will be discussed in Sec. 4.

[6] The "image force" F_t of the electron when close to the impurity will differ somewhat from that of the electron in the perfect lattice because of difference in polarizabilities of a lattice atom and an impurity atom. However, the difference of F_t should be small in comparison to the Coulomb force of the impurity and decays more rapidly with distance between the impurity and the electron. The effect has been estimated by W. Baltensperger [Phys. Rev. **83**, 1055 (1951)] for the case of the Si-lattice with a *P*-impurity.

[7] The field at a position r due to the spherically symmetric polarization is $-4\pi\mathbf{P}(r)$. The equation can be derived immediately, considering the polarization as an assembly of positive and negative charges. The field at r results only from the dipoles whose charges lie in part outside and in part inside of the sphere of radius r.

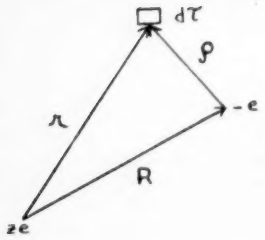

FIG. 1. Notation of vectors, pointing from the fixed extra charge ze to the position of electron $-e$, to the volume element $d\tau$ where polarization is considered, and from the electron to the volume element.

tion, derived from the field $\mathbf{F}_t$ is

$$\mathbf{P}_t^e = -\frac{w-1}{4\pi}\cdot\frac{e}{w\rho^3}\boldsymbol{\varrho}. \tag{3}$$

The time average of $\mathbf{F}_t$, $\langle\mathbf{F}_t\rangle$, is derived by averaging $\mathbf{F}_t$ over all positions of the electron, using the probability function $\psi\psi^*$ (ψ wave function of the electron):

$$\langle\mathbf{F}_t(\mathbf{r})\rangle = -\int\psi\psi^*\frac{e}{w\rho^3}\boldsymbol{\varrho}d\tau_1. \tag{4}$$

If $\psi\psi^*$ is spherically symmetrical (and we shall deal only with such cases in what follows) we have

$$\langle\mathbf{F}_t(\mathbf{r})\rangle = -\frac{pe}{wr^3}\mathbf{r}, \tag{5}$$

where

$$p = \int_0^r \psi\pi r^2\psi^*\psi dr \tag{6}$$

is the probability of finding the electron within the sphere of radius r. We shall now express $\mathbf{P}_i$ and $\mathbf{P}_e^e$ in terms of the time average of the total field $\langle\mathbf{F}\rangle$. The time average of the total polarization is $(s-1)/(4\pi)\cdot\langle\mathbf{F}\rangle$. The time average of the electronic polarization is $(w-1)/(4\pi)\cdot\langle\mathbf{F}\rangle$. The difference is the ionic polarization

$$\mathbf{P}^i = \frac{s-w}{4\pi}\cdot\langle\mathbf{F}\rangle. \tag{7}$$

The part of the electronic polarization $\mathbf{P}_e^e$, caused by the field due to the point charge ze, by the ionic polarization $\mathbf{P}^i$, and by the electronic polarization caused by them, is

$$\mathbf{P}_e^e = \frac{w-1}{4\pi}\left(\frac{ze}{wr^3}\mathbf{r} - 4\pi\cdot\frac{\mathbf{P}^i}{w}\right). \tag{8}$$

In Table I, we list the field $\langle\mathbf{F}\rangle$ causing the ionic polarization (line 1), the ionic polarization itself (line 2), and the field acting on the electron (line 3). In case (2) the ionic polarization is the same as in case (1), because the ions do not move, if the electron is inserted in a short time compared to the relaxation time of the lattice. For the same reason, the ionic polarization in case (4) is the same as in case (3). The subdivision of the polarization made in this section is not necessary to derive the field acting on the electron. However, we shall find this subdivision useful in the following discussion of the energy, associated with the various configurations.

III. THE ENERGY OF ELECTRON AND POLARIZATION

The energy of the polarization $\mathbf{P}$ caused by an external field $\mathbf{F}$ ($\mathbf{F}$ does not contain the contributions of $\mathbf{P}$ to the field) is

$$W = -\tfrac{1}{2}\int\mathbf{P}\mathbf{F}d\tau. \tag{9}$$

The factor $\frac{1}{2}$ results from consideration of the quasi-elastic energy of the dipoles. If the polarization $\mathbf{P}$ is not caused by $\mathbf{F}$, then the interaction energy between $\mathbf{P}$ and $\mathbf{F}$ would be $-\int\mathbf{P}\mathbf{F}d\tau$ (e.g., $\mathbf{P}$ ionic polarization, $\mathbf{F}$ field due to sudden insertion of an electron).

We shall apply the formula above first to the calculation of the energy W^i, involving ionic polarization, and then to the energy W^e, involving electronic polarization. We write down the expressions $\mathbf{PF}$ for a given volume element and a given position of the electron, then multiply by the probability $\psi\psi^*$ to find the electron at this position and then integrate over all positions of the electron and all volume elements. We obtain for case 1

$$W^i = -\tfrac{1}{2}\int\int\mathbf{P}^i\left(-\frac{ze}{r^3}\mathbf{r} - 4\pi\cdot\mathbf{P}_e^e\right)\psi\psi^*d\tau_1d\tau_2; \tag{10a}$$

for case 2

$$W^i = -\tfrac{1}{2}\int\int\mathbf{P}^i\left(-\frac{ze}{r^3}\mathbf{r} - 4\pi\cdot\mathbf{P}_e^e\right)\psi\psi^*d\tau_1d\tau_2 - \int\int\mathbf{P}^i\left(\frac{e}{w\rho^3}\boldsymbol{\varrho}\right)\psi\psi^*d\tau_1d\tau_2; \tag{10b}$$

for case 3,

$$W^i = -\tfrac{1}{2}\int\int\mathbf{P}^i\left(-\frac{ze}{r^3}\mathbf{r} - 4\pi\cdot\mathbf{P}_e^e + \frac{e}{w\rho^3}\boldsymbol{\varrho}\right)\psi\psi^*d\tau_1d\tau_2; \tag{10c}$$

for case 4,

$$W^i = -\tfrac{1}{2}\int\int\mathbf{P}^i\left(-\frac{ze}{r^3}\mathbf{r} - 4\pi\cdot\mathbf{P}_e^e + \frac{e}{w\rho^3}\boldsymbol{\varrho}\right)\psi\psi^*d\tau_1d\tau_2 + \int\int\mathbf{P}^i\left(\frac{e}{w\rho^3}\boldsymbol{\varrho}\right)\psi\psi^*d\tau_1d\tau_2. \tag{10d}$$

The second term on the right-hand side of Eq. (10b) does not contain the factor $\frac{1}{2}$ because the field $(e/w\rho^3)\boldsymbol{\varrho}$, due to the electron and its induced polarization, does not contribute to the displacement of ions in case 2. The origin of the second integral in Eq. (10d) is as

TABLE I. Time average of field $\langle \mathbf{F} \rangle$, ionic polarization $\mathbf{P}^i$, field acting on the electron $\mathbf{F}_e$ and total energy H related to an electron and an impurity, carrying an extra charge ze.[a]

Case	(1) Electron steadily separated from impurity	(2) Electron suddenly attached to impurity
(1) $\langle \mathbf{F} \rangle$	$-\frac{ze}{sr^3}\mathbf{r}$	
(2) $\mathbf{P}^i$	$-\frac{(s-w)ze}{4\pi \cdot sr^3}\mathbf{r}$	$-\frac{(s-w)ze}{4\pi \cdot sr^3}\mathbf{r}$
(3) $\mathbf{F}_e$		$-\frac{ze}{sr^3}\mathbf{r}$
(4) H	$-E_0-\frac{1}{2}\left(1-\frac{1}{s}\right)(ze)^2\int\frac{1}{r^2}dr$	$-E_0+K+U+\left(1-\frac{1}{s}\right)ze^2\int\frac{p}{r^2}dr$ $-\frac{1}{2}\left(1-\frac{1}{s}\right)(ze)^2\int\frac{1}{r^2}dr$
(5) $H-H_1$	0	$K+U+\left(1-\frac{1}{s}\right)ze^2\int\frac{p}{r^2}dr$
(6) $H-H_1$ for $\psi=\frac{1}{(\pi a^3)^{\frac{1}{2}}}\cdot e^{-r/a}$	0	$-R\cdot\frac{a_B}{a}\cdot\left(\frac{2z}{s}-\frac{a_B}{a}\right)$
(7) $H-H_1$ for proper value of a (Eq. 23)	0	$-R\cdot\frac{z^2}{s^2}$

Case	(3) Electron steadily attached to impurity	(4) Electron suddenly separated from impurity
(1) $\langle \mathbf{F} \rangle$	$\frac{-ze+pe}{sr^3}\mathbf{r}$	
(2) $\mathbf{P}^i$	$-\frac{(s-w)}{4\pi}\cdot\frac{(ze-pe)}{sr^3}\mathbf{r}$	$-\frac{(s-w)}{4\pi}\cdot\frac{(ze-pe)}{sr^3}\mathbf{r}$
(3) $\mathbf{F}_e$	$\left[\frac{-ze+pe}{sr^3}-\frac{pe}{wr^3}\right]\mathbf{r}$	
(4) H	$-E_0+K+U+\left(1-\frac{1}{s}\right)ze^2\int\frac{p}{r^2}dr$ $-\frac{1}{2}\left(\frac{1}{w}-\frac{1}{s}\right)e^2\cdot\int\frac{p^2}{r^2}dr$ $-\frac{1}{2}\left(1-\frac{1}{s}\right)(ze)^2\int\frac{1}{r^2}dr$	$-E_0-\frac{1}{2}\left(1-\frac{1}{s}\right)(ze)^2\int\frac{1}{r^2}dr$ $+\frac{1}{2}\left(\frac{1}{w}-\frac{1}{s}\right)e^2\int\frac{p^2}{r^2}$
(5) $-H_1$	$K+U+\left(1-\frac{1}{s}\right)ze^2\int\frac{p}{r^2}dr-\frac{1}{2}\left(\frac{1}{w}-\frac{1}{s}\right)e^2\int\frac{p^2}{r^2}dr$	$+\frac{1}{2}\left(\frac{1}{w}-\frac{1}{s}\right)e^2\int\frac{p^2}{r^2}dr$
(6) $H-H_1$ for $\psi=\frac{1}{(\pi a^3)^{\frac{1}{2}}}\cdot e^{-r/a}$	$-R\cdot\frac{a_B}{a}\left[\frac{2z}{s}+\frac{5}{8}\left(\frac{1}{w}-\frac{1}{s}\right)-\frac{a_B}{a}\right]$	$+R\cdot\frac{a_B}{a}\cdot\frac{5}{8}\cdot\left(\frac{1}{w}-\frac{1}{s}\right)$
(7) $H-H_1$ for proper value of a (Eq. 23)	$-R\left(\frac{5}{w}+\frac{16z-5}{s}\right)^2\Big/16^2$	$+R\left(\frac{1}{w}-\frac{1}{s}\right)\left(\frac{5}{w}+\frac{16z-5}{s}\right)\cdot 10\Big/16^2$

[a] $R=e^2/(2a_B)=2\pi^2me^4/h^2=13.53$ ev; $a_B=h^2/4\pi^2me^2=0.53$A.

follows: the average field of the electron and its induced polarization were included in the first integral, since the ionic polarization in case 4 is caused in part by them. However, the electron is removed in case 4, which is taken into account by the second term in Eq. (10d).

In a similar manner we obtain for the energy involving electronic dipoles, for the cases 1 and 4,

$$W^e=-\tfrac{1}{2}\int\int \mathbf{P}_e^e\left(-\frac{ze}{r^3}\mathbf{r}-4\pi\cdot\mathbf{P}^i\right)\psi\psi^* d\tau_1 d\tau_2$$

$$-\tfrac{1}{2}\int\int \mathbf{P}_t^e\left(\frac{e}{\rho^3}\boldsymbol{\varrho}\right)\psi\psi^* d\tau_1 d\tau_2; \quad (11a)$$

and for the cases 2 and 3,

$$W^e=-\tfrac{1}{2}\int\int (\mathbf{P}_e^e+\mathbf{P}_t^e)\left(-\frac{ze}{r^3}\mathbf{r}-4\pi\cdot\mathbf{P}^i+\frac{e}{\rho^3}\boldsymbol{\varrho}\right)$$

$$\times\psi\psi^* d\tau_1 d\tau_2; \quad (11b)$$

For $\mathbf{P}_e^e$, $\mathbf{P}^i$, and $\mathbf{P}_t^e$ the values of the Eqs. (8), (7), and (3) are to be inserted with $\langle\mathbf{F}\rangle$ given in Table I, line 1.

If we add W^i and W^e, we count twice the following energy terms, which arise from the interaction of electronic polarization with ionic polarization: for the cases 1 and 4,

$$W_{e,i}=-\int\int \mathbf{P}^i(-4\pi\mathbf{P}_e^e)\psi\psi^* d\tau_1 d\tau_2; \quad (12a)$$

and for the cases 2 and 3,

$$W_{e,i}=-\int\int (\mathbf{P}_e^e+\mathbf{P}_t^e)(-4\pi\mathbf{P}^i)\psi\psi^* d\tau_1 d\tau_2; \quad (12b)$$

In order to obtain the total energy of our configuration, we have to add to $W^i+W^e-W_{e,i}$ the kinetic energy of the electron

$$K=\frac{h^2}{2m}\int|\mathrm{grad}\psi|^2 d\tau \quad (13)$$

and the potential energy of the electron with respect to the extra charge ze

$$U=-ze^2\int_0^\infty\frac{p}{r^2}dr. \quad (14)$$

Furthermore, we have to add the energy $-E_0$ of the electron at the bottom of the conduction band, since the elimination of the periodic lattice potential from Schrödinger's equation yields the electronic energy relative to the bottom of the conduction band, as mentioned in the introduction. Now the term W^e [Eq. (11)] contains in all four cases the integral

$$W_{t,e}=-\frac{1}{2}\int\int \mathbf{P}_t^e\left(\frac{e}{\rho^3}\boldsymbol{\varrho}\right)\psi^*\psi d\tau_1 d\tau_2, \quad (15)$$

which represents the quasi-elastic energy of the electronic polarization $\mathbf{P}_t^e$, moving with the electron, and the interaction of $\mathbf{P}_t^e$ with the electron. The energy $W_{t,e}$ is present also if the electron moves in the conduction band and is already included in the energy $-E_0$ of the conduction band. Hence, we obtain for the energy of our configuration

$$H=-E_0+K+U+W^i+W^e-W_{e,i}-W_{t,e}. \quad (16)$$

Values of H are listed in Table I, line 4. In evaluating the integrals over the positions of the electron, occuring in Eqs. (10) to (12), the same procedure as in Eqs. (4) to (6) has been used.

In line 5 of Table I, the energies relative to that of configuration (1) are listed. The energy listed for case 4 is released during the readjustment of the ionic displacement after the electron is suddenly removed to the conduction band. Simpson[4] calculated this energy by the equation

$$H_4-H_1=\frac{1}{2}\left(\frac{1}{w}-\frac{1}{s}\right)\int\frac{p}{r^2}dr. \quad (17)$$

Simpson's equation is based on the incorrect use of Eq. (9), which is only valid when $\mathbf{F}$ is the field generating the polarization.

IV. WAVE FUNCTION OF THE ELECTRON

We have assumed a 1s-type wave function

$$\psi=\frac{1}{(\pi a^3)^{\frac{1}{2}}}\cdot e^{-r/a} \quad (18)$$

in cases (2) and (3). Integrals of this function which occur in formulas given previously in this paper are

$$\int_0^\infty\frac{p}{r^2}dr=\frac{1}{a};\quad \int_0^\infty\frac{p^2}{r^2}dr=\frac{5}{8a};\quad K=\frac{h^2}{(8\pi^2 ma^2)}. \quad (19)$$

With these integrals the Hamiltonian $H-H_1$ of line 5 of Table I becomes the expression of line 6 in Table I.

The proper value for the parameter a has been calculated by use of the variational principle. We form the total energy of the electron

$$E=K+e\int_0^\infty pF_e dr. \quad (20)$$

Both K and p depend on the parameter a. We calculate a from:[5]

$$\frac{dK}{da}+e\int_0^\infty F_e\cdot\frac{dp}{da}dr=0. \quad (21)$$

In evaluating Eq. (21), we have used the value of F_e listed in Table I, line 3, the integrals (19) and the

[5] In case 3, F_e depends on a also. However, the field is not varied in the variational method [see Peckar, J. Phys. (U.S.S.R.) **10**, 341, 347 (1946); and Simpson (reference 4)].

integral

$$\int_0^\infty \frac{p}{r^2}\cdot\frac{\partial p}{\partial a}dr=\frac{1}{2}\cdot\frac{\partial}{\partial a}\int_0^\infty \frac{p^2}{r^2}dr=-\frac{5}{16a^2}. \tag{22}$$

One obtains from Eq. (21): for case 2,

$$a=a_B\cdot s/z; \tag{23a}$$

for case 3,

$$a=a_B\cdot 16\Big/\left(\frac{5}{w}-\frac{5}{s}+\frac{16z}{s}\right); \tag{23b}$$

where $a_B=\hbar^2/4\pi^2me^2=0.53$A is the Bohr radius. Using these a values we derived the expressions listed in Table I, line 7.

In Fig. 2, the energy values for cases (1) to (4) are plotted *versus* a "configurational coordinate," characteristic for the displacement of ions near the fixed point charge ze. No quantitative significance is to be attributed to the location of the two abscissa values, characterizing the equilibrium displacement of ions for the cases "electron permanently removed from impurity (x_1)" and "electron in a stationary state attached to impurity (x_2)," respectively. Sudden changes of the state of the electron such as caused by interaction with light quanta (optical transitions) correspond to transitions at the same abscissa. "Slow" transitions such as caused by interaction with lattice vibration (thermal transitions) lead to transitions between the points (1) and (3). Notice that the activation energy for the optical transition from state (3) to the conduction band

$$H_4-H_3=\frac{R}{16^2}\cdot\left(\frac{5}{w}+\frac{16z-5}{s}\right)\left(\frac{15}{w}+\frac{16z-15}{s}\right) \tag{24}$$

is higher than that for the corresponding thermal transition, H_1-H_3 ("Frank-Condon principle"). From the values of Table I, line 7, one obtains for the ratio: optical activation/thermal activation

$$f=\frac{H_4-H_3}{H_1-H_3}=\left[15\left(\frac{1}{w}-\frac{1}{s}\right)+\frac{16z}{s}\right]\Big/\left[5\left(\frac{1}{w}-\frac{1}{s}\right)+\frac{16z}{s}\right]. \tag{25}$$

For the limiting cases $s\to\infty$, $f\to 3$; whereas for $s=w$, $f=1$.

TABLE II. Ionization energies of some SiC crystals.

	Ionization energy in electron volts observed[a]	calculated (H_1-H_3)
Crystal # 10	1.57	1.55
Crystal # 18	0.909	0.913
Crystal # 12b	0.441	0.445

[a] Reference 9.

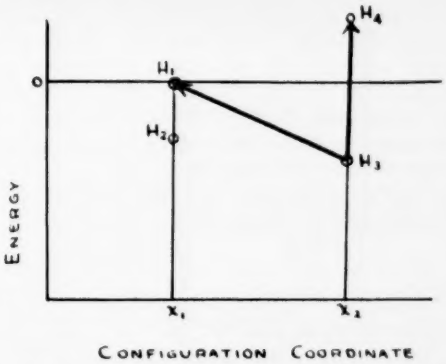

FIG. 2. Energy H of electron and impurity for the following configurations: (1) Electron moves in the conduction band at large distance from the impurity. (2) Electron is suddenly attached to the impurity. (3) Electron stays long enough at the impurity so that equilibrium of the surrounding lattice can occur. (4) Electron is suddenly removed from the impurity into the conduction band. $H_3\to H_4$ is the optical activation energy, and $H_3\to H_1$ is the thermal activation energy.

V. APPLICATION TO SILICON CARBIDE CRYSTALS

Busch[9] has measured the temperature dependence of the resistance of various SiC crystals, and has derived ionization energies of impurities. On three p-type crystals, the exceptionally high ionization energies listed in Table II, line 1 were observed. The ratio of these energies is close to $2^2:3^2:4^2$. It occurred to us that this may be related to presence of impurities carrying a multiple charge. We have applied tentatively the formula, listed in Table I, line 7, case 3, for $z=2$, 3, 4, respectively, with $w=6.55$ as derived from optical measurements on SiC.[10] We do not know the effective mass which enters R and the static dielectric constant. We presume that the static dielectric constants of SiC is higher than the high-frequency dielectric constant w, because of the existence of a strong reststrahl absorption.[11] We have obtained a good fit for the observed activation energies with an effective mass ratio $m^*/m=1$ and $s=12.7$ (Table II, line 2).

VI. CONCLUDING REMARKS

Our calculations were based on the approximation of the crystal polarization by that of a homogeneous medium. This approximation is bound to break down if the orbit radius a of the wave function of the electron is not large compared to the radius of the "Jost-sphere" (~interatomic distance).

We would like to emphasize that the electron need

[9] G. Busch, Helv. Phys. Acta **19**, 167 (1946).

[10] $n=2.56$, extrapolated from measurements by O. Weigel, Nachr. Ges. Wiss. Göttingen, Math.-phys. Kl., p. 264 (1915).

[11] C. Schaeffer and M. Thoma, Z. Physik **12**, 330 (1923); it is not impossible that the reststrahl absorption observed on SiC results from impurities and not from a partial ionic structure of this crystal. A strong infrared absorption is also observed in some diamonds [Robertson, Fox, and Martin, Proc. Roy. Soc. (London) **A157**, 579 (1936)].

not move in a hydrogen-like orbit. In many cases the wave function of the ground state of the electron at the impurity will resemble more the wave function of the electron at the impurity in free space[12] than that of a point charge imbedded in a dielectric. However, there exist always excited states, if not the ground state, of the type considered in this paper.

The optical absorption associated with the electron in a state such as the case (3) considered in this paper, is likely to result mainly from transitions $1s \rightarrow 2p$, rather than from transitions to the conduction band. However, the energy difference between the $2p$ state and the conduction band is rather small, and the formulas derived in this paper may still be of value for an interpretation of optical absorption associated with an electron in a hydrogen-like $1s$ orbit at a multivalent impurity in ionic crystals.

[12] F. Williams, J. Chem. Phys. **19**, 455 (1951).

PHYSICAL REVIEW VOLUME 92, NUMBER 2 OCTOBER 15, 1953

Atomic Heat of Indium below 20°K

J. R. CLEMENT AND E. H. QUINNELL
Naval Research Laboratory, Washington, D. C.

(Received May 28, 1953)

A calorimetric technique in which a carbon-composition resistor serves simultaneously as both heater and thermometer has been developed and is described briefly. Using this technique, the atomic heat of indium has been measured in the normal state from 1.7°K to 21.3°K and in the superconducting state from 1.8°K to 3.396°K, the transition temperature in zero magnetic field. Tables of smoothed values are given. A method of deducing the separate lattice and electronic contributions to the heat capacities, based on several empirically and/or theoretically tenable assumptions, has been developed and is described in some detail. This method of analysis, when applied to the indium data, led to the conclusion that a cubic analytic form for the critical magnetic field equation would allow conclusions consistent with all the assumptions but that the more commonly used parabolic form would not. Numerical values are given for the constants involved. The temperature dependence of the Debye characteristic temperature of the indium lattice over the entire range of measurement is shown to follow the theoretically expected behavior.

LOW temperature calorimetric measurements can yield information concerning three problems of fundamental importance in solid state physics: vibrational spectra of crystalline lattices, electronic structure, and superconductivity. Numerous theoretical and experimental investigations have shown that the discrete nature of the crystalline lattice causes significant deviations of its heat capacity from the Debye continuum theory only below about one-tenth the Debye characteristic temperature,[1] i.e., below 30°K or 40°K for most materials. The electronic structure of a material is the basis for theoretical calculations of the heat capacity of its electrons. However, only below about 15°K is the heat capacity of the electrons of sufficient magnitude relative to the lattice contribution to allow a reasonably precise test of any theory.[2] In superconductivity, a difference between the heat capacities in the normal and superconducting states is observed. While no present theory adequately explains this effect, any acceptable theory of superconductivity must eventually predict this difference. Superconductivity occurs among the metallic elements only below 10°K.[3]

In addition, the quantity actually measured in a calorimetric experiment on a solid body is the heat capacity at constant pressure C_p, while theoretical calculations ordinarily give the heat capacity at constant volume C_v. Therefore, in comparing theory and experiment, it is necessary to correct C_p to C_v. At moderately high temperatures, i.e., room temperature, this correction is of sufficient magnitude to require rather precise accounting but the data necessary for making an accurate calculation are usually not available.[4] At low temperatures, i.e., below 20°K, $C_p - C_v$ becomes vanishingly small so that only a slight correction, if any, need be made to the measured data to compare with theory.

Calorimetric measurements below 20°K were therefore undertaken. This report describes briefly the experimental technique employed and gives the results obtained on indium. There were several reasons why indium was chosen for investigation. First, there were no useful calorimetric data below room temperature in the literature; second, it is a metallic element and should have at low temperatures a measurable heat capacity due to the conduction electrons; and third, it becomes superconducting at about 3.4°K. Thus information related to all the problems mentioned

[1] M. Blackman, Repts. Progr. Phys. **8**, 11 (1941).
[2] F. Seitz, *Modern Theory of Solids* (McGraw-Hill Book Company, Inc., New York, 1940), Secs. 27, 28, and 101.
[3] D. Shoenberg, *Superconductivity* (Cambridge University Press, Cambridge, 1952), Chap. I and Appendix I.
[4] J. K. Roberts, *Heat and Thermodynamics* (Blackie and Son, Ltd., London, 1940), pp. 161–2.

above may be gained from a calorimetric study of indium. Also, indium has a low melting point and can be easily obtained in a state of high purity so that preparation of a sample was a relatively minor problem.

EXPERIMENTAL TECHNIQUE

It can be readily shown that with an electrical heater supplying heat to a body at the rate EI, under conditions of imperfect thermal isolation, the heat capacity of the body at temperature T (assuming perfect thermal conductivity) is

$$C_T = EI/(\dot{T}_m - \dot{T}_0), \tag{1}$$

where E is the voltage drop across the heater, I the current through it, $\dot{T}_m$ the time rate of change of temperature when $EI \neq 0$, and $\dot{T}_0$ the time rate of change of temperature when $EI = 0$, all quantities to be determined at the temperature T. Since the measurement of heat capacity intrinsically requires dynamic observations, it is impossible to determine directly all the quantities in Eq. (1) at a single temperature. In the technique described here, a carbon-composition resistor[5] is used simultaneously as both heater and thermometer, the principal observation during a calorimetric experiment being the electrical resistance of this resistor as a function of time. The E in Eq. (1) is maintained practically constant and the resistance-time data furnishes information for determining I and $\dot{T}_m$ directly and $\dot{T}_0$ indirectly.

The thermometer-heater is cemented into a close-fitting hole along the central axis of a cylindrical specimen of the material to be studied. This sample is suspended in an ordinary vacuum calorimeter, Fig. 1, consisting essentially of a brass can which may be either evacuated for making calorimetric measurements or filled with helium exchange gas for cooling the sample and calibrating the carbon-composition thermometer. The upper part of this can is a vapor pressure thermometer into which a small amount of liquid helium or hydrogen may be condensed.[6] A Wheatstone bridge having equal ratio arms and a three lead connection to the thermometer[7] is used to measure the resistance of the thermometer-heater. By using a dc amplifier whose output is fed into a General Electric photoelectric recorder, as the null detector for this bridge, a permanent record of the unbalance voltage as a function of time is obtained.

For making calorimetric measurements, a bridge voltage is chosen so that the heat developed in the thermometer-heater will cause the sample temperature to rise an amount between 0.05° and 0.5° in 300 seconds

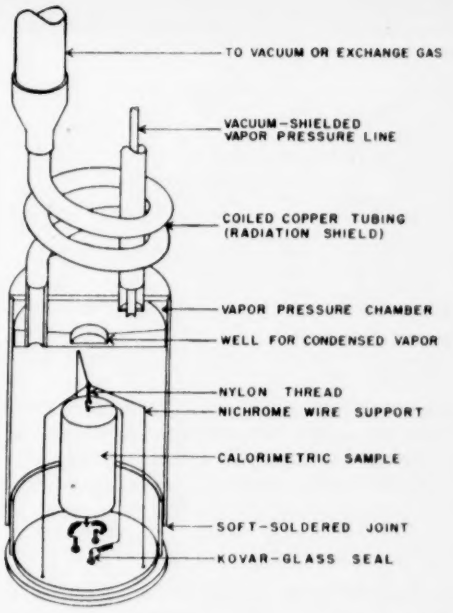

FIG. 1. Sketch of calorimeter can showing principal details of construction and assembly.

depending on the temperature range to be studied. During the 300-second heating period, the balancing resistor of the bridge is changed by fixed increments so that 10 or more resistance nulls are obtained. The values of the balancing resistor at the first and last nulls, as well as the size of the increments, are recorded separately and the exact time of each null can later be read from the recorder chart. At the end of this heating period the bridge voltage is turned off and no measurements made for the next 300 seconds, a "cooling" period. At the end of this "cooling" period another 300 second heating period follows immediately, and this process is continued without interruption until the desired temperature range has been covered. During the experiment, the temperature of the liquid helium surrounding the calorimeter can is maintained very nearly constant.

At the temperature prevailing at the mid-time of the nth heating period, the quantities in Eq. (1) are presumed to be as follows. First,

$$\dot{T}_{m,n} = (T_{f,n} - T_{i,n})/(t_{f,n} - t_{i,n}), \tag{2}$$

where $T_{f,n}$ is the final temperature, $T_{i,n}$ the initial temperature, $t_{f,n}$ the time at which heating stopped, and $t_{i,n}$ the time at which heating began for the nth heating period, the initial and final temperatures being obtained by extrapolation of a smooth curve through the actual data. In practice, instead of calculating a temperature corresponding to each resistance null, some simple function of resistance, such as $1/R$ or $\log R$,

[5] J. R. Clement and E. H. Quinnell, Rev. Sci. Instr. **23**, 213 (1952).

[6] Temperatures were obtained below 4.2°K from the vapor pressure of liquid helium using the "1949 scale" [H. van Dijk and D. Shoenberg, Nature **164**, 151 (1949)] and between 10° and 20°K from the vapor pressure of liquid hydrogen [Wooley, Scott, and Brickwedde, J. Research Natl. Bur. Standards **41**, 379 (1948)].

[7] Reference 4, p. 23.

TABLE I. Synopsis of calorimetric experiments on indium.

Experimental run	Date	Bridge voltage (volts)	Temperature range (°K)	Magnetic field (gauss)	Cooling times (seconds)	Helium bath temperature (°K)
H	5- 9-50	1.50	2.3- 3.8	0	300	1.85
J	5-18-50	1.50	1.7- 4.3	250	300	1.57
M_a	11- 2-50	1.92	1.9- 3.5	0	300	1.63
M_b	11- 2-50	1.92	1.8- 2.3	0	300	1.59
M_c	11- 2-50	1.92	1.7- 2.4	250	300	1.59
N	9-27-51	2.00	4.5- 9.6	0	300	4.21
O	9-27-51	4.00	10.3-13.7	0	150	4.21
P	9-27-51	10.00	17.2-21.3	0	150	4.21
Q	10- 4-51	4.00	5.9-19.2	0	200-400	4.21
R	10- 5-51	4.00	18.7-21.2	0	200-400	4.21

giving nearly linear curves for the heating periods, is plotted and actual temperatures calculated only for the initial, mid-time, and final resistance values.

The total voltage applied to the resistance bridge E_b is automatically maintained highly constant so that

$$(EI)_n=[E_b/2]^2[R_n/(R_n+r_n)^2], \tag{3}$$

where R_n is the resistance of the thermometer-heater at the mid-time of the nth heating period and r_n is the resistance at the time of the nth heating period of any one of the three (constantan) leads from outside the cryostat to the thermometer. A switching arrangement is incorporated in the bridge so that the series resistance of two of these three leads may be measured during a "cooling" period.

Finally,

$$\dot{T}_{0,n}=\frac{1}{2}\left[\frac{T_{i,n}-T_{f,n-1}}{t_{i,n}-t_{f,n-1}}+\frac{T_{i,n+1}-T_{f,n}}{t_{i,n+1}-t_{f,n}}\right], \tag{4}$$

i.e., simply the average of the rate of change of temperature during the "cooling" period just preceding and that just following the heating period under consideration. The time intervals in Eqs. (2) and (4) are independently measured on separate clocks, run by the same power source as the time scale of the General Electric recorder chart, so that they are known to ± 0.1 second.

If $\dot{T}_0$ be expanded in a power series of the time, Eq. (4) takes proper account only of the constant and first power term. A simple means of testing whether higher power terms are of sufficient magnitude to influence the results, and also for detecting other possible anomalies in the heat exchange correction, such as excessive heat loss through electrical leads, is to vary the cooling times during a calorimetric run. In the later work on indium, and also that on lead,[8] the cooling times were alternately 200 and 400 seconds, requiring, of course, an appropriate modification of Eq. (4). The $\dot{T}_0$'s obtained in these experiments lay on a reasonably smooth curve, when plotted as a function of average sample temperature, with no systematic difference for the two cooling times, justifying the use of Eq. (4) and indicating that no anomalous effects were contributing to the measured values of $\dot{T}_0$.

The over-all validity of the method rests primarily on two assumptions: (1) after the first few seconds, the temperature difference existing radially across the thermometer-heater[9] is essentially constant during the heating period; and (2) the temperature difference which exists radially across the sample during heating is negligibly small compared to the total temperature rise resulting from heating. The validity of these assumptions may be tested by making calorimetric measurements on the same sample over the same temperature range for two, or more, heating rates, i.e., bridge voltages. This was done for the indium data as will be noted later.

A study of these two effects has also been made by means of an electrical analog computer.[10] The results of this study indicated that the temperature difference in the thermometer is determined by the electrical power developed and is essentially independent of time, after a few seconds, if the thermometer is mounted in a sample of any practical size with any likely thermal diffusivity. The study further showed that the linearity of the temperature-time curves while heating, particularly the linearity during the first part of the heating, is an indication of the validity of the assumption (2) above. Therefore, the temperature at the mid-time of each heating period is compared with the average of the initial and final temperatures for that heating period. For each heating period so far analyzed, except those in which the transition from the superconducting to the normal state occurred, the mid-time temperature deviated from the average temperature by less than 1 percent of the total temperature rise for that heating period. Also, each heating period was examined graphically for abnormal curvature during the early portion. If $\dot{T}_m$ be expanded in a power series of the time, Eq. (2) takes proper account only of the constant and first power term. However, the linearity test shows that no higher terms of any significance occur in $\dot{T}_m$.

EXPERIMENTAL RESULTS

Calorimetric measurements were made on a cylindrical specimen of indium weighing 121.7 grams, cast from metal, obtained from the City Chemical Company, having a stated purity higher than 99.9 percent. Ten successful calorimetric experiments were carried out with this sample, and Table I, a synopsis of these runs, gives the resistance bridge voltage, the temperature range covered, the magnetic field applied externally to the sample, the cooling times employed, and the temperature of the helium bath during the run.

[8] J. R. Clement and E. H. Quinnell, Phys. Rev. **85**, 502 (1952).

[9] See reference 5, Eq. (3).

[10] V. Paschkis and H. D. Baker, Trans. Am. Soc. Mech. Engrs. **64**, 105 (1942).

In all, 180 data points were obtained in the normal state and 50 in the superconducting state.

Preliminary reports of part of this work have already been given.[11,12] Since the method of calculation used in obtaining the data in the earlier reports was not precisely that outlined in the preceding section, in particular, the thermometer calibration equation[13] was not used, all the data have been recalculated for this report according to the stated procedure. This recalculation changed the previous values slightly and reduced considerably the spread in the data. Table II gives smoothed values of the atomic heat in the normal state from 1.7°K to 21.0°K, and Table III smoothed values of the atomic heat in the superconducting state from 1.8°K to 3.396°K. The data in these tables have been corrected for the heat capacity of the thermometer-heater, estimated from the time required to establish the known temperature difference in it at the beginning of the heating periods. While such an estimate is probably not accurate to much better than 30 percent, the resulting error in the actual heat capacity of the sample is very much smaller since the heat capacity of the thermometer was less than 1 percent that of the sample.

The correction C_p-C_v has also been applied and was calculated from

$$C_p-C_v=AC_p^2T, \tag{5}$$

A being determined from the melting temperature.[4] Again the correction may not be very exact but is so small compared to the total heat capacity of the sample that the resulting error is negligible.

It is possible in the experimental technique described to obtain the relative uncertainty of each quantity involved in deducing the heat capacities since each

TABLE II. Atomic heat at constant volume of normal indium.

Temp. (°K)	Atomic heat (cal/mole deg)	Temp. (°K)	Atomic heat (cal/mole deg)	Temp. (°K)	Atomic heat (cal/mole deg)
1.7	0.002515	3.2	0.01351	9.0	0.3245
1.8	0.002893	3.3	0.01475	9.5	0.3738
1.9	0.003311	3.396	0.01602	10.0	0.4253
2.0	0.003772	3.6	0.01899	11.0	0.5330
2.1	0.004278	3.8	0.02233	12.0	0.6460
2.2	0.004831	4.0	0.02615	13.0	0.7631
2.3	0.005433	4.5	0.03860	14.0	0.8836
2.4	0.006087	5.0	0.05501	15.0	1.007
2.5	0.006797	5.5	0.07479	16.0	1.134
2.6	0.007563	6.0	0.09840	17.0	1.263
2.7	0.008389	6.5	0.1261	18.0	1.395
2.8	0.009278	7.0	0.1581	19.0	1.529
2.9	0.01023	7.5	0.1944	20.0	1.666
3.0	0.01125	8.0	0.2345	21.0	1.806
3.1	0.01234	8.5	0.2780		

[11] J. R. Clement and E. H. Quinnell, National Bureau of Standards Circular 519 (1952), p. 89.
[12] J. R. Clement and E. H. Quinnell, Phys. Rev. **79**, 1028 (1950).
[13] Reference 5, Eq. (1).

TABLE III. Atomic heat at constant volume of superconducting indium.

Temp. (°K)	Atomic heat (cal/mole deg)	Temp. (°K)	Atomic heat (cal/mole deg)	Temp. (°K)	Atomic heat (cal/mole deg)
1.8	0.002832	2.4	0.006614	3.0	0.01274
1.9	0.003323	2.5	0.007459	3.1	0.01403
2.0	0.003866	2.6	0.008371	3.2	0.01541
2.1	0.004464	2.7	0.009352	3.3	0.01687
2.2	0.005120	2.8	0.01041	3.396	0.01835
2.3	0.005837	2.9	0.01154		

should, for a single experimental run, ideally give a smooth curve when plotted as a function of average sample temperature. Such plots showed EI to be smooth to one part in 10 000 or better, $\dot{T}_m$ to about 2 parts in 1000 with occasional points in excess of this value and $\dot{T}_0$ to about 5 parts in 100. Since the magnitude of $\dot{T}_m$ was usually at least 10 times that of $\dot{T}_0$, the maximum relative error in heat capacity should be about 0.7 percent. For the data reported here 95 percent of the points deviated less than 1 percent from a smooth curve and a distribution curve of the deviations indicated a standard deviation between 0.3 and 0.4 percent. The smallness of the relative error is due to the high thermometric sensitivity of the carbon-composition resistors, to the precision with which the times of resistance nulls can be taken from the recorder tape ($\pm$0.2 second), to the relatively good thermal isolation achieved, and most of all, to the high precision in measuring resistance resulting from the use of the comparatively high voltage needed to heat the calorimetric sample as the measuring voltage of the resistance bridge.

The absolute error is more difficult to evaluate precisely. The temperature differences involved in calculating the heat capacities are rather sensitive to the thermometer calibration equation, and errors in the absolute thermodynamic temperatures are indistinguishable, when one compares theory and experiment, from errors in heat capacity values. However, the use of a temperature difference graph in conjunction with a closely fitting calibration equation reduces the error due to each of these sources to probably less than 0.2 percent. The instrumental error and the error due to the heat capacity of the thermometer-heater are both probably less than 0.3 percent. Thus, if the temperature values are regarded as exact, the absolute uncertainty in the atomic heat values appearing in Tables II and III is probably less than 1 percent.

Of these possible errors in absolute values, that due to the heat capacity of the thermometer-heater is undoubtedly systematic and those due to the thermometer calibration are very likely systematic. Therefore, differences in heat capacities, in particular differences between the heat capacities in the normal and superconducting states, would probably have, due to the small relative error in the data, a much higher accuracy than would be reflected by data consistent

with a 1 percent absolute uncertainty. For this reason, and also in order that the tabulated data would represent the best possible estimate of the accuracy of the results, four significant digits have been given for each value in Tables II and III. So that the roughly constant relative accuracy exhibited by the experimental data could be retained in the smoothed data, the smoothing process was essentially that of smoothing the Debye characteristic temperature and calculating smoothed atomic heats from smoothed characteristic temperatures.

DISCUSSION OF RESULTS

With these data, one has the opportunity to study the electronic atomic heat, the lattice atomic heat, and the thermodynamics of superconductivity as it relates the atomic heat differences between the normal and superconducting states to the temperature dependence of the magnetic field which just destroys superconductivity. Various methods of empirical analysis[14] have been used in the past to study these three effects, but the results have not always been mutually consistent. A method of analysis has been applied here which seeks results consistent with all the presently accepted ideas concerning these properties. In order to describe the method most efficiently, the principal assumptions involved are stated and discussed briefly below.

Assumptions

(1) The electronic atomic heat in the normal state is

$$C_{e,n}=\gamma T, \tag{6}$$

where γ is a constant at low temperatures. This assumption implies that the lattice and electronic heat capacities are independent and therefore additive, but this implication does not appear susceptible to a purely empirical test, since only the total effect of both the lattice vibrations and the electrons can be measured experimentally. Equation (6) results when Fermi-Dirac statistics is applied to a free electron gas[15] and the existence of a linear term in the low temperature atomic heat of many metallic elements has been demonstrated.[16]

(2) If the Debye characteristic temperature Θ is allowed to vary with temperature so that it represents the actual atomic heat of a crystalline lattice, then

$$\lim_{T\to 0}(d\Theta/dT)=0. \tag{7}$$

This condition on Θ appears to be a generally valid result of investigations of the lattice heat along the lines of the Born-von Kármán lattice dynamics, and it has received empirical support from the results of calorimetric measurements on materials which have only a lattice, and no electronic, contribution to the heat capacity.[1] For a three-dimensional lattice, this assumption is equivalent to the condition that a power series representing the heat capacity near 0°K contain no first, second, or fourth power temperature terms.

(3) Below the transition temperature in zero magnetic field, the heat capacity of the lattice is the same function of temperature in the normal and superconducting states. Measurements of the elastic constants[17–19] and the thermal expansion coefficient[20] on passing from one state to the other indicate that any difference in the lattice contributions in the two states is probably less than a few tenths percent and therefore within the experimental error of calorimetric measurements.

(4) No linear temperature term occurs in the atomic heat in the superconducting state. All the available evidence on superconducting elements supports this assumption.[21,22] The evidence considered here is that smooth curves drawn through plots of $C_{v,s}/T$ *versus* T^2 appear to extrapolate through the origin of coordinates, $C_{v,s}$ being the atomic heat in the superconducting state.

(5) Rather early in the study of superconductivity, it was noted that the magnetic field which just destroys superconductivity H_c varies almost parabolically with temperature.[23] Maxwell[24] has recently shown that the critical field data can be more adequately represented by the addition of a cubic term to the parabola. A convenient form for the cubic equation is

$$H_c=H_0[1-at^2+(a-1)t^3], \tag{8}$$

where H_0 is the critical field at 0°K, a is a numerical constant near unity, and t is the reduced temperature T/T_c, T_c being the transition temperature in zero magnetic field. Since the cubic form includes the parabola as a special case ($a\equiv 1$), Eq. (8) will be assumed as the analytic form for the critical field curve.

(6) The thermodynamics of superconductivity[25] gives correctly the difference in the atomic heats in the

[14] See, e.g., Burton, Grayson-Smith, and Wilhelm, *Phenomena at the Temperature of Liquid Helium* (Reinhold Publishing Company, New York, 1940), Chaps. 6 and 10.
[15] A. Sommerfeld, Z. Physik **47**, 1 (1928).
[16] Reference 14, Chap. 6 and Appendix C.
[17] W. J. de Haas and M. Kinoshita, Proc. Amsterdam Acad. Sci. **30**, 598 (1927).
[18] J. R. Clement [U. S. Office of Naval Research Cryogenics Conference, Yale University, 1948 (unpublished)] reported some observations of the elastic constants of tantalum which showed that they remained constant within 0.2 or 0.3 percent on passing from the normal to the superconducting state.
[19] W. C. Overton, Jr. [thesis, Rice Institute, 1950 (unpublished)] measured the elastic properties of tin and tantalum in the liquid helium range by an ultrasonic pulse technique. The moduli of both elements remained constant within 0.1 percent on passing from the normal to the superconducting state.
[20] McLennan, Allen, and Wilhelm, Trans. Roy. Soc. Can. **25**, 1 (1931).
[21] Reference 3, pp. 62 and 63.
[22] In one of the preliminary reports of the present data (reference 11), the possible existence of a small linear term in the atomic heat of superconducting indium was proposed. Recalculation of the data changed the absolute values of the atomic heat sufficiently that this conclusion of the earlier report is no longer valid.
[23] W. Tuyn and H. K. Onnes, J. Franklin Inst. **201**, 379 (1926).
[24] E. Maxwell, Phys. Rev. **86**, 235 (1952).
[25] C. J. Gorter and H. Casimir, Physica **1**, 306 (1934).

normal and superconducting states, that is,

$$C_{v,s}-C_{v,n}=[VT/8\pi][d^2(H_c^2)/dT^2], \qquad (9)$$

where V is the atomic volume, $C_{v,n}$ the atomic heat in the normal state, and the other quantities are as already defined. Many experimental investigations have yielded supporting evidence,[26] although in some cases the lack of agreement between calorimetric and magnetic results appears to be greater than experimental error. Since the heat capacity difference is a function of derivatives of the critical field curve, this lack of agreement may be due to the difficulty in accurately differentiating these curves. Fundamentally, this assumption implies the thermodynamic reversibility of transitions between the normal and superconducting states.

(7) The transition temperature in zero magnetic field can be determined with sufficient exactness from calorimetric and/or magnetic measurements to be taken as a known, unadjustable, quantity in any analysis of data.

A variety of ways to attempt to arrive at conclusions consistent with all these assumptions can be imagined. However, only the particular one finally adopted here will be discussed. Assumptions (1) and (2) applied simultaneously to normal state calorimetric data yield a value, or limits on the value, of γ in Eq. (6). The exact means of applying these two assumptions may vary, a more or less standard procedure being to plot $C_{v,n}/T$ *versus* T^2. If Θ is sufficiently constant over the temperature range in which data are available, such a plot will result in a straight line with an intercept equal to γ and a slope simply related to Θ for the lattice.

However, for materials with a relatively low value of Θ, such as indium, Θ may not become constant in the liquid helium temperature range so that erroneous values of γ result from such a procedure. An alternative method which takes account of the variation of Θ with T is suggested by the work of Blackman[27] on simple cubic lattices. He finds that near the absolute zero the heat capacity C_L of any three-dimensional lattice should become

$$C_L=AT^3+BT^5, \qquad (10)$$

where the constants A and B have been used in place of the exact expressions for his particular case.[28] It follows from Eq. (10) that

$$(d/dT)[(C_{v,n}-\gamma T)/T^3]=2BT. \qquad (11)$$

Thus, a plot of the rate of change of $(C_{v,n}-\gamma T)/T^3$ with T *versus* T should yield, for the correct value of γ, a straight line passing through the origin of coordinates. Figure 2 shows such plots for several values of γ, the plotted points being obtained by graphical differentiation of smooth curves of $(C_{v,n}-\gamma T)/T^3$ *versus* T.

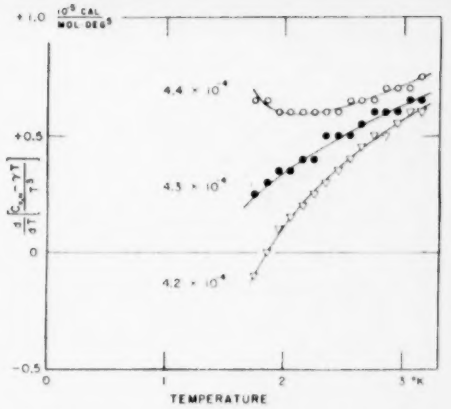

FIG. 2. Graphical application of Blackman's result (lattice heat $=AT^3+BT^5$) for finding the normal electronic heat, γT. The γ value associated with each curve is indicated in the figure.

Blackman makes no specific remarks in his paper concerning the temperature range over which Eq. (10) should be applicable. However, for the particular case which he has calculated it appears to be from 0°K up to about $\Theta/30$ and this range has been assumed valid for the present analysis. The curves in Fig. 2 indicate a value of γ a little greater than 4.3, and certainly between 4.2 and 4.4×10^{-4} cal/mole deg^2. Had indium not been a superconductor, values of γ between 4.3 and 4.4×10^{-4} would have been tried to find the most likely value. In this case, however, we seek results as consistent as possible with all the assumptions so we take only the outside limits on γ and continue the analysis to find if any value within these limits is consistent with the other assumptions.

Assumptions (5) and (6) yield the result that

$$C_{v,s}-C_{v,n}=[VH_0^2T/4\pi T_c^2][15(a-1)^2t^4-20a(a-1)t^3+6a^2t^2+6(a-1)t-2a]. \qquad (12)$$

Assumptions (1), (3), and (4) lead then to the following identification of terms in Eqs. (6) and (12),

$$\gamma=aVH_0^2/2\pi T_c^2. \qquad (13)$$

Using this result, it is possible to rearrange Eq. (12) in the following form,

$$\frac{2(C_{v,s}-C_{v,n})}{\gamma T(15t^4-20t^3+6t^2)}+\frac{15t^4-20t^3+2}{15t^4-20t^3+6t^2}=a-\alpha\left[\frac{15t^4-6t}{15t^4-20t^3+6t^2}\right], \qquad (14)$$

where

$$\alpha=1-(1/a). \qquad (15)$$

According to the definition of α in Eq. (15), Eq. (14) really involves two constants, γ and a, which are to be determined. However, Eq. (14) is quadratic in a, and

[26] Reference 3, Chap. III.

[27] M. Blackman, Proc. Roy. Soc. (London) **A159**, 416 (1937).

[28] From a purely empirical point of view, Eq. (10) may be interpreted as a theoretical justification for ignoring in the analysis the higher power terms permitted by the less stringent condition, Eq. (7).

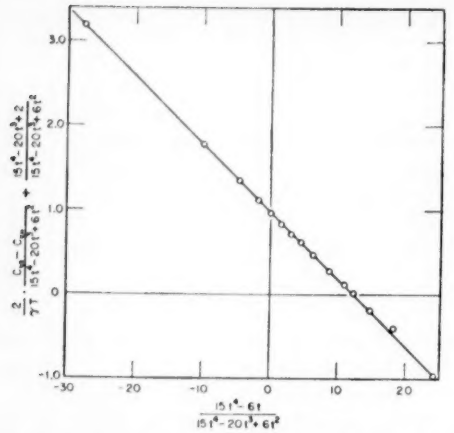

FIG. 3. Illustration of the method of determining a and α in Eq. (14), for the case $\gamma=4.2\times10^{-4}$ cal/mole deg^2.

no simple direct means could be found for evaluating the best values of these two constants. A rather convenient method which was used, and which has the advantage that both calorimetric and magnetic results can be compared in a single graph, is as follows. We suppose that Eq. (14) actually contains three constants, γ, a, and α. We choose a value for γ from the limits already determined from the normal state calorimetric data and evaluate a and α by the straight line graph method, which means that we plot the entire left side of Eq. (14) as a function of the bracketed portion on the right side. One such graph, for $\gamma=4.2\times10^{-4}$ cal/mole deg^2, is shown in Fig. 3. The points plotted in this figure were obtained from the differences in smoothed calorimetric data, and a point is included for each 0.1° interval between 1.8°K and 3.396°K. We now define, for a particular value of γ, two values of a in terms of the constants of the straight line like that in Fig. 3. One of these, $a(0)$, is the intercept of the line, and the other, $a(\alpha)$, results from substituting the slope of the line, α, into Eq. (15) and solving for $a(\alpha)$. After carrying out this procedure for several values of γ, curves can be constructed showing the dependence of $a(0)$ and $a(\alpha)$ on γ, and from the crossing point of these curves, if one exists, the set of values of γ and a which satisfy Eq. (14) can be found. Figure 4 shows such curves and yields the values, $\gamma=4.33\times10^{-4}$ cal/mole deg^2 and $a=1.105$.

The fact that the curves in Fig. 4 have a crossing point within the range of γ values obtained from the normal state data means that assumptions (2) and (3) can be satisfied with the values of a and γ indicated by the crossing point. However, a and γ also determine the critical field curve and it is not necessarily true that the crossing point of the $a(0)$ and $a(\alpha)$ curves will give a curve in agreement with magnetic data. Therefore, a shaded area has also been included in Fig. 4. This area represents the range of values of a and γ which can, within the spread in the existing data,[29-31] give critical field curves in agreement with experiment. The extent of this area was determined by drawing, for several values of a included on the curve, straight lines with reasonable maximum and minimum intercepts through plots of $H_c/(1-t^3)$ *versus* $(t^3-t^2)/(1-t^3)$. Such curves have intercepts equal to H_0 and slopes equal to aH_0. The maximum and minimum values of H_0 so determined were then substituted into Eq. (13) and the maximum and minimum values of γ calculated. From such a composite of experimental data as contained in Fig. 4 a set of values of a and γ which will be most nearly consistent with all the assumptions may be chosen. Since, in this particular case, the crossing point of the $a(0)$ and $a(\alpha)$ curves is within the shaded area, the exact values of a and γ at that point were used.

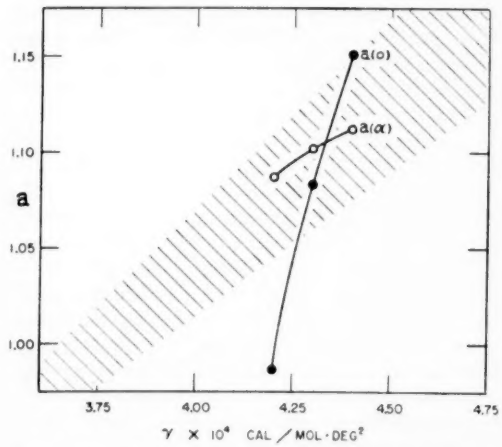

FIG. 4. Composite of experimental data for finding the values of a and γ most nearly consistent with the assumptions that $\Theta\rightarrow$constant as $T\rightarrow0$°K, the lattice heat is independent of the magnetic state, and transitions between the normal and superconducting states are thermodynamically reversible. The two curves, $a(0)$ and $a(\alpha)$, result from calorimetric data and the shaded area from magnetic data.

To carry out the analysis just described, numerical values for T_c and V were necessary. In two calorimetric runs on the indium sample, the transition from the superconducting to the normal state was observed with the sample in the earth's magnetic field. In both cases, the T_c value obtained was 3.390± about 0.005°K. Correcting for the earth's field, we get $T_c=3.396\pm0.005$°K. The transition of the sample was also determined magnetically by measuring the inductance of a coil wound directly on the sample as a function of temperature. This experiment gave a transition of 3.390°K in the earth's field and also results in a zero field transition of 3.396°K. The recent work of Stout

[29] J. W. Stout and L. Guttman, Phys. Rev. **88**, 703 (1952).
[30] Daunt, Horseman, and Mendelssohn, Phil. Mag. **27**, 754 (1939).
[31] A. D. Misener, Proc. Roy. Soc. (London) **A174**, 262 (1940).

and Guttman[29] on the critical fields of indium and indium-thallium alloys gave a zero field transition for pure indium of 3.396°K, that of Daunt *et al.*[30] on indium gave 3.4° and that of Misener[31] gave 3.386°K. The most likely value of T_c appears to be 3.396°K, and this value has been used throughout the analysis.

The V appearing in Eqs. (9), (12), and (13) should be the atomic volume at and below T_c. Since the thermal expansion vanishes, as required by the third law of thermodynamics, as the temperature approaches absolute zero, the atomic volume needed is simply that at absolute zero. The atomic volume at ordinary room temperatures, calculated from density[32,33] and x-ray crystallographic[34–36] measurements, ranges between 15.61 cm³ and 15.76 cm³, the most likely value being 15.76 cm³. Using the rather meager and conflicting data available on the thermal expansion of indium,[33]

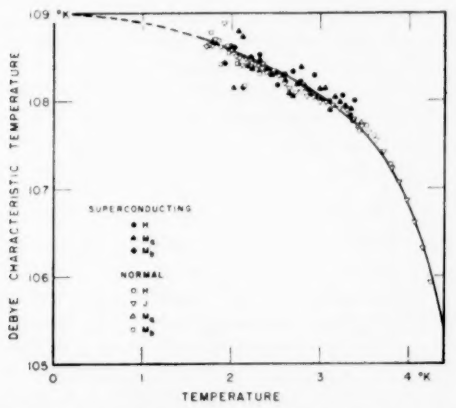

FIG. 5. Graphical test of compliance of the calorimetric data with the assumptions that $\Theta \to$ constant as $T \to 0$°K, the lattice heat is independent of the magnetic state, and the electronic heats may be deduced thermodynamically from a critical field equation of cubic analytic form. The legend in the figure identifies the experimental run (see Table I) in which the data were obtained.

with the Grueneisen[37] thermal expansion formula as an aid in extrapolating the data, the fractional change in volume between room temperature and the absolute zero is found to be between 0.020 and 0.037, the most likely value being about 0.027. From these data the atomic volume at 0°K should lie somewhere between 15.03 cm³ and 15.45 cm³. The most likely value appears to be 15.33 cm³, and this value has been used in the present analysis.

[32] *Handbook of Chemistry and Physics* (Chemical Rubber, Cleveland, 1947), 30th edition, p. 1686.
[33] P. Hidnert and M. G. Blair, J. Research Natl. Bur. Standards **30**, 427 (1943).
[34] Reference 32, p. 2016.
[35] L. K. Frevel and E. Ott, J. Am. Chem. Soc. **57**, 228 (1935).
[36] L. Guttman, J. Metals (Trans. Am. Inst. Mining Met. Engrs.) **188**, 1472 (1950).
[37] E. Grueneisen, *Handbuch der Physik* (J. Springer, Berlin, 1926), Vol. 10, p. 1.

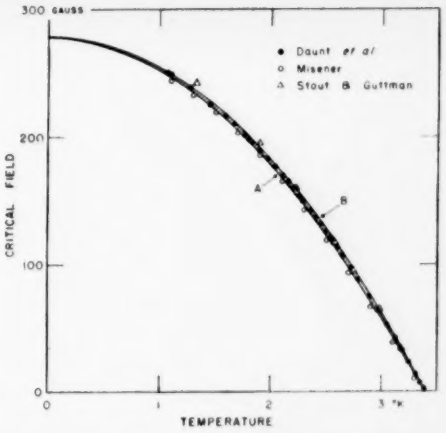

FIG. 6. Comparison of the experimental magnetic field data with two analytic curves deduced from calorimetric data. Curve A is the cubic form which corresponds to the results presented in Fig. 5 and curve B is the parabolic form which corresponds to the results presented in Fig. 7.

While Fig. 4 shows that a and γ can be chosen to give agreement with assumptions (2) and (3), it does not show directly how exact this agreement may be. For a more detailed examination, it is necessary to subtract the electronic atomic heats from the measured values for both the normal and superconducting states and compare the two Debye characteristic temperatures of the resulting lattice heats. Equations (12) and (13) lead to the conclusion that the electronic heat in the superconducting state $C_{e,s}$ is

$$C_{e,s}=(\gamma T/2a)[15(a-1)^2t^4-20a(a-1)t^3 +6a^2t^2+6(a-1)t]. \quad (16)$$

Using Beattie's[38] tabulated values of the Debye specific heat function, with $3R=5.960$ cal/mole deg, Θ values were calculated for each data point in the normal state after subtracting the normal electronic heat as given by Eq. (6) and for each point in the superconducting state after subtracting the value calculated according to Eq. (16), the constants being $\gamma=4.33\times10^{-4}$ cal/mole deg², $a=1.105$ and $T_c=3.396$°K. Figure 5 shows the results with the data from the different experimental runs distinguished from each other. Both assumptions (2) and (3) are seen to be satisfied within experimental error and the agreement between the data for different heating rates is evident.

Figure 4 also indicates that there will be some semblance of agreement between the measured critical field data and the cubic curve deduced from the chosen values of a and γ. However, there is even less indication in this case than in the preceding one of how exact this agreement may be. Figure 6 shows the data of Stout and Guttman,[29] Daunt *et al.*,[30] and Misener,[31] together with two smooth curves deduced directly from

[38] J. A. Beattie, J. Math. and Phys. **6**, 1 (1926–1927).

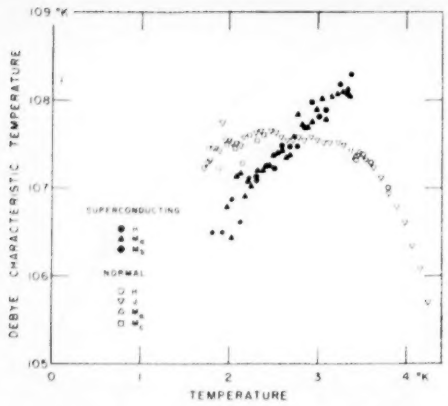

FIG. 7. Graphical test of compliance of the calorimetric data with the assumptions that $\Theta \to$ constant as $T \to 0°K$, the lattice heat is independent of the magnetic state, and the electronic heats may be deduced thermodynamically from a critical field equation of parabolic analytic form. The legend in the figure identifies the experimental run (see Table I) in which the data were obtained.

the calorimetric data. Curve A is calculated from Eq. (8) with $H_0 = 278.4$ gauss, $a = 1.105$, and $T_c = 3.396°K$. The value of H_0 results from substituting numerical data into Eq. (13). The measured values of Daunt *et al.* are rather close to this smooth curve while the other two sets of data fall on either side. Some uncertainty is present in the smooth curve because of uncertainty in the low temperature atomic volume. Based on the estimated uncertainty in the atomic volume noted above, however, the uncertainty in the critical field curve from this source should not exceed 1 percent.

One difficulty in the foregoing analysis is that it provides no indication of how well the several assumptions can be satisfied if the parabolic form of the critical field curve is used in place of the more flexible cubic form. From Fig. 4 it is apparent that some agreement between the critical field data and a parabolic curve can be obtained with γ values between 3.65×10^{-4} and 3.90×10^{-4} cal/mole deg^2. However, Fig. 2 shows that γ must be considerably higher than the highest of these values to be in agreement with assumption (2). The possibility of satisfying assumption (3) was investigated by calculating the lattice Θ's for the normal and superconducting states after subtracting the appropriate electronic atomic heats given by Eqs. (6) and (16) with $a \equiv 1$, $T_c = 3.396°K$ and γ values of 3.65, 3.90, and 4.33×10^{-4} cal/mole deg^2. In no case was assumption (3) satisfied even approximately within experimental error. The results obtained with $\gamma = 3.90 \times 10^{-4}$ cal/mole deg^2, the value most nearly consistent with both calorimetric data and a parabolic critical field curve, are shown in Fig. 7. The appearance of the data for $\gamma = 4.33 \times 10^{-4}$ was somewhat similar, the superconducting state data having about the same slope relative to the normal state data but crossing the normal data at a lower temperature. Curve B of Fig. 6 is the parabolic curve calculated from Eq. (8) with $H_0 = 278.3$ gauss and $a \equiv 1$. This value of H_0 results from substituting numerical data into Eq. (13), $a \equiv 1$, $T_c = 3.396°$, $\gamma = 3.90 \times 10^{-4}$ cal/mole deg^2 and $V = 15.33$ cm^3.

Figures 5 and 7 form a dramatic illustration of the sensitivity of the derived electronic heat capacities to the shape of the critical field curve. So far as the magnetic data are concerned, curve A, the cubic, and curve B, the parabola, of Fig. 6 are essentially the same. However, when thermodynamics is applied to these equations to obtain the electronic heats, the calorimetric results are remarkably different as shown by comparing Fig. 5, the results of the cubic curve, with Fig. 7, the results of the parabolic curve.

Finally, the temperature dependence of the Debye characteristic temperature of the lattice over the entire temperature range of measurement may be compared with theoretical results when the discrete nature of the lattice is taken into account in calculating a vibration spectrum. Generally, these calculations have resulted in qualitatively similar curves,[1,27] having the following principal features in the temperature range for which indium data are available. Θ starts from some roughly constant value near 0°K, drops with rising temperature, passes through a minimum, then rises again with further increase in temperature to some other value which may, or may not, represent a maximum. Indium crystallizes in the face-centered tetragonal structure so that no existing calculations can be applied in any quantitative manner. However, Fig. 8, a plot of Θ *versus* T for indium, shows that the variation of Θ with T follows the general behavior outlined above. The agreement between data obtained with different heating rates is apparent. It might also be noted that the Θ curve extrapolates, as indicated in Fig. 5, to 109.0°K at the absolute zero, the absolute uncertainty in this extrapolated value being perhaps $\pm 0.3°K$.

SUMMARY

A calorimetric technique employing a carbon-composition resistor simultaneously as both heater and thermometer was developed. The principal observations during a calorimetric experiment, the time dependence of the resistance of this thermometer-heater, are automatically recorded. Heat capacities are deduced from the initial data by a time derivative method, and criteria for testing the validity of the method on the basis of results of a single run were given.

Using this technique, the atomic heat of indium was measured in the normal state from 1.7°K to 21.3°K and in the superconducting state from 1.8°K to 3.396°K, the transition temperature in zero magnetic field. The results exhibited a high degree of consistency, the standard deviation of the data from a smooth curve

being between 0.3 and 0.4 percent. Tables of smoothed values were given, the absolute uncertainty in the tabulated values being probably less than 1 percent.

A method of deducing the separate lattice and electronic contributions to the heat capacities, based on several empirically and/or theoretically tenable assumptions was developed. Among these assumptions were that the Debye characteristic temperature of the lattice approaches a constant as the temperature approaches the absolute zero, the lattice heat of a superconductor is independent of the magnetic state, the heat capacity of a superconductor has no linear temperature term, and the equation of the critical magnetic field is of cubic analytic form. The method of analysis was applied to the indium data and yielded conclusions consistent with all the assumptions. The numerical values of several constants deduced for, or resulting from, this analysis are collected in Table IV. It was further demonstrated that such mutually consistent conclusions could not be found if a parabolic form for the critical field equation was assumed, even though the parabola used was in essentially as good agreement with critical field data as the cubic curve.

Finally, the temperature dependence of the Debye characteristic temperature of the lattice over the entire range of measurement was shown to be in qualitative agreement with that which would be expected on the basis of the few existing calculations which take more complete account of the discrete nature of the crystalline lattice than the Debye continuum theory.

TABLE IV. Low temperature physical constants of indium.

Constant	Numerical value
γ	4.33×10^{-4} cal/mole deg^2
a	1.105
T_c	3.396°K
V (0°K)	15.33 cm^3
H_0	278.4 gauss
Θ (0°K)	109.0°K

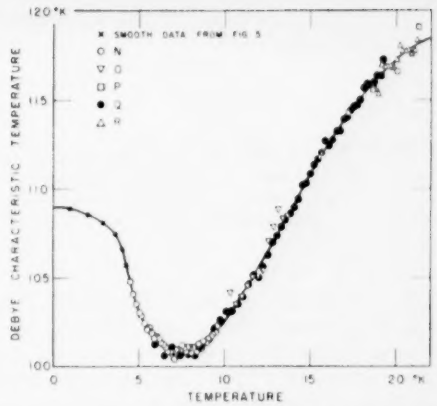

FIG. 8. Curve showing the variation of Θ of the indium lattice with T over the entire range of measurement. The legend in the figure identifies the experimental run (see Table I) in which the data were obtained.

The authors wish to express their appreciation to the various members of the Cryogenics Branch of this Laboratory, in particular to R. L. Dolecek, J. R. de Launay, M. F. M. Osborne, and R. T. Webber, for many helpful discussions during the course of this investigation.

Note added in proof:—Since the completion of this report, the results of some calorimetric measurements on indium between 12°K and 273°K [K. Clusius and L. Schachinger, Z. angew. Physik **4**, 442 (1952)] have come to the authors' attention. The two sets of data are in good agreement at about 21°K but gradually deviate from each other with decreasing temperature, becoming finally 4 to 5 percent different at about 12°K, the data of Clusius and Schachinger being the higher.

The actual experimental data on which the present report was based are contained in Naval Research Laboratory Document No. 106435 (August 1953).

Sign of the Quadrupole Interaction of Li^6 in LiCl†

P. KUSCH
Columbia University, New York, New York
(Received June 23, 1953)

The sign of the quadrupole interaction energy of Li^6 in LiCl has been found to be positive. Previous determinations have shown that the quadrupole interaction energy of Li^7 in the same molecule is also positive. It may, therefore, be concluded that both of the stable isotopes of lithium have a quadrupole moment of the same sign, though the sign itself is not known.

THE signs of the quadrupole interaction energies of certain of the alkali atoms in the homonuclear diatomic molecules and in some of the alkali halides have been determined[1,2] by a method which involves the selection of states of either positive or negative magnetic moment for observation by the molecular beam magnetic resonance method. The sign of the quadrupole interaction energy (eqQ) does not, of course, yield information as to the sign of the electric quadrupole moment, Q, of the nucleus. Considerable uncertainty exists[3] in determination of the sign of $Q(Li^7)$ from the data on $(Li^7)_2$ because of the limited accuracy of the electronic wave functions of Li_2 in the determination of the gradient, q, of the electric field at the Li nucleus. Nevertheless, both the sign and the magnitude of the ratio of the quadrupole moments of two isotopic nuclei can be determined unambiguously from a measurement of the sign and magnitude of the quadrupole interaction energies in the same molecule, since q is very closely the same for both isotopes. The magnitude of the ratio of the quadrupole moments $|Q(Li^6)/Q(Li^7)|$ has been found[4] to be 0.023 ± 0.002, but the sign of the ratio has not previously been determined. In LiCl $(eqQ)_7=192$ kc/sec, so that, in the same molecule, $(eqQ)_6=4.4$ kc/sec.

In the work of Feld and Lamb,[5] the high field resonance spectrum of Li^6 or any other nucleus of spin 1 in a diatomic molecule is shown to consist of two intensity distributions resulting from the transitions $m_I=1\leftrightarrow m_I=0$ and $m_I=0\leftrightarrow m_I=-1$, whose maxima are symmetrical about the frequency $g_I(Li^6)\mu_0H/h$ and are separated from each other by a frequency interval of $3eqQ/8h$, which is here 1.7 kc/sec. The spectrum is actually observed[6] as a single unresolved maximum with a half-width of 5.5 kc/sec. The lack of resolution can be accounted for solely in terms of the natural half width of the separate lines which compose the spectrum since in the presently available apparatus with a transition length of 28 cm over which the rf amplitude is applied, the natural half-width is 2.2 kc/sec. The width of the resonance spectrum is, in addition, increased by the distribution within a finite frequency interval of the lines which contribute to the spectrum, both because of the quadrupole interaction and because of an interaction between the nuclear magnetic moment and the magnetic field arising from the molecular rotation.

The determination of the sign of the quadrupole interaction energy depends on a redistribution of intensity within the spectrum when states characterized by either positive or negative m_I are removed from a molecular beam. It is possible, by presently available methods, to select molecules characterized by either a total positive or a total negative magnetic moment. In order that this selection should be effective in selecting states in which the moment of the nucleus in question is either positive or negative, it is necessary that the other nucleus which comprises the diatomic molecule have a relatively small magnetic moment. Clearly, the the only lithium halide in which the Li^6 nucleus gives a major contribution to the total molecular magnetic moment is LiCl. In all the other halides of Li,[6] the preferential removal of states in which the moment of Li^6 is, say, positive, is extremely inefficient.

The preferential removal of states of positive m_I by an obstacle is limited by the small magnetic moment of the Li^6 nucleus. At the position of the obstacle in the present apparatus the width of the beam is about 4×10^{-3} cm and the deflection of an Li^6Cl^{35} molecule of maximum moment and velocity α the most probable velocity in the oven, is 2.9×10^{-3} cm. Accordingly, since the deflection pattern is comparable in width to the beam itself, a reduction in the intensity of the total beam to half of its original value by interposition of the obstacle from one side of the beam has only a limited effect in removing molecules characterized by a magnetic moment of a particular sign. A detailed calculation for Li^6Cl^{35} for the particular conditions of these experiments indicates that interposition of an obstacle to the center of the undeflected beam from the side of the beam on which m_I for Li^6 is positive, decreases the populations of states for which m_I is $+1$ from 1 to 0.28, that of states for which m_I is 0 from 1 to 0.50 and that of states for which m_I is -1 from 1 to 0.72.

The calculation of line intensities from the popula-

† This research was supported in part by the U. S. Office of Naval Research.
[1] P. Kusch, Phys. Rev. **76**, 138 (1949).
[2] Logan, Coté, and Kusch, Phys. Rev. **86**, 280 (1952).
[3] E. G. Harris and M. A. Melkanoff, Phys. Rev. **90**, 585 (1953).
[4] N. A. Schuster and G. E. Pake, Phys. Rev. **81**, 157 (1951).
[5] B. T. Feld and W. E. Lamb, Phys. Rev. **67**, 15 (1945).
[6] P. Kusch, Phys. Rev. **75**, 887 (1949).

tions of the states is subject to a considerable uncertainity. If it is assumed that the two components of the spectrum are independent, the intensities of the components are proportional to the sums of the population of the terminal states; in the case here discussed the intensities of the lines $1\leftrightarrow 0$ and $0\leftrightarrow -1$ are then 0.78 and 1.22 respectively. As a further approximation it is possible to assume that each of the two components can be represented by the usual resonance curve with a width at half-intensity of 5.0 kc/sec. The superposition of two such curves, whose centers are separated by 1.7 kc/sec and of relative intensities 0.78 and 1.22, yields a maximum which is shifted by about 0.22 kc/sec from the maximum obtained by the superposition of two curves of equal intensity. Since the shift may be reversed in sign by interposition of the obstacle into the beam from the side on which m_I is negative, a total displacement of the maximum by 0.44 kc/sec when the obstacle is shifted from one side of the beam to the other may be anticipated.

Because of the considerable overlapping of the two components of the pattern there will be a competition for the $m_I=0$ state. In the limiting case, when at any frequency the probability of transition to $+1$ and -1 is equally great, the relative intensities of the two components are 0.53 and 0.97. An estimate of the shift of the maximum as the obstacle is moved from one side of the beam to the other is then 0.54 kc/sec. It is to be noted that the spectrum becomes slightly unsymmetrical in shape when the beam is partially cut. The center of the intensity distribution is here determined at a point midway between two points of $\frac{3}{4}$ the maximum intensity, since such a determination can much more readily be made experimentally than can a determination of the point of maximum intensity. The difference between the center as here determined and the true maximum is very small and is much less than the errors introduced by the approximations of the model.

The nuclear resonance of Li^6 in LiCl has been observed at a field of about 3100 gauss. At this field the Li^6 nucleus is wholly decoupled from the molecular rotation and the high-field treatment of Feld and Lamb is completely applicable. The experimental arrangements have been discussed previously.[2] For the present purposes, LiCl in which the Li^6 was enriched to 95.2 percent was used. With this sample, the Li^6 resonance had a maximum depth of about 13 percent of the beam and it was possible to determine the center of the resonance with considerable accuracy.

The experimental procedure is to reduce the intensity of the beam at the detector to some fraction of its original value by interposing an obstacle first on the side of the beam on which the total moment is positive and then on the side on which it is negative. The frequency of the center is determined in each case by observation of points of equal intensity on either side of the center of the resonance. During a run a small drift in the field may occur which may give rise to a frequency shift between successive observations comparable to the shift arising from the selection of states. It is obviously possible to avoid significant error by a sufficiently long sequence of observations. The result of a typical run is shown in Fig. 1, where the frequency of the resonance center is plotted as a function of the current in the magnet coils as the beam is alternately cut from the two sides to one half of its full intensity. The data indicate that $(eqQ)_6$ is positive, as for the quadrupole interaction energy of Li^7 in the same molecule. Other data taken under different experimental conditions in which the direction of all fields in the apparatus was reversed and in which the fraction of the beam removed by the obstacle was varied give the same clear result as that shown in Fig. 1, both in the magnitude and the sign of the shift. A number of runs made with LiCl with a normal abundance of Li^6 also give a positive $(eqQ)_6$, though the data are inferior to those obtained with the enriched sample. The mean shift observed in enriched LiCl, where the data are good, when the beam was cut to one-half of its full value is 0.44 kc/sec, in excellent agreement with that obtained from the approximate calculations.

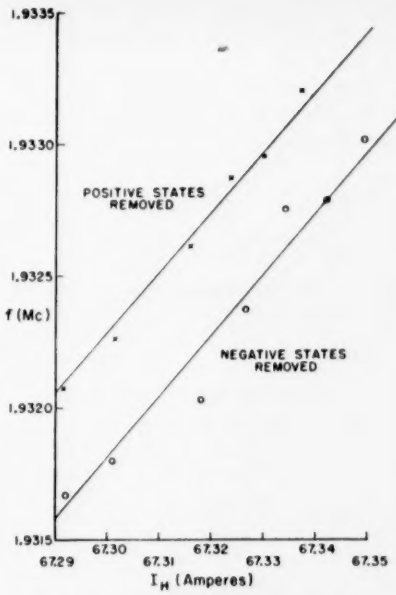

FIG. 1. The frequency of the center of the Li^6 resonance in LiCl as a function of field current as states of either positive or negative m_I are selectively removed from the beam.

While a small variation of q may be expected between the molecules of LiCl of different isotopic constitution because of a small variation of the internuclear distance, this variation can hardly be of sufficient magnitude to reverse the sign of q. The consistency of the shift observed in these experiments with the ratio $|Q_6/Q_7|$ found by Schuster and Pake[4] from

observations on $LiAl(SiO_3)_2$ offers experimental evidence that q is not markedly different for a molecule containing Li^6 or Li^7. It is, therefore, concluded that the sign of the quadrupole moment of Li^6 is the same as that of Li^7. Previous data obtained by the method of molecular beams have been able to give only an upper limit for $|Q_6/Q_7|$. The present data indicate that Q_6 is other than zero and give at least a rough quantitiative verification of the result of Schuster and Pake of the value of $|Q_6/Q_7|$.

The aid of Mr. Thomas Eck in obtaining the data of the experiment is gratefully acknowledged.

PHYSICAL REVIEW VOLUME 92, NUMBER 2 OCTOBER 15, 1953

Change in the Inversion Spectrum of ND_3 from Resonant to Nonresonant Absorption*

G. Birnbaum and A. A. Maryott
National Bureau of Standards, Washington D. C.
(Received July 2, 1953)

The absorption due to the inversion spectrum of ND_3 centered near 1600 Mc/sec was measured at pressures from 0.3 to 80 cm Hg in the frequency interval 1100 to 2600 Mc/sec. The inversion frequency was found to decrease with increasing pressure and became substantially zero at about 9 cm Hg. This change occurs at pressures about 15-fold lower than for NH_3, a result in accord with Margenau's theory. At the higher pressures where the absorption is of the nonresonant or Debye type, the collision diameter is about 6.9A, a value roughly one-half that associated with resonant absorption at low pressures.

1. INTRODUCTION

COLLISION broadening in the microwave inversion spectrum of NH_3 near 24 000 Mc/sec has been studied extensively, both at pressures below 1 mm Hg where the considerable fine structure is completely resolved and at higher pressures where the lines become so broad that this structure is completely obliterated. Working in the pressure region from 10 cm Hg to several atmospheres, Weingarten[1] and Bleaney and Loubser[2] found that the unresolved spectrum could be represented by a single Van Vleck-Weisskopf line shape factor provided empirical values were chosen for the line width and resonance frequency. They showed that the resonance frequency decreased as the pressure was increased and became substantially zero for pressures above two atmospheres. The line width was found to rise much less rapidly than the pressure in the transition region, but, as shown by the more detailed experiments of Bleaney and Loubser, to become proportional to the pressure above four atmospheres. The effective collision diameter appeared to change from an initial value in the neighborhood of 13A to about 7.7A at the higher pressures, a change which was attributed to the effect of multiple collisions.

A similar behavior is to be expected for the completely deuterated ammonia ND_3 which in its ground vibrational state has an inversion resonance near 1600 Mc/sec.[3,4] However, on the basis of the theoretical treatment of Margenau,[5] the shift in the inversion frequency should occur at pressures about 15-fold lower than in the case of NH_3. In this event the effect of multiple collisions on the spectral broadening process should be relatively unimportant.

Measurements of the absorption in ND_3 were made at a number of pressures between 0.3 and 80 cm Hg in the frequency interval 1100 to 2600 Mc/sec. The results are in accord with the predictions from Margenau's theory. A definite shift in frequency is evident at a pressure as low as 1 cm Hg. Above 9 cm Hg the inversion frequency has become effectively zero and the transition from resonant to nonresonant or Debye absorption is virtually complete.

2. EXPERIMENTAL

A hybrid mode cylindrical cavity,[6] tunable by a movable center post from 1100 to 2600 Mc/sec, was used as the gas absorption cell. Over this frequency range the loaded Q of the empty cavity varied from 3000 to 5000. The absorption coefficient of the gas was determined as described previously[7,8] from the cavity response curve displayed on an oscilloscope. At the lower pressures the absorption was obtained from the initial Q and relative power transmitted by the cavity. At the higher pressures the absorption was also obtained from measurements of the Q's of the empty and gas-filled cavity.

Calibrated attenuators were used to obtain the law of the crystal detector several times throughout the course of the investigation. The power level at the

* Presented at the St. Louis meeting of the American Physical Society, 1952 [Phys. Rev. 89, 895 (1953)].

[1] I. R. Weingarten, Thesis, Columbia University, New York, 1948 (unpublished).

[2] B. Bleaney and J. H. N. Loubser, Proc. Phys. Soc. (London) A63, 483 (1950).

[3] Nuckolls, Rueger, and Lyons, Phys. Rev. 89, 1101 (1953).

[4] Unpublished calculations of J. R. Madigan, A. Javan, and J. F. Lotspeich.

[5] H. Margenau, Phys. Rev. 76, 1423 (1949).

[6] L. Essen, Wireless Engr. 23, 126 (1946).

[7] G. Birnbaum and A. A. Maryott, J. Chem. Phys. (to be published).

[8] Birnbaum, Kryder, and Lyons, J. Appl. Phys. 22, 95 (1951).

crystal was in the neighborhood of several microwatts, and the crystal was found to exhibit square law behavior in all instances.

The ND_3 gas[9] was condensed in a liquid nitrogen trap and used repeatedly. However, frequent checks of the absorption with fresh samples showed that no detectable contamination occurred in the sample. All measurements were made at a temperature of about 25°C.

The sensitivity of measurement corresponded to about 5×10^{-7} cm^{-1} in absorption. From the reproducibility of the data, test measurements on NH_3 whose absorption had been determined previously,[7] and a search for systematic errors, it is felt that the experimental accuracy is in the neighborhood of 5 percent except where limited by sensitivity at lower pressures.

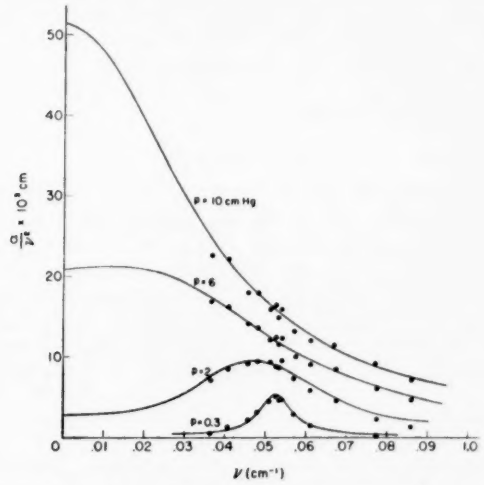

FIG. 1. Variation of $\alpha/\nu^2\times10^3$ with wave number ν at various pressures for ND_3.

3. RESULTS

Since the experimental results are interpreted with the aid of the Van Vleck-Weisskopf equation, it is convenient to describe first the manner in which this equation is used. When the widths of the individual lines become large compared with their separation, it becomes possible to represent approximately the absorption due to the unresolved band by the Van Vleck-Weisskopf formula[10] in the form,

$$\frac{\alpha}{\nu^2}=\frac{4\pi^2N}{3kT}\sum_{J,K}f_{J,K}|\mu_{JK}|^2 \times\left(\frac{\Delta\nu}{\Delta\nu^2+(\nu_0-\nu)^2}+\frac{\Delta\nu}{\Delta\nu^2+(\nu_0+\nu)^2}\right), \quad (1)$$

[9] Synthesized from 99.8 percent D_2O by the Texas Research Foundation, Renner, Texas.

[10] J. H. Van Vleck and V. F. Weisskopf, Revs. Modern Phys. **17**, 227 (1945).

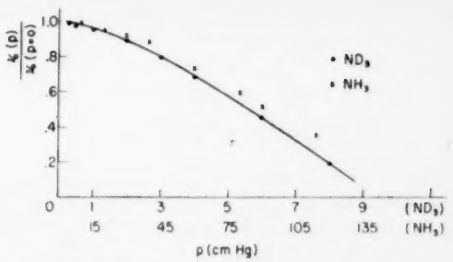

FIG. 2. Variation of the ratio of the inversion frequency at finite pressures $\nu_0(p)$ to that at zero pressure $\nu_0(p=0)$ as a function of pressure: ●ND_3—present data; ×NH_3—Bleaney and Loubser.

where the individual line shape factors have been replaced by a single term having an effective line breadth $\Delta\nu$ and a resonance frequency, ν_0. The quantities α, ν_0, ν, and $\Delta\nu$ are in cm^{-1}. The quantity $f_{J,K}$ is the fractional number of molecules occupying the J, K rotational energy levels, $|\mu_{J,K}|^2=\mu^2K^2/(J^2+J)$, and N is the number of molecules per cc. Calculations made at 25°C gave

$$\sum_{J,K}f_{J,K}|\mu_{J,K}|^2=0.40_0\mu^2,$$

a result virtually the same as that for NH_3. With the permanent dipole moment μ taken to have the value 1.47×10^{-18} esu,[11] Eq. (1) reduces to

$$\frac{\alpha}{\nu^2}=9.00\times10^{-5}p\left(\frac{\Delta\nu}{\Delta\nu^2+(\nu_0-\nu)^2}+\frac{\Delta\nu}{\Delta\nu^2+(\nu_0+\nu)^2}\right), \quad (2)$$

where p is the pressure in cm Hg.

Experimental values of α/ν^2 plotted against ν for several pressures are shown in Fig. 1 together with the curves computed from Eq. (2) by using empirical values of ν_0 and $\Delta\nu$ to give the best fit at each pressure. The calculated curves show satisfactory agreement with the experimental data. At a pressure of 0.3 cm Hg, the absorption maximum appears at a wave number of 0.0526 cm^{-1}. However, a plot of ν_0 *versus* pressure suggests that even at this low pressure a slight shift in resonance frequency has occurred. Extrapolation to zero pressure gives an effective value of 0.0532 cm^{-1}. This value is in very close agreement with that calculated by Madigan *et al.*[4] for the inversion splitting of the ground vibrational level, namely 0.0534 cm^{-1}. As the pressure increases, there is a progressive shift in the frequency of maximum absorption to lower frequencies. When the pressure reaches about 10 cm Hg, the resonance frequency appears to be indistinguishable from zero.

In Fig. 2 the ratio of the inversion frequency of ND_3 at some pressure p to the value extrapolated to zero pressure is plotted for each pressure examined in the region 0.3 to 8 cm Hg. Values at the two highest pres-

[11] Within the experimental accuracy, $\mu(NH_3)=\mu(ND_3)$. See A. A. Maryott and F. Buckley, "Table of dielectric constants and electric dipole moments of substances in the gaseous state," National Bureau of Standards Circular 537.

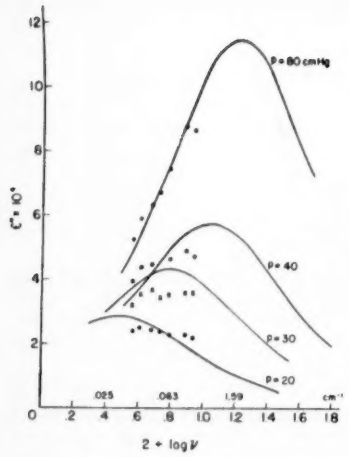

FIG. 3. Variation of the dielectric loss factor $\epsilon'' \times 10^4$ of ND_3 with $\log\nu$ at various pressures above 10 cm Hg.

sures where the calculated absorption is relatively insensitive to the choice of ν_0 are rather approximate. For comparison, the data of Bleaney and Loubser[12] on NH_3 are included but on a pressure scale reduced by a factor of 15. The significance of the close parallelism of the two sets of data when compared on this basis will be discussed subsequently.

At the higher pressures where the resonance frequency is zero, Eq. (2) reduces to

$$\frac{\alpha}{2\pi\nu}=\epsilon''=2.86\times10^{-5}p\left(\frac{\nu\Delta\nu}{\Delta\nu^2+\nu^2}\right), \tag{3}$$

where ϵ'' is the dielectric loss factor. In this case it is convenient to represent the data by plots of ϵ'' against $\log\nu$, as shown in Fig. 3. Such plots are customarily used for the nonresonant absorption found in polar liquids and solids, and as may be easily verified, ϵ'' has a maximum value when $\nu=\Delta\nu$.

In view of the considerable breadth of the nonresonant absorption band, the present data cover a rather limited portion of the pertinent frequency region. However, at pressures of 60 (not shown) and 80 cm Hg, the data are in good agreement with the curves calculated by empirical adjustment of $\Delta\nu$. At 20, 30, and 40 cm Hg the absorption band appears to be somewhat broader than that required by Eq. (3). Such behavior is observed in liquids and solids when there is a distribution of relaxation times, or in the present terminology a distribution of $\Delta\nu$'s. On the other hand, data at 10 cm Hg where ν_0 was also zero show no such anomaly. However, data over a more extended range of frequencies are needed before any particular significance can be attached to the deviations noted.

Values of the line breadth parameter $\Delta\nu/p$ obtained by fitting Eqs. (2) or (3) to the data at each pressure are plotted in Fig. 4. For comparison the corresponding values obtained for NH_3 by Bleaney and Loubser[12] are included but on a pressure scale reduced by a factor of 15. Except for the ND_3 points at 20 and 30 cm Hg where the significance of a single $\Delta\nu$ appears to be uncertain, the line breadth parameters show comparable variations for both gases.

[13] Reference 2 and a private communication.

4. DISCUSSION

A qualitative interpretation of the observed frequency shift in NH_3 has been given by Anderson[13] and a quantitative treatment has been attempted by Margenau.[5] They pointed out that the dipole interaction between two isolated ammonia molecules can become large enough to cause a change in the molecular wave functions and hence in the selection rules for the inversion transition. In this case Margenau found that two possible transitions with different frequencies are produced, one smaller and the other larger than the normal frequency. With increasing interaction the strength of the lower frequency transition increases greatly at the expense of the other. By considering only the dominant or low-frequency component, the resonance frequency for a pressure p is given by

$$\nu_0'=\nu_0[(1+\lambda^2)^{\frac{1}{2}}-\lambda],$$

where $\lambda\approx2\mu^2N/\Delta E$ and $\Delta E=h\nu_0 c$ is the transition energy associated with the unperturbed inversion. As $\Delta E(NH_3)/\Delta E(ND_3)=14.8$, a given fractional shift in resonance frequency for each gas should occur at pressures in the inverse ratio.[14] This relationship is substantiated by the data of Fig. 2 which show that a given fractional change in the resonance frequency of ND_3 takes place at a pressure approximately 15 times lower

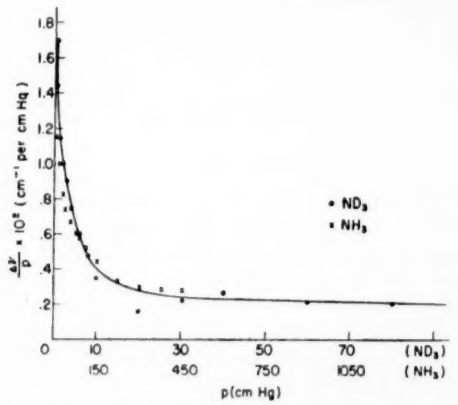

FIG. 4. Variation of the bandwidth parameter $\Delta\nu/p$ with pressure: $\bullet ND_3$—present data; $\times NH_3$—Bleaney and Loubser.

[13] P. W. Anderson, Phys. Rev. **75**, 1450 (1949).

[14] The absorption spectrum of ND_3 in its first excited vibrational state was measured between 24 000 and 145 000 Mc/sec at 20, 50, and 76 cm Hg by J. H. N. Loubser and J. A. Klein [Phys. Rev. **78**, 348 (1950) and Columbia Radiation Laboratory Quarterly Report, Sept. 1949 (unpublished)]. At these pressures the absorption curves show that the resonance frequency is at 1.2×10^5 Mc/sec. It would be interesting to see if this frequency shifts downward at higher pressures.

than in NH_3. At a pressure of 6 cm Hg where $\lambda=0.81$ for ND_3, $\nu_0'/\nu_0=0.48$ which is virtually the same as the experimental value of 0.45. At higher pressures the resonance frequency drops to zero more rapidly than predicted from a consideration of two interacting molecules. As indicated by Margenau, such behavior would be expected if interactions between three or more molecules become effective at these higher pressures.

We next wish to consider the observed variation of the band width parameter ($\Delta\nu/p$) with pressure. However, before doing so, it will be instructive to consider the variation of the individual line widths with pressure from pressures where the lines are completely resolved up to pressures where the fine structure is completely obliterated but the frequency shift is not appreciable.[15] Bleaney and Penrose[16] have shown that $\Delta\nu_{JK}$ is proportional to p for NH_3 in the region in question by demonstrating close agreement between the experimental peak absorption and that obtained by summing the Van Vleck-Weisskopf equation over the rotational states. We proceeded similarly for ND_3 by using the empirical formula of Nuckolls *et al.*[3] for the resonance frequencies and the formula of Bleaney and Penrose[16] for the line widths. The latter formula is based on measurements of the individual NH_3 lines, but according to Anderson's theory[17] it should apply without large error to the ND_3 lines, whose widths have not been measured as yet. The theoretical value of α/ν^2 (at 0.3 cm Hg and at 0.0526 cm^{-1}) was thus found to be 4.7×10^{-3} cm, about 10 percent lower than the experimental value. However, this difference might easily arise from the error in the measured value and from inaccuracies in the line width and frequency formulas.

With reference to Fig. 4, it is seen that $\Delta\nu/p$ for both NH_3 and ND_3 first decreases very rapidly in the transition region, and finally becomes substantially constant as the pressure is increased to the highest values. At the lowest pressures the separation of the individual unresolved lines is not yet negligible compared with their widths. Thus the values of $\Delta\nu/p$ which represent the width of the band of lines are significantly larger than the average width of the individual lines. Therefore the initial rapid change of the apparent $\Delta\nu/p$ with pressure does not necessarily imply a nonlinear variation of widths or a change in collision diameters of the individual lines.

At intermediate pressures $\Delta\nu/p$ falls well below the value calculated from the low-pressure collision diameters. Bleaney and Loubser[2] attributed this behavior in the case of NH_3 to the effect of multiple collisions. On this basis they derived the expression:

$$\Delta\nu/p \propto 1-(4\pi b^3N)/3,$$

which fitted surprisingly well their measured variation of $\Delta\nu/p$ in the transition region. In the above expression b is the collision diameter for which they used an average value of 13A. This expression, however, cannot account for the corresponding $\Delta\nu/p$ variation in ND_3 for this occurs at pressures 15-fold lower, yet the value of b is almost the same as that for NH_3. Thus $(4\pi b^3N)/3$, the term arising from multiple collisions, should be small and $\Delta\nu/p(ND_3)$ in contrast with experiment should be rather insensitive to pressure in the region under consideration.

At the highest pressures where $\Delta\nu/p$ is substantially constant, the collision diameter for ND_3 calculated from the usual kinetic formula,

$$\Delta\nu=\frac{2N}{c}\left(\frac{RT}{\pi M}\right)^{\frac{1}{2}}b^2,$$

reaches the limiting value of 6.9A, which is somewhat lower than the value 7.7A reported for NH_3. It is interesting to observe that these collision diameters are considerably less than those associated with the resonance absorption but still definitely larger than the kinetic diameters. There appears to be no theoretical treatment of collision diameters for non-resonant absorption in dilute gases.[18]

In the preceding discussion it may have been noticed that use was made of both statistical and impact theories. Thus on the one hand, the molecules were considered always under the influence of intermolecular interactions which are sufficiently strong to destroy the inversion resonance at a pressure of only 9 cm Hg (ND_3) where the average intermolecular distance is 70A. On the other hand, the line-shape equation used is based on impact theory. Furthermore, collision cross sections were obtained on this basis which requires that most of the time a molecule is sufficiently far from other molecules so that it may be considered as free. As yet there appears to be no unified treatment of the ammonia problem.

ACKNOWLEDGMENT

The authors take pleasure in thanking Mr. S. J. Kryder for assisting with the measurements, Dr. C. R. Greenhow for several valuable discussions, and Dr. H. Lyons for his interest in this work.

[15] About 0.3 cm Hg for ND_3 and 10 cm Hg for NH_3.

[16] B. Bleaney and R. P. Penrose, Proc. Phys. Soc. (London) **69**, 418 (1947).

[17] Provided that broadening arising from rotational resonance is neglected, Anderson's theory shows that $\Delta\nu$ is proportional to $\bar{\mu}_2$, the dipole moment along the axis of total angular momentum averaged over the states of the colliding molecule. [See W. F. Smith and R. Howard, Phys. Rev. **79**, 132 (1950)]. The quantity $\bar{\mu}_2$ for ND_3 equals 0.797×10^{-18} esu, about 3 percent higher than that for NH_3. Consequently, corresponding line widths for ND_3 should differ by the same amount.

[18] A suggestion in this direction has been made by P. W. Anderson in reference 13.

One-to-Two Millimeter Wave Spectroscopy. II. H_2S†

CHARLES A. BURRUS, JR.,* AND WALTER GORDY
Department of Physics, Duke University, Durham, North Carolina

(Received June 24, 1953)

Pure rotational transitions of H_2S^{32}, H_2S^{33}, and H_2S^{34} have been measured with high precision in the region of one to two millimeters. From these measurements the SH bond length is found to be 1.3226A and the bond angle to be 92° 6′. The S^{33} nuclear quadrupole coupling observed along the principal inertial axes are $eQq_{aa}=-32$ Mc/sec, $eQq_{bb}=-8$ Mc/sec, and $eQq_{cc}=+40$ Mc/sec. Approximate analysis of the quadrupole coupling constants shows that the bonding orbitals of S are *spd* hybrids and yields a value of -0.06×10^{-24} cm² for the quadrupole moment of the S^{33} nucleus. From the known ratio Q^{33}/Q^{35} this gives $Q^{35}=0.04\times10^{-24}$ cm². Zeeman studies show that the molecular g_J factor is approximately, but not exactly, equal for different rotational states. A mean value of 0.24 nuclear magneton is found for g_J.

INTRODUCTION

HARMONIC generators and detectors recently developed in this laboratory[1] extend the bounds of microwave spectroscopy down to one millimeter wavelength. A rotational line of OCS has been measured at 1.03 mm wavelength with a precision of three parts in 10^6. The line strength at this point was several times the noise level. One of the advantages of this new development is the wider frequency coverage afforded for the investigation of asymmetric-top molecules. The easily analyzed, low J transitions of asymmetric rotors very frequently fall only in the short millimeter-wave region. This is true for H_2S, the molecule which is the subject of the present investigation. It has three low J transitions between 1 mm and 1.8 mm but none at lower frequencies. Internal (Q-branch) transitions in HSD have been measured in the lower frequency microwave region by Hillger and Strandberg.[2] Because of the large difference between the zero-point vibrational energies of SH and SD they could not improve upon the accuracy of the structure as determined with infrared spectra.

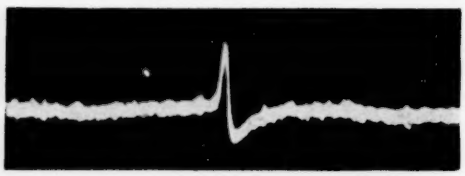

FIG. 1. Cathode-ray display of the $1_{0,1}\rightarrow1_{1,0}$ line of H_2S^{34} with the natural concentration of S^{34} of 4.2 percent.

The hydrogen sulfide molecule has been the subject of numerous studies in optical spectroscopy.[3] The transitions $1_{1,0}\rightarrow1_{2,0}$ and $2_{1,1}\rightarrow2_{2,0}$ predicted by King, Hainer, and Cross[4] to fall at 5.67 cm^{-1} and 7.28 cm^{-1} respectively, are the ones observed here. They were found to fall near the predicted frequencies.

EXPERIMENTAL METHOD

The millimeter-wave generator and detector are those described briefly in Part I of this series by King and Gordy.[1] It will be described in more detail by these authors in a paper to follow. An improvement in sensitivity by a factor of 10 or more over the performance described in Part I has been made by the use of a phase-lock-in amplifier with frequency modulation of the klystron and an automatic recording of the lines.[5] The lock-in amplifier was tuned to 4000 kc/sec, which was twice the frequency of the klystron modulation. This tuning of the amplifier to the harmonic of the modulation discriminates against reflections and hence tends to make the base line flat.

Figure 1 is a cathode-ray display of the $1_{0,1}\rightarrow1_{1,0}$ line of H_2S^{34} taken with S^{34} in its natural concentration of 4.2 percent with a 60-cps video sweep spectrometer. For this presentation an ordinary P amplifier with a bandwidth of about 6000 kc/sec was employed. Figure 2 shows similar video presentations of the $1_{0,1}\rightarrow1_{1,0}$ and $2_{1,1}\rightarrow2_{2,0}$ lines of H_2S^{32}. Figure 3 represents an automatic recording of the $1_{0,1}\rightarrow1_{1,0}$ transition of H_2S^{33} with S^{33} in its natural concentration of 0.7 percent.

SPECTRAL CONSTANTS AND MOLECULAR STRUCTURE

Table I gives the observed frequencies. The notation used, $J_{K-1,K+1}$, is that of King, Hainer, and Cross.[4] Explicit expressions can be obtained for these low J transitions. They are, for the rigid asymmetric rotor:

$$\nu(1_{0,1}\rightarrow1_{1,0})=C-B, \qquad (1)$$

† This research was supported in part by the U. S. Air Force under Contract No. AF18(600)-497, monitored by the Office of Scientific Research, Air Research and Development Command.
A preliminary report on this work was given by one of the authors (W. G.) at the North Carolina Meeting of the American Physical Society, March, 1953.

* Texas Company Fellow. The information contained in this paper will be the basis for part of a thesis to be submitted by the author in partial fulfillment of the requirements for the Ph.D. degree at Duke University.

[1] W. C. King and W. Gordy, Phys. Rev. **90**, 319 (1953).
[2] R. E. Hillger and M. W. P. Strandberg, Phys. Rev. **83**, 575 (1951).
[3] For reference see G. Herzberg, *Infrared and Raman Spectra* (D. Van Nostrand Company, New York, 1945), p. 489.
[4] King, Hainer, and Cross, Phys. Rev. **71**, 433 (1947).
[5] Gordy, Smith, and Trambarulo, *Microwave Spectroscopy* (John Wiley and Sons, Inc., New York, 1953), p. 11.

and

$$\nu(2_{1,1}\rightarrow 2_{2,0}) = A - 2B + C + 2[(B-C)^2 + (A-C)(A-B)]^{\frac{1}{2}}, \quad (2)$$

where $A=h/(8\pi^2 I_a)$, $B=h/(8\pi^2 I_b)$, and $C=h/(8\pi^2 I_c)$, in which I_a, I_b, and I_c are the moments of inertia about the principal axes a, b, and c with $I_a<I_b<I_c$. For a rigid planar molecule there are only two independent inertial moments to be evaluated in the approximation of the rigid rotor. Sufficient data are available for evaluation of these constants for H_2S^{32}. The number of frequencies measured is insufficient, however, for evaluation of the centrifugal distortion constants. Fortunately, the rotational states involved in the observed transitions are so low that the effects of centrifugal distortion can be safely neglected in the evaluation of the molecular structure. Even for the low J states involved here centrifugal distortions may shift the observed frequency by an amount of the order of megacycles per second. Nevertheless, the error in the structural determination caused by neglect of zero point vibrational effects is likely to be greater than that caused by the neglect of centrifugal distortion. The internal consistency of the structural parameters which were evaluated in three different ways indicate that neither of these effects caused large errors.

TABLE I. Observed transitions of H_2S.

	Transition	Observed frequency in Mc/sec
H_2S^{32}	$1_{0,1}\rightarrow 1_{1,0}$	168 762.51±0.35
H_2S^{33}	$2_{1,1}\rightarrow 2_{2,0}$	216 710.42±0.45
H_2S^{33}	$1_{0,1}\rightarrow 1_{1,0}$	168 322.63±0.35[a]
H_2S^{34}	$1_{0,1}\rightarrow 1_{1,0}$	167 910.57±0.35

[a] Corrected for nuclear quadrupole effects.

TABLE II. H_2S structure.[a]

∠HSH	SH distance, A	Transitions employed
92° 6′	1.32261	H_2S^{32}, $1_{0,1}\rightarrow 1_{1,0}$ and $2_{1,1}\rightarrow 2_{2,0}$
92° 6′	1.32259	H_2S^{32} and H_2S^{33}, $1_{0,1}\rightarrow 1_{1,0}$
92° 6′	1.32257	H_2S^{32} and H_2S^{34}, $1_{0,1}\rightarrow 1_{1,0}$
92° 6′	1.32259±0.00002	Averaged value

[a] Masses and other constants used are those listed in reference 5, Table A1.

For H_2S the axis of intermediate moment of inertia, b, lies along the symmetry axis; a lies in the plane of the molecule perpendicular to b; and c, the axis of greatest moment of inertia is perpendicular to the plane of the molecule. The principal moments of inertia are readily found to be

$$I_a = [(2M_H M_S)/(M_S+2M_H)]d_{SH}^2\cos^2(\theta/2); \quad (3)$$

$$I_b = 2M_H d^2 \sin^2(\theta/2); \quad (4)$$

$$I_c = I_a + I_b, \quad (5)$$

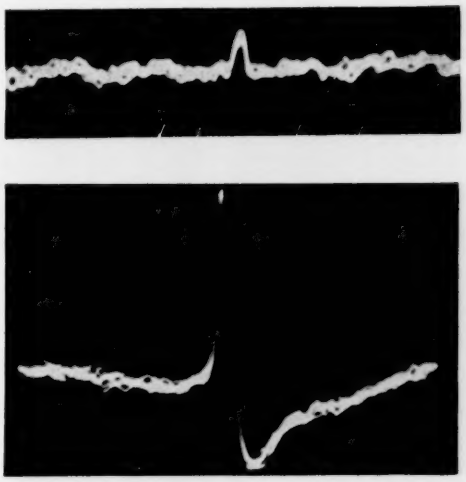

FIG. 2. Cathode-ray display of the $1_{0,1}\rightarrow 1_{1,0}$ (lower) and the $2_{1,1}\rightarrow 2_{2,0}$ (upper) lines of H_2S^{32} at 168.7 kMc and 216.7 kMc, respectively.

where d_{SH} is the bond length and θ is the bond angle HSH.

With the above equations and the observed frequencies, the structure of the molecule can be obtained. Since there are only two structural parameters and four observed frequencies (including those for different isotopic combinations), the parameters can be evaluated in more than one way. Table II gives the results. It is seen that the internal consistency is remarkably good. Certainly for the $1_{0,1}\rightarrow 1_{1,0}$ transition, where the centrifugal stretching is small, the differences in the stretching effects for the different S isotopes are negli-

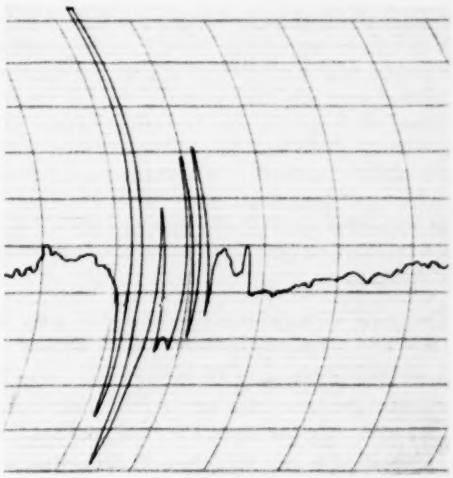

FIG. 3. Recorder trace of the $1_{0,1}\rightarrow 1_{1,0}$ transitions of H_2S^{33} at 168.3 kMc showing S^{33} nuclear quadrupole splitting. Concentration of S^{33} is 0.7 percent.

TABLE III. Spectral constants from averaged dimensions[a] of Table II.

	Moments of inertia in 10^{-40} g cm^2		
	I_a	I_b	I_c
H_2S^{32}	2.6522	3.0339	5.6861
H_2S^{33}	2.6570	3.0339	5.6909
H_2S^{34}	2.6615	3.0339	5.6954
	Spectral constants in Mc/sec		
	A	B	C
H_2S^{32}	316 304	276 512	147 536
H_2S^{33}	315 735	276 512	147 412
H_2S^{34}	315 201	276 512	147 296

[a] Masses and other constants employed are those listed in reference 5, Table A1.

gible. Also, as the change in the reduced mass of the molecule for the S substitution is slight, the difference in zero-point vibrational energy is small. It seems, therefore, that isotopic substitution may yield the most accurate structural determination. Nevertheless, it is seen that the values obtained from the two rotational lines of H_2S^{32} are in excellent agreement with those obtained by isotopic substitution. One should mention that both determinations include errors from zero point vibrational energy. Relation (5) does not hold exactly for the actual non rigid molecule but involves the so called quantum defect, $\Delta=I_c-(I_a+I_b)$. The error limits may be somewhat larger than the mean deviation indicated in Table II. Nevertheless, this small deviation is indicative of small error limits, and it seems likely that the structural parameters are determined to at least four significant figures. Without attempting to estimate the error limits we give the most probable values, $d_{SH}=1.3226$A and $\angle$HSH $=92°\,6'$.

The presumably more accurate values of the bond distances and bond angles here obtained are slightly lower than the previously accepted values. The best previous values are probably those given by Herzberg,[3] $d_{SH}=1.334$A and $\angle HSH=92°\,16'$, as obtained from the infrared work of Crawford and Cross.[6] It should be mentioned that our values, as well as those quoted from infrared data, are the effective values for the ground vibrational state. The hypothetical equilibrium values have not been obtained.

The moments of inertia and the constants A, B, and C are sometimes needed. They are given to five figures in Table III.

S^{33} NUCLEAR QUADRUPOLE COUPLING AND THE NATURE OF CHEMICAL BONDING IN H_2S

The rotational lines of H_2S^{33} are split into a multiplet structure by the interaction of the S^{33} nuclear quadrupole moment with the molecular field gradient.‡ This structure has been resolved and measured in the $1_{0,1}\rightarrow 1_{1,0}$ line, with S^{33} in its natural concentration of 0.7 percent. A recorder tracing of the transition is shown in Fig. 3. The spin of S^{33} is $\frac{3}{2}$. There are, in all, seven components for the $1_{0,1}\rightarrow 1_{1,0}$ transition. The weakest of these does not show on the tracing, and two of the stronger components fall at essentially the same frequency (see Table V) and hence are not resolved.

The quadrupole splitting is readily analyzed with the formula:[7]

$$E_Q=eQ\left\{\left(\frac{\partial^2V}{\partial a^2}\right)\left[J(J+1)+E(\kappa)-(\kappa+1)\left(\frac{\partial E(\kappa)}{\partial\kappa}\right)\right]+2\left(\frac{\partial^2V}{\partial b^2}\right)\left(\frac{\partial E(\kappa)}{\partial\kappa}\right)+\left(\frac{\partial^2V}{\partial c^2}\right)\left[J(J+1)-E(\kappa)+(\kappa-1)\left(\frac{\partial E(\kappa)}{\partial\kappa}\right)\right]\right\}\left(\frac{1}{J(J+1)}\right)Y(F),$$

where

$$Y(F)=\frac{\frac{3}{4}C(C+1)-J(J+1)I(I+1)}{2(2J-1)(2J+3)I(2I-1)},$$

TABLE IV. S^{33} nuclear quadrupole coupling constants in H_2S^{33}.

Coupling in Mc	
$eQq_{aa}=-32$	Spin $=3/2$
$eQq_{bb}=-\ 8$	$Q^{33}=-0.06\times10^{-24}$ cm^2
$eQq_{cc}=+40$	

values of which are tabulated by Gordy, Smith, and Trambarulo[5] for J up to 20. The quantities $eQ(\partial^2V/\partial a^2)=\chi_{aa}$, $eQ(\partial^2V/\partial b^2)=\chi_{bb}$, and $eQ(\partial^2V/\partial c^2)=\chi_{cc}$ are the quadrupole coupling constants measured along the principal inertial axes. $E(\kappa)$ is the reduced energy of the asymmetric rotor, and $\kappa=(2B-A-C)/(A-C)$ is the asymmetry parameter. For the $1_{0,1}$ level, $E(\kappa)=\kappa-1$ and $\partial E(\kappa)/\partial\kappa=1$; for the $1_{1,0}$ level, $E(\kappa)=\kappa+1$ and $\partial E(\kappa)/\partial\kappa=1$. With these values and the additional simplification $\chi_{bb}=-(\chi_{aa}+\chi_{cc})$ provided by Laplace's equation, the level energies can be written

$$(E_Q)_{1_{1,0}}=-\chi_{cc}Y(F),\quad (E_Q)_{1_{0,1}}=-\chi_{aa}Y(F).$$

These relations, with the selection rules $\Delta F=0,\pm1$ and the Bohr relation with the observed frequencies, yield the coupling constants listed in Table IV. Table V shows the calculated and observed spectrum for this transition.

The most surprising feature of the quadrupole splitting is the large difference in the coupling constants χ_{aa} and χ_{bb}. The asymmetry in the coupling measured

[6] B. L. Crawford, Jr., and P. C. Cross, J. Chem. Phys. **5**, 621 (1937).

‡ Partial resolution of the S^{33} quadrupole hyperfine structure of the $2_{2,1}\rightarrow 2_{2,0}$ transition in HDS^{33} has been accomplished by Hillger and Strandberg (reference 2). This transition has been further investigated by G. R. Bird and C. H. Townes, who have obtained preliminary values for the coupling constants in HDS^{33} (Quarterly Progress Report, Columbia Radiation Laboratory, March 31, 1953).

[7] J. K. Bragg and S. Golden, Phys. Rev. **75**, 735 (1949).

by the parameter

$$\epsilon=(\chi_{aa}-\chi_{bb})/\chi_{cc}=-0.60$$

is remarkably large. From the fact that the bond angle is so nearly a right angle, one would expect the bonds to be formed with nearly p orbitals of the S. In fact, from the deviation of only 2 degrees from 90 one would expect no more than 3 percent of s contribution to the bonding orbitals, yet it is not possible to account even approximately for the large difference in χ_{aa} and χ_{bb} with nearly pure p bonding orbitals of the S, as is indicated by the angles.

It is possible to account for the bond angle as well as the nuclear couplings by postulating roughly equal s and d contributions to the bonding orbitals. The amount of energy required to promote a $3s$ electron of S to a $3p$ orbital is roughly equal that required to promote a $3p$ electron to a $3d$ orbital. Hence, s, p, d hybridization, a possibility called to our attention by Dehmelt, is a promising solution to the problem. If equal s and d contributions to the bonding orbitals are assumed with one non-bonding pair in a pure p orbital (normal to the molecular plane) and the other in an sp hybrid directed along the symmetry axis, then 15 percent s and 15 percent d character of each bonding orbital is indicated by the coupling with 30 percent p character for the sp hybrid containing the non-bonding pair. Qualitative estimates indicate that this type of hybridization is also in harmony with the observed bond angles. More quantitative calculations of the s, p, and d admixture are being attempted.

NUCLEAR QUADRUPOLE MOMENTS OF S^{33} AND S^{35}

With the hybridized orbitals as postulated above and 20 percent ionic character of the bonds estimated from the difference in electronegativity of S and H the number of unbalanced p electrons along c is -0.81. This leads to

$$\chi_{cc}=-0.81Qq_{3,1,0},$$

if we neglect the small contributions of d electrons. The $q_{3,1,0}$ here represents the electronic field gradient at the nucleus for one unbalanced p electron and can be estimated from the doublet splitting $\Delta\nu=574$ cm^{-1} in the atomic spectrum of S as 13.8×10^{15} esu. With this value one obtains for S^{33}:

$$Q^{33}=-0.06\times10^{-24}\text{ cm}^2;$$

and for S^{35}, from the ratio[8]

$$Q^{33}/Q^{35}=-0.695,$$

$$Q^{35}=+0.04\times10^{-24}\text{ cm}^2.$$

[8] Cohn, Koski, and Wentink, Phys. Rev. **81**, 948 (1951).

TABLE V. Calculated and observed structure of the $1_{0,1}\rightarrow1_{1,0}$ transition of H_2S^{32}.

$F\rightarrow F'$	Frequency Mc/sec calculated	Frequency Mc/sec observed	Relative intensity calculated	Relative intensity observed
1/2→1/2	168 304.58	...	7.9	....
5/2→5/2	168 318.98	168 318.93	100	140
3/2→1/2	168 318.98	168 318.93	39.7	
1/2→3/2	168 322.58	168 322.63	39.7	40
3/2→5/2	168 326.98	168 326.90	42.9	40
5/2→3/2	168 328.98	168 329.03	42.5	45
3/2→3/2	168 337.18	...	12.7	...

These values include a factor 1.05 to correct for polarization of the inner electron shells[9] by Q. From OCS, Townes and Geschwind[10] estimates $Q^{33}=-0.055$ to -0.103. From the pure quadrupole coupling in rhombic sulfur Dehmelt[11] estimates $Q^{33}=-0.050$.

MOLECULAR g FACTOR

The Zeeman effect of the $1_{0,1}\rightarrow1_{1,0}$ line of H_2S^{32} was observed with a field of 2.93 kilogauss. The field was found to split the line into a doublet with separation $2\Delta\nu=1.08$ Mc/sec when imposed at right angles to the E vector of the microwaves. This arrangement gives the σ or $\Delta M=\pm1$ Zeeman components. When the magnet was placed so that H was parallel to the E vector, no splitting was observed although the line was noticeably broadened by the field of 2.93 kilogauss. If the g factor of the upper and lower states were equal, there would be no splitting for the latter arrangement ($\Delta M=0$). Since broadening was observed it is apparent that g for the upper state is nearly but not exactly equal to g for the lower state. From the $\Delta M=\pm1$ component we obtain

$$g_J\approx\Delta\nu/762H=0.24\text{ nuclear magnetons.}$$

This factor is approximately 40 percent of that[12] for H_2O, 0.586 nuclear magnetons.

More extensive Zeeman studies on H_2S are planned. Also, a millimeter wave Stark cell is being designed with which it is hoped that the electric dipole moment of H_2S can be obtained.

We wish to thank Dr. H. G. Dehmelt for his helpful discussion of the quadrupole coupling and Dr. W. C. King and Mr. H. G. Robinson for their suggestions about experimental details.

[9] R. Sternheimer, Phys. Rev. **86**, 316 (1952).
[10] C. H. Townes and S. Geschwind, Phys. Rev. **74**, 626 (1948).
[11] H. G. Dehmelt, Phys. Rev. **91**, 314 (1953).
[12] C. K. Jen, Physica **17**, 379 (1951).

Eigenfunctions of S^2 by a Spin Operator Method*

GEORGE W. PRATT, JR.
Lincoln Laboratory, Massachusetts Institute of Technology, Cambridge, Massachusetts

(Received April 13, 1953)

An operator is derived which is a function of step-up and step-down operators pertaining to spin angular momentum, and which creates a state of definite multiplicity when operating on a single determinant of spatial and spin orbitals. This paper is concerned with the problem of finding all of the orthogonal singlets for a $2N$-electron system in terms of the spin operator. The five orthogonal singlets corresponding to the six-electron spin degeneracy problem are studied in detail by means of the branching diagram. The fourteen orthogonal singlets corresponding to the eight-electron problem and the forty-two orthogonal singlets corresponding to the ten-electron problem are written down. Some remarks are made concerning the application of this method to a configuration interaction investigation.

INTRODUCTION

IN the investigation of molecules by configuration interaction, one is faced with the problem of setting up the states of definite multiplicity for the various configurations and of taking the matrix components of the energy between the different configurations. The following paper deals primarily with the singlet states, as they are usually of greatest interest in these problems. A simple and direct method of constructing all of the orthogonal singlets for a $2N$-electron system is presented. A brief discussion is given of the application of the operator techniques developed to the problem of configuration interaction. The reader is referred to Condon and Shortley[1] and the work of Racah[2] for a more general treatment of these problems.

For a set of $2N$ electrons occupying $2N$ distinct orbitals, it is possible to form many states of a given multiplicity by associating either α or β spin with the collection of orbitals in a variety of ways. In fact, one can construct

$$(2N)!/N!(N+1)!$$

orthogonal singlet states. One means of setting up all of the singlets is the valence-bond method which leads to the correct number of linearly independent singlets, but the states so obtained are not orthogonal.[3] Another method of constructing all of the singlets is by using the branching diagram,[4] a pictorial description of adding the spin angular momentum of electrons one by one. This scheme shows, for any number of electrons, how many states of various multiplicities there are, and what the parentage of each state is. The method of the branching diagram will be used in the following discussion.

A spin operator method is given here for setting up all of the orthogonal singlets. The five orthogonal singlets corresponding to a six-electron system are analyzed in some detail, and from this analysis a spin operator O is derived which when operating on a single determinant creates an eigenfunction of S^2. All of the orthogonal singlets for the six-, eight-, and ten-electron systems are written down in terms of the operator O.

THE SIX-ELECTRON PROBLEM

In Fig. 1 the branching diagram for a six-electron system is given. This diagram not only shows how many states of a given multiplicity there are for n electrons, but by applying the methods of vector addition of angular momentum, the branching diagram also shows how the states are actually constructed. In Figs. 1(b) through 1(e) the five possible ways of obtaining a singlet state for the six-electron problem are illustrated. Let us consider in some detail the state described in Fig. 1(b). The branching diagram tells us that this state results from the combination of two three-electron systems, say A and B, each of which are in a state of $S=\frac{3}{2}$. Let us order the six orbitals for this problem φ_1, φ_2, φ_3, φ_4, φ_5, and φ_6. These orbitals are assumed to be orthonormal and distinct. Let φ_1, φ_2, and φ_3 and three electrons make up set A and φ_4, φ_5, and φ_6 and three electrons comprise set B. The singlet in Fig. 1(b) can be expressed as

$$\begin{aligned}\Psi_1(S=0)=&C_0\varphi_A(S=\tfrac{3}{2},M_S=\tfrac{3}{2})\cdot\varphi_B(S=\tfrac{3}{2},M_S=-\tfrac{3}{2})\\&+C_1\varphi_A(S=\tfrac{3}{2},M_S=\tfrac{1}{2})\cdot\varphi_B(S=\tfrac{3}{2},M_S=-\tfrac{1}{2})\\&+C_2\varphi_A(S=\tfrac{3}{2},M_S=-\tfrac{1}{2})\cdot\varphi_B(S=\tfrac{3}{2},M_S=+\tfrac{1}{2})\\&+C_3\varphi_A(S=\tfrac{3}{2},M_S=-\tfrac{3}{2})\cdot\varphi_B(S=\tfrac{3}{2},M_S=+\tfrac{3}{2}).\end{aligned}\quad(1)$$

The states representing by $\varphi_A(S,M_S)$ and $\varphi_B(S,M_S)$ are

$$\varphi_A(S=\tfrac{3}{2},M_S=\tfrac{3}{2})=\begin{vmatrix}\varphi_1(1)\alpha(1)\varphi_1(2)\alpha(2)\varphi_1(3)\alpha(3)\\\varphi_2(1)\alpha(1)\varphi_2(2)\alpha(2)\varphi_2(3)\alpha(3)\\\varphi_3(1)\alpha(1)\varphi_3(2)\alpha(2)\varphi_3(3)\alpha(3)\end{vmatrix}\equiv|\alpha\alpha\alpha|,\quad(2)$$

$$\varphi_B(S=\tfrac{3}{2},M_S=-\tfrac{3}{2})=\begin{vmatrix}\varphi_4(4)\beta(4)\varphi_4(5)\beta(5)\varphi_4(6)\beta(6)\\\varphi_5(4)\beta(4)\varphi_5(5)\beta(5)\varphi_5(6)\beta(6)\\\varphi_6(4)\beta(4)\varphi_6(5)\beta(5)\varphi_6(6)\beta(6)\end{vmatrix}\equiv|\beta\beta\beta|,\quad(3)$$

* The research in this document was supported jointly by the Army, Navy, and Air Force under contract with the Massachusetts Institute of Technology.

[1] E. U. Condon and G. H. Shortley, *Theory of Atomic Spectra* (Cambridge University Press, London, 1935).

[2] G. Racah, Phys. Rev. **61**, 186 (1942); **62**, 438 (1942); **63**, 367 (1943); **76**, 1352 (1949).

[3] Eyring, Walter, and Kimball, *Quantum Chemistry* (John Wiley and Sons, Inc., New York, 1944), Chap. XIII.

[4] E. M. Corson, *Perturbation Methods in the Quantum Mechanics of n-Electron Systems* (Hafner, New York, 1951), Chap. X.

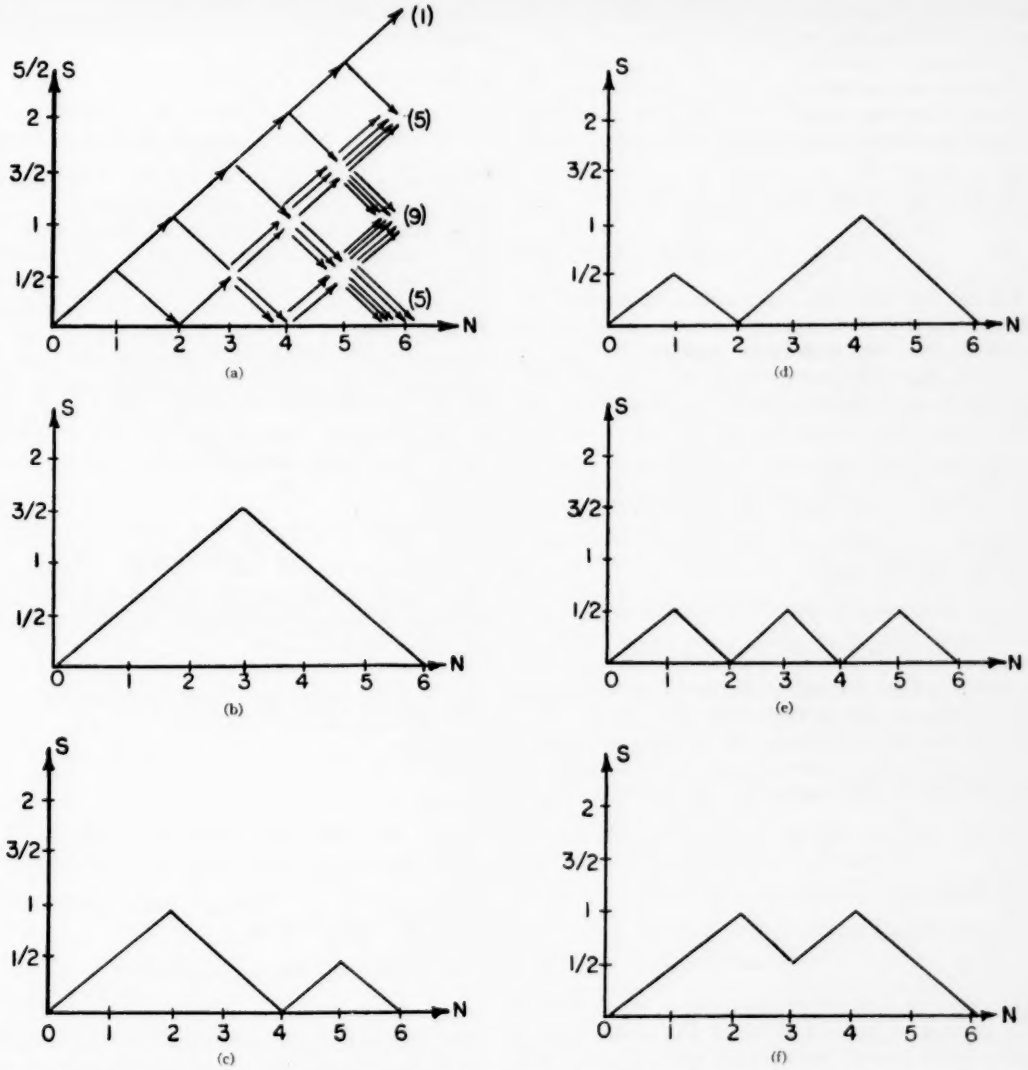

FIG. 1. (a) Branching diagram for a six-electron system; (b) first path; (c) second path; (d) third path; (e) fourth path; and (f) fifth path.

$$\varphi_A(S=\tfrac{3}{2}, M_S=\tfrac{1}{2})=[\,|\beta\alpha\alpha|+|\alpha\beta\alpha|+|\alpha\alpha\beta|\,]/\sqrt{3}, \quad (4)$$

$$\varphi_B(S=\tfrac{3}{2}, M_S=-\tfrac{1}{2})=[\,|\beta\beta\alpha|+|\beta\alpha\beta|+|\alpha\beta\beta|\,]/\sqrt{3}, \quad (5)$$

$$\varphi_A(S=\tfrac{3}{2}, M_S=-\tfrac{1}{2})=[\,|\alpha\beta\beta|+|\beta\alpha\beta|+|\beta\beta\alpha|\,]/\sqrt{3}, \quad (6)$$

$$\varphi_B(S=\tfrac{3}{2}, M_S=+\tfrac{1}{2})=[\,|\alpha\alpha\beta|+|\beta\alpha\alpha|+|\alpha\beta\alpha|\,]/\sqrt{3}, \quad (7)$$

$$\varphi_A(S=\tfrac{3}{2}, M_S=-\tfrac{3}{2})=|\beta\beta\beta|, \quad (8)$$

$$\varphi_B(S=\tfrac{3}{2}, M_S=+\tfrac{3}{2})=|\alpha\alpha\alpha|. \quad (9)$$

All determinants are assumed to be normalized.

The expression $\varphi_A(S=\frac{3}{2}, M_S)\cdot\varphi_B(S=\frac{3}{2}, -M_S)$ involves the combination of the determinants which make up the states. The "product" of two determinants is taken to mean

$$|\alpha\beta\alpha|\cdot|\beta\beta\alpha| = \begin{vmatrix} \varphi_1(1)\alpha(1) & \cdots & \varphi_1(6)\alpha(6) \\ \varphi_2(1)\beta(1) & \cdots & \varphi_2(6)\beta(6) \\ \varphi_3(1)\alpha(1) & \cdots & \varphi_3(6)\alpha(6) \\ \varphi_4(1)\beta(1) & \cdots & \varphi_4(6)\beta(6) \\ \varphi_5(1)\beta(1) & \cdots & \varphi_5(6)\beta(6) \\ \varphi_6(1)\alpha(1) & \cdots & \varphi_6(6)\alpha(6) \end{vmatrix}. \quad (10)$$

In general the "product" of an $n\times n$ determinant and an $m\times m$ determinant is an $(m+n)\times(m+n)$ determinant. We also note that the order must be preserved, i.e., $|\alpha\beta\alpha|\cdot|\beta\beta\alpha|$ is not equal to $|\beta\beta\alpha|\cdot|\alpha\beta\alpha|$. It is to be borne in mind that the $\varphi_{A,B}(S, M_S)$ are normalized

states of definite multiplicity. The coefficients C_i in (1) are the transformation amplitudes for the vector addition of angular momentum, and sometimes called the Clebsch-Gordon coefficients. They may be obtained in this case from the general expression for combining two systems of spin S to form a resultant singlet. This is

$$\Psi(S=0)=\sum_{M_S=-S}^{+S}(-1)^{S-M_S}\varphi_A(S,M_S)\cdot\varphi_B(S,-M_S). \quad (11)$$

Let us now look into the question of forming the various $\varphi_{A,B}(S,M_S)$ states. $\varphi_A(S=\frac{3}{2},\ M_S=+\frac{1}{2})$ is obtained by the step-down operator acting on $\varphi_A(S=\frac{3}{2},\ M_S=+\frac{3}{2})$, and $\varphi_B(S=\frac{3}{2},\ M_S=-\frac{1}{2})$ is gotten by the step-up operator acting on $\varphi_B(S=\frac{3}{2},\ M_S=-\frac{3}{2})$. Thus except for a constant we have

$$\varphi_A(S=\tfrac{3}{2},\ M_S=+\tfrac{1}{2})=S_A{}^-\varphi_A(S=\tfrac{3}{2},\ M_S=+\tfrac{3}{2}),$$
$$\varphi_B(S=\tfrac{3}{2},\ M_S=-\tfrac{1}{2})=S_B{}^+\varphi_B(S=\tfrac{3}{2},\ M_S=-\tfrac{3}{2}),$$

where $S_A{}^-=S_1{}^-+S_2{}^-+S_3{}^-$ and $S_B{}^+=S_4{}^++S_5{}^++S_6{}^+$. Writing this out, we get

$$S_A{}^-|\alpha\alpha\alpha|=[|\beta\alpha\alpha|+|\alpha\beta\alpha|+|\alpha\alpha\beta|]. \quad (12)$$

$$S_B{}^+|\beta\beta\beta|=[|\alpha\beta\beta|+|\beta\alpha\beta|+|\beta\beta\alpha|]. \quad (13)$$

In order to have normalized states, we must multiply the right-hand side of both (12) and (13) by $(3)^{-\frac{1}{2}}$, which is the number of ways of reversing one spin in set A or B taken to the $-\frac{1}{2}$ power. We can write the second term in (1), except for the factor of -1, as

$$[(S_A{}^-S_B{}^+)/3]\varphi_A(S=\tfrac{3}{2},\ M_S=\tfrac{3}{2})\cdot\varphi_B(S=\tfrac{3}{2},\ M_S=-\tfrac{3}{2}). \quad (14)$$

The third term in (1) may be written as

$$[(S_A{}^-S_B{}^+)^2/3\times4]\varphi_A(S=\tfrac{3}{2},\ M_S=\tfrac{3}{2})\cdot\varphi_B(S=\tfrac{3}{2},\ M_S=-\tfrac{3}{2}). \quad (15)$$

The factor of 3 in the denominator is the product of the number of ways of reversing two spins in set A taken to the $\frac{1}{2}$ power and the number of ways of reversing two spins in B taken to the $\frac{1}{2}$ power. The factor of 4 in the denominator arises because in the expansion of $(S_A{}^-S_B{}^+)^2$ we encounter equivalent terms of the type $S_1{}^-S_2{}^-S_4{}^+S_5{}^++S_1{}^-S_2{}^-S_5{}^+S_4{}^++S_2{}^-S_1{}^-S_4{}^+S_5{}^+ +S_2{}^-S_1{}^-S_5{}^+S_4{}^+$. Thus if there are M spin reversals in set A and in set B, we must divide out the permutations among set A and set B as in the case above.

The fourth term in (1) may be written

$$[(S_A{}^-S_B{}^+)^3/36]\varphi_A(S=\tfrac{3}{2},\ M_S=\tfrac{3}{2})\cdot\varphi_B(S=\tfrac{3}{2},\ M_S=-\tfrac{3}{2}). \quad (16)$$

Here there is just one way of reversing all the spins in A and in B. The factor of 36 in the denominator is necessary because there are 3! ways of expressing the reversals in A, i.e., $S_1{}^-S_2{}^-S_3{}^-$, $S_2{}^-S_1{}^-S_3{}^-$, etc., and 3! ways in B.

We can combine (14), (15), and (16) and write the singlet (1) as

$$\Psi_1(S=0)=\{(S_A{}^-S_B{}^+)^0-\tfrac{1}{3}(S_A{}^-S_B{}^+)^1 +(1/12)(S_A{}^-S_B{}^+)^2-(1/36)(S_A{}^-S_B{}^+)^3\}\times\varphi_A(S=\tfrac{3}{2},\ M_S=\tfrac{3}{2})\cdot\varphi_B(S=\tfrac{3}{2},\ M_S=-\tfrac{3}{2}). \quad (17)$$

We must multiply the right-hand side of (17) by $\frac{1}{2}$ in order that the final state will be normalized.

We have now expressed the singlet shown in Fig. 1(a) as the result of an operator acting on the "product" of $\varphi_A(S=\frac{3}{2},\ M_S=\frac{3}{2})$ and $\varphi_B(S=\frac{3}{2},\ M_S=-\frac{3}{2})$. We seek now to generalize this operator to the $2N$-electron case. That is, given a $2N$-electron system, a collection of N electrons and N orbitals will be terms as set A, and the remaining N electrons and N orbitals denoted by set B. We wish to form the $2N$-electron-orbital singlet state by combining sets A and B, each of which is to be in a state of maximum multiplicity, i.e., $S_{A,B}=N/2$. Our composite state will be

$$\Psi(S=0)=O_1[\varphi_A(S=N/2,\ M_S=+N/2)\cdot\varphi_B(S=N/2),\ M_S=-N/2)]. \quad (18)$$

Denoting the number of spin reversals in A or B by M, the general form of the operator, which will be represented by O_1, is

$$O_1=\sum_{M=0}^{N}(-1)^M[(N-M)!/(N!M!(N+1)^{\frac{1}{2}})]\times(S_A{}^-S_B{}^+)^M, \quad (19)$$

where

$$S_A{}^-=S_{1A}{}^-+S_{2A}{}^-+S_{3A}{}^-+\cdots+S_{NA}{}^-.$$
$$S_B{}^+=S_{1B}{}^++S_{2B}{}^++S_{3B}{}^++\cdots+S_{NB}{}^+. \quad (20)$$

The $(-1)^M$ is the Clebsch-Gordon coefficient. The factor $(N-M)!/N!M!$ is

$$[(N-M)!M!/N!]^{\frac{1}{2}}\cdot[(N-M)!M!/N!]^{\frac{1}{2}}\cdot1/M!\cdot1/M!. \quad (21)$$

The first factor in (21) is the number of ways of making M reversals in set A, which contains N elements, taken to the $-\frac{1}{2}$ power. The second factor is the number of ways of making M reversals of spin in set B taken to the $-\frac{1}{2}$ power. The third factor divides out equivalent permutations in set A, as explained above. The fourth factor does the same in set B.

Therefore, we have found an operator O_1 which, when acting on the "product" of two N-electron systems, each in a state of maximum S and one with $M_S=S$ and the other with $M_S=-S$, produces a composite state of $2N$-electrons which is a singlet. It turns out that the present operator O_1 is not general enough to be a really powerful tool. In the course of events a number of modifications will suggest themselves.

Let us now investigate the creation of the remaining singlets for the six-electron problem. The reader is referred to Figs. 1(c), 1(d), 1(e), and 1(f) for a pictorial

description of the structure of these states. In Fig. 1(c) our resultant singlet is the "product" of a singlet state made up of the first four orbitals and four electrons, and the singlet made from the last two orbitals and electrons. Equation (11) shows that if we combine two systems each of which is in a singlet state to form a resultant singlet, that the composite state is merely the "product" of $\varphi_1(s=0)$ and $\varphi_2(S=0)$. Our plan is, therefore, to generate the two singlets inferred from Fig. 1(b) and to take their "product" to get the final state. The singlet formed from the first four orbitals and four electrons is the result of combining two states $\varphi_A(S=1, M_S=1)$ and $\varphi_B(S=1, M_S=-1)$. The singlet formed from the last two orbitals and two electrons is the result of combining two states $\varphi_A'(S=\frac{1}{2}, M_S=\frac{1}{2})$ and $\varphi_B'(S=\frac{1}{2}, M_S=-\frac{1}{2})$. Thus the six-electron singlet for Fig. 1(b) is simply

$$\Psi_2(S=0)=O_1|\alpha\alpha\beta\beta|\cdot O_1'|\alpha\beta|, \tag{22}$$

which when expanded is

$$\Psi_2(S=0)=(1/\sqrt{6})[|\alpha\alpha\beta\beta|-\tfrac{1}{2}\{|\alpha\beta\alpha\beta|+|\alpha\beta\beta\alpha| +|\beta\alpha\alpha\beta|+|\beta\alpha\beta\alpha|\}+|\beta\beta\alpha\alpha|]\cdot[|\alpha\beta|-|\beta\alpha|]. \tag{23}$$

For the purpose of illustration let us write out O_1 and O_1'. For O_1, $N=2$; and for O_1', $N=1$. Thus from (19) we get

$$O_1=(1/\sqrt{3})[1-\tfrac{1}{2}\{S_1^-S_3^++S_1^-S_4^++S_2^-S_3^++S_2^-S_4^+\} +\tfrac{1}{4}\{S_1^-S_2^-S_3^+S_4^++S_2^-S_1^-S_3^+S_1^+ +S_1^-S_2^-S_4^+S_3^++S_2^-S_1^-S_4^+S_3^+\}].$$

Since $S_i^-S_j^+$ commute for $i\neq j$,

$$O_1=[1-\tfrac{1}{2}\{S_1^-S_3^++S_1^-S_4^++S_2^-S_3^++S_2^-S_4^+\} +S_1^-S_2^-S_3^+S_4^+]/\sqrt{3}, \tag{24}$$

and O_1' is

$$O_1'=[1-S_5^-S_6^+]/\sqrt{2}. \tag{25}$$

The singlet in Fig. 1(d) is constructed in the same manner as $\Psi_2(S=0)$, only now the first two orbitals and two electrons are combined to form a singlet, and the last four orbitals and four electrons are combined to form a singlet. The composite singlet is just the "product" of these singlets. Hence

$$\Psi_3(S=0)=O_1'|\alpha\beta|\cdot O_1|\alpha\alpha\beta\beta|, \tag{26}$$

$$\Psi_3(S=0)=(1/\sqrt{6})[|\alpha\beta|-|\beta\alpha|] \cdot[|\alpha\alpha\beta\beta|-\tfrac{1}{2}\{|\alpha\beta\alpha\beta|+|\alpha\beta\beta\alpha|+|\beta\alpha\alpha\beta| +|\beta\alpha\beta\alpha|\}+|\beta\beta\alpha\alpha|]. \tag{27}$$

Theorem I, which is proved in Appendix I, and which states that different paths on the branching diagram terminating at the same destination lead to orthogonal states, shows us that Ψ_2 and Ψ_3 are indeed orthogonal.

The singlet formed in Fig. 1(e) is obtained by taking the "product" of three singlets, each made up of two orbitals and two electrons. Thus

$$\Psi_4(S=0)=O_1^{(1)}|\alpha\beta|\cdot O_1^{(3)}|\alpha\beta|\cdot O_1^{(5)}|\alpha\beta|, \tag{28}$$

where $O_1^{(i)}$ is

$$O_1^{(i)}=[1-S_i^-S_{i+1}^+]/\sqrt{2}. \tag{29}$$

It is of interest to note that this state is one of the familiar valence-bond singlets. In valence-bond language one would describe the state as having a bond between φ_1 and φ_2, a bond between φ_3 and φ_4, and a bond between φ_5 and φ_6. The expanded form of this state is

$$\Psi_4(S=0)=[(|\alpha\beta|-|\beta\alpha|)\cdot(|\alpha\beta|-|\beta\alpha|) \cdot(|\alpha\beta|-|\beta\alpha|)]/\sqrt{8}. \tag{30}$$

Let us now consider the last singlet, that shown in Fig. 1(f). The singlets formed so far have been either the "product" of subsidiary singlets formed by the application of O_1, or in the case of Fig. 1(b), a total singlet formed directly by the use of O_1. The state shown in Fig. 1(f) is the result of combining two states each made up of three orbitals and three electrons and both in a state of $S=\frac{1}{2}$. Our plan is now to find out how to use O_1 so that it can operate on a determinant made up of an odd number of electrons; therefore, not in a state of $M_S=0$. We want the result of operating with O_1 on, for example, $|\alpha\alpha\beta|$ to be a state of $\Psi(S=\frac{1}{2})$. The formation of a state of $\Psi(S=\frac{1}{2})$ from three electrons may be accomplished in two different ways as indicated by the branching diagram, Fig. 1. The two possible states are shown in Figs. 2(a) and 2(b). The state illustrated in Fig. 2(a) is the result of the combination of a singlet formed by the first two orbitals and two electrons and a state $\varphi(S=\frac{1}{2})$ formed from the third orbital and an electron. That is

$$\begin{aligned}\Psi_{2a}&=[|\alpha\beta|-|\beta\alpha|]\cdot|\alpha|/\sqrt{2},\\ \Psi_{2a}&=\{O_1|\alpha\beta|\}\cdot|\alpha|.\end{aligned} \tag{31}$$

The state shown in Fig. 2(b) is the result of the combination of a state $\varphi(S=1)$ formed from the first two electrons, and a state $\varphi(S=\frac{1}{2})$ formed from the third orbital and an electron. The method of creating such a state by the vector addition of angular momentum is well known, and the result is

$$\Psi(S_i=\tfrac{1}{2}, M_S=\tfrac{1}{2})=(2/\sqrt{6})|\alpha\alpha|\cdot|\beta| -(1/\sqrt{6})[|\alpha\beta|+|\beta\alpha|]\cdot|\alpha|. \tag{32}$$

We can factor this state as follows:

$$\Psi(S=\tfrac{1}{2}, M_S=\tfrac{1}{2})=(1/\sqrt{6})\{|\alpha|\cdot(|\alpha\beta|-|\beta\alpha|) +(|\alpha\cdot|\alpha|\cdot\beta|-|\beta\cdot|\alpha|\cdot\alpha|)\}. \tag{33}$$

This defines a new way of writing a "product"; for example,

$$|\alpha\beta\cdot\{|\alpha\beta|-|\beta\alpha|\}\cdot\beta\beta|=|\alpha\beta\alpha\beta\beta\beta|-|\alpha\beta\beta\alpha\beta\beta|. \tag{34}$$

We can generate the state $\Psi(S=\frac{1}{2}, M_S=\frac{1}{2})$ by the application of an operator,

$$(1-S_2^-S_3^+)+(1-S_1^-S_3^+), \tag{35}$$

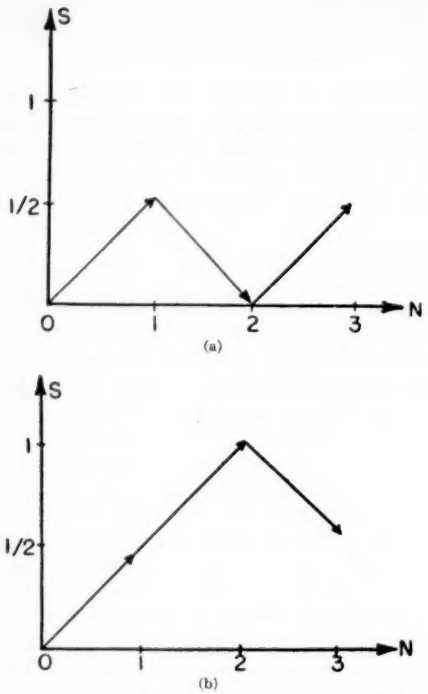

FIG. 2. (a) and (b) Three-electron system of $S=\frac{1}{2}$, $M_S=\frac{1}{2}$.

which operates on $|\alpha\alpha\beta|$. We have

$$(1-S_2^-S_3^+)|\alpha\alpha\beta| = |\alpha\alpha\beta| - |\alpha\beta\alpha|,$$
$$(1-S_1^-S_3^+)|\alpha\alpha\beta| = |\alpha\alpha\beta| - |\beta\alpha\alpha|.$$

Therefore, except for the proper normalization constant

$$[(1-S_2^-S_3^+)+(1-S_1^-S_3^+)]|\alpha\alpha\beta| = 2|\alpha\alpha\beta| - |\alpha\beta\alpha| - |\beta\alpha\alpha|. \quad (36)$$

Thus the state $\Psi(S=\frac{1}{2}, M_S=\frac{1}{2})$ can be created by use of O_1, since (36) can be written

$$\Psi(S=\tfrac{1}{2}, M_S=\tfrac{1}{2}) = [O_1^{(2,3)}+O_1^{(1,3)}]|\alpha\alpha\beta|/\sqrt{3} = [2|\alpha\alpha\beta| - |\alpha\beta\alpha| - |\beta\alpha\alpha|]/\sqrt{6}. \quad (37)$$

Similarly,

$$\Psi(S=\tfrac{1}{2}, M_S=-\tfrac{1}{2}) = [O_1^{(4,5)}+O_1^{(4,6)}]|\alpha\beta\beta|/\sqrt{3} = [2|\alpha\beta\beta| - |\beta\alpha\beta| - |\beta\alpha\alpha|]/\sqrt{6}. \quad (38)$$

Since we have found the two states $\Psi(S=\frac{1}{2}, M_S=\pm\frac{1}{2})$ corresponding to those involved in the formation of the singlet in $\Psi_b(S=0)$, Fig. 1(e), we can create the composite six-electron singlet as

$$\Psi_b(S=0) = O_1[\Psi(S=\tfrac{1}{2}, M_S=\tfrac{1}{2})\cdot\Psi(S=\tfrac{1}{2}, M_S=-\tfrac{1}{2})]. \quad (39)$$

When written out, this is

$$\Psi_b(S=0) = \tfrac{1}{6}O_1[4|\alpha\alpha\beta\alpha\beta\beta| - 2|\alpha\alpha\beta\beta\alpha\beta| - 2|\alpha\alpha\beta\beta\beta\alpha| - 2|\alpha\beta\alpha\alpha\beta\beta| + |\alpha\beta\alpha\beta\alpha\beta| + |\alpha\beta\alpha\beta\beta\alpha| - 2|\beta\alpha\alpha\alpha\beta\beta| + |\beta\alpha\alpha\beta\alpha\beta| + |\beta\alpha\alpha\beta\beta\alpha|], \quad (40)$$

where the orbitals associated with spin α comprise set A and the orbitals associated with spin β comprise set B. For example, the first determinant in (40) has φ_1, φ_2, and φ_4 in A and φ_3, φ_5, and φ_6 in B.

With expression (40) we have completed the task of writing down all of the orthogonal singlets for the six electron case with the help of the operator O_1. Now we wish to generalize this operator so that it can be used for a wider variety of situations. Equations (37), (38), and (40) show that it is sometimes necessary to use more than one definition of sets A and B. It would be much more convenient to have a form of O_1 which would automatically operate on all possible choices for sets A and B. We can easily modify O_1 to do this, and the generalized form of O_1 will be written as O. It is

$$O = \frac{1}{(N+1)^{\frac{1}{2}}}\sum_i\Big[1+\sum_{M=1}^{N}\frac{(-1)^M(N-M)!}{N!M!} \times\{(S_{Ai}^-S_{Bi}^+)^M+(S_{Ai}^+S_{Bi}^-)^M\} \times\prod_{jAi,kBi}^{N}(S_{jAi}^+S_{jAi}^-S_{kBi}^-S_{kBi}^+ + S_{jAi}^-S_{jAi}^+S_{kBi}^+S_{kBi}^-)\Big], \quad (41)$$

where the sum over i is the sum over all different divisions of the orbitals φ_1 to φ_{2N} into two groups of N orbitals. O is to operate on a determinant with total M_S equal to zero. The rules for applying O to determinants with total M_S not zero will be given in a later section. The properties of O will now be written down and the proofs of these statements is given in the various appendices.

I. O is hermitian.
II. O commutes with S^2.
III. O commutes with the Hamiltonian H.
IV. O^2 equals $(N+1)^{\frac{1}{2}}\{n[1+(n-1)/(N+1)]\}^{\frac{1}{2}}O$.[5]
V. O commutes with the antisymmetrizing operator A.

We are now in a position to illustrate how O operates on a determinant. Consider for example O operating on $|\alpha\beta\alpha\beta|$. First, since O commutes with the antisymmetrizing operator, we can write $O|\alpha\beta\alpha\beta|$ as $AO\varphi_1(1)\alpha(1)\varphi_2(2)\times\beta(2)\varphi_3(3)\alpha(3)\varphi_4(4)\beta(4)$, where O now operates on a spin-product function. We can divide our four orbitals φ_1, φ_2, φ_3, and φ_4 into two groups in three different ways φ_1, $\varphi_2-\varphi_3$, φ_4; φ_1, $\varphi_3-\varphi_2$, φ_4; φ_1, $\varphi_4-\varphi_2$, φ_3. Let us first consider the

$$\prod_{jAi,kBi}^{N}(S_{jAi}^+S_{jAi}^-S_{kBi}^-S_{kBi}^+ + S_{jAi}^-S_{jAi}^+S_{kBi}^+S_{kBi}^-)$$

part of O operating on

$$\varphi_1(1)\alpha(1)\varphi_2(2)\beta(2)\varphi_3(3)\alpha(3)\varphi_4(4)\beta(4).$$

[5] See Eq. (49) for the definition of n.

Suppose we take the division φ_1, $\varphi_2-\varphi_3$, φ_4 and let φ_1 and φ_2 comprise set A, and φ_3 and φ_4 make up set B. Then we have

$$[S_1^+S_1^-S_2^+S_2^-S_3^-S_3^+S_4^-S_4^+ + S_1^-S_1^+S_2^-S_2^+S_3^+S_3^-S_4^+S_4^-] \times\varphi_1(1)\alpha(1)\varphi_2(2)\beta(2)\varphi_3(3)\alpha(3)\varphi_4(4)\beta(4). \quad (42)$$

This is clearly zero. Hence this choice of dividing our four orbitals into two groups yields nothing. Similarly the choice φ_1, $\varphi_4-\varphi_2$, φ_3 gives nothing. For the selection φ_1, $\varphi_3-\varphi_2$, φ_4 we have

$$[S_1^+S_1^-S_3^+S_3^-S_2^-S_2^+S_4^-S_4^+ + S_1^-S_1^+S_3^-S_3^+S_2^+S_2^-S_4^+S_4^-] \times\varphi_1(1)\alpha(1)\varphi_2(2)\beta(2)\varphi_3(3)\alpha(3)\varphi_4(4)\beta(4) = \varphi_1(1)\alpha(1)\varphi_2(2)\beta(2)\varphi_3(3)\alpha(3)\varphi_4(4)\beta(4). \quad (43)$$

Thus when operating on a spin product function with the $\prod_i$ operator, we get zero for all choices of i except one, which leaves the spin product function invariant. Let us now examine the factor

$$[(S_{Ai}^-S_{Bi}^+)^M+(S_{Ai}^+S_{Bi}^-)^M].$$

The term $(S_{Ai}^+S_{Bi}^-)^M$ gives zero for all M, since in this example we have associated α spin with all orbitals in set A. Thus we see that O effectively reduces to

$$O=[1-\tfrac{1}{2}(S_1^-S_2^+ + S_1^-S_4^+ + S_3^-S_2^+ + S_3^-S_4^+) + S_1^-S_3^-S_2^+S_4^+]/\sqrt{3},$$

which is the same as (24) if we interchange the 2's and 3's in that expression. One should note that we would have obtained the same result had we associated β spin with all orbitals in A. This is as it should be, for the assignment of spin to set A or B is entirely arbitrary.

Using our new operator O, let us look back at the five singlets we have set up for the six-electron problem. $\Psi_1(S=0)$, originally given in (17), is just

$$\Psi_1(S=0)=O|\alpha\alpha\alpha\beta\beta\beta|. \quad (44)$$

Here O reduces to just the original operator. $\Psi_2(S=0)$, given in (22), is

$$\Psi_2(S=0)=O|\alpha\alpha\beta\beta|\cdot O|\alpha\beta|. \quad (45)$$

$\Psi_3(S=0)$, given in (26), is

$$\Psi_3(S=0)=O|\alpha\beta|\cdot O|\alpha\alpha\beta\beta|. \quad (46)$$

$\Psi_4(S=0)$, given in (28), is

$$\Psi_4(S=0)=O|\alpha\beta|\cdot O|\alpha\beta|\cdot O|\alpha\beta|. \quad (47)$$

In the case of $\Psi_5(S=0)$ we encounter operands, i.e. $|\alpha\alpha\beta|$ or $|\alpha\beta\beta|$, with $M_S\neq 0$ as in (37) and (38). If we operate on $|\alpha\alpha\beta|$ with O, taking N to be 1 and letting the sum over i range over all possibilities of dividing the three orbitals into two groups with one orbital per group and excluding the remaining orbital, then the expanded form of O is

$$O=(1-\{S_1^-S_2^+ + S_1^+S_2^-\}) \times(S_1^+S_1^-S_2^-S_2^+ + S_1^-S_1^+S_2^+S_2^-)/\sqrt{2} + (1-\{S_1^-S_3^+ + S_1^+S_3^-\}) \times(S_1^+S_1^-S_3^-S_3^+ + S_1^-S_1^+S_3^+S_3^-)/\sqrt{2} + (1-\{S_2^-S_3^+ + S_2^+S_3^-\}) \times(S_2^+S_2^-S_3^-S_3^+ + S_2^-S_2^+S_3^+S_3^-)/\sqrt{2}. \quad (48)$$

As a result of operating on $|\alpha\alpha\beta|$, this gives

$$O|\alpha\alpha\beta|=[2|\alpha\alpha\beta|-|\alpha\beta\alpha|-|\beta\alpha\alpha|]/\sqrt{2}.$$

This is indeed a state of $S=\frac{1}{2}$, $M_S=\frac{1}{2}$; however, it is not properly normalized. We must multiply by $3^{-\frac{1}{2}}$ to effect normalization. Let us derive this extra coefficient and set down the rules for the operation of O on any spin-product function with $M_S\neq 0$.

Suppose O operates on a spin-product function with $x\alpha$ spins and $y\beta$ spins, let us assume x is greater than y. First, the constant N in O is to be taken as equal to y. We have $x-y$ excess α spins, hence $M_S=(x-y)/2$. In the sum over i in the operator O, the number of choices of i that will give a nonvanishing result in the number of ways of choosing y electrons out of the collection of x electrons, i.e.,

$$n=x!/(x-y)!y!. \quad (49)$$

Operation with O on this spin-product function will produce n states with $S=(x-y)/2$ and $M_S=(x-y)/2$. Thus

$$O\cdot\text{spin-product}=\psi_1+\psi_2+\cdots+\psi_n=\Phi,$$

each of the ψ_i being normalized. We have $(\psi_i,\psi_i)=1$, $(\psi_i,\psi_j)=1/(N+1)$. Thus

$$(\Phi,\Phi)=\textstyle\sum_i(\psi_i,\psi_i)+2\sum_{i>j}(\psi_i,\psi_j) = n[1+(n-1)/(N+1)].$$

Therefore, if we multiply O by $\{n[1+(n-1)/N+1)]\}^{-\frac{1}{2}}$, we will produce a normalized resultant state. We can modify the form of O given in (41) so that it can operate on any spin product function. That is,

$$O=\frac{1}{(N+1)^{\frac{1}{2}}\{n[1+(n-1)/(N+1)]\}^{\frac{1}{2}}} \times\sum_i\left[1+\sum_{M=1}^{N}\frac{(-1)^M(N-M)!}{N!M!} \times\{(S_{Ai}^-S_{Bi}^+)^M+(S_{Ai}^+S_{Bi}^-)^M\} \prod_{jA_i,kB_i}^{N}(S_{jA_i}^+S_{jA_i}^-S_{kB_i}^-S_{kB_i}^+ + S_{jA_i}^-S_{jA_i}^+S_{kB_i}^+S_{kB_i}^-)\right]. \quad (50)$$

This will be taken to be the final form of the operator O. We can now write down $\Psi_5(S=0)$ directly as

$$\Psi_5(S=0)=O[O|\alpha\alpha\beta|\cdot O|\alpha\beta\beta|]. \quad (51)$$

THE EIGHT-ELECTRON PROBLEM

Before passing on to applications of the operator O other than the creation of the orthogonal singlets for an n-electron problem, the use of this operator may be further illustrated by writing down the fourteen orthogonal singlets for the eight-electron problem. It is to be recalled that the singlets for the six-electron problem were found by partitioning the six orbitals in the various ways suggested by the branching diagram. The construction of this diagram is not necessary in general, and we shall write down the singlets for the eight-electron case without recourse to it. The fourteen orthonormal singlets for the eight-electron problem are:

$$\Psi_1(S=0)=O|\alpha\beta|\cdot O|\alpha\beta|\cdot O|\alpha\beta|\cdot O|\alpha\beta|, \quad (52)$$

$$\Psi_2(S=0)=O|\alpha\beta|\cdot O|\alpha\alpha\beta\beta|, \quad (53)$$

$$\Psi_3(S=0)=O|\alpha\alpha\alpha\beta\beta\beta|\cdot O|\alpha\beta|, \quad (54)$$

$$\Psi_4(S=0)=O|\alpha\alpha\alpha\alpha\beta\beta\beta\beta|, \quad (55)$$

$$\Psi_5(S=0)=O|\alpha\beta|\cdot O|\alpha\alpha\beta\beta|\cdot O|\alpha\beta|, \quad (56)$$

$$\Psi_6(S=0)=O|\alpha\beta|\cdot O|\alpha\beta|\cdot O|\alpha\alpha\beta\beta|, \quad (57)$$

$$\Psi_7(S=0)=O|\alpha\alpha\beta\beta|\cdot O|\alpha\beta|\cdot O|\alpha\beta|, \quad (58)$$

$$\Psi_8(S=0)=O|\alpha\alpha\beta\beta|\cdot O|\alpha\alpha\beta\beta|, \quad (59)$$

$$\Psi_9(S=0)=O[O|\alpha\alpha\alpha\beta\beta|\cdot O|\alpha\beta\beta|], \quad (60)$$

$$\Psi_{10}(S=0)=O[O|\alpha\alpha\beta|\cdot O|\alpha\alpha\beta\beta\beta|], \quad (61)$$

$$\Psi_{11}(S=0)=O[O|\alpha\alpha\beta\alpha|\cdot O|\beta\alpha\beta\beta|], \quad (62)$$

$$\Psi_{12}(S=0)=O[O|\alpha\alpha\alpha\beta|\cdot O|\alpha\beta\beta\beta|], \quad (63)$$

$$\Psi_{13}(S=0)=O[O|\alpha\alpha\beta|\cdot O|\alpha\beta\beta|]\cdot O|\alpha\beta|, \quad (64)$$

$$\Psi_{14}(S=0)=O|\alpha\beta|\cdot O[O|\alpha\alpha\beta|\cdot O|\alpha\beta\beta|], \quad (65)$$

THE TEN-ELECTRON PROBLEM

The forty-two orthogonal singlets for a ten-electron system are:

$$\Psi_1=O|\alpha\beta|\cdot O|\alpha\beta|\cdot O|\alpha\beta|\cdot O|\alpha\beta|\cdot O|\alpha\beta|, \quad (66)$$

$$\Psi_2=O|\alpha\alpha\beta\beta|\cdot O|\alpha\beta|\cdot O|\alpha\beta|\cdot O|\alpha\beta|, \quad (67)$$

$$\Psi_3=O|\alpha\beta|\cdot O|\alpha\alpha\beta\beta|\cdot O|\alpha\beta|\cdot O|\alpha\beta|, \quad (68)$$

$$\Psi_4=O|\alpha\beta|\cdot O|\alpha\beta|\cdot O|\alpha\alpha\beta\beta|\cdot O|\alpha\beta|, \quad (69)$$

$$\Psi_5=O|\alpha\beta|\cdot O|\alpha\beta|\cdot O|\alpha\beta|\cdot O|\alpha\alpha\beta\beta|, \quad (70)$$

$$\Psi_6=O|\alpha\alpha\beta\beta|\cdot O|\alpha\beta|\cdot O|\alpha\alpha\beta\beta|, \quad (71)$$

$$\Psi_7=O|\alpha\beta|\cdot O|\alpha\alpha\alpha\beta\beta\beta|\cdot O|\alpha\beta|, \quad (72)$$

$$\Psi_8=O|\alpha\alpha\beta\beta|\cdot O|\alpha\alpha\alpha\beta\beta\beta|, \quad (73)$$

$$\Psi_9=O|\alpha\alpha\alpha\beta\beta\beta|\cdot O|\alpha\alpha\beta\beta|, \quad (74)$$

$$\Psi_{10}=O[O|\alpha\alpha\beta|\cdot O|\alpha\beta\beta|]\cdot O|\alpha\beta|\cdot O|\alpha\beta|, \quad (75)$$

$$\Psi_{11}=O|\alpha\beta|\cdot O[O|\alpha\alpha\beta|\cdot O|\alpha\beta\beta|]\cdot O|\alpha\beta|, \quad (76)$$

$$\Psi_{12}=O|\alpha\beta|\cdot O|\alpha\beta|\cdot O[O|\alpha\alpha\beta|\cdot O|\alpha\beta\beta|], \quad (77)$$

$$\Psi_{13}=O|\alpha\alpha\beta\beta|\cdot O|\alpha\alpha\beta\beta|\cdot O|\alpha\beta|, \quad (78)$$

$$\Psi_{14}=O|\alpha\beta|\cdot O|\alpha\alpha\beta\beta|\cdot O|\alpha\alpha\beta\beta|, \quad (79)$$

$$\Psi_{15}=O|\alpha\alpha\alpha\alpha\beta\beta\beta\beta|\cdot O|\alpha\beta|, \quad (80)$$

$$\Psi_{16}=O|\alpha\beta|\cdot O|\alpha\alpha\alpha\alpha\beta\beta\beta\beta|, \quad (81)$$

$$\Psi_{17}=O|\alpha\alpha\alpha\beta\beta\beta|\cdot O|\alpha\beta|\cdot O|\alpha\beta|, \quad (82)$$

$$\Psi_{18}=O|\alpha\beta|\cdot O|\alpha\beta|\cdot O|\alpha\alpha\alpha\beta\beta\beta|, \quad (83)$$

$$\Psi_{19}=O|\alpha\alpha\beta\beta|\cdot O[O|\alpha\alpha\beta|\cdot O|\alpha\beta\beta|], \quad (84)$$

$$\Psi_{20}=O[O|\alpha\alpha\beta|\cdot O|\alpha\beta\beta|]\cdot O|\alpha\alpha\beta\beta|, \quad (85)$$

$$\Psi_{21}=O[O|\alpha\alpha\alpha\beta|\cdot O|\alpha\beta\beta\beta|]\cdot O|\alpha\beta|, \quad (86)$$

$$\Psi_{22}=O|\alpha\beta|\cdot O[O|\alpha\alpha\alpha\beta|\cdot O|\alpha\beta\beta\beta|], \quad (87)$$

$$\Psi_{23}=O[O|\alpha\alpha\beta|\cdot O|\alpha\alpha\beta\beta\beta|]\cdot O|\alpha\beta|, \quad (88)$$

$$\Psi_{24}=O|\alpha\beta|\cdot O[O|\alpha\alpha\beta|\cdot O|\alpha\alpha\beta\beta\beta|], \quad (89)$$

$$\Psi_{25}=O[O|\alpha\alpha\alpha\beta\beta|\cdot O|\alpha\beta\beta|]\cdot O|\alpha\beta|, \quad (90)$$

$$\Psi_{26}=O|\alpha\beta|\cdot O[O|\alpha\alpha\alpha\beta\beta|\cdot O|\alpha\beta\beta|], \quad (91)$$

$$\Psi_{27}=O|\alpha\beta|\cdot O[O|\alpha\alpha\beta\alpha|\cdot O|\beta\alpha\beta\beta|], \quad (92)$$

$$\Psi_{28}=O[O|\alpha\alpha\beta\alpha|\cdot O|\beta\alpha\beta\beta|]\cdot O|\alpha\beta|, \quad (93)$$

$$\Psi_{29}=O|\alpha\alpha\alpha\alpha\beta\beta\beta\beta|, \quad (94)$$

$$\Psi_{30}=O[O|\alpha\alpha\alpha\beta|\cdot O|\alpha\beta\beta\beta\beta|], \quad (95)$$

$$\Psi_{31}=O[O|\alpha\alpha\alpha\beta|\cdot O|\alpha\alpha\beta\beta\beta|], \quad (96)$$

$$\Psi_{32}=O[O|\alpha\alpha\alpha\alpha\beta\beta|\cdot O|\alpha\beta\beta\beta|], \quad (97)$$

$$\Psi_{33}=O[O|\alpha\alpha\alpha\beta\beta|\cdot O|\alpha\alpha\beta\beta\beta|], \quad (98)$$

$$\Psi_{34}=O[O|\alpha\alpha\beta|\cdot O|\alpha\alpha\alpha\beta\beta\beta\beta|], \quad (99)$$

$$\Psi_{35}=O[O|\alpha\alpha\alpha\alpha\beta\beta\beta|\cdot O|\alpha\beta\beta|], \quad (100)$$

$$\Psi_{36}=O[O|\alpha\alpha\beta\alpha\alpha|\cdot O|\beta\beta\alpha\beta\beta|], \quad (101)$$

$$\Psi_{37}=O[O|\alpha\alpha\alpha\beta\alpha\beta\beta|\cdot O|\alpha\beta\beta|], \quad (102)$$

$$\Psi_{38}=O[O|\alpha\alpha\beta|\cdot O|\alpha\alpha\beta\alpha\beta\beta\beta|], \quad (103)$$

$$\Psi_{39}=O[O|\alpha\alpha\beta\alpha\beta|\cdot O|\alpha\alpha\beta\beta\beta|], \quad (104)$$

$$\Psi_{40}=O[O|\alpha\alpha\alpha\beta\beta|\cdot O|\alpha\beta\alpha\beta\beta|], \quad (105)$$

$$\Psi_{41}=O[O|\alpha\alpha\beta\alpha\beta|\cdot O|\alpha\beta\alpha\beta\beta|], \quad (106)$$

$$\Psi_{42}=O[O|\alpha\alpha\alpha\beta\alpha|\cdot O|\beta\alpha\beta\beta\beta|]. \quad (107)$$

APPLICATIONS TO CONFIGURATION INTERACTION

Let us now turn from the consideration of how to set up the orthogonal singlets and very briefly investigate some of the aspects of a configuration interaction calculation. The determination of the expectation value of the Hamiltonian H with respect to a particular state will be considered as an example of how the spin operator O can be used. Suppose we wish to find the expectation value of H with respect to the six electron

singlet given in (44), i.e., $O|\alpha\alpha\alpha\beta\beta\beta|$.

$$\begin{aligned}(\psi|H|\psi)&=[O|\alpha\alpha\alpha\beta\beta\beta|\cdot|H|\cdot O|\alpha\alpha\alpha\beta\beta\beta|]\\&=[OA(\alpha\alpha\alpha\beta\beta\beta)|H|OA(\alpha\alpha\alpha\beta\beta\beta)]\\&=[AO^2A(\alpha\alpha\alpha\beta\beta\beta)|H|(\alpha\alpha\alpha\beta\beta\beta)]\\&=(N+1)![AO(\alpha\alpha\alpha\beta\beta\beta)|H|(\alpha\alpha\alpha\beta\beta\beta)],\\(\psi|H|\psi)&=2AO(\alpha\alpha\alpha\beta\beta\beta)|H|(\alpha\alpha\alpha\beta\beta\beta).\end{aligned}\tag{108}$$

The spatial orbitals in the spin-product function $(\alpha\alpha\alpha\beta\beta\beta)$ are assumed to be orthonormal. In the expansion of $AO(\alpha\alpha\alpha\beta\beta\beta)$ the only terms which will make nonzero contributions to the matrix element are those for which a given electron is assigned the same spin on both sides of the matrix element. Therefore, we need only consider those terms in the expansion which lead to $\alpha(1)\alpha(2)\alpha(3)\beta(4)\beta(5)\beta(6)$. Let us write the antisymmetrizing operator as

$$A=\sum_P(-1)^pP^qP^\sigma.\tag{109}$$

Because of the orthogonality of the spatial orbitals in the spin-product function, the only spatial coordinate permutations in A that will give rise to nonvanishing integrals are the P^q's which effect a single interchange. When O operates on $(\alpha\alpha\alpha\beta\beta\beta)$, all those values of M in O greater than one cause two or more spin interchanges between sets A and B. Therefore, in order to match spins on both sides of H, we will need a permutation from A which is the product of at least two interchanges of spin and space coordinates. This will, therefore, lead to a zero contribution due to the spatial orthogonality. Hence the only terms that give contributions from the operator O are those from M values of zero or one. For $M=0$, we will get nonvanishing integrals from all possible interchanges of a single pair of spatial coordinates within set A or within set B. For $M=1$ in O the terms arising from the operation of O on the spin-product are all the possible single spin interchanges between sets A and B. Therefore, in order to match spins for a nonzero integral, we will need those permutations in A which put the spins back in place. But these permutations involve the interchange of a single pair of spatial coordinates between sets A and B, and will therefore give rise to exchange integrals. Let us now write down $(\psi|H|\psi)$.

$$\begin{aligned}(\psi|H|\psi)=\Big\{\Big[1-\sum_{jA=1}^{3}\sum_{kA=1\neq jA}^{3}P_{jAkA}{}^q-\sum_{jB=4}^{6}\sum_{kB=4\neq jB}^{6}P_{jBkB}{}^q\\+\frac{1}{3}\sum_{jA=1}^{3}\sum_{kB=4}^{6}P_{jAkB}{}^q\Big]\varphi_1(1)\alpha(1)\varphi_2(2)\alpha(2)\varphi_3(3)\\\times\alpha(3)\varphi_4(4)\beta(4)\varphi_5(5)\beta(5)\varphi_6(6)\beta(6)\\\times|H|\varphi_1(1)\alpha(1)\varphi_2(2)\alpha(2)\cdots\varphi_6(6)\beta(6)\}.\end{aligned}\tag{110}$$

This expression may seem complicated, but the reader will also note that this matrix element is taken with respect to a singlet state which is a linear combination of twenty determinants. This leads to the direct product of twenty determinants and contributions from 180 nonzero cross products.

This general procedure for treating matrix elements can be extended to nondiagonal matrix elements and can be generalized to systems with a rather large number of electrons.

ACKNOWLEDGMENTS

The author wishes to thank R. H. Parmenter and G. F. Koster for most helpful discussions concerning this work.

APPENDIX I

Theorem I

Different paths on the branching diagram terminating at the same destination lead to orthogonal states.

Proof

It is assumed that all spatial orbitals are orthonormal. A one to one correspondence exists between a determinant D and spin-product function ϕ, and it is $D=A\phi$ where A is the antisymmetrizing operator. If two spin-product functions composed of the same set of spatial orbitals differ in the assignment of spin to these spatial orbitals, then the spin-product functions, or the determinants corresponding to them, are orthogonal. It is understood that if two states of the same multiplicity are orthogonal, then the orthogonality is independent of the M_S quantum number of the states. Having made these preliminary remarks, let us proceed.

The first case in the branching diagram where one encounters two different paths leading to the same end point is for three electrons as shown in Figs. 2(a) and 2(b). The two states are

$$\begin{aligned}\Psi_{2a}&=(1/\sqrt{2})\{|\alpha\beta\alpha|-|\beta\alpha\alpha|\}=(A/\sqrt{2})[(\alpha\beta\alpha)-(\beta\alpha\alpha)],\\\Psi_{2b}&=(1/\sqrt{6})\{2|\alpha\alpha\beta|-|\alpha\beta\alpha|-|\beta\alpha\alpha|\}\\&=(A/\sqrt{6})[2(\alpha\alpha\beta)-(\alpha\beta\alpha)-(\beta\alpha\alpha)],\end{aligned}$$

where $(\alpha\beta\alpha\alpha\beta\cdots)$ will in general denote a spin-product function. Ψ_{2a} and Ψ_{2b} are orthogonal.

Let us now consider an arbitrary x-electron terminal point on the branching diagram corresponding to an arbitrary multiplicity, say S. We shall assume that all of the different paths leading to this terminal point correspond to orthogonal states of multiplicity S. It will be shown that all of the states arising from the combination of an additional electron with the various states corresponding to a given terminal point are orthogonal. It will also be shown that any two $(x+1)$-electron states of the same multiplicity which arise from the combination of the $(x+1)$st electron with x-electron states of different multiplicities are orthogonal.

Consider the addition of the $(x+1)$st electron to the ith state corresponding to the x-electron terminal point of multiplicity S which results in an $(x+1)$-electron

state of $S+\frac{1}{2}$ and $M_S=S+\frac{1}{2}$. The composite state is

$$\psi_i(S+\tfrac{1}{2}, M_S=S+\tfrac{1}{2})=\varphi_i(S, M_S=S)\cdot\varphi(S=\tfrac{1}{2}, M_S=\tfrac{1}{2}),$$

where $\varphi(s=\frac{1}{2}, M_S=\frac{1}{2})$ is just $\varphi_{x+1}(x+1)\alpha(x+1)$. Now φ_i is equal to A_x operating on some linear combination of x-electron spin-product functions, where A_x antisymmetrizes a function of x coordinates. $\psi_i(S+\frac{1}{2}, S+\frac{1}{2})$ is equal to A_{x+1} operating on that same linear combination of spin-product functions each spin-product being multiplied by $\varphi_{x+1}(x+1)\alpha(x+1)$. Consider any $\psi_j(S+\frac{1}{2}, S+\frac{1}{2})$ for $j\neq i$. This is A_{x+1} operating on the linear combination of spin-product functions corresponding to $\varphi_j(S, S)$, each spin-product being multiplied by $\varphi_{x+1}(x+1)\alpha(x+1)$. $\varphi_i(S, S)$ has been assumed orthogonal to $\varphi_j(S, S)$. Therefore, $\psi_i(S+\frac{1}{2}, S+\frac{1}{2})$ is orthogonal to $\psi_j(S+\frac{1}{2}, S+\frac{1}{2})$, for the orthogonality of two linear combinations of x-electron spin-product functions is not changed when it is multiplied by $\varphi_{x+1}(x+1)\alpha(x+1)$ and operated on by A_{x+1}.

Now consider the addition of the $(x+1)$st electron to the ith state which corresponds to the x-electron terminal point at multiplicity S and which results in an $(x+1)$-electron state $\psi_i(S-\frac{1}{2}, M_S=S-\frac{1}{2})$. We have

$$\psi_i(S-\tfrac{1}{2}, M_S=S-\tfrac{1}{2})=C_1\varphi_i(S, S)\varphi(\tfrac{1}{2}, -\tfrac{1}{2})+C_2\varphi_i(S, S-1)\varphi(\tfrac{1}{2}, +\tfrac{1}{2}).$$

Consider any other $\psi_j(S-\frac{1}{2}, S-\frac{1}{2})$ obtained by adding the $(x+1)$st electron to $\varphi_j(S, M_S)$. We have

$$\psi_j(S-\tfrac{1}{2}, S-\tfrac{1}{2})=C_1\varphi_j(S, S)\varphi(\tfrac{1}{2}, -\tfrac{1}{2})+C_2\varphi_j(S, S-1)\varphi(\tfrac{1}{2}, +\tfrac{1}{2}).$$

Since $\varphi_j(S, S)$ is orthogonal to $\varphi_i(S, S)$ and $\varphi_j(S, S-1)$ is orthogonal to $\varphi_i(S, S-1)$, we have that $\psi_i(S-\frac{1}{2}, S-\frac{1}{2})$ is orthogonal to $\psi_j(S-\frac{1}{2}, S-\frac{1}{2})$ by the same arguments given above.

Therefore, it has been shown that all of the states arising from the combination of an additional electron with the various states corresponding to a given terminal point are orthogonal.

Suppose now that we have two $(x+1)$-electron states of the same multiplicity which arise from the combination of the $(x+1)$st electron with x-electron states of different multiplicities. Two x-electron states of different multiplicity are orthogonal. Therefore, by proceeding in the same manner as above. it is easily shown that the two $(x+1)$-electron states are orthogonal.

Therefore, the theorem is proved.

APPENDIX II

Theorem II

The spin operator O given in (49) commutes with S^2.

Proof

The operator S^2 may be expressed as

$$S^2=\text{const}+\sum_{i>j}P_{ij}^{\sigma}. \tag{A-1}$$

The commutation of S^2 and O is clearly a question of the commutation of $\sum_{i>j}P_{ij}^{\sigma}$ and O. It will be established that P_{st}^{σ} commutes with O for arbitrary s and t and therefore, that S^2 commutes with O. It has been shown that the following properties hold for P_{st}^{σ}.[6]

$$S_s^{+}P_{st}^{\sigma}=P_{st}^{\sigma}S_t^{+}, \tag{A-2}$$

$$S_s^{-}P_{st}^{\sigma}=P_{st}^{\sigma}S_t^{-}, \tag{A-3}$$

$$(S_s^{-}S_k^{+})^M P_{st}^{\sigma}=P_{st}^{\sigma}(S_t^{-}S_k^{+})^M, \tag{A-4}$$

$$(S_t^{+}S_t^{-}S_s^{+}S_s^{-})P_{st}^{\sigma}=P_{st}^{\sigma}(S_t^{+}S_t^{-}S_s^{+}S_s^{-}), \tag{A-5}$$

$$(S_t^{+}S_t^{-}S_k^{+}S_k^{-})P_{st}^{\sigma}=P_{st}^{\sigma}(S_s^{+}S_s^{-}S_k^{+}S_k^{-}). \tag{A-6}$$

We will speak here about the operation of O on a spin-product function, as this allows one to treat the electrons as being distinguishable, which is convenient. We can break down the sum over i in the operator O into two cases:

1. All choices of i for which both s and t are in the same group, i.e., A or B.
2. All of those choices of i for which s and t are in different groups, i.e. s in A and t in B.

Let us consider case 1. For (5), we have

$$(S_{sA}^{+}S_{sA}^{-}S_{tA}^{+}S_{tA}^{-})P_{st}^{\sigma}=P_{st}^{\sigma}(S_{sA}^{+}S_{sA}^{-}S_{tA}^{+}S_{tA}^{-}).$$

The expression $(S_{Ai}^{-}S_{Bi}^{+})^M$ consists of all possible M tuples, i.e.,

$$S_{x1Ai}^{-}S_{x2Ai}^{-}\cdots S_{xMAi}^{-}S_{y1Bi}^{+}S_{y2Bi}^{+}\cdots S_{yMBi}^{+}.$$

If neither S_{sA}^{-} nor S_{tA}^{-} appear in a given M tuple, then that M tuple commutes with P_{st}^{σ}. If just S_{sAi}^{-} appears, then

$$(S_{x1Ai}^{-}\cdots S_{sAi}^{-}\cdots S_{xMAi}^{-}S_{y1Bi}^{+}\cdots S_{yMBi}^{+})P_{st}^{\sigma}=P_{st}^{\sigma}(S_{x1Ai}^{-}\cdots S_{tAi}^{-}\cdots S_{xMAi}^{-}S_{y1Bi}^{+}\cdots S_{yMBi}^{+}).$$

Therefore, the sum of the two M tuples, one with just S_{sAi}^{-} and the other with S_{tAi}^{-} in place of S_{sAi}^{-} but otherwise identical, commutes with P_{st}^{σ}. Hence P_{st}^{σ} commutes with the sum of all possible M tuples which contain either S_{sAi}^{-} or S_{tAi}^{-} but not both at the same time. If both S_{sAi}^{-} and S_{tAi}^{-} appear in an M tuple, then P_{st}^{σ} commutes with that M tuple. Therefore, it follows that P_{st}^{σ} commutes with all O_i in which both s and t are in the same group.

Let us now consider case 2. We can easily show that

$$(S_{sA}^{+}S_{sA}^{-}S_{tB}^{-}S_{tB}^{+})P_{st}^{\sigma}=P_{st}^{\sigma}(S_{tA}^{+}S_{tA}^{-}S_{sB}^{-}S_{sB}^{+}).$$

Therefore,

$$(S_{sA}^{+}S_{sA}^{-}S_{tB}^{-}S_{tB}^{+}+S_{tA}^{+}S_{tA}^{-}S_{sB}^{-}S_{sB}^{+})P_{st}^{\sigma}=P_{st}^{\sigma}(S_{sA}^{+}S_{sA}^{-}S_{tB}^{-}S_{tB}^{+}+S_{tA}^{+}S_{tA}^{-}S_{sB}^{-}S_{sB}^{+}).$$

As in case 1, we can examine all of the M tuples which

[6] P. Dirac, *Quantum Mechanics* (Oxford University Press, London, 1947), p. 222.

appear in the expansion of O, those where neither s nor t occur, those where one or the other occur, and those where both s and t appear. In quite the same way as in case 1, it can be shown that P_{st}^{σ} commutes with the collection of all possible M tuples.

Therefore, in this fashion one can show that P_{st}^{σ} commutes with O, which implies that S^2 commutes with O.

APPENDIX III

Theorem III

The spin operator O is Hermitian.

Proof

Every term in O appears symmetrically with its hermitian conjugate. Therefore, O is Hermitian.

Theorem IV

The spin operator O commutes with the Hamiltonian H.

Proof

This is a matter of restricting ourselves to spin-free Hamiltonians.

Theorem V

The spin operator O squared is

$$(N+1)^{\frac{1}{2}}\{n[1+(n-1)/(n+1)]\}^{\frac{1}{2}}O.$$

Proof

It will be shown first that $O^2=\text{const}\cdot O$. The value of the constant will be determined later. We shall consider an N-electron problem and the effect of O^2 operating on a single $N\times N$ determinant D_0, the generalization of O^2 operating on any linear combination of $N\times N$ determinants being trivial.

Let OD_0 be written as

$$OD_0=C_0D_0+C_1\{D_1^{(1)}+D_2^{(1)}+\cdots+D_{X^2}^{(1)}\}+C_2\{D_1^{(2)}+D_2^{(2)}+D_3^{(2)}+\cdots D_{X(X-1)/2}^{(2)}+\cdots+C_XD_1^{(X)}.$$

where, in $D_k^{(j)}$, j refers to the number of reversals in set A or B and k denotes the kth determinant with j reversals. Let us now order these determinants such that

$$D_1^{(1)}=P_{1A1B}^{\sigma}D_0\cdots D_{X^2}^{(1)}=P_{XAXB}^{\sigma}D_0,$$

$$D_1^{(2)}=P_{1A1B}^{\sigma}P_{2A2B}^{\sigma}D_0,\ D_2^{(2)}=P_{1A1B}^{\sigma}P_{2A3B}^{\sigma}D_0,\ \cdots,$$

and so forth.

Let us consider O^2D_0 term by term. The first term is just C_0OD_0. The second term may be written

$$C_1O\{P_{1A1B}^{\sigma}+P_{1A2B}^{\sigma}+\cdots+P_{XAXB}^{\sigma}\}D_0.$$

In Appendix II it was shown that any P_{st}^{σ} commutes with O. Therefore, the second term can be expressed as

$$C_1\{P_{1A1B}^{\sigma}+P_{1A2B}^{\sigma}+\cdots+P_{XAXB}^{\sigma}\}OD_0.$$

We know that OD_0 is an eigenfunction of S^2 which is

$$S^2=\text{const}+\sum_{i>j}P_{ij}^{\sigma}.$$

Thus

$$\sum_{i>j}P_{ij}^{\sigma}(OD_0)=\text{const}OD_0.$$

We can write $\sum_{i>j}P_{ij}^{\sigma}$ as

$$\sum_{i>j}P_{ij}^{\sigma}=\sum_{jA>kA}P_{jAkA}^{\sigma}+\sum_{jB>kB}P_{jBkB}^{\sigma}+\sum_{jAkB}P_{jAkB}^{\sigma}.$$

Since P_{jAkA}^{σ} and P_{jBkB}^{σ} commute with O and since they leave D_0 invariant, we have

$$\sum_{jAkB}P_{jAkB}^{\sigma}(OD_0)=\text{const}OD_0.$$

However, the second term in O^2D_0 is just

$$C_1[\sum_{jAkB}P_{jAkB}^{\sigma}]OD_0,$$

and is, therefore, a constant times OD_0.

The third term can be written as

$$C_2[\sum_{jAkB}\sum_{sAtB}P_{jAkB}^{\sigma}P_{sAtB}^{\sigma}]OD_0.$$

However, we see from

$$[\sum_{jAkB}P_{jAkB}^{\sigma}]OD_0=\text{const}OD_0,$$

that

$$[\sum_{jAkB}P_{jAkB}^{\sigma}]^2OD_0=[\sum_{jAkB}P_{jAkB}^{\sigma}\sum_{sAtB}P_{sAtB}^{\sigma}]OD_0.$$

Hence, the third term in O^2D_0 is just a constant times OD_0. Proceeding in this manner it is clear that

$$O^2D_0=\text{const}OD_0.$$

Now let

$$OD_i=\psi_i.$$

We have

$$(\psi_i,\psi_i)=(OD_i,OD_i)=(O^2D_i,D_i)=\text{const}\,(OD_i,D_i)=1.$$

However,

$$OD_i=\frac{1}{(N+1)^{\frac{1}{2}}\{n[1+(n-1)/(N+1)]\}^{\frac{1}{2}}}D_i+\text{orthogonal } D_j\text{'s}.$$

Therefore,

$$\text{const}\left[(N+1)^{-\frac{1}{2}}\left\{n\left(1+\frac{n-1}{N+1}\right)\right\}^{-\frac{1}{2}}\right](D_i,D_i)=1,$$

and

$$\text{const}=\left[(N+1)^{\frac{1}{2}}\left\{n\left(1+\frac{n-1}{N+1}\right)\right\}^{\frac{1}{2}}\right];$$

so

$$O^2=\left[(N+1)^{\frac{1}{2}}\left\{n\left(1+\frac{n-1}{N+1}\right)\right\}^{\frac{1}{2}}\right]O.$$

APPENDIX IV

Theorem VI

The spin operator O commutes with the antisymmetrizing operator A.

Proof

The antisymmetrizing operator A can be written as

$$A=\sum_P(-1)^P P^q P^\sigma,$$

where P^q is a permutation of the spatial coordinates and P^σ is a permutation of the spin coordinates. Any spatial permutation operator clearly commutes with O. Any spin permutation operator can be written as a product of $P_{ij}{}^\sigma$'s. But, any $P_{ij}{}^\sigma$ commutes with O. Therefore, any spin permutation operator commutes with O. Hence every permutation in A commutes with O, which implies that A commutes with O.

PHYSICAL REVIEW VOLUME 92, NUMBER 2 OCTOBER 15, 1953

The 1.25-Minute Rb^{82m} Daughter of 27-Day Sr^{82}

L. M. LITZ, S. A. RING, AND W. R. BALKWELL
California Research and Development Company, Livermore, California

(Received June 29, 1953)

The 3.15-Mev positron associated with the decay of the 27-day Sr^{82} has been found to arise from the decay of a 1.25-minute metastable Rb^{82} isomer by an allowed transition to the Kr^{82} ground state. No isomeric transition to the 6.3-hour Rb^{82} ground state was observed. A tentative decay scheme and spin and parity assignments are discussed.

INTRODUCTION

THE 27-day Sr^{82} was observed to have a positron radiation of 3.15 Mev.[1,2] Castner and Templeton suggested this radiation was due to a short-lived Rb daughter because of its high energy. However, they were unable to find this Rb isotope because of the time required for the chemical separation used. Also, they established that the 6.3-hour Rb^{82} was not the daughter of the 27-day Sr^{82}.

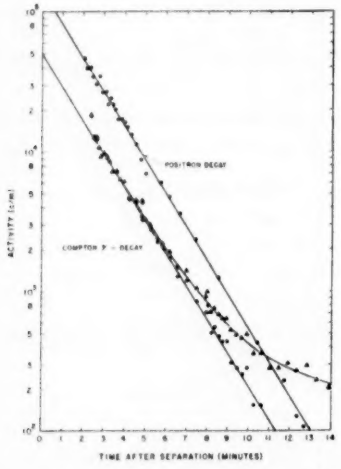

FIG. 1. Positron and Compton γ decay of Rb^{82m}.

It was the purpose of this work to clarify the decay scheme. The pertinent results have been published in Hollander, Perlman, and Seaborg's revised Table of Isotopes.[3]

PROCEDURE

Chemical Separation

Purified strontium fractions containing the 27-day Sr^{82} were prepared from target materials containing either strontium or zirconium which had been bombarded with 350-Mev protons or 190-Mev deuterons on the University of California's 184-in. cyclotron. Fuming nitric acid precipitations of $Sr(NO_3)_2$ followed by cation resin adsorption and elution of the strontium fraction was used for this purification. Holdback agents were used to keep the preparation free of the other spallation products.

The purified strontium fraction was allowed to stand to insure adequate growth of any daughter activity of several hours half-life. Perchloric acid, strontium, and rubidium carrier were added and the solution boiled to fuming. After cooling to ice temperature, the rubidium perchlorate was precipitated by rapid addition of chilled

[1] S. V. Castner and D. H. Templeton, Phys. Rev. **88**, 1126 (1952); S. V. Castner, M.S. thesis, University of California Radiation Laboratory Unclassified Report UCRL-942, October, 1950 (unpublished).

[2] K. C. Maclure, Ph.D. thesis, McGill University, September, 1952 (unpublished).

[3] Hollander, Perlman, and Seaborg, Revs. Modern Phys. **25**, 469 (1953).

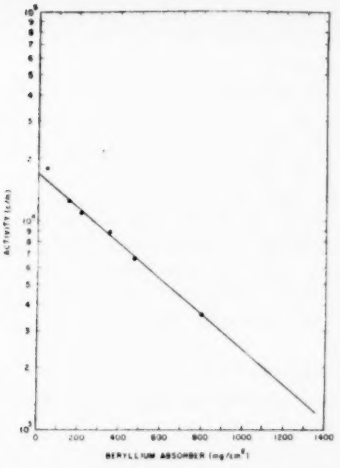

FIG. 2. Beryllium absorption curve of 1.25-min Rb^{82m}.

absolute alcohol. The precipitate was separated by vacuum filtration on a sintered glass filter, washed with alcohol and the filter placed in the Geiger counter.

Samples have been counted within one minute after the precipitation by this technique. Purification factors of 250 from the parent strontium activity were readily attained.

Measurement Techniques

The positron activity was followed with a standard alcohol-quenched Geiger counter. All counts were corrected for background and coincidence.

The γ spectrum was studied with a forty-channel pulse analyzer utilizing a thallium-activated NaI scintillation counter. The γ decay was followed with a single-channel pulse analyzer using a similar detector. The positron and conversion electrons from the strontium were observed using a 180° spectrometer and a magnetic lens spectrometer.

Absorption curves to determine the positron energy were taken with beryllium absorbers. Beryllium was preferred to aluminum in this region of the periodic table because of the appreciable half-thickness in the latter of x-rays of the elements around strontium which interferes with the resolution of the positron absorption curve.

RESULTS

Decay Rate

Four different rubidium samples gave half-lives of 1.25 ± 0.03 minutes when followed on the Geiger counter for at least six half-lives. Figure 1 shows a typical positron decay curve. The purity of this sample is evident from the absence of a long-lived tail through more than eight half-lives. The decay of the peak in the Compton γ spectrum also yielded a half-life of this magnitude. One of these decay curves is also shown in Fig. 1. The tail due to the γ activity of the longer lived strontiums is a larger fraction of the total activity than in the case of the particulate decay.

In the course of this work, quite a few strontium fractions were followed which showed a twenty-seven day half-life for Sr^{82} in agreement with Maclure.[2]

Radiations

Two types of experiments were used to show that the hard positron was associated with the Rb^{82} daughter of the Sr^{82}. In one, the strontium was separated from the rubidium by precipitation of the carbonate. The growth of the daughter was followed on the Geiger counter. Assuming all of the observed activity was due to this growth from the strontium, half-lives of the order of one minute were calculated from the growth. Since the major portion of the activity observed with a Geiger counter for this system is that of 3.15-Mev positron, it is indicated that this radiation accompanies the Rb daughter.

We were also able to obtain a beryllium absorption curve on a separated rubidium faction. This curve, Fig. 2, gave a half-thickness of 360 mg/cm² which is equivalent to approximately 2.8-Mev positrons. The agreement is quite satisfactory. Corrections were made for the decay during the time required to take the data assuming a 1.25-minute half-life. The variation in the activity of the long-lived tail with different absorber thickness was also taken into account. This long-lived tail had the absorption curve of a 3.15-Mev positron. The slope of the absorption curve was used to determine the energy rather than the end point because the short time available made it impossible to obtain the complete absorption curve.

The γ radiation of the separated rubidium fraction and of the strontium equilibrium mixture were essentially the same. This is indicated in the γ-pulse analysis curves of Fig. 3. No γ peaks above 0.6 Mev were observed. The γ spectra below this energy appears to be made up of the 0.51-Mev peak from the positron annihilation and the accompanying Compton radiation. The peaking at about 0.18 Mev has been observed with

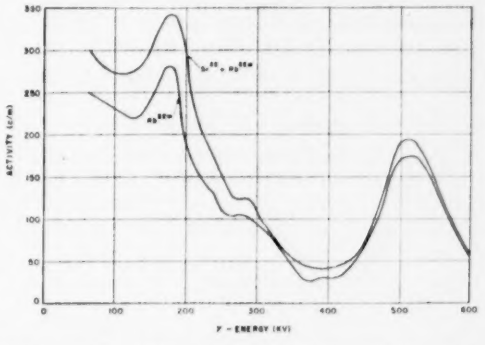

FIG. 3. γ spectra of Rb^{82m} and of Sr^{82}–Rb^{82m} equilibrium mixture.

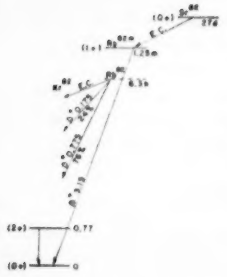

FIG. 4. Decay scheme of neutron-deficient mass-82 chain.

other isotopes having annihilation or other γ radiation in this energy region such as Na^{22} or Cs^{137}. This is due to γ radiation inelastically scattered from the bottom of the shielding.

The magnetic lens spectrometer showed only the electron spectrum characteristic of annihilation radiation.

6.3-Hour Rb^{82}

No activity which could be attributed to the 6.3-hour Rb^{82} was observed in either the gamma or positron decay curves of the separated rubidium fraction. An upper limit of 0.1 percent could be set on the percentage of the decay which goes through this isomer. Also, the strong γ peaks reported for this isomer[4,5] were not observed in the γ spectrum of Sr^{82} in equilibrium with its daughter activities.

DISCUSSION

Decay Scheme

A tentative decay scheme for the neutron-deficient mass-82 chain is shown in Fig. 4. The levels suggested by Huddleston and Mitchell[5] in the decay of the 6.3-hour Rb^{82} isomer were omitted because their position was felt to be uncertain in light of the evidence given below from which Fig. 4 was derived.

1. The minimum energy of 1.25-minute Rb^{82m} state above the Kr^{82} ground state is, from the positron energy, 4.17 Mev.

2. The existence of the first excited level of Kr^{82} at 0.77 Mev is strongly indicated by the fact that the intensity of the γ rays of this energy which were found in both the 6.3-hour Rb^{82} decay[5] and in the Br^{82} decay[6,7] is appreciably greater than that of any of the other γ's.

3. The transition from Rb^{82m} goes to the Kr^{82} ground state because neither the 0.77-Mev γ ray, nor any others, appears in the γ spectrum.

4. The $\log(ft)$ value calculated for the 3.15-Mev positron of the 1.25-minute Rb^{82m} is 4.35. This and the shape of the Fermi plot[1] indicate that this positron arises from an allowed transition.

Since the spin and parity of the Kr^{82} ground state are 0 and even, the Rb^{82m} state must have a spin of 1 with even parity for an allowed transition. If Nordheim's rules apply to the odd-odd nucleons of this excited state, the configuration available from the shell-model of the nucleus in this region would allow only the spin 1.

The question as to the proper placing of the levels in the tentative scheme proposed by Huddleston and Mitchell then arises because of the absence of the transition between the two Rb^{82} isomers. Their scheme, which places the Rb^{82} ground state at 2.57 Mev above the Kr^{82} ground state, would allow 1.6 Mev between the two states of the Rb isomers. With this energy available, one would expect the isomeric transition to have a half-life so short that even with maximum forbiddenness to the transition, the positron decay would not be observed. It is therefore suggested that the spacing of the two levels is much less than 1.6 Mev. Also, it is likely that the shell configuration of the Rb^{82} ground state is such so as to give a higher spin difference and possibly a change in parity between the ground and the excited level of Rb^{82}. This would require that the positron decay from the ground state would occur to levels higher in the Kr^{82} system than those suggested by Huddleston and Mitchell.

Another question arising out of the decay scheme of Fig. 4 is the absence of positron decay from the higher state of Rb^{82} to the first excited state of Kr^{82}. The energy available, on the basis of the scheme shown, would yield a positron of 2.38 Mev. The absence of positrons of this energy as well as the gamma rays of 0.77 Mev indicates that this is a forbidden transition.

The authors wish to express their appreciation to J. M. Hollander of the University of California Radiation Laboratory and F. E. Bjorklund of the California Research and Development Company for helpful discussion of the decay scheme, to J. Olson of the California Research and Development Company for obtaining and interpreting the magnetic lens β-ray spectrograms and to the crew of the 184-in. Berkeley cyclotron for carrying out the necessary bombardments. This work was carried out under a U. S. Atomic Energy Commission contract.

[4] D. G. Karraker and D. H. Templeton, Phys. Rev. **80**, 646 (1950).
[5] C. M. Huddleston and A. C. G. Mitchell, Phys. Rev. **88**, 1350 (1952).
[6] Siegbahn, Hedgran, and Deutsch, Phys. Rev. **76**, 1263 (1949).
[7] P. Hubert and J. Laberrigue-Frowlow, Compt. rend. **232**, 2420 (1951).

PHYSICAL REVIEW VOLUME 92, NUMBER 2 OCTOBER 15, 1953

The Elastic Scattering of Particles by Atomic Nuclei*

N. C. FRANCIS AND K. M. WATSON†
Department of Physics, Indiana University, Bloomington, Indiana
(Received June 1, 1953)

The description of the elastic scattering of particles by atomic nuclei in terms of the optical model is studied. It is shown that the optical model does not represent only an approximation to the many-body problem, although the optical model potential must in general be considered to contain spin-orbit couplings. An explicit expression is obtained for the optical model potential in terms of the amplitudes for scattering of the incident particle by the individual neutrons and protons of the nucleus. The potential also depends upon correlations in the positions of the nuclear particles. A calculation of the parameters of the optical model seems to be in good agreement with some meson scattering experiments.

I. INTRODUCTION

IN a previous publication[1] a general theory of the multiple scattering of particles by complex systems was developed. The multiple scattering was described by the solution to a set of coupled integral equations, the number of equations being equal to the number of scattering centers in the scattering medium. When the number of scatterers is large a direct solution of the coupled integral equations is not feasible; however, in this case it was shown that the integral equations can be considerably simplified when the coherent (elastic) scattering is separated from the inelastic scattering. From this form of the equations it was possible to show that the inelastic scattering could be (approximately) described by a transport equation. The elastic scattering could be approximately described by the conventional "optical models"[2] when the energy of the incident particle was high.

In the present paper we consider the elastic scattering in more detail. The theory is applied specifically to the scattering of particles by atomic nuclei, but the formal arguments are quite general. In particular, we shall see that the "optical model" has in principle a wide range of validity and thus does not necessarily represent only an approximation to the many-body problem.

By the term "optical model," we mean that the elastic scattering can be obtained from the solution to a Schrödinger equation with an interaction potential which depends only upon the coordinate of the incident particle relative to (let us say) the center of mass of the nucleus. If the incident particle and the nucleus have spins, the potential may also depend upon these—but it does not depend upon individual coordinates of the neutrons and protons of the nucleus. In other words, the many-body problem is reduced to a two-body problem. This reduction is somewhat formal, since an analysis of the many-body problem is in principle required to find the equivalent *two-body* interaction. The advantage gained by such an approach is that in some cases the problem of finding the two-body potential is much simpler than is that of tackling directly the many-body Schrödinger equation. Also, for many problems it appears possible to make reasonable guesses concerning the form of the two-body interaction.

The use of such an "equivalent two-body potential" has been frequently made. Such an approach was employed by Ostrofsky, Breit, and Johnson[3] in calculating Coulomb barrier penetration. Bethe[4] has given a theory of nuclear reactions at low energies in terms of such an interaction. The model was also used by Feshbach, Peaslee, and Weisskopf[5] in the discussion of nuclear reactions. Fernbach, Serber, and Taylor[2] based their theory of nuclear reactions at high energies on an effective two-body potential. The latter model has been applied in particular to meson interactions.[6,7]

The purpose of the present paper is to study the relation of these models to the many-body problem. A special case of our results is an exact expression for the index of refraction for an extended scattering medium given in terms of the solution to an integral equation.

II. DEFINITIONS AND GENERAL PROPERTIES OF THE ELASTIC SCATTERING

Several useful characteristics of the elastic scattering of particles by atomic nuclei can be obtained quite generally without use of the more explicit multiple scattering theory of reference 1. In particular, we shall see that the elastic scattering can be obtained as the solution to a Schrödinger equation for a particle moving in the "potential" of a single heavy scatterer. That is, the potential involves only the coordinates and spin of the scattered particle, as well as the nuclear spin, but does not involve explicitly the coordinates of the neutrons and protons in the nucleus. Therefore, only the solution of a two-body (rather than a many-body) problem is required to determine the elastic scattering, once the "potential" is known.

To begin, we formulate the many-body problem

* Supported in part by a grant from the National Science Foundation.
† Now at the University of Wisconsin, Madison, Wisconsin.
[1] K. M. Watson, Phys. Rev. **89**, 575 (1953). This paper will hereafter be referred to as I.
[2] Fernbach, Serber, and Taylor, Phys. Rev. **75**, 1352 (1949).
[3] Ostrofsky, Breit, and Johnson, Phys. Rev. **49**, 22 (1936); Also B. Freeman and J. McHale, Phys. Rev. **89**, 223 (1953).
[4] H. A. Bethe, Phys. Rev. **57**, 1125 (1940).
[5] Feshbach, Peaslee, and Weisskopf, Phys. Rev. **71**, 145 (1947).
[6] H. A. Bethe and R. R. Wilson, Phys. Rev. **83**, 690 (1951).
[7] Brueckner, Serber, and Watson, Phys. Rev. **84**, 258 (1951).

which describes the interaction of the incident particle with an atomic nucleus. Let the nuclear hamiltonian be H_N and suppose that $g_\gamma(\xi)$ represent a complete set of nuclear wave functions, where ξ is some appropriate set of many-body coordinates and γ represents a specific nuclear state of energy W_γ. Then

$$H_N g_\gamma = W_\gamma g_\gamma. \tag{1}$$

We suppose that before bombardment the nucleus is in the initial state $\gamma_0 \equiv (A, M)$, where M is the azimuthal quantum number associated with the nuclear spin J. It is further assumed that the only degeneracy of this state is that due to different spin orientations (i.e., different values of M).

Let the incident particle have a spin s and a wave function $\lambda_q(\nu)$ when it is in a plane wave state with momentum $\mathbf{q}$ and has an azimuthal spin component ν. (We shall frequently omit the symbol "ν" from λ_q.) It will be convenient to consider the nucleus to be very heavy, so that $\mathbf{q}$ can be interpreted as the momentum of the incident particle *relative* to the nucleus. If we designate the kinetic energy operator and kinetic energy by h and ϵ_q, respectively, the Schrödinger equation for the incident particle is

$$h\lambda_q = \epsilon_q \lambda_q, \tag{2}$$

as long as it is far from the nucleus.

We define

$$H_0 \equiv H_N + h, \tag{3}$$

and V to be the many-body interaction between the incident particle and the nucleus. Then the Schrödinger equation which describes the interaction of the incident particle with the nucleus is

$$(H_0 + V)\Psi_a = E_a \Psi_a. \tag{4}$$

The solution Ψ_a has the boundary condition that, for large distances of the incident particle from the nucleus,

$$\Psi_a \rightarrow g_{(A,M)}\lambda_q(\nu). \tag{5}$$

We then have

$$E_a = W_a + \epsilon_q,$$

where ϵ_q is the energy of the incident particle [Eq. (2)]. A further boundary condition on Ψ_a is that it have only *outgoing* scattered waves. Associated with Ψ_a is a solution $\Psi_a^{(-)}$ to Eq. (4) which has *incoming* scattered waves. These solutions are related by the time reversal operator[8] K:

$$\mu_a \Psi_a^{(-)} = K\Psi_{(-a)}. \tag{6}$$

Here the state $(-a)$ is the state $(A, -M, -q, -\nu)$, and μ_a is a complex number of modulus one (i.e., a phase factor).[9]

We may formally write Ψ_a and $\Psi_a^{(-)}$ as

$$\begin{aligned} \Psi_a &= \sum_{\gamma,p,\nu'} (g_\gamma \lambda_p(\nu'), \Psi_a) g_\gamma \lambda_p(\nu'); \\ \Psi_a^{(-)} &= \sum_{\gamma,p,\nu'} (g_\gamma \lambda_p(\nu'), \Psi_a^{(-)}) g_\gamma \lambda_p(\nu'). \end{aligned} \tag{7}$$

We are interested in the elastic scattering by the nucleus. This is scattering which does *not* excite the nucleus. It is given by those terms in Eqs. (7) for which the energy W_γ of the nuclear state γ is equal to W_A, the energy of the initial state (A, M). The "elastic part" of Ψ_a and $\Psi_a^{(-)}$ is then obtained from Eqs. (7) as

$$\begin{aligned} \Phi_a &= \sum_{M',p,\nu'} (g_{(A,M')}\lambda_p(\nu'), \Psi_a) g_{(A,M')}\lambda_p(\nu'); \\ \Phi_a^{(-)} &= \sum_{M',p,\nu'} (g_{(A,M')}\lambda_p(\nu'), \Psi_a^{(-)}) g_{(A,M')}\lambda_p(\nu'). \end{aligned} \tag{8}$$

That is, the sum over nuclear states is a sum over spin orientations only, since it has been assumed that there is no further degeneracy of the state (AM). In analogy to Eq. (6) we have

$$\mu_a \Phi_a^{(-)} = K\Phi_a^{(-)}. \tag{9}$$

We wish now to see if the "elastic wave functions" Φ, as given by Eq. (8), represent solutions to a Schrödinger equation. For this purpose it is convenient to introduce the Møller wave matrix Ω_s and employ the operator algebra of Chew and Goldberger.[10] That is, the relations (7), when restated in formal matrix notation, read

$$\Psi_a = \Omega_s g_{(A,M)}\lambda_q(\nu), \quad \Psi_a^{(-)} = \Omega_s^{(-)} g_{(A,M)}\lambda_q(\nu). \tag{10}$$

The matrices Ω_s and $\Omega_s^{(-)}$ satisfy the Lippmann and Schwinger[11] integral form of the Schrödinger equation [see Eq. (4)]:

$$\Omega_s = 1 + a^{-1}V\Omega_s, \quad \Omega_s^{(-)} = 1 + (a^\dagger)^{-1}V\Omega_s^{(-)}, \tag{11}$$

where we have defined

$$a \equiv E_a + i\eta - H_0. \tag{12}$$

[Here η is a small positive parameter which is set equal to zero after the implied integrations in Eqs. (11) are done.]

The Eqs. (11) are more general than are required for the wave functions (10), since we may suppose Eqs. (11) to also define Ω_s and $\Omega_s^{(-)}$ for initial states whose energy is not equal to E_a. This generalization is useful for the description of "virtual scatterings" off the energy shell (a problem which one encounters in studying multiple scattering and also in field theory).[12]

If we write $T = V\Omega_s$, then

$$\Omega_s = 1 + a^{-1}T, \tag{13}$$

[8] E. P. Wigner, Gött. Nachr. **31**, 546 (1932).

[9] See, for instance, K. M. Watson, Phys. Rev. **88**, 1163 (1952). The reason for introducing Eqs. (6) and (9) is that these give simple relations between the solutions Ψ and $\Psi^{(-)}$, etc., making it unnecessary to solve the Schrödinger equation for these separately.

[10] G. F. Chew and M. L. Goldberger, Phys. Rev. **87**, 778 (1952).

[11] B. Lippmann and J. Schwinger, Phys. Rev. **79**, 469 (1950). If the incident particle has a charge, it is convenient to assume that the Coulomb potential is screened at large distances.

[12] K. Brueckner and K. Watson Phys. Rev. **90**, 699 (1953).

which satisfies the first of Eqs. (11) if T satisfies

$$T=V+Va^{-1}T. \tag{14}$$

The solution of this equation may be put into the form

$$\begin{aligned} T&=V+V\Omega_s a^{-1}V \\ &=V+Ta^{-1}V. \end{aligned} \tag{15}$$

This is easily verified by direct substitution into Eq. (14), making use of Eqs. (11) for Ω_s.

Forming the adjoint of the second of Eqs. (11), we have

$$\Omega_s^{(-)\dagger}=1+\Omega_s^{(-)\dagger}Va^{-1}, \tag{11'}$$

which is satisfied by

$$\Omega_s^{(-)\dagger}=1+Ta^{-1}. \tag{13'}$$

This is verified upon substitution into Eq. (11'), making use of Eq. (15).

In analogy to Eqs. (10) we may write the "elastic wave functions" Φ as

$$\Phi_a=\Omega_c g_{(A,M)}\lambda_q(\nu), \quad \Phi_a^{(-)}=\Omega_c^{(-)}g_{(A,M)}\lambda_q(\nu), \tag{16}$$

where

$$\Omega_c=1+a^{-1}T_c, \quad \Omega_c^{(-)\dagger}=1+T_c a^{-1}. \tag{17}$$

The quantities Ω_c and T_c are obtained from Ω_s and T [Eq. (13)] by keeping only those matrix elements of the latter which connect nuclear states of the same energy. That is, Ω_c and T_c are contained in Ω_s and T and are defined as follows:

$$\begin{aligned} \Omega_c&=(\gamma', \mathbf{k}', \nu'|\Omega_s|\gamma, \mathbf{k}, \nu), \quad W_{\gamma'}=W_\gamma \\ &=0, \quad W_{\gamma'}\neq W_\gamma. \end{aligned} \tag{18}$$

Here $(\mathbf{k}', \nu')$ and $(\mathbf{k}, \nu)$ represent any two plane wave states for the incident particle. T_c is obtained from T and $\Omega_c^{(-)}$ from $\Omega_s^{(-)}$ in the same manner.

The primary problem of our investigation is to find a potential $\mathcal{U}_c$, such that [see Eq. (14)]

$$T_c=\mathcal{U}_c+\mathcal{U}_c a^{-1}T_c. \tag{19}$$

If $\mathcal{U}_c$ exists, then T_c is the scattering amplitude which results from the potential $\mathcal{U}_c$. We may, however, consider Eq. (19) to be an integral equation to determine $\mathcal{U}_c$ in terms of T_c. If this equation has a solution then $\mathcal{U}_c$ exists.[13] In the next section we shall turn to the problem of actually calculating $\mathcal{U}_c$.

When the incident particle is a neutron or proton some modification of the above analysis is needed in order that the Pauli principle not be violated. If we employ the isotopic spin formalism, so that we may call either a neutron or proton a "nucleon," then the wave functions (10) must be made antisymmetric with respect to a permutation of any two "nucleon" coordinates. This may be easily done since Ψ_a [or $\Psi_a^{(-)}$], as given by Eqs. (10) is still a solution to Eq. (4) if we interchange the coordinates ξ_{A+1} of the incident nucleon with the coordinates ξ_α of any other nucleon ($\alpha=1, 2, \cdots A$, where A is the mass number of the nucleus). To obtain an antisymmetrized wave function, we then operate on Ψ_a [or $\Psi_a^{(-)}$] with the projection operator

$$\Lambda=\frac{1}{(A+1)!}\left[I-\sum_{\alpha=1}^{A}P_\alpha\right]. \tag{20}$$

Here I is the identity permutation and P_α interchanges ξ_{A+1} and ξ_α.

If the "exchange scattering" terms in Eqs. (10) are unimportant, then our previous analysis needs no modification. (The exchange scattering refers to processes in which the incident nucleon changes places with one of the nucleons which was originally in the nucleus.) More generally, we must replace the T_c in Eq. (17) by the direct minus the exchange scattered amplitudes. If there still exists a potential $\mathcal{U}_c$ such that Eq. (19) is satisfied (with T_c in this equation including the exchange terms), then we can again describe the scattering by means of the "optical model," as developed in the next few paragraphs. However, the multiple scattering analysis of the next section is greatly complicated by the exchange scattering. For this reason we shall in the *subsequent* sections assume either that the incident particle is not a nucleon or that the exchange scattering is negligibly small.

The potential $\mathcal{U}_c$, which appears in Eq. (19), is the "optical model potential" which we have set out to find. We note that $\mathcal{U}_c$ is *not* a many-body interaction. It is obtained from T_c [Eq. (19)], which has the matrix elements

$$T_c=(A, M'; \mathbf{k}', \nu'|T|A, M; \mathbf{k}, \nu), \tag{21}$$

when operating on any nuclear state (A, M) which follows from Eq. (18). Consequently, $\mathcal{U}_c$ has the form

$$\mathcal{U}_c=(M', \mathbf{k}', \nu'|\mathcal{U}_c|M, \mathbf{k}, \nu)=\mathcal{U}_c(\mathbf{J}, \mathbf{S}, \mathbf{k}', \mathbf{k}), \tag{22}$$

if we drop the symbol A. The last expression results from writing the $(M'\mu', M\mu)$ dependence in terms of the spin operators $\mathbf{J}$ and $\mathbf{S}$.

From Eqs. (17) and (19) it follows that

$$\Omega_c=1+a^{-1}\mathcal{U}_c\Omega_c, \tag{23}$$

and

$$\Omega_c^{(-)\dagger}=1+\Omega_c^{(-)\dagger}\mathcal{U}_c a^{-1}. \tag{24}$$

These are recognized as being the generalized Schrödinger equations for the elastic scattering [see Eqs. (11), for instance].

The nuclear wave functions can be eliminated from the Schrödinger equation for Φ_a by writing this as

$$\Phi_a=\textstyle\sum_{M'}\varphi_q{}^{M'}g_{(A,M')}. \tag{25}$$

Then the Schrödinger equation for the column matrix $\varphi_q\equiv(\varphi_q{}^M)$ is

$$[h+\mathcal{U}_c(\mathbf{J}, \mathbf{S})]\varphi_q=\epsilon_q\varphi_q. \tag{26}$$

[13] The formal Chew-Goldberger (reference 10) solution to Eq. (19) is $\mathcal{U}_c=T_c-T_c(a+T_c)^{-1}T_c$, so $\mathcal{U}_c$ exists at least formally.

This follows directly from Eq. (23), when it is noted that $a \equiv E_a + i\eta - H_0$ [see Eq. (12)] when operating on the state $g_{(A,M)}$ is equal to $\epsilon_q + i\eta - h$. The related wave function $\varphi_q^{(-)}$, obtained as in Eq. (25) from $\Phi_a^{(-)}$, satisfies the Schrödinger equation

$$[h + \mathcal{U}_c^\dagger]\varphi_q^{(-)} = \epsilon_q \varphi_q^{(-)}. \tag{27}$$

We emphasize once again that $\mathcal{U}_c$ depends only upon the coordinates of the incident particle and the spin of of the nucleus, so Eqs. (26) and (27) are not many-body equations. These equations represent the rigorous formulation of what may be called the "optical models" of nuclear interactions. They do not involve a high-energy approximation, nor do they represent approximations to the many-body problem.

The potential $\mathcal{U}_c$ is not in general hermitean, so there is no conservation of particle and current density associated with φ_q. This is, of course, necessary in order that there be conservation of probability for the original wave function Ψ_a. The state Φ_a describes the scattering in only one of the possible nuclear "channels" into which the reaction can go. As Φ_a is "feeding" the other channels, its normalization must become less than unity as one traces the wave through the scattering event.

It is just this feature, on the other hand, which permits us to use φ_q to calculate the cross section for inelastic scattering. From the general conservation theorem[11] which relates the imaginary part of the transition operator for forward scattering to the total transition rates for all scattering, we have

$$-2\,\mathrm{Im}\langle T\rangle_0 = -2\,\mathrm{Im}\langle T_c\rangle_0 = P_t \tag{28}$$

as the total rate at which the particle is scattered from its initial state.[14] The symbol "$\langle\cdots\rangle_0$" means the "diagonal matrix element of '$(\cdots)$' with respect to both nuclear states and the momentum and spin states of the incident particle." By means of a little algebra and the relation

$$\delta(E_a - H_0) = \frac{i}{2\pi}\left(\frac{1}{a} - \frac{1}{a^\dagger}\right),$$

we can easily express Eq. (28) as

$$P_i = 2\pi\langle T_c^\dagger \delta(E_a - H_0) T_c\rangle_0 - 2\,\mathrm{Im}(\varphi_q, \mathcal{U}_c\varphi_q). \tag{29}$$

To derive this, we note that

$$-2\pi i T_c^\dagger \delta(E_a - H_0) T_c = T_c^\dagger\left(\frac{1}{a} - \frac{1}{a^\dagger}\right)T_c$$

$$= T_c^\dagger \Omega_c - \Omega_c^\dagger T_c + T_c - T_c^\dagger$$

by Eq. (17). If we write $\Omega_c^\dagger T_c = \Omega_c^\dagger \mathcal{U}_c \Omega_c$ and $\langle \Omega_c^\dagger \mathcal{U}_c \Omega_c\rangle_0 = (\varphi_q, \mathcal{U}_c\varphi_q)$, etc., Eq. (29) follows.[15] In terms of cross sections, Eq. (29) may be written [see reference (14)]:

$$\sigma_t = \sigma_{el} + \sigma_{ab},$$

where

$$\sigma_{el} = \frac{(2\pi)^4}{v_\pi}\langle T_c^\dagger \delta(E_a - H_0) T_c\rangle_0$$

and

$$\sigma_{ab} = -\frac{2(2\pi)^3}{v_\pi}\,\mathrm{Im}(\varphi_q, \mathcal{U}_c\varphi_q). \tag{30}$$

Here σ_{el} is the total cross section for elastic scattering, and σ_{ab} is that for inelastic scattering by the nucleus. The relations (30) are equal to the cross sections which one would obtain from a solution to the *many-body* Schrödinger Eq. (4), but are obtained in terms of the solution to Eq. (26) only. In other words, the solution to Eq. (26) gives not only the detailed features of the elastic scattering but also the total cross section for inelastic scattering.

For incident particle energies above the resonance region it is quite plausible that the dependence of $\mathcal{U}_c$ (and of T_c) upon the nuclear spin may be weak. This is qualitatively understandable since the interaction at higher energies represents the effect of many interactions with individual nucleons, whose spins tend to take all orientations. If at such energies we approximate $\mathcal{U}_c$ by dropping $\mathbf{J}$, then the only possible dependence upon $\mathbf{S}$, the spin of the incident particle (if it has spin one-half), is a spin-orbit interaction of the form

$$\mathbf{S}\cdot(\mathbf{q}\times\mathbf{q}').$$

If this dependence is weak (or the energy high enough that the scattering tends to be in the forward direction), we may take $\mathcal{U}_c$ independent of spin interactions.

If furthermore the nuclear diameter is large compared to the wavelength of the incident particle, it seems quite plausible that $\mathcal{U}_c$ will be approximately constant inside the nucleus and vanish outside (in a coordinate representation). In this case $\mathcal{U}_c$ depends upon only two parameters at a given energy (its real and its imaginary parts), and Eq. (26) is quite simple. If we write $\epsilon_q = q^2/2\mu$ (μ is the mass of the incident particle), and $\varphi_q = e^{i\mathbf{k}\cdot\mathbf{x}}$ within the nucleus, Eq. (26) becomes

$$[k^2/2\mu + \mathcal{U}_c] = q^2/2\mu,$$

or

$$k^2/q^2 \equiv n^2 = 1 - (2\mu/q^2)\mathcal{U}_c. \tag{31}$$

We may interpret n to be the *index* of *refraction* of the nuclear medium. When Eq. (26) can be expressed in this form, the resulting analysis is usually referred to as "the optical model." To obtain the optical model in this form, we have neglected the dependence of $\mathcal{U}_c$ upon the spin of the nucleus and the incident particle (if it

[14] We normalize our wave functions in momentum space, so the total cross section is $\sigma_t = (2\pi)^3 P_t/v_\pi$, where v_π is the velocity of the incident particle. For convenience we have supposed the nucleus to be infinitely heavy—otherwise it would be necessary to factor a δ function expressing momentum conservation from Eq. (28).

[15] This result, in a somewhat more restrictive context, has been obtained by M. Lax, Phys. Rev. **78**, 306 (1950).

has a spin) and assumed that $\mathcal{U}_c$ is constant within the nucleus. These approximations seem quite reasonable except for low energies and the smaller nuclei. We emphasize, however, that Eq. (26) represents a very general formulation of the "optical model," and that Eq. (31) is only an approximation to this.

In the next section we shall calculate $\mathcal{U}_c$ directly in terms of the many-body interactions. As mentioned in the Introduction, however, it is possible for many applications to treat $\mathcal{U}_c$ just as a phenomenological parameter.[16]

III. CALCULATION OF THE POTENTIAL

In the present section we consider the calculation of the potential in terms of the interaction of the incident particle with the nucleus. To do this we employ the multiple scattering theory of reference 1. We suppose the potential V of Eq. (4), which describes the interaction of the incident particle with the nucleus, to be

$$V=\sum_{\alpha=1}^{A} V_\alpha, \tag{32}$$

where the summation runs over the A neutrons and protons of the nucleus. V_α is the interaction of the incident particle with the αth nucleon in the nucleus. [If we were to suppose that many-body forces were of importance, so that the incident particle interacts directly with clusters of nucleons, we could extend the summation in Eq. (32) to include these more general interactions. This would not modify the formal multiple scattering theory, since it would be only necessary to let the sum "over nucleons" have this more general interpretation in the multiple scattering Eqs. (33).] Then it was shown in I that the solution to Eqs. (11) for Ω_c is

$$\Omega_s=1+\frac{1}{a}\sum_{\alpha=1}^{A} t_\alpha\Omega_s(\alpha), \quad \Omega_s(\alpha)=1+\frac{1}{a}\sum_{\beta\neq\alpha}^{A} t_\beta\Omega_s(\beta). \tag{33}$$

The energy denominator a was defined by Eq. (12). The quantity t_α is the *effective scattering matrix* for the αth nucleon when it is *bound*, as described in I.

When true absorption of the incident particle can occur (as is the case with mesons), it was shown in I that a is to be replaced by

$$b=a-\Delta, \tag{34}$$

where

$$\Delta=(-iv_r/2\lambda_a)v(z).$$

v_r is the velocity of the incident particle, λ_a is the *mean free path for true absorption*, and $v(z)$ is the nucleon density in the nucleus normalized to

$$\int v(z)d^3z=V_A,$$

the nuclear volume.

Again following I, we decompose t_α into its matrix elements I_α which refer to inelastic scatterings (corresponding to a change in nuclear excitation energy) and those matrix elements C which correspond to elastic scattering.[17] That is

$$C=\langle t_\alpha\rangle. \tag{35}$$

The symbol $\langle\cdots\rangle$ means a matrix element between nuclear states having the same binding energy. In this notation, for instance,

$$\Omega_c=\langle\Omega_s\rangle$$

[see Eq. (18)]. If we use the isotopic spin formalism, so that the nuclear wave function is antisymmetric in all nucleon variables, it is clear that C is independent of the index α, and so is

$$t_c=AC. \tag{36}$$

Then it was shown in I that

$$\Omega_s=F[1+e^{-1}t_c], \tag{37}$$

where

$$e=b-t_c=a-\Delta-t_c, \tag{38}$$

and F is defined by the integral equations

$$F=1+\frac{1}{e}\sum_{\alpha=1}^{A} I_\alpha F_\alpha, \quad F_\alpha=1+\frac{1}{e}\sum_{\beta\neq\alpha}^{A} I_\beta F_\beta. \tag{39}$$

When true absorption of the particles is possible, we must replace Ω_s in Eq. (37) by

$$\Omega=[1+a^{-1}R]F[1+e^{-1}(t_c+\Delta)], \tag{40}$$

[see Eq. (34)] as was shown in I. The "absorption operator" R was described in reference 1. Equation (37) represents an approximation to Eq. (33) (which is rigorous), the relative error being of order $(1/A)$.

To calculate the elastic scattering [i.e., Eq. (16)], we need

$$\langle\Omega\rangle=\langle\Omega_s\rangle\equiv\Omega_c=\langle F\rangle[1+e^{-1}(t_c+\Delta)]. \tag{41}$$

This follows since the operator R, which absorbs the particle, can obviously not lead to elastic scattering (see reference 1 for a further discussion). The last step in Eq. (41) results from the fact that $(t_c+\Delta)$ is by definition diagonal in nuclear states, except for spin orientation. To obtain Ω_c we must calculate $\langle F\rangle$, which in I was approximated by

$$\langle F\rangle=1. \tag{42}$$

This is reasonable for high-energy scatterings. Indeed, the corrections to Eq. (42) result from several

[16] In a forthcoming publication the authors will present a theory of the deuteron-stripping reaction which makes use of the concepts of the present section. In this analysis $\mathcal{U}_c$ arises in a natural manner and can be treated as a phenomenological quantity.

[17] In reference 1, only high-energy scatterings were considered, so C was defined to be diagonal in nuclear states. Here we wish also to consider the possibility of nuclear spin interactions and so give a more general definition of C.

inelastic scatterings, the net result of which is to leave the nucleus in its initial state. When the scatterings are very energetic, corresponding to high nuclear excitation, the probability that the *last* inelastic scattering should happen to leave the nucleus in its ground state would appear to be negligibly small, so Eq. (42) appears quite reasonable. However, for lower energies and especially for lighter particles such as mesons we may expect that Eq. (42) will require modification.

To calculate $\langle F\rangle$, we refer to Eq. (39) and write

$$\langle F\rangle = 1 + e^{-1}L, \tag{43}$$

where

$$L = \sum_{\alpha=1}^{A} \langle I_\alpha F_\alpha\rangle. \tag{44}$$

We now introduce a new notation which will prove useful in the subsequent discussion. If Γ is a matrix involving nuclear states, we introduce

$$'\Gamma$$

to mean the matrix obtained from Γ by removing all nuclear matrix elements of the form

$$(A, M|\Gamma|\gamma),$$

for all M, where A refers to the initial state of the nucleus and γ is any nuclear state.[18] For example, in this notation we can write

$$L = \sum_{\alpha=1}^{A} \langle I_\alpha\, 'F_\alpha\rangle, \tag{44'}$$

since the prime notation tells us that there are to be no states (A, M')—for all M'—in the sum over states in the matrix product $\sum_\gamma \langle I_\alpha|\gamma\rangle(\gamma|'F_\alpha\rangle$. If we let

$$'F_\alpha\rangle \equiv \sum_\gamma (\gamma|'F_\alpha|A, M)g_\gamma,$$

for some value of M, etc., we have from Eq. (39)

$$\begin{aligned} 'F_\alpha\rangle &= '1\rangle + \frac{1}{e}\sum_{\beta\neq\alpha} 'I_\beta F_\beta\rangle \\ &= -\frac{1}{e}\sum_{\beta\neq\alpha} 'I_\beta\rangle\langle F_\beta\rangle + \frac{1}{e}\sum_{\beta\neq\alpha} 'I_\beta\, 'F_\beta\rangle, \end{aligned} \tag{45}$$

since $'1\rangle$ vanishes identically because of the definition of the prime notation. The second step is just the explicit decomposition of $'I_\beta F_\beta\rangle$ into intermediate states (A, M') and those not equal to (A, M').

Now the quantity

$$F_c \equiv \langle F_\beta\rangle, \tag{46}$$

which occurs in Eq. (45), is independent of the index β for the same reason that C in Eq. (35) was. Thus Eq. (45) can be written as

$$'F_\alpha\rangle = -\frac{1}{e}\sum_{\beta\neq\alpha} 'I_\beta\rangle F_c + \frac{1}{e}\sum_{\beta\neq\alpha} 'I_\beta\, 'F_\beta\rangle. \tag{47}$$

To solve this integral equation we write $'F_\alpha\rangle$ as

$$'F_\alpha\rangle = (G_\alpha - 1)\rangle F_c, \tag{48}$$

which when substituted into Eq. (47), leads to

$$\left[G_\alpha - 1 - \frac{1}{e}\sum_{\beta\neq\alpha} 'I_\beta G_\beta\right]\Big\rangle F_c = 0. \tag{49}$$

This is satisfied when G_α is the solution to the set of equations

$$G_\alpha = 1 + \frac{1}{e}\sum_{\beta\neq\alpha} 'I_\beta G_\beta. \tag{50}$$

If we substitute Eq. (48) into Eq. (44'), we obtain

$$\begin{aligned} L &= \left[\sum_{\alpha=1}^{A} \langle I_\alpha G_\alpha\rangle - I_c\right] F_c \\ &\equiv \mathcal{U}_1 F_c. \end{aligned} \tag{51}$$

Here the symbol $\mathcal{U}_1$, has been introduced for brevity as

$$\mathcal{U}_1 \equiv \sum_{\alpha=1}^{A} \langle I_\alpha G_\alpha\rangle - I_c. \tag{52}$$

From Eqs. (46) and (39) we have

$$\begin{aligned} \sum_{\alpha=1}^{A} \langle F_\alpha\rangle &= AF_c = A + \frac{1}{e}\sum_{\alpha=1}^{A}\sum_{\beta\neq\alpha} \langle I_\beta F_\beta\rangle \\ &= A + (A-1)\frac{1}{e}L, \end{aligned} \tag{53}$$

if we use Eq. (39) and the defining Eq. (44) for L. From Eq. (43), we have to relative order $1/A$ (the accuracy to which we are restricting ourselves)

$$F_c = 1 + e^{-1}L = \langle F\rangle. \tag{54}$$

The first Eq. (54) can be written as

$$F_c = 1 + e^{-1}\mathcal{U}_1 F_c, \tag{55}$$

since $L = \mathcal{U}_1 F_c$ by Eq. (51). The Chew-Goldberger[10] solution to Eq. (55) is

$$F_c = 1 + \frac{1}{e - \mathcal{U}_1}\mathcal{U}_1. \tag{56}$$

If we substitute this value of $\langle F\rangle$ into Eq. (41), we obtain after some algebra

$$\Omega_c = 1 + \frac{1}{e - \mathcal{U}_1}[I_c + \Delta + \mathcal{U}_1]. \tag{57}$$

[18] Expressed somewhat differently, the "prime" represents a projection operator standing to the left of Γ, which vanishes when operating on a ground state eigenfunction of the nucleus but which has the eigenvalue unity for all other nuclear states.

From the definition of e [Eq. (38)]

$$e-\mathcal{U}_1=a-[t_c+\mathcal{U}_1+\Delta],$$

so

$$\Omega_c=1+a^{-1}[t_c+\mathcal{U}_1+\Delta]\Omega_c, \tag{58}$$

as in Eq. (23). Therefore, the optical model potential $\mathcal{U}_c$ is

$$\mathcal{U}_c=t_c+\mathcal{U}_1+\Delta$$

$$=\sum_{\alpha=1}^{A}\langle t_\alpha G_\alpha\rangle+\Delta \tag{59}$$

[by Eq. (52)]. Comparison with Eq. (26) shows that φ_q satisfies that equation with $\mathcal{U}_c$ as given by Eq. (59). When there is no true absorption, $\Delta=0$, so

$$\mathcal{U}_c=\sum_{\alpha=1}^{A}\langle t_\alpha G_\alpha\rangle. \tag{59'}$$

The calculation of $\mathcal{U}_c$ is seen to involve the solution to the set of integral Eqs. (50).

IV. FURTHER DISCUSSION OF THE POTENTIAL $\mathcal{U}_c$

To obtain the potential $\mathcal{U}_c$ it is necessary to solve the integral Eqs. (50) for the quantities G_α. The possibility of doing this quantitatively evidently depends upon the complexity of the scattering medium. In the case of an atomic nucleus we are limited to semiphenomenological calculations if it is necessary to improve the simpler version of the optical model which was given in I.

For purposes of making a definite calculation we shall suppose that the incident particle is a high-energy π meson and assume that $\mathcal{U}_c$ does not depend upon the nuclear spin (although some of our results, such as Eq. (80), are more general). We shall also suppose that the nuclear radius is large compared to the wavelength of the incident particle.

We define a "wave function" ψ_α as

$$\psi_\alpha=G_\alpha\lambda_k, \tag{60}$$

where $\lambda_k=(2\pi)^{-\frac{3}{2}}e^{i\mathbf{k}\cdot\mathbf{z}}$. In terms of ψ_α, Eq. (50) is

$$\psi_\alpha(z)=\lambda_k(z)+\frac{1}{e}\sum_{\beta\neq\alpha}{}'I_\beta\psi_\beta(z). \tag{61}$$

If we have solved Eq. (61), which is just Eq. (50) in an explicit representation, we can immediately obtain $\mathcal{U}_c$.

The first observation concerning Eq. (61) is that there is no attenuation or coherent modification of the "incident wave" λ_k. This results from

$$\langle\psi_\alpha\rangle=\lambda_k, \tag{62}$$

which follows from the *prime* condition on $'I_\beta$.

The next observation is that for a large homogeneous scattering medium

$$(\mathbf{k}'|\,\mathcal{U}_c\,|\mathbf{k})=B\delta(\mathbf{k}'-\mathbf{k}), \tag{63}$$

where B is a numerical function of k. This conclusion follows from a study of the individual terms in a series expansion of Eq. (50) in powers of $'I_\beta$. A somewhat improved form of Eq. (63) is

$$\mathcal{U}_c(z)=Bv(z), \tag{63'}$$

where $v(z)$ was defined in connection with Eq. (34) and $\mathbf{z}$ is the coordinate of the meson. In I, Eqs. (63) and (63') were referred to as approximations I and II, respectively.

We can obtain the approximate value of $\mathcal{U}_c$ which was obtained in I by setting

$$\psi_\alpha(z)=\lambda_k(z),$$

so

$$(\mathbf{k}'|\,\mathcal{U}_c\,|\mathbf{k})=(\mathbf{k}'|\,t_c\,|\mathbf{k})+(\mathbf{k}'|\,\Delta\,|\mathbf{k}). \tag{64}$$

As in I, we write $(\mathbf{k}'|\,\Delta\,|\mathbf{k})=-(iv_\pi/2\lambda_a)\delta(\mathbf{k}'-\mathbf{k})$. [See Eq. (34).] Also, as in I,

$$(\mathbf{k}'|\,t_c\,|\mathbf{k})=\sum_\alpha\langle(\mathbf{k}'|\,t_\alpha\,|\mathbf{k})\rangle$$
$$\simeq B_s\delta(\mathbf{k}'-\mathbf{k})$$

[see Eqs. (35) and (37)], where B_s is given in terms of t_α. If we refer to Eq. (63), we see Eq. (64) implies the approximation

$$B\simeq B_0\equiv B_s-(iv_\pi/2\lambda_a). \tag{65}$$

If we assume the impulse approximation,[10] t_α is related to the meson scattering amplitude a_s from a free nucleon by

$$t_\alpha\simeq a_s/(2\pi)^2\epsilon',$$

where ϵ' is the meson energy (rest plus kinetic) evaluated in the nuclear medium. Then

$$B_s=\frac{A}{V_A}\frac{2\pi}{\epsilon'}[a_s(0)], \tag{66}$$

as was shown in I. Here $a_s(0)$ is the value of a_s for scattering in the *forward* direction and should be taken as the average scattering amplitude for the neutrons and protons in the nucleus. If we use the relationship between the imaginary part of the forward scattering amplitude and the total cross section, Eq. (66) can be rewritten as

$$B_s=\frac{A}{V_A}\frac{2\pi}{\epsilon'}\mathrm{Re}[a_s(0)]-\frac{iv_\pi}{2\lambda_s}. \tag{66'}$$

$\mathrm{Re}[a_s(0)]$ is the real part of $a_s(0)$, and $\lambda_s=(A\sigma_s/V_A)^{-1}$ is the mean free path for a single scattering from an individual nucleon in the nuclear medium, assuming that the cross section σ_s is the same as for an unbound nucleon (this follows from the impulse approximation). The velocity v_π is that which the meson has in the nuclear medium.

These results were obtained in I and provide a first approximation to $\mathcal{U}_c$. In order to test the validity of this approximation we can calculate B_s by means of

Eq. (66′) from the experimental phase shifts of Anderson *et al.*[19] These are available for the scattering of pions on protons at an energy of 78 Mev. The calculated value of B_s can be compared with the value of B [Eq. (63)] deduced by Lederman *et al.*[20] for the scattering of 65-Mev mesons by carbon.

From the Fermi phase shifts and Eq. (66′), we obtain

$$B_s=-[24+11i]\ \text{Mev}. \tag{67}$$

The value of B obtained by Lederman *et al.* is

$$B=-[18+9i]\ \text{Mev}. \tag{68}$$

In view of the experimental uncertainties these values seem to be quite compatible with each other. As is seen from Eq. (65), however, we must subtract $iv_\pi/2\lambda_\alpha$ from B_s to obtain B_0. λ_α is known only roughly, but is expected to be at least no larger than λ_s at 65 Mev.[7] It thus seems that the imaginary parts of Eqs. (67) and (68) are in definite disagreement with each other.

The most apparent source of this error is associated with our use of the free nucleon scattering amplitude a_s in Eq. (66). As mentioned above this is the so-called "impulse approximation" as discussed by Chew and Goldberger[10] and others. However, the validity of the impulse approximation seems, perhaps, least certain for the calculation of the imaginary part of the forward scattering amplitude, since this is related to the total cross section.

To obtain a correction to the impulse approximation, we note that

$$-\operatorname{Im}\langle t_\alpha\rangle_0=\pi\langle t_\alpha{}^\dagger\delta(E_\alpha-H_0)t_\alpha\rangle_0. \tag{69}$$

[This is easily derived in the same manner as was Eq. (29).] Here t_α is the effective scattering operator for the αth nucleon when it is bound, as discussed in I [see also Eq. (33)]. According to the impulse approximation, the t_α's are to be replaced by the corresponding quantities for *free* nucleons, which also implies setting $E_\alpha-H_0=\epsilon_q-h$ in the δ function in Eq. (69).[21] For a first correction to the impulse approximation, it seems reasonable to replace the t_α's on the right hand side of Eq. (69) by the corresponding free nucleon t_α's, but to keep the energy of excitation of the nucleus in $\delta(E_\alpha-H_0)$. This then corrects the total scattering cross section from the bound nucleon for binding effects in the final state.

Making a simplified evaluation of the right hand side of Eq. (69), using a degenerate Fermi gas model of the nucleus, we obtain a modified B_s, which seems to be in agreement with experiment:[20]

$$B_s\simeq-[24+5i]\ \text{Mev}. \tag{67′}$$

[19] Anderson, Fermi, Martin, and Nagle, Phys. Rev. **91**, 155 (1953).

[20] Byfield, Kessler, and Lederman, Phys. Rev. **86**, 17 (1952).

[21] The energy ϵ_q should be replaced by the effective energy of the meson in the nuclear medium, according to the Appendix A of I.

Here again we have to use the impulse approximation for the $\operatorname{Re}[a_s(0)]$ so the real part of B_s is unchanged.

To obtain further corrections to Eq. (67′), we return to the integral Eqs. (50). A first "Born approximation" to these is

$$G_\alpha=1+\frac{1}{e}\sum_{\beta\neq\alpha}{}'I_\beta.$$

When this is substituted into Eq. (59) for $\mathcal{V}_e$, we obtain

$$\begin{aligned}\mathcal{V}_e&=\Delta+t_e+\sum_{\alpha_1\neq\alpha_2,\alpha_2}\left\langle I_{\alpha_1}\frac{1}{e}I_{\alpha_2}\right\rangle\\&=\Delta+t_e+\sum_{\alpha_1\neq\alpha_2,\alpha_2}\langle I_{\alpha_1}(a-t_e-\Delta)^{-1}I_{\alpha_2}\rangle.\end{aligned} \tag{70}$$

The second equation follows from the expression (38) for e.

Now

$$\langle I_{\alpha_1}e^{-1}I_{\alpha_2}\rangle=\langle t_{\alpha_1}e^{-1}t_{\alpha_2}\rangle-\langle t_{\alpha_1}\rangle e^{-1}\langle t_{\alpha_2}\rangle \tag{71}$$

follows directly from the definition of I_α. If we neglect the energy of excitation of the nucleus in e, then

$$e\simeq\epsilon_q+i\eta-p_0-B_0,$$

when operating on a meson wave having momentum $\mathbf{p}$. Here $p_0=[p^2+\mu^2]^{\frac{1}{2}}$, where μ is the rest mass of the meson, and B_0 is defined by Eq. (65). For simplicity we neglect the spin and isotopic spin dependence of t_α and write

$$t_\alpha=(\mathbf{p}|t^0|\mathbf{k})\exp[-i(\mathbf{p}-\mathbf{k})\cdot\mathbf{z}_\alpha] \tag{72}$$

in a momentum representation. Then (also in a momentum representation),

$$\begin{aligned}\sum_{\alpha_1\neq\alpha_2}\left\langle I_{\alpha_1}\frac{1}{e}I_{\alpha_2}\right\rangle=\sum_{\alpha_1\neq\alpha_2}\int d^3z_{\alpha_1}d^3z_{\alpha_2}d^3p\\ \times[P(\mathbf{z}_{\alpha_1},\mathbf{z}_{\alpha_2})-P(\mathbf{z}_{\alpha_1})P(\mathbf{z}_{\alpha_2})]\\ \times\left[\frac{(\mathbf{k}'|t^0|\mathbf{p})(\mathbf{p}|t^0|\mathbf{k})}{\epsilon_q+i\eta-p_0-B_0}\right]\\ \times\exp[-i(\mathbf{k}'-\mathbf{p})\cdot\mathbf{z}_{\alpha_1}]\\ \times\exp[-i(\mathbf{p}-\mathbf{k})\cdot z_{\alpha_2}].\end{aligned} \tag{73}$$

$P(\mathbf{z}_{\alpha_1},\mathbf{z}_{\alpha_2})$ is the joint probability of finding nucleon α_1, at the point $\mathbf{z}_{\alpha_1}$, and nucleon α_2 at the point $\mathbf{z}_{\alpha_2}$. $P(\mathbf{z}_{\alpha_1})$ is the probability of finding nucleon α_1, at the point $\mathbf{z}_{\alpha_1}$, etc. The combination of the P's in Eq. (73) follows directly from Eq. (71).

If the nucleus is large we can write

$$\begin{aligned}&[P(\mathbf{z}_{\alpha_1},\mathbf{z}_{\alpha_2})-P(\mathbf{z}_{\alpha_1})P(\mathbf{z}_{\alpha_2})]\\&\qquad=(1/V_A)^2v(\mathbf{z}_{\alpha_1})C(|\mathbf{z}_{\alpha_1}-\mathbf{z}_{\alpha_2}|),\end{aligned} \tag{74}$$

where $v(z)$ is defined in connection with Eq. (34). $C(|\mathbf{z}_{\alpha_1}-\mathbf{z}_{\alpha_2}|)$ is a function describing the correlation

between nucleon positions. Then, if the nucleus is large

$$\sum_{\alpha_1\neq\alpha_2}\left\langle I_{\alpha_1}\frac{1}{e}I_{\alpha_2}\right\rangle=(2\pi)^3\left(\frac{A}{V_A}\right)^2\delta(\mathbf{k}'-\mathbf{k})\times\int d^3r d^3p\frac{(\mathbf{k}'|f^0|\mathbf{p})(\mathbf{p}|f^0|\mathbf{k})}{\epsilon_q+i\eta-p_0-B_0}\times\exp[i(\mathbf{p}-\mathbf{k})\cdot\mathbf{r}]C(\mathbf{r}),\quad(75)$$

where we have written $\mathbf{r}=\mathbf{z}_{\alpha_1}-\mathbf{z}_{\alpha_2}$.

Equation (75) represents a correction to $t_c+\Delta$ due to correlation in nucleon positions (or, in other words, to the mutual interaction of two nucleons). It corresponds to two inelastic scatterings, the second of which returns the nucleus to its original state. To calculate this effect more carefully, we note that by Eq. (59),

$$\begin{aligned}\mathcal{U}_c&=\Delta+\sum_{\alpha_1}\langle t_{\alpha_1}G_{\alpha_1}\rangle\\&\simeq\Delta+t_c+\sum_{\alpha_1\neq\alpha_2}\langle I_{\alpha_1}\Gamma_{\alpha_1\alpha_2}{}'I_{\alpha_2}\rangle,\end{aligned}\quad(76)$$

where the quantity $\Gamma_{\alpha_1\alpha_2}$ results from expanding the solution to Eq. (50) in a series in the $'I_\alpha$'s; that is,

$$\Gamma_{\alpha_1\alpha_2}=1+\sum_{(\alpha)}\left\{\frac{1}{e}{}'I_{\alpha_3}+\frac{1}{e}{}'I_{\alpha_3}\frac{1}{e}{}'I_{\alpha_4}+\cdots\right\}.\quad(77)$$

The sum over (α) is such that no two indices on adjacent $'I_\alpha$'s are the same when $\Gamma_{\alpha_1\alpha_2}$ is substituted into Eq. (76). We have neglected in Eq. (76) those terms for which $\alpha_1=\alpha_2$.

Now if we neglect all correlations except those between pairs of nucleons—that is, except those of the form given by Eq. (75)—then the nuclear states of the $'I_\alpha$'s must be so paired. Since the nuclear ground state occurs in the matrix elements of only the first and last I_α in Eq. (76), these two must be paired and we can write $\mathcal{U}_c$ as

$$\mathcal{U}_c=t_c+\Delta+\sum_{\gamma}\sum_{\alpha_1\neq\alpha_2}(A,M'|I_{\alpha_1}|\gamma)(\gamma|\Gamma_{\alpha_1\alpha_2}|\gamma)\times\left(\gamma\left|\frac{1}{e}{}'I_{\alpha_2}\right|AM\right),\quad(78)$$

where the "γ" represent a complete set of nuclear states. (If there is spin dependent scattering, we should interpret $(\gamma|\Gamma_{\alpha_1\alpha_2}|\gamma)$ to be off diagonal in the nuclear spin orientation, as before.) Now a comparison of the quantity $(\gamma|\Gamma_{\alpha_1\alpha_2}|\gamma)=\langle\Gamma_{\alpha_1\alpha_2}\rangle$ with the $\langle F\rangle$ of Eq. (41) shows that these have the same structure. There are only two differences: (1) the indices α_1 and α_2 are suppressed for the first and last scatterings, respectively, in $\Gamma_{\alpha_1\alpha_2}$. This should not be important if the mass number A is large. (2) $\langle F\rangle$ contains I_α's while $\langle\Gamma_{\alpha_1\alpha_2}\rangle$ contains $'I_\alpha$'s. Since we have started the system in an excited state γ in $(\gamma|\Gamma_{\alpha_1\alpha_2}|\gamma)$, the ground state has lost its preferred role here, so this distinction is probably not of great importance. Therefore, we set

$$(\gamma|\Gamma_{\alpha_1\alpha_2}|\gamma)=\langle F\rangle=F_c\quad(79)$$

in Eq. (78). Since by Eq. (56)

$$F_c=1+(1/e-\mathcal{U}_1)\mathcal{U}_1,$$

we have, on doing a little algebra,

$$F_c(1/e)=1/(e-\mathcal{U}_1)=1/(a-\mathcal{U}_c).$$

If we substitute this into Eq. (78), we obtain

$$\mathcal{U}_c=t_c+\Delta+\sum_{\alpha_1\neq\alpha_2,\alpha_2}\left(I_{\alpha_1}\frac{1}{a-\mathcal{U}_c}I_{\alpha_2}\right).\quad(80)$$

This is an integral equation for $\mathcal{U}_c$ and has a simple interpretation. It differs from Eq. (70) only in that the approximate propagation function $1/e$ is replaced by the "correct function" $(a-\mathcal{U}_c)^{-1}$. If we write

$$(\mathbf{k}'|\mathcal{U}_c|\mathbf{k})=B\delta(\mathbf{k}'-\mathbf{k}),$$

it is evident that Eq. (75) is modified in that B_0 is replaced by B in the energy denominator. When the integrals in Eq. (75) are evaluated, Eq. (80) becomes an *algebraic* equation to be solved for B (if we can neglect the dependence of B on the energy when evaluating the integral).

For a qualitative evaluation of B we shall assume that

$$\begin{aligned}C(r)&=\pm1,\quad r<r_0;\\&=0,\quad r>r_0.\end{aligned}$$

If, for instance, we choose the negative sign, we can interpret $C(r)$ as describing the net effect of the Pauli principle and a possible short range repulsion in the nuclear interaction. A choice of the positive sign would imply a net "bunching together" of nucleons as short distances. We interpret r_0 to be a parameter measuring the strength of this correlation.

To obtain a rough estimate of $\mathcal{U}_c$ from Eq. (80), we assume that and that the nucleons are point scatterers. Then the integral (75) is easily evaluated and we obtain

$$B\simeq\frac{B_0\mp iB_0{}^2\epsilon_q r_0/q}{1\pm iB_0{}^2\epsilon_q{}^2r_0/q^3},\quad(81)$$

the sign depending upon that of $C(r)$.

Equation (81) provides us with an additional correction to Eq. (67′). For $r_0\leq(\hbar/\mu c)$ the correction to B_0 is no more than 10–20 percent and is thus negligible compared to the experimental uncertainties. It is reassuring to find this correction small, since it implies that Eq. (65) is a useful approximation for the optical model. On the other hand, one may hope eventually to have sufficiently precise measurements so that it is necessary to use Eq. (80). In this case the results might be used to obtain a measure of nucleon correlations in nuclear structure.

We finally observe that by keeping more terms in the expansion of Eq. (50) it is possible to obtain the effect of three-particle and four-particle correlations, etc., on $\mathcal{U}_c$.

V. APPLICATIONS TO MESON INTERACTIONS

By way of further application of the theory which has been developed, we shall briefly discuss the scattering and photoproduction of π mesons from complex nuclei. We shall employ the same simple model of the photoproduction which was used in I (i.e., that the matrix elements for the photoproduction from a bound nucleon are the same as for a free nucleon). From the point of view of the formal theory this means that there is a uniformly distributed source density in a median which can both scatter and reabsorb.

We shall arrive at essentially the same conclusions which were obtained in I. However, we are now able to ascribe a much more general validity to our results. Indeed, we shall obtain some specific predictions which may provide a test of the model for photoproduction (that the mechanism is the same for a bound as for an unbound nucleon, as discussed in more detail in I).

The scattering of mesons by nuclei is described by the theory already developed. The meson wave function $\varphi_q=\Omega_c\lambda_q$ satisfies Eq. (26). $\mathcal{U}_c$ does not of course now depend upon the spin $\mathbf{S}$ since the meson has no spin and we may also suppose it to not depend upon the nuclear spin $\mathbf{J}$.

As was shown in I, the transition operator T for photomeson production is

$$T=T_\pi+T_s+T_a,$$

where

$$T_a=RFe^{-1}H', \tag{82}$$

and

$$T_\pi+T_s=[1+(t_c+\Delta)e^{-1}][1+\textstyle\sum_\alpha I_\alpha F_\alpha e^{-1}]H'. \tag{83}$$

The quantity H', as defined in I, is the sum of the matrix elements for photomeson production from the individual nucleons in the nucleus. R is the absorption operator introduced in Eq. (40). Thus T_a is the transition operator for photomeson production followed by reabsorption. $T_\pi+T_s$ describes photoproduction with possible scattering of the meson before it leaves the nucleus. T_π is now explicitly defined as the transition amplitude for producing mesons which are *not* subsequently scattered *inelastically* or absorbed by the nucleus. That is,

$$T_\pi=[1+(t_c+\Delta)e^{-1}][1+\textstyle\sum_\alpha\langle I_\alpha F_\alpha\rangle e^{-1}]H'. \tag{84}$$

The quantity

$$\textstyle\sum_\alpha\langle I_\alpha F_\alpha\rangle\equiv L=\mathcal{U}_1+\mathcal{U}_1(e-\mathcal{U}_1)^{-1}\mathcal{U}_1,$$

as was shown in Sec. III. On introducing this into Eq. (84) and on rearranging, we obtain

$$T_\pi=\left[1+\mathcal{U}_c\frac{1}{a-\mathcal{U}_c}\right]H'$$

$$=\Omega_c^{(-)\dagger}H' \tag{85}$$

[see Eq. (24)]. This represents the rigorous form of the T_π which was given in the approximation of Eq. (64) in I. The matrix element of T_π for photoproduction of a meson of momentum $\mathbf{q}$ when the nucleus is excited to a state γ is then

$$\begin{aligned}(\gamma q|T_\pi|A,M)&=(\lambda_q,\Omega_c^{(-)\dagger}\langle\gamma|H'|A,M\rangle)\\&=(\varphi_q^{(-)},\langle\gamma|H'|A,M\rangle).\end{aligned} \tag{86}$$

The symbol $\langle\gamma|H'|A,M\rangle$ means the matrix element of H' with respect to the *nuclear* states (A,M) and γ. Equation (86) differs from a simple lowest order perturbation calculation of T_π only in that the "distorted wave" $\varphi_q^{(-)}=\Omega_c^{(-)}\lambda_q$ [see Eq. (27)] is used for the final state rather than the plane wave λ_q.

When the photoproduction from a given nucleon is localized at the point of production, the photoproduction cross section, as obtained from Eq. (86), can be written approximately as[22,23]

$$\frac{d\sigma_\pi}{d\Omega}=A\frac{d\sigma_f}{d\Omega}\frac{(2\pi)^3}{V_A}\eta\int d^3x|\varphi_q^{(-)}(x)|^2. \tag{87}$$

$d\sigma_f/d\Omega$ is the cross section for photomeson production from a free nucleon (actually, a suitably weighted average for the neutrons and protons in the nucleus, taking into account the charge of the meson). η is a parameter introduced to account for the effects of nuclear binding on the photoproduction and is expected to be independent of A to a fair approximation.[23]

We consider $d\sigma_\pi/d\Omega$ to correspond to the experimentally observed photomeson cross section when the very low energy (i.e., inelastically scattered mesons) are not observed. This conclusion is further justified since true absorption seems to predominate over the inelastic scattering for meson energies below 100 Mev.

From Eq. (30) we obtain the cross section for inelastic scattering or absorption of mesons by a nucleus to be

$$\sigma_{ab}=-2\frac{(2\pi)^3}{v_\pi}\operatorname{Im}[(\varphi_q,\mathcal{U}_c\varphi_q)]. \tag{88}$$

If $\mathcal{U}_c$ is considered to be a constant within the nucleus and to vanish outside, the integrals of Eqs. (87) and (88) are the same and can be eliminated from these two equations to give

$$\frac{d\sigma_\pi}{d\Omega}=\left[\frac{d\sigma_f}{d\Omega}\eta\lambda\frac{A}{V_A}\right]\sigma_{ab}, \tag{89}$$

[22] This was discussed in reference 1 and in more detail in reference 23.

[23] N. Francis and K. Watson, Phys. Rev. **89**, 328 (1953).

a result discussed in more detail in reference 23. To obtain Eq. (89), $\mathrm{Im}\mathcal{U}_e$ was set equal to $-v_\pi/2\lambda$, where λ is the mean free path for scattering or absorption.

Since we have defined T_π, T_s is also defined. This corresponds to photomeson production followed by inelastic scattering in the nucleus in which it was produced. We now wish to calculate the cross section σ_{star}, which corresponds to the photoproduction of a meson which is either reabsorbed or scattered inelastically. σ_{star} is expected to lead to considerable nuclear excitation. We first calculate the cross section σ_t for the production of a meson, irrespective of its subsequent behavior.

σ_t can most easily be evaluated by calculating the transition amplitude for the elastic, forward scattering of a high energy γ ray by the nucleus:

$$\langle T_\gamma\rangle_0=\langle H'Fe^{-1}H'\rangle_0 \tag{90}$$

as shown in I [the notation is that of Eq. (28)]. Now photomeson production seems to involve considerable nuclear excitation (recoil nucleons seem to have been observed)[24] and may reasonably be thought not to interfere coherently with the subsequent scattering of the meson. In this case, we can write Eq. (90) as

$$\langle T_\gamma\rangle_0=\sum_\gamma(A,M|H'|\gamma)(\gamma|F|\gamma)(\gamma|e^{-1}H'|A,M), \tag{91}$$

where the "γ" represent a complete set of nuclear states. [Equation (91) is similar to Eq. (78).] Now $(\gamma|F|\gamma)=\langle F\rangle$, as given by Eq. (56). But

$$\langle F\rangle\frac{1}{e}=\frac{1}{a-\mathcal{U}_e},$$

so

$$\langle T_\gamma\rangle_0=\left\langle H'\frac{1}{a-\mathcal{U}_e}H'\right\rangle_0. \tag{92}$$

The cross section σ_t is then[11]

$$\sigma_t=-\frac{2(2\pi)^2}{v_\pi}\,\mathrm{Im}\left\{\left\langle H'\frac{1}{a-\mathcal{U}_e}H'\right\rangle_0\right\}. \tag{93}$$

For the same reasons which led to Eq. (91) it seems reasonable that the coherent interference of T_π and T_s can be neglected, so

$$\sigma_{\mathrm{star}}=\sigma_t-\sigma_\pi. \tag{94}$$

As argued in I, the quantity $\mathcal{U}_e$ is not expected to be of much importance in Eq. (93), so

$$\sigma_t\simeq A\sigma_f\eta, \tag{95}$$

where σ_f is the total weighted cross section for the protons and neutrons of the nucleons if they were free. We can take into account the effect of $\mathcal{U}_e$ in Eq. (93) by rewriting Eq. (95) as

$$\sigma_t=A\sigma_f\eta\eta', \tag{96}$$

where η' is the factor correcting Eq. (95). η' can be calculated from the optical model. Integrating the differential cross section (89) gives

$$\sigma_\pi=A\sigma_f\eta(\lambda\sigma_{\mathrm{ab}}/V_A),$$

so Eq. (94) becomes

$$\sigma_{\mathrm{star}}=A\sigma_f\eta[\eta'-(\lambda\sigma_{\mathrm{ab}}/V_A)], \tag{97}$$

on using Eq. (96). Equations (89) and (97) represent two relations between the four cross sections σ_f, σ_{ab}, σ_π and σ_{star}, each of which has been studied experimentally.

An approximate evaluation of η', if we use Eq. (93), and assume that the nucleus is large, gives

$$\eta'=1-\frac{3v_\pi}{8A}\left(\frac{a_0}{\lambda}\right)\left(\frac{B_R}{\epsilon_q}\right)\frac{1}{[(B_Ra_0)^2+(v_\pi a_0/2\lambda)^2]^2}, \tag{98}$$

where a_0 is related to the nuclear radius R by

$$a_0=R/A^{\frac{1}{3}}.$$

B_R is the real part of the part of B [Eq. (65)], the well depth. Taking $\sigma_{\mathrm{ab}}=\pi R^2$ and the values of B_R and λ obtained by Lederman *et al.*[20] for 65-Mev mesons, we obtain

$$\eta'=1+4.4/A,$$

and

$$\sigma_{\mathrm{star}}=A\sigma_f\eta[1+4.4/A-1.86/A^{\frac{1}{3}}]. \tag{99}$$

This is in qualitative agreement with the magnitude of the observed high energy photostar cross section.[24] These phenomena are complicated, however, and it appears that the meson reabsorption may be just one of several contributing causes. The relation (89) seems to be well satisfied experimentally.[23]

VI. FINAL COMMENTS

Our discussion indicates that the optical models have a wide range of validity. For applications one may ignore the problem of actually calculating the potential $\mathcal{U}_e$ and attempt to describe it by means of parameters which are determined by experiment. On the other hand, the arguments of Sec. IV suggest that it is not unfeasible to try calculating $\mathcal{U}_e$ directly in terms of free nucleon scattering amplitudes and certain gross parameters describing nuclear structure. In this case it is reasonable to hope that the theory can be useful in deducing such nuclear properties as density and strength of correlations.

The role played by spin-orbit interactions is of interest, although we have made no attempt to explicitly calculate such effects. If the spin dependence of the t_α's is known, then the methods of Sec. IV can be applied to calculate the spin dependence of $\mathcal{U}_e$. For the elastic scattering of slow nucleons by nuclei it is tempting to relate $\mathcal{U}_e$ to the "one-body potential" used in the shell model. In this case one may very well expect appreciable spin-orbit interactions.

[24] S. Kikuchi, Phys. Rev. **86**, 41 (1952).

In the Appendix we give an alternate derivation of the potential $\mathcal{U}_c$. This alternate derivation has the advantage that it does not involve an approximation which assumes that the number of scatterers is large, as was done in Sec. III. The corrections for a finite number of scatterers appear in a somewhat curious and surprisingly simple manner—and permit us to define the optical model even for the somewhat singular (and trivial) case of a single bound scatterer.

We are indebted to Professor K. A. Brueckner for several helpful discussions.

APPENDIX

An Alternate Derivation of the Potential $\mathcal{U}_c$

We shall give an alternate development of the optical model potential $\mathcal{U}_c$ which has an advantage over that of Sec. III in that it is both simpler and of greater rigor. (It does not make the approximation that the number of scatterers is large.) For simplicity we shall assume that there is no true absorption, so $\Delta=0$.

The present derivation begins with the original (rigorous) multiple scattering Eqs. (33):

$$\Omega_s=1+\frac{1}{a}\sum_{\alpha=1}^{A} t_\alpha\Omega_s(\alpha), \quad \Omega_s(\alpha)=1+\frac{1}{a}\sum_{\beta\neq\alpha}^{A} t_\beta\Omega_s(\beta). \tag{A-1}$$

If we use the notation of Sec. III,

$$\Omega_c\equiv\langle\Omega_s\rangle=1+\frac{1}{a}\sum_{\alpha=1}^{A}\langle t_\alpha\Omega_s(\alpha)\rangle. \tag{A-2}$$

Define

$$\mathfrak{L}\equiv\sum_{\alpha=1}^{A}\langle t_\alpha\Omega_s(\alpha)\rangle \tag{A-3}$$

and

$$\mathfrak{F}_c\equiv\langle\Omega_s(\alpha)\rangle. \tag{A-4}$$

Compare with the notation of Eqs. (44) and (46). Then using the "prime" notation and that of Eq. (45), the second set of Eqs. (A-1) lead to

$$\begin{aligned}\langle'\Omega_s(\alpha)\rangle&=\langle'1\rangle+\frac{1}{a}\sum_{\beta\neq\alpha}^{A}\langle't_\beta\Omega_s(\beta)\rangle\\&=-\frac{1}{a}\sum_{\beta\neq\alpha}^{A}[\langle't_\beta\rangle\mathfrak{F}_c+\langle't_\beta\,'\Omega_s(\beta)\rangle].\end{aligned} \tag{A-5}$$

Setting

$$\langle'\Omega_s(\alpha)\rangle=(\mathcal{G}_\alpha-1)\rangle\mathfrak{F}_c. \tag{A-6}$$

Equation (A-5) is satisfied if the $\mathcal{G}_\alpha$, satisfy the set of integral equations

$$\mathcal{G}_\alpha=1+\frac{1}{a}\sum_{\beta\neq\alpha}^{A}{}'t_\beta\mathcal{G}_\beta. \tag{A-7}$$

Then, from Eqs. (A-3) and (A-6), we find that

$$\mathfrak{L}=\mathfrak{U}_c\mathfrak{F}_c, \tag{A-8}$$

where $\mathfrak{U}_c$ is defined as

$$\mathfrak{U}_c\equiv\sum_{\alpha=1}^{A}\langle t_\alpha\mathcal{G}_\alpha\rangle. \tag{A-9}$$

From the second of Eqs. (A-1), we obtain

$$\langle\Omega_s(\alpha)\rangle=1+\frac{1}{a}\sum_{\beta\neq\alpha}^{A}\langle t_\beta\Omega_s(\beta)\rangle. \tag{A-10}$$

Since $\mathfrak{F}_c\equiv\langle\Omega_s(\alpha)\rangle$, and is independent of α, we obtain on summing Eq. (A-10) over α,

$$A\mathfrak{F}_c=A+(A-1)a^{-1}\mathfrak{L}. \tag{A-11}$$

If we divide by A (we do not here drop the $1/A$ term as was done in Sec. III) and use Eq. (A-8), we obtain an integral equation for $\mathfrak{F}_c$:

$$\mathfrak{F}_c=1+a^{-1}\delta\mathfrak{U}_c\mathfrak{F}_c \tag{A-12}$$

where we have defined

$$\delta\equiv1-1/A. \tag{A-13}$$

The approximation used in Sec. III was to neglect terms of relative order $1/A$. If we did that there we could set $\delta=1$ and obtain the optical model directly. More generally, let us define a "pseudopotential" $\mathfrak{U}_\delta$ as

$$\mathfrak{U}_\delta=\delta\mathfrak{U}_c. \tag{A-14}$$

Then Eq. (A-12) can be written as

$$\mathfrak{F}_c=1+a^{-1}\mathfrak{U}_\delta\mathfrak{F}_c. \tag{A-12'}$$

In a formal sense, Eq. (A-12') defines a scattering problem with the pseudopotential $\mathfrak{U}_\delta$. The coefficient of $1/a$ is the "transition operator" T_δ for this scattering:

$$T_\delta=\mathfrak{U}_\delta\mathfrak{F}_c. \tag{A-15}$$

We return now to the actual problem, Eq. (A-2) is

$$\begin{aligned}\Omega_c&=1+a^{-1}\mathfrak{L}\\&=1+a^{-1}\mathfrak{U}_c\mathfrak{F}_c,\end{aligned} \tag{A-16}$$

by Eq. (A-8). The actual transition operator T_c is the coefficient of $1/a$ in Eq. (A-16), or

$$\begin{aligned}T_c&=\mathfrak{U}_c\mathfrak{F}_c\\&=\delta^{-1}T_\delta.\end{aligned} \tag{A-17}$$

The last step follows upon comparison with Eqs. (A-14) and (A-15). When the number of scatterers A is large enough that one can set $\delta=1$, then $\Omega_c=\mathfrak{F}_c$ [see Eqs. (A-12) and (A-16)] and $T_c=T_\delta$. (We may also verify that $T_c=\mathfrak{U}_c\mathfrak{F}_c$ holds even when $A=1$!)

In general, however, the actual transition operator differs from that obtained with the pseudopotential only by the factor δ^{-1}. The scattering cross sections are then related by δ^{-2}. This implies that in comparing an observed cross section with the predictions from the model with $\mathfrak{U}_c\simeq t_c$, for instance (as was done in Sec. IV), one should multiply the observed cross section by

δ^2. The potential deduced from the experimental cross section is then $\mathfrak{U}_\delta$, which should be divided by δ to obtain $\mathfrak{U}_c$.

It appears that the $1/A$ corrections occur in a rather simple manner and indeed tend to cancel each other somewhat.

Equations (A-7) seem to be more difficult to tackle than Eqs. (50). That is, Eqs. (A-7) includes *elastic* scatterings in excited nuclear states. These are already taken into account in Eqs. (50) by the appearance in that equation of $1/e$ rather than $1/a$.

Another (related) difference between Eqs. (50) and (A-7) is that the scattering operators t_a are different in these two equations. The incident energy in the t_a of Eqs. (50) is corrected to be the energy of the particle *in the medium*. [This point was discussed in Appendix (A) of reference 1.] As was also shown in I, the fact that this energy has a small imaginary part does not lead to significant corrections—at least, where the imaginary part is no larger than it seems to be for mesons. It thus appears that certain complicated properties of Eqs. (A-7) appear in a more natural and simple manner in Eqs. (50).

As a final remark, we note that our rather free use of operators such as $(a-\mathfrak{V})^{-1}$ is justified if there exists the Møller wave matrix,

$$\omega=1+a^{-1}\mathfrak{V}\omega,$$

since $(a-\mathfrak{V})^{-1}$ can be defined to be

$$\omega a^{-1}.$$

Therefore, all the results of this paper and of reference 1 depend upon the existence of such quantities ω. In particular, the entire derivation may be carried out in terms of the solution to integral equations and without the use of the more formal algebraic treatment which was actually employed.

PHYSICAL REVIEW VOLUME 92, NUMBER 2 OCTOBER 15, 1953

The Nuclear Moments of Technetium-99

KARL G. KESSLER AND R. E. TREES
National Bureau of Standards, Washington, D. C.
(Received May 15, 1953)

The hyperfine structure in the optical spectrum of technetium has been investigated in the region 3600–7000A with a Fabry-Perot interferometer crossed with a quartz prism spectrograph. The light source was a liquid-nitrogen-cooled hollow cathode discharge tube. The nuclear-spin, magnetic moments previously reported by one of us are confirmed ($I=9/2\hbar$ and $\mu=5.5\pm0.3$ nm) and are in agreement with a more recent nuclear induction measurement. The quadrupole moment of Tc^{99} is found to be: $Q=(+0.34\pm0.17)\times10^{-24}$ cm^2.

I. INTRODUCTION

ELEMENT 43 was first prepared in 1937 in the Berkeley cyclotron by neutron bombardment of molybdenum, and was named technetium (Tc) by Perrier and Segrè.[1,2] In 1948, milligram amounts of Tc^{99} were separated from uranium fission products by Parker, Reed, and Ruch.[3] A 3-mg sample of Tc^{99} was received by the spectroscopy laboratory of the National Bureau of Standards in January, 1949, for a preliminary investigation of the arc and spark spectra of the element.[4,5] In July, 1950, an additional amount of 3 mg was received from the Atomic Energy Commission for further work on the spectra of Tc. Wavelength measurements on 2121 lines in Tc I and Tc II were published by Meggers and Scribner,[6] and a preliminary analysis identifying 20 terms of Tc I and 4 terms of Tc II was published by Meggers.[7]

Of the second sample received, 2 mg were saved for an investigation of the hyperfine structure (hfs) of Tc. The nuclear spin (9/2) was determined by Kessler and Meggers[8] and a preliminary value (5.2 ± 0.5 nm) of the magnetic moment of the Tc nucleus was reported.[9] More recently a 7-mg sample of Tc^{99} has been received from the Oak Ridge National Laboratory. Four mg have been used to improve the descriptions of the arc and spark spectra, and the remainder was devoted to the investigation of the hfs of Tc reported below.

A nuclear induction experiment on 156 mg of Tc^{99} by Walchli, Livingston, and Martin[10] yielded for the magnetic moment a value of 5.6805 ± 0.0004 nm, consistent with our preliminary value.

[1] C. Perrier and E. Segrè, J. Chem. Phys. **5**, 712 (1937); **7**, 1 (1939).
[2] C. Perrier and E. Segrè, Nature **159**, 24 (1947).
[3] Parker, Reed, and Ruch, Clinton National Laboratory Report CNL-1, 1949 (unpublished).
[4] W. F. Meggers and B. F. Scribner, Y-476, Oak Ridge Spectroscopy Symposium, Abstracts of Papers, March 24 to 25, 1949 (unpublished).
[5] W. F. Meggers and B. F. Scribner, J. Opt. Soc. Am. **39**, 1059 (1949).
[6] W. F. Meggers and B. F. Scribner, J. Research Natl. Bur. Standards **45**, 476 (1950).
[7] W. F. Meggers, J. Research Natl. Bur. Standards **47**, 7 (1951).
[8] K. G. Kessler and W. F. Meggers, Phys. Rev. **80**, 905 (1950).
[9] K. G. Kessler and W. F. Meggers, Phys. Rev. **82**, 341 (1951).
[10] Walchli, Livingston, and Martin, Phys. Rev. **85**, 479 (1952).

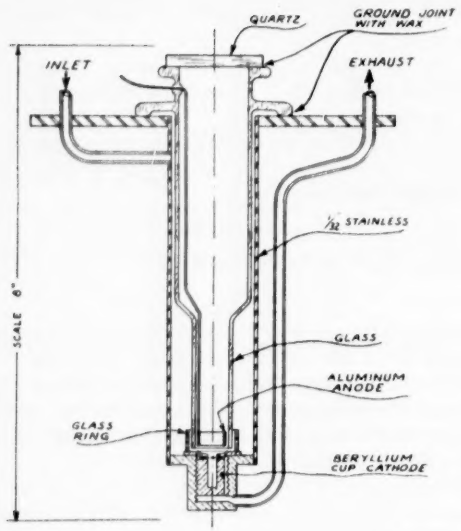

FIG. 1. Beryllium cup, liquid-nitrogen-cooled hollow cathode discharge tube. The technetium compound is deposited on the inner wall of the cathode cup. A stream of helium or argon gas passes down the tube, through the cup, and out through the bottom of the tube. The lower 4 inches of the tube is immersed in liquid nitrogen during operation.

II. EXPERIMENTAL PROCEDURE

(a) The Light Source

The source used was a liquid-nitrogen-cooled hollow cathode tube, shown in Fig. 1. The body of the tube is constructed of stainless steel to minimize the longitudinal heat flow. The lower end of the tube, which consists of a threaded brass plug, is immersed in liquid nitrogen to reduce the Doppler broadening of the spectral lines. The slow flow of heat down the tube walls permits the upper end to remain moderately warm, thus avoiding brittleness and cracking of the wax joints, and condensation on the window.

The beryllium-cup cathode is a modification of a design suggested by Schüler and Gollnow.[11] Three radial holes are drilled near the upper end of the cup, and these are connected to a longitudinal slot in the outside surface of the threaded cup. In operation, the carrier gas flows into the upper part of the cup, out through the radial holes, down the channel and out through the bottom of the tube. The flow pattern is such as to inhibit the loss of material out of the cup, while supplying clean gas for the discharge. The gas cleaning and circulating system consists of two liquid nitrogen traps, one on either side of the discharge tube, a mercury diffusion pump to circulate the gas, and a heated quartz tube filled with copper oxide to remove hydrogen gas. Carrier gases used were argon and helium at pressures of approximately 1-mm Hg. In the case of the helium carrier, one of the liquid nitrogen traps was filled with activated charcoal.

The cathode and anode were connected in series with a ballast resistor to a 1000-volt dc power supply. In normal operation, the potential fall across the discharge tube was 100 to 125 volts at a current of 85 to 120 ma.

The Tc^{99} was received in the form of the soluble ammonium pertechnate NH_4TcO_4. The salt was dissolved in pure water and slowly evaporated to dryness inside the beryllium cup. By careful manipulation, a thin layer of the salt was formed on the inside surface of the cathode.

Because the mechanism of the hollow cathode discharge depends on the excitation of ions sputtered into the discharge column by the gas ions striking the cathode surface, it is advantageous to use for the cathode a metal that has a low rate of sputtering. Beryllium has an extremely low rate,[12] and therefore this metal was used in the construction of the cathode cup.

(b) Dispersive Apparatus

The light from the hollow cathode discharge was collimated by a simple quartz lens mounted above the tube window. The collimated beam was reflected in a horizontal direction by a front-surface mirror and passed through a Fabry-Perôt interferometer. The interference pattern was then focused on the slit of a large Gaertner quartz spectrograph by a quartz-fluorite achromat of 50-cm focal length. Quartz interferometer plates coated with either aluminum or silver were used with 3.75 and 5 mm separators of invar. The plate curvature in the spectrograph was modified to yield optimum focus for the interferometer pattern. Eastman 103aF plates were used, and exposure times varied from 15 to 45 minutes.

III. RESULTS

(a) Data

Interference spectrograms covering the wavelength region 3600–7000A yielded 72 lines of Tc I. Of these, 36 were sufficiently resolved so that the hfs splitting factors could be calculated for at least one of the energy levels involved. The hfs patterns on these plates were measured with a comparator, by using the standard eyepiece and crosshairs on all lines. Those lines used in the calculation of the quadrupole moment were also measured on the same comparator, with a photo-electric scanning device.[13]

(b) Nuclear Spin

As many as 9 resolved hfs components have been observed in lines of Tc I, and all interval ratios observed are in agreement with a value of $I=9\hbar/2$, as previously reported.[8]

[11] H. Schüler and H. Gollnow, Z. Physik **93**, 611 (1935).

[12] E. O. Hulburt, Rev. Sci. Instr. **5**, 85 (1934).

[13] F. S. Tomkins and M. Fred, J. Opt. Soc. Am. **41**, 641 (1951).

(c) Nuclear Magnetic Moment

Preliminary investigation[9] of the hfs of Tc^{99} yielded a value of $+5.2\pm0.5$ nuclear magnetons for the magnetic moment of the Tc^{99} nucleus. Walchli, Livingston, and Martin[10] subsequently reported a value of $\mu=+5.6805\pm0.0004$ nm which they measured by nuclear-induction methods. The precision attained by nuclear resonance techniques cannot be matched by optical methods. However, comparison of the optical data with the resonance value is helpful in studying the the validity of approximations involved in the optical experiment. Insufficient information on the energy levels in Tc I and Tc II contributes to considerable uncertainty in the ionization potentials, and more particularly in the quantum defect corrections. In several terms, deviations from the nuclear induction value may be attributed to a mixture of term parentage.

In the case of the ^6D term, the term parentage is pure and the value of the energy to remove the electron is reasonably well known. The good agreement with the nuclear induction value (within 2.5 percent) supports the statement by Breit[14] that in some cases there is experimental evidence that the accuracy of the Goudsmit-Fermi-Segrè formula is good, despite the lack of sound theoretical foundation.

The interval factors for the five principal terms are given in Table I. These factors were derived for the $a\,^6D$, $a\,^4D$, and $e\,^6S$ terms by the method of graphical analysis suggested by Fisher and Goudsmit.[15] Nearly all of the estimated errors in the interval factors for these configurations are attributable to the uncertainty in determining the proper interval factor ratio for the two terms involved in the transition. The $z\,^8P^\circ$ and $z\,^6P^\circ$ terms are analyzed in transitions to the ground state $a\,^6S$, which has nearly zero hfs splitting. The interval factors for these terms are derived by the formula[5] given in the following section on the quadrupole moment.

The electron coupling constants for the individual electrons were calculated from the interval factors with the formulas of Table II. These formulas were derived by one of us in the accompanying paper.[16] The values of the coupling constants, a_l, calculated from the above formula [formula (3) in RET] by the method of least squares, are given in Table III.

The magnetic moments were calculated by use of the Goudsmit formula:[17]

$$\mu=0.431IZ_0a_s\times10^{10}/Z_iW^{\frac{1}{2}}\kappa, \qquad (1)$$

where $I=9/2$; Z_0 is the effective charge outside the nucleus and is taken to be 1 for the neutral and 2 for the singly ionized atom; a_s is the coupling constant for s electrons; Z_i, the effective charge near the nucleus, is taken as 43 for the s electron; W is the energy in units[18] of K necessary to remove the electron in question and $\kappa=1.22$ is the relativity correction. Thus, Eq. (1) reduces to

$$\mu=3.70\times10^8Z_0a_s/W^{\frac{1}{2}}. \qquad (2)$$

Values of μ are listed in Table III for the following five terms:

(1) $(4d^6(a\,^5D)5s)a\,^6D$.

This configuration has pure parentage and should give a reliable value for μ. The principal errors involved are: (a) the uncertainty in the value of the ionization potential (58 297K),[19] (b) the uncertainty introduced in determining the interval factors by graphical analysis,[14] and (c) the omitted Fermi-Segrè correction.[20]

By using a value of 4161.2K for the centroid value of $a\,^5D$ in Tc II[21] and 3277K for $a\,^6D$ in Tc I, the energy to remove the $5s$ electron becomes $W=59\,181$K, yielding $\mu=5.93$ nm. There are insufficient data available in Tc to calculate the Fermi-Segrè quantum defect correction. It is possible, however, to obtain a rough approximation to this correction from the corresponding terms in Mn I. If the magnetic moment is divided by the correction factor $[(1-d\sigma/dn)=1.07]$ from Mn I, the corrected value of the magnetic moment, shown in Table III, becomes $\mu=5.54$ nm. In view of the approximations involved, the agreement with the nuclear induction value of $\mu=5.68$ is good.

(2) $(4d^5(a\,^7S)5p)z\,^8P^\circ$.

The energy necessary to remove the $5s$ electron was calculated for the second spectrum. Removal of the $5p$ electron leaves the configuration $(4d^5(a\,^6S)5s)a\,^7S$, the ground state of Tc II. The energy to remove the $5s$

TABLE I. Interval factors.

Configuration	Term symbol	J	Interval factor (A)	Coupling factor (B) $\times10^4$
$4d^6(a\,^6D)5s$	$a\,^6D$	9/2	$+0.025\pm0.001$	···
		7/2	$+0.030\pm0.001$	···
		5/2	$+0.032\pm0.001$	···
		3/2	$+0.039+0.001$	···
		1/2	$+0.07\pm0.02$	···
$4d^5(a\,^7S)5p$	$z\,^8P^\circ$	7/2	$+0.0345\pm0.0001$[a]	-3.7 ± 2.2[a]
		5/2	$+0.0351\pm0.0001$[a]	-1.9 ± 2.2[a]
$4d^6(a\,^5D)5s$	$a\,^4D$	7/2	-0.018 ± 0.002	···
		5/2	-0.016 ± 0.002	···
$4d^5(a\,^7S)5p$	$z\,^6P^\circ$	7/2	$+0.0292\pm0.0004$	0.0 ± 4
		5/2	$+0.0336\pm0.0004$	-6.8 ± 4
		3/2	$+0.0442\pm0.0004$	$+3.0\pm4$
$4d^5(a\,^7S)6s$	$e\,^6S$	5/2	$+0.048\pm0.001$	···

[a] Errors marked are standard deviation, others are estimated.

[14] G. Breit, "Report of Subcommittee h, Joint Commission for Spectroscopy," J. Opt. Soc. Am. **43**, 427 (1953).
[15] R. A. Fisher and S. Goudsmit, Phys. Rev. **37**, 1057 (1931).
[16] R. E. Trees, following paper [Phys. Rev. **92**, 308 (1953)], hereafter referred to as RET.
[17] S. Goudsmit, Phys. Rev. **43**, 636 (1933).
[18] We have used the notation K (kayser) for cm^{-1}, the unit of wave numbers, in accordance with recommendations of the Joint Commission for Spectroscopy, J. Opt. Soc. Am. **43**, 410 (1953).
[19] M. A. Catalán and F. R. Rico, Anales fís. y quím. (Madrid) **A48**, 328 (1952).
[20] E. Fermi and E. Segrè, Z. Physik **82**, 729 (1933).
[21] W. F. Meggers (unpublished).

TABLE II. Interval factor formulas.

$a\ ^6D$	$a\ ^4D$
$A(9/2)=0.1111a_s+0.5079a_d$	$A(7/2)=-0.086a_s+0.498a_d$
$A(7/2)=0.1175a_s+0.3574a_d$	$A(5/2)=-0.074a_s+0.719a_d$
$A(5/2)=0.1314a_s+0.2090a_d$	$\zeta(\alpha SL)=-(3/10)\zeta_d$
$A(3/2)=0.1733a_s+0.0076a_d$	$z\ ^6P^\circ$
$\zeta(\alpha SL)=-1/5\zeta_d$	$A(7/2)=0.1361a_s+0.3265a_p$
$z\ ^8P^\circ$	$A(5/2)=0.1687a_s-0.0065a_p$
$A(7/2)=0.1338a_s+0.1814a_p$	$A(3/2)=0.2667a_s-0.3200a_p$
$A(5/2)=0.1837a_s-0.3592a_p$	$B(7/2)=0.0381b_p$
$B(7/2)=-0.0508b_p$	$B(5/2)=-0.0914b_p$
$B(5/2)=+0.0285b_p$	$B(3/2)=0.0533b_p$
$\zeta(\alpha SL)=(1/7)\zeta_p$	$\zeta(\alpha SL)=-(1/7)\zeta_p$
	$e\ ^6S$
	$A(5/2)=0.1905a_{6s}-0.1429a_{6s}$

electron is then the ionization limit of Tc II, or $W=120\,000$K.[19] The calculated value of the magnetic moment ($\mu=4.11$ nm) is low, but perhaps not unreasonably so in view of the uncertainty in the ionization limit and the approximation involved in going to the second spectrum. Inclusion of the Fermi-Segrè correction is this calculation would further lower this value.

(3) $(4d^6(a\ ^5D)5s)a\ ^4D.$

The energy necessary to remove the $5s$ electron is equal to the difference between the $a\ ^4D$ term ($W=11\,030$K) and the $a\ ^5D$ term in Tc II ($W=58\,297+4161$K). The resultant value ($W=51\,428$K) gives $\mu=6.78$ nm. If we take the quantum defect correction factor 1.07 from Mn I, the value of the magnetic moment becomes $\mu=6.34$ nm. Part of the discrepancy here may lie in the approximation involved in the Fermi-Segrè correction. A correction factor of 1.12 would yield complete agreement.

(4) $(4d^5 5s(a\ ^7S)5p)z\ ^6P^\circ.$

The energy to remove the $5s$ electron must again be taken from the second spectrum. As in $z\ ^8P^\circ$, the energy to remove the $5s$ electron is $W=120\,000$K. The corresponding value of μ ($=3.35$ nm) is low, again for reasons pointed out in $z\ ^8P^\circ$. The parentage here is also a mixture of ^7S and ^5S, which would lower the value of the magnetic moment, as observed.

(5) $(4d^5 5s(a\ ^7S)6s)e\ ^6S.$

In order to remove the $5s$ electron we must again go to the second spectrum ($W=120\,000$K). This yields a value of $\mu=4.98$ nm. A principal source of uncertainty here lies in the assumption of the value 8.1 for the ratio a_{5s}/a_{6s}. This approximation to the interval factor ratio for the two s electrons was derived from the Goudsmit formula:

$$\frac{a_{5s}}{a_{6s}}=\frac{(Z_0)_{6s}}{(Z_0)_{5s}}\left(\frac{W_{5s}}{W_{6s}}\right)^{\frac{1}{2}}=8.1. \qquad (3)$$

The quantum defect correction here reduces the value of the magnetic moment to $\mu=4.33$ nm.

The values of a_p and a_d, empirical values of which are shown in Table III, can be calculated from Eq. (10) in RET as a check on the internal consistency of the measurements. Using values of $\lambda=1.03$ and $g=1.26$, we have:

$$a_l=\frac{0.545\times1.26\times10^{-3}\zeta_l}{1.03Z_i}=0.667\times10^{-3}\frac{\zeta_l}{Z_i}. \qquad (4)$$

A discussion of the values of ζ_l as determined from the fine structure is given in the Appendix. For a p electron, $\zeta_p=960$ and $Z_i=41$, then $a_p=0.016$. This is in moderately good agreement with the observed values of $a_p=0.017$ for the $z\ ^6P^\circ$ level and $a_p=0.021$ for the $z\ ^8P^\circ$ level. In the case of a d electron, $\zeta_d=670$ and $Z_i=33$, therefore $a_d=0.013$. This value is considerably larger than the observed values of 0.003 and $\leqslant0.001$ for the $a\ ^6D$ and $a\ ^4D$ terms respectively. Both these terms are derived from transitions in which the other level involved does not have zero splitting, and the graphical analysis necessary in such cases involves errors of the order of ±0.005.

The average of the corrected values of the magnetic moment from Table III is $\mu=5.40$ nm. The most reliable value is that from the $a\ ^6D$ term, $\mu=5.54$ nm.

(d) Nuclear Electric Quadrupole Moment

Calculations of the quadrupole moment were found to be feasible only with the data derived from transitions in which one of the terms involved has negligible hfs splitting. In all other cases, the uncertainty introduced in fitting the observed pattern to the combined effect of two splitting factors was greater than the quadrupole effect. The transitions from which quadrupole data were derived are from the $z\ ^8P^\circ$ and $z\ ^6P^\circ$ terms to the ground state $a\ ^6S$.

Values of the magnetic splitting factor A and the quadrupole coupling factor B were calculated from the observed intervals with the interaction formula

$$W_F=W_J+\tfrac{1}{2}AK+BK(K+1),$$
$$K=F(F+1)-I(I+1)-J(J+1). \qquad (5)$$

Values of A and B are tabulated in Table I, together with the standard deviation of the mean in each case. Six exposures were available for each line, and measurements on each were repeated at least four times.

The relations between the coupling factor B and the parameter b_p, taken from Eq. (12) of RET, are given in Table II. The value of the quadrupole moment Q can be calculated with formula 15 of RET:

$$b_l=\frac{0.253\zeta_l Q\times10^{21}}{\lambda Z_i I(2I-1)},$$

where $\lambda=1.03$, $I=9/2$ and $Z_i=41$ for the p electron. The value $\zeta_p=960$ was used in both $z\,^6P^\circ$ and $z\,^8P^\circ$ for reasons discussed in the Appendix.

The values of b_I and Q calculated from the $z\,^8P^\circ$ and $z\,^6P^\circ$ levels are given in Table III. The final value of Q has been calculated by using as a weighting factor in each case the reciprocal of the standard deviation squared of the individual measurements from Table III. The final value of the nuclear quadrupole moment is $Q=+0.34\times10^{-24}$ cm² with a standard deviation of the mean of 0.17×10^{-24} cm².

The observed value of Q corresponds to a shift of the order of 1 percent in the energy level spacing, and it is, therefore, very close to the limit of precision attainable in the measurement of these intervals. A significant result could be obtained only by combining the calculated Q values from five different levels, where the hfs of each level was measured some 25 times.

It is also possible that the regular variation in intensity and spacing found in hfs patterns may introduce a small systematic bias into the determination of line centers. Such a systematic error of the same sign and approximate magnitude would affect the $^8P_{7/2}$ and $^6P_{5/2}$ terms in one direction and the $^8P_{5/2}$, $^6P_{7/2}$ and $^6P_{3/2}$ terms in the opposite direction. The fact that the Q values of the latter set of levels are generally smaller than those in the first pair may indicate the presence of such a systematic error. The direction of this bias would be opposite to that required to produce an error in the sign of Q.

Sources of perturbations are discussed from the theoretical viewpoint in RET. None of these errors is likely to affect significantly the Q value obtained in Tc. A similar analysis of the homologous spectrum of Mn I in RET yielded a positive Q value somewhat higher than the positive value obtained from recent microwave experiments.

If one assigns 95 percent confidence limits to the value of the quadrupole moment, one has:

$$Q=(+0.34\pm0.34)\times10^{-24}\text{ cm}^2.$$

A small negative Q is not excluded, however.[22]

Complete details of the hfs patterns will be published in the National Bureau of Standards Journal of Research in conjunction with an extended analysis of both Tc I and Tc II. We wish to express our appreciation to Mr. Joseph Cameron of the National Bureau of Standards Statistical Engineering Laboratory for valuable aid in analyzing the quadrupole moment data.

This work has been carried out in the Spectroscopy Section of the National Bureau of Standards as part of the program initiated by W. F. Meggers to study the spectra of technetium. We are indebted to G. W. Parker of the Oak Ridge National Laboratories for supplying the excellent samples of Tc^{99}.

[22] The plot of Q values given by Townes, Foley, and Low [Phys. Rev. **76**, 1415 (1949)] indicates a small Q for Tc. The empirical rule of Bene, Denis, and Extermann [Phys. Rev. **76**, 1255 (1949)] indicates that the Q of Tc should be greater than the Q in Nb. Since no limits are given on the value $Q\approx0$ in Nb [W. W. Meeks and R. A. Fisher, Phys. Rev. **72**, 451 (1947)] it would not be safe to conclude from this that a positive Q is expected in Tc. It has been pointed out to us that, according to the shell model, the Q of Tc should be negative in contradiction to our observed result.

TABLE III. Dipole and quadrupole moments from the terms of Tc I.

Term	Coupling constant	Magnetic moment (nm) Uncorrected	Corrected	J	b_I	$Q\times10^{+24}$ (cm²)
$a\,^6D$	$a_s=0.231$ $a_d=0.003$	5.93	5.54			
$z\,^8P^\circ$	$a_s=0.0231$ $a_p=0.021$	4.11	···	7/2 5/2	+0.72 −0.67	+0.47±0.28 −0.44±0.51
$a\,^4D$	$a_s=0.214$ $a_d\leq0.001$	6.78	6.34			
$z\,^6P^\circ$	$a_s=0.188$ $a_p=0.018$	3.35	···	7/2 5/2 3/2	0.00 +0.75 +0.57	+0.00±0.69 +0.49±0.29 +0.37±0.49
$e\,^6S$	$a_{5s}=0.277$ $a_{6s}=0.034$	4.98	4.33			
		Mean	5.4		Mean	+0.34±0.17

APPENDIX

Evaluation of the Parameters ζ_p and ζ_d

The parameter $\zeta(\alpha SL)$ is calculated from the observed fine structure. It is equal to the fine structure intervals divided by the higher J value. Formulas for calculating the parameters for the individual electrons, ζ_p and ζ_d, from $\zeta(\alpha SL)$ taken from formula 51, RET, are given in Table II. For $z\,^8P^\circ$, $\zeta_p=960$, which is consistent with the data on four other terms analyzed. In the case of $z\,^6P^\circ$, however, $\zeta_p=380$. This low value is probably the result of a mixture of $4d^55s\,^7S$ and $4d^55s\,^5S$ parentage in this term. Such a mixture would make the calculated value of the magnetic moment too small, as is the case. The value $\zeta_p=960$ was therefore used in calculating the quadrupole moment from the $z\,^6P^\circ$ term. The values of B_J are the same for both $z\,^6P^\circ$ and $y\,^6P^\circ$ terms, so that mixing of parents will not effect the matrix element needed to calculate the quadrupole moment. The value of $\zeta_d=670$ used in calculating a_d in the section on the magnetic moment is the same for both $a\,^6D$ and $a\,^4D$ terms and is in good agreement with the values calculated for five out of eight terms analyzed.

Hyperfine Structure Formulas for *LS* Coupling

R. E. TREES
National Bureau of Standards, Washington, D. C.
(Received May 15, 1953)

Formulas for the interval factor A and the quadrupole coupling factor B in the hyperfine structure formula,

$$W=W_J+\tfrac{1}{2}AK+BK(K+1),$$

are derived with Racah's tensor algebra. The results are directly applicable to light atoms ($Z<50$) that show good *LS* coupling. Data of White and Ritchl for manganese are analyzed, and an approximate value of the nuclear quadrupole moment in Mn^{55} of $Q=1\times10^{-24}$ cm² is obtained. This confirms another approximate value of $Q=0.5\times10^{-24}$ cm² recently obtained by microwave methods. An error in the calculation carried out by Brown and Tomboulian to evaluate the Q of tantalum is noted. A relation satisfied by X functions is derived, which simplifies their numerical evaluation.

A. GENERAL THEORY

THE interaction between the nucleus and electrons of an atom is usually given by the formula,[1]

$$W_F=W_J+\tfrac{1}{2}AK+BK(K+1), \tag{1}$$

where

$$K=F(F+1)-I(I+1)-J(J+1). \tag{2}$$

The dependence of W_F on F (and, practically, on I also) is given by K and the dependence on electronic quantum numbers is included in A and B. The term with A as coefficient arises from the magnetic dipole interaction between the nucleus and the electrons while the term containing B arises from the electric quadrupole moment interaction. The dependence of A and B on the electronic quantum numbers has been calculated only for special electronic configurations,[2-4] usually by writing out the wave functions explicitly, or by use of Goudsmit's sum rule.[3] We give here expressions for A and B that can be evaluated easily with Racah's tensor algebra.[5] The expressions are directly applicable to atoms showing *LS* coupling. Since relativistic effects[2,4,6] are largely neglected, the atom considered should not have too great an atomic number (say $Z<50$).

Goudsmit[3] has given the following formula which expresses the J dependence of A for an atom showing *LS* coupling.

$$A(J)=\lambda(2-g)-\sigma\frac{6\Gamma(2-g)-2(g-1)L(L+1)}{(2L-1)(2L+3)}+\beta(g-1), \quad (J\neq0), \tag{3}$$

where[7]

$$\Gamma=\tfrac{1}{2}\{J(J+1)-L(L+1)-S(S+1)\}, \tag{4}$$

$$g=1+\frac{J(J+1)+S(S+1)-L(L+1)}{2J(J+1)}. \tag{5}$$

Goudsmit's derivation by means of the diagonal-sum rule was too cumbersome to publish; we give a more direct derivation of this in Sec. D. Goudsmit did not define the coefficients λ, σ, and β explicitly in terms of one-electron parameters. The procedure outlined in Sec. D yields the following values of λ, σ, and β in terms of double-barred submatrices and tensor operators defined in II; the necessary submatrices are diagonal in αSL, where α represents the quantum numbers needed to specify the electron state (exclusive of S and L).

$$\lambda=\frac{(\alpha SL||\sum_i(a_l)_i\mathbf{l}_i||\alpha SL)}{[L(L+1)(2L+1)]^{\frac{1}{2}}}, \tag{6}$$

$$\sigma=-[(2L-1)(2L+3)]^{\frac{1}{2}}\times\frac{(\alpha SL||\sum_i(a_l)_i\mathbf{s}_i\mathbf{C}_i^{(2)}||\alpha SL)}{[S(S+1)(2S+1)L(L+1)(2L+1)]^{\frac{1}{2}}}, \tag{7}$$

$$\beta=\frac{(\alpha SL||\sum_i(a_s)_i\delta(l_i,0)\mathbf{s}_i||\alpha SL)}{[S(S+1)(2S+1)]^{\frac{1}{2}}}. \tag{8}$$

In these expressions $\mathbf{s}_i$ and $\mathbf{l}_i$ are the spin and angular momentum respectively of the ith electron and $\mathbf{C}^{(2)}$ is the second degree tensor operator defined by Racah in II, Eq. (46). The one-electron parameters a_s and a_l are defined in agreement with the definitions of Fermi[8] and Goudsmit:[3]

$$a_s=\frac{8\pi}{3}R\alpha^2a_o^3\left(\frac{m_e}{M_P}\right)|\psi(0)|^2g(I), \tag{9}$$

$$a_l=R\alpha^2a_o^3\left(\frac{m_e}{M_P}\right)\left\langle\frac{1}{r_l^3}\right\rangle_{Av}g(I) \quad (l\neq0). \tag{10}$$

[1] H. Kopfermann, *Kernmomente* (Akad. Verlag. M.B.H., Leipzig, 1940), referred to as I.
[2] H. B. G. Casimir, Verhandel. Teyler's Tweede Genootschap, Haarlem (1936).
[3] S. Goudsmit, Phys. Rev. **37**, 663 (1931).
[4] G. Breit, Phys. Rev. **38**, 463 (1931); G. Breit and L. A. Wills, Phys. Rev. **44**, 470 (1933).
[5] G. Racah, Phys. Rev. **62**, 438 (1942); **63**, 367 (1943), referred to as II and III respectively.
[6] G. Racah, Z. Physik **71**, 431 (1931); Nuovo cimento **8**, 178 (1931).
[7] Tables of g values have been prepared by C. C. Kiess and W. F. Meggers, J. Research Natl. Bur. Standards **1**, 641 (1928).
[8] E. Fermi, Z. Physik **60**, 320 (1930).

In these relations, R is the Rydberg constant; α is the fine structure constant ($=1/137$); a_0 is the Bohr hydrogen radius; m_e/M_p is the ratio of the electron mass to the proton mass ($=1/1836$); and $g(I)$ is the nuclear g factor.

In Eq. (9), $\psi(0)$ is the value of the eigenfunction of the s-electron at the nucleus. It is usually evaluated by use of a formula given by Fermi and Segrè.[9] When this evaluation is used, a_s takes on a form similar to that suggested by Goudsmit.[10]

$$a_s=\frac{8}{3}\frac{m_e}{M_P}\frac{\alpha^2}{R^{\frac{1}{2}}}\frac{Z}{Z_0}W^{\frac{1}{2}}g(I)\kappa(\tfrac{1}{2},Z)\left(1-\frac{ds}{dn}\right)$$

$$=2.32\times10^{-10}W^{\frac{1}{2}}\frac{Z}{Z_0}g(I)\kappa(\tfrac{1}{2},Z)\left(1-\frac{ds}{dn}\right). \quad (11)$$

In this expression a_s is measured in kaysers.[11] W is the energy in kaysers needed to remove the s electron from the atom in that stage of ionization in which it is the outer electron; Z is the atomic number; and Z_0 is one for neutral atoms, two for singly ionized atoms, etc. The factor $\kappa(\frac{1}{2},Z)$ is a relativistic correction[6] tabulated in I. The rate of change of the quantum defect ds/dn can be evaluated if other members of the series are known; neglecting this factor will generally make the calculated value of a_s a little too small.

The value of $\langle 1/r_i^3\rangle_{Av}$ in Eq. (10) can be related to the spin-orbit parameter ζ_l by the equation

$$\zeta_l=R\alpha^2a_0^3Z_i\langle 1/r_i^3\rangle_{Av}\lambda(l,Z). \quad (12)$$

Z_i is an effective nuclear charge, about two less than Z for p-electrons and 10 less than Z for d electrons, and $\lambda(l,Z)$ is another relativistic correction[6] which is tabulated in I. The value of ζ_l is determined from an analysis of the experimentally-observed fine structure of the term by methods outlined in Appendix II. By means of Eq. (12), relation (10) takes the form

$$a_l=\frac{m_e}{M_P}\frac{\zeta_l}{\lambda(l,Z)Z_i}g(I)=0.545\frac{\zeta_l}{\lambda(l,Z)Z_i}g(I)\times10^{-3}. \quad (13)$$

Both a_l and ζ_l are measured in kaysers.

The expression usually given for B is that due to Casimir.[2]

$$B=-\frac{3}{8}\frac{e^2Q}{I(2I-1)J(2J-1)}$$

$$\times\left\langle\left\{\sum_i\frac{(3\cos^2\theta_i-1)}{r_i^3}\right\}_{M_J=J}\right\rangle_{Av}. \quad (14)$$

The electric quadrupole moment Q of the nucleus is defined in Sec. E (it is measured in cm^2); θ_i is the angle which the radius vector r_i of the ith electron makes with the Z axis. The J dependence of B is not shown explicitly in this formula. To express this dependence we have derived in Sec. E the following expression for B:

$$B(J)=\gamma\frac{8\{3(2-g)[J(J+1)(2-g)-\frac{1}{2}]-L(L+1)\}}{(2J-1)(2J+3)(2L-1)(2L+3)},$$

$$(J\neq0,\tfrac{1}{2}). \quad (15)$$

The coefficient γ, which is independent of J, is given by:

$$\gamma=-[(2L-1)(2L+3)]^{\frac{1}{2}}$$

$$\times\frac{(\alpha SL||\sum_i(b_l)_i\mathbf{C}_i^{(2)}||\alpha SL)}{[L(L+1)(2L+1)]^{\frac{1}{2}}}. \quad (16)$$

The one-electron parameter is defined as

$$b_l=\frac{3e^2Q}{16I(2I-1)}\langle 1/r_i^3\rangle_{Av}. \quad (17)$$

By use of (12), since $e^2=2Ra_0$, it can be evaluated as

$$b_l=\frac{3}{8\alpha^2a_0^2}\frac{\zeta_l}{\lambda(l,Z)Z_i}\frac{Q}{I(2I-1)}$$

$$=\frac{0.253\zeta_l}{\lambda(l,Z)Z_i}\frac{Q}{I(2I-1)}\times10^{21}, \quad (18)$$

where b_l and ζ_l are in kaysers and Q in units of cm^2. If b_l is measured in millikaysers and Q in units of barns (10^{-24} cm^2), then the factor 10^{21} can be omitted.

For one-electron configurations, the values of A and B have a particularly simple form. Entering the following expressions from II into the general formulas (6), (7), (8), and (16),

$$(l||\mathbf{l}||l)=[l(l+1)(2l+1)]^{\frac{1}{2}}, \quad (19)$$

$$(\tfrac{1}{2}||\mathbf{s}||\tfrac{1}{2})=\sqrt{\tfrac{3}{2}}, \quad (20)$$

$$(l||\mathbf{C}^{(2)}||l)=-\left[\frac{l(l+1)(2l+1)}{(2l-1)(2l+3)}\right]^{\frac{1}{2}}, \quad (21)$$

one finds for the one-electron configurations that $\lambda=\sigma=a_l$, $\beta=a_s$, and $\gamma=b_l$. Entering these values into (3) and (15) we have,

$$A=a_s, \qquad (l=0), \quad (22)$$

$$A(J)=\frac{l(l+1)}{j(j+1)}a_l, \quad (l\neq0), \quad (23)$$

$$B(J)=\frac{b_l}{j(j+1)}, \qquad (j\neq\tfrac{1}{2}). \quad (24)$$

[9] E. Fermi and E. Segrè, Z. Physik **82**, 729 (1933).
[10] S. Goudsmit, Phys. Rev. **43**, 636 (1933).
[11] "Kayser" is the name adopted by the Joint Commission for Spectroscopy for the unit of wave number, cm^{-1}. It is abbreviated "K."

The expressions for A have been given by many authors;[12] $A(l+\frac{1}{2})$ and $A(l-\frac{1}{2})$ are usually denoted by a' and a'', respectively. The expression (24) for B is in agreement with results given by Casimir[2] and Racah.[6]

For a term made up of equivalent electrons we write in the notation of II:

$$\sum_i (a_l)_i \mathbf{C}_i^{(2)} = a_l(l||\mathbf{C}^{(2)}||l)\mathbf{V}^{(12)},$$
$$\sum_i (b_l)_i \mathbf{C}_i^{(2)} = b_l(l||\mathbf{C}^{(2)}||l)\mathbf{U}^{(2)}. \quad (25)$$

Relations (7) and (16) become now

$$\sigma = -a_l(l||\mathbf{C}^{(2)}||l)[(2L-1)(2L+3)]^{\frac{1}{2}} \times \frac{(l^n\alpha SL||\mathbf{V}^{(12)}||l^n\alpha SL)}{[L(L+1)(2L+1)S(S+1)(2S+1)]^{\frac{1}{2}}} \quad (26)$$

$$\gamma = -b_l(l||\mathbf{C}^{(2)}||l)[(2L-1)(2L+3)]^{\frac{1}{2}} \times \frac{(l^n\alpha SL||\mathbf{U}^{(2)}||l^n\alpha SL)}{[L(L+1)(2L+1)]^{\frac{1}{2}}}. \quad (27)$$

The double barred submatrices of $\mathbf{V}^{(12)}$ and $\mathbf{U}^{(2)}$ are tabulated in III for configurations made up of equivalent p or d electrons; the double barred submatrix of $\mathbf{C}^{(2)}$ has already been given in (21). Because of a relation analogous to (19), $\lambda = a_l$ for groups of equivalent electrons (this is also true for a group of equivalent electrons plus any number of s electrons).

If configurations of non equivalent electrons are coupled together, A and B are evaluated by straightforward application of the decoupling formulas [relations (44)] of II; the results are omitted here for brevity.

B. QUADRUPOLE MOMENT OF MANGANESE

The data of White and Ritchl[13] has been analyzed in an effort to evaluate the quadrupole moment of manganese (Mn^{55}). The two lines $\lambda 5394 (^8P_{7/2} \rightarrow {}^6S_{5/2})$ and $\lambda 4033 (^6P_{5/2} \rightarrow {}^6S_{5/2})$ lead to the respective Q values 1.10×10^{-24} cm^2 and 1.01×10^{-24} cm^2 and from this we conclude that

$$Q = 1\times10^{-24} \text{ cm}^2.$$

This value is probably less accurate than the approximate value,

$$Q = 0.5\times10^{-24} \text{ cm}^2,$$

recently obtained by microwave methods,[14] but the two determinations do tend to confirm each other.

The Q given above was determined by least squares from the first three line-component intervals only. Successive intervals are less and less well-defined as the lines get wider, weaker, and more closely spaced, and the reproducibility of measurements becomes poor. White and Ritschl give no estimate of the accuracy of their interval measurements, but the increased difficulty involved in the measurements can be appreciated from inspection of the photometer traces they have given for several of their patterns. In the homologous spectra of technetium—where the generally wider spacing allows for better resolution—a weighting procedure was used with the weights defined by the reproducibility of the measurements of the intervals. In some cases this procedure amounted practically to disregarding all but the first two intervals.

The Q values obtained from three other lines of the spectrum, namely $\lambda 5432$ ($^8P_{5/2} \rightarrow {}^6S_{5/2}$), $\lambda 4030$ ($^6P_{7/2} \rightarrow {}^6S_{5/2}$), and $\lambda 4034$ ($^6P_{3/2} \rightarrow {}^6S_{5/2}$), were disregarded; the Q values for these three lines were -2.6, -0.3, and -2.7×10^{-24} cm^2, respectively. This procedure is justified on the basis of the sensitivity of the intervals to the effects of the quadrupole moment. A suitable criterion for this sensitivity is the difference between the position of the third of three levels with consecutive F values when predicted from the interval between the first two levels with a Landé rule, and when predicted according to the full formula (1); this difference has the value $4B(F-1)(2F-1)$. The quadrupole moment will be determined most accurately from terms in which this quantity is large compared to the accuracy with which the intervals are measured. If we assume $Q = 10^{-24}$ in Mn, and calculate this difference, we get the values for $^8P_{7/2}$, $^6P_{5/2}$, $^8P_{5/2}$, $^6P_{7/2}$, $^6P_{3/2}$ as 0.0035, 0.0036, -0.0013, -0.0022 and -0.0013 kaysers respectively (in Mn I, $\zeta_d = 250$, $Z_i = 15$, $I = 5/2$). These numbers are indicative of the much stronger effect to be expected in the $^8P_{7/2}$ and $^6P_{5/2}$. In technetium, the Q values obtained from the lines corresponding to those neglected in Mn were also too small. The data in technetium were weighted heavily in favor of the $^8P_{7/2}$ and $^6P_{5/2}$ patterns by making a statistical analysis with weights based on the estimated errors of each Q determination as judged by the variability of the Q values obtained from different observations.

Reliable B values can be obtained most easily from lines in which the splitting of one level is zero. In both Mn and Tc, the analysis neglects possible splitting of the $^6S_{5/2}$ ground level. Theoretically, both A and B are zero for this level if it is a pure $d^5s^2\ {}^6S$, and no splitting of this level has been observed directly. By an indirect procedure, White and Ritschl determined an overall splitting of 0.030 K in this ground level in Mn I. They corrected the intervals of the ^8P and ^6P hfs to account for this nonzero splitting. Though these corrections are two or three times as large as the effects of Q evaluated above, the analysis of these corrected intervals leads to very nearly the same Q values as we obtained above from the direct measurements of the lines. The large splitting found by White and Ritchl in the ^6S ground term of Mn is hard to explain, and their analysis may be in error. However, a moderate Landé splitting of this ground term, especially for the transitions in-

[12] For notes on the literature and a simple derivation see G. Breit, Phys. Rev. **37**, 51 (1931). See also G. Breit and F. W. Doermann, Phys. Rev. **36**, 1732 (1930).

[13] H. E. White and R. Ritchl, Phys. Rev. **35**, 1146 (1930).

[14] Javan, Silvey, Townes, and Grosse, Phys. Rev. **91**, 222 (1953).

volving large F values in Mn and Tc, would have negligible effect on the Q values.

In manganese the levels $^6P_{5/2}$ and $^6P_{3/2}$ are only 8.73 K apart so that second-order effects of the magnetic interaction might produce perturbations of the hfs pattern and invalidate the determination of Q given above. The matrix elements of the interaction between hfs levels with the same F value in the two fine structure levels were determined by the methods of Sec. D, and found in all cases to be less than $\frac{1}{6}a_s$ (only effects of the s electron were calculated). As a_s has a value of about 0.14 K in Mn I the maximum perturbation to be expected is less than 0.00006 K, so this effect is too small to influence the results.

Observations on Mn I have also been made by Fisher and Peck.[15] Their measurements on λ5394 ($^6P_{7/2}\rightarrow{}^6S_{5/2}$) and λ5432 ($^6P_{5/2}\rightarrow{}^6S_{5/2}$) lead to Q values of 3×10^{-24} and -4×10^{-24} cm², respectively. The first of these Q values is probably too large since, if it were correct, we would expect more consistent Q values for all lines considered. The second determination is disregarded because of the previously noted low sensitivity of the measurements to effects of Q.

Fisher and Peck evaluated the coefficients λ and σ experimentally in the $d^6(^5D)s\ ^6D$ term of Mn I, obtaining the values $\lambda=0.0094$ and $\sigma<0.0001$. From relations (6) and (7) it follows that $\lambda=a_d$ and $\sigma=-a_d/5$. From relation (13) we expect $a_d=0.011$ ($\zeta_d=250$, $Z_i=15$, $g=1.2$), which is in good agreement with the observed value of λ. On this basis, σ should have the value -0.002. It seems unlikely that σ can be evaluated accurately enough from the observed data to make the disagreement between theory and experiment significant.

C. QUADRUPOLE MOMENT OF TANTALUM

Schmidt[16] has determined Q values of tantalum from the $^4F_{3/2}$, $^4F_{5/2}$, $^4F_{9/2}$, and $^4P_{3/2}$ levels of the $5d^36s^2$ configuration of Ta I. These Q values are $6.3, 6, 2, 4.2\times10^{-24}$ cm², respectively; from these data he has given the value $Q=6\times10^{-24}$ cm² for Ta^{181}. Assuming this value of Q, the values of $4B(F-1)(2F-1)$ for these terms are -0.023, -0.010, -0.012, and -0.053 kaysers, respectively (in Ta I, $\zeta_d=1500$, $Z_i=62$, $I=7/2$ as given by Schmidt), so that effects of Q should be easily observable in all patterns. The lower accuracy of the measurement would justify disregarding the low value of Q obtained from the $^4F_{9/2}$. The low value of Q obtained for the $^4P_{3/2}$ may be attributed to breakdown of *LS*-coupling. Our unpublished calculations of the energy levels of Ta I in intermediate coupling show that the purities of the four levels considered above are 0.92, 0.97, 0.91, and 0.70, respectively, which tends to bear out this conclusion. The fact that the observed g value of the $^4P_{3/2}$ level is much too small (observed $g=1.524$; theoretical $g=1.733$) also confirms this conclusion.

In the non relativistic limit, formulas (15) and (16) lead to the same values of $\langle\{\sum_i(3\cos^2\theta_i-1)\}_{M_J=J}\rangle_{\text{Av}}$ as Schmidt obtained by writing out the eigenfunctions explicitly. In general, to check values of this quantity (when the sum is over a group of equivalent electrons), B is evaluated with (15) and (16) and then multiplied by $-J(2J-1)/2b_l$.

Brown and Tomboulian[17] have recently obtained the value $Q=5.9\times10^{-24}$ cm² for Ta^{181} from observations on the $5d^36s\ ^5F_1$ level of Ta II. We found by the use of relation (15) that their calculation of the matrix element for this level is in error by a factor of two (in the nonrelativistic limit), so that the observed data actually lead to the unreasonably large value of $Q=11.8\times10^{-24}$ cm². It is likely that departures from *LS* coupling, which may be greater in Ta II than in Ta I, are the cause of the discrepancy with respect to Schmidt's value.[18]

D. MAGNETIC DIPOLE INTERACTION BETWEEN THE NUCLEUS AND AN ELECTRON

The interaction of the nuclear magnetic moment with the spin magnetic moment of an electron is that of two magnetic dipoles, and according to (3, 8)I, it has the form

$$H_{I,s}=-a_l\mathbf{I}\cdot\{\mathbf{s}-3\mathbf{r}\mathbf{r}\cdot\mathbf{s}/r^2\},\quad (l\neq0),\qquad(28)$$

where a_l is defined by (10), $\mathbf{I}$ is the vector representing the total nuclear spin, $\mathbf{s}$ is the electron's spin vector, and $\mathbf{r}$ is the radius vector from the nucleus to the electron. The quantity in { } in (28) is a tensor product of order one; according to relation (40) in Appendix I it is equal to $\sqrt{10}[\mathbf{s}\times\mathbf{C}^{(2)}]^{(1)}$ where $\mathbf{C}^{(2)}$ is the tensor operator introduced in II, Eq. (46). The interaction (28) is the scalar product of two vectors, one in the space of nuclear coordinates, the other in the space of electronic coordinates. We have by Eq. (38) in II and Eq. (36) in II,

$$(\alpha J,I,F|H_{I,s}|\alpha J,I,F)=\left\{-\frac{\sqrt{10}(\alpha SLJ||a_l[\mathbf{s}\times\mathbf{C}^{(2)}]^{(1)}||\alpha SLJ)}{[J(J+1)(2J+1)]^{\frac{1}{2}}}\right\}\frac{K}{2},\qquad(29)$$

where

$$K=F(F+1)-I(I+1)-J(J+1).$$

[15] R. A. Fisher and E. R. Peck, Phys. Rev. **55**, 270 (1939). In their notation, $\lambda=a(3d^6)$ and $\sigma=b(3d^6)$.

[16] T. Schmidt, Z. Physik **121**, 63 (1943).

[17] B. M. Brown and D. H. Tomboulian, Phys. Rev. **88**, 1158 (1952).

[18] In commenting on the original manuscript of this paper, G. Racah has pointed out that in *jj* coupling the level $(d_{\frac{3}{2}})^2s$ with $J=1$ has $\langle\sum_i(3\cos^2\theta_i-1)\rangle_{\text{Av}}=\frac{1}{5}$, which is about three times the value of 12/175 valid for the $d^2s\ ^5F_1$ in *LS* coupling. Thus the departures from *LS* coupling are likely to act in the right direction to explain the result. In another private communication, B. M. Brown has informed us that if the worst possible view of the errors is taken, then the λ3042−λ2702 combinations of Ta II lead to the value $B=-0.77\pm0.12$, so that very little of the discrepancy can be due to experimental error.

Using (43) of Appendix I the expression in { } in (29) becomes

$$-\left[\frac{30(2J+1)}{J(J+1)}\right]^{\frac{1}{2}} X \begin{Bmatrix} SLJ \\ SLJ \\ 121 \end{Bmatrix} (\alpha SL||a_l \mathbf{sC}^{(2)}||\alpha SL). \quad (30)$$

The X function in (30) has been evaluated in terms of W functions in relation (50) of Appendix I. When the W functions in (50) are explicitly evaluated with (36)II, and the resulting explicit form of the X function is substituted in (30), an expression equal to the second term on the right of (3) [where σ is defined by (7)] is obtained.

The first and last terms on the right of (3) can be obtained similarly. The first term arises from the interaction of the magnetic moment of the nucleus with the field generated by the electron's orbital motion. By (3, 5)I, this interaction has the form:

$$H_{I,l} = a_l \mathbf{I}\cdot\mathbf{l}, \quad (l \neq 0), \quad (31)$$

where $\mathbf{l}$ is the electron's orbital angular momentum. The interaction giving rise to the last term of (3) is derived from the Dirac equation;[12] it applies only to s electrons. According to Eqs. (3) and (28) of I it has the form:

$$H_{I,s} = a_s \mathbf{I}\cdot\mathbf{s}, \quad (l=0), \quad (32)$$

where a_s is defined in (9). However, it is simpler and more direct to use II, Eq. (38) and II, Eq. (44) in carrying out the derivation of these two terms in (3).

All three magnetic interactions (28), (31), and (32), are scalar products of two vectors and have the form:

$$H_v = a_v \mathbf{I}\cdot\mathbf{V}.$$

The Racah method also enables us to calculate nondiagonal elements of these interactions [as well as the diagonal elements needed in deriving (3)]. By Eq. (38) of II we have, in general,

$$(\alpha J, I, F|H_v|\alpha' J', I, F) = (-1)^{J+I-F}[I(I+1)(2I+1)]^{\frac{1}{2}} \cdot (\alpha J||a_v \mathbf{V}||\alpha' J') W(JIJ'I; F1). \quad (33)$$

When $J=J'$, the W function in (33) is proportional to the quantity K which is defined in (29) [in deriving (29) the explicit form of the W function was used]. The general relation (33) is used in conjunction with (43) of Appendix I, which is needed to evaluate the double-barred submatrix, to calculate nondiagonal matrix elements of the electron-nuclear magnetic interactions. The perturbations due to these nondiagonal matrix elements are sometimes responsible for departures of the hfs intervals from the Landé ratio,[2,19] and the production of forbidden electronic transitions.[20]

[19] S. Goudsmit and R. F. Bacher, Phys. Rev. **43**, 894 (1933).

[20] S. Mrozowski, Phys. Rev. **67**, 161 (1945); K. G. Kessler, Phys. Rev. **77**, 559 (1950); F. F. Deloume and J. R. Holmes, Phys. Rev. **76**, 174 (1949).

E. ELECTRIC QUADRUPOLE INTERACTION BETWEEN THE NUCLEUS AND AN ELECTRON

The quadrupole interaction between the nuclear and electronic charge distributions is given by Eqs. (11) and (1) of I as,

$$H_Q = -e^2 \int\int \frac{\rho_k r_k^2 \rho_e}{r_e^3} (\tfrac{3}{2}\cos^2\vartheta - \tfrac{1}{2}) d\tau_k d\tau_e, \quad (34)$$

where ϑ is the angle between the radius vector $\boldsymbol{r}_k$ of an element $e\rho_k d\tau_k$ of nuclear charge and the electronic radius vector $\boldsymbol{r}_e$ and ρ_k and ρ_e are the nuclear and electronic densities, respectively. By II, Eq. (45) the angular factor in (34) is represented as a scalar product of tensor operators,

$$\tfrac{3}{2}\cos^2\vartheta - \tfrac{1}{2} = \mathbf{C}_e^{(2)}\cdot\mathbf{C}_k^{(2)}, \quad (35)$$

and then by (38)II

$$(\alpha_e SLJ, \alpha_k I, F|H_Q|\alpha_e SLJ, \alpha_k I, F) = -e^2(-1)^{J+I-F}(\alpha_e SLJ||r_e^{-3}\mathbf{C}_e^{(2)}||\alpha_e SLJ) \cdot (\alpha_k I||r_k^2 \mathbf{C}_k^{(2)}||\alpha_k I) W(JIJI; F2). \quad (36)$$

The quadrupole moment Q of the nucleus is defined as a matrix element over the space of nuclear coordinates, evaluated when I has its largest component in the z direction;[2] i.e.,

$$Q = \langle r_k^2(3\cos^2\theta_k - 1)_{M_I=I}\rangle_{av}. \quad (37)$$

By utilizing II, Eq. (29), and II, Eq. (17), we put this in the form

$$Q = 2\left[\frac{I(2I-1)}{(I+1)(2I+1)(2I+3)}\right]^{\frac{1}{2}} (\alpha_k I||r_k^2 \mathbf{C}_k^{(2)}||\alpha_k I). \quad (38)$$

When this is substituted in (36), and the W function is evaluated explicitly with Eq. (36) of II we get:

$$(\alpha_e SLJ, \alpha_k I, F|H_Q|\alpha_e SLJ, \alpha_k I, F) = \left\{\frac{-3e^2 Q}{2I(2I-1)}\left\langle\frac{1}{r_e^3}\right\rangle_{av}\left[\frac{(2J-2)!}{(2J+3)!}\right]^{\frac{1}{2}} \cdot (\alpha_e SLJ||\mathbf{C}_e^{(2)}||\alpha_e SLJ)\right\} \cdot [K(K+1) - (4/3)I(I+1)J(J+1)], \quad (39)$$

with K again defined as in (29). The first term in brackets [i.e., $K(K+1)$] contributes the third term on the right to the hfs formula (1); its coefficient, the factor in braces, is therefore equal to $B(J)$. This can also be shown more directly by evaluating the expression for $B(J)$ given in (14) with Eq. (29) of II. The contribution of the second term in brackets of (39) is included in W_J [the first term on the right in (1)].

The J dependence of $B(J)$ is obtained by evaluating the submatrix in the factor in braces in (39) with

Eq. (44) of II; this leads directly to the formula given in (15) and (16).

This work has been carried out in the Spectroscopy Section of the National Bureau of Standards as part of the program initiated by W. F. Meggers to study the spectrum of technetium. I wish to thank Professor Racah and Dr. Fano for a critical reading of the original manuscript of this paper.

APPENDIX I

An extension of the theory in II is given in Sec. I of this Appendix. This extension is equivalent to results given by G. Racah and U. Fano in unpublished manuscripts.

1. *J* Dependence of an Irreducible Tensor in *LS* Coupling

The interactions encountered in atomic spectroscopy are generally (a) scalars with respect to J, or else (b) they commute with either L or S; Eqs. (38) and (44), respectively, of II are adequate to specify the J dependence of the interactions in such cases. The interactions (31), (32), and (34) are examples of the type (b). However, the interaction (28) behaves as a vector with respect to J and does not commute with either L or S. The following extension of the theory in II allows us to calculate the J dependence in such cases.

A tensor of degree k_1 which is irreducible with respect to S and commutes with L can be combined with a tensor of degree k_2, irreducible with respect to L and commuting with S, to produce a tensor of degree k ($k_1+k_2\geqslant k\geqslant|k_1-k_2|$) called the tensor product, which is irreducible with respect to J by use of the relation,[21]

$$\mathbf{P}_q^{(k)}\equiv[\mathbf{T}^{(k_1)}\times\mathbf{U}^{(k_2)}]_q^{(k)}=\sum_{q_1q_2}\mathbf{T}_{q_1}^{(k_1)}\mathbf{U}_{q_2}^{(k_2)}(k_1q_1k_2q_2|k_1k_2kq). \quad (40)$$

To obtain matrix elements of such a tensor between states showing LS coupling, Eqs. (16) and (29) of II are first utilized:

$$\begin{aligned}(\alpha SLJM|\mathbf{P}_q^{(k)}|\alpha'S'L'J'M')&=(-1)^{J+M+k+q}(2k+1)^{\frac{1}{2}}\sum_{\alpha''J''}(-1)^{J''}\\&\cdot(\alpha SLJ||\mathbf{T}^{(k_1)}||\alpha''S'LJ'')\\&\cdot(\alpha''S'LJ''||\mathbf{U}^{(k_2)}||\alpha'S'L'J')\\&\cdot\{\sum_{q_1q_2M''}(-1)^{M''}V(k_1k_2k;q_1q_2-q)\\&\cdot V(JJ''k_1;-MM''q_1)V(J''J'k;-M''M'q_2)\}. \quad (41)\end{aligned}$$

The sum over the V functions is carried out with (41)II, and then (44)II is used to obtain the result:

$$\begin{aligned}(\alpha SLJM|\mathbf{P}_q^{(k)}|\alpha'S'L'J'M')&=(-1)^{J+M}V(JJ'k;-MM'q)\\&\cdot[(2k+1)(2J+1)(2J'+1)]^{\frac{1}{2}}\\&\cdot(\alpha SL||\mathbf{T}^{(k_1)}\mathbf{U}^{(k_2)}||\alpha'S'L')\\&\cdot\{(-1)^{k-J-J'}\sum_{J''}(2J''+1)W(k_1Jk_2J';J''k)\\&\cdot W(SJS'J'';Lk_1)W(LJ''L'J';S'k_2)\}. \quad (42)\end{aligned}$$

By comparing this with Eq. (29) of II, and representing the summation in braces as an X function in agreement with the definition of Fano,[22] we put this result in the final form,

$$\begin{aligned}(\alpha SLJ||\mathbf{P}^{(k)}||\alpha'S'L'J')&=(\alpha SL||\mathbf{T}^{(k_1)}\mathbf{U}^{(k_2)}||\alpha'S'L')\\&\cdot[(2k+1)(2J+1)(2J'+1)]^{\frac{1}{2}}X\begin{pmatrix}SLJ\\S'L'J'\\k_1k_2k\end{pmatrix}, \quad (43)\end{aligned}$$

where

$$\begin{aligned}X\begin{pmatrix}SLJ\\S'L'J'\\k_1k_2k\end{pmatrix}&=(-1)^{k-J-J'}\sum_{J''}(2J''+1)\\&\cdot W(k_1Jk_2J';J''k)W(SJS'J'';Lk_1)\\&\cdot W(LJ''L'J';S'k_2). \quad (44)\end{aligned}$$

The following are some miscellaneous properties of the X function. If any of the 9 arguments is zero, the X function reduces to a W function; in particular, if $k=0$ then (43) is equivalent to Eq. (38) of II, while if $k_1=0$ or $k_2=0$ it is equivalent to Eq. (44) of II. The function vanishes if the triangular condition is not satisfied by any of the six triads forming the rows and columns of the function. The function is invariant with respect to interchange of rows and columns. Interchange of two rows or columns multiplies the function by

$$(-1)^{S+L+J+S'+L'+J'+k_1+k_2+k}.$$

As a consequence, when $(SLJ)=(S'L'J')$ the function vanishes unless k_1+k_2+k is even.

2. An Identity Satisfied by *X* Functions

We have derived an identity which can be used to simplify the numerical calculation of the X function. Relation (44) is multiplied on both sides by $(-1)^k(2k+1)W(J'k\beta k_2;Jk_1)$, and a sum over k is carried out on the right by using Eqs. (40) and (43)

[21] G. Racah, "Group Theory and Spectroscopy," lecture notes, Princeton University, 1951 (unpublished).

[22] U. Fano, Natl. Bur. Standards Rep. No. 1214 (unpublished) 1951.

of II to obtain

$$\sum_k (-1)^k(2k+1)W(J'k\beta k_2; Jk_1)X\begin{pmatrix} SLJ \\ S'L'J' \\ k_1k_2k \end{pmatrix} = (-1)^{L-\beta-S'-2k_2}\sum_{J''} W(LJ''Sk_1; S'J) \cdot W(J'J''\beta J; k_2k_1)W(LJ''L'J'; S'k_2). \quad (45)$$

By using the following identity given by Biedenharn:[23]

$$\sum_k (2\lambda+1)W(a'\lambda\alpha c; ac')W(b\lambda\beta c'; b'c)W(a'\lambda\gamma b; ab') = W(a\alpha b\beta; c\gamma)W(a'\alpha b'\beta; c'\gamma), \quad (46)$$

relation (45) can be reduced to the following form:

$$\sum_k (-1)^k(2k+1)W(J'k\beta k_2; Jk_1)X\begin{pmatrix} SLJ \\ S'L'J' \\ k_1k_2k \end{pmatrix} = (-1)^{L-\beta-S'-2k_2}W(S'SJ'\beta; k_1L') \cdot W(k_2\beta LS; JL'). \quad (47)$$

By making use of the symmetry properties of the X function, summation can be carried out over any other argument (to permit this, no use has been made of the integral nature of anv argument in the X function). For instance, to simplify the X function needed in Sec. D we use

$$\sum_{k_2} (-1)^{k_2}(2k_2+1)W(Lk_2\beta k; L'k_1)X\begin{pmatrix} SLJ \\ S'L'J' \\ k_1k_2k \end{pmatrix} = (-1)^{J'-\beta-S-2k}W(SS'L\beta; k_1J) \cdot W(k\beta J'S'; L'J). \quad (48)$$

In the case where $k_1=k=1$ and $(S'L'J')=(SLJ)$, the X-function in the sum of (48) with $(k_1k_2k)=(111)$ vanishes as indicated in the last sentence of Sec. 1 of this Appendix. Hence, taking $\beta=L$, relation (48) becomes,

$$W(L1L1; L0)X\begin{pmatrix} SLJ \\ SLJ \\ 101 \end{pmatrix} + 5W(L1L1; L2)X\begin{pmatrix} SLJ \\ SLJ \\ 121 \end{pmatrix} = W(SLSL; J1)W(LJLJ; S1). \quad (49)$$

Noting that $W(L1L1; L0) = -[3(2L+1)]^{-\frac{1}{2}}$ and that the X-function containing zero reduces to a W function, this finally becomes

$$X\begin{pmatrix} SLJ \\ SLJ \\ 121 \end{pmatrix} = \frac{3(2L+1)W(LSLS; J1)W(LJLJ; S1) - (-)^{L-S-J}W(SJSJ; L1)}{15(2L+1)W(L1L1; L2)}. \quad (50)$$

In general it would require the evaluation of nine W functions for each J value to calculate the X function in (50) directly from the sum in (44); the relation (50) simplifies this so that only three W functions need be evaluated for each J value.

In the calculation of X functions for which $(SLJ) \neq (S'L'J')$, simplification may result from the vanishing of certain X functions in the sum in (48) because of failure of the triangular conditions.

APPENDIX II

In the first-order approximation, the spin-orbit interaction displaces a level by the amount $\zeta(\alpha SL)\Gamma$,[24] where Γ is defined by (4) and where

$$\zeta(\alpha SL) = \frac{(\alpha SL||\sum_i(\zeta_l)_i\mathbf{s}_i\mathbf{l}_i||\alpha SL)}{[S(S+1)(2S+1)L(L+1)(2L+1)]^{\frac{1}{2}}}. \quad (51)$$

In this expression, ζ_l is the radial parameter given in (12) according to the evaluation with a Coulomb field.[24]

For one-electron configurations we have:

$$(l||\mathbf{sl}||l) = [\tfrac{3}{2}l(l+1)(2l+1)]^{\frac{1}{2}}. \quad (52)$$

In this case $\zeta(l)=\zeta_l$ and the doublet separation is

$$E_J - E_{J-1} = J\zeta(\alpha SL) = (l+\tfrac{1}{2})\zeta_l. \quad (53)$$

The doublet separation is sometimes denoted by δ.

In configurations of equivalent electrons

$$\zeta(l^n\alpha SL) = [l(l+1)(2l+1)]^{\frac{1}{2}} \cdot \frac{(l^n\alpha SL||\mathbf{V}^{(11)}||l^n\alpha SL)}{[S(S+1)(2S+1)L(L+1)(2L+1)]^{\frac{1}{2}}}\zeta_l. \quad (54)$$

Values of the tensor $\mathbf{V}^{(11)}$ are tabulated in III for p and d electrons.

If nonequivalent electrons are coupled together relations (44) of II are used to calculate $\zeta(\alpha SL)$.

[23] L. C. Biedenharn, J. Math. Phys. **31**, 287 (1953).

[24] E. U. Condon and G. H. Shortley, *The Theory of Atomic Spectra* (Cambridge University Press, London, 1951), pp. 194 and 123.

The Radiations of $_{64}Gd^{159}$(18 hr) and $_{64}Gd^{161}$(3.7 min)

W. C. JORDAN, J. M. CORK,* AND S. B. BURSON
Argonne National Laboratory, Lemont, Illinois

(Received July 6, 1953)

The radiations from $_{64}Gd^{159}$(18 hr) and $_{64}Gd^{161}$(3.7 min) are studied with 180° photographic electron spectrometers and a scintillation coincidence spectrometer.

$_{64}Gd^{159}$(18 hr): Internal conversion lines corresponding to gamma transitions of 57.5±0.3 and 364±3 kev are observed. Peaks due to the K x-ray and the 364-kev gamma ray are observed in the NaI pulse-height distribution. The results of coincidence measurements indicate that the two gamma transitions are not in cascade, but that the 57-kev one is preceded by a beta transition of ~1.1 Mev, while the 364-kev one is preceded by a beta transition of ~0.9 Mev.

$_{64}Gd^{161}$(3.7 min): The half-life of this activity is found to be 3.73±0.10 min. Aluminum absorption measurements indicate an energy of ~1.6 Mev for the beta transition. Peaks are observed in the pulse-height distribution corresponding to 44±1 (Tb K x-ray), 102±3, ~165, and ~360 kev. The high-energy peak is resolved into two peaks in coincidence distributions, showing the 360-kev transition to be coincident with the x-ray, and a 316-kev transition to be coincident with the 102-kev gamma ray. The K internal conversion line for the 316-kev transition is observed, plus some other weak conversion lines corresponding to the other transitions. All of the electromagnetic radiation appears to be coincident with a beta transition of ~1.6 Mev. The existence of a gamma transition of ~60 kev is suggested.

INTRODUCTION

IN 1938 Pool and Quill[1] produced 18-hr and 3.5-min activities by means of both fast and slow neutrons on gadolinium. Both activities were tentatively assigned to mass number 159. Subsequent investigations[2–4] have indicated that the 18-hr activity does belong to mass 159, but that the short activity is associated with mass 161. Absorption measurements[2,3,5] have shown that the 18-hr activity decays by emission of a beta ray of about 0.9 Mev and electromagnetic radiations of approximately 0.055 and 0.35 Mev.

Reported values for the half-life of the short activity have varied from 3.3 to 4.5 minutes.[5–7] Absorption measurements[5,7] have indicated that a beta transition of about 1.5 Mev, a gamma ray of 0.37 Mev, and internal conversion electrons of approximately 0.066 Mev are associated with this activity. Church[8] has recently investigated both of these activities with a scintillation spectrometer. He has detected a 0.360-Mev gamma ray in the 18-hr activity and gamma rays of 0.110 and 0.320 Mev in the short activity.

In the present investigation, the radiations associated with these activities are studied with photographic electron spectrometers as previously described,[9] and a scintillation coincidence spectrometer. The scintillation coincidence spectrometer[10] is equipped with a ten-channel pulse-height analyzer on one side and a single-channel analyzer on the other. Either side can be operated independently as a single spectrometer. In coincidence studies, the output pulse from the single-channel side triggers the recording pulse in the ten-channel side. The coincidence resolving time is about 2 microseconds. NaI(Tl) and anthracene crystals are used as scintillators for gamma and beta radiations, respectively. Some of the preliminary scintillation spectrometer data were obtained with a twenty-channel spectrometer kindly made available by B. Hamermesh. We are grateful for the use of this instrument.

Sources of gadolinium oxide were irradiated in the Argonne heavy-water-moderated reactor. The gadolinium oxide was supplied by Research Chemicals Incorporated, Burbank, California and was specified to be 99.9 percent pure. Upon activation it was found that a trace of europium was present. (The 9.3-hr Eu^{152} activity was easily detected by means of K, L, and M conversion lines associated with the 122-kev transition. Also, peaks indicating this, as well as other higher energy europium gamma rays, were observed in the pulse-height distribution.)

RESULTS

$_{64}Gd^{159}$(18 hr): A sample of the gadolinium oxide was irradiated for approximately 55 hours in the reactor to produce sources for the conversion electron study. Initial spectrograms revealed the presence of many electron groups. Some of these are associated with activities of longer life than the 18-hr activity, and some with a 9.3-hr europium contaminant. By a series of exposures it was found that six lines were attributable to the 18-hr activity. These may be interpreted as arising from internally converted gamma rays of

* University of Michigan, Ann Arbor, Michigan.

[1] M. Pool and L. Quill, Phys. Rev. **53**, 437 (1938).

[2] Krisberg, Pool, and Hibdon, Phys. Rev. **74**, 44 (1948).

[3] B. Ketelle, Brookhaven National Laboratory Report No. C-9, 109, 1949 (unpublished).

[4] F. Butement, Proc. Phys. Soc. (London) **A64**, 395 (1951).

[5] F. Butement, Phys. Rev. **75**, 1276 (1949).

[6] M. Inghram and R. Hayden, U. S. Atomic Energy Commission Report MDDC-525 (1946) (unpublished).

[7] der Mateosian, Goldhaber, and Smith, Argonne National Laboratory Report ANL-4237, 64 (1949) (unpublished).

[8] E. Church, private communication.

[9] Rutledge, Cork, and Burson, Phys. Rev. **86**, 775 (1952); Argonne National Laboratory Report ANL-4735 (unpublished).

[10] S. Burson and W. Jordan, Phys. Rev. **91**, 498 (1953).

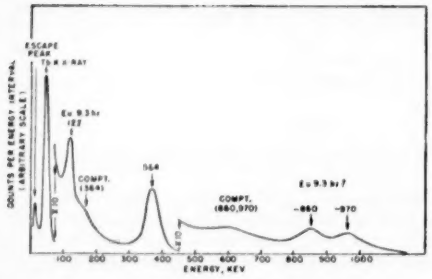

FIG. 1. Gamma ray pulse-height distribution resulting from $_{64}Gd^{159}$(18 hr). Peaks due to europium contamination are also present.

57.5±0.3 and 364±3 kev, using the electron binding energies of terbium (see Table I).

Although K conversion of the 57.5-kev gamma ray is energetically possible, the electrons would have an energy below the minimum detectable by the spectrometer. Visual estimates of the line intensities indicate that L conversion occurs mostly in the L_1 sub-shell, which suggests an $M1$ transition.[11] The K and L electron lines of the 364-kev transition are weak. The K/L ratio appears to be large, but it is not determined with sufficient accuracy to identify the character of the radiation.

The pulse-height distribution obtained from a sample of gadolinium oxide several hours after irradiation is shown in Fig. 1. The peaks corresponding to the 364-kev gamma ray and the Tb K x-ray (as well as its associated escape peak) were observed to decay with the 18-hr period. The other peaks decayed with a half-life of about 10 hours. By comparison with peaks resulting from a europium source, these were shown to be due to europium contamination. There is a small contribution to the x-ray peak due to a 49-kev transition

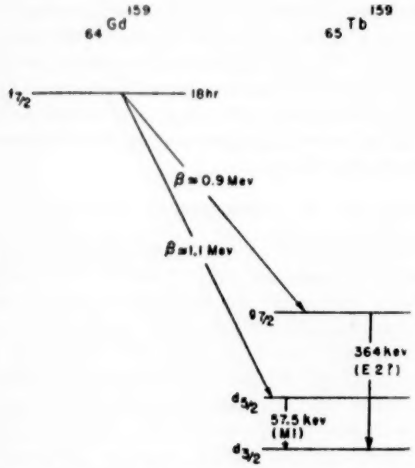

FIG. 2. Proposed decay scheme for $_{64}Gd^{159}$(18 hr).

[11] J. Mihelich, Phys. Rev. 87, 646 (1952).

following the beta decay of Tb^{161}(6.8 day), which is the daughter of Gd^{161}(3.7 min). The unconverted portion of the 57.5-kev transition is apparently small relative to the intense 44-kev Tb K x-ray and is unresolved.

Coincidence experiments failed to reveal any (x-ray)–(364-kev gamma) coincidences, indicating that the 57.5 and 364-kev transitions are not in cascade. Although some of the pulses contributing to the 44-kev peak were in coincidence with others of about the same energy, these coincidences are attributable to the K capture activity of either the europium contaminant or that of 236-day Gd^{153}.

Coincidences between beta rays and the 364-kev gamma ray and between beta rays and x-rays were observed. The (beta)–(gamma) coincidence rate is attenuated by aluminium absorbers on the beta side with a half-value thickness of about 29 mg/cm², while the (beta)–(x-ray) coincidence rate is attenuated with a half-value thickness of about 43 mg/cm². These absorption values indicate the presence of two beta components whose energies are approximately 0.9 and 1.1 Mev. The (beta)–(x-ray) coincidence rate was observed to decay with the 18-hr half-life, and the slope of the absorption curve was the same on two successive days after the initial experiment. Hence, these coincidences may be assigned to the 18-hr activity.

TABLE I. Internal conversion electrons associated with $_{64}Gd^{159}$(18 hr).

Electron energy (kev)	Proposed interpretation	Energy sum (kev)	Transition energy (kev)	Estimate of intensity ratios
48.8	L_1(Tb)	57.5	57.5±0.3	$L_1/L_3 \gg 1$
50.0	L_3(Tb)	57.5		
55.5	M_1(Tb)	57.5		
56.9	N(Tb)	57.3		
312	K(Tb)	364	364 ±3	K/L large
~353	L(Tb)	~362		$\gtrsim 5$

From these data it may be concluded that two beta-ray branches exist, each followed by a single gamma ray. It seems reasonable to propose the nuclear energy level scheme as shown in Fig. 2.

The spin of the ground state of Tb^{159} has been measured[12] and found to be 3/2. Shell theory predicts the ground state of Gd^{159} to be $f_{7/2}$, while $g_{7/2}$ and $d_{5/2}$ are possible assignments for low lying states of Tb^{159}. If one postulates an equal branching ratio for the two beta transitions, the log ft values would be about 6.8 and 7.3, indicating both would be first forbidden with spin change 0 or 1. A $d_{5/2}$ assignment to the 57.5-kev level is consistent if the transition is magnetic dipole ($M1$). A $g_{7/2}$ assignment to the 364-kev level is also consistent if this transition is electric quadrupole ($E2$).

$_{64}Gd^{161}$(3.7 min): Measurements of the half-life of the short-lived gadolinium activity yield an average

[12] H. Schüler and T. Schmidt, Naturwiss. 22, 730 (1934).

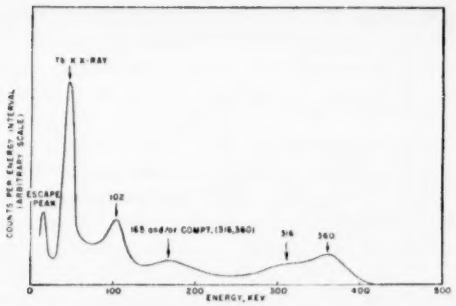

FIG. 3. Gamma ray pulse-height distribution resulting from $_{64}Gd^{161}$(3.7 min).

value of 3.73±0.10 min. Aluminum absorption of the beta radiation indicates a maximum energy of approximately 1.6 Mev. Internal conversion electron lines associated with this activity are not strong. A line at 264 kev may be interpreted as due to K conversion of a 316-kev gamma ray. Other weak lines, possibly associated with this activity, are observed at 47.4, 53.4, ~305, ~310, and ~350 kev. In one attempt to build up the intensity of the weak lines, three hundred successive irradiations and exposures were made on a single spectrogram.

The pulse-height distribution obtained with the scintillation spectrometer is shown in Fig. 3. There are peaks corresponding to energies of 44±1 (Tb K x-ray), 102±3, ~165, and ~360 kev. All of these were observed to decay with the 3.7-min period. The "360"-kev peak is broad and distorted in comparison with other single gamma-ray peaks of approximately this energy. The appearance suggests the presence of another gamma ray of about 320 kev, which may be interpreted as the 316-kev transition, previously mentioned. These two peaks are well resolved in coincidence pulse-height distributions as shown in Fig. 4. The 316- and 102-kev gamma rays are in coincidence, while the 360-kev gamma ray is coincident with the K x-ray. A shoulder at 316 kev appears in the coincidence distribution

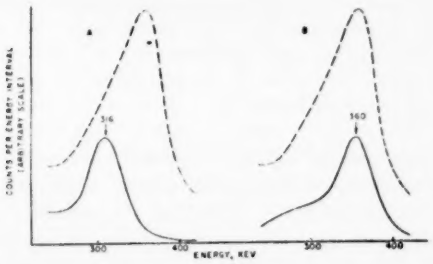

FIG. 4. Gamma coincidence pulse-height distributions resulting from $_{64}Gd^{161}$(3.7 min). A. Coincidence distribution in region of "360"-kev peak with the single-channel spectrometer set at the 102-kev peak; B. Corresponding distribution with single-channel spectrometer set at the x-ray peak. For comparison, the normal distribution is shown with a dashed curve in both figures. Only the position of the peaks is to be compared, since the scales are not the same.

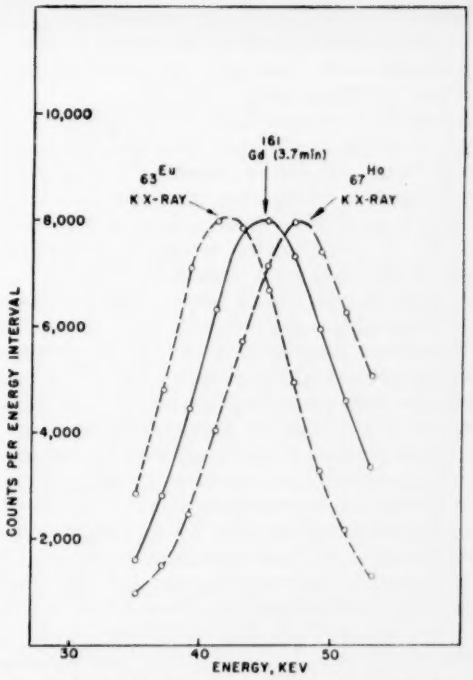

FIG. 5. Pulse-height distribution in the region of the K x-ray. The solid curve is the distribution resulting from $_{64}Gd^{161}$(3.7 min). The dashed curves are distributions resulting from K x-rays of europium ($Z=63$) and holmium ($Z=67$).

corresponding to the latter combination. This may be attributed to coincidences between the 316-kev gamma ray and K x-rays resulting from conversion of the 102-kev gamma ray. The coincidence rates in each case were observed to decay with the 3.7-min period.

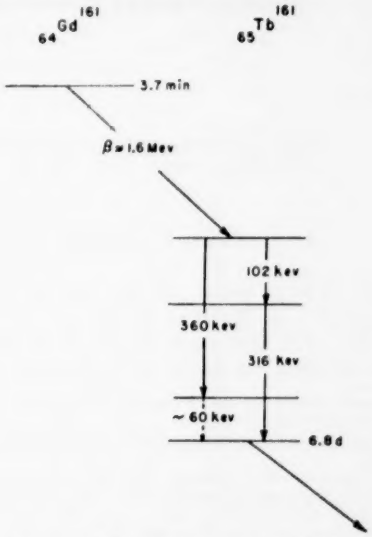

FIG. 6. Proposed decay scheme for $_{64}Gd^{161}$(3.7 min).

No coincidences between the 316- and 360-kev gamma rays were observed. Except for the possible existence of a metastable state, this precludes the possibility of these two transitions being in cascade.

The results of (gamma)–(gamma) coincidence experiments involving the 165-kev peak are inconclusive. A peak in the coincidence pulse-height distribution is observed in this region when the single-channel spectrometer is set at 150–200 kev. These coincidences are probably due to Compton scattering of the higher energy gamma rays in the detecting crystals.

Because the coincidences between the K x-ray and the 360-kev gamma ray are easily observed (the ratio of coincidence counting rate to single counting rate being approximately the geometry factor), and since conversion lines are not easily observed, the possible presence of a K capture activity was suspected. K capture in gadolinium would result in the emission of x-rays characteristic of europium; x-rays associated with internal conversion following beta decay would be characteristic of terbium. The energy resolution of the spectrometer is not good enough to permit a reliable Z assignment to the x-ray. However, by comparing the pulse-height distribution with those due to x-rays of europium and holmium (Fig. 5), it is evident that the x-ray peak is not due to europium and is probably characteristic of terbium. As an additional check, the attenuation of the peak due to absorbers of La, Ce, Pr, and Nd was observed. The relative attenuation effected by each of these absorbers was approximately the same. This also indicates that the x-ray is not the Eu x-ray, since if it were, its energy would lie between the critical edges of Ce and Pr, and a striking difference in absorption should be noted. Additional evidence indicating that no K capture activity is present was obtained from (beta)–(gamma) and (beta)–(x-ray) coincidence experiments. The results of such experiments indicate that all of the electromagnetic radiation is coincident with a beta ray of approximately 1.6 Mev.

The foregoing data may be explained by postulating the existence of a highly K converted transition of about 60 kev which is in cascade with the 360-kev transition in Tb. A careful inspection of the pulse-height distribution in the region of 60 kev failed to reveal any evidence of an unconverted gamma ray of this energy. Electrons resulting from K conversion of such a transition would have an energy below the detection limit of the conversion electron spectrometers, hence would not be observed on the photographic plates. The weak 47.4- and 53.4-kev internal conversion lines may be due to L and M conversion electrons for this transition. However, one or the other of these might also be attributed to K conversion of the ~102-kev gamma ray.

The 165-kev peak in the pulse-height distribution may be interpreted either as resulting from a gamma ray of this energy or as the Compton distribution due to the 316- and 360-kev radiations. Although the former interpretation is preferred from a consideration of the line shape, the decay scheme (Fig. 6) which is proposed is consistent with all of the remaining data without inclusion of the possible 165-kev transition.

PHYSICAL REVIEW VOLUME 92, NUMBER 2 OCTOBER 15, 1953

Gamma-Gamma Directional Correlation Experiments with Mo^{93m}†

J. J. KRAUSHAAR*
Brookhaven National Laboratory, Upton, New York
(Received July 8, 1953)

Three directional correlations have been measured involving the three successive γ rays emitted following the 7.0 hour state in Mo^{93m}. The data characterize the spins and multipoles as

$$J+8 \xrightarrow{2^4} J+4 \xrightarrow{2^2} J+2 \xrightarrow{2^2} J,$$

which is consistent with Goldhaber's postulation on the basis of "core isomerism."

THE 7.0-hour isomer of Mo has now been assigned[1–3] to Mo^{93m} and three γ rays of 0.264, 0.685, and 1.479 Mev are known[1–5] to be emitted in cascade following the decay of the isomeric state. It has been pointed out by Goldhaber[6] that the main features of the decay scheme suggest a phenomenon of "core isomerism," where the odd neutron (presumably in a $g_{7/2}$ state) couples to the even-even core which successively goes through states with spins 8+, 4+, 2+, 0+ to give a total spin to the four states involved of 23/2+, 15/2+, 11/2+, and 7/2+. As one means of establishing the spins of the four levels experimentally, directional correlation measurements

† Research carried out under contract with the U. S. Atomic Energy Commission.
* Now at Physics Department, Stanford University, Stanford, California.
[1] G. E. Boyd and R. A. Charpie, Phys. Rev. **88**, 681 (1952).
[2] D. E. Alburger and S. Thulin, Phys. Rev. **89**, 1146 (1953).
[3] R. Bernas and S. Beydon, Compt. rend. **236**, 194 (1953).
[4] Kundu, Holt, and Pool, Phys. Rev. **77**, 71 (1950).
[5] L. Ruby and J. R. Richardson, Phys. Rev. **83**, 698 (1951).
[6] M. Goldhaber, Phys. Rev. **89**, 1146 (1953).

have been made between the three cascade gamma rays. Stevenson and Deutsch[7] have measured the anisotropy at 180° of the γ-γ directional correlation as $+0.20$, but lack of energy discrimination prevented any definite conclusions.

Sources were prepared by bombarding Nb foil with 20-Mev deuterons in the Brookhaven 60-inch cyclotron. Mo^{93m}, formed by the $Nb(d,2n)Mo^{93m}$ reaction was chemically separated from Nb by an ether extraction. About 0.1 ml of an aqueous solution were used for the individual sources.

The first directional correlation studied was that between the 0.685- and 1.479-Mev γ rays which have been tentatively assigned (Fig. 1) as γ_2 and γ_3. The counters were integrally biased at just above 320 kev, and 2.5 mm of Pb placed in front of them. In this way, neither the 0.264-Mev γ ray nor back-scattered radiation were counted. The measurements are shown in Fig. 1. The lower solid curve represents the least squares fit and the dashed curve is the least squares fit corrected for the finite geometry involved. Because the three γ rays have energies considerably different

TABLE I. The corrected least squares values of the coefficients in $W(\theta)=1+A_2P_2(\cos\theta)+A_4P_4(\cos\theta)$.

Correlation	Measured values		Theoretical values	
	A_2	A_4	A_2	A_4
$\gamma_1-\gamma_2$ Basic 2^4-2^2	0.208 ± 0.103	-0.027 ± 0.028	0.2208	-0.0180
$\gamma_2-\gamma_3$ Basic 2^2-2^2	0.098 ± 0.031	0.006 ± 0.009	0.1020	0.0091
$\gamma_1-\gamma_3$ Basic 2^4-2^2 (one-three)	0.210 ± 0.096	-0.001 ± 0.027	0.2208	-0.0180

from annihilation radiation, the collimated beam method[8] was employed for the geometry correction. This involved measuring the angular resolution with γ-ray beams of the appropriate energy under the various conditions of pulse-height selection.

The theoretical curve in Fig. 1 (basic,[9] 2^2-2^2) can be seen to be in good agreement with the data. All other basic correlations and other reasonable assignments involving pure radiation can be excluded. For example, the spins consistent with the assignments for γ_2 and γ_3 made by Forsthoff, Goeckermann, and Naumann[10] would require a basic 2^1-2^2 cascade. This correlation has a value of -0.0714 for A_2 which is in decided disagreement with the experimental value (see Table I).

[7] D. T. Stevenson and M. Deutsch, Phys. Rev. **83**, 1202 (1951).
[8] J. S. Lawson Jr., and H. Frauenfelder Phys. Rev. **91**, 648 (1953).
[9] S. P. Lloyd, Phys. Rev. **83**, 716 (1951). As defined by Lloyd, "basic" correlations are of the type:

$$J\pm l_1 \xrightarrow{2^{l_1}} J \xrightarrow{2^{l_2}} J\mp l_2.$$

The coefficients for such correlations are independent of J.
[10] Forsthoff, Goeckermann, and Naumann, Phys. Rev. **90**, 1004 (1953).

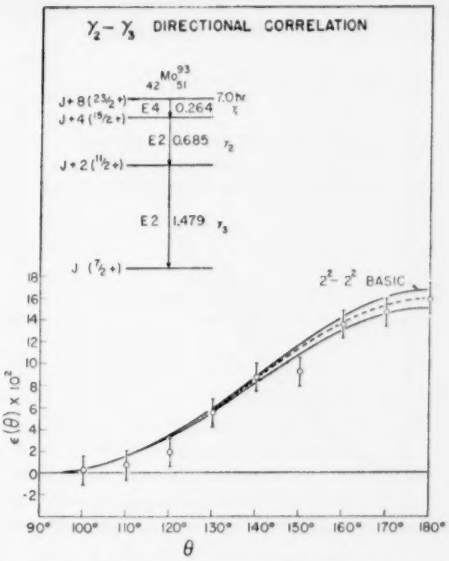

FIG. 1. The decay scheme of Mo^{93m} [See M. Goldhaber and R. D. Hill, Revs. Modern Phys. **24**, 179 (1952)] and the directional correlation measurements between the 0.685- and 1.479-Mev γ rays. The corrected least-squares curve (dashed) is to be compared with the theoretical one.

The second correlation studied was that between γ_1 and γ_2. For this, two differential pulse-height discriminators were used in conjunction with the usual coincidence circuit. The channels were positioned to cover the appropriate photo peaks. The results are shown in Fig. 2. The experimental points have been corrected for contributions from the other possible

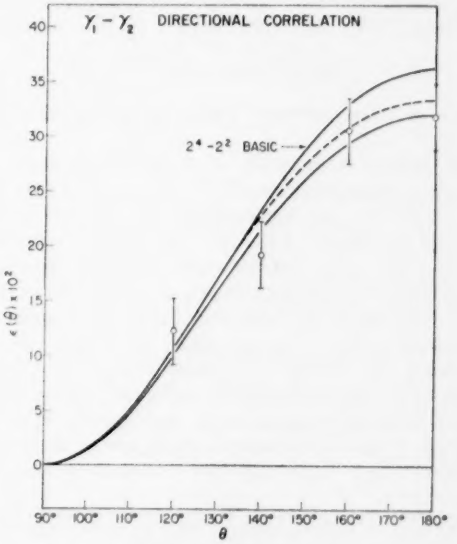

FIG. 2. The directional correlation measurements between the 0.264- and the 0.685-Mev γ rays.

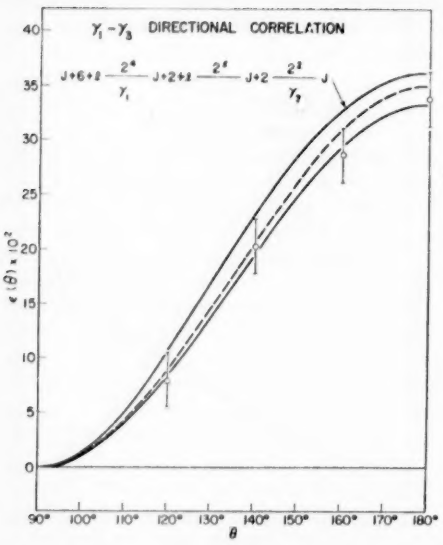

FIG. 3. The directional correlation measurements between the 0.264- and 1.479-Mev γ rays.

coincidence events due to a portion of the Compton distribution being under the photo peak of a lower energy γ ray. It will be shown later that the $\gamma_1-\gamma_3$ cascade has the identical correlation as $\gamma_1-\gamma_2$. Thus, the correction only involved the contribution from the $\gamma_2-\gamma_3$ cascade, and this amounted approximately to a six percent increase in the anisotropy.

The final dashed curve in Fig. 2 can be seen to be in agreement with the theoretical curve shown, which is that for a basic 2^4-2^2 correlation.[11] These data then characterize the spin changes and multipoles of the γ rays as

$$J+8 \xrightarrow{2^4} J+4 \xrightarrow{2^2} J+2 \xrightarrow{2^2} J,$$

which is quite consistent with the postulated assignments.[6]

As further verification of these assignments, the one-three directional correlation of γ_1 and γ_3 has been measured. For this measurement the channel for one counter was placed on the photo peak of the 0.264-Mev γ ray. The other counter was integrally biased at 0.800 Mev in addition to having 4.5 mm of Pb in front of it. The results are shown in Fig. 3. Here again the measured points have been corrected for a small contribution from the $\gamma_2-\gamma_3$ cascade. The explicit calculations of Arfken, Biedenharn, and Rose[12] for one-three correlations unfortunately do not include cases involving 2^4-pole radiation. Examination of their work indicated that basic one-three correlations were apparently not only independent of J, but when the intermediate transition is also basic, such correlations were identical to the corresponding one-two correlation.[13,‡] Thus in this case, the one-three correlation to be expected is just the basic 2^4-2^2 pole correlation as shown in Fig. 3. Such a correlation can be seen to be in agreement, within the uncertainty, with the measured points. This then is corroborative evidence for the spins indicated in Fig. 1.

In addition to demonstrating the feasibility of measuring a one-three directional correlation, it was hoped that such a measurement would establish the order of γ_2 and γ_3. There is some indirect evidence[14] that the order shown in Fig. 1 is correct and that order has been assumed in the above discussion. However, because of the basic nature of the transitions, the measurements reported here are independent of the order assumed for γ_2 and γ_3.

Internal conversion electron data[2,4,5,10] indicate that γ_1 is an $E4$ transition, which is in agreement with the directional correlation measurements. Inasmuch as the values of Z^2/E are low for γ_2 and γ_3, one must rely principally on conversion coefficients rather than the K/L ratios in determining the type of transition. The measured coefficients[10] are in satisfactory agreement with either $M1$ or $E2$ radiation.[15] The $E2$ assignment is shown in Fig. 1 because the results reported here indicate both γ rays are 2^2-pole.

A summary of the numerical results for the three directional correlation measurements is shown in Table I. The fact that the three corrected experimental curves all fall slightly below the theoretical curves is perhaps an indication that the correlations are being attenuated by extra-nuclear fields or that small amounts of mixtures of radiations are present.

In the light of Goldhaber's[6] "core isomerism" and the data reported here, a study of the energies and spins of the levels of Mo^{92} would be particularly interesting.

I am indebted to M. Goldhaber for suggesting the problem and for helpful discussions and to J. Weneser and M. Fuchs for considerations of the one-three directional correlation. Thanks are also due W. M. Harris, C. P. Baker, and the cyclotron crew for numerous irradiations and to J. Hudis for performing the equally numerous chemical separations.

[11] Apparently the value of A_4 for this correlation in Lloyd's tables[9] is in error by a factor of 10. The correct value being -0.0180 instead of the listed value -0.0018.

[12] Arfken, Biedenharn, and Rose, U. S. Atomic Energy Commission Document ORNL 1103, 1952 (unpublished).

[13] It has been shown [J. Weneser and D. R. Hamilton, following paper, Phys. Rev. **92**, 321 (1953)] that for a series of basic transitions of any character such that the spins of the levels form a monotonic sequence, the correlation depends only on the character of the particular radiations being measured.

‡ *Note added in proof.*—It has been pointed out by M. E. Rose that numerical results for any one-three angular correlation can be obtained by using Eq. (141) in the paper of Biedenharn and Rose, Revs. Modern Phys. (to be published) in conjunction with tables of Racah coefficients.

[14] Based on the assumption of "core isomerism" and the energy expected for the first excited state of Mo^{92} [G. Scharff-Goldhaber, Phys. Rev. **90**, 587 (1953)], γ_3 should be the 1.479-Mev transition.

[15] Rose, Goertzel, Spinrad, Harr, and Strong, Phys. Rev. **83**, 79 (1951).

A Theorem Concerning Angular Correlations

J. WENESER AND D. R. HAMILTON*
Brookhaven National Laboratory, Upton, New York†

(Received July 15, 1953)

It is shown that in a cascade of any number of basic transitions between states of monotonically increasing or decreasing angular momenta the angular correlation between any two of the radiations is independent of the spins, the number and character of the intermediate steps, and the order in which the radiations occur. It depends only on the character of the measured radiations.

IT will be shown here that for a series of basic[1] transitions of any character such that the spins of the levels form a monotonic sequence, the correlation depends only on the character of the particular two radiations being measured; it is independent of the number of transitions intervening between the two measured radiations and the character of the intervening transitions, and is unaltered if a constant is added to all the level spins.[2] That is, suppose we have the pure radiations of angular momentum $L_1, L_2 \cdots L_n$ and the sequence of spins $j_0, j_1 \cdots j_n$:

$$j_0 \xrightarrow{L_1} j_1 \xrightarrow{L_2} j_2 \cdots \xrightarrow{L_n} j_n,$$

such that $j_0 = j_1 + L_1$, $j_1 = j_2 + L_2$, $\cdots j_{n-1} = j_n + L_n$; then, the correlation between the L_1 and L_n radiations is independent of their position in the sequence and independent of the spins. The same result holds if the sequence obeys the rule: $j_0 = j_1 - L_1$, $j_1 = j_2 - L_2 \cdots j_{n-1} = j_n - L_n$; we restrict ourselves here only to the first case.

This fact is of particular interest in the case of electromagnetic radiation. In the great majority of experimental cases a specific transition is both pure and basic; this is certainly not true in the case of the transition $j \to j$, which is rather an exceptional case and one with which we shall here assume we are not concerned. Let us suppose that we have a fast cascade of radiations $L_1, L_2, \cdots, L_n$. Then the level scheme remains undetermined because we have not fixed the order in which the radiations occur. With the assumption that all transitions are basic, it is, then, the point of the above remarks that angular correlation measurements alone will in no way fix the order in which the radiations occur.

The theorem applies, of course, to β radiation too. In practice we need consider the β only as the first radiation. However, the requirement that the transition be basic is not commonly validated. It would, for example, apply to the β transition characterized by

$$(\Delta J = 2 \text{ yes});$$

it would apply to ($\Delta J = 1$ yes), ($\Delta J = 2$ no) only if $j_0 = 0$. Similar considerations apply to other radiations, which we do not further consider here.

The theorem is easily proved using the Racah techniques.[3] The matrix element for the $i \to (i+1)$ transition can be written in the form—for single particle radiation:

$$(j_i \| L_{i+1} \| j_{i+1}) C(j_i, L_{i+1}, j_{i+1}; m_i, M_{i+1}) \times D(L_{i+1}, M_{i+1}, \tau_{i+1}; R_{i+1}) c_{\tau i+1}(L_{i+1}),$$

where $C(j_i, L_{i+1}, j_{i+1}; m_i, M_{i+1})$ is the usual Clebsch-Gordan coefficient, $D(L_{i+1}, M_{i+1} \tau_{i+1}; R_{i+1})$ is the L_{i+1} irreducible representation of the rotation group, R_{i+1} is the rotation characterizing the directions that describe the L_{i+1} radiation, and $c_{\tau i+1}$ are the parameters that depend on the kind and character of the radiation. Thus, for α particles $c_\tau = \delta_{\tau,0}$; for circularly polarized γ rays $c_\tau = \delta_{\tau,\pm 1}$; for linearly polarized γ rays $c_{+1} = +1$, $c_{-1} = \pm i$. Then, the correlation between the L_1 and L_n radiations is $W(1, n)$, where

$$\begin{aligned} W(1,n) = \sum_{\substack{m_0, m_1, \cdots m_f \\ m_1', \cdots m_{n-1}' \\ \tau_1, \cdots \tau_n \\ \tau_1', \cdots \tau_n'}} \int dR_2 \cdots dR_{n-1} \\ \times c_{\tau_1}(1) c_{\tau_1'}(1) D(L_1, M_1, \tau_1; R_1) \\ \times D^*(L_1, M_1', \tau_1'; R_1) C(j_0, L_1, j_1; m_0, M_1) \\ \times C(j_0, L_1, j_1; m_0, M_1') \\ \times c_{\tau_2}(2) c_{\tau_2'}(2) D(L_2, M_2, \tau_2; R_2) \\ \times D^*(L_2, M_2'; \tau_2'; R_2) C(j_1, L_2, j_2; m_1, M_2) \\ \times C(j_1, L_2, j_2; m_1', M_2') \\ \times \cdots \\ \times c_{\tau_n}(n) c_{\tau_n'}(n) D(L_n, M_n, \tau_n; R_n) \\ \times D^*(L_n, M_n', \tau_n'; R_n) \\ \times C(j_{n-1}, L_n, j_f; m_{n-1}, m_f - m_{n-1}) \\ \times C(j_{n-1}, L_n, j_f; m_{n-1}', m_f - m_{n-1}'). \end{aligned}$$

* On leave from Physics Department, Princeton University, Princeton, New Jersey.

† Work done under the auspices of the U. S. Atomic Energy Commission.

[1] A *basic transition* between two levels the spins of which are j_1, j_2, respectively, is defined as the emission of radiation of angular momentum L, where $L = |j_1 - j_2|$.

[2] Special case of this for dipole and quadrupole transitions are given in: Biedenharn, Arfken, and Rose, Phys. Rev. **83**, 586 (1951); Arfken, Biedenharn, and Rose, Oak Ridge National Laboratory Report 1103 (unpublished).

[3] Use has been made throughout of the simplified and unified approach formulated by: L. C. Biedenharn and M. E. Rose, Revs. Modern Phys. (to be published). The notation of these authors has been used throughout. We wish to thank these authors for making preprints available to us.

Using the facts that:

$$\int D(L, M, \tau; R)D^*(L, M', \tau'; R)dR = 8\pi^2/(2L+1)\delta_{M,M'}\delta_{\tau,\tau'},$$

$$D(L, M, \tau; R)D^*(L, M', \tau'; R) = (-1)^{M'-\tau'}\sum_\nu C(L, L, \nu; M, -M') \times C(L, L, \nu; \tau, -\tau')D(\nu, M-M', \tau-\tau'; R),$$

and the Racah relation:

$$\sum_{m_0}(-1)^{m_0}C(j_0, L, j_1; m_0, m_1-m_0) \times C(j_0, L, j_1; m_0, m_1'-m_0)C(L, L, \nu; m_0-m_1, m_1'-m_0) = -j_0-2L(-1)(2j_1+1)^{\frac{1}{2}}C(j_1, j_1, \nu; m_1, -m_1') \times W(j_1, j_1, L, L; \nu, j_0),$$

and carrying out first the m_0, m_f summation, then the M_2, $M_3\cdots M_{n-1}$, m_{n-1} summation, in that order, we immediately obtain, after dropping irrelevant factors:

$$\sum_q(-1)^q[\sum_{\tau_1} c_{\tau_1}{}^{(1)}c_{\tau_1}{}'^{(1)}(-1)^{\tau_1'}C(L_1, L_1, \nu; \tau_1, -\tau_1') \times D(\nu, q, \tau_1-\tau_1'; R_1)]W(j_1j_1L_1L_1; \nu j_0) \times W(j_2j_2j_1j_1; \nu L_1)\cdots W(j_{n-1}j_{n-1}j_{n-2}j_{n-2}; \nu L_{n-1}) \times[\sum_{\tau_n} c_{\tau_n}{}^{(n)}c_{\tau_n}{}'^{(n)}(-1)^{\tau_n'}C(L_n, L_n, \nu; \tau_n, -\tau_n') \times D(\nu; -q, \tau_n-\tau_n'; R_n)]W(j_{n-1}j_{n-1}L_nL_n; \nu j_n),$$

or, in the more usual form:

$$[\sum_{\substack{\tau_1, \tau_n \\ \tau_1', \tau_n'}}(-1)^{\tau_1'+\tau_n}c_{\tau_1}{}^{(1)}c_{\tau_1}{}'^{(1)}c_{\tau_n}{}^{(n)}c_{\tau_n}{}'^{(n)} \times C(L_1, L_1, \nu; \tau_1, -\tau_1')C(L_n, L_n, \nu; \tau_n, -\tau_{n'}) \times D(\nu, \tau_n'-\tau_n, \tau_1-\tau_1'; R)]W(j_1j_1L_1L_1; \nu j_0) \times W(j_2j_2j_1j_1; \nu L_2)\cdots W(j_{n-1}j_{n-1}j_{n-2}j_{n-2}; \nu L_{n-1}) \times W(j_{n-1}j_{n-1}L_nL_n; \nu j_f),$$

where $R=R_n^{-1}R_1$ represents the directions between the L_1 and L_n radiations. We have, then, only to examine the products of the Racah coefficients. This is easily done since for the special case here considered the usual sum becomes a single, simple term;[4] dropping irrelevant factors, we have:

$$W(j_1j_1L_1L_1; \nu j_0)\rightarrow \left\{\frac{1}{(2j_1-\nu)!(2L_1-\nu)!(2j_1+\nu+1)!(2L_1+\nu+1)!}\right\}^{\frac{1}{2}},$$

$$W(j_{n-1}j_{n-1}L_nL_n; \nu, j_f)\rightarrow \left\{\frac{(2j_{n-1}-\nu)!(2j_{n-1}+\nu+1)}{(2L_n-\nu)!(2L_n+\nu+1)!}\right\}^{\frac{1}{2}}(-1)^{-\nu},$$

$$W(j_2j_2j_1j_1; \nu L_2)\rightarrow \left\{\frac{(2j_1-\nu)!(2j_2+2L_2+\nu+1)!}{(2j_2-\nu)!(2j_2+\nu+1)!}\right\}^{\frac{1}{2}}(-1)^{\nu}.$$

[4] G. Racah, Phys. Rev. **62**, 438 (1942), especially Eq. (36′).

The product of the Racah coefficients becomes, after again dropping irrelevant factors,

$$\left\{\frac{1}{(2L_1-\nu)!(2L_1+\nu+1)!}\,\frac{1}{(2L_n-\nu)!(2L_n+\nu+1)!}\right\}^{\frac{1}{2}}.$$

Since this is the same as

$$W(jjL_1L_1; \nu j_1)W(jjL_nL_n; \nu j_f)$$

if $j_0=j+L_1$ and $j=L_n+j_f$, we have proved the desired theorem.

It is interesting to consider from a different viewpoint how this result comes about. Suppose we choose the Z axis along the direction of the first quantum. The relative population of the different m_1 sublevels of j_1 is, then:

$$\sum_\nu[(-1)^{\tau_1}C(L_1, L_1, \nu; -\tau_1, \tau_1)c_{\tau_1}{}^2(1)](-1)^{m_1'} \times C(j_1, j_1, \nu; m_1, -m_1) \times\left\{\frac{1}{(2j_1-\nu)!(2L_1-\nu)!(2j_1+\nu+1)!(2L_1+\nu+1)!}\right\}^{\frac{1}{2}}.$$

The relative population of the m_2 sublevels of j_2, following the unobserved L_2 radiation, turns out to be the same function with j_1, m_1 replaced by j_2, m_2. This "standard population" is transmitted down to the j_{n-1} level. That is, the population in the j_{n-1} level, when we have observed the L_1 radiation emitted along the Z axis, is the same as the population produced by the following hypothetical transition: an L_1 radiation is emitted along the Z axis in a transition from an isotropic state of spin $(j_{n-1}-L_1)$ to the state j_{n-1}. The cascade thus reduces in effect to a single basic-basic correlation, which is known[5] to be independent of the j values; this implies the theorem.

The extension to transitions in which two particles are emitted—as in beta decay—is only slightly more difficult. We omit the details, but it is sufficient to point out that

$$\int(j_0, m_0|\quad|j_1, m_1)(j_0, m_0|\quad|j_1, m_1')^*d\omega_\nu,$$

which replaces the factor

$$(j_0m_0|L_1|j_1m_1)(j_0m_0|L_1|j_1m_1')^*,$$

can be written in the form

$$(-1)^{m_1'}C(j_1, j_1, \nu; m_1, -m_1') \times W(j_1j_1L_1L_1; \nu j_0)(\text{function of } L_1).$$

The derivation then goes through as before.

We wish to thank Dr. J. Kraushaar for suggesting this problem, and both him and Dr. M. Goldhaber for stimulating discussions.

[5] S. P. Lloyd, Phys. Rev. **83**, 716 (1951).

Total Neutron Cross Section of Liquid Argon*

JANET B. GUERNSEY AND CLARK GOODMAN
Department of Physics and Laboratory for Nuclear Science, Massachusetts Institute of Technology, Cambridge, Massachusetts
(Received July 8, 1953)

Using liquid argon in a specially designed Dewar flask, $Li^7(p,n)$ neutrons, and a hydrogen recoil counter, we have measured $\sigma_t(A)$ at 2-kev intervals in the range 450 to 1100 kev of neutron energy. The experiment was performed in good geometry using the transmission method.

THE total neutron cross section of argon for fast neutrons apparently has not been measured previously.[1] Recent measurements of the total cross section of chlorine[2] and phosphorus[3] both odd-odd compound nuclei, have been made in this laboratory. It was thought that similar measurements might prove interesting for argon, a nearby even-odd compound nucleus (principal isotope: A^{40}, 99.6 percent abundant).

Neutrons of well-defined energy in the range 0.45 to 1.1 Mev were obtained using the Rockefeller electrostatic generator, and the $Li^7(p,n)$ reaction. Thin targets (2–3 kev) were evaporated on 10-mil tantalum in the target chamber of the machine. Energy calibration was made using the threshold of the $Li^7(p,n)$ reaction as 1.882 Mev.[4] This threshold was checked after each run against the frequency of the proton resonance control of the analyzing magnet. Target thickness was estimated by the "rise" method at the Li threshold, and was checked against the 585-kev resonance of sulfur which has a width of <2 kev.[5]

The experiment itself consisted of transmission measurements, made in good geometry, using liquid argon as a scatterer. The argon was contained in a specially constructed Dewar bottle, previously used in

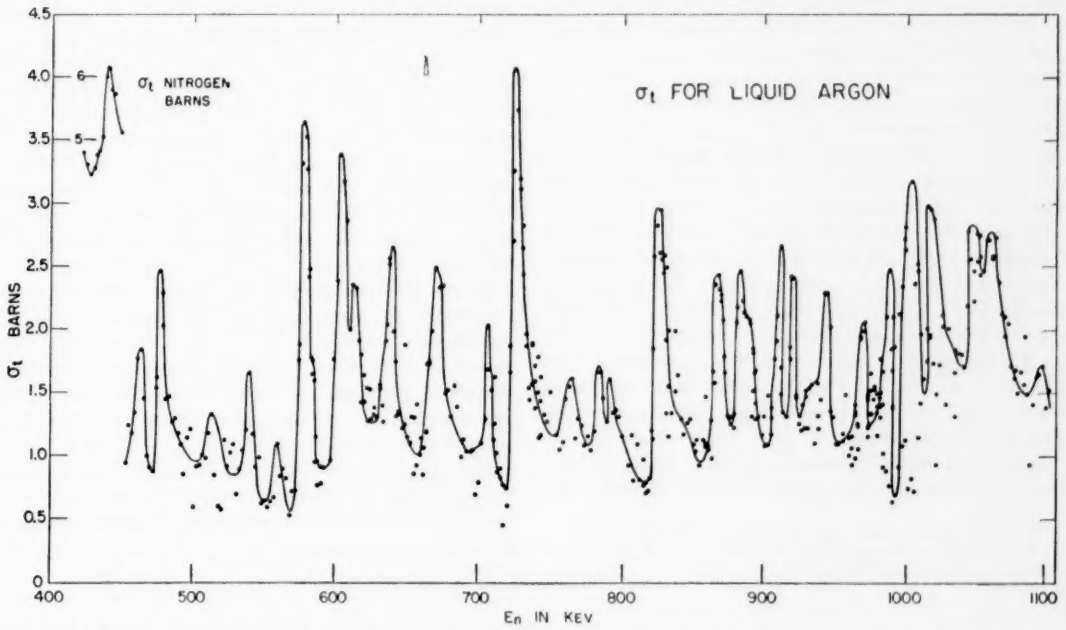

FIG. 1. Total neutron cross section of liquid argon. The major resonances are well defined, but the scatter of points near the base level makes graphical averaging difficult. In this region the line drawn is only suggestive of the general trend. The peak for liquid nitrogen was one of several used as a check with Hinchey, *et al.* (see reference 6).

* This work was supported by the U. S. Bureau of Ships and the U. S. Office of Naval Research.
[1] *Neutron Cross Sections*, U. S. Atomic Energy Commission Report AECU-2040 (Office of Technical Services, Department of Commerce, Washington, D. C., 1952).
[2] Kiehn, Goodman, and Hansen, Phys. Rev. **91**, 66 (1953).
[3] Hansen, Kiehn, and Goodman (to be published).
[4] Herb, Snowdon, and Sala, Phys. Rev. **75**, 246 (1949).
[5] Peterson, Barschall and Bockelman, Phys. Rev. **79**, 593 (1950).

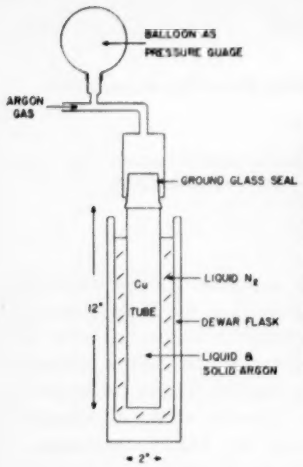

FIG. 2. Apparatus for liquefying argon. Tank argon enters through a ground-glass seal with a rubber balloon as pressure gauge. The argon condenses on the walls of the thin-walled copper tube immersed in liquid N_2. After opening the ground joint, the argon is poured out of the copper tube into a storage Dewar from which it is transferred to the scattering Dewar.

the measurement of σ_t for liquid nitrogen.[6] A pressurized hydrogen recoil counter (70 psi)[7] was used as a neutron detector, operated at 3600–3800 volts. This counter has the advantage of being insensitive to neutrons of low energy, 200 to 400 kev, depending on the voltage of the center wire; thus background caused by room scattering was negligible. Measurements were made at intervals of slightly less than 2 kev over the range 450 to 1100 kev of neutron energy (see Fig. 1). At each energy, measurements were made with and without the scatterer in the beam, in order to eliminate the effects of drift in the electronic equipment over a period of time. A later check of several resonances made by taking measurements over a range of energies with the scatterer in the beam, then repeating without the scatterer, showed essentially no deviation from the results obtained by the first method. The beam was monitored by a BF_3 long counter, placed at 90° with the neutron beam, and about 2 meters away, and also by beam current integration. It was determined that the monitor was far enough away from the recoil counter that no correction need be made for neutrons scattered by the argon.

No correction for the second group of neutrons from the $Li^7(p,n)$ reaction was made since it fell within the statistics of the experiment. Corrections for scattering by the Dewar were made by running a transmission experiment on the empty flask at intervals of about 50 kev. These corrections were found to be essentially constant over the whole range of energies, amounting to about 9 percent. The region near 440 kev (the prominent resonance in oxygen) was checked carefully, and the correction in this region increased by a factor of two. A similar observation in the vicinity of the major silicon resonance at 570 kev revealed no detectable resonant scattering.

The argon used in this experiment was liquefied by flowing it from the storage cylinder into a cylindrical metal container provided with a gas-tight glass top.[8] (See Fig. 2.) The metal container was immersed in liquid nitrogen, whose boiling point is −196°C. The boiling point of argon is −187°C, and its freezing point −192°C. Thus the argon formed both the solid and liquid state. It was stored in a pre-cooled Dewar flask until ready for use in the target bottle. The liquefying apparatus was flushed with gaseous argon to remove all air before liquefaction took place. The argon contained less than 0.1 percent impurity (N_2).

The data were taken over a period of several months, using different Li targets. Each time the experiment was set up several previously obtained resonances were rechecked. The nitrogen resonances obtained by Hinchey, *et al.*[6] at 430 and 639 kev, using liquid nitrogen in the target bottle, were also checked several times. Our results were in excellent agreement with theirs.

The average resonant cross section was found to be about 3 barns, the nonresonant cross section about 0.75 barn. The average level spacing over the range of neutron energies is about 25 kev; the level widths of the prominent resonances are about 4 kev. There is evidence that several of the larger resonances are probably unresolved doublets. The resolution does not permit assignments of l values to any of the resonances. At higher energies the nonresonant scattering cross section seems to be somewhat greater on the average than at lower energies. This may result from unresolved resonances.

We wish to thank Dr. J. H. Marshall for the use of his equipment for liquefying argon. The assistance of the other members of the Neutron Physics Group is gratefully acknowledged.

[6] Hinchey, Stelson, and Preston, Phys. Rev. **86**, 483 (1952).
[7] F. S. Replogle, Servomechanisms Engineering Memo No. 29, Massachusetts Institute of Technology, March 18, 1952 (unpublished).
[8] J. H. Marshall, Phys. Rev. **91**, 905 (1953).

Hyperfine Structure of the Spectra of Dysprosium, Cobalt, Vanadium, Manganese, and Lanthanum

KIYOSHI MURAKAWA AND TOHRU KAMEI
Institute of Science and Technology, Komaba-machi, Meguro-ku, Tokyo, Japan
(Received June 17, 1953)

Study of the hyperfine structure of the spectra of Dy I and D II yielded the result that the nuclear spins of Dy^{161} and Dy^{163} are very probably 7/2 and their nuclear magnetic moments are approximately equal. The quadrupole moments of Co, V, Mn, and La were deduced by hyperfine structure investigation to be $Q(Co^{59}) = (0.5\pm0.2)\times10^{-24}$ cm², $Q(V^{51}) = (0.3\pm0.2)\times10^{-24}$ cm², $Q(Mn^{55}) = (0.4\pm0.2)\times10^{-24}$ cm², $Q(La^{139}) = (0.9\pm0.1)\times10^{-24}$ cm². The eccentricities of odd-proton nuclei were calculated from the existing data, and they were plotted *versus* the proton number. It was found that they attain large maxima in light and heavy elements.

I. HYPERFINE STRUCTURE OF THE SPECTRA OF Dy I AND Dy II

THE hyperfine structure (hfs) of the spectrum of dysprosium was studied, using a water-cooled hollow cathode discharge tube and a Fabry-Perot etalon.

Unfortunately no classification of the spectrum of Dy I or Dy II is available. Natural dysprosium consists of seven isotopes:[1] Dy^{164} (28.18 percent), Dy^{163} (24.97 percent), Dy^{162} (25.53 percent), Dy^{161} (18.88 percent), Dy^{160} (2.294 percent), Dy^{158} (0.0902 percent) and Dy^{156} (0.0524 percent), where a number in parentheses represents the isotopic abundance. The abundances of Dy^{158} and Dy^{156} are so small that their existence will be neglected in the discussion of the hfs.

The hfs of the line Dy I λ6259 is shown in Fig. 1. The intensity ratio of the components A to a is equal to the ratio of the abundance of Dy^{163} to Dy^{161} within experimental error, and this indicates that the nuclear spins of Dy^{163} and Dy^{161} must be equal. Approximate equality of the distances AB and ab shows that the magnetic moments of Dy^{163} and Dy^{161} are approximately equal.

There are many lines of Dy I in which the displacement effect of Dy^{164} against Dy^{162} is of the order of 0.035 cm^{-1}. When 0.035 cm^{-1} is assumed to be the isotopic effect due to the transition $6s-6p$, the order of magnitude is very reasonable.[2]

Meggers[3] published a constant difference (828.3 cm^{-1}) between Dy II lines among which strong lines and especially the strongest line λ3968 are included. This line appears even when the condition of the discharge is unfavorable for the production of the Dy II spectrum. Thus we may assume that the final level of this line belongs to the ground multiplet or nearby multiplet of Dy II. The theoretical electron configuration of Dy II is given by Meggers as $4f^95d6s^2$. It is, therefore, expected that the ground state of Dy II has a sufficiently high J value. We may assume that the final level of Dy II λ3968 has also a sufficiently high J value. The observed hfs of λ3968 is shown in Fig. 1 and is in harmony with the assumption of the high J values of the levels involved.

The central strong component of λ3968 corresponds to the even isotopes, the remaining components belonging to the odd isotopes. The number of components and the intensity distribution in λ3968 show that the spin of Dy^{163} and Dy^{161} is very probably 7/2.

II. QUADRUPOLE MOMENTS OF Co, V, Mn AND La

In order to determine the quadrupole moments of Co, V, Mn, and La, the hfs of the spectra of Co I, V I, Mn I, La I, and La II were studied, using a liquid-air cooled hollow cathode discharge tube and a Fabry-Perot etalon. Each of these elements consists of only one isotope and the interpretation of the hfs is simple. Previous authors found that the nuclear spins of Co, V, and La are 7/2 and that of Mn is 5/2.

The hfs of the Co I spectrum was studied by several authors.[4-6] Rasmussen[6] detected for the first time a

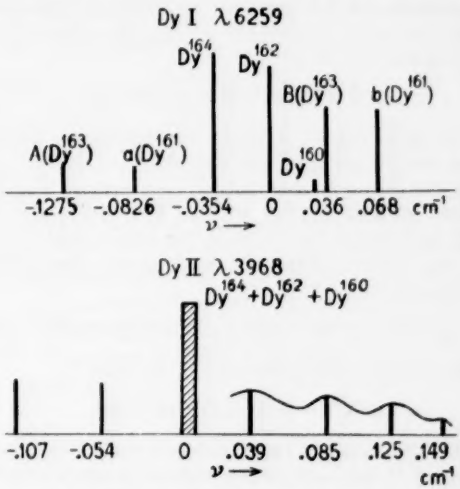

FIG. 1. Hfs of the lines Dy I λ6259 and Dy II λ3968.

[1] M. G. Inghram and D. C. Hess, quoted by G. T. Seaborg and I. Perlman, Revs. Modern Phys. **20**, 585 (1948).
[2] See, for example, Fig. 2 of the work of K. Murakawa and J. S. Ross, Phys. Rev. **83**, 1272 (1951).
[3] W. F. Meggers, Revs. Modern Phys. **14**, 96 (1942).
[4] K. R. More, Phys. Rev. **46**, 470 (1934).
[5] H. Kopfermann and E. Rasmussen, Z. Physik **94**, 58 (1935).
[6] E. Rasmussen, Z. Physik **102**, 229 (1936).

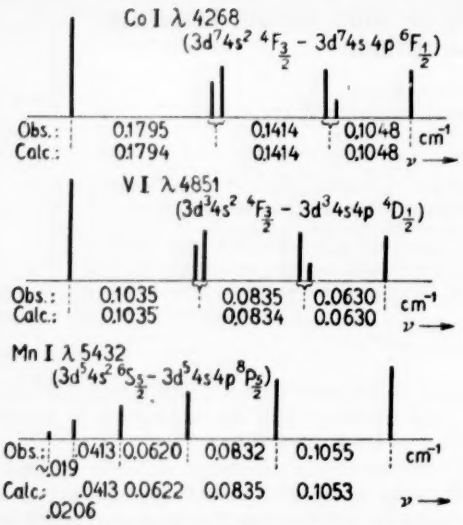

FIG. 2. Hfs of the lines Co I λ4268, V I λ4851 and Mn I λ5432.

deviation from the cosine interval rule in the term $3d^74s^2\ {}^4F_{\frac{9}{2}}$. In the present work the line λ4268 ($3d^74s^2\ {}^4F_{\frac{9}{2}} - 3d^74s4p\ {}^6F_{\frac{9}{2}}$) was studied, and the result is given in Fig. 2. Rasmussen got the intervals 0.179, 0.140, and 0.105 cm^{-1} in the same line. The hfs splitting of the initial term must be very small. Denoting the interval factor and the quadrupole constant of the final level by A and B, respectively, and the interval factor of the initial level by δ, we get from the observed hfs the values: $A-\frac{1}{12}\delta=35.53\times10^{-3}$ cm^{-1}, $B=0.015\times10^{-3}$ cm^{-1}. The structure of λ4268 that was calculated using these values of $A-\frac{1}{12}\delta$ and B is also shown in Fig. 2.

Assuming an LS coupling for the final level and using the usual procedure,[7] we get the value of the quadrupole moment:

$$Q(Co^{59})=(0.5\pm0.2)\times10^{-24}\ cm^2.$$

The hfs of the V I spectrum was studied by Kopfermann and Rasmussen,[8] but they detected no deviation from the cosine interval rule in any term of V I. The present authors studied the line V I λ4851, and the result is shown in Fig. 2. Using the same notation as in the case of Co I λ4851, we get from the observed hfs the values:

$$A-\tfrac{1}{12}\delta=20.81\times10^{-3}\ cm^{-1},\quad B=-0.0046\times10^{-3}\ cm^{-1}.$$

As in the case of Co, the value of B yields

$$Q(V^{51})=(0.3\pm0.2)\times10^{-24}\ cm^2.$$

The hfs of the Mn I spectrum was studied by several authors,[9–13], but none of the previous authors detected any deviation from the cosine interval rule in any term of Mn I. The present authors studied the hfs of Mn I λ5432 ($3d^54s^2\ {}^6S_{\frac{5}{2}} - 3d^54s4p\ {}^8P_{\frac{5}{2}}$), and the result is shown in Fig. 2. It is well known that the final level is of an LS-coupling type, so that it has a vanishing interval factor and a vanishing quadrupole constant. The hfs of λ5432 therefore gives directly the hfs of the initial level $3d^53s4p\ {}^8P_{\frac{5}{2}}$. Denoting the interval factor and the quadrupole constant of the initial level by A and B respectively, we get from the observed hfs the values:

$$A=20.90\times10^{-3}\ cm^{-1},\quad B=0.005\times10^{-3}\ cm^{-1}.$$

Assuming an LS coupling for the initial level, we get

$$Q(Mn^{55})=(0.4\pm0.2)\times10^{-24}\ cm^2.$$

Recently Javan, Silvey, and Townes[14] deduced $Q(Mn^{55})=0.5\times10^{-24}$ cm^2 by means of microwave spectroscopy. This is in good agreement with the value deduced here.

It would be desirable to check the value of Q by studying the hfs of the line Mn I λ5395 ($3d^54s^2\ {}^6S_{\frac{5}{2}} - 3d^54s4p\ {}^8P_{7/2}$). However, unfortunately the hfs obtained by different spacers were not sufficiently consistent, so that such an attempt has been abandoned for the time being.

The hfs of La I spectrum was studied by Anderson,[15] but he found no deviation from the cosine interval rule in any level of La I.

The hfs of the line La I λ5106 [$5d^26s\ {}^4F_{\frac{9}{2}} - 5d^2({}^3F)6p\ {}^4D_{\frac{7}{2}}$][16] obtained in the present work is shown in Fig. 3. The deviation from the cosine interval rule in $5d^26s\ {}^4F_{\frac{9}{2}}$ is considerable, and the interval factor A and the quadrupole constant B of this level are calculated to be

$$A=-16.7\times10^{-3}\ cm^{-1},\quad B=0.011\times10^{-3}\ cm^{-1}.$$

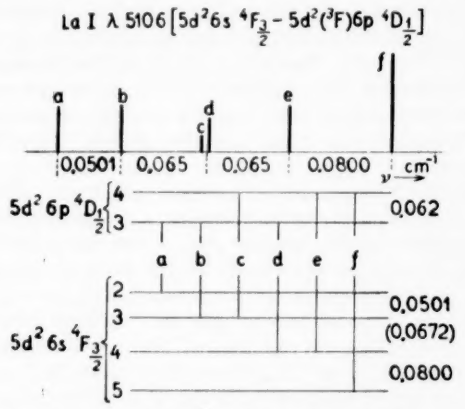

FIG. 3. Hfs of the line La I λ5106 and the transition scheme.

[7] See, for example, T. Schmidt, Z. Physik **121**, 63 (1943).
[8] H. Kopfermann and E. Rasmussen, Z. Physik **98**, 624 (1936).
[9] L. Janicki, Ann. Physik **29**, 833 (1909).
[10] Wali-Mohammad, Astrophys. J. **39**, 185 (1914).
[11] H. E. White and R. Ritschl, Phys. Rev. **35**, 1146 (1930).
[12] Wali-Mohammad and P. N. Sharma, Phil. Mag. **18**, 1144 (1934).
[13] R. A. Fisher and E. R. Peck, Phys. Rev. **55**, 270 (1939).
[14] Javan, Silvey, Townes, and Grosse, Phys. Rev. **98**, 222 (1953).
[15] O. E. Anderson, Phys. Rev. **46**, 473 (1934).
[16] The classification of the spectra La I, La II, and La III was published by H. N. Russell and W. F. Meggers, J. Research Natl. Bur. Standards **9**, 625 (1932).

Using the formula published by Crawford,[17] the quadrupole moment is calculated to be

$$Q(\mathrm{La}) = (0.95 \pm 0.20) \times 10^{-24}\ \mathrm{cm}^2.$$

The line La II $\lambda 4809$ ($5d6s\ ^3D_1 - 5d4f\ ^3P_0$) was observed to consist of three components: 0 (3), 0.137 (4), 0.305 (5) cm^{-1}, where a number in parentheses represents the relative intensity. The interval factor A and the quadrupole constant B of $5d6s\ ^3D_1$ deduced from the hfs are

$$A = -38.1 \times 10^{-3}\ \mathrm{cm}^{-1}, \quad B = 0.057 \times 10^{-3}\ \mathrm{cm}^{-1}.$$

Using the formula published by Casimir,[18] we get the quadrupole moment:

$$Q(\mathrm{La}) = (0.91 \pm 0.10) \times 10^{-24}\ \mathrm{cm}^2.$$

Summarizing the results obtained from the hfs of the La I and La II spectra, we can conclude that

$$Q(\mathrm{La}^{139}) = (0.9 \pm 0.1) \times 10^{-24}\ \mathrm{cm}^2.$$

Regularities in the quadrupole moments of atomic nuclei were discussed by Gordy[19] and Townes[20] some time ago. More values have been found since then, and it will not be out of place to discuss the regularities again here.

Wageningen and de Boer[21] calculated the quadrupole moments of some nuclei and verified that the intrinsic quadrupole moment Q_0 that was introduced by Bohr[22] is more adequate than the experimentally found quadrupole moment Q for use in the calculation. Under the assumption of spin-orbit coupling, Q_0 is expressed by the equation:

$$Q_0 = Q\frac{(I+1)(2I+3)}{I(2I-1)}. \tag{1}$$

Then the relation between Q_0 and the eccentricity ϵ is given by

$$\epsilon = (r_1^2 - r_2^2)/(r_1^2 + r_2^2) = 5Q_0/(4ZR^2), \tag{2}$$

where Z is the charge number (=proton number), R is the radius of the nucleus, and the nucleus is assumed to have the form of a spheroid with semi-axes r_1 and r_2. ϵ is positive for a prolate spheroid and negative for an oblate spheroid.

Using the values of Q listed in the review articles of Mack[23] and Klinkenberg,[24] values of ϵ of odd-proton nuclei were calculated and plotted *versus* the proton number Z (see Fig. 4).[25]

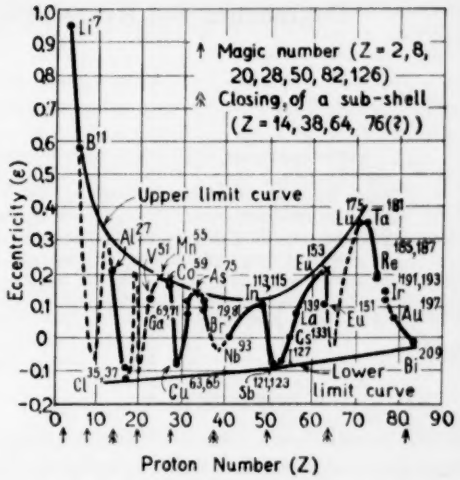

FIG. 4. Plot of eccentricity *versus* proton number.

Each of the nuclei Na^{23}, Mn^{55}, As^{75}, and Eu^{153} is anomalous in that the magnetic moment deviates to some extent from that predicted by the Mayer-Jensen shell model. However, in the present work it was assumed that the shell model is still valid for these nuclei and their Q_0 values were calculated by Eq. (1). In Fig. 4 the values of ϵ for these nuclei are plotted by x.

Figure 4 shows that two curves can be drawn in such a way that all the observed ϵ values lie between them. The upper-limit curve is flat for medium proton numbers but steep for small and large proton numbers. All of the above-mentioned anomalous nuclei except Na are observed to have ϵ lying on the upper limit curve. No data for Na are available, but it is probable that ϵ of Na also lies on the upper-limit curve, and it is predicted that $\epsilon(\mathrm{Na}^{23}) = 0.3$, $Q(\mathrm{Na}^{23}) = +8.4 \times 10^{-26}\ \mathrm{cm}^2$.

It will be useful to plot ϵ *versus* neutron number for odd-neutron nuclei also, but since the available data for such nuclei are still meager, such an attempt has been abandoned for the time being.

Note added in proof.—Recently K. Murakawa and S. Suwa [J. Phys. Soc. Japan (to be published)] have shown that $Q(\mathrm{Pr}^{141}) = -0.05 \times 10^{-24}\ \mathrm{cm}^2$, $\epsilon(\mathrm{Pr}^{141}) = -0.005$, and according to the recent article of D. R. Inglis [Revs. Modern Phys. **25**, 390 (1953)] $Q(\mathrm{Li}^7)$ is probably negative. Figure 4 of the present paper, therefore, requires correction with respect to Pr^{141} and Li^7.

[17] M. F. Crawford, Phys. Rev. **47**, 768 (1935).
[18] H. Casimir, (Verhandel. Teylers Tweede Genootschap, Haarlem (1936), 11.
[19] W. Gordy, Phys. Rev. **76**, 139 (1949).
[20] C. H. Townes, Phys. Rev. **76**, 1415 (1949).
[21] R. van Wageningen and J. de Boer, Physica **18**, 369 (1952).
[22] A. Bohr, Phys. Rev. **81**, 134 (1951).
[23] J. E. Mack, Revs. Modern Phys. **22**, 64 (1950).
[24] P. F. A. Klinkenberg, Revs. Modern Phys. **24**, 63 (1952).

[25] Closing of a sub-shell at neutron number 76 in the case of odd-neutron nuclei is evident from the negative Q value of Xe^{131} ($N = 77$). However, in the case of odd-proton nuclei, closing of a sub-shell at $Z = 76$ is not so clear.

Degradation and Range Straggling of High-Energy Radiations*

U. FANO
National Bureau of Standards, Washington, D. C.
(Received April 16, 1953)

A general analysis of the energy spectrum resulting from the degradation of ionizing radiations is presented in part A (Secs. 2–6) and of the range-energy straggling in part B (Secs. 7–13). A method for calculating the energy spectrum is developed, which requires that the differential cross sections of successive collisions are nearly equal. This method is applied to the slowing down of mesons and other heavy charged particles (Sec. 6). The same requirement on the cross section for successive collisions underlies the analysis of straggling into contributions from separate energy intervals traversed in the course of degradation. Successive approximation formulas for the straggling parameters (cumulants) are derived (Sec. 12) and applied to the case of heavy charged particles (Sec. 13). The connections among the theoretical approaches of several authors are discussed.

1. INTRODUCTION

IONIZING radiations which travel through a material experience a succession of inelastic collisions. Each collision results in a subdivision, or "degradation," of the radiation energy and in a deflection of its line of flight and may also change the nature of the incident radiation; for example, a photon may be replaced by a photoelectron. Therefore the propagation of high-energy radiation through a large mass of matter leads to a complex process of degradation and diffusion.

This process has been the object of much study in the case of *neutrons*.[1] Work on x-rays and γ rays up to energies of about 10 Mev has been in progress for several years in this laboratory. *Heavy charged particles*, including mesons, are scattered only to a minor extent and therefore do not experience true diffusion. Their multiple small-angle scattering is fairly complex, but the simpler problems of heavy particle degradation and range straggling have been solved long ago in a good approximation which will be discussed further below. The penetration, degradation, and diffusion of *electrons* up to about 10 Mev offers serious difficulties and is being approached systematically only now. The theory of high energy *electron-photon* showers has, for the most part, taken advantage of the smallness of deflections and of simplified cross sections for the elementary processes at very high energies. A recent semiempirical study by Wilson[2] has pointed up the errors due to unrealistic approximations. Here, too, a systematic study is still to come. The problems encountered in the study of different radiations have much in common.

A comprehensive formulation of a process of penetration, diffusion, and degradation in an infinite medium, with a point isotropic source or with any plane source, involves at least three independent variables: (1) the distance from the source, (2) the obliquity of propagation with respect to a fixed direction, and (3) the energy attained in the course of degradation. A more general type of source, namely point collimated, requires the introduction of two additional variables. Experience with neutrons[1] and x-rays emphasizes the convenience of proceeding by steps, taking into account *one variable at a time*. This is done by averaging out the distribution of radiation over the other variables.

The process of energy degradation may be isolated in this manner from the other aspects of penetration and diffusion, by averaging over all variables other than the energy of a particle or photon. The single-variable problem of simple energy degradation inquires about the distribution-in-energy of the particles or photons which result from a succession of collisions, irrespective of their positions in space. Once this problem has been solved, one may consider a two-variable problem. The second variable may be either the path length traveled by a particle from its source, or the obliquity of its direction. The study of the distribution-in-path length of radiation particles of various energies pertains to the problem of range-energy straggling. The study of the distribution-in-direction of particles of various energies, irrespective of their position in space, has received less attention than the other, but has proven instructive in the x-ray problem.[3] Either of the two-variable problems may be reduced to a set of independent single-variable, energy degradation problems (see Sec. 8, and Appendix I, respectively). Even the more complete three-variable problem, including the distribution-in-distance from the source, can be reduced to a set of energy degradation problems, at least in certain cases.[4]

As a preliminary to an effort to solve the electron problems it was desired to make a general study of the energy degradation problem and of the two-variable problem of range-energy straggling. These studies are reported in parts *A* and *B* of the present paper, respec-

* Work supported by the U. S. Office of Naval Research and the U. S. Atomic Energy Commission Reactor Division.

[1] See, e.g., R. E. Marshak, Revs. Modern Phys. **19**, 185 (1947), and in particular, the work of Placzek, Adler, and Wick quoted therein; also, I. Waller, Arkiv. Mat. Astron. Fysik **34A**, No. 3 (1948).

[2] R. R. Wilson, Phys. Rev. **86**, 261 (1952).

[3] See, e.g., L. V. Spencer and F. A. Jenkins, Phys. Rev. **76**, 1885 (1949).

[4] See, e.g., L. V. Spencer and U. Fano, J. Research Natl. Bur. Standards **46**, 446 (1951).

tively. Each problem is first surveyed qualitatively, mostly on the basis of ideas developed in the study of the neutron[1] and of the x-ray problems. Direct methods of solution, which work well in the case of neutrons or x-rays, are inadequate for charged-particle problems where the distribution of energy losses in individual collisions is extremely skew. A different line of approach is afforded by the fact that the energy degradation process exhibits a steady-state feature when successive energy losses obey *nearly equal* statistical laws, that is, when the differential cross section changes little from one collision to the next. This condition is fulfilled by "elastic" neutron collisions,[1] by all heavy charged particle collisions owing to the smallness of the maximum fractional energy loss and by most electron collisions. (The occasional hard knock-on collisions and the radiative collisions experienced by electrons do not fit into this class.) The steady-state feature is exploited in the development of an analytical method of successive approximations (Sec. 5) which assumes a slow variation of the cross sections for successive collisions. This method is not yet adequate to solve the electron problems, but it applies to heavy charged particles and serves to calculate corrections to the earlier elementary theories. These corrections are of little quantitative importance, however, because they correspond to an expansion in powers of m/M (electron mass divided by the mass of the incident particle). The steady-state feature is also shown to afford the necessary basis for resolving the range-energy straggling into a sum of contributions due to the various energy intervals traversed by particles in the course of degradation (Sec. 9).

In conclusion, this paper intends to clarify a number of concepts in the theories of energy degradation and of range-energy straggling as well as the relationships among earlier theories. As a by product it contributes new corrective terms on the slowing-down and straggling of heavy charged particles.

A. ENERGY DEGRADATION

2. Formulation of the Problem

Consider a uniform medium containing a source of high energy particles or photons. The initial energy of each particle or photon is reduced in discrete steps as a consequence of successive collisions. Other secondary radiations may arise from these collisions. What is the resulting energy spectrum of the primary radiation and of its secondaries?

This problem belongs to a broad class of one-dimensional random walk problems and much of the following treatment appears to have a correspondingly broad range of applications.

The problem is, perhaps, formulated most visually if one considers a uniformly distributed source of constant intensity which emits $S(E)dE$ particles or photons of energy between E and $E+dE$ per unit volume and per unit time. Spectral equilibrium of the radiation in the medium requires that the rate of destruction of radiation of each energy (number of particles absorbed per unit volume and per unit time) equal the rate of generation of the same radiation by the source or by degradation from higher energy radiation. If $n(E)$ indicates the spectral density of the *flux* of particles or photons of energy E at each point (number traversing a small spherical probe of unit cross-sectional area per unit time per unit spectral range), $\mu(E)$ the total probability of inelastic collision per unit path, $k(E, \epsilon)d\epsilon$ the differential probability per unit path of a particle of energy E to undergo a collision with an energy loss between ϵ and $\epsilon+d\epsilon$, the degradation obeys the equation

$$\mu(E)n(E)=\int_0^\infty k(E+\epsilon, \epsilon)n(E+\epsilon)d\epsilon+S(E). \quad (1)$$

The range of integration is indicated as extended to infinity, but in practice infinitely large losses cannot occur and $k(E, \epsilon)$ will vanish for ϵ larger than some maximum value ϵ_M. The probability distribution $k(E, \epsilon)$ may contain terms $k_i\delta(\epsilon-\epsilon_i)$ corresponding to the excitation of discrete levels of energy ϵ_i in the atoms or nuclei of the medium.

Actually, the source need not be considered as uniformly distributed in space and time. $S(E)dE$ may be regarded as the *total number* of particles or photons, emitted with energy between E and $E+dE$, no matter where or when. The spectral distribution $n(E)dE$ is then normalized as the total *track length* covered by particles or photons while their energy lies between E and $E+dE$. This normalization will be adhered to in the following. For convenience we shall also assume a unit source strength, $\int_0^\infty S(E)dE=1$.

If one considers secondary radiations, such as the delta rays ejected by protons, one may classify the different kinds of radiation by an index $\alpha=1, 2\cdots$. The degradation obeys then the system of equations

$$\mu(\alpha, E)n(\alpha, E)=\sum_{\alpha'}\int_0^\infty k(\alpha, \alpha'; E+\epsilon, \epsilon)n(\alpha', E+\epsilon)d\epsilon+S(\alpha, E), \quad (2)$$

where α takes all its values and $k(\alpha, \alpha'; E, \epsilon)$ indicates the differential probability that a particle of radiation α', with energy E collides and generates a particle of radiation α with energy $E-\epsilon$. The terms of the $\Sigma_{\alpha'}$ with $\alpha'\neq\alpha$ represent in effect additional sources of the radiation α. The whole system (2) is more complicated but in principle no more difficult to solve than the single equation (1), provided that there are only a few kinds of radiation. In this paper, we consider only the single equation (1).

Knowledge of the spectral distribution $n(E)$ serves to answer numerous questions such as the following one: "How much energy is radiated as *Bremsstrahlung* by electrons in the course of their degradation?" The basic data to be provided by *Bremsstrahlung* theory is the energy $W(E)$ radiated per unit distance by electrons of energy E. The total energy radiated is then obtained by multiplying $W(E)$ by the track length $n(E)$ of electrons of energy E and integrating over the energy, $\int_0^\infty n(E)W(E)dE$. Notice that the usual calculations of this quantity assume that $n(E)$ is given by the approximate formula (3), below, which is inadequate just when *Bremsstrahlung* is intense.

3. Qualitative Discussion

(a) *The Limiting Case of Continuous Slowing Down*

Heavy charged particles dissipate their energy in such small bits that their slowing down may be regarded for many purposes as a continuous process. According to this model the track length covered by particles of energy E is given by the reciprocal of the stopping power $\langle -dE/ds \rangle$. This is to say that for this model the degradation Eq. (1) has the solution

$$n(E) \sim \langle -dE/ds \rangle^{-1} = \left[\int_0^\infty k(E, \epsilon) \epsilon d\epsilon \right]^{-1}. \quad (3)$$

Much of the effort of this paper is directed to formulate the specific assumptions which underlie the approximate solution (3) and to develop a procedure for taking into account the fact that individual losses are actually finite.

The model of continuous slowing down applies to a considerable extent also to electrons. However, an electron occasionally loses a large fraction of its energy in a single collision especially when *Bremsstrahlung* is important. These rare events have a great influence on the range straggling of electrons. Hence there arises a need for considering radical departures from the model of continuous slowing down, but also for making the best use of this model in so far as it offers a valid approximation.

(b) *Direct Integration*

The degradation Eq. (1) determines $n(E)$ if a knowledge of $n(E+\epsilon)$ is assumed ($\epsilon > 0$). (Similarly, the system (2) determines $n(\alpha, E)$ if all $n(\alpha', E+\epsilon)$ are known.) Therefore, one is naturally led to stepwise methods of solution, beginning with the highest source energy E_0, such that $n(E_0+\epsilon)$ vanishes, and progressing from high to low energies along the course of energy degradation.

Placzek[1] approached the neutron slowing-down problem along this line, solving (1) stepwise in successively lower energy intervals by analytical means. The degradation of x-ray photons by successive Compton scatterings has been treated by Karr and Lamkin by numerical evaluation of the integral in (1) at successively lower values of the energy.[5]

The numerical procedure may well be the most expeditious one in many circumstances. One of its main limitations lies in the necessity of extrapolating the knowledge of $n(E+\epsilon)$ over the last finite interval of integration. This leads into difficulties unless $n(E+\epsilon)$ and $k(E+\epsilon, \epsilon)$ vary smoothly and not too rapidly with ϵ. In the slowing down of charged particles the energy loss distribution $k(E+\epsilon, \epsilon)$ is sharply peaked at low values of ϵ, so that this direct approach is not immediately applicable.

(c) *Transient and Steady State*

An additional element in the qualitative analysis of the degradation problem emerges from the following considerations. Both in neutron and in x-ray degradation the spectral distribution tends to a shape independent of the source energy, at all energies sufficiently lower than the source energy itself. This trend arises from the randomness of the energy loss in individual collisions, which erases the "memory" of the initial energy of each particle or photon after a few collisions. (As noted below, not every collision need be equally significant in this connection.) One may say that the process of energy degradation consists of an initial "transient" phase, which involves the first few collisions, followed by a simpler "steady state."

(d) *Expansion According to Orders of Scattering*

The first few collisions can be treated, if necessary, by an elementary iteration procedure, or expansion according to "orders of scattering." According to (1), the spectrum of undegraded (unscattered) particles is $n_0(E) = S(E)/\mu(E)$, that of "first scattered" particles is $n_1(E) = \int_0^\infty k(E+\epsilon, \epsilon) n_0(E+\epsilon) d\epsilon / \mu(E)$; the recurrence formula $n_r(E) = \int_0^\infty k(E+\epsilon, \epsilon) n_{r-1}(E+\epsilon) d\epsilon / \mu(E)$ gives the spectrum of particles that have experienced r collisions.[6] This iteration procedure is laborious and has been found to be of value only under special circumstances. A direct application to the energy loss of a charged particle, where a significant energy loss involves an extremely large number of collisions, appears unpromising.

(e) *Discussion of the Steady State*

The spectrum under steady-state conditions can be easily formulated in favorable circumstances, where the spectral density $n(E)$ equals the reciprocal of a suitable average of the energy loss per unit path. This situation was pointed out by Placzek for the neutron problem.[1] It would also obtain for low-energy x-rays if one could disregard the photoelectric absorption.[7] Notice finally that the solution (3) to the degradation equation, in the limiting case of continuous slowing down, is also equal to the reciprocal of the mean energy loss. We seek here to identify the common element in these examples.

The concept of a "steady state" implies, usually, more than independence of the initial conditions. In addition it tends to imply, in our case, a smooth variation of the spectral density $n(E)$. This implies, in turn, a smooth variation of the degradation law $k(E, \epsilon)$

[5] P. R. Karr and J. C. Lamkin, Phys. Rev. **76**, 1843 (1949). The same method has been applied in references 3 and 4 and in further extensive work still in progress, by means of desk and of automatic computers.

[6] See, e.g., G. H. Peebles and M. S. Plesset, Phys. Rev. **81**, 430 (1951).

[7] The actual steady-state shape of the x-ray degradation spectra can be qualitatively understood in this manner, as pointed out by M. H. Johnson in a private discussion.

as a function of the energy E.[8] After all, any convenient treatment of the problem must rely on some regularity of the degradation law.

In fact the examples mentioned above have this in common, that their degradation law can be expressed in a form independent of the energy of the incident particle or photon. Neutrons below 10 Mev are slowed down by elastic scattering against nuclei with a probability of deflection which is uniform in the center-of-mass system. Consequently the probability of a neutron losing various *fractions* of its energy depends only on the ratio of its mass to the mass of the nuclei in the medium and not on the energy of the incident neutron. The variations of the *logarithm* of the energy in successive collisions obey identical probability laws. The steady-state spectrum of neutrons in a *logarithmic energy scale* is the reciprocal of the *mean logarithmic energy* loss per unit path. Similarly the Compton scattering of x-rays approaches a constant angular distribution at low energies. Therefore the *wavelength changes* of the x-rays in successive scatterings obey identical probability laws and the x-ray spectrum in the *wavelength scale* tends to the reciprocal of the *mean wavelength increase* per unit path. In the slowing down of protons, on the other hand, the determining factor is not so much that the relative probability of various energy losses varies slowly with the energy of the incident particle. Rather the energy loss in each collision is so small that successive collisions obey practically equal probability laws. Therefore, the approximate solution (3) of the degradation equation for protons does not rely strictly on the model of continuous slowing down but on the fact that the individual energy losses are so small that the changes of cross section from one collision to the next can be disregarded.

The neutron slowing down with constant probability law has been treated analytically by Adler.[1] This treatment brings out clearly the emergence of a steady state after a transient stage of damped oscillations. It is presented in Sec. 4, in a form suitable for application to any radiation, because it constitutes the point of departure for further development.

(*f*) *Proposed Line of Advance*

The Adler treatment assumes that successive energy losses experienced by a particle are governed by identical probability laws. In order to permit a flexible exploitation of the regularities indicated above, we shall develop in Sec. 5 an analytical solution of the degradation equation, assuming only that successive energy losses obey "nearly equal" probability laws. More specifically we shall calculate corrective terms to the approximate solution (3) for the slowing down of protons. Since the maximum fraction of energy lost by a proton in a collision is of the order m/M (i.e., electron mass/proton mass), successive corrections to the results based on continuous slowing down will involve successively higher powers of m/M.

As indicated in the introduction, the justification for deriving these corrections does not lie primarily in their practical importance for proton problems (where $m/M \sim 10^{-3}$) or even for mesons (where $m/M \sim 10^{-2}$). Rather, it is desired to ascertain whether the qualitative argumentation of the preceding sections can be developed into a consistent formalism.

The solution of the problem of the degradation of electron energy will still have to wait for the development of a technique to deal with the rare collisions with large energy loss. The "order of scattering" procedure indicated above in Sec. 3 might perhaps serve for this purpose, when combined with the techniques appropriate to the smaller energy losses. Large energy losses are not so rare for high-energy electrons, when bremsstrahlung is important. Here too, however, one may see some hope in the fact that the spectrum of bremsstrahlung losses is nearly energy-independent when expressed in a logarithmic scale.†

In order to improve the initial approximation represented by the Adler treatment, one may want to express the energy variable in any scale suitable for minimizing the variations of the probability law. Furthermore, for simplicity, we may assume that the radiation source is monochromatic, with energy

$$E_0,\ S(E)=\delta(E-E_0). \tag{4}$$

(No generality is lost here, since the degradation equation is linear.) Therefore the energy will be indicated by a general variable x, such that $x=0$ when $E=E_0$ and $x>0$ when $E<E_0$. We also set

$$y(x)dx=n(E)dE, \quad K(x,\xi)d\xi=k(E,\epsilon)d\epsilon. \tag{5}$$

The degradation equation (1) becomes then

$$\mu(x)y(x)=\int_0^\infty K(x-\xi,\xi)y(x-\xi)\,d\xi+\delta(x). \tag{6}$$

The near equality of probability laws in successive collisions does not apply so much to the absolute as to the relative probability of different energy losses. Therefore it is not $K(x,\xi)$ which should vary slowly with x but rather $K(x,\xi)/\mu(x)$, and it is convenient to introduce the additional substitution:

$$\bar{y}(x)=\mu(x)y(x), \quad \bar{K}(x,\xi)=K(x,\xi)/\mu(x). \tag{7}$$

Equation (6) takes now the simpler form:

$$\bar{y}(x)=\int_0^\infty \bar{K}(x-\xi,\xi)\bar{y}(x-\xi)d\xi+\delta(x). \tag{8}$$

[8] Sharp, localized, irregularities of the degradation law can be treated separately from the smooth variations. For example, Placzek has treated the absorption of neutrons in a sharp spectral line as a "negative source" which gives rise to a new transient (see reference 1).

† *Note added in proof:*—A solution of the electron degradation problem, which combines the features of continuous slowing down and of direct integration, is presented in a forthcoming paper by L. V. Spencer and U. Fano.

However, the final results will be expressed just as easily in terms of $K(x, \xi)$ as of $\bar{K}(x, \xi)$.

Equation (8) is a general one-dimensional random walk equation, with the restriction that every step is forward, i.e., $K(x, \xi)$ vanishes for $\xi<0$. Therefore it corresponds to the games of chance of the parcheesi type. $K(x, \xi)$ is by its nature a non-negative function (except in the applications of Appendix I).

Since $k(E, \epsilon)$ represents the probability of collision with a finite energy loss ϵ, the $\int_0^\infty k(E, \epsilon)d\epsilon$ represents the probability of all collisions with a finite energy loss. This probability cannot exceed the total probability $\mu(E)$ of all collisions. On the other hand $\mu(E)$ may exceed $\int_0^\infty k(E, \epsilon)d\epsilon$ if there is some process of outright absorption of the particles. Thus we have, in general:

$$\int_0^\infty k(E, \epsilon)d\epsilon \leqslant \mu(E), \tag{9}$$

$$\int_0^\infty K(x, \xi)d\xi \leqslant \mu(x), \tag{9.1}$$

$$\int_0^\infty \bar{K}(x, \xi)d\xi \leqslant 1, \tag{9.2}$$

where the equality sign holds in the absence of absorption, the inequality in the presence of absorption.

4. Constant Degradation Law

If $\bar{K}(x, \xi)=\bar{K}(\xi)$ in (8),

$$\bar{y}(x)=\int_0^\infty \bar{K}(\xi)\bar{y}(x-\xi)d\xi+\delta(x). \tag{10}$$

The homogeneous portion of this equation is invariant with respect to translations along x and, therefore, must have exponential solutions. One takes advantage of this fact by a Laplace transformation. In this type of problem many formulas are expressed more conveniently by introducing a Laplace transform variable p with sign opposite to the usual one, i.e., by setting

$$\begin{aligned}\bar{v}(p)&=\int_0^\infty \exp(px)\bar{y}(x)dx,\\ \bar{F}(p)&=\int_0^\infty \exp(p\xi)\bar{K}(\xi)d\xi.\end{aligned} \tag{11}$$

Multiplying the degradation equation (10) by $\exp(px)$ and integrating over x from 0 to ∞, we obtain the transform equation

$$\bar{v}(p)=\bar{F}(p)\bar{v}(p)+1. \tag{12}$$

The solution of (12) is $\bar{v}(p)=[1-\bar{F}(p)]^{-1}$, and the solution of (10) is represented by the inverse transform

$$\bar{y}(x)=(2\pi i)^{-1}\int_{-a-i\infty}^{-a+i\infty} \exp(-px)[1-\bar{F}(p)]^{-1}dp. \tag{13}$$

The singularities of the transform $\bar{v}(p)$ are poles located at the points $p=p_j$ which are roots of the equation

$$\bar{F}(p)=\int_0^\infty \bar{K}(\xi)\exp(p\xi)d\xi=1. \tag{14}$$

Assuming that these roots are simple, which appears in the following to be true, the integral (13) can be evaluated by shifting the path of integration toward $p=\infty$ and reduces to the residues at the poles,

$$\begin{aligned}\bar{y}(x)&=\textstyle\sum_j \exp(-p_jx)/\bar{F}'(p_j)\\ &=\textstyle\sum_j \exp(-p_jx)\Big/\int_0^\infty \bar{K}(\xi)\exp(p_j\xi)\xi d\xi.\end{aligned} \tag{15}$$

Since Eq. (13) is real, its roots are real or complex conjugate in pairs; pairs of terms of (15) with complex conjugate p_j's represent real damped sinusoids.

The distribution of the roots of (14) may be discussed by setting $p=\alpha+i\beta$ so that (14) splits into two real equations:

$$\int_0^\infty \bar{K}(\xi)\exp(\alpha\xi)\cos(\beta\xi)d\xi=1, \tag{14.1}$$

$$\int_0^\infty \bar{K}(\xi)\exp(\alpha\xi)\sin(\beta\xi)d\xi=0. \tag{14.2}$$

Equation (14.2) has a solution $\beta=0$. When $\beta=0$, $\cos\beta\xi=1$ in (14.1); the resulting expression $\int_0^\infty \bar{K}(\xi)\times\exp(\alpha\xi)d\xi$ is an increasing function of α, since $\bar{K}(\xi)$ is non-negative. Therefore (14) has a single real root, which we indicate as $p=p_0=\alpha_0$, $\beta=0$. In the absence of absorption $\int_0^\infty \bar{K}(\xi)d\xi=1$ and $p_0=0$; otherwise $\int_0^\infty \bar{K}(\xi)d\xi<1$ and $p_0>0$.

The other roots of (14), if any, must have values of β of such magnitude that the positive and negative values of the integrand of (14.2) average out. This requires that $\beta \gtrsim \pi/\xi_M$, where ξ_M is the largest value of ξ, beyond which $\bar{K}(\xi)$ vanishes. The $\cos(\beta\xi)$ in the integrand of (14.1) oscillates also, and therefore α will have to be larger than α_0 if (14.1) has to be fulfilled despite the partial cancellation of positive and negative values of the integrand. Two examples may be quoted. If $\bar{K}(\xi)=b\exp(-a\xi)$, there is no root other than $p_0=a-b$. If $\bar{K}(\xi)=1/a$ for $0\leqslant\xi\leqslant a$, $\bar{K}(\xi)=0$ for $\xi>a$, and we set $\beta_n=\pm(2n\pi+\epsilon_n)$, then $\epsilon_0=0$, $\epsilon_1\sim\pi/4$, $\lim_{n\to\infty}\epsilon_n=\pi/2$ and $\alpha_n=(1/a)\log[(2n\pi+\epsilon_n)/\sin\epsilon_n]$.

This discussion indicates that all terms of the sum (15) other than $j=0$ are damped out more rapidly than the $j=0$ term, as x increases, because $\alpha_j>\alpha_0$ for $j\neq 0$. The rate of damping is inversely related to the magnitude of the maximum energy loss ξ_M. All these terms together represent the "transient."

The $j=0$ term is a constant in the absence of absorption, where $p_0=0$. Its value, which represents the *steady-*

state value of $\bar{y}(x)$, is

$$\bar{y}(x)=1\Big/\int_0^\infty \bar{K}(\xi)\xi d\xi=1/\bar{M}_1 \text{ (steady state, no absorption)}, \quad (16)$$

where

$$\bar{M}_1=\int_0^\infty \bar{K}(\xi)\xi d\xi \quad (17)$$

represents the first moment of the probability distribution $\bar{K}(\xi)$. According to (7) we have also

$$y(x)=1\Big/\int_0^\infty K(x,\xi)\xi d\xi=1/M_1(x) \text{ (steady state, no absorption)}, \quad (18)$$

with

$$M_1(x)=\int_0^\infty K(x,\xi)\xi d\xi, \quad (19)$$

whenever $K(x,\xi)=\mu(x)\bar{K}(\xi)$ is the product of $\mu(x)$ and of a function of ξ, that is, whenever the relative probability of different energy losses is independent of x. Equation (18) includes (3) and the results for neutrons and x-rays mentioned in Sec. 3*e*.

In the presence of absorption, the formulas (16), (17), (18), and (19) become:

$$\bar{y}(x)=\exp(-p_0x)\Big/\int_0^\infty \bar{K}(\xi)\exp(p_0\xi)\xi d\xi$$

$$=\exp(-p_0x)/\bar{L}_1 \text{ (steady state)}, \quad (20)$$

$$\bar{L}_1=\int_0^\infty \bar{K}(\xi)\exp(p_0\xi)\xi d\xi, \quad (21)$$

$$y(x)=\exp(-p_0x)\Big/\int_0^\infty K(x,\xi)\exp(p_0\xi)\xi d\xi$$

$$=\exp(-p_0x)/L_1(x) \text{ (steady state)}, \quad (22)$$

and

$$L_1(x)=\int_0^\infty K(x,\xi)\exp(p_0\xi)\xi d\xi. \quad (23)$$

The parameters $\bar{L}_1$ and L_1 are the first moments of the statistical distributions $\bar{K}(\xi)\exp(p_0\xi)$ and $K(x,\xi)\times\exp(p_0\xi)$, respectively. These are not the probability distributions of the "energy losses" ξ which can be experienced by the particles with "energy" x, but rather the distributions of the "energy losses" experienced in the preceding collision which had led to x. The factor $\exp(p_0\xi)$ takes into account the fact that there were $\exp(p_0\xi)$ as many particles at $x-\xi$ than at x, the balance, $\exp(p_0\xi)-1$, having been absorbed.

The procedure of this section is still applicable if the source term in the initial equation (10) is a function $s(x)$ instead of $\delta(x)$. The unit term in the transform equation (12) must be replaced by the transform of the source function, $g(p)=\int_0^\infty s(x)\exp(px)dx$. When one evaluates the inverse transform

$$\bar{y}(x)=(2\pi i)^{-1}\int_{-a-i\infty}^{-a+i\infty}\exp(-px)[1-\bar{F}(p)]^{-1}g(p)dp$$

$$=(2\pi i)^{-1}\int_{-a-i\infty}^{-a+i\infty}\exp(-px)[1-\bar{F}(p)]^{-1}dp\int_0^\infty s(x')\times\exp(px')dx', \quad (24)$$

the source strength at $x'>x$ does not contribute anything to $\bar{y}(x)$, as one would expect, that is the integral over x' is effectively limited at $0\leqslant x'\leqslant x$. This is verified by shifting the path of integration over p toward $p=-\infty$, since $\exp[p(x'-x)]$ vanishes there when $x'>x$. The separation of the steady state from the transient according to (15) is also applicable, but the transient does not become negligible unless the source strength $s(x')$ is confined to values of x' sufficiently smaller than x.

The procedure of this section is also applicable if the kernel $\bar{K}(x,\xi)$ of (8) is not constant but equal to different constant functions $\bar{K}_1(\xi)$, $\bar{K}_2(\xi)$, etc. in successive intervals $0\leqslant x\leqslant x_1$, $x_1\leqslant x\leqslant x_2$, etc. The constant kernel problem can be solved for each interval taking as a source the input of particles which are degraded from higher energy intervals. A new transient will occur at the beginning of each interval, but it will have a low amplitude if the difference of the kernels in successive intervals is small. Thus one might approach the problem of a continuous kernel variation $K(x,\xi)$ by regarding it as the limit of a succession of variations by finite steps.

5. Slowly Variable Degradation Law

The preceding results suggest that, when the degradation kernel $\bar{K}(x,\xi)$ is a slowly variable function of x, Eq. (8) should have solutions similar to individual terms of (15), $\exp(-p_jx)/\bar{L}_1$, modified by a slow variation of the parameter p_j. A form of this type is:

$$\bar{y}(j,x)\sim\exp\left[-\int^x p_j(x')dx'\right]\Big/\bar{L}_1(j,x), \quad (25)$$

$$y(j,x)\sim\exp\left[-\int^x p_j(x')dx'\right]\Big/L_1(j,x). \quad (25.1)$$

Here $\bar{L}_1$ and L_1 are given by (21) and (23), with p_j in place of p_0 and $p_j(x)$ is defined, for each value of x, as a root of the equation.

$$\int_0^\infty \bar{K}(x,\xi)\exp[p(x)\xi]d\xi=1, \quad (26)$$

or

$$\int_0^\infty K(x,\xi)\exp[p(x)\xi]d\xi=\mu(x), \quad (26.1)$$

which is analogous to (14).

This surmise is supported by the following developments. In particular, it will be shown that:

(a) For all values of $x>0$, where there is no source and the degradation equation is homogeneous, there is a set of solutions $y(j,x)$, whose form is approximately (25.1).

(b) The accuracy of each solution can be improved progressively by a procedure of successive approximations.

(c) The solutions of the homogeneous equation can be superposed, with suitable coefficients, so that

$$y(x)=\sum_j A_jy(j,x) \quad (27)$$

obeys the degradation equation (6) over the whole range of x, inclusive of the point $x=0$ where there is the source $\delta(x)$.

(d) As x increases, all terms of the $\sum_j$ in (27) with $j>0$ are rapidly damped out and the term with $j=0$ emerges as the steady-state solution.

The homogeneous equations corresponding to (8) and (6) are

$$\bar{y}(x)=\int_0^\infty \bar{K}(x-\xi,\xi)\bar{y}(x-\xi)d\xi \tag{28}$$

and

$$\mu(x)y(x)=\int_0^\infty K(x-\xi,\xi)y(x-\xi)d\xi, \tag{28.1}$$

respectively.

For purpose of orientation we consider first the case of no absorption, where $\int_0^\infty \bar{K}(x,\xi)d\xi=1$ and (26) has the solution $p_0(x)=0$. The corresponding spectral distribution of the form (26) reduces then to $\bar{y}(0,x)\sim 1/\bar{M}_1(x)$ and is, therefore, a slowly variable function of x. To determine this spectral distribution in a deductive manner, rather than by surmise, one may treat (28) by expanding $\bar{K}(x-\xi,\xi)\bar{y}(x-\xi)$ in the form $\bar{K}(x,\xi)\bar{y}(x)-\xi\partial[\bar{K}(x,\xi)\bar{y}(x)]/\partial x+\cdots$. This procedure is carried out in Appendix II. The solution $y(0,x)$ of the equation (28.1) in terms of the moments of the "degradation step size" ξ, averaged over the step-size distribution $K(x,\xi)$, i.e., in terms of

$$M_n(x)=\int_0^\infty K(x,\xi)\xi^n d\xi, \tag{29}$$

is

$$\begin{aligned} y(0,x)=(C/M_1)[1&+\tfrac{1}{2}(d/dx)(M_2/M_1)\\ &+\tfrac{1}{4}(d/dx)(M_2/M_1)(d/dx)(M_2/M_1)\\ &-\tfrac{1}{6}(d^2/dx^2)(M_3/M_1)+\cdots], \end{aligned} \tag{30}$$

where C is an undetermined integration constant.

The factor $1/M_1$ in front of the bracket coincides with (25.1), with $p_0=0$, as expected. To visualize the expression (30) as an expansion into successive orders of approximation, one may analyze the dimensions of its terms as follows. A ratio M_{n+1}/M_1 represents the mean of the nth power of the "step size" ξ averaged over the distribution $K(x,\xi)\xi$, and has the dimensions of ξ^n. The percent-variations of the ratios M_r/M_1 depend on the variations of the kernel $K(x,\xi)$, which are assumed to be small and are represented by the logarithmic derivatives of the ratios. A term of the expansion (30) which contains a total of n logarithmic differentiations-in-x, together with ratios M_r/M_1 with total dimensions ξ^n, constitutes a quantity small of the nth order. Thus, e.g., the second term within the bracket of (30) may be written in the form $\frac{1}{2}\{d[\log(M_2/M_1)]/dx\}(M_2/M_1)$ and clearly represents a first-order correction. Similarly the last two terms of (30) may be expressed by means of terms like $\{d^2[\log(M_2/M_1)]/dx^2\}(M_2/M_1)$ and represent second-order corrections.

As an illustration, consider the example: $K(x,\xi)=\mu(x)/a(x)$ for $0\leqslant\xi\leqslant a(x)$, $K(x,\xi)=0$ for $\xi>a(x)$. According to (29), $M_n(x)=\mu(x)a^n(x)/(n+1)$, and, according to (30), $y(0,x)=[2C/\mu(x)a(x)]\cdot[1+\frac{1}{3}da/dx-(1/36)d^2(a^2)/dx^2+\cdots]$.

Consider now the general case where one does not assume $p=0$ in the tentative solution (25). This case is of importance for various reasons, even though the steady-state distribution of particles corresponds ordinarily to $p=0$. In the first place the treatment of transients requires one to work with $p_j\neq 0$. Even with regard to steady states only, one may want to consider some outright absorption of particles by nuclear collisions. Moreover, in the degradation of electrons it might prove convenient to treat unusually large energy losses as separate processes which deplete the number of electrons that have experienced only small losses. Finally, the applications to two-variable problems, considered in part B and in Appendix I, introduce in effect an additional, positive or negative, absorption.

The variations of $\bar{y}(j,x)$ as a function of x need not be "slow" according to (25), when $p_j\neq 0$, unless p_j itself happens to be so small that $p_j(\xi)\ll 1$. On the other hand, p_j itself, as a solution of (26), varies only on account of variations of $\bar{K}(x,\xi)$ and can therefore be assumed to vary slowly. This argument suggests the replacement of y with a slowly varying dependent variable. This is achieved by the substitution

$$y(j,x)=\exp\left[-\int_0^x q(j,x')dx'\right], \tag{31}$$

where $q(j,x)$ need not be small and is expected to be approximately equal to the root $p_j(x)$ of (26) and to vary slowly as a function of x. The lower limit of the integral in (31) is fixed arbitrarily in such a way that $y(j,0)=1$. The treatment of the homogeneous equation (28) by means of the substitution (31) is developed in Appendix III and we give here only the results.

Whereas the solution (30) for $p=0$ is expressed in terms of the moments M_n, the general solution for $p\neq 0$ is expressed in terms of the moments

$$L_n(j,x)=\int_0^\infty K(x,\xi)\exp[p_j(x)\xi]\xi^n d\xi \tag{32}$$

of the modified distribution $K(x,\xi)\exp[p_j(x)\xi]$. L_n corresponds to M_n in the same way as the first moment L_1 of (23) corresponds to the M_1 of (19). The index j will be dispensed with whenever it is not necessary for clarity.

The calculations of Appendix III show that $q(j,x)$

is given, up to second-order corrections inclusive, by

$$q(j,x)=p_j(x)+\left\{\frac{d\log L_1}{dx}-\frac{1}{2}\frac{dp_j}{dx}\frac{L_2}{L_1}\right\}$$
$$-\frac{1}{2}\left\{\frac{d^2}{dx^2}\frac{L_2}{L_1}-\frac{dp_j}{dx}\frac{d}{dx}\left[\frac{L_3}{L_1}-\frac{3}{4}\left(\frac{L_2}{L_1}\right)^2\right]\right.$$
$$+\left(\frac{dp_j}{dx}\right)^2\left[\frac{1}{4}\frac{L_4}{L_1}-\frac{L_3}{L_1}\frac{L_2}{L_1}+\frac{1}{2}\left(\frac{L_2}{L_1}\right)^3\right]$$
$$\left.-\frac{2}{3}\frac{d^2p_j}{dx^2}\left[\frac{L_3}{L_1}-\frac{3}{4}\left(\frac{L_2}{L_1}\right)^2\right]\right\}+\cdots. \quad (33)$$

The first term, $p_j(x)$, indicates a solution of (26) or (26.1). The discussion of these solutions is the same as for the equivalent equation (14). The solution with $j=0$ is the only one which is real; all other solutions have a real part, $\alpha_j(x)$, larger than $p_0(x)$. The solution of (26) for each particular kernel $K(x,\xi)$ constitutes a special problem, which may have to be solved numerically. The terms in the two curly brackets of (33) represent the first- and second-order corrections to the zero-order value p_j, respectively. The classification of these terms according to order of approximation is given by the number of differentiations which they contain.

To obtain $y(j,x)$, one enters the expression (33) for $q(j,x)$ into the substitution (31). The terms of q which do not contain p_j explicitly can be integrated directly. The first-order term $d\log L_1/dx$ contributes to y a factor $\exp(-\log L_1)=1/L_1$. This yields just the denominator of the expression (25.1) which had been surmised to indicate the approximate form of $y(j,x)$. The second-order term $-\frac{1}{2}d^2(L_2/L_1)/dx^2$ contributes to y a factor $\exp[\frac{1}{2}d(L_2/L_1)/dx]\sim 1+\frac{1}{2}d(L_2/L_1)/dx$ which is analogous to the first-order correction term in (30). Thus, first- and second-order terms in the expansion of $q(j,x)$, yield zeroth and first-order effects on $y(j,x)$, after integration over x. In general, the integration of the "small" terms of (33) over x implies an accumulation of corrective effects from all along the course of energy degradation. Accordingly, care must be exercized in determining what approximation is required in the calculation of $q(j,x)$.

There remains now to construct a solution to the full inhomogeneous degradation equation (6) by superposing the various solutions $y(j,x)$ of the homogeneous equation with suitable coefficients A_j, as indicated in (27). To determine the A_j's we construct the solution $\bar{y}(x)=\mu(x)y(x)$ of the inhomogeneous equation (8) by an entirely different method valid only for $x\sim 0$. The degradation kernel $\bar{K}(x-\xi,\xi)$ is expanded into powers of $x-\xi$, that is, beginning with its value at $x-\xi=0$ rather than at $x-\xi=x$. The calculation, whose details are given in Appendix IV, proceeds by the method of the Laplace transform, as in Sec. 4. The result is expressed in terms of the transforms of the derivatives $[\partial^n\bar{K}(x,\xi)/\partial x^n]_{x=0}$, namely,

$$\bar{F}_n(p)=\int_0^\infty [\partial^n\bar{K}(x,\xi)/\partial x^n]_{x=0}\exp(p\xi)d\xi, \quad (34)$$

which are treated as small quantities of order n. [If $\bar{K}$ is independent of x, as in Sec. 4, $\bar{F}_n$ vanishes for $n>0$, and $\bar{F}_0(p)$ coincides with $\bar{F}(p)$ of (11).] The solution, carried to first-order corrections only, is

$$\bar{y}(x)=(2\pi i)^{-1}\int_{-a-i\infty}^{-a+i\infty}\exp(-px)[1-\bar{F}_0(p)]^{-1}$$
$$\times[1+\bar{F}_1\bar{F}_0'/(1-\bar{F}_0)^2]dp$$
$$=\sum_j\{[\exp(-px)/\bar{F}_0'][1+\tfrac{1}{2}(\bar{F}_1''/\bar{F}_0'$$
$$-\bar{F}_1'\bar{F}_0''/\bar{F}_0'^2-\tfrac{3}{2}\bar{F}_1\bar{F}_0''^2/\bar{F}_0'^3)$$
$$-(\bar{F}_1'/\bar{F}_0'-\tfrac{1}{2}\bar{F}_1\bar{F}_0''/\bar{F}_0'^2)x$$
$$+\tfrac{1}{2}(F_1/\bar{F}_0')x^2+\cdots]\}_{p=p_j}, \quad (35)$$

where the primes indicate differentiation with respect to p.

We shall now compare this expression of $\bar{y}(x)$ with the expression derived from (27) and (31), namely,

$$\bar{y}(x)=\mu(x)y(x)$$
$$=\mu(x)\sum_j A_j\exp\left[-\int_0^x q(j,x')dx'\right]. \quad (36)$$

At $x=0$ this expression reduces to $\mu(0)\sum_j A_j$ and it coincides with the corresponding value of (35) provided we set

$$A_j=[1/\mu(0)]\{(1/\bar{F}_0')[1+\tfrac{1}{2}(\bar{F}_1''/\bar{F}_0'$$
$$-\bar{F}_1'\bar{F}_0''/\bar{F}_0'^2-\tfrac{3}{2}\bar{F}_1\bar{F}_0''^2/\bar{F}_0'^3)-\cdots]\}_{p=p_j}. \quad (37)$$

The $\bar{F}$'s and their derivatives with respect to p can be expressed in terms of the L's or L's and of their derivatives with respect to x. Thereby (37) may be rewritten in the form

$$A_j=\left\{\frac{1}{L_1}\left[1+\frac{1}{2}\frac{d}{dx}\frac{L_2}{L_1}+\frac{1}{2}\frac{dp_j}{dx}\left(\frac{L_3}{L_1}+\frac{1}{2}\frac{L_2^2}{L_1^2}\right)+\cdots\right]\right\}_{x=0}. \quad (38)$$

The comparison of (36) with (35) has been extended to values of $x\neq 0$ by expanding (36) into powers of x up to x^3. The expansion is found to coincide with (35) provided A_j has the value (37). This comparison verifies the consistency of the independent calculations which lead to (33) and to (35).

6. Application to Heavy Charged Particles

As mentioned before, the formulas of the preceding section cannot be applied immediately to the slowing down of electrons but rather to protons and other heavy charged particles for which the maximum value

of ξ is small, so that the successive approximations [the successive terms of (30)] are bound to converge rapidly. This application serves to calculate corrective terms to the elementary equation (3).

Protons and other heavy charged particles are not subject to outright absorption except at high energies where the chance of head-on nuclear collisions becomes appreciable. If the absorption is disregarded, i.e. if p_0 is assumed to vanish, the steady-state term of the spectral density (27) reduces to

$$A_0 y(0, x)=\frac{1}{M_1}\left\{1+\frac{1}{2}\frac{d}{dx}\frac{M_2}{M_1}+\cdots\right\}, \tag{39}$$

taking into account (31), (33) and (38). [Notice that this expression (39) coincides with the homogeneous solution (28), as it should, provided the integration constant C of (28) is set equal to 1.]

We take $x=E_0-E$, where E is the proton energy and E_0 its initial value. The moment

$$M_1=\int_0^\infty K(x, \xi)\xi d\xi=\int_0^\infty k(E, \epsilon)\epsilon d\epsilon$$

represents the stopping power (average energy loss per unit path). Its value may be indicated as

$$M_1=(k/2E)B, \quad B=\log(\gamma E/I)^2, \tag{40}$$

where $k=2\pi NZz^2e^4M/m$; M, E, and ze are the mass, energy, and charge of the incident particle; NZ is the number of electrons per unit volume; e, m, and I are the charge, mass, and effective binding energy of the electrons in the medium; and $\gamma=4(m/M)(1+m/M)^{-2}\sim 4m/M$ is the maximum energy fraction lost in a single collision. B represents the stopping number.

The moment $M_2=\int_0^\infty K(x, \xi)\xi^2 d\xi=\int_0^\infty k(E, \epsilon)\epsilon^2 d\epsilon$ represents the mean square energy loss per unit path. From the theory of stopping power it follows that M_2 is given to a good approximation by[9]

$$M_2=(k/2E)[\gamma E+(4/3)TB], \tag{41}$$

where T indicates the mean kinetic energy of the electrons in the medium. Therefore we have

$$M_2/M_1=\gamma E/B+(4/3)T. \tag{42}$$

Taking into account the relationship between x and E, the spectral distribution (39) becomes in the energy scale,

$$n(E)=\frac{1}{M_1}\left[1-\frac{1}{2}\frac{d}{dE}\frac{M_2}{M_1}+\cdots\right]$$
$$=\frac{2E}{kB}\left[1-\frac{1}{2}\frac{\gamma}{B}+\frac{\gamma}{B^2}+\cdots\right]. \tag{43}$$

The factor in front of the brackets coincides with the elementary solution (3). The first-order corrective terms in the brackets are proportional to γ, as expected. The term γ/B^2 arises from the derivative of B, and is considerably smaller than $\frac{1}{2}\gamma/B$, since B is of the order of 10.

The corrective terms are, of course, small owing to the smallness of γ. It may be worth noticing, however, that the accuracy attained in the zero-order approximation depends on the relationship between x and E which one assumes. For example, one might take into account from the outset that the maximum *fraction* of energy lost in a collision, γ, is independent of the energy. Accordingly, the degradation kernel $\bar{K}(x, \xi)$ is more nearly energy independent if represented in a logarithmic energy scale, that is, if one takes $x=\log(E_0/E)$. This choice of x leads to a result equivalent to (43), but with the corrective term $\frac{1}{2}\gamma/B$ incorporated in the zero-order approximation $1/M_1$ (see also Appendix VII).

The corrected value (43) of $n(E)$ is a little lower than the value $2E/kB$ derived from the model of continuous slowing down. This shows that the finite size of the degradation steps effectively shortens the average track length traveled by protons of each energy. A related effect of the fluctuations of energy loss is familiar from the theory of neutron slowing down, where the mean number of collisions required for a certain degradation depends on the mean logarithmic energy loss per collision rather than on the simple mean energy loss. However, it should not be concluded here that the mean range of protons is a little shorter than expected from the model of continuous slowing down. The systematic treatment of the range distribution in Sec. 13 will show that the range shortening effect considered above is overcompensated by the chance of unusually low energy losses during the transient phase of slowing down, at energies just below the initial energy.

B. RANGE-ENERGY STRAGGLING

7. Background

The energy loss of radiations along their path in a material is subject to statistical fluctuations. This effect of "straggling" is rather small for heavy charged particles and rather large for electrons; for neutrons and x-rays the fluctuations are so large that the mean energy loss per unit path length is hardly a significant parameter.

Certain basic features of the phenomenon of straggling were established in Bohr's early theory of stopping power.[10] Among these is the fact that successive intervals of energy degradation contribute additive amounts to the mean square fluctuation of energy loss. The Bohr theory applies primarily to heavy charged particles since it regards the fluctuations as sufficiently small to be well represented by a Gaussian distribution.

[9] The inelastic collisions may be classified according to the energy Q that an atomic electron would receive if it could recoil freely. The probability of collision can then be written as $k(E, \epsilon, Q)d\epsilon dQ=(k/2E)(dQ/Q^2)|F(\epsilon, Q)|^2 d\epsilon$ where $|F(\epsilon, Q)|^2$ is the "generalized form factor." One finds from sum rules that $\int_0^\infty|F(Q, \epsilon)|^2 d\epsilon=Q$ and $\int_0^\infty|F(Q, \epsilon)|^2\epsilon^2 d\epsilon=Q^2+4QT/3$. The first of these formulas serves to calculate the stopping power M_1, the second serves to calculate M_2.

[10] N. Bohr, Phil. Mag. **30**, Series 6, 581 (1915).

In the following sections we propose to formulate a general treatment of the energy distribution of particles which have traveled a certain path length from their source and of the path length distribution of particles which have been degraded to a certain energy. Attention will be directed to the conditions under which successive intervals of energy degradation contribute additively to the straggling. The problem will be treated as a two-variable problem from the point of view outlined in Sec. 1. The treatment will rely heavily on the concepts and techniques of the energy degradation problem. Since these techniques are primarily applicable to the slowing down of heavy charged particles, the immediate application of our methods will be to verify, analyze and extend the recent results of Lewis.[11]

It is hoped that these methods will also prove useful for analyzing and developing further the work of Wilson,[12] of Blunck,[13] and of Landau and Symon,[14] on the straggling of electrons. These authors, as well as Lewis, rely on simplified representations of the collision cross sections and do not make it quite obvious how critically their results depend on the initial assumptions.

Finally, it should be noted that the study of the distribution in energy and path length finds a direct application to certain penetration problems. Whenever the penetration of radiation in a material is accompanied by only small deflections, the depth of penetration attained is approximately equal to the path length traveled. Increments of path length and increments of depth of penetration are in a ratio equal to the cosine of the angle φ between the instantaneous direction of travel and the initial direction. Approximate theories are often based on the assumption $\cos\varphi \sim 1$, which is called the "straight ahead" approximation. These theories may be regarded as theories dealing with the distribution in path length rather than with the distribution in depth.

8. The Energy-Path Length Equation and Its Laplace Transform

Consider the energy-path length distribution function $f(E, s)$ of particles or photons which have an energy E and which have traveled a path length s from their source. The distance s is to be measured along the zigzag path actually followed. If one deals with a source distributed uniformly in space and time, with a strength measured in particles emitted per unit volume and per unit time, $f(E, s)dEds$ represents the flux of particles traversing a small spherical probe of unit cross-sectional area per unit time, with energy between E and $E+dE$ and pathlength between s and $s+ds$ (see Sec. 2). If, on the contrary, one considers only the total number of particles emitted in the medium, no matter where and when, then $f(E, s)dEds$ represents the track length covered by the particles while their energy and path length lie within the specified limits, again as in Sec. 2. We shall follow the latter point of view, so that $f(E, s)dEds$ has the dimensions of a length and $f(E, s)$ the dimensions of a reciprocal energy. Accordingly, $\int_0^\infty f(E, s)dE$ is a number, the number of particles which travel at least a distance s in the course of their degradation. On the other hand, $\int_0^\infty f(E, s)ds$ coincides with the spectral density $n(E)$ of part A.

The distribution function obeys a familiar transport equation, which is formulated on the same basis as the degradation equation (1) and is

$$\partial f(E, s)/\partial s = -\mu(E)f(E, s) + \int_0^\infty k(E+\epsilon, \epsilon)f(E+\epsilon, s)d\epsilon + S(E)\delta(s), \quad (44)$$

with the boundary condition $f(E, s)=0$ for $s<0$. The Dirac function $\delta(s)$ indicates that the source constitutes the point of zero path length.

It will prove advantageous to treat the distribution function $f(E, s)$ in terms of its Laplace transform

$$\phi(E, \sigma) = \int_0^\infty \exp(\sigma s)f(E, s)ds. \quad (45)$$

(Here, as in part A, it is convenient to define the transform variable σ with a sign opposite to that of common practice.) The transform of the transport equation (44), obtained by multiplication by $\exp(\sigma s)$ and integration over s, is

$$[\mu(E)-\sigma]\phi(E, \sigma) = \int_0^\infty k(E+\epsilon, \epsilon)\phi(E+\epsilon, \sigma)d\epsilon + S(E). \quad (46)$$

This is a degradation equation of the type (1), with $\mu(E)-\sigma$ in the place of $\mu(E)$. The variable σ may be regarded as a parameter and the equation may be solved separately for different values of σ, that is, as though it were an equation with the single variable E.

By inverting the Laplace transform we represent the distribution function as

$$f(E, s) = (2\pi i)^{-1}\int_{-a-i\infty}^{-a+i\infty} \exp(-\sigma s)\phi(E, \sigma)d\sigma. \quad (47)$$

The integral

$$\int_0^\infty f(E, s)ds = \phi(E, 0) \quad (48)$$

represents the spectral distribution without reference to the path length traveled and is the solution of (46) for $\sigma=0$, i.e., of the degradation equation (1), as men-

[11] H. W. Lewis, Phys. Rev. **85**, 20 (1952).
[12] R. R. Wilson, Phys. Rev. **84**, 100 (1951).
[13] O. Blunck, Z. Physik **131**, 354 (1952).
[14] L. D. Landau, J. Phys. (U. S. S. R.) **8**, 201 (1944); K. R. Symon, Harvard thesis, 1948 (unpublished).

tioned above. Accordingly the ratio

$$f(E, s)/\phi(E, 0) \tag{49}$$

represents the *path length distribution* of all particles which happen to have the energy E.

Often one may want to consider the related distribution of the path length at which the particle *energy drops below* the value E. This distribution is

$$g(E, s) = -(d/ds)\int_E^\infty f(E', s)dE', \tag{50}$$

and its transform is

$$\Gamma(E, \sigma) = \int_0^\infty \exp(\sigma s) g(E, s) ds = \sigma \int_E^\infty \phi(E', \sigma) dE'. \tag{51}$$

The distributions (49) and (50) must tend to coincide in the limiting case of continuous slowing down (Sec. 3a). Their relationship will be discussed in the following sections.

9. Laplace Transform and the Additivity of Straggling

The representation of the distribution function by a Laplace transform serves not only to "separate" the energy and path length variables in the transport equation (46) but also to combine conveniently the effects of independent statistical fluctuations. This is a well-known method of statistics which can be illustrated by the following schematic example.

Suppose that a quantity x is the sum of two quantities x_1 and x_2, which are subject to independent statistical fluctuations. Call $f_1(x_1)$ the statistical distribution of x_1 and $f_2(x_2)$ that of x_2; call $\phi_1(\sigma)$ and $\phi_2(\sigma)$ the Laplace transforms of f_1 and f_2. The statistical distribution of $x = x_1 + x_2$ is $f(x) = \int_0^x f_1(x_1) f_2(x - x_1) dx_1$. According to the well-known "folding" theorem, which can be easily verified, the Laplace transform of $f(x)$, $\phi(\sigma)$, is simply the product of $\phi_1(\sigma)$ and of $\phi_2(\sigma)$. Thus the combination law of the independent statistical fluctuations of x_1 and x_2 takes a simple form when expressed in terms of the distribution transforms ϕ_1 and ϕ_2. The combination law can be cast in the form of an addition, corresponding to the addition of x_1 and x_2 by writing

$$\log\phi(\sigma) = \log\phi_1(\sigma) + \log\phi_2(\sigma). \tag{52}$$

Let us see how this combination law applies to the straggling of charged particles. Bohr's theory of straggling relies on the model of "continuous slowing down" (Sec. 3*a*). According to this model each particle traverses every small energy interval dE in the course of its progressive degradation. The statistical fluctuations of pathlength within different intervals dE are, of course, independent and should accordingly contribute additive amounts to $\log\phi(E, \sigma)$. This argument is formulated by writing

$$\log\phi(E, \sigma) = \int_E \varphi(E', \sigma) dE'; \tag{53}$$

$\varphi(E', \sigma)dE'$ represents the logarithm of the transform of the distribution of path lengths traveled during the degradation through dE'.

The relationship between ϕ and φ in (53) is essentially the same as that between y and $-q$ in (31), which suggests a close connection between the additivity of pathlength fluctuations and the solution of the degradation problem by the method of Sec. 5. True enough, one can always introduce the relationship (53) in a formal manner, by defining φ as the logarithmic derivative of ϕ. However, the substitution of ϕ with φ appears physically meaningful only when the value of φ for each energy interval can be calculated independently of its values in other energy intervals. Independent calculation is, in fact, achieved in Sec. 5, where $q(x)$ is given in terms of the values at x of the "moments" L_n, i.e., of the kernel $K(x, \xi)$, and of their derivatives. Therefore the path length fluctuations will be determined by adding contributions from successive energy intervals provided the transform equation can be solved by the method of Sec. 5 and the solution represented adequately by its steady-state component. In other words, the additivity of straggling hinges on the near equality of the probability laws in successive collisions and on the attainment of a steady state rather than on the model of continuous slowing down.

10. Inversion of the Laplace Transform

In general one may expect to have to solve the transform equation (46) numerically for particular values of σ. Even so, the subsequent problem of inverting the transform by means of (47) need not be very difficult. This was shown, for example, by Spencer in an analogous study of x-ray penetration.[15]

The topography of the Laplace transform on the complex plane has an important common feature in the penetration problem and in the present one, namely, that the singularities are confined to the portion of the positive real axis where $\sigma = \mu(E)$. Inspection of the transform equation (46) shows that a singularity arises when $\sigma = \mu(E)$. If the right side of (46) is finite and $\mu(E) - \sigma$ vanishes, $\phi(E, \sigma)$ becomes infinite. Furthermore, if $\phi(E, \sigma)$ is infinite for a certain value of E, this infinity will appear in the right side, under the integral, when the equation is solved for lower values of E and thereby will propagate through the rest of the degradation process. This is to say that the transform $\phi(E, \sigma)$ is singular whenever σ equals any value which μ takes in the whole energy range between E and the source energy. The smallest value of σ which leads to a singularity equals the smallest value, μ_s, of $\mu(E)$ in the range of integration. To avoid singularities σ must remain $< \mu_s$, if it is real. Owing to this topography, the steepest descent path of integration in the inverse transform (47) passes through a single saddle point to the left of $\sigma = \mu_s$.[15,16]

[15] L. V. Spencer, Phys. Rev. **88**, 793 (1952).

[16] See also U. Fano, Phys. Rev. **76**, 739 (1949) which deals with the equivalent problem of x-ray penetration in the straight-ahead approximation and a more general discussion by U. Fano, J. Research Natl. Bur. Standards **51**, 95 (1953).

As discussed by Spencer,[15] it is possible under these conditions to evaluate the inverse transform integral (47) on the basis of the values of $\phi(E,\sigma)$ for a few values of σ on both sides of the saddle point. One method of evaluation consists of approximating $\phi(E,\sigma)$ over an interval of the real axis by a suitable analytical function of σ, whose inverse transform is known. The resulting analytical function of s constitutes a good approximation to $f(E,s)$ for values of s such that the saddle point of $\exp(-\sigma s)\phi(E,\sigma)$ lies within the interval where the approximation holds.

11. Survey of the Path Length Distribution

In order to apply the technique indicated above, or any similar procedure, one must have good understanding of the topography of $\phi(E,\sigma)$, particularly on the real axis of σ. The calculation by Landau[14] of the energy straggling of charged particles after a short travel serves as an illustration of the questions which arise in this connection. This calculation is discussed in Appendix V. Examination of the transform equation (46) shows that $\phi(E,\sigma)$ diverges when $\sigma \geqslant \mu_s$, and is finite when $\mu(E)-\sigma$ remains positive for all values of E. Any decrease of σ, toward the left on the real axis, makes $\mu(E)-\sigma$ larger and therefore causes $\phi(E,\sigma)$ to decrease. In fact, not only $\phi(E,\sigma)$ but also its slope and all the higher derivatives are increasing functions of σ. This is seen by taking successive derivatives of (46) with respect to σ, which yields

$$[\mu(E)-\sigma]\phi^{(n)}(E,\sigma)=\int_0^\infty k(E+\epsilon,\epsilon)\phi^{(n)}(E+\epsilon,\sigma) + S(E)\delta_{n0}+n\phi^{(n-1)}(E,\sigma), \quad (54)$$

where $\phi^{(n)}=\partial^n\phi/\partial\sigma^n$. This equation shows that each derivative obeys the same Eq. (46) as ϕ itself but with a "source" proportional to the previous derivative. Therefore, since $\phi(E,\sigma)$ is itself positive, all its derivatives are in turn positive. Furthermore this chainwise relationship among the derivatives makes it so that successive derivatives increase more and more steeply as σ increases toward μ_s and also as the energy E decreases.

It follows that the saddle point, whose position is defined by the condition[17]

$$-\sigma s+\log\phi(E,\sigma)=\min, \quad (55)$$

or

$$\phi^{(1)}(E,\sigma)/\phi(E,\sigma)=s, \quad (56)$$

moves steadily to the right, toward $\sigma=\mu_s$, as s increases. Accordingly, the trend of the transform $\phi(E,\sigma)$ for positive σ, approaching μ_s, determines the trend of the path length distribution $f(E,s)/\phi(E,0)$ over the largest values of s, i.e., it determines the long path length tail of the distribution. Similarly, the trend of $\phi(E,\sigma)$ for negative σ, approaching $-\infty$, determines the short path length side of the distribution. The trend of $\phi(E,\sigma)$ for intermediate values of σ, near $\sigma=0$, determines the features of the middle and main part of the distribution.

[17] H. and B. S. Jeffreys, *Mathematical Physics* (Cambridge University Press, Cambridge, 1946), Chap. 17.

(a) *The Middle Portion of the Path Length Distribution*

It is widely known, and can be verified easily from (47), that the moments of a statistical distribution are equal to the derivatives of its transform, at $\sigma=0$. Thus the nth moment of the path length distribution (49), of the particles with energy E is

$$\langle s^n\rangle_E=\int_0^\infty ds s^n f(E,s)/\phi(E,0)=\phi^{(n)}(E,0)/\phi(E,0). \quad (57)$$

Similarly the nth moment of the distribution (50) pertaining to particles whose energy drops below E is

$$\langle s^n\rangle_{[E]}=\int_0^\infty ds s^n g(E,s)=\Gamma^{(n)}(E,0)=n\int_E^\infty \phi^{(n-1)}(E',0)dE'.^{18} \quad (58)$$

Notice that the mean path length $\langle s\rangle_E$ equals $\phi^{(1)}(E,0)/\phi(E,0)$. Hence, according to (56), the saddle point lies exactly at $\sigma=0$ when s equals its mean value $\langle s\rangle_E$.

In order to take advantage of the additivity of straggling, discussed in Sec. 9, we consider parameters of the statistical distribution which relate to the derivatives of $\log\phi(E,\sigma)$ rather than to the derivatives of ϕ itself. These parameters are familiar to statisticians and are called *cumulants* because of their additivity property or also "semi-invariants of Thiele."[19] They have been used by Lewis[11] to characterize the range distribution of heavy charged particles.

According to (53) the derivatives of $\log\phi$ are straggling parameters which are represented as the sum of contributions from different energy intervals,

$$\partial^n\log\phi(E,\sigma)/\partial\sigma^n=\int_E \varphi^{(n)}(E',\sigma)dE'. \quad (59)$$

The cumulants are just the values of these parameters

[18] The relationship between the moments (57) and (58) is as follows. The expression (57) is the ratio of the solutions $\phi^{(n)}$ and ϕ of the equations (54) and (46). These differ only in their source terms which are $n\phi^{(n-1)}(E,\sigma)$ and $S(E)$, respectively. On the other hand (58) may be regarded as the ratio of the integrals of the sources, since the total source strength $\int_E^\infty S(E')dE'$ is understood to equal 1. Therefore (57) relates to (58) as the ratio of two solutions of the transform equations relates to the ratio of the corresponding source strengths. This relationship is obviously very nearly an identity under steady-state conditions, as we shall verify later on.

[19] See, e.g., H. Cramér, *Mathematical Methods of Statistics* (Princeton University Press, Princeton, 1946), p. 185 ff. The relationships between the first four cumulants κ_n and the moments $\langle s^n\rangle_E$ are listed here for convenience.

$$\kappa_1=\langle s\rangle_E,\quad \kappa_2=\langle s^2\rangle-\langle s\rangle^2=\langle[s-\langle s\rangle]^2\rangle,$$

$$\kappa_3=\langle s^3\rangle-3\langle s^2\rangle\langle s\rangle+2\langle s\rangle^3=\langle[s-\langle s\rangle]^3\rangle,$$

$$\kappa_4=\langle s^4\rangle-3\langle s^2\rangle^2-4\langle s^3\rangle\langle s\rangle+12\langle s^2\rangle\langle s\rangle^2-6\langle s\rangle^4 = \langle[s-\langle s\rangle]^4\rangle-3\langle[s-\langle s\rangle]^2\rangle^2,$$

$$\langle s\rangle=\kappa_1,\quad \langle s^2\rangle=\kappa_2+\kappa_1^2,\quad \langle s^3\rangle=\kappa_3+3\kappa_2\kappa_1+\kappa_1^3,$$

$$\langle s^4\rangle=\kappa_4+3\kappa_2^2+4\kappa_3\kappa_1+6\kappa_2\kappa_1^2+\kappa_1^4.$$

for $\sigma=0$ and are usually indicated by

$$\kappa_n=[\partial^n \log\phi(E,\sigma)/\partial\sigma^n]_{\sigma=0}. \quad (60)$$

They represent, of course, the coefficients of the power-series expansion of $\log\phi(E,\sigma)$, that is of the following expansion of ϕ,

$$\phi(E,\sigma)=\phi(E,0)\exp\left(\textstyle\sum_n \kappa_n\sigma^n/n!\right).$$

In Sec. 12 we shall calculate $\phi(E,\sigma)$ by the method of Sec. 5, i.e., by means of (27), (31) and (33), for the slowing down of heavy charged particles, to which the method is applicable. The cumulants will then be given, in the main, by an integral over the derivatives of the parameter q, which coincide with the $\varphi^{(n)}$ of (59).

The corresponding calculation for electrons will have to wait until the method of Sec. 5 is suitably adapted (see Sec. 3f). The additivity property of cumulants is not easily exploited in the slowing down of x rays and neutrons. However in these cases the equation (54) for successively higher values of n can be solved in succession, by direct numerical approach (see Sec. 3*b*).

Information on the transform $\phi(E,\sigma)$ for $\sigma\sim 0$, as represented by a knowledge of a few terms of its power expansion, i.e., of a few $\phi^{(n)}(E,0)$, can be utilized in various manners to construct an approximation to the path length distribution $f(E,s)/\phi(E,0)$ (see Appendix VI).

(*b*) *The Long Path Length Tail of the Distribution*

The behavior of $\phi(E,\sigma)$ when σ approaches μ_s has been studied particularly for the equivalent problem of x-ray penetration in the straight-ahead approximation.[16] For example, in the usual case where $\mu(E)$ increases monotonically as E decreases, ϕ turns out to vary in proportion to $\mu_s-\sigma$ raised to a power of the order of -1 or -2, which depends on the logarithmic derivative of $\mu(E)$ at the source energy. The range straggling of neutrons is rather analogous to that of x-rays.

The occurrence of an unusually long path length is favored by a succession of numerous collisions with a particularly low-energy loss. The calculation of $\phi(E,\sigma)$ for σ near μ_s reflects this relationship and can take advantage of it. A positive value of σ in the transform equation (46) is equivalent to a decrease of the absorption coefficient μ. Such a decrease may be visualized as indicating an effective multiplication of the particles at every collision. Therefore the particle population of low energies grows larger as σ begins to approach μ_s. It also consists to an increasing extent of particles that have experienced a long succession of small energy losses and thus have been boosted by repeated "effective multiplication." The preference, in the region of σ near μ_s, of low energy losses as compared to large energy losses tends to improve the accuracy of calculations in this region by the method of Sec. 5 which assumes a small change of probability law from one collision to the next.

To verify this surmise, we begin the application of Sec. 5 and specifically of Eq. (26.1), which reads now:

$$\mu(E)-\sigma=\int_0^\infty k(E,\epsilon)\exp(p_0\epsilon)d\epsilon. \quad (61)$$

The parameter p_0 pertains to the steady-state solution of the transform equation (46). As σ grows positive and $\mu-\sigma$ grows small, p_0 is forced to take negative values of increasingly large magnitude. Now, the solution of the transform equation by means of (31) and (33) depends on the moments L_n of the modified distribution of energy losses $k(E,\epsilon)\exp(p_0\epsilon)$. As p_0 grows large and negative, this distribution becomes increasingly confined to small energy losses ϵ. The convergence of the approximation method of Sec. 5 depends on the smallness of moment ratios such as L_2/L_1 and will obviously improve rapidly when p_0 grows large and negative.

The solution of the problem of straight-ahead x-ray penetration[16] was in effect a resort to the zero-order approximation of Sec. 5, justified by the large negative values of p_0.

In addition, that solution took advantage of the circumstance that the differential cross section $k(E,\epsilon)$ for x-rays and neutrons varies slowly for $\epsilon\sim 0$. As a result the $\int_0^\infty k(E,\epsilon)\exp(p_0\epsilon)d\epsilon$ in (61) converges rapidly toward a limit

$$\int_0^\infty k(E,\epsilon)\exp(p_0\epsilon)d\epsilon$$

$$\sim k(E,0)\int_0^\infty \exp(p_0\epsilon)d\epsilon=-k(E,0)/p_0, \quad (62)$$

and the solution of (61) becomes

$$p_0\sim -k(E,0)/[\mu(E)-\sigma]. \quad (63)$$

This is just the result of reference 16. Its new and more general derivation points to possible improvements in the approximation.

The corresponding study for charged particles requires a different approach since $k(E,\epsilon)$ is peaked sharply at $\epsilon\sim 0$. For particles that have lost only a small fraction of their total energy, the answer is provided by the Landau theory[14] (see Appendix V). For larger energy losses, this study may be of minor importance in so far as excessively long path lengths of charged particles, and especially of heavy particles, are quite unlikely and their distribution might be determined rather well by the behavior of $\phi(E,\sigma)$ near $\sigma=0$.

(*c*) *The Short Path Length Tail of the Distribution*

The trend of $\phi(E,\sigma)$ for σ negative and large corresponds to the probability distribution of unusually short path lengths. It depends on the occurrence of an

unusually large proportion of collisions with large energy losses. No general analysis of this problem has been given. For x-rays and neutrons this problem is not of great interest. For heavy or light charged particles that have lost a small fraction of their energy, it is solved by the Landau theory.[14] For heavy charged particles that have lost much energy, extreme fluctuations of this kind are unlikely and the tail of the distribution can be predicted by the behavior of $\phi(E,\sigma)$ near $\sigma=0$ as was done by Symon[14] (see Appendix V).

12. Calculation of the Cumulants

We propose here to calculate the cumulants of the path length distribution, i.e., the parameters

$$\kappa_n=[\partial^n \log\phi/\partial\sigma^n]_{\sigma=0} \tag{64}$$

of Sec. 11*a*, under the assumption of a slowly variable degradation law, i.e., by the approximation method of Sec. 5. This method, in its present form, yields results which are applicable primarily to the slowing down of heavy charged particles.

In order to maintain flexibility in the choice of the energy scale and to utilize the formulas of part *A*, we proceed as in *A*, Sec. 3*f*, and represent the energy by a variable x, such that $x=0$ at a fixed source energy, $E=E_0$. The transform equation (46) will be written here in a form analogous to (6), namely

$$[\mu(x)-\sigma]y(x,\sigma)=\int_0^\infty K(x-\xi,\xi)y(x-\xi,\sigma)+\delta(x), \tag{65}$$

where $y(x,\sigma)dx=\phi(E,\sigma)dE$. Since dE/dx is independent of σ, the cumulants are given by

$$\kappa_n=[\partial^n \log y(x,\sigma)/\partial\sigma^n]_{\sigma=0}. \tag{66}$$

The solution of (65), for any particular value of σ, is given by (31) and (27) in the form

$$y(x,\sigma)=\textstyle\sum_j A_j(\sigma)\exp\left[-\int_0^x q(j,x',\sigma)dx'\right]. \tag{67}$$

Confining ourselves to the steady-state term, $j=0$, which is permissible whenever x is much larger than its maximum change in a single collision, we take

$$y(x,\sigma)=A_0(\sigma)\exp\left[-\int_0^x q(0,x',\sigma)dx'\right]$$

(steady state). (68)

Dropping from now on the index $j=0$, we write

$$\log y(x,\sigma)=\log A(\sigma)-\int_0^x q(x',\sigma)dx'$$

and

$$\kappa_n=[\partial^n \log A(\sigma)/\partial\sigma^n]_{\sigma=0}-\int_0^x q^{(n)}(x')dx$$

(steady state), (69)

where $q^{(n)}=[\partial^n q/\partial\sigma^n]_{\sigma=0}$.

The parameters q and A are given, in turn, by the successive approximation formulas (33) and (38) in terms of still other parameters, p and L_n. Like q and A, p and the L_n's should be calculated, in principle, for each value of σ. However, the cumulants κ_n which we want to calculate are coefficients of the expansion of $\log y(x,\sigma)$ into powers of σ. Therefore we seek here the expansion of each parameter (p, L_n, q and A) into powers of σ. This problem is straightforward but its solution is algebraically complicated since it involves a double expansion, into powers of σ and into orders of approximation of the procedure of Sec. 5.

The expansion of $p(x,\sigma)$ may be written as

$$p(x,\sigma)=\textstyle\sum_n p^{(n)}(x)\sigma^n/n!. \tag{70}$$

Since $p(x,\sigma)$ itself—the zero-order approximation value of $q(x,\sigma)$—has to be determined by solving Eq. (26.1),

$$\mu(x)-\sigma=\int_0^\infty K(x,\xi)\exp[p(x,\sigma)\xi]d\xi=L_0(\xi), \tag{71}$$

the coefficients $p^{(n)}(x)$ of (70) are to be found through the expansion of (71) into powers of σ. To begin with, the expansion of the factor $\exp[p(x,\sigma)\xi]$ yields[20]

$$\begin{aligned}&\exp[p(x,\sigma)\xi]\\&=\exp[p^{(0)}(x)\xi]\exp[\textstyle\sum_{n>0} p^{(n)}(x)\xi\sigma^n/n!]\\&=\exp[p^{(0)}(x)\xi]\{1+\sigma p^{(1)}\xi+\tfrac{1}{2}\sigma^2[p^{(2)}\xi+p^{(1)2}\xi^2]\\&\quad+\tfrac{1}{6}\sigma^3[p^{(3)}\xi+3p^{(2)}p^{(1)}\xi^2+p^{(1)3}\xi^3]+\cdots\}.\end{aligned} \tag{72}$$

From this expansion we derive the expansion of the L_n's by multiplying each side of (72) by $K(x,\xi)\xi^n$ and integrating over ξ. There result integrals of the type $\int_0^\infty K(x,\xi)\exp[p^{(0)}(x)\xi]\xi^n d\xi$. These integrals have the same form as the L_n's, but with $p^{(0)}$ in the place of p. They are the L_n values for $\sigma=0$, i.e., the L_n values pertaining to the simple degradation process, irrespective of path length distribution. Accordingly they will be indicated as $L_n{}^{(0)}(x)$.

$$\begin{aligned}L_n(x)=L_n{}^{(0)}&+\sigma p^{(1)}L_{n+1}{}^{(0)}\\&+\tfrac{1}{2}\sigma^2[p^{(2)}L_{n+1}{}^{(0)}+p^{(1)2}L_{n+2}{}^{(0)}]\\&+\tfrac{1}{6}\sigma^3[p^{(3)}L_{n+1}{}^{(0)}+3p^{(2)}p^{(1)}L_{n+2}{}^{(0)}\\&\qquad+p^{(1)3}L_{n+3}{}^{(0)}]+\cdots.\end{aligned} \tag{73}$$

The expansion of Eq. (71), which determines the $p^{(n)}$'s, results when the expansion (73) of L_0 is entered

[20] Each of the expressions in the brackets that multiply σ^2, $\sigma^3\cdots$ has the same structure as the expression in the footnote (17) which gives $\langle s^2\rangle$, $\langle s^3\rangle\cdots$ in terms of the cumulants κ_1, $\kappa_2\cdots$, with $p^{(n)}\xi$ in the place of κ^n. If $\exp[\Sigma_{n>0} p^{(n)}\xi\sigma^n/n!]=\Sigma_{\nu\geq 1}B_\nu\sigma^\nu/\nu!$, the coefficients B_ν are determined in the following manner. Consider all the partitions of the number ν, which are represented by a set of numbers ν_r such that $\Sigma_{r=1}^{\nu} r\nu_r=\nu_1+2\nu_2+\cdots=\nu$. For example, for $\nu=4$ the sets of ν_r's are (4000), (2100), (0200), (1010), (0001). We find that

$$B_\nu=\sum_{\text{all partitions}}\nu!\prod_r\frac{1}{\nu_r!}\left(\frac{p^{(r)}}{r!}\xi\right)^{\nu_r}.$$

into (71):

$$\mu(x)-\sigma=L_0^{(0)}+\sigma p^{(1)}L_1^{(0)}+\tfrac{1}{2}\sigma^2[p^{(2)}L_1^{(0)}+p^{(1)2}L_2^{(0)}]+\tfrac{1}{6}\sigma^3[p^{(3)}L_1^{(0)}+3p^{(2)}p^{(1)}L_2^{(0)}+p^{(1)3}L_3^{(0)}]+\cdots. \quad (74)$$

Separating out the groups of terms with the same power of σ, we obtain the set of equations:

$$L_0^{(0)}=\mu(x), \quad L_1^{(0)}p^{(1)}=-1,$$
$$L_1^{(0)}p^{(2)}+L_2^{(0)}p^{(1)2}=0, \quad (75)$$
$$L_1^{(0)}p^{(3)}+3L_2^{(0)}p^{(2)}p^{(1)}+L_3^{(0)}p^{(1)3}=0.$$

The first of these equations,

$$L_0^{(0)}(x)=\int_0^\infty K(x,\xi)\exp[p^{(0)}(x)\xi]d\xi=\mu(x),$$

is the equation (2.61) pertaining to the simple degradation process. From the standpoint of the path length distribution problem we regard this equation as solved in advance. (In the absence of absorption, $p_0=0$, of course.) If $p^{(0)}(x)$ is regarded as known, all the $L_n^{(0)}$ are known as well.

From this point on, the successive equations (75) yield the successive parameters $p^{(n)}(x)$ in terms of the moments $L_n^{(0)}(x)$, and one finds

$$\begin{aligned}
p^{(1)}(x)&=-1/L_1^{(0)},\\
p^{(2)}(x)&=-L_2^{(0)}/(L_1^{(0)})^2,\\
p^{(3)}(x)&=L_3^{(0)}/(L_1^{(0)})^4-3(L_2^{(0)})^2/(L_1^{(0)})^5,\\
p^{(4)}(x)&=-L_4^{(0)}/(L_1^{(0)})^5+10L_3^{(0)}L_2^{(0)}/(L_1^{(0)})^6\\
&\qquad -15(L_2^{(0)})^3/(L_1^{(0)})^7,\\
p^{(5)}(x)&=L_5^{(0)}/(L_1^{(0)})^6-[15L_4^{(0)}L_2^{(0)}+10L_3^{(0)}]^2/(L_1^{(0)})^7\\
&\quad +105L_3^{(0)}(L_2^{(0)})^2/(L_1^{(0)})^8-105(L_2^{(0)})^4/(L_1^{(0)})^9.
\end{aligned} \quad (76)$$

The expression (69) of the cumulants κ_n is obtained in zero-order approximation, by replacing $q^{(n)}$ with its zero-order value $p^{(n)}$ given by (76). Here one may disregard $[\partial^n \log A/\partial\sigma^n]_{\sigma=0}$, since this term yields only a first-order correction as shown further below. Thus we write

$$\kappa_n(x)\sim-\int_0^x p^{(n)}(x')dx'. \quad (77)$$

The values thus obtained are those which measure the straggling according to the model of "continuous slowing down."

To obtain the higher order approximations of κ_n one must now take Eqs. (33) for $q(x)$ and (38) for A and expand them into powers of σ, utilizing the expansion (73) of the L_n's. This procedure is tedious but straightforward. We give here only the values of $q^{(1)}(x)$ and of $[\partial \log A/\partial\sigma]_{\sigma=0}$, calculated to first-order corrections inclusive:

$$\begin{aligned}
q^{(1)}(x)&=-\frac{1}{L_1^{(0)}}\left\{1+\left[\frac{d}{dx}\frac{L_2^{(0)}}{L_1^{(0)}}-\frac{1}{2}\frac{d\log L_1^{(0)}}{dx}\frac{L_2^{(0)}}{L_1^{(0)}}\right.\right.\\
&\qquad\left.\left.-\frac{dp^{(0)}}{dx}\left(\frac{L_3^{(0)}}{L_1^{(0)}}-\frac{(L_2^{(0)})^2}{(L_1^{(0)})^2}\right)\right]+\cdots\right\}\\
&=-\frac{1}{L_1^{(0)}}\left\{1+\left[\frac{1}{2}\frac{d}{dx}\frac{L_2^{(0)}}{L_1^{(0)}}\right.\right.\\
&\qquad\left.\left.-\frac{dp^{(0)}}{dx}\left(\frac{L_3^{(0)}}{L_1^{(0)}}-\frac{(L_2^{(0)})^2}{(L_1^{(0)})^2}\right)\right]+\cdots\right\}\\
&\qquad -\frac{1}{2}\frac{d}{dx}\frac{L_2^{(0)}}{(L_1^{(0)})^2}+\cdots;
\end{aligned} \quad (78)$$

$$\left[\frac{\partial \log A}{\partial\sigma}\right]_{\sigma=0}=\left[\frac{L_2^{(0)}}{(L_1^{(0)})^2}-\frac{1}{2}\frac{d}{dx}\left(\frac{L_3^{(0)}}{(L_1^{(0)})^2}-\frac{(L_2^{(0)})^2}{(L_1^{(0)})^3}\right)+\cdots\right]_{x=0}. \quad (79)$$

The value of the first cumulant κ_1 is given by (69), which combines the two formulas (78) and (79)[21] into

$$\begin{aligned}
\kappa_1(x)=\langle s\rangle_x&=\left(\frac{L_2^{(0)}}{(L_1^{(0)})^2}\right)_{x=0}\\
&\quad+\int_0^x\frac{dx'}{L_1^{(0)}(x')}\left\{1+\left[\frac{1}{2}\frac{d}{dx'}\frac{L_2^{(0)}}{L_1^{(0)}}\right.\right.\\
&\qquad\left.\left.-\frac{dp^{(0)}}{dx'}\left(\frac{L_3^{(0)}}{L_1^{(0)}}-\frac{(L_2^{(0)})^2}{(L_1^{(0)})^2}\right)\right]+\cdots\right\}\\
&\quad+\frac{1}{2}\left(\frac{L_2^{(0)}}{(L_1^{(0)})^2}\right)_x-\frac{1}{2}\left(\frac{L_2^{(0)}}{(L_1^{(0)})^2}\right)_{x=0}+\cdots.
\end{aligned} \quad (80)$$

The significance of the various terms of this expression may be illustrated by comparing it with the expression for the related mean path length,

$$\langle s\rangle_{[E]}=\int_E^\infty\phi(E',0)dE'=\int_0^x y(x',0)dx', \quad (81)$$

of Eq. (58). We assume here absence of absorption, i.e., $p^{(0)}=0$ and $L_n^{(0)}=M_n$. Under these conditions, the integrand of (80), $(1/M_1)\{1+\frac{1}{2}d(M_2/M_1)dx+\cdots\}$ represents the steady-state value of $y(x',0)$ in (81), according to (30). The sum of the first and the last term of (80), namely, $\frac{1}{2}(M_2/M_1^2)_{x=0}$ can be shown to equal the integral of the transient terms of $y(x',0)$, which are appreciable only for $x\sim0$.[22] The remaining term of (80), $\frac{1}{2}(L_2^{(0)}/(L_1^{(0)})^2)_x$

[21] Only the zero-order term of $[\partial \log A/\partial\sigma]_{\sigma=0}$ has been carried, because the next term has an effect comparable to that of the second-order terms of $q^{(1)}$.

[22] To evaluate $\int_0^x y(x',0)dx'$ in (81) correctly in the range $x\sim0$ one can use the solution (35) valid in this range and carry out the integration over x before the integration over p. The error that would have been made by integrating over p first and then discarding the transient terms is seen to equal $\frac{1}{2}[L_2^{(0)}/(L_1^{(0)})^2]_{x=0}$. See also the treatment at the end of Appendix VII.

does not appear in the evaluation of (81) and therefore represents the true difference between the mean path lengths $\langle s\rangle_E$ and $\langle s\rangle_{[E]}$. Notice that the corrective terms,

$$[L_2^{(0)}/(L_1^{(0)})^2]_{x=0}-\tfrac{1}{2}[L_2^{(0)}/(L_1^{(0)})^2]_{x=0}=\tfrac{1}{2}[L_2^{(0)}/(L_1^{(0)})^2]_{x=0}$$

and $\frac{1}{2}[L_2^{(0)}/(L_1^{(0)})^2]_x$, are approximately equal to $\int dx'/L_1^{(0)}$ extended respectively, over one half-interval of $L_2^{(0)}/L_1^{(0)}$ at $x=0$ and over a similar interval at x. The ratio $L_2^{(0)}/L_1^{(0)}$ represents one "step of degradation." Therefore one may visualize the value (80) of the cumulant as equal to the integral of the steady-state value of $y(x',0)$ from 0 to x, plus one half-step of degradation at the beginning of the degradation and one half-step at the end. These corrections represent effects of the discontinuity of the process of degradation.

13. Application to Heavy Charged Particles. Comparison with the Lewis Results

The formulas of the preceding section can be applied directly to the calculation of the mean path length and of the straggling of heavy charged particles. As in the application of the formulas on spectral distribution, we assume that there is no true absorption, so that $p^{(0)}(x)=0$ and $L_n^{(0)}(x)=M_n(x)$. We also choose $x=E_0-E$.

The first moment M_1, that is, the stopping power, will be indicated by $(k/2E)B$, as in (40). The higher moments can be shown to be, approximately

$$M_n\sim\tfrac{1}{2}k\gamma^{n-1}E^{n-2}/(n-1). \tag{82}$$

This approximation disregards corrective terms of the order of the atomic binding energy divided by the maximum energy loss in a collision, γE. [The second term in the bracket of (41), which constitutes a correction $4T/3B\gamma E$, is an example of the terms disregarded in (82).] These assumptions about the M's rely on the ordinary, nonrelativistic, theory of stopping power. Improved formulas may be entered in the theory without any additional difficulty.

The Bohr theory[10] of the mean range and of the mean square straggling may be described here as a calculation of the first and second cumulant in zero-order approximation. It utilizes (77), that is,

$$\kappa_n(E=0)\sim-\int_0^{E_0}p^{(n)}(E_0-E)dE, \tag{83}$$

with the values of $p^{(1)}$ and $p^{(2)}$ from (74). Blunck[12] gives also the formulas for κ_3 and κ_4.

An explicit calculation of the cumulants up to κ_5 in this approximation has been carried out by Lewis.[11] The Lewis results can be derived by entering the values (76) of $p^{(n)}$ into (83), substituting the M_n values (81) in place of the $L_n^{(0)}$ and performing the integration over the energy. If the stopping number B is regarded as constant (as in the Lewis "simplified problem") one obtains the Lewis formula (L23),[23] with B and γ in the place of Lewis' A_1 and ϵ_1. If the dependence of B on the energy is taken into account, one obtains (L23.1).

Lewis also introduced a new notion in the theory of the mean range, namely the need for a correction of the order of $\gamma\sim m/M$, which amounts to a fraction of 1 percent for μ mesons. The Lewis correction should appear in the present treatment as a first-order correction. According to (80) the "mean range," i.e., the mean path length of particles with no remaining energy, is

$$\begin{aligned}\kappa_1(0)=\langle s\rangle_0&=\frac{1}{2}\left(\frac{M_2}{M_1^2}\right)_{E=E_0}\\&+\int_0^{E_0}\frac{dE}{M_1}\left\{1-\frac{d}{dE}\frac{M_2}{M_1}+\cdots\right\}+\frac{1}{2}\left(\frac{M_2}{M_1^2}\right)_{E=0}\\&=\frac{\gamma E_0^2}{kB^2}+\int_0^{E_0}\frac{2EdE}{kB}\left\{1-\frac{1}{2}\frac{\gamma}{B}+\frac{\gamma}{B^2}+\cdots\right\}.\end{aligned} \tag{84}$$

The last term in the middle expression vanishes at $E=0$. Otherwise it would have to be discounted in the comparison with the Lewis theory, since Lewis calculates the mean $\langle s\rangle_{[0]}$, according to (58), instead of $\langle s\rangle_0$. The comparison must be made at $E=0$ because the Lewis theory deals only with the path length for zero energy.

The Lewis formula for the mean range (L20) is $\langle R\rangle=\int_0^{E_0}2EdE/kA_1$, where $A_1=B-\frac{1}{2}\gamma$.[24] If A_1 is expanded into powers of γ, $\langle R\rangle=\int_0^{E_0}(2EdE/kB)\times(1+\frac{1}{2}\gamma/B+\cdots)$. The discrepancy in sign between the correction term in this formula and the term γ/B in the curly bracket of (84) is compensated by the term in front of the integral of (84), whose value is $\int_0^{E_0}(2EdE/kB)(\gamma/B-2\gamma/B^2)$. However, the term γ/B^2 of (84) has no counterpart in the Lewis treatment. This discrepancy is small, since $(\gamma/B^2)/(\gamma/B)=1/B\sim0.1$, but real. The corrective terms γ/B^2 arise from the derivative of B which is disregarded by Lewis.[25]

A further discussion of the Lewis theory is given in Appendix VII.

ACKNOWLEDGMENTS

It is a pleasure to acknowledge the help of Dr. C. H. Blanchard and Dr. L. V. Spencer in extensive discussions throughout this work and in the revision of the manuscript. I also wish to thank Professor H. A. Bethe for his continued interest in this program and especially for a very helpful discussion in the Fall of 1951.

[23] The Lewis equation numbers will be accompanied by the letter L. The coefficient 230 in β_5 of (L23) should apparently be replaced with 210. Notice also that B does not quite coincide with Lewis' $A_1=B-\frac{1}{2}\gamma$ nor does γ coincide with $\epsilon_1=\gamma(1-\gamma)$. However this difference is immaterial in the zero-order approximation. It does not seem consistent for Lewis to regard A_1 as different from B in this calculation, since terms of the order of ϵ have been disregarded in his derivation of (L23).

[24] In Lewis's notation γ and B are called ϵ and $\log(\epsilon/\delta)$. The value of A_1 given by Lewis is equal to $\log(\epsilon/\delta)+\epsilon/2$ and appears to be incorrect, possibly because of confusion between his symbols ϵ and ϵ_1. The final statement that the range is lengthened by a factor $1+3\epsilon_1/2\log(\epsilon/\delta)+\cdots$ seems to be incorrect for the same reason, since the stopping number in the Bohr formula is $B=2\log(\epsilon E/I)$ as shown in (L2) and not $2\log(\epsilon_1E/I)$.

[25] Lewis begins by treating a "simplified problem" in which B is regarded as constant and then allows for the variation of B only *after* having obtained the formula $\langle R\rangle=\int_0^{E_0}2EdE/k(B-\frac{1}{2}\gamma)$.

APPENDIX I. DISTRIBUTION IN DIRECTION AND ENERGY

Suppose that particles or photons diffuse in a medium under the conditions of Sec. 2 and that the source is nonisotropic, though with cylindrical symmetry. The angle between a direction ω and the axis of symmetry will be indicated by ϑ. The number of particles emitted with energy between E and $E+dE$ and with obliquity between ϑ and $\vartheta+d\vartheta$ will be indicated by $S(E, \vartheta)dE2\pi \times \sin\vartheta d\vartheta$. The track length of particles in the same energy range and in the same range of obliquity will be called $N(E, \vartheta)dE2\pi \sin\vartheta d\vartheta$. The probability per unit track of a collision with energy loss from ϵ to $\epsilon+d\epsilon$ and with a deflection of Θ to $\Theta+d\Theta$ will be called $k(E, \epsilon, \cos\Theta)d\epsilon 2\pi \sin\Theta d\Theta$. (This probability includes elastic scattering, for which $\epsilon=0$.)

The degradation and deflection equation is:

$$\mu(E)N(E, \vartheta)=\int_0^\infty d\epsilon \int_{4\pi} d\omega' k(E+\epsilon, \epsilon, \omega\cdot\omega') \times N(E+\epsilon, \vartheta')+S(E, \vartheta). \quad (85)$$

The source distribution, the scattering probability, and the particle distribution will be represented by Legendre polynomial expansions:

$$S(E, \vartheta)=\sum_l (2l+1)S_l(E)P_l(\cos\vartheta)/4\pi, \quad (86)$$

$$k(E, \epsilon, \cos\Theta)=\sum_l (2l+1)k_l(E, \epsilon)P_l(\cos\Theta)/4\pi, \quad (87)$$

$$N(E, \vartheta)=\sum_l (2l+1)N_l(E)P_l(\cos\vartheta)/4\pi. \quad (88)$$

It is well known that this expansion effectively separates the variables, as long as the kernel k depends only on $\cos\Theta=\omega\cdot\omega'$ and not on ω and ω' separately. For example if the source is isotropic the distribution will remain isotropic; if the source were distributed like $P_1(\cos\vartheta)=\cos\vartheta$, the particles would also be distributed in this manner. Multiplication of Eq. (85) by $P_l(\cos\vartheta)$ and integration over all directions ω yields the set of equations

$$\mu(E)N_l(E)=\int_0^\infty d\epsilon\, k_l(E+\epsilon, \epsilon)N_l(E+\epsilon)+S_l(E). \quad (89)$$

The equations with different values of l can be solved independently of one another. Each of the equations has the same form as (1) and can be treated accordingly. The equation with $l=0$ is identical with (1) and $N_0(E)$ with $n(E)$ of Sec. 2.

One difference, which may be important at times, is the fact that neither $N_l(E)$ nor $k_l(E, \epsilon)$ need be positive for $l\neq 0$. Each distribution $N_l(E)$ has no physical reality *per se*, since it corresponds to a source distribution P_l which is negative in some directions and therefore unrealistic. The discussion of the roots of (14) given in Sec. 4 hinges on the fact that $K(\xi)$ is positive. No study of the more general problem with a nonpositive K seems to have been made yet.

Spencer and Jenkins[3] solved the set (89) for x-ray degradation up to $l=5$, by the direct method of Sec. 3*b*. There was formerly some feeling that the breakdown of the problem in terms of Legendre coefficients, as in (89), is convenient only in the absence of peaked angular distributions, i.e., when only a few N_l's are significant. However it has become apparent that one can also handle long sequences of Legendre coefficients provided their values vary smoothly with l. For example, the Molière theory of multiple electron scattering[26] takes advantage, in essence, of the independence of the different Legendre coefficients and replaces the Σ_l in (88) with an integration. A procedure to carry out the Σ_l when many terms are important has recently been developed by Spencer.[27]

When the directional distribution of particles is peaked sharply at the source, it becomes progressively smeared out by multiple scattering. The smearing out is described, in the Legendre polynomial representation, by a damping of the coefficients N_l, for $l>0$, in the course of degradation. The larger l, the faster is the damping. This picture has been developed particularly in treatments where the directional distribution is considered as a function of the pathlength traversed.[28] Since the cross sections are functions of the energy, rather than of the path length, the formulation given here is a little more appropriate. A more complete treatment would combine the procedure of this appendix and of part *B* to give a combined distribution in energy, direction and path length.

The damping of the Legendre coefficients $N_l(E)$ comes about as follows. According to (9), $\int_0^\infty k_0(E, \epsilon)d\epsilon \leqslant \mu(E)$. Moreover, since $k(E, \epsilon, \cos\Theta)$ is non-negative, $k_l(E, \epsilon)=2\pi\int_0^\infty k(E, \epsilon, \cos\Theta)P_l(\cos\Theta)\sin\Theta d\Theta \leqslant k_0(E, \epsilon)$, for $l\neq 0$, owing to the oscillations of $P_l(\cos\Theta)$ which become increasingly rapid as l increases. Therefore the integral $\int_0^\infty k_l(E, \epsilon)d\epsilon$ over the kernel of (89) amounts to a smaller and smaller fraction of $\mu(E)$ as l increases and the solution p of Eq. (26.1), $\mu(E)=\int_0^\infty k_l(E, \epsilon) \times \exp(p\epsilon)d\epsilon$, tends to become large and positive. The value of p determines the damping of the solution of (89), $N_l(E)$, in the course of degradation.

APPENDIX II. CALCULATION OF THE STEADY STATE IN ABSENCE OF ABSORPTION

We wish to solve the equation

$$\bar{y}(x)=\int_0^\infty \bar{K}(x-\xi, \xi)\bar{y}(x-\xi)d\xi \quad (28)$$

with $\int_0^\infty \bar{K}(x, \xi)d\xi=1$, assuming that both $\bar{K}$ and $\bar{y}$

[26] G. Molière, Z. Naturforsch **3a**, 78 (1948). See particularly the derivation by H. W. Lewis, Phys. Rev. **78**, 526 (1950) and by H. A. Bethe, Phys. Rev. **89**, 1256 (1953).

[27] L. V. Spencer, Phys. Rev. **90**, 146 (1953); also L. V. Spencer and C. H. Blanchard, Phys. Rev. (to be published).

[28] See, e.g., S. Goudsmit and J. L. Saunderson, Phys. Rev. **57**, 24 (1940); **58**, 36 (1940), H. W. Lewis, reference 26, and also C. H. Blanchard and U. Fano, Phys. Rev. **82**, 767 (1951).

are slowly variable functions of x. In view of this assumption we utilize the expansion

$$\bar{K}(x-\xi,\xi)\bar{y}(x-\xi)=\sum_{n=0}^{\infty}\frac{(-\xi)^n}{n!}\frac{\partial^n}{\partial x^n}\bar{K}(x,\xi)\bar{y}(x). \quad (90)$$

This expansion reduces (28) to the form

$$\bar{y}(x)=\sum_n(-d/dx)^n[\bar{M}_n(x)\bar{y}(x)]/n!, \quad (91)$$

where $\bar{M}_n=\int_0^\infty \bar{K}(x,\xi)\xi^n d\xi$, according to (29). The $\bar{y}(x)$ on the left side cancels with the $n=0$ term on the right, since $\bar{M}_0=1$. Integration of (91) yields

$$\sum_{n=0}(-d/dx)^n[\bar{M}_{n+1}(x)\bar{y}(x)]/(n+1)!=C, \quad (92)$$

where C is an integration constant.

In a zero-order approximation one would disregard all derivatives and consider only the term $n=0$ in the sum. A procedure of successive approximations may be established by writing

$$\bar{y}(x)=\bar{y}_0(x)+\bar{y}_1(x)+\bar{y}_2(x)+\cdots, \quad (93)$$

with the understanding that the rth term of the expansion, $\bar{y}_r$, is small of the rth order, i.e., that it contains r differential factors. This expansion brings (92) to the form

$$\sum_n\sum_r(-d/dx)^n[\bar{M}_n(x)\bar{y}_r(x)]/(n+1)!=C. \quad (94)$$

Since $\bar{y}_r$ contains r differentiations, the total number of differentiations in each term of (94) is $n+r$. The procedure of successive approximations requires that (94) be fulfilled separately by each group of terms with the same value of $n+r$. Thereby (94) separates out into the set of equations:

$$\begin{aligned}
&\bar{M}_1\bar{y}_0=C, \quad (n+r=1),\\
&\bar{M}_1\bar{y}_1-\tfrac{1}{2}(d/dx)(\bar{M}_2\bar{y}_0)=0, \quad (n+r=2),\\
&\bar{M}_1\bar{y}_2-\tfrac{1}{2}(d/dx)(\bar{M}_2\bar{y}_1)+\tfrac{1}{6}(d/dx)^2(\bar{M}_3\bar{y}_0)=0,\\
&\qquad\qquad (n+r=3).\\
&\cdots\cdots\cdots\cdots\cdots
\end{aligned} \quad (95)$$

The first equation yields $\bar{y}_0$, the second $\bar{y}_1$, etc., and the resulting expressions, when entered in (93), give

$$\begin{aligned}
\bar{y}(x)=&\frac{C}{\bar{M}_1}+\frac{1}{2}\frac{1}{\bar{M}_1}\frac{d}{dx}\bar{M}_2\frac{C}{\bar{M}_1}+\frac{1}{4}\frac{1}{\bar{M}_1}\frac{d}{dx}\frac{\bar{M}_2}{\bar{M}_1}\frac{d}{dx}\bar{M}_2\frac{C}{\bar{M}_1}\\
&-\frac{1}{6}\frac{1}{\bar{M}_1}\frac{d^2}{dx^2}\bar{M}_3\frac{C}{\bar{M}_1}+\cdots.
\end{aligned} \quad (96)$$

Since $\bar{M}_n/\bar{M}_{n'}=M_n/M_{n'}$, Eq. (96) reduces to the expression (30) for $y(x)$, when divided by $\mu(x)$.

APPENDIX III. CALCULATION OF SOLUTIONS OF THE HOMOGENEOUS EQUATION

We wish to solve Eq. (28),

$$\bar{y}(x)=\int_0^\infty \bar{K}(x-\xi,\xi)\bar{y}(x-\xi)d\xi,$$

without assuming that $\bar{y}(x)$ varies slowly. The equation may be written by means of operator symbols in the form

$$\bar{y}(x)=\int_0^\infty \exp[-\xi d/dx]\bar{K}(x,\xi)\bar{y}(x)d\xi. \quad (97)$$

The substitution (31), $\bar{y}(x)=\exp[-\int_0^x q(x')dx']$, is such that $(d/dx)\bar{y}(x)=\bar{y}(x)[(d/dx)-q(x)]$ and, therefore,

$$\exp[-\xi d/dx]\bar{y}(x)=\bar{y}(x)\exp\{\xi[q(x)-d/dx]\}. \quad (98)$$

In this manner $\bar{y}(x)$ can be factored out of (97), which reduces to

$$\int_0^\infty \exp\{\xi[q(x)-d/dx]\}\bar{K}(x,\xi)d\xi=1. \quad (99)$$

We wish to set up a procedure of approximation in which $q(x)$ and $\bar{K}(x,\xi)$ are regarded as varying slowly with x. To this end we must expand the exponential operator of (99) into powers of the differential operator d/dx. The Feynman operator calculus[29] yields the expansion formula

$$\begin{aligned}
\exp(\alpha+\beta)=&\exp\alpha+\int_0^1\exp[(1-s)\alpha]\beta\exp(s\alpha)ds\\
&+\int_0^1 ds\int_0^s ds'\exp[(1-s)\alpha]\beta\\
&\times\exp[(s-s')\alpha]\beta\exp(s'\alpha)+\cdots.
\end{aligned} \quad (100)$$

In our problem, $\alpha=\xi q(x)$ and $\beta=-\xi d/dx$ and the commutator of β and $\exp[(1-s)\alpha]$ is independent of β. Therefore β may be shifted everywhere to the left of α, after which the integrals in (100) reduce to ordinary integrals. This procedure gives

$$\begin{aligned}
&\exp\left\{\xi\left[q(x)-\frac{d}{dx}\right]\right\}\\
&=\left\{1-\xi\left[\frac{d}{dx}-\xi\frac{dq}{dx}\right]+\frac{1}{2}\xi^2\left[\frac{d^2}{dx^2}-\xi\frac{dq}{dx}-\frac{2}{3}\xi\frac{d^2q}{dx^2}\right.\right.\\
&\qquad\left.\left.+\frac{1}{4}\xi^2\left(\frac{dq}{dx}\right)^2\right]+\cdots\right\}\exp[q(x)\xi].
\end{aligned} \quad (101)$$

If we enter this expansion in Eq. (99), the integrals over ξ can be represented as the moments

$$N_t(x)=\int_0^\infty \bar{K}(x,\xi)\exp[q(x)\xi]\xi^t d\xi \quad (102)$$

of a distribution $\bar{K}(x,\xi)\exp[q(x)\xi]$, and (99) takes the

[29] R. P. Feynman, Phys. Rev. **84**, 108 (1951), Sec. 1.

form:

$$\bar{N}_0-\left[\frac{d\bar{N}_1}{dx}-\frac{1}{2}\frac{d\bar{q}}{dx}\bar{N}_2\right]+\left[\frac{1}{2}\frac{d^2\bar{N}_2}{dx^2}-\frac{1}{2}\frac{d\bar{q}}{dx}\frac{d\bar{N}_3}{dx}-\frac{1}{3}\frac{d^2\bar{q}}{dx^2}\bar{N}_3+\frac{1}{8}\left(\frac{d\bar{q}}{dx}\right)^2\bar{N}_4\right]+\cdots=1. \quad (103)$$

The terms in successive brackets contain an increasing number of differentiations.

At this point we proceed as in Appendix II, i.e., we represent $\bar{q}(x)$ as a sum of terms of successively smaller order, with the understanding that the term of rth order contains an r-fold differential. In the zero-order approximation, (103) reduces to $\bar{N}_0=1$, which coincides with (26) and shows that the zero-order value of $\bar{q}(x)$ is in fact $p(x)$. Hence we write:

$$\bar{q}(x)=p(x)+\bar{q}_1(x)+\bar{q}_2(x)+\cdots. \quad (104)$$

The exponential in the integral of (101) can be expanded into powers of $\sum_{r>0}\bar{q}_r(x)\xi$. The value of $\bar{N}_n$ with $\bar{q}=p$ is the moment $\bar{L}_n$ analogous to that of (32), so that

$$\bar{N}_n(x)=\sum_h[\textstyle\sum_r \bar{q}_r(x)]^h\bar{L}_{n+h}(x)/h!. \quad (105)$$

We must now enter this expansion into (103) and separate out the groups of terms of the same order, for which the number of differential factors plus the sum of the indices of the factors $\bar{q}_r$ equals a given total. The groups of terms of the same order must fulfil the equation separately. In this manner we obtain a system of equations of which the first three are written out explicitly:

$$\bar{L}_0=1,$$

$$\bar{q}_1\bar{L}_1-\frac{d\bar{L}_1}{dx}+\frac{1}{2}\frac{dp}{dx}\bar{L}_2=0,$$

$$\bar{q}_2\bar{L}_1+\frac{1}{2}\bar{q}_1^2\bar{L}_2-\frac{d\bar{q}_1\bar{L}_2}{dx}+\frac{1}{2}\frac{d\bar{q}_1}{dx}\bar{L}_2+\frac{1}{2}\frac{dp}{dx}\bar{q}_1\bar{L}_3+\frac{1}{2}\frac{d^2\bar{L}_2}{dx^2}-\frac{1}{2}\frac{dp}{dx}\frac{d\bar{L}_3}{dx}-\frac{1}{3}\frac{d^2p}{dx^2}\bar{L}_3-\frac{1}{8}\frac{d^2p}{dx^2}\bar{L}_4=0. \quad (106)$$

The first equation coincides with (26) and yields $p(x)$. The second yields $\bar{q}_1(x)$ in terms of $p(x)$, the third yields $\bar{q}_2(x)$ in terms of $p(x)$ and $\bar{q}_1(x)$, etc. When the $\bar{q}_r$'s are expressed entirely in terms of $p(x)$ and of the $\bar{L}_n$'s, it turns out that the $\bar{L}_n$'s are combined in ratios $\bar{L}_n/\bar{L}_{n'}=L_n/L_{n'}$ with the exception of one term, $d\log\bar{L}_1/dx$, in $\bar{q}_1$. On the other hand the relationship $\bar{y}(x)=\mu(x)y(x)$ implies $\bar{q}(x)=q(x)-d\log\mu/dx$, so that one can pass from the $\bar{q}_r$'s to the q_r's simply by replacing the $\bar{L}_n$'s with L_n's. In this manner one arrives at (33).

APPENDIX IV. CALCULATION OF THE SOLUTION FOR ENERGIES NEAR THE SOURCE

We wish to solve the equation

$$\bar{y}(x)=\int_0^x \bar{K}(x-\xi,\xi)\bar{y}(x-\xi)d\xi+\delta(x) \quad (8)$$

by means of the expansion

$$\bar{K}(x-\xi,\xi)=\textstyle\sum_n[\partial^n\bar{K}(x,\xi)/\partial x^n]_{x=0}(x-\xi)^n/n!. \quad (107)$$

The Laplace transform of (8) is

$$\begin{aligned}\bar{v}(p)&=\int_0^\infty \exp(px)\bar{y}(x)dx\\&=\int_0^\infty dx\exp(px)\int_0^x \bar{K}(x-\xi,\xi)\bar{y}(x-\xi)d\xi+1\\&=\int_0^\infty d\xi\int_0^\infty d\eta\exp[-p(\xi+\eta)]\bar{K}(\eta,\xi)\bar{y}(\eta)+1\\&=\sum_n n!^{-1}\int_0^\infty[\partial^n\bar{K}(x,\xi)/\partial x^n]_{x=0}\\&\quad\times\exp(p\xi)d\xi\int_0^\infty\eta^n\bar{y}(\eta)\exp(p\eta)d\eta+1\\&=\sum_n\frac{\bar{F}_n(p)}{n!}\left(\frac{d}{dp}\right)^n\bar{v}(p)+1, \quad (108)\end{aligned}$$

where $\bar{F}_n(p)$ is the transform of $[\partial^n\bar{K}/\partial x^n]_{x=0}$, according to (34).

The $\bar{F}_n$'s are treated as small quantities of order u and $\bar{v}(p)$ is represented as a sum of terms of successively smaller order,

$$\bar{v}(p)=\bar{v}_0(p)+\bar{v}_1(p)+\cdots+\bar{v}_r(p)+\cdots. \quad (109)$$

This expansion, entered into (108), yields

$$\textstyle\sum_r\bar{v}_r(p)=\sum_n\sum_r\bar{F}_n(p)(d/dp)^n\bar{v}_r(p)/n!+1. \quad (110)$$

The groups of terms of equal order, i.e., with equal $n+r$, when separated out yield the system of successive equations:

$$\begin{aligned}\bar{v}_0(p)&=\bar{F}_0(p)\bar{v}_0(p)+1,\\\bar{v}_1(p)&=\bar{F}_0(p)\bar{v}_1(p)+\bar{F}_1(p)d\bar{v}_0/dp, \quad (111)\\\bar{v}_2(p)&=\bar{F}_0(p)\bar{v}_2(p)+\bar{F}_1(p)d\bar{v}_1/dp+\tfrac{1}{2}\bar{F}_2(p)d^2\bar{v}_0/dp^2,\\&\cdots\cdots\cdots\cdots\cdots\end{aligned}$$

the first of which coincides with (12). The system, solved chainwise, has the solution

$$\begin{aligned}\bar{v}_0(p)&=[1-\bar{F}_0(p)]^{-1},\\\bar{v}_1(p)&=\bar{F}_1(1-\bar{F}_0)^{-1}d\bar{v}_0/dp=\bar{F}_1(d\bar{F}_0/dp)(1-\bar{F}_0)^{-3}, \quad (112)\\\bar{v}_2(p)&=\bar{F}_1(1-\bar{F}_0)^{-1}d\bar{v}_1/dp\\&\quad+\tfrac{1}{2}\bar{F}_2(1-\bar{F}_0)^{-1}d^2\bar{v}_0/dp^2,\\&\cdots\cdots\cdots\cdots\cdots\end{aligned}$$

All the terms $\bar{v}_r(p)$ have poles only at values of p which are roots of Eq. (14), $\bar{F}_0(p)=1$. The Laplace transform (109) can be inverted in the same manner as (13), by reducing the integral to loops around the poles. To evaluate the residues at the pole $p=p_j$ one can use the expansion:

$$\frac{1}{1-\bar{F}_0(p)}=\frac{1-\frac{1}{2}(p-p_j)\bar{F}_0''(p_j)/\bar{F}_0'(p_j)-\frac{1}{6}(p-p_j)^2\{\bar{F}_0'''(p_j)/\bar{F}_0'(p_j)-\frac{3}{2}[\bar{F}_0''(p_j)]^2/[\bar{F}_0'(p_j)]^2\}+\cdots}{[-\bar{F}_0'(p_j)](p-p_j)}. \quad (113)$$

The inverse transform of the sum of two terms $\bar{v}_0+\bar{v}_1$, is (35).

APPENDIX V. CONNECTION WITH THE LANDAU-SYMON THEORY

Landau[14] has given a theory of the energy straggling of charged particles which traverse thin layers of matter. This theory applies to total energy losses so small, that the collision probabilities $\mu(E)$ and $k(E,\epsilon)$ may be regarded as independent of E. Under this assumption the transform equation (46) can be solved by the method of Sec. 4. The initial energy of the particles is fixed at E_0, i.e., one takes $S(E)=\delta(E-E_0)$. The solution, equivalent to (13) is

$$\phi(E,\sigma)=(2\pi i)^{-1}\int_{-a-i\infty}^{-a+i\infty}\exp[-p(E_0-E)]\times\left[\mu-\sigma-\int_0^\infty k(\epsilon)\exp(p\epsilon)d\epsilon\right]^{-1}dp, \quad (114)$$

or, since $\mu=\int_0^\infty k(\epsilon)d\epsilon$,

$$\phi(E,\sigma)=(2\pi i)^{-1}\int_{-a-i\infty}^{-a+i\infty}\exp[-p(E_0-E)]\times\left\{\int_0^\infty k(\epsilon)[1-\exp(p\epsilon)]d\epsilon-\sigma\right\}^{-1}dp. \quad (115)$$

The Landau formula is obtained by entering (115) into the inverse transform (47) and carrying out the integration over σ before that over p. The integral over σ is given by the residue at

$$\sigma=\int_0^\infty k(\epsilon)[1-\exp(p\epsilon)]d\epsilon,$$

$$f(E,s)=(2\pi i)^{-1}\int_{-a-i\infty}^{-a+i\infty}\exp\left\{-p(E_0-E)-s\int_0^\infty k(\epsilon)[1-\exp(p\epsilon)]d\epsilon\right\}dp. \quad (116)$$

This is just Eq. (5) of Landau except for the replacement of p with $-p$.

In the evaluation of $\int_0^\infty k(\epsilon)[1-\exp(p\epsilon)]d\epsilon$, Landau took advantage of the fact that $k(\epsilon)=\text{const}/\epsilon^2$ over a large range of values of ϵ, for charged particles. For the sake of analytical convenience, Landau assumed that the ϵ^{-2} dependence extends to $\epsilon=\infty$ instead of stopping at some value $\epsilon_{\max}$. Thereby he introduced a spurious possibility of energy losses $>\epsilon_{\max}$, but the resulting error can be disregarded as long as the total probability of any such spurious loss over the pathlength s, $s\,\text{const}/\epsilon_{\max}$, remains much smaller than one. However, the possibility of the spurious losses raises to infinity the mean energy loss over a finite path length. Correspondingly, the saddle point of the integrand of (116), which must lie at $p=0$ for $E_0-E=\langle E_0-E\rangle$ (see p. 43) and at $p>0$ for $E_0-E>\langle E_0-E\rangle$, remains, in the Landau calculation, at $p<0$. Indeed the Landau value for $\int_0^\infty k(\epsilon)[1-\exp(p\epsilon)]d\epsilon$, namely $\text{const}\,p\log(-1.56p\epsilon')$, has a spurious singularity at $p=0$. It is interesting that the topography of the Laplace transform is thus seriously altered even though the Landau assumption is actually realistic over a broad range of conditions and even though the inverse transform remains unaffected, as it should.

The Landau calculation breaks down when the probability of spurious losses, of the order of $\epsilon_{\max}$, becomes appreciable. This happens, for heavy charged particles, including mesons, before a very substantial fraction of the initial energy has been dissipated, owing to the smallness of $\epsilon_{\max}$. In the situation opposite to that of the Landau approximation, the energy degradation has proceeded so far that the frequency of actual losses of the order of $\epsilon_{\max}$ has become rather large instead of very low. In this situation the "transient" phase of the degradation is over, the "steady-state" analysis of part A, as applied in Secs. 13 and 12, becomes quite appropriate, and the straggling distribution approaches a Gaussian shape.

Symon[14] has bridged the gap between ranges of validity of the Landau analysis and of the steady-state analysis by a skilled and elaborate interpolation procedure.[30] He characterizes the distribution in energy, for a given path length, by: (1) the value of the most probable energy, (2) a factor which measures the scale of the fluctuations and which is related to the mean square energy fluctuation, (3) a skewness parameter λ whose value ranges from zero for a Gaussian distribution of straggling to 1.48 for the Landau distribution. The shape of the distribution depends only on λ. Symon constructs a standard set of distribution curves for $0<\lambda<1.48$, whose shapes vary gradually from Gaussian to Landau. The curves for $\lambda\leqslant 1$ are Gaussians modified

[30] Much of this procedure has been reproduced by B. Rossi, *High Energy Particles* (Prentice Hall, Inc., New York, 1952), p. 32ff.

by a suitably applied Edgeworth expansion. The curves for $\lambda > 1$ are obtained from the Landau theory corrected to the first order for the error caused by the inclusion of the "spurious losses." For path lengths so small that $k(E, \epsilon)$ and $\mu(E)$ are effectively independent of E, the Symon parameters can be calculated directly. For large path lengths Symon fits his distribution to values of the mean, mean-square and mean-cube energy loss calculated to an accuracy equivalent to that of the first three cumulants in (76) and (77).

APPENDIX VI. UTILIZATION OF MOMENTS TO INVERT THE LAPLACE TRANSFORM

Lewis[11] has utilized a standard method of statistics, the Edgeworth series, which amounts to fitting initially a Gaussian distribution with the correct mean range and mean square deviation and then of improving this distribution on the basis of data on higher moments. This method is appropriate to the path length distribution of heavy charged particles, which involves rather small fluctuations and therefore is well approximated by the initial Gaussian.

Another type of approach has been developed to construct approximate distributions of x-rays in an infinite medium.[4] The idea is to represent $\phi(E, \sigma)$ for $\sigma \sim 0$ by an expansion especially chosen to converge rapidly over a broad interval of σ. Thus, for example, if ϕ is expanded into powers of $\sigma/(\mu_s - \sigma)$, each term of the expansion diverges as σ aproaches μ_s. Since we know that ϕ itself actually diverges in this limit, this expansion is more realistic than a simple power expansion. The coefficients of the first n terms of the expansion in powers of $\sigma/(\mu_s - \sigma)$ are linear combinations of the first n coefficients of the expansion in powers of σ and therefore their determination requires no additional information. The additional information, provided by independent knowledge on the behavior of $\phi(E, \sigma)$ far from $\sigma = 0$, is embodied in the choice of the *type of expansion*. Many types of expansion allow analytical inversion of the transform term by term; e.g., the expansion in powers of $\sigma/(\mu_s - \sigma)$ yields an expansion of $f(E, s)$ in a series of Laguerre polynomials.[4]

APPENDIX VII. DISCUSSION OF THE LEWIS THEORY

A discussion of the range straggling theory of Lewis,[11] especially of his "simplified problem," serves to illustrate various points previously raised in the present paper.

Lewis assumes that the differential collision probability for heavy charged particles is

$$k(E, \epsilon) = k/2E\epsilon^2, \tag{117}$$

where $k = 2\pi N Z z^2 e^4 M/m$, as in (40). The values of the energy loss ϵ are supposed to vary from a lower limit δE to the upper limit $\gamma E \sim 4(m/M)E$ (γ is called ϵ by Lewis),

$$\delta E \leqslant \epsilon \leqslant \gamma E. \tag{118}$$

The assumption (117) is not realistic for low values of ϵ, but the value of δ is adjusted so that $M_1 = \int_0^\infty k(E, \epsilon)\epsilon d\epsilon$ has the correct value (40). The error in the moments $M_2, M_3 \cdots$ is also negligible and therefore the law (117) gives the correct results for the purpose at hand. The corresponding value of $\mu(E)$ is

$$\mu(E) = (k/2E^2)(\delta^{-1} - \gamma^{-1}). \tag{119}$$

The transport equation (44) is, then,

$$\partial f/\partial s = -(k/2E^2)(\delta^{-1} - \gamma^{-1}) f(E, S) + (k/2)\int_{\delta E}^{\gamma E} f(E+\epsilon, s) d\epsilon/(E+\epsilon)\epsilon^2 + \delta(E - E_0)\delta(s). \tag{120}$$

The main part of the Lewis treatment deals with the "simplified problem" in which he regards as constant the minimum fractional energy loss δ and therefore the stopping number $B = \log(\gamma/\delta)$. His calculation can be simplified by considering the moments of the spectrum, $m_n(s) = \int_0^{E_0} E^{2n} f(E, s) dE$, which coincide with the Lewis expression (L15). The $\int_0^{E_0}$ has to be understood as $\lim_{\Delta=0} \int_\Delta^{E_0}$, so that particles whose energy drops below Δ are effectively "absorbed." Multiplication of (120) by E^{2n} and integration over E yields

$$dm_n/ds = -kA_n m_{n-1}(s) + E_0^{2n}\delta(s), \tag{121}$$

equivalent to (L16), where

$$A_n = \tfrac{1}{2}\int_\delta^\gamma du u^{-2}[1 - (1-u)^{2n}].$$

This expression of A_n, is obtained by setting $u = \epsilon/E = 1 - (1+\eta)^{-1}$ in Lewis's expression. The moments (58) of the range distribution, $\langle s^n \rangle_{[0]}$ are equal to $n\int_0^\infty ds s^{n-1} m_0(s)$ according to (50). To evaluate them one can express m_0 in terms of $d^n m_n/ds^n$ and of $\delta(s)$ by repeated application of (121) and then integrate by parts n times. The result is (L19).

The fluctuations of energy loss in the simplified problem remain *constant throughout the degradation*, if expressed in a logarithmic energy scale. If we take $x = \log(E_0/E)$ and $\xi = \log[E/(E-\epsilon)] = \log[(1-u)^{-1}]$, the collision probability becomes

$$k(E, \epsilon)d\epsilon = \tfrac{1}{2}kE_0^2 \exp(2x)\exp(-\xi)[1 - \exp(-\xi)]^{-2} d\xi = K(x, \xi)d\xi. \tag{122}$$

Similarly

$$\mu(E) = \mu(x) = \tfrac{1}{2}kE_0^{-2}\exp(2x)(\delta^{-1} - \gamma^{-1}) = \mu(0)\exp(2x). \tag{123}$$

The transform equation (65) can then be solved, for $\sigma = 0$, by the method of Sec. 4 without any approximation procedure. According to (13) and (7) the result is

$$y(x, 0) = [2\pi i \mu(x)]^{-1}\int_{-a-i\infty}^{-a+i\infty} \times \exp(-px)[1 - \bar{F}(p)]^{-1} dp, \tag{124}$$

where

$$\bar{F}(p)=(\delta^{-1}-\gamma^{-1})^{-1}\int_{-\log(1-\delta)}^{-\log(1-\gamma)}\times\exp(-\xi)d\xi[1-\exp(-\xi)]^{-2}\exp(p\xi) \quad (125)$$

$$=(\delta^{-1}-\gamma^{-1})\int_{\delta}^{\gamma}duu^{-2}(1-u)^{-p}.$$

Evaluation of (123) by taking the residues at the poles gives the steady-state solution, valid for $x\gg\gamma$,

$$y(x,0)=[\mu(x)\bar{F}'(0)]^{-1}$$

$$=E_0^2 2\exp(-2x)\left\{k\int^{\gamma}duu^{-2}\log[(1-u)^{-1}]\right\}^{-1}$$

$$=E_0^2 2\exp(-2x)/k[B+\tfrac{1}{2}(\gamma-\delta)+\cdots]. \quad (126)$$

As anticipated in Sec. 6, the exact solution obtained in this manner is equivalent to the corresponding solution (43), if the expression

$$\{\textstyle\int_{\delta}^{\gamma}duu^{-2}\log[(1-u)^{-1}]\}^{-1}=[B+\tfrac{1}{2}(\gamma-\delta)+\ldots]^{-1} \quad (127)$$

is expanded into powers of γ/B. The fraction δ can be disregarded in this expansion (as it is effectively disregarded in (41)), because it is extremely small. The term γ/B^2 of (43) cannot appear here since it arises from the variation of B.

It was pointed out in Sec. 13 that an evaluation of the mean path length by the formula $\langle s\rangle_{[x]}=\int_0^x y(x',0)dx'$ yields an incorrect result if one utilizes the steady-state expression (126) for y even in the interval of integration $x'\sim 0$. In this manner one would find only the integral of (84), without the additional term in front of it. To obtain the correct value of $\langle s\rangle_{[x]}$ one must take into consideration the exact solution (124) of the simplified problem, which includes the transient effect,

$$\langle s\rangle_{[x]}=\int_0^x y(x',0)dx'=\int_0^x dx'\exp(-2x')[2\pi i\mu(0)]^{-1}$$

$$\times\int_{-a-i\infty}^{-a+i\infty}\exp(-px')[1-\bar{F}(p)]^{-1}dp=\frac{1}{\mu(0)}\int_{-a-i\infty}^{-a+i\infty}dp\frac{1-e^{-(p+2)x}}{p+2}\frac{1}{1-\bar{F}(p)}.$$

Since x itself is large, the factor $\exp[-(p+2)x]$ becomes very small in the residues at all poles of $1-\bar{F}$ except at $p=0$. Therefore we may apply the steady-state approximation to the portion of the integral which contains $\exp[-(p+2)x]$. This portion yields

$$-\exp(-2x)/2\mu(0)\bar{F}'(0)=-[2\mu(x)F'(0)]^{-1}$$
$$=-E_0^2/k[B+\cdots]. \quad (128)$$

The remaining part of the integral, which does not contain the exponential, converges for p large and negative and reduces to the residue at $p=-2$ plus a half contour at $p=-\infty$, that is, to

$$[1/\mu(0)]\{[1-F(-2)]^{-1}-\tfrac{1}{2}\}=E_0^2/kA_1-1/2\mu(0). \quad (129)$$

Here $A_1=\frac{1}{2}(\delta^{-1}-\gamma^{-1})[1-F(-2)]$ is just the parameter which appears in the Lewis range formula (L20), $1/2\mu(0)\sim(E_0^2/k)\delta$ is a very small distance, of the order of the mean distance between collisions.

At $E=0$, (128) vanishes and (129) coincides with the Lewis value of the mean range, to within the insignificant term $1/2\mu(0)$. For purpose of comparison with (84) one may add $E_0^2/k[B+\cdots]$ to (128) and subtract it from (129). With this addition (128) becomes essentially equal to the integral in (84), i.e., to the integral over the steady state (126), and (129) becomes $(E_0^2/k)\{A_1^{-1}-[B+\cdots]^{-1}\}$ and coincides with the corrective term in front of the integral in (84).

It may be concluded from the discussion that, whereas the Lewis mean range E_0^2/kA_1 is correct, its interpretation as the integral of contributions from different energy intervals $\int_0^{E_0}2EdE/kA_1$ is not quite correct. End-effects, as discussed in Sec. 13, are primarily responsible for the fact that the range is not $\int_0^{E_0}2EdE/k[B+\frac{1}{2}\gamma+\cdots]$.

Angular Distributions from (n,p) Nuclear Reactions*

N. AUSTERN AND S. T. BUTLER,† *Laboratory of Nuclear Studies, Cornell University, Ithaca, New York*

AND

H. MCMANUS, *Atomic Energy of Canada, Limited, Chalk River, Ontario, Canada*

(Received July 1, 1953)

It is shown that angular distributions of high-energy proton groups from (n,p) reactions should evidence sharp maxima near the forward direction, which arise from neutrons with large impact parameters interacting with protons out in the "tails" of the initial nucleus. The positions of these peaks are characterized by the allowed values of orbital angular momenta l_n with which the neutron can be captured to form the final state. A study of such distributions therefore may well lead to information concerning spins and parities of nuclear energy levels, as in the case of stripping reactions. For most nuclei, compound nucleus formation should contribute little to such proton groups. For light nuclei, in order that the sharp maxima stand out above the compound nucleus background, it is probably necessary that the incident neutron energy not be near a resonance of the compound nucleus.

I. INTRODUCTION

ANALYSIS of the total cross sections for processes of the type $X(n,p)Y$ for neutron energies of 14 Mev and for fairly heavy nuclei[1] has indicated that an important contribution comes from interaction with surface protons. This is because there is an appreciable probability that a surface proton can receive by direct collision almost all the energy of the incident neutron, thus overcoming the Coulomb barrier, and leaving the final nucleus in a state of low excitation. Compound nucleus formation, on the other hand, due to the rapid increase in density of states with excitation for the final nucleus, favors the emission of lower-energy protons, which in these cases are subject to a large Coulomb barrier and can contribute little to the reaction.

The energy range in which the surface effect is important is most likely to be about 10–30 Mev. Nuclear "transparency" establishes the high-energy limit. At energies below 10 Mev the immediate formation of a compound nucleus may be suppressed,[2] so the interaction of the incident neutron with just one other nucleon might be possible throughout the entire target nucleus, rather than only at the surface.

The conclusion of reference 1 raises the question as to the appearance of the angular distributions resulting from such surface interactions, i.e., the angular distributions resulting from neutrons with large impact parameters interacting with protons which have penetrated outside the main core of the initial nucleus and whose wave functions in this region are the familiar "exponential" tails. In the present paper it is shown that these angular distributions are similar to those obtained in stripping reactions[3] and possess sharp maxima near the forward direction, maxima which depend on the allowed values of the orbital angular momenta with which the neutron can be captured. Moreover, since these sharp peaks involve many partial waves of the incident neutrons, it seems quite possible that they will stand out against the background due to compound nucleus formation even for considerably lighter nuclei than those considered in reference 1. The possibility exists, therefore, that (n,p) angular distribution experiments can yield information about the properties of the energy levels of a wide range of nuclei.

Such experiments should be most satisfactory for the higher-energy discrete proton groups. Energy discrimination for these groups can distinguish them from the background of protons from compound nucleus formation since, even for these nuclei whose Coulomb barriers cannot suppress it, this background mostly includes protons having energies considerably less than the incident neutron energy, and having a practically continuous energy distribution. For quite light nuclei, where there is no great increase in density of states with excitation for the final nucleus, it would probably be necessary that the incident neutron energy not be near a resonance of the compound nucleus. The anticipated total cross section for one high-energy group might be estimated as several millibarns for each initial participating proton. This is computed, for 14 Mev, by correcting the 0.6-barn total $(n$-$p)$ scattering cross section both for the fraction of time the initial and final particles spend outside their respective nuclei, and for certain angular effects.

If the process should be dominated by the least bound single-particle proton state of the initial nucleus, i.e., that state whose tail extends furthest from the nuclear core, the angular distributions become especially simple. They are then characterized by the set of values for l where,

$$l_n+l_p \geq l \geq |l_n-l_p|\,;$$

l_p and l_n are, respectively, the orbital angular momentum of a proton in the state of least binding of the

* Supported in part by the U. S. Office of Naval Research.

† Now at the Research School of Physical Sciences, Australian National University, Canberra, Australia.

[1] H. McManus and W. T. Sharp, Phys. Rev. **87**, 188 (1952), and (to be published).

[2] Feshbach, Porter, and Weisskopf, Phys. Rev. **90**, 166 (1953).

[3] S. T. Butler, Proc. Roy. Soc. (London) **A208**, 559 (1951).

initial nucleus, and the orbital angular momentum of the captured neutron (which in this event goes into a neutron state of least binding of the final nucleus).

Of course, the considerations of this paper not only apply to (n,p) reactions, but also to the types (n,n'), (p,n), and (p,p').

Our calculations are done in the impulse approximation. Section II presents the analysis of the simple case where only the least-bound states of the initial and final nuclei are important, while Sec. III considers what can be learned if such a strong selection cannot be imposed.

II. TRANSITIONS BETWEEN SINGLE STATES

In this section we consider those cases where the incident neutron interacts only with protons of the initial nucleus which we assume to be both outside the main body of the nucleus and also in a single state, *viz.*, the proton state of least binding. These considerations will apply therefore only to cases where protons in other states are substantially more tightly bound. Then contributions from the tightly bound protons are suppressed because the neutrons with the large impact parameters which are needed to get a rapidly varying angular distribution see mainly the proton tails of greatest extent, and also because the neutrons with sufficiently small impact parameter to see proton tails with small extension are more likely to be captured into a compound nucleus. The considerations of this section are later applied in Sec. III, where many tails participate. Although the simple rules of Sec. II are not likely to apply for many nuclei, their possible application in any one experiment should not be overlooked.

Experiments suggest that protons of least binding frequently have a definite orbital angular momentum, even in those cases where spin coupling considerations allow an admixture of two or more orbital momenta. On such a picture the proton is ejected from the state of least binding and known orbital momentum; the neutron is captured into a similar state, also characterized by a definite orbital momentum, leaving the final nucleus in one of its low-lying states.

We assume then that a proton, initially in a bound state of orbital angular momentum l_p and projection m_p, is knocked out by the incoming neutron, which is captured into a state of orbital angular momentum l_n and projection m_n. We also suppose that the interaction between the two particles takes place only outside the nucleus. These assumptions suggest using the "impulse approximation" method of Chew,[4] for the assumption that the reaction takes place outside the nucleus means just that neither particle interacts with the nucleus during the time they are interacting with each other. Indeed, our case is almost exactly the simple example Chew treats in Sec. II of his paper.

Suppose $G_l(\mathbf{r}_p)$ and $G_{l'}'(\mathbf{r}_n)$ are the wave functions of the bound neutron and proton in states l and l', respectively, and $e^{i(\mathbf{k}\cdot\mathbf{r}_n)}$ and $e^{i(\mathbf{k}'\cdot\mathbf{r}_p)}$ are the incident and outgoing plane waves. Also, suppose $V_{np}(\mathbf{r}_p-\mathbf{r}_n)$ is the neutron-proton interaction, r_0 is the nuclear radius, and $\mathbf{R}=\frac{1}{2}(\mathbf{r}_p+\mathbf{r}_n)$, $\mathbf{r}=(\mathbf{r}_p-\mathbf{r}_n)$. Then the matrix element for the transition may be written as

$$\int_{r_n,\,r_p\geq r_0} d^3r_n d^3r_p G_{l'}'^{*}(\mathbf{r}_n)e^{-i(\mathbf{k}'\cdot\mathbf{r}_p)}V_{np}\Psi(\mathbf{r}_n,\mathbf{r}_p). \quad (1)$$

Here Ψ is the complete wave function for the process. Following Chew, we introduce the impulse approximation by replacing Ψ by the approximate function Ψ_a, where

$$\Psi_a=\int d^3k_p g_l(\mathbf{k}_p)\varphi_{\mathbf{k}_p,\,\mathbf{k}}(\mathbf{r}_n,\mathbf{r}_p) \quad (2)$$

$$=\int d^3k_p g_l(\mathbf{k}_p)e^{i(\mathbf{R}\cdot\mathbf{k}_p)+i(\mathbf{R}\cdot\mathbf{k})}\varphi_{\frac{1}{2}(\mathbf{k}_p-\mathbf{k})}(\mathbf{r}). \quad (3)$$

The functions φ are two-body scattering wave functions, $\varphi_{\mathbf{k}_p,\mathbf{k}}$ giving a complete description of the collision between a proton of momentum $\hbar\mathbf{k}_p$ and a neutron of momentum $\hbar\mathbf{k}$, while $\varphi_{\frac{1}{2}(\mathbf{k}_p-\mathbf{k})}$ describes the same collision, but in the center-of-mass coordinate system. The function $g_l(\mathbf{k}_p)$ is the Fourier transform of $G_l(\mathbf{r}_p)$, for $r_p\geq r_0$.

It is convenient also to represent $G_{l'}'(\mathbf{r}_n)$ by its Fourier transform, for $r_n\geq r_0$,

$$g_{l'}'(\mathbf{k}_n)\equiv\int_{r_n\geq r_0} d^3r_n e^{-i(\mathbf{k}_n\cdot\mathbf{r}_n)}G_{l'}'(\mathbf{r}_n). \quad (4)$$

Inserting (3) and (4) into (1), we find directly:

$$\int d^3k_p g_{l'}'^{*}(\mathbf{k}_p+\mathbf{k}-\mathbf{k}')g_l(\mathbf{k}_p)$$
$$\times\langle\mathbf{k}'-\tfrac{1}{2}(\mathbf{k}_p+\mathbf{k})|r_{np}|\tfrac{1}{2}(\mathbf{k}_p-\mathbf{k})\rangle, \quad (5)$$

the matrix element of the r matrix being defined as

$$\langle\mathbf{q}'|r_{np}|\mathbf{q}\rangle\equiv\int d^3r e^{-i(\mathbf{q}'\cdot\mathbf{r})}V_{np}\varphi_{\mathbf{q}}(\mathbf{r}).$$

The r matrix, as in Chew's work, is to be obtained phenomenologically from the two-body scattering experiments.

The integral of Eq. (5) leads directly to the cross section. It can be evaluated once the r matrix is known, the functions g_l and $g_{l'}'$, by assumption, being known for the outside region of the nucleus. Now a phenomenological derivation of $\langle\mathbf{q}'|r_{np}|\mathbf{q}\rangle$ is obtained from the free-scattering cross sections through the relation

$$\sigma_{np}=(2\pi/\hbar)M^2|\langle\mathbf{q}'|r_{np}|\mathbf{q}\rangle|^2. \quad (6)$$

Using (6) we deduce from the data that $\langle\mathbf{q}'|r_{np}|\mathbf{q}\rangle$ is a very slowly varying function of $\mathbf{q}$ and $\mathbf{q}'$. With this fact we simplify (5) by taking out the matrix element of r_{np}

[4] G. Chew, Phys. Rev. **80**, 196 (1950).

from under the integral sign, approximating it by its value at $k_p=0$.

A first observation on the free n-p scattering cross section[5] is that it is hardly at all a function of angle. Thus for the free scattering we can write the matrix element in the simpler form, $r_{np}(q)$. Although this form may seem inadequate for our discussion of "bound" n-p scattering, which involves an off-energy-shell matrix element of r_{np}, closer inspection shows that for outgoing protons at small forward angles, where $\mathbf{k}'\approx\mathbf{k}$, our process actually is close to the energy shell. In addition to this, we have been able to derive a semiphenomenological form which shows that r_{np} changes slowly as it leaves the energy shell.

The energy variation of $r_{np}(q)$ follows from (6) as being proportional to $(\sigma_{np})^{\frac{1}{2}}$. In (5), if k_p were small compared to k and k' then we could immediately take out the matrix element from the integral. Now k and k' pertain to energies of, say, 14 Mev. Aside from some oscillations which are introduced by the cutoffs, the ranges of important arguments in g_l and $g_{l'}$ are determined by the binding energies of the initial and final nuclei, about 8 Mev. Now suppose the magnitude of $\mathbf{k}_p$ is related to the binding energy, and suppose $\mathbf{k}_p$ is permitted to swing through all angles. In this case the energy of the equivalent free-scattering experiment from which $r_{np}(q)$ must be found for (5) will range over about 3–30 Mev, a region in which σ_{np} changes by a factor of 7, so $r_{np}(q)$ by a factor $\sqrt{7}$. Most of even this variation of r_{np} occurs when $\mathbf{k}_p$ is within about 30° of being parallel to $\mathbf{k}$. Since such a localized angle variation is unimportant if g_l and $g_{l'}$ are not very rapid functions of angle, we merely limit ourselves to nuclear states of low orbital angular momentum, and safely approximate $k_p\approx 0$ in the matrix element of r_{np}. Equation (5) thus becomes approximately[6]

$$r_{np}(k/2)\int d^3k_p g_{l'}{}^*(\mathbf{k}_p+\mathbf{k}-\mathbf{k}')g_l(\mathbf{k}_p). \qquad (7)$$

This is the matrix element for our n-p process.

The second factor of (7) gives the form of the angular distribution. It is most easily treated by returning to coordinate space, where it becomes

$$\int_{r_p\geq r_0} d^3r_p \exp(i\mathbf{Q}\cdot\mathbf{r}_p)G_l(\mathbf{r}_p)G_{l'}{}^*(\mathbf{r}_p), \qquad (8)$$

and $\mathbf{Q}\equiv\mathbf{k}-\mathbf{k}'$.

On expanding $\exp(i\mathbf{Q}\cdot\mathbf{r}_p)$ in spherical harmonics and integrating over angles, (8) becomes

$$\sum_l i^l\{(2l_n+1)(2l_p+1)\}^{\frac{1}{2}}C_{l_n l_p}(l,0;0,0) \times C_{l_n l_p}(l,0;-m_n,m_p)\int_{r_0}^{\infty} r_p^2 dr_p \times j_l(Qr_p)f_l(r_p)f_{l'}{}^*(r_p), \qquad (9)$$

where the C's are Clebsch-Gordan coefficients,[7] f_l and $f_{l'}$ are the radial parts of the wave functions, $Q=|\mathbf{k}-\mathbf{k}'|$, and j_l is the spherical Bessel function. Now for $r_p\geq r_0$ the functions $r_p f_l$ and $r_p f_{l'}$ are "exponentially" decreasing, since they correspond in general to bound states. The variation of the Bessel function is, in general, slow compared with this decrease (the momentum difference $\mathbf{Q}$ being small at small angles of scattering), and the integral of (9) may therefore be approximated by

$$j_l(Qr_0)\int_{r_0}^{\infty} r_p^2 dr_p f_l(r_p)f_{l'}(r_p) = (\text{say}) \quad \epsilon(r_0)j_l(Qr_0).$$

When the sum and average over initial and final states is carried out, we obtain therefore for the differential cross section:

$$\sigma \propto |\langle|r_{np}|\rangle|^2 = |r_{np}(k/2)|^2\times\epsilon^2(r_0)\times(2l_p+1) \times\sum_l C_{l_n l_p}{}^2(l,0;0,0)\{j_l(Qr_0)\}^2, \qquad (10)$$

where l is restricted to the values $l_n+l_p\geq l\geq|l_n-l_p|$, and, to conserve parity, can take only all odd or even values in this range.

The angular distribution given by (10) is analogous to that obtained in the case of deuteron stripping, although the straightforward physical interpretation which the parameter l has in stripping is not applicable here. However, the spherical Bessel functions do introduce peaks which are characteristic of the particular l values allowed, and, as in stripping, there is no interference between different l values. Unlike the deuteron case, there is no form factor which suppresses the maxima from higher l values. Still it is not necessary to study all the maxima, as the position of the first maximum is adequate for determining the lowest allowed value of l, i.e., $|l_n-l_p|$. Thus l_n, the orbital angular momentum of the captured neutron, is given by

$$l_n = l_p \pm l_{\min}, \qquad (11)$$

the negative sign being omitted if $l_{\min}>l_p$. Thus, information concerning the spins and parities of the final state should be obtainable in much the same way as is done for deuteron stripping reactions.

For the above picture to be valid we require an initial nucleus in which there are some relatively lightly bound protons, all in the same orbital momentum state, surrounding a main core in which the protons are sub-

[5] R. K. Adair, Revs. Modern Phys. **22**, 249 (1950).

[6] One further justification for dropping $\mathbf{k}_p$ in the matrix element of r_{np} is that it cancels identically in the Born approximation limit of the exchange part of the matrix element. Production of protons in the forward direction, the direction of interest in this paper, is most likely to be by exchange scattering.

[7] J. M. Blatt and V. F. Weisskopf, *Theoretical Nuclear Physics* (John Wiley and Sons, Inc., New York, 1952), Appendix A.

stantially more tightly bound. In this event we consider the reaction to proceed by one of the outer protons being replaced by a neutron with orbital angular momentum appropriate for formation of the particular state of the final nucleus under consideration, contributions from protons within the core being suppressed by the effects which were previously discussed.

On the independent particle model an initial nucleus well suited for the above picture should be one in which the protons of the (in general incompleted) last shell are all of the same orbital angular momentum. In this event the value l_p appropriate to this shell is employed in (11). For any one nucleus in which protons occupy more than one subshell of the last major shell, the energy differences are sufficiently small so that, on energetic grounds alone, all the subshells are apt to participate in an (n,p) reaction. Nevertheless, even in such cases, the formation of at least the ground state of the final nucleus, and perhaps the first excited state or two, might involve the replacement of one of the protons in the last subshell by a neutron, hence for these few final states the appropriate value of l_p to employ in (11) would also be known.

Finally, it might be remarked that, because of the use of free waves in the impulse approximation, we do not expect Eq. (10) to give accurate angular distributions. We wish merely to suggest that (n,p) angular distributions can give information about the properties of nuclear levels, and to use (10) to obtain a qualitative idea of the way in which the distributions depend on the orbital angular momentum change l. If the need arises, a more accurate theory can be developed.

In order to confirm that (10) is indeed qualitatively correct, we have considered a simple model, in which the incident neutron beam is permitted to interact with the core. In this model it is assumed that, in the incident neutron beam, all partial neutron waves l' for $l' \leqslant kr_0$ are absorbed by the nucleus, all other partial waves being unaffected. This should overestimate the effects of neutron scattering. Thus, the neutron wave

$$e^{i(\mathbf{k}\cdot\mathbf{r}_n)}=\sum_{l'} i^{l'}[4\pi(2l'+1)]^{\frac{1}{2}} j_{l'}(kr_n)Y_{l',0}(\boldsymbol{\theta}_n),$$

was replaced in the matrix element (1) by the sum

$$\sum_{l'} i^{l'}[4\pi(2l'+1)]^{\frac{1}{2}} f_{l'}(kr_n)Y_{l',0}(\boldsymbol{\theta}_n),$$

where

$$\begin{aligned} f_{l'} &= j_{l'}, \quad \text{if } l' > kr_0 \\ &= \tfrac{1}{2}(j_{l'}+in_{l'}), \quad \text{if } l' \leqslant kr_0, \end{aligned}$$

$n_{l'}$ being the irregular spherical Bessel function. Also, as the previous discussion showed that the $(n$-$p)$ potential itself gave little angular dependence, this potential was assumed to have very small range.

A comparison of the results of this calculation with those of formula (10) is shown in Fig. 1, in which all cases refer to a nucleus of $A=34$ and a neutron energy of 14 Mev.

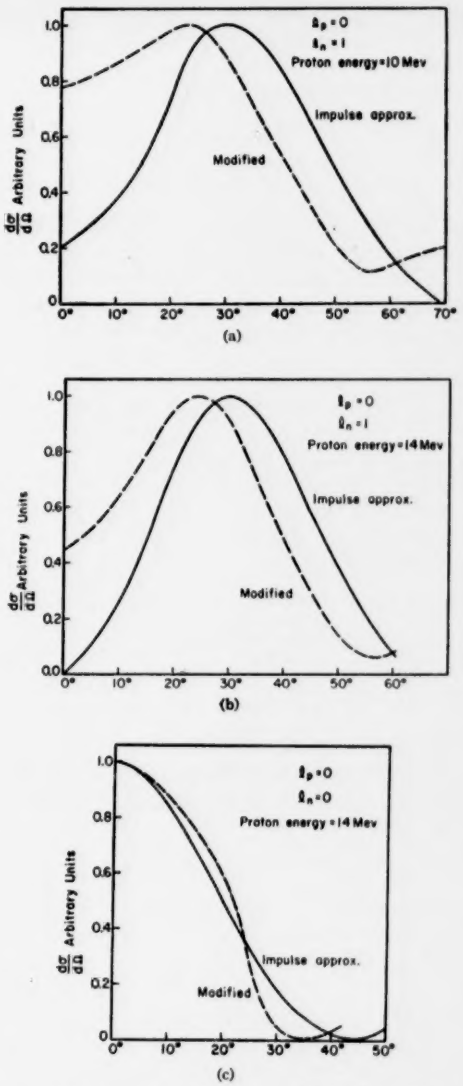

FIG. 1. Some typical (n,p) angular distributions. The solid curves are calculated from Eq. (10), while the dotted curves show the results of an alternative calculation which overestimates the effects of neutron scattering. The curves all apply to the case of 14-Mev neutrons incident on a nucleus with $A=27$.

III. TRANSITIONS INVOLVING MANY STATES

In this section we consider briefly those cases where there are no particular reasons for picking out special orbitals for the neutron and proton. Here the shape of the differential cross section arising from surface interactions still has restrictions, and these are shown to be determined by the change of nuclear spin, and by any change of parity.

We expand the antisymmetrical wave function $\Psi(J_X, M_X)$ of the initial nucleus (spin J_X and pro-

jection M_X) with respect to a complete set of one-particle states for the αth proton, and with respect to the energy eigenstates of the system composed of the remaining nucleons; i.e.,

$$\Psi(J_X, M_X)=\sum_{s,\,l,\,m_s,\,\mu_p} A_{sl}{}^{\alpha}(j_s, m_s, j_p, \mu_p) \times\psi_s{}^{\alpha}(j_s, m_s)G_l(j_p, \mu_p; \mathbf{r}_p{}^{\alpha}), \quad (12)$$

where the $\psi_s{}^{\alpha}(j_s, m_s)$ are the antisymmetrical wave functions of the states s of the nucleus with the αth proton absent. These states have total spins designated by j_s and projections m_s. The spatial coordinates of the αth proton are given by $\mathbf{r}_p{}^{\alpha}$ and the total angular momentum of this particle is represented by j_p (with projection μ_p). Thus $\mathbf{J}_X=\mathbf{j}_s+\mathbf{j}_p$.

In the expression (12) the antisymmetrization of $\Psi(J_X, M_X)$ exhibits itself in certain properties of the $A_{sl}{}^{\alpha}$. It is, of course, equally possible to perform the expansion in terms of wave functions $\psi_s{}^{\alpha'}$ and $G_l(\mathbf{r}_p{}^{\alpha'})$ where the coordinates of a different particle (the α'th) have been chosen for the single particle wave function. Then, because of the antisymmetry of Ψ, we will have

$$A_{sl}{}^{\alpha'}=\pm A_{sl}{}^{\alpha}=(\text{say})\pm A_{sl}(j_s, m_s, j_p, \mu_p).$$

Similarly, the antisymmetrized wave function of the final nucleus can be written

$$\Psi(J_Y, M_Y)=\sum B_{s'l'}{}^{\lambda}(j_{s'}, m_{s'}, j_n, \mu_n) \times\psi_{s'}{}^{\lambda}(j_{s'}, m_{s'})G_{l'}(j_n, \mu_n; \mathbf{r}_n{}^{\lambda}), \quad (13)$$

where λ designates the particular neutron coordinates chosen for the single particle wave functions. Then again,

$$B_{s'l'}{}^{\lambda'}=\pm B_{s'l'}{}^{\lambda}=(\text{say})\pm B_{s'l'}(j_{s'}, m_{s'}, j_n, \mu_n).$$

In analogy to (1) we now compute the matrix element of the interaction, $\sum_{\alpha} V_{n\lambda,p\alpha}$ and obtain

$$\pm Z^{\frac{1}{2}}\sum_{s,\,l,\,l'} A_{sl}(j_s, m_s, j_p, \mu_p)B_{sl'}(j_s, m_s, j_n, \mu_n) \times\langle e^{i(\mathbf{k}'\cdot\mathbf{r}_p)}G_{l'}(j_n, \mu_n)\,|\,V_{np}\,|\,\Psi_l(\mathbf{k}, \mathbf{r}_n, j_p, \mu_p)\rangle. \quad (14)$$

The symmetry properties of A and B are used in deriving (14). There are no transitions between different states of the nucleus represented by ψ, i.e., $s=s'$, $j_s=j_{s'}$; hence

$$\mathbf{j}_p-\mathbf{j}_n=\mathbf{J}_X-\mathbf{J}_Y. \quad (15)$$

The cross section is proportional to the absolute square of (14).

Now $\langle e^{i(\mathbf{k}'\cdot\mathbf{r}_p)}G_{l'}(j_n, \mu_n)\,|\,V_{np}\,|\,\Psi_l(\mathbf{k}, \mathbf{r}_n, j_p, \mu_p)\rangle$ is a linear combination of matrix elements of the type $\langle e^{i(\mathbf{k}'\cdot\mathbf{r}_p)}\psi(l_n, m_n)\,|\,V_{np}\,|\,\Psi(\mathbf{k}, \mathbf{r}_n, l_p, m_p)\rangle$ already considered, where $l_n=j_n\pm\frac{1}{2}$ and $l_p=j_p\pm\frac{1}{2}$. Each of these we have seen to be a sum of the form (9), where l is restricted to the possible magnitudes of the vector l_p-l_n. But $l_p-l_n=\mathbf{j}_p-\mathbf{j}_n+\mathfrak{s}$, where $\mathfrak{s}$ is a vector of unit magnitude; so, by (15), $l_p-l_n=\mathbf{J}_X-\mathbf{J}_Y+\mathfrak{s}$. The possible values of l are therefore given by

$$J_X+J_Y+1\geqslant l\geqslant|\,\mathbf{J}_X+\mathbf{J}_Y+\mathfrak{s}\,|_{\min}. \quad (16)$$

Conservation of parity yields the further restriction that l can take only odd or even values, according to whether or not there is a change of nuclear parity.

In the cases, therefore, where there are no special reasons for choosing particular orbitals for the neutron and proton, the angular distribution from surface interactions will still exhibit a series of peaks in the forward direction [arising from the same factor $j_l(Qr_0)$] except that now the selection rules governing these peaks are somewhat less stringent. Thus $l_{\min}$ (obtained from the first peak) is the first even (no) or odd (yes) integer not less than the minimum value of $|\,\mathbf{J}_X+\mathbf{J}_Y+\mathfrak{s}\,|$. If we write $|J_X-J_Y|=\Delta J$, a peak directly forward indicates $\Delta J=0$ or 1 (no). If there is no peak directly forward, then either $\Delta J\geqslant 0$ (yes) or $\Delta J\geqslant 2$ (no). If $l_{\min}$ is observed to be 3, $\Delta J=3$ or 4 (yes), and so on.

ACKNOWLEDGMENT

We are indebted to Dr. E. E. Salpeter, Dr. W. T. Sharp, and Professor H. A. Bethe for interesting discussions in connection with this work.

Penetration of Gamma Radiation through Iron

L. A. Beach, R. B. Theus, and W. R. Faust
Naval Research Laboratory, Washington, D. C.

(Received June 12, 1953)

Measurements have been made on the penetration through iron by Cs^{137}, Co^{60}, and Na^{24} gamma radiation in plane parallel geometry. Good agreement was obtained between the experimental transmissions and theoretical values computed from Spencer's polynomial method.

SOLUTIONS of the transport equation appropriate for the penetration of gamma radiation in an infinite medium have been devised by Spencer and Fano by expansion of the photon distribution in Legendre polynomials.[1] This method has given theoretical predictions in good agreement with experimental results[2–4] for Co^{60} radiation in lead and water.

Experimental results of plane parallel Cs^{137}, Co^{60}, and Na^{24} gamma radiation diffusing through iron are compared with computations of Spencer. The shield used in these experiments was constructed of $\frac{1}{4}$-inch plates four feet square which were secured in a perpendicular position ten feet above the ground to insure a minimum contribution to the counting rate by ground-scattered radiation. The sources were placed fifteen feet from the iron plates providing a beam intensity that was constant to within ten percent over the shield surface. A copper Geiger-Mueller counter, centered behind the plates, detected the radiation penetrating the barrier. Correction for air-scattered radiation was established by observing the difference in counting rates with and without two inches of lead protecting the sides and bottom of the detector.

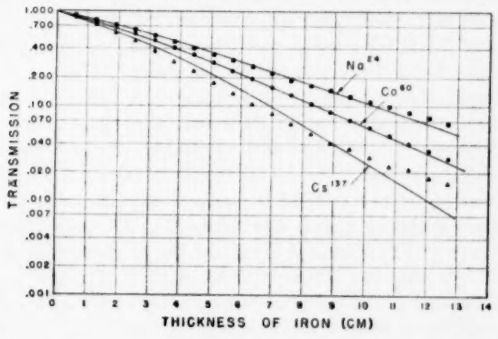

FIG. 1. Transmission of gamma radiation through iron. ▲, Cs^{137} radiation of 0.66 Mev; ●, Co^{60} radiation of 1.17 and 1.33 Mev; ■, Na^{24} radiation of 1.38 and 2.76 Mev. The solid curves represent theoretical transmission values compiled by Spencer's polynomial method.

Figure 1 shows the comparison between experimental results and theoretical predictions of the polynomial method as a function of penetration depth. The solid curves represent theoretical values computed for plane parallel radiation incident upon an iron medium by integrating the spectral intensity,[5] weighted by the detector response, over all energies. Corrections have been made to the experimental points for air-scattered radiation which is larger and more difficult to evaluate for lower energy radiation. The experimental values for Co^{60} and Na^{24} radiation are in good agreement with the theoretical curves and the slight deviations at large penetration depths are due to incomplete correction for air scattering.

The experimental points for Cs^{137} radiation fall below the theoretical curve because less radiation is incident on the detector in our slab geometry than if it was imbedded in an infinite medium. This effect is most important for Cs^{137} since large angle scattering is more probable for low-energy radiation.

This experiment extends the verification of the polynomial method to intermediate weights and verifies that the polynomial method contains the proper energy dependence in that the build-up factors increase as the primary energy decreases.

The authors wish to express their appreciation to Dr. E. H. Krause for his aid and support.

[1] L. V. Spencer and U. Fano, Phys. Rev. **88**, 446 (1951).
[2] G. R. White, Phys. Rev. **80**, 154 (1950).
[3] E. Hayward, Phys. Rev. **86**, 493 (1952).
[4] J. O. Elliot *et al.*, Phys. Rev. **85**, 1048 (1952).
[5] Curves were obtained from L. V. Spencer prior to publication.

Disintegration Scheme of Br^{80} (18 min)

GERTRUDE SCHARFF-GOLDHABER AND MICHAEL MCKEOWN
Brookhaven National Laboratory, Upton, New York*

(Received July 15, 1953)

The 18-min isomer Br^{80} is shown to emit γ rays of 620-kev energy which follow a low intensity (9 ± 2 percent) β-ray branch. Beta-gamma coincidences are observed, indicating that the gamma transition takes place in Kr^{80}. No γ-ray transition was found to follow the positron or K capture branch. The intensity observed is compatible with a spin and parity assignment 1+ for the ground state of Br^{80}, while the 620-kev state in Kr^{80} is probably 2+. The gamma-ray energy observed fits well into the pattern for the energy of the first excited state of even-even nuclei.

THE 18-min isomer of Br^{80} has been reported by several authors[1,2] to have a complex beta-ray spectrum. The two most energetic β rays showed an energy difference of about 0.9 Mev. A recent search,[3] by means of a scintillation spectrometer, for the γ transition going to the ground state of Kr^{80} following the low-energy beta-ray branch, revealed no γ rays except annihilation radiation due to a low-intensity positron branch. The mean of the values reported[1,2] for the ratio β^+/β^- is 0.03.

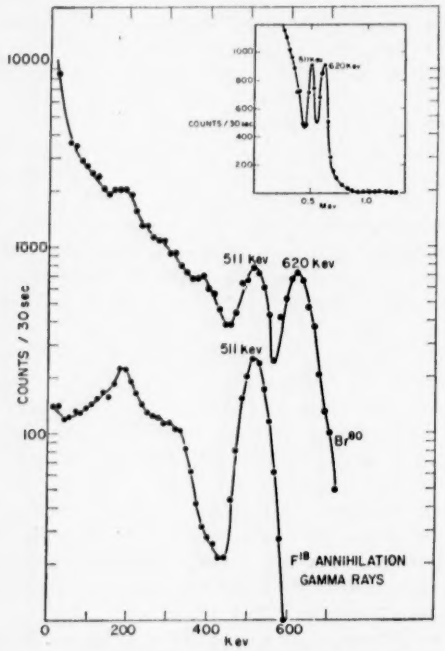

FIG. 1. Pulse-height distribution of Br^{80} (18-min) γ radiation obtained with a scintillation spectrometer. For calibration purposes, the pulse-height distribution of the annihilation gamma rays from F^{18} is shown (lower curve). The peaks below 200 kev are the result of reflection of the gamma rays. The inset shows the continuation of the spectrum at higher energy.

A survey of first excited states of even-even nuclei[4,5] shows that an excited state in Kr^{80} of about 0.6 Mev might be expected. Consequently, a new effort was made to detect the corresponding γ rays with a high resolution scintillation spectrometer. For this purpose a 1-cm^3 NaI(Tl) crystal was used. A Br^{80} sample produced by a 1-sec irradiation of 1-mg NH_4Br in the Brookhaven reactor served as a source. A (620 ± 10) kev γ radiation was indeed detected. Figure 1 shows a spectrogram obtained with a single channel pulse-height analyzer. The annihilation γ rays are clearly resolved from the 620-kev peak. For calibration purposes a similar curve was taken for the annihilation γ rays of F^{18}. Figure 2 gives the decay curves for the 511-kev and the 620-kev peaks of Br^{80}, showing that 90 percent of the radiations initially emitted decay with a half-life of 18 min. The intensity of the 620-kev γ rays, after correction for efficiency, is found to be 50 percent higher than that of the annihilation γ rays. Using the ratio $\beta^+/\beta^-=0.03$ mentioned above, we arrive at a branching ratio $\gamma_{620\text{ kev}}/\beta^-=0.09\pm0.02$.

In order to show that the 620-kev radiation follows indeed a beta-ray branch, beta-gamma coincidences were studied. The 620-kev γ-ray pulses were again selected by means of a differential pulse-height analyzer. Figure 3 shows a decay curve of the $\beta-\gamma$ coincidences which is in good agreement with $T_{1/2}=18$ min. The coincidence efficiency per beta ray was calibrated with a source of Au^{198}. The branching ratio $\gamma_{620\text{ kev}}/\beta^-$ deduced from the coincidence rate per beta ray, after correcting for the γ-ray efficiency, agrees within limits of error with the value obtained from a comparison of the intensity of the 620-kev γ rays with that of the annihilation radiation.

In order to exclude the possibility that the γ rays follow the positron or K capture branch, a search for 511-kev–620-kev γ-γ coincidences as well as for coincidences of the 620-kev γ rays with Se K x-rays was made. No coincidences were found.

* Work carried out under the auspices of the U. S. Atomic Energy Commission.

[1] Hollander, Perlman, and Seaborg, Revs. Modern Phys. **25**, 469 (1953).

[2] K. Way *et al.*, National Bureau of Standards Bulletin No. 499 and Supplement 1 (U. S. Government Printing Office, Washington, D. C., 1950 and 1951).

[3] Laberrigue-Frolow, Bernas, and Langevin, Compt. rend. **236**, 1246 (1953).

[4] P. Preiswerk and P. Stähelin, Helv. Phys. Acta **24**, 623 (1952).

[5] G. Scharff-Goldhaber, Phys. Rev. **90**, 587 (1953).

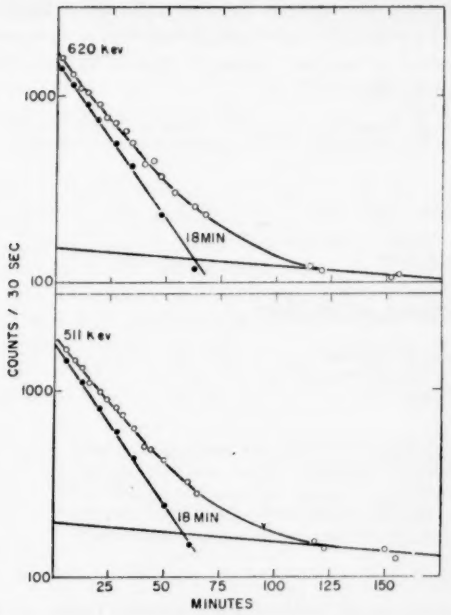

FIG. 2. Decay curves of the 620-kev γ rays (upper curve) and annihilation radiation (lower curve) from Br^{80}. The curves show that about 90 percent of these radiations decay with a half-life of 18 min.

Figure 4 shows the disintegration scheme[6] for Br^{80}. A spin of 1+ for the Br^{80} ground state is compatible with the logft values for the two β^- branches. That the logft value for the transition from Br^{80} to Se^{80} is much

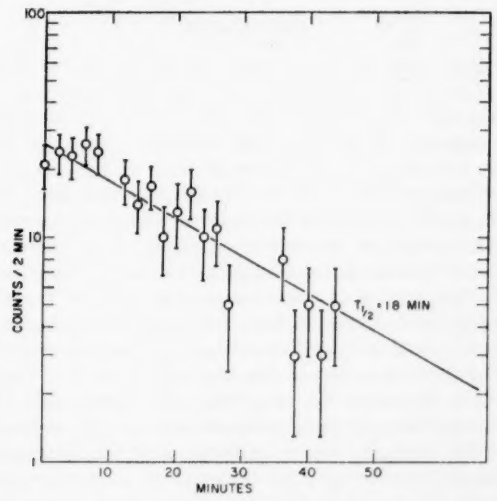

FIG. 3. Decay curve of the $\beta-\gamma_{620\ kev}$ coincidences from Br^{80}. At least 90 percent of the coincidences decay with a half-life of 18 min.

[6] For spin assignments of the Br^{80} states see M. Goldhaber and R. D. Hill, Revs. Modern Phys. **24**, 179 (1952).

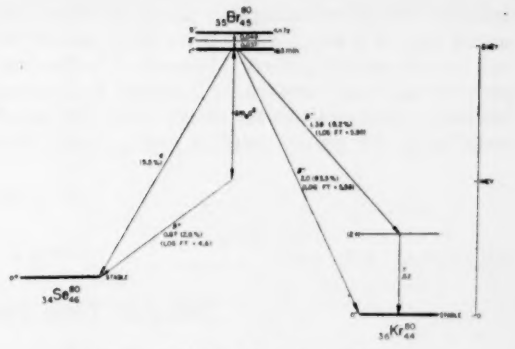

FIG. 4. Disintegration scheme of Br^{80}.

lower than that for the transitions to Kr^{80} is due to the fact that in both Se^{80} and Kr^{80} one may expect to find a $p_{1/2}$ neutron pair with high probability.[7] Consequently, the transition from the ground state of Br^{80} with, presumably, a $p_{3/2}$ proton and a $p_{1/2}$ neutron to Se^{80} will be favored, whereas the transition to Kr^{80} can only take place to the much less probable neutron configuration $g_{9/2}{}^6p_{1/2}{}^0$.—From the generally observed regularity[5] we may assume that the 620-kev state is 2+.

Figure 5 represents the trend, with increasing neutron number, of the energy of the first excited state of

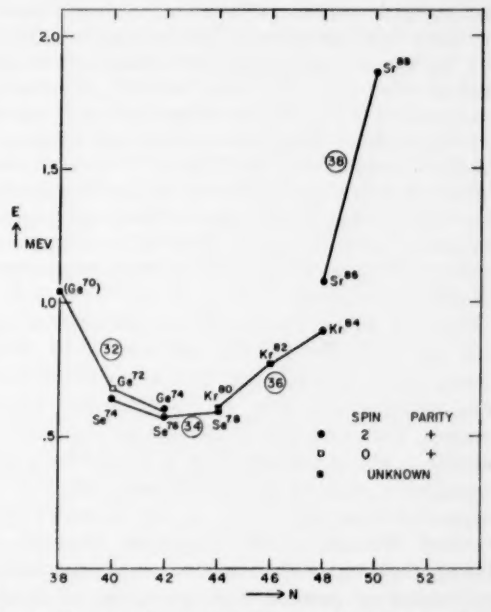

FIG. 5. Energy of first excited state, plotted against number of neutrons in even-even nuclei for N below 50. Points for isotopes of an element are connected with straight lines. The encircled numbers indicate the atomic number.

[7] In support of this argument see Sunyar, Mihelich, Scharff-Goldhaber, Goldhaber, Wall, and Deutsch, Phys. Rev. **86**, 1023 (1952) and A. de Shalit and M. Goldhaber, Phys. Rev. (to be published).

even-even nuclei in the region with which we are concerned here. It is seen that the point found for Kr^{80} fits well into the general pattern. Moreover, it further supports the rule[6] that addition of 2 protons to a nucleus has only a slight effect on the energy of the first excited state except for proton numbers near a closed shell: Se^{78} has a first excited state of 0.60 ± 0.025 Mev, deduced by Kinsey and Bartholomew[8] from the energy difference of the two capture γ rays of highest energy observed from $(Se^{77}+n)$.

[8] B. B. Kinsey and G. A. Bartholomew (private communication). This will appear in the *Canadian Journal of Physics*.

PHYSICAL REVIEW VOLUME 92, NUMBER 2 OCTOBER 15, 1953

Neutron Total Cross Sections at 20 Mev

ROBERT B. DAY AND RICHARD L. HENKEL
Los Alamos Scientific Laboratory, Los Alamos, New Mexico
(Received July 1, 1953)

With the $T(d,n)He^4$ reaction as a monoenergetic source of neutrons of about 20 Mev, the total cross sections of 13 elements have been measured by a transmission experiment. These cross sections vary approximately as $A^{\frac{1}{3}}$ as is to be expected from the continuum theory of nuclear reactions. The cross section for hydrogen at 19.93 Mev is 0.504 ± 0.01 barn. This result, together with other results at lower energies, seems to require a Yukawa potential in both the singlet and triplet n-p states and a singlet effective range that is lower than that obtained from p-p scattering data.

INTRODUCTION

UNTIL very recently most work on neutron cross sections at energies from 10 to 25 Mev was done with sources such as $Li^7(d,n)Be^8$ which do not produce monoenergetic neutrons. Therefore, to obtain results ascribable to a particular neutron energy it was necessary to use an energy-sensitive detector. The two methods most commonly used were (1) detection of recoil protons of a particular energy emitted in a given direction from a hydrogenous radiator[1] and (2) use of a threshold detector such as $C^{12}(n,2n)$.[2,3] Both of these methods suffer from rather severe defects. The first has very low efficiency if one wishes to obtain good energy resolution, while the second gives only a complicated average of the cross section over the energy region above the effective threshold.

With the production of sufficient quantities of tritium, the $T(d,n)He^4$ reaction can now serve as an intense source of high-energy monoenergetic neutrons, thus releasing one from the troublesome detector problem. With a 3.5-Mev accelerator, for example, it is possible to obtain neutrons from 12 to 20 Mev with a homogeneity that is determined essentially by the target thickness and hence by the source strength required. Because of the low-energy resonance in $T(d,n)$, Cockcroft-Walton accelerators are particularly well suited to produce high intensities of 14-Mev neutrons by this reaction. Coon *et al.*[4] have recently published a survey of the total cross sections of over 50 elements for 14-Mev neutrons, while Poss *et al.*[5] have also reported a few measurements of total cross sections at this energy.

Using this reaction as a source of monoenergetic neutrons in the 20-Mev region, we have measured the total cross sections of a number of elements to an accuracy of about 3 percent and the total cross section of hydrogen to 2 percent. The results vary approximately as $A^{\frac{1}{3}}$, as is to be expected from the continuum theory of nuclear reactions of Feshbach and Weisskopf.[6]

PROCEDURE

Fast neutrons of the order of 20-Mev energy were obtained by bombarding a tritium gas target with deuterons from the large Los Alamos electrostatic accelerator. To obtain a sufficiently high neutron flux, the tritium pressure was usually such that it produced an energy loss of about 200 kev for the deuterons traversing the target. This variation in deuteron energies throughout the target produced a corresponding spread in neutron energies which was much larger than the spread due to other causes. The average neutron energy was calculated from the dynamics of the reaction, including a small correction for relativistic effects. The corrections to the deuteron energy for the energy loss in the target and the nickel entrance foil were calculated from calibrations made with the proton beam.

The detector was a stilbene scintillation counter placed 148 cm from the target at 0° to the deuteron beam. To keep the background low the counter was biased to count only neutrons of about 14 Mev or higher. A similar scintillation counter at 30° to the

[1] W. Sleator, Jr., Phys. Rev. **72**, 207 (1947).
[2] R. Sherr, Phys. Rev. **68**, 240 (1945).
[3] Amaldi, Bocciarelli, Cacciapuoti, and Trabacchi, Report of an International Conference on Fundamental Particles **1**, 97 (1947).
[4] Coon, Graves, and Barschall, Phys. Rev. **88**, 562 (1952).
[5] Poss, Salant, Snow, and Yuan, Phys. Rev. **87**, 11 (1952).
[6] H. Feshbach and V. F. Weisskopf, Phys. Rev. **76**, 1550 (1949).

beam served as a monitor for the neutron flux, while a precision current integrator was used to measure the deuteron beam incident on the target.

The total cross sections σ_t were obtained from transmission measurements by means of the relation:

$$T=e^{-n\sigma_t},$$

where n is the number of target nuclei per square cm of beam. In making the transmission measurements, samples 2.54 cm in diameter were placed midway between the source and detector. To measure the effect produced by neutrons scattered from the walls and floor of the room a long copper bar with essentially zero transmission was placed at the sample position. The counting rate with this in place was always less than 1.5 percent of the rate obtained from the direct neutron beam. A second correction must be made for neutrons (and any possible gamma rays) that are produced by (d,n) reactions where the deuteron beam strikes the collimating diaphragms, entrance foil, etc. This correction was obtained by replacing the tritium in the target cell with hydrogen and repeating the transmission measurements. In order to remove all tritium from the target it was necessary to flush it out several times with hydrogen. The removal of the tritium was considered satisfactory when the monitor counting rate no longer decreased with further flushing. The detector counting rate was then a maximum of 3 percent of the rate obtained with tritium in the target.

For the hydrogen and helium measurements the sample was a cell 100.0 cm long and 2.38 cm in diameter filled with the gas to a pressure of about 2000 psi. The filling was done by R. L. Mills and F. Edeskuty, who also determined the amount of gas present by weighing the cell full and empty. For the hydrogen filling an independent check was made by accurate PVT measurements. The two methods agreed to ½ percent. A mass-spectroscopic analysis of the hydrogen showed a purity of 99.75 percent, with deuterium being the principal contaminant. No special analyses of the other samples were made since they were known to have a purity of better than 99 percent and the accuracy expected from the cross sections did not justify this procedure.

TABLE I. Total cross sections. Unless otherwise indicated the cross-section accuracy is ±3 percent. The accuracy in the neutron energy is ±0.025 Mev.

Element	E_n(Mev)	Neutron energy spread (Mev)	σ_t(barns)	Sample form
H	19.93	0.26	0.504±0.01	gas
He	17.97	0.44	0.848	gas
	19.00	0.32	0.816	
	20.07	0.25	0.770	
C	17.20	0.54	1.39	graphite
	19.00	0.32	1.45	
	20.07	0.25	1.52	
F	19.00	0.32	1.84	Teflon
Al	19.00	0.32	1.84	metal
Si	19.00	0.32	1.94	compacted powder
Fe	19.00	0.32	2.23	metal
Cu	19.00	0.32	2.56	metal
Br	17.20	0.54	3.12	liquid
	19.00	0.32	2.98	
	20.07	0.25	2.96	
Zr	19.00	0.32	3.60	metal
Pb	19.00	0.32	5.96	metal
Bi	19.00	0.32	5.69	metal
U	17.97	0.44	6.14	metal
	19.00	0.32	5.94	
	20.07	0.25	6.29	

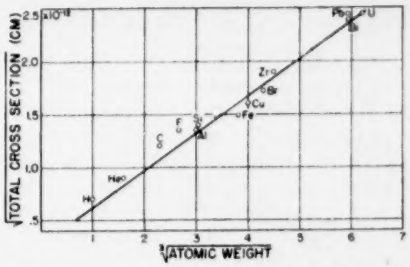

FIG. 1. The square root of the total cross section as a function of the cube root of the atomic weight. Neutron energy = 19 Mev. The straight line is the function $(\sigma_t)^{\frac{1}{2}}=(2\pi)^{\frac{1}{2}}(r_0A^{\frac{1}{3}}+\lambda)$, $r_0=1.4\times10^{-13}$ cm.

RESULTS

The results of the total cross-section measurements are summarized in Table I. Generally, several series of measurements were made from which the cross section could be calculated, and these always agreed within 2 or 3 percent. Since the possible errors arising from other causes are considerably less than this, we believe that these cross sections are good to 3 percent.

A correction for in-scattering has been applied using the formula for in-scattering given in the appendix. Because of the good geometry used in these experiments the correction was never larger than 1.4 percent, and for the lighter elements it was negligible. The increased correction necessitated by the long length of the gas cell in the hydrogen and helium experiments has been calculated, but it is still negligible. The effects of multiple scattering were also considered and were found to be so small as to produce no detectable effect.

The cross sections are displayed graphically in Fig. 1, where we have plotted the square root of the total cross section as a function of the cube root of the atomic number. The solid curve is the function $(\sigma_t)^{\frac{1}{2}}=(2\pi)^{\frac{1}{2}}\times(R+\lambda)$, which is the asymptotic form of the expression for the total cross section given by the theory of Feshbach and Weisskopf.[6] Deviations from this curve are not significant, since the theory has already proved to be inadequate to explain the variation of total cross sections at lower energies.[7] A more refined theory has recently been announced,[8] which gives better agreement with the lower-energy data, and perhaps it will be satisfactory at these energies also.

[7] H. H. Barschall, Phys. Rev. **86**, 431 (1952).
[8] Feshbach, Porter, and Weisskopf, Phys. Rev. **90**, 166 (1953).

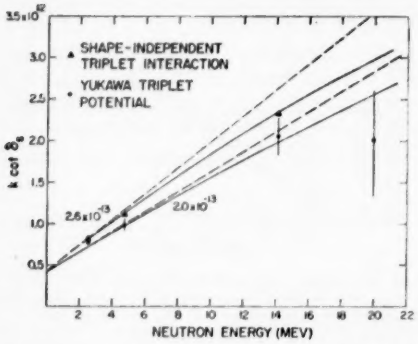

FIG. 2. $k\cot\delta_s$ for the singlet scattering state, calculated under the assumption of both a shape-independent triplet interaction and a Yukawa triplet potential. At 20 Mev, $k\cot\delta_s$ is practically independent of assumptions as to the nature of the triplet potential. The dotted and solid curves are the predictions of the effective range theory for the shape-independent and Yukawa potentials, respectively, for the two values of the singlet effective range indicated here.

More attention was given to the measurements of the total cross section of hydrogen. From five different determinations of the transmission, the cross section was found to be 0.504 ± 0.01 barn, where the error quoted is the standard deviation of the measurements. This error arises principally from the fact that the transmission was fairly high (0.734) and therefore the error in the cross section was several times the transmission error. With twice the hydrogen pressure this error could be reduced by a factor of two without increasing the counting time to any great extent. Other possible sources of error have been considered and are considerably less than that quoted here.

DISCUSSION OF *n-p* SCATTERING RESULTS

With the aid of the effective range theory for *s*-wave neutrons,[9,10] the results of the *n-p* total cross section have been compared with the most accurate experimental results obtained at lower energies. The other results used were (1) $\sigma=2.525$ barns at 2.532 Mev (Fields, Becker, and Adair[11]); (2) $\sigma=1.690$ barns at 4.749 Mev (Hafner, Hornyak, Falk, Snow, and Coor[12]); and (3) $\sigma=0.689$ barn at 14.10 Mev (Poss, Salant, Snow, and Yuan[5]). Using the triplet scattering length and effective range given by Snow,[13] we have calculated $k\cot\delta_s$ for the singlet scattering at each of these energies for both a shape-independent triplet interaction and a Yukawa triplet potential. At 19.93 Mev the effect of *d*-wave scattering was considered, and a small correction for it was subtracted, using the results of calculations by Christian.[14] However, the *d*-wave contribution at this energy is actually negligible compared to our experimental error and could have been left out. Effects from *p* waves were not estimated since the symmetry in the scattering about 90° found at higher energies leads one to expect that they are very small.[14] It is interesting to note that the triplet phase shift is very close to 90° at this energy; consequently, the total cross section is practically independent of any assumptions as to the nature of the triplet interaction. Unfortunately, the singlet scattering is only about $\frac{1}{3}$ of the total cross section, and therefore a very precise measurement of the total cross section is necessary to get much accuracy in $k\cot\delta_s$.

The values for $k\cot\delta_s$ have been plotted in Fig. 2 as a function of neutron energy. The uncertainties indicated are those resulting from errors in the cross sections only and do not include any errors in the scattering parameters. From this graph it appears that the singlet effective range must be smaller than the value 2.6–2.7×10^{-13} cm obtained from *p-p* scattering data at low energies,[15] although if one assumes a shape-independent interaction for the triplet state a shape-independent singlet effective range of 2.6×10^{-13} cm is consistent with the three experiments at lower energies. Considering all the data, the best fit is obtained if one assumes a Yukawa potential for both the singlet and triplet states, with a singlet effective range of about 2×10^{-13} cm.

Since the low value for $k\cot\delta_s$ at 20 Mev is the main factor in the conclusions reached above, we must reconsider the possibility of a systematic error in the cross-section measurement. Of the various possibilities, the only one which could amount to more than a few tenths of a percent is in the measurement of backgrounds when the tritium in the target is replaced by hydrogen. In recent experiments some unusually high backgrounds were found to be produced by impurities in the hydrogen used as the replacement gas; however, at the time the total cross-section measurements reported here were made a different tank of hydrogen was in use and there was no suggestion of an abnormal background. If the hydrogen background measured then were ignored completely, the result would be a 2.7-percent decrease in the *n-p* cross section and a corresponding increase of 40 percent in $k\cot\delta_s$. Because the magnitude of this background depends on several unknown factors, among which are the bias used on the scintillation counter and the way in which the deuteron beam was focused, it is not possible to say how large it should have been.

We would like to thank Robert L. Mills and Frederick Edeskuty for filling the gas cells and determining the amount of gas present, and James H. Coon for the use of the gas cells and detection equipment.

[9] J. M. Blatt and J. D. Jackson, Phys. Rev. **76**, 18 (1949).
[10] H. A. Bethe, Phys. Rev. **76**, 38 (1949).
[11] Fields, Becker, and Adair, Phys. Rev. **89**, 908 (1953).
[12] Hafner, Hornyak, Falk, Snow, and Coor, Phys. Rev. **89**, 204 (1953).
[13] G. Snow, Phys. Rev. **87**, 21 (1952).
[14] R. S. Christian, Repts. Progr. Phys. **15**, 68 (1952).
[15] J. D. Jackson and J. M. Blatt, Revs. Modern Phys. **22**, 77 (1950).

APPENDIX

In-Scattering Corrections

Since there seems to be no general agreement as to how in-scattering should be treated we wish to derive here the corrections required for a transmission experiment.[16] We assume that the scattering sample is midway between the source and detector and that the incident and in-scattered neutrons make small angles with the axis of the system. Considering only singly scattered neutrons, the increase in transmission due to in-scattering is given by

$$T_1=\frac{4B}{(\frac{1}{2}L)^2}\int e^{-\mu z}f(0)\mu dz e^{-\mu(t-z)},$$

where $B=\frac{1}{4}\pi D^2$=area of scattering sample, L=source to detector distance, t=thickness of scattering sample, $\mu=n\sigma_t$; σ_t=total cross section, and

$$f(\theta)=\frac{1}{\sigma_t}\frac{d\sigma(\theta)}{d\Omega}.$$

After integrating this expression one can obtain a simple formula for the relative correction to be applied to the cross section, namely

$$\Delta\sigma/\sigma=4\pi(D/L)^2f(0).$$

For the quantity $f(0)$ we have used $\frac{1}{2}(kR+1)^2/4\pi$, where k is the neutron wave number and $R=r_0A^{\frac{1}{3}}$ is the nuclear radius. The factor $(kR+1)^2/4\pi$ is obtained from the diffraction theory of Feld *et al.*[17] based on the continuum model; the factor $\frac{1}{2}$ arises from our assumption that half of the total cross section is due to diffraction scattering. There is excellent justification for using this diffraction theory. With the fast beam of the Los Alamos Fast Reactor as a source, Jurney[18] has measured the neutron angular distributions for a number of elements from iron to bismuth. In all cases the results were in very good agreement with the predictions of the theory for angles up to 60°. At the higher energies used in our experiments one would expect the theory to apply equally well.

Since in some experiments the effects of multiple scattering may be important we have considered them also. For elements which scatter principally in a narrow forward cone the increase in transmission caused by double scattering is

$$T_2=\frac{4B}{(\frac{1}{2}L)^2}\int\int e^{-\mu z}f(\theta)\mu dz[1-e^{-\mu(t-z)}]f(\theta)2\pi\sin\theta d\theta.$$

The expression in brackets, which is the probability that a second collision will occur, has been simplified by assuming that $\cos\theta\approx 1$. We have also neglected the attenuation of the neutrons after the second scattering. The ratio of the effects due to double and single in-scattering is now given by

$$\frac{T_2}{T_1}=\frac{2\pi\int f^2(\theta)\sin\theta d\theta}{f(0)}\frac{1-e^{-\mu t}-\mu te^{-\mu t}}{\mu te^{-\mu t}}.$$

An upper limit to this ratio can be obtained by letting $f(\theta)=f(0)$ within the first lobe of the scattering pattern and $f(\theta)=0$ outside. One then finds that for a uranium sample with a transmission of 0.5 the ratio of T_2/T_1 at 20 Mev is about $\frac{1}{2}$. A better estimate can be made by a numerical integration of the curves given in reference 17. This indicates that the ratio of $\frac{1}{2}$ may be an order of magnitude too large. Since in our experiments the greatest correction required for single in-scattering was 1.4 percent, we conclude that the correction for double in-scattering is negligible.

[16] The correct formula taking single scattering into account has previously been given by the following authors: Amaldi, Bocciarelli, Cacciapuoti, and Trabacchi, Atti accad. nazl. Lincei **1**, 29 (1946); R. Ricamo and W. Zünti, Helv. Phys. Acta **24**, 419 (1951); Hafner, Hornyak, Falk, Snow, and Coor, Phys. Rev. **89**, 204 (1953).

[17] Feld, Feshbach, Goldberger, Goldstein, and Weisskopf, Final Report of the Fast Neutron Data Project, NYO-636 (January 31, 1951) (unpublished).

[18] E. T. Jurney (private communication).

Photoprotons from In, Ce, and Bi*

M. E. Toms and W. E. Stephens
University of Pennsylvania, Philadelphia, Pennsylvania
(Received June 18, 1953)

The charged particles ejected from indium, cerium, and bismuth foils by x-rays from a 24-Mev betatron were observed in nuclear emulsions. The yields of photoprotons, photodeuterons, and photoalpha particles were determined, and the energy and angular distributions of the photoprotons were measured and compared with theoretical calculations based on the evaporation process and on the direct photoeffect. The energy distributions observed indicate a large fraction of direct photoeffect. A marked forward asymmetry was observed in the angular distributions from indium and bismuth.

INTRODUCTION

THE photodisintegration of medium elements has been shown to consist primarily of a dipole absorption of photons with the subsequent evaporation of a nuclear particle.[1–6] Nevertheless, several indications suggested that a direct photoeffect is also present.[5–8] We have investigated this possibility further by observing the photoprotons from heavier elements, where the yield of evaporation protons is reduced by the Coulomb barrier, thus relatively enhancing other processes. The charged photoparticles ejected by 24-Mev bremsstrahlung x-rays were observed in nuclear emulsions. This made identification of the particles by grain counting possible, as well as measurement of angular and energy distributions. Preliminary results have already been described.[9] A similar investigation of the photoprotons from Mo^{100} and Mo^{92} has been reported by Butler and Almy[10] and from aluminum and tantalum by Cameron and Hoffman.[11]

EXPERIMENT

The experimental arrangement is essentially the same as described previously.[4,6] An improved plate holder was installed in the nuclear emulsion camera to ensure the accurate positioning of the nuclear emulsion plates. Ten $\frac{1}{4}$-in.$\times$1-in. Ilford E-1, 200-micron nuclear emulsion plates were cemented on plate holders at angles of 30°, 50°, 70°, 90°, 110°, to the left and 70°, 90°, 110° 130°, and 150° to the right of the target foil with their front edges 1.9 cm away from a vertical line through the center of the target. The plane of the surface of the plates was 0.65 cm below the center of the beam. The plates from a single run were developed together by a temperature change method. A double camera was used so that two separate foils could be exposed in each

Table I. Exposure details.

Run Foil	Ia In	IIa Bi	IIb Ce	IIIa Bi	IIIb Ba[a]	IVb Ce	Va ···
(mg/cm²)	18.6	17.5	23	54.7	22.6	28	···
(mils)	1.0	0.8	1.31	2.2	2.36	1.6	···
Betatron energy (Mev)	24	24	24	24	24	23	23
Roentgens at foil	51 800	44 600	37 800	28 400	24 200	23 800	34 000
Emulsion type	E-1	E-1	E-1	E-1	E-1	E-1	C-2
Area scanned (cm²)	0.396	0.724	0.14	1.37	scanned sideways	0.6	0.32
Total tracks measured	625	116	219	480	(62)	584	8
Target half-thickness in Mev for 10-Mev protons	0.2	0.2	0.25	0.5	0.2	0.3	···
Comments		Repeated in IIIa for more intensity	Repeated in IVb as a check				Background

[a] Possible oil contamination on foil.

* Aided in part by the Air Research and Development Command and by the joint program of the U. S. Office of Naval Research and the U. S. Atomic Energy Commission.

[1] J. S. Levinger and H. A. Bethe, Phys. Rev. **78**, 115 (1950).
[2] M. Goldhaber and E. Teller, Phys. Rev. **74**, 1046 (1948).
[3] V. F. Weisskopf and D. H. Ewing, Phys. Rev. **57**, 472 (1940).
[4] M. E. Toms and W. E. Stephens, Phys. Rev. **82**, 709 (1951).
[5] B. C. Diven and G. M. Almy, Phys. Rev. **80**, 407 (1950).
[6] P. R. Byerly, Jr., and W. E. Stephens, Phys. Rev. **83**, 54 (1951).
[7] O. Hirzel and H. Wäffler, Helv. Phys. Acta **20**, 373 (1947).
[8] E. D. Courant, Phys. Rev. **82**, 703 (1951).
[9] M. E. Toms and W. E. Stephens, Phys. Rev. **88**, 160 (1952); Stephens, Toms, Carroll, and Rosenblum, Phys. Rev. **89**, 893 (1953).
[10] W. A. Butler and G. M. Almy, Phys. Rev. **89**, 893 (1953).
[11] A. G. W. Cameron and M. M. Hoffman, Bull. Am. Phys. Soc. **28**, No. 3, 49 (1953).

run. The details of the various exposures are given in Table I. The first row gives the run number, with the suffix a to indicate the camera nearer to the betatron and b the camera farther from the betatron.The second row gives the element irradiated. The purities of these elements are: Bi 99.9 percent, Ce 98.6 percent, Ba 98 percent, and In 99.9 percent. We can estimate that about 5 to 10 percent of the barium protons might be from the calcium and strontium impurities; for cerium, about 5 percent of the cerium protons may be from iron; and that less than 1 percent of the indium or bismuth protons would be due to impurities. The third and fourth rows show the effective thickness of the foil in milligrams per square cm and in mils. Since the foils were placed at an angle of 30° to the beam, this thickness is greater than the target thickness for the protons emerging normally from the foil. The betatron energy, the roentgen units delivered to the foil, and the emulsion type are given in the next rows. Row eight shows the areas of the emulsion which were

TABLE II. Yield data.

Run Foil	Ia In	IIa Bi	IIb Ce	IIIa Bi	IIIb Ba	IVb Ce	Va ···
Foil width (cm)	1.1	1.1	0.9	0.9	1.1	0.9	···
A (cm²)	0.292	0.292	0.283	0.240	0.335	0.283	···
$t\times10^{-3}$ (cm)	5.09	4.06	6.68	11.36	13.4	8.16	···
Protons	623	116	216	475	(62)	556	8
Deuterons	0			4		24	0
Alphas	2		3	1		4	0
(P/w) $\times10^{-3}$	5.82			1.70		3.50	0.11
$Y_p\times10^{-4}$	11.7	4	10	5.20	11	12.9	
p/wR	11.2			6.0		11.8	0.32
Estimated background tracks	18			25		16	

scanned, and row nine gives the total tracks observed which fulfilled the criteria of coming from the foil and entering the top surface of the emulsion. The barium plates were scanned perpendicular to the track directions in order to survey the yield. Since there was a possible oil contamination on the surface of the barium foil, these plates were not scanned further. Run IIa for bismuth gave a low yield of protons per field of view and was repeated in run IIIa with a thicker foil. Run IIb with cerium showed a difference between the 90° right and 90° left plate indicating a misalignment. Cerium was therefore repeated in run IVb. In all accepted runs, the 90° right and 90° left plate agreed within the statistical probable error.

Table II gives additional data from which the yields were calculated. The beam did not cover the foils in the horizontal direction. Consequently the area of interception A was calculated from the known geometry. The effective thickness t was calculated from the weight and area of the foils. The sixth, seventh, and eighth rows give the observed protons, deuterons, and alpha particles as identified by grain counting. Alphas

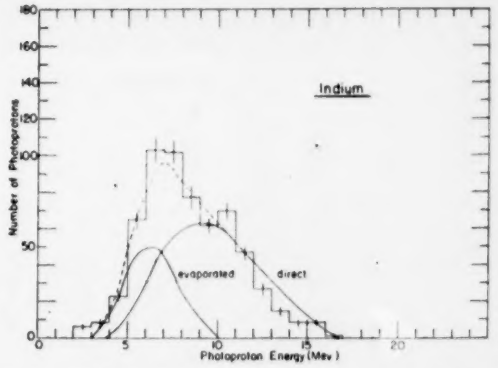

FIG. 1. Histogram of the number of photoprotons observed from indium as a function of proton energy. The calculated curves for the direct and evaporated protons are shown for comparison.

could in general be identified visually. All tracks with a range less than that of a 5-Mev proton were grain-counted in their last 60 microns and compared with the grain counts of recoil protons in the same emulsion. The grain counts in E-1 emulsions scattered more than in C-2 emulsions, and because of the small numbers of deuterons involved the identification was not as clear cut as for the copper photodeuterons.[6] Row nine gives the numbers of protons per total solid angle corrected for the observed angular distribution. The proton yields are stated in row ten in protons per mole per roentgen unit. Row eleven gives protons per roentgen in order to compare with the background determined in run Va. This is used to estimate the background tracks for runs Ia, IIIa, and IVb as indicated in row twelve. These background protons are in the energy range from 2.5 to 5 Mev.

Figures 1–3 show the observed energy distributions for indium, cerium, and bismuth. In the indium and bismuth curves, the few tracks identified as alphas or deuterons by grain counting were removed from the

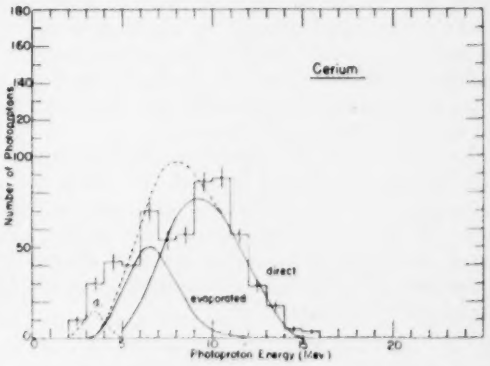

FIG. 2. Histogram of the number of photoprotons observed from cerium as a function of proton energy. The calculated curves for the direct and evaporated protons are shown for comparison. The tracks identified as deuterons are also shown.

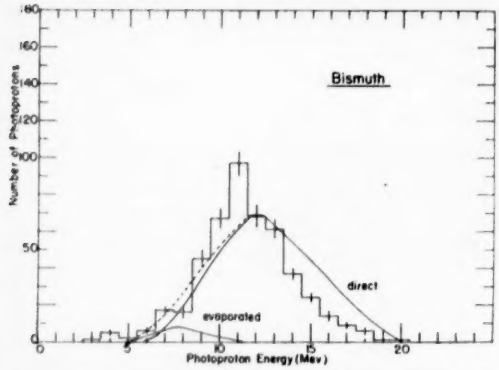

FIG. 3. Histogram of the number of photoprotons observed from bismuth as a function of proton energy. The calculated curves for the direct and evaporated protons are shown for comparison.

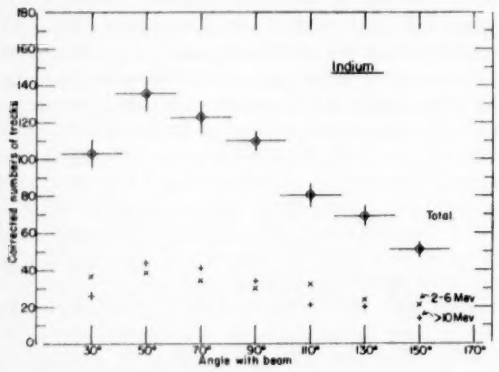

FIG. 4. The angular distribution of the photoprotons from indium. The crosses show the angular distribution of the high-energy and the low-energy protons separately.

energy distribution curve. The deuterons identified from cerium are indicated as a dotted line in the proton energy distribution. These deuterons are plotted against the energy of a proton of the same range as a deuteron. Tracks which passed through the emulsions were grain counted and corrected to their estimated true range. E-1 emulsions were used in all but the background run to reduce fogging due to Compton electrons from the target and thereby permit longer exposures.

Figures 4–6 show the angular distributions observed from indium, cerium, and bismuth. The three sets of points give the total distribution and also the distribution of the low-energy particles and of the high-energy particles. The points for the total distribution are marked with the statistical probable error and the angular spread of observation.

DISCUSSION

The yields of photoparticles corrected for angular distribution and with background subtracted off can be summarized as follows:

bismuth photoprotons	5×10^4 protons mole^{-1} r^{-1}
cerium photoprotons	1.2×10^5 protons mole^{-1} r^{-1}
cerium photodeuterons	6×10^3 deuterons mole^{-1} r^{-1}
cerium photoalphas	8×10^2 alphas mole^{-1} r^{-1}
indium photoprotons	1.1×10^5 protons mole^{-1} r^{-1}

The major uncertainties are in the determination of the solid angles subtended by the emulsions and in the calibration of the x-ray beam. It is estimated that the uncertainty in the proton yields is of the order of 20 percent. There is additional uncertainty in the deuteron and alpha yields due to identification uncertainty and statistical fluctuations. The barium yield in Table II is only an estimate subject to possible contamination errors and poor statistics.

Mann and Halpern[12] give a photoproton yield from indium of 1.3×10^5 protons mole^{-1} r^{-1} as determined by a ZnS scintillation detector.

In order to compare these results with theoretical values, we have made calculations using both the

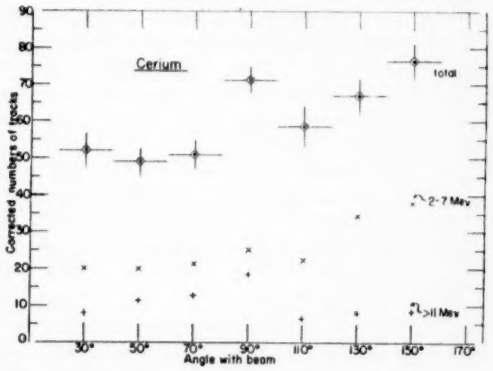

FIG. 5. The angular distribution of the photoprotons from cerium. The crosses show the angular distribution of the high-energy and the low-energy protons separately.

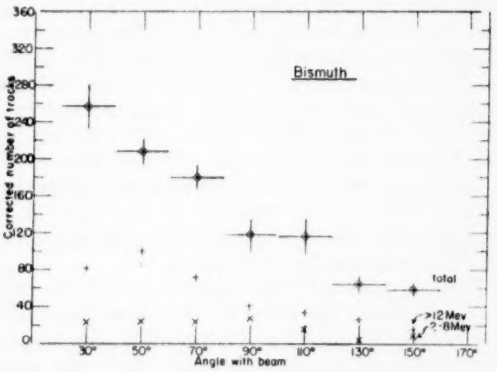

FIG. 6. The angular distribution of the photoprotons from bismuth. The crosses show the angular distribution of the high-energy and the low-energy protons separately.

[12] A. K. Mann and J. Halpern, Phys. Rev. 82, 733 (1951).

evaporation process[3] of emission and the direct photoeffect.[8] In each case the charged particle yields are determined by the bremsstrahlung spectrum, the photon absorption, the binding energies, and the Coulomb barrier. The pertinent binding energies for the nuclei involved are given in Table III. In each element the values for the dominant isotope were used. The bremsstrahlung distribution was calculated from Schiff's[13] formula as adapted by Johns *et al.*[14] The photon absorption curves are not known but are presumed to be well approximated by the (γ,n) cross section curves. Bi(γ,n) is given by Halpern, Nathans, and Mann[15] while the Ce and In curves were adapted from the Ta(γ,n) curve[16] normalized to the neutron yield data of Price and Kerst[17] corrected by the multiplicity factor of Heidmann and Bethe.[18] The Coulomb penetration factors are taken from Weisskopf's tables[19] using $r_0=1.5\times10^{-13}$ cm or $r_0=1.3\times10^{-13}$ cm.

In calculating the photoproton yields to be expected on the evaporation model, it is simple and direct to determine the ratio of the (γ,p) cross section to the (γ,n) cross section from the F functions defined by Blatt and Weisskopf[19] (page 369). Using the binding energies given in our Table III, the excitation energies were determined for various photon energies. The corresponding F_n and F_p were read off the curves[20] for $r_0=1.5\times10^{-13}$ cm and their ratio weighted by the bremsstrahlung distribution and photon absorption values. The resulting theoretical $(\gamma,p)/(\gamma,n)$ ratios are 1.3×10^{-3}, 8×10^{-5}, 6×10^{-5}, and 6×10^{-4} for indium, barium, cerium, and bismuth. The ratios for $r_0=1.3\times10^{-13}$ cm or for older penetration factors give even smaller values. Photoneutron yields[17] of 0.9×10^{7}, 1.1×10^{7}, 1.2×10^{7}, and 2.5×10^{7} neutrons per mole per roentgen units combine with our photoproton yields of 1.1×10^{5}, 1×10^{5}, 1.2×10^{5}, and 0.5×10^{5} protons per mole per r for indium, barium, cerium and bismuth to give observed $(\gamma,p)/(\gamma,n)$ ratios of 1.2×10^{-2}, 1×10^{-2}, 1×10^{-2}, and 0.2×10^{-2}, respectively. In every case the observed ratio is higher than the calculated.

These results confirm and extend the results of Wäffler,[7] who measured the radioactivity produced by some (γ,p) reactions induced by monochromatic gamma rays. Although the F functions are not very well known (especially for even-A isotopes), such results imply some marked departure from the evaporation process. In order to further elucidate these discrepancies, we have calculated the energy distributions to be expected from evaporated and direct photoprocesses.

[13] L. I. Schiff, Phys. Rev. **83**, 252 (1951).
[14] Johns, Katz, Douglas, and Haslam, Phys. Rev. **80**, 1062 (1950).
[15] Halpern, Nathans, and Mann, Phys. Rev. **88**, 679 (1952).
[16] L. Katz and A. G. W. Cameron, Can. J. Phys. **29**, 518 (1951).
[17] G. A. Price and D. W. Kerst, Phys. Rev. **77**, 806 (1950).
[18] J. Heidmann and H. A. Bethe, Phys. Rev. **84**, 274 (1951).
[19] J. M. Blatt and V. Weisskopf, *Theoretical Nuclear Physics* (John Wiley and Sons, Inc., New York, 1952), pp. 352.
[20] Fast Neutron Data, Atomic Energy Commission Report NYO-632, 1950 (unpublished).

TABLE III. Binding energies.[a]

Z	Element	A	Abundance	B_n (Mev)	B_p (Mev)	B_d (Mev)	B_α (Mev)
49	In	113	0.04	9.4	6.1	12.9	2.1
		115	0.96	9.05[b]	6.8	13.1	2.5
56	Ba	138	0.72	7.5	9.6	14.7	2.3
58	Ce	140	0.89	9.05[b]	8.5	14.1	1.2
		142	0.11	7.15[b]	9.1	14.3	1.6
83	Bi	209	1.00	7.44[e]	3.76[d]	10.4	−3.15[e]

[a] N. Metropolis and G. G. Reitwiesner, *Tables of Atomic Masses*, U. S. Atomic Energy Commission Report NP 1980, 1950 (unpublished).
[b] Sher, Halpern, and Mann, Phys. Rev. **84**, 387 (1951).
[c] J. A. Harvey, Phys. Rev. **81**, 353 (1951).
[d] K. Way (private communication).
[e] H. Faraggi and A. Berthelot, Compt. rend. **232**, 2093 (1951).

TABLE IV. Direct and evaporation yields of photoprotons (particles per mole per roentgen unit).

	In	Ce	Bi
Observed			
direct	8×10^{4}	9×10^{4}	5×10^{4}
evaporation	3.5×10^{4}	4×10^{4}	0.3×10^{4}
Theoretical			
direct	2×10^{4}	0.7×10^{4}	1.5×10^{4}
evaporation	1.1×10^{4}	0.07×10^{4}	0.3×10^{4}

The energy distribution of the photoprotons evaporated from a compound nucleus can be calculated as described before.[6] Here we have used the level density from a statistical model: $W(E)=C\exp2(aE)^{\frac{1}{2}}$, where C and a are given in the Fast Neutron Data report.[20] The relative energy distributions calculated were matched to the experimental curves as in Figs. 1–3 and the "observed-evaporation" partial yields so determined are tabulated in Table IV. The evaporation calculated yields are also given in Table IV. In addition, the evaporation yields of deuterons and alpha particles were similarly calculated to be: 100 alphas mole^{-1} r^{-1} and 2 deuterons mole^{-1} r^{-1} for bismuth. These are to be compared with the very approximate observed values of 200 alphas mole^{-1} r^{-1} and 400 deuterons mole^{-1} r^{-1}. The calculated yield for bismuth, given as 0.3×10^{4} protons mole^{-1} r^{-1}, is for $r_0=1.3\times10^{-13}$ cm. The bismuth yield for $r_0=1.5\times10^{-13}$ cm would be calculated to be 1.3×10^{4} protons mole^{-1} r^{-1}. For cerium and indium, on the other hand, the nuclear radius seems to favor $r_0=1.5\times10^{-13}$ cm and so the calculated evaporated yields are based on $r_0=1.5\times10^{-13}$ cm. In comparing the observed energy distributions to those expected from evaporated protons, it is evident that a large number of the photoprotons have energies greater than calculated. The calculated yields of evaporated protons for indium and bismuth is at least consistent with a portion of the observed particles. However, in cerium, the evaporated yield is so depressed by the large proton binding energy that practically no evaporated protons should be observed.

It is interesting, then, to calculate the energy distribution and yield of photons to be expected from a

direct photoeffect. Courant's[8] formula has been extended to allow a determination of the energy distribution by simplifying its dependence on photon energy and rearranging it to give

$$y(\epsilon) \approx (Z^2/4A^{4/3})aF(\epsilon)\int_{E_{\min}}^{E_{\max}} (N_\gamma(E)/E^3)dE,$$

where $y(\epsilon)$ is the number of protons of energy ϵ per mole per r ejected by a beam of photons of energy distribution $N_\gamma(E)$ with a maximum energy $E_{\max}$ and $E_{\min}=\epsilon+B_p$ (B_p is the proton binding energy); a is Avogadro's number and $F(\epsilon)$ is the Coulomb barrier penetration cross section. The total yield can be determined more directly by

$$Y = (34.3aZ^2/A^{4/3})\int_{B_p}^{E_{\max}}\left[(N_\gamma(E)/E^3)\int_0^{x_1} F(x)dx\right]dE,$$

where $x_1=(E_{\max}-B_p)/C_B$ (C_B is Coulomb barrier height). Using these relations, the curves marked "direct" in Figs. 1–3 were calculated and the direct yields given in Table IV were determined. Again the relative energy distribution curves were matched to the observed histograms, and the yields so deduced are given in Table IV as "observed-direct" protons. Since Courant's formulation is quite approximate, the agreement in the case of indium is regarded as excellent. For bismuth the yield is in good agreement, but the calculated energy distribution is somewhat too high in energy. The cerium calculated yield is low by a factor of 10 although the energy distribution is in reasonable agreement. Nevertheless, in every case the interpretation of appreciable direct photoprotons is evident.

The observed angular distribution of the photoprotons show rather striking anisotropies. Indium and especially bismuth show a large forward asymmetry. This is rather unexpected, since evaporated protons should be essentially isotropic and direct photoeffect protons should have a distribution of the form $A+B\sin^2\theta$, where the rate of A to B depends on the proton angular momentum[8] (assuming dipole absorption). Each of these effects is symmetric about 90°. The photon momentum is not large enough to affect this symmetry. Several explanations can be considered for the observed effects. An asymmetry can be caused by a dipole-quadrupole interference effect[21] producing an angular distribution of the form $I(\theta)=a+b(\sin\theta+p\sin\theta\cos\theta)^2$, where a is an isotropic component (evaporated protons), and b is the asymmetric component (direct protons) with $p^2/5=\sigma_q/\sigma_d$, the ratio of the electric quadrupole to electric dipole absorption cross sections. The total photoprotons from indium shown in Fig. 4 can be fitted by an angular distribution of this type, with p between $\frac{3}{4}$ and 1 together with $b/a=0.85$ to 0.95. The total photoprotons from bismuth shown in Fig. 6 have an excess of protons at 30° which cannot be fitted by a curve of this type. The bismuth photoprotons of greater than 10 Mev can, however, be fitted with this type of angular distribution with a p of approximately 2 and a b/a about $\frac{3}{2}$. The cerium photoprotons, on the other hand, show no evidence of such an effect.

Schiff[22] has suggested (on the assumption of virtual deuterons in the nucleus) that a forward asymmetry will result from the variation in cross section of the deuteron photoeffect, depending on the approach or recession of the deuteron relative to the photon.

We wish to acknowledge with gratitude discussions with Dr. Arnold Feingold and Dr. Sherman Frankel, which have contributed to our calculations of the direct photoeffect, the aid of E. E. Carroll, Jr. in scanning the indium plates, and the help of the late G. K. Rosenblum in some of the photoeffect calculations.

[21] Mann, Halpern, and Rothman, Phys. Rev. **87**, 146 (1952); L. I. Schiff, Phys. Rev. **78**, 733 (1950); J. F. Marshall and E. Guth, Phys. Rev. **78**, 738 (1950); J. S. Levinger, Phys. Rev. **84**, 43 (1951).

[22] L. I. Schiff (private communication).

The Radioactive Decay of Calcium 47*

J. M. Cork, J. M. LeBlanc, M. K. Brice, and W. H. Nester
Department of Physics, University of Michigan, Ann Arbor, Michigan

(Received June 8, 1953)

Spectrometric studies have been made of the beta and gamma radiations from calcium 47 (5.35 day) and its radioactive daughter scandium 47 (3.4 day). Using conversion and photoelectrons and the scintillation spectrometer, gamma rays of energy 149.5, 234, 495, 800, and 1303 kev are found in scandium following beta emission from the calcium. The beta spectrum is complex with energies of 0.46 and 1.4 Mev.

Scandium 47 decays with a single allowed beta transition with upper energy limit of 0.64±0.03 Mev and a single gamma ray of 159.5 kev. A satisfactory level scheme is proposed for the decay and checked in some of its details by coincidence observations.

THE irradiation of normal calcium by neutrons and by deuterons was found[1] to yield a beta-emitting activity of half-life 5.8 days. This was attributed to the isotope of mass 47 although calcium 46 from which it would be derived exists with a natural abundance of only 0.0033 percent. Subsequent studies have substantiated the assignment and have shown that a previously observed[2] activity, scandium 47, which decays by beta emission to titanium 47, with a half-life of 3.4 days, exists[3] as a daughter product in the decay.

From its absorption in aluminum the beta energy of the calcium 47 has been reported[3] as 1.1 or 1.2 Mev and that from scandium 47 as 0.61 Mev. A single gamma ray, whose energy appeared by absorption in lead to be 1.3 Mev, has been reported to exist in scandium 47 following the first beta emission.

In the present investigation samples of calcium enriched 3000-fold in mass 46, up to 9.45 percent, were irradiated for two weeks in the Argonne heavy water pile. The scandium daughter product was chemically separated from the irradiated specimens and spectrometric studies made of each activity. The gamma energies have been evaluated both by a scintillation crystal spectrometer and more accurately by observing both conversion and photoelectrons in photographic magnetic spectrometers. The beta radiations have been observed in a double-focusing magnetic spectrometer. The half-life of the calcium 47 activity is found to be 5.35±0.10 days and that of the separated scandium 47 is 3.40±0.05 days.

The composite beta spectrum resolves into four components as shown in Fig. 1. These beta transitions have upper energy limits of 0.46±0.02, 0.64±0.03, and 1.4 ±0.10 Mev. The low-energy component at 260±20 kev is probably due to long-lived calcium 45. The 0.64-Mev beta ray is associated with the decay of the 3.4-day daughter product, scandium 47. The branching ratio for the 0.46- and 1.4-Mev transitions is about 60 to 40 percent, and their log ft values are 5.7 and 7.7, respectively. The log ft for the 0.64-Mev radiation is 5.6, thereby indicating an allowed transition.

The strongest electron conversion lines are observed for a gamma ray of energy 159.5 kev. Both the K and L lines are observed in the photographic spectrometer with work functions characteristic of titanium. The K/L ratio is large (visual estimate ~10) which at this low Z^2/W (2.7) does not discriminate as to its multipolarity. Single K electron conversion lines are observed for the gamma rays of energy 149.5, 234, and 495 kev. By using a lead radiator, photoelectrons are observed for the gamma rays of energy 160, 495, and 1303 kev. The scintillation spectrometer revealed the existence of

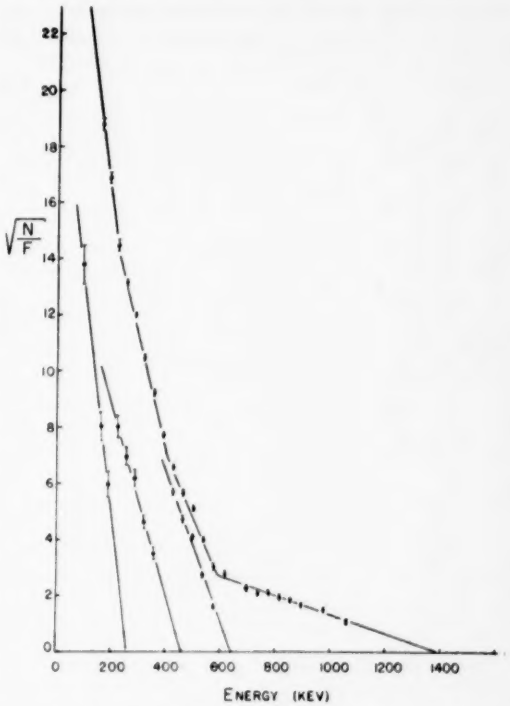

FIG. 1. Resolution of the beta spectra of Ca^{47} and Sc^{47}.

* This project received the joint support of the Office of Naval Research and the U. S. Atomic Energy Commission.

[1] D. Matthews and M. Pool, Phys. Rev. **72**, 163 (1947).

[2] C. Hibdon and M. Pool, Phys. Rev. **67**, 313 (1945); N. Krisberg and M. Pool, Phys. Rev. **75**, 1693 (1949); R. Hein and A. Voigt, Phys. Rev. **74**, 1265 (1948).

[3] Batzel, Miller, and Seaborg, Phys. Rev. **84**, 671 (1951); Rudstam, Stevenson, and Folger, Phys. Rev. **87**, 358 (1952).

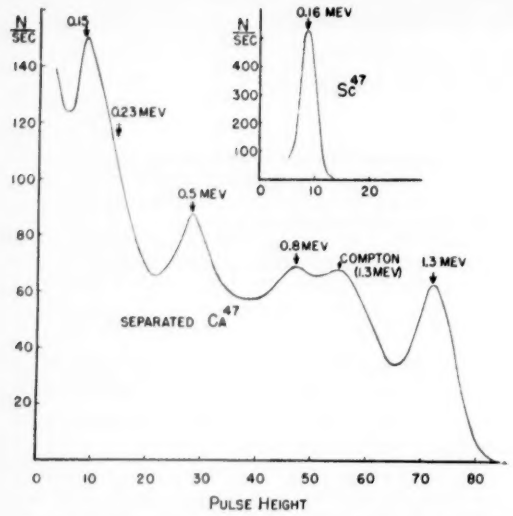

FIG. 2. Gamma distribution by scintillation spectrometer.

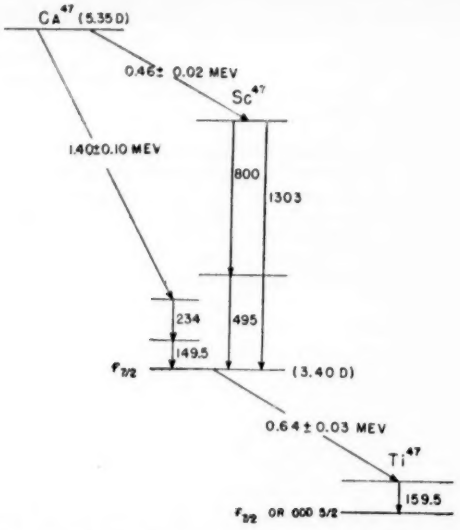

FIG. 4. Proposed nuclear level scheme for Ca^{47}-Sc^{47}-Ti^{47}.

several gamma rays, some of which showed little internal conversion. Figure 2 shows the gamma-energy distribution for the chemically separated isotopes as revealed by the scintillation spectrometer. The separated calcium probably contained some scandium. The uncertainty in the energy of the lines at 495, 800, and 1300 kev may be as great as plus or minus 3 percent. The low-energy peak near 0.15 Mev is probably largely due to the 159.6-kev gamma radiation in the incompletely separated scandium. The gamma ray at 234 kev lies on the edge of this peak and is so weak that it cannot be resolved. The fact that both the 149.5- and the 234-kev gamma rays appear by internal conversion and not by photoelectrons indicates that although weak, their conversion coefficients are large.

A summary of the observed gamma energies and the methods of detection is presented in Table I.

Using an anthracene crystal to detect beta radiations and a NaI crystal for gamma energies, certain important coincidence data are obtained. In the separated scandium isotope a "Feather" absorption curve for the beta spectrum is shown singly in Curve *A*, Fig. 3. A similar trace in which only coincident counts between the beta radiation and the gamma radiation of energy 160 kev is shown in Curve *B*. It is apparent that the end point is the same in both curves, thus showing that the 0.64-Mev beta transition does not terminate in the ground state of Ti^{47}. The background count is probably due to coincidence between backscattered Compton gamma rays and their associated electrons. In the separated calcium the anthracene was shielded by about 0.25 g per cm^2 of aluminum so as to respond to energies greater than 600 kev. In this arrangement definite coincidence counts occurred with gamma

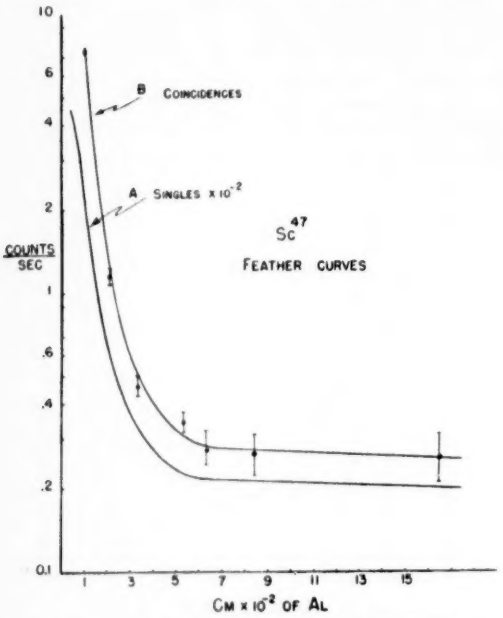

FIG. 3. Feather curve for the beta radiation from Sc^{47}.

TABLE I. Gamma energies in Ca^{47} and Sc^{47}.

Gamma energy kev	Observed by—*A*. Conversion electrons. *B*. Photoelectrons. *G*. Scintillation
149.5	*A*
159.5 (Sc)	*A*, *B*, *C*
234.0	*A*
495	*A*, *B*, *C*
800	*C*
1303	*B*, *C*

energies around 200 kev. When unshielded so as to respond to low-energy betas, coincidence counts were observed with gamma energies greater than 250 kev.

It is thus possible to arrange the observed transitions in a rather simple decay scheme which essentially satisfies every observation, as shown in Fig. 4.

The final titanium 47 nucleus with 22 protons and 25 neutrons, from shell theory, would have five particles in the $f_{7/2}$ level and an $f_{7/2}$ ground state. It is, however, possible that the five $f_{7/2}$ particles couple to form a 5/2 odd ground state, similar to the coupling observed in Mn^{55}. In this event the first excited level is $f_{7/2}$ and the beta transition goes to the excited state with no change in spin or parity, since the scandium 47 is likely to have an $f_{7/2}$ ground state as does the similar Sc^{45}. Selection rules do not forbid a decay to the 5/2 odd ground state. Such a transition, however, would not be a simple one-particle process, thus it would probably have a much longer lifetime than the simple $f_{7/2}$ to $f_{7/2}$ transition. The 159.5-kev radiation is then an $M1$ transition. The Ca^{47} nucleus is given an assignment of $f_{7/2}$ from the shell theory. It then seems difficult to explain the lack of a beta transition to the ground state of Sc^{47}.

PHYSICAL REVIEW VOLUME 92, NUMBER 2 OCTOBER 15, 1953

A Long-Lived Activity in Neutron-Irradiated Niobium

DAVID L. DOUGLAS, ANITA C. MEWHERTER, AND ROBERT P. SCHUMAN
Knolls Atomic Power Laboratory, Schenectady, New York*

(Received July 8, 1953)

An activity has been found in samples of niobium metal irradiated for long periods in the Chalk River reactor. Extensive chemical tests showed that the activity is niobium. The activity is most likely the long-lived ground state of Nb^{94}. If so, its half-life is estimated as $(2.2\pm0.5)\times10^4$ years from its yield. It has a 0.50 ± 0.05-Mev beta and three gammas, 0.70 ± 0.01 Mev (92 percent), 0.87 ± 0.01 Mev (92 percent), and 1.57 ± 0.02 Mev (8 percent). The capture cross section of Nb^{94} is 15 ± 4 barns.

I. INTRODUCTION

A NUMBER of investigators have reported the presence of a 6.6-min activity in neutron-irradiated niobium.[1,2] The same activity has also been produced by a (d,p) reaction on niobium.[3] This activity has been assigned as class A (element and mass number certain) to Nb^{94}.[4] The activity has been found to decay almost entirely by isomeric transition to a long-lived ground state.[5,6] The energy of the transition is 41.5 kev as determined from the energies of the K, L, and M conversion electrons.[7] In addition, about 0.1 percent of the activity has been found to decay by emitting a 1.3-Mev β[8] and a 0.9-Mev γ.[9]

Goldhaber and Muehlhause[6] set a lower limit of $\gg$100 years for the half-life of the ground state. Hein, Fowler, and McFarland,[10] who studied niobium metal that had been irradiated four months in the Argonne reactor, set a minimum half-life of 5×10^4 years.

This laboratory has had some samples of niobium irradiated for a long period in the Chalk River reactor in order to look for a long-lived activity which might be the ground state of Nb^{94}. An activity has been found which the authors feel is the ground state of Nb^{94}.

II. CHEMICAL SEPARATIONS

Two samples of niobium metal were irradiated in the Chalk River reactor at an average flux of $4-5\times10^{13}$ n/cm^2 sec, one sample for a total $nvt=1.33\times10^{21}$ n/cm^2, the other for a total $nvt=2.5\times10^{21}$ n/cm^2. The total nvt received was checked by cobalt flux monitors. The niobium metal was spectrographically standardized niobium powder. A spectrographic analysis, made by the supplier, showed very faint lines of Mg, Cu, Fe, Si, and Ca, and no lines of Al, Ag, B, Co, Cr, Mn, Mo, Ni, Pb, Sn, Ta, Th, Ti, V, Zr, or Zn.

The samples were returned to the laboratory about two months after the end of irradiation. Decay curves and aluminum absorption curves on the irradiated metal showed that the major beta activity was Ta^{182}. Scintillation spectrometer scans on the metal showed the 0.76-Mev gamma of Nb^{95} in addition to the characteristic spectrum of Ta^{182}. Aluminum absorption curves made with a low-absorption counter also showed the presence of the weak beta of Nb^{95}.

An initial chemical purification of the niobium by

* Operated by the General Electric Company for the U. S. Atomic Energy Commission.

[1] Pool, Cork, and Thornton, Phys. Rev. **52**, 239 (1937).
[2] Sagane, Kojima, Miyamoto, and Ikawa, Phys. Rev. **54**, 970 (1938).
[3] D. N. Kundu and M. L. Pool, Phys. Rev. **70**, 111 (1946).
[4] Hollander, Perlman, and Seaborg, University of California Radiation Laboratory Report UCRL 1928, 1952 (unpublished).
[5] M. Goldhaber and W. J. Sturm, Phys. Rev. **70**, 111 (1946).
[6] M. Goldhaber and C. O. Muehlhause, Phys. Rev. **74**, 1248 (1948).
[7] R. L. Caldwell, Phys. Rev. **78**, 407 (1950).
[8] M. Goldhaber and R. D. Hill, Revs. Modern Phys. **24**, 179 (1952).
[9] E. der Mateosian, Phys. Rev. **83**, 233 (1951).
[10] Hein, Fowler, and McFarland, Phys. Rev. **85**, 138 (1952).

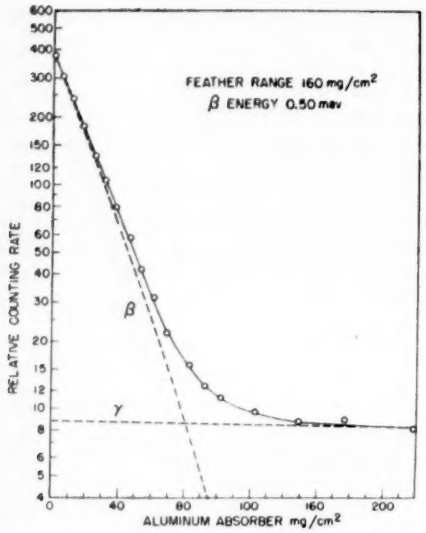

FIG. 1. Aluminum absorption curve of Nb^{94}.

the procedure used in analyzing niobium in fission products[11] showed that the bulk of the activity was niobium or tantalum which follows Nb in the procedure. Two methods have been used to purify the niobium from radioactive tantalum. The first method is based on the extraction of the niobium from 8*N* HCl into a solution of methyldioctlyamine in xylene.[12] A sample of

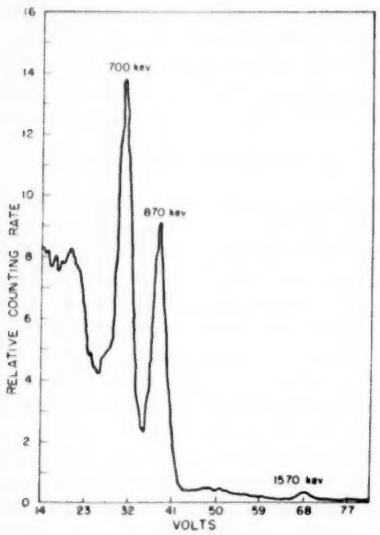

FIG. 2. Scintillation spectrogram of Nb^{94}.

niobium was purified by four methyldioctlyamine extractions plus three cupferron scavenging extractions. A small yield of niobium was obtained which was fairly free from Ta^{182}. The purified niobium contained mainly Nb^{95}, and, when followed for decay, showed in addition, Ta^{182} plus a still longer-lived activity.

The other method that has been used to separate the niobium from the tantalum impurity is based on partition chromatography.[13] In this method, the niobium is complexed with HF, a little Ta carrier is added, and the sample added to a cellulose packed column. The column is then treated with three solutions; first with water saturated methyl ethyl ketone to remove the Ta, then methyl ethyl ketone containing about 1 percent HF to fix Ti, Sn, and Zr on the column, then finally methyl ethyl ketone containing $12\frac{1}{2}$ percent HF to elute the niobium. The niobium containing solution is then evaporated, the residue ignited, and the resulting Nb_2O_5 purified further by the standard niobium fission product procedure.[11] Scintillation spectrograms showed that the above procedure gave a very clean separation of Ta and Nb. The purified niobium from a sample that had decayed about fourteen months showed only the long-lived activity; the niobium from a sample that had decayed five months showed mainly Nb^{95} plus a little of the same long-lived activity.

TABLE I. Specific beta and gamma activities of long-lived niobium.

Radiation	Energy, Mev	Counts/min mg
β^-	0.50	530 000
γ	0.70	455 000
γ	0.87	470 000
γ	1.57	41 000

In order to prove that the long-lived activity is actually niobium, further chemical tests were run. Neither an AgCl or an Sb_2S_3 scavenging precipitation carried the activity. Some of each sample of the cellulose column purified niobium was then run through an anion exchange column. The column, packed with Dowex-1, is similar to the one used by Kraus and Moore[14] to separate Nb and Zr. The long-lived activity and the Nb^{95} in the five-month decay sample showed no fractionation in going through the column as shown by scintillation spectrograms. The long-lived activity in the 14-month decay sample gave the same elution pattern as the Nb^{95}.

Since the long-lived activity follows niobium chemistry and is not fractionated from Nb^{95} in the anion exchange column, it can be assigned to an isotope of niobium. Also, the niobium from the same irradiation and purified by the two different methods has the same specific activity of the long-lived isotope. The specific

[11] L. E. Glendenin, *Radiochemical Studies: The Fission Products* (McGraw-Hill Book Company, Inc., New York, 1951), paper 253, National Nuclear Energy Series, Plutonium Project Record, Vol. 9, Div. IV, p. 1523.

[12] G. W. Leddicotte and F. L. Moore, J. Am. Chem. Soc. **74**, 1618 (1952).

[13] A. F. Williams, J. Chem. Soc. **1952**, 3155.

[14] K. A. Kraus and G. E. Moore, J. Am. Chem. Soc. **73**, 9 (1951).

activity of the long-lived isotope in the niobium from the two irradiations is proportional to the *nvt* received.

III. DETERMINATION OF ENERGY OF RADIATIONS AND SPECIFIC ACTIVITY

The long-lived activity is most likely the ground state of Nb^{94}. The beta energy of the activity has been determined by Feather analysis of aluminum absorption curves taken on samples known to be free of Ta^{182} (see Fig. 1). An energy of 0.50 ± 0.05 Mev has been obtained for the beta. The energies of the gamma rays have been determined with a scintillation spectrometer by comparison with the known energies of the Cs^{137}-Ba^{137} gamma and the Co^{60} gammas (see Fig. 2). The energies found are 0.70 ± 0.01, 0.87 ± 0.01, and 1.57 ± 0.02 Mev.

The specific beta activity of the niobium has been obtained by counting with an end-window proportional counter. Approximate specific gamma activities have also been obtained by comparing the scintillation spectrograms of the niobium with those of $Cs^{137}-Ba^{137}$, Nb^{95}, and Co^{60} of known disintegration rates. Table I gives the specific β and γ activities found on a sample

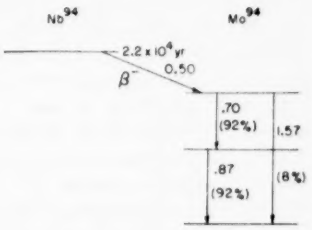

FIG. 3. Decay scheme of Nb^{94}.

in which all the Nb^{95} had decayed and which was free of Ta^{182}.

The specific activity of Nb^{95} in the purified niobium from the two irradiations has also been obtained by 4π counting, by gamma counting, and by beta counting with a low absorption counter. A specific activity corrected back to the end of irradiation of 2.2×10^8 β/min mg was obtained for the shorter irradiation, and 6.5×10^8 β/min mg for the longer irradiation.

The activity of the highly purified niobium in which all the Nb^{95} has decayed has been followed for several months and has shown no decay. From the decay

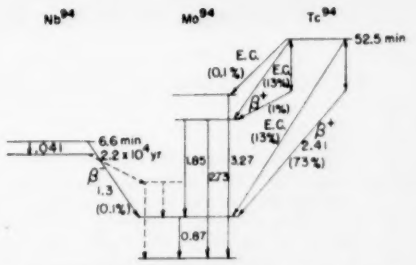

FIG. 4. Decay schemes of Nb^{94m} and Tc^{94} (after Goldhaber and Hill see reference 8). The broken lines indicate our proposed decay scheme of Nb^{94}.

curve, a half-life of >3 years can be set. A proportional counter x-ray spectrometer did not show the presence of an appreciable amount of x-ray activity; consequently the activity decays largely, if not entirely, by β emission.

IV. DISCUSSION OF RESULTS

A half-life of the Nb^{94} has been calculated from the specific activity, the total *nvt*, and the capture cross section of Nb^{93}. Based upon a capture cross section of Nb^{93} of 1.1 ± 0.1 barns,[15] a half-life of $(2.2\pm0.5)\times10^4$ years is obtained for the Nb^{94}. An approximate capture cross section of 15 ± 4 barns for Nb^{94} has been calculated from the specific activity of Nb^{95}, the average flux during the irradiation, and a capture cross section of 1.1 ± 0.1 barns for Nb^{93}.

A possible decay scheme for the Nb^{94} has been proposed based upon the results of this investigation and upon the decay schemes given for Nb^{94m} and Tc^{94}. The proposed decay scheme is given in Fig. 3, while the decay schemes given by Goldhaber and Hill[8] for Nb^{94m} and Tc^{94} are given in Fig. 4. On the basis of the Tc^{94} and Nb^{94m} decay schemes, it is expected that the 0.70-Mev gamma precedes the 0.87-Mev gamma in the gamma cascade.

The authors wish to give special thanks to the Chalk River Laboratories for making possible the long-term irradiation of the niobium. They also wish to thank Dr. A. B. Carlson for his help in setting up and testing the scintillation spectrometer.

[15] D. J. Hughes *et al.*, *Atomic Energy Levels*, U. S. Atomic Energy Commission Report AECU-2040, May, 1952 (unpublished).

Polarization of the Gamma Rays in the $F^{19}(p,\alpha\gamma)O^{16}$ Reaction*

L. W. Fagg and S. S. Hanna
Department of Physics, Johns Hopkins University, Baltimore, Maryland
(Received July 15, 1953)

The polarizations of the 6.13-, 6.9-, and 7.1-Mev gamma rays from the $F^{19}(p,\alpha)O^{16*}(\gamma)O^{16}$, $E_p=0.87$ Mev, reaction have been observed using the photodisintegration of the deuteron to detect polarization. Range measurements on the photoprotons separated the 6.13-Mev gamma ray from the other two, which were only slightly resolved. Knowing the relative intensities of the 6.9- and 7.1-Mev gamma rays and their unresolved angular distribution coefficient, it is possible, nevertheless, to deduce the separate polarizations from the observed total polarization. Polarization ratios, $I(0°)/I(90°)$, of 0.9 ± 0.1, 1.9 ± 0.3, and 0.4 ± 0.3 were obtained for the 6.13-, 6.9-, and 7.1-Mev gamma rays, respectively, emitted at 90° to the proton beam. These values are in good agreement with the polarizations expected for the assignment of a 2^- state in Ne^{20} and 3^-, 2^+, and 1^- states in O^{16} as deduced by Seed and French from directional correlation measurements on this reaction.

I. INTRODUCTION

FOLLOWING a suggestion by Madansky, it was shown by Falkoff[1] that parity changes in successive nuclear transitions could be determined from polarization measurements on the emitted gamma rays. Hamilton[2] has given the theory for the case in which the polarization of one gamma ray is measured relative to the direction of emission of a second gamma ray in a cascade process. Experiments of this type have been performed by Metzger and Deutsch.[3] The theory can be readily applied to a process in which a material particle replaces the gamma ray whose polarization is not determined. An alpha-gamma correlation of this type has been measured by French and Newton[4] in the reaction, $F^{19}(p,\alpha)O^{16*}(\gamma)O^6$, $E_p=0.34$-Mev, $E_\gamma=6.13$ Mev.

The theory can also be extended to the case of a gamma ray and a bombarding particle in a nuclear reaction. In such an experiment it is not necessary to detect radiations in coincidence, since the entering particles are unidirectional. In this case nuclear plates can be used as the detectors of the radiation and its polarization. In the experiments mentioned above, scintillation counters were employed and the Compton effect provided the polarization sensitive mechanism. For gamma-ray energies above about 4 Mev, however, it would seem desirable to use the photodisintegration of the deuteron as the polarization sensitive reaction. In the energy range of the present work, 6 to 7 Mev, this reaction proceeds chiefly by photoelectric disintegration. The yield of photoprotons is, to a good approximation, proportional to $\cos^2\alpha$, where α is the angle between the direction of the photoproton and the direction of polarization of the gamma ray.[5] With a favorable experimental arrangement, therefore, a very large polarization effect can be achieved for a completely polarized gamma ray, as has been recently demonstrated by Wilkinson[6] in observing the distribution of photoprotons produced by the gamma ray in the $H^2(p,\gamma)He^3$ reaction. The Compton scattering in the same energy range produces only about a 20 percent effect for a perfectly polarized gamma ray in a practical experimental arrangement.

The aim of the present work was to detect the polarizations of the 6.13-, 6.9-, and 7.1-Mev gamma rays relative to the proton in the $F^{19}(p,\alpha)O^{16*}(\gamma)O^{16}$, $E_p=0.874$-Mev, reaction.[7] The detection was accomplished by observing the photoprotons in the $D(\gamma,p)n$ process in nuclear emulsions impregnated with D_2O.[6,8] A complete measurement of the polarization correlation would consist in determining the intensity and the polarization of the gamma rays as a function of the correlation angle. Since Sanders[9] has obtained the intensity distribution of the gamma rays, it was in fact only necessary to establish the polarization of the radiation emitted at 90°, at which angle there is a maximum effect. Recently, the proton-alpha and alpha-gamma directional correlations at this resonance have been measured by Seed and French,[10] so that a very complete description of the reaction has now been obtained.

II. EXPERIMENTAL METHOD

Thin fluorine targets were prepared by exposing various metals to bromine trifluoride gas. Tantalum fluoride targets were generally suitable, but with beams of high-intensity water-cooled copper fluoride targets were employed. Four separate runs were made. The first two ($\sim$100 μa-hr) were obtained with the statitron in the Physics Department at Johns Hopkins University. The last two runs ($\sim$250 μa-hr) were made with the statitron at the Department of Terrestrial

* Assisted by a contract with the U. S. Atomic Energy Commission.
[1] D. L. Falkoff, Phys. Rev. **73**, 518 (1948).
[2] D. R. Hamilton, Phys. Rev. **74**, 782 (1948).
[3] F. Metzger and M. Deutsch, Phys. Rev. **78**, 551 (1950).
[4] A. P. French and J. O. Newton, Phys. Rev. **85**, 1041 (1952).
[5] H. A. Bethe and R. F. Bacher, Revs. Modern Phys. **8**, 122 (1936).
[6] D. H. Wilkinson, Phil. Mag. **43**, 659 (1952).
[7] An earlier report on this experiment is given by L. W. Fagg and S. S. Hanna, Phys. Rev. **88**, 1205 (1952).
[8] G. Goldhaber, Phys. Rev. **81**, 930 (1951).
[9] J. E. Sanders, Phil. Mag. **43**, 630 (1952).
[10] J. Seed and A. P. French, Phys. Rev. **88**, 1007 (1952).

Magnetism of the Carnegie Institute of Washington. The standard practice for each run was to expose two plates impregnated with D_2O and one control plate with H_2O.

The target chamber was an aluminum cylinder, $9\frac{1}{2}$ in. long, $2\frac{1}{2}$ in. in diameter, with a $\frac{1}{16}$-in. wall. The target made an angle of 45° with the beam and with the planes of the nuclear emulsions. The latter were placed outside the chamber, normal to the radiation emitted at 90°. The emulsions, soaked in D_2O or H_2O, were held in water tight cassettes made of stainless steel and mounted on copper bars which were maintained at the low temperature at which the plates were soaked. The temperature control was necessary to avoid spoiling the emulsion and to prevent changes in emulsion thickness.

Four hundred micron Ilford C-2 emulsions were soaked in D_2O (or H_2O) until saturated, at a fixed temperature between 10°C and 16°C. Saturation was desirable to obtain maximum photoproton intensity and to insure uniform water density throughout the emulsion. The resulting decrease in grain density of the tracks did not seriously impair range measurements. The shrinkage factor (ratio of thickness during exposure to thickness after development) of each emulsion was measured by means of a micrometer. Although, for the most part, track depths were not measured, a depth criterion was used, and knowledge of the shrinkage factor was necessary in order to interpret the results. The shrinkage factor varied from about 6 to 9, the value depending mostly on the temperature at which the plates were soaked. The emulsions were developed using the "dry development" procedure prescribed by Dainton *et al.*[11] with a few modifications. The use of amidol bisulfite as a developer was effective in preventing stain in the developed emulsions.

With the targets used, there were very few gamma rays, other than those from O^{16*}, which could produce photoprotons from the photodisintegration of the deuteron. Protons from all other origins could be detected in the H_2O control plates. Possible sources of background were (γ,p) reactions on other nuclei in the emulsion, or (p,n) reactions in the target emitting neutrons which would produce recoil protons in the emulsion. The threshold energies for both types of reactions, however, are above the proton and gamma energies of this experiment. In fact virtually the only background observed was that accumulated in the emulsion before a run was made.

The plates were scanned with a Leitz binocular microscope using a magnification of 900, 450, or 250. The center of the scanning area, usually circular, was located at the point at which gamma rays emitted at 90° to the beam were normal to the emulsion plane. For each acceptable track the projected range and direction in the emulsion plane were measured. When using the 900 magnification the depth of a track was also recorded.

The criteria for acceptance of a track were as follows. (1) The track must not be scattered through an angle greater than 10° as seen in the emulsion plane. This limit was extended to 20° when the sense (direction) of the track could be determined. (2) The track must lie entirely in the emulsion. (3) The track must be in "sharp" focus along its entire length. (4) The track must not have an observed length indefinite by more than 2.5 microns. The third criterion was not used with the 900 magnification, since depths were measured.

Actually the high magnification was used only on one plate of the first run. It was then found that the third criterion could be successfully applied and the labor greatly reduced. Furthermore, the energy discrimination based on projected range and the third criterion was found to be as good as that based on actual range which involved a depth measurement.

II. ANALYSIS OF THE MEASUREMENTS

If the photodisintegration is electric dipole in nature, the angular distribution of photoprotons is given by:

$$I(\alpha)d\Omega = I_0 \cos^2\alpha d\Omega, \tag{1}$$

where α is the angle between the proton direction and the polarization direction of the gamma ray. If a polar axis is established along the propagation direction of the gamma ray, Eq. (1) in polar coordinates becomes:

$$I(\theta,\phi)d\theta d\phi = I_0 \sin^3\theta \cos^2\phi d\theta d\phi. \tag{2}$$

The complement of θ is the dip angle of the photoproton in the emulsion. ϕ is the azimuthal angle measured experimentally. If R is the range of the photoproton, its projection on the emulsion plane is $p = R\sin\theta$; hence

$$I(p,\phi)dpd\phi = I_0 R^{-3} p^3 (R^2 - p^2)^{-\frac{1}{2}} \cos^2\phi dpd\phi. \tag{3}$$

Then

$$I(p)dp = \int_0^{2\pi} I(p,\phi)d\phi dp = I_0 \pi R^{-3} p^3 (R^2 - p^2)^{-\frac{1}{2}} dp, \tag{4}$$

and

$$I(\phi)d\phi = \int_{p_c}^{R} I(p,\phi)dpd\phi = C_0 \cos^2\phi d\phi, \tag{5}$$

where $C_0 = (I_0/3)R^{-3}(p_c^2 + 2R^2)(R^2 - p_c^2)^{\frac{1}{2}}$.

Equation (4) gives the distribution in projected range p expected from the microscope measurements. A lower limit p_c of the projected range is established by the criterion that the tracks be in sharp focus in the microscope. Its value depends on the depth of focus and the shrinkage factor. A comparison of the theoretical distribution with an experimental distribution is shown in Fig. 3. The quantity p_c for the 6-Mev distribution is shown at 46μ and for the 6.9-Mev distribution it falls at 69μ, well above R for the 6-Mev distribution.

Equation (5) gives the distribution in ϕ expected for a gamma ray polarized along the beam direction, $\phi = 0°$.

[11] Dainton, Gottiker, and Lock, Phil. Mag. **42**, 596 (1951).

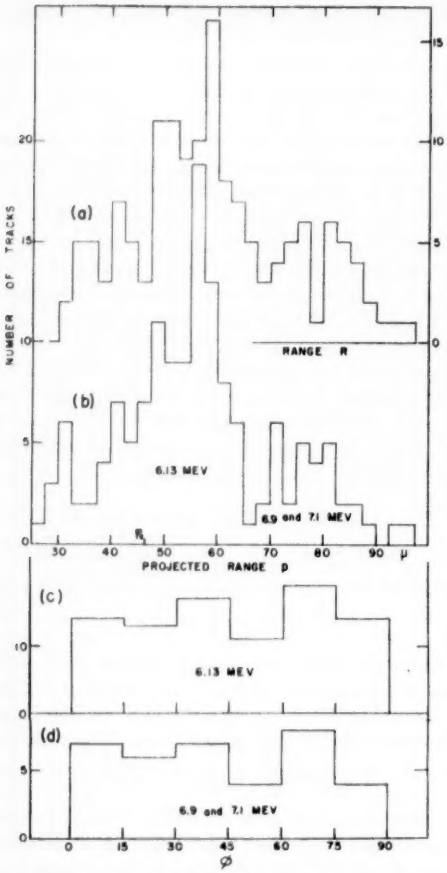

FIG. 1. (a) Actual range distribution of photoprotons from the first run; (b) projected range distribution of photoprotons, (c) polarization distribution for the 6.13-Mev gamma; (d) for the 7-Mev group.

If the gamma ray is partially polarized, it can be treated as two waves with random phases and with mutually perpendicular polarizations, one parallel and the other perpendicular to the proton beam. Adding the distributions corresponding to each component we get a resultant ϕ dependence of the form:

$$I(\phi)=1+B\cos^2\phi, \tag{6}$$

where $1+B=I(0°)/I(90°)$ is the polarization ratio P.

The effect of the extended scanning area on the polarization ratios measured in the experiment was investigated and found to be negligible. The ratios were, however, corrected for the contribution of the magnetic dipole interaction in the photodisintegration process, as given by theory,[5] but not for the small admixture of quadrupole interaction.

IV. RESULTS

The results from three runs are presented in Figs. 1 to 4. Since it was not possible in many cases to determine the sense of a track, no effort was made to do so, and it was only necessary to use two quadrants in recording the azimuthal angle. Because of the symmetry in the polarization distributions, most of the distributions are shown folded about $\phi=0°$.

The results of the first run are presented in Fig. 1. Since depth measurements were made in this run, it was possible to make a comparison between the distribution achieved by plotting actual range [Fig. 1(a)] and that achieved by plotting projected range [Fig. 1(b)]. Both distributions contain only tracks of dip angle $<35°$. The two groups in Fig. 1 correspond to photoprotons produced by the 6.13-Mev gamma and the unresolved 6.9- and 7.1-Mev gammas. The distributions in ϕ for the 6.13-Mev gamma [Fig. 1(c)] and the 7-Mev group [Fig. 1(d)] were plotted using tracks with projected ranges between 45μ and 62.5μ, and between 65μ and 90μ, respectively.

The short-range tail (below ρ_c) in the range distribution of the 6.13-Mev gamma ray indicates that background was fairly high in this run, and the polar-

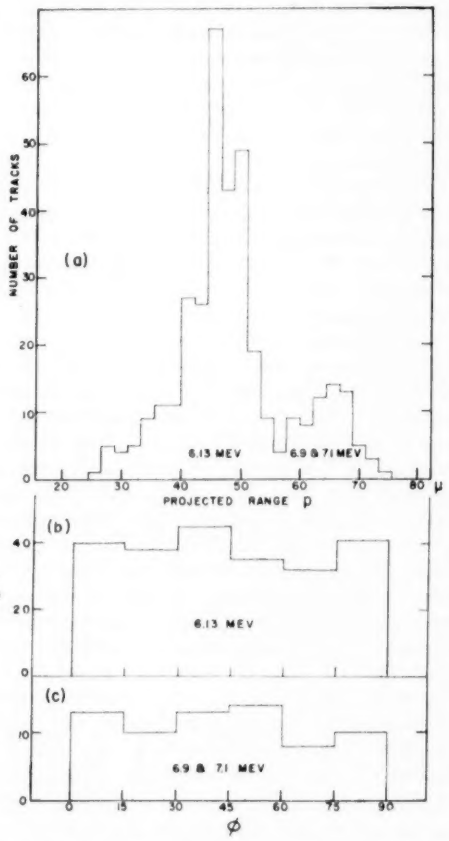

FIG. 2. (a) Projected range distribution from the third run; (b) polarization distribution for the 6.13-Mev gamma; (c) for the 7-Mev group.

ization distributions are not considered entirely reliable, although they do agree with the work of later runs. This background was even more pronounced in the second run, and it is believed that it was due to a previous exposure to fast neutrons which produced recoil protons in the emulsion. Since the (n,p) process has a relatively high cross section, a very low neutron flux would produce a troublesome background.

Because of these background difficulties, the next run was made with freshly eradicated emulsions. The results are presented in Fig. 2. The improvement in the background situation is established by the fact that no acceptable tracks were found in the portion of the H_2O plate that was scanned (about $\frac{1}{12}$ that scanned in the D_2O plates). The improvement is also apparent from Fig. 2(a), where p_c (at 41μ) and R (at 50μ) are well defined for the 6.13-Mev distribution. The polarization distributions in Figs. 2(b) and 2(c) are made up of tracks of projected range, $40\mu<p<53.5\mu$ and $56\mu<p<76\mu$.

To improve statistics and in particular to study the 7-Mev group, a run of greater intensity was obtained. Uneradicated plates which hold more D_2O were used, but stringent background precautions were taken. The background as determined from the H_2O control plate

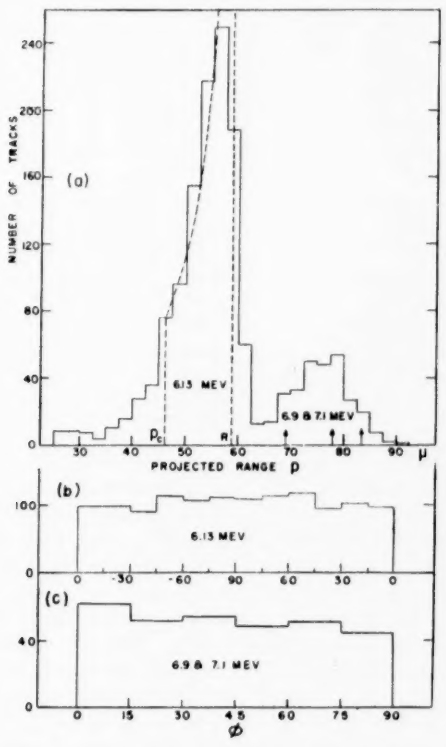

FIG. 3. (a) Projected range distribution from the fourth run; (b) unfolded polarization distribution, 6.13-Mev gamma; (c) folded, 7-Mev group.

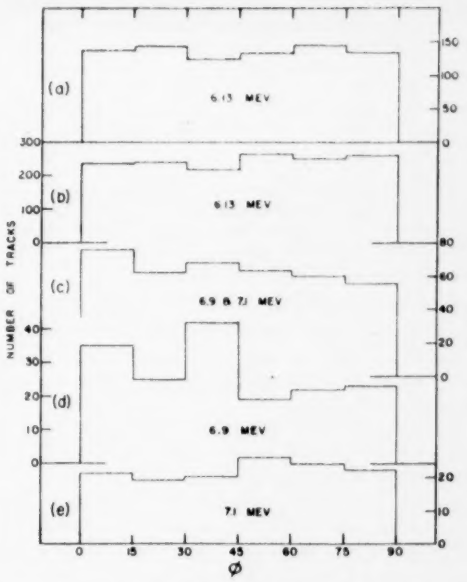

FIG. 4. (a) Total polarization distribution for 6.13-Mev gamma from the third and fourth runs (excepting one plate in the fourth run); (b) total polarization distribution for 6.13-Mev gamma (all plates); (c) for the 7-Mev group; (d) attempted resolution of the distribution for the 6.9-Mev gamma; (e) for the 7.1-Mev gamma.

was estimated to be 2 percent. The results of this run are presented in Fig. 3. The arrows at 78μ and 83.5μ give the predicted ranges R for the two unresolved distributions of the 7-Mev group. The ratio of the 6.13-Mev yield to the unresolved 6.9 and 7.1 yield is 2.9 ± 0.4, in good agreement with other investigations.[9]

The polarization distribution for the 6.13-Mev gamma (tracks with $45\mu<p<62.5\mu$) is shown unfolded in Fig. 3(b). The small increase in intensity toward 90° in evidence in this distribution was present only in one of the plates of this run. The other plate, and the other runs gave little evidence of a polarization effect for the 6.13-Mev gamma, and the discrepancy has not yet been adequately explained. Figure 3(c) gives the polarization distribution for the 7-Mev group (tracks with $67.5\mu<p<92.5\mu$), which shows a definite polarization effect.

The combined polarization distributions for the last two runs are plotted in Fig. 4. For the 6.13-Mev distribution in Fig. 4(a), however, data from the plate showing the intensity increase toward 90° are not included. The total 6.13-Mev distribution is shown in Fig. 4(b). Figure 4(c) gives the distribution for the 7-Mev group. Figures 4(d) and 4(e) represent an attempt to resolve the 6.9- and 7.1-Mev distributions by plotting tracks from the extremities of the 7-Mev group. There are noticeable intensity increases in the 6.9-Mev and 7.1-Mev distributions toward 0° and 90°, respectively.

TABLE I. Polarization ratios for radiation emitted at 90° and for an angular distribution of the form $1+A\cos^2\theta$.

Radiation	Parity	$P=I(0°)/I(90°)$
$E1$, $M2$	−	$(1-A)/(1+A)$
$M1$, $E2$	+	$(1+A)/(1-A)$
$E3$	−	$(1+\frac{2}{3}A)/(1-\frac{2}{3}A)$
$M3$	+	$(1-\frac{2}{3}A)/(1+\frac{2}{3}A)$

The dipole and quadrupole expressions are given by Hamilton (see reference 2). Expressions for higher poles may be obtained by means of the formulas (for magnetic radiation):

$$I_\theta = 4M^2[(2L+1)(L+1)L]^{-1}\sin^{-2}\theta[Y_L{}^M]^2,$$

$$I_\phi = [(2L+1)(L+1)L]^{-1}\{[(L-M)(L+M+1)]^{\frac{1}{2}}Y_L{}^{M+1} - [(L+M)(L-M+1)]^{\frac{1}{2}}Y_L{}^{M-1}\}^2.$$

V. DISCUSSION

Table I gives the polarization ratios for radiation emitted at 90° to the proton beam and for an angular distribution of the form $1+A\cos^2\theta$. A_2 and A_3 will represent the angular distribution coefficients, and P_2 and P_3 the polarization ratios of γ_2 (6.9-Mev) and γ_3 (7.1-Mev), respectively. A_t and P_t will designate these quantities for the unresolved group.

Table II gives all possible assignments of polarization for γ_2 and γ_3 taking into account only the form (dipole or quadrupole) of the polarization ratios and the sign of the coefficients. Taking $A_t=0.33$, as given by Sanders,[9] values of P_t are calculated for each case. It is seen that the value $P_t=1.32\pm0.24$, obtained from a least square analysis of the data in Fig. 4, eliminates all but two of the possibilities. Of these only case 8 in Table II gives $P_2>1$ and $P_3<1$, in qualitative agreement with the polarization trends in Fig. 4. The other choice, case 5, gives just the reverse trends for P_2 and P_3. If one or both of the gamma rays are octupole, the possible values of P_t given in Table II are altered somewhat, but the above conclusion is unchanged. Hence we take $P_2=(1+A_2)/(1-A_2)$, $P_3=(1-A_3)/(1+A_3)$, $A_2>0$, and $A_3>0$, with it understood that the coefficient is multiplied by $\frac{2}{3}$ in the polarization ratio for octupole radiation.

Table III gives the computed angular distribution coefficients and polarizations for those spin and parity assignments to states in Ne^{20} and O^{16} which lead to short-range alpha particles and to distributions of the type $1+A\cos^2\theta$. These coefficients were calculated by the method of Biedenharn, Arfken, and Rose.[12] The lowest possible values of the orbital quantum numbers, l_p and l_α are assumed in each case. The effect of mixed values of l_p and l_α was investigated, but in no case in which the spin of Ne^{20} is 2 or greater is the sign of the coefficient altered by any reasonable admixture of higher l-values.[12] For the 1^+ case, it is necessary to consider $l_p=0$ and 2 in order to obtain non-zero values of A. For any states in O^{16} leading to the correct polarizations, however, opposite signs for A_2 and A_3 are obtained in this case. Among all the possibilities in Table III the only ones in qualitative agreement with $P_2>1$, $P_3<1$, $A_2>0$, and $A_3>0$ are those for which the Ne^{20} state is 2^-, γ_2 is $E2$ or $E3$, and γ_3 is $E1$, $M2$, or $M3$.

Finally, these possibilities are investigated quantitatively in Table IV. Experimental values for A_2 and A_3 were computed using $A_t=0.33$, $P_t=1.32$, and a 3.3:1 ratio for the intensities of γ_2 and γ_3 at 90°. This ratio was obtained from an analysis of the range distribution in Fig. 3. The results are, however, quite insensitive to the precise value of this ratio, but the preponderance of 6.9-Mev radiation makes the computed values of A_3 more uncertain than those for A_2, as indicated by the errors given in the table. It is noticed also that different experimental values for A_2 and A_3 are obtained if one or both of the gamma rays are octupole because of the factor of $\frac{2}{3}$ in the octupole expression for the polarization. The best numerical agreement in Table IV is obtained when γ_2 is $E2$ and γ_3 is $E1$. It is necessary, however, to consider the effect on the coefficients of higher values of l_p and l_α. For a 2^- state in Ne^{20} both $l_p=1$ and 3 are allowed. An investigation of the terms introduced by $l_p=3$ shows that the coefficients of $\cos^4\theta$ and $\cos^2\theta$ are of comparable

TABLE II. Polarization assignments for the 6.9- and 7.1-Mev gamma rays. The only datum used in computing values of P_t is that $A_t=0.33$, which also eliminates the possibility that A_2 and A_3 are both negative.

Case	P_2	A_2	P_3	A_3	P_t
1	$\frac{1+A_2}{1-A_2}$	Any	$\frac{1+A_3}{1-A_3}$	Any	2.0
2	$\frac{1-A_2}{1+A_2}$	Any	$\frac{1-A_3}{1+A_3}$	Any	0.5
3	$\frac{1-A_2}{1+A_2}$	<0	$\frac{1+A_3}{1-A_3}$	>0	>2.0
4	$\frac{1-A_2}{1+A_2}$	>0	$\frac{1+A_3}{1-A_3}$	<0	<0.5
5	$\frac{1-A_2}{1+A_2}$	>0	$\frac{1+A_3}{1-A_3}$	>0	$0.5\rightarrow2.0$
6	$\frac{1+A_2}{1-A_2}$	<0	$\frac{1-A_3}{1+A_3}$	>0	<0.5
7	$\frac{1+A_2}{1-A_2}$	>0	$\frac{1-A_3}{1+A_3}$	<0	>2.0
8	$\frac{1+A_2}{1-A_2}$	>0	$\frac{1-A_3}{1+A_3}$	>0	$0.5\rightarrow2.0$

[12] Biedenharn, Arfken, and Rose, Phys. Rev. **83**, 586 (1951). For 1^+ and 2^- states in Ne^{20} Seed and French (reference 10) have tabulated the correlation functions in a very convenient form for investigating the effect of mixed l values.

magnitude (except of course for $E1$ radiation). To the extent that a term in $\cos^4\theta$ has not been observed in the angular distributions, therefore, contributions from $l_p=3$ may be neglected. For all the cases in Table IV except $E1$, two or more values of l_α are allowed. In each case, however, the contribution of higher values of l_α has the effect of *reducing* the magnitude of the angular distribution coefficients, and therefore the choice of $E2$ radiation for γ_2 is the most likely one.

For γ_3 the choice of $E1$ radiation gives agreement just within the uncertainty in the measurement. Since only one value of l_α is allowed by the selection rules in this case, a closer agreement for A_3 could be obtained only by allowing a large contribution from an incoming $l_p=3$ wave. For $M2$ and $M3$ radiation it is possible to reduce the theoretical values of A_3 by assuming contributions from higher values of l_α. In both cases, however, the amplitudes of the $l_\alpha+2$ and the l_α waves must be in a ratio greater than 1:2 in order to obtain agreement within the experimental uncertainty.

TABLE III. Computed angular distribution coefficients and polarization ratios for those cases having distributions of the form $1+A\cos^2\theta$. The smallest values of l_p and l_α are used in each case.

Ne^{20}	l_p	O^{16}	l_α	A	P	Possible assignment 6.9-Mev	7.1-Mev
1^+	0	Any	···	0	1	No	No
2^-	1	1^-	2	0.64	0.22	No	Yes
		1^+	1	−0.45	0.38	No	No
		2^-	0	1.00	0.00	No	Yes
		2^+	1	0.43	2.51	Yes	No
		3^-	2	0.24	1.38	Yes	No
		3^+	1	1.29	0.08	No	Yes
3^+	2	1^-	3	0.82	0.10	No	Yes
		1^+	2	−0.44	0.39	No	No
4^-	3	1^-	4	0.89	0.06	No	Yes
		1^+	3	−0.42	0.40	No	No

The selection of $E2$ radiation for γ_2 and the value $A_2=0.30$ are in complete agreement with the results of Seed and French[10] on the directional alpha-gamma correlations. If one uses their parameters, one obtains $A_2=0.32$. For γ_3 Seed and French obtain the assignment of $E1$, and the value $A_3=0.64$ follows from the fact that they find no evidence in their work for $l_p=3$ waves. The discrepancy between 0.64 and the experimental value of 0.41 can undoubtedly be attributed to the uncertainty in the latter value. As noted above, small errors in either A_t or P_t could account for the discrepancy without materially affecting the good agreement for A_2. A value of $A_3\simeq 0.6$ would of course give rise to a marked polarization for γ_3; the lack of a strong trend in the γ_3 distribution in Fig. 4 must be attributed to the poor resolution coupled with the very low relative intensity of γ_3, and to the poor statistics.

TABLE IV. Quantitative comparison of theoretical and experimental angular distribution coefficients.

γ_2 (6.9-Mev)	A_2 Theor.	A_2 Exp.	γ_3 (7.1-Mev)	A_3 Theor.	A_3 Exp.
$E2$	0.43	0.30±0.08	$E1$	0.64	0.41±0.24
$E2$	0.43	0.30±0.08	$M2$	1.00	0.41±0.24
$E2$	0.43	0.28±0.08	$M3$	1.29	0.50±0.29
$E3$	0.24	0.36±0.10	$E1$	0.64	0.21±0.24
$E3$	0.24	0.36±0.10	$M2$	1.00	0.21±0.24
$E3$	0.24	0.35±0.10	$M3$	1.29	0.26±0.31

A least-square analysis of the 6.13 distributions presented in Figs. 4(a) and 4(b) yields polarization ratios of $P_1=0.99\pm0.10$ and 0.89 ± 0.08, respectively. Considering the statistical uncertainty and the experimental error (particularly the somewhat anomalous behavior of one plate) the ratio is too close to unity to establish the polarization of the 6.13-Mev gamma ray, and a parity assignment cannot be made. The work of Arnold[13] and Barnes *et al.*[14] on the directional correlation and of French and Newton[4] on the polarization correlation involving this state in O^{16} has, however, established the assignment of 3^- ($E3$ radiation).

An approximately isotropic polarization for the 6.13-Mev gamma ray is expected from the value of $+0.01\pm0.04$ given by Sanders[9] for the angular distribution coefficient. If we use the values found above for the 6.13-Mev polarization ratio, we arrive at values of -0.01 ± 0.08 [from Fig. 4(a)] and -0.09 ± 0.06 [from Fig. 4(b)] for the angular distribution coefficient in essential agreement with Sanders' value.

We are greatly indebted to the members of the cosmic ray group of the Nucleonics Division, Naval Research Laboratory, for their help in acquainting the authors with the thick emulsion development technique and for performing all of the plate eradications. We are also greatly indebted to Dr. N. P. Heydenberg for the use of the D.T.M. statitron. Thanks are due to Mr. F. Levin for assistance with the microscope readings.

[13] W. R. Arnold, Phys. Rev. **80**, 34 (1950).
[14] Barnes, French, and Devons, Nature **166**, 145 (1950).

Neutron and Spontaneous Fission in Uranium Ores

W. H. FLEMING* AND H. G. THODE
Departments of Physics and Chemistry, Hamilton College, McMaster University, Hamilton, Ontario, Canada
(Received June 1, 1953)

The fission yields of the stable isotopes of xenon and krypton in natural fission have been determined for six samples of pitchblende and one sample of uraninite. The fission yields observed varied markedly from sample to sample. The nature of these variations and particularly the changes that occur in the "fine structure" of the mass yield curves at Xe^{132} and Xe^{134} indicate that both spontaneous fission of U^{238} and neutron fission of U^{235} occur in uranium minerals, the proportion of each depending on the uranium concentration, geological age, and the impurities in the mineral. This conclusion is consistent with estimates of the neutron flux in these ores based on the abundance of Pu^{239} in pitchblende.

INTRODUCTION

THE spontaneous fission of uranium was first reported in 1940[1,2] and a number of attempts were made to measure the fission half-life. More recently, Segrè[3] has reported on the spontaneous fission half-life of the individual isotopes of uranium and other heavy elements. The values given for U^{238} and U^{235} are, respectively, $8.04\pm0.3\times10^{15}$ and $1.87\pm0.6\times10^{17}$ years. In 1950 Macnamara and Thode identified fission products in gases extracted from uranium minerals. Their results showed the existence of five fission product isotopes of Xe and three of Kr, the distribution of which indicated an asymmetric mass fission yield curve similar to that obtained in the thermal neutron fission of U^{235}.[4] However, the curves were steeper, indicating a more selective process, and the ratio of Xe to Kr was larger. Both these facts suggested that some spontaneous fission of U^{238} was involved. Also the amount of fission product Kr and Xe obtained per gram of uranium in the mineral was of the order of magnitude expected, considering the spontaneous fission half-life and the age of the mineral.

Finally, some "fine structure" in the mass yield curve was evident from the high yield of Xe^{132}. Previous mass spectrometer studies of fission gas from $U^{235}+n$ fission had shown abnormally high yields at Xe^{133} and Xe^{134}.[5-7] This shifting of the fine structure to the lower masses again pointed to the spontaneous fission of U^{238} as the source of fission products in uranium minerals, since the Glendenin mechanism[8] put forth to explain these abnormal yields would qualitatively account for such a shift. Experimental evidence today[7,9] indicates that abnormal yields or fine structure in the mass yield curve are due to two closed shell effects; first, the structural preference in the initial fission process; second, the preferential liberation of fission neutrons from nuclides having 1 or 3 neutrons more than a closed shell. The latter explanation of fine structure, first suggested by Glendenin, would predict a shifting of fine structure to the lower masses by 1–2 mass units as we go from U^{235} to U^{238} fission.

Several years ago it was found in our laboratory[10] that the fission pattern of isotopes for Xe and Kr varied to some extent between gases extracted from Great Bear (Canada) and Belgian Congo pitchblendes. Both patterns showed the same characteristics, but the fission gases from the richer and younger Belgian Congo ore gave a pattern of isotopes closer to that obtained for $U^{235}+n$ fission; suggesting that both $U^{235}+n$ and spontaneous fission of U^{238} might be involved. Since that time, we have investigated a number of uranium ores to determine the nature and extent of natural fission. The results indicate that both neutron fission of U^{235} and spontaneous fission of U^{238} are involved, the extent of each depending on the concentration of uranium, the age of the mineral and the nature of the impurities. The results are given in this paper.

EXPERIMENTAL

The apparatus used in this laboratory for the extraction of Xe and Kr from neutron irradiated uranium metal has been described elsewhere.[11] The same apparatus, with minor modifications, was used for the extraction and purification of the rare gases from uranium minerals. A trap containing ascarite was inserted in the chemical drying train to remove the large quantities of CO_2 produced from carbonates in some of the minerals. A simple calcium furnace was installed after the drying train to carry out the initial rough purification of the released gases, which contained large quantities of nitrogen and oxygen. The final purification and volume measurement was identical to that described previously.[11]

* Holder of a Research Council of Ontario Scholarship 1951–1952.
[1] G. N. Flerov and K. A. Petrzhak, J. Exptl. Theor. Phys. U. S. S. R. **3**, 275 (1940).
[2] G. N. Flerov and K. A. Petrzhak, Phys. Rev. **58**, 89 (1940).
[3] E. Segrè, Los Alamos Scientific Laboratory Report, LADC-975, 1945 (unpublished).
[4] J. Macnamara and H. G. Thode, Phys. Rev. **80**, 471 (1950).
[5] H. G. Thode and R. L. Graham, Can. J. Research **A25**, 1 (1947).
[6] Macnamara, Collins, and Thode, Phys. Rev. **78**, 129 (1950).
[7] Wiles, Smith, Horsley, and Thode, Can. J. Phys. **31**, 418 (1953).
[8] L. E. Glendenin, Phys. Rev. **75**, 337 (1949).
[9] Dr. R. Wiles, M.Sc. thesis, McMaster University, Hamilton, Ontario, August, 1950 (unpublished).
[10] H. G. Thode, Trans. Roy. Soc. (Canada) **45**, 1 (1951).
[11] Arrol, Chackett, and Epstein, Can. J. Research **B27**, 757 (1949).

In the preliminary work, the mineral, in the form of a fine powder, was dissolved in concentrated sulfuric acid for 1½ to 2 hours. This procedure produced satisfactory samples, but it was later found that the sulfuric acid contained large quantities of dissolved argon accompanied by traces of normal Xe and Kr. For this reason the later samples were prepared by heating the powdered mineral in an Inconel combustion tube to 1000–1200°C at which temperatures the pitchblende began to sinter. The rare gas samples obtained in this way contained a much smaller amount of normal Xe and Kr and the final samples removed at the highest temperatures contained almost pure fission product Xe and Kr. These samples made possible a more accurate determination of the fission yields and also permitted a study of the argon isotope abundances in the minerals. The final volume of the purified rare gas samples obtained from 200 gram samples of ore varied from 10 to 30 cubic millimeters. Mass spectrometer analysis showed the approximate composition to be 99.5 percent A, 0.25 percent Kr and 0.25 percent Xe.

All rare gas samples were analyzed on a conventional 180° direction focusing Nier-type mass spectrometer. The ion currents were amplified by an Applied Physics Corporation vibrating reed electrometer. The mass spectrometer had previously been calibrated with standard mixtures of xenon and krypton so that it was possible to determine the ratio of xenon to krypton from the mass spectrometer results. This permitted normalizing both the xenon and krypton fission yield data to an arbitrary value assumed for one of the xenon isotopes. The results of the earlier argon isotope studies have already been published.[12]

RESULTS

Figure 1 shows a typical mass spectrogram of the Xe isotopes in uraninite all recorded at one sensitivity. As noted previously,[4] stable Xe^{129} is present and 10-year Kr^{85} is absent in these naturally occurring fission product samples because of their great age. The particular sample for which the mass spectrogram in Fig. 1 was obtained was remarkably free from normal Xe gas as indicated by the absence of Xe^{130}. Other samples were found to contain a small percentage of normal Xe for which corrections had to be made to obtain the true fission isotope pattern. This correction was less than 20 percent in one case and less than 10 percent in all others. Also the argon present in the uraninite sample was almost free of A^{36}; the A^{38} to A^{36} ratio being 10 to 1 rather than 1 to 5 as in natural argon. This result confirms strikingly the earlier results of Fleming and Thode, which showed that A^{38} is formed in uranium minerals by nuclear processes.

The relative yields of the fission isotopes of Xe obtained for Xe gas extracted from 6 different samples of pitchblende and 1 sample of uraninite are given in Table I. In each case Xe^{136} was arbitrarily assigned a

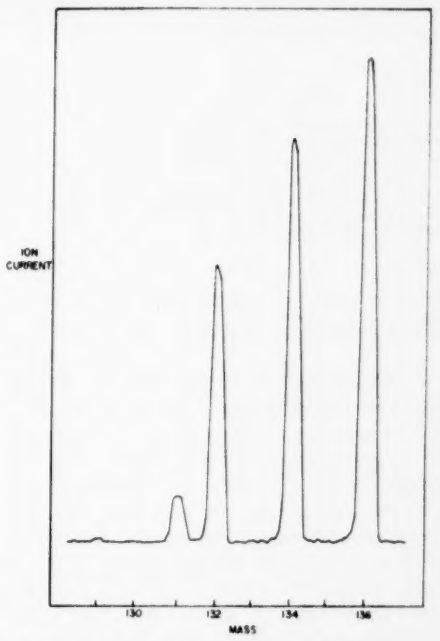

FIG. 1. Mass spectrogram of xenon from uraninite, Cardiff Township, Ontario.

value of 6.5 percent to coincide approximately with the smooth yield curve at this mass in the neutron fission of U^{235}.[13] Table I also gives the average uranium concentration and the geological age of each sample. The later value was determined by the lead isotope method.[14] It can be seen that the relative yields of the Xe isotopes vary markedly from sample to sample. Table II gives the relative fission yields of the Kr isotopes in gases extracted from two different uranium ores. Here again the values are normalized at 6.5 percent for Xe^{136}, the ratio of Xe to Kr having been determined. Although the errors involved in the Kr yield measurements are larger than for the xenon yields, because the absolute yields are lower, and because the contamination with normal Kr gas is greater (larger corrections necessary), the results nevertheless show significant differences between the two samples investigated.

These different patterns of isotopes found for the fission gas samples extracted from different uranium minerals cannot be due to isotope fractionation in sample preparation or to isotope fractionation due to different rates of diffusion of the isotopes from the minerals over the millions of years. (From He age studies it has been found that the loss of He from minerals is not great. The losses of Xe and Kr by

[12] W. H. Fleming and H. G. Thode, Phys. Rev. **90**, 857 (1953).

[13] The yield of 6.5 percent for Xe^{136} is based on a value of 3.0 percent for the yield of I^{131}. Recently this yield has been revised upward to 3.2 percent [Bartholomew, Brown, Hawkings, Merrit, Thode, and Yaffe, paper given at Annual Conference Chemical Institute of Canada, June 4–6, 1953 (unpublished)].

[14] A. O. Nier, Phys. Rev. **55**, 153 (1939).

TABLE I. Xenon fission yields.

Sample	% U_3O_8	Age (million years)	Fission yields (%) 129	131	132	134	136
Pitchblende, Katanga, Belgian Congo	65.21	640	0.217±0.036	1.27 ±0.04	3.91±0.06	6.03±0.03	6.50[a]
Pitchblende, Eagle Mine, Beaverlodge	45.5	1630	0.223±0.037	1.16 ±0.04	3.91±0.06	5.93±0.03	6.50
Pitchblende, Ace Mine, Beaverlodge	16.95	1600	0.226±0.035	1.07 ±0.04	3.89±0.07	5.79±0.06	6.50
Pitchblende, Lake Athabaska	13.99	1690	0.093±0.042	0.799±0.040	3.79±0.07	5.58±0.04	6.50
Pitchblende, Nesbitt Labine, Beaverlodge	27.55	...	0.107±0.060	0.830±0.059	3.80±0.06	5.56±0.05	6.50
Pitchblende, Great Bear Lake	36.46[b]	1370	0.103±0.062	0.798±0.054	3.73±0.08	5.54±0.6	6.50
Uraninite, Cardiff Township, Ontario	approx. 60% uranium	...	0.029±0.002	0.613±0.010	3.74±0.03	5.41±0.03	6.50
$U^{235}+n$	...	...	...	3.28	4.92	8.64	7.10

[a] Yield of 136 mass chain arbitrarily chosen to be 6.50 percent. Errors shown are "standard deviations."
[b] A mill concentrate, original concentration unknown.

diffusion should be very much smaller.) Several gas samples were prepared from each mineral studied and, where the gases were obtained by the heating of the powdered mineral, samples were taken off at different temperatures. In all cases the agreement between samples was within experimental error. Further, the difference found for each isotope are not proportional to the percentage mass differences and in the case of Xe^{132} the yields differ in quite a different way from that expected if diffusion processes were involved in the fractionation of the isotopes. Also, the mass yield curves for the different samples (see Fig. 3) are not displaced according to the age of the mineral involved. Finally, any fractionation of isotopes by a diffusion process which resulted in the depletion of the light isotopes of Xe to the extent found between samples would be accompanied by an almost complete loss of Kr which was not observed. It is apparent, therefore, that the differences in the yield patterns found between samples are due to the nature of the fission processes involved in uranium minerals.

Figure 2 shows a comparison of the mass fission yield curves (masses 129–136) for $U^{235}+n$ fission and for natural fission in Great Bear pitchblende. Figures 3 and 4 show how these mass yield curves vary from one uranium mineral sample to another in the Xe and Kr isotope ranges, respectively. Two points stand out. First the mass yield curves for natural fission are steeper, and second the "fine structure" characteristics are different. In the case of $U^{235}+n$ fission, Xe^{133} and Xe^{134} have abnormally high yields, whereas in natural fission the yield of Xe^{132} is abnormally high and the yield of Xe^{134} is markedly down. These considerations, together with the higher Xe to Kr ratio found for natural fission, led previously to the conclusion that spontaneous fission of U^{238} was involved in natural fission.

In recent investigations of fast neutron fission of U^{238},[15] it has been found that the slope of the fission yield curve in the Xe and Kr mass ranges for neutron fission of U^{238} is almost identical with that for neutron fission of U^{235}. Neutron fission of U^{238} cannot, therefore, account for the steepness of the fission yield curve observed in this mass range for natural fission. The fission cross section of U^{238} is so low that little neutron fission of U^{238} would be expected. This confirms the earlier conclusion that the main source of fission products in uranium ores is from the spontaneous fission of U^{238}.

However, a close study of the present results indicate that there is an appreciable amount of $U^{235}+n$ fission involved as well. The uranium mineral fission gas samples are listed in Table III in order of increasing steepness of the mass fission yield curves plotted in Fig. 3. Columns 2 and 3 give the "fine structure" effects for masses 132 and 134, respectively, in terms of the percentage that their yields are above a smooth curve drawn through the other yield points (masses 129, 131, 136). Column 4 gives the ratio of Xe to Kr in the fission gas samples. The results obtained for thermal neutron fission of U^{235} and for fast neutron fission of ordinary uranium are included for comparison. The latter results were obtained by irradiating ordinary uranium with fast neutrons, the energy distribution being such that an appreciable amount of $U^{238}+n$

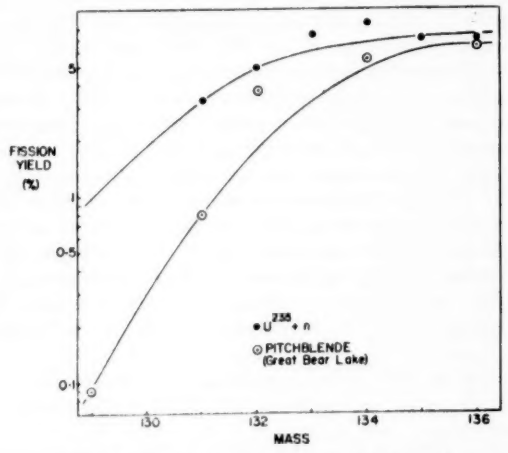

FIG. 2. Mass yield curves for natural fission and neutron induced fission of U^{238}.

[15] R. K. Wanless, Ph.D. thesis, McMaster University, October, 1953 (unpublished).

fission could be expected. It is clear from the results plotted in Fig. 5 and given in Table III that the effect of this contribution of $U^{238}+n$ fission is to increase the Xe to Kr ratio because of a shift in the whole mass yield curve toward the heavier masses and to decrease the yield of Xe^{134} and increase the yield of Xe^{132}. The fission yield results obtained for gases extracted from uranium minerals differ from those for $U^{235}+n$ fission in precisely the same way except that the curves are steeper, possibly due to the fact that spontaneous fission of U^{238} is involved rather than $U^{238}+n$ fission. It was pointed out previously[4] that since in spontaneous fission there is less energy available the process might be more selective and that a sharper grouping of the light and heavy fission fragments might be expected.

It can be seen from Table III and Fig. 3 that as the fine structure at masses 132 and 134 decreases and increases, respectively, the general shape of this mass yield curve approaches more closely to that of $U^{235}+n$ fission, indicating an increased contribution of $U^{235}+n$ fission in the samples. The remarkable relationship between the fine structure effects, steepness of the mass yield curves, and the ratio of Xe to Kr for the different

TABLE II. Krypton fission yields.

Sample	Fission yield (%) 83	84	86
$U^{235}+n$	0.67	1.27	2.45
Natural uranium, fast neutrons ($U^{235}+n$ and $U^{238}+n$)	0.47	0.98	1.63
Pitchblende, Belgian Congo	0.30±0.06	0.50±0.13	1.62±0.12
Pitchblende, Great Bear Lake	0.073±0.022	0.34±0.06	1.19±0.05

samples all confirm our conclusion that both spontaneous fission of U^{238} and neutron fission of U^{235} take place in uranium minerals, the proportion of each depending on the uranium content, the age of the

TABLE III. Fine structure variations.

Sample	% above smooth curve Mass 132	Mass 134	Xe/Kr
$U^{235}+n$ fission	0	24.5	5.05
Natural uranium irradiated with fast neutrons, average energy 0.5 Mev ($U^{235}+n$ and $U^{238}+n$)	6	17.9	6.7
Pitchblende, Belgian Congo	40	9.6	7.4
Pitchblende, Eagle Mine	40	7.8	...
Pitchblende, Ace Mine	47	6.1	...
Pitchblende, Lake Athabaska	75	3.1	...
Pitchblende, Nesbitt Labine	75	1.8	...
Pitchblende, Great Bear Lake	72	1.4	10.3
Uraninite, Cardiff Township	93	0.7	...

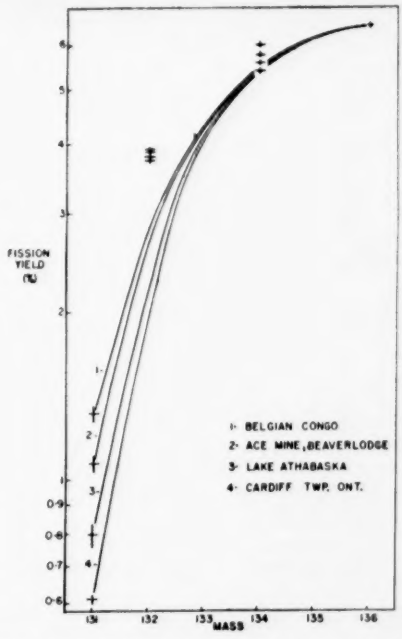

FIG. 3. Xenon fission yield variations in natural fission.

mineral, and the mineral impurities. Although there is little evidence of any fine structure in the Kr isotope mass range, the fission yield results for the Kr isotopes nevertheless support this conclusion.

The largest contribution of $U^{235}+n$ fission would be expected in very old ores, because of the higher U^{235}/U^{238} ratio when the ore was just deposited and in ores with high uranium concentrations. It is evident from Table I

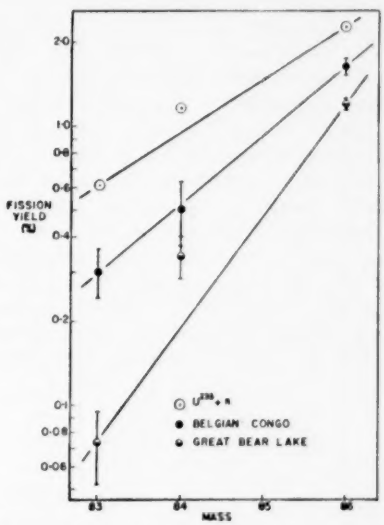

FIG. 4. Krypton fission yield variations in natural and neutron induced fission.

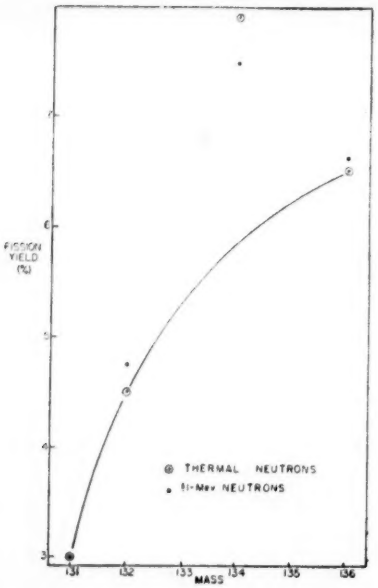

FIG. 5. Variation of neutron induced fission yields with neutron energy.

that in general the xenon fission yields most closely resembling those for $U^{235}+n$ fission are associated either with very high uranium content (Belgian Congo) or with a combination of high uranium content and old geological age (Eagle Mine). The uraninite sample appears to be an exception since it has a very high uranium content, but gives the lowest yields found. However, this sample contains the rare earth elements to the extent of several percent and the large neutron capture cross sections of some of these elements could account for the small amount of neutron fission observed. The fission gas from the Ace mine samples of pitchblende shows a higher proportion of $U^{235}+n$ fission in the ore in comparison to the others, considering its age and concentration. It is just possible that (α, n) reactions may be more important in this ore.

The fission isotope pattern for the uraninite mineral from Cardiff Township may represent that for spontaneous fission of U^{238}, although the results do not preclude some small amount of $U^{235}+n$ fission involved as well. An upper limit to the possible contribution of $U^{235}+n$ fission (and/or $U^{238}+n$ fission) can be set at 5 percent for this sample, since the yield of the 129 mass chain in $U^{235}+n$ (or $U^{238}+n$) fission is approximately 1 percent and the observed yield in this sample is certainly less than 0.05 percent allowing for a possible error in the value assumed for Xe^{136}.

DISCUSSION

The conclusion that both $U^{235}+n$ and spontaneous fission occur in nature in varying proportions seems a reasonable one in view of other considerations. First of all, the spontaneous fission rates of U^{235} and U^{238} as reported by Segrè show that only the spontaneous fission of U^{238} can be a factor. It is interesting to point out that the amounts of fission gas extracted from uranium ores per gram of uranium are of the order of magnitude expected considering the spontaneous fission half-life of U^{238} and the age of the samples. In this connection more quantitative measurements are now being made.

In regard to $U^{235}+n$ fission, Seaborg[16] has found appreciable quantities of Pu^{239} in uranium minerals which must have been formed by (n, γ) reactions of U^{238}. He calculates that the spontaneous fission neutrons would be sufficient to maintain the concentration of plutonium actually found. By the same reasoning, Seaborg[17] suggests that the neutron fission rate of U^{235} in these ores could be comparable to the spontaneous fission of U^{238}. Another source of neutrons for such reactions would be (α, n) reactions involving the light elements present in the minerals. The argon isotope studies reported previously[12] indicate that (α, n) and (α, p) reactions occur to an appreciable extent in uranium ores.

Studies of neutron and spontaneous fission in uranium and thorium minerals are being continued. A quantitative measure of the amount of fission gas present in ores per gram of uranium and a knowledge of the proportion of spontaneous fission that has occurred should make age calculations possible.

ACKNOWLEDGMENTS

This work was made possible by the financial assistance of the National Research Council of Canada and the Atomic Energy of Canada Limited. The authors wish to thank A. Thunaes of the Department of Mines for determining the uranium content of the samples and W. H. Walker who carried out the lead isotope age determinations. The assistance of S. C. Robinson of the Department of Mines in obtaining samples of uranium minerals is gratefully acknowledged.

[16] G. T. Seaborg, Chem. Eng. News **23**, 2190 (1945).
[17] G. T. Seaborg (private communication).

A Study of the H^3+He^3 Reactions*

C. D. Moak
Oak Ridge National Laboratory, Oak Ridge, Tennessee
(Received June 29, 1953)

The reactions $H^3(He^3,d)He^4$, $H^3(He^3,p)He^5$ and $H^3(He^3,p)He^4,n^1$ have been studied in the 100-kev to 800-kev region of bombarding energy. In the case of $H^3(He^3,p)He^5$, the proton energy was measured with a scintillation spectrometer; from this measurement, the energy of breakup of He^5 into a neutron and an α particle was found to be 0.95 ± 0.07 Mev. At a bombarding energy of 360 kev, the deuterons from the $H^3(He^3,d)He^4$ were found to be isotropic in the center-of-mass system. The spectrum of protons from the three-body breakup, $H^3(He^3,p)He^4,n^1$, was found to be flat within experimental error from 2 to 8 Mev. Competitions among the various modes of decay of the compound nucleus of Li^6 do not vary beyond an experimental uncertainty of ±2 percent from 200-kev to 600-kev bombarding energy. The shape of the total cross-section curve, measured from 100 kev to 800 kev, appears to indicate a nonresonant behavior, similar to the case of the *d-d* reaction.

INTRODUCTION

THE following three reactions are known to take place when H^3 is bombarded by He^3:

$$H^3+He^3\rightarrow Li^{6*}\rightarrow He^4+H^2+14.31 \text{ Mev} \quad (1)$$

$$\rightarrow He^4+H^1+n^1+12.08 \text{ Mev} \quad (2)$$

$$\rightarrow He^{5*}+H^1+Q. \quad (3)$$

These reactions have been reported by Almqvist, Allen, Dewan, and Pepper.[1] In reaction (3) the value of Q will depend upon the energy of excitation left in the He^5 nucleus. If He^5 is left in its ground state Q will be equal to $12.08-E(He^5)$ where $E(He^5)$ is the energy of breakup of He^5 into a neutron and an α particle.

The purpose of the present experiments was to determine the binding energy of the ground state of He^5 and to determine the individual cross sections of reactions (1), (2), and (3) as a function of energy in the 100- to 800-kev region of bombarding energy. Some information has been obtained concerning the excited state of Li^6 formed as a compound nucleus.

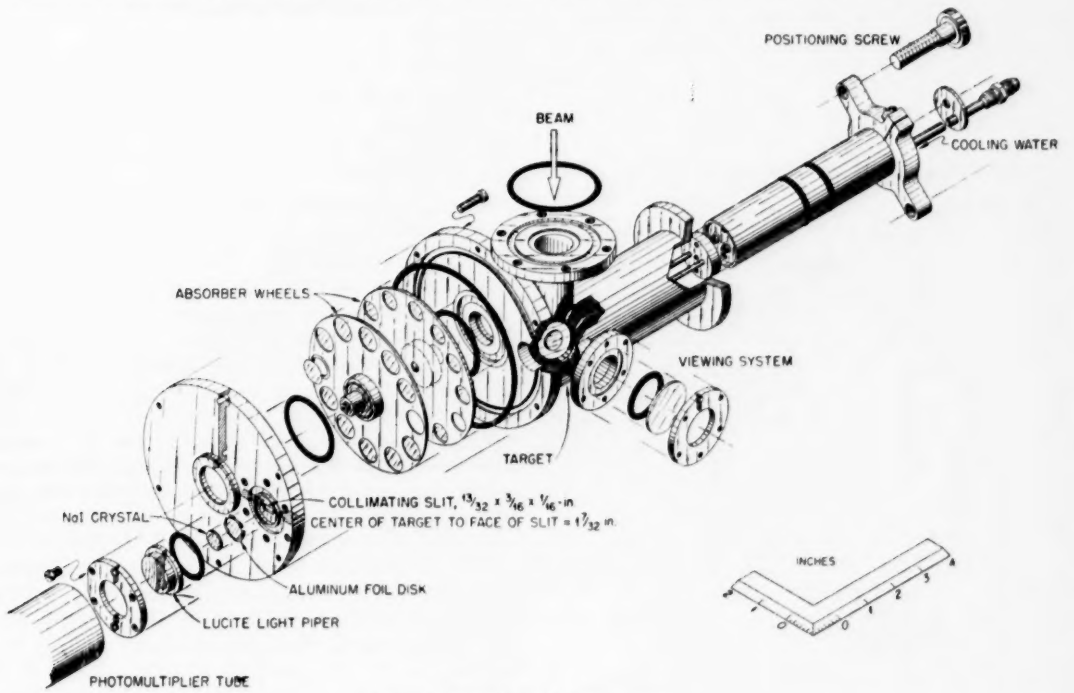

FIG. 1. Charged particle spectrometer.

* This work represents part of a thesis being prepared in partial fulfillment of the requirements for the degree of Doctor of Philosophy at the University of Tennessee.

[1] Almqvist, Allen, Dewan, and Pepper, Phys. Rev. **83**, 202 (1951).

EXPERIMENTAL ARRANGEMENTS

Accelerator

The Cockcroft-Walton accelerator is to be described in a forthcoming article. It consists of a four-stage 400-kv voltage supply and an accelerator fitted with equipment for handling He^3, an rf ion source and a 15° analyzing magnet for separating the beam components. By using the doubly charged He^3 ions, energies up to 800 kev are made available with the 400-kv generator.

Targets

For measurements of the charged particle distributions the targets were approximately 50 kev thick (at 300 kev). In the case of the cross-section measurements the target used was less than 20 kev thick throughout the range of bombarding energies used. All targets were made by heating Zr films in a tritium atmosphere. The Zr films were evaporated onto Pt backings.

Counting Arrangements

Three counting arrangements were used. The first arrangement, shown in Fig. 1, was designed for small solid angle and high resolution for use in studying the spectrum of the charged-particle reaction-products. In the arrangement of Fig. 1 a NaI crystal was mounted behind a collimator so that particles could not strike the crystal edges. Provision was made for rotating Al foils, of thickness varying in 100 steps from zero to 300 mg/cm², into the region between the target and the NaI crystal. Light from the NaI crystal was piped out of the vacuum by a Lucite button mounted on an O-ring. The light was then collected by an RCA 5819 photomultiplier. The resultant pulses were amplified by a type A-1 linear amplifier and pulse-height distributions were taken with a single-channel differential pulse-height selector. The second arrangement is shown in Fig. 2. This arrangement has been designed for accurate measurement of target current, with provision for suppression of secondary electron currents, and was made to have a larger solid angle so that current on the thin target used in the cross section measurements could be kept at a minimum. The counting circuits were the same as those for Fig. 1. The third counting arrangement is shown in Fig. 3. A scintillation counter with a window of 1-mil Al was mounted on a goniometer. The target was mounted in the vacuum system at the center of rotation of the goniometer. A cylindrical window of 1-mil steel was used to pass charged particles from the target out of the vacuum and into the scintillation counter. With this arrangement, provision was made for tilting the target so that the scintillation counter could be rotated through the range of angles from 20° to 135° with respect to the beam.

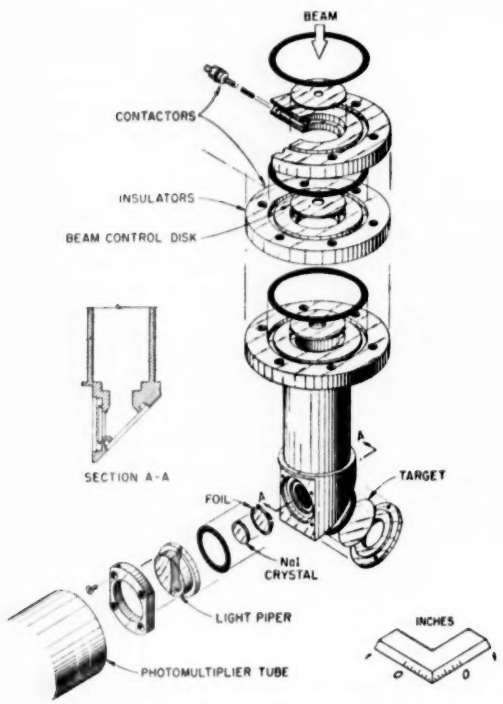

FIG. 2. Close geometry counting arrangement.

SPECTROMETER CALIBRATION

The response of the scintillation spectrometer (i.e., pulse height *vs* proton energy) has been measured by using two nuclear reactions giving protons of accurately known energies and by interpolating between these points with a set of Al absorbers. The reactions used were the following:

$$H^2+H^2\rightarrow H^3+H^1+4.036\pm0.022 \text{ Mev} \quad (4)$$

$$He^3+H^2\rightarrow He^4+H^1+18.34\pm0.024 \text{ Mev}. \quad (5)$$

For 0.3-Mev deuterons, the protons of reactions (4) and (5) have energies of 3.10 ± 0.02 Mev and 14.77 ± 0.02 Mev, respectively, at 90° to the incident beam. By using absorbers of various thicknesses, the energy of the protons from reaction (5) was reduced through the energy range bracketed by reactions (4) and (5). The residual proton energies, following passage through the various absorbers were computed using the range-energy data given by Smith.[2] The calibration data are plotted in Fig. 4. The circles shown are points gotten with Al absorbers placed between the counter and a target emitting 14.77-Mev protons. The double circles are points gotten with absorbers placed between the counter and a target emitting 3.10-Mev protons. The line drawn through the circles is quite straight, indicating that NaI responds linearly from 3 Mev to 14 Mev. It can be seen that the circles do not lie on a line (dashed line) drawn between the two points of known energy.

[2] J. H. Smith, Phys. Rev. **71**, 32 (1947).

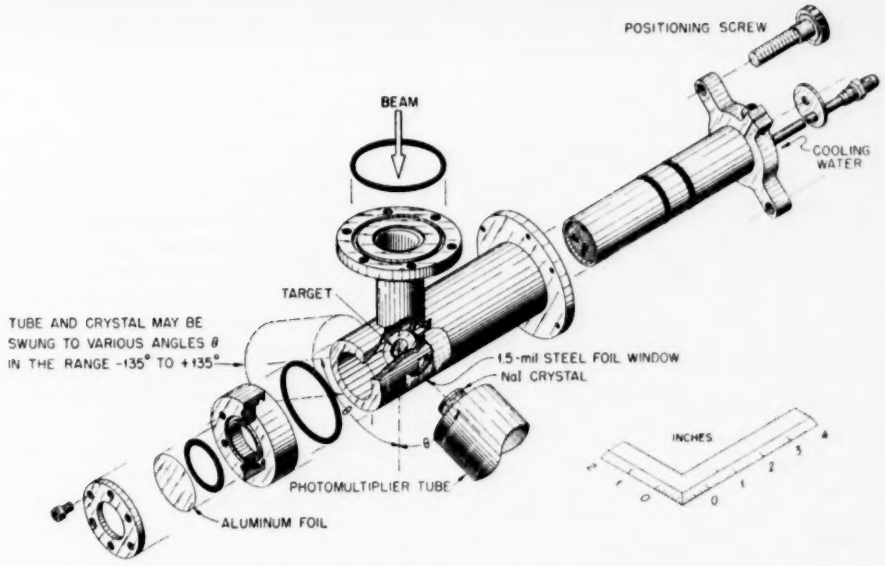

FIG. 3. Angular distribution counting arrangement.

This discrepancy indicates either that all the absorber thicknesses have been over-estimated or that the range-energy curves are slightly in error. Since all the absorbers were prepared in the same fashion, the possibility of a consistent error in the estimation of absorber thicknesses cannot be ruled out. On the other hand, some recent measurements of the range of protons in Al indicate that the values given by Smith are low by about 1 percent.[3,4] The discrepancy is in the same direction as that reported here and is of approximately the same magnitude. Until further experiments now in progress have removed this discrepancy, an error of ± 50 kev, for protons with energy in the neighborhood of 10 Mev, must be added to the experimental error. Beyond this source of error is the uncertainty of ± 20 kev in reactions (4) and (5). Errors of measurement are ± 20 kev for protons at 10 Mev. The resultant experimental error is estimated as ± 70 kev.

THE He^5 GROUND STATE

The charged particle spectrum, observed in NaI when a tritium target is bombarded with 0.3-Mev He^3 ions, is shown in Fig. 5. This curve was taken with a 600-$\mu g/cm^2$ Al absorber to stop scattered beam particles and was obtained using the geometry of Fig. 1. The peaks at each end of the spectrum are due to deuterium contamination giving rise to the protons and α particles of reaction (5). The two remaining peaks are due to the deuterons and α particles of reaction (1). Between these two peaks is the continuous spectrum of protons from reaction (2). A peak in the spectrum of protons, corresponding to the ground state of He^5 is obscured by the deuterons of reaction (1). In order to uncover this peak an absorber was used, which reduced the deuteron energy and the proton energies by different amounts; in this way the deuteron peak was displaced with respect to the spectrum of protons. The result is

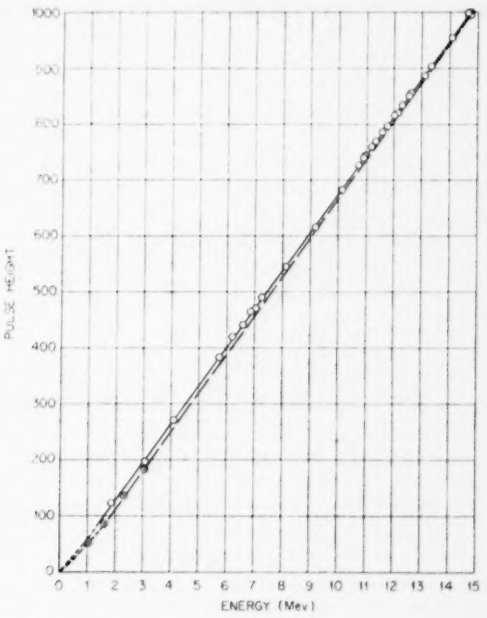

FIG. 4. Pulse height vs proton energy for NaI scintillation spectrometer.

[3] E. L. Hubbard and K. R. McKenzie, Phys. Rev. **85**, 107 (1952).
[4] H. Bichsel and R. F. Mozley, Phys. Rev. **90**, 354 (1953).

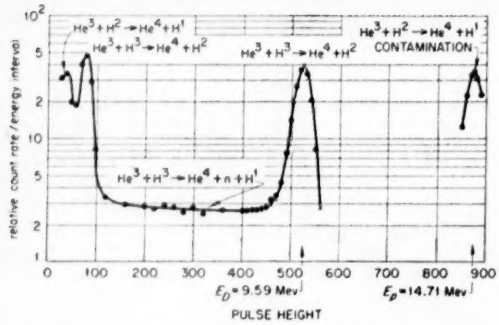

FIG. 5. Pulse spectrum in NaI of particles from H^3+He^3, bombarding energy 300 kev.

shown in Fig. 6. The first peak is that due to the deuterons of reaction (1). Displacement of this peak uncovers a peak in the proton spectrum corresponding to the formation of He^5 in its ground state. By measuring the energy of the protons in this peak, the energy of breakup of He^5 into a neutron and an α particle was determined. The upper end point of the proton spectrum is computed from the mass defect values given by Li, Whaling, Fowler, and Lauritsen.[5] Using exact masses and taking center-of-mass motion for 0.3-Mev bombarding energy into account, the end point for protons at 90° to the incident beam is at 10.16 Mev. For the energy of breakup of He^5 into an α particle and a neutron the following relation holds:

$$E(He^5)=12.20-1.201E_p, \qquad (6)$$

where E_p is the proton energy for the He^5 peak of Fig. 6

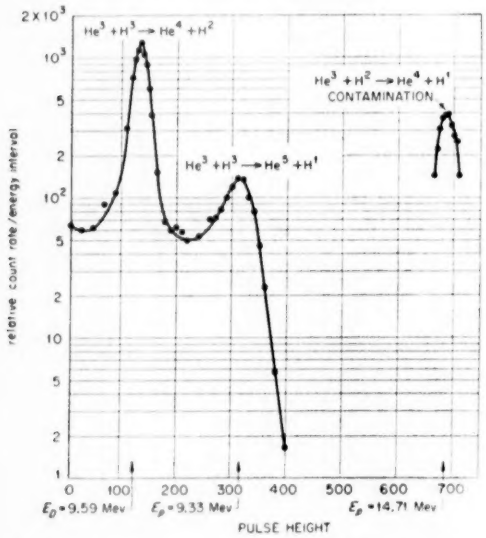

FIG. 6. Pulse spectrum in NaI of particles from H^3+He^3, bombarding energy 300 kev; particles passing through 11 mils Al into NaI crystal.

[5] Li, Whaling, Fowler, and Lauritsen, Phys. Rev. **83**, 512 (1951).

and $E(He^5)$ is the breakup energy of He^5 into an α particle and a neutron.

In order to eliminate as many systematic errors as possible in the measurement of E_p, the following procedure was used:

1. The pulse height of the He^5 peak was measured using a 60.2-mg/cm² Al absorber to shift the deuterons from the peak being measured, as in Fig. 6.

2. Absorbers were used to reduce the energy of the 14.71-Mev protons, obtained from reaction (5) which occurs due to deuterium contamination of the targets, down to the energy required to give the same pulse height as was measured in 1.

3. Using the range energy values of Smith,[3] the energy of the protons in the He^5 peak was obtained.

It was found that 240.5 mg/cm² Al for reaction (5) gave the same pulse height in the crystal counter as did 60.2 mg/cm² Al for the He^5 peak. The total range of a 14.71-Mev proton is 328.1 mg/cm² Al. The total range of the protons of the He^5 peak is then 328.1 − 240.5 + 60.2 = 147.8 mg/cm² corresponding to a value for E_p of 9.33 Mev. From the relation (6) the energy of breakup of He^5 is

$$E(He^5)=12.20-1.201\times 9.33=1.00 \text{ Mev}.$$

As pointed out in the section on calibration the absorber thicknesses may be in error by 0.8 percent; if this is the case the value of $E(He^5)$ would be 0.90 Mev. Giving equal weight to these two values and assuming the errors given in the section on calibration, the best estimate for $E(He^5)$ is 0.95 ± 0.07 Mev. This would give for the mass of He^5 a value 5.01388 ± 0.00007 a.m.u.

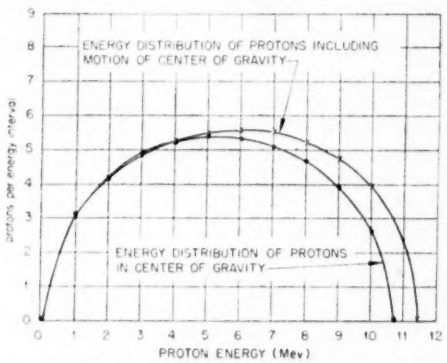
ENERGY DISTRIBUTION OF PROTONS INCLUDING MOTION OF CENTER OF GRAVITY
ENERGY DISTRIBUTION OF PROTONS IN CENTER OF GRAVITY
protons per energy interval
PROTON ENERGY (Mev)

FIG. 7. Statistical mechanics energy distribution for the $H^3(He^3\,\alpha)n,p$ three-body breakup.

THE THREE-BODY BREAKUP

The reaction (2) may be considered as a real three-body breakup or as two distinct two-body breakups in rapid succession. Thus far no satisfactory theory of three-particle breakup has been derived. If one calculates the spectrum on the basis of simple statistical mechanical arguments, assuming constant density in

phase-space, the result is as shown in Fig. 7. Referring to Fig. 5 the observed three-body breakup spectrum is quite flat in contrast to the downward curvature seen in Fig. 7. The same disagreement with the shape of the curve in Fig. 7 is found in the case of the three-body reaction $He^3+He^3 \rightarrow He^4+H^1+H^1$.[6]

RELATIVE INTENSITIES OF THE REACTIONS

Using the curve of Fig. 6 an estimate was made of the relative intensities of reactions (1) and (3). This estimate was then used to break down the total spectrum of Fig. 5 into its components. The principal source of error lay in the fact that the He^5 peak was superimposed over a three-body breakup spectrum whose shape was not known. Thus the area left under the He^5 peak was somewhat dependent upon the assumed shape of the curve subtracted for that energy region. Since the He^5 peak is small compared to the other components of the spectrum, the competition between reaction (1) and (2) could be estimated with a fair degree of accuracy. By measuring the areas under

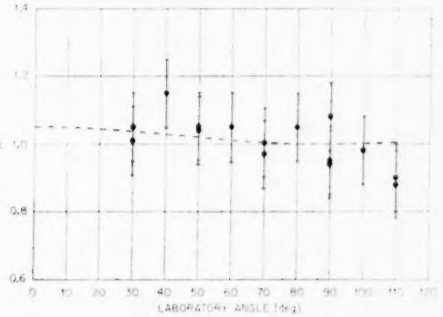

FIG. 8. Ratio (R) of $H^2(He^3,\alpha)d$ count to $H^2(He^3,\alpha)p$ count as a function of laboratory angle.

the various components of the total spectrum the following was found:

Reaction	*Percent of the times occurring*
(1) $H^3+He^3 \rightarrow He^4+H^2$	43 ± 2 percent
(2) $H^3+He^3 \rightarrow He^4+H^1+n^1$	51 ± 2 percent
(3) $H^3+He^3 \rightarrow He^5+H^1$	6 ± 2 percent

The relative intensities were measured for various bombarding energies ranging from 225 kev to 600 kev. No variation of the relative intensities beyond experimental error was found through the range of bombarding energies used.

ANGULAR DISTRIBUTION OF THE DEUTERONS

The counting arrangement of Fig. 3 was used to measure the angular distribution of the deuterons from reaction (1). The bombarding energy used was 360 kev. For this experiment the $H^2(He^3,\alpha)H^1$ reaction (5) was

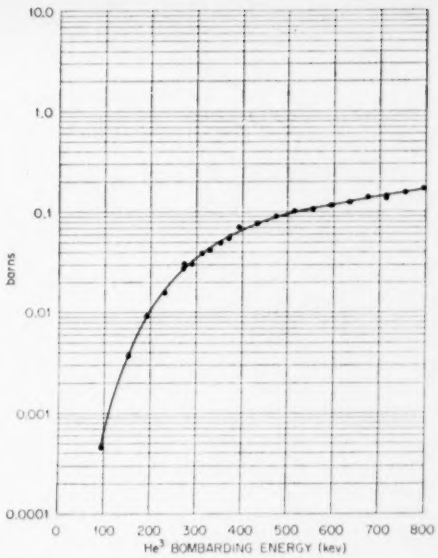

FIG. 9. Total reaction cross section for the H^3+He^3 reactions.

used as a control. The protons from this reaction are known to be isotropic in the center of mass with respect to the incident beam at bombarding energies below 500 kev.[7] A target containing both deuterium and tritium was used to produce simultaneously the isotropic protons of reaction (5) and the deuterons of unknown angular distribution from reaction (1). The electronic circuits were arranged to count the deuterons of reaction (1) and the protons of reaction (5) separately. Measurements of the ratio of deuteron counts to proton counts were made for various laboratory angles. The ratio was normalized to unity at 90° and the results are shown in Fig. 8. The smooth curve is the variation of the ratio in the laboratory assuming isotropy of the deuterons in the center-of-mass system. The experimental points indicate either that the deuterons are isotropic or that the variations with angle are smaller than the present experimental error. In particular, if the angular distribution is $1+a\cos^2\theta$, then the value of $|a|$ must be less than 0.1.

THE CROSS SECTION

The counting arrangement of Fig. 2 was used for the measurement of the cross section for reactions (1), (2), and (3). The electronic instruments were so arranged that counts due to deuterium giving rise to reaction (5) could be subtracted out. The differential cross section was measured at 90° for the total spectrum of protons and deuterons from reactions (1), (2), and (3). The cross section was obtained by dividing the differential cross section by the solid angle subtended by the crystal counter on the assumption that all particles

[6] Good, Kunz, and Moak, Oak Ridge National Laboratory Report ORNL-1415, p. 5.

[7] W. E. Kunz (private communication).

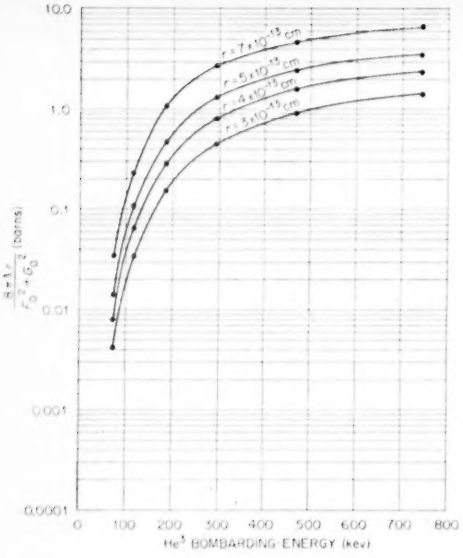

FIG. 10. Theoretical energy dependence of the H^3+He^3 cross section for $L=0$.

emerged isotropically with respect to the beam. The result is shown in Fig. 9. The effective target thickness in kev and the number of tritium atoms per cm^2 were measured by analysis of the geometric peak at the threshold of the $H^3(p,n)He^3$ reaction. The target used was 8 ± 1 kev thick for 1-Mev protons and was found to have $8\pm1\times10^{16}$ tritium atoms per cm^2. Although the incident He^3 beam passed through small collimating apertures which helped to define its position on the target, there remained some uncertainty in the solid angle subtended by the crystal counter due to uncertainty in the exact position of the beam. The uncertainty in the cross section measured is estimated to be ±20 percent. Target thickness corrections were made at each value of the bombarding energy using the data of Warshaw.[8] The target thickness did not exceed 20 kev throughout the range of bombarding energies used.

Coulomb penetrability curves for the *s*-wave and *p*-wave cases have been calculated using the tables of Bloch, Hull, Broyles, Bouricius, Freeman, and Breit,[9] for various values of the interaction radius. The results are plotted without statistical factor in Figs. 10 and 11. Comparison of the shape of the experimental curve of Fig. 9 to the theoretical curves of Figs. 10 and 11 indicates no pronounced resonance behavior and seems to indicate a behavior similar to that of the *d-d* reactions.

[8] S. D. Warshaw, Phys. Rev. **76**, 1759 (1949).
[9] Bloch, Hull, Broyles, Bouricius, Freeman, and Breit, Revs. Modern Phys. **23**, 147 (1951).

SUMMARY

The value of 0.95 ± 0.07 Mev for the energy of breakup of He^6 into a proton and an α-particle is in close agreement with the value of 1.00 ± 0.1 Mev assumed by Ajzenberg and Lauritsen.[10] Their value was derived from analyses of neutron scattering on He^4,[11–13] and from experiments on the reaction $He^4(d,p)He^5$.[14]

The isotropy of the deuterons from reaction (1) does not rule out a mixture of *s*-wave and *p*-wave interactions because the *p*-wave part of the interactions could proceed through a $J=0$ level in Li^6. The constancy of the relative intensities of reactions (1), (2), and (3) with bombarding energy does not rule out a similar mixture since all three reactions may proceed through the same set of entrance channels.

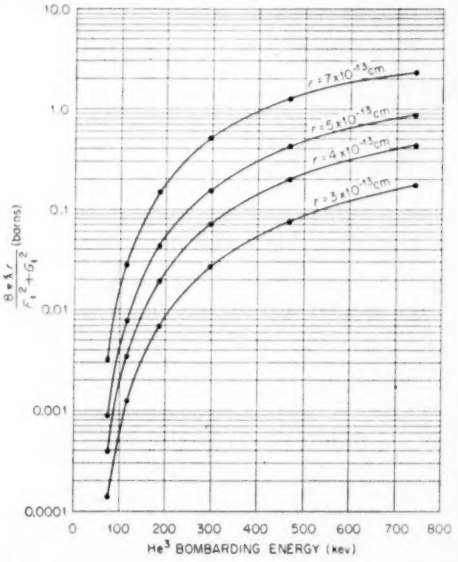

FIG. 11. Theoretical energy dependence of the H^3+He^3 cross section for $L=1$.

The author wishes to thank Dr. W. M. Good for his help and advice in performing the experiments. The author is indebted to Dr. M. E. Rose for discussions concerning the problem of three-body breakup, to Dr. A. Simon for discussions of the angular distribution problem, to Dr. H. B. Willard and the 6-Mev Van de Graaff group for the thin target calibrations, and to Dr. H. E. Banta of Instrument Division at Oak Ridge National Laboratory for the preparation of the tritium targets.

[10] F. Ajzenberg and T. Lauritsen, Revs. Modern Phys. **24**, 321 (1952).
[11] Bashkin, Mooring, and Petree, Phys. Rev. **82**, 378 (1951).
[12] R. K. Adair, Phys. Rev. **86**, 155 (1952).
[13] P. Huber and E. Baldinger, Helv. Phys. Acta **25**, 435 (1952).
[14] Burge, Burrows, Gibson, and Rotblat, Proc. Roy. Soc. (London) **A210**, 534 (1951).

The Neutron Spectrum from the $O^{18}(d,n)F^{19}$ Reaction*†

ROBERT L. SEALE‡
Physics Department, University of Texas, Austin, Texas
(Received July 1, 1953)

The neutron spectrum from the $O^{18}(d,n)F^{19}$ reaction has been investigated. $BaCO_3$ targets enriched in O^{18} were bombarded with 2-Mev deuterons and the emitted neutrons were detected using 100- and 200-micron Ilford nuclear plates. The method of analyzing the data is discussed in detail. The results of the experiment indicates the presence of 4 excited levels in the F^{19} which had not been previously reported. These levels are at 0.9 Mev, 2.2 Mev, 5.2 Mev, and 5.5 Mev.

INTRODUCTION

AN investigation of the excited states in the F^{19} nucleus has been made using the $O^{18}(d,n)F^{19}$ reaction. The Q value for the reaction as calculated from the atomic mass values is 5.73 ± 0.05 Mev.

Several investigations of excited levels in F^{19} have been made; none, however, with this reaction. A summary of these previous studies is given by Ajzenberg and Lauritsen.[1]

EXPERIMENTAL TECHNIQUE

O^{18} is a relatively rare isotope (0.20 percent) of oxygen, making the investigation of this reaction quite difficult under ordinary conditions. However, a sample of CO_2 enriched in O^{18} to 14 atom percent was obtained from the Temple University Research Foundation, Philadelphia, Pennsylvania. $BaCO_3$ was prepared using the O^{18} enriched CO_2. The concentration of O^{18} in the $BaCO_3$ produced was 9.3 atom percent.

It was decided that a solid target be used. Targets were prepared by painting a suspension of the $BaCO_3$ in distilled water on silver disks and allowing the water to evaporate. Uniform targets 100 kev thick could be prepared using this method.

A preliminary exposure of an O^{18}-enriched target was made on the Carnegie Institution of Washington Van de Graaff machine. The target used was 300 kev thick. The thickness of the target was estimated by extrapolating the data in Livingston and Bethe.[2] An exposure of 280 000 microcoulombs of atomic deuterons of 2-Mev energy was made with packs of nuclear plates placed at 0° and 90° with respect to the incident deuteron beam. These plates were processed and scanned in the conventional manner. An analysis of the results showed that the neutron spectrum was quite complex and that the neutron groups due to the different levels in the F^{19} nucleus overlapped considerably. There were on the average five usable tracks in each field of view suggesting that the bombardment could be readily decreased.

With these results in mind a second exposure was made on the University of Texas Van de Graaff machine as soon as it was in operation. In this exposure the bombardment was reduced to 108 000 microcoulombs of (2 ± 0.04) Mev deuterons and the target used was only 100 kev thick. Nuclear plates were placed in several positions about the target relative to the incident beam. Plates exposed at 0° and 20° were scanned.

ANALYSIS OF DATA

The results were thus obtained in the form of a plot of number of recoil protons *versus* range. However, the distribution of neutrons emitted from the target *versus* neutron energy was desired. A neutron energy interval of 100 kev was selected for the energy distribution plot. To express these energy increments in terms of observed recoil proton lengths the following conversion was made:

(1) The recoil proton energy corresponding to a given neutron energy is given by

$$E_p = E_n\langle\cos^2\theta\rangle_{Av},$$

where θ is the angle between the path of the incident neutron and the path of the recoil proton. The value of θ for tracks read is a function of the size of the source and the acceptance criteria for recoil tracks. The average value of $\cos^2\theta$ was calculated for the geometry of the system used.[3]

(2) Using the range-energy curve for protons in Ilford C-2 emulsion[4] the proton energies calculated above were converted to track lengths.

(3) The track lengths read in the procedure used were the projections of the track lengths on the long axis of the plate. The plates were arranged in the exposure so that their long axes were coplanar with the incident deuteron beam. The observed track lengths are given by

$$L_{obs} = L_{true}\langle\cos\theta'\rangle_{Av},$$

* Part of a dissertation presented to the Faculty of the Graduate School of the University of Texas as a partial fulfillment of the requirements for the degree of Doctor of Philosophy.

† Assisted by the U. S. Atomic Energy Commission.

‡ Now at Consolidated Vultee Aircraft Corporation, Fort Worth, Texas.

[1] F. Ajzenberg and T. Lauritsen, Revs. Modern Phys. **24**, 321 (1952).

[2] M. S. Livingston and H. A. Bethe, Revs. Modern Phys. **9**, 261–286 (1951).

[3] J. C. Allred and A. H. Armstrong, *Laboratory Handbook of Nuclear Spectroscopy* (Los Alamos Scientific Laboratory of the University of California, 1951) (unpublished).

[4] Lattes, Fowler, and Cuer, Proc. Phys. Soc. (London) **59**, 883 (1947).

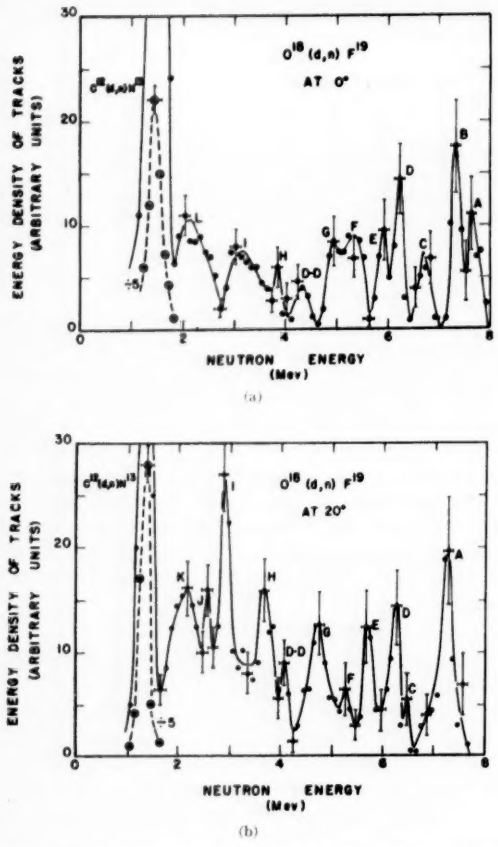

FIG. 1. The energy density of tracks *versus* neutron energy is shown (a) at 0° and (b) at 20° for the bombardment of O^{18} with 2-Mev deuterons.

where $\langle\cos\theta'\rangle_{Av}$ is the average value $\cos\theta'$, θ' being a function of the track acceptance criteria.

By using the scheme outlined, neutron energy increments could be converted to the corresponding observed track lengths. The neutron energy increments were then marked off on the number of recoil proton *versus* observed track length histogram. The tracks falling within a given 100-kev energy interval were counted and plotted as an ordinate at the center of the interval, the abscissas still linear in track length. A smooth curve was then drawn through these points. The area under this curve within each energy interval was taken as a measure of the energy density of tracks in that interval. The energy densities of tracks thus obtained were then plotted as ordinates against a linear energy scale after the corrections for the variations of the *n-p* cross section with energy and for the thickness of the emulsion were applied.

The results of a plot of energy density of tracks *versus* energy at 0° and 20° are shown in Fig. 1.

The probable error in the energy density of tracks was taken as the normalized square root of the energy density of track. Again the *n-p* cross section and emulsion thickness corrections were applied.

The energies assigned to the groups shown in Fig. 1 were obtained by making an integral plot of track density *versus* energy of each group and "extrapolating" the steepest tangent on the curve after the method of Livingston and Bethe.[2]

A neutron group from the dueteron on deuteron reaction was observed. This group is probably due to the surface absorption of deuterons from the gas in the vacuum system by the target.

The energies of neutron groups from the transitions to the ground state of the $O^{18}(d,n)F^{19}$, the $C^{12}(d,n)N^{13}$, and the $H^2(d,n)He^3$ reactions as determined from the data shown and from the calculated Q values check with one another within the limits of experimental error. This serves as a check on the absolute energy of each of the groups.

TABLE I. Experimental determination of energy levels of F^{19}.

Group	Extrapolated group energy[a] (Mev) At 0°	At 20°	Q-value of group[a] (Mev) At 0°	At 20°	Energy of excited levels[a] (Mev) At 0°	At 20°	Av	Known levels[b]
A	7.7	7.6	5.7	5.7	0.0	0.0	0.0	0.0
B	7.5	···	5.5	···	0.2	···	0.2	0.19
C	6.9	6.6	4.9	4.7	0.8	1.0	0.9	···
D	6.3	6.1	4.3	4.3	1.4	1.4	1.4	1.37
E	6.0	5.9	4.0	4.0	1.6	1.6	1.6	1.59
F	5.5	5.4	3.5	3.5	2.2	2.2	2.2	···
G	4.9	4.9	2.9	3.0	2.8	2.7	2.75	2.82
H	3.8	3.8	1.8	1.9	3.9	3.8	3.85	3.94
I	3.2	3.1	1.2	1.2	4.5	4.5	4.5	4.48
J	···	2.9	···	0.9	···	4.8	4.8	4.76
K	···	2.5	···	0.5	···	5.2	5.2	···
L	2.2	···	0.2	···	5.5	···	5.5	···

[a] All values ±0.1 Mev.
[b] See reference 1.

The energies assigned to the excited levels of F^{19} as well as the excitation energies for known levels in F^{19} are summarized in Table I.

At excitation energies above 4 Mev the levels become closely spaced and resolution of the individual groups becomes very difficult. However, there are a few definite peaks which appear superimposed on a rather heavy background.

Four additional levels in F^{19} are indicated. These are at 0.9±0.1 Mev, 2.2±0.1 Mev, 5.2±0.1 Mev, and 5.5±0.1 Mev.

A normal $BaCO_3$ target was also bombarded and scanned as a check against the possibility of assigning a spurious group to the F^{19} spectrum.

The author wishes to express his appreciation to Dr. E. L. Hudspeth for many helpful suggestions throughout the course of this work, to Dr. N. P. Heydenberg of the Carnegie Institution, Department of Terrestrial Magnetism, Washington, D. C., for making the preliminary exposures, and to acknowledge the assistance of the entire Van de Graaff group of the University of Texas.

PHYSICAL REVIEW VOLUME 92, NUMBER 2 OCTOBER 15, 1953

The Production of Protons from Carbon by Monoenergetic Gamma Rays*

JOHN W. WEIL† AND BOYCE D. MCDANIEL
Cornell University, Ithaca, New York

(Received July 14, 1953)

A technique is described for selecting from the interactions produced by a bremsstrahlung spectrum only those arising from essentially monoenergetic quanta. These interactions are selected by requiring a coincidence with the degraded electron which produced the interacting quanta.

A study of the photoproduction of protons from carbon was made using 190-Mev monochromatic quanta from the 310-Mev Cornell synchrotron. An energy distribution of the emitted protons was observed at 60 degrees and an angular distribution of 70-Mev protons was also obtained. Interpretation of these results in terms of a deuteron model gives satisfactory agreement and indicates that the photoproduction process involves only a few nucleons on the average and probably involves just two nucleons a large fraction of the time. Rough quantitative agreement is obtained with experiments on the photodisintegration of the deuteron.

INTRODUCTION

THE study of photoproton production from nuclei containing more than two nucleons is hampered by the fact that gamma-ray sources are not capable of producing line spectra at high energies. Because of this, and because of the many particles in the nucleus, the measurement of the energy and angle of the energent proton is not sufficient to determine the parameters of the photodisintegration process. Analysis of the results of conventional experiments must include an integration over the bremsstrahlung spectrum and direct physical interpretation becomes difficult.

Photoproduction of protons from carbon has been studied by a number of experimenters.[1-6] Of the light elements carbon has been chosen as a target material for a number of practical considerations including density and convenience of preparation. While the results of these experiments are in general agreement with each other, theoretical interpretation has not been particularly successful. Levinthal and Silverman[1] assumed that the process was essentially a photoelectric process with the entire nucleus taking up the recoil of the emitted proton. This calculation gave reasonable agreement with the low-energy region of their energy spectrum but did not explain the features of the spectrum which occurred in the high proton-energy region. Levinger[7] proposed a deuteron model in which the participating nucleons were only two in number. Rather poor agreement with experiment was obtained by this calculation, due in part to the use of the simple, low-energy (below 140 Mev) theoretical results for the photodisintegration of the deuteron. Because of the integration over the bremsstrahlung spectrum it was not easy to adjust the theory in the light of newer experimental results. Yoshida[8] has made a calculation of the photoproduction process using a model in which the number of particles available to take up the recoil is left as an adjustable constant. These results do not include any mesonic effects, and the absolute cross sections obtained are much too low at the energies under consideration. Some reasonable results for angular distributions of the photoprotons were obtained, but it is not possible to conclude that the calculation is either right or wrong from this evidence alone. Yoshida does not compute an energy distribution to be expected for the protons.

The simplification in interpretation that would result from the study of photoprotons produced by an essentially monochromatic source of quanta has recently led to an effort at this laboratory in the direction of achieving experimental situations in which results from gamma rays of a narrow energy interval could be obtained. Keck and Perry[5] have studied photoprotons from carbon using the conventional subtraction technique with various synchrotron energies. However, it was felt desirable to be able to perform the experiment using a different method in order to check the results obtained by this difference technique and in order to attempt to discover a more direct approach (and perhaps a less tedious approach) to the study of photoproduction processes using essentially monoenergetic quanta for the incident spectrum.

THE MONOCHROMATIC GAMMA-RAY PRINCIPLE

The technique for selecting individual monoenergetic gamma rays which has been used in this work was originally suggested independently by Koch at Illinois and by Camac at Cornell. Maximum energy electrons circulating in the donut of the synchrotron are allowed to spiral in and strike a thin target. Some of these electrons radiate in the target and emerge from the

* This work was supported in part by the U. S. Office of Naval Research and was submitted by John W. Weil to the Graduate School of Cornell University in partial fulfillment of the requirements for the degree of Doctor of Philosophy.

† U. S. Atomic Energy Commission Predoctoral Fellow. Present address: Knolls Atomic Power Laboratory, General Electric Company, Schenectady, New York.

[1] C. Levinthal and A. Silverman, Phys. Rev. **82**, 822 (1951).
[2] J. C. Keck, Phys. Rev. **85**, 410 (1952).
[3] J. W. Rosengren and J. M. Dudley, University of California Radiation Laboratory Report UCRL-1913, revised (unpublished).
[4] Wattenberg, Feld, and Godbole, Phys. Rev. **90**, 380 (1953).
[5] J. C. Keck and A. M. Perry (private communication); also Phys. Rev. **86**, 629 (1952).
[6] D. Walker, Phys. Rev. **81**, 634 (1951).
[7] J. S. Levinger, Phys. Rev. **84**, 43 (1951).
[8] S. Yoshida, Prog. Theoret. Phys. **6**, 1032 (1951).

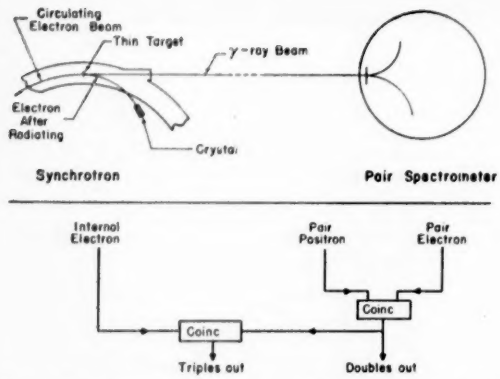

FIG. 1. Experimental arrangement for the measurement of the resolution of the monochromatic gamma-ray line.

target correspondingly degraded in energy. Because of the high energies involved the degraded electrons will emerge from the target essentially in the forward direction. Furthermore, although a nuclear field must take part in the bremsstrahlung process, it does not carry off an appreciable amount of energy because of its large mass. As a result, the sum of the energy of the degraded electron and the energy of the emitted quantum is, to a good approximation, equal to the energy of the incident electron. Multiple interactions in the synchrotron target can be avoided by use of a sufficiently thin target.

The electrons emerging from the target after interaction are analyzed by the guide field of the synchrotron, electrons of different energies being physically separated. By placing a detector in the path of certain of these electrons it is possible to detect the creation of quanta of an energy corresponding to the energy of the circulating beam minus the energy of the detected electrons. By using this detector to gate apparatus which is examining effects produced by the x-ray beam, results due to essentially monochromatic gamma rays may be obtained.

THE INTERNAL ELECTRON DETECTOR

In order to obtain gamma rays of as high an energy as possible it is desirable to detect electrons of the lowest possible energy. This would necessitate placing an electron detector inside the synchrotron donut. For a variety of technical reasons having to do with convenience in handling and with assurance of continued synchrotron operation, this step was deemed inadvisable, and the electron detector was located outside of the donut. To avoid loss of efficiency due to vertical defocusing of the electrons by the fringe magnetic field, the detector was placed directly against the wall of the donut. Finally, the dual considerations of available space and of having sufficient electron energy to penetrate two centimeters of glass donut wall without excessive scattering dictated placing the detector in such a position that it would receive electrons of about 100 Mev when the synchrotron operated at full 310-Mev excitation. The corresponding monochromatic gamma-ray beam had an energy of roughly 200 Mev.

The electron detector was constructed by using a stilbene scintillation crystal mounted on a $2\frac{1}{4}$-inch diameter Lucite light-pipe and a 5819 photomultiplier. To remove the photomultiplier from the fringe field of the magnet, the Lucite light-pipe was required to be about three feet long and additional magnetic shielding was needed around the tube. Care was taken to provide the 5819 with a low-resistance bleeder to avoid variations of tube voltages at high counting rates. Two stilbene crystals, each 4 cm in diameter, were provided. The length of one of these was 2 cm while the other measured 4 cm. Either crystal could be used. When in position the crystal was oriented with the electrons entering along a diameter so that the longer crystal would intercept a larger band of electron energies.

To test the operation of the scheme and the quality of the resolution, the Cornell pair spectrometer[9] was used in the manner described earlier.[10] The spectrometer was located in the beam and a thin (10-mil) Cu foil was used as a radiator. The synchrotron target consisted of a 12-mil Ni foil. Figure 1 shows the geometry and the circuit arrangement which was employed. Pulses from the central channel of the pair spectrometer were counted in coincidence with pulses from the internal electron detector, hereafter referred to as the pit counter. This coincidence rate was then observed as the magnetic field of the pair spectrometer was varied. The known energy calibration of the pair spectrometer allowed this coincidence counting rate to be converted into a measured gamma-ray spectrum.

To minimize random coincidences the synchrotron beam was spread over about three milliseconds in time by shaping the rf envelope. Even then the resolution of the electronics was sufficiently slow (about one microsecond) to necessitate running the synchrotron at a very low beam of less than 10^6 effective quanta per minute. Maximum counting rates were a few per minute.

Results of these energy resolution measurements are given in Fig. 2. The results shown include the resolution of the pair spectrometer which is approximately triangular with a 10 percent full width at half-maximum. In order to be able to estimate the true gamma-ray spectrum, a theoretical synthesis of the line shape was attempted. The results are shown in Fig. 3. One theoretical curve, $J(E)$, represents the spectrum as it would be seen by the pair spectrometer and is a reasonable fit to the experimental data. The other curve, $S(E)$, is the gamma-ray spectrum with the effects of the resolution of the pair spectrometer not included and has been assumed to represent the true gamma-ray spectrum for later theoretical work. Both the data presented here and the theoretical curves are for the 4

[9] DeWire, Ashkin, and Beach, Phys. Rev. **83**, 505 (1951).
[10] J. W. Weil and B. D. McDaniel, Phys. Rev. **86**, 582 (1952).

cm crystal which was used in all following work in order to obtain the higher counting rate which results.

FAST COINCIDENCE CONSIDERATIONS

Keck's data for photoproduction of protons indicated that for a reasonable solid angle subtended by the proton detector and for about a 20-Mev detection interval, more than 10^6 effective quanta were required to produce one proton. If roughly one-tenth of these protons is produced by quanta lying in the energy band detected by the monochromatic gamma-ray scheme, then a beam of over 10^7 Q per minute is required for a counting rate of one per minute with one hundred percent efficiency in all detectors.

It can be shown that, independent of the spectral efficiency of the pit detector, the chance-to-true or real-to-random ratio in the counting circuits will be given approximately by

$$\frac{1}{2KT\ln(E_0/E_1)},$$

where T is the resolution of the coincidence circuits; K is the instantaneous beam intensity in effective quanta per second; and E_0 and E_1 are, respectively, the maximum bremsstrahlung beam energy and the effective low-energy cutoff of the external counter. Because of the duty cycle of the Cornell synchrotron of about 1/15 for a three-millisecond beam and because of the 30-cycle repetition rate, the instantaneous intensity must be multiplied by a factor of about four to obtain the number of effective quanta per minute. In an experiment of the type currently performed on synchrotrons the factor due to the spectral sensitivity of the external detector will not give more than a factor of two in real-to-random ratio. Thus, in order to obtain the necessary beams of about 10^8 effective quanta per minute, coincidence resolving times of the order of 4×10^{-9} second are needed.

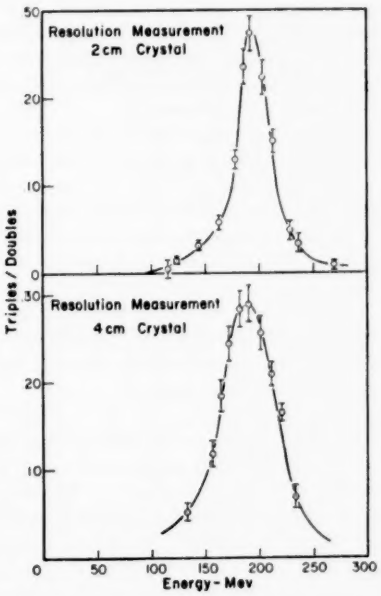

FIG. 2. Line shape of the monochromatic gamma ray as observed with the pair spectrometer. Curves are given for two crystals which intercept different fractions of the internal electron spectrum. The 4 cm crystal was used in the photoproton experiments.

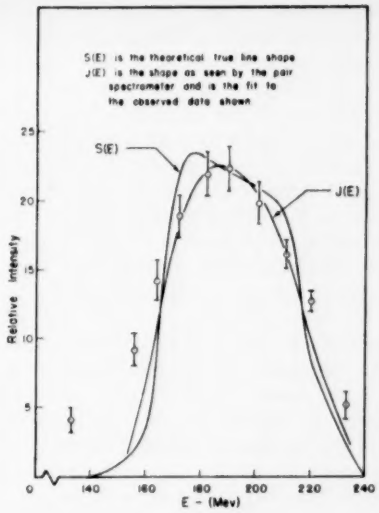
S(E) is the theoretical true line shape
J(E) is the shape as seen by the pair spectrometer and is the fit to the observed data shown
S(E)
J(E)
Relative Intensity
E - (Mev)

FIG. 3. Theoretical resolution for the monochromatic gamma-ray technique.

The coincidence circuit first constructed was of the Bell and Jordon type in which the incoming negative signal is used to cut off a pentode, the pentode plate signal being clipped by a shorted stub and mixed with a similar signal from the other input. A diode discriminator, followed by suitable amplification and further discrimination, then examines the pulses from the pentode plates. Coincidence pulses, being the sum of identical signals from the two input tubes, are twice the height of the singles pulses and may be distinguished accordingly. This type of circuit proved to work quite nicely at short resolving times, but was found to have two important difficulties. Primarily, the input grids are normally biased at their point of maximum sensitivity with the result that if they are connected to a source of signals which contains a very large amount of small-amplitude, spurious signal (such as the pit counter), the pentode is continually being cut off by this background. The resulting singles rate is much higher than the true singles rate due to the electrons of interest, and the random rate is correspondingly much too high. Secondly, the two-to-one ratio of coincidence-pulse amplitude to singles-pulse amplitude was poor in that the discriminator time constant would stretch the singles pulses, so that at high input rates singles

feed-through would appear. It was thus desirable to find a coincidence circuit which could be biased off to avoid seeing the spurious background from the pit counter and which would not feed through.

The requirements for a satisfactory coincidence circuit for this application are quite different from those for situations usually published in the literature. Not only must the circuit be able to distinguish the relative times of arrival of input pulses to a few times 10^{-9} second or better, but it must be able to do so at a very high rate (many times per microsecond). Some of the coincidence circuits available, while able to distinguish relative times of arrival to a fraction of a millimicrosecond, must take about a microsecond to do so and would thus be useless at very high counting rates.

The circuit finally adopted for use was of the 6BN6 type similar to that of Fischer and Marshall[11] (see Fig. 4). Here the input grids may be biased off and are thus insensitive to small-amplitude noise. In addition the ratio of the amplitudes of coincidence pulses to singles pulses is much larger with the result that for properly biased tubes with properly limited input pulses singles feed-through is entirely absent.

For correct operation of such a 6BN6 circuit, the input pulses should be over 6 volts. To get pulses of this magnitude it was found necessary to amplify the input pulses since the newer, high-gain photomultipliers were not yet available and since pulsed operation of the present photomultipliers was not practical for a three millisecond counting span. 200-ohm distributed amplifiers were used which would deliver 8 volts positive to an unterminated output. Above this point the amplifiers are badly nonlinear and thus provide a poor sort of limiting which is effective if the input pulses do not vary too drastically in amplitude. Since the pulses from the pit counter were all roughly the same height, this limiting was satisfactory for use there, where the high rate would have precluded the use of any more normal form of limiting.

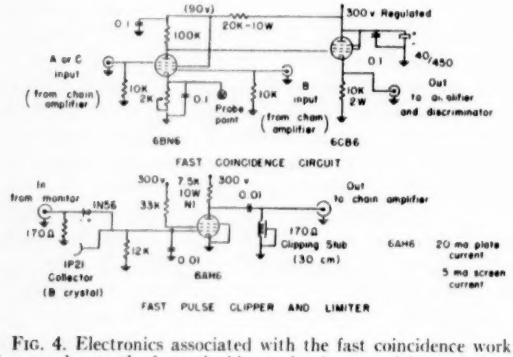

FIG. 4. Electronics associated with the fast coincidence work. Input pulses to the fast coincidence circuit are positive and about 8 volts in amplitude.

[11] J. Fischer and J. Marshall, Rev. Sci. Instr. **23**, 417 (1952).

In all the work to be described two complete coincidence circuits were used, with one serving as a delayed or random channel. The coincidence tubes were so arranged that the signal from the external counter could be applied directly to the appropriate grid of both 6BN6's simultaneously. Since this pulse was in general faster than the pulse from the pit counter, the slight additional capacitive loading did not prove to be a limitation on the resolving time. The pulses from the pit counter required amplification through two chain amplifiers in series. The output of the first of these amplifiers was split in a constant-impedance network and each of the two output signals was fed to a separate chain amplifier for the remaining amplification. Each of these amplifiers then drove a single grid in one of the 6BN6 coincidence tubes. It was possible to insert different lengths of delay cable in the two parallel pit inputs in order to set up either channel as a random channel. By varying the delay in the external counter side, both channels could be moved together.

Output pulses from the 6BN6's were stretched to one microsecond in the plate circuit of the 6BN6, amplified by 501 amplifiers, and then discriminated suitably. The use of "slow" amplifiers is found to be important here because the coincidence pulse amplitude is not much larger than the amplitude of the capacitive, singles feed-through pulses, although, because they are conductive in nature, the total area under them is much larger than the area under the feed-through pulses. Hence an amplifier which integrates over a time long compared to the capacitive feed-through-pulse duration is necessary.

The characteristics of the 6BN6 are useful in another fashion. While there is considerable capacitive coupling between the third (quadrature) grid and the plate, the capacitance between the first grid and the plate is negligibly small. Thus the high-counting-rate source (the pit counter) can be connected to the first grid to avoid capacitive pulse pile-up in the integrating amplifiers which follow. The low counting-rate input is connected to the third grid. Very large pulses on the third grid can sometimes feed through capacitively and be recorded. It has been found necessary to provide effective limiting action on this signal input. A 6AH6 clipper-limiter, as shown in Fig. 4, has been used very successfully. No trouble with feed-through was ever experienced with this arrangement.

A resolving time of about 4 to 5×10^{-9} second was used throughout. Because the input pulses were not square but bell-shaped due to the chain amplifiers, the resolving time was to some extent a function of the gain and of the discrimination following the 6BN6. Thus, the use of a random channel was imperative. The length of cable used in forming the delay channel relative to the true channel was 560 cm, corresponding to the time of one revolution around the synchrotron of the electrons in the circulating beam. This length of cable was used to avoid false random rates in the

event that the beam from the synchrotron was bunched as it traveled around the machine just before hitting the target. In the stable orbit the beam is sharply bunched, but as it spirals in and is lost from the synchronous rf cycle this bunching would be expected to decrease. A measurement was made of the variation of random rate as a function of delay cable used, using signals from the pit counter and from an external detector situated directly in the beam. A ten percent variation of accidental rate as a function of delay was observed, even when the beam was spread to a full three milliseconds. Thus, to avoid false measurements in the random channel a delay equal to one rf cycle was always used.

As a preliminary exercise in the handling of both the monochromatic gamma-ray technique and the fast coincidence apparatus, a measurement was made of the velocity of 190-Mev light quanta.[12] A value for the velocity was obtained of $(2.974\pm0.03)\times10^{10}$ cm/sec.

In the study of photoprotons the fast coincidence circuit was used to record the simultaneous arrival of electrons in the pit counter and protons in the external detector. The identification of a proton required three counters forming a telescope, so that the fast coincidence indicated only the occurrence of a monochromatic gamma ray and some event in the telescope which could produce a sufficiently large pulse in the individual crystal which provided the fast external output. The fast output could have been taken from either of the two counters in the proton telescope which were counted in slow coincidence with each other. In practice it was found that the use of the rear of the two coincidence crystals cut down the counting rate in the external detector input to the fast circuit and thus decreased the random coincidence rate. Pulses from the second crystal were taken off the collector for the fast coincidence and off the last dynode for the slow coincidence circuitry which was used to detect the protons. Because very large pulses could occur in this crystal, the fast clipper-limiter described earlier was used in this fast coincidence output. At no time did the counting rate in this crystal come near saturating the clipping tube.

It was found during the initial runs on the photoproduction of protons from carbon that it was not possible to reproduce the data to a sufficient accuracy, and analysis of the data indicated a drifting efficiency in the fast coincidence circuitry. With a choice of either attempting to find the instability or monitoring the fast coincidence efficiency in some fashion, the latter was chosen as providing a more certain solution to the problem.

A fast monitor would also have another advantage in the present experiment. This fast monitor could be calibrated in terms of absolute intensity in the monochromatic gamma-ray beam and would allow absolute measurements to be made directly.

[12] D. Luckey and J. W. Weil, Phys. Rev. **85**, 1060 (1952).

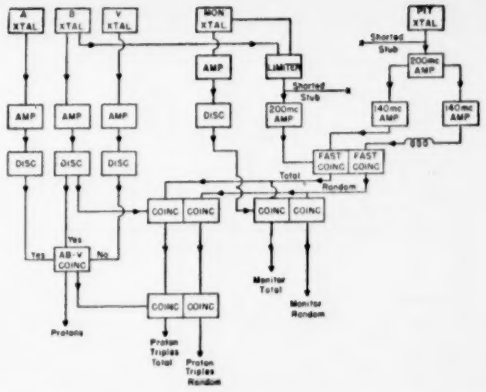

FIG. 5. Complete block diagram of the electronics. Each fast coincidence circuit indicated is actually a coincidence circuit (Fig. 4) followed by an amplifier and a discriminator. All six discriminators have provision for being gated by the floating trigger from the synchrotron, so that they are sensitive only during the period surrounding the beam pulse.

To provide such a monitor a separate, fixed, stilbene crystal is allowed to observe an independent graphite target situated in the beam. The signal from the 1P21 photomultiplier associated with this crystal is mixed, through a short terminated cable and a 1N56 diode, with the signal on the grid of the clipping tube which comes from the second crystal in the proton telescope. This is indicated in Fig. 4. These pulses go through the fast coincidence circuitry in exactly the same manner as the pulses from the proton-detection crystal itself. After detection in the fast coincidence circuit the resulting coincidence pulses (now about one microsecond long) are sent to a sorting circuit consisting of a number of coincidence tubes. If the fast coincidence signal arrives at the same time as a pulse from the slow output of the second proton-detection crystal, it is sorted out as a coincidence having to do with proton detection. If the fast coincidence arrives in time with a pulse from the slow output of the monitor crystal, it is sorted out as a monitor coincidence. The net monitor count should be a steady counting rate independent of anything done to the proton telescope or to the proton target. Variation in the net fast monitor counting rate should then be the result of either variation in the beam intensity or variation in the fast coincidence efficiency. The only changes in the fast coincidence circuitry not followed by the monitor would be those in the second proton-detection crystal itself. Since all phototubes were operated off the same high-voltage supply, these remaining variations should be cancelled out to first order.

Some idea of this monitor technique can be obtained from Fig. 5 which shows a block diagram of the complete circuitry. In addition to the outputs shown the monitor circuit was provided with a slow output for recording monitor singles.

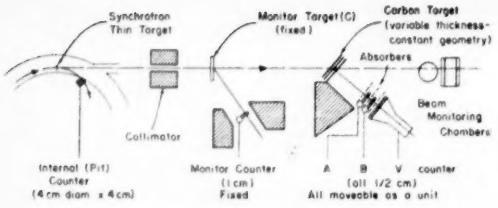

FIG. 6. Schematic of the experimental geometry. All crystals are stilbene.

An absolute calibration of the monochromatic beam intensity was obtained by placing the three-crystal telescope used in the proton work directly in the beam. The front crystal was used as a veto counter while the rear two were counted in coincidence. All three crystals were set to have high efficiency for counting individual electrons of minimum ionization. A curve was then taken of counting rate as a function of Pb converter placed between the front two crystals. The slope of this curve provides an absolute calibration of the beam in terms of the known interaction cross section for gamma rays of this energy in Pb as measured by DeWire, Ashkin, and Beach.[9] All this was done without disturbing the monitor counter so that the monitor counting rate (singles) could be calibrated directly in terms of monochromatic beam intensity. Because the monitor crystal was not located in the beam, a number of intermediate monitors had to be used because of the very low-beam intensity at which this measurement was necessarily made. The very low intensity also avoided any possible corrections due to random coincidences. A straight line was observed as a function of thickness of Pb and the resulting calibration is estimated to be good to about seven percent.

It is possible to use this calibrated monochromatic gamma-ray beam for measurements of the efficiency of various detectors for quanta of this energy. Some work of this nature has been done by A. Silverman and B. D. McDaniel and has been referred to by Cocconi and Silverman.[13]

PHOTOPROTONS FROM CARBON

The telescope used in observation of the photoproduction of protons contained three scintillation counters. The first two were stilbene crystals 0.5 $\times$3.5$\times$5.0 cm mounted on 1P21 photomultipliers. The third counter was a large anticoincidence counter made up of a 5819 receiving light from a mosaic of four crystals similar to those in the first two counters. The effective area of this veto counter was 7$\times$10 cm. This counter was found to have very good sensitivity and resolution over its entire area.

The first two counters, A and B, were counted in coincidence with each other and in anticoincidence with the third, V, counter. The resulting AB-V signal was used in the conventional manner to select protons of a given energy by measuring the specific ionization of particles with a fixed residual range. Copper absorbers were used to vary the telescope settings. In making the various preliminary settings on the telescope care was taken to insure that the effective biases in all counters were set in the slow electronics rather than in the more unstable and less precise fast-coincidence circuitry.

In practice it was found necessary to use a geometry in which the telescope subtended a rather large solid angle at the target. Reduction of this solid angle was not possible because of the low counting rates which resulted. Hence the angular resolution used was rather poor, about $\pm$15 degrees. In order to be able to line up the apparatus easily, slab targets were used where possible. These were set perpendicular to the axis of the telescope. However, because of the rather wide variation of target thicknesses encountered (from 0.75 cm to 2.50 cm) the geometry of the experiment would have had to be calibrated for each target thickness. To avoid this, variable-density, constant-geometry targets were constructed.

For the angular distribution measurements a cylindrical target 2.5 cm in diameter was used, placed with its axis perpendicular to both the beam direction and the telescope axis. This target necessitated careful alignment of the beam in order to prevent changes in the effective spectrum of protons during observation at various angles.

The geometry of the entire arrangement as it was used for the energy spectrum measurements at 60 degrees is shown in Fig. 6. The beam from the synchrotron target is collimated by a one-inch Pb collimator and then strikes the auxiliary graphite target used for the monitor. This target was roughly 0.5 inch thick. The beam then strikes the target used for the production of protons and passes through into several auxiliary monitoring chambers. Both the monitor crystal and the proton telescope were surrounded by Pb shielding to protect them from stray background and to prevent them from seeing the incorrect target.

In addition to the fast coincidence connections mentioned earlier, all crystals except the pit counter had "slow" outputs which were connected through amplifiers to discriminators. The outputs of the A, B, and V discriminators were used to provide an AB-V signal indicating the arrival of a proton. This signal was then mixed with the appropriate fast coincidence signal to give the proton triples signal which indicated the production of a proton by a monochromatic gamma ray. The full block diagram of the electronics is given in Fig. 5.

Because of the complexity of the apparatus and because of the low real-to-random ratio in the fast circuit it was found necessary to keep continuous check on the functioning of the electronics. The two fast coincidence circuits which provided the real and random

[13] G. Cocconi and A. Silverman, Phys. Rev. **88**, 1230 (1952).

coincidence counting rates had their functions interchanged at regular intervals by removing the extra delay cable from the random side and placing it into what had been the real side. In addition, all data for the energy distribution of the photoprotons was taken in pairs of points, with the telescope settings for two adjoining energies being identical except for the insertion or removal of additional Cu absorber from in front of the entire telescope. In both of these ways checks on the internal consistancy of the data were available.

A typical single run on any point would take about one hour with from 40 to 120 real triples being recorded and with roughly one-quarter to one-third as many being recorded in the random channel.

Throughout the experiment calibration runs with delay cables in both fast coincidence circuits were taken to determine the relative widths of the two channels. This information was then used to correct the data taken in regular runs for any disparity in channel widths.

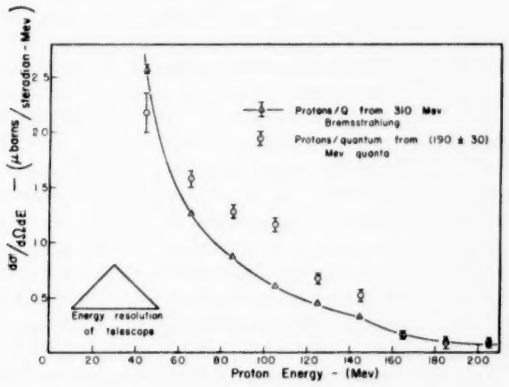
dσ/dΩdE — (μ barns / steradian - Mev)
Protons/Q from 310 Mev Bremsstrahlung
Protons/quantum from (190 ± 30) Mev quanta
Energy resolution of telescope
Proton Energy - (Mev)

FIG. 7. Proton energy distributions from carbon at 60±15 degrees.

All data were corrected for random counts and for nuclear absorption in the telescope. Absolute calibration of the monochromatic beam intensity was made in the manner described above. The absolute calibration of the intensity of the full bremsstrahlung beam was made using the standard Cornell ionization chambers.

RESULTS AND INTERPRETATION

The results obtained from the energy spectrum measurements are given in Figs. 7 and 8. On each graph the results from both the full bremsstrahlung beam and the monochromatic gamma ray are given for purposes of comparison. The indicated errors are standard deviations due to counting statistics and indicate the relative error in the position of the points. In addition, from the absolute calibration, there is an uncertainty of seven percent in the numbers used and a rough uncertainty of perhaps 20 percent because of possible errors in the estimate of solid angle of the target

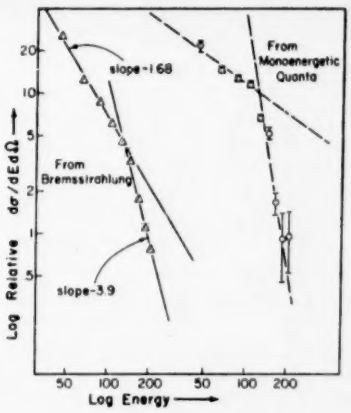

FIG. 8. Proton energy distributions from carbon at 60±15 degrees. This is a log-log plot of the data given in Fig. 7.

subtended at the telescope. The net absolute error of the cross sections is estimated to be about 25 percent.

From the linear plot of the data it can be seen that the two energy distributions obtained at 60 degrees for the two kinds of incident gamma-ray spectra are not the same, there being more protons at intermediate energies in the case of the monochromatic incident spectrum. The log-log plot shows the more conventional features of such spectra. In agreement with previous workers the proton distribution from incident 310-Mev bremsstrahlung is seen to fall essentially on two straight lines. The slope of the low-energy line is found to be -1.68 in good agreement with the -1.7 found at 67 degrees by Keck,[2] by Rosengren and Dudley at 45 and 90 degrees,[3] and by Levinthal and Silverman at 90 degrees.[1] The upper part of the curve has a slope of -3.9 which agrees well with the results of Rosengren and Dudley and is not in serious disagreement with the data given by Keck. Levinthal and Silverman did not extend their measurements to these higher proton energies. In agreement with all these workers, the break in the spectrum appears to come at roughly half the maximum energy of the bremsstrahlung distribution. Recently Wattenberg, Feld, and Godbole[4] have reported results at 30 degrees in qualitative agreement with those given here but differing somewhat in the actual numerical values obtained.

The proton spectrum resulting from bombardment with monochromatic gamma rays also falls roughly on two straight lines with, however, different slopes from the bremsstrahlung case. The low-energy portion of the curve is flatter, and the high-energy portion falls off more rapidly. The break occurs somewhere in the vicinity of 100 or 110 Mev.

No attempt will be made to explain the bremsstrahlung-produced spectrum because of the interpretive difficulty mentioned earlier. Rather, an effort towards explaining the results from the monochromatic beam will be made in detail with the hope that any success

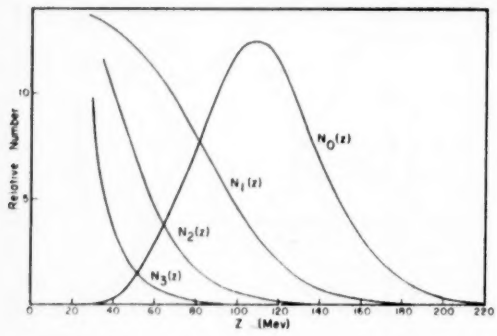

FIG. 9. Theoretical energy distributions of protons from disintegration of a pseudo-deuteron within the carbon nucleus, for various numbers of collisions during escape from the nucleus.

along this line may be extended to the bremsstrahlung results.

As has been noted by others, perhaps the most suggestive thing about the results of energy distribution measurements of protons from carbon has been the location of the break in the log-log plot. This feature would seem to indicate that the recoil from proton emission was being taken up by some light sub-unit of the nucleus. Specifically, if the deuteron photodisintegration were being studied at 60 degrees, a peaked spectrum centering at a little over 110 Mev would be expected for incident 200-Mev quanta. The fact that the break in the observed energy distribution comes just at this point has led to an attempt to construct the experimental results in terms of a two-particle model.

Three effects will modify the spectrum of protons observed in the laboratory from such a deuteron interaction in carbon. The motion of the individual nucleon at the time it is struck will smear out the line spectrum of protons otherwise expected from a deuteron disintegration. In addition, the motion of the center-of-mass of the pseudo-deuteron will smear out the proton energy spectrum observed at a fixed laboratory angle. It can be shown that the second of these two effects is much more important because of the heavier mass of the moving system, with the result that the motion of the individual nucleon will not appreciably affect our results and will be neglected in the following calculations. The third effect due to the motion of the nuclear particles is that this motion will shift the center-of-mass energy available to the reaction and will therefore affect the cross section somewhat. It will be assumed that the energy dependence of the cross section is sufficiently flat to be neglected. If the deuteron model is to be taken literally, some speculative support for this assumption can be obtained from the flat energy dependence of the deuteron photodisintegration cross section as measured at these energies.

The momentum distribution of the center-of-mass of the pseudo-deuteron can be obtained by a folding of the momentum distributions of the two participating nucleons. An individual nucleon is assumed to have a momentum distribution given by a Fermi distribution at zero temperature. While this is not strictly correct it should be pointed out that the 8-Mev temperature often used in the literature is not correct either in light of the model which is being considered. More important, however, is the fact that the calculations to follow are extremely insensitive to the detailed shape of the momentum distribution assumed, so long as the general shape and approximate relation of the various portions of the distribution are maintained. The resulting momentum distribution for the center-of-mass of the pseudo-deuteron is denoted by $P(p_d)$.

The spectrum of protons ejected from the pseudo-deuteron is then given by the expression

$$X(E_p)=\int_{E'} P(p_d)\frac{dp_d}{dE_p}S(E')dE',$$

where $X(E_p)$ is the spectrum of protons emerging at the angle of observation, E' is the incident gamma-ray energy, $S(E')$ is the spectrum of incident gamma-rays, and E_p is the observed proton energy. The gamma-ray spectrum which has been used in the present calculations is derived from the theoretical fit to the monochromatic gamma-ray spectrum measurements.

If this integral is carried out numerically a spectrum of protons from the pseudo-deuteron is obtained. A certain fraction of these protons will escape from the nucleus without making further collisions. The spectrum of these protons is called $N_0(E)$ and is shown in Fig. 9. The energy scale has its zero referred to the bottom of the well within the nucleus and is not yet the energy in the laboratory. This energy may be converted to the laboratory system by subtracting some average nucleon binding energy. This subtraction is to allow for the depth of the well minus some average energy of the individual nucleons within it and is a quantity not already taken into account in the above calculations involving the motion of the center of mass of the pseudo-deuteron. The amount to be subtracted is roughly 15 Mev.

In a manner adapted from Keck[14] it is possible to compute the energy spectrum of protons which are scattered on the way out of the nucleus. This is done by computing the escape probability of nucleons from a spherical nucleus using a collision cross section derived from the work of Goldhaber[15] and of Fernbach *et al.*[16] It is then assumed that protons of energy E which do make a collision are scattered with equal probability into any portion of the energy interval from 20 Mev to $E-10$ Mev. The exclusion of regions at both ends of the energy scale is the result of the use of a Fermi gas model. A correction factor is then added to the scattering

[14] J. C. Keck, Cornell University thesis, 1951 (unpublished).
[15] M. L. Goldhaber, Phys. Rev. **74**, 1269 (1948).
[16] Fernbach, Serber, and Taylor, Phys. Rev. **75**, 1352 (1949).

calculation to allow for the fact that a proton may collide with another proton thus giving rise to two protons emitted. This factor also includes the initial production of an equal number of neutrons which can then produce protons upon scattering. This factor is taken to be 2 for one collision, 4 for two collisions, and 8 for three collisions. Because all of the above scattering calculations are admittedly rough and because of the simplification involved, it is also assumed that there is no angular effect in the scattering, that is, that in-scattering into the solid angle of observation equals out-scattering.

With these approximations the relative magnitudes and shapes of the spectra of protons after one, two, and three scatterings can be computed and are shown in Fig. 9 as N_1, N_2, and N_3, respectively. The sum of all four of these spectra then roughly represents the spectrum of outgoing protons. By subtraction of 15 Mev from the energy of each proton the spectrum is then converted into an energy spectrum in the laboratory.

Finally, these resulting spectra are to be folded with a representative resolution function for the proton telescope. The energy resolution function of the telescope is roughly triangular with full width at half-maximum of 20 Mev. Because of the correlation between proton energy and angle in the pseudo-deuteron disintegration assumed, an additional energy spread is caused by the poor angular resolution of the telescope. To allow for this the net resolution has been taken to be triangular with a 30-Mev full width at half-maximum. The results of this folding are given in Fig. 10 where both the entire spectrum and the spectrum of those escaping without scattering are shown. While this last folding has smoothed the curves out a little, it is seen that the results are largely insensitive to any detailed choice of telescope resolution function. The curves have been normalized for best fit to the monochromatic gamma-ray data which are also shown on the same graph. The theoretical curve has also been arbitrarily moved up the energy scale by 5 Mev to improve the fit. This amount is within the uncertainties involved in absolute calibration of the gamma-ray energy since the synchrotron target was moved and certain organic modifications of the synchrotron were made in the period between the pair-spectrometer measurements of the monochromatic spectrum and the measurements of the proton energy spectrum.

The success of the fit to experiment is indeed surprising, but a rather careful distinction must be made in the interpretation of the significance of this fit. The upper portion of the curve shows a nice fit which is probably rather strongly indicative of the approximate correctness of the deuteron model. It is probably true that any momentum distribution reasonably similar to the Fermi distribution would give as good a fit to the present data. But the general confirmation of the type of model is probably significant. On the other hand, the good fit to the lower portion of the curve, where the large scattering contributions have been added, must be considered largely fortuitous. The magnitude of the scattering corrections is extremely sensitive to the exact choice of escape probabilities, and probably the only important result is that such calculations can indeed give curves of the general character of those which are observed. These curves should not be taken to exclude the possibility of a significant contribution from other processes in the low-energy region.

The area under the curve of those protons which have escaped without scattering is some 76 microbarns, representing 55 percent of the protons initially produced from the assumed pseudo-deuteron process. This means that the integrated cross section for the photoproduction of protons at 60 degrees from the carbon nucleus by the mechanism under discussion is about 138 microbarns. If this cross section is then divided by the number of effective deuterons in the carbon nucleus (shown by Levinger[7] to be 1.6A if the deuteron is composed of a proton and a neutron) a cross section for the photodisintegration of the pseudo-deuteron within the carbon nucleus can be obtained. The value obtained here is 7 microbarns/Mev-steradian with an estimated absolute error somewhat larger than 25 percent. It is interesting to note that this cross section is essentially within the experimental error of measurements made by a number of workers of the cross section for the photodisintegration of a real deuteron at this energy and angle.[17–21] Of course, if the pseudo-deuteron is also allowed to be a pair of protons or a pair of neutrons the cross section resulting from our measure-

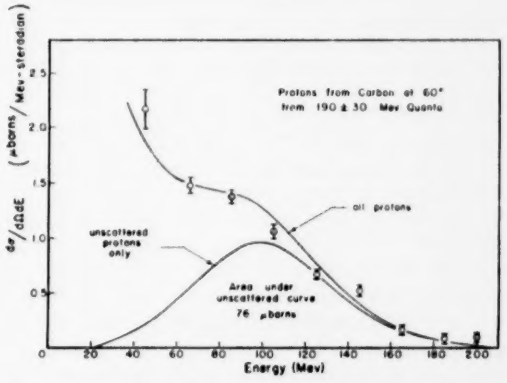

FIG. 10. Theoretical synthesis of the energy distribution. The curve for all protons is the result of the full theoretical synthesis and represents the attempted fit to the data. The curve for unscattered protons is given for comparison and for use in computing an effective cross section for photodisintegration of the pseudo-deuteron within the carbon nucleus.

[17] J. C. Keck and R. M. Littauer, Phys. Rev. **86**, 1051 (1952).
[18] S. Kikuchi, Phys. Rev. **85**, 1062 (1952).
[19] W. S. Gilbert and J. W. Rosengren, Phys. Rev. **88**, 901 (1952).
[20] T. S. Benedict and W. M. Woodward, Phys. Rev. **85**, 924 (1952).
[21] O'Neill, Perry, and Woodward (private communication).

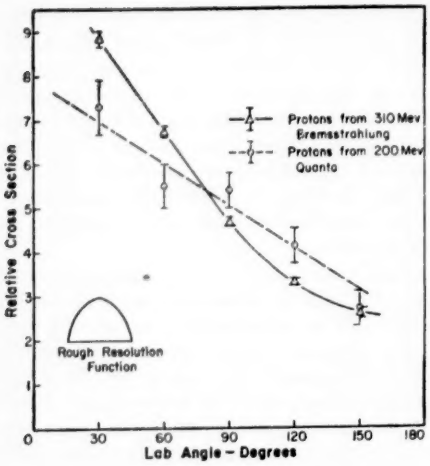

FIG. 11. The angular distribution of photoprotons of 70±17 Mev from carbon. The dotted line is a straight line drawn for purposes of comparison only through the data from an incident monochromatic gamma-ray spectrum.

ments would be somewhat lower, but the data here and the present data for the photodisintegration of the deuteron do not allow a real distinction to be made.

Keck and Perry[5] at this laboratory have also measured the energy distribution of protons produced at 60 degrees by monochromatic gamma rays. They used the bremsstrahlung subtraction technique and obtained results from quanta centered about 280 Mev. Their results, combined with theoretical considerations similar to those used here, agree in principle with those given above.

Figure 11 shows the angular distribution observed for 70-Mev protons. It is possible to say, first, that the present distribution is not inconsistent with a two-particle model which breaks up isotropically in the center-of-mass system. The various resolution functions and the nuclear scattering would perhaps be expected to make the distribution somewhat more isotropic than the observed curve, but this is not entirely clear. In addition it is not unlikely that the experimental point taken at 30 degrees is too high by 10 percent or so because of the large electron background experienced in this position with the rather poor angular resolution of the apparatus and the consequent rather poor resolution of protons in the pulse-height spectrum. Because of this perhaps all that can be said is that the angular distribution of protons from the monochromatic gamma-ray spectrum is not in disagreement with the model proposed for explaining the energy distribution.

The angular distribution data taken for protons produced by the entire bremsstrahlung spectrum are in essential agreement with those given by other workers. As expected, it shows a sharper peak in the forward direction and a lower cross section in the backward direction when compared to the results from monochromatic quanta.

EVALUATION OF THE MONOCHROMATIC METHOD

It has been established that by this technique one may perform experiments with a narrow spectrum of quanta selected from the bremsstrahlung spectrum. But there are a number of additional facts which should be noted in comparing this technique with some other approach, such as the difference spectrum technique. First, the apparatus is complex, not only in magnitude but also in the interlacing of the various functions. This is clear from examination of the block diagram of the electronics discussed elsewhere. Excluding the pulse-height analyzer, the electronic equipment devoted solely to this experiment contained some three hundred vacuum tubes. Secondly, with the duty cycles available from present synchrotrons and with the present limitations on coincidence resolving times, the monochromatic beam intensity (and hence the net counting rate) is severely limited. About four weeks of continuous running time were devoted to setting up for and taking the energy distribution curve, even after all difficulties had been eliminated and the experiment had been shown to be working. It is probably so that the same results on photoproduction of protons could have been obtained more conveniently and more rapidly by the difference spectrum technique. However, it was felt a valuable check to be able to obtain results by a new method in order to prove the validity of the difference technique.

For experiments requiring only very low-beam intensities (such as the calibration of the efficiency of gamma-ray counters) the electronics may be greatly simplified to permit rapid and easy measurement. Even for those experiments requiring greater beam intensities, the occasion may arise for the application of the technique. The present technique should also be re-evaluated when some of the higher energy machines come into operation, particularly those of race-track design. In this case much greater convenience in detecting the internal electron would be possible, and running a number of energy channels simultaneously would be a feasible method of significantly increasing the effective counting rates. One may, of course, hope for some improvement in resolving times and coincidence techniques.

We are greatly indebted to Professor P. Morrison for discussions concerning the interpretation of this experiment and to Doctors R. M. Littauer, J. C. Keck, and A. M. Perry for the communication of unpublished experimental results and theoretical calculations as well as their assistance in the design of the circuits. In addition, grateful acknowledgement is made to Professor J. W. DeWire for the use of the pair spectrometer and to the many students and members of the staff who helped operate and maintain the synchrotron.

Metastable States of Ge^{73}†*

JOAN P. WELKER, A. W. SCHARDT, G. FRIEDLANDER, AND J. J. HOWLAND, JR.‡
Brookhaven National Laboratory, Upton, New York

(Received July 3, 1953)

The decay of As^{73} to Ge^{73} has been investigated with scintillation counters. The K capture is followed by a 53.9-kev gamma ray which in turn is followed by a 13.5-kev transition to the ground state. The total conversion coefficient of the 53.9-kev gamma is 4.7 and the lifetime is between 900 microseconds and 10 seconds. The half-life of the 13.5-kev transition is 4.6 microseconds. The available evidence points to the 53.9-kev transition being $M2$ and the 13.5-kev transition $E2$ with a possible small admixture of $M1$. Spin and parity assignments are discussed.

AS part of a general search for nuclear isomers with lifetimes in the millisecond range, it seemed pertinent to examine further the disintegration scheme of As^{73}. Johansson,[1] on evidence obtained from measurements with a β-ray lens spectrometer, suggested the decay scheme shown in Fig. 1. It was of particular interest to investigate the lifetime of the 53.9-kev transition, as half-lives in the millisecond range are not expected to be very common.[2] A knowledge of the lifetimes is also helpful in verifying the spin and parity changes involved. In addition, it was desirable to confirm the existence of the 13.5- and 53.9-kev gamma rays by means of scintillation spectrometer techniques. The order of emission of the gamma rays was also investigated and found to be the reverse of that proposed by Johansson on the basis of shell theory.

SOURCE PREPARATION

As^{73} was obtained from Oak Ridge as carrier-free arsenite in 2.8M HCl. Metallic arsenic was precipitated from a hot concentrated HCl solution to which had been added 0.2-mg arsenic carrier (as AsO_2^-) and a few tenths of a gram of sodium hypophosphite. In order to make sources, portions of the precipitate were transferred to 0.001-inch Al foils, dried, and covered with a film of 1 percent zapon. In addition, a NaI crystal was grown from a melt containing some of the metallic arsenic and 0.5 percent TlI. This crystal retained only a small fraction of the added activity and gave a somewhat poorer resolution than commercial NaI(Tl) crystals.

At the time the final measurements were made, the As^{74} activity was less than 1 percent of As^{73}, and no difficulties were encountered due to the presence of As^{74}. No other radioactive contaminants were found.

EXPERIMENTAL RESULTS

Gamma-Ray Spectrum

The spectrum of the arsenic source was investigated with a scintillation spectrometer using a $\frac{1}{2}\times\frac{1}{2}\times\frac{3}{2}$-inch cleaved NaI(Tl) crystal[3] which was sealed against moisture with a 0.001-inch aluminum foil. The associated electronic equipment consisted of DuMont K1186 photomultipliers, regulated high-voltage power supplies,[4] a modified version of the non-overload amplifier,[5] and a gray wedge pulse-height analyzer.[6] The spectra were photographed on Kodak type IV-0 spectroscopic film, then printed with such magnification that the intensity scale corresponds to that of commercial semilog paper. Different points on an isodensity line, traced on such paper, would then have the correct relative intensities.

Figure 2 shows a trace of the pulse-height spectrum obtained with an external As^{73} source. The energy scale was calibrated with silver K x-rays (22.0 kev) from a Cd^{109} source. Since the gray wedge used covers an intensity ratio of only 1:100, different exposures were required in order to examine the desired range. In

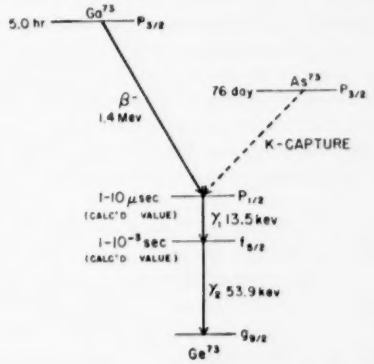

FIG. 1. Johansson's decay scheme for As^{73} and Ga^{73}.

† A preliminary report was given at the American Physical Society Meeting, Washington, D. C. (April 30–May 2, 1953).

* This work was carried out under the auspices of the U. S. Atomic Energy Commission.

‡ Now at the Radiation Laboratory, University of California, Berkeley, California.

[1] S. Johansson, Arkiv. Fysik **4**, 273 (1952).

[2] M. Goldhaber and A. W. Sunyar, Phys. Rev. **83**, 906 (1951).

[3] The NaI(Tl) was supplied by the Harshaw Chemical Company.

[4] W. A. Higinbotham, Rev. Sci. Instr. **22**, 429 (1951).

[5] R. L. Chase and W. A. Higinbotham, Rev. Sci. Instr. **23**, 34 (1952).

[6] Bernstein, Chase, and Schardt, Rev. Sci. Instr. **24**, 437 (1953).

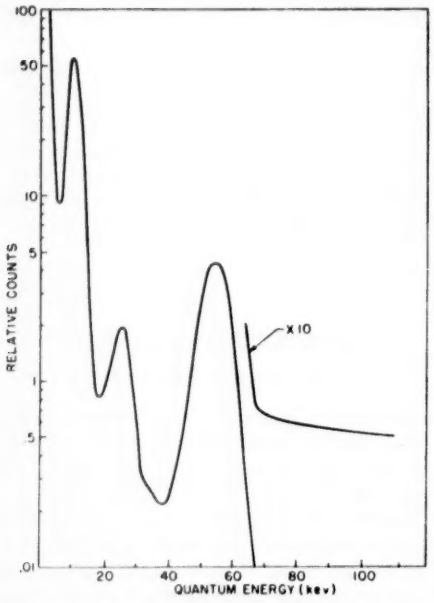

FIG. 2. Pulse-height spectrum of an As^{73} source external to a NaI(Tl) crystal.

addition to the 9.9-kev germanium x-rays and 53.9-kev gamma rays,[7] a line appears at 25 kev which is caused by 53.9-kev quanta ejecting photoelectrons from iodine in the NaI(Tl) scintillator without subsequent capture of the iodine K radiation in the crystal. The 13.5-kev gamma ray[1] is not detectable because of its very high conversion coefficient (see Table II). No line at 81 kev, corresponding to the 75-kev conversion electrons reported by Johansson, was observed. The statistics in the background are such that it would have been possible to see a line 0.2 percent as strong as the 53.9-kev line. Johansson measured the ratio in intensity of the 75-kev conversion electrons to the K conversion electrons associated with the γ_2 transition and found it to be 0.1 percent. Thus, the 81-kev quanta, if present in our source, must have almost as high an internal conversion coefficient as the 53.9-kev line. Similarly, the crossover transition, which would appear at 67.4 kev, is not found.

The pulse height spectrum obtained with the NaI(Tl) crystal containing As^{73} is shown in Fig. 3a. Since this source was much weaker than the external source, the tail of the photomultiplier noise is more noticeable and decreases the peak-to-trough ratio of the 9.9-kev line. The escape peak at 25 kev is absent because the activity is distributed throughout the volume of the crystal. There is still no indication of the 13.5-kev transition reported by Johansson.[1] The gray wedge analyzer requires 200 microseconds to record an event and is insensitive during this period. Consequently, the 13.5-kev transition, if it exists, must follow either the 9.9- or 53.9-kev radiations within this time. Visual observation of individual sweeps on a Tektronix oscilloscope showed small pulses following the 53.9-kev pulses within a few microseconds, but no pulses were observed after the 9.9-kev pulses. Figure 3b shows the spectrum of these delayed events. Special trigger circuits were used to make the gray wedge analyzer sensitive only during the time from 5 to 20 microseconds following a pulse with an amplitude between 40 and 60 kev. Two separate energy measurements gave values of 13.7 and 14.1 kev, respectively, in agreement with Johansson's γ_1 transition. However, this transition definitely follows rather than precedes the 53.9-kev gamma ray. The observation that no 53.9-kev pulses were seen following the 9.9-kev x-rays on the Tektronix scope proves that the 53.9-kev transition must be delayed by more than a few microseconds.

Observations with the internal source permit some qualitative conclusions regarding transitions from As^{73} to the 13.5-kev and ground levels in Ge^{73}. If a long time constant is used in the amplifier, pulses delayed by only 2 or 3 microseconds will add to the height of the original pulse. Pictures taken in this way showed a pronounced asymmetry on the high side of the 53.9-kev line, but left the 9.9-kev line unchanged. This indicates that, at most, few delayed 13.5-kev quanta follow directly after a K capture; in other words, no direct decay was observed from As^{73} to the 13.5-kev level. The relative areas under the 9.9- and 53.9-kev peaks (Fig. 3a) give directly the ratio of K captures to total 53.9-kev transitions. Because the photomultiplier noise background could not be evaluated accurately, only an upper limit of 1.5 can be given for this ratio. This shows that K capture to the ground state is not a very probable mode of decay.

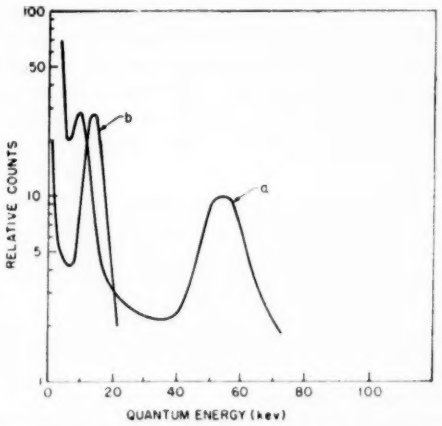

FIG. 3. Pulse-height spectra of an As^{73} source incorporated in a NaI(Tl) crystal. Curve a shows the singles spectrum, curve b the spectrum of pulses following the 53.9-kev gamma ray.

[7] Because of their greater accuracy, Johansson's energy values have been used throughout the paper.

The relative intensities of the 9.9-, 13.5-, and 53.9-kev photolines can be used to evaluate conversion coefficients. The ratio of the number of K x-rays to that of unconverted 53.9-kev gamma rays was measured with the $\frac{3}{32}$-inch NaI(Tl) crystal and external source. The best value of this ratio was obtained from the ratio of the steps in the integral bias curve, the escape radiation being included with the 53.9-kev photoline. After correction for absorption in the 0.001-inch aluminum foil, the ratio is 6.2.

To look for unconverted 13.5-kev gammas, a proportional counter filled to two atmospheres with a mixture of 90 percent argon and 10 percent methane was used. No evidence for 13.5-kev photons was found, but an upper limit of 1/1400 could be set for the ratio of 13.5-kev quanta to K x-rays. A smaller contribution of 13.5-kev gammas would have been masked by the high energy tail of the x-ray peak. In arriving at the upper limit, account was taken of the relative counting efficiencies (88 and 59 percent) and resolutions (14 and 12 percent full width at half-maximum) at 9.9 and 13.5 kev, respectively, and of absorption in the 1.27 g/cm² of beryllium used to absorb the betas from As^{74}.

The experimental intensity ratios listed in Table I were used to calculate the total internal conversion coefficient (α_2) of the 53.9-kev gamma ray, the K/L conversion ratio (K_1/L_1) and a lower limit for the total internal conversion coefficient (α_1) of the 13.5-kev transition. All As^{73} disintegrations were assumed to proceed according to the decay scheme of Fig. 5. The fluorescence yield of the germanium K x-rays was taken as 0.56,[8] the fraction of L capture in As^{73} as 0.11; this latter value was computed according to Rose and Jackson[9] for a decay energy of 320±30 kev.[10] The results of these calculations for α_2, K_1/L_1, and α_1 are given in Table II. As a check on the internal consistency of the data, the ratio $(K_2+L_2+M_2)/(L_1+M_1)$ was evaluated using (L_1+M_1)/Auger, K x-rays/γ_2, and α_2. The calculated ratio is in good agreement with Johansson's experimental value.

TABLE I. Experimental ratios of the intensities of various radiations from As^{73}.

Intensity ratio	Experimental value
$K_2/(L_2+M_2)$	5.6±0.3[a]
L_1/M_1	5.4±0.5[a]
(L_1+M_1)/Auger	0.77[a,b]
(K x-rays)/γ_2	6.2±0.6
(K x-rays)/γ_1	≥1400

[a] See reference 1.
[b] For purposes of calculation, a 10 percent experimental error was assigned to this value.

[8] Broyles, Thomas, and Haynes, Phys. Rev. **89**, 715 (1953).
[9] M. E. Rose and J. L. Jackson, Phys. Rev. **76**, 1540 (1949).
[10] This decay energy was obtained from the threshold of the $Ge^{73}(p,n)As^{73}$ reaction reported by C. C. Trail and C. H. Johnson, Phys. Rev. **91**, 474 (1953).

TABLE II. Conversion coefficients and ratios of conversion electron intensities for the two transitions in Ge^{73}.

Intensity ratio	Values: Calculated from the data of Table I	Values: Measured by Johansson
$\alpha_2=(K_2+L_2+M_2)/\gamma_2$	4.7±0.6	
K_1/L_1	0.63±0.22	<0.5
$\alpha_1=(K_1+L_1+M_1)/\gamma_1$	≥1300	
$(K_2+L_2+M_2)/(L_1+M_1)$	1.25	1.2

Measurements of Half-Lives

A gray wedge time-delay analyzer[11] was used to record the data. In this instrument the radiation preceding the delayed transition triggers the blanked, horizontal time sweep of an oscilloscope. The delayed event stops the horizontal sweep and is displayed as a vertical line trace. The face of the oscilloscope is photographed through a gray wedge mounted in such a way that its transparency decreases in the vertical direction. The gray wedge was calibrated as described by Bernstein *et al.*;[6] the time markers from a DuMont 256D oscilloscope were used to calibrate the horizontal sweep. The performance of the analyzer was checked by triggering the horizontal and vertical sweeps by random events. This gave the expected horizontal line.

Since γ_1 is completely internally converted, the internal source was used to measure the half-life of the 13.5-kev level. The discriminators on the time-delay analyzer were set such that any pulse between 40 and 70 kev would start the time sweep. A subsequent pulse between 7 and 70 kev started the display sweep. Figure 4 shows the resulting picture taken on Kodak type IV-O film. The average half-life measured from it and another picture is 4.6±0.5 microseconds. The assigned error is due to the uncertainty in the wedge calibration. Another possible source of error lies in the random after-pulses[12] created in the photomultiplier by the 53.9-kev pulses. This effect was minimized by using a photomultiplier with silver-magnesium dynodes.[13] It was not determined exactly how much of an error this effect could have introduced, but Fig. 3b shows very little evidence of after-pulses.

In an attempt to measure the half-life of the second excited level of Ge^{73}, a krypton-filled proportional counter, channeled on germanium K x-rays, was used to trigger the time sweep of the analyzer. The display sweep was triggered by the photoline of the 53.9-kev gammas as detected with a $\frac{3}{4}$-inch diameter by $\frac{1}{16}$-inch thick NaI(Tl) crystal. Pictures were taken with a Polaroid Land camera; although this results in decreased accuracy for half-life measurements, the data are obtained more rapidly. Time sweeps of 3, 8, 26, 60, 150, and 400 microseconds were used. The source strengths were progressively decreased as the sweep

[11] Schardt, Bernstein, and Chase, Phys. Rev. **90**, 353 (1953).
[12] Mueller, Best, Jackson, and Singletary, Nucleonics **10**, No. 6, 53 (1952).
[13] DuMont K1186.

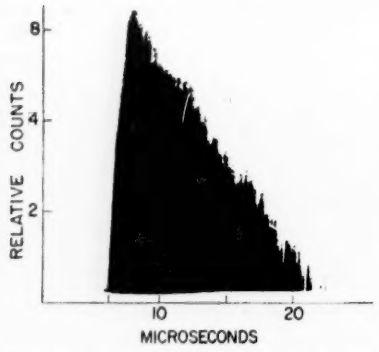

FIG. 4. The decay of the 13.5-kev level as observed on the time-delay analyzer. The measured half-life is 4.6±0.5 microseconds.

time was increased so that, if one half-life occurred during the sweep duration, the number of real coincidences would have been at least ten times the number of chance coincidences. There was no evidence of any decay even when using the 400-microsecond sweep.

Measurements with the 900-microsecond sweep of the time-delay analyzer were made with the internal source in order to take advantage of its greater detection efficiency and improved geometry.[14] The discriminators associated with the time and display sweeps were set to trigger on pulses from 5.5 to 65 kev and 40 to 65 kev, respectively. Again no decay was found, though a lifetime comparable to the sweep time would have been observable on the Polaroid prints. Thus a lower limit of 900 microseconds was set for the half-life of the 53.9-kev transition.

It was possible to set an upper limit on the lifetime of the 53.9-kev transition by making a rapid chemical separation of arsenic from germanium and looking immediately for a decay in the germanium fraction. The procedure[15] used is as follows: An equal volume of 47 percent hypophosphite-free HI was added to a solution of pentavalent As^{73} (containing 0.2-mg As carrier) in $3N$ HCl. The AsI_3 formed was extracted into $CHCl_3$, 2–4 mg of germanium holdback carrier (as GeI_4) were added and the $CHCl_3$ layer was extracted with $1M$ H_2SO_4. Less than 0.4 percent germanium is carried into the H_2SO_4 acid layer, while the arsenic is removed as AsO_2^- with an efficiency >95 percent. The time required for the layers to separate and to drain the $CHCl_3$ layer into a thin-walled glass vessel for counting is ~15 seconds. γ_2 was detected by means of a standard scintillation spectrometer connected to a Brush recorder. In the two experiments performed the germanium fraction had decayed to background within the time of separation. Thus the half-life must be less than 10 seconds, since otherwise the decay of γ_2 would have been discernable on the recorder tape.

While this work was in progress, Campbell[16] measured the half-life of the 53.9-kev transition. His value is 0.33±0.05 second.

DISCUSSION

The available evidence on the decay schemes of As^{73} and Ga^{73} is summarized in Fig. 5. Johansson's spin and parity assignments,[1] which were made partly on the basis of shell theory, have been revised to take into account the order of emission of the two gamma rays. The Ge^{73} ground state is known to be $g_{9/2}$ from the measured spin[17] and from shell theory. The ground states of Ga^{73} and As^{73} are almost certainly $p_{3/2}$ states, in agreement with shell structure and in analogy to the measured spins and moments[17] of Ga^{71} and As^{75}. The logft values for the transitions from Ga^{73} and As^{73} to the second excited state (67.4 kev) of Ge^{73} are 5.9 and 5.4, respectively, indicating allowed transitions. Thus the 67.4-kev level could be $p_{1/2}$, $p_{3/2}$, or $f_{5/2}$; any of these assignments is compatible with the single-particle model. However, the $f_{5/2}$ assignment can be eliminated because the 67.4-kev crossover transition was unobserved ($<2\times10^{-3}$ of unconverted 53.9-kev transitions). According to Blatt and Weisskopf,[18] the theoretical $M2$ gamma half-life for an $f_{5/2} \longrightarrow g_{9/2}$ transition of 67.4 kev is $\sim10^{-3}$ sec, a factor of about 10^5 shorter than the experimental lower limit.

The 53.9-kev transition can be labeled fairly definitely as $M2$. Extrapolation of the K conversion coefficient data of Rose *et al.*[19] to lower energies with the aid of Spinrad's[20] threshold values shows that the experimental value, $\alpha_K=4.0$, is compatible only with a $M2$ or $E2$ assignment. The measured K/L ratio of 6 to 7[1] is in excellent agreement with the value 6.8 obtained from Goldhaber and Sunyar's[2] curve for $M2$, but not with the value 1.7 for $E2$. In the case of the 13.5-kev transition, the evidence points to an $E2$ assignment, with a possible small admixture of $M1$. Transitions of multipole order greater than two can be ruled out on the basis of lifetime considerations. The threshold values for the total K conversion coefficients,[20] ~64 ($E1$), ~44 ($M1$), ~670 ($E2$) can be used to eliminate pure $E1$ and $M1$ type transitions since the experimental lower limit for α_K is 450. The measured K/L ratio, 0.63±0.22 is higher than the value, ~0.15, obtained by extrapolating Goldhaber and Sunyar's[2] curve for $E2$ from $Z^2/E=60$ to $Z^2/E=75$.

[14] With the external source, processes resulting in Auger and internal conversion electrons could not be detected. The calculated accidental rate is low enough with the internal source to permit use of a 10-millisecond sweep time. However, 900 microseconds is the longest sweep for which the analyzer was designed.

[15] We are indebted to Dr. René J. Prestwood, Los Alamos Scientific Laboratory, for suggesting the separation method.

[16] E. C. Campbell (private communication).

[17] Way, Fano, Scott, and Thew, *Nuclear Data*, National Bureau of Standards Circular 499 and Supplements (U. S. Government Printing Office, Washington, D. C., 1950).

[18] J. M. Blatt and V. F. Weisskopf, *Theoretical Nuclear Physics* (John Wiley and Sons, Inc., New York, 1952).

[19] Rose, Goertzel, Spinrad, Harr, and Strong, Phys. Rev. **83**, 79 (1951).

[20] B. I. Spinrad and L. B. Keller, Phys. Rev. **84**, 1056 (1951).

However, a recent accurate measurement[21] of the K/L ratio for the 84-kev transition in Yb^{170}, 0.36 ± 0.04 at $Z^2/E=57$, indicates that the $E2$ curve is too low for large values of Z^2/E; considering the experimental accuracy of the original data used to construct the curve, such a displacement is not unreasonable. Even so, the observed K/L ratio for the 13.5-kev transition appears to be somewhat high for pure $E2$, and a small admixture of $M1$ ($K/L\sim7.4$)[2] cannot be excluded.

Since the 67.4-kev level of Ge^{73} is either $p_{1/2}$ or $p_{3/2}$, the 13.5-kev level must be either $5/2+$ or $7/2+$, respectively. Thus the two possible assignments for the gamma cascade are

$$p_{1/2}\xrightarrow{M2}5/2+\xrightarrow{E2}g_{9/2},\quad p_{3/2}\xrightarrow{M2}7/2+\xrightarrow{M1+E2}g_{9/2}.$$

The intermediate level cannot be interpreted on the basis of the single particle model since no low-lying $d_{5/2}$ or $g_{7/2}$ levels can be expected for the forty-first neutron in Ge^{73}. A reasonable assumption would be that three neutrons are in the $g_{9/2}$ shell and that this $(g_{9/2})^3$ configuration has spin $5/2+$ or $7/2+$. The $(g_{9/2})^3$ configuration is also compatible with the fact that the 53.9-kev transition has a half-life about 600 times longer than would be expected for a single particle $M2$ transition. The gamma half-life of the 13.5-kev transition ($\gtrsim6\times10^{-3}$ sec) is to be compared with the theoretical values,[18] 4×10^{-2} sec for $E2$, and 9×10^{-9} sec for $M1$. Thus, at first glance, the lifetime would appear to favor a pure $E2$ assignment for the transition and therefore a $5/2+$ designation for the 13.5-kev level. However, as discussed above, this level most likely has a $(g_{9/2})^3$ configuration and therefore one would expect the transition to the ground state to be considerably slower than a single particle $E2$ transition. A $7/2+$ assignment for the 13.5-kev state and a mixed $M1+E2$ transition to the ground state is thus a definite possibility, although this interpretation would require an exceedingly small matrix element for the $M1$ transition.

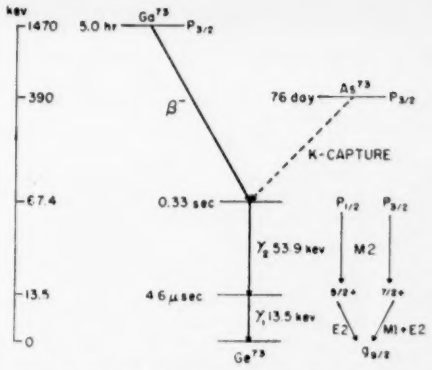

FIG. 5. Revised decay scheme of As^{73} and Ga^{73}.

The fact that the lifetimes of the two gamma transitions are long compared with those expected for $M2$ and $M1$ transitions, respectively, points to a relatively high purity of the postulated $(g_{9/2})^3$ configuration of the intermediate level. This is in accord with recent considerations on mixed configurations[22] which make it plausible that purer configurations occur at the beginning than in the middle of shells.

The authors would like to thank Dr. M. Goldhaber and Dr. J. Mihelich for valuable discussions. A great deal of help with electronic problems was given by Mr. R. L. Chase, who also designed the time-delay analyzer.

Note added in proof.—In a recent paper (Compt. rend. **236**, 1872 (1953)) R. Barloutaud and M. Sartory propose a decay scheme for As^{73} substantially different from that of Fig. 5 and incompatible with the evidence given in the present paper. However, Dr. Barloutaud has kindly informed us that his experimental data are consistent with our decay scheme.

[21] Graham, Wolfson, and Bell, Can. J. Phys. **30**, 459 (1952).

[22] A. De-Shalit and M. Goldhaber (private communication).

Search for Highly Absorbable Negative Cosmic-Ray Particles at Sea Level*

CHARLES E. MILLER, JOSEPH E. HENDERSON, DAVID S. POTTER, WILLIAM R. DAVIS, WAYNE M. SANDSTROM, GERALD R. GARRISON, AND FRANCIS M. CHARBONNIER
Applied Physics Laboratory,† University of Washington, Seattle, Washington
(Received June 22, 1953)

A search has been made at sea level for negative cosmic-ray particles (other than electrons) which are absorbed in 147 g/cm² of lead and which have momenta greater than that of mu mesons of this range. The momentum and sign of the charge of those particles stopping in the absorber were determined by means of a counter controlled cloud chamber operated in a magnetic field. During 1400 hours of operation no negatively charged particle in the momentum interval 0.4–1.7 Bev/c was recorded as stopping in the absorber. This result has been used to show that the intensity of negative particles with strong nuclear interaction cannot amount to as much as 0.05 percent of the total intensity of negative particles in this momentum interval. It has been shown that the local production of negative mu mesons in the momentum interval 0.5–1.0 Bev/c is less than 8.8×10^{-5} particle/(cm² steradian hr meter). A lower limit of 6.9×10^{5} g/cm² of lead has been set on the removal path length of mu mesons in the momentum interval 0.4–1.6 Bev/c.

I. INTRODUCTION

FROM many studies it is clear that the cosmic radiation at sea level and mountain altitudes consists principally of an electronic cascade component, positive and negative mu mesons, protons, and neutrons. Even at these low altitudes high-energy nuclear events occur which produce secondary particles not included in the above list. These are the pi mesons, V particles, and other types of mesons. Such particles have been detected only in association with highe-nergy nuclear events or when they chance to decay in cloud chambers or nuclear emulsions. With the possible exception of the pi meson, the net flux of these particles must be exceedingly small because of the low production rates and short decay times.

By improving a technique previously used to determine the intensity of protons at lower altitudes,[1,2] a careful search has been made at sea level for negatively charged particles of such nature as to be more readily absorbed than mu mesons. In the previous experiments the proton flux density was determined by using an experimental arrangement similar to that used in the present experiment (Fig. 1). The magnetic cloud chamber was triggered by an arrangement of counters designed to select those ionizing particles stopping in the absorber below the chamber. All particles selected in this way lie in the same range interval. By suitable choices of absorber thicknesses protons and mesons selected in this way will lie in well-separated momentum intervals because of the different range-momentum relationships of these particles. For ionization ranges of 0.5 to 5.5 cm of lead, well-resolved maxima corresponding to mesons and protons were obtained by plotting the number of particles as a function of momentum.[3]

While the negatively charged particles selected in this way were grouped strongly in the momentum interval to be expected for mu mesons on the basis of their ionization range, small numbers of negatively charged particles were recorded up to the highest momentum measured (2.5 Bev/c). In these observations the coverage of the anticoincidence tray was not nearly so complete as in the present experiment. This led to an error of inclusion in which mesons of momentum greater than that corresponding to the maximum ionization range were recorded as a result of being scattered outside the anticoincidence coverage. However, multiple scattering could not account for the negative particles recorded with momenta greater than 1 Bev/c. Inclusion of these high-energy negative particles was attributed to inefficiency of the anticoincidence Geiger tubes resulting from dead time. In later observations[2] with larger absorber thicknesses and much better anticoincidence coverage such high-energy negative particles were still recorded. At an altitude of 3.4 km and with an absorber thickness of 15 cm of lead the recorded intensity of negative particles above 1 Bev/c amounted to about 2.5 percent of the total negative meson intensity at the same momentum. In this case apparently neither scattering nor counter inefficiency could account for the inclusion of these negative particles. For similar observations[4] at sea level the corresponding percentage of negative particles was 0.4 percent, which can be accounted for by leakage due to dead time of the anticoincidence Geiger tubes.

In the present experiment the effects of scattering and counter inefficiency have been greatly reduced in order to place an upper limit on the total intensity of all negative particles (other than electrons) with momenta greater than 0.4 Bev/c and of such nature as to be absorbed in 10 cm of lead. In 1400 hours of operation at sea level, with the single exception of one heavily ionizing particle which seemed to be a back-scattered deuteron, no negative particles with momenta

* This work supported by the U. S. Office of Naval Research.
† A division of the Department of Physics.
[1] Miller, Henderson, Potter, Todd, and Wotring, Phys. Rev. 79, 459 (1950).
[2] G. R. Garrison *et al.* (to be published).
[3] Miller, Henderson, Potter and Todd, Phys. Rev. 84, 981 (1951).
[4] J. Todd, Jr. *et al.* (to be published).

greater than 0.4 Bev/c were found to stop. For the same momenta some 200 positive particles stopped in the absorber; these are assumed to consist almost entirely of protons.

II. APPARATUS AND EXPERIMENT

The experimental arrangement is shown schematically in Fig. 1. The chamber is expanded by C-A events in which Geiger tubes C_1 and C_2 are discharged in coincidence while none of the anticoincidence tubes in groups A_1 and A_2 are discharged. Therefore cloud-chamber photographs are obtained of those tracks produced by particles which pass through C_1 and C_2 and are absorbed in the 10 cm of lead below the chamber. The term "absorption" here refers to those events in which not only the incident particle but also all ionizing secondary particles are stopped in the absorber.

The cloud chamber has a diameter of 7 inches and an illuminated depth of 1 inch and is operated at a pressure of 1.8 atmospheres in a magnetic field of 8200 gauss. The coincidence tubes C_1 and C_2 that define the acceptance beam have copper cathodes $\frac{3}{4}$ inch in diameter and 6 inches long and are separated by a distance of 12 inches. The anticoincidence tubes below the absorber are $1\frac{1}{4}$ inches in diameter and 30 inches long. To insure complete coverage, the width and length of the anticoincidence tray are such that the tray extends several inches beyond the limits of the acceptance beam. The A tubes at the sides of the absorber prevent the recording of events due to wide angle scattering and reduce the probability of recording events in which high-energy charged particles entering the absorber from the side undergo nuclear collisions in the lead from which secondary particles pass upward through the cloud chamber and coincidence tubes. Errors resulting from the inefficiency of the anticoincidence tray because of counter dead time are eliminated by providing a blanking pulse which prevents the recording of any C-A events during the recovery time of the A tubes. Using the method described by Stever[5] the maximum recovery time of the A tubes used in this experiment was found to be about 450 microseconds. Following the discharge of any A tube a positive 600-microsecond pulse is applied to one side of a C-A mixer and prevents the recording of C-A events during the recovery time of the A tube. This blanking pulse was retriggered by each A pulse (even though the pulse occurred in the middle of a blanking cycle) so that no C-A pulse could be recorded for 600 microseconds following the last discharge of an A tube. The effect of introducing this blanking pulse is only to reduce the total time of observation by about 4 percent. During the effective time of observation it in no way reduces the probability of detecting those particles stopping in the absorber. To make sure that no events

[5] H. G. Stever, Phys. Rev. **61**, 38 (1942).

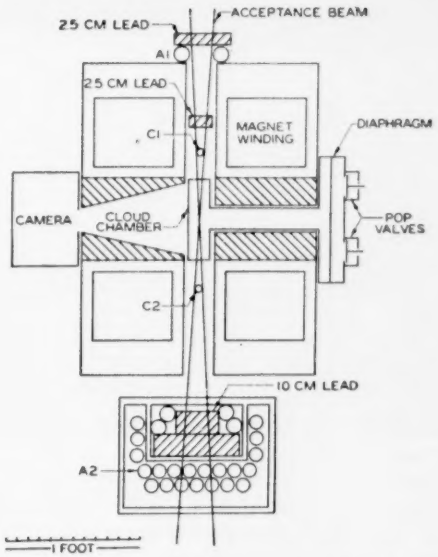

FIG. 1. Schematic diagram of the experimental arrangement.

were recorded due to the failure of one or more A tubes, all tubes were scaled twice each day. Provision was made to do this without removing the tubes being checked from the anticoincidence circuit. During the experiment only one A tube had to be replaced, and all data were discarded which had been obtained between the previous check period and the detection of the bad tube.

Lead absorbers were placed above the chamber so that electrons would produce with a high probability cascade showers which would either trigger the anticoincidence tubes A_1 or be revealed by the presence of several time-coincident tracks in the cloud chamber.

As described in detail in a previous paper[1] the curvature of the cloud-chamber tracks was determined by comparing the track photographs with a set of standard curves.

The equipment was operated for 9 weeks during the summer of 1952 at Seattle, Washington, at an elevation of 20 feet above sea level.

III. RATE DETERMINATION

A. Track Selection

Since this experiment is primarily concerned with singly occurring nonelectronic particles that produce C-A events, only those photographs were retained in the pertinent data which showed a single track time-coincident with the chamber expansion. Of these tracks, those near the chamber wall are not suitable for accurate curvature measurement because of their short length and the turbulence of the gas near the wall. The curvature was determined only for those "single tracks" of length at least 75 percent of the

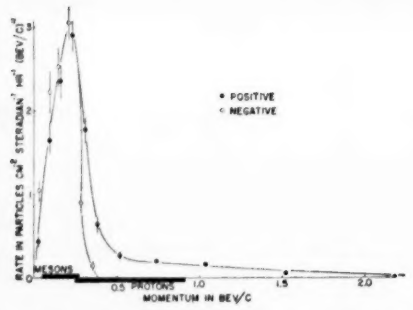

FIG. 2. Momentum spectra of those particles stopping in 147 g/cm² of lead equivalent at sea level plotted separately for positive and negative particles.

chamber diameter. These tracks constitute the "measured tracks." With the exception of the single track requirement, none of these criteria biases in any way the selection of particles of a specific type. The single track requirement does discriminate against electrons (which produce cascade showers) and those particles emitted from energetic nuclear collisions in the material immediately above the chamber since these particles are often accompanied by penetrating showers. Such discrimination is advantageous since we are concerned with the flux of nonelectronic particles in the atmosphere rather than with local production.

B. Normalization

As described in an earlier paper,[3] the absolute directional differential intensity is given by $I=(1/A)\times fr(n/m)(1/\Delta P)$, where A is the admittance of the counter telescope C_1 and C_2 in cm² steradian, f is the fraction of all C-A events associated with single tracks, r is the average hourly rate of C-A events and n/m is the ratio of the number of measured tracks in the momentum interval ΔP to the total number of measured tracks. This expression for the intensity depends only on the assumptions that the momentum distribution among measured tracks is the same as that among all single tracks and that the distribution of events producing C-A counts is the same whether or not the cloud chamber control circuits are in such a configuration that a C-A event would trigger a chamber expansion.

The admittance of the counter telescope computed from the effective length, width, and separation of tubes C_1 and C_2 is 0.97 cm² steradian. This value is in satisfactory agreement with the value 0.94 cm² steradian found in a separate experiment by a comparison of the intensity of the hard component as determined by this equipment with the absolute value determined by Rossi.[6]

[6] B. Rossi, Revs. Modern Phys. **20**, 537 (1948).

IV. RESULTS

The experimental results obtained during 1400 hours of operation are listed in Table I and shown graphically in Fig. 2. Every track satisfying the criteria discussed under Track Selection is included in this table. The most significant feature of the results is that with one possible exception no negative particles with momenta greater than 0.4 Bev/c were recorded as stopping in the absorber. As will be shown later, the exceptional track was produced by a heavily ionizing particle which was probably positively charged and moving upward through the chamber; it is therefore omitted in the following discussion.

For particles with momenta near the maximum at which momentum measurement is attempted (2.5 Bev/c) there is a possibility that occasionally the sign of the charge of the particle will be mistaken because of turbulance in the cloud chamber or bias of the observer. Since relatively large numbers of high momentum positive particles were expected it was decided before the experiment was conducted that the quantitative results should be based only upon those particles with momenta less than 1.6 Bev/c in order to avoid even small numbers of errors of inclusion among the negative particles recorded. Therefore, even though no negative particles were recorded with momenta between 0.4 and 2.5 Bev/c, the results stated below are based on the momentum interval 0.4–1.6 Bev/c.

The exceptional track is track "a" of Fig. 3. Its curvature corresponds to a momentum of 0.54 Bev/c and the direction of curvature is such that if the particle moved downward through the chamber it must have been negatively charged. The density of the track has been estimated by comparing it with a large number of tracks produced by heavily ionizing positive particles, presumably protons. Tracks "b" and "c" are included in Fig. 3 as examples. Track "d" is a track of minimum ionization. All of the tracks of Fig. 3 were obtained within a period of 14 hours; the photographic treatment was therefore the same for all tracks, and the cloud-chamber conditions were at least approximately the

TABLE I. Momentum distribution at sea level of particles stopping in 147 g/cm² of lead.

Momentum interval in Bev/c	Positive particles: Number of particles	Positive particles: Intensity in particles per (cm² steradian hr Bev/c)	Negative particles: Number of particles	Negative particles: Intensity in particles per (cm² steradian hr Bev/c)
0.00–0.08	32	0.46±0.07	72	1.05±0.12
0.08–0.13	71	1.65±0.19	90	2.22±0.23
0.13–0.17	120	2.34±0.21	121	2.53±0.23
0.17–0.27	214	2.90±0.20	208	3.10±0.21
0.27–0.35	115	1.77±0.16	52	0.89±0.12
0.35–0.43	49	0.65±0.09	10	0.15±0.05
0.43–0.61	41	0.28±0.04	1	0.00
0.61–0.88	55	0.23±0.03	0	0.00
0.88–1.20	55	0.19±0.03	0	0.00
1.20–1.85	27	0.05±0.01	0	0.00
1.85–2.50	10	0.02±0.01	0	0.00

same. Track "c" was produced by a proton with a momentum of 0.54 Bev/c (the same momentum as particle "a") and track "b" corresponds to a momentum of 0.37 Bev/c. Much detail has been lost in the reproduction of these tracks, but a comparison of the tracks as they appeared on the original film shows that track "a" is much denser than track "c" and that it is at least as dense as and perhaps denser than track "b." It follows that particle "a" (if singly charged) has a mass at least $1\frac{1}{2}$ times that of a proton. This conclusion is consistent with the comparison of track "a" with other heavily ionizing tracks of positive curvature. Additional but perhaps less certain conclusions can be drawn from a comparison between the range required for a particle to traverse the chamber wall and trigger the second coincidence tube and the range of various heavy particles corresponding to the momentum indicated by the curvature of track "a." It is found that neither the triton nor the alpha particle of this curvature has sufficient ionization range to pass through the wall of the cloud chamber. It is conceivable that track "a" was produced by a negative particle, but since there is no reliable evidence for the existence of a negative particle of mass $1\frac{1}{2}$ times that of the proton, the most credible explanation of track "a" seems to be that it was produced by a deuteron emitted in an energetic nuclear event in the lower absorber and projected upward through the cloud chamber. It has therefore been omitted in the discussion of the experimental results.

With the possible exception just discussed, no negative particles in the momentum interval 0.4–1.6 Bev/c were found to stop in 147 g/cm² of lead. If the absolute intensity of such particles were such that on the average one would be detected during the experiment, the probability of the actual result (i.e., of detecting no such particles) would be 37 percent. An upper limit for the absolute intensity of such particles at sea level is computed on the basis that on the average one would be detected during the course of the experiment. In this way, using the normalization procedure mentioned above, an upper limit of 1.0×10^{-3} particle/(cm² steradian hr) is found. That is to say, the absolute intensity of negative particles in the momentum interval 0.4–1.6 Bev/c that are absorbed in 147 g/cm² of lead equivalent is $\left(0.0\,{}^{+1.0}_{-0.0}\right)\times10^{-3}$ particle/(cm² steradian hr). Integrating Rossi's[6] sea level momentum spectrum for mu mesons over this momentum interval and taking 1.2 as the positive-negative ratio, it is found that the intensity of negative particles in the momentum interval that are absorbed in 147 g/cm² of lead is less than 0.02 percent of the total intensity of negative mu mesons in the momentum interval.

In the same momentum interval 198 positive particles (presumably protons) stopped in the absorber, corresponding to an intensity of 0.36 particle/(cm² steradian hr) or 6 percent of the total intensity of positive particles in the momentum interval.

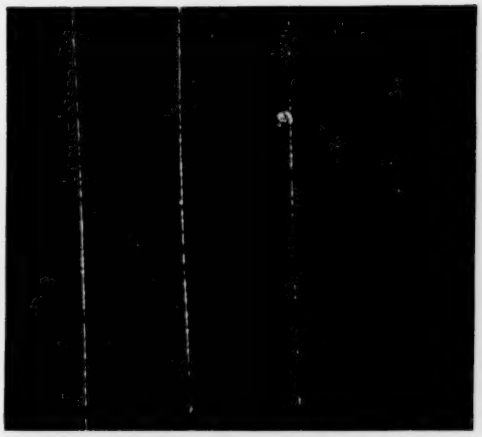

(a) (b) (c) (d)

FIG. 3. Cloud-chamber tracks produced by (a) heavy particle showing negative curvature, (b) 0.37 Bev/c proton, (c) 0.54 Bev/c proton, (d) particle of minimum ionization.

The results of this experiment may be compared with the results of a similar experiment by Mylroi and Wilson.[7] For the momentum interval 0.6–10 Bev/c, these authors found that of 1975 negative particles passing through the apparatus 4 were recorded as stopping in 1–10 cm of lead, none in 10–15 cm, and 8 in 15–20 cm. The 8 events for the range interval 15–20 were attributed to inefficiency of the anticoincidence tray. Two of the 4 events for 1–10 cm were attributed to erroneous information from the magnetic spectrometer, leaving two events that might have been due to electrons or absorption of negative particles with strong nuclear interaction. The authors therefore set an upper limit of 0.1 percent on the fraction of high-energy negative particles that are absorbed in 10 cm of lead.

V. DISCUSSION OF RESULTS

Since in the course of the present experiment no negative particles in the momentum interval 0.4–1.6 Bev/c were recorded, there is no necessity for a discussion of errors of inclusion. The detection efficiency for C-A events is considered to be 100 percent. Effects of dead times of the C counters are negligible for the present purpose. That the equipment was operating properly is shown by the detection of those mesons with range less than 147 g/cm² of lead with intensities in agreement with previous work of this and other laboratories.[4,6] In arriving at an upper limit for the intensities of specific types of negative particles assumptions will have to be made regarding the probability of such particles producing C-A events.

[7] M. G. Mylroi and J. G. Wilson, Proc. Phys. Soc. (London) **A64**, 404 (1951).

A. Sea Level Intensity of Pi Mesons

In order to derive an upper limit for the intensity of negative pi mesons it is necessary to introduce a removal path length L, which is defined by the expression $J_0-J_x=J_0(1-e^{-x/L})$, where J_0-J_x is the intensity of particles that are "removed" in an absorber distance x, and J_0 is the intensity of particles incident at the top of the absorber. An event is recorded as a "removal" only if all ionizing secondary particles as well as the primary particles are stopped in the absorber. The removal path length is therefore always equal to or greater than the mean path for nuclear interaction.

The removal path length of the pi meson is assumed to be approximately equal to that of the proton. Experimental evidence for the validity of this assumption is given by the nuclear emulsion studies of Camerini *et al.* and others.[8] Within the statistical accuracy of these experiments the nuclear interaction cross section for fast pi mesons was found to be the same as that for protons, or approximately equal to the nucleon geometrical cross section. Furthermore the types of stars produced by pi mesons and those produced by protons were identical within the experimental accuracy. Previous work of this laboratory[2] has shown that the removal path length of protons in the momentum interval considered in the experiment is about 200 g/cm² of lead. This value has been assumed for the removal path length of pi mesons.

Since the nuclear collision of particles is a statistical process, not all pi mesons passing through the chamber would be absorbed in the lead below the chamber and some pi mesons interacting in the 60 g/cm² of material above the chamber would not be detected because of absorption or because of production of secondaries which would cause them to be rejected by the single track criterion. Taking account of these two effects and the loss of momentum as the particles pass through the material above the chamber, it is found that the intensity of pi mesons in the momentum interval 0.5–1.7 Bev/c at the top of the equipment is less than 2.5×10^{-3} particle/cm² steradian hr, or less than 0.05 percent of the total flux of negative mu mesons in this momentum interval.

In deriving this result the production of pi mesons in the absorber above the chamber was not considered. Pi mesons produced in the absorber and accompanied by secondary particles would be overlooked because of the single track criterion used in data selection. Those pi mesons produced locally but not accompanied by other particles would contribute to the observed intensity and have been included in the upper limit. This upper limit can be applied to each of the components contributing to the observed intensity and therefore is valid for the atmospheric intensity of singly occurring negative pi mesons in the momentum interval considered.

Although no negative particles were observed which could have been negative protons, the detection efficiency for such particles would probably be small because the energy released upon annihilation could produce secondaries penetrating the absorber.

B. Local Production of Mu Mesons

The preceding result can be used to set an upper limit on the local production of mu mesons. The fraction of pi mesons that decay in a distance x is given by $f=1-e^{-x/\gamma\beta\tau_0 c}$, where τ_0 is the proper mean lifetime, taken as 2.5×10^{-8} second. $\gamma\beta$ is the momentum of the pi meson in units of $m_\pi c$ and for this momentum interval has a mean value of about 8. The fraction of pi mesons in this momentum interval that decay in a distance of 1 meter is 0.016.

From the conservation of energy and momentum, it can be shown that pi mesons with momenta P_π decay to mu mesons with momenta P_μ in the interval $U_{\mu0}P_\pi-P_{\mu0}U_\pi<P_\mu<U_{\mu0}P_\pi+P_{\mu0}U_\pi$, where P_π and P_μ are in terms of $m_\pi c$ and $m_\mu c$. U_π is the energy of the pi meson in units of $m_\pi c^2$; $U_{\mu0}$ and $P_{\mu0}$ are the energy and momentum of a mu meson in the center-of-mass system of the parent pi meson. Only those pi mesons in the momentum interval 0.5–1.7 Bev/c can decay to mu mesons in the interval 0.4–1.0 Bev/c.

Applying the results of the previous section, it is found that the local production at sea level of mu mesons in the momentum interval 0.4–1.0 Bev/c is less than 8.8×10^{-5} particle/(cm² steradian hr meter).

C. Removal Path Length of Mu Mesons

In recent years many investigations have been made of the nuclear collisions of energetic mu mesons.[9–12] Most of these experiments have been conducted underground in order to reduce the number of events caused by nucleons and the soft component. Because of poor statistics and the diversity of techniques and event selection criteria only rough agreement is found among these experiments. The cross section for nuclear collisions (attributed to electromagnetic interaction) is found to be of the order of 10^{-29} cm²/nucleon.

The results of the present experiment can be used to set a lower limit on the removal path length of mu mesons. From Rossi's absolute mu meson momentum spectrum and the effective admittance and operation time, it is found that 10 300 mu mesons in the momentum interval 0.4–1.6 Bev/c passed through the apparatus during the effective time of the experiment. Taking 1.2 as the positive-negative ratio, the number of

[8] Camerini, Fowler, Lock, and Muirhead, Phil. Mag. **41**, 413 (1950).

[9] E. Amaldi and G. Fidecaro, Phys. Rev. **81**, 339 (1951).
[10] G. Cocconi and V. C. Tongiorgi, Phys. Rev. **84**, 29 (1951).
[11] E. P. George and P.T. Trent, Proc. Phys. Soc. (London) **A64**, 1134 (1951).
[12] Barrett, Bollinger, Cocconi, Eisenberg, and Greisen, Revs. Modern Phys. **24**, 133 (1952).

negative mu mesons in this momentum interval is 4700. Since none of these particles was absorbed in 147 g/cm² of lead the removal path length must be greater than 6.9×10^5 g/cm². The upper limit for the corresponding removal cross section is 2.4×10^{-30} cm²/nucleon. The statistical significance placed on these limits is the same as that placed on the previously determined upper limit for the intensity of pi mesons.

This result is more direct than the results obtained by the earlier experiments in the sense that no corrections have to be made for instrumental errors or for nuclear events produced by particles other than mu mesons, e.g., pi mesons and protons in equilibrium with the mu meson flux. However, it should be pointed out that the cross section corresponding to a removal path length refers only to those collisions in which a large fraction of the incident energy is distributed among several heavily ionizing particles.

PHYSICAL REVIEW VOLUME 92, NUMBER 2 OCTOBER 15, 1953

Polarization of Nuclei in Metals

ALBERT W. OVERHAUSER*
Department of Physics, University of Illinois, Urbana, Illinois
(Received June 25, 1953)

A new method for polarizing nuclei, applicable only to metals, is proposed. It is shown that if the electron spin resonance of the conduction electrons is saturated, the nuclei will be polarized to the same degree they would be if their gyromagnetic ratio were that of the electron spin. This action results from the paramagnetic relaxation processes that occur by means of the hyperfine structure interaction between electron and nuclear spins. A shift of the electron spin resonance due to the same interaction will occur for large amounts of polarization and should provide a direct indication of the degree of polarization.

I. INTRODUCTION

A NUMBER of methods[1] have been proposed for producing polarization or alignment of nuclear spins. A new method, applicable to the nuclei of atoms of a metallic solid, is made possible by the existence[2] of the electronic spin resonance from electrons in the conduction band. The interaction between the electron spin magnetic moment $\boldsymbol{\beta}_e$ and the nuclear spin magnetic moment $\boldsymbol{\beta}_n$ that is responsible for the polarizing action is that of the hyperfine coupling of an S state,[3]

$$H=-(8\pi/3)\boldsymbol{\beta}_e\cdot\boldsymbol{\beta}_n\delta(\mathbf{r}). \tag{1}$$

Here, $\delta(\mathbf{r})$ is a delta function of the relative coordinate of the electron and nucleus under consideration. The polarization is produced when the metallic sample, in a constant magnetic field $3\mathcal{C}_0$, is irradiated with a perpendicular microwave magnetic field, $2\mathcal{C}_1\cos\omega t$, of frequency such as to satisfy the electron spin resonance criterion,

$$h\omega=2\beta_e\mathcal{C}_0. \tag{2}$$

The metal is then in a nonequilibrium condition, and we shall show that the dynamical processes which tend to restore the system to its equilibrium state induce nuclear transitions via Eq. (1) in predominantly one direction, with a resulting steady state nuclear polarization. This action cannot be attributed to a large Boltzmann factor for the energy separations of adjacent nuclear magnetic states, and the spin-temperature concepts, familiar in the literature of magnetic resonance, do not apply.

The magnitude of the polarizing effect depends upon the degree to which the electron resonance can be saturated, and hence upon the microwave power available, the paramagnetic relaxation time, and the resonance line width. A number of spin relaxation processes have been studied by the writer in a paper,[4] hereafter referred to as A, and the methods used for those calculations will be followed here. We shall consider first the problem of resonance absorption in the electron spin system.

II. ELECTRON RESONANCE ABSORPTION

If a metal is placed in a magnetic field $3\mathcal{C}_0$, say in the z direction, the spin magnetic moments of the conduction electrons tend to line up parallel to the field. If N_+ and N_- are, respectively, the number of electrons per cc with spin up and down, the degree of bulk magnetization is proportional to the difference, $D=N_--N_+$, and the equilibrium value of D is

$$D_0=3N\beta_e\mathcal{C}_0/2\epsilon_f. \tag{3}$$

If, in addition, the metal is subjected to a perpendicular, alternating magnetic field, $2\mathcal{C}_1\cos\omega t$, of frequency such

* Now at the Department of Physics, Cornell University, Ithaca, New York.

[1] C. J. Gorter, Physica **14**, 504 (1948); M. E. Rose, Phys. Rev. **75**, 213 (1948); B. Bleaney, Proc. Phys. Soc. (London) **A64**, 315 (1951); R. V. Pound, Phys. Rev. **76**, 1410 (1949); A. Kastler, J. phys. et radium **11**, 255 (1950), Compt. rend. **233**, 1444 (1951).

[2] Griswold, Kip, and Kittel, Phys. Rev. **88**, 951 (1952).

[3] E. Fermi, Z. Physik **60**, 320 (1930).

[4] A. W. Overhauser, Phys. Rev. **89**, 689 (1953).

as to satisfy Eq. (2), the time variation of D is given by

$$dD/dt=(D_0-D)/T_1-\alpha D. \tag{4}$$

The first term in Eq. (4) is due to the relaxation processes that are effective in establishing the equilibrium degree of spin magnetization. A number of such processes have been studied in A, and the total relaxation can be described by a term of the above type with a characteristic relaxation time T_1. The second term is due to the alternating field, which tends to decrease the amount of magnetization since more transitions are induced from the spin state of greater population. The value of α can be derived by a simple calculation using time dependent perturbation theory and is given by

$$\alpha=4\pi\beta_e^2\mathfrak{IC}_1^2/hw. \tag{5}$$

Here, w is the integrated width of the resonance line. That is, if the shape of the resonance as a function of energy is given by $P(E)$, having a maximum value $P(E_0)$, then w is defined by the equation

$$wP(E_0)=\int_0^\infty P(E)dE.$$

After the alternating field has been turned on, a steady state will be reached such that $dD/dt=0$. A net rate of spin flips in one direction due to $\mathfrak{IC}_1$ will be balanced by a similar rate in the opposite direction due to relaxation interactions. Of these latter processes those due to Eq. (1) will bring about the nuclear polarization. From Eq. (4) the steady-state value of D is

$$D=D_0/(1+\alpha T_1). \tag{6}$$

In the limit of complete saturation of the resonance, large $\mathfrak{IC}_1$, $D\to 0$. It is convenient to define a parameter s which is 0 when there is no alternating field and is 1 for complete saturation:

$$s=1-(D/D_0). \tag{7}$$

From (6) we obtain

$$s=\alpha T_1/(1+\alpha T_1).$$

We shall see that the degree of nuclear polarization will be proportional to s, which is a function only of αT_1.

The electron spin resonance in lithium has been studied recently by Slichter,[5] using radio-frequencies and particles of the metal that were small compared to the skin depth. The resonance was found to be Lorentzian in shape. The width of the line between maximum slopes was 5 oersteds, corresponding to a transverse relaxation time T_2 of 10^{-8} sec. The relaxation time T_1 was measured by the method of saturation and found to be 10^{-8} sec. Thus, the expected agreement between T_1 and T_2 for conduction electrons was confirmed.

[5] C. P. Slichter, private communication.

For a Lorentzian line the integrated width w is given by

$$w=\pi h/T_2.$$

The fractional saturation can then be written:

$$s=\gamma_e^2\mathfrak{IC}_1^2T_1T_2/(1+\gamma_e^2\mathfrak{IC}_1^2T_1T_2). \tag{8}$$

Here, we have replaced $2\beta_e/h$ by γ_e, the gyromagnetic ratio of the electron spin. From Eq. (8) we see that appreciable saturation results only if

$$\gamma_e^2\mathfrak{IC}_1^2T_1T_2\sim 1.$$

The amplitude of the microwave field that is necessary to saturate the resonance is inversely proportional to the relaxation times, and at room temperature $\mathfrak{IC}_1$ must be of the order of 5 oersteds. At liquid helium temperature $\mathfrak{IC}_1$ need be less, perhaps, if T_1 and T_2 are correspondingly longer. The shortest relaxation time that was found in A, due to the spin-current interaction, was inversely proportional to the absolute temperature. However, the observed relaxation time is smaller by a factor of 100 than the value given by theory. An important relaxation mechanism has probably been overlooked, so that the correct temperature dependence of T_1 is as yet unknown.

III. PRODUCTION OF NUCLEAR POLARIZATION

The nuclear polarization that results when $s>0$ can be derived most easily from the results of Sec. IV of A, where the paramagnetic relaxation due to the hyperfine interaction (1) was studied. These calculations made use of the assumption that $\beta_e\mathfrak{IC}_0/\kappa\theta\ll 1$, but we shall show later that the results of interest here remain unaltered if this approximation is not used. The variation of D with time, (A31), was found to be

$$(dD/dt)'=(D_0-D)/T_1'+G(\Delta_0-\Delta)/T_n'. \tag{9}$$

The "prime" is used here to denote quantities that are associated with the hyperfine interaction. Thus, T_1' and T_n' are the electronic and nuclear relaxation times due to this interaction. The difference in population between adjacent nuclear magnetic levels is Δ, whose equilibrium value in the field $\mathfrak{IC}_0$ is

$$\Delta_0=Nh\gamma_n\mathfrak{IC}_0/(2I+1)\kappa\theta. \tag{10}$$

The quantity G is the constant of proportionality between the total excess z component of nuclear spin and $\frac{1}{2}\Delta$, and is

$$G=\tfrac{2}{3}I(I+1)(2I+1).$$

Since Eq. (1) conserves the total spin angular momentum, we have

$$(dD/dt)'=G(d\Delta/dt)'.$$

Equation (9) can then be written

$$(d\Delta/dt)'=(\Delta_0-\Delta)/T_n'+(D_0-D)/GT_1'. \tag{11}$$

If we assume, temporarily, that the only interaction

through which Δ is allowed to change is Eq. (1), the steady-state condition corresponds to Eq. (11) being zero. The steady-state value of Δ, with the use of Eq. (7), is then

$$\Delta=\Delta_0+sD_0T_n'/T_1'G. \tag{12}$$

Now, the ratio T_n'/T_1' from (A34) is

$$T_n'/T_1'=8I(I+1)\epsilon_f/9k\theta.$$

On using this result together with Eqs. (3) and (10), Eq. (12) becomes

$$\Delta=\frac{N\hbar\mathcal{H}_0}{(2I+1)k\theta}(\gamma_n+s|\gamma_e|). \tag{13}$$

We see, therefore, that the steady-state nuclear polarization is larger by an amount that would be expected if the nuclear gyromagnetic ratio were increased by $s|\gamma_e|$. If s is near unity, an enhanced polarization by a factor of about 2000 should result.

If there are interactions other than Eq. (1) which also produce nuclear magnetic relaxation, so that the total nuclear relaxation time is T_n, we must consider the total variation of Δ with time:

$$d\Delta/dt=(\Delta_0-\Delta)/T_n+(D_0-D)/GT_1'.$$

This equation must be set equal to zero instead of Eq. (11), and we find, similarly, that the polarization is as though the nuclei had an effective gyromagnetic ratio

$$\gamma_{\text{eff}}=\gamma_n+s(T_n/T_n')|\gamma_e|. \tag{14}$$

This equation expresses the general result, which has been reported earlier.[6] It should be appreciated that other electronic relaxation processes, of which there are many,[4] do not affect the polarizing action other than in making the electron resonance more difficult to saturate. The nuclear relaxation processes have been studied theoretically by Korringa[7] and experimentally by a number of workers. The results indicate that Eq. (1) is the important relaxation interaction, so that T_n/T_n' is close to unity.

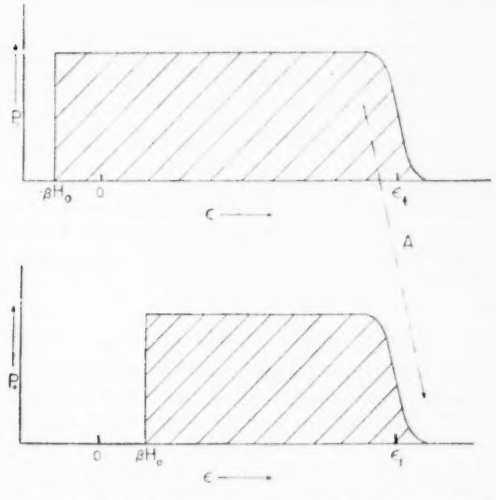

FIG. 1. Schematic diagram of the Fermi distributions of the two spin states in equilibrium.

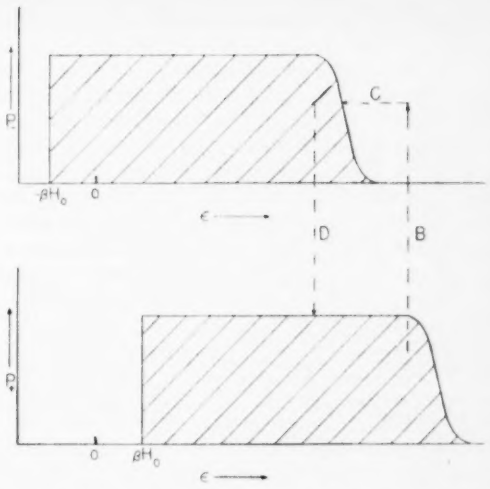

FIG. 2. Schematic diagram of the Fermi distributions of the two spin states for complete saturation.

The foregoing derivation gives little insight into the physical reasons why such a polarizing effect takes place. To understand this action one may consider the conduction band as consisting of two Fermi distributions, one for the electrons with spin up and the other for the electrons with spin down. Two such distributions are shown schematically in Fig. 1, where the occupation probability is plotted as a function of the energy of the electronic state, including the magnetic energy in the field $\mathcal{H}_0$. The equilibrium distributions are shown in Fig. 1, so that the Fermi energies are equal, and there is an excess number of electrons in the spin down distribution, corresponding to a net magnetization in the field direction. If the oscillating field is turned on, transitions represented by the arrow A will predominate, so that the number of electrons in each distribution will tend to be equalized. If the electron resonance is completely saturated, the two distributions will appear as in Fig. 2 and will have equal numbers of electrons. We need consider now only those relaxation processes due to the hyperfine interaction and which flip over nuclear spins. Such a process is represented by the vertical arrow B in Fig. 2, which corresponds to an electron spin being flipped down, so that a nuclear spin is flipped upwards. As was shown in A, the characteristic time of such processes is about 10^{-4} sec. As soon as the transition B has taken place, the electron will

[6] A. W. Overhauser, Phys. Rev. **91**, 476 (1953).

[7] J. Korringa, Physica **16**, 601 (1950).

undergo transitions into the surface of the Fermi distribution such as is represented by the arrow C. Such transitions are due to interactions with the lattice, familiar in the theory of electrical conductivity, and have a characteristic time of 10^{-13} sec. Transitions that flip nuclear spins in the reverse direction are represented by the arrow D in Fig. 2 and are forbidden because the final states are already occupied. The polarizing action takes place, therefore, because nuclear spins are flipped over in predominantly one direction by the relaxation processes due to Eq. (1) and cannot return. Actually, the reverse processes occur to some extent because the surfaces of the Fermi distributions are finite in width and have exponential tails. As can be seen from Eq. (14), the rates in the two directions must be so balanced that the excess polarization obeys Curie's law if $s(T_n/T_n')$ is kept constant.

A convenient definition for the degree of nuclear polarization $\mathcal{P}$ is the quotient of the z component of nuclear spin and the maximum possible value. Thus

$$\mathcal{P}=\left|\sum_{m=-I}^{I} me^{m\mu}\right| \Big/ \left(I\sum_{m=-I}^{I} e^{m\mu}\right), \tag{15}$$

where the ratio of the populations of adjacent magnetic states is

$$M_m/M_{m-1}=e^{\mu}. \tag{16}$$

We have shown that μ is given by

$$\mu=[\gamma_n+s(T_n/T_n')|\gamma_e|]\hbar\mathcal{H}_0/\kappa\theta, \tag{17}$$

but only if $\beta_e\mathcal{H}_0\ll\kappa\theta$ (so that $\mu\ll 1$), since this approximation was used in the derivation of Eq. (9).

In order to obtain a large degree of polarization, $\mathcal{P}$ near 1, μ must be of the order of magnitude of unity or greater, and we must now establish that Eq. (16) remains valid for larger μ. To do so we shall assume that interactions of the form (1) are the only source of nuclear relaxation, and hence that $T_n/T_n'=1$. We consider first the special case $I=\frac{1}{2}$ and calculate the number of nuclei per second $W_{+,-}$ flipped from the state $m=-\frac{1}{2}$ to the state $m=+\frac{1}{2}$. This quantity is given by (A29), and the indicated integration can be performed by elementary methods and yields

$$W_{+,-}=M_{-1/2}\mu/[2(1-e^{-\mu})T_n'].$$

Similarly, the number of nuclei flipped per second from $m=+\frac{1}{2}$ to $m=-\frac{1}{2}$ can be calculated and is

$$W_{-,+}=M_{+1/2}\mu/[2(e^{\mu}-1)T_n'].$$

When a steady state is established, $W_{+,-}$ and $W_{-,+}$ must be equal, and we find

$$M_{+1/2}/M_{-1/2}=e^{\mu}.$$

Thus, Eq. (16) is obtained as an exact result, with

$$\mu=(\gamma_n+s|\gamma_e|)\hbar\mathcal{H}_0/\kappa\theta.$$

The generalization required for $I>\frac{1}{2}$ is trivial. It is sufficient to calculate $W_{m,m-1}$ and $W_{m-1,m}$ and to observe that Eq. (16) is the condition that they be equal. If there are other nuclear relaxation processes, one can show that Eq. (16) is a good approximation, with μ given by Eq. (17), if T_n/T_n' is not too much smaller than 1.

In order to illustrate the degree of polarization that should be possible by this technique, consider the following example: $I=\frac{3}{2}$, $\mathcal{H}_0=10^4$ oersteds, $\theta=2°\mathrm{K}$, and $s=0.8$. One finds $\mu=0.54$, and Eq. (15) gives a value of 42 percent for the polarization. The electron resonance for this case would require microwaves in the 1-cm region.

It may be asked why the effect which we have described can occur only in metals, since the hyperfine interaction that is responsible certainly exists in other paramagnetic materials. The basic reason is that electrons in an unfilled band can change energy by small amounts, $\sim\kappa\theta$, by small changes in momentum or wave number. This freedom is necessary in order that energy be conserved during the simultaneous spin flip of an electron and a nucleus. In nonmetals, where the valence bands are full or, alternatively, where bound state wave functions are more appropriate, small energy changes necessary to compensate for jumps in magnetic energy can be taken up only by the emission, absorption, or scattering of phonons, and these processes do not couple electron and nuclear spins.

IV. ELECTRON RESONANCE SHIFT

The hyperfine interaction gives rise to a nuclear resonance shift in metals. This shift, first observed by Knight,[8] can be described as the effect of an extra magnetic field at the nucleus due to the feeble spin paramagnetism of the conduction electrons, which interact with the nucleus according to Eq. (1). A similar change in the electron-spin resonance will occur if there is an appreciable degree of nuclear polarization. Thus, the energy of an electron spin in the presence of a field $\mathcal{H}_0$ and the N nuclei per cc of metal is

$$H=-\boldsymbol{\beta}_e\cdot[\boldsymbol{\mathcal{H}}_0+(8\pi/3)|\psi(0)|^2\textstyle\sum\boldsymbol{\beta}_n].$$

Here, $|\psi(0)|$ is the magnitude of the wave function at the nucleus, normalized in 1 cc, of a conduction electron. Since the nuclear spins will be polarized in the direction of $\mathcal{H}_0$, the second term in Eq. (18) can be represented as an extra magnetic field parallel to $\mathcal{H}_0$ and of magnitude

$$\Delta\mathcal{H}=\mathcal{P}(\Delta\mathcal{H})_0, \tag{18}$$

where $(\Delta\mathcal{H})_0$ is the maximum value, for 100 percent nuclear polarization, and is given by

$$(\Delta\mathcal{H})_0=(8\pi/3)|\psi(0)|^2N\beta_n. \tag{19}$$

This shift can be relatively large, and the value of Eq. (19) for Li^7 is 217 oersteds. $|\psi(0)|^2$ was taken to be 34, a value based on the calculations of Kohn and

[8] W. D. Knight, Phys. Rev. **76**, 1259 (1949).

Bloembergen.[9] This effect will be even larger for other metals and will complicate the procedure for producing large amounts of polarization.

A more favorable feature of the electron resonance shift is that it should provide, in principle, a direct measurement of the degree of polarization obtained. For example, if one were to apply the microwave power, the resonance line would be shifted towards higher frequencies, or for fixed frequency, towards lower magnetic fields. The field would then have to be decreased gradually to a critical value at which maximum polarization is reached. Beyond this value the resonance would be lost suddenly, and the line would snap back to its original, low microwave power position. The polarization Φ is related to the critical shift by Eq. (18) and could be maintained by operating on the high field side of the resonance. For nuclei having a negative gyromagnetic ratio this shift would be in the opposite direction, since these nuclei will at first be depolarized and then lined up in the opposite direction by the action of the relaxation processes.

V. CONCLUSION

Within the framework of the single particle model an enhanced nuclear polarization is predicted as the result of relaxation processes that occur when the electron-spin resonance is saturated. The possibility of producing large amounts of polarization by this technique is of great experimental interest, although the problems that would have to be solved are by no means trivial. Microwaves in the 1-cm range are appropriate, and considerable power may be needed, depending upon the value of the electronic relaxation time at liquid helium temperature. In order to avoid eddy current losses as well as excessive breadth of the electron resonance,[2] it would be necessary to use finely divided metallic samples of particle size somewhat smaller than a micron. The use of chemically impure samples to increase the electrical resistivity at low temperatures would be helpful in this regard.

In nuclear resonance experiments the signal strength is proportional to the degree of nuclear polarization, which is ordinarily quite small. Such nuclear resonances would be enhanced by several orders of magnitude if the electron resonance were saturated simultaneously. This interdependence could be used as a means for detecting the electron resonance. Other effects would be a disappearance of the nuclear resonance shift at high saturation and a decrease in the dipolar broadening of the nuclear line for large polarizations.

[9] W. Kohn and N. Bloembergen, Phys. Rev. **82**, 263 (1951).

PHYSICAL REVIEW VOLUME 92, NUMBER 2 OCTOBER 15, 1953

Effects of the Geomagnetic Field on Solar Cosmic Rays

V. SARABHAI AND R. P. KANE
Physical Research Laboratory, Ahmedabad, India

(Received June 2, 1953)

The force acting on a charged solar cosmic ray due to the action of the geomagnetic field has been analyzed in terms of its components along the E-W, the N-S, and the vertical directions. With certain simplifying assumptions, the relative magnitudes of these components and their directions have been determined for specific values of the geographic latitude λ of the place of observation as well as the declination δ and the hour angle t of the sun. The deflection that can be produced in the trajectories of solar cosmic rays is qualitatively discussed in terms of the resulting changes which may be expected in the hour of maximum of the diurnal variation of cosmic rays assumed to be due to particles from the sun. It appears that the hour of maximum should become later with increase of latitude. In a northern latitude, a north-pointing cosmic-ray telescope should reveal a diurnal variation with an earlier maximum than a south-pointing telescope. There is a possibility therefore of being able to interpret the experimental results of directional studies of the diurnal variation of cosmic rays in terms of geomagnetic effects.

INTRODUCTION

EVIDENCE[1–5] has been accumulating recently indicating that the sun continuously emits cosmic rays. These rays are believed to be responsible for a daily variation in the pressure-corrected meson intensity measured in the lower atmosphere. The variation has a predominant 24 hourly harmonic component whose amplitude may be designated by M^D. The hour of maximum of the diurnal component can be expressed in terms of the angle $M\phi^D$ made by the radius vector of M^D with respect to midnight on a 24 hourly harmonic dial representation. In general, $M\phi^D$ is different from π as the maximum does not coincide with the local noon of the place of observation. This is believed to be due to the effect of the geomagnetic field on charged solar cosmic rays.

[1] Simpson, Fonger, and Wilcox, Phys. Rev. **85**, 366 (1952).
[2] H. V. Neher and S. E. Forbush, Phys. Rev. **87**, 889 (1952).
[3] Sarabhai, Desai, and Kane, Nature **171**, 122 (1953).
[4] Sarabhai, Desai, and Kane, Proc. Indian Acad. Sci. **A37**, 287 (1953).
[5] V. Sarabhai and R. P. Kane, Phys. Rev. **90**, 204 (1953).

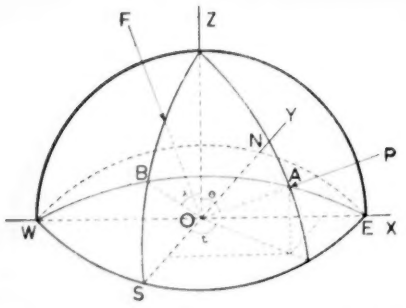

FIG. 1. Diagram showing the orientation of the initial momentum P of a solar cosmic ray and of the geomagnetic force F with respect to the E–W and N–S directions at a place in the northern hemisphere.

Considerable attention has been devoted in the past towards a theoretical understanding of the geomagnetic effects of cosmic rays. The main experimental facts that were sought to be explained concern the change of cosmic-ray intensity with latitude, longitude, zenith angle, and azimuth. The Lemaitre-Vallarta[6] theory, based on the equations of motion set out by Störmer in connection with the aurora borealis, has given a satisfactory explanation of the experimental observations. This theory, which uses Liouville's theorem, postulates an isotropic distribution of cosmic-ray primaries at great distances from the magnetic dipole. We cannot thus apply it for explaining the effects produced by the geomagnetic field on nonisotropic rays such as those coming from the sun.

Through extensive and laborious calculations involving numerical integration of the differential equations of motion, several workers, notably Störmer[7] and Lemaitre and Vallarta, have traced the orbits of charged particles directed from infinity towards a magnetic dipole. Brüche[8] and Malmfors[9] have studied the same in laboratory experiments, and Malmfors has discussed the implications of these results on the diurnal variation of intensity. However, no study appears to have been made specifically on the geomagnetic effects of solar cosmic rays, nor on the changes that could take place by such effects in the diurnal variation assumed to be caused by solar cosmic rays.

TABLE I. Components of P and F which produce deflection of the trajectory of a positively charged solar cosmic ray in the northern hemisphere when the sun is in the southern sky.

	Component of P	Component of F	Component of R	Deflection
1	P_{+z}	F_{+y}	R_{+x}	Eastwards
2	P_{+y}	F_{-x}	R_{-x}	Westwards
3	(a) Before noon P_{-x}	F_{-z}	R_{-y}	Southwards
	(b) Afternoon P_{+x}	F_{-z}	R_{+y}	Northwards
4	(a) Before noon P_{-z}	F_{+y}	R_{-z}	Downwards
	(b) Afternoon P_{+z}	F_{+y}	R_{+z}	Upwards

[6] G. Lemaitre and M. S. Vallarta, Phys. Rev. **43**, 87 (1933).
[7] C. Störmer, Astrophys. Norvegica **2**, No. 1 (1936).
[8] E. Brüche, Terr. Mag. Atmos. Elec. **36**, 41 (1931).
[9] K. G. Malmfors, Arkiv. Mat. Astron. Fysik **32A**, No. 8 (1945).

If we wish to study the effect of the earth's magnetic field on $M\phi^D$, we are not as much interested in estimating the minimum momentum of allowed particles, as in the direction and magnitude of the deflections of the trajectories of solar cosmic rays that reach the earth at any point. It is possible by elementary considerations to examine the force that deflects the trajectories of solar particles in different latitudes at different hours and seasons. We show in this communication how such an analysis enables us to understand qualitatively, in terms of solar cosmic rays, some features of the meson diurnal variation which have hitherto proved difficult to interpret.

TABLE II. Values of (R_x/Pk) for specific values of λ, δ and $\pm l$.

	$\delta=0$			$\delta=-23.5°$			$\delta=+23.5°$		
λ \ l	$\pm\pi/2$	$\pm\pi/4$	0	$\pm\pi/2$	$\pm\pi/4$	0	$\pm\pi/2$	$\pm\pi/4$	0
80	0	−1.35	−1.88				0.07	−1.11	−1.53
60	0	−0.98	−1.28			−1.67	0.17	−0.57	−0.63
40	0	−0.35	−0.23		−0.69	0.79	0.20	0.01	0.38
20	0	0.27	0.67		0.02	0.22	0.13	0.38	0.98
00	0	0.71	1.00	0	0.65	0.92	0	0.65	0.92
−20	0	0.27	0.67	0.13	0.38	0.98		0.02	0.22
−40	0	−0.35	−0.23	0.20	−0.01	0.38		−0.69	−0.79
−60	0	−0.98	−1.28	0.17	−0.57	−0.63			−1.67
−80	0	−1.35	−1.88	0.07	−1.11	−1.53			

FORCE DUE TO THE ACTION OF THE GEOMAGNETIC FIELD

For an elementary treatment, we only consider trajectories of solar cosmic rays of large enough "stiffness" so that after interaction with the field and on arrival on the surface of the earth, the initial components of the velocity of the particles in the vertical, the N–S and the E–W directions do not suffer a reversal of sign. We thereby exclude from consideration all cosmic rays of low momenta which are considerably deflected by the geomagnetic field. We also restrict ourselves to daylight hours when the sun is above the horizon. For the sake of simplification, we neglect the eccentricity of the geomagnetic dipole and the inclination of its axis with respect to the axis of rotation of the earth.

For any point 0 at geographic latitude λ, we can set up coordinate axes so that $+X$ points to the east, $+Y$ points to the north and $+Z$ points vertically upwards to the zenith. If 0 lies in the northern hemisphere at a latitude of about 50°N, Fig. 1 shows the orientation of the geomagnetic field F and the momentum P of a solar cosmic ray at equinox, before interaction with the field. The field F lies wholly in the meridian plane through 0 and has the component F_{-z} (or V) vertically downwards in the direction $-Z$, and F_{+y} (or H) pointing north. With the rotation of the

earth from west to east, the sun appears to move along the arc $EABW$ in the southern sky, crossing the meridian plane at B at noon. At all times of the day, the momentum of the particle has the components P_{+y} towards north and P_{-z} vertically downwards. Along the X axis, it has a component P_{-x} towards west before noon, and P_{+x} towards east in the afternoon. If, as a result of the geomagnetic field, a force R acts on the particle, one can consider its components along the coordinate axes in terms of the appropriate components of F and P.

Table I summarizes, for a positively charged solar cosmic ray, the components of force R that produce deflections of the trajectory in the east or west direction, the north or south direction and the vertically upward or downward direction. Since F has no component along the X axis, the components of P have effective interactions only with F_{+y} and F_{-z}. The indicated directions for the deflections are applicable to the northern hemisphere when the sun is in the southern half of the sky.

TABLE III. Values of (R_y/Pk) for specific values of λ, δ and $+t$ (in the afternoon). For the forenoon when t is negative, all signs in the table get reversed.

λ \ t	$\delta=0$			$\delta=-23.5°$			$\delta=+23.5°$		
	$\pi/2$	$\pi/4$	0	$\pi/2$	$\pi/4$	0	$\pi/2$	$\pi/4$	0
80	1.96	1.37	0				1.80	1.20	0
60	1.74	1.15	0			0	1.63	0.91	0
40	1.28	0.76	0		0.88	0	1.24	0.59	0
20	0.68	0.35	0		0.42	0	0.67	0.32	0
00	0	0	0	0	0	0	0	0	0
−20	−0.68	−0.35	0	−0.67	−0.32	0		−0.42	0
−40	−1.28	−0.76	0	−1.24	−0.59	0		−0.88	0
−60	−1.74	−1.15	0	−1.63	−0.91	0			0
−80	−1.96	−1.37	0	−1.80	−1.20	0			

It will be noticed that along the E–W axis, there are in general two component forces R_{+x} and R_{-x} of opposite sign, which act simultaneously on the particle. Along the N–S axis or the vertical axis only one component operates at any moment; but along these axes the forces get reversed in direction as the sun crosses the meridian plane at noon.

EVALUATION OF COMPONENTS OF THE FORCE

The components of the geomagnetic field F are given by

$$F_x=0, \quad F_y=k\cos\lambda \quad \text{and} \quad F_z=2k\sin\lambda, \tag{1}$$

where $k=(M/r^3)$. M is the magnetic moment of the earth and r is the distance of the point 0 from the center of the earth. F_z is directed downwards in the northern hemisphere but upwards in the southern hemisphere.

The angular zenith distance θ of the sun is given by

$$\cos\theta=\cos\delta\cos\lambda\cos t+\sin\delta\sin\lambda, \tag{2}$$

where δ is the declination of the sun and t is the hour angle of the sun measured from noon. δ takes the values 0, $+23.5°$, and $-23.5°$ at the equinoxes, the summer solstice, and the winter solstice, respectively.

TABLE IV. Values of (R_x/Pk) for specific values of λ, δ and $+t$ (in the afternoon). For the forenoon when t is negative, all signs in the table get reversed.

λ \ t	$\delta=0$			$\delta=-23.5°$			$\delta=+23.5°$		
	$\pi/2$	$\pi/4$	0	$\pi/2$	$\pi/4$	0	$\pi/2$	$\pi/4$	0
80	0.17	0.12	0				0.16	0.10	0
60	0.50	0.33	0			0	0.47	0.26	0
40	0.77	0.46	0		0.53	0	0.74	0.36	0
20	0.94	0.50	0		0.58	0	0.93	0.44	0
00	1.00	0.50	0	1.00	0.54	0	1.00	0.54	0
−20	0.94	0.50	0	0.93	0.44	0		0.58	0
−40	0.77	0.46	0	0.74	0.36	0		0.53	0
−60	0.50	0.33	0	0.47	0.26	0			0
−80	0.17	0.12	0	0.16	0.10	0			

The three components of the momentum P of the particle are

$$\begin{aligned} P_x&=P\sin t\sin\theta,\\ P_y&=P\cos t\sin\theta,\\ P_z&=P\cos\theta. \end{aligned} \tag{3}$$

Hence, for any momentum P, the components of the deflecting force R due to geomagnetic interaction are

$$\begin{aligned} R_x&=P_zF_y-P_yF_z,\\ R_y&=P_xF_z,\\ R_z&=P_xF_y. \end{aligned} \tag{4}$$

These equations can be used for evaluating the values of R_x, R_y, and R_z for different values of λ, δ, and t.

Tables II, III, and IV indicate relative values of the components of force R along the X, Y, and Z axes respectively for different latitudes, at equinoxes and at the solstices, at 0600, 0900, 1200, 1500, and 1800 hours local time.

It is seen from Table II that at noon R_x has a maximum positive value at the latitude where the sun is directly overhead. With change of latitude either towards the north or the south, R_x first decreases, then reverses in sign and becomes increasingly negative as the polar regions are approached. At equinoxes, the reversal of the sign of R_x takes place at $\lambda=37°$ in both hemispheres. Expressed differently, it can be stated that solar cosmic rays have a force acting on them in the E–W direction which is such that in low latitudes the particles are deflected towards east and in higher latitudes towards west.

Changes in R_y, the force along the N–S direction, are seen from Table III. In the northern hemisphere, during daylight hours before noon, R_y is negative and the particles are deflected towards south. In the afternoon, R_y is positive and the particles are deflected towards north. In the southern hemisphere, the sign of R_y gets altered and in consequence, during morning hours, the particles get deflected towards north, and during the afternoon towards south. In both hemispheres, the magnitude of R_y increases with latitude.

TABLE V. Values of (R/Pk) for specific values of λ, δ, $\pm t$.

λ \ t	$\delta=0$			$\delta=-23.5°$			$\delta=+23.5°$		
	$\pm\pi/2$	$\pm\pi/4$	0	$\pm\pi/2$	$\pm\pi/4$	0	$\pm\pi/2$	$\pm\pi/4$	0
80	1.97	1.93	1.88				1.81	1.64	1.53
60	1.81	1.55	1.28			1.67	1.71	1.10	0.63
40	1.49	0.95	0.23		1.24	0.79	1.46	0.69	0.38
20	1.16	0.67	0.67		0.72	0.22	1.15	0.66	0.98
00	1.00	0.87	1.00	1.00	0.84	0.92	1.00	0.84	0.92
−20	1.16	0.67	0.67	1.15	0.66	0.98		0.72	0.22
−40	1.49	0.95	0.23	1.46	0.69	0.38		1.24	0.79
−60	1.81	1.55	1.28	1.71	1.10	0.63			1.67
−80	1.97	1.93	1.88	1.81	1.64	1.53			

The value of the force R_z in the vertical direction is shown in Table IV. At all places, during the hours before noon, R_z is negative and there is a downward deflection of the particles. In the afternoon there is an upward deflection. The force is most pronounced in low latitudes and becomes progressively weaker with increase of latitude.

The magnitude of the total force R acting on a solar cosmic ray is shown in Table V. During the hours near noon, R has a minimum value at an intermediate latitude between 20° and 50°, depending on the season. It has a maximum value in polar latitudes.

THE HOUR OF MAXIMUM OF THE DIURNAL VARIATION

It has been stated earlier that if solar cosmic rays are responsible for the diurnal variation of meson intensity, the displacement of the hour of maximum $M\phi^D$ from noon is an indication of geomagnetic effects on the charged particles of the primary radiation. Effects which deflect the trajectories towards east would result in a maximum earlier than noon. Hence $M\phi^D$ would be less than π. For a deflection towards west, $M\phi^D$ would be greater than π on account of the maximum occurring in the afternoon. Besides, deflections occurring in the N–S direction or the vertical direction which change in magnitude and sense at different times of the day, could also alter the number of solar cosmic rays that are registered by an apparatus at any particular time. Thus, an ionization chamber can record a larger number of solar cosmic rays during the morning than in the afternoon on account of the vertical force acting on the particles. This would in effect tend to produce an earlier maximum and a decrease of $M\phi^D$.

Before one can draw conclusions concerning the change of $M\phi^D$ that can be expected, it is necessary to consider the stiffness (P/z) on which depends the curvature of a trajectory of a particle of momentum P and charge "z." The mean momentum $\bar{P}$ of primary particles whose secondaries are measured by the apparatus, changes with latitude and elevation of the station and with inclination of the sun during the day on account of alteration of the atmospheric path length for solar cosmic rays. $\bar{P}$ can also depend on the absorber used with the apparatus. It is difficult to estimate changes of $\bar{P}$ with latitude, elevation, and time as the true path length in the atmosphere depends on the direction of incidence of a deflected trajectory and not on one along an optical path from the sun. Therefore, unless the trajectories are calculated, one cannot proceed far on quantitative lines. Broadly speaking, it is nevertheless possible to consider that the stiffness increases with increase of latitude, but decreases with increase of elevation of the place of observation or with proximity to noon local time.

Taking into consideration the change of stiffness and of R_x and R_z, one expects that the hour of maximum would become later with increase of latitude and the geomagnetic effects should get magnified at high elevations.

(a) The Latitude Dependence of $M\phi^D$

Experimental evidence on this point is meager. It is obviously necessary to compare only those results which have been obtained under similar experimental conditions and where similar corrections are applied to the data. The Carnegie Institution studies at Huancayo, Christchurch, Cheltenham, and Godhavn as reported by Lange and Forbush,[10] furnish the most reliable data for this purpose. The mean diurnal variation for the period 1939 to 1946 has hours of maximum at the different stations as shown in Table VI. It will be noticed that there is qualitative agreement with our expectation concerning $M\phi^D$ at low and high latitudes.

TABLE VI. Latitude dependence of $M\phi^D$.

Station	Geo. lat.	Geomag. lat.	Elevation	$M\phi^D$
1 Huancayo	12°S	1°S	3350 m	$\pi-15°$
2 Christchurch	43°S	49°S	0	$\pi+41°$
3 Cheltenham	39°N	50°N	0	$\pi+38°$
4 Godhavn	69°N	80°N	0	$\pi+36°$

In the past, the occurrence of a maximum much later than noon at stations in high latitudes has been difficult to understand, for it was thought that positive solar cosmic rays can only be deflected towards the east. If a deflection towards the west at higher latitudes is indeed responsible for a maximum in the afternoon, the change of $M\phi^D$ with variation of stiffness at any particular latitude should take place in opposite directions at low and high latitudes. The stiffness can decrease with elevation, or there can be long term changes in the mean momentum of primary solar cosmic rays. For change of either kind, an increase of stiffness would displace the maximum nearer noon. Thus at low latitudes, $M\phi^D$ which is less than π, would increase and at high latitudes, $M\phi^D$ which is greater than π, would decrease.

This leads us to a new and a serious difficulty. We have shown elsewhere[5] by an examination of the Carnegie data that long-term changes of $M\phi^D$ are

[10] I. Lange and S. E. Forbush, Carnegie Inst. Wash. Publ. **175** (1948).

similar at all stations. If these are due to changes in the mean momentum of primary rays, we shall have to look elsewhere for an explanation of the late maxima that have been observed at stations in medium and high latitudes.

In connection with the latitude dependence of $M\phi^D$, Hogg's[11] data without external temperature correction and obtained with an ionization chamber at Canberra, are probably comparable with the Carnegie data. For $\lambda = 35°$S and geomagnetic latitude 45°S, we have for the years 1936 to 1940 a mean $M\phi^D = \pi + 38°$. This agrees well with the hour of maximum at Cheltenham, Christchurch, and Godhavn.

Thompson[12] has attempted to survey the change of the diurnal variation with change of latitude, in the Pacific. Thompson's data extend over a large range of latitudes but cover a very short period of time in each belt of latitude. He has reported that the amplitude and hour of maximum of the diurnal variation do not change significantly with latitude. However, we are inclined not to attach much weight to this result which is in contradiction to the Carnegie results of much greater reliability.

Geiger counter studies with vertically pointing telescopes have been made in London by Duperier[13] and by workers of our group[3,4] at Ahmedabad and Kodaikanal. Though the studies at London and in India have not been carried out with apparatus of identical design, the change of $M\phi^D$ follows broadly the pattern of the Carnegie studies.

(b) Directional Dependence of $M\phi^D$

We have discussed earlier the change in the sign of R_y, the force along the N–S direction, as the sun crosses the meridian plane. An important consequence of this is that in the northern hemisphere during the morning, solar cosmic rays would be preferentially recorded by a north-pointing telescope. However, in the afternoon, the rays would be preferentially recorded by a south-pointing telescope. Thus, the N telescope would show an earlier maximum of intensity than a S telescope and $(M\phi^D)_N$ should be less than $(M\phi^D)_S$. These conditions are expected to interchange in the southern hemisphere.

The directional studies of Alfven and Malmfors[14] at Stockholm, of Kolhörster[15] at Berlin, and of Elliot and Dolbear[16] at Manchester exhibit between the N and S telescopes just the type of difference in $M\phi^D$ that is expected qualitatively from the above considerations. At Stockholm, the difference in $M\phi^D$ in the two directions is about 80° as compared to the much smaller difference of about 28° at Manchester. This may result at least partly, from a larger value of R_y at the former place due to a higher latitude. Detailed comparison is however difficult because of dissimilarities in the telescopes used at the two stations. No experimental results are available from high southern latitudes, but it would be worthwhile to test if $(M\phi^D)_S$ is less than $(M\phi^D)_N$ as predicted here.

DISCUSSION

The most unsatisfactory aspect of the present analysis of the effect of the geomagnetic field on solar cosmic rays is that we neglect the contribution of particles of low momenta which suffer the greatest deflection. However, the qualitative analysis that is made here under a number of simplifying assumptions suggests a geomagnetic interpretation for the rather puzzling results of directional cosmic-ray studies.

We have earlier[4] expressed the view that the N–S difference curve may indicate little more than an arithmetic difference between the daily variation caused by secondaries of anisotropic cosmic rays measured in the N and S directions. Since a possibility has been shown here of explaining the observed facts in terms of geomagnetic effects, we might perhaps be able to get over the difficulties of the interpretation proposed by Elliot and Dolbear[17] wherein there is the necessity of a magnetic field in the space surrounding the sun.

It is now clearly necessary to pursue rigorously the theoretical problem of the geomagnetic effects on charged solar cosmic rays in order to get a fundamental insight into the daily variation of cosmic rays.

We are grateful to Professor K. R. Ramanathan for helpful discussions. One of us (R.P.K.) is indebted to the Atomic Energy Commission of India for financial support.

[11] A. R. Hogg, Mem. Commonwealth Observatory, Canberra, No. 10 (1949).
[12] J. L. Thompson, Phys. Rev. **54**, 93 (1938).
[13] A. Duperier, Proc. Phys. Soc. (London) **57**, 468 (1945).
[14] H. Alfven and K. G. Malmfors, Arkiv. Mat. Astron. Fysik **29A**, No. 24 (1943).
[15] W. Kolhörster, Physik. Z. **42**, 55 (1941).
[16] H. Elliot and D. W. N. Dolbear, Proc. Phys. Soc. (London) **A63**, 137 (1950).
[17] H. Elliot and D. W. N. Dolbear, J. Atmos. Terr. Phys. **1**, 205 (1951).

Bremsstrahlung and Electron Scattering Cross Sections in Au for 247-Mev Electrons and Positrons*

PHILIP C. FISHER†
University of Illinois, Urbana, Illinois
(Received June 29, 1953)

The absolute cross sections for gold for the top 40 percent of the bremsstrahlung spectrum have been measured for electrons and positrons of 247-Mev mean energy. A magnetic cloud chamber containing two Au foils was used. The foils were positioned to intercept an electron or alternately a positron beam provided by a magnetic field analysis of the electron-positron pair members produced in a Pb foil situated in the x-ray beam of the 300-Mev betatron. With the possible exception of the top 2 percent of the spectrum, electron and positron bremsstrahlung were the same. For quantum energies in the interval 0.604 to 0.927 of maximum, the Bethe-Heitler spectrum is 8.7 ± 2.3 percent above the experimental spectrum. In the same interval the Maximon-Bethe-Davies theory agrees with experiment. Scattering by electrons was also observed as a function of energy of the struck or lowest energy electron. For these particles having energies between 20 and 130 Mev, the scattering cross section ratios of experiment to theory are 0.96 ± 0.06 and 1.06 ± 0.08 for incident electrons and positrons, respectively. The cross section ratio of electrons to positrons in the same energy interval is 1.31 ± 0.13 for experiment and 1.46 for theory. All errors are probable errors.

INTRODUCTION

THE Bethe-Heitler[1] (hereafter referred to as BH) and Wheeler-Lamb[2] theories of bremsstrahlung, applicable for nuclear and electronic fields, respectively, have generally been used to describe the radiative energy losses experienced by electrons and positrons in passing through matter for particle energies much larger than mc^2. A first-order Born approximation was used for the BH derivation. For relativistic electrons or positrons on Au the possibly overly stringent conditions for the validity of this approximation are not fulfilled. Maximon, Bethe, and Davies[3,4] (hereafter referred to as MBD) have derived a nuclear bremsstrahlung cross section without the use of the Born approximation. The MBD theory yields a cross section of the order of 10 percent smaller than that predicted by the BH theory.

Curtiss[5] has investigated the shape and magnitude of the bremsstrahlung spectrum produced by 60-Mev electrons in traversing Pb foils. There have been no experiments with particles of energy greater than 60 Mev of sufficient accuracy to precisely determine either the shape or the absolute magnitude of the bremsstrahlung cross section. This experiment is primarily concerned with supplying these two pieces of information for both electrons and positrons striking Au, for particles radiating more than two-thirds of their energy.

When a particle experiences radiation on passage through a foil located in a magnetic cloud chamber, the straggling is detected from the different track curvatures exhibited on opposite sides of the foil. By determining the number and energy of such radiative events, the shape of the high-energy part of the bremsstrahlung spectrum is found. From the total number of foil traversals made by the incident particles and the energy spectrum of these particles the absolute cross section for radiation is found.

A by-product of the experiment is the information obtained on the elastic scattering of positrons and electrons by electrons in the foil if the struck or lowest energy electron receives more than 10 Mev. Comparisons with the Bhabha[6] and Moller[7] theories are made.

THE EXPERIMENT

Two Au foils of effective thickness 0.3799 ± 0.0009 g/cm^2 were placed parallel to one another in a 33 cm diameter cloud chamber. The foils were each 7.6 cm high and 20.3 cm long and were located 6.5 cm and 20 cm from the center of an Al-covered particle entrance window in the glass cloud-chamber ring. This thickness and arrangement was based on compromising four factors: first, thick enough foils to give a reasonable number of pictures; second, sufficient chord lengths of almost all straggled tracks to allow accurate energy measurement; third, thin enough foils to hold the occurrence of successive events to a minimum; fourth, sufficient distance in front of the first foil to distinguish electron produced events from stray x-ray produced events, and to allow rejection of obviously degenerate energy and/or poorly directed (collimator scattered) tracks.

The apparatus alignment is shown in Fig. 1. The source of particles was the pairs produced by allowing x-rays from the 300-Mev betatron to impinge on a $\frac{1}{16}$-in. thick, 1-cm by 2-cm Pb sheet placed in an 11 500-gauss

* This work was supported by the joint program of the U. S. Office of Naval Research and the U. S. Atomic Energy Commission.
† Now at Los Alamos Scientific Laboratory, Los Alamos, New Mexico.
[1] H. Bethe and W. Heitler, Proc. Roy. Soc. (London) **146**, 83 (1934).
[2] J. A. Wheeler and W. E. Lamb, Phys. Rev. **55**, 858 (1939).
[3] L. C. Maximon and H. A. Bethe, Phys. Rev. **87**, 156 (1952).
[4] H. Davies and H. A. Bethe, Phys. Rev. **87**, 156 (1952).
[5] C. D. Curtiss, Phys. Rev. **89**, 123 (1953).
[6] H. J. Bhabha, Proc. Roy. Soc. (London) **154**, 195 (1936).
[7] C. Moller, Ann. Physik **14**, 531 (1932).

analyzing field about 3.7 m from the betatron target. Electron pair members produced in the x-ray converter passed through two small primary collimators before entering the cloud chamber. The first collimator was formed by the 1.3-cm separated pole faces of the analyzing magnet and a Pb brick supposedly placed to intercept most electrons of energy less than 265 Mev. The second collimator was located at the cloud chamber and was a 5-cm thick Pb brick with a 0.3-cm by 12.6-cm aperture. Immediately behind and centered with respect to this was the 0.7-cm by 14-cm 5-mil Al foil covered slot in the glass cloud-chamber ring.

By simultaneously reversing polarity of the analyzer and cloud-chamber fields, oppositely charged pair members having the same energy distribution were brought into the chamber.

The cloud-chamber tracks were photographed stereoscopically using a pair of cameras and a single mirror. Pulsed lights provided a horizontal sheet of light in the chamber which was at least 5.8 cm high and a chamber diameter in width. A coating of Aquadag of about 0.00014 g/cm^2 was applied to each side of each Au foil to cut down reflection of light to the roof and floor of the chamber. Light scattered at approximately 90° from the track droplets sensitized the film. One hundred foot rolls of Kodak linograph-ortho films were employed because of this film's small shrinkage and good track to background contrast. Each roll of film recorded incident particles of one sign of charge, alternate rolls recording incident particles of the opposite sign.

A magnetic pulse time delay circuit[8] was used for timing and sequencing the cloud-chamber functions, the betatron, and the diesel driven generator which supplied the cloud chamber's pulsed magnetic field. The chamber was expanded when the magnetic field reached the maximum value. Particles entered the chamber 0.6 second after expansion and were allowed to grow 0.12 second before the pulse lights were flashed. The chamber was fast compressed 0.01 second later. A 15-second cycle time was used.

The maximum value of the magnetic field averaged over the whole experiment was 10 020±180 gauss. The true maximum fields were 0.5 percent higher for electrons and the same amount lower for positrons than the average field; the fields increased uniformly with time from −0.4 percent to +0.4 percent during the experiment. This drift produced a probable uncertainty of ±0.2 percent for which the data to be presented cannot be corrected. A calibrated fluxmeter was used to standardize a meter indicating coil current against the peak magnitude of the field pulse. The point on the current peak field curve corresponding to 1800 gauss was checked using a proton magnetic moment detector.

Analysis of the pictures involved counting all foil traversals and measuring the radii and angles of deflection, α and φ in planes parallel and perpendicular

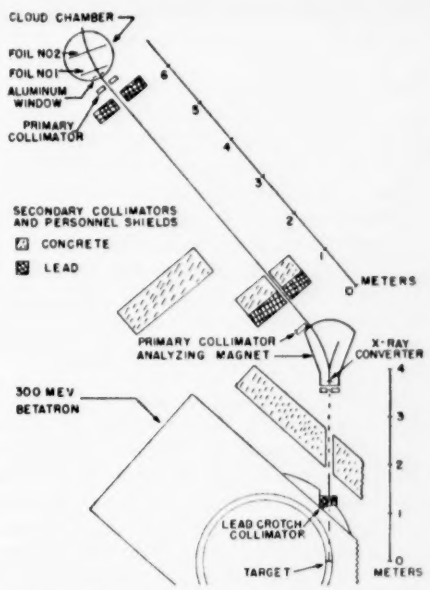

FIG. 1. Schematic for obtaining a particle beam in the chamber.

to the magnetic field, of any particles which had experienced events. Events were labeled as to type in accordance with the following conventions: bremsstrahlung if one particle came out of the foil with an energy $\leq$108 Mev; elastic electron scattering if two electrons came out each having an energy $\geq$10 Mev with their combined energy being $\geq$130 Mev; elastic positron scattering if an electron of energy $\geq$10 Mev came out, the combined energy of the electron and positron out being $\geq$130 Mev; and pair production if three or two particles came out with the particle with electric charge of opposite sign than that of the incident particle having an energy $\geq$10 Mev and the combined energy of the emergent particles being $\geq$130 Mev. The reasons for limitation of the accepted scattered electrons to energies $\geq$10 Mev were ease of observation and exclusion of events produced by a combined bremsstrahlung and Compton effect.

To avoid the difficulties of identification and measurement encountered when events occurred near the boundaries of the lighted region strict track acceptance criteria were established. These restricted to set values, α, φ, the horizontal and vertical positions in the chamber, and the minimum energy of particles entering either foil. In addition any aggregate of two or more tracks crossing the first foil which could not readily be resolved into its components before crossing the foil resulted in discarding the entire picture.

Angles were measured with a device similar to that described by Brueckner *et al.*[9] Energies up to 130 Mev were found using an instrument constructed from the

[8] C. R. Emigh, Rev. Sci. Instr. **21**, 142 (1950).

[9] Brueckner, Hartsough, Hayward, and Powell, Phys. Rev. **75**, 555 (1949).

design of Emigh.[10] Above 110 Mev an optical track straightening device employing a prism was used. This device will be described in a paper to be published later. The latter energy region is associated with the incident particles. To obtain this energy spectrum for the incoming electrons, all tracks of every tenth accepted picture were measured between the foils. Only one-thirtieth of the accepted pictures were measured to obtain the incident positron energy spectrum.

Energy lost by ionization in the foil was accounted for by adding to each measured energy $\Delta E \sec\alpha \sec\varphi$, the sum being called the total energy. ΔE is calculated from Bloch's theory[11] and the assumption that the radiative and scattering events occurred in the center of the foil.

During the initial stages of analysis, pictures were occasionally deliberately discarded because of elastic scattering and pair production events. About one-third of the pictures were analyzed before this discrimination was corrected. It was necessary to examine the remaining two-thirds of the pictures twice to be certain that all pair and scattering events were properly recorded.

THE THEORY

A. Bremsstrahlung

When high-energy electrons, or positrons, pass through a foil in a cloud chamber those bremsstrahlung events which are observed are caused by interaction of the incident particle with the two distinct entities of which the foil is composed; nuclei and electrons. In the process arising from the atomic electron interaction, the recoil momentum of the orbital electron is in general so small that it will not be seen in the chamber. Consequently this process cannot be distinguished from bremsstrahlung caused by a nucleus, and a correction must be applied to the number of events seen to find that component attributable to the nuclei alone. If the foil is sufficiently thick, corrections must also be made for multiple events. Thus consideration must be given those particles which undergo several successive radiations in passage through the foil, as the total emergent energy spectrum will be distorted from that due to a single radiation process. Another correction arises from the conversion of bremsstrahlung into electron-positron pairs and the resultant impossibility of identifying that particle which experienced the radiation straggling. Finally the possibility of a particle radiating more than one quantum while passing through the field of a single nucleus must be considered.

In 1934, BH published their theory of bremsstrahlung which took into account the electronic screening of the nucleus by using a Fermi-Thomas model atom. The perturbation which causes an incident particle of energy E_0 to transform to an energy E and a quantum of energy $k=E_0-E$ is the interaction of the particle with the atomic field and the interaction of the particle with the radiation field giving rise to the emission of the quantum E_0-E. As the Born approximation was used, the result is accurate provided $Zc/137v_1 \ll 1$ and $Zc/137v_2 \ll 1$, where v_1 and v_2 are the velocities of the electron in the initial and final state. For relativistic electrons in Au, these reduce to $0.58 \ll 1$ and indicate that some error may exist. The MBD theory accounts for the same process without the use of the Born approximation. To be valid this theory requires E_0, $E \gg mc^2$ and scattering angles of the order of mc^2/E_0, which are the only angles contributing significantly to the total cross section. With the exception of a constant the cross sections of the two theories are identical.

No difference between electron and positron bremsstrahlung is predicted by either theory. The reason being that the electric charge of the particle appears in the matrix element which when squared leads to the cross section. However some difference in behavior is expected for positive and negative particles. Emission of radiation is caused by the influence of the nuclear electric field, modified by the orbital electrons. A positive charge is repelled and should not approach the nucleus as closely as a negative charge, and so should interact less strongly than a negative particle.

Expressions for the probability of bremsstrahlung in an atomic field are

no screening, $2 \leq \gamma \leq 15$,

$$\varphi_r(E_0, E) = \{4Z^2/(137E_0^2k)\}\{e^2/mc^2\}^2 \times \{E_0^2+E^2-2EE_0/3\} \times \{\ln 2E_0E/(mc^2k) - \tfrac{1}{2} - c(\gamma) - f(Z)\}; \quad (1)$$

partial screening, $0 \leq \gamma \leq 2$,

$$\varphi_r(E_0, E) = \{Z^2/(137E_0^2k)\}\{e^2/mc^2\}^2 \times \{[E_0^2+E^2][\varphi_1(\gamma) - (4/3)\ln Z - 4f(Z)] - (2EE_0/3)[\varphi_2(\gamma) - (4/3)\ln Z - 4f(Z)]\}, \quad (2)$$

where $\gamma = 100mc^2k/E_0EZ^{\frac{1}{2}}$. Placing $f(Z)=0$ yields the BH theory while $f(Z)=0.287\pm0.004$ for Au gives the MBD theory.[12] The functions $\varphi_1(\gamma)$, $\varphi_2(\gamma)$, and $c(\gamma)$ are given in tabular form by BH.

Wheeler and Lamb have deduced the theory for bremsstrahlung when an incident particle interacts with an orbital electron. Their formula is sufficiently similar to the nuclear bremsstrahlung formula that for this experiment sufficient accuracy is obtained by using

$$\varphi_{\text{total}} = \varphi_{\text{nuclear}}\left[1+\frac{\varphi_{\text{electronic}}}{\varphi_{\text{nuclear}}}\right] = \varphi_{\text{nuclear}}[1.015]. \quad (3)$$

The cross section which includes the effect of two successive radiations has been formulated by Curtiss.[13]

[10] C. R. Emigh, Ph.D. thesis, University of Illinois, 1951 (unpublished).

[11] See, e.g., W. Heitler, *The Quantum Theory of Radiation* (Oxford University Press, London, 1944), 2nd edition, p. 218.

[12] H. A. Bethe (private communication).

[13] C. Curtiss, reference 5, Eq. (4).

Accurate numerical integration of his equation is difficult because the small number answer is obtained from a difference of large numbers. To avoid this, Eq. (2) was rearranged to give

$$\varphi(E_0, E)=B(E_0, E; \varphi_1)+C(E_0, E; \varphi_1-\varphi_2).$$

In this formulation B is roughly about ten times larger than C in the region of interest here. Using the approximation, arrived at empirically, $\varphi_1=(68.66+6.928\gamma)/(3.306+\gamma)$, Curtiss' formula can be integrated analytically for all terms of order B^2. The integrations are rather long but straightforward. The only analytic approximation for $\varphi_1-\varphi_2$ that was judged to be sufficiently accurate, lead to such tedious and involved numerical manipulation after integration that the small contribution of the BC and C^2 terms is found by numerical integration.

A cross section for the creation of pairs from bremsstrahlung may be derived by using the theories of BH. $\varphi(E_0, E_0-k)$ and $\varphi(k)$ are defined to be, respectively, the probabilities that an electron of energy E_0 will radiate a quantum of energy k, and that a quantum k will create an electron-positron pair. On the average the quantum will be produced halfway through the foil so that only the remaining half of the foil is available for the creation of a pair. Therefore the probability that in traversing the foil an electron will create a pair of energy between k and $k+dk$ by this two stage process is

$$d\sigma=nt\varphi(E_0, E_0-k)\cdot nt\varphi(k)dk/2. \quad (4)$$

As screening is partially effective in each stage of the event, this expression must be evaluated numerically. Since both φ's were derived using the Born approximation, Eq. (4) is valid regardless of whether an electron or a positron initiates the event.

B. Elastic Scattering by Electrons

For the incident energies used here scattering of electrons and positrons by electrons is of interest because different interactions of the incident and struck particle are predicted according to whether the charges carried by the particles are of the same or different sense. Since the interaction of the two particles is treated as a first-order perturbation by both Moller and Bhabha, their theories are accurate provided $c/137v \ll 1$. This condition is obviously fulfilled for particles of relativistic velocity. The actual scattering observed is distorted from that due to the processes under investigation because of the multiple events arising from the use of thick foils. After the scattering process has occurred the struck, or lowest energy electron, may radiate part of its energy in traversing the remainder of the foil.

The average radiative energy loss of the struck electron was computed with the aid of an approximate relation given by Rasetti,[14] corrected by a multiplying factor of 0.91 to correspond with the bremsstrahlung results found in the next section. In conjunction with this relation the Bloch ionization loss theory was used, this providing a sufficiently accurate result. The difference between the theoretically expected number of events for the true scattered energy and the theoretically expected number of events for the measured scattered energy which neglected radiation loss, may be applied as a correction to the experiment. The second and more important correction is due to those bremsstrahlung created pairs in which the energy sharing is so unequal that it allows only observation of the electron pair member. This correction was evaluated experimentally.

[14] F. Rasetti, *Elements of Nuclear Physics* (Prentice-Hall, Inc., New York, 1936), p. 72.

THE RESULTS

A. Bremsstrahlung

The data compiled from the analysis of 163 110-electron and 161 585-positron foil traversals for radiation events are presented in Table I.

TABLE I. The observed number of radiation events, the BH corrected experimental cross sections for the sum of the positron and electron events, and the theoretical cross sections found from integration of the BH theory over the incident spectrum of Fig. 2. The cross sections are in units of barns/Mev.

Straggled particle energy in Mev	Number of positron events	Number of electron events	BH corrected experimental cross sections	BH theoretical cross sections
0.511–6	167	155	0.0967±0.0064[a]	0.1025±0.0012
6–12	161	173	0.1326±0.0061	0.1668±0.0020
12–18	175	181	0.1436±0.0067	0.1891±0.0023
18–24	210	218	0.1764±0.0078	0.2027±0.0024
24–30	219	239	0.1909±0.0084	0.2128±0.0026
30–36	266	240	0.2128±0.0091	0.2215±0.0027
36–42	256	284	0.2284±0.0097	0.2297±0.0028
42–48	237	274	0.2166±0.0096	0.2377±0.0029
48–54	253	272	0.2234±0.0099	0.2459±0.0030
54–60	269	254	0.2233±0.0100	0.2545±0.0031
60–66	244	317	0.2405±0.0104	0.2641±0.0032
66–72	286	291	0.2479±0.0106	0.2747±0.0033
72–78	293	308	0.2589±0.0108	0.2868±0.0035
78–84	335	335	0.2896±0.0115	0.2996±0.0037
84–90	321	344	0.2881±0.0114	0.3137±0.0039
90–96	347	360	0.3070±0.0118	0.3304±0.0041
96–102	465	460	0.4024±0.0135	0.3484±0.0043
102–108	345	361	0.3077±0.0118	0.3675±0.0046

[a] Annihilation accounted for.

Numbers of straggled particles were determined for different energy bins, each of which was 6 Mev wide with the exception of that bin corresponding to the highest energy radiation which was (6–0.511) Mev wide. Analysis of the angular distribution of emerging particles showed symmetry and equality within statistics in both the horizontal and vertical cloud-chamber planes for any given bin. Within statistics the horizontal and vertical position distributions of the events in each bin were equal to the corresponding distributions of the incident particles. From these comparisons the asymmetry in the ease of observation and measurement of events introduced by the narrow vertical, as com-

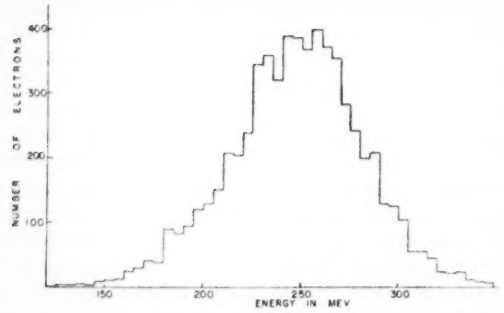

FIG. 2. Incident electron spectrum with energies computed from average magnetic field. Mean energy is 247.3 Mev.

pared to broad horizontal, lighted region does not appear to have affected the efficiency of the data collecting process which was 100 percent efficient for each bin.

For any bin the experimental cross section, φ_e, in units of cm^2/Mev is found from $\varphi_e = AN/TLdW$, where N is the number of straggled particles in the bin, T the number of foil traversals, A the atomic weight of the target, d the foil density, W the bin width, and L the Avogadro number. The errors assigned to φ_e are probable errors and are calculated from the statistical error in the number of events and from the experimentally found variation with energy of the number of events per bin, and the error in any one energy measurement. Because of this error in energy there is a displacement of events both in to and out of a bin occuring across both edges of a bin. As the bremsstrahlung process is statistical by nature the combined error is found by taking the square root of the sum of the squares of the errors in each one of the four component fluxes and in the number of events actually placed in a bin. The resulting probable error for the number in any one bin after including errors in foil thickness is found to vary approximately from $0.7\sqrt{N}$ to $1\sqrt{N}$ as the energy increases, instead of remaining a constant $0.675\sqrt{N}$ as would be the case if only the number of events actually found in the bin were considered.

The theoretical cross sections, φ_t, for a bin are found by integrating the theories over the incident electron energy distribution and then integrating these results over the straggled particle energies included in the bin. Figure 2 shows the incident electron spectrum used in the calculations. Because only 6300 elements are contained in the distribution, a statistical error amounting to about 1.2 percent is given φ_t. The spectrum is the weighted average of the measured second and calculated first foil distributions, the weights being assigned according to the number of particle traversals experienced by the respective foils. The spectrum incident on the first foil was found by assuming the *BH* bremsstrahlung theory to be 9 percent high and then calculating that spectrum which after traversal of the first foil would give the measured emergent spectrum. In terms of φ_e the resultant distribution is not critically dependent on the percentage chosen. Use of the 9 percent figure will, however, eventually receive some justification.

Before theory and experiment can be compared the corrections already discussed must be applied. These corrections are independent of the sign of the charge of the incident particle. Consequently it is feasible to compare electron and positron bremsstrahlung in all but the lowest straggled energy bin directly on the basis of the experimentally observed events, provided allowance is made in the errors assigned for the purely statistical error resulting from integration of the theoretical cross sections over the incident spectrum. The lowest straggled energy bin is excluded from this comparison because of the necessity of correcting the positron results for the annihilation processes still to be discussed.

The experimental ratio of positron to electron events must be increased by 3.0 ± 0.4 percent to yield the true ratio of the cross sections. Approximately one-third of this increase is due to the difference in the number of foil transits for the two types of particles. A correction in energy resulting from use for the energy measurements of a magnetic field averaged over the entire experiment accounts for the remaining 2 percent and the ±0.4 percent uncertainty. One-half of the 2 percent increase arises from the number of events being roughly proportional to the true bin width. The remaining 1 percent is due to the different average incident energies for the two types of particles, as these energies appear to be identical when the average magnetic field is used.

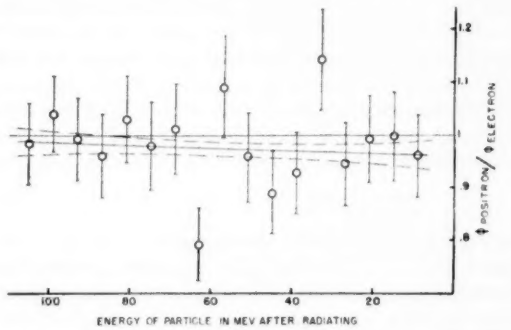

FIG. 3. Relative bremsstrahlung cross sections for positrons to electrons. The broken lines give the probable error in the straight line fitted to the data by the weighted least-squares method.

Figure 3 is a plot of the corrected ratio of positron to electron events. Following the method of Birge[15] a straight line was fitted to the data by a weighted least squares approximation. Taken over the whole range of 6 to 108 Mev the weighted average ratio is 0.973 $\pm0.013\pm$the error of 0.004 discussed above. It is

[15] R. T. Birge, Phys. Rev. **40**, 207 (1932).

apparent that for the interval of straggled energies considered, positrons and electrons yield very closely the same shape and magnitude for the bremsstrahlung cross section. On the basis of this conclusion positron and electron data in this interval are added to give experimental values to compare to the theoretical cross sections.

Table II gives the numerical values of the corrections made to the experimental cross section. The electronic bremsstrahlung is taken as $0.015\varphi_e$. Integration of Eq. (4) over the incident spectrum yields the correction for the double process involving bremsstrahlung and pair production. Here the assumption is made that the BH theories involved were too large by 9 percent. This conclusion has been established for pair production by the work of Lawson,[16] and DeWire *et al.*,[17] and will be seen to be approximately valid for bremsstrahlung on the basis of the present experiment. To the accuracy required here the theory of MBD yields the same result as the adjusted BH theory, and, as in the case of the input spectrum, the actual correction to φ_e is not critically dependent on the precise value by which the BH theory must be altered. The double bremsstrahlung correction was found by integration over the incident spectrum for both the BH and MBD theories. As this process contributes appreciably to φ_e it is necessary to first make the correction and then adjust the correction on the basis of the deviation found between theory and experiment. The appropriate numerical factor of $(0.92)^2$ for the adjusted BH theory was found by using the integrated cross section for straggled particle energies between 18 and 96 Mev. When this is done the MBD and BH double bremsstrahlung corrections are equal within 2 percent in all but the (6–0.511)-Mev bin. No correction is made for three successive radiations although on the basis of the double radiation process the triple radiation process could conceivably give a contribution of the order of 1 percent to the cross sections in the lowest straggled energy bins measured.

TABLE II. Corrections to bremsstrahlung cross sections, φ_e, of combined positron and electron events. All corrections in units of barns/Mev.

Straggled particle energy in Mev	$k/(E_0-mc^2)$ for center of bin	Electron electron bremsstrahlung	Bremsstrahlung pair production	Calculated BH double bremsstrahlung	Total corrected correction using BH theory
0.511–6	0.988	−0.0016	0.0015	−0.0131	−0.0588[a]
6–12	0.965	−0.0022	0.0029	−0.0186	−0.0150
12–18	0.940	−0.0024	0.0033	−0.0173	−0.0137
18–24	0.915	−0.0030	0.0036	−0.0157	−0.0127
24–30	0.890	−0.0030	0.0037	−0.0143	−0.0114
30–36	0.866	−0.0035	0.0039	−0.0133	−0.0108
36–42	0.841	−0.0037	0.0040	−0.0124	−0.0102
42–48	0.816	−0.0035	0.0041	−0.0116	−0.0092
48–54	0.791	−0.0036	0.0043	−0.0109	−0.0085
54–60	0.766	−0.0036	0.0044	−0.0102	−0.0078
60–66	0.742	−0.0038	0.0046	−0.0096	−0.0073
66–72	0.717	−0.0040	0.0047	−0.0091	−0.0070
72–78	0.692	−0.0041	0.0048	−0.0086	−0.0066
78–84	0.667	−0.0046	0.0050	−0.0081	−0.0064
84–90	0.642	−0.0045	0.0052	−0.0076	−0.0057
90–96	0.617	−0.0048	0.0054	−0.0071	−0.0054
96–102		−0.0063	0.0056	−0.0066	−0.0063
102–108		−0.0048	0.0058	−0.0061	−0.0042

[a] Includes positron annihilation correction of −0.0476.

In addition to the above factors, the phenomenon of positron annihilation requires consideration. The complete loss of energy of a positron by radiation is indistinguishable in the cloud chamber from a one or two quantum annihilation process. The theory for two quantum annihilation has been developed by Dirac[18] and has been confirmed within an experimental error of ±25 percent by Gilbert and Colgate,[19] who apparently assume that the positron and electron bremsstrahlung cross sections are equal. Heitler[20] has given the cross section for the one quantum process but this has not been tested experimentally. After integration over the incident spectrum the annihilation theories predict that of the 167 events found in the lowest positron energy bin, 46 should be ascribed to the two quantum and 3 to one quantum process. Making this correction the ratio of positron to electron bremsstrahlung in this bin is then 0.78±0.08. There is not sufficient accuracy to definitely determine whether a difference does or does not exist in the bremsstrahlung of the two types of particles. Consequently in comparing the experimental results with the theories, a triangular symbol is used in the figures for the annihilation corrected lowest energy bin instead of the circular symbol used for all other bins.

Figures 4 and 5 present the completely corrected data. It appears that the BH theory is incorrect in magnitude. It also appears that there is some discrepancy between theory and experiment near the tip of the spectrum.

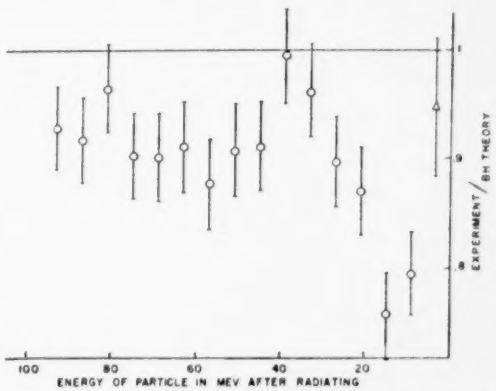

FIG. 4. Bremsstrahlung cross section relative to BH theory.

[16] T. L. Lawson, Phys. Rev. **75**, 433 (1949).
[17] DeWire, Ashkin, and Beach, Phys. Rev. **82**, 447 (1951).
[18] P. A. M. Dirac, Proc. Cambridge Phil. Soc. **26**, 361 (1930).
[19] F. C. Gilbert and S. A. Colgate, Phys. Rev. **88**, 164 (1952).
[20] W. Heitler, reference 11, p. 212.

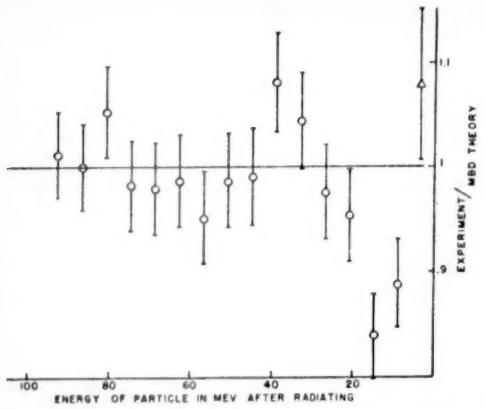

FIG. 5. Bremsstrahlung cross section relative to MBD theory.

The experimental result would be quite perplexing if data had not been taken for straggled particle energies greater than 42 Mev. Although the theories seem invalid for low straggled energies, the double bremsstrahlung corrections are fairly accurate because of their relative independence of observed straggled energies in this region.[21]

The corrected experimental cross sections in the 96 to 108 Mev interval given in Table I appear to contain systematic errors and so are not shown in Figs. 4, 5, and 6. In this interval the scale of the instrument used to determine straggled particle energies was greatly compressed. Inspection of the energy distributions of events in the various bins showed approximate equality with the theoretically expected distributions for bins containing energies less than 96 Mev. The energy distributions indicate that the observer definitely practiced a discrimination of putting almost all events near 102 Mev in the 96- to 102-Mev bin. Although more care was exercised near 108 Mev the tendency was to place possibly doubtful events in the 102- to 108-Mev bin. For fear of influencing the observer, the experimental results were deliberately not evaluated until the analyzing had been completed. Consequently the errors went unnoticed and no correction can be made. More care was taken in the measurement of the few scattered electrons having energies in this region and no systematic displacement was found.

The bremsstrahlung cross section found from adding the electron and positron results in the interval 18 to 96 Mev is 18.62±0.39 barns experimentally as compared to 20.24 barns for the BH and 18.60 barns for the MBD theories. Agreement with the latter theory is good while the BH theory is found to be 8.7±2.3 percent higher than experiment. In the 0.511 to 18 Mev interval the experimental cross sections are 91.7±4.3 percent of the MBD and 82.1±3.9 percent of the BH predictions for positrons, and 100.4±4.3 percent and 89.8±3.9 percent, respectively, for electrons. The errors given are the sums of the absolute values of the probable error, found from φ_e and φ_i, and 0.4 percent arising from the uncertainty in magnetic field. All results neglect the three successive radiation and two quanta from one nuclear encounter types of event, and assume the Wheeler-Lamb electronic bremsstrahlung theory. The result for the 0.511- to 18-Mev positron energy interval is additionally dependent on the validity of the annihilation theories.

TABLE III. The observed number of electron scattering events, and the observed number of obvious bremstrahlung plus pair production events.

Scattered electron energy in Mev	Number of positron-electron events	Number of positron-positron events	Number of electron-electron events	Number of electron-positron events
10–20	85	11	139	25
20–30	38	7	47	9
30–40	16	4	25	3
40–50	13	2	22	4
50–60	8	0	8	3
60–70	4	0	6	0
70–80	4	0	7	1
80–90	3	0	5	1
90–100	3	0	6	0
100–110	3	1	4	1
110–120	1	0	3	1
120–130	1	1	2	0
130	11	0	0	0

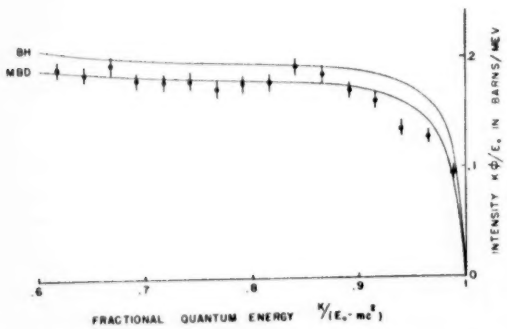

FIG. 6. Quanta spectrum resulting from superposition of spectra from all bins of incident particle spectrum.

Figure 6 summarizes the positron electron bremsstrahlung results in terms of intensity, $k\varphi/E_0$, as a function of the average fractional energy loss $k/(E_0-mc^2)$, where k equals the incident energy, E_0, minus the energy of the electron after radiating. The average values of k/E_0 and $k/(E_0-mc^2)$ were found by integration over the incident spectrum of Fig. 2. The corrected experimental values used are those found with the aid of the adjusted BH theory corrections.

[21] *Note added in proof.*—Bethe, Maximon, and Low, in Phys. Rev. **91**, 417 (1953) point out that an error was made by MBD in their calculation of the bremsstrahlung cross section. The comparison made here is with the uncorrected MBD calculation since the corrected calculation is not yet available.

B. Elastic Scattering by Electrons

Table III and Figs. 7 and 8 give the data compiled from the analysis of 97 833 positron and 113 125 electron foil traversal for elastic scattering by electrons. To draw attention to the small number of events observed the results are expressed in terms of events. The theoretical values are those found from integration over the incident spectrum of Fig. 2.

The total corrections to the experimental data are given in Figs. 7 and 8. The method of determining the correction for the radiation loss of the struck electron has already been described. Correction for those two stage bremsstrahlung plus pair production processes which were counted as scatterings was achieved using information found experimentally. If an electron enters

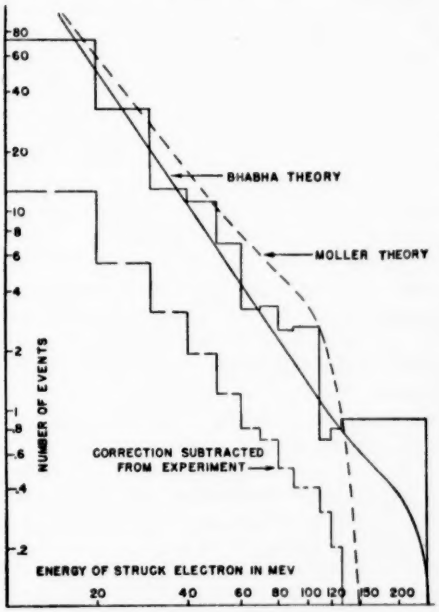

FIG. 7. Comparison of the observed positron-electron scattering events with the theoretically predicted values.

the foil and two electrons emerge the occurrence can be attributed to either elastic scattering or the double process. However it is also possible for an electron and positron to emerge. The number and positron energy distribution of the latter type of event was measured. On the assumption that the double process electron positron event occurs as often as the double process electron electron event the number of electron electron events due to the double process can be found. A similar behavior is exhibited by incident positrons. In the preceding section the bremsstrahlung of positrons and electrons was found to be approximately equal. Consequently it is permissible for the accuracy required here to combine the obvious double process events (i.e., incident electron emerging as positron and elec-

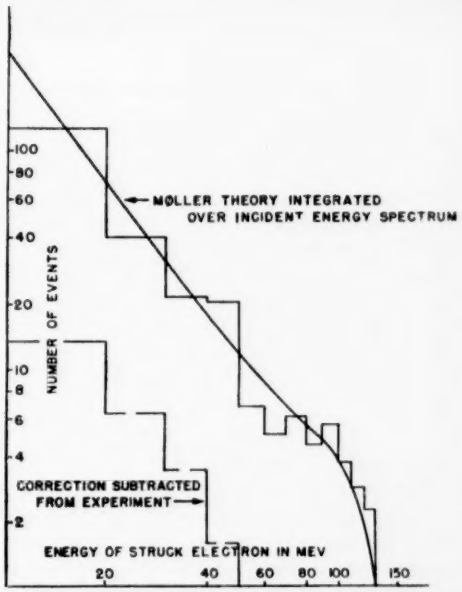

FIG. 8. Comparison of the observed electron-electron scattering events with the theoretically predicted values.

tron) of incident positrons and of incident electrons to achieve a slightly greater accuracy in the correction. This was the procedure followed.

Agreement with the Møller electron electron scattering theory is rather better than the statistics warrant. The same is true of the Bhabha theory of positron electron scattering, with the exception of the 10 to 20 Mev and 130- to 250-Mev bins. For energies of the struck electron between 20 and 130 Mev, where the best experimental fits are found, the ratio of experimental to theoretical cross section is 0.956 ± 0.057 for electrons and 1.065 ± 0.075 for positrons. The cross-section ratio of electrons to positrons in the same energy interval is 1.31 ± 0.13 for experiment and 1.46 for theory. Errors are probable errors based only on the corrected number of events.

It has been stated that the pictures were analyzed twice for scattering processes, the first examination having yielded results differing from the theories by as much as a factor of two for the lowest struck electron energy bins. In view of this and the large errors attendant on the final number of events found, the information presented should be regarded only as a rough substantiation of the theories involved.

The author wishes to express his gratitude for the guidance given him by Professor D. W. Kerst, under whose direction this experiment was performed. He also wishes to acknowledge the helpful discussions of the work held with Professor A. T. Nordsieck, Professor A. O. Hanson, and Dr. C. R. Emigh. Much of the cloud-chamber equipment was designed and built by the latter.

The Time Variation of Cosmic-Ray Heavy Nuclei*

VICTOR H. YNGVE†
Department of Physics, University of Chicago, Chicago, Illinois
(Received June 30, 1953)

Two 4×4 Ilford G-5 photographic emulsions in contact were exposed to the cosmic radiation in such a way that one plate was moved slowly and uniformly with respect to the other. By this technique it is possible to determine the time at which heavy nuclei pass through the plates. The plates were exposed above 90 000 feet on June 4, 1952, for 8 hours during the day. A reliable altitude record was available and was used to correct for the altitude changes during the 8 hours. 947 heavy nuclei with more than 10 delta rays per 100 microns, corresponding to Z greater than about 10, were traced through and their time of passage measured. This was done by new techniques which are described in detail. The data have been divided into three time intervals. The intensity during the middle interval between noon and 2 P.M. is greater by 25±8.5 percent than the average of the other two. It is concluded that this is due to a real fluctuation in the intensity of of cosmic-ray heavy nuclei at the top of the atmosphere. The possibility that this may be due to a dipole magnetic field of the sun is discussed.

I. INTRODUCTION

THE problem of the origin of cosmic rays has been a subject of speculation ever since their discovery in 1912 by Hess. Recently, theoretical approaches to this problem have been proposed by Fermi, Alfvén, Teller, and others. A great deal of experimental effort has gone into the study of the cosmic radiation and a great deal has been learned, but the problem of the origin has not been completely solved. The study of time variations probably will be important in the future if this problem is to be solved. The reason that time variation information is valuable is that by this means there is the possibility of deducing something about the direction from which the particles come and thus of obtaining information on the position and perhaps the nature of the source.

In order to deduce the original direction of the particles from observations of the direction and time of their arrival at the earth, one has to take into account the diurnal rotation of the earth and the effect of the earth's magnetic field in bending the paths of the cosmic-ray particles, a problem[1] which has been studied intensively for many years by Störmer, Vallarta, and others, and is still not completely solved in all detail. Then too, there are the effects of other magnetic fields which are less well known, such as a possible magnetic field of the sun. It may turn out that important additional evidence for the existence and nature of such fields will come from cosmic-ray measurements, principally from time variation work on the primaries.

The study of time variations is complicated by a number of disturbing factors. Work at low altitude is plagued by the well-known problems due to the presence of the atmosphere. Besides temperature and barometric effects, there is the effect of the lateral spread of the secondaries away from the original direction of the primary. But perhaps most serious is the complicated nature of the cascade of events through the atmosphere, so that measurement of any one component cannot easily be related to a given primary, but represents some sort of averaged out effect. Thus it is a great advantage in studies on time variations to carry them out at the top of the atmosphere on the primaries themselves.

This paper reports work on the heavy nucleus primaries with charge, $Z \geq 10$. For this range of charge, the method of delta-ray counting allows one to identify a group of particles which includes mostly primaries. Secondaries from nuclear events contribute only a very small amount.

Time variations at the top of the atmosphere which might be connected with a diurnal effect have been looked for and not found in the total ionizing component and in the gamma rays by Bergstralh and Schroeder[2]; in bursts and low Z heavy nuclei using a pulse ionization chamber by Pomerantz and McClure[3]; and in the heavy nuclei using photographic emulsions by Freier, Anderson, Naugle, and Ney[4] and by Anderson, Freier, and Naugle,[5] who quote an upper limit of ±20 percent for time variations. Lal, Pal, Kaplon, and Peters[6] have given an upper limit of 10 percent for time variations in the high-energy heavy nuclei.

Changes have been observed, however, by Neher, Peterson, and Stern[7] in the total ionizing component on one out of several flights; by Swetnick, Neuburg, and Korff,[8] who found a 17±7 percent change in the neutrons at high altitude; by Ney and Thon[9] who

* Supported in part by the joint program of the U. S. Office of Naval Research and the U. S. Atomic Energy Commission.
† Now at Research Laboratory of Electronics, Massachusetts Institute of Technology, Cambridge, Massachusetts.
[1] D. J. X. Montgomery, *Cosmic Ray Physics* (Princeton University Press, Princeton, 1949).
[2] T. A. Bergstralh and C. A. Schroeder, Phys. Rev. **81**, 244 (1951).
[3] M. A. Pomerantz and G. W. McClure, Phys. Rev. **86**, 536 (1952).
[4] Freier, Anderson, Naugle, and Ney, Phys. Rev. **84**, 322 (1951).
[5] Anderson, Freier, and Naugle, Bull. Am. Phys. Soc. **28**, No. 3, 7 (1953).
[6] Lal, Pal, Kaplon, and Peters, Phys. Rev. **86**, 569 (1952).
[7] Neher, Peterson, and Stern, Phys. Rev. **90**, 655 (1953).
[8] Swetnick, Neuburg, and Korff, Phys. Rev. **86**, 589 (1952).
[9] E. P. Ney and D. M. Thon, Phys. Rev. **81**, 1069 (1951).

found a change in alpha particles and heavy nuclei using scintillation counters; and by Lord and Schein.[10,11]

In their first investigation, Lord and Schein compared the intensity of heavy nuclei of $Z \geq 10$ on two day balloon flights and two night balloon flights. The intensity during the day was found to be about twice the nighttime intensity. However, there are difficulties in comparing the intensities on different flights, and so in order to overcome these, the drop-load technique was used. In this technique, two gondolas are carried aloft on the same balloon and after a certain time one is dropped, the other continuing at altitude. An experiment of this type, carried out on May 22, 1950, gave a day-night ratio of about 2.5. The zenith angle dependence of the heavy nuclei found in the plates was studied, and it was concluded that the effect could not have been due to error in the altitude measurement.[12]

It became clear that the development of a new technique was desirable because of the poor time resolution inherent in both previously used techniques and because of the uncertainties introduced in comparisons between different plates. Work was carried out in this laboratory[11] to develop an apparatus which moves one plate slowly in contact with another fixed plate. The time of traversal of a heavy nucleus can be deduced by measuring the relative positions of the tracks of the heavy nucleus in the two plates. It was found that a rate of motion of about $\frac{1}{4}$ mm per hour was sufficient to determine the time of a particle traversing the plates to within a few minutes. Similar work has been carried out at other laboratories. A description of the moving plate method of studying time variations follows, together with the results of the analysis by this method of one flight.

II. NEW DEVELOPMENTS IN MOVING PLATE TECHNIQUE—EXPERIMENTAL PROCEDURE

The plates selected for analysis had been exposed on a Skyhook balloon flight at Minneapolis, June 4, 1952. The flight was launched at 5:50 A.M. and reached an altitude of 91 000 ft at 9:45. It then spent 8 hours between 91 000 and 96 000 ft. It was released at 4:56 P.M., descended by parachute and reached the ground at 5:35 P.M. The altitude record was obtained by a barograph. The plates were 4×4 inches with 400-micron G-5 electron sensitive emulsions.

The relative orientation of the plates during the flight is shown in Fig. 1. The moving plate holder was driven against a spring by a screw and train of gears. The motor was a tuned reed controlled dc motor of constant speed. The rate of motion was 282 microns per hour. The whole apparatus was enclosed in an aluminum can so as to be made water and airtight.

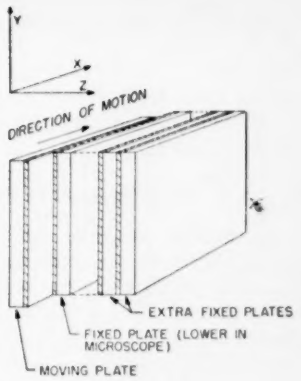

FIG. 1. The way in which the plates were oriented during the flight. The directions of the axes referred to in the text are shown.

The Microscope

The microscope that was used for determining the times of traversal of the heavy nuclei by measuring the relative position of their tracks in the two plates had been fitted with a special stage. This stage consists of two very accurate slides and screws. It is possible with this stage to reproducibly measure the relative position of two objects under the microscope, such as the ends of heavy nucleus tracks, to within about 3 microns. The availability of this precision stage made possible the refined techniques to be described. The stage is actually much more stable than the microscope nose piece. Changes in the position of the objective cause considerable difficulty in attempts to measure the absolute position of an object under the microscope, but relative positions can be measured quite accurately if care is taken not to touch the objective or its mounting between the two measurements involved. The procedures developed thus never rely upon absolute positions but only on relative positions.

Location of the Heavy Nuclei

In order to locate the heavy nuclei, the plate which had been fixed was scanned under a relatively low power, that is with a field of view of 1 mm. Tracks with greater than 10 delta rays per 100 microns were recorded. A delta ray was counted if it had three or more grains. Ten such delta rays per hundred microns corresponds to a Z of about 10 at minimum ionization. Slower particles with lower Z will contribute only a small fraction of the tracks. All delta-ray counts were made by one observer. Even if there is a systematic change of the delta-ray criterion during the course of the scanning, this is likely to have no effect on the final time distribution determined, because first all heavy nuclei were located, and then afterwards the times of traversal of these previously located tracks were determined.

No effects are to be expected from temperature changes during the flight since the flight was made

[10] J. J. Lord and M. Schein, Phys. Rev. **78**, 484 (1950).
[11] J. J. Lord and M. Schein, Phys. Rev. **80**, 304 (1950).
[12] Marcel Schein (private communication).

during daylight hours, and the equipment was enclosed in a Cellophane-covered gondola of the type which we have used often in the past. Temperature changes during a day flight in such a gondola are known to be small. The temperature of the barograph was constant to within $\pm 6°C$.

Alignment of the Plates

In order to determine the times of traversal of the heavy nuclei by the procedure to be described, it is necessary to place the plates in the microscope in the same relative position that they had at some one time during the flight. It is strongly recommended that future experiments use a mechanical method of alignment so that the relative y positions (Fig. 1) of the plates will be the same in the microscope as during the flight. This can be done easily by having the bottom edges of the two plates rest against a flat surface along which one plate can slide during the flight. Then when the plates are placed in the microscope against a stop, they will be in the same relative orientation with respect to the y direction. In this experiment, the y alignment had to be determined from tracks in the emulsions.

A special plate holder was added to the microscope stage so that the lower plate was held in place as before, and the upper plate could be placed on top with the emulsion in contact and adjusted in the y direction by two screws, one at each end, and in the x direction by a cam-shaped stop.

After much experimentation, the plates were aligned using large cosmic-ray stars. It was found that large stars near the surface of the emulsion frequently had several prongs which could be traced through into the the other emulsion even though there was a variable air gap between the plates probably caused by warping due to humidity changes during the flight. The limitations of this method are the shear distortions in the emulsion which cause events near the surface of the emulsion to be moved from their original positions.

Shear Distortions

In these plates the shear distortion amounted to about 25 microns displacement of the surface of the emulsion from its original position. It causes tracks which were originally straight to appear curved. An examination of such curved tracks in both emulsions revealed the fact that the direction of the projection of the tangent to the track at the air intercept in one emulsion closely matched the direction of the tangent at the air intercept in the other emulsion. In fact this direction was the same in the two plates to as close as the measurements could be made with a cross hair in a rotating eyepiece—about 0.01 radian. This result is reasonable since there can be no shear stress across a free surface, but there can be a large one at the emulsion glass interface. The stress curve can be expected to be smoothly varying through the thickness of the emulsion between these two extremes. It was thus assumed that the projection on the emulsion surface of the original *direction* of the tracks was closely given by the direction of the tangent at the air interface in either emulsion. It was also assumed that there was a good bond between the glass and the emulsion so that the *position* of the intercept of the track with the emulsion-glass surface was not affected by these distortions.

Procedure for Measuring the Time

In order to make sure that the plates remained in the same relative alignment throughout the measurements, two heavy nucleus tracks were chosen as standards, one at each end. Frequently during the measurements these tracks were returned to and remeasured. The relative positions of the emulsion-glass intercepts of the two tracks of each heavy nucleus in the two emulsions was reproducibly measured to within ± 2 microns.

To measure the time of a heavy nucleus, the low-power ($10\times$) objective was used which has a long enough working distance that it can see through the glass backing of the upper plate and into either of the two emulsions. In the procedure, a heavy nucleus is located in the lower emulsion by its previously determined coordinates. The cross hair in one of the occulars is turned so as to appear to line up exactly with the direction of the track. In the cases of those tracks which appear curved due to emulsion distortion, the cross hair is lined up so as to be tangent to the track at the emulsion-air intercept (see Fig. 2). The assumption is that this tangent is undistorted as to direction. The microscope is then focused up into the upper emulsion, and a search is made for the same track in the upper emulsion. After the track is found in the upper emulsion, a check is made of the direction of the tangent: it should be in line with the cross hair to within the accuracy of setting, which is about 0.01 radian. A check is also made to see that the density of the track is about the same as in the other emulsion, that the projected length is about the same, and that the apparent y distance between the air intercepts is reasonable considering the variable air gap between the emulsions. With all of these criteria, the traced-through track can be identified with considerable certainty. Then, with the precision screw, the x distance is measured between the two positions of the stage where the cross hair intersects the emulsion-glass intercepts of the track in the two emulsions. This x distance is proportional to the time of traversal of the heavy nucleus relative to an arbitrary zero.

In the case of tracks so long that the glass intercepts in the two plates cannot be seen without adjusting the y axis of the stage, this adjustment is made by moving the stage obliquely with the two screws together in the direction of the track as given by the cross hair. This

is done by moving some large grain or other landmark in the emulsion from one end of the cross hair to the other the required number of times to produce a sufficient motion in the y direction.

This procedure eliminates, in first approximation, the effects of the shear distortion in the emulsions and the variable air gap during the flight. Shear distortion does not affect the direction of setting of the cross hair which is determined by the direction of the track at the air intercepts, and it does not affect the x distance which is measured to the undistorted glass intercepts. The variable air gap has no effect because it only moves the tracks farther apart along the direction of the cross hair.

Reproducibility of the Measurements

The cross hair can be set to the end of the track or to a landmark to within ± 2 microns for each setting. The cross hair can be set tangent to the track to within about 0.01 radian. It can be shown that this gives an error

$$\Delta x = y \Delta\theta \sec^2\theta,$$

where y is the component of the distance between the two emulsion-glass ends of the track and θ is the cross hair angle, that is the angle between the y axis and the projection of the track in the x-y plane.

In order to check these estimates of precision, some of the tracks were remeasured. Over half of the measurements were reproducible to within 15 microns or three minutes of time. If all of this error is attributed to the setting of the angle of the cross hair, over $\frac{2}{3}$ of the measurements are reproducible to within 0.01 radian. In other words, the largest errors in the measurement of the time come from the tracks which are long, or from those which make a large angle with the vertical or y axis. Emulsion distortion contributes to the reproducibility error only through the fact that it is more difficult to set the cross hair tangent to the track if the track has a large curvature due to distortion. The variable air gap between the plates during the flight only contributes through increasing y in the above expression and sometimes by requiring more settings of the cross hair.

Effects of Misalignment

There are three possible sources of error which could be caused by misalignment of the plates.

The first type of alignment error could be caused by a difference between the direction of motion of the plate during the flight and the direction of the x axis of the microscope stage. If φ is the angle between these two directions, then there is an error introduced into the time

$$\Delta t = t \tan\theta \tan\varphi,$$

where θ is the eyepiece angle as before. It can be seen that this error is 0 for all vertical tracks. The effect on

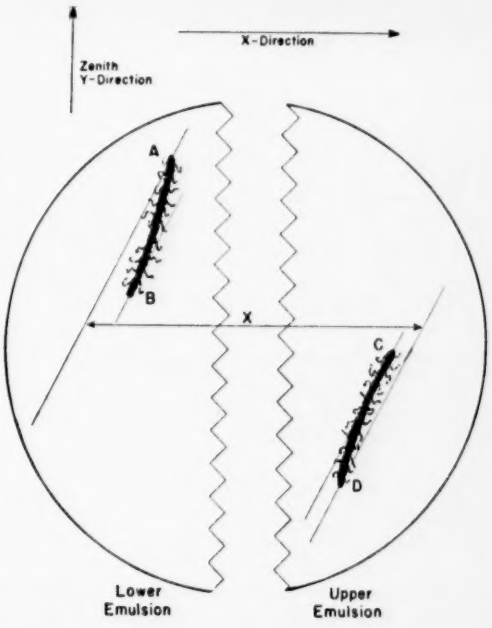

FIG. 2. The method of determining the time. B and C represent the intercepts of the track with the emulsion-air surface of the lower and upper emulsions. The cross hair is set parallel to the track at these two points. The distance x is measured with the precision screw by setting the cross hair to points A and D which are the intercepts of the track with the emulsion-glass surfaces.

tracks with eye-piece angle θ is to expand or contract the time scale slightly depending on the relative sign of θ and φ. It is estimated that this error is less than 1 percent in this experiment and thus is negligible.

The second type of error to consider could be caused by misalignment of the plates in the vertical or y direction. The error in x due to this cause is

$$\Delta x = \Delta y \tan\theta,$$

and again is 0 for vertical tracks. In this experiment it is estimated that Δy is of the order of ± 15 microns. This comes about because the emulsions were aligned using stars which are on the surface and are thus subject to translation errors due to distortions in the emulsion. Also it is possible that the plates did not follow exactly a straight line in the original motion.

The third type of error, which could be of the same order of magnitude but is probably less, could be caused by plates out of alignment by a small rotation about an axis perpendicular to the plane of the emulsion. At the ends of the plates this reduces to an error of the second type above, but at the top and bottom it becomes an error in the y alignment which will add to or subtract from the time measurement depending upon whether the track is at the top or bottom of the plate.

These errors can be reduced by using mechanical

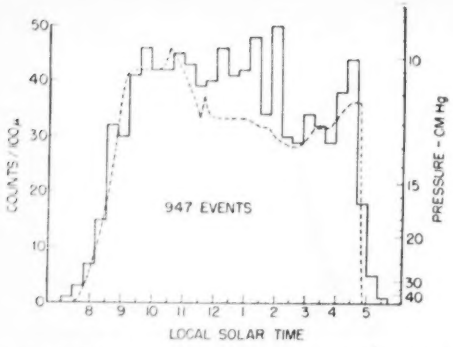

FIG. 3. The histogram is the number of tracks found in each interval of 100 microns of plate motion. The dotted curve is the calculated counting rate as a function of time assuming no changes in the flux with time at the top of the atmosphere and using the given altitude changes.

methods of alignment, but even with good mechanical methods one would probably want to check the alignment using traced-through star tracks.

In this experiment both the second and third type of error could have been accurately determined and corrected, if it had been found necessary. This could have been done by tracing through more than the 9 stars, and measuring the distortion in the emulsion at the star positions. It was decided that this was unnecessary, as these errors were found to be small.

III. ANALYSIS OF DATA AND EXPERIMENTAL RESULTS

The time was measured on 947 tracks. All of the time determinations were made by one person. Then all of the time measurements were repeated by another person, but readings were made to one less significant figure. All large discrepancies (greater than 50 microns) were carefully investigated by the original investigator, carefully remeasured if necessary, and the source of each discrepancy found. Thus it is probable that the 947 separate time measurements contain no more than one or two gross errors.

The raw data obtained are plotted in Fig. 3 in the form of a histogram of the number of events found per 100 micron interval of plate motion. 100 microns of plate motion is equivalent to 21.3 minutes of time. The observed variations with time can be caused by changes with time of the flux at the top of the atmosphere and by changes in the altitude of the balloon. In order to separate these two effects, the altitude curve provided by the barograph was used to correct for altitude changes.

To calculate what effect a change in altitude of the balloon will have on the flux of heavy nuclei through the plates, it is necessary to know how the particles are absorbed in the atmosphere. For nuclei of $Z \geqslant 10$, there seems to be agreement in the literature that the nuclear mean free path in air is 21 grams per cm^2. There is also the effect of ionization loss. The flux of particles per unit area through a vertical plate at depth D in the atmosphere is given by

$$\Phi(D) = \Phi_0 \frac{4}{\pi} \int_0^{\pi/2} \sin^2\theta f(D \sec\theta) d\theta,$$

where θ is the angle between the direction of the track and the vertical, and Φ_0 is the flux at the top of the atmosphere. The function $f(D \sec\theta)$, which is the measured linear attenuation function, was obtained from the curve given by the Minnesota group[4] on the basis of a number of flights. A curve for the altitude effect assuming a constant Φ_0 was obtained by numerical integration. It is shown in Fig. 3, superimposed on the cosmic-ray histogram.

It can be seen in Fig. 3 that there is a good fit between the two curves in the region of the slow rise of the balloon at the beginning of the flight and the rapid descent at the end. The total elapsed time of the flight, as measured by the moving plate mechanism and the heavy nuclei, agrees remarkably well with the total time as measured by the barograph clock. This is a very good indication that the moving plate mechanism was operating correctly. Since the local time of these altitude changes at the ends of the flight is known from visual observations of the launching and release time of the balloon, this excellent fit makes possible an absolute determination of the time of the cosmic-ray events. This has been done and the local solar time is given.

An examination of the portion of the curves between the initial rise and the final descent reveals that there is agreement between the two curves for the first and last thirds of the time at altitude, even to the detail of the small rise in the last third. In the center third, however, there is a large increase of the cosmic-ray histogram over the dotted altitude effect curve during the middle of the flight. In order to show this, the cosmic-ray histogram for the 21 intervals between the rise and descent has been corrected for altitude changes using the result of the numerical integration, and normalized to the flux per cm^2 per second through a vertical plane at a pressure of 1.1 cm Hg. This is shown in the histogram of Fig. 4. The increase of the center bar over the average of the other two amounts to 25 percent. If we use statistical errors which represent the square root of the number of counts, it could be as low as 17.5 percent or as high as 32.5 percent. The application of the chi square test gives a probability of 0.007 that a random sample will give no better fit to a straight line. The statistical error on each of the three points amounts to about 6 percent. The reproducibility of ± 3 minutes amounts to only 2 percent of these 150-minute time intervals. It is estimated that the alignment errors are also about 2 percent. These errors are not negligible, but they are smaller than the statistical errors. These

errors are much too small to account for the observed increase.

Altitude records can usually be relied upon to within about $\frac{1}{2}$ mm Hg pressure according to our previous experience. The record itself shows changes recognized and marked on the graph of about $\frac{1}{4}$ mm. In principle the altitude can be accurately determined from observed zenith angle distributions. For this purpose one would need to measure a much greater number of heavy nuclei. Also one would need better information on the attenuation of the heavy nuclei in the atmosphere and the zenith angle distribution averaged over all directions at the top of the atmosphere. Due to the fact that the absorption of heavy nuclei in the atmosphere is approximately exponential, the zenith angle distribution becomes much more peaked toward the vertical at lower altitudes. In other words, the altitude effect is much greater at the larger zenith angles than it is at the smaller zenith angles.

An examination of the zenith angle distribution of the heavy nuclei in this experiment yields a valuable qualitative check on the barometer record. The eyepiece angle and the y component of the length of each track in the emulsion was measured, and from these the zenith angle for each heavy nucleus was calculated. The 947 heavy nuclei were divided into four approximately equal groups according to the magnitude of the zenith angles. These zenith angle intervals turned out to be $0°-38\frac{1}{2}°$, $38\frac{1}{2}°-50\frac{1}{2}°$, $50\frac{1}{2}°-60\frac{1}{2}°$, $60\frac{1}{2}°-90°$. The heavy nuclei in these four groups were then plotted against time in the four histograms shown in Fig. 5.

An examination of Fig. 5 shows that the intensity during the first time interval increases relatively to the intensity during the last time interval as the zenith angle is increased. This clearly shows that during the first time interval the apparatus had a higher average altitude than during the second. There is a smaller difference between the intensities during the second and third time intervals which indicates that they represent more nearly equal altitudes. The third interval is perhaps higher than the second. Thus the altitude during the second interval was certainly lower than during the first interval and perhaps lower than the last interval too. This is in perfect agreement with the barograph record and in disagreement with what one would have to assume in order to explain the results in terms of an altitude change instead of a fluctuation in the primary flux. The observed increase cannot be attributed to errors in the barograph record.

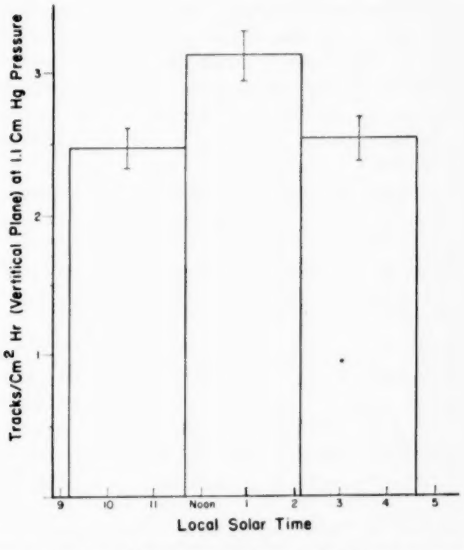

FIG. 4. The flux of heavy nuclei through the plates corrected to a constant altitude and plotted in three intervals of 700 microns each. This represents all of the data except the sections during the ascent and descent of the balloon.

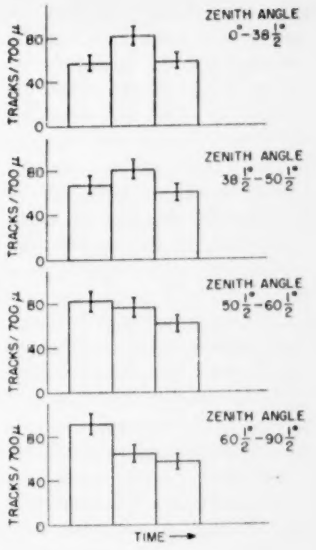

FIG. 5. The heavy nuclei have been divided into four nearly equal groups according to zenith angle. Each group is plotted in the same three time intervals used in Fig. 4.

The data at small zenith angles show that the center interval has an increase of 41 ± 18 percent over the average of the other two. This is without altitude correction which would make it an even greater increase. Though this is perhaps not statistically different from the 25 ± 8.5 percent deduced from all the data with the altitude correction, it possibly represents a first indication that the time changes observed here are confined to the low-energy heavy nuclei. It will be important to investigate this possibility in future experiments.

A large azimuthal asymmetry of the heavy nuclei coupled with a very slow rotation of the apparatus was looked for as a possible explanation for the effect. Because the photographic plates were flown with the emulsions in a vertical plane, they did not present the same projected area for the detection of particles in

different directions. Now if the balloon had rotated very slowly and there had been a large directional asymmetry in the flux of the heavy nuclei, the flux observed in the plates would fluctuate as the balloon turned. In order to investigate this possibility, the 947 heavy nuclei were divided into four groups depending upon which quadrant they were in with respect to the apparatus. An effect of the type postulated would show up as some sort of periodicity in each of these four quadrants. Careful examinations, comparison with a random separation of the data into four parts, and application of statistical tests revealed no evident periodicity. It is concluded that either there was no measurable azimuthal asymmetry in the heavy nuclei, or that the period of the rotation was sufficiently rapid to prevent its being resolved with 21.3-minute intervals. The observed increase cannot be attributed to a directional asymmetry and rotation effect.

However, there is one feature about the separation of the data into four quadrants that seems to be outside of experimental error, and that is that the number of heavy nuclei in quadrants 2 and 3 is 434 and the number in quadrants 1 and 4 is 513. Although there was a slight difference in the geometry of the apparatus between these two sides, in particular there were two other plates on the side of quadrants 2 and 3 which might have introduced some detectable absorption, it was found that the explanation was rather to be found in a small tilt of the apparatus by about 3°. This was discovered by plotting the distribution of the angles of the tracks with the vertical projected in the y-z plane. This distribution rises at small angles as the sine of the angle due to the vertical orientation of the plates. But at large angles it falls again becaue of absorption in the atmosphere. The fact that the difference between the number in quadrants 1 and 4 and the number in quandrants 2 and 3 appears mostly at the larger angles speaks strongly in favor of the tilt explanation rather than the local geometry explanation. There is no way in which such a tilt could affect the apparent time distribution, since there are no effects due to rotation.

The data were also divided up in other ways in an effort to detect discrepancies. For instance, the data at large eyepiece angles were divided into two groups, with angles of a given sign in each group. Since most of the plate orientation type of errors have a sign which depends systematically on the eyepiece angle, such errors might be expected to show up. They did not to within the statistical precision of the test.

In conclusion, these data show that there was a real increase in the flux of the heavy nuclei with $Z \geqslant 10$ at the top of the atmosphere around noon of June 4, 1952 in the vicinity of Minneapolis. No imaginable systematic error could have caused such an apparent increase, and the probability that it is a statistical fluctuation is low.

IV. DISCUSSION

The results of this experiment constitute strong evidence that the heavy nuclei do fluctuate with time. The average flux of heavy nuclei with $Z \geqslant 10$ measured here agrees remarkably well with the daytime flux obtained by Lord and Schein,[11] even though the delta-ray counts were made by different observers and the acceptance criterion may have been slightly different.

There have been large changes in cosmic-ray intensity at low altitude which have been attributed to charged particles accelerated by some mechanism on the sun.[13–15] On November 19, 1949, the ionization chamber at Climax, Colorado, recorded an extraordinary increase in the cosmic radiation at about 11 A.M. G.M.T. Forbush, Stinchcomb, and Schein[16] report that the increase amounted to 180 percent. Increases were observed at other stations around the world, but none at the equator. From the absorption in the atmosphere of the radiation responsible for the increase, it was deduced that the increase was due to the nucleonic component which is responsible for the production of stars in photographic emulsions. This increase coincided with a solar flare, as have similar smaller increases observed by Clay, Ehmert, Simpson, and others. It was concluded that nucleons are at times accelerated by some mechanism on the sun to cosmic-ray energies.

Changes correlated with solar flares have also been observed at balloon altitudes in the star rate but not in the heavy nuclei. Lord, Elston, and Schein[17] reported a 50 percent increase in the rate of star production during a small solar flare which produced no detectable increase at sea level. The flux of heavy nuclei showed no detectable increase. Freier, Anderson, Naugle, and Ney[4] also were not able to detect any increase in the heavy nuclei during solar activity. Thus we have some direct evidence that protons and possibly alpha particles are accelerated by the sun, but we have no direct evidence for the acceleration of heavy nuclei.

The steady emission of heavy nuclei coming directly from the vicinity of the sun would be expected to give a peak in the intensity in the morning due to the deflection of the particles in the earth's field. The fact that the observed peak is in the afternoon makes this explanation unlikely.

A peak in the flux of heavy nuclei near noon does not necessarily have to be interpreted as direct emission of heavy nuclei of cosmic-ray energy from the sun. One can postulate that the heavy nuclei arrive isotropically from all directions and still explain a diurnal effect, if one postulates a magnetic dipole field of the

[13] W. F. G. Swann, Phys. Rev. **43**, 217 (1933).
[14] Forbush, Gill, and Vallarta, Revs. Modern Phys. **21**, 44 (1949).
[15] K. O. Kiepenheuer, Phys. Rev. **78**, 809 (1950).
[16] Forbush, Stinchcomb, and Schein, Phys. Rev. **79**, 501 (1950).
[17] Lord, Elston, and Schein, Phys. Rev. **79**, 540 (1950).

sun. The effect that a solar magnetic dipole would have in producing diurnal variations has been considered by Janossy, Epstein, Vallarta and Godart, and Rossi. Such a dipole field would prevent particles with less than a certain energy from reaching the region of the earth's orbit. Particles with slightly higher energies would be able to reach the earth only from certain allowed directions. These directions would be such as to produce a maximum at 6:00 P.M. in the absence of a terrestial magnetic field and if the solar dipole were pointed in the same direction as the earth's. The effect of the earth's field is to deflect further the particles so that the maximum would be earlier in the afternoon. The precise shape of the intensity curve depends upon the strength and orientation of the solar dipole; upon the energy spectrum of the cosmic-ray particles detected; and upon the geomagnetic latitude of the point of observation. Alfvén[18] has suggested that such effects may be greatly reduced by the scattering of particles into trapped orbits around the sun by the earth's magnetic field. The theory has been investigated in detail by Kane, Shanley, and Wheeler,[19] and by Dwight.[20]

Neher, Peterson, and Stern[7] who used balloons and also Van Allen[21] who used rockets have shown that there are no additional primary particles arriving north of 58° geomagnetic latitude. It is postulated that this is probably due to a solar magnetic moment of 0.65×10^{34} gauss-cm^3. That the sun may have a magnetic field in spite of the apparently negative spectroscopic evidence is discussed by Alfvén.[22] He states on the basis of magnetohydrodynamic arguments that the observed turbulence on the surface of the sun would make it impossible to measure equatorial fields of the order of 20 gauss by the Zeeman effect method.

The observed peak in the early afternoon agrees qualitatively with the solar magnetic field effect calculated by Kane, Shanley, and Wheeler, and by Dwight. If the peak is present every day, it would constitute evidence for a solar magnetic dipole field of the same order of magnitude as deduced from the latitude cut-off. Observations of the changes of the effect with solar rotation and geomagnetic latitude would provide a new method for calculating the magnitude and orientation of a solar dipole. The effect should be largest near the knee of the latitude effect curve where these measurements were made.

The author wishes to express his sincere thanks to Professor Marcel Schein who suggested the experiment and gave much valuable help and advice. He also wishes to thank Dr. Jere J. Lord for help in the early stages of the experiment and Mr. David B. Williams for checking the time measurements and assisting with the angular distribution. The moving plate apparatus was developed in the Physical Sciences Central Development Shop with the help of Mr. T. J. O'Donnell and Mr. Walter Norlander. The precision stage was designed and made in the Physics Department Machine Shop by Mr. Ivar Kalberg.

[18] H. Alfvén, Phys. Rev. **72**, 88 (1947).
[19] Kane, Shanley, and Wheeler, Revs. Modern Phys. **21**, 51 (1949).
[20] K. Dwight, Phys. Rev. **78**, 40 (1950).
[21] J. A. Van Allen, Nuovo cimento **10**, 630 (1953).
[22] H. Alfvén, Nature **168**, 1036 (1951).

High-Energy Electron Scattering by Nuclei*

R. W. PIDD, C. L. HAMMER, and E. C. RAKA
Randall Laboratory of Physics, University of Michigan, Ann Arbor, Michigan
(Received June 19, 1953)

The Michigan race-track synchrotron has been used as a source of electrons for the study of elastic scattering of 30- to 45-Mev electrons by nuclei of $Z=46-52$ and $Z=74$. The experimental results for tungsten can be interpreted to give a value of the nuclear radius equal to $(1.0\pm0.1)\times10^{-13}A^{\frac{1}{3}}$ cm if a constant proton density is assumed for the nucleus. The radius of the tin nucleus is $(1.1\pm0.1)\times10^{-13}A^{\frac{1}{3}}$ cm. Any discontinuity in r_0 *versus* A at the closing of the $g_{9/2}$ shell is about 1 percent or less; a step increase of 2 percent at $Z=48$ gives a best fit to the lower Z data.

INTRODUCTION

THE angular dependence of the differential cross section for the scattering of electrons by nuclei depends on the nuclear charge distribution when the electron de Broglie wavelength is comparable with the nuclear size. Several measurements of the cross section have been made at incident electron energies between 30 and 45 Mev. The results for a tungsten target are in agreement with a nuclear radius given by $R=r_0A^{\frac{1}{3}}$, $r_0=(1.0\pm0.1)\times10^{-13}$ cm, for an assumed uniform spherical model of the nucleus. A somewhat larger value of r_0 is found for tin and neighboring elements. A comparison of these radii with the values obtained by other means shows the inadequacy of the simple uniform model and to some extent how it should be modified.

APPARATUS

The source of electrons is the internal beam of the Michigan synchrotron. A target is located in one of the field-free straight sections at a position just inside the equilibrium beam orbit. The beam is scattered by contracting the orbit to the target radius. Figure 1 shows the equilibrium orbit, target location, and the detecting systems.[1] Scattered electrons emerge from the vacuum chamber through 5-mil aluminum windows into the detecting systems on either side of the chamber. One detector fixed at 90° is used as an intensity monitor, while the other can be set at angles between 60° and 120° with respect to the incident beam direction. The detecting systems include a collimator, magnetic analyzer, and a pair of shielded Geiger counters, all shown approximately to scale in the figure. The scattered beam is deflected through an angle of 15° in the anlayzer magnetic field and then is detected as a coincidence in the pair of counters. Background coincidences are recorded in either of two ways, by plugging the collimator hole or by increasing the analyzer field so that electrons elastically scattered from the target cannot reach the counters. Both methods give the same result. A typical spectrum of the scattered electrons shows a symmetrical peak centered at the incident beam energy, an energy half-width of ±20 percent, and a height about 10 times the background level. The counting rate is adjusted to about $\frac{1}{8}$ count per synchrotron pulse. All data are corrected for systematic counting errors.

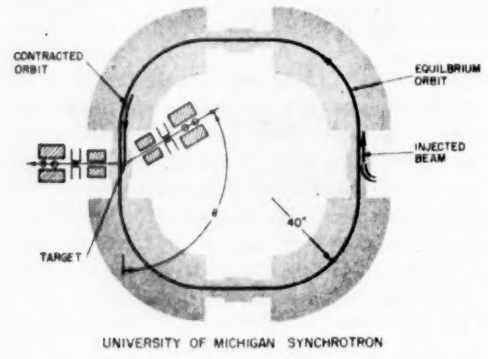

FIG. 1. Experimental layout.

EXPERIMENTAL RESULTS

In Fig. 2 are plotted the cross sections for a tungsten target at 33 Mev. For comparison, theoretical curves for 30-Mev electrons are drawn for a point nucleus[2] and a uniform spherical model,[3] $r_0=1.45\times10^{-13}$ cm. Both data and curves are normalized at 90°. It can be seen that the experimental points deviate from the uniform model toward the point nucleus. A choice of $r_0=1.0\times10^{-13}$ cm, about 30 percent smaller than the assumed value, leads to the best agreement between data and calculation. In this range of energies, the cross section is a function of the product of electron energy and nuclear radius. Therefore the uniform sphere prediction for $E=30$ Mev, $r_0=1.45\times10^{-13}$ cm, applies equally well for the combination, $E=43$ Mev, $r_0=1.0\times10^{-13}$ cm. The data obtained at 43 Mev, plotted in the same graph, are in much better agreement with this predicted angular distribution than the 33-Mev points.

The systematic errors in the experimental cross

* This research was supported by the U. S. Atomic Energy Commission.
[1] Raka, Hammer, and Pidd, Phys. Rev. **90**, 341 (1953).
[2] H. Feshbach, Phys. Rev. **88**, 295 (1952).
[3] L. K. Acheson, Jr., Phys. Rev. **82**, 488 (1951).

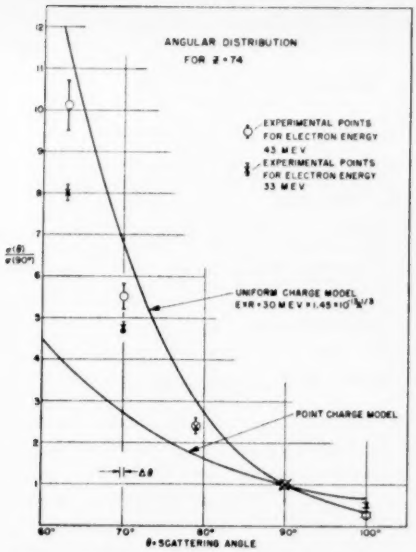

FIG. 2. Differential cross sections for tungsten.

sections are considerably less than the standard deviations which are shown. The tungsten target is 0.007 inch thick and is oriented at 45° with respect to the incident beam direction. The variable-angle detector is on the transmitting side of the target. Relative corrections depending on the target thickness at angles between 60° and 100° are less than 2 percent. The errors include corrections for multiple and plural scattering, and straggling in the target. At angles larger than 100° these errors become much larger especially due to plural scattering and the data are not considered reliable. Thus the conclusions reached in the preceding paragraph refer to the more reliable forward angles. The error calculations are confirmed experimentally by a repeat run with the target thickness reduced by one-half, in which no detectable change in the cross sections could be observed. The Schwinger correction, while important to the absolute cross section, would lead to a negligible differential correction within the angular range in the experiment.

Similar data have been obtained for a series of target elements from $Z=46$ to $Z=52$ at an energy of 34 Mev. In an effort to find any systematic differences from element to element, the targets were alternated inside the vacuum system in a series of runs so that any experimental bias could be minimized. A total of 12 500 counts was accumulated for each element at two angles, 60° and 90°. The ratios, $\sigma(60°)/\sigma(90°)$ are plotted in Fig. 3. The ratio predicted for a point nucleus[2] is 5.2 and for a uniform sphere,[3] $r_0=1.45\times10^{-13}$ cm, about 11 for all the elements. The value $r_0=(1.1\pm0.1)\times10^{-13}$ cm is consistent with the data, 10 percent larger than in the case of tungsten. Individual variations among the target elements are less than the standard deviation except for the break between $Z=48$ and $Z=49$.

CONCLUSIONS

Coefficients of the nuclear radius less than 1.45×10^{-13} cm have been found in other experimental work. In particular, electron scattering at 15.7 Mev,[4] and μ-meson absorption by nuclei[5] agree with a value of 1.2×10^{-13} cm. It appears from this that observations which depend only on the electric charge distribution in the nucleus may give a consistently smaller value for the nuclear size than the value obtained from reactions which depend on nuclear interaction. The data on beta decay of mirror nuclei, on the other hand, are consistent with the larger value of the radius, if the uniform model is used. Since these data extend only up to $Z=20$ they cannot be readily compared with electron scattering results now available.

Methods of measuring the nuclear size which are available at present fail to determine a nuclear model. In each case they measure an effective radius for an interaction and not a nuclear density distribution. It

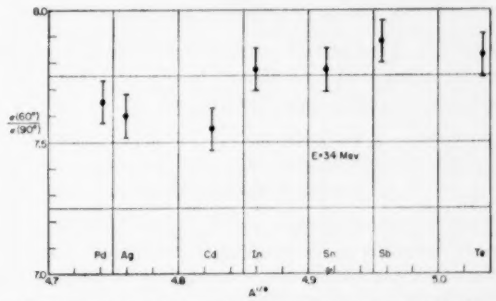

FIG. 3. Ratios of differential cross sections at 60° and 90° for elements from $Z=46$ to $Z=52$.

is not surprising then that different observations and different interactions should give conflicting results when interpreted on the basis of a uniform model with a sharp boundary. Nevertheless, saturation in nuclear structure is a common point of agreement among all measurements and any new model must retain this property. In view of this, the nuclear model suggested by Wilson,[6] a saturated core surrounded by an exponentially decreasing distribution, may lead to the best agreement among all data on the nuclear size. Some scattering models such as this have been used and they show that the angular dependence of the cross section for electron scattering depends mostly on the core size. It is possible that the radius measured by neutron scattering, for example, would extend toward the edge of the distribution. Electron scattering at much higher energies is model-dependent and should yield more detailed information about the shape of the proton distribution in the nucleus.

[4] Lyman, Hanson, and Scott, Phys. Rev. **84**, 626 (1951).
[5] L. N. Cooper and E. M. Henley, Bull. Am. Phys. Soc. **28**, No. 3, 56 (1953).
[6] R. R. Wilson, Phys. Rev. **88**, 350 (1952).

Properties of Heavy Unstable Particles

D. LAL, YASH PAL, AND B. PETERS
Tata Institute of Fundamental Research, Bombay, India
(Received June 22, 1953)

A block of emulsion consisting of unbacked emulsion sheets can be used as a very efficient detector for heavy unstable particles and provide favorable conditions for mass and energy determinations. The mass of the τ meson was obtained as $m_\tau = 3m_\pi + Q$, where $Q = 76.0 \pm 0.9$ Mev. Fairly accurate mass values are obtained for the positive K meson and four examples of the capture of negative heavy mesons are presented, two of them leading to emission of a π meson. A charged particle of mass higher than that of a proton which decays in flight into a meson is discussed. In most of these cases the nuclear event giving rise to the heavy mesons could be observed. The Q value of the V_1^0 particle was determined as 37 ∓ 2 Mev and other examples which may represent the decay of neutral particles are discussed.

IN this paper we give the result of measurements on 12 heavy charged unstable particles of which 10 are observed to be ejected from nuclear events. The particles are identified as

3 τ mesons,
4 K mesons (probably positive),
4 K mesons (negative),
1 $V^\pm$ particle decaying in flight.

We also give results on 4 events which probably represent the decay of neutral heavy particles. These particles are tentatively identified as

1 V_2^0 particle,
2 V_1^0 particles,
1 particle of mass $\sim 4100\, m_e$.

All the events were observed in a solid block of emulsions consisting of 24 emulsion sheets 6 in.$\times$4 in. and 600μ thick exposed in the stratosphere at geomagnetic latitude 19°. After exposure these emulsion sheets were mounted on glass plates and carefully aligned on slides such that particle tracks could be traced through the entire block. With such an emulsion arrangement it is comparatively easy to identify various types of particles and trace them to their origin. (The track length available for measurement is frequently of the order of several cm.)

τ MESONS

Three examples of τ mesons were found. One is emitted with an energy of 31.7 Mev from a star which according to the nomenclature of Brown *et al.*[1] is designated by $6+0p$. The decay products consist of one positive π meson of 22.4 Mev and one negative π meson of 15.4 Mev which come to rest in the emulsion block, as well as one meson which escapes.

The second τ meson is produced with 6.4-Mev energy in a star of the type $21+2\alpha$. Of the decay products two positive π mesons (of 25.8 and 16.2 Mev, respectively) come to rest in the block; the third escapes after traversing five emulsion sheets.

The third τ meson is emitted with 33.6 Mev from a star of the type $13+10\alpha$. In this case only one of the 3 decay products comes to rest in the block (a positive π meson of 6.63-Mev energy). Details on these three particles are given in Table I. In each case the Q values and masses quoted are those obtained by using the energy of the two decay products which can be determined with the greatest accuracy and calculating the energy of the third decay product from conservation of momentum assuming that all decay products are π mesons. Combining the results of these observations, we obtain as our best value for the mass of the τ meson

$$M_\tau = 969.3 \pm 1.7\, m_e, \quad Q_\tau = 72.2 \pm 0.8 \text{ Mev.}^2$$

TABLE I. τ mesons.

No.	Origin	Parent particle: Range (cm)	Parent particle: Energy (Mev)	Q value (Mev)	Mass	Decay products: Range (cm) observed (o) or total (t)	Decay products: Energy (Mev)	Angles of emission
1	$6+0p$	0.6650	31.7	72.2 ± 1.5	969.0 ± 3	(a) 0.898 (t)	22.4	$\measuredangle ab = 93°$
						(b) 0.478 (t)	15.4	$\measuredangle bc = 131°$
						(c) 0.37 (o)	34.4	$\measuredangle ca = 136°$
2	$21+2\alpha$	0.0367	6.4	72.8 ± 1.5	970.8 ± 3	(a) 1.1474 (t)	25.8	$\measuredangle ab = 105°$
						(b) 0.5369 (t)	16.2	$\measuredangle bc = 118°$
						(c) 0.46 (o)	30.8	$\measuredangle ca = 137°$
3	$13+10\alpha$	0.7468	33.6	71.7 ± 2.0	968.3 ± 4	(a) 0.1135 (t)	6.63	$\measuredangle ab = 78°$
						(b) 0.45 (o)	29.8	$\measuredangle bc = 168°$
						(c) 1.2161 (o)	35.3	$\measuredangle ca = 116°$

[1] R. H. Brown *et al.*, Phil. Mag. **40**, 862 (1949).
[2] *Note added in proof.*—These values were obtained before correcting for variations in individual emulsion thicknesses and for the effect of distortion on the angles between steep tracks. More refined measurements are described in the Proc. Indian Acad. Sci. (to be published) and yield $Q_\tau = 76.0 \pm 0.9$ Mev and $M_\tau = 996.8 \pm 1.8 m_e$.

TABLE II. Positive K mesons.

No.	Origin	Range (cm)	No. of emulsions traversed	Mass values (m_e) g/R	Sc/R	M.R.	Energy of secondary
1	$20+5n$	1.36	1	1090 ± 100	990 ± 120	1130 ± 130	$p\beta=226\pm20$ Mev/c
2	$14+2n$	1.2	1	1080 ± 100	940 ± 150	1140 ± 150	$g/g_{pl}=0.98\pm0.12$
3	Outside of block	5.20	14	1220 ± 100	1010 ± 100	920 ± 100	$g/g_{pl}\approx1$
4	$1+0n$	3.15	5	1070 ± 100	1010 ± 110	1050 ± 100	$g/g_{pl}=0.93\pm0.07$

Of the three τ mesons, two were discovered by tracing back towards their origin, the tracks of positive and negative π mesons which stopped in the emulsion. From the observed yield we estimate the ratio of slow (presumably positive) τ mesons to slow π mesons produced at this latitude and altitude as

$$\tau^+/\pi^\pm=1.0\pm0.7 \text{ percent.}$$

The same $13+10\alpha$ star which gives rise to the third τ meson also contains a $V^\pm$ *particle.* This particle has an observed range of 1.93 cm and decays just before it comes to rest. Its residual range at the point of decay is $0.35^{+0.25}_{-0.15}$ cm. The mass of the particle is 2520 ± 400 m_e. The decay product can be observed over a track length of 1.4 cm; its mass is 330 ± 60 m_e and $p\beta=160\pm13$ Mev/c. Thus, 1.9×10^{-10} sec after its creation, the V particle decayed into a (presumably) π meson of energy 103 ± 9 Mev. If together with the π meson a single neutral particle is emitted, its mass must be larger than 1570 m_e. The observed event is consistent with the decay scheme: $V^\pm\rightarrow\pi^\pm+\text{neutron}+Q$. If this scheme is assumed the mass of the V particle is $M=2330\pm30$ m_e and the Q value is $Q=135\pm35$ Mev.

POSITIVE K MESONS

Table II gives the measurements on four particles which come to rest in the emulsion before they decay; they seem to form a homogeneous group. The mass values in the fifth column are obtained from measurements of grain density *vs* particle range (g/R); the mass values in the sixth column are obtained from measurements of scattering *vs* range (Sc/R) by using a method of varying cell length which accurately takes into account the energy loss along the trajectory. (This method, which will be described elsewhere, is, we believe, capable of great accuracy.) The mass values in the seventh column are obtained from scattering *vs* range using the method described by Menon and Rochat (M.R.).[3] The last column gives the $p\beta$ value or the grain density (in terms of its plateau value) of the decay products.

The best mass value from scattering measurements for the 4 positive K mesons is

$$M_{K^+}=1025\pm50\ m_e.$$

Here the error given is the standard deviation based on statistical fluctuations only. An additional systematic error of the order of 50 m_e cannot be ruled out

TABLE III. Negative K mesons.

No.	Origin	Range	Mass (m_e)	Range total (t) or observed (o)	Visible prongs in capture star Mass (m_e)	Energy (Mev)	Remarks
1	$14+2n$	308μ	1000^{+720}_{-400}	15.8μ (t)			Probably proton.
				5.7μ (t)			Probably proton.
				0.39 cm (o)	300^{+70}_{-40}	24.7 ± 0.8	π meson.
2	$25+5n$	92μ	?	48μ (t)			Probably proton.
				5.5μ (t)			Probably proton.
				139μ (t)			Scatters very strongly.
				0.354 cm (o)	210^{+50}_{-40}	25.3 ± 1.0	This particle is a π meson since it produces a nuclear interaction in flight after traversing 3.5 mm of path.
3	$4+6n$	2.5 cm	1010 ± 150	385μ (t)			Probably proton.
				46μ (t)			Probably proton.
				140μ (t)			Probably proton.
				0.14 cm (o)		>20 Mev	Proton or deuteron.
				1.76 cm (o)	1836	>175 Mev	Proton.
4	Outside of block	2.926 cm	840 ± 200	407μ (t)			Probably proton.
				456μ (t)			Probably proton.

[3] M. G. K. Menon and O. Rochat, Phil. Mag. **42**, 1232 (1951).

TABLE IV. V_1^0 particles.

Angle between tracks	Decay products: Range (cm) Observed (o) or total (t)	Mass (m_e)	Energy (Mev)	Parent particles: Q Mev	Mass (m_e)
169° 48′	0.0725 (t) 1.85 (o)	276 1850±180	5.22 π^- 118±7 (p)	37±2	2184±4
168° 36′	0.5284 (t) 0.60 (o)	276 ~1800	16.5 π^- 42±3 (p)	38±3	2186±6
151°	0.80 (o) 0.917 (t)	240±40 3970^{+900}_{-600}	49.5±3.5 (π^-) 67.5 (d)	89±10	4120±20

until more calibration measurements have been carried out with our new scattering procedure. It is, therefore, not possible at this moment to state definitely whether or not the mass of these particles is different from that of the τ meson.

It is interesting to note that the last particle in Table II does not originate in a star but is produced by itself in the middle of the emulsion. There is, however, a very steep minimum ionization track which seems to cross the K-particle track about 3μ from its origin. Although we do not believe that the two tracks are associated, it is possible that the origin of this particle should be described as of the type $1+1p$ or $1+2n$.

NEGATIVE K MESONS

Table III contains data on four K mesons captured by nuclei at the end of their range. The first one originates in the same star as the positive K particle No. 2 listed in Table II.

Particles No. 1 and No. 2 give very similar capture stars, both giving a π meson of ~25 Mev and some unusually short black tracks.

Particle No. 3 suffers a 8° deflection 6 mm before the end of its range. There is some indication that the mass after this deflection is reduced ($680\pm150\ m_e$), but the evidence is not conclusive. The energy of the visible prongs emitted at capture put a lower limit of $480\ m_e$ on the mass of the particle after deflection.

Based on the fraction of capture stars investigated which led to the discovery of K^- mesons, we estimate the ratio of slow π^- to slow K^- mesons produced at this altitude and latitude as $K^-/\pi^- = (3\pm1.8)$ percent.

V_2^0 PARTICLE

A positive π meson of 11-Mev energy is emitted from a two-prong star and comes to rest in the emulsion block. The second track which makes an angle of 69° with the π^+ track can be observed over a distance of 1.2 cm. Grain density ($g/g_{pl}=0.9\pm0.04$) and scattering measurements ($\alpha_{100}=0.056\pm0.008$) show that the particles' mass is less than 30 percent of the proton mass and that it has a momentum $p\beta=450\pm70$ Mev/c. Assuming a two-body decay scheme $V_2^0\rightarrow\pi^++\pi^-$, we obtain

$$M(V_2^0)=810\pm35\ m_e, \quad Q(V_2^0)=132\pm17 \text{ Mev}.$$

V_1^0 PARTICLES

A group of 85 π mesons (34 π^+ and 51 π^-) whose tracks were traced from their point of decay or capture to their point of origin in the emulsion block can be classed according to their mode of production in the following way:

$^+\pi$	π^-	Total	
2	—	2	came from τ mesons.
1	—	1	came from the V_2^0 particle mentioned above.
30	43	73	came from stars with more than 2 prongs.
1	8	9	came from "two-prong stars."
34	51	85	

Some of the last mentioned 9 cases are undoubtedly genuine nuclear events; in one case a recoil is visible at the origin of the meson, and in two other cases a slow electron is emitted. There are also 3 cases where it cannot safely be ruled out that a δ ray in the neighborhood is associated with the production of the meson. These dubious cases will be discussed elsewhere. In 3 cases, however, there can be no doubt that only two charged particles originate at a point. They probably represent the decay of a neutral unstable particle, and in Table IV they have been analyzed on the assumption that they represent two-body decays. The Q values in the first two cases are in close agreement with those obtained in the analysis of V_1^0 particles observed in cloud chambers. The third case, if interpreted correctly, represents the decay of a particle which has not previously been observed.

Full details on the measurements reported in this paper will be published shortly in the *Proceedings of the Indian Academy of Sciences*. The technical details involved in preparing an accurately aligned solid block of emulsions as well as the new method of obtaining particle masses from range and scattering measurements with variable cell lengths will also be published shortly in the same journal.

We wish to express our gratitude to Dr. S. Biswas, Mr. R. R. Daniel, Miss S. Ghosh, and Mr. Rama for assistance in some of the measurements reported here.

Distribution of Arrival Times of Air Shower Particles*

P. Bassi,† G. Clark, and B. Rossi
Department of Physics and Laboratory for Nuclear Science, Massachusetts Institute of Technology, Cambridge, Massachusetts
(Received July 13, 1953)

We have studied the instantaneous distribution of particles in extensive air showers at sea level by measuring the relative delays between particles with three liquid scintillation counters. The delays measured were in the range from 5 to 300 mμsec. The sizes of the showers were in the range from 10^5 to 10^6 particles. Using statistical methods of analysis we have found that at a given instant most electrons with energies of ~20 Mev lie in a flat disk of thickness between 1 and 2 meters. The particles which can penetrate at least 20 cm of lead lie in a disk of thickness between 2 and 3 meters. The disk of penetrating particles follows behind the disk of electrons by less then 3 meters.

We measured the projected zenith angles of the axes of individual showers by measuring the delays between widely spaced counters. The standard deviation of a measurement of the sine of the projected zenith angle of a shower was 0.13. The root mean square of the sines of the projected zenith angles was found to be 0.24 ± 0.015. If we assume a $\cos^n\theta$ distribution law for the projected zenith angles we find $n=15\pm1.2$. We determined the spatial orientations of the axes of individual showers by measuring the projections of the zenith angles on two mutually perpendicular planes.

1. INTRODUCTION

PARTICLES in an extensive air shower, generated by a single high-energy particle incident on the top of the atmosphere, may be delayed with respect to one another at the plane of observation because

(1) path lengths may differ as the result of scattering,
(2) velocities may differ,
(3) the axis of the shower may not be perpendicular to the plane of observation.

Several attempts have been made to observe delays due to causes (1) and (2) by recording the times of arrival of air shower particles at detectors. McCusker, Ritson, and Nevin[1] found no particles in air showers which were delayed by more than 1500 mμsec (1500×10^{-9} sec). Mezzetti, Pancini, and Stoppini[2] have shown that the percentage of penetrating particles with delays greater than 100 mμsec is certainly less and probably much less than 15 percent. Delays of penetrating particles have been studied by Officer[3] who found an upper limit of 20 mμsec to the mean delay of particles able to penetrate 10 cm of lead. Jelley and Whitehouse[4] have measured the delays between successive pulses produced in a single large scintillation counter by air showers. They find that 0.6 percent of particles have delays from 30 to 700 mμsec and that the distribution of these delays can be described by an exponential function with half of the delays occurring before a time $\Delta t=100\pm20$ mμsec.

We describe here several experiments which we have carried out with an apparatus sensitive to delays in the range from 5 to 300 mμsec. Our results clarify several features of the instantaneous longitudinal distribution of particles in air showers. In addition they demonstrate that one can determine with fair precision the direction of arrival of air showers from measurements of the delays between widely spaced counters.

At any instant most particles in an air shower are concentrated in a disk-shaped region of space symmetric about the shower axis. This axis is the prolongation of the trajectory of the primary particle. The instantaneous spatial distribution of a certain type of particles will be described by a cylindrically symmetric volume density $\sigma(r, z, t)$, where z is the distance measured along the shower axis, r is the radial distance from the axis, and t is the time (measured from some convenient instant). After the first few radiation lengths from the top of the atmosphere, most of the shower particles will be electrons of about the critical energy traveling at various angles with respect to the shower axis. However, the shape of the spatial distribution will change slowly as the shower propagates downward. By measuring the times of arrival of air shower particles at several counters spread out on the ground, one can, therefore, obtain information about the instantaneous distribution of particles just before the shower struck the ground. In particular, we have measured the thickness of shower disks, the curvature of shower "fronts," the longitudinal distribution of penetrating particles relative to the electrons, and the angular distribution of shower axes.

2. EXPERIMENTAL ARRANGEMENT

Three large liquid scintillation counters, each with a sensitive area of 600 cm², were used both to detect the air showers and to record the times of arrival of the particles. The counters were constructed from the commercial five-gallon drums in which the benzene, used for the scintillation fluid, was delivered. RCA 5819 photomultipliers, selected for high photoelectric efficiency and high gain, were mounted on the tops of the drums by means of adapters as illustrated in Fig. 1. Aluminum foil was spread over the bottoms of the drums in order to increase the amount of light striking

* This work was supported in part by the joint program of the U. S. Atomic Energy Commission and the U. S. Office of Naval Research.
† On leave of absence from the University of Padova, Padova, Italy.
[1] McCusker, Ritson, and Nevin, Nature **166**, 400 (1950).
[2] Mezzetti, Pancini, and Stoppini, Phys. Rev. **81**, 629 (1951).
[3] V. C. Officer, Phys. Rev. **83**, 458 (1951).
[4] J. V. Jelley and W. J. Whitehouse, Proc. Phys. Soc. (London) **66**, 454 (1953).

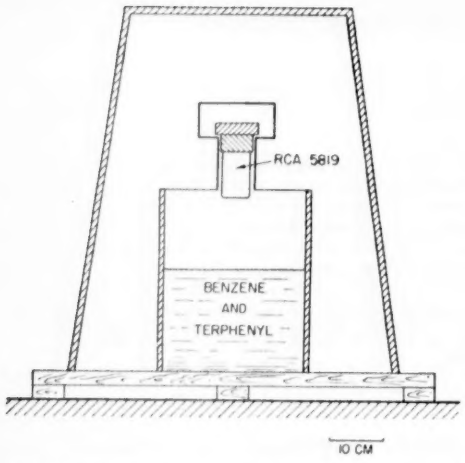

FIG. 1. A schematic diagram of the scintillation counter and protective housing.

the photomultiplier. The counters were filled to a depth of 20 cm with a solution of terphenyl in benzene (3 grams/liter).

A block diagram of the electronic apparatus is shown in Fig. 2. The positive pulses from the last dynodes were conducted by 100-ohm coaxial lines to the central station where they were amplified by fast R-C coupled amplifiers, each with a gain of 500 and a rise time of 20 mμsec. The amplifiers were connected to a crystal diode triple coincidence circuit, and the output of the coincidence circuit was fed into a fast discriminator, employing a secondary emission amplifier tube. Thus, whenever three pulses of sufficient size entered the coincidence circuit within an interval of 300 mμsec, a pulse was generated which triggered the sweep of the oscilloscope. The sweep speed was 100 mμsec/cm. The oscilloscope tube was of the aluminized screen type which permitted long exposures to be made without fogging due to stray light.

The negative pulses from the collecting anodes of the photomultipliers were also conducted by 100-ohm coaxial lines to the central station. At this point artificial delays were introduced between the pulses by suitable lengths of RC-65/U delay line so that the pulses from counters 1, 2, and 3 would appear in proper order in spite of small delays in the arrival of the particles. The pulses were then mixed, amplified (over-all gain of 6000, rise time 15 mμsec), and displayed on the oscilloscope. The oscilloscope traces were photographed with a camera which was automatically advanced one frame for each triple coincidence event. All measurements were made on the oscilloscope record by means of a film projector. We calibrated the sweep with a standard high frequency oscillator and determined that the time scale on the projected image was 1 mm per 5.3 mμsec.

Since much of the experiment was performed with the detectors in the open at temperatures below the freezing point of the scintillation liquid, it was necessary to provide protection for the counters from the weather. We placed the counters on light wooden frames and covered them with inverted ash cans. Electric heating cord was wrapped around the cans and covered with a layer of asbestos for heat insulation.

The total thickness of material between the air and the top surface of the scintillating fluid was approximately 2 g cm^{-2} of steel and brass.

The experiment was performed on the roof of a building at sea level. All the electronic equipment other than the photomultipliers was located in a shelter where daily checks of its performance were made.

We measured the resolving time of the coincidence circuit by determining the amount by which one of the three pulses had to be delayed in order to eliminate the triple coincidence trigger pulse. The resolving time was adjusted so that it was large compared to typical delays which were to be measured.

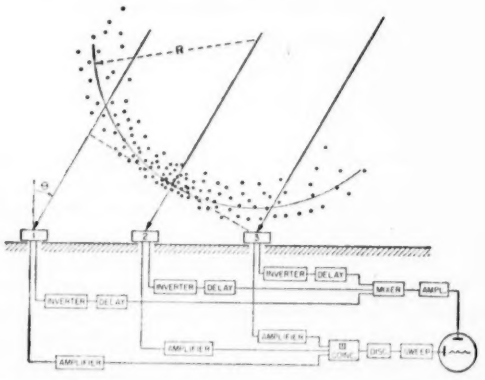

FIG. 2. Block diagram of the apparatus with a schematic representation of an air shower about to strike the counters. The counters are in arrangement II.

The pulses produced by cosmic-ray particles traversing the counters were not much larger than the thermal noise pulses from the photomultipliers. The amplification was fixed so that 300 countable pulses per second were admitted into the coincidence circuit from each counter. The accidental triple coincidence rate was 0.02 hr^{-1}. The efficiencies of the detectors at these settings were then determined by means of a conventional counter telescope arrangement which selected μ mesons traversing the scintillation counters. The efficiencies were ≈ 0.90.

Schematic diagrams of the various arrangements of counters used in our measurements are shown in Fig. 3. In the subsequent discussion it will be convenient to call these arrangements by the numerals indicated in the figure.

The photographic records of several events obtained with arrangement I are reproduced in Fig. 4. Most

triple coincidences with the counters in this vertical arrangement are due to traversals by single μ mesons. We interpret the wide variations in pulse heights as statistical fluctuations due to the small average number of photoelectrons produced in the photomultipliers by a particle of minimum ionization traversing the counters.

We determined the delays between the pulses by measuring the relative positions of the maxima of the three pulses. Approximately 10 percent of the events were rejected because the height of one of the pulses was less than a certain preset minimum height, and 2 percent because one of the pulses was so large as to saturate the amplifier and produce an irregular maximum.

3. THEORY OF DELAY MEASUREMENTS AND METHOD OF ANALYSIS

A. Relations between the Spatial Distribution of Particles, Particle Fluxes, and Delay Distributions

As was mentioned in Sec. 1, the shape of the spatial density distribution $\sigma(r, z, t)$ changes slowly as the shower propagates along the z axes. Therefore, the time dependence of σ around the time t_0 at a detector located at r_0, z_0 will be related to the z dependence of σ around r_0, z_0 at the time t_0. Specifically,

$$\sigma(r_0, z_0, t) = \sigma(r_0, z', t_0), \tag{1a}$$

where

$$z' = z_0 - v(t - t_0), \tag{1b}$$

and v is the velocity of propagation of the shower disk which is practically the velocity of light. $\sigma(r_0, z', t_0)$ is the instantaneous longitudinal density distribution of particles at r_0 at the time t_0.

We shall call $f(r, z_0, t)$ the instantaneous flux of particles through the plane $z = z_0$. Thus $f(r, z_0, t)dtdA$ is the probability that a particle traverses an area dA in the plane $z = z_0$ at a distance r from the axis between the times t and $t+dt$. f and σ are related by the equation

$$f(r, z_0, t)dtdA = \sigma(r, z_0, t)vdtdA = \sigma(r, z', t_0)vdtdA. \tag{2}$$

We shall call $F(r, z_0, t)$ the normalized probability distribution for the time of arrival of the first particle at a counter struck by a shower. Thus $F(r, z_0, t)dt$ is the probability that, if at least one particle traverses a counter of area A at r, z_0, the first particle to do so arrives between the times t and $t+dt$. F and f are related by the equation

$$F(r, z_0, t)dt = \frac{Af(r, z_0, t)dt \exp\left[-A\int_{-\infty}^{t} f(r, z_0, t')dt'\right]}{1-\exp(-m)}, \tag{3}$$

where

$$m = A\int_{-\infty}^{+\infty} f(r, z_0, t)dt$$

is the average number of particles that traverse the counter. The exponential in the numerator represents the probability that no particle has traversed the counter up to the time t. The denominator is the probability that at least one particle traverses the counter.

The shower "front" can now be rigorously defined in terms of F. Suppose $F(r, z_0, t)$ characterizes a shower that arrives at the plane $z = z_0$ near the time t_0. Consider the quantity

$$z_f(r) = \int_{-\infty}^{+\infty} z' F\left(r, z_0, t_0 = \frac{z' - z_0}{v}\right)\frac{dz'}{v}. \tag{4}$$

$z_f(r)$ is the expectation value of z at the time t_0 of the first particle that will eventually strike the counter. This quantity depends upon the area of the counter. We call the surface of points $z_f(r)$ the shower front.

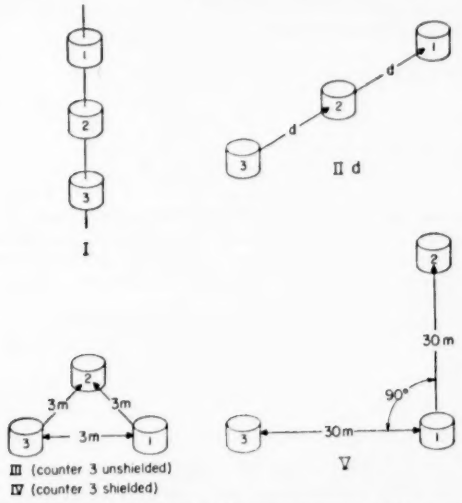

FIG. 3. Schematic diagrams of the arrangements of the counters.

B. Interpretation of Correlated Delays

Above the detection apparatus in Fig. 2 we have shown an "instantaneous profile" of a shower about to strike the counters. Individual shower particles are represented by dots. For the purpose of illustration let us imagine that the axis of this shower strikes counter 2, and that it lies in the plane determined by the counters and the zenith. θ is the angle between the axis and the

FIG. 4. Photographic records of three shower events showing the pulses from the three scintillation counters.

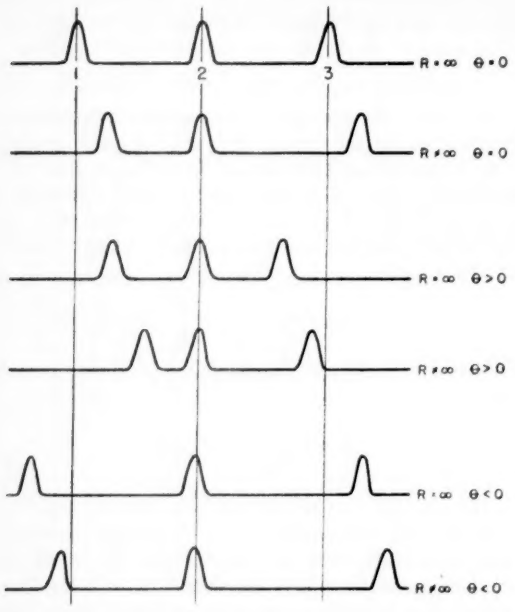

FIG. 5. Idealized diagrams of several types of events showing only the effect of front curvature and axis orientation on the relative positions of the pulses.

vertical. We shall approximate the shape of the front by a spherical surface of radius R.

The sweeps in Fig. 5 illustrate several combinations of pulses corresponding to showers with various values of R and θ, if the thickness of the shower disks and the instrumental fluctuations are negligible. It is important to notice that the effect of a finite value of R is not the same on the time intervals s_{12} (between pulses 1 and 2) and s_{23} (between pulses 2 and 3). Since both pulses 1 and 3 come later with respect to 2 when R is finite than when R is infinite, s_{12} will be decreased and s_{23} will be increased by a curvature of the shower front.

In order to interpret the experimental data we require expressions for s_{12} and s_{23} involving the geometrical properties of showers that we wish to measure, and which take into account the thickness of the shower disks and the instrumental fluctuations. For each event one can compute the relative delays between the arrival times of the first pulses from the three counters. The apparent magnitudes of the delays will depend upon the sweep speed of the oscilloscope which may be subject to small fluctuations. The observed delay will be written as the product of the true delay and a variable factor $(1+a)$ which represents the sweep speed in terms of its average value. Then

$$s_{12}=(1+a)(T_2-T_1+d\sin\theta/v-d^2\cos\theta/2Rv + t_2-t_1+\tau_2-\tau_1), \quad (5a)$$

$$s_{23}=(1+a)(T_3-T_2+d\sin\theta/v+d^2\cos\theta/2Rv + t_3-t_2+\tau_3-\tau_2). \quad (5b)$$

t_1, t_2, and t_3 are the differences between the arrival times of the front at the three counters and the actual arrival times of the first particles at the counters. τ_1, τ_2, and τ_3 represent the random instrumental errors. The t's and τ's are random uncorrelated delays. T_1, T_2, and T_3 are the fixed delays artifically introduced for display purposes. The differences in the arrival times of the front at the various counters due to axis orientation and front curvature give rise to correlated delays which are represented by terms involving d, the distance between counters; θ, the zenith angle; and R the radius of curvature. (Note that $d^2/2R$ is an approximate expression for the sagitta of a spherical segment which is valid if $R\gg d$.)

It can be shown that Eqs. (5) are accurate for any shower provided the axis strikes within a distance from counter 2 small compared to R, and provided θ is the projected zenith angle. Furthermore, the effect of a finite curvature is, in general, at least as great as that represented by the term involving R in Eqs. (5). Thus if one analyzes our data by means of Eqs. (5), one obtains a value of R which is a lower limit on the radius of curvature of shower fronts.

If we add and subtract Eqs. (5) we find

$$(s_{12}+s_{23})=(1+a)(T_3-T_1+2d\sin\theta/v + t_3-t_1+\tau_3-\tau_1), \quad (6a)$$

$$(s_{12}-s_{23})=(1+a)(2T_2-T_1-T_3-d^2\cos\theta/Rv + 2t_2-t_1-t_3+2\tau_2-\tau_1-\tau_3). \quad (6b)$$

In the following discussion we shall frequently refer to the statistical concepts of expectation value, dispersion, and standard deviation. In order to make clear the meanings we attach to these concepts and to the symbols we shall use, we state here several definitions.

Let x be a random variable which assumes the values $x_1, \cdots, x_n$. We call

$$E(x)=\frac{1}{n}\sum_{i=1}^{i=n} x_i$$

the expectation value of x. We call

$$D(x)=E\{[x-E(x)]^2\}$$

the dispersion of x. We call $[D(x)]^{\frac{1}{2}}$ the standard deviation of x. Two random variables x and y are said to be independent if

$$E\{[x-E(x)][y-E(y)]\}=0.$$

The following theorems will be used.

Let x and y be independent random variables. Then

$$E(x+y)=E(x)+E(y),$$

$$E(xy)=E(x)E(y),$$

and

$$D[f(x,y)]=[\partial f/\partial x]^2D(x)+[\partial f/\partial y]^2D(y),$$

where the partial derivatives are evaluated for the expectation values of the variables.

We define T_1, T_2, and T_3 so that

$$E(\tau_1)=E(\tau_2)=E(\tau_3)=0.$$

The definition of the shower front that we have given implies that $E(t_1)=E(t_2)=E(t_3)=0$. Then, since a is

independent of the other delay variables and $E(a)=0$,

$$E(s_{12}-s_{23})=2T_2-T_1-T_3-E(d^2\cos\theta/Rv). \quad (7a)$$

As we shall see, all air showers detected in our experiment are strongly collimated in the vertical direction. We can therefore put $\cos\theta=1$ in Eq. (7a). It follows that

$$E_{II}(s_{12}-s_{23})=2T_2-T_1-T_3-(d^2/v)E(1/R). \quad (7b)$$

(Subscripts on the symbols E and D indicate the experimental arrangement used.) The curvature of the shower front has practically no effect on the delays observed with arrangement III. Therefore,

$$E_{III}(s_{12}-s_{23})=2T_2-T_1-T_2. \quad (7c)$$

If we combine Eqs. (7b) and (7c) we find that

$$E(1/R)=(v/d^2)[E_{III}(s_{12}-s_{23})-E_{II}(s_{12}-s_{23})]. \quad (8)$$

Consider now the dispersions of the measured quantities. Anticipating the experimental results, we state that we can neglect the term involving $1/R$. Thus we can write

$$D(s_{12}+s_{23})=D(2d\sin\theta/v)+D(t_3)+D(t_1)+D(\tau_3)+D(\tau_1)+(T_3-T_1)^2D(a), \quad (9a)$$

and

$$D(s_{12}-s_{23})=4D(t_2)+D(t_1)+D(t_3)+4D(\tau_2)+D(\tau_1)+D(\tau_3)+(2T_2-T_1-T_3)^2D(a). \quad (9b)$$

$D(a)$ can be estimated from measurements with arrangement I. As we mentioned earlier, most of the triple coincidences with arrangement I are produced by single μ mesons. Thus

$$D(t_1)=D(t_2)=D(t_3)=0.$$

We shall assume in our analysis that the instrumental fluctuations are the same for all three pulses, i.e.,

$$D(\tau_1)=D(\tau_2)=D(\tau_3)=D(\tau).$$

If we omit the term $D(2d\sin\theta/v)$, we have from Eqs. (9a) and (9b)

$$D_I(s_{12}+s_{23})=2D(\tau)+(T_3-T_1)^2D(a), \quad (9c)$$

and

$$D_I(s_{12}-s_{23})=6D(\tau). \quad (9d)$$

In Eq. (9b) the term $(2T_2-T_1-T_2)^2D(a)$ can be neglected because we have adjusted the instrumental delays so that $(2T_2-T_1-T_3)\approx 0$. Then, from Eqs. (9c) and (9d) it follows that

$$D(a)=[D_I(s_{12}+s_{23})-\tfrac{1}{3}D_I(s_{12}-s_{23})]/(T_3-T_1)^2. \quad (10)$$

In the case of the measurements with arrangement II we will put

$$D(t_1)=D(t_2)=D(t_3)=D(t).$$

Thus,

$$D_{II}(s_{12}+s_{23})=(4d^2/v^2)D(\sin\theta)+2D_{II}(t)+2D(\tau)+(T_3-T_1)^2D(a), \quad (9e)$$

$$D_{II}(s_{12}-s_{23})=6D_{II}(t)+6D(\tau), \quad (9f)$$

where we have again neglected the term $(2T_2-T_1-T_3)^2D(a)$. From Eqs. (9e) and (9f) it follows that

$$(4d^2/v^2)D(\sin\theta)=D_{II}(s_{12}+s_{23})-\tfrac{1}{3}D_{II}(s_{12}-s_{23})-(T_3-T_1)^2D(a). \quad (11)$$

C. Interpretation of Uncorrelated Delays

One can estimate the thickness of the shower disks by combining the measurements of $D(s_{12}-s_{23})$ made with arrangements I and II or III. From Eqs. (9d) and (9f) one obtains

$$D_{IId}(t)=\tfrac{1}{6}[D_{IId}(s_{12}-s_{23})-D_I(s_{12}-s_{23})]. \quad (12a)$$

Also, since d is small in arrangement III,

$$D_{III}(t)=\tfrac{1}{6}[D_{III}(s_{12}-s_{23})-D_I(s_{12}-s_{23})]. \quad (12b)$$

Electrons are the particles primarily responsible for the discharge of the unshielded counters in a shower. Therefore, $D_{IId}(t)$ and $D_{III}(t)$ are the dispersions of arrival times of first electrons averaged over ranges of shower sizes and over ranges of distances from the shower axes. $v[D_{IId}(t)]^{\frac{1}{2}}$ and $v[D_{III}(t)]^{\frac{1}{2}}$ are measures of the thickness of the shower disks (see Section IVC).

It is possible to shield a counter so that it can be discharged only by penetrating particles. If one compares the arrival times of pulses from a shielded counter and from unshielded counters one can obtain information about the difference between the arrival times of the front of penetrating particles and of the front of electrons. We shall call this difference Λ_{ep}. If counter 3 is shielded (arrangement IV) and if t_1, t_2, and t_3 are all measured with respect to the front of electrons, then

$$E_{IV}(t_1)=E_{IV}(t_2)=0; \quad E_{IV}(t_3)=\Lambda_{ep}.$$

From Eq. (6b) we deduce that

$$E_{IV}(s_{12}-s_{23})=2T_2-T_1-T_3+\Lambda_{ep}. \quad (7d)$$

If one compares Eqs. (7c) and (7d) one then finds

$$\Lambda_{ep}=E_{IV}(s_{12}-s_{23})-E_{III}(s_{12}-s_{23}). \quad (13)$$

$v[D_{IV}(t_3)]^{\frac{1}{2}}$ is a measure of the thickness of the disk of penetrating particles. We shall assume that

$$D_{IV}(t_1)=D_{IV}(t_2)=D_{III}(t).$$

We can then write

$$D_{III}(s_{12}-s_{23})=6D_{III}(t)+6D(\tau),$$

and

$$D_{IV}(s_{12}-s_{23})=5D_{III}(t)+D_{IV}(t_3)+6D(\tau)$$

from which one obtains

$$D_{IV}(t_3)=D_{IV}(s_{12}-s_{23})-\tfrac{5}{6}D_{III}(s_{12}-s_{23})-\tfrac{1}{6}D_I(s_{12}-s_{23}). \quad (14)$$

The advantage of using the delay differences instead of the sums is, of course, that the differences are not affected by fluctuations in the sweep speed.

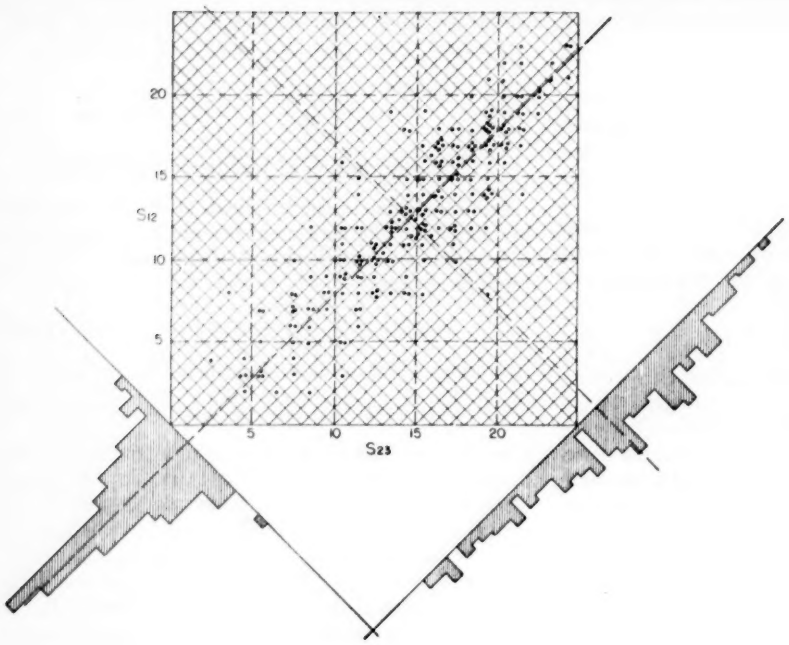

FIG. 6. Graphical summary of data obtained with arrangement II 30. Each shower event is represented by a dot with Cartesian coordinates s_{12}, s_{23}. The scales are 5.3 mμsec per division. The location of the origin is arbitrary.

D. Graphical Presentation of Data; Orientation of Shower Axes

Figure 6 illustrates a way of plotting the experimental data which clarifies the statistical problems involved in the analysis. We recorded a large number of shower events with a certain disposition of counters, and for each event we obtained the measured quantities s_{12} and s_{23}. Each event is then represented by a point with Cartesian coordinates s_{12} and s_{23} (Fig. 6). The points for a typical experimental run with arrangement II 30 are distributed in an approximately elliptical region whose major axis is inclined at 45°. From Eqs. (5) it is clear that if R were infinite and the uncorrelated delays negligible, then all the points would lie on the 45° line. (Note that if $T_2-T_1\neq T_3-T_2$, the major axis does not pass through the origin.) The breadth of the elliptical region is related to the thickness of the shower disks. The projected distribution of points on the major axis is related to the distribution of zenith angles of shower axes. In Fig. 6 two histograms have been plotted which represent the projected distributions of points on the 45° and 135° lines. The 45° histogram is the histogram of $1/\sqrt{2}(s_{12}+s_{23})$; the other is the histogram of $1/\sqrt{2}(s_{12}-s_{23})$.[5]

[5] These assertions can be demonstrated in the following way: Represent an experimental point by the vector $\mathbf{X}=(s_{12}, s_{23})$. Consider the unit vectors $\mathbf{U}_+=1/\sqrt{2}(1, 1)$ and $\mathbf{U}_-=1/\sqrt{2}(-1, 1)$ parallel to the 45° and 135° lines, respectively. Then the projection of $\mathbf{X}$ on the 45° line is

$$\mathbf{X}\cdot\mathbf{U}_+=1/\sqrt{2}(s_{12}+s_{23})$$

and on the 135° line is

$$\mathbf{X}\cdot\mathbf{U}_-=1/\sqrt{2}(s_{12}-s_{23}).$$

The coordinates of the "center of gravity" of the delay distribution are

$$\delta_{12}=E(s_{12}); \quad \delta_{23}=E(s_{23}).$$

With the counters close together in arrangement III the center of gravity corresponds to the point representing the simultaneous discharge of the three counters. With the counters in arrangement II d, the increase in the dispersion of correlated delays due to variations in the zenith angles produces an elongation of the distribution of points. In addition, the effect of any general curvature of shower fronts will be to move the center of gravity down and to the right. The displacement of the center of gravity will be proportional to the separation, d, of the counters.

One can determine the projected zenith angle, within certain errors by measuring the delay between the discharges of two widely separated counters. With three counters placed at the vertices of a right triangle as in arrangement V, one can therefore measure the projection of the zenith angle on two mutually perpendicular planes and from these projected angles obtain the spatial orientation of the axis. The accuracy of this method depends, of course, on the relative magnitudes of the delays due to uncorrelated fluctuations and axis orientation.

With arrangement V the plot of s_{12} *vs* s_{23} for a large number of showers takes on a different appearance and meaning (Fig. 10). The experimental points are distributed in a circular region whose center of gravity corresponds to a vertical shower. The plotted dis-

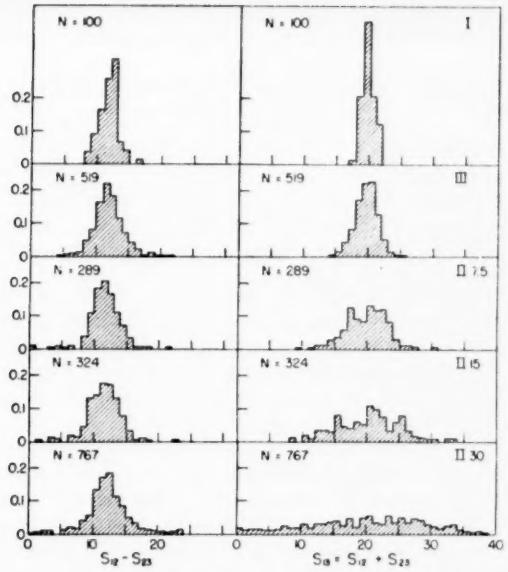

FIG. 7. Histograms of the sums and differences of the observed relative delays. The scale on the horizontal axes is 5.3 mμsec per division. The histogram intervals are 5.3 mμsec. The areas of the histograms are normalized to 1. N indicates the number of recorded events.

tribution is the projection of the spherical distribution of shower axes onto the equatorial plane. The azimuth and altitude (zenith angle) of each shower axis can therefore be determined directly from the plot. An annular ring with radii S_a and S_b contains points representing axes with zenith angles in the range

$$\arcsin(S_a v/d) < \Theta < \arcsin(S_b v/d).$$

If one measures the frequency of counts within successive annular rings, one can determine the distribution in zenith angle of shower axes.

Although the use of this graphical representation is not absolutely necessary in the interpretation of our data, we have found that it clarifies the statistical problems and facilitates the numerical evaluation of the experimental results.

4. EXPERIMENTAL RESULTS

A. Instrumental Fluctuations

Sweep speed fluctuations result from slow changes in circuit constants and operating conditions and are not random. It is not, possible, therefore, to subtract the dispersion due to sweep speed fluctuations from the measured dispersions in a rigorous way. However, we have made an estimate of $[D(a)]^{\frac{1}{2}}$ using Eq. (10) and the data collected in several runs with arrangement I over a period of twenty days. We found

$$[D(a)]^{\frac{1}{2}} = 0.02,$$

which is equivalent to 5 mμsec on a length of sweep equal to $T_3 - T_2 = T_2 - T_1 = 250$ mμsec.

The other instrumental fluctuations are random and uncorrelated. They arise partly from fluctuating delays in the counters and electronic circuits, and mostly from errors in the measurement of the positions of the pulses. Figures 7-I are histograms of $s_{12} - s_{23}$ and $s_{12} + s_{23}$ obtained in one short run with arrangement I in which the apparatus responds primarily to single penetrating particles. Over the short period of time occupied by this run $D(a) \approx 0$. From Eqs. (9c) and (9d) we see that we should find

$$D(s_{12} - s_{23})/D(s_{12} + s_{23}) = 3.$$

From several short runs we find for the above ratio a value of 2.3 ± 0.6 which agrees roughly with the expected ratio. Assuming the dispersions of τ_1, τ_2, and τ_3 to be equal, we find

$$[D(\tau)]^{\frac{1}{2}} = [\tfrac{1}{6} D(s_{12} - s_{23})]^{\frac{1}{2}} = 3.0 \text{ mμsec}.$$

B. Determination of a Lower Limit on the Radius of Curvature of Shower Fronts

We measured $E_{\text{II }30}(S_{12} - s_{23})$ and $E_{\text{III}}(s_{12} - s_{23})$. Using Eq. (8) we evaluated $E(1/R)$. As a precaution against slow instrumental changes, we made measurements alternately with the two arrangements. Figure 8 is a plot of the values of $E(s_{12} - s_{23})$ for successive experimental runs. No large systematic difference was found in the results obtained with arrangements II 30 and III. The combined data from the two runs with arrangement II 30 and the three runs with arrangement III were used in computing $[E(1/R)]^{-1}$. We found

$$[E(1/R)]^{-1} = 2600 \text{ m}.$$

If we consider the statistical errors, the lower limit on the radius of curvature of the fronts of showers detected with arrangement II 30 is 1300 m.

C. Thickness of Shower Disks

Since, as we have seen, the fronts are nearly plane, we can find $D(t)$ from Eqs. (12) using measured values

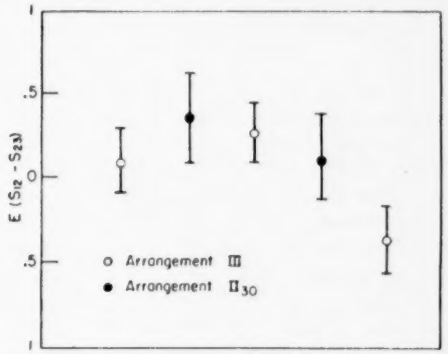

FIG. 8. Plot of the expectation values of $s_{12} - s_{23}$ obtained from successive experimental runs with arrangements II 30 and III.

TABLE I. Summary of statistical results obtained with various arrangements of counters.

Arrangement of counters	No. of showers observed	$[D(S_{13}-S_{23})]^{\frac{1}{2}}$ (mμsec)	$[D(S_{12}+S_{23})]^{\frac{1}{2}}$ (mμsec)	$[D(t)]^{\frac{1}{2}}$ (mμsec)	$v[D(t)]^{\frac{1}{2}}$ meters	$[D_{IV}(t_2)]^{\frac{1}{2}}$ (mμsec)	$v[D_{IV}(t_2)]^{\frac{1}{2}}$ meters	$D(S_{12}+S_{13})-\frac{1}{4}D(S_{12}-S_{13})$ $\times 10^{-18}$ sec^2
I	300	7.4±0.4	4.8±0.2	...	...	...	...	...
III	519	12.1±0.4	9.0±0.3	4.0±1	1.2±0.3	...	...	...
II 7.5	289	13.4±0.5	17.6±0.7	4.5±1	1.35±0.3	...	...	250±26
II 15	324	16.2±0.6	26.5±1.0	5.8±1	1.7±0.3	...	...	615±50
II 30	767	21.0±0.5	50.3±1.5	8.0±1	2.4±0.3	...	...	2383±150
IV	...	14.1±0.5	...	...	...	8.2±2.0	2.5±0.6	...

of $D_I(s_{12}-s_{23})$, $D_{IId}(s_{12}-s_{23})$, and $D_{III}(s_{12}-s_{23})$. The histograms in Fig. 7 summarize our data. In Table I we have listed the values of $[D(s_{12}-s_{23})]^{\frac{1}{2}}$ and the numbers of events used in the evaluations. We have also listed the corresponding values of $v[D(t)]^{\frac{1}{2}}$ which, as we shall discuss in more detail below, are indications of the thickness of the shower disks. It should be noted that $[D(t)]^{\frac{1}{2}}$ increases with d.

If we assume the validity of the Molière radial distribution function and use a method similar to that of Blatt,[6] we estimate that the range of sizes of showers detected with these counter arrangements is from 10^5 to 10^6 particles. The median size of showers detected with arrangement IId increases with d. The ratio of median shower sizes for arrangements II 7.5, II 15, and II 30 are approximately 1:3:9.

In order to draw from the measurements a clear conclusion as to the thickness of shower disks, we must consider in detail the significance of the quantity $[D(t)]^{\frac{1}{2}}$. Let us represent the instantaneous fluxes of electrons through all these counters by the single function $f_e(t)$. Then $D(t)$ is the dispersion of the corresponding first particle time distribution $F_e(t)$. According to Eq. (3), F_e differs more and more from $(1/m)f_e$ as the average number of electrons traversing a counter increases. Our method of selecting showers insures that the average number of traversals is close to one. However, in order to form an idea of the relation between the two functions, we evaluated $F_e(t)$ for a selected form of $f_e(t)$ and for several values of the average number of traversals m. We assume that

$$f_e(t)=\exp(-t/\lambda_e), \quad t>0$$
$$=0, \quad t<0.$$

and values of m from 0.5 to 3. The results of these calculations are presented in Fig. 9. For the sake of comparison we have plotted a dashed line to represent $(1/m)f_e(t)$. The dispersion of F_e is clearly smaller than the dispersion of f_e. One must expect, therefore, a significant difference between the dispersion in arrival times of first particles and the dispersion in arrival times of all particles. However, our measurements are not sufficiently accurate to insure that we measure only first particles. In practice, when two particles traverse a counter within a time interval comparable to our instrumental fluctuations, they produce a deflection of the oscilloscope beam which looks like a single pulse whose maximum occurs at a time corresponding, more or less, to the average of the two arrival times. Thus the dispersion that we actually measure is the dispersion of a function which lies between f_e and F_e.

Scattering of the electrons in the last radiation length above the counters is sufficient in itself to account for the thickness of the shower disks as can be seen from the following argument: the lower limit of the energy of the electrons detected by the counters is about 20 Mev. The mean energy is about 50 Mev. The root-mean-square angle of scattering in the last radiation length for electrons with a residual energy of 50 Mev is approximately 0.2 radian. In one radiation length in air at sea level this scattering results in an increase of path length of about 3 m, which corresponds to a delay of 10 mμsec. If the electrons are produced in a circular region of radius 30 m at a distance of 300 m above the plane of observation, then this amount of scattering would result in an almost flat shower disk of thickness 3 m, which is roughly the same as the measured values of $v[D(t)]^{\frac{1}{2}}$.

The apparent increase of the disk thickness with d may be due to the increase of the mean shower size with d. It seems unlikely that the effect could be due to a general thickening of shower disks with increasing distance from the shower axis, since this would almost certainly cause the fronts to be curved contrary to the observation we have reported.

The small thickness of the electron shower disk points to a conclusion regarding the mechanism of production of the shower. Certainly many of the electrons present in the disk at sea level are descendents of the neutral π mesons produced in the first nuclear interaction of the primary particle near the top of the atmosphere. If an appreciable fraction of the electrons at sea level come from later generations in the nucleonic cascade, then the N particles which link these later generations with the first nuclear interaction must be of very high energy since their descendent electrons are observed to be not greatly delayed with respect to the first electrons which arrive at sea level. Specifically, the energy of a proton which is delayed by 10 mμsec (3 m) with respect to a particle traveling with the velocity of light over a length of 100 g cm^{-2} at sea level is 12 Bev, and at 14 km is 27 Bev. These values are,

[6] J. Blatt, Phys. Rev. 75, 1584 (1949).

therefore, conservative lower limits on the energies of the nucleon links.

D. Average Projected Zenith Angle of Shower Axes

From measurements of $D(s_{12}+s_{23})$ and $D(s_{12}-s_{23})$ with arrangement II*d* one can determine $D(\sin\theta)$ [see Eq. (11)] if the term involving $D(a)$ can be neglected. As we observed before, an exact evaluation of $D(a)$ is impossible. However, from the measurements reported in IVA it is possible to estimate that the magnitude of $(T_3-T_1)^2D(a)$ is not greater than 100×10^{-18} sec^2. From the numbers quoted in column 9 of Table I it is clear that this quantity is small compared to the values of $D_{\mathrm{II}d}(s_{12}+s_{23})-\frac{1}{3}D_{\mathrm{II}d}(s_{12}-s_{23})$ obtained with $d=7.5$, 15 and 30 m. Certainly for $d=30$ m the error introduced by the sweep speed fluctuations is negligible. For $d=30$ m we deduce

$$D_{\mathrm{II}\,30}(\sin\theta)=0.059\pm0.004$$

for the dispersion of the sine of the projected zenith angles of shower axes.

In order that this result may be compared with previous experiments and with theoretical predictions, we have assumed that the distribution of projected zenith angles follows a $\cos^n\theta$ law, and we have calculated the value of n which would give the observed dispersion of $\sin\theta$. It can be shown that

$$D(\sin\theta)=\int_0^{\pi/2}\sin^2\theta\cos^n\theta d\theta\Big/\int_0^{\pi/2}\cos^n\theta d\theta=1/n+2.$$

From this equation and the measured value of $D(\sin\theta)$ we find

$$n=15\pm1.2.$$

It should be emphasized that these results on the projected zenith angle distribution do not depend on the detailed interpretation of the first particle dispersion which we gave in IVC.

Jánossy[7] has calculated the zenith angle distribution in approximation *A* for showers of 10^5 and 10^6 particles initiated by photons near the top of the atmosphere. He finds $n=16$. We have calculated the distribution in approximation *B* using graphical integrations, and we found the same value of n.

E. Determination of the Orientations of Shower Axes; Distribution of the Zenith Angles of Showers

We shall now evaluate the error in a measurement of the projected zenith angle of a shower axis using two counters. From Eq. (5) it can be seen that the principal effect of fluctuations in a on $D(s_{12})$ is through the term involving the artificial delays between pulses, since T_2-T_1 is large compared to $E(d\sin\theta/v+t_2-t_1+\tau_2-\tau_1)$. Now, $T_2-T_1=250$ mμsec. Since $[D(a)]^{\frac{1}{2}}=0.02$, the error introduced by this term is of the order of 6 mμsec. From $D_{\mathrm{II}d}(s_{12}-s_{23})$ we can evaluate the errors due to disk thickness and instrumental fluctuations. We find $[D(t+\tau)]^{\frac{1}{2}}=12$ mμsec. Therefore, the standard deviation of a measurement of s_{12} due to instrumental fluctuations and disk thickness is

$$[2D(t+\tau)+(T_2-T_1)2D(a)]^{\frac{1}{2}}=13\text{ m}\mu\text{sec}.$$

This results in an error in the determination of the sine of the projected zenith angle amounting to 0.13. Using counters 1 and 3, the error in the sine is 0.15, which is greater than with counters 1 and 2 because the greater sweep length emphasizes fluctuations in sweep speed. The fundamental limitation on the accuracy of angle measurements made by this method is, of course, the dispersion in arrival times of first particles which in our case accounts for an error of 0.12 in the determination of $\sin\theta$.

Using arrangement IV we measured the spatial orientation of 350 shower axes. The data is summarized in Fig. 10. The plot illustrates clearly the strong vertical collimation of shower axes. Figure 11 is a histogram of the spatial zenith angles computed from Fig. 10 by counting the frequencies of points within successive annular rings.

F. Delays of Penetrating Particles

The delays of penetrating particles were measured with arrangement IV in which counter 3 was shielded on the top and sides by lead 20 cm thick. In addition, counter 3 was located under a concrete roof 60 g cm^{-2} thick.

From our data we computed $E_{\mathrm{IV}}(s_{12}-s_{23})$. $E_{\mathrm{III}}(s_{12}-s_{23})$ was obtained with all three counters unshielded in arrangement III. If we apply Eq. (13) we

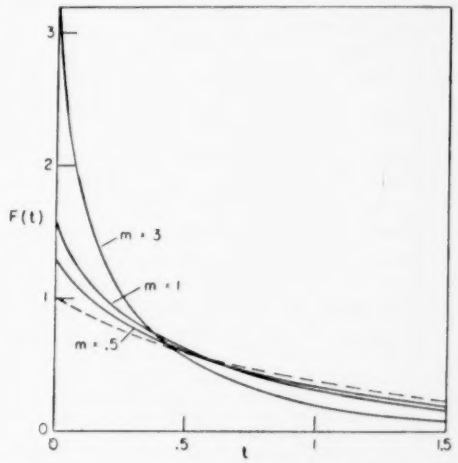

FIG. 9. Comparison of $F_s(t)$ (solid lines) and $f_s(t)$ (dashed line) for several values of m.

[7] Jánossy, *Cosmic Rays* (Oxford University Press, London, 1950), second edition, p. 337.

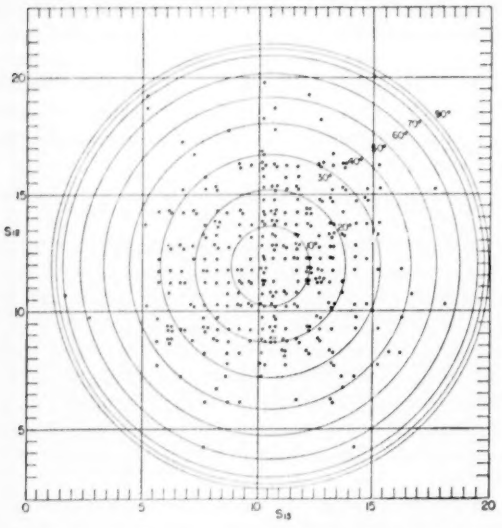

FIG. 10. Graphical summery of the data on the spatial orientation of shower axes obtained with arrangement V. The scales are 5.3 mμsec per division. The zenith angles of the shower axes are indicated by the concentric circles.

find the difference in the arrival times of the front of electrons and the front of penetrating particles to be

$$\Lambda_{ep}=9.5 \text{ m}\mu\text{sec.}\dagger$$

If we combine $D_{\text{IV}}(s_{12}-s_{23})$ and $D_{\text{III}}(s_{12}-s_{23})$ according to Eq. (14) we find

$$[D_{\text{IV}}(t_3)]^{\frac{1}{2}}=8\pm 2 \text{ m}\mu\text{sec.}$$

The values of Λ_{ep} and $[D_{\text{IV}}(t_3)]^{\frac{1}{2}}$ quoted here are subject to a statistical bias introduced by the coincidence circuit which accepts an event only if the three pulses occur within an interval of 300 mμsec. These results, therefore, apply to penetrating particles that are delayed by less than 300 mμsec.

The experiments of Cocconi, Tongiorgi, and Greisen[8] demonstrated that penetrating particles are present in air showers at sea level to the extent of approximately 2 percent of the total ionizing radiation. The small absorption suffered by this penetrating component in air and in lead and iron indicated that it consists mostly of μ mesons. Recent work of McCusker[9] has shown that approximately 35 percent of the penetrating radiation in showers at sea level consist of N particles. Since the shielding over counter 3 in our measurements absorbs at least 50 percent of the N component incident from the atmosphere, it is probable that most of the penetrating particles detected in our experiment were μ mesons. The observed delay in the arrival of the penetrating particle front is consistent with this picture as can be seen from the following argument: in Fig. 12 we have evaluated the delays of μ-mesons and of protons of various $\gamma=E/mc^2$ with respect to particles traveling with the speed of light on different paths in the atmosphere. The numbers in parentheses indicate the initial γ's at 20 km and the final γ's at sea level. We can estimate the delay of the penetrating particle front by adding $[D(t)]^{\frac{1}{2}}$ (a measure of the delay of the electron front) to Λ_{ep} (the delay of the penetrating particle front relative to the electron front). This delay is 13 mμsec. If we assume that the average energy of μ mesons in showers at sea level is between 2 and 4 Bev, than the altitude of production corresponding to the observed delay is between 5 and 20 km. If the average energy of nucleons in showers were between 2 and 4 Bev, the altitude of production corresponding to the observed delay would be between 30 m and 120 m. For this reason we can exclude nucleons as a main component of the penetrating particles we detected. The height of production we have deduced for μ mesons is consistent with the usual picture of air showers.

5. CONCLUSIONS

If we add our results to the description of air showers which has been deduced from other experiments, one can construct the following picture of an extensive air shower. A primary proton striking an air nucleus at an altitude near 20 km initiates a cascade of nuclear interactions. The neutral π mesons produced in these interactions give rise to the electromagnetic component; the charged π mesons give rise to the μ mesons. Because a large fraction of the electron component observed at

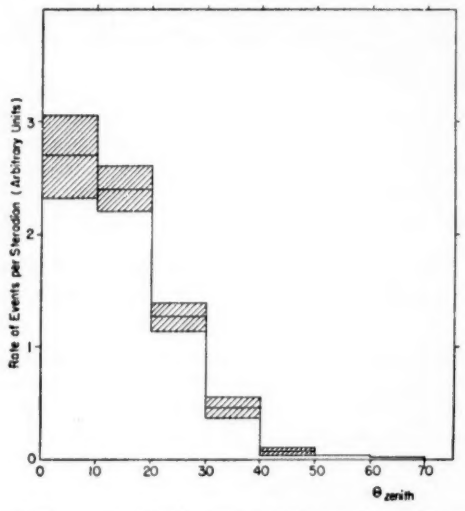

FIG. 11. Histogram of the frequency of showers with zenith angle Θ per unit solid angle as a function of Θ.

† Of course, Λ_{ep} does not represent the difference between the mean arrival times of electrons and penetrating particles, because the numbers, m, of electrons and penetrating particles are not the same (see discussion in Sec. 3C).

[8] Cocconi, Cocconi-Tongiorgi, and Greisen, Phys. Rev. **75**, 1063 (1949).

[9] C. B. A. McCusker, Proc. Phys. Soc. (London) **A63**, 1240 (1950).

sea level probably comes from the neutral π mesons generated in the first few interactions of the nucleonic cascade, a large production of electronic radiation at lower altitudes by low-energy nucleons would result in an increase in the thickness of the electron shower disk due to the kinematic delays of the nucleons. From the observed thickness, which can be accounted for on the basis of scattering alone, we deduce a conservative lower limit of $\sim$20 Bev on the energy of nucleons which are responsible for the production of an appreciable fraction of the electrons we observe at sea level.

Charged π mesons produced in the first few nuclear interactions partly interact and partly decay into μ mesons. From the delay between the front of penetrating particles and the front of electrons, we conclude that the main production of the μ mesons observed at sea level occurs at an altitude of approximately 10 km.

When an air shower reaches sea level most electrons in the shower are concentrated in a flat disk of radius 60 m and thickness between 1 and 2 m. The disk of particles which can penetrate 20 cm of lead has the same lateral dimensions, a thickness between 2 and 3 m, and its front follows behind the front of electrons by about 3 m. The penetrating particles we detected consisted mostly of μ mesons.

The dispersion of the sines of the projected zenith angles of shower axes is 0.059 which, assuming a $\cos^n\theta$ law, corresponds to $n=15$. The orientation of individual shower axes can be determined by delay measurements. The error (standard deviation) in our determination of the sine of the projected zenith angle of an individual shower axis is 0.13. The error is due principly to the thickness of the shower disk.

In conclusion we wish to express our gratitude to Professor W. L. Kraushaar for the design of the fast amplifiers, and to Dr. S. Olbert for valuable discussions of several phases of this work. We thank Dr. J. V. Jelley and Dr. W. Whitehouse for sending us the results of their experiments before publication. We also thank Mr. W. Smith and Mr. J. Strickland for their assistance in the construction and operation of the equipment.

One of us (P.B.) acknowledges the financial assistance he received from the Fulbright Program and from the Associazione Industrali di Trieste.

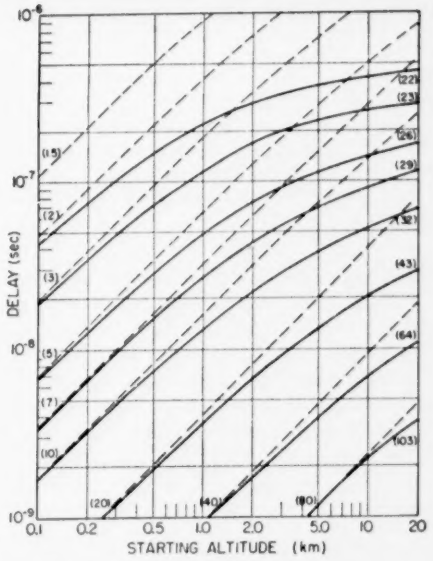

FIG. 12. Plot of the delays of protons (dashed lines) and μ mesons (solid lines) relative to particles traveling with the speed of light over various paths in the atmosphere. The numbers in parentheses indicate the values of $\gamma=E/mc^2$ at sea level and at 20 km. One finds the delay of a particle, which reaches sea level with a certain γ_0, over a path from altitude h_0 to sea level, by reading from the graph the value of the delay which corresponds to h_0 along the curve with residual $\gamma=\gamma_0$.

Multiple Production of Pions in Nucleon-Nucleon Collisions at Cosmotron Energies*

E. FERMI
Institute for Nuclear Studies, University of Chicago, Chicago, Illinois
(Received July 3, 1953)

The statistical theory of multiple pion production is applied in some detail to the discussion of nucleon-nucleon collisions for primary energies of 1.75 Bev and 2.2 Bev. Probabilities are given for single and multiple productions of pions and nucleons with different charges.

THE availability of high-energy nucleons from the Brookhaven cosmotron makes it now possible to compare the results of the statistical theory[1] of multiple pion production with experiment.[2] In Table I of A, a tentative estimate of the relative probabilities that in a nucleon-nucleon collision various numbers n of pions are emitted together with two nucleons was given. According to formula (22) of A, these probabilities for for bombarding energies of a few Bev should be proportional to

$$f_n(w)=\left\{\frac{251}{w}(w-2)^3\right\}^n \Big/ \left(\frac{3}{2}\times\frac{5}{2}\times\cdots\times\frac{6n+1}{2}\right). \quad (1)$$

In this formula w is the total energy of the two colliding nucleons in the center-of-mass system including their rest energy. The nucleon rest energy is taken as unit of energy. A number of crude simplifying approximations have been introduced in A in deriving the preceding formula. One of them was to neglect the effects of the different possible charges of the nucleons and of the pions. We propose to improve the earlier results by a consideration of this factor. This will be done for low multiplicity production up to a maximum number of pions $n=3$. In doing this we shall make use of the conservation of isotopic spin as a limitation to the possible types of transitions.

The fundamental hypothesis of the statistical calculation of high-energy nuclear events is that in a collision process, all possible final states are formed with a probability proportional to the statistical weight of the final state. In listing all the possible final states, however, one should exclude all those that cannot be reached from the ground state because of conservation theorems. In addition to the classical conservation theorems of energy, momentum, and angular momentum, one should include in the present discussion also the conservation of isotopic spin and, of course, of charge. To be sure, the conservation of isotopic spin is not exact. It is believed, however, that only weak transitions are possible between states of different isotopic spin. Therefore, the statistical equilibrium postulated in A will normally not have time to be established except for states of equal isotopic spin.

TABLE I. Number of states of isotopic spin 1 and 0 for a system of two nucleons and n pions.

n	0	1	2	3
p_n	1	2	4	9
q_n	1	1	2	4

In a collision of two nucleons, the initial state may have either isotopic spin $T=1$ or $T=0$. In computing the final states, only those with isotopic spin 1 or 0 shall have to be counted. For each final state characterized, for example, by the momenta of its particles, there are a number of different charge possibilities. Let p_n be the number of such possibilities for states of isotopic spin 1 with the given total charge, and q_n the similar number for isotopic spin 0. In Table I, we list the numbers p_n and q_n for states of two nucleons and n pions.

For example, in the collision of two high-energy protons, the isotopic spin of the initial state is $T=1$. A final state will be formed abundantly only when its isotopic spin is also 1 and we may assume that the probability of its formation will be proportional to $f_n(w)$ given by Eq. (1). In computing the relative probabilities for the formation of n pions, we shall take into account, however, that there are p_n states of isotopic spin 1. Therefore, the probabilities to form n pions will be proportional to $p_n f_n$ and be given by

$$P_n=p_n f_n/\sum p_n f_n. \quad (2)$$

If the two colliding nucleons are a neutron and a proton, the initial state is a mixture of 50 percent isotopic spin 1 and 50 percent isotopic spin 0. If the initial state has $T=1$, the probability to form n pions will again be given by Eq. (2). For $T=0$, the probability will be given by a similar expression with p_n replaced by q_n:

$$Q_n=q_n f_n/\sum q_n f_n. \quad (3)$$

The resultant probability will be, therefore, the arithmetic average of Eqs. (2) and (3).

In discussing the comparison of these figures with experiment, it is important to give not only the number of pions that accompany the two nucleons in the final state, but also their charges. In order to do this, we must subdivide the numbers p_n and q_n of states with n pions into numbers of states corresponding to the

* Research supported by a joint program of the U. S. Office of Naval Research and the U. S. Atomic Energy Commission.
[1] E. Fermi, Progr. Theoret Phys. (Japan) 5, 570 (1950), quoted as A; Phys. Rev. 81, 683 (1951).
[2] Fowler, Shutt, Thorndike, and Whittemore, Phys. Rev. (to be published).

different possible charges of the particles emitted. For example, according to Table I there are two states of isotopic spin 1 containing two nucleons and one pion. If we are discussing the collision of two protons (total charge = 2) the two states can be written as follows:

$$(-1/\sqrt{2})(pp0)+(1/2)(pn+)+(1/2)(np+) \quad (4)$$

and

$$(1/\sqrt{2})(pn+)-(1/\sqrt{2})(np+), \quad (5)$$

where, for example, $(pn+)$ means a state in which the first nucleon is a proton, the second a neutron, and the pion is a positive pion. If the final state were Eq. (4), the probability would be $\frac{1}{2}$ that in the final state there is a proton, a neutron, and a positive pion and $\frac{1}{2}$ that there are two protons and a neutral pion. If the final state were Eq. (5), the only possible final state would be a neutron, a proton, and a positive pion. In this case, therefore, the number $P_2=2$ is divided in a part 3/2 for the formation of a neutron, a proton and positive pion, and a part 1/2 corresponding to the formation of two protons and a neutral pion. The weights computed in this manner for the various cases are listed in Tables II and III.

TABLE II. Weights for different final states in a collision of two protons.

State	Weight	Number of pions	Number of prongs	Probabilities for primaries of energy 1.75 Bev	2.2 Bev
pp	1	0	2	8.6	4.0
$pp0$	$\frac{1}{3}$	1	2	14.1	11.3
$pn+$	$\frac{2}{3}$	1	2	42.3	32.7
$pp+-$	1.2	2	4	9.1	12.2
$pp00$	0.4	2	2	3.0	4.0
$pn+0$	1.8	2	2	13.6	18.2
$nn++$	0.6	2	2	4.6	6.0
$pp+-0$	154/60	3	4	1.4	3.2
$pp000$	18/60	3	2	0.2	0.4
$pn++-$	175/60	3	4	1.5	3.7
$pn+00$	121/60	3	2	1.0	2.5
$nn++0$	72/60	3	2	0.6	1.5

Table II illustrates the case of a collision between two protons. The first column gives the different types of particles that may appear in the final state compatible with charge conservation. The second column gives the weight of the state, the third is the number n of pions emitted and the fourth column is the number of charged particles emitted. The fifth and sixth columns will be discussed later.

Table III gives similar data for a neutron-proton collision. In this case two isotopic spins, $T=1$ and $T=0$, are possible, and therefore, two weights are given for each case in columns 2 and 3. Columns 4 and 5 give respectively the number of pions and the number of charged particles emitted. Again, the last two columns will be discussed later.

In order to show the use of the tables, we consider

TABLE III. Weights for different final states in a collision of a proton and a neutron for the cases $T=1$ and $T=0$.

Final state	$T=1$	$T=0$	Number of pions	Number of prongs	Probabilities for primaries of energy 1.75 Bev	2.2 Bev
pn	1	1	0	1	12.3	6.0
$pp-$	$\frac{1}{3}$	$\frac{1}{3}$	1	3	15.7	12.9
$pn0$	$\frac{1}{3}$	$\frac{1}{3}$	1	1	22.8	18.5
$nn+$	$\frac{1}{3}$	$\frac{1}{3}$	1	1	15.7	12.9
$pp-0$	0.8	$\frac{1}{3}$	2	3	5.3	7.3
$pn00$	0.6	$\frac{1}{3}$	2	1	4.6	6.3
$pn+-$	1.8	1	2	3	13.8	18.9
$nn+0$	0.8	$\frac{1}{3}$	2	1	5.3	7.3
$pp-00$	0.9	0.4	3	3	0.4	1.0
$pp--+$	1.2	0.6	3	5	0.6	1.5
$pn000$	0.6	0.2	3	1	0.2	0.6
$pn+-0$	4.2	1.8	3	3	2.0	4.6
$nn+00$	0.9	0.4	3	1	0.4	1.0
$nn++-$	1.2	0.6	3	3	0.6	1.5

first the collisions of 1.75-Bev and 2.2-Bev protons against a proton at rest. One finds in this case $w=2.781$ for 1.75 Bev and $w=2.948$ for 2.2 Bev. The corresponding values of f_n are

$f_0=1$; $f_1=3.28$; $f_2=0.88$; $f_3=0.062$; for 1.75 Bev.
$f_0=1$; $f_1=5.53$; $f_2=2.49$; $f_3=0.30$; for 2.2 Bev.

The probability that the collision gives rise to an event of the type listed in the first column of Table II is given by the product of the weight listed in column 2 of the same table times the appropriate f_n. The probabilities calculated in this manner and normalized to 1 are listed in columns 5 and 6.

A similar calculation can be carried out for a collision of 1.75-Bev and 2.2-Bev neutrons with a proton. In this case, one should first compute in a similar manner the probabilities corresponding to isotopic spin 1 and 0, and then take the average of the results. These averages are given in columns 6 and 7 of Table III. For example, one can see from Table III that the probabilities of having a star with 1, 3, or 5 prongs in a neutron-proton collision of 1.75 Bev are 61.3, 37.8, 0.6 percent, and for a 2.2-Bev neutron are 52.6, 46.2, 1.5 percent. In particular, notice the very low probability of 5-pronged stars at these energies.

In statistics of 3-pronged stars, one will expect the probabilities of events in which a single negative pion, or at least a negative and a neutral pion, or a positive and a negative pion are produced should be 42, 15, 43 percent at 1.75 Bev and 28, 18, 54 percent at 2.2 Bev.

It should be stressed that all these figures are at best indicative of orders of magnitude. Obviously, a statistical theory of the type under discussion can, at best, yield qualitative results. In addition, in deriving formula (1) in A, many features like statistical correlation of the various particles and conservation of angular momentum have been neglected and it is to be expected that some sizeable error may be introduced thereby in the results.

PHYSICAL REVIEW VOLUME 92, NUMBER 2 OCTOBER 15, 1953

Atmospheric Effects on Cosmic-Ray Intensity Near Sea Level*†

S. OLBERT
Department of Physics and Laboratory for Nuclear Science, Massachusetts Institute of Technology, Cambridge, Massachusetts
(Received June 30, 1953)

The effects of atmospheric temperature and pressure on the μ-meson intensity are studied theoretically for locations near sea level. The analysis is based on a unidimensional equation for the vertical differential intensity of μ mesons, studied originally by Sands. The treatment is rigorous in the sense that it includes the continuous production as well as the ionization losses of μ mesons in the atmosphere. With the help of a newly derived range spectrum of μ mesons at production and the exact expression for the survival probability of μ mesons, a three-term regression formula for the relative changes of the μ-meson intensity is derived and discussed in detail. According to this formula, the relative intensity changes are correlated not only with the average production height and the ground pressure (a customarily employed two-term correlation) but also with the average tropospheric temperature. This additional correlation, resulting from the ionization losses of μ mesons in the air, seems to remove some apparent difficulties in the interpretation of experimental data. In particular, it seems to explain the discrepancies found in the decay coefficients determined from diurnal and seasonal observations, respectively.

I. INTRODUCTION

NUMEROUS experiments[1] of the last two decades have shown that the intensity of cosmic rays is influenced by the atmospheric conditions existing during the period of observation. It has been found from experiments on the ground that the variations of the cosmic-ray intensity are closely related to the changes of pressure and temperature of the atmosphere above the observer. While the pressure effect indicates the dependence of cosmic radiation on the amount of air traversed, the temperature effect has its origin in the instability of μ mesons[2] which form the preponderant part of the penetrating component of cosmic rays at sea level. The following simple argument shows qualitatively that an increase of the temperature causes a decrease of the μ-meson intensity at sea level. Each μ meson produced at a certain atmospheric depth (i.e., at a given pressure level) has to travel the distance from the production layer to the level of detection. An increase of the temperature will increase this distance and thus enhance the probability of decay in flight. If all mesons were produced at the same atmospheric depth, and if one could neglect their ionization losses, the fluctuations in the height H, of a single pressure level—the production level—would suffice to account for the temperature effect on the μ-meson intensity. One could then express the variations of the μ-meson intensity I with an equation of the following type:

$$\delta I/I = A_H'\delta H + A_P'\delta x_0, \qquad (1)$$

where δH and δx_0 are the variations of the height of production and of the ground pressure, respectively. The coefficients A_H' and A_P' are often referred to as the "decay" and "absorption" coefficients, respectively.

Early investigations seemed to confirm the approximate validity of the above regression formula. Duperier,[3,4] in particular, found through the statistical analysis of the observed data, that the ground pressure and the height corresponding to the atmospheric depth of 100 g cm^{-2} were the controlling factors in the variations of cosmic-ray intensity at sea level. However, the more recent studies by the same author,[5] as well as those by Dolbear and Elliot,[6] have shown that the two-term Eq. (1) is inadequate to account fully for the variations of the cosmic-ray intensity at sea level. The inconsistencies have not been explained quantitatively in a satisfactory manner.

In this paper we attempt to give a more rigorous, quantitative treatment of the problem outlined above. In particular, the two following facts, neglected thus far, are taken into account in present calculations: (1) the fact that the μ mesons are produced *continuously* throughout the atmosphere, and (2) the fact that the μ mesons suffer *ionization losses* during their propagation through air. As we shall see in the following sections, the first fact will justify and clarify the notion of an average production layer for the bulk of μ mesons, and the second fact will introduce a third term into the regression formula discussed above. This additional term will turn out to be primarily controlled by the temperature changes in the *lower* atmosphere, where the ionization losses are relatively more important than in the upper atmosphere.

All considerations in this paper apply only to the *vertical* intensities (both differential and integral) of μ mesons measured at locations near sea level.

* Part of a thesis submitted in partial fulfillment of the requirements for the degree of Doctor of Philosophy at the Massachusetts Institute of Technology.

† This work was supported in part by the joint program of the U. S. Office of Naval Research and the U. S. Atomic Energy Commission.

[1] For a review, see, e.g., H. Elliot, *Progress in Cosmic-Ray Physics* (North-Holland Publishing Company, Amsterdam, 1952), Chap. VIII.

[2] P. M. S. Blackett, Phys. Rev. **54**, 973 (1938).

[3] A. Duperier, Terrestial Magnetism and Atm. Elec. **49**, 1 (1944).

[4] A. Duperier, Proc. Phys. Soc. (London) **61**, 34 (1948).

[5] A. Duperier, Proc. Phys. Soc. (London) **62**, 684 (1949).

[6] D. W. N. Dolbear and H. Elliot, J. Atmos. Terr. Phys. **1**, 215 (1951).

II. SURVIVAL PROBABILITY OF μ MESONS

In order to see the manner in which the temperature of the atmosphere enters into the expression of the μ-meson intensity, we must first consider the expression for the survival probability of μ mesons. For a μ meson produced at the elevation z and traveling vertically toward the earth with the velocity $c\beta$, the survival probability is given by[7]

$$w=\exp\left[-\int_{z_0}^{z}\frac{(1-\beta^2)^{\frac{1}{2}}}{c\tau\beta}dz'\right], \tag{2}$$

where τ is the mean life of the μ meson at rest, and z_0 the elevation of the point of observation. The factor $(1-\beta^2)^{\frac{1}{2}}$ accounts for the relativistic time dilatation. It is convenient to express the distance dz' in terms of the increment of atmospheric depth dx'. Since $dx'=\rho(x')dz'$, one may write for Eq. (2)

$$w(x, R)=\exp\left[-\frac{\mu}{\tau}\int_{x}^{x_0}\frac{dx'}{\rho(x')p(R')}\right], \tag{2'}$$

where now x and x_0 denote the atmospheric depths at the points of production and observation, respectively; μ is the rest mass of the μ meson, and $p(R')$ is the momentum at the depth x' expressed as a function of the corresponding residual range $R'=R+x_0-x'$. R is the residual range of the μ meson at the point of observation. It is useful to approximate $p(R')$ by the following analytical formula:

$$\frac{\mu c}{p(R)}=\frac{B}{b+R'}-\kappa, \tag{3}$$

where $B=53.5$ g cm^{-2} and $b=56$ g cm^{-2} if R is measured in g cm^{-2}; $\kappa=$ constant $=2.07\times10^{-3}$. With the numerical values of the constants quoted above, Eq. (3) is applicable for all μ mesons with residual ranges R', between 30 g cm^{-2} and 6000 g cm^{-2} air equivalent. In this region, it reproduces the theoretical curve[8] within an accuracy of one percent. Sinceal most all μ mesons recorded at sea level have residual ranges from 30 to 6000 g cm^{-2}, Eq. (3) may be considered as sufficient for the purposes of this paper.

The evaluation of Eq. (2') also requires the knowledge of the vertical behavior of the air density $\rho(x')$ or of the atmospheric temperature T. These two quantities are related by the following equation:

$$x'/\rho(x')=\Re T(x')/Mg, \tag{4}$$

where $\Re$ is the universal gas constant, M is the effective molecular weight of air, and g is the acceleration of gravity. If the temperature $T(x')$ is measured in absolute units, $\Re/Mg=2.87\times10^{3}$ cm/°C. It is more appropriate to discuss the survival probability w in terms of $T(x')$ rather than in terms of $\rho(x')$, because $T(x')$ is a quantity that can be measured directly by means of radio sondes.

By combining Eqs. (2'), (3), and (4) one may write for the survival probability

$$w(x, R)=\exp\left[-\frac{\Re}{c\tau Mg}\int_{x}^{x_0}\frac{T(x')}{x'}\left(\frac{B}{x_e-x'}-\kappa\right)dx'\right], \tag{5}$$

where $x_e=x_0+R+b$. Since $1/[x'(x_e-x')]=1/[x_e(x_e-x')]+1/(x_ex')$ one may also express Eq. (5) as follows:

$$w(x, R)=\exp[\alpha_H(R)H(x)+\alpha_K(R)K(x, R)], \tag{5'}$$

where

$$\alpha_H(R)=-\frac{1}{c\tau}\left(\frac{B}{x_e}-\kappa\right)=-\frac{\mu}{\tau p(x_0+R)}, \tag{6}$$

$$\alpha_K(R)=-\Re B/Mgc\tau x_e^2, \tag{6'}$$

and

$$H(x)=\frac{\Re}{Mg}\int_{x}^{x_0}\frac{T(x')}{x'}dx', \tag{7}$$

$$K(x, R)=x_e\int_{x}^{x_0}\frac{T(x')}{x_e-x'}dx'. \tag{7'}$$

The representation of $w(x, R)$ given by Eq. (5') has some advantages over those given by Eqs. (2') or (5). The two terms in the exponent of Eq. (5') have a direct physical significance. The function $H(x)$, defined by Eq. (7), represents simply the distance from the pressure level x_0 (the ground) to the pressure level x (the production level). The first term in Eq. (5'), $\exp[\alpha_H H(x)]$, is the main term; it represents the survival probability for a μ meson produced at x and traveling the distance $H(x)$ with a *fixed* momentum $p(x_0+R)$ [see Eq. (6)]. Since, for most mesons, x is considerably smaller than x_0 the fixed momentum $p(x_0+R)$ will not differ significantly from the actual momentum at production $p(x_0+R-x)$, so that

$$\exp[\alpha_H H(x)]\approx\exp\left[-\frac{\mu H(x)}{\tau p(x_0+R-x)}\right].$$

One recognizes in the right-hand side expression a formula often quoted in the interature; it represents the survival probability of μ mesons if one neglects their *ionization losses* in the air. The second term in Eq. (5'), $\exp(\alpha_K K)$, may be regarded as a corrective term accounting for the *ionization losses* of μ mesons in the air. The function $K(x, R)$, defined by Eq. (7'), will, in general, depend not only on $T(x)$ but also on the residual range of the μ mesons R. However, for sufficiently large R (say $R>1000$ g cm^{-2}), $K(x, R)$ may be written roughly as

$$K(x, R)\approx\int_{x}^{x_0}T(x')dx'; \tag{8}$$

[7] See, e.g., B. Rossi, *High Energy Particles* (Prentice-Hall, Inc., New York, 1952), p. 157.
[8] See reference 7, pp. 40–41.

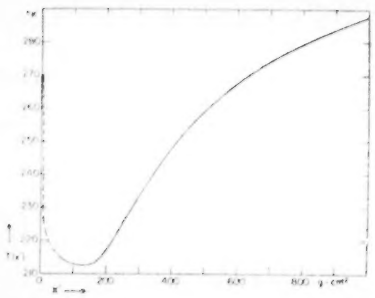

FIG. 1. Vertical distribution of the annual mean of the temperature at 40°N geographic latitude plotted as a function of the atmospheric depth. The curve was computed from the graph given by B. Haurwitz and J. M. Austin in *Climatology* (McGraw-Hill Book Company, Inc., New York and London, 1944), p. 37.

i.e., in the case of fast mesons, the function $K(x, R)$ is closely related to the temperature averaged over the region between the level of production and the ground.

For the numerical evaluation of Eq. (5′) one needs the function $T(x')$ which will, in general, be different for different seasons, different geographical locations, etc. We have based our calculations of $w(x, R)$ on the annual average of $T(x')$ for 40°N geographical latitude (see Fig. 1). Figure 2 shows graphically the behavior of the negative logarithm of this "average" survival probability *versus* the atmospheric depth x for various residual ranges R and for $x_0 = 1000$ g cm^{-2}.

In order to study the deviations from the average survival probability, $w_{\delta T}(x, R)$, which are due to the departure of the temperature from its annual mean, one may make use of the first-order perturbation with respect to $T(x')$. From Eq. (5′), one then gets

$$\delta_T w(x, R) = w_{\delta T}(x, R)[\alpha_H \delta H(x) + \alpha_K \delta K(x, R)], \quad (9)$$

where

$$\delta H(x) = \frac{\mathcal{R}}{Mg}\int_x^{x_0} \frac{\delta T(x')}{x'} dx', \quad (10)$$

and

$$\delta K(x, R) = x_e \int_x^{x_0} \frac{\delta T(x')}{x_e - x'} dx'. \quad (10')$$

As we shall see in the next section, the above Eqs. (9), (10), and (10′) will be of primary importance for the evaluation of the temperature coefficient of the differential intensity of μ mesons.

III. TEMPERATURE EFFECT ON THE COSMIC-RAY INTENSITY AT SEA LEVEL

We now turn to our main problem: the evaluation of the variations of the cosmic-ray intensity caused by changes of atmospheric temperature. As we have mentioned in the introduction, we shall limit ourselves to the case of the *vertical* intensities of the hard component at sea level. Thus we may follow the treatment given by Sands[9] and assume that differential intensity may be represented by

$$i_v(R) = \int_0^{x_0} G(R_s) e^{-x/L} w(x, R) dx, \quad (11)$$

where L is the absorption mean free path of the meson-producing radiation and $G(R_s)$ is the range spectrum of μ mesons at production. $G(R_s)$ will be assumed to be a function of the residual range $R_s = R + x_0 - x$ *only*. We shall use, for the purpose of this paper, the following approximate expression for this function:

$$G(R_s) = \frac{7.31 \times 10^4}{(520 + R_s)^{3.58}} (\text{g}^{-2}\ \text{cm}^2\ \text{sec}^{-1}\ \text{sterad}^{-1}), \quad (12)$$

where R_s is measured in g cm^{-2}. This empirical formula for the production spectrum of μ mesons has been derived on the basis of more recent experimental data,[10]

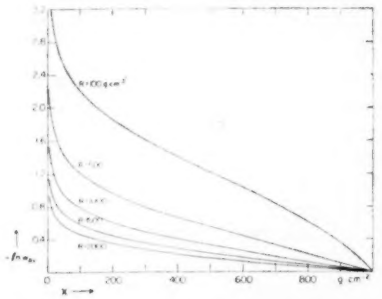

FIG. 2. Negative natural logarithm of the survival probability of μ mesons produced at the atmospheric depth x and reaching sea level with various residual ranges between 100 and 2000 g cm^{-2}. The curves correspond to the annual mean of the vertical temperature distribution at 40°N geographic latitude.

and is believed to be slightly better than the expression given by Sands. It is compatible with measurements at 50° geomagnetic latitude for the residual ranges at production extending from $R_s = 100$ g cm^{-2} to $R_s = 7000$ g cm^{-2}.

Let us discuss first the case where the ground pressure x_0 is kept *constant*. Then the variation of $i_v(R)$ due to the temperature changes $\delta T(x')$ is given, according to Eqs. (11) and (9), by

$$\delta_T i_v(R) = \int_0^{x_0} [\alpha_H \delta H(x) + \alpha_K \delta K(x, R)] \Phi(x, R) dx, \quad (13)$$

where we have put for short

$$\Phi(x, R) = G(R_s) e^{-x/L} w_{\delta T}(x, R). \quad (14)$$

[9] M. Sands, Technical Report No. 28, Laboratory for Nuclear Science, Massachusetts Institute of Technology, 1949 (unpublished); Phys. Rev. 77, 180 (1950).

[10] For a detailed discussion on this subject, the reader is referred to S. Olbert, thesis, Massachusetts Institute of Technology, June, 1953 (unpublished).

In order to evaluate Eq. (13) we shall make use of the mean value theorem which states that a definite integral of a product of two regular functions, say $f(z)$ and $g(z)$, may be written as follows:

$$\int_a^b g(z)f(z)dz=g(\xi)\int_a^b f(z)dz, \tag{15}$$

where $a<\xi<b$. One can estimate the actual value of ξ rather accurately if the following two conditions are satisfied: (1) $g(z)$ is a slowly varying function in the interval (a, b), and (2) $f(z)$ displays a sharp maximum in (a, b). One then finds, by expanding $g(z)$ into a Taylor series at ξ and neglecting the terms of second order or higher, that

$$\xi\int_a^b f(z)dz=\int_a^b zf(z)dz. \tag{16}$$

The error that one makes in Eq. (15) by applying the above estimate of ξ is of the order of

$$\frac{1}{2g(\xi)}\left[\frac{d^2g(z)}{dz^2}\right]_{z=\xi}(\eta^2-\xi^2), \tag{17}$$

where

$$\eta^2\int_a^b f(z)dz=\int_a^b z^2f(z)dz. \tag{18}$$

Evidently, the function $\Phi(x, R)$, defined by Eq. (14), satisfies the condition (2) very well for $R>100$ g cm^{-2}; furthermore, according to Eq. (10′), the function $\delta K(x, R)$ satisfies the condition (1). Hence, we may apply the method outlined above directly to the second term in Eq. (13). We cannot apply it directly to the first term, because the function $H(x)$ displays a logarithmic divergence at $x=0$. However, if we consider separately the functions $\delta H(x)/\ln(x_0/x)$ and $\Phi(x, R)\ln(x_0/x)$, rather than the functions $\delta H(x)$ and $\Phi(x, R)$, we readily verify that these two functions do satisfy conditions (1) and (2), respectively. Consequently, we may write Eq. (13) as follows:

$$\delta_T i_v(R)=\frac{\alpha_H\delta H(x_1)}{\ln(x_0/x_1)}\int_0^{x_0}\ln(x_0/x)\Phi(x, R)dx + \alpha_K\delta K(x_2, R)\int_0^{x_0}\Phi(x, R)dx \tag{19}$$

or

$$\delta_T i_v/i_v=\gamma\alpha_H\delta H(x_1)+\alpha_K\delta K(x_2, R), \tag{20}$$

where, according to Eq. (16),

$$x_1=\int_0^{x_0}x\ln(x_0/x)\Phi(x, R)dx\Big/\int_0^{x_0}\ln(x_0/x)\Phi(x, R)dx, \tag{21}$$

$$x_2=\int_0^{x_0}x\Phi(x, R)dx\Big/\int_0^{x_0}\Phi(x, R)dx, \tag{22}$$

and

$$\gamma=\left[\int_0^{x_0}\ln(x_0/x)\Phi(x, R)dx\right]\Big/\left[\ln(x_0/x_1)\int_0^{x_0}\Phi(x, R)dx\right]. \tag{23}$$

The three quantities, x_1, x_2, and γ, according to their definitions, are functions of the residual range R of μ mesons at x_0. Figures 3 and 4 show these quantities plotted *versus* $R(100<R<4000$ g cm$^{-2})$ for $x_0=1000$ g cm^{-2}. Note that the factor γ is practically one for all $R>500$ g cm^{-2}; note further that the atmospheric depths x_1 and x_2 are slowly decreasing functions of R. We shall discuss the physical significance of these results in Sec. V.

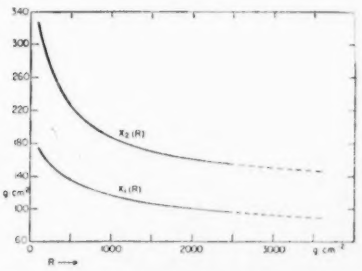

FIG. 3. Characteristic atmospheric depths $x_1(R)$ and $x_2(R)$ defined by Eqs. (21) and (22) and entering into the regression formula for the temperature effect on the differential μ-meson intensity near sea level.

In order to give Eq. (20) a simpler physical interpretation, it is useful to approximate the function $\delta K(x, R)$ by the following expression:

$$\delta K(x_2, R)=\frac{x_e}{x_0-x_2}\left(\ln\frac{x_e-x_2}{x_e-x_0}\right)\int_{x_2}^{x_0}\delta T(x')dx';$$

one may readily verify that the above formula is a good approximation to Eq. (10′) if $\delta T(x')$ does not

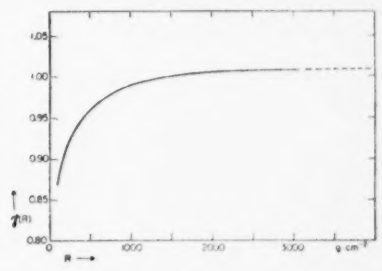

FIG. 4. Factor $\gamma(R)$ defined by Eq. (23) and entering into the regression formula for the temperature effect on the differential μ-meson intensity near sea level.

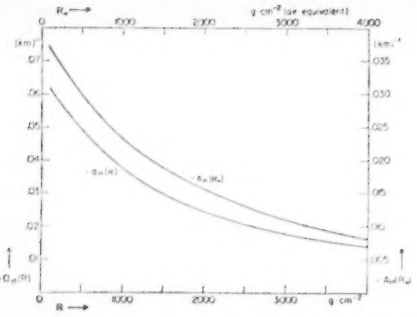

FIG. 5. The coefficients a_H and A_H correlating the differential and integral intensity changes with the variations of the mean production height; a_H and A_H are plotted *versus* the residual range R and the cut-off thickness R_0, respectively.

vary too strongly with x' in the region between x_0 and x_2. In this case Eq. (20) simplifies to

$$\delta_T i_v/i_v = a_H(R)\delta H(x_1) + a_K(R)[\delta T(x_2)]_{Av}, \quad (24)$$

where

$$a_H(R) = \alpha_H(R)\gamma(R)$$

$$a_K(R) = \frac{\Re B}{Mgc\tau x_e} \ln\left(\frac{x_e - x_2}{x_e - x_0}\right)$$

$$[\delta T(x_2)]_{Av} = \frac{1}{x_0 - x_2}\int_{x_2}^{x_0} \delta T(x')dx'. \quad (25)$$

Equation (24), although not so accurate as Eq. (20), gives us an insight into the problem in question: The temperature effect on the differential intensity i_v at sea level can be described by means of a two-term regression formula. The variations of i_v are correlated with the variations of the height of x_1, and the variations of the temperature averaged between x_2 and x_0. Figures 5 and 6 show the coefficients a_H and a_K plotted *versus* the residual ranges R.

We conclude this section with a few remarks concerning the temperature effect for the *integral* intensity near sea level, I_v. Evidently one obtains an expression applicable to this effect by integrating Eq. (20) or Eq. (24) over all residual ranges R above a certain cut-off value, R_0, determined by the experimental arrangement, *viz.*:

$$\delta_T I_v(R_0) = \int_{R_0}^{\infty} a_H(R) i_v(R)\delta H dR + \int_{R_0}^{\infty} a_K(R) i_v(R)(\delta T)_{Av} dR. \quad (26)$$

Since the functions δH and $(\delta T)_{Av}$ vary slowly with respect to R, Eq. (26) may be evaluated by means of the mean value theorem. Thus, according to Eqs. (15) and (16),

$$\delta_T I_v/I_v = A_H(R_0)\delta H(\bar{x}_1) + A_K(R_0)[\delta T(\bar{x}_2)]_{Av}, \quad (26')$$

where

$$A_{H,K}(R_0) = \frac{1}{I_v(R_0)}\int_{R_0}^{\infty} a_{H,K}(R) i_v(R) dR;$$

$$\bar{x}_1 = x_1(R_1), \quad \bar{x}_2 = x_2(R_2);$$

$$R_{1,2}\int_0^{\infty} a_{H,K} i_v dR = \int_{R_0}^{\infty} R a_{H,K} i_v dR. \quad (27)$$

Figures 5 and 6 show the coefficients A_H and A_K plotted against the cut-off range R_0. These curves are convenient for comparative purposes with experimental observations. We shall return to them in Sec. V.

The numerical values of $\bar{x}_1$ and $\bar{x}_2$ for the case of $I_v(R_0)$ may be estimated directly from Fig. 3 where one has to take those values of x_1 and x_2 which correspond to the average residual ranges, R_1 and R_2, respectively. One finds that $\bar{x}_1$ will lie somewhere between 115 and 110 g cm^{-2}, and $\bar{x}_2$ between 190 and 160 g cm^{-2}, depending on the experimental value of R_0.

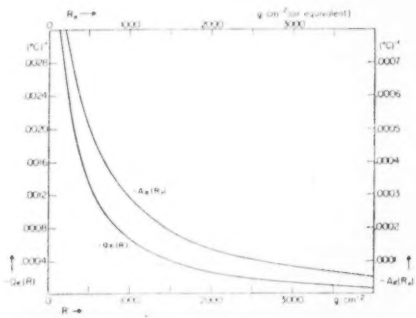

FIG. 6. The coefficients a_K and A_K correlating the differential and integral intensity changes with the variations of the mean temperature of the troposphere; a_K and A_K are plotted *versus* the residual range R and the cut-off thickness R_0, respectively.

IV. PRESSURE EFFECT ON THE COSMIC-RAY INTENSITY AT SEA LEVEL

To complete the discussion of the atmospheric effects on the cosmic-ray intensity, it remains to evaluate the effect of the atmospheric pressure. This evaluation may be carried out by a method analogous to that discussed in the preceding section. If the temperature overhead is kept constant, the partial variation of the differential intensity $i_v(R)$, due to the changes of the ground pressure x_0, is given by

$$\delta_P i_v = (\partial i_v/\partial x_0)\delta x_0. \quad (28)$$

Assuming that i_v may be represented by Eq. (11), one finds by differentiation

$$\delta_P i_v = \left\{G(R)e^{-x_0/L} + \int_0^{x_0} \partial/\partial x_0[\ln G(R_a) + \ln w(x, R)]\Phi dx\right\}\delta x_0. \quad (28')$$

The first term in Eq. (28′) is negligible at sea level. The two last terms may be evaluated by means of the mean value theorem discussed previously. By substituting Eqs. (12) and (5) for $G(R_s)$ and $w(x, R)$, respectively, one gets

$$\delta_P i_v/i_v = a_P(R)\delta x_0, \tag{29}$$

where the "pressure" coefficient a_P is given by

$$a_P(R) = \frac{3.58}{x_0+R-x_2+520} + \gamma\frac{\partial \alpha_H}{\partial x_0} H(x_1) + \alpha_H \frac{\Re T}{Mgx_0} + \frac{\partial}{\partial x_0}[\alpha_K K(x_2, R)]. \tag{30}$$

The evaluation of Eq. (30) with help of Eqs. (6) and (7′) shows that the first term above is predominant. We have computed the pressure coefficient a_P for $100<R<4000$ g cm^{-2} under the assumption that the temperature, $T(x)$, is given by Fig. 1. The result is presented in Fig. 7, where a_P is plotted *versus* R.

For the convenience of the reader we have also computed the pressure coefficient of the integral intensity, i.e., the quantity

$$A_P(R_0) = \frac{1}{I_v(R_0)}\int_{R_0}^{\infty} a_P(R) i_v(R) dR. \tag{31}$$

The behavior of A_P, as a function of R_0, is shown in Fig. 7.

Before concluding this section, we should like to point out that the coefficient a_P is directly related to the measurements on the altitude dependence of the differential intensity i_v; according to its definition, a_P simply represents the slope of the intensity-depth curve. Therefore, referring to Eq. (30), the observed values of a_P may be alternately used as part of the data needed for the determination of the range spectrum at production $G(R_s)$.

V. SUMMARY—COMPARISON WITH EXPERIMENTS

(a) Atmospheric Effect on the Differential Intensity

According to the results obtained in Secs. III and IV, the total variation of the differential intensity near sea level may be represented by a three-term regression formula, *viz.*:

$$\delta i_v/i_v = a_H\delta H(x_1) + a_K[\delta T(x_2)]_{Av} + a_P\delta x_0; \tag{32}$$

i.e., the fractional changes in i_v are correlated with the following variables of the atmosphere:

(1) the departures, $\delta H(x_1)$, from the mean height of the pressure level $x_1(R)$;

(2) the departures from the mean temperature overhead averaged between the pressure level $x_2(R)$ and the sea level pressure, x_0, *viz.*:

$$[\delta T(x_2)]_{Av} = \frac{1}{x_0-x_2}\int_{x_2}^{x_0} \delta T(x')dx';$$

(3) the departures from the mean pressure at sea level, δx_0. The numerical values of the two characteristic pressure levels, x_1 and x_2, are to be taken from Fig. 3. For the numerical values of the three coefficients, a_H, a_K, and a_P, one is referred to Figs. 5, 6, and 7.

(b) Atmospheric Effect on the Integral Intensity

Similarly to case (a), the total variation of the integral intensity near sea level is given by

$$\delta I_v/I_v = A_H\delta H(\bar{x}_1) + A_K[\delta T(\bar{x}_2)]_{Av} + A_P\delta x_0. \tag{33}$$

Here the coefficients A_H, A_K, and A_P are constant quantities for a given experimental arrangement. Their numerical values will be, however, different from case to case, depending on the amount of shielding material above the detector. Taking 400 g cm^{-2} air equivalent of shielding material as a typical case, we find from Figs. 5, 6, and 7

$$A_H = -3.15 \text{ percent per km},$$
$$A_K = -0.059 \text{ percent per °C},$$
$$A_P = -1.79 \text{ percent per cm Hg}. \tag{34}$$

In order to determine the above coefficients experimentally, one has to correlate the observed changes in I_v with the three atmospheric variables $\delta H(\bar{x}_1)$, $[\delta T(\bar{x}_2)]_{Av}$, and δx_0. The characteristic pressure levels, $\bar{x}_1$ and $\bar{x}_2$, have now practically fixed values: $\bar{x}_1 \simeq 115$ g cm^{-2}, and $\bar{x}_2 \simeq 190$ g cm^{-2}, if the amount of shielding above the detector is of the order of a few hundred grams per square centimeter. It is worth mentioning that the pressure level $\bar{x}_2$ nearly coincides with that of the tropopause at moderate latitudes. This implies that the vertical average of the temperature changes above the observer $(\delta T)_{Av}$, extends only over the region of the

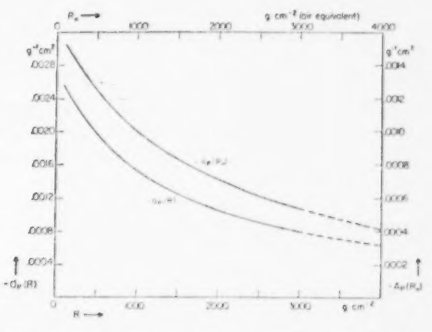

FIG. 7. The coefficients a_P and A_P correlating the differential and integral intensity changes with the variations of the sea-level pressure; a_P and A_P are plotted *versus* the residual range R and the cut-off thickness R_0, respectively.

troposphere, and does not include the temperature of the stratosphere.

(c) Comparison with Experiments

As we have mentioned in the Introduction, it has been customary to correlate the observed variations of the μ-meson intensity to only two atmospheric variables, δH and δx_0. Lack of knowledge of the third variable $(\delta T)_{Av}$, makes an exact comparison of our results with those found experimentally impossible. However, the following semiquantitative considerations appear to indicate substantial agreement between observations and theory.

In the first place, our value of 115 g cm^{-2} for the "mean pressure level" of μ-meson production is in agreement with the observations. For example, A Duperier obtained the best correlation between changes in cosmic-ray intensity and changes in the height of a given pressure level by choosing a value of this pressure level in the proximity of 100 g cm^{-2}.

In the second place, if one writes Eq. (33) in the form

$$\delta I_v/I_v=\left(A_H+A_K\frac{(\delta T)_{Av}}{\delta H}\right)\delta H+A_P\delta x_0, \qquad (35)$$

one sees that the so-called "decay" coefficient of Eq. (1), A_H', is related to our coefficients A_H and A_K by the equation

$$A_H'=A_H+A_K[(\delta T)_{Av}/\delta H]. \qquad (36)$$

The ratio $(\delta T)_{Av}/\delta H$ will depend, of course, on the geographic location, the season during which the experiment was performed, etc. Meteorological observations indicate that, for moderate latitudes, the above ratio will have on the average the following approximate values:

for diurnal departures of $(T)_{Av}$ and H from their means:

$$[(\delta T)_{Av}/\delta H]_{\text{diurnal}}\simeq 50°\text{C/km},$$

for seasonal departures of $(T)_{Av}$ and H from their means:

$$[(\delta T)_{Av}/\delta H]_{\text{seasonal}}\simeq 20°\text{C/km}.$$

It follows that the decay coefficient A_H' will be different depending on whether it is inferred from the diurnal or the seasonal changes of the intensity. According to Eqs. (34) and (36), one would expect for A_H' in these two cases:

$$[A_H']_{\text{diurnal}}\simeq -6.1\%\text{ per km},$$

$$[A_H']_{\text{seasonal}}\simeq -4.3\%\text{ per km}.$$

Indeed, the diurnal and seasonal decay coefficients estimated above are in substantial agreement with those observed experimentally. For instance, Dolbear and Elliot[6] deduced for A_H' the values -5.7 percent km^{-1} and -3.6 percent km^{-1} from the daily and monthly correlations, respectively.[11]

Regarding the pressure effect on the μ-meson intensity, we shall limit ourselves to the remark that the values of the pressure coefficient A_P, given in Fig. 7, seem to be in essential agreement with those observed experimentally. The agreement may be considered as a partial check for the consistency of the assumptions made about the production spectrum of μ mesons [see Eqs. (11) and (12)].

In conclusion we would like to discuss briefly the problem of the so-called "positive temperature effect." As we have mentioned in the Introduction, recent observations by Duperier have shown that the two-term regression formula given by Eq. (1) was inadequate to account fully for the observed variation of the cosmic-ray intensity. The analysis of the correlation coefficients indicated that there must be an additional atmospheric variable which, together with H and x_0, plays a controlling role in the intensity variations. Duperier assumed this variable to be the temperature of the pressure layer between 100 and 200 mb (lower stratosphere). Hence, he replaced Eq. (1) by the following:

$$\delta I/I=A_H\delta H+A_T\delta T+A_P\delta x_0, \qquad (37)$$

where δT is the deviation from the mean of the temperature of the 100–200 mb pressure layer, and the other symbols have the same meaning as before. The temperature coefficient A_T, deduced from the observational data, turned out to be positive ($A_T=+0.12$ percent per °C). Duperier attempted to interpret this positive temperature effect as due to the competing processes of nuclear capture and decay of π mesons. However, a quantitative estimate of the effect of these processes, based on more recent data for the mean life and the cross section for nuclear capture of π mesons, has shown that the observed value of A_T is much too high to be ascribed exclusively to the finite life span of π mesons.

It is interesting to compare Duperier's regression formula, Eq. (37), with that given by Eq. (33). Since the coefficients A_H and A_P determined by Duperier are roughly in numerical agreement with those calculated in this paper, the ratio $(\delta T)_{Av}/\delta T$ should be equal to A_T/A_K. The value of our coefficient A_K is about -0.06 percent per °C while the experimental value of A_T is 0.12 percent per °C from which it follows that $(\delta T)_{Av}/\delta T\simeq -2$. The negative sign of the ratio $(\delta T)_{Av}/\delta T$ is not in contradiction with the general behavior of the free atmosphere. For it is well known that the warming of the troposphere [$(\delta T)_{Av}$ positive] is, as a rule, ac-

[11] In the experimental arrangement used by Dolbear and Elliot the threefold counter coincidence set was inclined at 45° to the vertical. Therefore the results of these authors are to be corrected before being compared with the results corresponding to the vertical intensity. It can be shown, however, that this correction is not crucial, and can be neglected in our semiquantitative discussion.

companied by a cooling of the lower stratosphere (δT negative) and vice versa. The magnitude of the above ratio is probably too large. However, a knowledge of the actual values of $(\delta T)_{A_0}$ for the period and location of Duperier's experiment is needed to check our results quantitatively.

In view of the above discussion we conclude that the additional term, $A_K(\delta T)_{A_0}$, in the regression formula may possibly remove the apparent variability of Elliot's decay coefficient as well as the anomalous value of Duperier's coefficient for the positive temperature effect. An experimental verification of this conclusion would be desirable. Unfortunately, because of the strong correlation between δH and $(\delta T)_{A_0}$, it will be very difficult to separate experimentally the effects caused by δH from those caused by $(\delta T)_{A_0}$.

The author would like to express his gratitude to Professor Bruno Rossi for his interest and assistance in the preparation of this paper, and to Professor H. Elliot and Professor A. Duperier for their criticisms. The author is also grateful to Professor J. M. Austin of the Meteorology Department at Massachusetts Institute of Technology for valuable discussions concerning meteorological data.

PHYSICAL REVIEW VOLUME 92, NUMBER 2 OCTOBER 15, 1953

Multiple Cores in Air Showers*

OSMAN EL-MOFTY†
Department of Physics, University of California, Berkeley, California
(Received July 6, 1953)

Multiple cores in cosmic-ray air showers are difficult to observe because of the overlapping of the cores. After transition to equilibrium with water the cores are much smaller and readily identified. Decoherence measurements of the coincidences between pulses in ionization chambers have been made for depths in water from 0 to 3 meters and with separation of the chambers up to 6 meters. The decoherence measurements are consistent with an average air shower at 9000 feet which has about 20 cores within a distance of about 5 meters from the shower's center.

INTRODUCTION

SEVERAL experiments have been performed to study the structure of the extensive showers in cosmic rays. Calculations[1] based on the hypothesis of the cascade origin of these showers have been shown to be in agreement with experiments performed with Geiger counters[2] and ionization chambers.[3] It has been proposed by Lewis, Oppenheimer, and Wouthuysen[4] that the originating particles are produced in nucleon-nucleon collisions with high multiplicity. Hence, the resulting showers should have multiple cores corresponding to the multiplicity of the events. However, experiments[2,3] failed to detect any multiplicity in the cores of the extensive showers. These negative results have been explained by Blatt.[5] He pointed out that statistical fluctuations in experimental data are responsible for this apparent agreement between Molière[1] distribution and the experimental data.

Fretter and Ise[6] have reported another type of experiment to detect the presence of multiple cores, using water as an absorber and Geiger tubes as detectors. The experiments were carried out by Barrett,[7] and results were reported to agree with the single core distribution.

In the research reported here, another experimental arrangement was applied to study further the structure of the shower cores. Water was used as an absorber and fast ionization chambers as detecting instruments. The reason for these two choices can be explained as follows:

In water, the characteristic quantities for electron showers are quite different from those in air. Table I gives numerical values of the characteristic quantities for electron showers in both materials.

The unit r_1 was introduced by Euler and Wergeland[8] as a convenient unit for studying the spatial distribu-

TABLE I. Characteristic quantities for electron showers in air and water.

	Critical energy E_f $\times 10^9$ ev	Radiation length X_0 cm	Lateral unit r_1 cm
Air	11.3	33 000	5950
Water	11.3	43	7.8

* Assisted by the joint program of the U. S. Office of Naval Research and the U. S. Atomic Energy Commission.
† Now at the Department of Physics, Faculty of Engineering, Fouad University, Giza, Egypt.
[1] G. Molière, *Cosmic Radiation*, edited by W. Heisenberg (Dover Publications, New York, 1946).
[2] Cocconi, Cocconi Tongiorgi, and Greisen, Phys. Rev. **76**, 1020 (1949).
[3] R. W. Williams, Phys. Rev. **74**, 1689 (1948).
[4] Lewis, Oppenheimer, and Wouthuysen, Phys. Rev. **73**, 127 (1948).
[5] J. M. Blatt, Phys. Rev. **75**, 1584 (1944).
[6] W. B. Fretter and J. Ise, Jr., Phys. Rev. **78**, 92 (1950).
[7] P. H. Barrett, Phys. Rev. **84**, 339 (1951).
[8] H. Euler and H. Wergeland, Astrophysica Norwegica **3**, 165 (1940).

TABLE II. Experimental results at Lake Sabrina (elevation 2765 meters).

Depth under water, D in cm	Separation of the chambers, S in cm	Twofold coincidence counting rates counts/hr
0	87	0.870±0.1
91	87	1.024±0.15
185	87	0.469±0.046
	345	0.294±0.039
	440	0.175±0.033
	645	0.046±0.034
274	87	0.277±0.043
	158	0.196±0.04
	345	0.162±0.037
	440	0.075±0.039

tion in the showers, and can be defined by: $r_1=E_sX_0/E_j$, where X_0 is the radiation length, E_j the critical energy, and E_s is a constant ($E_s=21$ Mev). The value of r_1 for any material can then be shown to be of the order of magnitude of the lateral dimension of the showers in equilibirum with this material. This lateral dimension being sometimes expressed as a half radius, meaning the radius enclosing half the total number of particles in the shower at any depth.

From the value of r_1 (the lateral unit of length), it is clear that showers which extend in air to distances of several meters, after reaching equilibrium in water, will shrink to a few centimeters. X_0 the radiation length, being only 43 cm in water, indicates that the transition effect will have disappeared at a depth of two meters or so. The multiplicity of cores which escapes detection in air due to overlapping, is more readily revealed if the showers are studied under water.

Fast ionization chambers were chosen as the detecting instrument in the experiment because of their proportionality. The pulse output of a chamber is proportional in height to the amount of ionization in the chamber. The instrument can then be applied to record events larger than any arbitrary value when used in conjunction with a discriminating circuit.

EXPERIMENTAL ARRANGEMENT

The apparatus for the experiment consisted of two spherical ionization chambers, the necessary amplifiers, registering circuits, and power supplies. The equipment was carried on a raft and floated on Lake Sabrina (elevation 2765 meters) near Bishop, California. The chambers were then lowered in water by ropes. The depth D of the chambers below the surface of the lake as well as the separation S between the chambers were changed throughout the experiment and the twofold coincidence counting rate was recorded.

Each ionization chamber consisted[9] of two spun-aluminum hemispheres, 13.25 in. in diameter and $\frac{1}{8}$ in. thick, welded together, enclosing a small, hollow aluminum sphere 3 in. in diameter serving as a collecting electrode. The ionization chambers were fitted to steel boxes with watertight covers leaving the top hemispheres exposed. The boxes housed the lower halves of the chambers, the high voltage circuits and the preamplifiers. Power and signals were conducted to and from the chambers by cables which entered the boxes through watertight glands. The chambers were filled with pure argon gas at a pressure of 2.85 atmospheres. A high degree of purity of the gas was achieved by having a calcium gas purifier[10] connected permanently to each chamber.

Signals from the chambers after going through the preamplifiers are transmitted through long cables to the linear amplifier.[11] Each linear amplifier has a rise time of 0.7 μsec and a clipping time of 50 μsec. The overall gain of amplification is 8×10^5. The output from the amplifiers is then fed into a discriminator circuit, a twofold coincidence circuit, and registering circuits. The registering circuits recorded the individual channels' counts as well as the twofold coincidences on separate registers. The resolving time of the coincidence circuit was measured to be 5 μsec.

For calibration, each chamber was provided with a weak polonium source placed on the inside of the outer wall. A bias curve was obtained for each chamber and the discriminator was set during the experiment to correspond to $\frac{1}{2}$ the energy of a polonium α particle. This energy corresponds to 20 shower particles in the chamber or a density of 230 particles per square meter.

RESULTS AND ANALYSIS

The experimental data are given in Table II. Counting rates were corrected for accidentals and the errors indicated are standard deviations due to statistical fluctuations. Other errors were too small, compared to the statistical fluctuations, to be of significance.

Calculations were carried out to determine the shape of the twofold decoherence curve expected for this experimental arrangement assuming the Molière distribution is valid and a single core. If the apparatus is biased to detect densities above a certain value ρ, the twofold coincidence counting rate $W(\rho,S)$ for any separation of chambers, S, can be calculated. An expression was given by Blatt[5] for $W(\rho,S)$ as a function of the density distribution function $f(r)$ and the integral number spectrum of showers. This expression in conjunction with the Ise and Fretter[12] discussion of shower spectra and the Molière[1] distribution function can be reduced to

$$W(\rho,S)=CS^{-4}, \tag{1}$$

where C is a proportionality constant. Equation (1) is

[9] Osman H. El-Mofty, Ph.D. thesis, University of California, 1953 (unpublished).

[10] B. Rossi and H. H. Staub, *Ionization Chambers and Counter's Experimental Techniques* (McGraw-Hill Book Company, Inc., New York, 1949).

[11] Elmore and M. Sands, *Electronics Experimental Techniques* (McGraw-Hill Book Company, Inc., New York, 1949).

[12] J. Ise and W. B. Fretter, Phys. Rev. **76**, 933 (1949).

shown in Fig. 1 by the dotted curve 4. It was normalized at the experimental values at the smallest separation.

It is obvious that the calculated curve does not fit the experimental data. This is expected, in view of the argument presented in connection with Table I. It actually means that the values of S used in the experiment are so large compared to the dimensions of showers in water, that the counting rate function drops very rapidly.

As the idea of single cores was found inconsistent with the experimental data, an assumption was made that showers have multiple cores. This assumption is also supported by meson production theories and theories on the origin of showers, as was pointed out in the Introduction. An attempt was then made to obtain information about the distribution of these cores.

Let the cores of the shower be distributed around the axis, according to a function $\phi(r)$. In other words, let $\phi(r)$ be the probability of finding a core at a distance r in the horizontal plane from the axis of the shower. If ν is the total number of cores within the individual shower, and σ is the density of cores at a distance r, then

$$\sigma = \nu \cdot \phi(r).$$

An expression can then be set up for the twofold coincidence counting rate W as a function of the above-mentioned variables. A linear function was assumed for $\phi(r)$, decreasing from a value corresponding to density of cores of σ_0 at the center, to the value of 0 at a limiting distance r_0. Calculations were carried out for an average shower, hence no assumption as to the form of dependence of the shower frequency on ν was necessary. By choosing arbitrary values for the multiplicity ν and the limiting radius r_0 it was possible to calculate graphically the value of the counting rate W as a function of the separation S. The results of the calculations are shown in Fig. 1. Curve 1 was calculated for $r_0=7$ meters and $\nu=30$, curve 2 for $r_0=7$ meters, $\nu=35$, and curve 3 for $r_0=5$ meters and ν ranging from 10 to 15.

The fairly good fit of curve 3 to the experimental points suggests that the assumptions introduced in the analysis are consistent with the experimental data. It was noticed that the shape of the curve is sensitive to changes in r_0 but rather insensitive to changes in ν. The values of r_0 indicate that the cores of the shower extend to a distance of the order of 5 meters from the axis. No definite value for ν can be evaluated. However, upper and lower limits can be estimated as 30 and 10, respectively.

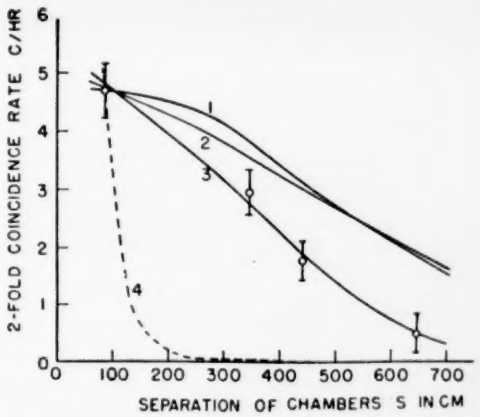

FIG. 1. Calculated decoherence curves assuming multiple cores (curves 1, 2, and 3) and for single core (curve 4). Experimental points taken at a depth of 185 cm are also shown.

CONCLUSIONS

The conclusions that may be drawn from the experiments and calculations are somewhat qualitative. The decoherence curve calculated from the Molière[1] distribution was found to be inconsistent with the experimental results. The observed decoherence can be satisfactorily explained by the presence of multiple cores in extensive showers. It is reasonable to assume that the density of cores in the average extensive shower decreases linearly with the distance from the center of the shower to a value of zero at a distance r_0.

A density of cores σ_0 of about 1 per square meter at the center and a limiting radius of $r_0=5$ meters appear to fit the observed data. This gives a total number of cores in the average shower of about 20.

ACKNOWLEDGMENTS

The writer wishes to express his gratitude to Professor Robert B. Brode for his help and guidance in the research, and to Professor W. B. Fretter who suggested the experiment and guided its progress. Great help in electronics technique was given by Mr. R. M. MacIntyre and Mr. E. Mundt. Appreciation is also expressed to the California Electric Power Company and the U. S. Forestry Service, for the cooperation of their employees and the use of their facilities during the experimental research at Lake Sabrina.

The author also acknowledges the support of the Egyptian Government in providing a fellowship that made his graduate studies and research possible.

Relative Ionization by Cosmic-Ray μ Mesons in a Liquid Scintillator*

R. BASKIN† AND J. R. WINCKLER
University of Minnesota, Minneapolis, Minnesota

(Received January 22, 1953; revised manuscript received June 8, 1953)

Measurements of the rise in energy loss of μ mesons of energy between 385 Mev and 2200 Mev in traversing an xylene solution have been made. The observed pulse-height distribution is compared with the most probable energy loss and median energy loss as found using the Landau theory without a density correction and with a density correction as calculated by Sternheimer. The result of this measurement favors a density correction to the theory of energy loss.

INTRODUCTION

AN attempt has been made to measure the increase in energy loss for a μ meson of increasing relativistic velocity in traversing a condensed material.

The theory of energy loss of charged particles in passing through matter was first proposed by Bohr.[1] Later work by Bethe and Bloch[2] using quantum mechanics improved quantitatively the agreement between measured and calculated energy loss. The equation Bethe and Bloch arrived at has come to be known as the Bethe-Bloch formula[3] and represents what is commonly called the mean energy loss. Further calculations on the energy loss of relativistic particles in passing through condensed material have been recently made.[4–7] The influence of the electric polarization of the medium on the electric field of the passing particle reduces the energy loss for incident particles of relativistic velocities. A search for this effect, which is called the density effect, in anthracene, sodium iodide, and silver chloride has recently been reported by Bowen and Roser,[8] Hudson and Hofstadter[9] and Whittemore and Street.[10]

One of the problems in this investigation is to arrive at a satisfactory basis for comparison of the experimental results with theory. The problem arises because the energy loss of a charged particle of unique velocity in passing through matter is not unique, but there is a distribution in energy loss. The form of the distribution depends on the amount of loss in relation to the kinetic energy of the particle. For the case of this experiment, where the loss is very much less than the kinetic energy, the distribution is nonsymmetrical with a high-energy tail. As the loss begins to be appreciable relative to the particles' kinetic energy, the distribution becomes more symmetrical. The form of the distribution function and values for the most probable, mean, and median energy loss of the distribution have been given by Landau[11] and Symon,[12] using the Bethe-Bloch formula in deriving the distribution function. The mean energy loss given by the Bethe-Bloch formula coincides with the most probable energy loss of the fluctuation theory only for the symmetrical type distribution, i.e., when the energy loss is a considerable fraction of the kinetic energy of the particle. The comparisons of the experimental and theoretical values are here carried out, firstly on the basis of the median energy loss of the Landau distribution, which can be obtained by an objective numerical analysis of the data, and secondly by estimating the most probable value of the experimental histograms, which is less objective, but not necessarily less accurate, than the first method. Also calculated for comparison is the mean energy loss of the Bethe-Bloch type, as given recently by Sternheimer.[7]

The development of liquid scintillators and high-gain photomultipliers in the past several years has made possible the determination of the density correction in a condensed material. Liquid scintillators permit the material in which the ionization loss is to be measured to be of large cross-sectional area and thus allow reasonably high counting rates when the particle is a cosmic ray μ meson. In other respects liquid scintillators are generally inferior to good crystal scintillators.

EXPERIMENTAL ARRANGEMENT

The experimental arrangement for this experiment consists of a Geiger counter telescope in which is placed the liquid scintillator. The liquid scintillator was 5 g of *p*-diphenylbenzene, plus 10 mg of diphenylhexatriene per 1000 cc of xylene. The photomultiplier used was RCA 5819 run with photocathode at ground potential, the first two stages at 100 volts and the remaining stages at 50 volts. The energy of the μ meson whose pulse height is measured is obtained from its range in lead. The experiment was performed in two parts:

* This work supported by the joint program of the U. S. Atomic Energy Commission and the U. S. Office of Naval Research.

† Present address: Radioisotope Unit, Veterans Administration Hospital, Minneapolis, Minnesota.

[1] N. Bohr, Phil. Mag. **25**, 10 (1913); **30**, 581 (1915).
[2] H. Bethe, Ann. Physik **5**, 325 (1930); Z. Physik **76**, 293 (1932); F. Bloch, Ann. Physik **16**, 285 (1933); Z. Physik **81**, 363 (1933).
[3] See B. Rossi and K. Greisen, Revs. Modern Phys. **13**, 247 (1941).
[4] E. Fermi, Phys. Rev. **57**, 485 (1940).
[5] G. C. Wick, Nuovo cimento **1**, 302 (1943).
[6] G. Halpern and A. Hall, Phys. Rev. **73**, 477 (1948).
[7] R. M. Sternheimer, Phys. Rev. **88**, 851 (1952).
[8] T. Bowen and F. X. Roser, Phys. Rev. **85**, 992 (1952).
[9] A. Hudson and R. Hofstadter, Phys. Rev. **88**, 589 (1952).
[10] W. L. Whittemore and J. C. Street, Phys. Rev. **76**, 1786 (1949).
[11] L. Landau, J. Phys. (U.S.S.R.) **8**, 201 (1944).
[12] K. R. Symon, Harvard thesis (1948) published in *High Energy Particles* by B. Rossi (Prentice-Hall, Inc., New York, 1952).

(a) the relativistic μ mesons were selected as shown in Fig. 1 and (b) the nonrelativistic arrangement similar to Fig. 1 with the exception that 8 inches of Pb was placed above the telescope to absorb electrons. For the relativistic case two groups of energies were selected at a time and in this case there were a total of six groups of energy. For the nonrelativistic case two groups of energies were also run simultaneously, and for this case, only two groups were obtained. The meson energy is obtained from the differential range in lead. Column 1 of Table I is the average meson energy. The highest meson energy looked at is obtained by counting all mesons of range greater than 864.5 g/cm^2 and computing the effective energy by using the sea-level spectrum[13] modified by the fact that the experiment was performed beneath several feet of concrete. No correction has been made for multiple scattering in the lead or the accidental rate, which is relatively high in a differential experiment of this kind. However, these effects do not invalidate the conclusions drawn from the data.

TABLE I. Calculated energy loss in 5-cm xylene for several meson energies.

Average meson energy Mev	$t\frac{dE}{dx}$ (Mev) with density correction	E_p (Mev) no density correction	E_p (Mev) with density correction	$\bar{E}$ (Mev) with density correction
80	10.42	10.61	10.61	11.01
135	9.39	9.26	9.26	9.82
385	8.98	8.56	8.13	8.94
425	9.07	8.57	8.13	8.94
630	9.34	8.65	8.13	8.95
740	9.48	8.72	8.14	8.95
875	9.61	8.82	8.15	8.95
995	9.66	8.88	8.15	8.95
1400	9.88	9.09	8.15	8.95
3000	10.42	9.52	8.15	8.95

The energy loss is determined by measuring the pulse heights from the scintillation counter, and the light output is taken to be proportional to the energy loss. This proportionality of energy loss to light output does not break down until much lower kinetic energies than that used in this experiment. The work of Chow[14] shows that saturation of π mesons in phenylcyclohexane occurs at energies below 32 Mev.

The pulses from the scintillation counter were amplified and fed to the vertical deflection plates of an oscilloscope which was triggered by a threefold coincidence ABC. The pulse and neon lights indicating whether counters D, E, and F were discharged at the same time the threefold coincidence occurred were photographed. Counters D and E set the limits on the differential energy of the meson, and counters F were for the purpose of eliminating a fraction of the side showers. The pulse from the phototube was shaped to have a 2-μsec rise time and a 7-μsec decay time. The threefold coincidence generated a 20-μsec square wave with a rise time less than 1 μsec.

[13] J. G. Wilson, Nature **158**, 415 (1946).
[14] C. N. Chow, Phys. Rev. **87**, 903 (1952).

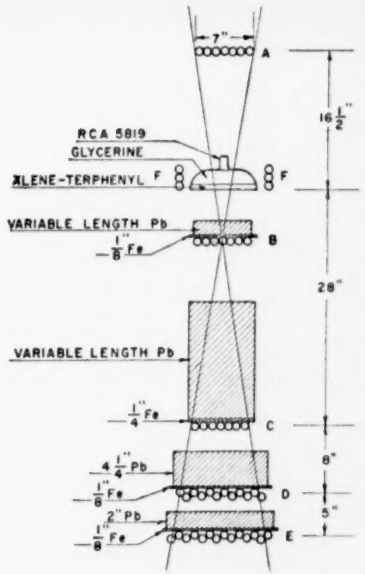

FIG. 1. Experimental arrangement. (Xlene should read xylene in the above figure.)

The liquid scintillator, which was 2 inches thick, was placed in a magnesium oxide coated hemisphere of 8 inches diameter. The upper section of the hemisphere was filled with glycerine for optical coupling and the photomultiplier was set into the hemisphere as shown in Fig. 1.

RESULTS

Pulse-height distributions for eight differential energy groups and for two integral energies have been obtained. The distribution obtained for mesons between 560 and 700 Mev is shown in Fig. 2. The distributions are typical of the distribution in energy loss as calculated by Landau[11] and Symon,[12] the major difference being in the much greater percent half-width of the experimental distributions. On the basis of Symon's work the calculated percent half-width in the energy loss distribution for a minimum ionizing μ meson in traversing 2 inches of xylene should be about 20 percent; however, the experimental relativistic distributions give a percent half-width of approximately 60 percent. The nonrelativistic distribution for a meson of energy 80 Mev is slightly broader than the relativistic ones. This might be explained by the fact that the distributions are differential, and in the nonrelativistic region before minimum ionization the energy loss is falling rapidly with increasing energy. The broadening of the experimental distributions can be accounted for on the basis of the following factors:

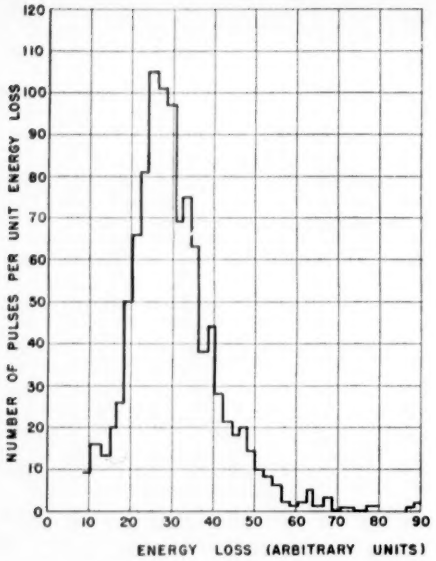

FIG. 2. Pulse-height histogram for meson energy 630 Mev.

(1) photoelectron statistics,
(2) difference in path length of the meson through the scintillator,
(3) attenuation of the light due to variations in the focusing from different parts of the cell,
(4) absorption by the liquid of its own radiation in varying amounts depending on source positions.

By measuring the gain of the photomultiplier at the voltage operated, the number of photoelectrons from the most probable pulse size has been calculated. From the work of Garlick and Wright[15] it is estimated that the photoelectron statistics has a full width at half-maximum of approximately 15 percent. The attenuation of the light at the photocathode was determined by measuring the output current from the photomultiplier when a polonium alpha source was placed in different positions of the liquid cell. This showed the light to fall off by a factor of two in going from the center of the cell to the end of the cell along any diameter. The weighting of this attenuation with the solid angle of the telescope and the cosmic-ray flux shows that the pulse-height distribution is shifted to the left, and that its standard deviation is increased. The exact value, however, is difficult to determine. The standard error if increased because of this large standard deviation or large half-width, but by taking more events the standard error can be made small. For all the differential energies used, the pulse height distribution represents approximately 1000 events.

[15] G. F. J. Garlick and G. T. Wright, Proc. Phys. Soc. (London) **B65**, 415 (1952).

COMPARISON WITH THEORY

As discussed above, in order to compare the results with theory, we calculated the energy loss with a density correction in three different ways. The theoretical expression for the rate of loss of energy with the density correction as given by Sternheimer[7] is

$$\frac{1}{\rho}\frac{dE}{dx}=\frac{A}{\beta^2}\left[B+2\ln\frac{\beta}{(1-\beta^2)^{\frac{1}{2}}}+\ln T'+1-\beta^2-\delta\right], \quad (1)$$

where

$$A=0.15\times10^6\Sigma Z/\Sigma A,$$

$$B=\ln(mc^2\times10^6\ \text{ev}/I^2),$$

$$T'=\frac{E^2-\mu^2c^4}{\mu c^2(\mu/2m+m/2\mu+E/\mu c^2)}. \quad (2)$$

In this formula ρ is the density of the material, μ is the mass of the incident particle, m is the mass of the electron, E is the energy of the incident particle, I is the ionization potential of the material, δ is the density correction, Z and A are the atomic number and mass of the material. The ionization potential for xylene, I_x, was computed by using the following equation

$$\ln I_x=\frac{8\times6\ln I_C+10\times1\ln I_H}{8\times6+10\times1} \quad (3)$$

$I_C=76.4$ ev and $I_H=15.6$ ev are the ionization potentials of carbon and hydrogen, respectively.[16] The number multiplying $\ln I_C$ and $\ln I_H$ are weighting numbers obtained from the formula of xylene, which is C_8H_{10}. The density correction is obtained from the curves as given by Sternheimer.[7] For xylene, $A=0.0821$ Mev/g/cm^2, $I=58$ ev, and $B=18.8$. Column 2 of Table I is the product of Eq. (1) and the thickness of xylene in g/cm^2.

Using the Landau distribution we computed the most probable energy loss E_p, which is the peak of the distribution. The most probable energy loss for a small

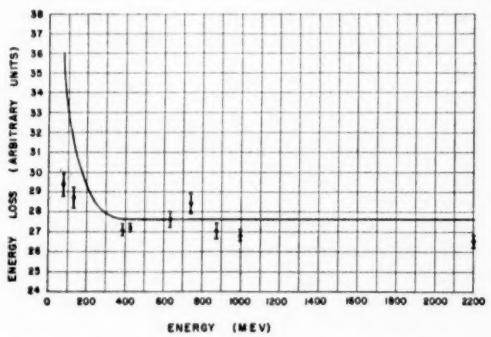

FIG. 3. The most probable energy loss as a function of meson energy. Solid curve—calculated with density correction.

[16] C. J. Bakker and E. Segrè, Phys. Rev. **81**, 489 (1951).

thickness of material, where by small thickness is meant that the average energy loss is less than one-tenth the kinetic energy of the incident particle, is

$$E_p=\frac{At}{\beta^2}\left[B+2\ln\frac{\beta}{(1+\beta^2)^{\frac{1}{2}}}+\ln\frac{At}{\beta^2}+1.37-\delta\right], \quad (4)$$

where t is the thickness of the material in g/cm². E_p for several meson energies is given in column 4 of Table I. It should be noticed that the rise in energy loss as given from Eq. (1) is much larger than is predicted by the most probable energy loss, Eq. (4), using the Landau distribution (thin absorber, skewed distribution).

The rise in energy loss, for μ mesons of energy 385 Mev and 3000 Mev, using the *Bethe-Bloch* formula with and without the density correction for 2 inches of xylene is 14 percent and 21 percent, respectively. This rise for mesons of same kinetic energy using the *most probable* loss of energy from the Landau theory with and without the density correction is 2 percent and 10 percent, respectively.

Using curves obtained from Symon's thesis[12] and knowing the most probable energy loss, the *median* energy loss $\bar{E}$ has been calculated. This median energy loss is that energy loss which divides the Landau distribution into equal areas, and it is not the same as the energy loss obtained from Eq. (1) by multiplying by thickness of the material in g/cm². The results of this calculation are given in column 5 of Table I, which shows the expected rise in median energy loss is 2 percent and 10 percent with and without the density correction.

For the nonrelativistic energies, 80 Mev and 135 Mev, the most probable energy loss was obtained from the experimental data by drawing a smooth curve through the experimental histograms. This was done by six individuals. The average of these six observations and the average error of these observations are the points plotted in Fig. 3. For the relativistic energies, a slightly different method was used to find the peak of the distributions. The peak of histograms of the relativistic energies were all in the same energy loss interval and so all the relativistic histograms were added together. From this histogram a smooth curve was drawn. The seven relativistic histograms were normalized to give the same area as the sum of all the relativistic histograms. Using the smooth curve obtained from the sum, the peaks of seven normalized histograms were found by observing how much the smooth curve had to be shifted along the abscissa in order to best fit the histograms. This operation was performed by six individuals, and the average of these results is plotted in Fig. 3.

The median energy loss was computed directly from the histogram data for the relativistic and nonrelativistic energies. The errors used are the standard errors, also obtained directly from the data. The result is plotted in Fig. 4.

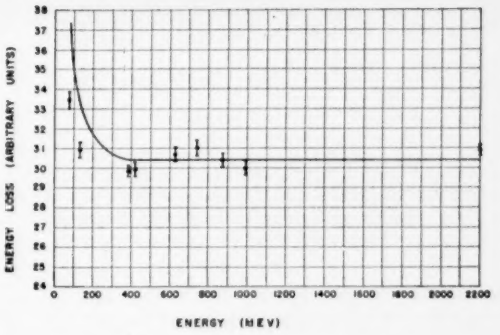

FIG. 4. The median energy loss as a function of meson energy. Solid curve—calculated with density correction.

The smooth curves in Figs. 3 and 4 are the calculated most probable and median energy loss using the Landau distribution with a density correction. The ordinate of Figs. 3 and 4 is in arbitrary units. The ordinates for the theoretical curves were found by normalizing the calculated median energy loss to the observed median energy loss at 385 Mev. One notes that when this is done, the curve representing the most probable energy loss falls, in general, slightly above the experimental points, but hardly outside the experimental error. One also notes that the experimental rise in energy loss cannot be as much as 10 percent and is not in disagreement with the theory corrected for the density effect.

The ratio of the median energy loss found by experiment for a meson of energy 80 Mev to the median energy loss for a meson of energy 385 Mev is about 15 percent too low if compared with theory. The ratio of an energy loss for mesons of 135 Mev and 385 Mev as found from experiment is about 8 percent too low. If this is evidence for saturation in the scintillator, it occurs at higher kinetic energies than found by Chow[14] for phenylcyclohexane. However, the range method used in this experiment presents greater difficulties in determining particle energy in this range due to scattering and other spurious effects, and more uncertainty is thereby introduced.

SUMMARY

The results of this experiment show that the rise in energy loss past minimum in a condensed material is in much better agreement with a theory[4–7] which takes account of the polarization of the medium. A comparison of the energy loss of a meson of 135 Mev with a meson of 385 Mev shows that an experiment of this nature can detect about a 3 percent change.

The authors are very grateful to Dr. Joseph W. Weinberg and Dr. Charles L. Critchfield for discussions on the theoretical aspects of this paper. We wish to thank Lenore Sausser for the construction of the Geiger counters used in this experiment.

Strong Coupling Theory of Meson Scattering*

ALLAN N. KAUFMAN
Department of Physics, University of Chicago, Chicago, Illinois
(Received June 12, 1953)

The strong coupling theory of meson scattering by nucleons is extended to second order in the inverse of the coupling parameter g for the case of a charged scalar field. The ordinary and charge exchange scattering amplitudes for positive and negative mesons are calculated by a perturbation expansion in g^{-1}, in terms of the normal modes of the g^0 order Hamiltonian, taking into account the inelasticity caused by the existence of isobaric levels of the compound nucleon.

1. INTRODUCTION

IT is now generally believed that pions are pseudoscalar particles and that they are coupled to nucleons with a strength that is neither weak nor strong, but intermediate. In order to investigate the nature of the pion-nucleon interaction, scattering experiments have been performed.[1] There is at present no satisfactory field-theoretic treatment of pion-nucleon scattering available which treats the case of intermediate coupling.[2] Some idea of the probable results of intermediate coupling may be obtained by studying the cases of weak and strong coupling. Whereas extensive field-thoretic calculations have been carried out for the scattering cross sections in the weak coupling limit, calculations in the strong coupling limit[3–6] have been performed only to zero order in the inverse of the coupling parameter. It is the purpose of this paper to extend the calculations to second order in the inverse coupling parameter.

Because the strong coupling treatment of the (charge-symmetric) pseudoscalar field[4,6] is quite complicated, and because many of the essentials of this problem arise already in simpler theories, it was thought advisable to investigate the mathematical structure of the problem by first studying the relatively simple case of the charged scalar field.[3,5] This paper restricts itself to this case.

Strong coupling theories[3–6] have treated the nucleon as a fixed extended source of the meson field. (The use of a point source leads to divergences.) These theories thus neglect recoil of the nucleon,[7] and transitions of the nucleon to negative-energy states. Although an extended source is required throughout the calculation, for the charged scalar field the final results are finite in the limit of a point source (without the necessity of renormalization).

Strong coupling between the nucleon and the meson field leads to the existence of isobaric nucleon states, which are states of the system composed of the bare nucleon and many bound (or possibly virtually bound) mesons. In the charged scalar theory, the bare proton or neutron has many charged mesons bound to it, and as a result the compound nucleon may have any integral charge. The theory[3,5] shows that these states have an energy equal to $4\pi g^{-2}\mu I_N^2$, where g is the coupling parameter, μ is the meson rest mass, and I_N is the isotopic spin, defined here as charge minus one-half, of the compound nucleon. (In a charge-symmetric theory, this is called the 3-component of the vector isotopic spin.) The strong coupling treatment requires that g be much greater than one, while I_N is assumed to be of the order of one. Thus the isobaric states have energy differences much less than the meson mass, and this makes them stable against meson emission. Hence resonance scattering of mesons is not possible in the scalar theory. (For the pseudoscalar theory, on the other hand, the isobaric energies can be made greater than μ by a suitable choice of the nucleon radius; this leads to an expectation of resonance scattering,[8] as suggested by the experimental results.[1])

The following scattering processes occur:

$$\Pi^{\pm}+N^{I_N}\rightarrow\Pi^{\pm}+N^{I_N}$$

$$\Pi^{\pm}+N^{I_N}\rightarrow\Pi^{\mp}+N^{I_N\pm 2}.$$

The first reaction is ordinary elastic scattering from an isobaric state; the second is charge-exchange inelastic scattering, and involves a change of kinetic energy equal to $\mp 16\pi g^{-2}\mu I$, where $I=I_N\pm 1$ is the total isotopic spin of the system. For scattering from a proton or neutron, which is the doubly degenerate ground state of the compound nucleon ($I_N=\pm\frac{1}{2}$), both charge-exchange processes have thresholds.

In Sec. 2, the Hamiltonian describing a charged meson field with a scalar interaction is successively transformed until an expansion in descending powers of g can be made. Terms beyond order g^{-2} are dropped.

* This paper is based on a thesis submitted in partial fulfillment of the requirements for the degree of Doctor of Philosophy at the University of Chicago.

[1] Anderson, Fermi, Martin, and Nagle, Phys. Rev. **91**, 155 (1953).

[2] Recently the Tomonaga approximation has been applied to the intermediate coupling problem by T. D. Lee and R. S. Christian, and by B. D. Fried and R. J. Riddell, Jr. (to be published).

[3] G. Wentzel, Helv. Phys. Acta **13**, 269 (1940); **14**, 633 (1941).

[4] W. Pauli and S. M. Dancoff, Phys. Rev. **62**, 85 (1942).

[5] R. Serber and S. M. Dancoff, Phys. Rev. **63**, 143 (1943).

[6] A. Houriet, Helv. Phys. Acta **18**, 473 (1945).

[7] Recoil corrections have been investigated by G. Wentzel, Phys. Rev. **91**, 1573 (1953).

[8] G. Wentzel, Phys. Rev. **86**, 437 (1952); K. A. Brueckner, Phys. Rev. **86**, 106 (1952).

In Sec. 3, the zero-order (g^0) terms of the Hamiltonian are diagonalized by a transformation to normal modes, which represent the strong scattering of mesons by the nucleon; in Sec. 4 the Hamiltonian is expressed in terms of these normal modes. The isobaric levels are found in Sec. 5, and in Sec. 6 the ordinary and charge-exchange scattering amplitudes are calculated to order g^{-2}. Section 7 contains a discussion of the results.

It is found that, at least to order g^{-2}, a rigorous perturbation calculation of the scattering can be made using the normal modes of the zero-order Hamiltonian as the unperturbed states, with g^{-1} as the perturbation parameter. It is expected that a similar calculation can be performed for the physically more interesting, but mathematically more difficult, case of the charge-symmetric pseudoscalar field. Whereas in the present problem, the transition to a point source can be made in the final results, this would not be possible for the pseudoscalar field, and the nucleon radius would remain as an adjustable parameter.

2. THE HAMILTONIAN

For a charged scalar field in scalar interaction with an extended source, the Hamiltonian is, in natural units ($\hbar=c=1$),

$$H=H_0+H_I,$$

$$H_0=\int d\mathbf{r}(\pi^*\pi+\varphi^*\omega^2\varphi), \quad \omega^2\equiv\mu^2-\nabla^2,$$

$$H_I=\sqrt{2}g\int d\mathbf{r}U(r)[\tau_+\varphi(\mathbf{r})+\tau_-\varphi^*(\mathbf{r})], \tag{2.1}$$

where

$$i[\pi(\mathbf{r}),\varphi(\mathbf{r}')]=i[\pi^*(\mathbf{r}),\varphi^*(\mathbf{r}')]=\delta(\mathbf{r}-\mathbf{r}'). \tag{2.2}$$

The spherically symmetric source function $U(r)$ represents the spatial extension of the bare nucleon, and is normalized to unity:

$$\int d\mathbf{r}U(r)=1. \tag{2.3}$$

Its radial extension a is to be taken much smaller than μ^{-1} and the wavelengths of scattered mesons, and will be allowed to go to zero whenever possible.

The only degree of freedom of the fixed bare nucleon is its isotopic spin, or charge variable, on which operate $\tau_\pm\equiv\frac{1}{2}(\tau_1\pm i\tau_2)$. The bare proton and neutron are eigenstates of τ_3 with eigenvalues $+1$ and -1, respectively; τ_+ changes a neutron into a proton. In the sense defined in the Introduction, the total isotopic spin of the system is

$$I=\tfrac{1}{2}\tau_3+Q, \tag{2.4}$$

where

$$Q=-i\int d\mathbf{r}(\varphi\pi-\varphi^*\pi^*) \tag{2.5}$$

is the total charge of the meson field. The operator I commutes with the Hamiltonian H.

If the field $\varphi(\mathbf{r})$ is analyzed into spherical harmonics, one sees that only the $l=0$ part interacts with the nucleon. Hence scattering will occur for S waves only. In order to put the Hamiltonian into a form from which the scattering can be calculated in increasing powers of g^{-1}, a succession of transformations (indicated by boldface capital letters) will be made. (Those used here are similar to but somewhat different from those of Wentzel[3] and Serber and Dancoff.[5])

The first transformations are designed to diagonalize the Hamiltonian in τ space. The term H_I can be put into a readily diagonalizable form by the transformations (**A**) and (**B**):

$$\varphi(\mathbf{r})=\varphi_0NU(r)+\varphi_1(\mathbf{r}),$$

$$\pi(\mathbf{r})=\pi_0NU(r)+\pi_1(\mathbf{r}); \tag{A}$$

where

$$N^2\int d\mathbf{r}U^2(r)=1, \tag{2.6}$$

$$\int d\mathbf{r}U(r)\varphi_1(\mathbf{r})=\int d\mathbf{r}U(r)\pi_1(\mathbf{r})=0, \tag{2.7}$$

$$i[\pi_0,\varphi_0]=i[\pi_0^*,\varphi_0^*]=1, \tag{2.8}$$

$$i[\pi_1(\mathbf{r}),\varphi_1(\mathbf{r}')]=i[\pi_1^*(\mathbf{r}),\varphi_1^*(\mathbf{r}')]$$
$$=\delta(\mathbf{r}-\mathbf{r}')-N^2U(r)U(r'), \tag{2.9}$$

and other pairs commute. Under (**A**) the interaction term becomes

$$H_I=\sqrt{2}gN^{-1}(\tau_+\varphi_0+\tau_-\varphi_0^*). \tag{2.10}$$

Now let us express the operator φ_0 in terms of Hermitian "polar coordinates":

$$\varphi_0=q_0e^{-i\theta}/\sqrt{2}, \quad \varphi_0^*=q_0e^{+i\theta}/\sqrt{2}, \quad q_0\geq 0. \tag{B}$$

Then H_I takes the form

$$H_I=gN^{-1}q_0(\tau_+e^{-i\theta}+\tau_-e^{+i\theta}). \tag{2.11}$$

The unitary transformation

$$S\equiv\exp(i\tau_3\theta/2) \tag{C}$$

transforms H_I to

$$SH_IS^*=gN^{-1}q_0\tau_1, \tag{2.12}$$

which is diagonal with respect to the nucleon variable if we choose a representation in which τ_1 is diagonal. Note that the eigenstates of τ_1 are not proton or neutron but half-proton, half-neutron states.

Transformation (**B**) must be completed, that is, made quasi-canonical. This can be done in such a way as to make H_0 independent of θ, which is very con-

venient.

$$\varphi_1(\mathbf{r})=q_1(\mathbf{r})e^{-i\theta},\quad \varphi_1^*(\mathbf{r})=q_1^*(\mathbf{r})e^{+i\theta},$$
$$\pi_1(\mathbf{r})=p_1(\mathbf{r})e^{+i\theta},\quad \pi_1^*(\mathbf{r})=p_1^*(\mathbf{r})e^{-i\theta},$$
$$\pi_0=e^{+i\theta}[p_0+iq_0^{-1}(p_\theta+\tfrac{1}{2}-Q_1)]/\sqrt{2},$$
$$\pi_0^*=e^{-i\theta}[p_0-iq_0^{-1}(p_\theta-\tfrac{1}{2}-Q_1)]/\sqrt{2}; \qquad \text{(B)}$$

where

$$i[p_0, q_0]=i[p_\theta, \theta]=1; \qquad (2.13)$$

(p_1, q_1), like (π_1, φ_1), satisfy Eqs. (2.7) and (2.9); and

$$Q_1\equiv -i\int d\mathbf{r}(q_1p_1-q_1^*p_1^*). \qquad (2.14)$$

The form of H_0 is simplified by the following recombination:

$$q''(\mathbf{r})=q_1(\mathbf{r})+q_0NU(\mathbf{r})/\sqrt{2},$$
$$p''(\mathbf{r})=p_1(\mathbf{r})+p_0NU(\mathbf{r})/\sqrt{2}. \qquad \text{(B')}$$

After transformations (**A**), (**B**), (**B'**), (**C**), the Hamiltonian becomes

$$SHS^*=\int d\mathbf{r}(p''^*p''+q''^*\omega^2q'')+gN^{-1}q_0\tau_1 +\tfrac{1}{2}q_0^{-2}[(p_\theta-Q_1)^2-\tau_3(p_\theta-Q_1)], \qquad (2.15)$$

where q_0 and $q''(\mathbf{r})$ are related, by (**B'**), as follows:

$$q_0=\sqrt{2}N\int d\mathbf{r}U(\mathbf{r})q''(\mathbf{r})=\sqrt{2}N\int d\mathbf{r}U(\mathbf{r})q''^*(\mathbf{r}). \qquad (2.16)$$

After (**A**) and (**B**), the meson charge Q [Eq. (2.5)] becomes simply p_θ. Thus the transform of the total isotopic spin I [Eq. (2.4)] is

$$IS^*=p_\theta. \qquad (2.17)$$

Since the eigenvalues of $\frac{1}{2}\tau_3$ and Q are, respectively, $\pm\frac{1}{2}$ and all the integers, the operator I (and hence its transform p_θ) has half-odd integral eigenvalues. Note that since p_θ commutes with the Hamiltonian SHS^*, it may be considered as the quantum number denoting total isotopic spin.

The term in τ_3 in SHS^* prevents us from eliminating the nucleon variable entirely, but we shall show later that this term can be neglected if we restrict ourselves to effects of order g^{-2}. We therefore ignore this term temporarily, and fix our attention on the states $\tau_1=-1$, which by (2.15) lie lower than the states $\tau_1=+1$. The expression

$$\int d\mathbf{r}(p''^*p''+q''^*\omega^2q'')-gN^{-1}q_0 \qquad (2.18)$$

can be made wholly bilinear by a translation in $q''(\mathbf{r})$:

$$q''(\mathbf{r})=q'(\mathbf{r})+g\omega^{-2}U(\mathbf{r})/\sqrt{2},$$
$$p''(\mathbf{r})=p'(\mathbf{r}); \qquad \text{(D)}$$

whence (2.18) becomes

$$\int d\mathbf{r}(p'^*p'+q'^*\omega^2q')-\tfrac{1}{2}g^2\int d\mathbf{r}U(\mathbf{r})\omega^{-2}U(\mathbf{r}). \qquad (2.19)$$

The inverse differential operator ω^{-2} is an integral operator on spatial functions:

$$\omega^{-2}f(\mathbf{r})=\int d\mathbf{r}'(4\pi|\mathbf{r}-\mathbf{r}'|)^{-1}e^{-\mu|\mathbf{r}-\mathbf{r}'|}f(\mathbf{r}'). \qquad (2.20)$$

The second integral of (2.19) depends, like N^2 [Eq. (2.6)], on the particular choice of source function $U(\mathbf{r})$. We shall define the source radius[9] explicitly:

$$\hat{a}\equiv N^2\left[\int d\mathbf{r}U(\mathbf{r})\omega^{-2}U(\mathbf{r})\right]^2. \qquad (2.21)$$

It can be shown from Eqs. (2.3), (2.6), (2.21) (for example by choosing a particular $U(\mathbf{r})$) that $\hat{a}$ is of the order of the radial extension of $U(\mathbf{r})$, and that

$$N\sim\hat{a}^{\frac{1}{2}}. \qquad (2.22)$$

The complete Hamiltonian (2.15) is now

$$SHS^*=\int d\mathbf{r}(p'^*p'+q'^*\omega^2q')-\tfrac{1}{2}g^2\hat{a}^{\frac{1}{2}}N^{-1} +g(\bar{q}+g\hat{a}^{\frac{1}{2}}N^{-1})(1+\tau_1)+\tfrac{1}{2}N^{-2}(\bar{q}+g\hat{a}^{\frac{1}{2}}N^{-1})^{-2} \times[(p_\theta-Q_1)^2-\tau_3(p_\theta-Q_1)], \qquad (2.23)$$

where, by (2.16), (**D**), (2.14), (**B'**),

$$\bar{q}\equiv N^{-1}(q_0-g\hat{a}^{\frac{1}{2}})=\sqrt{2}\int d\mathbf{r}Uq'=\sqrt{2}\int d\mathbf{r}Uq'^*, \qquad (2.24)$$

$$Q_1=Q'-g\hat{a}W', \qquad (2.25)$$

$$Q'\equiv -i\int d\mathbf{r}(q'p'-q'^*p'^*), \qquad (2.26)$$

$$W'\equiv\hat{a}^{-1}\int d\mathbf{r}i(p'-p'^*)\omega^{-2}U/\sqrt{2}. \qquad (2.27)$$

We shall now expand the exact Hamiltonian (2.23) in ascending powers of g^{-1}, using Eq. (2.25) for Q_1, and shall keep terms only through g^{-2}:

$$SHS^*=\int d\mathbf{r}(p'^*p'+q'^*\omega^2q')+\tfrac{1}{2}\hat{a}W'^2 +g^{-1}[(p_\theta-Q')W'-\hat{a}^{\frac{1}{2}}N\bar{q}W'^2] +g^{-2}[\tfrac{1}{2}\hat{a}^{-1}(p_\theta-Q')^2-2\hat{a}^{-\frac{1}{2}}N\bar{q}(p_\theta-Q')W' +\tfrac{3}{2}N^2\bar{q}^2W'^2]-\tfrac{1}{2}g^2\hat{a}^{\frac{1}{2}}N^{-1}+g^2\hat{a}^{\frac{1}{2}}N^{-1} \times(1+g^{-1}\hat{a}^{-\frac{1}{2}}N\bar{q})(1+\tau_1)-\tfrac{1}{2}g^{-1}\tau_3\mathfrak{W}, \qquad (2.28)$$

[9] Note that this definition differs from that of Pauli and Dancoff (reference 4); their a is defined as the reciprocal of $\int d\mathbf{r}U\omega^{-2}U$. The two definitions differ only by a constant factor of order one.

where, in the case of noncommuting factors like $Q'W'$, the symmetrized product $[\frac{1}{2}(Q'W'+W'Q')]$ is to be understood. $\mathfrak{W}$ is an expression of order g^0. The last term can be removed to higher order in g^{-1} by a unitary transformation similar to (**C**):

$$S' \equiv \exp[\tfrac{1}{4} i\tau_2 g^{-3}\hat{a}^{-\frac{1}{2}} N\mathfrak{W}(1+g^{-1}\hat{a}^{-\frac{1}{2}}N\dot{q})^{-1}]. \quad \text{(E)}$$

The transform of the Hamiltonian, $S'SHS^*S'^*$, to order g^{-2}, is just SHS^* (2.28) without the last term. To this order the Hamiltonian is now diagonal in τ-space, and we may select the lower states $\tau_1=-1$, which differ in energy from the upper states $\tau_1=+1$, by $\sim g^2\hat{a}^{-1}$; this energy separation becomes infinite in the limit of a point source ($\hat{a}\to 0$). Note that the state function is unaffected to order g^{-2} by S', for $S'-1$ is of the order g^{-3}.

Among the g^{-1} terms in the Hamiltonian, the one in $\dot{p}_\theta$ is linear, whereas the others are trilinear, in the field operators. It is convenient to remove the former term by a translation, as in (**D**); for in the result, terms representing the isobaric levels will manifest themselves.

$$q'(\mathbf{r}) = q(\mathbf{r}),$$
$$p'(\mathbf{r}) = p(\mathbf{r}) - ig^{-1}\mu' p_\theta(\omega^{-2}-\hat{a}^{\frac{1}{2}}N)U(r)/\sqrt{2}, \quad \text{(F)}$$

where

$$\mu' \equiv \left[\int d\mathbf{r} U(r)\omega^{-4}U(r)\right]^{-1}. \quad (2.29)$$

(In the limit $\hat{a}\to 0$, $\mu'\to 8\pi\mu$.) (2.30)

Under (**F**) the Hamiltonian becomes (dropping the constant term), to order g^{-2},

$$\int d\mathbf{r}(p^*\dot{p}+q^*\omega^2\dot{q}) + \tfrac{1}{2}\hat{a}W^2 - g^{-1}(\bar{Q}W+\hat{a}^{\frac{1}{2}}N\dot{q}W^2) + g^{-2}(\tfrac{1}{2}\mu' p_\theta^2 - \mu' p_\theta\bar{Q} + \tfrac{1}{2}\hat{a}^{-1}\bar{Q}^2 - \mu' p_\theta WD + 2\hat{a}^{-\frac{1}{2}}N\dot{q}\bar{Q}W + \tfrac{3}{2}N^2\dot{q}^2W^2 - \hat{a}^{\frac{1}{2}}N\mu' p_\theta\dot{q}W), \quad (2.31)$$

where

$$W \equiv \hat{a}^{-1}\int d\mathbf{r} i(p-p^*)\omega^{-2}U/\sqrt{2}, \quad (2.32)$$

$$D \equiv \int d\mathbf{r}(q+q^*)\omega^{-2}U/\sqrt{2}, \quad (2.33)$$

and

$$\bar{Q} \equiv -i\int d\mathbf{r}(qp-q^*p^*) \quad (2.34)$$

is the charge of the field (q, p). The field is subject, by (2.7), (**B**), (**B'**), (**D**), (2.24), (**F**), to the constraints

$$\sqrt{2}\int d\mathbf{r}U(r)q(\mathbf{r}) = \sqrt{2}\int d\mathbf{r}U(r)q^*(\mathbf{r}) = \bar{q} \geq -g\hat{a}^{\frac{1}{2}}N^{-1},$$

$$\int d\mathbf{r}U(r)p(\mathbf{r}) = \int d\mathbf{r}U(r)p^*(\mathbf{r}); \quad (2.35)$$

and has, by (2.9), (**B**), (**B'**), (2.13), (**D**), (**F**), the commutators

$$i[p(\mathbf{r}), q(\mathbf{r}')] = i[p^*(\mathbf{r}), q^*(\mathbf{r}')] = \delta(\mathbf{r}-\mathbf{r}') - \tfrac{1}{2}N^2U(r)U(r'),$$
$$i[p(\mathbf{r}), q^*(\mathbf{r}')] = i[p^*(\mathbf{r}), q(\mathbf{r}')] = +\tfrac{1}{2}N^2U(r)U(r'). \quad (2.36)$$

3. THE NORMAL MODES

A conceivable method of handling the Hamiltonian (2.31) is to diagonalize the zero-order terms (g^0), and then to utilize perturbation theory for the effects of the higher-order terms (g^{-1}, g^{-2}). Such a procedure breaks down in that the term $\sim g^{-2}\bar{Q}$ has infinite matrix elements between equal-energy eigenstates (normal modes) of the zero-order Hamiltonian, making perturbation theory inapplicable. Fortunately, the bilinearity of this term makes it possible to include it with the zero-order terms to be diagonalized exactly, and thus the use of perturbation theory for this term can be avoided.

The Hamiltonian we wish to diagonalize exactly is then

$$H^0 \equiv \int d\mathbf{r}(p^*\dot{p}+q^*\omega^2\dot{q}) + \tfrac{1}{2}\hat{a}W^2 - g^{-2}\mu' p_\theta\bar{Q}, \quad (3.1)$$

subject to Eqs. (2.35), (2.36). This diagonalization can be accomplished by a transformation of the form

$$q(\mathbf{r}) = \int d\mathbf{k}[\mathfrak{U}_\mathbf{k}^{++}(\mathbf{r})A_\mathbf{k} + \mathfrak{U}_\mathbf{k}^{+-*}A_\mathbf{k}^* + \mathfrak{U}_\mathbf{k}^{-+}B_\mathbf{k} + \mathfrak{U}_\mathbf{k}^{--*}B_\mathbf{k}^*],$$
$$p(\mathbf{r}) = \int d\mathbf{k}[\mathfrak{V}_\mathbf{k}^{+-}(\mathbf{r})A_\mathbf{k} + \mathfrak{V}_\mathbf{k}^{++*}A_\mathbf{k}^* + \mathfrak{V}_\mathbf{k}^{--}B_\mathbf{k} + \mathfrak{V}_\mathbf{k}^{-+*}B_\mathbf{k}^*]; \quad \text{(G)}$$

where

$$[A_\mathbf{k}, A_{\mathbf{k}'}^*] = [B_\mathbf{k}, B_{\mathbf{k}'}^*] = \delta(\mathbf{k}-\mathbf{k}'), \quad (3.2)$$

other pairs commuting. The Hamiltonian is to take the form

$$H^0 = \int d\mathbf{k}\tfrac{1}{2}[E_k^+(A_\mathbf{k}^*A_\mathbf{k} + A_\mathbf{k}A_\mathbf{k}^*) + E_k^-(B_\mathbf{k}^*B_\mathbf{k} + B_\mathbf{k}B_\mathbf{k}^*)]. \quad (3.3)$$

We shall show that $A_\mathbf{k}$ and $B_\mathbf{k}$ are absorption operators for one-meson eigenstates representing the (elastic ordinary and inelastic charge-exchange) scattering of a meson of momentum $\mathbf{k}$ and of positive or negative charge, respectively. The spatial functions $\mathfrak{U}$, $\mathfrak{V}$ are, in a certain sense, the wave functions of these states; the first superscript refers to the charge of the incident meson of the state, the second to that of the component described. The constants $E_k^\pm$ are the eigenvalues of H^0 for these eigenstates.

In the normal mode representation, the equations of motion are,[10] by (3.2), (3.3),

$$\dot{A}_{\mathbf{k}}=-iE_k{}^{+}A_{\mathbf{k}}, \quad \dot{A}_{\mathbf{k}}{}^{*}=+iE_k{}^{+}A_{\mathbf{k}}{}^{*},$$
$$\dot{B}_{\mathbf{k}}=-iE_k{}^{-}B_{\mathbf{k}}, \quad \dot{B}_{\mathbf{k}}{}^{*}=+iE_k{}^{-}B_{\mathbf{k}}{}^{*}. \tag{3.4}$$

Similarly, the equations of motion for (p, q) can be found from (3.1) and (2.36). The substitution of (**G**), (3.4) into these equations leads to sets of differential equations for $\mathfrak{U}, \mathfrak{V}$ which are quite complicated because of the anomalous commutator (2.36) and the term $\sim\bar{Q}$ in (3.1). Nevertheless, these differential equations can be solved exactly after a great deal of algebra (if one disregards the inequality of (2.35), which will be shown [Eq. (3.44)] to be unimportant if g is large). The result is sufficiently complicated to be rather meaningless on inspection. Fortunately, it will be sufficient for our purpose to know the solution in two limits: (**1**) $\hat{a}\to 0$, $r\to\infty$; (**2**) $g\to\infty$. Hence the exact solution will not be presented here.

Certain of the results obtained for the two limiting cases are valid in general. These are the eigenvalues $E_k{}^{\pm}$ and the physical interpretation of the functions $\mathfrak{U}, \mathfrak{V}$. For the sake of simplicity and clarity these are discussed only for the limiting cases, but their general validity can be inferred. We shall denote by the subscript 0, A, 1 or 2 attached to the number of an equation whether the equation is valid in general (or at least to order g^{-2}), in general asymptotically, or for one of the two limiting cases.

The parts of the Hamiltonian not included in H^0 give rise to energy and scattering effects of order g^{-2}, for the g^{-1} terms, being trilinear, contribute only in second order. Since we shall calculate these effects only to order g^{-2}, transformation (**G**) need be correct only to order g^0 when substituted into those terms. We must keep $\hat{a}$ finite here, for many of the terms are separately divergent in the limit $\hat{a}\to 0$, and we must carry through the whole calculation before letting $\hat{a}\to 0$. In this connection we shall use the limiting case (**2**).

In deducing the scattering amplitudes of the normal modes, transformation (**G**) must be valid to order g^{-2}. Then we shall be interested in the asymptotic region $r\to\infty$ and in the limit $\hat{a}\to 0$, and so shall need limiting case (**1**). It turns out that if we replace the anomalous commutators (2.36) by the normal commutators

$$i[p(\mathbf{r}), q(\mathbf{r}')]=i[p^{*}(\mathbf{r}), q^{*}(\mathbf{r}')]=\delta(\mathbf{r}-\mathbf{r}'), \tag{3.5}$$

and drop the auxiliary conditions (2.35), the resultant normal modes $\mathfrak{U}, \mathfrak{V}$ in the limit $\hat{a}\to 0$, $r\to\infty$, are the same as the exact modes in that limit. (That this is so may be suspected intuitively and can be checked by direct calculation.) Hence, for simplicity, we shall solve the problem in that way here.

[10] $\dot{O}=i[H^0, O]$.

The equations of motion for (p, q) are, by (3.1), (3.5),

$$\dot{q}(\mathbf{r})-ig^{-2}\mu' p_\theta q(\mathbf{r}) = p^{*}(\mathbf{r})-\tfrac{1}{2}\hat{a}^{-1}\omega^{-2}U(r)\int d\mathbf{r}'(p-p^{*})\omega^{-2}U,$$
$$\dot{p}^{*}(\mathbf{r})-ig^{-2}\mu' p_\theta p(\mathbf{r})=-\omega^2 q(\mathbf{r}), \tag{3.6}$$

and the Hermitian conjugate equations. Substituting (**G**) into (3.6), and using (3.4), yields the equations for the normal modes. From the coefficient of $A_{\mathbf{k}}$, we obtain

$$\begin{cases} -i\omega_{++}\mathfrak{U}_{\mathbf{k}}{}^{++}(\mathbf{r})=\mathfrak{V}_{\mathbf{k}}{}^{++}(\mathbf{r}) \\ \qquad -\tfrac{1}{2}\hat{a}^{-1}\omega^{-2}U(r)\int d\mathbf{r}'(\mathfrak{V}_{\mathbf{k}}{}^{+-}-\mathfrak{V}_{\mathbf{k}}{}^{++})\omega^{-2}U, \\ -i\omega_{++}\mathfrak{V}_{\mathbf{k}}{}^{++}(\mathbf{r})=-\omega^2\mathfrak{U}_{\mathbf{k}}{}^{++}(\mathbf{r}), \end{cases} \tag{3.7}$$

where

$$\omega_{+\pm}\equiv E_k{}^{+}\pm g^{-2}\mu' p_\theta; \tag{3.8}$$

and from the coefficients of $A_{\mathbf{k}}{}^{*}$, $B_{\mathbf{k}}$, and $B_{\mathbf{k}}{}^{*}$, similar sets. By eliminating $\mathfrak{V}_{\mathbf{k}}{}^{+\pm}$ from the first two sets, we find for $\mathfrak{U}_{\mathbf{k}}{}^{+\pm}$:

$$\mp\omega_{+\mp}(\omega^2-\omega_{+\pm}{}^2)\mathfrak{U}_{\mathbf{k}}{}^{+\pm}(\mathbf{r})=\tfrac{1}{2}\hat{a}^{-1}\omega^{-2}U(r)M, \tag{3.9}$$

where

$$M\equiv\int d\mathbf{r}[\omega_{+-}\mathfrak{U}_{\mathbf{k}}{}^{++}(\mathbf{r})-\omega_{++}\mathfrak{U}_{\mathbf{k}}{}^{+-}(\mathbf{r})]U(r). \tag{3.10}$$

Boundary conditions are now chosen in accordance with the desired physical interpretation, and incorporated into the equivalent integral equations:[11]

$$\begin{cases} \mathfrak{U}_{\mathbf{k}}{}^{++}(\mathbf{r})=(2\pi)^{-\frac{3}{2}}(2\omega_{++})^{-\frac{1}{2}}e^{i\mathbf{k}\cdot\mathbf{r}} \\ \qquad -\tfrac{1}{2}(\hat{a}\omega_{+-})^{-1}(\omega^2-\omega_{++}{}^2-i\epsilon)^{-1}\omega^{-2}U(r)M, \\ \mathfrak{U}_{\mathbf{k}}{}^{+-}(\mathbf{r})=+\tfrac{1}{2}(\hat{a}\omega_{++})^{-1}(\omega^2-\omega_{+-}{}^2-i\epsilon)^{-1} \\ \qquad\qquad \times\omega^{-2}U(r)M. \end{cases} \tag{3.11}$$

The plane wave is a solution of the homogeneous equation

$$(\omega^2-\omega_{++}{}^2)e^{i\mathbf{k}\cdot\mathbf{r}}=0$$

if we set

$$\omega_{++}=\omega_k\equiv(\mu^2+k^2)^{\frac{1}{2}}. \tag{3.12}$$

It follows from (3.8) that

$$E_k{}^{+}=\omega_k-g^{-2}\mu' p_\theta,$$
$$\omega_{+-}=\omega_k-2g^{-2}\mu' p_\theta. \tag{3.13}$$

The normalization of the plane wave is so chosen that the normal modes will be properly normalized. The inverse differential operator $(\omega^2-\omega_k{}^2-i\epsilon)^{-1}$ is, like ω^{-2}

[11] The question of bound state solutions is discussed in connection with case (**2**).

[Eq. (2.20)], an integral operator on space functions:

$$(\omega^2-\omega_k^2-i\epsilon)^{-1}f(\mathbf{r})$$

$$=\int d\mathbf{r}'(4\pi|\mathbf{r}-\mathbf{r}'|)^{-1}e^{ik|\mathbf{r}-\mathbf{r}'|}f(\mathbf{r}'). \quad (3.14)$$

The operator $(\omega^2-\omega_{+-}^2-i\epsilon)^{-1}$ is similar, with k replaced by $k_-\equiv(\omega_{+-}^2-\mu^2)^{\frac{1}{2}}$. The $-i\epsilon$ selects outgoing waves; hence the asymptotic behavior of Eq. (3.11) is plane wave+outgoing spherical waves.

Equation (3.11), with (3.10), is easily solved for the normal modes. These are, asymptotically and in the limit $\hat{a}\to 0$,

$$\mathfrak{U}_{\mathbf{k}}{}^{+\pm}(\mathbf{r})=(2\pi)^{-\frac{1}{2}}(2\omega_{+\pm})^{-\frac{1}{2}}\phi_{\mathbf{k}}{}^{+\pm}(\mathbf{r}), \quad (3.15)_A$$

with $\phi_{\mathbf{k}}$ given in Eq. (3.17) below. From Eq. (3.7), we find, in the same limit,

$$\mathfrak{V}_{\mathbf{k}}{}^{+\pm}(\mathbf{r})=-i\omega_{+\pm}\mathfrak{U}_{\mathbf{k}}{}^{+\pm}(\mathbf{r}). \quad (3.16)_A$$

The other ($B_{\mathbf{k}}$) type of mode is found in a similar way. The relevant equations can be obtained from those above by replacing the first super- (or sub-) script + by − in Eqs. (3.7–10) and (3.15–16), and by assigning the plane wave $e^{i\mathbf{k}\cdot\mathbf{r}}$ to $\mathfrak{U}_{\mathbf{k}}{}^{--}$, with $\omega_{--}=\omega_k$.

The ordinary scattering is then given by ϕ^{++} and ϕ^{--} for positive and negative incident mesons respectively, and the corresponding charge-exchange scattering by ϕ^{+-} and ϕ^{-+}:

$$\phi_{\mathbf{k}}{}^{\pm\pm}(\mathbf{r})=e^{i\mathbf{k}\cdot\mathbf{r}}-(8\pi\omega_k{}^{\frac{1}{2}}J^{\pm})^{-1}e^{ikr}/r,$$

$$\phi_{\mathbf{k}}{}^{\pm\mp}(\mathbf{r})=+(8\pi\omega_k{}^{\frac{1}{2}}\omega_{\mp}{}^{\frac{1}{2}}J^{\pm})^{-1}\exp(ik_{\mp}r)/r, \quad (3.17)_1$$

where

$$\omega_{\pm}=\omega_k\pm 16\pi g^{-2}\mu p_0, \quad (3.18)_1$$

$$8\pi J^{\pm}=(\mu-ik)^{-1}+(\mu-ik_{\mp})^{-1}, \quad (3.19)_1$$

$$k_{\pm}\equiv(\omega_{\pm}{}^2-\mu^2)^{\frac{1}{2}}. \quad (3.20)$$

The physical interpretation is obtained from the expectation values of the momentum density and charge density operators:[12]

$$\mathbf{G}(\mathbf{r})=-[\pi(\mathbf{r})\nabla\varphi(\mathbf{r})+\nabla\varphi^*(\mathbf{r})\pi^*(\mathbf{r})],$$

$$\rho(\mathbf{r})=-i[\varphi(\mathbf{r})\pi(\mathbf{r})-\varphi^*(\mathbf{r})\pi^*(\mathbf{r})].$$

We shall be interested in the expectation values in the asymptotic region only; for this region the transformations (**A**), (**B**), (**B′**), (**D**), (**F**) lead to

$$\mathbf{G}(\mathbf{r})\to\mathbf{G}_A(\mathbf{r})\equiv-(p\nabla q+\nabla q^*p^*),$$

$$\rho(\mathbf{r})\to\rho_A(\mathbf{r})\equiv-i(qp-q^*p^*); \quad (3.21)_A$$

transformation S (**C**) commutes with these operators.

Let the normalized vacuum state Ψ_0 be defined:

$$A_{\mathbf{k}}\Psi_0=B_{\mathbf{k}}\Psi_0=0 \text{ for all } \mathbf{k};\ (\Psi_0,\Psi_0)=1. \quad (3.22)_0$$

[12] G. Wentzel, *Quantum Theory of Fields* (Interscience Publishers, New York, 1949), Sec. 8.

The δ-normalized one-meson states $\Psi_{\mathbf{k}}{}^{\pm}$ are defined:

$$\Psi_{\mathbf{k}}{}^{+}\equiv A_{\mathbf{k}}{}^*\Psi_0,\quad \Psi_{\mathbf{k}}{}^{-}\equiv B_{\mathbf{k}}{}^*\Psi_0. \quad (3.23)_0$$

From (3.2) it follows that

$$A_{\mathbf{k}}\Psi_{\mathbf{k}'}{}^{+}=\Psi_0\delta(\mathbf{k}-\mathbf{k}');\ (\Psi_{\mathbf{k}}{}^{+},\Psi_{\mathbf{k}'}{}^{+})=\delta(\mathbf{k}-\mathbf{k}'). \quad (3.24)_0$$

These states are eigenstates of H^0 [Eq. (3.3)]:

$$H^0\Psi_{\mathbf{k}}{}^{\pm}=E_k{}^{\pm}\Psi_{\mathbf{k}}{}^{\pm}, \quad (3.25)_0$$

where, by (3.13) and the discussion above,

$$E_k{}^{\pm}=\omega_k\mp g^{-2}\mu' p_0. \quad (3.26)_0$$

The addition to the kinetic energy is due to the last term of (3.1), and represents the effect of the isobaric energy.

A normalized one-meson state can be formed by a superposition of the δ-normalized states:

$$\Psi_{\mathbf{k}}{}^{+}(t)=\int d\mathbf{k}'c_{\mathbf{k}}(\mathbf{k}')\Psi_{\mathbf{k}'}{}^{+}\exp(-iE_{k'}{}^{+}t), \quad (3.27)_0$$

where

$$\int d\mathbf{k}'|c_{\mathbf{k}}(\mathbf{k}')|^2=1. \quad (3.28)_0$$

The function $c_{\mathbf{k}}(\mathbf{k}')$ is to be strongly peaked about $\mathbf{k}$ with a spread $\Delta\ll k$. The Fourier transform of $c_{\mathbf{k}}(\mathbf{k}')$ is then a wave packet in ordinary space, of spread Δ^{-1}. In the limit $\Delta\to 0$, the wave packet spreads out into a plane wave of wave number $\mathbf{k}$.

For the state (3.27), the expectation values of (3.21) are, by (**G**), (3.15)–(3.16), (3.23)–(3.24),

$$\langle\mathbf{G}_A(\mathbf{r})\rangle_{\mathbf{k}}{}^{+}=\textstyle\sum_{\pm}\mathrm{Re}[\psi_{\mathbf{k}}{}^{+\pm*}(\mathbf{r},t)(-i\nabla)\psi_{\mathbf{k}}{}^{+\pm}(\mathbf{r},t)],$$

$$\langle\rho_A(\mathbf{r})\rangle_{\mathbf{k}}{}^{+}=\textstyle\sum_{\pm}(\pm 1)|\psi_{\mathbf{k}}{}^{+\pm}(\mathbf{r},t)|^2; \quad (3.29)_A$$

where

$$\psi_{\mathbf{k}}{}^{+\pm}(\mathbf{r},t)\equiv(2\pi)^{-\frac{1}{2}}\int d\mathbf{k}'c_{\mathbf{k}}(\mathbf{k}')\phi_{\mathbf{k}'}{}^{+\pm}(\mathbf{r})$$

$$\times\exp(-iE_{k'}{}^{+}t). \quad (3.30)_A$$

Let us first drop the normalization requirement (3.28) and choose $c_{\mathbf{k}}(\mathbf{k}')=(2\pi)^{\frac{1}{2}}\delta(\mathbf{k}'-\mathbf{k})$. Then Eq. (3.30) reduces to

$$\psi_{\mathbf{k}}{}^{+\pm}(\mathbf{r},t)=\phi_{\mathbf{k}}{}^{+\pm}(\mathbf{r})\exp(-iE_k{}^{+}t). \quad (3.31)_A$$

It is then evident from (3.29) and (3.17) that $\phi_{\mathbf{k}}{}^{++}(\mathbf{r})$ and $\phi_{\mathbf{k}}{}^{+-}(\mathbf{r})$ are, respectively, the positive charge and negative charge parts of the wave function of a positive meson which is scattered with and without charge-exchange. (The case of an incident negative meson is completely analogous.) It is readily verified that the wave function (3.17) satisfies the S-matrix unitarity requirement, which relates the total cross section to the imaginary part of the elastic amplitude in the forward direction. If the normalization (3.28) is retained,

the wave function (3.30) will be normalized:

$$\int d\mathbf{r} \sum_{\pm} |\psi_{\mathbf{k}}{}^{+\pm}(\mathbf{r}, t)|^2 = 1. \qquad (3.32)_0$$

It can then be shown that (in the limit $\Delta \to 0$)

$$\int d\mathbf{r} \langle \mathbf{G}_A(\mathbf{r}) \rangle_{\mathbf{k}}{}^{+} = \mathbf{k},$$

$$\int d\mathbf{r} \langle \rho_A(\mathbf{r}) \rangle_{\mathbf{k}}{}^{+} = 1; \qquad (3.33)_0$$

for only the plane wave parts of $\phi_{\mathbf{k}}(\mathbf{r})$ contribute to the integrals (3.33) in that limit. Equation (3.33) confirms that we are indeed dealing with a single (incident) positive meson of momentum $\mathbf{k}$.

The isobaric levels of the compound nucleon, which give rise to the inelasticity of the charge-exchange scattering, will be derived in Sec. 5. Note that if p_θ is positive, and $\omega_k < \mu + 16\pi g^{-2}\mu p_\theta$, k_- will be imaginary (it is to be taken positive imaginary), and only elastic scattering of positive mesons results, for their kinetic energy is below threshold for charge-exchange scattering (similarly for negative mesons and p_θ negative).

We shall now treat the other limiting case, (**2**), retaining Eqs. (2.35)–(2.36). The Hamiltonian (3.1) for $g \to \infty$ is

$$H^{0\prime} \equiv \int d\mathbf{r} (p^* p + q^* \omega^2 q) + \tfrac{1}{2}\hat{a} W^2. \qquad (3.34)_2$$

It is now advantageous to separate the field into real and imaginary parts:

$$q(\mathbf{r}) = [q_r(\mathbf{r}) + i q_i(\mathbf{r})]/\sqrt{2},$$
$$p(\mathbf{r}) = [p_r(\mathbf{r}) - i p_i(\mathbf{r})]/\sqrt{2}; \qquad (\mathbf{H})$$

where (p_r, q_r) and (p_i, q_i) are Hermitian fields, and, by (2.35)–(2.36),

$$\int d\mathbf{r} U(r) q_r(\mathbf{r}) = \bar{q} \geq -g\hat{a}^{\frac{1}{2}} N^{-1}, \qquad (3.35)$$

$$\int d\mathbf{r} U(r) q_i(\mathbf{r}) = \int d\mathbf{r} U(r) p_i(\mathbf{r}) = 0, \qquad (3.36)$$

$$i[p_r(\mathbf{r}), q_r(\mathbf{r}')] = \delta(\mathbf{r} - \mathbf{r}'), \qquad (3.37)$$

$$i[p_i(\mathbf{r}), q_i(\mathbf{r}')] = \delta(\mathbf{r} - \mathbf{r}') - N^2 U(\mathbf{r}) U(\mathbf{r}'). \qquad (3.38)$$

$H^{0\prime}$ then becomes $H_r + H_i$, where

$$H_r = \frac{1}{2}\int d\mathbf{r} (p_r{}^2 + q_r \omega^2 q_r), \qquad (3.39)$$

$$H_i \equiv \frac{1}{2}\int d\mathbf{r} (p_i{}^2 + q_i \omega^2 q_i) + \tfrac{1}{2}\hat{a} W^2, \qquad (3.40)$$

$$W = \hat{a}^{-1} \int d\mathbf{r} p_i(\mathbf{r}) \omega^{-2} U(r). \qquad (3.41)_0$$

If it were not for the condition (3.35), H_r could be immediately diagonalized by

$$\begin{cases} q_r(\mathbf{r}) = \int d\mathbf{k} (u_{\mathbf{k}}'(\mathbf{r}) a_{\mathbf{k}} + \text{c.c.}), \\ p_r(\mathbf{r}) = \int d\mathbf{k} (v_{\mathbf{k}}'(\mathbf{r}) a_{\mathbf{k}} + \text{c.c.}), \end{cases}$$

$$\begin{cases} u_{\mathbf{k}}'(\mathbf{r}) = (2\pi)^{-\frac{3}{2}} (2\omega_k)^{-\frac{1}{2}} e^{i\mathbf{k}\cdot\mathbf{r}}, \\ v_{\mathbf{k}}'(\mathbf{r}) = -i\omega_k u_{\mathbf{k}}'(\mathbf{r}), \end{cases} \qquad (\mathbf{I})$$

where

$$[a_{\mathbf{k}}, a_{\mathbf{k}'}{}^*] = \delta(\mathbf{k} - \mathbf{k}'), \qquad (3.42)$$

and c.c. means Hermitian conjugate. H_r would then become

$$H_r = \int d\mathbf{k} \omega_k \tfrac{1}{2} (a_{\mathbf{k}}{}^* a_{\mathbf{k}} + a_{\mathbf{k}} a_{\mathbf{k}}{}^*). \qquad (3.43)_2$$

However, we show below that condition (3.35) is quite well satisfied by (**I**) if $g \gg 1$. Since this is assumed anyway for the semiconvergence of the perturbation expansion in powers of g^{-1}, we may use the transformation (**I**).

From (3.35), (**I**), we have

$$\bar{q} = (2\pi)^{-\frac{3}{2}} \int d\mathbf{k} (2\omega_k)^{-\frac{1}{2}} U_k (a_{\mathbf{k}} + a_{\mathbf{k}}{}^*), \qquad (3.44)_2$$

where

$$U_k \equiv \int d\mathbf{r} U(r) e^{i\mathbf{k}\cdot\mathbf{r}} \qquad (3.45)$$

is the Fourier transform of $U(r)$, and, by Eq. (2.3), equals one for $k \ll \hat{a}^{-1}$. For the vacuum state, or any state with a finite number of mesons, it follows that

$$\langle \bar{q}^2 \rangle = (2\pi)^{-3} \int d\mathbf{k} (2\omega_k)^{-1} U_k{}^2 \sim \hat{a}^{-2},$$

while Eq. (3.35) demands

$$\langle \bar{q}^2 \rangle \ll g^2 \hat{a} N^{-2} \sim g^2 \hat{a}^{-2}.$$

Thus, $g^2 \gg 1$ insures that (3.35) is satisfied. The error introduced may be estimated to be of order e^{-g^2}, by analogy to the problem of the bounded harmonic oscillator,[13] and thus less than the effects (g^{-2}) calculated in Secs. 5 and 6 by perturbation theory.

The diagonalization of H_i [Eq. (3.40)], using the anomalous commutator (3.38), proceeds in much the same way as that of H^0 [Eq. (3.1)] in case (**1**), with a few modifications. Because the fields are Hermitian, the

[13] N. F. Mott and I. N. Sneddon, *Wave Mechanics and Its Applications* (Clarendon Press, Oxford, 1948), Sec. 11.2.

canonical transformation is of the form

$$\begin{cases} q_i(\mathbf{r})=\int d\mathbf{k}(u_\mathbf{k}(\mathbf{r})b_\mathbf{k}+\text{c.c.}), \\ p_i(\mathbf{r})=\int d\mathbf{k}(v_\mathbf{k}(\mathbf{r})b_\mathbf{k}+\text{c.c}); \end{cases} \quad (\mathbf{J})$$

where

$$[b_\mathbf{k}, b_{\mathbf{k}'}{}^*]=\delta(\mathbf{k}-\mathbf{k}'), \quad (3.46)$$

resulting in

$$H_i=\int d\mathbf{k}\omega_k\tfrac{1}{2}(b_\mathbf{k}{}^*b_\mathbf{k}+b_\mathbf{k}b_\mathbf{k}{}^*). \quad (3.47)_2$$

Because of Eq. (3.36), we must impose the conditions

$$\int d\mathbf{r}u_\mathbf{k}(\mathbf{r})U(r)=\int d\mathbf{r}v_\mathbf{k}(\mathbf{r})U(r)=0. \quad (3.48)$$

The anomalous commutator (3.38) affects the derivation of the equations of motion, and we find, in analogy to Eq. (3.7),

$$\begin{cases} -i\omega_k u_\mathbf{k}(\mathbf{r})=v_\mathbf{k}(\mathbf{r}) \\ \qquad\qquad +\hat{a}^{-1}(\omega^{-2}-\hat{a}^{\frac{1}{2}}N)U(r)\int d\mathbf{r}'v_\mathbf{k}\omega^{-2}U, \\ -i\omega_k v_\mathbf{k}(\mathbf{r})=-\omega^2 u_\mathbf{k}(\mathbf{r})+N^2U(r)\int d\mathbf{r}'u_\mathbf{k}\omega^2U. \end{cases} \quad (3.49)_2$$

It is easily verified that these equations themselves insure that Eq. (3.48) is satisfied, except for the case $\omega_k=0$. For that case (3.49) has the solution

$$u(\mathbf{r})\sim\omega^{-2}U(r), \quad v(\mathbf{r})=0.$$

This bound state must be ruled out because of Eq. (3.48).

The solution of Eq. (3.49) is

$$\begin{cases} u_\mathbf{k}(\mathbf{r})=(2\pi)^{-\frac{3}{2}}(2\omega_k)^{-\frac{1}{2}}\{e^{i\mathbf{k}\cdot\mathbf{r}} \\ \qquad -(\omega^2-\omega_k{}^2-i\epsilon)^{-1}\omega^{-2}U(r)U_k/J_k\}, \\ v_\mathbf{k}(\mathbf{r})=-i\omega_k(2\pi)^{-\frac{3}{2}}(2\omega_k)^{-\frac{1}{2}}\{e^{i\mathbf{k}\cdot\mathbf{r}} \\ \quad -[(\omega^2-\omega_k{}^2-i\epsilon)^{-1}-\hat{a}^{\frac{1}{2}}N]U(r)U_k/\omega_k{}^2J_k\}, \end{cases} \quad (3.50)_2$$

where

$$J_k\equiv\int d\mathbf{r}U(r)(\omega^2-\omega_k{}^2-i\epsilon)^{-1}\omega^{-2}U(r)$$
$$=(2\pi)^{-3}\int d\,\mathbf{p}U_p{}^2(p^2-k^2-i\epsilon)^{-1}(p^2+\mu^2)^{-1}. \quad (3.51)$$

Asymptotically, the expression in brackets is, for both $u_\mathbf{k}$ and $v_\mathbf{k}$,

$$e^{i\mathbf{k}\cdot\mathbf{r}}+f_k e^{ikr}/r, \quad (3.52)_{2A}$$

where

$$f_\mathbf{k}=-U_k{}^2/4\pi\omega_k{}^2J_\mathbf{k}. \quad (3.53)_2$$

In the limit $\hat{a}\to 0$, we have

$$U_k\to 1, \quad J_k\to[4\pi(\mu-ik)]^{-1}, \quad (3.54)_1$$

$$f_k\to-(\mu+ik)^{-1}, \quad (3.55)_{1,2}$$

$$e^{2i\delta_k}\equiv 1+2ikf_k=J_k{}^*/J_k$$
$$\to(\mu-ik)/(\mu+ik). \quad (3.56)_{1,2}$$

The transformations (**H**), (**I**), (**J**), with Eq. (3.50), form the solution of the problem of the diagonalization of H^0 [Eq. (3.1)] in the limit $g\to\infty$. They are related to (**G**) *in this limit* as follows:

$$\begin{cases} A_\mathbf{k}=(a_\mathbf{k}+ib_\mathbf{k})/\sqrt{2}, \\ B_\mathbf{k}=(a_\mathbf{k}-ib_\mathbf{k})/\sqrt{2}; \end{cases} \quad \begin{cases} a_\mathbf{k}=(A_\mathbf{k}+B_\mathbf{k})/\sqrt{2}, \\ b_\mathbf{k}=(A_\mathbf{k}-B_\mathbf{k})/\sqrt{2}i; \end{cases} \quad (3.57)_2$$

$$\begin{cases} \mathfrak{U}_\mathbf{k}{}^{++}=\mathfrak{U}_\mathbf{k}{}^{--}=\tfrac{1}{2}(u_\mathbf{k}'+u_\mathbf{k}), \\ \mathfrak{U}_\mathbf{k}{}^{+-}=\mathfrak{U}_\mathbf{k}{}^{-+}=\tfrac{1}{2}(u_\mathbf{k}'-u_\mathbf{k}); \end{cases} \quad (3.58)_2$$

and the same with $\mathfrak{U}_\mathbf{k}$, $u_\mathbf{k}'$, $u_\mathbf{k}\to\mathfrak{V}_\mathbf{k}$, $v_\mathbf{k}'$, $v_\mathbf{k}$. We recall that the functions $\phi_\mathbf{k}$ of Eq. (3.17), with Eqs. (3.15–16), etc., represented the functions $\mathfrak{U}_\mathbf{k}$, $\mathfrak{V}_\mathbf{k}$ in the limit $r\to\infty$, $\hat{a}\to 0$. It is easily seen that the two sets of limiting expressions agree in the common limit $r\to\infty$, $\hat{a}\to 0$, $g\to\infty$.

4. THE HAMILTONIAN IN TERMS OF THE NORMAL MODES

The total Hamiltonian (2.31) will now be expressed in terms of the normal mode operators $A_\mathbf{k}$, $B_\mathbf{k}$ of transformation (**G**). The terms comprising H^0 [Eq. (3.1)] are diagonalized by (**G**) to (3.3), which, by (3.26), is

$$H^0=E_\text{II}-g^{-2}\mu' p_\theta Q_\text{II}+\text{constant}, \quad (4.1)_0$$

where

$$E_\text{II}\equiv\int d\mathbf{k}\omega_k(A_\mathbf{k}{}^*A_\mathbf{k}+B_\mathbf{k}{}^*B_\mathbf{k}), \quad (4.2)_0$$

$$Q_\text{II}\equiv\int d\mathbf{k}(A_\mathbf{k}{}^*A_\mathbf{k}-B_\mathbf{k}{}^*B_\mathbf{k}). \quad (4.3)_0$$

E_II is the kinetic energy of the plane wave parts of the normal modes, and Q_II is their charge. The constant is an infinite zero-point energy, independent of p_θ, and can be dropped.

For the rest of the Hamiltonian (2.31), we may use (**H**), (**I**), (**J**) of case (**2**). By (3.41), (**J**), (3.50), we have

$$W=\int d\mathbf{k}(w_k b_\mathbf{k}+\text{c.c.}), \quad (4.4)_2$$

where

$$w_k\equiv\hat{a}^{-1}\int d\mathbf{r}v_\mathbf{k}(\mathbf{r})\omega^{-2}U(r)$$
$$=-i\omega_k(2\pi)^{-\frac{3}{2}}(2\omega_k)^{-\frac{1}{2}}U_k/\omega_k{}^2J_k. \quad (4.5)_2$$

By (3.44), we have

$$\bar{q}=\int d\mathbf{k}x_k(a_\mathbf{k}+a_\mathbf{k}{}^*), \quad (4.6)_2$$

where

$$x_k \equiv (2\pi)^{-\frac{1}{2}}(2\omega_k)^{-\frac{1}{2}}U_k; \quad w_k = -ix_k/\omega_k J_k. \quad (4.7)_2$$

By (2.33), (**H**), (**I**), we have

$$D = \int d\mathbf{k} x_k \omega_k^{-2}(a_k + a_k^*). \quad (4.8)_2$$

The relations (3.57), which are valid only to order g^0, imply that

$$Q_\Pi = i\int d\mathbf{k}(a_k^* b_k - b_k^* a_k) \quad (4.9)_2$$

to that order. Then by (2.34), (**H**), (**I**), (**J**), (3.50), (4.6), and some integration, we find that

$$\bar{Q} = Q_\Pi + L - \hat{a}^{\frac{1}{2}} N \bar{q} W, \quad (4.10)_2$$

where

$$L \equiv \int d\mathbf{k}\int d\mathbf{k}'[a_k b_{k'}\xi_+(k,k') + \text{c.c.} + a_k^* b_{k'}\xi_-(k,k') + \text{c.c.}], \quad (4.11)$$

$$\xi_\pm(k,k') = x_k \omega_k^{-1} w_{k'}(\omega_k \pm \omega_{k'} - i\epsilon)^{-1}, \quad (4.12)$$

the $-i\epsilon$ referring to the pole in ξ_-. In Eq. (4.10) the charge is decomposed into the charge of the plane wave parts of the normal modes, Q_Π, and that of the scattered waves, L. (The third term vanishes in the limit $\hat{a}\to 0$.) It is seen that the charge is not diagonal in the normal mode representation. Note that the matrix elements ξ_- of L are singular for $k = k'$; this is a reflection of the inelasticity of the charge-exchange scattering. It is this fact which prevents the use of perturbation theory in calculating the scattering due to the term $\sim g^{-2}\bar{Q}$ in (2.31) and which necessitates its incorporation into (3.1).

With (4.1), (4.10), and some algebra, the total Hamiltonian (2.31), valid to order g^{-2}, becomes

$$E_\Pi - g^{-1}(Q_\Pi + L)W + g^{-2}[\tfrac{1}{2}\mu'(p_\theta - Q_\Pi)^2 + \tfrac{1}{2}Q_\Pi^2(\hat{a}^{-1} - \mu') + \hat{a}^{-1}(Q_\Pi L + \tfrac{1}{2}L^2) - \mu' p_\theta W D + \cdots], \quad (4.13)$$

where $\cdots$ stands for several terms whose matrix elements vanish in the limit $\hat{a}\to 0$. We may drop those terms, for the scattering amplitudes will be evaluated in this limit.

5. THE ISOBARIC LEVELS

The energy levels of the compound nucleon are found by calculating the perturbation of the energy of a normalized eigenstate, Ψ', of E_Π and Q_Π [Eqs. (4.1)–(4.3)]; Ψ' is to represent a finite number of mesons of given total energy E_Π' and total charge Q_Π'. An example of such an eigenstate is $\Psi'_k{}^+$ of Eq. (3.27) (in the limit $\Delta\to 0$); it represents *one* positive meson (with its scattered waves). The state of the system is further specified by the quantum number p_θ, the total isotopic spin.

The perturbation of the energy, to order g^{-2}, is obtained from the expectation value of the g^{-2} terms in (4.13) and from the second-order contribution of the g^{-1} terms, there being no first-order effects from the latter. The former is

$$g^{-2}[\tfrac{1}{2}\mu'(p_\theta - Q_\Pi')^2 + \tfrac{1}{2}Q_\Pi'^2(\hat{a}^{-1} - \mu')], \quad (5.1)_0$$

for the other terms have zero expectation value. Of the g^{-1} terms, LW contributes the same value for all states; such an additive constant can be neglected. The other term, $-g^{-1}\frac{1}{2}(Q_\Pi W + WQ_\Pi)$, contributes [see Eq. (4.4)]

$$g^{-2}\int d\mathbf{k}\,|(\Psi_k', \tfrac{1}{2}(Q_\Pi W + WQ_\Pi)\Psi')|^2/[E_\Pi' - (E_\Pi' + \omega_k)], \quad (5.2)_0$$

where $\Psi_k' \equiv b_k^*\Psi'$. By (4.4) and (4.9), this equals

$$-g^{-2}Q_\Pi'^2\int d\mathbf{k}\,|w_k|^2\omega_k^{-1}. \quad (5.3)_0$$

In the Appendix it is proved that

$$2\int d\mathbf{k}\,|w_k|^2\omega_k^{-1} = \hat{a}^{-1} - \mu'. \quad (5.4)_0$$

Thus (5.3) just cancels the second term of (5.1), and the perturbation of the energy is

$$\tfrac{1}{2}g^{-2}\mu'(p_\theta - Q_\Pi')^2, \quad (5.5)_0$$

where $(p_\theta - Q_\Pi')$ is the isotopic spin of the compound nucleon, denoted by I_N in the Introduction. For $\hat{a}\to 0$, by Eq. (2.30), this isobaric energy of the nucleon equals

$$4\pi g^{-2}\mu(p_\theta - Q_\Pi')^2. \quad (5.6)_1$$

6. THE SCATTERING AMPLITUDES

Before applying perturbation theory to the Hamiltonian (4.13) for the calculation of the scattering amplitudes, it is convenient to S order the g^{-1} terms. The notation $:\mathcal{O}:$ will be used to indicate that in $\mathcal{O}$ the order of the operators is to be rearranged so that all absorption operators stand on the right. Then, by (4.9), (4.11), (4.4), we obtain

$$(Q_\Pi + L)W = :(Q_\Pi + L)W: + \frac{1}{2}\int d\mathbf{k} y_k(a_k + a_k^*),$$

where y_k is a real function of k.

The term in y_k is linear in the operators and can therefore be removed by a translation, as has been done twice before:

$$a_k \to a_k + \tfrac{1}{2}g^{-1}y_k/\omega_k. \quad (6.1)$$

Then, referring to (4.2), (4.9), (4.11), (3.57), we find

$$E_\Pi - \tfrac{1}{2}g^{-1}\int d\mathbf{k} y_k(a_k + a_k^*) \to E_\Pi + \text{constant}, \quad (6.2)$$

$$Q_\Pi + L \to Q_\Pi + L + \tfrac{1}{2}g^{-1}\int d\mathbf{k}(z_k b_k + \text{c.c.}), \quad (6.3)$$

where z_k is defined by (6.3), (6.1). With these substitutions, the Hamiltonian (4.13) becomes, valid to order g^{-2},

$$E_\Pi+g^{-2}[\tfrac{1}{2}\mu'(p_\theta-Q_\Pi)^2+\tfrac{1}{2}Q_\Pi{}^2(\hat{a}^{-1}-\mu')] +g^{-1}H_1+g^{-2}H_2, \quad (6.4)$$

where

$$H_1\equiv -:(Q_\Pi+L)W:, \quad (6.5)$$

$$H_2\equiv\hat{a}^{-1}(Q_\Pi L+\tfrac{1}{2}L^2)-\mu' p_\theta WD -\tfrac{1}{2}:W\int d\mathbf{k}(z_k b_\mathbf{k}+\text{c.c.}):. \quad (6.6)$$

In (6.4) the bracketed terms are diagonal in the $A_\mathbf{k}$, $B_\mathbf{k}$ representation, which we shall use, and thus do not contribute to the scattering; H_1 contributes in second order, and H_2 in first order, producing effects of order g^{-2}. To derive the necessary formulas, we shall first disregard H_1 and consider only H_2.

The effective time development of a state, such as (3.27), is then

$$id\Psi(t)/dt=(E_\Pi-g^{-2}\mu' p_\theta Q_\Pi+g^{-2}H_2)\Psi(t). \quad (6.7)$$

Inasmuch as we are to calculate the scattering only to order g^{-2}, we need keep in H_2 only those terms which produce scattering to first order, of the type $a_\mathbf{k}{}^*a_{\mathbf{k}'}$, and drop such terms as $a_\mathbf{k}a_{\mathbf{k}'}$. Thus $\Psi(t)$ can remain a superposition of one-meson states. The term in Q_Π must be included, since Q_Π can change sign in a transition between normal modes; the other diagonal terms, in $p_\theta{}^2$ and $Q_\Pi{}^2$, need not, for they contribute just additive constants to the energy.

We generalize (3.27) to the form

$$\Psi_\mathbf{k}{}^+(t)=\int d\mathbf{k}'\sum_\pm\alpha_\mathbf{k}{}^\pm(\mathbf{k}',t)\Psi_{\mathbf{k}'}{}^\pm\exp(-iE_{k'}{}^\pm t), \quad (6.8)$$

where $\alpha_\mathbf{k}{}^-(\mathbf{k}',t_0)=0$, and $\alpha_\mathbf{k}{}^+(\mathbf{k}',t_0)$ can be taken to be $(2\pi)^{\frac{1}{2}}\delta(\mathbf{k}'-\mathbf{k})$ if we drop the normalization requirement on $\Psi(t)$. Thus $\Psi_\mathbf{k}{}^+(t_0)$ is an eigenstate of H^0 representing a normal mode with the incident meson positive and of momentum $\mathbf{k}$. The perturbation H_2 induces transitions to other normal modes. As from Eq. (3.29), from (3.21) and (6.8) we deduce the equivalent wave function, analogous to (3.30):[14]

$$\psi_\mathbf{k}{}^{+\pm}(\mathbf{r},t) =(2\pi)^{-\frac{1}{2}}\int d\mathbf{k}'[\alpha_\mathbf{k}{}^+(\mathbf{k}',t)\phi_{\mathbf{k}'}{}^{+\pm}(\mathbf{r})\exp(-iE_{k'}{}^+t) +\alpha_\mathbf{k}{}^-(\mathbf{k}',t)\phi_{\mathbf{k}'}{}^{-\pm}(\mathbf{r})\exp(-iE_{k'}{}^-t)], \quad (6.9)_A$$

where the $\phi_{\mathbf{k}'}$ are given in Eq. (3.17). We substitute (6.8) into (6.7) and find, by conventional first-order perturbation theory,

$$\alpha_\mathbf{k}{}^\pm(\mathbf{k}',t)=(2\pi)^{\frac{1}{2}}\delta(\mathbf{k}'-\mathbf{k})(\tfrac{1}{2}\pm\tfrac{1}{2}) +g^{-2}(2\pi)^{\frac{1}{2}}(\Psi_{\mathbf{k}'}{}^\pm, H_2\Psi_\mathbf{k}{}^+)[\exp(-i\Omega^\pm t) -\exp(-i\Omega^\pm t_0)]/\Omega^\pm, \quad (6.10)$$

where $\Omega^\pm\equiv E_k{}^+-E_{k'}{}^\pm$. Inserting (6.10) into (6.9), we obtain

$$\psi_\mathbf{k}{}^{+\pm}(\mathbf{r},t)=\exp(-iE_k{}^+t)\Big\{\phi_\mathbf{k}{}^{+\pm}(\mathbf{r}) +g^{-2}\int d\mathbf{k}'\{\phi_{\mathbf{k}'}{}^{+\pm}(\mathbf{r})(\Psi_{\mathbf{k}'}{}^+, H_2\Psi_\mathbf{k}{}^+) \times[1-\exp(i\Omega^+(t-t_0))]/\Omega^+ +\phi_{\mathbf{k}'}{}^{-\pm}(\mathbf{r})(\Psi_{\mathbf{k}'}{}^-, H_2\Psi_\mathbf{k}{}^+) \times[1-\exp(i\Omega^-(t-t_0))]/\Omega^-\}\Big\}. \quad (6.11)$$

In the g^{-2} terms in (6.11), we may use the $\phi_\mathbf{k}(\mathbf{r})$ of Eq. (3.17) in the limit $g\to\infty$ in the amplitudes, but not in the phase:

$$\phi_\mathbf{k}{}^{\pm\pm}(\mathbf{r})=e^{i\mathbf{k}\cdot\mathbf{r}}+\tfrac{1}{2}f_k e^{ikr}/r,$$

$$\phi_\mathbf{k}{}^{\pm\mp}(\mathbf{r})=-\tfrac{1}{2}f_k e^{ikr}/r,$$

where f_k is given in Eq. (3.55). Since the matrix elements are isotropic, we may immediately integrate over the direction of $\mathbf{k}'$ in (6.11). We may then remove slowly varying functions of k' from under the integral sign, since the only contribution comes from $E_{k'}{}^\pm\approx E_k{}^+$. The integrals over k' can be evaluated by standard methods of contour integration, with approximations valid for $t_0\to-\infty$, $r\to\infty$, and with the help of Eq. (3.26). Then (6.11) becomes

$$\psi_\mathbf{k}{}^{++}(\mathbf{r},t)=\exp(-iE_k{}^+t)\{\phi_\mathbf{k}{}^{++}(\mathbf{r}) -g^{-2}(2\pi)^2\omega_k(e^{ikr}/r)\tfrac{1}{2}[(e^{2i\delta_k}+1)(+|H_2|+) -(e^{2i\delta_k}-1)(-|H_2|+)]\}, \quad (6.12)$$

where $(-|H_2|+)\equiv(\Psi_{k'}{}^-, H_2\Psi_k{}^+)$ with $k'=k$, and so on. There is an analogous equation for $\psi_\mathbf{k}{}^{--}$ from (6.11).

Equation (6.12) shows that the ordinary scattering amplitude for positive mesons is, with Eq. (3.17),

$$(+|f|+)=-(8\pi\omega_k{}^2J^+)^{-1}-g^{-2}(2\pi)^2\omega_k\tfrac{1}{2}[(e^{2i\delta_k}+1) \times(+|H_2|+)-(e^{2i\delta_k}-1)(-|H_2|+)]. \quad (6.13)_1$$

The effects of H_1, which have up to now been disregarded, can be taken into account by replacing $(|H_2|)$ by $(|H_g|)$, where

$$(|H_g|)\equiv(|H_2|) +\textstyle\sum_i(|H_1|i)(i|H_1|)/(E_k-E_i+i\epsilon). \quad (6.14)_0$$

[14] The translation (6.1) does not affect these asymptotic expressions.

This result can be derived by the usual methods of second order-perturbation theory. The sum is actually an integral over suitably normalized intermediate states which lead from the initial state to the final state.

By analogous procedure one can find the other amplitudes: $(-|f|+)$ from $\psi_k{}^{+-}(\mathbf{r},t)$ of (6.11), giving the charge-exchange scattering of a positive meson; and $(\pm|f|-)$ for the scattering of a negative meson. The matrix elements are more easily calculated in the a_k, b_k representation than in the $A_k, B_k(\pm)$ representation used above. Hence we use (3.57) to relate the matrix elements:

$$(+|H_g|+)=\tfrac{1}{2}[(a|H_g|a)+(b|H_g|b)+i(b|H_g|a)-i(a|H_g|b)], \quad (6.15)_2$$

and so forth. We find for the scattering amplitudes, using (6.13)–(6.15) and the analogous equations,

$$(\pm|f|\pm)=(\pm|f_0|\pm)+f_1,$$
$$(\mp|f|\pm)=(\mp|f_0|\pm)+f_2; \quad (6.16)_1$$

where

$$(\pm|f_0|\pm)\equiv-(8\pi\omega_k{}^2J^{\pm})^{-1}\pm f_3,$$
$$(\mp|f_0|\pm)\equiv+(8\pi\omega_k{}^{\frac{1}{2}}\omega_{\mp}{}^{\frac{1}{2}}J^{\pm})^{-1}\pm f_4; \quad (6.17)$$

$$f_{1,2}\equiv-g^{-2}(2\pi)^2\omega_k{}^{\frac{1}{2}}[e^{2i\delta_k}(b|H_g|b)\pm(a|H_g|a)], \quad (6.18a)$$

$$f_{3,4}\equiv-g^{-2}(2\pi)^2\omega_k(i/2)[e^{2i\delta_k}(b|H_g|a)\mp(a|H_g|b)]. \quad (6.18b)$$

The first term of $(|f_0|)$ is valid for $\hat{a}\to0$; the matrix elements are also to be calculated eventually in this limit. Note that the factor $e^{2i\delta_k}$ appears only when the final state is a "b" state. This factor always occurs when a final state normal mode involves scattering; it is equivalent to replacing the outgoing-wave normal mode by an incoming-wave normal mode in the final state.[15]

We shall first calculate $(b|H_g|a)$. It can be seen from the operators in H_1 [Eqs. (6.5), (4.3), (4.4), (4.11)], that H_1 contributes to $(a|H_g|a)$ and $(b|H_g|b)$ to second order, but not to $(b|H_g|a)$ or $(a|H_g|b)$. Thus, defining $\Psi_k{}^a\equiv a_k{}^*\Psi^*{}_0$, $\Psi_k{}^b\equiv b_k{}^*\Psi^*{}_0$, we have

$$(b|H_g|a)=(b|H_2|a)\equiv(\Psi_k{}^b, H_2\Psi_k{}^a)=(\Psi_k{}^b, [-\mu' p_\theta WD]\Psi_k{}^a),$$

the other terms of H_2 not contributing; and we obtain, by (4.4), (4.8),

$$(b|H_g|a)=-\mu' p_\theta w_k{}^* x_k/\omega_k{}^2.$$

Using (3.56) and (4.7), we find

$$ie^{2i\delta_k}(b|H_g|a)=+\mu' p_\theta x_k{}^2/\omega_k{}^3 J_k.$$

Similarly, we find

$$i(a|H_g|b)=-\mu' p_\theta x_k{}^2/\omega_k{}^3 J_k.$$

It follows that $f_4=0$ and

$$f_3=-2g^{-2}\mu p_\theta/\omega_k{}^3 J_k, \quad (6.19)_1$$

where we have used Eqs. (4.7), (3.54), (2.30). We now insert (6.19) into (6.17):

$$(\pm|f_0|\pm)=-(8\pi\omega_k{}^2J^{\pm})^{-1}\mp2g^{-2}\mu p_\theta/\omega_k{}^3J_k. \quad (6.20)_1$$

$$(\mp|f_0|\pm)=+(8\pi\omega_k{}^{\frac{1}{2}}\omega_{\mp}{}^{\frac{1}{2}}J^{\pm})^{-1}. \quad (6.21)_1$$

With the help of (3.18), the two terms of (6.20) can be combined, to order g^{-2}:

$$(\pm|f_0|\pm)=-(8\pi\omega_+\omega_-J^{\pm})^{-1}. \quad (6.22)_1$$

The appearance of $\omega_-{}^{-1}$ in $(+|f_0|+)$ may suggest some sort of pseudo-resonance, for ω_- is less than ω_k (for p_θ positive) and could, for g not very large, be quite small. Since this expression was derived under the assumption of large g, such an extrapolation is dangerous. To find out whether such an effect actually exists, the relevant term ($\sim WD$) of H_2 can be incorporated into the original normal mode derivation, for it is bilinear in the fields. It is then found that for the modified normal modes, the scattering amplitudes in the limit $g\to\infty$, $\hat{a}\to0$ depend on the order in which the limits are taken. This situation arises from the fact that the added term would contribute effects diverging in the limit $\hat{a}\to0$, if a perturbation expansion to order g^{-6} were made. As a result, the modified normal modes, for $\hat{a}\to0$, bear no resemblance to the original normal modes. From this we conclude that an extrapolation of results here obtained to intermediate values of g is of doubtful validity.

We proceed to the calculation of $(a|H_g|a)$. From Eq. (6.6), we have

$$(a|H_2|a)=\hat{a}^{-1}(a|Q_{\Pi}L+\tfrac{1}{2}L^2|a). \quad (6.23)$$

Because the matrix elements of the two terms are separately singular, a distinction must be made wherever necessary between the initial and final energies, until the singularities have disappeared in the sum. After some calculation, with particular care in handling the singularities, we obtain

$$(a|H_2|a)=\frac{x_k{}^2}{2\omega_k{}^2\hat{a}}\left[\frac{d}{d\omega_k}\left(\mathrm{Re}\frac{1}{J_k}+\mathrm{P}\int d\mathbf{k}'\frac{|w_{k'}|^2}{\omega_{k'}-\omega_k}\right)+\int d\mathbf{k}'\frac{|w_{k'}|^2}{(\omega_{k'}+\omega_k)^2}\right]. \quad (6.24)$$

The contribution of H_1 to $(a|H_g|a)$ is given by Eqs. (6.14) and (6.5). Its evaluation is similar to but more lengthy than that of (6.23). The sum of the former and

[15] N. F. Mott and H. S. W. Massey, *The Theory of Atomic Collisions* (Clarendon Press, Oxford, 1949), second edition, Chap. VI; M. Gell-Mann and M. L. Goldberger, Phys. Rev. **91**, 398 (1953).

(6.23) yields $(a|H_g|a)$. Practically all the terms of this expression diverge separately in the limit of a point source ($\hat{a}\to 0$). However, with the use of Eq. (5.4) to express $\hat{a}^{-1}$ of (6.24) as an integral, it is possible to collect the divergent terms of the sum into a single expression which converges. We may then let $\hat{a}\to 0$, and find, after a lengthy calculation.

$$(a|H_g|a)=\mu(k^2-2\mu^2)(\pi^2\omega_k{}^4k)^{-1}\sinh^{-1}(k/\mu)$$
$$-3\mu/\pi^2\omega_k{}^3-2\mu^2/\pi\omega_k{}^4-\frac{2}{\pi^3\omega_k}\int_0^\infty\frac{k'^2dk'}{\omega_{k'}}\cdot\frac{\mathrm{P}}{k'^2-k^2}$$
$$\times\int_0^\infty\frac{k''^2dk''}{\omega_{k''}{}^2}\cdot\frac{\mathrm{P}}{k''^2-k^2}\cdot\frac{\omega_{k'}\omega_{k''}+2\omega_k{}^2}{(\omega_{k'}+\omega_{k''})^2-\omega_k{}^2-i\epsilon}. \quad (6.25)$$

The first integration of the double integral above can be performed in terms of elementary functions; for the second integration, we may use standard methods of contour integration to obtain a sum of elementary functions and an elliptic integral which cannot be completely reduced to tabulated forms. The result is

$$(a|H_g|a)=\mu(k^2-\mu^2)(\pi^2\omega_k{}^4k)^{-1}\sinh^{-1}(k/\mu)$$
$$+(2\pi\omega_k{}^2)^{-1}-2\mu/\pi^2\omega_k{}^3-2\mu^2/\pi\omega_k{}^4$$
$$-k(4\omega_k{}^2-\mu^2)^{\frac{1}{2}}(2\pi\omega_k{}^4)^{-1}+\frac{1}{\pi^2\omega_k{}^2}\int_\mu^{\omega_k+\mu}k'\frac{d\omega_{k'}}{\omega_{k'}{}^2}$$
$$\cdot\frac{\mathrm{P}}{k^2-k'^2}\cdot\frac{\omega_{k'}{}^2+2\omega_k{}^2}{2\omega_k-\omega_{k'}}[\mu^2-(\omega_k-\omega_{k'})^2]^{\frac{1}{2}}; \quad (6.26)_{1,2}$$

where, in the integral, the radical is to take the value $-i[(\omega_k-\omega_{k'})^2-\mu^2]^{\frac{1}{2}}$ for $\mu\leq\omega_{k'}\leq\omega_k-\mu$, in accordance with the $-i\epsilon$ in (6.25).

The calculation of $(b|H_g|b)$ is similar to that of $(a|H_g|a)$, but even more lengthy, with the result

$$(b|H_g|b)=-\mu(\pi^2\omega_k{}^2k)^{-1}\sinh^{-1}(k/\mu)$$
$$+(2\pi\omega_k{}^2)^{-1}+k^2/\pi\omega_k{}^4+\frac{1}{\pi^2\omega_k{}^3}\int_\mu^{\omega_k+\mu}k'\frac{d\omega_{k'}}{\omega_{k'}{}^2}$$
$$\times[\mu^2-(\omega_k-\omega_{k'})^2]^{\frac{1}{2}}. \quad (6.27)_{1,2}$$

The remark after Eq. (6.26) applies here, too.

7. RESULTS

The ordinary and charge-exchange scattering amplitudes are found by substituting Eqs. (6.26–27) into Eq. (6.18a), and Eqs. (6.18a), (6.22), (6.21) into Eq. (6.16). These expressions are valid in the perturbation sense, to order g^{-2}, if g is much larger than one, and in the limit of a point source ($\hat{a}\to 0$). The fundamental limitations of the theory were discussed in the Introduction. It is reasonable to suppose that an approach similar to that used above for the charged scalar theory should be possible for the strong coupling treatment of the charge-symmetric pseudoscalar field.

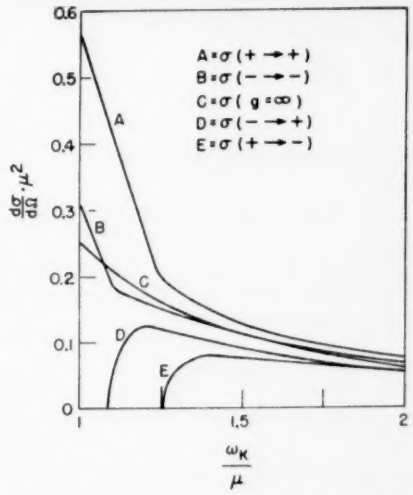

FIG. 1. Differential cross sections for ordinary and charge-exchange scattering of scalar mesons by a proton, as a function of incident meson total energy. Curves A, B, D, E are for $g=(96\pi)^{\frac{1}{2}}$. Curve C is for $g=\infty$.

The differential cross sections corresponding to the four scattering amplitudes (6.16) have been calculated numerically as a function of incident meson energy for scattering from a proton ($I_N=\frac{1}{2}$), for a particular value of g, $g=(96\pi)^{\frac{1}{2}}$. They are shown in Fig. 1, together with the common curve for $g=\infty$, in terms of natural units: the cross sections in the unit μ^{-2}, or $(\hbar/\mu c)^2$; the energy in the unit μ, or μc^2. Note that, because of the nature of the interaction, only S-wave scattering occurs, so that the cross sections are isotropic.

The deviations from the $g=\infty$ curve are surprisingly large, especially for the low-energy ordinary scattering of positive mesons; this is a result primarily of the factor $\omega_-{}^{-1}$ in Eq. (6.22). Thus this choice of g is not large enough to make the perturbation treatment a particularly good approximation; it serves rather to accentuate the effects of order g^{-2}.

These curves are, of course, not to be compared with experiment. They may, however, give some intuitive indication of the results to be expected with intermediate values of g, or for the pseudoscalar theory. It seems fairly certain that the intermediate coupling results would differ radically from the extreme strong coupling ($g=\infty$) results at low energies.

It should be pointed out that we have ignored other possible processes which arise from our Hamiltonian, to order g^{-2}, such as meson production in connection with inelastic meson scattering. These can be calculated by perturbation theory in similar fashion, there being no g^0 effects of this type.

The author wishes to express his deep gratitude to Professor M. L. Goldberger and Professor G. Wentzel for

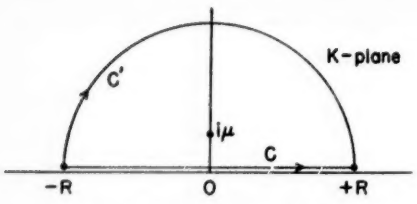

FIG. 2. Contours for Appendix.

the suggestion of this problem and for their encouragement and guidance, and to Dr. M. Gell-Mann and Mr. F. T. Solmitz for valuable discussions.

APPENDIX

It will be proved by contour integration that

$$\vartheta \equiv 2\int d\mathbf{k}|w_k|^2\omega_k^{-1} = \hat{a}^{-1}-\mu', \tag{A1}$$

where w_k and J_k are defined in Eqs. (4.5) and (3.51), respectively,

$$\mu'^{-1} = (2\pi)^{-3}\int d\mathbf{k}U_k^2\omega_k^{-4}, \tag{A2}$$

$$N^{-2} = (2\pi)^{-3}\int d\mathbf{k}U_k^2, \tag{A3}$$

$$N^{-2}\hat{a} = \left[(2\pi)^{-3}\int d\mathbf{k}U_k^2\omega_k^{-2}\right]^2, \tag{A4}$$

and U_k is an arbitrary regular real function of k, equal to one for $k=0$, and decreasing sufficiently fast so that N^{-2} [Eq. (A3)] exists. It will be noted that some of the definitions above differ from those used in the body of the paper in that integration over momentum space, rather than ordinary space, is used. We shall make use of the fact that, from (3.51),

$$\mathrm{Im}J_k = kU_k^2/4\pi\omega_k^2. \tag{A5}$$

By (4.5), (A5), we have

$$\vartheta = (2\pi)^{-3}4\pi\int_0^\infty k^2dkU_k^2/\omega_k^4|J_k|^2 = (2/\pi)\int_0^\infty kdk$$

$$\times \mathrm{Im}J_k/\omega_k^2|J_k|^2 = \frac{2}{\pi}\lim_{R\to\infty}\mathrm{Im}\int_0^R \frac{kdk}{\omega_k^2J_k^*}$$

$$= \frac{i}{\pi}\left[\int_0^R \frac{kdk}{\omega_k^2J_k} - \int_0^R \frac{kdk}{\omega_k^2J_k^*}\right].$$

The imaginary part must be taken before going to the limit $R\to\infty$, as the integral diverges. Henceforth this limiting process will be implicit.

The analytic continuation of J_k into the upper half of the complex k plane is

$$J(k) \equiv (2\pi)^{-3}\int d\mathbf{p}U_p^2/(p^2-k^2)(p^2+\mu^2). \tag{A6}$$

$J(k)$ is defined at all points for which $\mathrm{Im}k>0$, and exists in the limit $\mathrm{Im}k\to 0+$. Along the real axis $J(k)$ has a discontinuity, but we shall restrict ourselves to the upper half-plane. For k real and positive,

$$J_k = \lim_{\epsilon\to 0} J(k+i\epsilon),$$

$$J_k^* = \lim_{\epsilon\to 0} J(-k+i\epsilon).$$

Then

$$\vartheta = (i/\pi)\int_C kdk/(k^2+\mu^2)J(k),$$

where the contour C is shown in Fig. 2. The integrand has a pole at $i\mu$. Deform the contour from C to C':

$$\vartheta = (i/\pi)\int_{C'} kdk/(k^2+\mu^2)J(k) + (i/\pi)(2\pi i)\ \mathrm{Res}(k=i\mu).$$

The residue at $i\mu$ involves $[J(i\mu)]^{-1}$, which, by (A6) and (A2), equals μ'. For the contour C', we break up the integrand in the definition of $J(k)$ (A6) into partial fractions:

$$J(k) = [I(k)-I(i\mu)]/(k^2+\mu^2),$$

where

$$I(k) \equiv (2\pi)^{-3}\int d\mathbf{p}U_p^2/(p^2-k^2). \tag{A7}$$

Then we obtain

$$\vartheta+\mu' = (i/\pi)\int_{C'} kdk/[I(k)-I(i\mu)].$$

Expanding the denominator, we have

$$\vartheta+\mu' = [\pi iI(i\mu)]^{-1}\int_{C'} kdk\sum_{n=0}^\infty \left(\frac{I(k)}{I(i\mu)}\right)^n.$$

Now it may be shown that

$$\lim_{R\to\infty} R|I(Re^{i\theta})| = 0. \tag{A8}$$

Therefore we may interchange the order of summation and integration:

$$\vartheta+\mu' = [\pi iI(i\mu)]^{-1}\sum_n [I(i\mu)]^{-n}\int_{C'} kdk[I(k)]^n.$$

For $n>1$, (A8) insures that the integral vanishes as $R\to\infty$. The term $n=0$ also gives zero since $\int_{C'} kdk = 0$.

Thus only $n=1$ remains, and for it we deform the contour back to C:

$$g+\mu'=(2/\pi)[I(i\mu)]^{-2}\int_0^\infty kdk\ \mathrm{Im}I_k,$$

where we have introduced

$$I_k\equiv\lim_{\epsilon\to 0}I(k+i\epsilon)\text{ for }k\text{ real, positive.}\qquad\text{(A9)}$$

Since

$$\mathrm{Im}I_k=kU_k^2/4\pi\text{ by (A7), (A9),}$$

and

$$[I(i\mu)]^2=N^{-2}\hat{a}\text{ by (A7), (A4),}$$

we find

$$g+\mu'=(2/\pi)N^2\hat{a}^{-1}\int_0^\infty k^2dkU_k^2/4\pi=\hat{a}^{-1}\text{ by (A3),}$$

and (A1) is proved.

PHYSICAL REVIEW VOLUME 92, NUMBER 2 OCTOBER 15, 1953

The Virial Theorem for Dirac's Equation

N. H. MARCH
Department of Physics, The University, Sheffield 10, England
(Received June 16, 1953)

A general discussion is given of the form of the virial theorem when Dirac's equation is obeyed. The result reduces to that found by Fock when, as for example in the case of the hydrogen atom, the wave function tends to zero at infinity. With other boundary conditions, however, an additional term arises, which has not been considered hitherto.

THE virial theorem in nonrelativistic quantum mechanics has been discussed by a number of writers[1-3] and recently a rather general formulation has been given by Cottrell and Paterson.[4]

However, for a system described by Dirac's equation, the only discussion of which the writer was aware when this work was begun was that of Fock,[2] who used a variational method. Since then, however, a letter by Rose and Welton[5] (who were apparently unaware of Fock's earlier work) has appeared.

On examination it is clear that neither of these discussions is sufficiently general to apply to certain problems of physical interest and it seemed to us worthwhile therefore to record here a quite different proof of the theorem, which is more akin to the nonrelativistic treatments[3,4] and which leads to a more general result than has been found hitherto.

The Dirac equation for an electron in an electrostatic field may be written[6]

$$ihc\sum_i\alpha_i\frac{\partial}{\partial x_i}\psi-\alpha_mmc^2\psi=(E-V)\psi,\qquad(1)$$

and the corresponding equation for ψ^* as

$$-ihc\sum_i\frac{\partial\psi^*}{\partial x_i}\alpha_i-\psi^*\alpha_mmc^2=\psi^*(E-V).\qquad(2)$$

Differentiating (1) with respect to x_j and multiplying through on the left by ψ^*x_j, we obtain

$$ihc\psi^*x_j\sum_i\alpha_i\frac{\partial^2\psi}{\partial x_j\partial x_i}-\psi^*x_j\alpha_m\frac{\partial\psi}{\partial x_j}mc^2=\psi^*x_j(E-V)\frac{\partial\psi}{\partial x_j}-\psi^*x_j\frac{\partial V}{\partial x_j}\psi.\qquad(3)$$

Now we substitute for $\psi^*(E-V)$, sum over j, and integrate over coordinate space, and we have

$$ihc\int\sum_j x_j\left\{\psi^*\sum_i\alpha_i\frac{\partial^2\psi}{\partial x_j\partial x_i}+\sum_i\frac{\partial\psi^*}{\partial x_i}\alpha_i\frac{\partial\psi}{\partial x_j}\right\}d\tau=-\int\sum_j\psi^*x_j\frac{\partial V}{\partial x_j}\psi d\tau=\langle\textstyle\sum_j x_jF_j\rangle,\qquad(4)$$

where $F_j=-\partial V/\partial x_j$, and the angular brackets denote the quantum-mechanical average. We now make use of the identity,

$$\sum_i x_j\left\{\psi^*\alpha_i\frac{\partial^2\psi}{\partial x_j\partial x_i}+\frac{\partial\psi^*}{\partial x_i}\alpha_i\frac{\partial\psi}{\partial x_j}\right\}=\frac{\partial}{\partial x_i}\left[\psi^*\alpha_i\left(\sum_i x_j\frac{\partial\psi}{\partial x_j}\right)\right]-\psi^*\alpha_i\frac{\partial\psi}{\partial x_i},\qquad(5)$$

and hence

$$ihc\int\sum_i\frac{\partial}{\partial x_i}\left[\psi^*\alpha_i\left(\sum_i x_j\frac{\partial\psi}{\partial x_j}\right)\right]d\tau-ihc\int\psi^*\sum_i\alpha_i\frac{\partial\psi}{\partial x_i}d\tau=\langle\sum_i x_jF_j\rangle.\qquad(6)$$

[1] B. N. Finkelstein, Z. Physik **50**, 293 (1928).
[2] V. Fock, Z. Physik **63**, 855 (1930).
[3] J. C. Slater, J. Chem. Phys. **1**, 687 (1933).
[4] T. L. Cottrell and S. Paterson, Phil. Mag. **42**, 391 (1951).
[5] M. E. Rose and T. A. Welton, Phys. Rev. **86**, 432 (1952).
[6] V. Rojansky, *Introductory Quantum Mechanics* (Prentice-Hall, Inc., New York, 1946), p. 510.

Following Fock,[2] let us denote the operator $ihc\sum_i \alpha_i \partial/\partial x_i$ by L, and its quantum-mechanical average by L_0. Then from Eq. (6)

$$-L_0 = -ihc \int \sum_i \frac{\partial}{\partial x_i}\left[\psi^* \alpha_i \left(\sum_j x_j \frac{\partial \psi}{\partial x_j}\right)\right] d\tau + \langle \sum_j x_j F_j \rangle. \tag{7}$$

For the case of a hydrogen atom, for example, ψ vanishes at infinity, the first term on the right of (7) is zero, and we arrive at Fock's result. However, in some cases of physical interest other boundary conditions arise. Einbinder,[7] for example, has considered a system of free electrons enclosed in a finite volume. He has applied Fock's result to this case, arguing that the virial of the pressure p is $-3pv$, where v is the volume. In fact, however, Fock's result is not applicable to this problem, whereas Eq. (7) can be used. The boundary conditions in this case are the periodicity conditions, and one can evaluate the first term on the right of (7) using the explicit wave functions of Darwin,[8] representing an electron confined in a volume v. The result is simply $-3pv$, thus verifying Einbinder's form of the theorem.

In this case, then, it appears that the first term on the right of (7) can be interpreted as the contribution to the virial arising from the forces represented through the boundary conditions rather than through an explicit potential in the Dirac equation.

It would be necessary to consider the first term on the right of (7) when dealing with the problem of an electron in a spherical hole in the manner of Broch,[9] and it is also clear from (7) why the result of Rose and Welton[5] cannot be applied to continuum states.

The writer wishes to thank Dr. G. L. Sewell for a critical reading of the manuscript.

[7] H. Einbinder, Phys. Rev. **74**, 803 (1948).

[8] C. G. Darwin, Proc. Roy. Soc. (London) **A118**, 654 (1928).

[9] E. K. Broch, Phys. Rev. **51**, 586 (1937).

PHYSICAL REVIEW VOLUME 92, NUMBER 2 OCTOBER 15, 1953

Relativistic Correction to the Lamb Shift*†

M. BARANGER‡ AND H. A. BETHE, *Cornell University, Ithaca, New York*

AND

R. P. FEYNMAN, *California Institute of Technology, Pasadena, California*

(Received June 24, 1953)

The relativistic corrections to the Lamb shift, i.e., terms of order $\alpha(Z\alpha)^5 mc^2$, are calculated. For this purpose, the Lamb shift is separated into one term in which the Coulomb potential acts only once, and another term in which it acts two or more times (Sec. II). The one-potential term is shown to be equal to the expression calculated in previous papers except for corrections of order $\alpha(Z\alpha)^6$ (Sec. III), and a method is given by which these corrections could be evaluated if desired (Appendix). The many-potential term can be separated into a nonrelativistic part which is again equal to the term calculated in previous papers, and a relativistic term which can be calculated by considering the intermediate states as free (Sec. IV). The calculation of the latter term which, of course, involves the Coulomb potential exactly twice, is described in Sec. V. A correction to the vacuum polarization term which is of the same order, is evaluated in Sec. VI.

The result for the relativistic correction is 7.13 Mc/sec, and is in agreement with the result of Karplus, Klein, and Schwinger which was obtained by an independent method. The result for the complete Lamb shift has been given in a recent paper by Salpeter. The small remaining discrepancy of 0.6 Mc/sec between theory and experiment might be due to the next order relativistic correction which should be of order $\alpha(Z\alpha)^6 \ln(Z\alpha)$.

I. INTRODUCTION

SINCE the first accurate measurement by Lamb and Retherford[1] of the displacement of the 2*S* level of the hydrogen atom now known as the "Lamb shift," theoretical calculations, based on quantum electrodynamics and using the mass renormalization procedure, have been given by several authors.[2–6] A simple way to obtain their result is to start from the operator for the radiative corrections to scattering[7] [F II, Eq. (22)], or more exactly its limit for small momentum

* Part of the material presented in this paper, in particular Sec. V, is taken from the Ph.D. thesis of M. Baranger (Cornell University, June, 1951).

† Partially supported by the U. S. Office of Naval Research.

‡ Now at the California Institute of Technology, Pasadena, California.

[1] W. E. Lamb, Jr., and R. C. Retherford, Phys. Rev. **72**, 241 (1947).

[2] H. A. Bethe, Phys. Rev. **72**, 339 (1947).

[3] N. M. Kroll and W. E. Lamb, Phys. Rev. **75**, 388 (1949).

[4] J. B. French and V. F. Weisskopf, Phys. Rev. **75**, 1240 (1949).

[5] R. P. Feynman, Phys. Rev. **74**, 1436 (1948), corrected by Phys. Rev. **76**, 769 (1949), reference 13 on p. 777.

[6] J. Schwinger, Phys. Rev. **76**, 790 (1949).

[7] R. P. Feynman, Phys. Rev. **76**, 769 (1949), referred to as F II.

transfer [F II, Eq. (24)],[8]

$$\frac{e^2}{4\pi}\left[\frac{1}{2m}(qV-Vq)+\frac{4q^2}{3m^2}V\left(\ln\frac{m}{\lambda}-\frac{3}{8}\right)\right], \qquad (1)$$

where q is the 4-momentum transferred by the potential V and λ a fictitious "photon mass." The level shift is simply the expectation value of this operator for the state in consideration. But there is an infrared catastrophy, i.e., the result becomes infinite when λ goes to 0. For this reason, λ is not put equal to 0, but the result is added to the nonrelativistic Lamb shift,[2]

$$\frac{2e^2}{3\pi m^2}\sum_n|\mathbf{p}_{n0}|^2(E_n-E_0)\ln\frac{K}{|E_n-E_0|}, \qquad (2)$$

which is certainly correct for very small photon energy. $\mathbf{p}_{n0}$ is the matrix element of the electron momentum between the state under study ψ_0 and another state ψ_n of the hydrogen atom. E_0 and E_n are the energies of these two states. K is an ultraviolet cutoff. French[4] has shown that the correspondence relation,

$$\ln\lambda=\ln(2K)-\tfrac{5}{6}, \qquad (3)$$

should be used. It is then found that λ or K disappears from the total. To terms (1) and (2) should still be added the so-called "vacuum polarization" term, considered here in Sec. VI. The numerical work given by Bethe, Brown, and Stehn,[9] and corrected by Salpeter[10] for effect of the finite mass of the nucleus, gives the result 1051.0 Mc/sec for the $2S_{\frac{1}{2}}-2P_{\frac{1}{2}}$ transition in hydrogen.

In the meantime, experimental accuracy has been much improved. The recent experiments of Triebwasser, Dayhoff, and Lamb[11] yielded 1057.77±0.10 Mc/sec for hydrogen and 1059.00±0.10 Mc/sec for deuterium, thus leaving room for more accurate calculations.

It can be seen [reference 2, Eq. (11)], that the nonrelativistic term (2) is of order $\alpha(Z\alpha)^4\ln(Z\alpha)$. The expectation value of the operator (1), called in the following the "one-potential Lamb shift," is of order $\alpha(Z\alpha)^4$. The purpose of this paper is to evaluate all corrections of order $Z\alpha$ with respect to the main term, that is terms of order $\alpha(Z\alpha)^5\ln(Z\alpha)$ or $\alpha(Z\alpha)^5$. Among all terms in α^6, these can be characterized as the one-photon part of the Lamb shift, represented by the diagrams of Fig. 1.

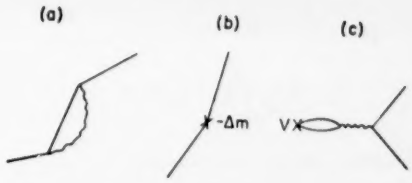

FIG. 1. Diagrams for the one-photon part of the Lamb shift. In these diagrams, the electrons should not be considered as free, but as bound electrons propagating in the field of the nucleus.

Terms of order $\alpha^2(Z\alpha)^4$, or two-photons parts, are not considered. Terms of order $\alpha(Z\alpha)^6$ or $\alpha(Z\alpha)^6\ln(Z\alpha)$ are neglected throughout. However, a method for evaluating some of them is given in the appendix.

The main part of the paper is concerned with diagrams 1(a) and 1(b). The vacuum polarization diagram 1(c) is evaluated at the end.

II. SEPARATION OF TERMS

The energy shift contributed by diagram 1(a) is easy to write down by a straightforward modification for a bound particle of the argument given in F II, p. 773.

$$\Delta E_a=e^2\int\bar{\psi}_0(\mathfrak{x}_2)\gamma_\mu K_+{}^V(\mathfrak{x}_2,\mathfrak{x}_1)\gamma_\mu\psi_0(\mathfrak{x}_1)\cdot\delta_+[(\mathfrak{x}_2-\mathfrak{x}_1)^2]d^3\mathbf{x}_2d^3\mathbf{x}_1d(t_2-t_1),$$

where $\psi_0(\mathfrak{x})$ is the electronic wave function, normalized by

$$\int\bar{\psi}_0(\mathfrak{x})\beta\psi_0(\mathfrak{x})d^3\mathbf{x}=\int\psi_0^*(\mathfrak{x})\psi_0(\mathfrak{x})d^3\mathbf{x}=1, \qquad (4)$$

$K_+{}^V(\mathfrak{x}_2,\mathfrak{x}_1)$ is the kernel for propagation of an electron bound in a hydrogen atom[12] [F I, Eq. (15)], δ_+ is defined in F II, and t is the time component of $\mathfrak{x}$.

Diagram 1(b) comes from the following cause: We use everywhere the propagation kernel $K_{+1}{}^V$, computed with the physical or measured mass m_1, and solution of the equation[13]

$$(i\nabla_2-V(\mathfrak{x}_2)-m_1)K_{+1}{}^V(\mathfrak{x}_2,\mathfrak{x}_1)=i\delta(\mathfrak{x}_2-\mathfrak{x}_1). \qquad (5)$$

But we really should use the kernel $K_{+0}{}^V$, computed with the bare mass $m_0=m_1-\Delta m$, and solution of the equation

$$(i\nabla_2-V(\mathfrak{x}_2)-m_1+\Delta m)K_{+0}{}^V(\mathfrak{x}_2,\mathfrak{x}_1)=i\delta(\mathfrak{x}_2-\mathfrak{x}_1).$$

A solution of the last equation correct to first order in Δm is

$$K_{+0}{}^V(\mathfrak{x}_2,\mathfrak{x}_1)=K_{+1}{}^V(\mathfrak{x}_2,\mathfrak{x}_1)+i\int K_{+1}{}^V(\mathfrak{x}_2,\mathfrak{x}_3)\Delta mK_{+1}{}^V(\mathfrak{x}_3,\mathfrak{x}_1)d^4\mathfrak{x}_3.$$

[8] Units and notations: $\hbar=c=1$. m is the electronic mass, e the positive quantum of charge in nonrationalized units. $e^2=\alpha=1/137$. $V=-Ze^2/r$ is the Coulomb potential energy. $\mathbf{A}$ is a 3-vector, of components A_i ($i=1, 2, 3$) and length A. $\mathfrak{A}$ is a 4-vector, of components A_μ ($\mu=0, 1, 2, 3$). The summation convention is $A_\mu B_\mu=A_0B_0-A_1B_1-A_2B_2-A_3B_3$. The fundamental tensor $\delta_{\mu\nu}$ is such that $\delta_{\mu\nu}A_\nu=A_\mu$ and $\delta_{\mu\mu}=4$. The conventions for Dirac matrices are: $\gamma_i=\beta\alpha_i$, $\gamma_0=\beta$, $\boldsymbol{A}=\gamma_\mu A_\mu$, $V=\gamma_\mu V_\mu=-\beta Ze^2/r$. Dirac's equation reads $(p-m)\psi=V\psi$. $\bar{\psi}=\psi^*\beta$ is the relativistic adjoint of ψ, ψ^* being the ordinary Hermitian conjugate. λ is the infinitesimal mass of the photon.

[9] Bethe, Brown, and Stehn, Phys. Rev. **77**, 370 (1950).

[10] E. E. Salpeter, Phys. Rev. **87**, 328 (1952); **89**, 92 (1953).

[11] Triebwasser, Dayhoff, and Lamb, Phys. Rev. **89**, 98 (1953).

[12] R. P. Feynman, Phys. Rev. **76**, 749 (1949), referred to as F I.

[13] Here ∇_μ stands for the vector $(\partial/\partial t, -\partial/\partial x, -\partial/\partial y, -\partial/\partial z)$.

The correction gives the following contribution to the transition amplitude from ψ_0 to ψ_0:

$$i\Delta m\int\bar{\psi}_0(\underline{x})\psi_0(\underline{x})d^4\underline{x},$$

and therefore the following energy shift:

$$\Delta E_b=-\Delta m\int\bar{\psi}_0(\underline{x})\psi_0(\underline{x})d^3\mathbf{x}. \tag{6}$$

In this paper, the convergence factor defined in F II, p. 776, will be used. Therefore, we replace Δm by[14]

$$\Delta m=(e^2/2\pi)m[3\ln(\Lambda/m)+\tfrac{3}{4}]. \tag{7}$$

The most important part of the Lamb shift is therefore given by $\Delta E_a+\Delta E_b$. As usual, it is easier to work in momentum space. Define

$$\psi_0(\underline{x})=\psi_0(\mathbf{x})\exp(-iE_0t), \tag{8}$$

$$\varphi_0(\mathbf{p})=(2\pi)^{-\frac{3}{2}}\int\psi_0(\mathbf{x})\exp(-i\mathbf{p}\cdot\mathbf{x})d^3\mathbf{x}, \tag{8a}$$

$$\begin{aligned}V(\mathbf{q})&=(2\pi)^{-3}\int V(\mathbf{x})\exp(-i\mathbf{q}\cdot\mathbf{x})d^3\mathbf{x}\\&=-(Ze^2/2\pi^2)\beta/\mathbf{q}^2,\end{aligned} \tag{8b}$$

$$K_+{}^V(\underline{\mathfrak{p}}_2,\underline{\mathfrak{p}}_1)=(2\pi)^{-4}\int K_+{}^V(\mathfrak{p}_2,\mathfrak{p}_1)\times\exp(-i\mathfrak{p}_2\cdot\underline{x}_2+i\mathfrak{p}_1\cdot\underline{x}_1)d^4\mathfrak{p}_2d^4\mathfrak{p}_1, \tag{9}$$

$$K_+{}^V(\mathfrak{p}_2,\mathfrak{p}_1)=\delta(E_2-E_1)K_+{}^V(E;\mathbf{p}_2,\mathbf{p}_1), \tag{9a}$$

where E is the time component of $\mathfrak{p}$. This part of the Lamb shift then becomes

$$\begin{aligned}\Delta E_{a+b}=&-(e^2/\pi)\int\bar{\varphi}_0(\mathbf{p}_2)\gamma_\mu K_+{}^V(E_0-\omega;\mathbf{p}_2-\mathbf{k},\mathbf{p}_1-\mathbf{k})\\&\cdot\gamma_\mu\varphi_0(\mathbf{p}_1)\mathbf{f}^{-2}d^4\mathbf{f}_F d^3\mathbf{p}_2d^3\mathbf{p}_1\\&-\Delta m\int\bar{\varphi}_0(\mathbf{p})\varphi_0(\mathbf{p})d^3\mathbf{p}.\end{aligned} \tag{10}$$

ω is the time component of $\mathbf{f}$. $d^4\mathbf{f}_F$ means $d^4\mathbf{f}/4\pi^2$ and will make it easier to use the formulas in the appendix of F II, where $d^4\mathbf{f}$ is defined in this manner [see appendix of F II, second line after Eq. (1a)].

Expression (10) is exact, for diagrams 1a and 1b, i.e., for the part of the Lamb shift involving one virtual photon, exclusive of vacuum polarization (diagram 1c). The difficulty of the problem comes entirely from the lack of a convenient expression for $K_+{}^V$. In previous treatments, e.g., F II, the kernel $K_+{}^V$ was approximated in the relativistic region by an expression of first order in the Coulomb potential V, and in the nonrelativistic region by the ordinary Schrödinger kernel; these parts were then fitted together. Our first aim will now be to make a rigorous separation of (10) into one part which is of first order in V, and another part involving the potential twice or more often.

We can perform this separation most easily using operator notation. The kernel $K_+{}^V$ may be written as:

$$\begin{aligned}-iK_+{}^V=&(\boldsymbol{p}-m)^{-1}+(\boldsymbol{p}-m)^{-1}\boldsymbol{V}(\boldsymbol{p}-m)^{-1}\\&+(\boldsymbol{p}-m)^{-1}\boldsymbol{V}(\boldsymbol{p}-m)^{-1}\boldsymbol{V}(\boldsymbol{p}-m)^{-1}+\cdots,\end{aligned} \tag{11}$$

where $\boldsymbol{p}$ stands for the momentum operator $\boldsymbol{p}=i\boldsymbol{\nabla}$. Equation (11) may be formally simplified into

$$-iK_+{}^V=(\boldsymbol{p}-\boldsymbol{V}-m)^{-1}. \tag{12}$$

In (12) there occur the noncommuting operators $\boldsymbol{p}$ and $\boldsymbol{V}$; Eq. (11) defines the order in which these operators should be applied.

The expression (12) for $K_+{}^V$ follows, of course, naturally from (5). We shall use (12) essentially in one way only. We know that

$$-i(\boldsymbol{p}-\boldsymbol{V}-m)K_+{}^V=-iK_+{}^V(\boldsymbol{p}-\boldsymbol{V}-m)=1, \tag{13}$$

where 1 is the unit operator. This follows directly from (5), or from (11), by straightforward algebra.

The expression for ΔE_a is

$$\begin{aligned}\Delta E_a=&-i(e^2/\pi)\int\bar{\varphi}_0\gamma_\mu\exp(-i\mathbf{f}\cdot\underline{x})\\&\cdot(\boldsymbol{p}-\boldsymbol{V}-m)^{-1}\gamma_\mu\exp(i\mathbf{f}\cdot\underline{x})\varphi_0\mathbf{f}^{-2}d^4\mathbf{f}.\end{aligned} \tag{14}$$

The exponentials give the space-time variation for the emitted and absorbed photon which has been expanded into components of momentum $\mathbf{f}$. The operator $\boldsymbol{p}=i\boldsymbol{\nabla}$ acts on everything that follows it, i.e., on φ_0, on $\boldsymbol{V}$ inasmuch as is required by the defining Eq. (11), and on $\exp(i\mathbf{f}\cdot\underline{x})$. The $\exp(i\mathbf{f}\cdot\underline{x})$ commutes with all quantities except $\boldsymbol{p}$, and $\exp(-i\mathbf{f}\cdot\underline{x})\boldsymbol{p}\exp(i\mathbf{f}\cdot\underline{x})=\boldsymbol{p}-\boldsymbol{k}$ so that (14) becomes[15]

$$\Delta E_a=-i(e^2/\pi)\int\bar{\varphi}_0\gamma_\mu(\boldsymbol{p}-\boldsymbol{k}-\boldsymbol{V}-m)^{-1}\gamma_\mu\varphi_0\mathbf{f}^{-2}d^4\mathbf{f}. \tag{15}$$

Now $\boldsymbol{p}=i\boldsymbol{\nabla}$ only acts on φ_0 and on $\boldsymbol{V}$ as required, no longer on $\exp(i\mathbf{f}\cdot\underline{x})$; $\mathbf{f}$ is a c number. The function φ_0 satisfies the Dirac equation,

$$(\boldsymbol{p}-\boldsymbol{V}-m)\varphi_0=0. \tag{16}$$

We shall now rearrange the integrand in (15),

$$\bar{\varphi}_0\gamma_\mu(\boldsymbol{p}-\boldsymbol{k}-\boldsymbol{V}-m)^{-1}\gamma_\mu\varphi_0, \tag{15a}$$

[14] Λ and λ stand for λ and $\lambda_{\min}$ of F II, respectively.

[15] In any expression involving operators one can perform an equivalence transformation:

$$Sf(A,B,\cdots)S^{-1}=f(A',B',\cdots),$$

where $A'=SAS^{-1}$, etc. With $S=\exp(-i\mathbf{f}\cdot\underline{x})$, and $f=(\boldsymbol{p}-\boldsymbol{V}-m)^{-1}$ we get

$$\exp(-i\mathbf{f}\cdot\underline{x})(\boldsymbol{p}-\boldsymbol{V}-m)^{-1}\exp(i\mathbf{f}\cdot\underline{x})=(\boldsymbol{p}'-\boldsymbol{V}'-m)^{-1},$$

$$\boldsymbol{V}'=\exp(-i\mathbf{f}\cdot\underline{x})\,\boldsymbol{V}\exp(i\mathbf{f}\cdot\underline{x})=\boldsymbol{V},$$

and $\boldsymbol{p}'=\exp(-i\mathbf{f}\cdot\underline{x})\boldsymbol{p}\exp(i\mathbf{f}\cdot\underline{x})=\boldsymbol{p}-\boldsymbol{k}$.

by use of the following lemma:

$$A\equiv(\not p_b-m)\frac{\not p_b A+A\not p_a}{\mathfrak{p}_b^2-\mathfrak{p}_a^2}-\frac{\not p_b A+A\not p_a}{\mathfrak{p}_b^2-\mathfrak{p}_a^2}(\not p_a-m), \quad (17)$$

which is valid for any operator A which causes the momentum to change[16] from $\mathfrak{p}_a$ to $\mathfrak{p}_b$.

The identity (17) is verified by direct algebra using the fact that $\not p_a^2=\mathfrak{p}_a^2$ is free of Dirac operators. We apply (17) to re-express the left hand γ_μ in (15a) (which replaces A), with $\mathfrak{p}_b=\mathfrak{p}$, $\mathfrak{p}_a=\mathfrak{p}-\mathfrak{k}$ and obtain

$$\bar\varphi_0[(\not p-m)B_\mu-B_\mu(\not p-\not k-m)]\times(\not p-\not k-V-m)^{-1}\gamma_\mu\varphi_0, \quad (18)$$

with

$$B_\mu=\frac{\not p\gamma_\mu+\gamma_\mu(\not p-\not k)}{\mathfrak{p}^2-(\mathfrak{p}-\mathfrak{k})^2}=\frac{2p_\mu-\gamma_\mu\not k}{\mathfrak{p}^2-(\mathfrak{p}-\mathfrak{k})^2}. \quad (19)$$

(18) may be rewritten:

$$\bar\varphi_0[(\not p-V-m)B_\mu-B_\mu(\not p-\not k-V-m)]\times(\not p-\not k-V-m)^{-1}\gamma_\mu\varphi_0+\bar\varphi_0(VB_\mu-B_\mu V)(\not p-\not k-V-m)^{-1}\gamma_\mu\varphi_0. \quad (20)$$

The first term vanishes because φ_0 satisfies the Dirac equation (16), and the second term is simply

$$\mathrm{I}=-\bar\varphi_0 B_\mu\gamma_\mu\varphi_0. \quad (21)$$

In the last term of (20) we now transform the second γ_μ, again using the lemma (17). This time $\mathfrak{p}_a=\mathfrak{p}$ and $\mathfrak{p}_b=\mathfrak{p}-\mathfrak{k}$ and the last term of (20) becomes

$$\begin{aligned}\mathrm{II}+\mathrm{III}&=\bar\varphi_0(VB_\mu-B_\mu V)(\not p-\not k-V-m)^{-1}\cdot[(\not p-\not k-V-m)B_\mu^\dagger-B_\mu^\dagger(\not p-V-m)]\varphi_0 \quad (22)\\&+\bar\varphi_0(VB_\mu-B_\mu V)(\not p-\not k-V-m)^{-1}(VB_\mu^\dagger-B_\mu^\dagger V)\varphi_0,\end{aligned}$$

with

$$B_\mu^\dagger=\frac{(\not p-\not k)\gamma_\mu+\gamma_\mu\not p}{(\mathfrak{p}-\mathfrak{k})^2-\mathfrak{p}^2}=\frac{2p_\mu-\not k\gamma_\mu}{(\mathfrak{p}-\mathfrak{k})^2-\mathfrak{p}^2}. \quad (19a)$$

The first term of (22) gives

$$\mathrm{II}=\bar\varphi_0(VB_\mu-B_\mu V)B_\mu^\dagger\varphi_0 \quad (21a)$$

the second vanishes, and the last term is

$$\mathrm{III}=\bar\varphi_0(VB_\mu-B_\mu V)(\not p-\not k-V-m)^{-1}\times(VB_\mu^\dagger-B_\mu^\dagger V)\varphi_0. \quad (21b)$$

The term (21b) is now the only one which still contains the propagation kernel in the Coulomb field, $K_+{}^V$. Of the other two terms, (21) does not contain the potential at all but is a self-energy for a free particle which will largely cancel the mass renormalization Δm. (21a) is the one-potential part of the Lamb shift. In (21b), the potential acts at least twice, once with the emission of the virtual photon (term $VB^\dagger-B^\dagger V$) and once with its absorption. In addition, the potential may also act in the propagation kernel $K_+{}^V$. Thus in (21b) are contained all terms in which the potential acts twice or more, and they are cleanly separated from the terms involving only one or no potential, thus fulfilling the first point of our program.[17]

It is interesting to note that in (21b) the emission and absorption of a virtual photon is coupled with the action of the potential. This expresses the physical fact that emission and absorption can only take place when there is an external field acting on the electron.

It is convenient to introduce an abbreviation for the expression which occurs repeatedly, *viz*:

$$VB_\mu-B_\mu V=M_\mu, \quad (23)$$

and $M_\mu^\dagger$ correspondingly. Then we have explicitly:

$$M_\mu(\mathfrak{p}_f,\mathfrak{p}_i-\mathfrak{k})=V(\mathbf{p}_f-\mathbf{p}_i)\frac{2p_{i\mu}-\gamma_\mu\not k}{2\mathfrak{p}_i\cdot\mathfrak{k}-\mathfrak{k}^2}-\frac{2p_{f\mu}-\gamma_\mu\not k}{2\mathfrak{p}_f\cdot\mathfrak{k}-\mathfrak{k}^2}V(\mathbf{p}_f-\mathbf{p}_i), \quad (24)$$

and

$$\begin{aligned}M_\mu^\dagger(\mathfrak{p}_f-\mathfrak{k},\mathfrak{p}_i)&=V(\mathbf{p}_f-\mathbf{p}_i)\frac{2p_{i\mu}-\not k\gamma_\mu}{\mathfrak{k}^2-2\mathfrak{p}_i\cdot\mathfrak{k}}-\frac{2p_{f\mu}-\not k\gamma_\mu}{\mathfrak{k}^2-2\mathfrak{p}_f\cdot\mathfrak{k}}V(\mathbf{p}_f-\mathbf{p}_i) \quad (24a)\\&=\bar M_\mu(\mathfrak{p}_i,\mathfrak{p}_f-\mathfrak{k}),\end{aligned}$$

where $\bar M_\mu$ is the operator relativistic adjoint of M_μ.

$V(\mathbf{p}_f-\mathbf{p}_i)$ is the Fourier component of the Coulomb potential corresponding to a momentum change $\mathbf{p}_f-\mathbf{p}_i$. The operator $M_\mu^\dagger$ corresponds to the emission of a quantum of momentum $\mathfrak{k}$ and polarization μ; the electron has initially the momentum $\mathfrak{p}_i$ and after emission the momentum $\mathfrak{p}_f-\mathfrak{k}$, so that the total final momentum of electron plus quantum is $\mathfrak{p}_f$; the initial and final momentum of the electron are put in evidence as the arguments of $M_\mu^\dagger$. M_μ corresponds to the absorption of the same quantum; the momentum of the electron before absorption is $\mathfrak{p}_i-\mathfrak{k}$, after absorption $\mathfrak{p}_f$. We shall call $M_\mu^\dagger$ and M_μ "radiation operators" or, specifically, emission and absorption operators.[18]

We can now collect the various parts of the Lamb

[16] More generally, $\mathfrak{p}_b$ and $\mathfrak{p}_a$ can be thought of as operators ordered according to the rule [see R. P. Feynman, Phys. Rev. **84**, 108 (1951)] that $\mathfrak{p}_a$ precedes and $\mathfrak{p}_b$ follows the variables in A; the γ's operate in the order in which they are written.

[17] The same aim could have been achieved by using the more straightforward identity:

$$K_+{}^V=K_+{}^0-iK_+{}^0VK_+{}^0-K_+{}^0VK_+{}^VVK_+{}^0.$$

But our method presents certain advantages which will become evident later.

[18] The method given here for separating the electrodynamic shift into three terms such as (21), (21a), and (21b), has been used previously, in connection with the radiative corrections to hyperfine structure, by N. M. Kroll and F. Pollock, Phys. Rev. **86**, 876 (1952).

shift and get

$$\Delta E_{a+b}=\Delta E_2+\Delta E_1$$

$$\begin{aligned}\Delta E_2=&-(e^2/\pi)\int \bar{\varphi}_0(\mathbf{p}_2)M_\mu(\mathfrak{p}_2,\mathfrak{p}_2-\mathfrak{s}_2-\mathfrak{k})\\&\times K_+{}^V(E_0-\omega;\mathbf{p}_2-\mathbf{s}_2-\mathbf{k},\mathbf{p}_1+\mathbf{s}_1-\mathbf{k})\\&\times M_\mu{}^\dagger(\mathfrak{p}_1+\mathfrak{s}_1-\mathfrak{k},\mathfrak{p}_1)\\&\times\varphi_0(\mathbf{p}_1)\mathfrak{k}^{-2}d^4\mathfrak{k}_F d^3\mathfrak{p}_1 d^3\mathbf{p}_2 d^3\mathbf{s}_1 d^3\mathbf{s}_2,\end{aligned}\tag{25}$$

$$\Delta E_1=\Delta E_{11}+\Delta E_{12}+\Delta E_{13}+\Delta E_{14},$$

$$\Delta E_{11}=\frac{e^2}{\pi i}\int\bar{\varphi}_0(\mathbf{p}_2)\frac{2p_{2\mu}-\gamma_\mu k}{\mathfrak{k}^2-2\mathfrak{p}_2\cdot\mathfrak{k}}V(\mathbf{p}_2-\mathbf{p}_1)\cdot\frac{2p_{1\mu}-k\gamma_\mu}{\mathfrak{k}^2-2\mathfrak{p}_1\cdot\mathfrak{k}}\varphi_0(\mathbf{p}_1)\mathfrak{k}^{-2}d^4\mathfrak{k}_F d^3\mathbf{p}_1 d^3\mathbf{p}_2,$$

$$\Delta E_{12}=-\frac{e^2}{\pi i}\int\bar{\varphi}_0(\mathbf{p}_2)V(\mathbf{p}_2-\mathbf{p}_1)\frac{2p_{1\mu}-\gamma_\mu k}{\mathfrak{k}^2-2\mathfrak{p}_1\cdot\mathfrak{k}}\cdot\frac{2p_{1\mu}-k\gamma_\mu}{\mathfrak{k}^2-2\mathfrak{p}_1\cdot\mathfrak{k}}\varphi_0(\mathbf{p}_1)\mathfrak{k}^{-2}d^4\mathfrak{k}_F d^3\mathbf{p}_1 d^3\mathbf{p}_2,\tag{26}$$

$$\Delta E_{13}=\frac{e^2}{\pi i}\int\bar{\varphi}_0(\mathbf{p})\frac{2p_\mu-\gamma_\mu k}{\mathfrak{k}^2-2\mathfrak{p}\cdot\mathfrak{k}}\gamma_\mu\varphi_0(\mathbf{p})\mathfrak{k}^{-2}d^4\mathfrak{k}_F d^3\mathbf{p},$$

$$\Delta E_{14}=-\Delta m\int\bar{\varphi}_0(\mathbf{p})\varphi_0(\mathbf{p})d^3\mathbf{p}.$$

In (25) and (26) the $\mathfrak{p}$'s have time component E_0 and the $\mathfrak{s}$'s have time component 0. $M_\mu(\mathfrak{p}_2,\mathfrak{p}_2-\mathfrak{s}_2-\mathfrak{k})$ is obtained from Eq. (24) by replacing $\mathfrak{p}_f$ by $\mathfrak{p}_2$ and $\mathfrak{p}_i$ by $\mathfrak{p}_2-\mathfrak{s}_2$; similarly $M_\mu{}^\dagger$ comes from (24a) replacing $\mathfrak{p}_i$ by $\mathfrak{p}_1$ and $\mathfrak{p}_f$ by $\mathfrak{p}_1+\mathfrak{s}_1$.

Of the terms in ΔE_1, Eq. (26), ΔE_{11} and ΔE_{12} arise from (21a) and thus contain one potential; ΔE_{13} arises from (21) and contains no potential at all; ΔE_{14} is the mass renormalization term, i.e., the last term of (10). The entire term ΔE_1 will be called "one-potential Lamb shift" and treated in Sec. III. ΔE_1 is identical with the term evaluated in references 3 to 6, except for the fact that, here, the momenta are not free particle ones: $\mathfrak{p}_1^2$, $\mathfrak{p}_2^2$, $\mathfrak{p}^2\neq m^2$, and $\mathfrak{p}\varphi_0\neq m\varphi_0$. ΔE_2 will be called "many-potential Lamb shift." It arises from (21b) and it contains the nonrelativistic Lamb shift (2); it will be treated in Secs. IV and V. It should be noted that Eqs. (25) and (26) are still exact, and approximations will only be made in the evaluation.

The poles that appear in the propagation factors $(\mathfrak{p}-m)^{-1}$ and $\mathfrak{k}^{-2}$ will be defined in the usual way by giving to the masses of electron and photon a small negative imaginary part. But, in Eqs. (17), (24), (24a) above, a new kind of pole, $(\mathfrak{k}^2-2\mathfrak{p}\cdot\mathfrak{k})^{-1}$, has been introduced, and has to be defined in some way. Since these poles are spurious, i.e., disappear when the two terms in the right side of Eq. (17) are added, it does not make any difference which way they are defined, provided it is done consistently. One could for instance take their principal values, but it seems easier to define them in the same way as the others, the ones that come in the propagation factors. Therefore when integrating over k_0 we shall take the contour of integration to go below the left-hand pole of $(\mathfrak{k}^2-2\mathfrak{p}\cdot\mathfrak{k})^{-1}$, and above the right-hand one, as usual. In subsequent integrations, in case a pole still appears, we shall assume that the absolute value of the time component of $\mathfrak{p}$, E_0, has a small negative imaginary part. These poles might then give imaginary contributions. But we expect the whole imaginary contribution from them to cancel at the end, since they are just artificial poles. Therefore we shall ignore it.

III. THE ONE-POTENTIAL LAMB SHIFT

The integration over $\mathfrak{k}$ in (26) can be performed by using the methods of the appendix of F II. First define I_1 and I_2, functions of $\mathbf{p}_1$ and $\mathbf{p}_2$, and I_3, function of $\mathbf{p}$, by

$$\Delta E_{11}=(e^2/\pi)\int\bar{\varphi}_0(\mathbf{p}_2)I_1\varphi_0(\mathbf{p}_1)d^3\mathbf{p}_1 d^3\mathbf{p}_2,$$

$$\Delta E_{12}=(e^2/\pi)\int\bar{\varphi}_0(\mathbf{p}_2)I_2\varphi_0(\mathbf{p}_1)d^3\mathbf{p}_1 d^3\mathbf{p}_2,$$

$$\Delta E_{13}+\Delta E_{14}=(e^2/\pi)\int\bar{\varphi}_0(\mathbf{p})I_3\varphi_0(\mathbf{p})d^3\mathbf{p}.$$

I_1, for instance, can be written

$$I_1=\frac{1}{i}\int\frac{2p_{2\mu}-\gamma_\mu k}{\mathfrak{k}^2-2\mathfrak{p}_2\cdot\mathfrak{k}}V\frac{2p_{1\mu}-k\gamma_\mu}{\mathfrak{k}^2-2\mathfrak{p}_1\cdot\mathfrak{k}}\frac{C(\mathfrak{k}^2)}{\mathfrak{k}^2}d^4\mathfrak{k}_F,$$

where $C(\mathfrak{k}^2)$ is a convergence factor, which will enable the integral to be performed at the limits of both small and large $\mathfrak{k}$. Specifically, we take

$$\mathfrak{k}^{-2}C(\mathfrak{k}^2)=(\mathfrak{k}^2-\lambda^2)^{-1}-(\mathfrak{k}^2-\Lambda^2)^{-1}=-\int_{\lambda^2}^{\Lambda^2}dL(\mathfrak{k}^2-L)^{-2}.$$

Next we define three expressions J_0, J_σ, and $J_{\sigma\tau}$ by

$$J_{(0;\sigma;\sigma\tau)}=\frac{1}{i}\int\frac{(1;k_\sigma;k_\sigma k_\tau)}{(\mathfrak{k}^2-2\mathfrak{p}_2\cdot\mathfrak{k})(\mathfrak{k}^2-2\mathfrak{p}_1\cdot\mathfrak{k})}\frac{C(\mathfrak{k}^2)}{\mathfrak{k}^2}d^4\mathfrak{k}_F.$$

These integrals are easily evaluated by the usual technique of combining denominators with auxiliary variables [F II, Eq. (14a)]. The result is

$$J_0=-\frac{1}{8}\int_0^1(dx/\mathfrak{p}_x^2)\ln(\mathfrak{p}_x^2/\lambda^2),$$

$$J_\sigma=-\frac{1}{4}\int_0^1(p_{x\sigma}/\mathfrak{p}_x^2)dx,$$

$$J_{\sigma\tau}=-\frac{1}{8}\int_0^1 dx\left[\frac{p_{x\sigma}p_{x\tau}}{\mathfrak{p}_x^2}-\frac{\delta_{\sigma\tau}}{2}\left(\ln\frac{\Lambda^2}{\mathfrak{p}_x^2}-\frac{1}{2}\right)\right],$$

where

$$\mathfrak{p}_x = x\mathfrak{p}_2 + (1-x)\mathfrak{p}_1, \tag{27}$$

and it has been assumed that Λ and λ are, respectively, very large and very small, compared to all momenta involved. I_1 is given in terms of J_0, J_σ, and $J_{\sigma\tau}$ by

$$I_1 = 4p_{2\mu}Vp_{1\mu}J_0 - 2(p_{2\mu}V\gamma_\sigma\gamma_\mu + \gamma_\mu\gamma_\sigma Vp_{1\mu})J_\sigma + \gamma_\mu\gamma_\sigma V\gamma_\tau\gamma_\mu J_{\sigma\tau}.$$

After summing over repeated indices, and making some algebraic manipulation in order to bring $\not{p}_2$ to the left and $\not{p}_1$ to the right of V, we find

$$I_1 = -\tfrac{3}{8}V - \tfrac{1}{2}\mathfrak{p}_2\cdot\mathfrak{p}_1 V\int_0^1 (dx/\mathfrak{p}_x^2)\ln(\mathfrak{p}_x^2/\lambda^2) + \tfrac{1}{4}V\int_0^1 dx\ln(\Lambda^2/\mathfrak{p}_x^2) + \tfrac{1}{2}\int_0^1 (dx/\mathfrak{p}_x^2) \cdot\{[(1-x)\mathfrak{p}_1^2 + x\mathfrak{p}_2^2 + 2\mathfrak{p}_2\cdot\mathfrak{p}_1]V + \not{p}_2V\not{p}_1 - E_0V\not{p}_x\}. \tag{28}$$

I_2 is computed in a similar fashion. The J's are the same as for I_1, with the additional simplification that the two momenta are the same and that there is no auxiliary variable x.

$$I_2 = -\frac{1}{i}V\int \frac{2p_\mu - \gamma_\mu \not{k}}{\mathfrak{k}^2 - 2\mathfrak{p}\cdot\mathfrak{k}}\frac{2p_\mu - \not{k}\gamma_\mu}{\mathfrak{k}^2 - 2\mathfrak{p}\cdot\mathfrak{k}}\frac{C(\mathfrak{k}^2)}{\mathfrak{k}^2}d^4\mathfrak{k}_F = V[\tfrac{1}{2}\ln(\mathfrak{p}^2/\lambda^2) - \ln(\Lambda^2/\mathfrak{p}^2)]. \tag{28a}$$

In I_2, $\mathfrak{p}$ has been written instead of $\mathfrak{p}_1$, since the result is symmetric between $\mathfrak{p}_1$ and $\mathfrak{p}_2$. One can, for instance, use $I_2/2$ with $\mathfrak{p}$ replaced by $\mathfrak{p}_1$, plus $I_2/2$ with $\mathfrak{p}$ replaced by $\mathfrak{p}_2$. For I_3 we find, after using Eq. (7),

$$I_3 = \frac{1}{i}\int \frac{2p_\mu - \gamma_\mu \not{k}}{\mathfrak{k}^2 - 2\mathfrak{p}\cdot\mathfrak{k}}\gamma_\mu\frac{C(\mathfrak{k}^2)}{\mathfrak{k}^2}d^4\mathfrak{k}_F - \frac{\pi}{e^2}\Delta m = \tfrac{3}{4}[(\not{p} - m)(\ln(\Lambda^2/\mathfrak{p}^2) + \tfrac{1}{2}) + m\ln(m^2/\mathfrak{p}^2)]. \tag{28b}$$

In I_3, we can replace $\not{p} - m$ by V, since it operates on φ_0, solution of Dirac's equation. When I_1, I_2, and I_3 are added together, we find that Λ disappears, as expected. After some rearranging, the result is

$$\Delta E_1 = (e^2/\pi)\int \bar{\varphi}_0(\mathbf{p}_2)(I_a + \cdots + I_f)\varphi_0(\mathbf{p}_1)d^3\mathbf{p}_1 d^3\mathbf{p}_2, \tag{29}$$

$$I_a = V\ln(\lambda/E_0)\left[\int_0^1 (\mathfrak{p}_1\cdot\mathfrak{p}_2/\mathfrak{p}_x^2)dx - 1\right], \tag{29a}$$

$$I_b = (V/2)\int_0^1 (dx/\mathfrak{p}_x^2)[(1-x)\mathfrak{p}_1^2 + x\mathfrak{p}_2^2 + 2\mathfrak{p}_1\cdot\mathfrak{p}_2] - 3V/2, \tag{29b}$$

$$I_c = (3V/8)\int_0^1 dx\ln[\mathfrak{p}_1^2\mathfrak{p}_2^2/(\mathfrak{p}_x^2)^2], \tag{29c}$$

$$I_d = -(V/2)\int_0^1 dx[(\mathfrak{p}_1\cdot\mathfrak{p}_2/\mathfrak{p}_x^2) - 1]\ln(\mathfrak{p}_x^2/E_0^2), \tag{29d}$$

$$I_e = \tfrac{1}{2}\int_0^1 (dx/\mathfrak{p}_x^2)(\not{p}_2V\not{p}_1 - E_0V\not{p}_x), \tag{29e}$$

$$I_f = (3m/4)\ln(m^2/\mathfrak{p}^2)\delta^3(\mathbf{p}_2 - \mathbf{p}_1) + 3V/2. \tag{29f}$$

It will now be shown that, except for a non-gauge-invariant part discussed later and which is canceled by a similar term in the many-potential Lamb shift, the terms of order $\alpha(Z\alpha)^4$ in ΔE_1 are given by the expectation value of the operator (1). Moreover, as discussed in the appendix, there are no corrections of order $\alpha(Z\alpha)^5$ to that.[19] Therefore, to the approximation desired, the first-order Lamb shift is just equal to what has already been calculated in references 3 to 6.

First, let us examine I_a. $\mathfrak{p}_x^2$ can be replaced by $x^2\mathfrak{p}_2^2 + (1-x)^2\mathfrak{p}_1^2 + 2x(1-x)\mathfrak{p}_1\cdot\mathfrak{p}_2$ and $\mathfrak{p}_1\cdot\mathfrak{p}_2 = \frac{1}{2}(\mathfrak{p}_2^2 + \mathfrak{p}_1^2 - \mathfrak{q}^2)$, where $\mathfrak{q} = \mathfrak{p}_2 - \mathfrak{p}_1$, so that

$$I_a = V\ln\frac{\lambda}{E_0}\int_0^1 dx \times \frac{[2x(1-x)-1]\mathfrak{q}^2 + (1-2x)(\mathfrak{p}_2^2 - \mathfrak{p}_1^2)}{2\mathfrak{p}_x^2}. \tag{30}$$

Since the most important momenta in the hydrogen atom are of order αm, the main contribution can be obtained by replacing $\mathfrak{p}_x^2 = E_0^2 - \mathbf{p}_x^2$ by E_0^2. Also $E_0 = m(1 - \text{order } \alpha^2)$ can be replaced by m. After integration over x, we obtain

$$I_a \simeq \tfrac{1}{3}(\mathfrak{q}^2/m^2)V\ln(m/\lambda). \tag{30a}$$

It is shown in the appendix that the error is actually of order $\alpha(Z\alpha)^6\ln Z\alpha$. The same reasoning can be applied to

$$I_b = \frac{V}{2}\int_0^1 dx\frac{[3x(1-x)-1]\mathfrak{q}^2 + (1-2x)(\mathfrak{p}_2^2 - \mathfrak{p}_1^2)}{\mathfrak{p}_x^2} \tag{31}$$

$$\simeq -\tfrac{1}{4}(\mathfrak{q}^2/m^2)V. \tag{31a}$$

For I_c, we write

$$I_c = \frac{3V}{8}\int_0^1 dx\ln\frac{(E_0^2 - \mathbf{p}_1^2)(E_0^2 - \mathbf{p}_2^2)}{(E_0^2 - \mathbf{p}_x^2)^2}, \tag{32}$$

and we can keep only the first term of an expansion in powers of $\mathbf{p}^2/E_0^2$:

$$I_c \simeq (3V/8)\int_0^1 dx(2\mathbf{p}_x^2 - \mathbf{p}_1^2 - \mathbf{p}_2^2)/E_0^2.$$

After replacing E_0 by m, and integrating over x, we obtain

$$I_c \simeq \tfrac{1}{8}(\mathfrak{q}^2/m^2)V. \tag{32a}$$

[19] This fact was first pointed out to the authors by N. M. Kroll.

That this is true including order $\alpha(Z\alpha)^5$, and also that I_d does not contribute in the same order, is shown in the appendix.

I_e can be transformed by writing its numerator

$$(\not p_2-m)V(\not p_1-m)+m[(\not p_2-m)V+V(\not p_1-m)] -E_0V(\not p_2-m)+m^2V-E_0mV,$$

and using Dirac's equation to replace the $\not p-m$ operators by V operators:

$$\begin{aligned}\Delta E_{1e}&=(e^2/\pi)\int\bar\varphi_0(\mathbf{p}_2)I_e\varphi_0(\mathbf{p}_1)d^3\mathbf{p}_2d^3\mathbf{p}_1\\&=(e^2/2\pi)\int d^3\mathbf{p}_f d^3\mathbf{p}_i d^3\mathbf{p}_2 d^3\mathbf{p}_1\int_0^1(dx/\mathfrak{p}_x^2)\\&\quad\cdot\bar\varphi_0(\mathbf{p}_f)[\beta V(\mathbf{p}_f-\mathbf{p}_2)V(\mathbf{p}_2-\mathbf{p}_1)V(\mathbf{p}_1-\mathbf{p}_i) \qquad (33)\\&\quad+(m-E_0x\beta)V(\mathbf{p}_f-\mathbf{p}_2)V(\mathbf{p}_2-\mathbf{p}_1)\delta^3(\mathbf{p}_1-\mathbf{p}_i)\\&\quad+(m-E_0(1-x)\beta)V(\mathbf{p}_2-\mathbf{p}_1)V(\mathbf{p}_1-\mathbf{p}_i)\delta^3(\mathbf{p}_f-\mathbf{p}_2)\\&\quad+m(\beta m-E_0)V(\mathbf{p}_2-\mathbf{p}_1)\delta^3(\mathbf{p}_f-\mathbf{p}_2)\delta^3(\mathbf{p}_1-\mathbf{p}_i)]\varphi_0(\mathbf{p}_i).\end{aligned}$$

The term with $3V$'s is of order $\alpha(Z\alpha)^6\ \ln Z\alpha$, since it involves essentially $\alpha(Z\alpha)^3$ times the expectation value of r^{-3}, with a cutoff for radii of the order of the Compton wavelength. For the other terms, we shall use again the approximation, justified in the appendix, of replacing $\mathfrak{p}_x^2$ by m^2. For brevity, we write the result in operator form:

$$\Delta E_{1e}\simeq(e^2/2\pi m^2)\langle\varphi_0^*|(2m\beta-E_0)V^2 +m(m-\beta E_0)V|\varphi_0\rangle. \qquad (33a)$$

This can be transformed, by use of the equations

$$\begin{aligned}\langle\varphi_0^*|\beta(\boldsymbol\alpha\cdot\mathbf{p}V-V\boldsymbol\alpha\cdot\mathbf{p})|\varphi_0\rangle&=-\langle\varphi_0^*|\boldsymbol\alpha\cdot\mathbf{p}\beta V+\beta V\boldsymbol\alpha\cdot\mathbf{p}|\varphi_0\rangle\\&=-\langle\varphi_0^*|(E_0-\beta m-V)\beta V+\beta V(E_0-\beta m-V)|\varphi_0\rangle\\&=2\langle\varphi_0^*|\beta V^2+(m-\beta E_0)V|\varphi_0\rangle.\end{aligned}$$

Therefore

$$\Delta E_{1e}\simeq(e^2/2\pi m^2)\langle\varphi_0^*|(m\beta-E_0)V^2 +(m/2)\beta(\boldsymbol\alpha\cdot\mathbf{p}V-V\boldsymbol\alpha\cdot\mathbf{p})|\varphi_0\rangle.$$

$(m\beta-E_0)V^2$ is negligible, within the accuracy desired, so that, going back to the momentum representation,

$$I_e\simeq(1/4m)\boldsymbol\alpha\cdot\mathbf{q}V(\mathbf{q})=(1/8m)(\boldsymbol\sigma\boldsymbol V-\boldsymbol V\boldsymbol\sigma). \qquad (34)$$

Finally, I_f can be replaced by

$$I_f=\tfrac{3}{4}m\delta^3(\mathbf{p}_2-\mathbf{p}_1)\int_0^1dx\left[\frac{2(\not p-m)}{m}-\frac{\not\mathfrak{p}-m^2}{\mathfrak{p}^2x+m^2(1-x)}\right].$$

By repeated use of the formula

$$\not\mathfrak{p}-m^2=(\not p-m)^2+2m(\not p-m),$$

the integrand in I_f can be written

$$\begin{aligned}&\frac{2x(\not p-m)(\not\mathfrak{p}-m^2)}{m[\mathfrak{p}^2x+m^2(1-x)]}-\frac{(\not p-m)^2}{\mathfrak{p}^2x+m^2(1-x)}\\&\quad=\frac{2x[2m(\not p-m)^2+(\not p-m)^3]}{m[\mathfrak{p}^2x+m^2(1-x)]}-\frac{(\not p-m)^2}{\mathfrak{p}^2x+m^2(1-x)}.\end{aligned}$$

Finally

$$I_f=\frac{3m}{4}\delta^3(\mathbf{p}_2-\mathbf{p}_1)\int_0^1\left[\frac{(4x-1)(\not p-m)^2}{\mathfrak{p}^2x+m^2(1-x)} +\frac{2x(\not p-m)^3}{m[\mathfrak{p}^2x+m^2(1-x)]}\right]dx. \qquad (35)$$

The first term in the bracket of (35) can be approximated by replacing its denominator by m^2. The error involved in this and in neglecting the second term is of order $\alpha(Z\alpha)^6\ \ln Z\alpha$, as shown in the appendix. Therefore, using Dirac's equation for the first term,

$$\Delta E_{1f}\simeq(3e^2/4\pi m)\langle\varphi_0^*|\beta V^2|\varphi_0\rangle. \qquad (36)$$

However, such a term cannot contribute on physical grounds, because its value depends on the gauge and would be changed if a constant were added to the potential. Indeed, it will be shown that this term is canceled by an equal and opposite one arising in the many-potential Lamb shift. This term being omitted, the first-order Lamb shift (29) is equal, within the accuracy desired, to the expectation value of e^2/π times the sum of the operators (30a), (31a), (32a), (34), that is exactly the expectation value of (1), so that no corrections of order $\alpha(Z\alpha)^5$ have been found here.

IV. THE MANY-POTENTIAL LAMB SHIFT

The many-potential Lamb shift is expression (25), where $\mathfrak{M}$ and $\mathfrak{M}^\dagger$ are given by (24) and (24a). It is interesting to note that the transversality condition

$$k_\mu M_\mu^\dagger=k_\mu M_\mu=0 \qquad (37)$$

is satisfied, so that the time component of a radiation operator can be written in terms of its space components by

$$M_0=\mathbf{k}\cdot\mathbf{M}/\omega. \qquad (38)$$

The emission operator (24a) can be transformed by using the identity

$$\gamma_0\not k\gamma_\mu=2\omega\gamma_\mu-2\delta_{0\mu}\not k+\not k\gamma_\mu\gamma_0 \qquad (39)$$

in its first term. One obtains

$$\begin{aligned}&M_\mu^\dagger=M_\mu^{\dagger\mathrm{I}}+M_\mu^{\dagger\mathrm{II}},\\&M_\mu^{\dagger\mathrm{I}}=[2p_{i\mu}/(\mathfrak{f}^2-2\mathfrak{p}_i\cdot\mathfrak{f})-2p_{f\mu}/(\mathfrak{f}^2-2\mathfrak{p}_f\cdot\mathfrak{f})\\&\qquad+\not k\gamma_\mu((\mathfrak{f}^2-2\mathfrak{p}_f\cdot\mathfrak{f})^{-1}\\&\qquad-(\mathfrak{f}^2-2\mathfrak{p}_i\cdot\mathfrak{f})^{-1})]\gamma_0V(\mathbf{p}_f-\mathbf{p}_i),\\&M_\mu^{\dagger\mathrm{II}}=2[(\delta_{0\mu}\not k-\omega\gamma_\mu)/(\mathfrak{f}^2-2\mathfrak{p}_i\mathfrak{f})]V(\mathbf{p}_f-\mathbf{p}_i). \qquad (40)\end{aligned}$$

The first two terms of $M_\mu^{\dagger I}$ are essentially the Schrödinger expression for the current, the last term is related to the contribution of the magnetic moment to the current. In a similar fashion we get

$$\begin{aligned} &M_\mu = M_\mu^{\rm I} + M_\mu^{\rm II}, \\ &M_\mu^{\rm I} = \gamma_0[-2p_{i\mu}/(\mathfrak{k}^2 - 2\mathfrak{p}_i\cdot\mathfrak{k}) + 2p_{f\mu}/(\mathfrak{k}^2 - 2\mathfrak{p}_f\cdot\mathfrak{k}) \\ &\qquad -\gamma_\mu \mathfrak{k}((\mathfrak{k}^2 - 2\mathfrak{p}_f\cdot\mathfrak{k})^{-1} \\ &\qquad -(\mathfrak{k}^2 - 2\mathfrak{p}_i\cdot\mathfrak{k})^{-1})]V(\mathbf{p}_f - \mathbf{p}_i), \\ &M_\mu^{\rm II} = 2[(\delta_{0\mu}\mathfrak{k} - \omega\gamma_\mu)/(\mathfrak{k}^2 - 2\mathfrak{p}_f\cdot\mathfrak{k})]V(\mathbf{p}_f - \mathbf{p}_i). \end{aligned} \tag{40a}$$

It is easy to see that $M_\mu^{\dagger II}$ and $M_\mu^{\rm II}$ taken alone satisfy also the transversality condition (37) or (38). The same is therefore true of $M_\mu^{\dagger I}$ and $M_\mu^{\rm I}$.

One advantage of the separation into two parts is that both $\mathfrak{M}^{\rm I}$ and $\mathfrak{M}^{\rm II}$ reduce to very simple (but very different) expressions in the nonrelativistic limit. We have for the spatial components of $\mathfrak{M}^{\rm I}$:

$$\begin{aligned} &M_j^{\rm I} \approx (p_{ij} - p_{fj})V(\mathbf{p}_f - \mathbf{p}_i)/m\omega \equiv R_j \quad (j=1,2,3), \\ &M_j^{\dagger I} \approx (p_{fj} - p_{ij})V(\mathbf{p}_f - \mathbf{p}_i)/m\omega \equiv R_j^* \\ &\qquad\qquad \text{(Hermitian conjugate)}, \end{aligned} \tag{41}$$

and the zero-component can be calculated by using the transversality condition,

$$R_0 = \mathbf{k}\cdot\mathbf{R}/\omega. \tag{42}$$

Similarly, the nonrelativistic limit for $\mathfrak{M}^{\rm II}$ is simply

$$M_j^{\rm II} \approx M_j^{\dagger II} \approx m^{-1}\gamma_j V(\mathbf{p}_f - \mathbf{p}_i) \equiv Q_j, \tag{43}$$

where again the transversality condition can be used to obtain Q_0.

The major obstacle to the evaluation of (25) is still the lack of a convenient expression for $K_+{}^V$. However, the splitting of the radiation operator into $\mathfrak{M}^{\rm I}$ and $\mathfrak{M}^{\rm II}$ will be very helpful: In fact, only in the part $\langle \mathfrak{M}^{\rm I} K_+{}^V \mathfrak{M}^{\rm I}\rangle$ will it be necessary to use the kernel in the Coulomb field, $K_+{}^V$; in all other contributions, it will be sufficient to replace $K_+{}^V$ by the propagation kernel for free electrons, $K_+{}^0$. Moreover, it will be shown that the main contribution to $\langle \mathfrak{M}^{\rm I} K_+{}^V \mathfrak{M}^{\rm I}\rangle$ arises from intermediate states of the electron with nonrelativistic energy so that both $K_+{}^V$ and $\mathfrak{M}^{\rm I}$ can be replaced by their nonrelativistic approximations which are simple. We thus get a separation into two main parts; in the first, the radiation operator is very simple and relativity can be neglected but the effect of the Coulomb field on the electron in the intermediate state must be taken into account. This part reduces essentially to the nonrelativistic Lamb shift; in the second part, the radiation operator is more complicated and must be treated relativistically, but the electrons may be considered as free in the intermediate state.

This section will serve two purposes. The first is to show that the separation into these two parts, nonrelativistic Coulomb and relativistic-free, is actually possible. In particular, it will be shown (in Subsection A) that $\langle \mathfrak{M}^{\rm II} K_+{}^V \mathfrak{M}^{\rm II}\rangle$ can be evaluated with free intermediate states, and it will be indicated (in *D*) that the same is true of the mixed term $\langle \mathfrak{M}^{\rm I} K_+{}^V \mathfrak{M}^{\rm II}\rangle$. It will further be shown (in *D*) that even in $\langle \mathfrak{M}^{\rm I} K_+{}^V \mathfrak{M}^{\rm I}\rangle$ the Coulomb potential needs to be taken into account only in nonrelativistic intermediate states, and that it is never required to take into account Coulomb potential and relativity simultaneously.

The second purpose is to evaluate those parts of the many-potential Lamb shift which are of order $\alpha(Z\alpha)^4$. They arise from $\langle \mathfrak{M}^{\rm II} K_+{}^V \mathfrak{M}^{\rm II}\rangle$ (Subsection A) and from $\langle \mathfrak{M}^{\rm I} K_+{}^V \mathfrak{M}^{\rm I}\rangle$ (Subsection B), but not from the mixed term. The $\mathfrak{M}^{\rm II}$ contribution will cancel the non-gauge-invariant term (36) from the one-potential Lamb shift, the $\mathfrak{M}^{\rm I}$ contribution provides the "nonrelativistic Lamb shift." In Subsection C, the relativistic correction to the Lamb shift is finally separated explicitly from the nonrelativistic terms: It is shown that the many-potential Lamb shift can be separated into terms of order $\alpha(Z\alpha)^4$ and terms of order $\alpha(Z\alpha)^5$; the former are the nonrelativistic terms evaluated in Subsections A and B; the latter represent the desired relativistic corrections and can be calculated with free intermediate states, and will be actually evaluated in Sec. V.

For our investigations, it will obviously be necessary to examine the propagation kernel $K_+{}^V$. For this purpose, we note that $K_+{}^V$ can be built up of the wave functions φ_n of the electron in the Coulomb field. For instance, in the nonrelativistic case, F I Eq. (3) gives

$$\begin{aligned} K_{NR}{}^V(\mathfrak{x}_2, \mathfrak{x}_1) &= \textstyle\sum_n \psi_n(\mathbf{x}_2)\psi_n^*(\mathbf{x}_1)\exp[-iE_n(t_2-t_1)] \\ &\qquad\qquad \text{for } t_2 - t_1 > 0, \\ &= 0 \qquad\qquad \text{for } t_2 - t_1 < 0, \end{aligned} \tag{44}$$

the summation being extended over all stationary states of the aton, with energies E_n. Going to momentum space,

$$\begin{aligned} &K_{NR}{}^V(E_0-\omega;\, \mathbf{p}_4,\, \mathbf{p}_3) \\ &= (2\pi)^{-3}\int \exp[-i\mathbf{p}_4\cdot\mathbf{x}_2 + i\mathbf{p}_3\cdot\mathbf{x}_1 + i(E_0-\omega)(t_2-t_1)] \\ &\qquad\qquad \cdot K_{NR}{}^V(\mathfrak{x}_2, \mathfrak{x}_1) d^3\mathbf{x}_2 d^3\mathbf{x}_1 d(t_2-t_1) \\ &= -i\textstyle\sum_n \varphi_n(\mathbf{p}_4)\varphi_n^*(\mathbf{p}_3)(E_n - E_0 + \omega)^{-1}, \end{aligned} \tag{45}$$

where φ_n is a momentum wave function and E_n is considered as having a small negative imaginary part. We shall refer to the states n as "intermediate states."

A. The Contribution $\langle \mathfrak{M}^{\rm II} K_+{}^V \mathfrak{M}^{\rm II}\rangle$

We shall first merely examine the intermediate states for the radiation operator $\mathfrak{M}^{\rm II}$; and for this purpose we shall replace $\mathfrak{M}^{\rm II}$ by the approximation Q_j, Eq. (43), with $j=1, 2, 3$. We shall disregard for the moment Q_0 and we shall use the nonrelativistic expression (45) for $K_+{}^V$. Later on (Eq. (50) ff.) we shall actually *calculate* $\langle \mathfrak{M}^{\rm II} K_+{}^V \mathfrak{M}^{\rm II}\rangle$, to order $\alpha(Z\alpha)^4$, and this will be done with the full expression for $\mathfrak{M}^{\rm II}$ and with the relativistic

propagation kernel K_+^0. Finally, we shall prove that the use of K_+^0 rather than K_+^V is justified.

With the approximations mentioned, the contribution of $\mathfrak{M}^{II}$, or rather $\mathbf{Q}$, to (25) becomes

$$\{M^{II}\}=\frac{ie^2}{\pi^2m^2}\sum_n\int\frac{V(\mathbf{s}_1)V(\mathbf{s}_2)k^2dkd\omega d^3\mathbf{p}_1d^3\mathbf{p}_2d^3\mathbf{s}_1d^3\mathbf{s}_2}{(\omega^2-k^2-\lambda^2)(E_n-E_0+\omega)}$$
$$\cdot\bar\varphi_0(\mathbf{p}_2)\gamma_\mu\varphi_n(\mathbf{p}_2-\mathbf{s}_2-\mathbf{k})\bar\varphi_n(\mathbf{p}_1+\mathbf{s}_1-\mathbf{k})\gamma_\mu\varphi_0(\mathbf{p}_1). \quad (46)$$

The integration over ω is carried out by giving a small negative imaginary part to both λ, the mass of the photon, and E_n, the energy of the intermediate state. Then

$$\{M^{II}\}=\frac{e^2}{\pi m^2}\sum_n\int\frac{V(\mathbf{s}_1)V(\mathbf{s}_2)k^2dkd^3\mathbf{p}_1d^3\mathbf{p}_2d^3\mathbf{s}_1d^3\mathbf{s}_2}{(k^2+\lambda^2)^{\frac{1}{2}}[E_n-E_0+(k^2+\lambda^2)^{\frac{1}{2}}]}$$
$$\cdot\bar\varphi_0(\mathbf{p}_2)\gamma_\mu\varphi_n(\mathbf{p}_2-\mathbf{s}_2-\mathbf{k})\bar\varphi_n(\mathbf{p}_1+\mathbf{s}_1-\mathbf{k})\gamma_\mu\varphi_0(\mathbf{p}_1). \quad (47)$$

Clearly, λ can be replaced by zero, and the main contribution comes from large values of k. This in turn means that the momentum of the electron in the intermediate state is essentially $-\mathbf{k}$ because $\mathbf{k}$ is in general much larger than those values of $\mathbf{s}$ and $\mathbf{p}$ for which φ_0 and $V(\mathbf{s})$ are large; these are both[20] of order $Z\alpha m$. The energy E_n is then nearly $(m^2+k^2)^{\frac{1}{2}}$.

The matrix element

$$(\bar\varphi_n(\mathbf{p}_1+\mathbf{s}_1-\mathbf{k})\gamma_\mu\varphi_0(\mathbf{p}_1))$$

is then of order

$$(k_\mu/m)(\bar\varphi_n\varphi_0)$$

if $k\ll m$, and of order $(\bar\varphi_n\varphi_0)$ if $k>m$. Since

$$\sum_n\varphi_n(\mathbf{p}_2-\mathbf{s}_2-\mathbf{k})\bar\varphi_n(\mathbf{p}_1+\mathbf{s}_1-\mathbf{k})$$
$$=\delta(\mathbf{p}_1+\mathbf{s}_1+\mathbf{s}_2-\mathbf{p}_2), \quad (47a)$$

we get approximately

$$\{M^{II}\}\sim(e^2/\pi m^2)\left[\int_0^m(k^2/m^2)dk+\int_m^\infty dk\right]$$
$$\cdot\int V(\mathbf{s}_1)V(\mathbf{q}-\mathbf{s}_1)\bar\varphi_0(\mathbf{p}_2)\varphi_0(\mathbf{p}_1)d^3\mathbf{p}_1d^3\mathbf{p}_2d^3\mathbf{s}_1, \quad (48)$$

with $\mathbf{q}=\mathbf{p}_2-\mathbf{p}_1=\mathbf{s}_1+\mathbf{s}_2$. The main contribution comes clearly from the relativistic region.[21]

Having now shown that the important intermediate states are all of high energy, we may in first approximation regard them as free. (See below for further proof.)

[20] What matters is actually

$$\chi(\mathbf{p}_3)=\int\varphi_0(\mathbf{p}_1)V(\mathbf{p}_3-\mathbf{p}_1)d^3\mathbf{p}_1,$$

with $\mathbf{p}_3=\mathbf{p}_1+\mathbf{s}_1$; and this can be shown to be large only for $\mathbf{p}_3$ of order $Z\alpha m$.

[21] In fact, the integral (48) diverges for large k. However, we shall show presently that when the full expression (40) for M^{II} is used rather than (43), the integrand is sufficiently reduced for large k to make the integral converge.

This enables us to go back to the full expression (40) for $\mathfrak{M}^{II}$ (including the component $\mu=0$), and to evaluate its contribution to (25) by the techniques of F II. To simplify this evaluation, $\mathfrak{p}_i$ and $\mathfrak{p}_f$ in the denominators of (40) and (40a) are replaced by the momentum vector for an electron at rest, $\mathfrak{p}=(m,0,0,0)$, (but in the arguments of $V(\mathbf{p}_f-\mathbf{p}_i)$, the correct momenta are retained); the error due to this approximation will be discussed below. We use the usual expression for the propagation kernel of free electrons:

$$K_+^0(E_0-\omega;\ \mathbf{p}_2-\mathbf{s}_2-\mathbf{k},\ \mathbf{p}_1+\mathbf{s}_1-\mathbf{k})$$
$$=\frac{i\delta^3(\mathbf{p}_1+\mathbf{s}_1+\mathbf{s}_2-\mathbf{p}_2)}{\mathfrak{r}-\mathfrak{k}-\mathfrak{m}}, \quad (48a)$$

where $\mathfrak{r}$ denotes the common value of the vectors $(E_0,\ \mathbf{p}_1+\mathbf{s}_1)$ and $(E_0,\ \mathbf{p}_2-\mathbf{s}_2)$ that is the intermediate 4-momentum. We replace E_0 simply by m, and call the intermediate 3-momentum $\mathbf{s}$. Therefore

$$\mathbf{p}_1+\mathbf{s}_1=\mathbf{p}_2-\mathbf{s}_2=\mathbf{s}, \quad (48b)$$

$$\mathfrak{r}=(m,\ \mathbf{s}). \quad (48c)$$

Then, the contribution of $\mathfrak{M}^{II}$ becomes

$$\{\mathfrak{M}^{II}\}\equiv\langle\mathfrak{M}^{II}K_+^0\mathfrak{M}^{II}\rangle=(e^2/\pi)\int d^3\mathbf{p}_1d^3\mathbf{p}_2d^3\mathbf{s}$$
$$\cdot\bar\varphi_0(\mathbf{p}_2)V(\mathbf{p}_2-\mathbf{s})N(\mathfrak{p},\ \mathbf{s})V(\mathbf{s}-\mathbf{p}_1)\varphi_0(\mathbf{p}_1), \quad (49)$$

with

$$N(\mathfrak{p},\ \mathbf{s})$$
$$=\frac{4}{i}\int\frac{(\delta_{0\mu}\mathfrak{k}-\omega\gamma_\mu)(\mathfrak{r}-\mathfrak{k}+\mathfrak{m})(\delta_{0\mu}\mathfrak{k}-\omega\gamma_\mu)}{(\mathfrak{k}^2-2\mathfrak{p}\cdot\mathfrak{k})^2(\mathfrak{k}^2-2\mathfrak{r}\cdot\mathfrak{k}-s^2)\mathfrak{k}^2}d^4\mathfrak{k}_F. \quad (49a)$$

The integral in (49a) is to be evaluated with $\mathfrak{p}=(m,0)$.

The integral (49a) can be evaluated for any $\mathbf{s}$, using the methods of Sec. V. The result can be expanded in a power series in $\mathbf{s}$, starting with a constant term and continuing with a term proportional to s^2. If the constant term is inserted into (49), one obtains a result of order $\alpha(Z\alpha)^4$, while the term in s^2 (and the higher terms) give results of order $\alpha(Z\alpha)^5$ or less. Moreover, the latter terms get their main contribution from *large* values of s, of order m, while the constant term comes mostly from small values of s, of order αZm. Therefore the exact momenta $\mathbf{p}_1$ and $\mathbf{p}_2$ contained in φ_0 and $\bar\varphi_0$ will matter for the constant term but not for the higher ones; for the latter terms, only the integral $\int\varphi_0(\mathbf{p}_1)d^3\mathbf{p}_1$ matters. This is the approximation which will be made in Sec. V, and this approximation is thus shown to be sufficient for all but the constant term.

We shall therefore need to evaluate here only the constant term, whose contribution to (49) will be denoted by $\{\mathfrak{M}^{II}\}_0$. This term is obtained by setting $\mathbf{s}=0$ in (49a), which simplifies this expression greatly and

makes it into

$$N(\mathfrak{p},0)$$
$$=\frac{4}{i}\int\frac{(\delta_{0\mu}\boldsymbol{k}-\omega\gamma_\mu)(\boldsymbol{p}-\boldsymbol{k}+m)(\delta_{0\mu}\boldsymbol{k}-\omega\gamma_\mu)}{(\mathfrak{f}^2-2\mathfrak{p}\cdot\mathfrak{f})^3\mathfrak{f}^2}d^4\mathfrak{f}_F$$
$$=4(\gamma_\sigma\delta_{0\mu}-\delta_{0\sigma}\gamma_\mu)(\boldsymbol{p}+m)(\gamma_\tau\delta_{0\mu}-\delta_{0\tau}\gamma_\mu)J^0{}_{\sigma\tau} \qquad (49b)$$
$$-4(\gamma_\sigma\delta_{0\mu}-\delta_{0\sigma}\gamma_\mu)\gamma_\omega(\gamma_\tau\delta_{0\mu}-\delta_{0\tau}\gamma_\mu)J^0{}_{\sigma\tau\omega},$$

where $J^0{}_{\sigma\tau}$ and $J^0{}_{\sigma\tau\omega}$ are two tensors given by the following integrals:

$$J^0{}_{(\sigma\tau;\sigma\tau\omega)}$$
$$=-i\int(k_\sigma k_\tau;\,k_\sigma k_\tau k_\omega)(\mathfrak{f}^2-2\mathfrak{p}\cdot\mathfrak{f})^{-3}\mathfrak{f}^{-2}d^4\mathfrak{f}_F. \qquad (49c)$$

Integrals of this sort will be calculated later, in Sec. V, and $J^0{}_{(\sigma\tau;\sigma\tau\omega)}$ is seen to be a particular case of $J_{(\sigma\tau;\sigma\tau\omega)}$ given by Eq. (75), where $\mathbf{s}$ is set equal to 0 and therefore $\mathfrak{r}$ replaced by $\mathfrak{p}$. From formulas (75a; 75b) for $J_{(\sigma\tau;\sigma\tau\omega)}$, one obtains immediately

$$J^0{}_{\sigma\tau}=\tfrac{1}{8}m^{-2}(\delta_{0\sigma}\delta_{0\tau}-\tfrac{1}{2}\delta_{\sigma\tau}),$$
$$J^0{}_{\sigma\tau\omega}=\tfrac{1}{16}m^{-1}[\delta_{0\sigma}\delta_{0\tau}\delta_{0\omega}$$
$$-\tfrac{1}{2}(\delta_{0\sigma}\delta_{\tau\omega}+\delta_{0\tau}\delta_{\sigma\omega}+\delta_{0\omega}\delta_{\sigma\tau})]. \qquad (49d)$$

Carrying these values back in (49b) and taking the expectation value for the state of rest of the electron, which in this case amounts simply to replacing γ_0 by $\mathbf{1}$, one finds

$$N(\mathfrak{p},0)=-3/4m. \qquad (50)$$

Thus the result for $\{\mathfrak{M}^{II}\}_0$ is

$$\{\mathfrak{M}^{II}\}_0=-(3\alpha/4\pi m)$$
$$\cdot\int\bar{\varphi}_0(\mathbf{p}_2)\varphi_0(\mathbf{p}_1)V(\mathbf{p}_2-\mathbf{s})V(\mathbf{s}-\mathbf{p}_1)d^3\mathbf{p}_1d^3\mathbf{p}_2d^3\mathbf{s}. \qquad (51)$$

To evaluate (51) we note that

$$\int d^3\mathbf{s}V(\mathbf{p}_2-\mathbf{s})V(\mathbf{s}-\mathbf{p}_1)=(2\pi)^{-3}\int V^2(\mathbf{x})e^{-i\mathbf{q}\cdot\mathbf{x}}d^3\mathbf{x}, \qquad (52)$$

which is the Fourier component $\mathbf{q}$ of the *square* of the spatial potential where $\mathbf{q}=\mathbf{p}_2-\mathbf{p}_1=\mathbf{s}_1+\mathbf{s}_2$. Changing (51) back to an integral in coordinate space, one obtains easily

$$\{\mathfrak{M}^{II}\}_0=-(3\alpha/4\pi m)\int\bar{\psi}_0(\mathbf{x})\psi_0(\mathbf{x})V^2(\mathbf{x})d^3\mathbf{x}$$
$$=-(3\alpha/4\pi m)\langle\varphi_0{}^*|\beta V^2|\varphi_0\rangle. \qquad (53)$$

This is a complete evaluation of $\{\mathfrak{M}^{II}\}_0$, subject to the justification of our approximations which we shall give presently. It will be noted that our result, (53), cancels exactly the term (36) from the one-potential Lamb shift and thus removes the lack of gauge invariance which that term introduced.

We have made two errors in this evaluation of $\mathfrak{M}^{II}$, namely (a) the replacement of $\mathfrak{p}_i$ and $\mathfrak{p}_f$ by $\mathfrak{p}$, corresponding to a free electron at rest, in the evaluation of the integral over $\mathfrak{f}$, and (b) the neglect of the potential in the intermediate states. Concerning (a), we note that the functions $\varphi_0(\mathbf{p}_1)$ and $V(\mathbf{s}_1)$ are large only if $\mathbf{p}_1$ and $\mathbf{s}_1$ are of order $Z\alpha$. (See also footnote 20.) Therefore $\mathfrak{p}_i$ and $\mathfrak{p}_f$ in (40) differ from $\mathfrak{p}$ by an amount of order $Z\alpha$ in the spatial components, and $(Z\alpha)^2$ in the time component. Clearly, the relative error introduced by this can only be of order:

(Correction to spatial momentum/
undisturbed momentum in intermediate state)^2

or

(Correction to energy/
unperturbed energy in intermediate state),

both of which are of order $(Z\alpha)^2/k^2$. Since the contribution of a given k to (49) goes as k^2dk for $k<m$, the error will be proportional to

$$(Z\alpha)^2\int_0^m dk=\mathcal{O}[(Z\alpha)^2]. \qquad (54)$$

Since the main term (53) is of order $\alpha(Z\alpha)^4$, an error of relative order $(Z\alpha)^2$ will be of absolute order $\alpha(Z\alpha)^6$ which has been consistently neglected in this paper.

To evaluate the error due to the neglect of the potential energy in the intermediate state, we imagine that one extra potential $V(\mathbf{s}_3)$ acts between $\mathfrak{M}^{III\dagger}$ and $\mathfrak{M}^{III}$. This introduces an extra factor of order

$$\int d^3\mathbf{s}_3Ze^2/s_3{}^2k, \qquad (55)$$

where k represents the additional energy denominator. Now $\mathbf{s}_3$ must again be of order αZ, in order that $\mathbf{p}_1+\mathbf{s}_1$ and $\mathbf{p}_2-\mathbf{s}_2$ be of that order, and therefore we get a correction of order

$$(Z\alpha)^2\int^m kdk\sim(Z\alpha)^2, \qquad (56)$$

which is again negligible.

We have thus shown that, in the evaluation of $\mathfrak{M}^{II}$, the intermediate state may indeed be regarded as free, which justifies the result (53).

B. The Contribution $\langle\mathfrak{M}^I\boldsymbol{K}_+{}^V\mathfrak{M}^{I\dagger}\rangle$

The contribution of $\mathfrak{M}^I$ from *relativistic* intermediate states is only of order $\alpha(Z\alpha)^5$. That $\mathfrak{M}^I$ for relativistic states is less important than $\mathfrak{M}^{II}$, is easily seen for the main part, $\mathfrak{R}$, of $\mathfrak{M}^I$ as follows: If we choose ω of order m in (41), then $\mathbf{R}$ differs from $\mathbf{Q}$, Eq. (43), by a factor

$(\mathbf{p}_f-\mathbf{p}_i)/m$ which is small (of order $Z\alpha$). The second part of $\mathfrak{M}^1$, Eq. (40), is similarly small.

On the other hand, $\mathbf{R}$ contains the factor ω in its denominator and can therefore be expected to be large in the *nonrelativistic* region. Here the potential must be taken into account in the intermediate states φ_n. However, for all intermediate states for which V matters, nonrelativistic wave functions may be used, and moreover, $\mathfrak{M}^1$ may be replaced by its nonrelativistic limit, $\mathfrak{R}$. The validity of this approximation will be proved in Subsection D.

We can make the further approximation of neglecting the recoil of the electron due to the emission of the virtual quantum. That is, we shall take the momentum of the electron in the intermediate state to be $\mathbf{p}_1+\mathbf{s}_1$ or $\mathbf{p}_2-\mathbf{s}_2$, rather than $\mathbf{p}_1+\mathbf{s}_1-\mathbf{k}$ or $\mathbf{p}_2-\mathbf{s}_2-\mathbf{k}$. This amounts to leaving out the retardation factor, $e^{i\mathbf{k}\cdot\mathbf{x}}$, in the spatial integral. The justification for this is that the momentum of the quantum, $\mathbf{k}$, is generally small compared with the other part of the electron momentum, $\mathbf{s}=\mathbf{p}_1+\mathbf{s}_1$. To see this, consider Eq. (60a), below: For a given energy E_n of the intermediate state, the main contribution comes from quanta whose energy k is of the order of E_n-E_0. But for nonrelativistic states, E_n-E_0 is of the order of magnitude of $s^2/2m$, where s is the predominant electron momentum in the intermediate state n. The quantum momentum k is therefore of the order of $s^2/2m$, which is small compared with the electron momentum s for nonrelativistic states, for which $s\ll m$ by definition. We are therefore justified in neglecting retardation, along with relativity, in our present first approximation.

Using the nonrelativistic kernel in the Coulomb field, (45), and neglecting retardation, the contribution of $\mathfrak{R}$, Eq. (41), to the many-potential Lamb shift (25) becomes:

$$\begin{aligned}\langle\mathfrak{R}K_{NR}{}^{V}\mathfrak{R}\rangle=&-\frac{e^2}{\pi i}\sum_n\int\frac{d^4\mathbf{f}_F d^3\mathbf{p}_1 d^3\mathbf{p}_2 d^3\mathbf{s}_1 d^3\mathbf{s}_2}{(\mathbf{f}^2-\lambda^2)(\omega+E_n-E_0)}\\&\cdot\varphi_0{}^*(\mathbf{p}_2)R_\mu(\mathbf{s}_2)\varphi_n(\mathbf{p}_2-\mathbf{s}_2)\\&\cdot\varphi_n{}^*(\mathbf{p}_1+\mathbf{s}_1)R_\mu{}^*(\mathbf{s}_1)\varphi_0(\mathbf{p}_1)\end{aligned}\tag{57}$$

$$=-\frac{e^2}{\pi i}\int\frac{d^4\mathbf{f}_F}{\mathbf{f}^2-\lambda^2}\sum_n\frac{\sum_\mu|\langle\varphi_n|R_\mu|\varphi_0\rangle|^2}{\omega+E_n-E_0}.\tag{57a}$$

According to (42), we can replace $\sum_\mu|\langle\varphi_n|R_\mu|\varphi_0\rangle|^2$ by

$$\omega^{-2}|\langle\varphi_n|\mathbf{R}|\varphi_0\rangle\cdot\mathbf{k}|^2-|\langle\varphi_n|\mathbf{R}|\varphi_0\rangle|^2.\tag{57b}$$

The integral on the angles of $\mathbf{k}$ will introduce a factor $\frac{1}{3}$ in the first term.

$$\langle\mathfrak{R}K_{NR}{}^{V}\mathfrak{R}\rangle=\frac{e^2}{\pi^2 i}\int_0^\infty k^2dk\int_{-\infty}^{+\infty}\frac{d\omega}{\mathbf{f}^2-\lambda^2}\times\sum_n\frac{|\langle\varphi_n|\mathbf{R}|\varphi_0\rangle|^2}{\omega+E_n-E_0}\left(1-\frac{1}{3}\frac{k^2}{\omega^2}\right).\tag{58}$$

$\langle\varphi_n|\mathbf{R}|\varphi_0\rangle$ is found from (41):

$$\begin{aligned}\langle\varphi_n|\mathbf{R}|\varphi_0\rangle&=(m\omega)^{-1}\langle\varphi_n|\mathbf{p}V-V\mathbf{p}|\varphi_0\rangle\\&=(m\omega)^{-1}\langle\varphi_n|\mathbf{p}H-H\mathbf{p}|\varphi_0\rangle\\&=-(m\omega)^{-1}(E_n-E_0)\langle\varphi_n|\mathbf{p}|\varphi_0\rangle,\end{aligned}\tag{59}$$

H being the Hamiltonian,

$$H=\mathbf{p}^2/2m+V.$$

$$\langle\mathfrak{R}K_{NR}{}^{V}\mathfrak{R}\rangle=(e^2/i\pi^2m^2)\sum_n(E_n-E_0)^2|\langle\varphi_n|\mathbf{p}|\varphi_0\rangle|^2\cdot\int_0^\infty k^2dk\int_{-\infty}^{+\infty}\frac{(1-k^2/3\omega^2)d\omega}{\omega^2(\omega^2-k^2-\lambda^2)(\omega+E_n-E_0)}.\tag{60}$$

The integration over ω is performed by giving a small negative imaginary part to both λ, the mass of the photon, and E_n, the energy of the intermediate state. The imaginary part of $\langle\mathfrak{R}K_{NR}{}^{V}\mathfrak{R}\rangle$ gives the lifetime of the state φ_0 for decay into φ_n by real photon emission, if there is a state $E_n<E_0$ which combines optically with state φ_0. Only the real part is wanted here. Integration[22] over ω gives for the k integral

$$\pi i\int_0^\infty k^2\omega_0{}^{-3}(\omega_0+E_n-E_0)^{-1}(1-k^2/3\omega_0{}^2)dk,\tag{60a}$$

where $\omega_0=(k^2+\lambda^2)^{\frac{1}{2}}$. The further integration over k yields, in the limit λ very small:

$$\langle\mathfrak{R}K_{NR}{}^{V}\mathfrak{R}\rangle=\frac{2e^2}{3\pi m^2}\sum_n|\langle\varphi_n|\mathbf{p}|\varphi_0\rangle|^2\times(E_n-E_0)\left(\ln\frac{\lambda}{2|E_n-E_0|}+\frac{5}{6}\right),\tag{61}$$

---

[22] The pole at $\omega=0$ is slightly disturbing. However, if the complete denominator in (40) had been used, the $2m\omega$ of the denominator in (41) would be replaced by

$$2\mathbf{p}\cdot\mathbf{f}-\mathbf{f}^2=2E_0\omega-2\mathbf{p}\cdot\mathbf{k}-\omega^2+\mathbf{k}^2,$$

resulting in two poles, located at

$$\omega=E_0\pm(\mathbf{k}^2-2\mathbf{p}\cdot\mathbf{k}+E_0{}^2)^{\frac{1}{2}}.$$

According to the convention made at the end of Sec. II, we are supposed to integrate on a contour passing below the left-hand pole (corresponding to the minus sign) and above the right-hand one. When we make our nonrelativistic approximation of considering $\mathbf{p}$, $\mathbf{k}$, and ω small compared to E_0, the left-hand pole is the one that tends toward $\omega=0$, while we neglect the contribution from the right-hand one. This shows that the pole $\omega=0$, arising from the first factor ω^2 in the denominator of (60), must be considered as lying above the contour of integration. Therefore, if the integral is carried out around the negative-imaginary halfplane (which is convenient anyway, since it also avoids getting a contribution from $\omega=E_0-E_n$), no contribution arises from this pole.

There remains the last term in (60), $k^2/3\omega^2$, arising from the elimination of the longitudinal waves by means of (42). The nature of the pole there can be understood if one uses for $M_\mu{}^1$, (40), an approximation slightly better than $\mathfrak{R}$, (41), namely

$$(p_{i\mu}/\mathfrak{p}_i\cdot\mathbf{f}-p_{f\mu}/\mathfrak{p}_f\cdot\mathbf{f})V(\mathbf{p}_f-\mathbf{p}_i).\quad(\mu=0,1,2,3).$$

This satisfies the transversality condition (37), and the 0 component is

$$E_0(\mathbf{p}_i-\mathbf{p}_f)\cdot\mathbf{k}(E_0\omega-\mathbf{p}_i\cdot\mathbf{k})^{-1}(E_0\omega-\mathbf{p}_f\cdot\mathbf{k})^{-1}V(\mathbf{p}_f-\mathbf{p}_i),$$

which reduces to $\mathbf{k}\cdot\mathbf{R}/\omega$ for $\mathbf{p}$ very small. But in this form it is evident that the pole in the last term of (60) is of the same nature as the one treated in the first part of this footnote, and therefore gives no contribution for the contour chosen.

that is, precisely the nonrelativistic Lamb shift (2), the relationship between K and λ being given by (3).

C. Explicit Separation of Relativistic Lamb Shift

We have now evaluated the contributions of order $\alpha(Z\alpha)^4$, arising from the interactions $\mathfrak{R}$ and $\mathfrak{M}^{II}$. We shall now consider the *difference* between the full contribution from $\mathfrak{M}$, Eq. (40), and the contributions from $\mathfrak{R}$ and $\mathfrak{M}^{II}$ as calculated in Subsections A and B. This difference is of order $\alpha(Z\alpha)^5$ because it consists of the relativistic contributions to $\mathfrak{M}^{I}$ and $\mathfrak{M}^{II}$ which were shown to be of this order in Subsections B and A, and of the interference term between $\mathfrak{M}^{I}$ and $\mathfrak{M}^{II}$ which will be discussed at the end of D. Both types of terms arise mainly from intermediate states of relativistic energy. For such states, the influence of the Coulomb potential may be neglected, being of relative order $Z\alpha$ and hence absolute order $\alpha(Z\alpha)^6$. (For further discussion, see Subsection D.) It is therefore permissible to calculate the *difference*

$$D\equiv\langle\mathfrak{M}K_+{}^{V}\mathfrak{M}\rangle-\langle\mathfrak{R}K_+{}^{V}\mathfrak{R}\rangle-\langle\mathfrak{M}^{II}K_+{}^{V}\mathfrak{M}^{II}\rangle_0, \quad (62)$$

by replacing the kernel K^V by K^0, the propagation kernel for free electrons, thus:

$$D=\langle\mathfrak{M}K_+{}^{0}\mathfrak{M}\rangle-\langle\mathfrak{R}K_+{}^{0}\mathfrak{R}\rangle-\langle\mathfrak{M}^{II}K_+{}^{0}\mathfrak{M}^{II}\rangle_0. \quad (62a)$$

Thus, at last, we have realized the purpose of our separation of the Lamb shift into various parts: The difference D can be calculated using the usual methods of F II.

Our aim is, of course, to calculate the total many-potential Lamb shift, which may be written:

$$\langle\mathfrak{M}K_+{}^{V}\mathfrak{M}\rangle=\langle\mathfrak{R}K_+{}^{V}\mathfrak{R}\rangle+\langle\mathfrak{M}^{II}K_+{}^{V}\mathfrak{M}^{II}\rangle_0+D. \quad (62b)$$

Of the terms on the right-hand side, D will be calculated later on the basis of Eq. (62a). The second term on the right has been evaluated in (53); the subscript 0 in this term denotes, as it did in (51) to (53), that only the leading term (first term), (50), of the expansion of (49a) in powers of s^2 is being considered. The first term in (62b), however, has not been actually evaluated in Subsection B because we have used there nonrelativistic rather than relativistic intermediate states in the Coulomb field. However, we shall show in Subsection D that the Coulomb field and the relativity correction need not be taken into account *simultaneously* for the same intermediate state; therefore we may write

$$\langle\mathfrak{R}K_+{}^{V}\mathfrak{R}\rangle=\langle\mathfrak{R}K_{NR}{}^{V}\mathfrak{R}\rangle+\langle\mathfrak{R}K_+{}^{0}\mathfrak{R}\rangle-\langle\mathfrak{R}K_{NR}{}^{0}\mathfrak{R}\rangle. \quad (63)$$

Here $\langle\mathfrak{R}K_{NR}{}^{V}\mathfrak{R}\rangle$ denotes the contribution of $\mathfrak{R}$ as evaluated in Subsection B, i.e., with the intermediate states treated in the Coulomb field but nonrelativistically. $\langle\mathfrak{R}K_+{}^{0}\mathfrak{R}\rangle$ is evaluated with free relativistic intermediate states, and $\langle\mathfrak{R}K_{NR}{}^{0}\mathfrak{R}\rangle$ with free *nonrelativistic* intermediate states. Inserting (63) and (62a) into (62b), the term $\langle\mathfrak{R}K_+{}^{0}\mathfrak{R}\rangle$ cancels[23] and we obtain

$$\langle\mathfrak{M}K_+{}^{V}\mathfrak{M}\rangle=\langle\mathfrak{M}^{II}K_+{}^{V}\mathfrak{M}^{II}\rangle_0+\langle\mathfrak{R}K_{NR}{}^{V}\mathfrak{R}\rangle+D', \quad (64)$$

$$D'=\langle\mathfrak{M}K_+{}^{0}\mathfrak{M}\rangle-\langle\mathfrak{R}K_{NR}{}^{0}\mathfrak{R}\rangle-\langle\mathfrak{M}^{II}K_+{}^{0}\mathfrak{M}^{II}\rangle_0 \equiv A-B-C. \quad (65)$$

The first term in (64) cancels (36), as was remarked after (53); the second is the ordinary nonrelativistic Lamb shift (61); both terms are strictly of order $\alpha(Z\alpha)^4$ and do not contain any component of order $\alpha(Z\alpha)^5$. Therefore *D' represents the relativistic correction which is now completely separated from the nonrelativistic parts.* From our previous discussion it follows that D' is of order $\alpha(Z\alpha)^5$. It can be evaluated by taking exclusively free intermediate states, i.e., the relativistic correction has been reduced to an expression in which the potential acts twice and only twice, once with the emission and once with the absorption of the virtual quantum.

Since D' arises entirely from high-energy intermediate states, a further simplification is possible, namely D' can be evaluated with the initial and final state of the electron assumed to be free states of momentum zero. Indeed, using the same argument as for error (a) in Subsection A, we find that the error due to this assumption is expected to be only of relative order $(Z\alpha)^2$.

We shall understand from now on that all three terms in (65) are to be evaluated with zero momentum in initial and final state. The first term in (65), A, will be evaluated in Sec. V. In this section, we shall still calculate the last two terms in (65). The contribution of $\mathfrak{M}^{II}$, with initial and final momentum set equal to zero, is obtained from (51) by considering $\mathbf{p}_1$ and $\mathbf{p}_2$ small compared to $\mathbf{s}$. Now, from the definition (8a),

$$\int\varphi_0(\mathbf{p}_1)d^3\mathbf{p}_1=(2\pi)^{\frac{1}{2}}\psi_0(0), \quad (66)$$

i.e., the wave function in coordinate space at the origin, and from (8b),

$$V(\pm\mathbf{s})=-Ze^2/2\pi^2s^2. \quad (66a)$$

Thus the approximation to (51) for $\mathbf{p}_1=\mathbf{p}_2=0$ becomes

$$C=-6\alpha(Z\alpha)^2(\pi m)^{-1}\psi_0{}^2(0)\int ds/s^2. \quad (67)$$

This integral clearly diverges at $s=0$, but this is just what will be needed to cancel a similar divergence in term A (see Sec. V).

Next we must calculate B, i.e., the contribution of $\mathfrak{R}$, evaluated with free nonrelativistic intermediate states and with initial and final state having momentum zero. To do this, we replace in Eq. (57) (E_n-E_0) by $s^2/2m$; then the summation over n can be carried out and gives $\delta(\mathbf{p}_1+\mathbf{s}_1-\mathbf{p}_2+\mathbf{s}_2)$, which permits evaluation

[23] This is fortunate because this term would diverge for large energy of the intermediate state.

of $\int d^3\mathbf{s}_2$. Further, since $\mathbf{p}_2 \approx \mathbf{p}_1 \approx 0$, we may set $\mathbf{s}_2 = -\mathbf{s}_1$ in R_μ; we also drop the subscript in $\mathbf{s}_1$. From (41), $-\mathbf{R} = \mathbf{R}^* = \mathbf{s}V(\mathbf{s})/(m\omega)$, and we obtain:

$$B = \frac{e^2}{i\pi m^2}\left|\int \varphi_0(\mathbf{p})d^3\mathbf{p}\right|^2 \int \frac{V^2(\mathbf{s})[s^2-(\mathbf{s}\cdot\mathbf{k})^2/\omega^2]d^4\mathbf{f}_F d^3\mathbf{s}}{\omega^2(\omega+s^2/2m)(\mathbf{f}^2-\lambda^2)}$$

$$= \frac{8\alpha(Z\alpha)^2}{\pi}|\psi_0(0)|^2\int_0^\infty \frac{ds}{s^2}\frac{4}{3m}\left(\ln\frac{m\lambda}{s^2}+\frac{5}{6}\right). \tag{68}$$

To obtain the last line, the integration over ω and $\mathbf{k}$ has been carried out in analogy with that leading from (60) to (61). The integral (68), just as (67), diverges for $s=0$, but just as in that case, this divergent term will exactly cancel a similar divergence in contribution A of (65).

D. Further Discussion of Approximations

We shall now show (1) that the potential has been taken into account in all intermediate states for which this is required, and (2) that it is not necessary for any intermediate state to consider potential and relativity simultaneously.

We have already shown in Subsection A that the potential in the intermediate states need not be taken into account for $\langle \mathfrak{M}^{II} K_+{}^V \mathfrak{M}^{II}\rangle$. The mixed terms, $\langle \mathfrak{M}^{II} K_+{}^V \mathfrak{M}^{I}\rangle$ and $\langle \mathfrak{M}^{I} K_+{}^V \mathfrak{M}^{II}\rangle$ will be discussed briefly at the end of this Subsection. We shall therefore now take up once more the term $\langle \mathfrak{M}^{I} K_+{}^V \mathfrak{M}^{I}\rangle$ (see also Subsection B) and shall examine in detail how strongly the contribution of intermediate states of various energies is influenced by the Coulomb potential in the intermediate state.

As has been shown already above, Eq. (57), for any given nonrelativistic intermediate state E_n, the main contribution comes from quanta k which are of order $E_n - E_0$ and are therefore small compared to the predominant *momentum* in the intermediate state; since $\mathbf{p}_i$ is mostly of order $Z\alpha$, it follows that $\mathbf{p}_n$ is essentially equal to $\mathbf{s}_1$, i.e., the momentum in the intermediate state comes mainly from the potential acting in R_μ.

The relative effect of the potential V on the wave function φ_n of the intermediate state is measured by the well-known quantity Ze^2/hv which, in our units, is $Z\alpha/p_n \approx Z\alpha/s$. The contribution of $\mathfrak{R}$ for *free* intermediate states is given by (68); and since $\psi^2(0) \approx (Z\alpha)^3$ (see end of Sec. V), the order of magnitude of (68) is given by

$$B \sim Z^5\alpha^6 \int ds/s^2. \tag{69}$$

The Coulomb effect on the intermediate state wave function gives, as we have seen, a correction of relative order $Z\alpha/s$ which therefore amounts to

$$B_c \sim Z^6\alpha^7 \int ds/s^3. \tag{70}$$

We are considering in this paper contributions of the order $Z^5\alpha^6$. In order to get a contribution of this order or greater from (70), we must consider values of s smaller than $(Z\alpha)^{\frac{1}{2}}$, or excitation energies less than $\frac{1}{2}Z\alpha m = 137$ Rydberg, which is intermediate between the Rydberg energy $\frac{1}{2}(Z\alpha)^2 m$ and the rest mass of the electron. We thus find that, in our order of approximation, the Coulomb potential needs to be taken into account only for intermediate states of less energy than $137Z$ Rydberg; in particular, it does not need to be considered for states of relativistic energy.

This consideration already shows that it is presumably unnecessary to apply a relativity correction simultaneously with a Coulomb correction. To put this argument in quantitative form, we note that the relativity correction for an intermediate state of momentum $\mathbf{p}_n$ is of relative order $(p_n/m)^2$, or in our case about s^2/m^2. Therefore the relativity correction to the Coulomb effect (70) is

$$B_{cr} \sim Z^6\alpha^7 \int ds/s \sim Z^6\alpha^7 \ln Z\alpha, \tag{71}$$

which is negligible in our approximation.

In Subsection B, *retardation* was left out along with relativity. We must therefore show that also retardation does not need to be considered simultaneously with the potential. Retardation changes the momentum of the electron by $k \sim s^2/2m$, and since the "unretarded" electron momentum is $\mathbf{s}$, the relative change is of order s/m. Since the vector $\mathbf{k}$ may have any direction relative to $\mathbf{s}$, the effect of retardation will be of order $k^2/s^2 \sim (s/m)^2$. This is exactly the same order as the relativistic correction, and is therefore negligible for all those intermediate states for which the potential must be taken into account.

We now examine whether it was justified to replace $\mathfrak{M}^{I}$ by $\mathfrak{R}$ for the evaluation of the effect of the Coulomb potential in the intermediate state. The difference $\mathfrak{M}^{I} - \mathfrak{R}$ is of order

$$k\gamma_\mu(\mathfrak{p}_f - \mathfrak{p}_i)\cdot\mathfrak{f}V/(2m^2\omega^2), \tag{71a}$$

and its ratio to R_μ is therefore about

$$k\gamma_\mu k/(m\omega) \sim k_\mu/m, \tag{72}$$

because $k \approx \omega$. Since we have already seen that the important values of k are of order $E_n - E_0 \sim s^2$, the contribution of $\mathfrak{M}^{I} - \mathfrak{R}$, for intermediate states for which the Coulomb forces matter, is of the same order as the relativistic correction to $\mathfrak{R}$ and hence negligible.

Finally, it can be shown by direct evaluation that the cross term between $\mathfrak{M}^{I}$ and $\mathfrak{M}^{II}$ does not give a contribution for low-energy intermediate states. This is

due to the fact that the matrix elements of $\mathfrak{M}^{II}$ to non-relativistic states are extremely small. The cross term gives altogether a result of order $\alpha^6 Z^5$. The potential correction to the cross term can again be shown to be of order $Z^6\alpha^7 \log Z\alpha$.

V. RELATIVISTIC CORRECTIONS TO THE MANY-POTENTIAL LAMB SHIFT

According to (65) and other discussions in the preceding section, the corrections of order $\alpha(Z\alpha)^5$ to the Lamb shift are given by $A-B-C$. B is given by (68) and C by (67). A is given by (25) where the electron is assumed at rest initially and finally, E_0 is replaced by m, and the intermediate state is taken to be a free state, that is K_+^{ν} is replaced by the free kernel (48a)

$$i(\mathfrak{r}-\boldsymbol{k}-m)^{-1}\delta^3(\mathbf{s}_2+\mathbf{s}_1),$$

where $\mathfrak{r}$ is defined by (48c). Therefore

$$A=8\pi^3|\psi(0)|^2\frac{e^2}{\pi i}\int d^3\mathbf{s}\,{}_0\!\left\langle\int M_\mu\frac{1}{\mathfrak{r}-\boldsymbol{k}-m}M_\mu^\dagger\frac{d^4\mathfrak{k}_P}{\mathfrak{k}^2-\lambda^2}\right\rangle_0,$$

where ${}_0\langle\cdots\rangle_0$ means that the expectation value is taken for the state of rest of the electron. Using for $M_\mu^\dagger$ expression (24a), with $\mathfrak{p}_i=(m,0)=\mathfrak{p}$, $\mathfrak{p}_f=\mathfrak{r}$, and using for M_μ expression (24) with $\mathfrak{p}_i=\mathfrak{r}$, $\mathfrak{p}_f=\mathfrak{p}$, this can also be written

$$A=8\alpha(Z\alpha)^2\pi^{-1}|\psi(0)|^2\int_0^\infty ds(T_1+T_2+T_3)/s^2, \tag{73}$$

$$T_1={}_0\!\left\langle\frac{1}{i}\int\frac{(2p_\mu-\gamma_\mu\boldsymbol{k})\beta(\mathfrak{r}-\boldsymbol{k}+m)\beta(2p_\mu-\boldsymbol{k}\gamma_\mu)}{(\mathfrak{k}^2-2\mathfrak{p}\cdot\mathfrak{k})^2(\mathfrak{k}^2-2\mathfrak{r}\cdot\mathfrak{k}-s^2)(\mathfrak{k}^2-\lambda^2)}d^4\mathfrak{k}_P\right\rangle_0,$$

$$T_3={}_0\!\left\langle\frac{1}{i}\int\frac{\beta(2r_\mu-\gamma_\mu\boldsymbol{k})(\mathfrak{r}-\boldsymbol{k}+m)(2r_\mu-\boldsymbol{k}\gamma_\mu)\beta}{(\mathfrak{k}^2-2\mathfrak{r}\cdot\mathfrak{k})^2(\mathfrak{k}^2-2\mathfrak{r}\cdot\mathfrak{k}-s^2)(\mathfrak{k}^2-\lambda^2)}d^4\mathfrak{k}_P\right\rangle_0,$$

$$T_2={}_0\!\left\langle-\frac{1}{i}\int\frac{\beta(2r_\mu-\gamma_\mu\boldsymbol{k})(\mathfrak{r}-\boldsymbol{k}+m)\beta(2p_\mu-\boldsymbol{k}\gamma_\mu)+(2p_\mu-\gamma_\mu\boldsymbol{k})\beta(\mathfrak{r}-\boldsymbol{k}+m)(2r_\mu-\boldsymbol{k}\gamma_\mu)\beta}{(\mathfrak{k}^2-2\mathfrak{p}\cdot\mathfrak{k})(\mathfrak{k}^2-2\mathfrak{r}\cdot\mathfrak{k})(\mathfrak{k}^2-2\mathfrak{r}\cdot\mathfrak{k}-s^2)(\mathfrak{k}^2-\lambda^2)}d^4\mathfrak{k}_P\right\rangle_0.$$

All poles are to be resolved by giving m and λ small negative imaginary parts. The integrals can be evaluated by using the methods in the appendix of F II. As an illustration, we consider T_1 in some detail.

$$\begin{aligned}T_1={}_0\langle&4m^2\beta(\mathfrak{r}+m)\beta J_0-2[\gamma_\mu\gamma_\sigma\beta(\mathfrak{r}+m)\beta p_\mu\\&+p_\mu\beta(\mathfrak{r}+m)\beta\gamma_\sigma\gamma_\mu+2m^2\beta\gamma_\sigma\beta]J_\sigma+[2\gamma_\mu\gamma_\sigma\beta\gamma_\tau\beta p_\mu\\&+2p_\mu\beta\gamma_\tau\beta\gamma_\sigma\gamma_\mu+\gamma_\mu\gamma_\sigma\beta(\mathfrak{r}+m)\beta\gamma_\tau\gamma_\mu]J_{\sigma\tau}\\&-\gamma_\mu\gamma_\sigma\beta\gamma_\tau\beta\gamma_\omega\gamma_\mu J_{\sigma\tau\omega}\rangle_0,\end{aligned} \tag{74}$$

with the definitions

$$J_{(0;\sigma;\sigma\tau;\sigma\tau\omega)}=\frac{1}{i}\int\frac{(1;k_\sigma;k_\sigma k_\tau;k_\sigma k_\tau k_\omega)d^4\mathfrak{k}_P}{(\mathfrak{k}^2-2\mathfrak{p}\cdot\mathfrak{k})^2(\mathfrak{k}^2-2\mathfrak{r}\cdot\mathfrak{k}-s^2)(\mathfrak{k}^2-\lambda^2)}$$

$$=\frac{6}{i}\int_0^1(1-y)dy\int_0^1 x^2dx$$

$$\times\int\frac{(1;k_\sigma;k_\sigma k_\tau;k_\sigma k_\tau k_\omega)d^4\mathfrak{k}_P}{[\mathfrak{k}^2-2x\mathfrak{p}_y\cdot\mathfrak{k}-xys^2-(1-x)\lambda^2]^4}, \tag{75}$$

$$\mathfrak{p}_y=y\mathfrak{r}+(1-y)\mathfrak{p}=(m,ys),$$

$$\mathfrak{p}_y^2=m^2-y^2s^2.$$

The integral over $\mathfrak{k}$ is performed using formula (13a) of the appendix of F II, and also the following one:

$$\frac{24}{i}\int\frac{k_\sigma k_\tau k_\omega d^4\mathfrak{k}_P}{(\mathfrak{k}^2-2\mathfrak{p}\cdot\mathfrak{k}-\Delta)^4}=\frac{p_\sigma p_\tau p_\omega}{(\mathfrak{p}^2+\Delta)^2}-\frac{1}{2}\frac{p_\sigma\delta_{\tau\omega}+p_\tau\delta_{\sigma\omega}+p_\omega\delta_{\sigma\tau}}{\mathfrak{p}^2+\Delta}.$$

The result is

$$J_0=\frac{1}{4}\int_0^1(1-y)dy\int_0^1 dx\frac{x^2}{[x^2\mathfrak{p}_y^2+xys^2+(1-x)\lambda^2]^2},$$

$$J_\sigma=\frac{1}{4}\int_0^1(1-y)dy\int_0^1 dx\frac{xp_{y\sigma}}{(x\mathfrak{p}_y^2+ys^2)^2},$$

$$J_{\sigma\tau}=\frac{1}{4}\int_0^1(1-y)dy\int_0^1 dx\left[\frac{x^2p_{y\sigma}p_{y\tau}}{(x\mathfrak{p}_y^2+ys^2)^2}-\frac{1}{2}\frac{x\delta_{\sigma\tau}}{x\mathfrak{p}_y^2+ys^2}\right], \tag{75a}$$

$$J_{\sigma\tau\omega}=\frac{1}{4}\int_0^1(1-y)dy\int_0^1 dx\left[\frac{x^3p_{y\sigma}p_{y\tau}p_{y\omega}}{(x\mathfrak{p}_y^2+ys^2)^2}-\frac{x^2}{2}\frac{p_{y\sigma}\delta_{\tau\omega}+p_{y\tau}\delta_{\sigma\omega}+p_{y\omega}\delta_{\sigma\tau}}{x\mathfrak{p}_y^2+ys^2}\right]. \tag{75b}$$

λ has been put equal to 0 whenever this does not introduce a divergence. For all J's, except J_0, the integral

over x is easy to perform. For J_0, we can first compute an easier integral, where we replace $\mathfrak{p}_y^2$ by m^2:

$$\int_0^1 x^2dx\int_0^1 \frac{(1-y)dy}{[x^2m^2+xys^2+(1-x)\lambda^2]^2}$$
$$=-\frac{1}{m^4\sigma^2}\left[\ln\frac{\lambda}{m}+\frac{1+\sigma^2}{\sigma^2}\ln(1+\sigma^2)-\ln\sigma^2\right], \quad (76)$$

where

$$\sigma=s/m, \quad (77)$$

and $\lambda/m\ll 1$ has been assumed. In the difference between this and J_0,

$$\int_0^1(1-y)dy\int_0^1 x^2dx[\{x^2\mathfrak{p}_y^2+xys^2+(1-x)\lambda^2\}^{-2}$$
$$-\{x^2m^2+xys^2+(1-x)\lambda^2\}^{-2}],$$

λ can be put equal to 0, yielding

$$\int_0^1(1-y)dy(ys^2)^{-1}[(\mathfrak{p}_y^2+ys^2)^{-1}-(m^2+ys^2)^{-1}]$$
$$=\int_0^1 y(1-y)dy(\mathfrak{p}_y^2+ys^2)^{-1}(m^2+ys^2)^{-1}. \quad (78)$$

The sum of (76) and (78) is $4J_0$. The J's have the coefficients appearing in formula (74), and the expectation value for the rest state of the electron has to be taken. For this, the following formulas are useful, in addition to those in the appendix of F II:

$${}_0\langle\beta M\beta\rangle_0={}_0\langle M\beta\rangle_0={}_0\langle\beta M\rangle_0={}_0\langle M\rangle_0,$$

M being any operator.

$$\mathfrak{p}=\beta m,$$
$${}_0\langle\mathfrak{p}\rangle_0={}_0\langle\mathfrak{p}_y\rangle_0={}_0\langle\mathfrak{r}\rangle_0=m,$$
$$\mathfrak{p}\cdot\mathfrak{p}_y=\mathfrak{p}\cdot\mathfrak{r}=m^2,$$
$$\mathfrak{r}\cdot\mathfrak{p}_y=m^2-ys^2,$$
$$\mathfrak{ABC}+\mathfrak{CBA}=2(\mathfrak{A}\cdot\mathfrak{B}\mathfrak{C}+\mathfrak{B}\cdot\mathfrak{C}\mathfrak{A}-\mathfrak{A}\cdot\mathfrak{C}\mathfrak{B}),$$
$$\mathfrak{ABA}=2\mathfrak{A}\cdot\mathfrak{B}\mathfrak{A}-\mathfrak{A}^2\mathfrak{B}.$$

Take for instance the coefficient of J_0:

$${}_0\langle 4m^2\beta(\mathfrak{r}+m)\beta\rangle_0=4m^2\,{}_0\langle\mathfrak{r}+m\rangle_0=8m^3.$$

Coefficient of J_0/p_{y0}:

$$-2\,{}_0\langle\mathfrak{p}\mathfrak{p}_y\beta(\mathfrak{r}+m)+(\mathfrak{r}+m)\beta\mathfrak{p}_y\mathfrak{p}+2m^2\mathfrak{p}_y\rangle_0$$
$$=-2m\,{}_0\langle\mathfrak{p}_y\beta\mathfrak{r}+\mathfrak{r}\beta\mathfrak{p}_y\rangle_0-2m^2\,{}_0\langle\mathfrak{p}_y\beta+\beta\mathfrak{p}_y\rangle_0-4m^3$$
$$=-2m\,{}_0\langle 2m\mathfrak{r}+2m\mathfrak{p}_y-2\mathfrak{p}_y\cdot\mathfrak{r}\beta\rangle_0-8m^3$$
$$=-16m^3+4m(m^2-ys^2)=-4m(3m^2+ys^2)$$

The other coefficients are computed in the same way. The result is, for T_1:

$$2mT_1=-\frac{4}{\sigma^2}\left(\ln\frac{\lambda}{m}+\frac{1+\sigma^2}{\sigma^2}\ln(1+\sigma^2)-\ln\sigma^2\right)$$
$$+\int_0^1(1-y)dy\left\{\frac{4y^3}{[y+(1-y)u^2](y+u^2)}\right.$$
$$+\left[\frac{-6}{(1-u^2)^2}+\frac{1}{y}\frac{u^4-5u^2}{(1-u^2)^3}+\frac{2}{y^2}\frac{u^6+5u^4}{(1-u^2)^4}\right]\ln\frac{y+(1-y)u^2}{u^2}$$
$$+\left[y\frac{9-u^2}{1-u^2}+2\frac{u^2(3-u^2)}{(1-u^2)^2}+\frac{1}{y}\frac{u^6-5u^4}{(1-u^2)^3}\right]\frac{1}{y+(1-y)u^2}$$
$$\left.+\frac{3u^2-1}{(1-u^2)^2}-\frac{1}{y}\frac{3u^4+5u^2}{(1-u^2)^3}\right\}, \quad (79)$$

where σ is defined by (77) and $u=y\sigma$. Although powers of $(1-u^2)=\mathfrak{p}_y^2/m^2$ appear in the denominators, this is only an apparent pole and the whole expression stays finite for $u=1$.

T_3 is similar to T_1, only simpler. The denominators are combined according to

$$(\mathfrak{f}^2-2\mathfrak{r}\cdot\mathfrak{f})^{-2}(\mathfrak{f}^2-2\mathfrak{r}\cdot\mathfrak{f}-s^2)^{-1}(\mathfrak{f}^2-\lambda^2)^{-1}$$
$$=6\int_0^1(1-y)dy\int_0^1 x^2dx[\mathfrak{f}^2-2x\mathfrak{r}\cdot\mathfrak{f}-xys^2-(1-x)\lambda^2]^{-4}.$$

$$2mT_3=-\frac{4}{\sigma^2}\ln\frac{\lambda}{m}+\left[\frac{4}{\sigma^2}+\frac{7}{2}\frac{1}{1-\sigma^2}-\frac{1}{2}\frac{1}{(1-\sigma^2)^2}\right]\ln\sigma^2$$
$$+\frac{1}{\sigma^2}\left(\frac{6}{\sigma^2}+\frac{3}{2}\right)\ln|1-\sigma^2|+\frac{2}{\sigma^2}-\frac{1}{2}\frac{1}{1-\sigma^2}. \quad (80)$$

Here again, the powers of $(1-\sigma^2)=\mathfrak{r}^2/m^2$ in the denominators do not constitute a pole. Poles arise in the integrations over the auxiliary variables x and y, and the way of going around them is defined by giving m a small negative imaginary part. Only the real contribution from these integrations is written above. For each integration, the imaginary contribution can be dropped after we have made sure that no real term can arise in it from a pole in subsequent integrations.

For T_2, an additional auxiliary variable z has to be introduced:

$$[(\mathfrak{f}^2-2\mathfrak{p}\cdot\mathfrak{f})(\mathfrak{f}^2-2\mathfrak{r}\cdot\mathfrak{f})(\mathfrak{f}^2-2\mathfrak{r}\cdot\mathfrak{f}-s^2)(\mathfrak{f}^2-\lambda^2)]^{-1}$$
$$=6\int_0^1 ydy\int_0^1 x^2dx\int_0^1 dz$$
$$\times[\mathfrak{f}^2-2x\mathfrak{p}_y\cdot\mathfrak{f}-xyzs^2-(1-x)\lambda^2]^{-4}.$$

If the integration over z is performed immediately after integrating on $\mathfrak{f}$, we get expressions very similar

to T_1:

$$2mT_2=-\frac{4}{\sigma^3}\int_0^1\frac{dx}{[x^2+(1-x)\lambda^2/m^2]^{\frac{1}{2}}}\ln\frac{x\sigma+[x^2+(1-x)\lambda^2/m^2]^{\frac{1}{2}}}{|x\sigma-[x^2+(1-x)\lambda^2/m^2]^{\frac{1}{2}}|}$$
$$+\int_0^1 dy\left\{\left[\frac{8y^2}{u^2(1-u^2)}+\frac{12y}{(1-u^2)^2}-\frac{4u^2}{(1-u^2)^2}-\frac{2u^2(1+u^2)}{y(1-u^2)^3}\right]\ln\frac{y+(1-y)u^2}{u^2}\right.$$
$$\left.+4u^2(1-u^2)^{-2}+2\sigma^{-2}\ln[(1+y(1-y)\sigma^2)/|1-y^2\sigma^2|]\right\}. \quad (81)$$

This is only the real part. The imaginary part has been dropped, because it cannot give any real term in subsequent integrations. There is a real pole, this time, for $u=y\sigma=1$. But if one subtracts from $2mT_2$ the following expression:

$$\int_0^1 dy u^2(12y^2-2y-2)(1-u^2)^{-1}, \quad (82)$$

one cancels the principal part of the pole. Moreover the contribution of the subtracted part (82) in later integrations is 0.

The last step is to compute

$$\int_0^\infty \sigma^{-2}d\sigma 2m(T_1+T_2+T_3) \quad (83)$$

according to (73). But, since this integral is divergent for small σ, its "small-σ limit" will be subtracted from each term before integrating. By small-σ limit is meant the terms in σ^{-4}, σ^{-2}, $\sigma^{-4}\ln\sigma^2$, $\sigma^{-2}\ln\sigma^2$, in the expansion for small σ, after (79), (80), (81) have been divided by σ^2. The integral is then convergent. It will be seen at the end that the small-σ limit cancels with terms B and C of (65).

We find for instance, for $2mT_3$, from (80), in the small-σ limit:

$$-4\sigma^{-4}\ln(\lambda/m)+4\sigma^{-4}\ln\sigma^2+3\sigma^{-2}\ln\sigma^2-4\sigma^{-4}-5\sigma^{-2} \quad (84)$$

$$-\frac{4}{\sigma^5}\int_0^1\frac{dx}{[x^2+(1-x)\lambda^2/m^2]^{\frac{1}{2}}}\left[\frac{2x\sigma}{[x^2+(1-x)\lambda^2/m^2]^{\frac{1}{2}}+\frac{2}{3}}\frac{x^3\sigma^3}{[x^2+(1-x)\lambda^2/m^2]^{\frac{1}{2}}}\right]$$
$$=8(\sigma^{-4}+\tfrac{1}{3}\sigma^{-2})\ln(\lambda/m)+(4/3)\sigma^{-2}\ (\text{assuming } \lambda/m\ll 1) \quad (88)$$

and no contribution to (83), by virtue of

$$\int_0^\infty\frac{d\sigma}{\sigma^5}\left[\ln\frac{1+k\sigma}{|1-k\sigma|}-2k\sigma-\tfrac{2}{3}k^3\sigma^3\right]=0.$$

We note that λ appears only in the small-σ limit, which is to be canceled against B and C, and this supports the consistency of our calculation. For the last term in the curly bracket of (81), we find, in the small-σ limit:

$$\sigma^{-2}; \quad (89)$$

and the contribution to (83) is then

$$\int_0^\infty \sigma^{-2}d\sigma(2mT_3-\text{small-}\sigma\text{ limit})=-(11/8)\pi^2, \quad (85)$$

by making use of the integrals:

$$\int_0^\infty d\sigma[\sigma^{-6}\ln|1-\sigma^2|+\sigma^{-4}+\tfrac{1}{2}\sigma^{-2}]=0,$$
$$\int_0^\infty d\sigma[\sigma^{-4}\ln|1-\sigma^2|+\sigma^{-2}]=0,$$
$$\text{p.v.}\int_0^\infty d\sigma(1-\sigma^2)^{-1}=0$$
$$\int_0^\infty d\sigma(1-\sigma^2)^{-1}\ln\sigma^2=-\pi^2/2$$
$$\text{p.v.}\int_0^\infty d\sigma(1-\sigma^2)^{-2}\ln\sigma^2=-\pi^2/4$$

(p.v. means principal value). In the same way the first line of (79) gives, in the small-σ limit:

$$-4\sigma^{-4}\ln(\lambda/m)+4\sigma^{-4}\ln\sigma^2-4\sigma^{-4}-2\sigma^{-2}; \quad (86)$$

and the contribution to (83) is then

$$8\pi/15. \quad (87)$$

The first term of (81) gives for the small-σ limit:

and the contribution to (83) is then

$$-\pi^2/2^6. \quad (90)$$

For the remainder of (79) and (81), the small-σ limit is

$$-8\sigma^{-4}\ln\sigma^2-(3+8/3)\sigma^{-2}\ln\sigma^2$$
$$+8\sigma^{-4}+(5+7/18)\sigma^{-2}. \quad (91)$$

The contribution to (83) of this last part is easily evaluated by using y and $u=y\sigma$ as new variables of integration, so that

$$\int_0^\infty\sigma^{-2}d\sigma\int_0^1 dy\cdots$$

becomes

$$\int_0^\infty u^{-2}du\int_0^1 ydy\cdots.$$

This change of variables presents no difficulty since there is no pole in the integrand for either $\sigma=0$ or $y\sigma=1$, after subtraction of the small-σ limit and of (82). One can first transform the term containing $\ln[(y+(1-y)u^2)/u^2]$ by an integration by parts, such as

$$\int_0^1 y^n dy \ln\frac{y+(1-y)u^2}{u^2}=\frac{(1-u^2)}{n+1}\int_0^1\frac{1-y^{n+1}}{y+(1-y)u^2}dy$$

(for $n\geq 0$).

Then the integration over u is carried on first, by taking a contour running along the real axis and closed by an infinite semicircle above. The only singularities are poles inside the contour, for $u=i[y/(1-y)]^{\frac{1}{2}}$ and $u=iy^{\frac{1}{2}}$. Then the residues are integrated over y. We find

$$-8\pi/15+\pi^2(5/2-3/128-\tfrac{1}{2}\ln 2) \qquad (92)$$

as the contribution of that part to (83).

The reader can now check that the sum of the various parts, (84), (86), (88), (89), (91), of the small-σ limit is equal to $B+C$. Adding the contributions (85), (87), (90), (92), we obtain the corrections to the many-potential Lamb sift:

$$D'=4\alpha(Z\alpha)^2\pi m^{-2}|\psi(0)|^2(1+11/128-\tfrac{1}{2}\ln 2) \qquad (93)$$

which is the result previously reported.[24] For the $2S$ state, $|\psi(0)|^2=(Z\alpha m)^3/8\pi$. For the $2P$ state, it is 0, in this approximation.

VI. VACUUM POLARIZATION TERM

To the desired approximation, the electrons forming the loop in diagram 1(c) can be considered free. This is because, due to Furry's theorem, the next correction to this is a diagram which contains a loop with 4 vertices, which is expected to be of order $\alpha(Z\alpha)^6$. Diagram 1(c) with free electrons in the loop is known[25] to be equivalent to the potential

$$\frac{e^2}{4\pi m^2}V(q)\int_0^1 du\frac{u^2(1-u^2/3)q^2}{1+(1-u^2)q^2/4m^2},$$

where q is the magnitude of the 3-momentum transferred. This is after charge has been renormalized. To get the shift due to vacuum polarization effects, we just have to take the expectation value of this potential. Moreover, we can use the Schrödinger approximation to the wavefunction, which is, for the $2S$ state,

$$\frac{(Z\alpha m)^{5/2}}{\pi}\frac{p^2-\frac{1}{4}(Z\alpha m)^2}{[p^2+\frac{1}{4}(Z\alpha m)^2]^3}.$$

That this is correct can be easily shown by the methods developed in the appendix. The integration involved in taking the expectation value is straightforward, if one does not integrate over u until the end, and yields the result:

$$-\frac{\alpha(Z\alpha)^4}{8\pi}m\int_0^1 u^2\left(1-\frac{u^2}{3}\right)\frac{1+\frac{1}{8}(Z\alpha)^2(1-u^2)}{[1+\frac{1}{2}Z\alpha(1-u^2)^{\frac{1}{2}}]^4}du.$$

Expanding in powers of $Z\alpha$, we first find

$$-(1/30\pi)\alpha(Z\alpha)^4m,$$

which is the well-known contribution of about -27 megacycles. The next term is

$$(5/384)\alpha(Z\alpha)^5m. \qquad (94)$$

The same calculation for the $2P$ state gives a result of order $\alpha(Z\alpha)^6$, which we do not consider.

VII. RESULT AND DISCUSSION

Adding (93) and (94), we find all $\alpha(Z\alpha)^5$ corrections to the Lamb shift:[26]

$$\tfrac{1}{2}\alpha(Z\alpha)^5m(1+11/128-\tfrac{1}{2}\ln 2+5/192).$$

There is a question of determining whether we should use the mass of the free electron m_0, or the reduced mass in the hydrogen atom, $m_r=m_0(1+m_0/M)^{-1}$. This question is of no consequence with the present accuracy (theoretical and experimental). However, it could be settled after the very small corrections of order $Z\alpha m/M$ with respect to the main Lamb shift, coming from the 2-body aspect of the problem, have been calculated.[27] At the present time, the most logical course to take is to use m_r in $|\psi(0)|^2$ and m_0 everywhere else. This has also proved to be the best way for the main term of the Lamb shift. Therefore, we write the $\alpha(Z\alpha)^5$ corrections in the form

$$\begin{aligned}&\tfrac{1}{2}\alpha(Z\alpha)^5(m_r^3/m_0^2)(1+11/128-\tfrac{1}{2}\ln 2+5/192)\\&\quad=\alpha(Z\alpha)^3Ry_H[1-m_0/(M+m_0)]^2\\&\qquad\qquad\times(1+11/128-\tfrac{1}{2}\ln 2+5/192)\\&\quad=7.130\text{ Mc/sec.}\end{aligned}$$

The result for the whole Lamb shift, and the comparison with experiment, has been given in a recent paper by Salpeter.[28] The discrepancy between theory and experiment has now been reduced to 0.6 Mc/sec, with the experimental value still higher than the theoretical. With the discrepancy reduced to such a small amount, there can no longer be any doubt that the general principles of quantum electrodynamics, especially the idea of renormalization, are correct. In pr-a ticular, it can now be considered as experimentally established that the vacuum polarization term (-27 Mc/sec) must be included.

It is also interesting to compare the remaining discrepancy of 0.6 Mc/sec with the total energy of the $n=2$ state, 8×10^5 Mc/sec. This means that there

[24] M. Baranger, Phys. Rev. **84**, 866 (1951).

[25] For instance, see E. A. Uehling, Phys. Rev. **48**, 55 (1935), Eq. (14), and integrate by parts over u.

[26] The same result has been obtained by Karplus, Klein, and Schwinger, Phys. Rev. **86**, 288 (1952).

[27] See E. E. Salpeter, Phys. Rev. **89**, 92 (1953). We are indebted to Professor Salpeter for the remarks of this paragraph.

[28] See reference in footnote 27.

cannot be an over-all deviation from the Coulomb field between proton and electron of as much as 1 part in a billion.

It is very unlikely that the small remaining discrepancy of 0.6 Mc/sec can be attributed to experimental error since the given experimental accuracy is 0.1 Mc/sec. In principle, the discrepancy could be attributed to a small deviation from the Coulomb field at small distances, due to the mesonic structure of the proton; a repulsion of 80 kev over a sphere of radius e^2/mc^2 would give the desired effect. However, it is known that the neutron-electron interaction amounts to only 4 kev (attractive) over this radius, and it is reasonable to assume that the proton-electron interaction (apart from the Coulomb force) has about the same magnitude. Moreover, if the discrepancy was of nuclear origin, one would expect it to have different values for hydrogen and deuterium. But the experimental value of the difference between the hydrogen and deuterium Lamb shifts is in good agreement with the present theoretical value.[28]

On the other hand, it does not seem to us unreasonable that the discrepancy could be explained by the relativistic correction of next order. We have shown in Sec. IV that the ratio of this correction to the correction calculated in this paper, is of order $\alpha Z \ln(\alpha Z)$, i.e., 1/28. Since our result is 7 Mc/sec, the next order is expected to be about 0.25 Mc/sec. Our result in this paper has also shown that higher order effects are apt to have a larger numerical coefficient, and only twice the coefficient is needed to give 0.5 Mc/sec.

The authors are happy to acknowledge several illuminating discussions with Professor N. M. Kroll.

APPENDIX

In this appendix, we give a method for computing the corrections to the one-potential Lamb shift, in order $\alpha(Z\alpha)^6$. Because these corrections contain many non-gauge-invariant terms, and an infrared catastrophy, which are supposed to cancel against contributions from the many-potential Lamb shift, they are rather uninteresting as long as similar corrections for the many-potential part are not available. For this reason, we shall not carry out the calculations, but limit ourselves to showing that terms of order $\alpha(Z\alpha)^5$ do not arise.

We can consider two kinds of corrections: (1) Corrections arising when (29) is evaluated exactly, but with the approximate nonrelativistic Schrödinger wavefunction in place of $\varphi_0(\mathbf{p})$, (2) Corrections arising from the use of the exact Dirac wave function.

The first kind can be obtained in closed form, by using integrals such as

$$K_{ab}=\Re\int\frac{d^3\mathbf{p}_1 d^3\mathbf{p}_2}{(\mathbf{p}_1^2+a^2)(\mathbf{p}_2^2+b^2)\mathbf{q}^2(E^2-\mathbf{p}_x^2)}$$
$$=\frac{2\pi^4}{E^2+(1-x)a^2+xb^2}\ln\frac{(E^2+a^2)(E^2+b^2)}{(a+b)^2[E^2+((1-x)a+xb)^2]},$$

$$J_{a^3b}=\Re\int\frac{d^3\mathbf{p}_1 d^3\mathbf{p}_2}{(\mathbf{p}_1^2+a^2)^2(\mathbf{p}_2^2+b^2)(E^2-\mathbf{p}_x^2)}$$
$$=-\frac{2\pi^4}{ax}\frac{(1-x)a+xb}{E^2+[(1-x)a+xb]^2},$$

where $\Re$ means the real part, and

$$\mathbf{q}=\mathbf{p}_2-\mathbf{p}_1,$$
$$\mathbf{p}_x=x\mathbf{p}_2+(1-x)\mathbf{p}_1.$$

From these two integrals and a similar one, J_{ab^3}, one can, by differentiating with respect to a and b and taking various combinations, obtain the values of all other integrals of this sort. In particular, we shall need

$$K_{21}=\Re\int\frac{d^3\mathbf{p}_1 d^3\mathbf{p}_2}{(\mathbf{p}_1^2+a^2)^2(\mathbf{p}_2^2+a^2)\mathbf{q}^2(E^2-\mathbf{p}_x^2)}$$
$$=\frac{2\pi^4(1-x)}{(E^2+a^2)^2}\ln\frac{E^2+a^2}{4a^2}+\frac{2\pi^4}{E^2+a^2}\left(\frac{1}{2a^2}-\frac{x}{E^2+a^2}\right),$$

$$K_{12}=\Re\int\frac{d^3\mathbf{p}_1 d^3\mathbf{p}_2}{(\mathbf{p}_1^2+a^2)(\mathbf{p}_2^2+a^2)^2\mathbf{q}^2(E^2-\mathbf{p}_x^2)}$$
$$=\frac{2\pi^4 x}{(E^2+a^2)^2}\ln\frac{E^2+a^2}{4a^2}+\frac{2\pi^4}{E^2+a^2}\left(\frac{1}{2a^2}-\frac{1-x}{E^2+a^2}\right),$$

$$K_{22}=\Re\int\frac{d^3\mathbf{p}_1 d^3\mathbf{p}_2}{(\mathbf{p}_1^2+a^2)^2(\mathbf{p}_2^2+a^2)^2\mathbf{q}^2(E^2-\mathbf{p}_x^2)}$$
$$=\pi^4\left[\frac{2x(1-x)}{(E^2+a^2)^3}\left(2\ln\frac{E^2+a^2}{4a^2}+3\right)\right.$$
$$\left.-\frac{2}{(E^2+a^2)^3}+\frac{1-x(1-x)}{a^2(E^2+a^2)^2}+\frac{1}{4a^4(E^2+a^2)}\right],$$

$$K_{20}=\Re\int\frac{d^3\mathbf{p}_1 d^3\mathbf{p}_2}{(\mathbf{p}_1^2+a^2)^2\mathbf{q}^2(E^2-\mathbf{p}_x^2)}=-\frac{2\pi^4}{x}\frac{1}{E^2+a^2},$$

$$J_{21}=\Re\int\frac{d^3\mathbf{p}_1 d^3\mathbf{p}_2}{(\mathbf{p}_1^2+a^2)^2(\mathbf{p}_2^2+a^2)(E^2-\mathbf{p}_x^2)}=-\frac{2\pi^4}{x}\frac{1}{E^2+a^2},$$

$$J_{12}=\Re\int\frac{d^3\mathbf{p}_1 d^3\mathbf{p}_2}{(\mathbf{p}_1^2+a^2)(\mathbf{p}_2^2+a^2)^2(E^2-\mathbf{p}_x^2)}=-\frac{2\pi^4}{1-x}\frac{1}{E^2+a^2},$$

$$J_{22}=\Re\int\frac{d^3\mathbf{p}_1 d^3\mathbf{p}_2}{(\mathbf{p}_1^2+a^2)^2(\mathbf{p}_2^2+a^2)^2(E^2-\mathbf{p}_x^2)}=\frac{\pi^4}{a^2}\frac{E^2-a^2}{(E^2+a^2)^2}.$$

For the sake of simplicity, let us consider the shift of the $1S$ level. The treatment of the $2S$ level is quite similar. For the $1S$ level, we have the normalized Schrödinger wave function

$$\pi^{-1}(8Z^5\alpha^5m^5)^{\frac{1}{2}}(\mathbf{p}^2+Z^2\alpha^2m^2)^{-2}.$$

Taking for instance I_b, Eq. (31), and using (8b),

$$I_b=-\frac{Z\alpha\beta}{4\pi^2}\int_0^1 dx\left[\frac{1-3x(1-x)}{\mathfrak{p}_x^2}-\frac{(1-2x)(\mathbf{p}_2^2-\mathbf{p}_1^2)}{\mathfrak{p}_x^2\mathbf{q}^2}\right],$$

we obtain for the corresponding energy-shift:

$$\Delta E_{1b}=(\alpha/\pi)\int\bar{\varphi}_0(\mathbf{p}_2)I_b\varphi_0(\mathbf{p}_1)d^3\mathbf{p}_2d^3\mathbf{p}_1$$

$$=-2\pi^{-5}\alpha(Z\alpha)^6m^5\int_0^1 dx[(1-3x(1-x))J_{22}(E_0,Z\alpha m)-(1-2x)(K_{21}-K_{12})_{(E_0,Z\alpha m)}],$$

where $J_{22}(E_0, Z\alpha m)$ means that, in the expression for J_{22}, we replace E by E_0 and a by $Z\alpha m$. The first term of the expansion of ΔE_{1b} in powers of $Z\alpha$ is of order $\alpha(Z\alpha)^4$, and the next one is of order $\alpha(Z\alpha)^6\ln(Z\alpha)$. No term of order $\alpha(Z\alpha)^5$ occurs, due to the fact that J_{22}, K_{21}, K_{12}, etc.$\cdots$ are functions of a^2 only, not of a. I_a can be dealt with in the same way, while I_c can be written

$$I_c=\tfrac{3}{8}V\int_0^1 dx\int_{E_0^2}^\infty d(E^2)[2(E^2-\mathbf{p}_x^2)^{-1}-(E^2-\mathbf{p}_1^2)^{-1}-(E^2-\mathbf{p}_2^2)^{-1}],$$

giving an energy shift

$$\Delta E_{1c}=(\alpha/\pi)\int\varphi_0(\mathbf{p}_2)I_c\varphi_0(\mathbf{p}_1)d^3\mathbf{p}_1d^3\mathbf{p}_2$$

$$=-\tfrac{3}{2}\pi^{-5}\alpha(Z\alpha)^6m^5\int_0^1 dx\int_{E_0^2}^\infty d(E^2)$$

$$\times[2K_{22}(E,Z\alpha m)-K_{22}{}^0(E,Z\alpha m)-K_{22}{}^1(E,Z\alpha m)],$$

where x has been put equal to 0 and 1, respectively, in $K_{22}{}^0$ and $K_{22}{}^1$. The bracket is equal to

$$2\pi^4x(1-x)\left[\frac{2}{(E^2+a^2)^3}\left(2\ln\frac{E^2+a^2}{4a^2}+3\right)-\frac{1}{a^2(E^2+a^2)^2}\right]_{(a=Z\alpha m)},$$

and there again no term of order $\alpha(Z\alpha)^5$ is found. For the next term I_d, we write

$$I_d=\tfrac{1}{2}V\int_0^1 dx[(\mathfrak{p}_1\cdot\mathfrak{p}_2/\mathfrak{p}_x^2)-1]\int_{E_0^2}^\infty[(E^2-\mathfrak{p}_x^2)^{-1}-E^{-2}]d(E^2)$$

$$=-(Z\alpha\beta/8\pi^2\mathbf{q}^2)\int_0^1 dx\int_{E_0^2}^\infty d(E^2)\{[1-2x(1-x)]\mathbf{q}^2-(1-2x)(\mathbf{p}_2^2-\mathbf{p}_1^2)\}\{(E^2-E_0^2)^{-1}[(E_0^2-\mathbf{p}_x^2)^{-1}-(E^2-\mathbf{p}_x^2)^{-1}]-E^{-2}(E_0^2-\mathbf{p}_x^2)^{-1}\},$$

$$\Delta E_{1d}=-\pi^{-5}\alpha(Z\alpha)^6m^5\int_0^1 dx\int_{E_0^2}^\infty d(E^2)\cdot\left\{[1-2x(1-x)]\left[\frac{1}{E^2-E_0^2}(J_{22}(E_0)-J_{22}(E))-\frac{1}{E^2}J_{22}(E_0)\right]-(1-2x)\left[\frac{1}{E^2-E_0^2}(K_{21}(E_0)-K_{12}(E_0)-K_{21}(E)+K_{12}(E))-\frac{1}{E^2}(K_{21}(E_0)-K_{12}(E_0))\right]\right\}_{(a=Z\alpha m)}.$$

$K_{21}-K_{12}$ is of order $\ln a$, while the $1/a^2$ factor in J_{22} actually disappears, so that ΔE_{1d} is of order $\alpha(Z\alpha)^6\times\ln(Z\alpha)$, in the Schrödinger approximation.

Before investigating I_s, we consider the second type of corrections, coming from the use of the Dirac wave function. For the $1S_{\frac{1}{2}}$ state, and $m=+\frac{1}{2}$, the four components of the Dirac wave function are

$$\varphi_{01}=-Y_{00}(\theta,\varphi)G(p),$$
$$\varphi_{02}=0,$$
$$\varphi_{03}=(1/\sqrt{3})Y_{10}(\theta,\varphi)f(p),$$
$$\varphi_{04}=-(\sqrt{2}/\sqrt{3})Y_{11}(\theta,\varphi)f(p),$$

where the Y's are normalized spherical harmonics in momentum space,

$$Y_{00}=(\tfrac{1}{4}\pi)^{-\frac{1}{2}},$$
$$Y_{10}=(\tfrac{3}{4}\pi)^{-\frac{1}{2}}\cos\theta,$$
$$Y_{11}=-(\tfrac{3}{8}\pi)^{-\frac{1}{2}}\sin\theta e^{i\varphi},$$

and $G(p)$ and $f(p)$ are obtained from the corresponding functions in ordinary space by a Fourier-Bessel transformation. $G(p)$, the large component, is proportional to

$$p^{-1}[1+(p^2/Z^2\alpha^2m^2)]^{-(1+\epsilon)/2}\sin[(1+\epsilon)\,\mathrm{tg}^{-1}(p/Z\alpha m)],$$

where ϵ is the energy of the level (including rest energy) divided by m [$\epsilon=(1-\alpha^2Z^2)^{\frac{1}{2}}$]. $G(p)$ can be expanded in powers of $Z\alpha$ and one finds that, if one neglects terms of order $(Z\alpha)^2$ with respect to the main term, a good approximation for almost all p's is given by

$$G(p)\simeq[32(Z\alpha m)^5/\pi]^{\frac{1}{2}}(p^2+Z^2\alpha^2m^2)^{-2}(1+\pi Z\alpha p/8m);$$

while, for the small component $f(p)$, it is enough to keep only the main term

$$f(p)\simeq-[8(Z\alpha)^5m^3/\pi]^{\frac{1}{2}}p(p^2+Z^2\alpha^2m^2)^{-2}.$$

ΔE_1 involves expressions of the form

$$\int\bar{\varphi}_0(\mathbf{p}_2)\beta\Lambda(\mathfrak{p}_1^2,\mathfrak{p}_2^2,\mathfrak{q}^2)\varphi_0(\mathbf{p}_1)d^3\mathbf{p}_1d^3\mathbf{p}_2,\qquad\text{(A1)}$$

where Λ is a function containing no Dirac operator. (A1) is equal to

$$(4\pi)^{-1}\int d^3\mathbf{p}_1d^3\mathbf{p}_2\Lambda(\mathfrak{p}_1^2,\mathfrak{p}_2^2,\mathfrak{q}^2)[G(p_2)G(p_1)+(\mathbf{p}_1\cdot\mathbf{p}_2/p_1p_2)f(p_2)f(p_1)],\qquad\text{(A2)}$$

the difference between the integrands in (A1) and (A2) giving 0 in the integration. Since $\mathbf{p}_1\cdot\mathbf{p}_2$ can be expressed in terms of $\mathbf{p}_1^2$, $\mathbf{p}_2^2$, $\mathbf{q}^2$ by

$$2\mathbf{p}_1\cdot\mathbf{p}_2=\mathbf{p}_1^2+\mathbf{p}_2^2-\mathbf{q}^2,$$

the corrections involving the small component, $f(p)$, in I_a, I_b, I_c, can be immediately evaluated as combinations of the integrals K, J, etc.$\cdots$, again, and it is seen that, due to the fact that these integrals depend on a^2 only, and not on a, there is no term of order $\alpha(Z\alpha)^5$.[29] As for the correction involving a first power of $\not{p}$ in $G(p)$, we can transform it by use of the formula

$$(\pi/2)\not{p}=\int_0^\infty(\not{p}^2/p^2+b^2)db,$$

so that

$G(p)\simeq$Schrödinger wave function

$$+[2\pi^{-1}(Z\alpha)^7m^3]^{\frac{1}{2}}\int_0^\infty p^2(p^2+b^2)^{-1}(p^2+Z^2\alpha^2m^2)^{-2}db,$$

and we obtain combinations of the more general integrals, K_{ab}, J_{a^2b}, etc.$\cdots$, followed by an integration over b. In all cases, Dirac corrections prove to be of order $\alpha(Z\alpha)^6\ln(Z\alpha)$ or higher.

Going back to I_e now, we can first perform the integral over $\mathbf{p}_i$ and $\mathbf{p}_f$ in (33). Define 4 new functions by

$$\varphi_{0s}'(\mathbf{p})=\int V(\mathbf{p}-\mathbf{p}')\varphi_{0s}(\mathbf{p}')d^3\mathbf{p}'\quad(s=1,2,3,4).$$

φ_{0s}' has the same angular dependence as φ_{0s}. This is a consequence of Dirac's equation itself, which can be written (for an S state):

$$\int V(\mathbf{p}-\mathbf{p}')G(p')Y_{00}(\theta',\varphi')d^3\mathbf{p}'$$
$$=Y_{00}(\theta,\varphi)[(E_0-m)G(p)+pf(p)]\equiv Y_{00}(\theta,\varphi)G'(p),$$

$$\int V(\mathbf{p}-\mathbf{p}')f(p')Y_{1m}(\theta',\varphi')d^3\mathbf{p}'$$
$$=Y_{1m}(\theta,\varphi)[(E_0+m)f(p)+pG(p)]\equiv Y_{1m}(\theta,\varphi)f'(p),$$

defining two new functions $G'(p)$ and $f'(p)$. Approximations for $G'(p)$ and $f'(p)$ are given by

$$G'(p)\simeq-\frac{Z\alpha}{2\pi^2}\left(\frac{32(Z\alpha m)^5}{\pi}\right)^{\frac{1}{2}}\int\frac{d^3\mathbf{p}'}{(\mathbf{p}-\mathbf{p}')^2[p'^2+(Z\alpha m)^2]^2}$$
$$=-\left(\frac{8(Z\alpha)^5m^3}{\pi}\right)^{\frac{1}{2}}\frac{1}{p^2+(Z\alpha m)^2},$$

$$Y_{1m}f'(p)\simeq\frac{Z\alpha}{2\pi^2}\left(\frac{8(Z\alpha)^5m^3}{\pi}\right)^{\frac{1}{2}}\int\frac{p'Y_{1m}(\theta',\varphi')d^3\mathbf{p}'}{(\mathbf{p}-\mathbf{p}')^2[p'^2+(Z\alpha m)^2]^2}$$
$$=\left(\frac{8(Z\alpha)^7m^3}{\pi}\right)^{\frac{1}{2}}Y_{1m}(\theta,\varphi)\int_{Z\alpha m}^\infty\frac{pdb}{(p^2+b^2)^2}.$$

We can now evaluate the term with $3V$'s in (33), and find a result of order $\alpha(Z\alpha)^6\ln(Z\alpha)$. The other terms of (33) have already been evaluated with p_x^2 replaced by m^2; we now want the difference, involving

$$(1/\mathfrak{p}_x^2)-(1/m^2)=(m^2-E_0^2+\mathbf{p}_x^2)/m^2(E_0^2-\mathbf{p}_x^2).$$

Always by the same methods, this can be shown to yield linear combinations of integrals K, J, etc.$\cdots$ that depend only on a^2, and therefore there cannot be any term of order $\alpha(Z\alpha)^5$.

We complete the investigation of the one-potential Lamb shift by looking at I_f, given in (35), from which we subtract

$$\tfrac{3}{4}m\delta^3(\mathbf{p}_2-\mathbf{p}_1)\int_0^1(4x-1)(\not{p}-m)^2m^{-2}dx,$$

already evaluated in (36). The difference gives for the energy shift:

$$\frac{3}{4}\frac{e^2}{\pi}\int\bar\varphi_0(\mathbf{p})\int_0^1dx\left[x(4x-1)\frac{(\not{\mathfrak{p}}-m)^2(m^2-\not{\mathfrak{p}}^2)}{m[\mathfrak{p}^2x+m^2(1-x)]}+2x\frac{(\not{\mathfrak{p}}-m)^3}{\mathfrak{p}^2x+m^2(1-x)}\right]\varphi_0(\mathbf{p})d^3\mathbf{p}$$
$$=\frac{3}{4}\frac{e^2}{\pi}\int\bar\varphi_0(\mathbf{p}_f)V(\mathbf{p}_f-\mathbf{p})\int_0^1xdx\left[(4x-1)\frac{m^2-\not{\mathfrak{p}}^2}{m[\mathfrak{p}^2x+m^2(1-x)]}+2\frac{\not{p}-m}{\mathfrak{p}^2x+m^2(1-x)}\right]V(\mathbf{p}-\mathbf{p}_i)\varphi_0(\mathbf{p}_i)d^3\mathbf{p}_id^3\mathbf{p}_fd^3\mathbf{p}_i$$
$$=\frac{3}{4}\frac{e^2}{\pi}\int_0^\infty p^2dp\int_0^1xdx\left[(4x-1)\frac{m^2-E_0^2+\mathbf{p}^2}{m[\mathfrak{p}^2x+m^2(1-x)]}\{[G'(p)]^2-[f'(p)]^2\}\right.$$
$$\left.+\frac{2}{\mathfrak{p}^2x+m^2(1-x)}\{(E_0-m)[G'(p)]^2+(E_0+m)[f'(p)]^2-2pG'(p)f'(p)\}\right].$$

The integration can be performed with the help of

$$\Re\int_0^\infty\frac{p^2dp}{(\mathbf{p}^2+a^2)[\mathfrak{p}^2x+m^2(1-x)]}=-\frac{\pi}{2}\frac{a}{(E_0^2+a^2)x+m^2(1-x)},$$

and other formulas obtained by taking derivatives with respect to a. No term of order $\alpha(Z\alpha)^5$ is found.

[29] A similar procedure shows that there is no $\alpha(Z\alpha)^5$ term in the one-potential shift for the $2P$ state.

Letters to the Editor

PUBLICATION of brief reports of important discoveries in physics may be secured by addressing them to this department. The closing date for this department is five weeks prior to the date of issue. No proof will be sent to the authors. The Board of Editors does not hold itself responsible for the opinions expressed by the correspondents. Communications should not exceed 600 words in length and should be submitted in duplicate.

Single Crystal Metal Rotors*

J. W. BEAMS
University of Virginia, Charlottesville, Virginia
(Received August 24, 1953)

IN connection with studies of the tensile strength and adhesion of thin metal films by the spinning rotor method,[1] it became desirable to use single crystals of iron as high speed rotors. At first sight this might seem impractical because a crystal of iron at room temperature has a body-centered cubic structure and is very easily distorted along the (110), (112), and (123) slip planes.[2] However, the three planes have the same [111] direction of slip, so that if the stresses in the rotor along this direction could be sufficiently reduced, the rotor could be spun to high speed without distortion. An iron crystal carefully machined to a spherical shape (diameter 0.163 in.) was magnetically suspended in a vacuum and spun by a rotating magnetic field by a method previously described.[3] The sphere had a small flat milled on its surface perpendicular to the slip direction, which automatically constrained the rotor to spin about an axis parallel to the direction of slip. The rotor showed no observable distortion until it attained a rotational speed of about 19 000 rps when it became deformed. This deformation increased the moment of inertia, which in turn slowed down the rotor and allowed it to be brought to rest without destruction. The distortion was asymmetrical and mostly at an angle to the axis of rotation. The resultant rotor is shown in Fig. 1

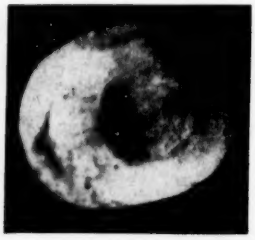

FIG. 1. Single crystal iron sphere with small flat after distortion by spinning.

with the small surface up which initially was flat. It was difficult to determine the initial slip planes from an examination of the resultant rotor as well as to calculate the maximum rotor stress. However, if we assume that the rotor was elastic up to maximum speed, the maximum stress was about 30 000 lb/in.^{2} while the maximum stress along the axis was about 1800 lb/in.^{2}. Both of these values are perhaps too high, but in any case a spherical single crystal of iron may reach considerable rotational speed if spun around the slip direction.

Since the body-centered cubic structure of iron made the interpretation of the above experiment difficult, a single crystal of zinc was next spun around a perpendicular to its only slip plane (0001). The zinc crystal was a short cylinder 0.6215 in. in diameter and 0.23 in. high with the (0001) slip plane parallel to the ends of the cylinder to better than 0.5 degree as determined by x-ray reflection. It was carefully machined and etched to remove the majority of strains. Zinc is not ferromagnetic, so it was spun by the air turbine method.[4] The crystal was so mounted that it was free to expand except for a few thousandths of an inch on each end of the cylinder. It was spun to various speeds of rotation and held for one minute before being brought to rest for examination. No change was observed until the rotor speed reached about 1600 rps (2750 lb/in.^{2}), when microscopic examination indicated some faint lines developing on the cylindrical surface at least at two angles to the axis of rotation. At 2300 rps (5800 lb/in.^{2}) the slip bands became distinct and an increase in the diameter of 0.003 in. was observed.

The above results may be interpreted as indicating that if a crystal at room temperature is prevented from slipping along the usual slip planes, at sufficiently high stresses slip will take place along other planes. Also in some cases twinning may possibly take place. These results probably should be expected from well-known experiments on the slip in crystals.[2,5] However, in the experiments here described the maximum stresses are at the center of the crystal and approach zero or a small value on the crystal surface. Also, in the case of iron, the crystal is not constrained in any way by clamps, etc., while in zinc the constraints are made very small.

The writer is much indebted to Drs. Allan Gwathmey, Fred Young, and Henry Leidheiser for the excellent iron and zinc crystals.

* Supported by a U. S. Navy Bureau of Ordnance contract.

[1] Beams, Walker, and Morton, Phys. Rev. **87**, 542 (1952).
[2] C. S. Barrett, *Structure of Metals* (McGraw-Hill Book Company, Inc., New York, 1952), second edition.
[3] Beams, Young, and Moore, J. Appl. Phys. **17**, 886 (1946).
[4] J. W. Beams, J. Wash. Acad. Sci. **37**, 221 (1947).
[5] W. T. Read, Jr., *Imperfections in Nearly Perfect Crystals* (John Wiley and Sons, Inc., New York, 1952).

Hall Effect in AgCl at Low Temperature*

FREDERICK C. BROWN†
Department of Physics, University of Illinois, Urbana, Illinois
(Received August 28, 1953)

THE method of Redfield[1] for detecting the Hall effect in insulating crystals has been applied to silver chloride. Measurements of Hall mobility were made at liquid nitrogen temperature on a specimen cut from a single crystal carefully grown from the melt. Crystal counter techniques using high-energy beta particles had previously yielded estimates of the drift mobility as a function of temperature in this crystal.[2]

Difficulty was experienced in directly applying the Redfield method to AgCl because of low-frequency noise and drift. A pulse technique was developed in which the photoconducting crystal was illuminated with a 15-microsecond flash of light from a strobotron. This was synchronized with the maximum of a much slower electric field pulse applied to the resistance film (in this case a relatively low resistance evaporated platinum film). Charge flow in the crystal was detected by a non-overloading linear amplifier and an oscilloscope. The repetition rate of the pulses was low, of the order of one every few seconds. Since the electric field applied to the crystal was zero, except during the pulse, depolarization could be effected by low-intensity steady illumination. A thin Mylar film separated the crystal and electrodes and prevented the possibility of charge entering the crystal from the electrodes. An analysis of the experiment shows the importance of releasing charge uniformly throughout the volume of the crystal. This was accomplished by filtering the light with an orange filter having a cutoff at 5200A. Care was taken to properly ascertain the true temperature of the crystal as it was mounted in the cryostat.

In itself the fast-pulse technique appears to be useful for studying photoeffect and polarization. Induced charges of the

order of 2×10^{-16} coulomb were readily detected in the Hall experiment. As expected the primary photoresponse of the AgCl crystal was fast, less than one microsecond.

An approximate value of the Hall mobility for this one sample at $89\pm6°$K is 370 ± 70 cm²/volt-sec and is shown in Fig. 1 along

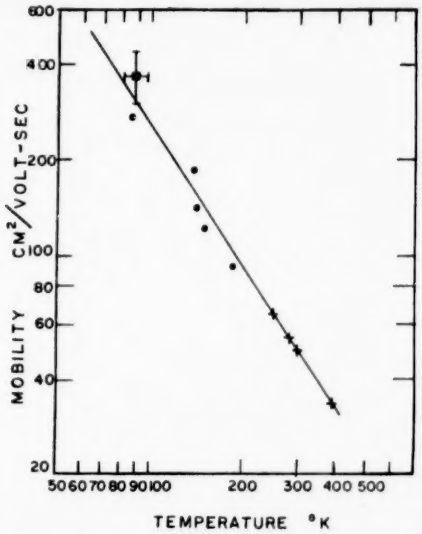

FIG. 1. Electron mobility in silver chloride. ■ Hall mobility for crystal No. IV; ● electron drift mobility for crystal No. IV; ✦ data of Haynes and Shockley for AgCl (reference 3).

with the drift mobility values. The crosses at higher temperature in this graph are the values of Haynes and Shockley[3] utilizing the "print-out effect" in AgCl, a technique which is not applicable at liquid nitrogen temperature. Although the figure for Hall mobility at low temperature is approximate, the reproducibility was reasonably good. Under the conditions of the experiment one is led to believe that the effects of space charge are unimportant. The value of Hall mobility decreased with increasing temperature similar to the drift mobility, but accurate results are not available for intermediate temperatures at this time. Within experimental error the Hall voltage was linear with magnetic field up to at least 10 000 gauss. Since the crystal counter measurements indicate that there is no appreciable hole conductivity at 85°K, it may be reasonable to assume that we have measured here the electronic Hall mobility. The polarity of the effect was as expected for electrons.

It is interesting to compare the data with the theory of Low and Pines.[4] Their approximation $kT\ll\hbar\omega$ should be valid for AgCl at 85°K. We take values of $\epsilon=12.3$, $n^2=4.04$,[5] and $\lambda_i\simeq90\mu$.[6] The drift mobility value of 270 then agrees best with theory for an effective mass of the electron $m\simeq0.5$ electron masses.

The author would like to express his appreciation for discussions with Professor R. J. Maurer and Dr. A. G. Redfield. The crystal growing and measurements of drift mobility are being carried out at Reed College with support from the Research Corporation and the National Science Foundation. Results will be published shortly.

* Partially supported by the U. S. Office of Naval Research.
† Address: Reed College, Portland, Oregon. The Hall effect work was carried out at the University of Illinois during the summer of 1953.
[1] A. G. Redfield, Phys. Rev. **91**, 753 (1953).
[2] F. C. Brown, paper presented at the 1953 Rochester meeting of the American Physical Society [Bull. Am. Phys. Soc. **28**, No. 4, 22 (1953)].
[3] J. R. Haynes and W. Shockley, Phys. Rev. **82**, 935 (1951).
[4] F. E. Low and D. Pines, Phys. Rev. **91**, 193 (1953).
[5] K. Hojendahl, Kgl. Danske Vindenskab. Selskab, Mat.-fys. Medd. **16**, No. 2 (1938).
[6] R. B. Barnes, Z. Physik **75**, 723 (1932).

Perfect Crystals of Zinc Sulfide

WILLIAM W. PIPER AND W. L. ROTH
General Electric Research Laboratory, Schenectady, New York
(Received August 27, 1953)

IT is a well-known fact that crystals deform plastically at strains much lower than predicted for perfect crystals. This is usually interpreted to signify the presence in real crystals of dislocations which move under the influence of a relatively small stress.[1] Galt and Herring[2] have shown that the small (1.8×10^{-4} cm in diameter) "whiskers" of tin reported by Compton *et al.*[3] are relatively perfect single crystals in the sense that they may be bent elastically to a strain of 1 percent without plastic deformation.

We have recently grown crystals of zinc sulfide which similarly appear to be free of dislocations, and we have some preliminary information which suggest these perfect crystals have several unusual properties. The crystals are grown by sublimation in an atmosphere of hydrogen, and the crystals of interest crystallize as needles, up to about 5×10^{-3} cm in diameter and several millimeters long. It is believed these crystals may have grown from a single screw dislocation with its Burger's vector parallel to the needle axis.

X-ray diffraction patterns from the needles show that they are single crystals of hexagonal zinc sulfide (wurtzite) and that the needle axis coincides with the crystallographic c axis. Whereas most zinc sulfide crystals grown by this technique possess a high density of stacking faults (aperiodic errors in the sequence of layers normal to the c axis), these crystals appear free from such defects as is shown by the absence of diffuse streaking in the x-ray photographs. The crystals also fail to show under the polarizing microscopic the usual pattern of striations parallel to the basal planes characteristic of the non-perfect crystals.

The needles are remarkably flexible and may be bent elastically without plastic deformation. After measuring the deflection produced by hanging known loads from the tip of a crystal rigidly anchored at the opposite end, Young's modulus was estimated to be about 7×10^{11} dynes/cm². We have induced elastic strains up to 1½ percent by bending the crystal between a fixed plate and the face of a micrometer.

Hexagonal zinc sulfide is thermodynamically unstable at room temperature with respect to the cubic polymorph (sphalerite). Ordinary crystals of hexagonal zinc sulfide, which contain stacking faults and presumably the usual complement of dislocations, begin to disorder when heated to about 400°C and at higher temperatures will transform to a twinned single individual of the cubic form. In contrast to this, the flexible crystals must be heated to 750°C to produce a comparable disorder, thus showing the important role dislocations play in the mechanism of the transformation.

The photoconductivity of these perfect crystals has been compared with ordinary single crystals of zinc sulfide which possess the stacking faults described above. In each case the crystal was irradiated with a strong source of 3650Å light (B-H4 lamp) and a voltage applied between silver paste electrodes to produce a photocurrent density of the order of 10^{-6} amp/cm². The ordinary crystals took 50 to 500 sec to decay by a factor of 10^3, whereas the perfect crystals decayed too rapidly (less than 5 sec) to be detected by the electrometer. The slow response of the ordinary ZnS crystals has been associated with electron traps well below the conduction band. The concentration of these traps would thus appear to be significantly diminished. Hence, one might suspect these electron traps are associated with dislocations. An alternative is that the traps and dislocations are independent products of the presence of a foreign impurity or other generator of crystal imperfections.

We would like to acknowledge the assistance of D. Hallgren who made many of the measurements.

[1] L. Bragg and W. M. Lomer, Proc. Roy. Soc. (London) **A196**, 171 (1949).
[2] J. K. Galt and C. Herring, Phys. Rev. **85**, 1060 (1952).
[3] Compton, Mendizza, and Arnold, Corrosion **7**, 327 (1951).

Dielectric Properties and Phase Transitions of $Cd_2Nb_2O_7$ and $Pb_2Nb_2O_7$†

GEN SHIRANE* AND RAY PEPINSKY
Department of Physics, Pennsylvania State College, State College, Pennsylvania
(Received August 20, 1953)

RECENTLY Cook and Jaffe[1,2] reported a new ferroelectric $Cd_2Nb_2O_7$, which shows a Curie temperature at about 170°K. The crystal structure of cadmium niobate is a face-centered cubic lattice of the pyrochlore type, which has a three-dimensional framework of linked octahedra of NbO_6.[3] A comparison of the dielectric and structural properties of this new ferroelectric with those of the well-studied $BaTiO_3$ may provide information contributing to an understanding of oxide ferroelectrics in general.

Ceramic $Cd_2Nb_2O_7$ specimens were prepared by firing the mixture of $CdCO_3$ and Nb_2O_5 at about 1250°C after preliminary heating at 1150°C. The specimens were hard, non-porous ceramics of tan color. The dielectric constant *vs* temperature curve was measured at 10 kc/sec and 5 v/cm (see Fig. 1). At room temperature the dielectric constant is about 310, and it reaches a peak value of 1200 at 185°K. This value of the Curie temperature is higher than the value reported by Cook and Jaffe. These workers reported marked difference in the Curie temperatures in disks from the same mix, with the highest Curie point at 170°K. We have checked three kinds of specimens, with different firing temperatures ranging from 1200° to 1300°C, and obtained Curie temperatures between 182° and 188°K.

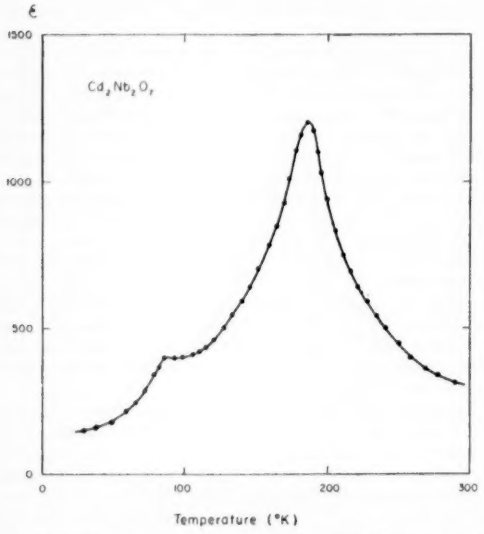

FIG. 1. Dielectric constant *vs* temperature curve of $Cd_2Nb_2O_7$ on heating.

The dielectric constant curve in Fig. 1 shows a small anomaly at 85°K, which suggests the existence of another phase change at this temperature. No other dielectric anomaly was found between 85°K and 4°K. Well-defined ferroelectric hysteresis loops were observed below the Curie temperature at 185°K down to 4°K (see Fig. 2). The spontaneous polarization estimated from these hysteresis loops under an ac field of 25 kv/cm is approximately 1.8 microcoulomb/cm² at 100°K. This value of spontaneous polarization is somewhat smaller than we expect from the remanent polarization of 3.2 microcoulomb/cm² reported previously.[2] The dielectric constant above the Curie temperature may be expressed to a good approximation by the Curie-Weiss law $\epsilon = C/(T-\theta)$, with $C = 4.6\times10^4$ and $\theta = 150$°K.

An increase in the dielectric constant of $Pb_2Nb_2O_7$ from room temperature down to liquid air temperature was reported by Cook and Jaffe, suggesting the possible existence of the Curie point below liquid air temperature. The $Pb_2Nb_2O_7$ ceramic was prepared in our laboratory by firing a mixture of $PbCO_3$ and Nb_2O_5 at 1000°C. We have measured the dielectric constant as a function of temperature down to 4°K at 10 kc/sec and 5 v/cm. The dielectric constant increases with decreasing temperature from a room temperature value of 185, and it reaches a maximum value of 360 at 14°K and decreases to 353 at 4°K. The shape of this small maximum suggests the existence of a phase transition at this temperature. However, the polarization *vs* field relation is quite linear even below 14°K under a field strength of 10 kv/cm. This leads us to doubt that $Pb_2Nb_2O_7$ is ferroelectric. Moreover, the crystal structure of $Pb_2Nb_2O_7$ at room temperature is not cubic but rhombohedral.[1] Thus any phase transition in $Pb_2Nb_2O_7$ at 14°K must be different from the upper ferroelectric phase transition in $Cd_2Nb_2O_7$.

(a) 100°K (b) 175°K

FIG. 2. Hysteresis loops of $Cd_2Nb_2O_7$ at an ac field of 25 kv/cm and 60 cycles/sec.

In order to examine a possible relation between these transitions in lead and cadmium niobates, a dielectric and structural study was made on solid solutions of $(Cd, Pb)_2Nb_2O_7$. Starting from the pure $Cd_2Nb_2O_7$ side, the Curie temperature decreases with increasing Pb concentration, appearing at 133°K in $(Cd_{0.9}, Pb_{0.1})_2Nb_2O_7$ and 41°K in $(Cd_{0.8}, Pb_{0.2})_2Nb_2O_7$. The lower transition point was not observed in these solid solutions down to 10°K. Powder photographs of solid solutions at room temperature show a cubic lattice for the compositions from pure $Cd_2Nb_2O_7$ to $(Cd_{0.1}, Pb_{0.9})_2Nb_2O_7$. Only a narrow composition range near pure $Pb_2Nb_2O_7$ shows a rhombohedral lattice. This result might be considered in conjunction with the fact[2] that $Pb_{1.5}Nb_2O_{6.5}$ shows a cubic pattern very similar to that of $Cd_2Nb_2O_7$. Exploration of the cubic *vs* rhombohedral phase line in this solid solution system, and an x-ray study of the two ferroelectric phases in pure $Cd_2Nb_2O_7$, are now underway.

Dr. Cook informed us, in a private communication, that Hulm[4] had found independently the lower phase transition in $Cd_2Nb_2O_7$ and the dielectric peak in $Pb_2Nb_2O_7$, in good agreement with the present results. We thank Dr. W. R. Cook, Jr., Dr. Hans Jaffe, and Dr. J. K. Hulm for their kind communication of unpublished data, and Mr. J. McLaughlin for the specimen preparation and dielectric measurements.

† Research supported by contract with the Air Research and Development Command.
* On leave from Tokyo Institute of Technology, Tokyo, Japan.
[1] W. R. Cook, Jr., and H. Jaffe, Phys. Rev. **88**, 1426 (1952).
[2] W. R. Cook, Jr., and H. Jaffe, Phys. Rev. **89**, 1297 (1953).
[3] A. Bystroem, Arkiv Kemi, Mineral Geol. **18A**, No. 21 (1944).
[4] J. K. Hulm (private communication, August, 1953) and following Letter [Phys. Rev. **92**, 504 (1953)].

Low-Temperature Dielectric Properties of Cadmium and Lead Niobates

J. K. HULM
Institute for the Study of Metals, University of Chicago, Chicago, Illinois
(Received August 24, 1953)

CADMIUM niobate, $Cd_2Nb_2O_7$, was reported by Wainer and Wentworth[1] to have a dielectric constant of about 500 with a high, negative temperature coefficient at room temperature; Cook and Jaffe[2] observed a ferroelectric Curie point at 170°K for this compound and also noted that its crystal structure was

of the pyrochlore type rather than of the perovskite or ilmenite types in which earlier double-oxide ferroelectrics were found.[3,4] The importance of cadmium niobate as the possible fore-runner of a new class of ferroelectrics led us to investigate the dielectric properties of this compound at temperatures down to 1.2°K. Figure 1 shows the temperature variation of dielectric constant (uncorrected for porosity) for two ceramic specimens fired in cadmium oxide vapor at 1180°C (*A*, density = 4.77) and at 1260°C (*B*, density = 5.72), respectively.

Although the difference between the dielectric constants for the two specimens in Fig. 1 is mainly due to the difference in densities, the two curves do not coincide exactly when a suitable porosity correction is applied. The striking maximum at the upper Curie point shifts from 187°K to 183°K as the firing temperature is changed from 1180°C to 1260°C, perhaps owing to slight deviations from the stoichiometric formula $Cd_2Nb_2O_7$. In addition to the main peak, a small, previously unreported, dielectric constant peak is clearly visible at about 80°K for both specimens in Fig. 1, the temperature of the peak again depending slightly upon the specimen firing temperature. Since with an alternating field of about 10 kilovolts per cm, hysteresis loops were observed over the whole range from the upper Curie point down to 1.2°K, it seems possible that the small peak at 80°K marks a phase change similar to the minor transitions occurring at about 180°K and 270°K in barium titanate,[5] where a symmetry change is associated with a discrete jump in the direction and magnitude of the spontaneous electric moment without, however, the disappearance of ferroelectricity. Such transitions are obviously favored in ferroelectrics of the perovskite and pyrochlore types which are cubic in the paraelectric range and may lose several degrees of symmetry with decreasing temperature.

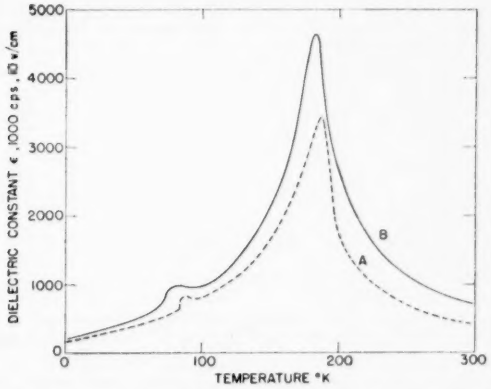

FIG. 1. Temperature variation of dielectric constant for specimens of cadmium niobate fired at 1180°C (A) and at 1260°C (B).

From dielectric observations above liquid nitrogen temperatures, Cook and Jaffe[2] suggested that lead niobate, $Pb_2Nb_2O_7$, which has an orthorhombic structure of a distorted pyrochlore type, should have a Curie point at very low temperatures. We have extended dielectric measurements on ceramic specimens of this compound down to 1.2°K, with the results shown in Fig. 2 for a specimen of density 6.53.

The dielectric constant of lead niobate rises steeply with decreasing temperature, obeying the Curie-Weiss law $\epsilon = C/(T-\theta)$, with $C = 6.26 \times 10^4$ and $\theta = -166$°K, down to 75°K. Below this temperature the curve flattens out, passing through a maximum at 15.4°K and dropping gradually down to 1.2°K, as shown in the enlarged inset of Fig. 2. Although the behavior of the dielectric constant is rather similar to that of potassium tantalate,[6] the polarization-field curve of lead niobate was found to be strictly linear at field strengths up to 15 kilovolts per cm and at temperatures down to 1.2°K, implying that lead niobate is not a ferroelectric crystal. While the dielectric constant peak may be associated with an antiferroelectric phase transition, it is difficult to reconcile either ferroelectric or antiferroelectric behavior with the negative Curie-Weiss temperature of lead niobate, which suggests paraelectric behavior down to absolute zero. Theory[7] indicates, however, that the dielectric constant of such a paraelectric should increase monotonically with decreasing temperature, as has been observed for strontium titanate.[8] Further work is thus required to establish the nature of the dielectric constant peak in lead niobate.

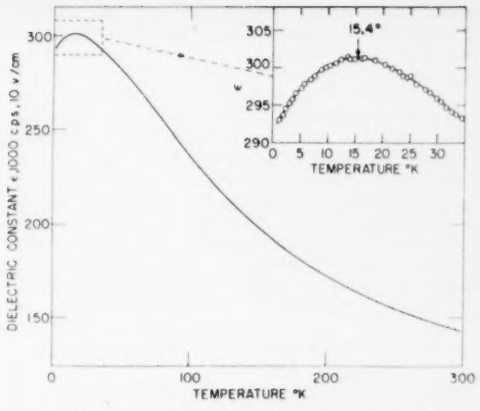

FIG. 2. Temperature variation of dielectric constant for specimen of lead niobate fired at 1180°C.

In conclusion it will be noted that no unusual dielectric properties were observed in $Cd_2Ta_2O_7$, $Pb_2Ta_2O_7$, $In_2Ti_2O_7$, $In_2Zr_2O_7$, $In_2Nb_2O_8$, $Y_2Nb_2O_8$, and $In_2Ta_2O_8$ between room temperature and liquid air temperature. The absence of ferroelectricity in the last three compounds is perhaps to be expected in view of the probable absence of NbO_6 or TaO_6 octahedra, which play such a vital role in the ferroelectricity of niobates and tantalates.[9]

I am grateful to Drs. Gen Shirane and Ray Pepinsky of Pennsylvania State College for kindly informing me of their unpublished data on cadmium and lead niobates,[10] which are in good agreement with the above results.

[1] E. Wainer and C. Wentworth, J. Am. Ceram. Soc. **35**, 207 (1952).
[2] W. R. Cook and H. Jaffe, Phys. Rev. **88**, 1426 (1952) and **89**, 1297 (1953).
[3] B. Wul and I. M. Goldman, Nature **156**, 480 (1945).
[4] B. T. Matthias and J. Remeika, Phys. Rev. **76**, 1886 (1949).
[5] Von Hippel, Breckenridge, Chesley, and Tisza, J. Ind. Eng. Chem. **38**, 1097 (1946).
[6] Hulm, Matthias, and Long, Phys. Rev. **79**, 885 (1950).
[7] J. H. Barrett, Phys. Rev. **86**, 118 (1952).
[8] J. K. Hulm, Proc. Phys. Soc. (London) **A63**, 1184 (1950).
[9] B. T. Matthias, Phys. Rev. **75**, 1771 (1949).
[10] Gen Shirane and R. Pepinsky (private communication, August, 1953 and preceding Letter [Phys. Rev. **92**, 504 (1953)].

Helium II Film Transport Rates over Machined Metal Surfaces*

BERNARD SMITH AND HENRY A. BOORSE†
Pupin Physics Laboratories, Columbia University, New York, New York
(Received August 11, 1953)

ONE widespread interpretation of previous transport measurements over metals maintains that ordinary, unpolished metal surfaces always show very high film transport rates (i.e., compared with glass).[1-3] The supposition is that, in contrast to glass, machined metal surfaces are characterized by a high degree of surface roughness which acts either to present a microperimeter many times larger than the measured macroperimeter,[3] or else to produce surface cracks which enhance the flow of bulk liquid.[1,2]

According to this view, "there may be only one transfer rate (that exhibited by the glass surfaces) and any higher rate would be due to the microstructure of the substrate."[3] Furthermore, it is maintained that "glass appears to be the only surface over which simple and reproducible phenomena of film flow have been observed."[4] The recent finding of Chandrasekhar and Mendelssohn[2] that highly polished stainless steel yielded a rate identical with that obtained for baked glass by Mendelssohn and White[1] is frequently cited in support of this interpretation.

In a previous note we have submitted evidence which does not support the assignment of this special role to glass. We wish now to report some new measurements which are at variance with the above view of transport over metals.

The method used to determine the rates listed in Table I was similar to that previously described.[5,6] The transport vessel-

TABLE I. Transport rate in cm²/sec-cm ×10⁵.

	1.2°	1.4°	1.6°	1.8°	2.0°
Stainless steel[a]	9.8	9.7	9.1	7.5	4.9
Aluminum[b]	9.8	9.8	9.3	7.1	3.8
Aluminum[c]	9.3	9.0	8.5	6.8	4.0
Nickel silver[d]	11.4	11.3	10.6	8.8	5.5
Nickel silver[e]	···	9.0	8.3	6.8	4.5
Nickel silver[f]	10.3	10.1	9.4	8.0	5.2
Silver[g]	8.6	8.3	7.9	7.0	5.2
Copper[h]	10.2	10.1	9.5	7.4	4.2

[a] (Type 303, 18 percent Cr, 8 percent Ni, 2 percent Mn, 1 percent Si): Six runs in a two month period.
[b] (Alcoa Alloy 11S—5.5 percent Cu, 0.5 percent Pb, 0.5 percent Bi) Sample 1: two runs six weeks apart.
[c] (Alcoa Alloy 11S) Sample 2: one run.
[d] (46.5 percent Cu, 40.75 percent Zn, 2.75 percent Pb, 10 percent Ni) Sample 1: three runs in a five week period.
[e] (same as d)—Sample 2: one run.
[f] (same as d)—Sample 2: two runs three weeks apart.
[g] (Fine, 99.9 percent pure): one run.
[h] (Oxygen free, high conductivity): one run.

capacitors were turned from solid cylindrical rods and no abrasives or polishes were used to modify the microfinish resulting from the turning process. The choice of metals was dictated by their suitability for various surface treatments in preparation for measurements to follow the initial work on turned surfaces.

The rather narrow range of flow rates obtained for these "rough" metallic surfaces appears noteworthy in view of the wide range of values which have been reported for metals on other occasions. The results for stainless steel are in good agreement with previous, but completely independent measurements made in this laboratory.[7,8] Furthermore, the results of Chandrasekhar and Mendelssohn for highly polished stainless steel[2] (in the absence of a prepolishing control measurement) do not seem sufficiently different to justify definitive conclusions concerning the effect of surface polish.

In view of these considerations, we therefore conclude that:

I. Machined metals do not always yield rates much higher than glass.

II. Transport rates over machined metals are capable of demonstrating a simplicity and reproducibility at least matching that of glass.

III. The effect of a highly polished metal subtrate on transport rates needs further clarification.

A series of control experiments on the role of polishing is now in progress in this laboratory.

* Assisted by the U. S. Office of Naval Research and the Linde Air Products Company.
† Barnard College, Columbia University, New York.
[1] K. Mendelssohn and G. K. White, Proc. Phys. Soc. (London) **A63**, 1328 (1950).
[2] B. S. Chandrasekhar and K. Mendelssohn, Proc. Phys. Soc. (London) **A65**, 226 (1952).
[3] W. C. Knudsen and J. R. Dillinger, Phys. Rev. **91**, 489 (1953).
[4] D. F. Brewer and K. Mendelssohn, Phil. Mag. **44**, 340 (1953).
[5] B. Smith and H. A. Boorse, Phys. Rev. **90**, 156 (1953).
[6] B. Smith and H. A. Boorse, Proc. Schenectady Cryo. Conf., Paper I.08, p. 34, Oct., 1952 (unpublished).
[7] J. G. Dash and H. A. Boorse, Phys. Rev. **82**, 851 (1951).
[8] J. G. Dash and H. A. Boorse, National Bureau of Standards Circular 519, 1952 (unpublished), p. 169.

Expectations from a Unified Field Theory

BEHRAM KURŞUNOĞLU
Laboratory of Nuclear Studies, Cornell University, Ithaca, New York
(Received April 8, 1953; revised manuscript received August 31, 1953)

IN classical field theories we have the following, completely independent, descriptions: (1) the electromagnetic field; (2) the gravitational field; (3) a prescribed distribution of charge in an elementary particle; (4) the equations of motion of a particle under the influence of fields.

A unification of (1) and (2) must, *inter alia*, also contain the statements (3) and (4); that is, a correct unified field theory must provide us with an acceptable distribution of charges and the law of motion for its carrier. A theory with the above characteristics is a field theory in an absolute sense; i.e., apart from the well-known features of a classical field it does not contain the constants e and m explicitly, but these constants are to be obtained as parameters in the solutions of the field equations with certain boundary conditions. This kind of field is very different from a mechanical theory since the latter contain in its equations the constants e and m. In this sense, classical electrodynamics also is not a pure field theory. The situation is the same in quantum mechanics, in which the Schrödinger and Dirac equations contain e and m. The passage to quantum field theory or to many-particle theory is achieved by the usual methods of second quantization but with the same mechanical equations that contain e and m explicitly. A quantized field in the above sense still bears the seeds of a mechanical concept even though it is called field theory.

We know from quantum electrodynamics that if the interaction between the radiation field and particles is considered to be small and the solution is worked out only to the first non-vanishing approximation in this interaction, the theory always gives correct results which agree with experiment up to the highest energies known. Thus the constants e and m appearing in the quantized equations fit in only for the first order perturbation theory; for higher order terms these constants have to be renormalized. Since the agreement of the first order calculations with experiment is satisfactory, one may regard the equations containing e and m, explicitly, as very good approximations to a future field theory from which e and m can be derived. The renormalization process is ample proof of the need for a field theory from whose equations the constants e and m are eliminated, so that there will be nothing left for renormalization.

The relativistic theory of gravitation is the only field theory in theoretical physics which has the above-mentioned desirable features of an absolute field theory. Its non-symmetric generalization, i.e., the unified field theory,[1] is a second example of an absolute field theory. Despite the great symmetry and beauty of its equations, it has not yet been possible to show its superiority over all other classical field theories. A much more difficult step is to discover a quantum version of the theory which, within the present realm of field quantization knowledge, may be regarded as Utopian. However, for the sake of argument, let us suppose that we have found a new method of quantization, which would mean a transition from a pure field theory to a mechanical theory having the properties of a quantized field; from this point of view it should be regarded as a unification of field and mechanics in an opposite sense to that of the usual quantized field, which is a unification of wave and particle concepts. Since, according to the above view, every physically measurable quantity is described by a field, then from its quantized version mass, and charge must result as quantum effects. In this fashion the so-called mass spectrum of elementary particles would be a natural consequence of the theory and all the divergent aspects of the present field theories might not arise. We are quite aware of the very ambitious form of the above statements, but it is conceivable that a complete field theory without the constants e and m may be reached in two big steps as described above. It also seems to us that trying to get agreement with all the experimental facts merely on the basis of the present form of the quantum field theories, is no less ambitious than the program outlined above.

Finally, we should like to illustrate some of the above ideas with an example from unified field theory. It is an entirely new and a most desirable feature of the theory that the distribution of charges in an elementary particle is subject, like everything else, to a field law and is not assigned arbitrarily. If we assume that the interactions between the electromagnetic and gravitational fields are negligible, then the antisymmetric parts of our field equations,

$$R_{\underset{\sim}{\alpha\beta},\gamma}+R_{\underset{\sim}{\beta\gamma},\alpha}+R_{\underset{\sim}{\gamma\alpha},\beta}=-\rho^2 I_{\alpha\beta\gamma},$$

reduce to

$$(\Box-\kappa^2)J_\alpha(x)=0,$$

where κ is an arbitrary constant which appears in the field equations and which under certain boundary conditions has been calculated as $\kappa^{-1}=e^2/2mc^2$; the latter is the range of the charge distribution in a charged particle. The above equation describes both signs of charge on an equal basis. For a static charge distribution we have $\rho=(e\kappa^2/4\pi)(\epsilon^{-\kappa r}/r)$, a result that may be verified experimentally by bombarding some kind of nuclear matter by high energy electrons (between 300 and 500 Mev) and studying the distribution of the emergent electrons and their cross sections. Such an experiment may also give some information about the deviation (if any) from the Coulomb interaction at distances of the order of 10^{-13} cm. Better information about charge distributions can only be obtained by solving the equations without any approximation; unfortunately this is found to be very difficult at present. The constant κ does not appear in Einstein's version of the theory. Our equations were derived by two methods, the first of which fixes the form of the Lagrangian uniquely. The existence of a constant in the field equations introduces additional terms in the Lagrangian of Einstein's theory, for which Einstein[2] remarks that (see the bottom of page 146) "All such additional terms bring a heterogeneity into the system of equations, and can be disregarded, provided that no strong physical argument is found to support them." Now, with $\kappa=0$ Einstein's charge distribution, at least to the assumed order of approximation, is given by $\Box J_\alpha(x)=0$, which implies an infinite range for the charges. Further difficulties about the theory not containing the constant κ have been discussed in detail.[1] From the results of our version of the unified field theory we infer that the nonexistence of a constant in a unified field theory implies precisely, that gravitational and electromagnetic forces are treated on the same footing and that there is nothing to differentiate between the two. It does not seem possible to derive such a constant from the field itself when there are compelling reasons for its introduction right at the beginning. The constant κ is to unified field theory what the constants c and h are to relativity and quantum theory.

[1] B. Kurşunoğlu, Phys. Rev. **88**, 1369 (1952).
[2] A. Einstein, *The Meaning of Relativity* (Princeton University Press, Princeton, 1953).

Superconductivity of Technetium

J. G. Daunt*
Department of Physics and Astronomy, Ohio State University, Columbus, Ohio
AND
J. W. Cobble†
Chemistry Division, Oak Ridge National Laboratory, Oak Ridge, Tennessee
(Received August 31, 1953)

IN view of the fact that pure rhenium was recently found by Daunt and Smith[1] to become superconducting at a relatively high temperature ($T_c=2.42$°K) and in view of the chemical similarities between rhenium and technetium,[2] it was considered of interest to investigate the latter for superconductivity.

The gram-atomic paramagnetic susceptibility of technetium has been found[3] at room temperature to be approximately four times that of rhenium and hence it would follow that the electronic specific heat, $C_{el}=\gamma T$, would be considerably larger in technetium than in rhenium. The exact one to one relationship between γ and the electronic paramagnetic susceptibility per gram, valid for a free electron gas system, however, would not be expected to hold rigidly owing to the possible effects of correlation forces, as for example has been discussed for palladium and platinum by Mott and Jones.[4] On the other hand, using this information that γ for technetium is larger than for rhenium and using the empirical correlation among superconductors between γ/V and the transition temperature, T_c, put forward previously by Daunt,[5] it was concluded that if technetium were to become superconductive its transition temperature would be several times higher than that of rhenium (2.42°K).

We have investigated experimentally a powdered sample of 0.1027 g of technetium metal of purity $\geq$ 99.9 percent prepared from fission product wastes.[6] The magnetic moment was first measured as a function of the applied exterior magnetic field in the liquid helium temperature region, by using first the same apparatus as had been used previously in the measurement of the superconductivity of rhenium.[1] By calibrating the apparatus with a pure tin spherical sample of known volume, it could be determined whether the subsequently observed technetium magnetic moment was para- or dia-magnetic, and what its numerical magnitude was. These experiments showed that the technetium sample was strongly diamagnetic over the entire liquid helium temperature range from 0.9° to 4.2°K, indicating it was superconductive.

The magnetic susceptibility of the technetium sample was next investigated by a ballistic mutual inductance method in an apparatus which had been used for similar susceptibility measurements in other experiments,[7] but which was modified to allow the temperature range 4°K to 20°K to be covered. This modification consisted in placing the technetium sample inside a copper block thermally connected to its surroundings at 4.2°K only by a poorly conducting brass rod, so that the copper block could be heated electrically to any desired temperature. The temperature was measured by a carbon resistance thermometer,[8] embedded in the copper block, and calibrated in the liquid helium and liquid hydrogen temperature regions. Temperatures between 4.2°K and 14°K were computed by graphical and analytical interpolation.

Typical results showing the diamagnetic susceptibility due to the superconductivity of the technetium sample in zero external magnetic field as a function of the absolute temperature, T, using the second apparatus is given in Fig. 1. The ordinates of Fig. 1 give the deflection of the ballistic galvanometer connected to the secondary of the mutual inductance which was around the specimen, and are directly proportional to the diamagnetic susceptibility of the sample. It will be seen that, whereas the temperature, T_c, at which the last trace of superconductive diamagnetism disappears is quite sharply defined (point "A"), the transition itself is spread over a broad range of temperature. This is attrib-

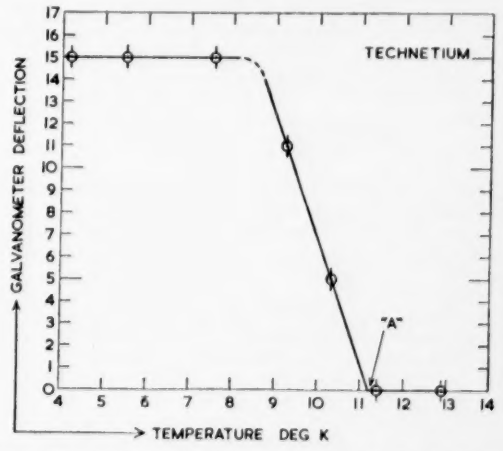

FIG. 1. Diamagnetic susceptibility (in arbitrary units) of technetium as a function of the absolute temperature.

uted largely to the geometrical form of the specimen, which having irregularly-shaped particles of different sizes, would also make the transition in a magnetic field highly irreversible![9] A similar behavior was observed in our rhenium experiments.[1] From a number of experiments of the type illustrated in Fig. 1 the average value of the superconductive transition temperature, T_c, in zero magnetic field was found to be 11.2°K.

Similar transitions were observed in constant external magnetic fields up to 209 gauss. These transitions were found to be highly irreversible, as would be expected from the geometry of the specimen. Owing to the small quantity of technetium available for these experiments, the slope of the magnetic threshold curve could not be obtained with high accuracy, but it appeared to show $(\partial H/\partial T)T=T_c$ of from 300 to 400 gauss/deg.

It is of interest to note that in Group 7 of the periodic table rhenium and technetium are superconductive whereas manganese is not,[10] and in Group 8 osmium and ruthenium are superconductive,[10] whereas iron is not.[11] It is of interest moreover that, whereas the transition temperatures of rhenium and technetium are high, that of technetium being exceptionally high, the transition temperatures of osmium and ruthenium are well below 1°K. The observed very high transition temperature of technetium is in accord with the considerations put forward earlier in this paper based on Daunt's empirical correlation among superconductors, and indeed it was expected by us some time before the experiments were undertaken. A fuller discussion of these general results in their relation to the *d*-band shape in the transition elements is given elsewhere by Horowitz and Daunt.[12]

We wish to thank Mr. Charles S. Ochs for his invaluable help in the experimental work.

* Assisted by a contract between the U. S. Atomic Energy Commission and the Ohio State University Research Foundation.
† Present address: Radiation Laboratory, University of California, Berkeley, California.
[1] J. G. Daunt and T. S. Smith, Phys. Rev. **88**, 309 (1952).
[2] Cobble, Boyd, and Smith, J. Am. Chem. Soc. (to be published).
[3] Nelson, Smith, and Boyd (to be published); C. M. Nelson, Ph.D. dissertation, University of Tennessee, 1952 (unpublished), p. 64.
[4] N. F. Mott and H. Jones, *Properties of Metals and Alloys* (Oxford University Press, London, 1936).
[5] J. G. Daunt, Phys. Rev. **80**, 911 (1950).
[6] Cobble, Nelson, Parker, Smith, and Boyd, J. Am. Chem. Soc. **74**, 1852 (1952).
[7] T. S. Smith and J. G. Daunt, Phys. Rev. **88**, 1172 (1952).
[8] This was a nominal 10-ohm 1-watt radio resistor. See J. R. Clement and E. H. Quinnell, Rev. Sci. Instr. **23**, 213 (1952); Brown, Zemansky, and Boorse, Phys. Rev. **84**, 1050 (1951).
[9] See Mendelssohn, Daunt, and Pontius, Proc. Intern. Congr. Refrig., 7th Congr., The Hague, Amsterdam **1**, 445 (1936).
[10] B. B. Goodman, Nature **167**, 111 (1951).
[11] W. Meissner and B. Voigt. Ann. Physik **7**, 892 (1930).
[12] M. Horowitz and J. G. Daunt, Phys. Rev. **91**, 1099 (1953).

Bifurcation of the *E* Region

J. R. Lien,* R. J. Marcou, J. C. Ulwick, and D. R. McMorrow
Air Force Cambridge Research Directorate,
Air Force Cambridge Research Center,
Cambridge, Massachusetts

and

D. B. Linsford and O. C. Haycock
University of Utah, Salt Lake City, Utah

(Received August 21, 1953)

EFFECTIVE electron measurements have been made directly in the *E* region by rocket-borne instruments. These data have been obtained by measuring the retardation time of a radio signal a Mc/sec or so above the critical frequency for the *E* region. The retardation times were found by comparing the time of arrival in the rocket of two synchronized signals sent from the ground, one of which is the probing signal and the other an uhf reference signal that suffers negligible retardation. On several occasions a profile curve relating the effective electron density *vs* altitude have been obtained for the regions between 90 and 130 kilometers.

Plots of the retardation time *vs* time of flight for the November 1946, April 1947, June and July 1953 flights from White Sands Proving Ground and Holloman Air Force Base, New Mexico are

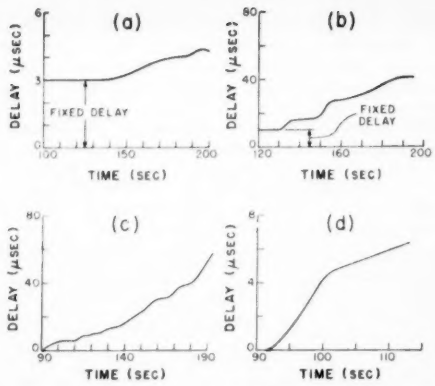

FIG. 1. Delay of probing signal *vs* time of flight of rocket. (a) 10:00 A.M., November 21, 1946; (b) 4:21 P.M., April 17, 1947; (c) 12:10 P.M., June 21, 1953; and (d) 10:52 A.M., July 1, 1953.

given in Fig. 1. The June and July 1953 data clearly indicate small-scale sporadic cloud effects, the study of which yields a method of "smoothing" which was applied to the November 1946 and April 1947 data with the results shown in Fig. 1. The effective electron density is found from these delay data in the following manner. Using Appleton's formula[1] with the collisional frequency, the Lorentz factor and the magnetic field set equal to zero, applying the theorem of Breit and Tuve[2] and ordinary ray-tracing techniques, one finds for the electron density, N,

$$N=\left[1-K_n^2-\frac{1}{c^2(dT_n/dh_n)^2}\right]\times 1.24\times 10^4 f^2.$$

In this formula, K_n is the sine of the angle between the ray and the vertical, dT_n/dh_n is the slope of the probing signal time *versus* altitude curve, and f is the probing frequency in Mc/sec. This

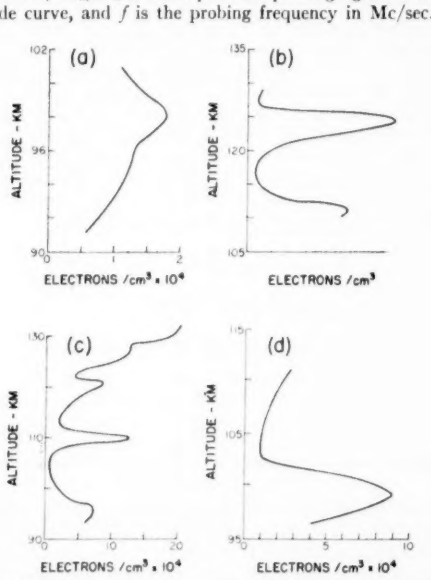

FIG. 2. Altitude *vs* electron concentration for (a) November 21, 1946, (b) April 17, 1947, (c) June 26, 1953 and (d) July 1, 1953.

formula was used to reduce the delay data given in Fig. 1, yielding the plots of altitude *vs* effective electron density shown in Fig. 2.

Examination of these curves yield a significant result. The June 1953 and April 1947 plots show clearly a bifurcation of the *E* region. The maximum electron density occurs at heights of

110 and 95 kilometers for the June plot and 124 and 111 kilometers for the April plot. A series of film records of $P'-f$ curves were taken on a Bureau of Standards Model C-3 Ionosphere Recorder a few moments before and after each of these rocket launchings to aid in the interpretation of the rocket data. Examination of these $P'-f$ curves for June 26 and April 17 show only one layer for the E region at heights of 110 and 120 kilometers, respectively, which compare favorably with the heights obtained by rocket measurement for the upper layer. Although data are lacking above 111 kilometers for July 1953 and above 105 kilometers for November 1946, nevertheless the lower layer is clearly indicated in both cases at altitudes of 99 and 98 kilometers, respectively. Ground station data shows one layer at 117 kilometers for July 1953 and 120 kilometers for November 1946. However, it is not expected that these particular ground measurements would show the lower layer since the critical frequency of this layer is approximately 2 Mc/sec. This frequency is in the region of high daytime absorption and consequently would require much more power than is available in the C-3 recorder to obtain a reflection.

On reducing the $P'-f$ curve to terms of maximum electron density and height for the E_1 and E_2 layers and comparing with the data from the June firing, the following is found. For the E_1 layer, rocket data give 1.3×10^5/cm³ effective electrons at a height of 110 kilometers; ground data give 1.5×10^5/cm³ also at a height of 110 kilometers. For the E_2 region the rocket data give a value of N approaching 2×10^5/cm³ at a height of 130 kilometers, while ground data give 2.5×10^5/cm³ at a height of 135 kilometers. This correlation is most striking, and lends much more credence to the belief that, had the C-3 recorder been capable of receiving reflections at this time in the 2-Mc/sec range, it would have recorded the lowermost E layer at 96 kilometers. It is of interest to note that the separation between peaks on these flights is in all cases not less than 13 kilometers, nor more than 18 kilometers.

* Now at Sylvania Electric Products Incorporated, Box 25, Mt. View, California.
† University of Utah, Salt Lake City, Utah.
[1] E. V. Appleton, Proc. Phys. Soc. (London) **37**, 160 (1925); J. Inst. Elec. Engrs. (London) **71**, 642 (1932).
[2] G. Breit and M. A. Tuve, Phys. Rev. **28**, 554 (1926).

The Conductivity of Germanium at 2.4×10^{10} cps

V. KLINGER
Imperial College, London, England
(Received May 26, 1953; revised manuscript August 31, 1953)

MEASUREMENTS have been carried out on a number of samples of germanium both polycrystalline and single crystals, of which the most interesting results—obtained on a highly purified single crystal ($11\times5\times1$ mm approx.)—are shown in Figs. 1, 2, and 3. The 1.24-cm results were obtained using a rectangular wave guide operating in the H_{01} mode by the method described by Roberts and Von Hippel.[1]

Figures 1 and 2 show the permittivity and loss tangent measured at 1.24 cm plotted as functions of temperature over the range 0–100°C, and Fig. 3 gives plots of the logarithms of the dc conductivity and of the derived effective conductivity at 1.24 cm against $1000/T$.

It will be observed that the sample is almost intrinsic (dc room temperature resistivity 56 ohm cm; estimated impurities 10^{12} cm^{-3}). If the conductivity is assumed given by $\sigma=\sigma_0\exp(-A/2kT)$, the figures give an activation energy A of 0.77$_5$ ev and 0.60 ev for the dc and 1.24-cm cases, respectively. The dc value is somewhat higher than the published figure (reference 3) of 0.75 ev. This is thought to be due to a small contribution of impurity scattering. The difference in conductivities between the dc and 1.24-cm cases is approximately in the ratio 2:1 at 100°C.

The conductivity and permittivity of electronically conducting materials at high frequency has been discussed theoretically by Kronig.[2] His theory is only approximate in nature, but, in the absence of a more rigorous analysis, it will be used here.

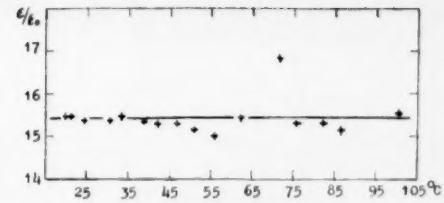

FIG. 1. Observed relative permittivity ϵ/ϵ_0 as a function of the temperature T°C at 1.24 cm.

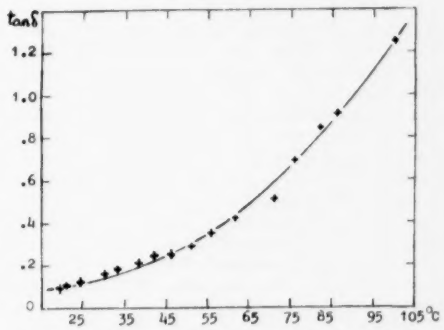

FIG. 2. Observed loss-tangent as a function of the temperature T°C at 1.24 cm.

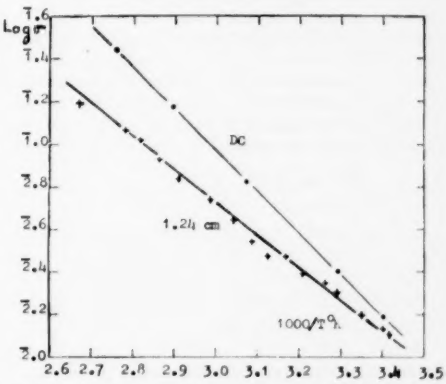

FIG. 3. $\log_{10}$ conductivity (ohm cm)$^{-1}$ *versus* $1/T°$ absolute at dc and 1.24 cm. The derived activation energies are 0.77$_5$ ev and 0.60 ev, respectively.

Kronig's conductivity and permittivity relations may be put in the form:

$$\sigma_\nu=\frac{\sigma_{dc}}{1+(\nu/\gamma)^2}=\frac{\sigma_{dc}}{1+(\omega\tau)^2}, \tag{1}$$

$$\kappa_\nu=\kappa_0-\sigma_\nu/\gamma, \tag{2}$$

where ν denotes the frequency in cps, $\omega=2\pi\nu$, and $\tau=2\pi/\gamma$ is the relaxation time of the charge carriers.

As is well known, the conductivity in semiconductors is given by:

$$\sigma=en\mu_n+ep\mu_p,$$

where n, p are the densities of electrons and holes, respectively, and μ_n, μ_p their corresponding mobilities. The relaxation time depends on the type of charge carrier considered, on the nature of the medium in which they move, and on the temperature.

In highly purified single crystals of germanium, τ is determined essentially by lattice scattering[3] such that

$$\tau\ (\text{lattice})=aT^{-\frac{3}{2}}. \tag{3}$$

However, this τ will be different for holes and electrons so that the conductivity relation for intrinsic germanium may be expected to be of the form:

$$\sigma_p = \tfrac{1}{2}\sigma_{dc}\left(\frac{1}{1+(\omega\tau_p)^2}+\frac{1}{1+(\omega\tau_n)^2}\right). \quad (4)$$

In the extrinsic range, where one type of charge carrier predominates and the mobility is determined by impurity scattering,

$$\sigma_p = \sigma_{dc}/[1+(\omega\tau_{imp})^2] \quad (5)$$

in which, according to reference 3,

$$\tau_{imp} \doteqdot bT^{-\frac{1}{2}}. \quad (6)$$

The corresponding equations for the permittivity are rather doubtful, particularly in the intrinsic case. This is due to the fact that κ_0, which appears as a constant in Eq. (2), is dependent on the number of electrons, since an electron in a bound state will contribute appreciably by virtue of its ease of polarizability. When an electron is excited into the conduction band, however, this contribution is lacking, and moreover, electronic inertia effects manifest themselves as a further reduction in the permittivity. A replacement of κ_0 by $\kappa_0(1-Cn)$ would probably be more accurate, where C, which accounts for the contribution of the ionizable electrons to the permittivity, will be a small fraction.

In the case of extrinsic semiconductors, the ionized impurities complicate matters even more. An ionized impurity and a nearby hole or electron (as the case may be) may be regarded as a very loosely held dipole.

The agreement between Kronig's simple theory and the experimental results on extrinsic germanium obtained recently[4] is of considerable interest in this connection.

In the small temperature range covered by the present measurements, no difficulty arises in getting an equation of type (4), with use of (3) and (6), to match the experimental results. If this is done, the relaxation times τ_p and τ_n turn out to be comparable with $\tau \sim 4\times10^{-11}$ sec, the period of the 1.24-cm excitation, whereas the dc measurements usually give:

$$\tau = \frac{\text{mean free path}}{\text{velocity}} \doteqdot \frac{10^{-5}\text{ cm}}{10^{7}\text{ cm/sec}} \doteqdot 10^{-12}\text{ sec}.$$

Kronig's formula (1) is, of course, a considerable simplification of the probable state of affairs. Lattice scattering takes place over a large number of atoms and is not localized as in the case of impurity scattering. The distribution of velocities of the electrons and the distribution of mean free paths are likely to give rather a wide distribution of relaxation times, which probably accounts for a relaxation phenomenon being observable at 1.24 cm.

[1] S. Roberts and A. Von Hippel, J. Appl. Phys. **17**, 610 (1946).
[2] R. de L. Kronig, Proc. Roy. Soc. (London) **133**, 255 (1931).
[3] E. M. Conwell, Proc. Inst. Radio Engrs. **40**, 1327 (1952).
[4] T. S. Benedict and W. Shockley, Phys. Rev. **89**, 1152 (1953).

The Exchange Potential in an Electron Gas at Nonzero Temperature

N. H. March
Department of Physics, University of Sheffield, Sheffield, England
(Received July 31, 1953)

In a recent paper with the above title, Zirin[1] has assumed that the simple Fermi-Dirac statistics can be applied when one is dealing with a free electron gas in which exchange interactions are considered, whereas it is known from the recent work of Koppe,[2] Wohlfarth,[3] and Lidiard[4,5] that this is not the case. A similar assumption was, in fact, made earlier by Yokota[6] when discussing the generalization of the Thomas-Fermi-Dirac method to nonzero temperature.

Assuming Fermi-Dirac statistics, Zirin finds effectively that the exchange energy of a system of N free electrons enclosed in a volume V and at temperature T is given by

$$A = -\tfrac{3}{4}N\epsilon_j\beta(kT/\epsilon_0) \quad (1)$$

where

$$\epsilon_0 = \frac{h^2}{8m}\left(\frac{3N}{\pi V}\right)^{\frac{1}{3}}, \quad \epsilon_j = e^2\left(\frac{3N}{\pi V}\right)^{\frac{1}{3}},$$

and he has given a short table of values of β.

Now in fact an approximation to the exchange energy when the distribution function is modified to take account of exchange can be obtained immediately from Lidiard's work.[4] The exchange energy cannot in general be written in the form (1), but only as

$$A = -\tfrac{3}{4}N\epsilon_j\beta\left(\frac{kT}{\epsilon_0},\frac{\epsilon_j}{\epsilon_0}\right) \quad (2)$$

β being a function of the two variables kT/ϵ_0 and ϵ_j/ϵ_0. In Fig. 1 we have plotted Zirin's results (curve1) and the results obtained from Lidiard's paper for $\epsilon_j/\epsilon_0=1$ (curve 4) in order to demonstrate in a particular case the effect of the modified distribution function

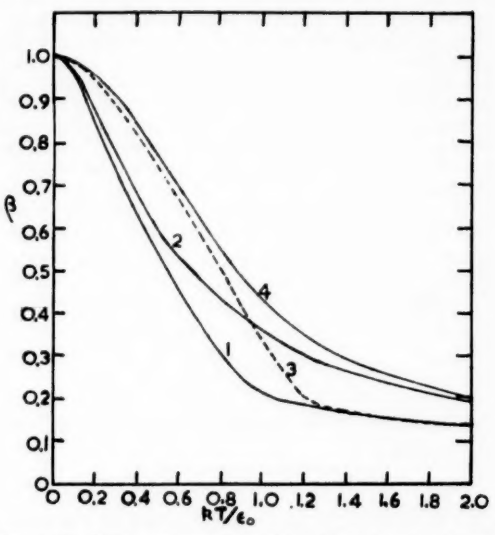

FIG. 1. β as function of temperature. Curve 1: Zirin's results. Curve 2: Lidiard approximation for $\epsilon_j=0$. Curve 3: Estimate for $\epsilon_j/\epsilon_0=1$. Curve 4: Lidiard approximation for $\epsilon_j/\epsilon_0=1$.

on the exchange energy. However, this approximation for $\epsilon_j/\epsilon_0=1$ is not likely to be very accurate, as the following considerations suggest. When $\epsilon_j=0$ the exchange energy is strictly zero. We can, however, still use Lidiard's function[4] when $\epsilon_j=0$ to calculate β, which we can compare with Zirin's curve. We have done this and the results are shown in curve 2 of Fig. 1. It can be seen that particularly for $kT/\epsilon_0>\frac{1}{2}$ curves 1 and 2 are considerably different, and we can infer that the results for finite values of ϵ_j may be quite seriously in error.

To obtain a better approximation we need a distribution function which reduces to the Fermi-Dirac function when $\epsilon_j=0$. Such a function has been proposed by Lidiard in a later paper,[5] and has been used by him to refine Wohlfarth's calculations of the specific heat of free electrons.[3] The distribution function he proposed is

$$f(|\mathbf{k}|) = \left[\exp\frac{1}{k\tau}\left(\frac{h^2|\mathbf{k}|^2}{8\pi^2m}-\zeta\right)+1\right]^{-1} \quad (3)$$

where τ, a "modified temperature," is to be found by putting $\partial F/\partial\tau=0$, F being the free energy. This function has also been

used by Umeda and Tomishima[7] in extending the Thomas-Fermi-Dirac method to nonzero temperatures.[8]

These applications were confined to low temperatures, but in principle Zirin's table now allows this distribution function to be used for all temperatures. For, choosing kT/ϵ_0 and ϵ_j/ϵ_0, we can obtain the free energy F as a function of τ, using Stoner's tables[9] to find the kinetic energy and entropy terms and Zirin's table to find the exchange energy. Then τ can be chosen to minimize the free energy and hence β can be found.

Unfortunately, however, in practice the accuracy of the calculations is limited by the nature of Zirin's table, since the free energy curve is very flat near the minimum, and it is not possible therefore to determine τ at all precisely. Thus the broken curve 3 in Fig. 1 is more of an estimate than the result of a precise calculation, for particularly in the neighborhood of $kT/\epsilon_0=1$ the possible errors are large. Nevertheless, it is possible to conclude that whereas Zirin's curve considerably underestimates β for $\epsilon_j/\epsilon_0=1$, Lidiard's work leads to values which are too great, particularly for $kT/\epsilon_0>1$. Curve 3 will certainly give a better approximation than either of these, but until a more accurate table than Zirin's is available it does not seem possible to be more precise than this.

In conclusion, it seems worthwhile to point out that though Lidiard's work does not lead to a very good approximation to the exchange energy, the free energy, which is the important quantity in most applications, for example in the calculation of specific heat,[3] ferromagnetic properties,[4] and spin paramagnetism,[10] is much less in error. This is shown quite clearly in Fig. 2, from

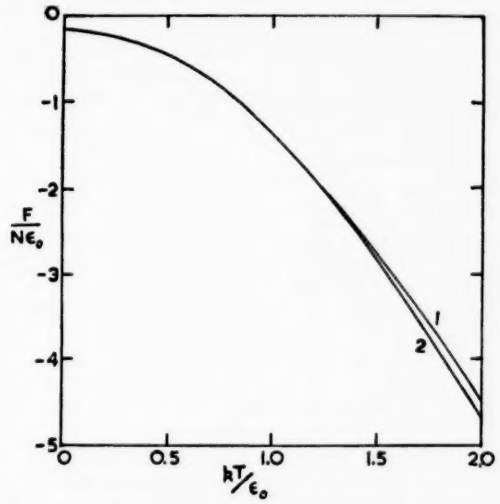

FIG. 2. Free energy as function of temperature for $\epsilon_j/\epsilon_0=1$. Curve 1: Lidiard approximation. Curve 2: Improved approximation.

which it can be seen that the free energy is insensitive to the choice of distribution function, and that, as we would expect, the function given by (3) is everywhere a better approximation than that used in Lidiard's first paper.[4]

[1] H. Zirin, Phys. Rev. **90**, 795 (1953).
[2] H. Koppe, Z. Naturforsch. **2A**, 429 (1947).
[3] E. P. Wohlfarth, Phil. Mag. **41**, 534 (1950).
[4] A. B. Lidiard, Proc. Phys. Soc. (London) **A64**, 814 (1951).
[5] A. B. Lidiard, Phil. Mag. **42**, 1325 (1951).
[6] I. Yokota, J. Phys. Soc. Japan **4**, 82 (1949).
[7] K. Umeda and Y. Tomishima, J. Phys. Soc. Japan **8**, 360 (1953).
[8] See also N. H. March, Phil. Mag. **44**, 346 (1953).
[9] E. C. Stoner, Phil. Mag. **28**, 257 (1939).
[10] N. H. March and B. Donovan (unpublished calculations).

Ionization Loss in Nuclear Emulsions*

JOHN R. FLEMING AND J. J. LORD
Department of Physics, University of Washington, Seattle, Washington
(Received July 22, 1953)

A STUDY has been made of the relationship between the velocity of singly charged particles and the resultant grain density produced in an Ilford G-5 emulsion. A single 2 in.×2 in., 400-micron thick place was exposed successively to slow negative muons (for their decay electrons) and to 227, 122, 81, and 31 Mev negative pions from the Chicago cyclotron.[1] The plate was rotated 45° after each exposure so that the tracks of particles of differing energies could be distinguished. This also made it possible to make grain and blob density measurements of tracks over a restricted portion of a single plate.

TABLE I. Data on grain counting.

Particle	Energy (Mev)	Total track length (microns)	Blob mean (100 μ)	Normal blob mean	Grain mean (100 μ)	E/Mc^2
e^-	34 ±10	40 400	30.44 ±0.08	0.983	41.9 ±0.1	66.6
π^-	224 ±5	112 500	27.78 ±0.08	0.897	37.1 ±0.1	1.61
π^-	121 ±5	24 600	31.69 ±0.08	1.023	43.6 ±0.6	00.87
π^-	80 ±4	34 900	36.71 ±0.15	1.185	52.0 ±0.3	00.58
π^-	24 ±2	40 800	45.16 ±0.11	1.458	75.7 ±0.4	00.173

Since the cyclotron meson beams contain 5 to 10 percent muons and electrons,[1] it was necessary to insure that only pion tracks were measured by selecting the tracks of particles which produced nuclear disintegrations in the emulsion. Each track was then followed back to the point where it entered the emulsion so that the average energy of the pion could be determined for the interval measured. The average energies of the pions in the measured portions of the tracks are given in Table I. The errors given for the pion energies in Table I include both the spread of energy of the incident pions and the variations of the path lengths of the pions in the emulsion. In the case of the electrons, the spread in energy is due to the natural muon decay energy spectrum.

All grain and blob counting was made by a single observer whose reproducibility was found to be 2.5 percent for grain and 0.5 percent for blob counting. The plate was calibrated for the variation of blob and grain densities with depth below the surface and the measured mean track density corrected accordingly. This was the largest single correction applied and amounted to −0.9, +2.59, +1.34, +2.14, and +1.50 percent for, respectively, the electrons, and the pions of 224, 121, 80, and 24 Mev. The track densities of the randomly distributed electrons were found to be independent of the azimuthal angle indicating the absence of any effects due to a possible preferential alignment of the AgBr crystals of the emulsion.

The corrected mean values for the grain and blob densities are given in Table I. These data for the blob densities are plotted in Fig. 1 together with theoretical curve for the restricted energy loss of electrons and heavy particles in AgBr for energy exchanges less than 5 kev. The data were normalized so that the point representing the average value of the decay electron blob density lies on the theoretical curve. This curve was obtained from the calculations of Sternheimer[2] based on the methods of treatment given by Fermi and Halpern and Hall.[3] The data (Fig. 1) agree reasonably well with this theory except for the point at $E/Mc^2=0.173$. This is due to the saturation of blob density which occurs in this range of high track densities. The close agreement of the data with the theory, which gives a 14.0 percent relativistic increase, implies that nearly all of the energy exchanges less than 5 kev go into the formation of grains.

Since Pickup and Voyvodic[4] first established the relativistic rise of track density in photographic emulsions, there have been a number of experimental investigations undertaken to establish these features.[5] The data reported herein were taken in order to give very precise information under more controlled conditions.

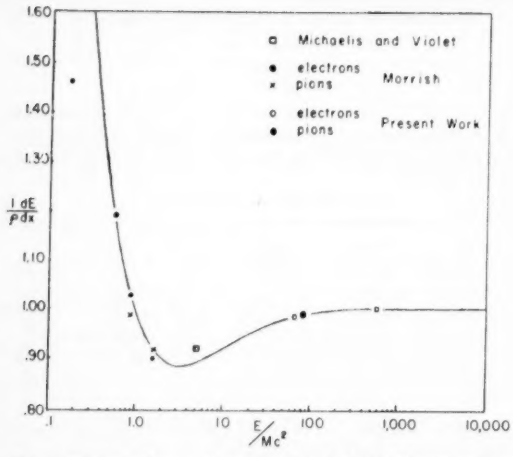

FIG. 1. Theoretical curve of energy loss in AgBr in Mev per gram per cm² as a function of E/Mc^2. Blob densities are plotted and normalized to the curve at the points for the decay electrons in the present investigation and that of Morrish. The data of Michaelis and Violet are normalized to the curve for their point at $E/Mc^2=580$.

Similar type experiments over restricted portions of the curve have been made at Berkeley[6] and by Morrish,[7] and these data have been included in Fig. 1. The points, Fig. 1, appear to be in reasonable agreement with the theoretical curve; however, the agreement between both the theory and the different observers would be quite good if all statistical errors were doubled. It is probable that this is due to some systematic errors, the nature of which are not known at present.

We would like to thank Professors Marcel Schein and H. L. Anderson for the photographic plate and the cyclotron exposure. It is also a pleasure to thank Professors E. A. Uehling and S. H. Neddermeyer for very helpful discussions.

* Assisted by the joint program of the U. S. Office of Naval Research and the U. S. Atomic Energy Commission.

[1] Anderson, Fermi, Martin, and Nagle, Phys. Rev. **91**, 155 (1953).
[2] R. M. Sternheimer, Phys. Rev. **88**, 851 (1952); **91**, 256 (1953).
[3] Enrico Fermi, Phys. Rev. **56**, 1242 (1939); O. Halpern and H. Hall, Phys. Rev. **73**, 477 (1948).
[4] E. Pickup and L. Voyvodic, Phys. Rev. **80**, 89 (1950).
[5] Daniel, Davies, Mulvey, and Perkins, Phil. Mag. **43**, 753 (1952); M. M. Shapiro and B. Stiller, Phys. Rev. **87**, 682 (1952).
[6] R. P. Michaelis and C. E. Violet, Phys. Rev. **90**, 723 (1953).
[7] A. H. Morrish, Phys. Rev. **91**, 423 (1953).

Negative μ-Meson Capture in Carbon*

T. N. K. GODFREY
Palmer Physical Laboratory, Princeton University, Princeton, New Jersey
(Received September 1, 1953)

WE are studying experimentally the behavior of cosmic-ray μ mesons stopped in carbon. Bell and Hincks[1] have shown that the mean life of negative μ mesons in carbon differs from the mean life of positive μ mesons. They compute the nuclear capture rate for negative μ mesons in carbon to be $A=(5.5\pm1.5)\times10^4$ sec^{-1}. The fraction of stopped negative μ mesons which are captured, $F=A/(A+1/\tau)$, is 0.11 ± 0.03, where τ is the mean life of positive μ mesons. The possible end products of the capture reaction are bound states of B^{12} or groups of fragments such as B^{11} plus a neutron. The object of our investigation is a determination of the probability for the end product to be B^{12} in its ground state. We present here a brief description of the method and some preliminary results.

The μ mesons to be studied are stopped in an organic liquid scintillation counter. The counter has a sensitive volume of 4 in.×4½ in.×5 in. viewed by two RCA type *C*7157 photomultipliers. The pulses from the counter are presented on an oscilloscope and photographed. An arrangement of coincidence and anticoincidence Geiger counters selects events and triggers the oscilloscope sweep. Details of the presentation scheme and of the means used to eliminate spurious events will be presented in a subsequent paper.

Two types of events are investigated. In the first, the pulse from the arriving μ meson is followed by a pulse with a 2 μsec mean delay, indicating that the meson decayed. In the second type of event, the arriving μ-meson pulse is followed by a pulse with a 39 millisecond mean delay, indicating that a C^{12} nucleus captured the meson, forming a B^{12} nucleus which subsequently decayed by β emission back to C^{12}.[2,3] The end product of the capture reaction in the second type of event is B^{12} in either the ground state or a bound excited state. (An unbound excited state would decay by neutron emission and a B^{12} β particle would never be observed.) A bound excited state would promptly decay by γ emission to the ground state and later a β particle would be emitted. With the present apparatus, the γ ray would in general not be detected, and the event would have the same appearance as if the ground state had been formed in the original capture reaction.

Let D be the number of events observed in which a negative meson decays, as determined from the total number of decays, corrected by the data of Bell and Hincks and by the known positive excess. Let C be the number of capture events observed. Then $P=C/D\tau$ is the rate of the μ-meson capture reaction that results in a B^{12} nucleus in the ground state or in a bound excited state. P is thus also an upper limit on the rate of the reaction whose end product is B^{12} in the ground state. Our preliminary result is that $P=(5\pm2)\times10^3$ sec^{-1}.

The ratio P/A is 0.09 ± 0.05. This indicates that only about a tenth of the capture reactions result in B^{12} in a bound state. If the unbound states of B^{12} usually break up into B^{11} plus a neutron, then from the low value of P/A one would expect the multiplicity of the neutrons emitted in the capture of μ mesons in carbon to be near unity. Although the neutron multiplicity has been measured[3] for the capture of μ mesons in several elements, it has not yet been done for carbon.

A full report will be published upon completion of this investigation.

* Supported by the joint program of the U. S. Atomic Energy Commission and the U. S. Office of Naval Research.
† National Science Foundation Predoctoral Fellow.
[1] W. E. Bell and E. P. Hincks, Phys. Rev. **88**, 1424 (1952).
[2] J. E. Brolley, Jr., *et al.*, Phys. Rev. **83**, 990 (1951).
[3] M. F. Crouch and R. D. Sard, Phys. Rev. **85**, 120 (1952); A. M. Conforto and R. D. Sard, Phys. Rev. **86**, 465 (1952); M. Widgoff, Phys. Rev. **90**, 891 (1953).

Liquid Scintillation Counting of Natural C^{14}†

F. N. HAYES, D. L. WILLIAMS, AND BETTY ROGERS
Los Alamos Scientific Laboratory, University of California, Los Alamos, New Mexico
(Received May 8, 1953; revised manuscript received September 2, 1953)

DURING an investigation of the natural C^{14} content of liquid scintillation solvents, samples of *p*-cymene were obtained which gave very different counting rates. A consistently high rate resulted from material whose primary origin, via certain trees, was contemporary atmospheric carbon dioxide[1] and an equally consistent low value was derived from samples synthesized entirely from petroluem chemicals.[2]

Accurate knowledge of these two counting rates and the accompanying backgrounds, along with careful standardization of the C^{14} detection efficiencies during the experiments, has allowed easy realization of a number which is the specific activity of natural C^{14} in *p*-cymene and in the constituents of turpentine from which it is derived.

A Los Alamos Model 530 Coincidence-Anticoincidence System[3] was used in this study. 2,5-diphenyloxazole[4] in a concentration of 4 g/l was the liquid scintillation solute and *p*-cymene volumes of 30 ml and 40 ml were employed. Five complete experiments were run, each at a different instrumental sensitivity. Absolute counting efficiencies were determined with C^{14}-benzoic acid as an internal standard. Mass spectrographic analyses gave a value of 6.00 ± 0.02 percent C^{14} in the carboxyl carbon of the benzoic acid. This was synthesized[5] from carbon dioxide containing 5.96 ± 0.01 percent $C^{14}O_2$. The benzoic acid specific activity was calculated from the C^{14} abundance and a half-life value of 5568 years.[6]

Experimental gross rates were corrected for background and converted to disintegration rates. The average value, from five experiments, of the specific activity of carbon in contemporary *p*-cymene was 12.9 ± 0.2 disintegrations per minute per gram. This number represents a rather startling departure from the usually quoted value of 15.3 ± 0.1 disintegrations per minute per gram of carbon in wood.[7] Such a difference is not altogether unexpected with both a new counting form and an instrument of twelve times higher efficiency than the Screen Wall Counter used by Libby and co-workers. The accuracy of either number depends on the efficiency calibration of the instrument used and not on the number of samples subsequently counted.

The liquid scintillation counter may soon be routinely used for radiocarbon dating. Further work is being carried out with methanol and methyl ether, both of which can easily be derived from carbon dioxide and which may be incorporated into the solvent system of liquid scintillators. The relatively high background of instruments such as the Los Alamos Model 530 Coincidence-Anticoincidence System is the only serious problem remaining before they can be converted to natural radiocarbon counters. Ways are being explored for lowering counting rates due to thermionic emission, light dark current, natural contamination in the apparatus, and external radiation. These will be reported at a later date.

The authors wish to thank R. L. Schuch for his valuable assistance and R. J. Kandel and W. H. Rogers for the mass spectrographic analyses.

† Work done under the auspices of the U. S. Atomic Energy Commission.
[1] Distillation Products Inc., Stock Number 83.
[2] Synthesized from propylene and toluene by the procedure of Ipatieff, Corson, and Pines, J. Am. Chem. Soc. **58**, 919 (1936).
[3] R. D. Hiebert and R. J. Watts, Nucleonics (to be published).
[4] Hayes, Hiebert, and Schuch, Science **116**, 140 (1952).
[5] D. L. Williams and A. R. Ronzio, Los Alamos Scientific Laboratory report, LADC-1385 (unpublished).
[6] Engelkemeir, Hamill, Ingrahm, and Libby, Phys. Rev. **75**, 1825 (1949).
[7] W. F. Libby, *Radiocarbon Dating* (The University of Chicago Press, Chicago, 1952), p. 16.

Crystal Structure and Nuclear Directional Correlation. I. Pb^{204}†

H. Frauenfelder, J. S. Lawson, Jr., W. Jentschke, and G. DePasquali
University of Illinois, Urbana, Illinois
(Received August 27, 1953)

THE Zürich group has recently shown in a beautiful experiment[1] that the $\gamma-\gamma$ directional correlation of Cd^{111} in a metallic indium single crystal depends markedly upon the orientation of the crystal axes with respect to the counter axes. Their experiment demonstrates that the main contribution to the effect of extranuclear fields on the directional correlation arises from the interaction between the nuclear quadrupole moment and electric field gradients.

Growing and orienting single crystals is, however, so time-consuming that the method is applicable only to nuclides with relatively long half-lives. In the case of Pb^{204} ($T_{\frac{1}{2}}=65$ min), we therefore chose a different approach to investigate the effect of crystal structure and studied the directional correlation of this isomer in Pb–Tl substitutional alloys. Pb and Tl form mixed crystals over a wide range of composition[2] and display at suitable compositions and temperatures face-centered cubic (f.c.c.), body-centered cubic (b.c.c.), and hexagonal close-packed (h.c.p.) lattices.

We determined the directional correlation function $W(\theta)$ of Pb^{204} for two types of sources at various temperatures. The first type (~100 percent Tl) was directly produced by irradiating Tl in the cyclotron with deuterons[3] and constitutes therefore a Pb–Tl crystal with vanishingly small Pb content. Such a crystal possesses an h.c.p. lattice below 235°C and a b.c.c. lattice between 235°C and the melting point 303°C. The second type (~40 percent Tl), prepared by adding Pb to the irradiated Tl, shows the f.c.c. structure of Pb and has a melting point of 365°C.

The measured anisotropies, $A=[W(180°)/W(90°)]-1$, are shown in Figs. 1(a) and 1(b) as a function of the source temperature T. (The indicated errors are statistical errors only. The measured anisotropies are corrected for scattering in the source[3] and the absolute values may therefore be in error by as much as a factor 1.1. However, this does not affect the relative values.)

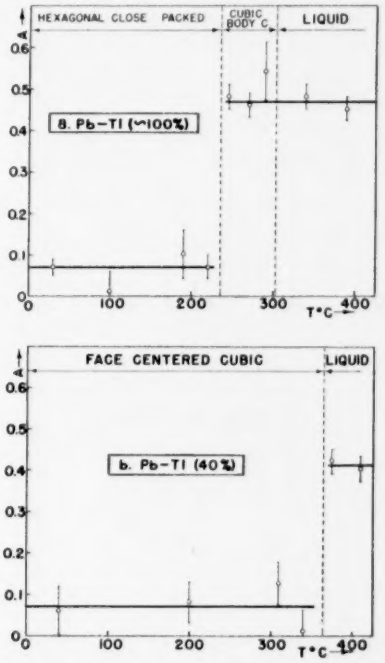

FIG. 1. Anisotropy A of the Pb^{204} $\gamma-\gamma$ cascade in Pb–Tl alloys as a function of the source temperature T. (a) 100 percent Tl. (b) 40 percent Tl.

The data in Fig. 1 show the importance of the crystal structure for the directional correlation of Pb^{204}. The highest anisotropy, 0.47 (±0.02) is obtained *both* in the solid b.c.c. lattice and in the liquid of corresponding composition.[3] The discussion of the Pb^{204} decay shows that no greater anisotropy is possible.[3] We therefore conclude that the interaction between the nucleus and its surroundings is vanishingly small in the b.c.c. lattice.

However, problems arise in the explanation of the anisotropies for the h.c.p. and the f.c.c. structures (0.07 ± 0.02, and 0.07 ± 0.03, respectively). These values are considerably lower than the lowest ("hard core") value 0.15 predicted by theory for a static quadrupole interaction in randomly oriented crystals.[4] (Attempts to show that a partial orientation of our crystals caused the low values were unsuccessful.) No value for the magnitude of the quadrupole interaction can therefore be given. The fact that the f.c.c. lattice yields the same low anisotropy as does the h.c.p. lattice is also unexplained.

The present results demonstrate the effect of crystal structure on the directional correlation of Pb^{204}. It is quite evident that more theoretical and experimental investigations are needed to clarify the major deviations from the expected behavior.

† Assisted by the joint program of the U. S. Office of Naval Research and and the U. S. Atomic Energy Commission.

[1] Albers-Schönberg, Hänni, Heer, Novey, and Scherrer, Phys. Rev. **90**, 322 (1953).
[2] V. C. Tang and L. Pauling, Acta Cryst. **5**, 39 (1952).
[3] Frauenfelder, Lawson, Jentschke, and DePasquali (to be published).
[4] A. Abragam and R. V. Pound (to be published).

Isomerism in Pb^{206}

D. E. Alburger,* *Nobel Institute of Physics, Stockholm, Sweden*
AND
M. H. L. Pryce, *Clarendon Laboratory, Oxford, England*
(Received August 24, 1953)

An investigation of the energy levels of Pb^{206}, formed in the electron capture decay of 6.4-day Bi^{206}, has been undertaken because of theoretical interest[1] in nuclei near closed-shell lead-208. Previous results[2] were inconclusive since the transition energies could not be determined with sufficient accuracy and a number of unresolved lines were known to be present.

The following measurements on Bi^{206} have been carried out at the Nobel Institute and at the Royal Institute of Technology, Stockholm; conversion line energies and intensities in a double-focusing spectrometer and in an intermediate-image spectrometer; coincidences between pairs of K conversion lines in a two-lens "spectrogoniometer"; and coincidences between conversion lines and gamma rays observed in the intermediate-image spectrometer modified with a NaI crystal detector near the source. The energy measurements, which establish a number of cascade crossovers, together with the coincidence data impose more than 50 restrictions on the level arrangement. Except for a few very weak unassigned gamma rays the tentative level scheme adopted contains 26 transitions and satisfies all of the conditions mentioned above.

Two sets of lines which are of special interest have their relative intensities listed in Table I. Both transitions are thought to

Table I. Relative conversion line intensities of $E3$ isomeric transitions in Pb^{206}.

E_γ	K	L_{I+II}	L_{III}	M	N
202.5	0.084	0.57	0.25	0.22	···
516.1	18	10	~1.8	3.3	~0.6

originate from a 7− fifth excited state at 2200.3 kev going to the fourth and third levels at 1998.1 and 1683.8 kev, respectively. The latter are each assigned 4+ not only because the K to L ratios of the two transitions appear to be consistent with $E3$ but because of other features of the decay scheme. It is possible that the 7− level is analogous to that responsible for the 68-min isomer of Pb^{204}.

A measurement of the lifetime of the Pb^{206} isomeric state has been carried out by placing a Bi^{206} source very close to a NaI crystal and EMI photomultiplier detector and allowing the output pulses to trigger the sweep of a Tektronix type 511AD synchroscope. When a sweep is started by the pulse from a gamma ray which is "prompt" with respect to K capture and occurs in the upper part of the level scheme there is a chance of observing a delayed pulse from either the main isomeric transition or gammas in the lower part of the scheme. The efficiency for detecting delayed events is expected to be reasonably high since, on the basis of the assumed level scheme, 10 strong gamma-ray transitions precede the isomeric level and 5 strong ones follow it.

For optimum conditions the integral pulse-height selector was set as low as possible, i.e., to the point where the room background and noise counting rate from the shielded detector was about 150 per minute. A scope sweep of 500 microseconds (10 cm) was used and its calibration and linearity were checked by feeding in a 200-kc/sec sine wave from a G.R. type 805C signal generator and then counting the number of cycles per cm. To record the data a cardboard mask covered the base line and all other parts of the scope face except a 1.5-cm wide slot whose distance from the origin pulse could be adjusted as desired. A large diameter short focal length lens placed at a distance of 50 cm from the scope screen focused the light pulses appearing in the mask opening onto a 931 photomultiplier. The latter was provided with a long-time-constant circuit in order to smooth out the "hashy" pulse arising from the decay characteristics of the scope screen phosphor. Even with this precaution reliable operation was not attained until a one-kick multivibrator having a time constant of several milliseconds was inserted between the discriminator and scalar.

Figure 1 shows the delayed pulse distribution obtained with a source of approximately 5×10^{-4} microcurie which gave a triggering rate of 1500 counts per min. A calculated background of 2.8 counts per min has been subtracted and corrections have been made for nonlinearity of the oscilloscope trace. The slope of the curve corresponds to a half-life of 145 ± 15 microseconds. This value is just above the region 10^{-7} to 10^{-4} sec within which no lifetimes had been observed[2] by means of the more commonly used delayed-coincidence techniques.

The bismuth sources were prepared by cyclotron bombardment of lead with 16-Mev deuterons followed by chemical separation.[2] Measurements on the conversion electron spectrum showed that a small amount of 50-year Bi^{207} and a very minute amount of 14-day Bi^{205} were present. The decay rate of the isomer was therefore studied and its intensity was observed to decrease at approximately the 6-day rate of Bi^{206}.

The 145-microsecond lifetime, which is determined almost entirely by the 516.1-kev transition, appears to be shorter than expected[3] although no multipole order other than $E3$ gives as reasonable a fit. Using the K conversion coefficients[4] of Rose *et al.*, one can compute from the conversion line intensities in Table I that the ratio of the 516.1- to 202.5-kev transition probabilities is 300 (with an error of perhaps 25 percent) if it is assumed that both are $E3$. This leads to a partial half-life of about 0.04 sec for the 202.5-kev transition. The computed ratio of unconverted gamma rays is about 1600. The fact that the ratio would be 700 on the basis of a seventh-power energy dependence[3] seems to be in agreement with the observations.

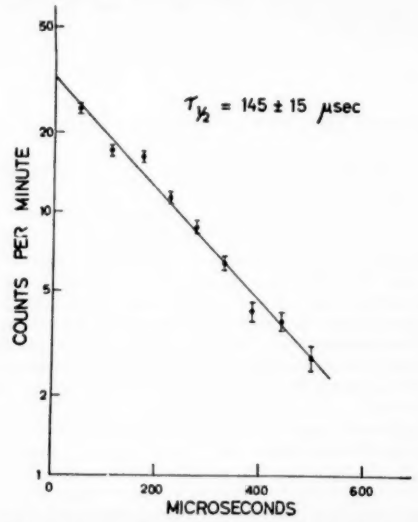

Fig. 1. Delayed pulse distribution resulting from the isomeric state of Pb^{206}.

A complete report on the Bi^{206} decay scheme will be published later. The authors are indebted to Dr. H. Atterling who arranged for the cyclotron irradiations and to Dr. W. Forsling and Mr. T. Karlsson who kindly performed the chemical separations. The first-named author would like to thank Professor Kai Siegbahn for the use of facilities at the Royal Institute of Technology and Professor Manne Siegbahn for extending the hospitality of the Nobel Institute during 1952–1953.

* National Science Foundation Fellow on leave from Brookhaven National Laboratory; now returned to latter address.

[1] M. H. L. Pryce, Proc. Phys. Soc. (London) **A65**, 773 (1952).
[2] D. E. Alburger and G. Friedlander, Phys. Rev. **81**, 523 (1951).
[3] M. Goldhaber and A. W. Sunyar, Phys. Rev. **83**, 906 (1951).
[4] Rose, Goertzel, Spinrad, Harr, and Strong (privately circulated tables).

Yields of Low-Energy Protons and Alphas Resulting from High-Energy Bombardment of Ag

ROBERT W. DEUTSCH*
Radiation Laboratory, University of California, Berkeley, California
(Received August 21, 1953)

IN this experiment, which has been previously described,[1,2] two experimental arrangements have been constructed to study the yield of charged secondary particles. For one arrangement, a thin foil of Ag (12.8 mg/cm²) has been bombarded by an internal beam of 332-Mev protons and 187-Mev deuterons. The secondary protons and alphas emitted at $0°\pm10°$ to the incident beam direction are detected in nuclear track plates located beneath the median plane of the cyclotron. There are five specific positions for these plates encompassing an energy region ranging from approximately 5 to 22 Mev for the secondary protons and alphas. Using a similar arrangement with the same thickness Ag foil, the angular distribution of secondary particles has been measured for 240-Mev alpha bombardment. Here, secondary protons and alphas emitted at $0°\pm10°$, $45°\pm10°$, and $135°\pm10°$ to the incident beam direction are detected in nuclear track plates at positions for which the mean energies are approximately 6 Mev.

Figure 1 shows the relative yield for the angular distribution of protons and alphas resulting from 240-Mev alpha bombardment. Figure 2 shows the relative yield of protons and alphas emitted at 0° to the incident beam direction for the two different bombardments as a function of their energy. In these plots, smooth curves have been arbitrarily drawn through the points.

Heretofore, there has been a considerable number of experiments performed in which nuclear emulsions have been directly bombarded either with cosmic-ray particles or with particles produced by artificial sources. The nuclear disintegrations which occur in the heavy nuclei (Ag and Br) in the emulsion have been studied extensively. The analysis of the black tracks (secondary particles having <30 Mev of energy) has generally been made using an evaporation model. Le Couteur[3] has probably made the most refinements using this model, and he has had considerable success predicting the low-energy spectrum of hydrogen and helium isotopes resulting from the cosmic ray bombardment of a heavy nucleus ($A=100$). However, recently Bernardini, Booth, and Lindenbaum,[4] in analyzing the results of their experiment, believe that at least 25 percent of the black tracks are knock-out protons.

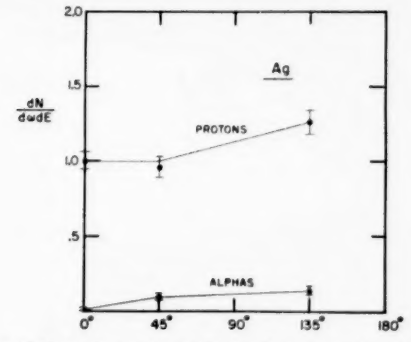

FIG. 1. Yields for the angular distribution of secondary protons (5.5 ± 0.6 Mev) and secondary alphas (6.8 ± 1.9 Mev) resulting from 240-Mev alpha bombardment. The yields of protons and alphas are relative to each other and the ordinate is in arbitrary units. The errors shown for the number of particles found are statistical standard deviations.

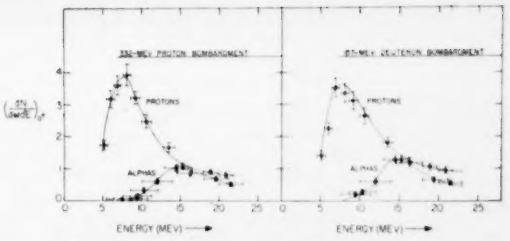

FIG. 2. Yields of secondary protons and alphas emitted at 0° to the incident beam direction as a function of their energy. The yields of protons and alphas are relative to each other and the ordinate is in arbitrary units. Smooth curves have been arbitrarily drawn through the points. The errors shown for the number of particles found are statistical standard deviations. The energy resolution for each point is the entire energy interval considered and is found by combining the energy spread determined by scanning a finite length of plate and the loss of energy by ionization in traversing the finite thickness of target.

The results of the angular distribution, Fig. 1, are consistent with isotropic emission. The rise in the backward direction for protons and alphas is attributed to the fact that the yields of these particles are strongly increasing functions of energy for the region around 6 Mev. If the residual nucleus retains a major portion of the incident momentum, then, for a constant laboratory energy, a proton emitted backwards in the center-of-mass system has ~1 Mev greater energy than a forward emitted proton. The increased yield for the higher energy would account for the backward rise. Similar considerations account for the alpha yield.

Figure 2 indicates that the shape of the spectra are quite similar for the two bombardments. This fact is significant since, according to an evaporation model, the only effect of the bombarding particle should be in the total excitation energy transferred to the nucleus. Le Couteur's analysis shows that the shape of the proton spectrum varies slowly with excitation, with a maximum at about 7 Mev independent of excitation energy. The predicted alpha spectra should have a maximum in the vicinity of 15 Mev for these excitation energies (presumed to be ~50–100 Mev). The results shown in Fig. 2 agree very well with these predictions. However, an evaporation model also implies an exponential fall off in the yield for energies higher than the most probable energy, and the yield is definitely not falling off exponentially for the proton spectra. It appears therefore that a considerable number of these higher-energy protons originate from another process, probably the knock-out process as postulated by Bernardini *et al.*

An analysis similar to reference 2 has been completed for 332-Mev proton bombardment and 187-Mev deuteron bombardment of Be, Al, Ni, Ag, Au, and U, as well as a similar analysis for the angular distribution of secondary particles resulting from 240-Mev alpha bombardment of Be, Al, Ni, and Ag. More detailed secondary proton and alpha energy spectra are also being found for these bombardments. The complete results will be published in the near future.

I am grateful to Dr. Walter H. Barkas for his guidance of this entire program.

* Present address: General Electric Knolls Atomic Power Laboratory, Schenectady, New York.

[1] W. H. Barkas and H. Tyren, Phys. Rev. **89**, 1 (1953).
[2] R. W. Deutsch, Phys. Rev. **90**, 499 (1953).
[3] K. J. Le Couteur, Proc. Phys. Soc. (London) **A63**, 259 (1950).
[4] Bernardini, Booth, and Lindenbaum, Phys. Rev. **88**, 1017 (1952).

Theory of High-Energy Deuteron Pickup*

B. J. MALENKA
Harvard University, Cambridge, Massachusetts
(Received August 31, 1953)

THE standard stationary state Green's function technique employed by Gerjuoy[1] for the (d,p) reaction can be used to determine the deuteron pickup[2,3] scattering amplitude. We will consider exactly the idealized (p,d) process where a proton impinges on a nucleus which is considered as a fixed center of force. Physically, this corresponds to the production of high-energy deuterons by high-energy protons where we neglect the energy exchanged with the residual nucleus. Spin and Coulomb effects are neglected also.

The Schrödinger equation for this problem is

$$(T_R+T_r+V_{NP}+V_N+V_P-E)\Psi=0 \tag{1}$$

where the potentials are defined as in reference 1, and for convenience, the kinetic energies T_R and T_r are expressed in terms of $\mathbf{R}=\frac{1}{2}(\mathbf{r}_p+\mathbf{r}_n)$ and $\mathbf{r}=\mathbf{r}_p-\mathbf{r}_n$. The solution of Eq. (1) at infinity is of the form

$$\Psi=\psi_0+\Phi, \tag{2}$$

where Φ is the outgoing part, and

$$\psi_0=e^{i\mathbf{K}\cdot\mathbf{r}_p}\varphi(\mathbf{r}_n,\lambda_0), \tag{3}$$

where $\varphi(\mathbf{r}_n,\lambda_0)$ is the initial bound state wave function of the picked-up neutron which has the energy λ_0, so that

$$(T_R+T_r+V_N-E)\psi_0=0. \tag{4}$$

For this problem, the scattering amplitude $A(\mathbf{K})$ can be determined by

$$A(\mathbf{K})\frac{e^{iKR}}{R}=\lim_{R\to\infty}\int d\mathbf{r}w^*(\mathbf{r},\epsilon_f)\Psi, \tag{5}$$

where $w(\mathbf{r},\epsilon_f)$ is the final bound state wave function of the deuteron.

In the symbolic notation,[1] we can write

$$\Psi=\psi_D-G(V_N+V_P)\Psi, \tag{6}$$

where

$$(T_R+T_r+V_{NP}-E)\psi_D=0, \tag{7}$$

$$(T_R+T_r+V_{NP}-E)G=\delta(\mathbf{r}-\mathbf{r}')\delta(\mathbf{R}-\mathbf{R}'). \tag{8}$$

The outgoing Green's function can be written in the form

$$G=\Sigma_\epsilon g(\mathbf{R}-\mathbf{R}',E-\epsilon)w(\mathbf{r},\epsilon)w^*(\mathbf{r}',\epsilon), \tag{9}$$

where

$$g(\mathbf{R}-\mathbf{R}',E-\epsilon)=\frac{1}{4\pi}\frac{4M}{\hbar^2}\frac{\exp[i(4M/\hbar^2)^{\frac{1}{2}}(E-\epsilon)^{\frac{1}{2}}|\mathbf{R}-\mathbf{R}'|]}{|\mathbf{R}-\mathbf{R}'|}. \tag{10}$$

M is the mass of a nucleon, and Σ_ϵ is the summation over the complete set of discrete and continuum deuteron wave functions which satisfy

$$(T_r+V_{NP}-\epsilon)w(\mathbf{r},\epsilon)=0. \tag{11}$$

From Eqs. (2) and (6), the difference between ψ_0 and ψ_D is outgoing. Then, if we rearrange Eq. (4) in the form

$$(T_R+T_r+V_{NP}-E)\psi_0=(V_{NP}-V_N)\psi_0 \tag{12}$$

we may write

$$\psi_0=\psi_D+G(V_{NP}-V_N)\psi_0. \tag{13}$$

If we use Eq. (13), we can eliminate ψ_D from Eq. (6), so that

$$\Psi=\psi_0-G(V_{NP}-V_N)\psi_0-G(V_N+V_P)\Psi. \tag{14}$$

Substituting the Ψ of Eq. (14) into Eq. (5), we have for the scattering amplitude, $A(\mathbf{K})=A_1(\mathbf{K})+A_2(\mathbf{K})$,

$$A_1(\mathbf{K})=-\frac{1}{4\pi}\frac{4M}{\hbar^2}\int d\mathbf{R}d\mathbf{r}e^{-i\mathbf{K}\cdot\mathbf{R}}w^*(\mathbf{r},\epsilon_f)(V_{NP}-V_N)\psi_0, \tag{15}$$

$$A_2(\mathbf{K})=-\frac{1}{4\pi}\frac{4M}{\hbar^2}\int d\mathbf{R}d\mathbf{r}e^{-i\mathbf{K}\cdot\mathbf{R}}w^*(\mathbf{r},\epsilon_f)(V_N+V_P)\Psi. \tag{16}$$

The ψ_0 term in Eq. (14) does not contribute to $A(\mathbf{K})$ since the bound state wave function of the neutron vanishes as $R\to\infty$. Likewise, since conservation of energy requires that

$$\frac{\hbar^2K^2}{4M}+\epsilon_f=E=\frac{\hbar^2k^2}{2M}+\lambda_0, \tag{17}$$

it can be readily shown from Eqs. (4) and (11) via integration by parts that

$$A_1(\mathbf{K})=0.^4 \tag{18}$$

Thus, $A(\mathbf{K})=A_2(\mathbf{K})$ describes the deuteron pickup scattering amplitude. Unlike the time-dependent theory, the explicit appearance of V_N instead of V_{NP} in $A_2(\mathbf{K})$ is not too surprising since the spherically scattered deuteron waves are already associated with the $-G(V_N+V_P)\Psi$ term in Eq. (6). If we make a Born approximation in $A_2(\mathbf{K})$ in which Ψ is replaced by ψ_0, we may then replace V_N by V_{NP} as a consequence of Eq. (18). With $V_P=0$, the scattering amplitude then takes the same form that is usually used, as in reference 2.

I would like to thank Dr. Walter Selove for his discussion of the deuteron pickup experiments being performed at Harvard. Scattering amplitudes are now being evaluated in conjunction with these experiments.

* This work was partially supported by the joint program of the U. S. Office of Naval Research and the U. S. Atomic Energy Commission.

[1] E. Gerjuoy, Phys. Rev. **91**, 645 (1953).
[2] G. F. Chew and M. L. Goldberger, Phys. Rev. **77**, 899 (1950).
[3] M. Gell-Mann and M. L. Goldberger, Phys. Rev. **91**, 398 (1953).
[4] Compare with Eq. (4.28) in reference 3, which also can yield this result.

Meson Production by 500-Mev Negative Pions*

M. BLAU, M. CAULTON,† AND J. E. SMITH
Brookhaven National Laboratory, Upton, New York
(Received August 27, 1953)

THE first event of meson production in meson interactions was found by the Bristol Group in nuclear emulsions,[1] exposed to cosmic radiation. Recently one event with two emitted mesons has been found by Fry[2] in the 220-Mev negative meson beam of the Chicago cyclotron. Among 460 meson interactions initiated by 500-Mev negative pions from the Brookhaven cosmotron, six events have been found in which two mesons leave the nucleus. These events represent production of mesons. It is highly probable that the created meson is produced directly in collisions of mesons on nucleons inside the nucleus, rather than indirectly by a nucleon recoiling in a meson scattering process.

Because of the large error in the energy determination of the emitted mesons and the uncertainty concerning the size of the nucleon aggregates involved, one cannot decide in each individual case which mechanism of production, by a single meson-nucleon

TABLE I. Characteristics of events with meson production. w is the energy of the emitted meson and θ is the space angle it makes with the direction of the incident meson.

No. of events	Emitted mesons w_1 in Mev	θ_1	w_2 in Mev	θ_2	Other particles emitted in interaction
1	2.5 ± 0.1	124°	80^{+30}_{-20}	95°	2 black tracks 1 recoil
2	50^{+15}_{-10}	32°	140^{+40}_{-25}	94°	1 black prong 1 recoil 1 slow electron
3	85^{+60}_{-40}	102°	42^{+16}_{-9}	130°	5 black prongs
4	80 ± 20	72°	90^{+80}_{-30}	154°	4 black prongs
5	25 ± 3	65°	29^{+8}_{-4}	137°	2 black prongs
6	3 ± 0.3	12°	85^{+80}_{-30}	115°	1 black prong
7	17 ± 3	7°	130 ± 40	102°	0

interaction, or by an interaction of a recoiling nucleon with another nucleon, occurred. Because of the low energy of the recoiling nucleons and therefore the small cross section (about 3×10^{-27} cm^2),[3] the latter process is improbable. Only 80 events where a backward scattered meson is observed, in the 460 analyzed, can lead to recoil nucleons more energetic than 250 Mev. These recoil nucleons would be expected to produce at most 0.2 meson, not six.

Table I describes the characteristics of the events, listing kinetic energy and angle of emission (laboratory system) of the two mesons and the number of additional particles emitted in the disintegration. The relatively great number of prongs in events 1, 3, and 4 suggest that these are processes occurring in light nuclei. Specifically, event 1 can be explained on energy grounds as having taken place in a carbon nucleus, disintegrating into two protons of 4.7 and 6.5 Mev (range determination) and a $_4Be^9$ nucleus of 2–3 Mev.

Figure 1 is a photomicrograph of event 1; *i* is the incoming meson and *a* and *b* the emitted mesons.

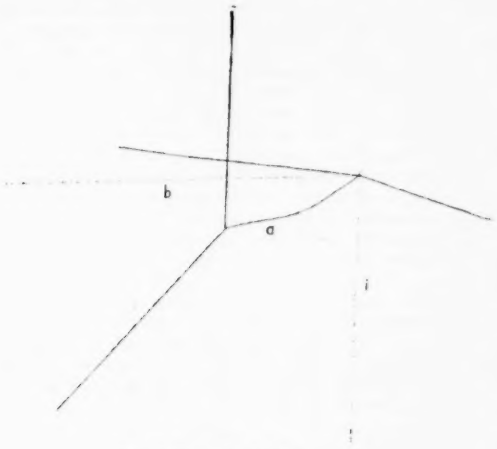

FIG. 1. Meson production, event 1.

Event 7 (Fig. 2) has been found after scanning more than the 460 events referred to. Here only the incoming meson *i* and the emitted mesons *a* and *b* can be seen. This event can, on the basis of energy and momentum considerations (within the limit of experimental errors), be explained as meson production in a hydrogen nucleus of the emulsion.

Thus far no positive mesons coming out of stars could be identified. However, in adjacent emulsions several π-μ-e decays have been observed, supporting the conclusions on meson production.

FIG. 2. Meson production, event 7.

In addition to the 6 events mentioned above, 8 more have been found which are consistent with interactions with meson production. However, the tracks are too short for unmistakable identification.

Therefore the percentage of events with two charged mesons is 1.3 percent to 3 percent, considering the 460 interactions among which the events have been found. This percentage has to be increased in order to take into account events where one or both mesons have been absorbed. We have found that with 500-Mev incident mesons, charged mesons leave the nucleus in only 38 percent of the interactions (55 percent if neutral mesons are considered). Since the energy of the emitted mesons is generally smaller in two-meson events, still fewer of these mesons escape. It is estimated (based on experiments with incident mesons of lower energy) that the number of 2-meson events reported here constitute at the most 25 percent of all events in which a charged meson—observed or absorbed—is produced. The above figure would then represent 5.2 percent to 12 percent of all interactions.

From these experiments nothing can be learned about the production of π^0 mesons, and therefore the actual cross section of meson-meson production at 500-Mev meson energy cannot be compared with theoretical data.

Recently Yang and Fermi[4] independently calculated the probabilities for meson-meson production for various meson energies available from the cosmotron. The calculations are based on the Fermi theory of meson production and on considerations concerning isotopic spin conservation; the calculations apply for meson-nucleon collisions and assume an interaction radius $r=\hbar/\mu c$.

Assuming (1) the validity of these calculations for meson-nucleon collisions inside the nucleus, (2) the equality of number of protons and neutrons for emulsion nuclei, and (3) the equality of π^--p and π^--n cross sections,[5] the fraction of events leading to two charged mesons is 16 percent or 18 percent (the second number includes events with 2 charged and 1 neutral meson). This figure is about twice the value calculated from experimental data, but considering the meager statistics and the simplified assumptions, the disagreement is probably not too serious

The authors wish to thank the entire staff of the Brookhaven cosmotron for their cooperation, Mrs. E. Medd and Mrs. B. Cozine for their efficient work in scanning and measuring the plates, Mrs. E. Schwarzer and Mrs. M. Carter for their help in developing the plates, and Mr. Robert F. Smith for making the photomicrographs. We are indebted to Drs. S. J. Lindenbaum and L. C. L. Yuan for their aid and advice in exposures and to Drs. C. N. Yang and G. Snow for interesting discussions.

* Research carried out under the auspices of the U. S. Atomic Energy Commission.
† Graduate Fellow from Rensselaer Polytechnic Institute, Troy, New York.
[1] Camerini, Davies, Franzinetti, Lock, Perkins, and Yekutieli, Phys. Rev. **42**, 1261 (1951).
[2] W. F. Fry, Phys. Rev. **91**, 1576 (1953). We are indebted to Dr. Fry for sending us the manuscript before publication.
[3] R. E. Marshak, *Meson Physics* (McGraw-Hill Book Company, Inc., New York, 1952), pp. 110–112.
[4] C. N. Yang and E. Fermi (private communications). We wish to express our gratitude to Professor Fermi and Dr. Yank for making their manuscripts accessible to us.
[5] S. Lindenbaum and L. C. L. Yuan, Phys. Rev. (to be published).

Operation of a Glaser Bubble Chamber with Liquid Hydrogen

ROGER H. HILDEBRAND AND DARRAGH E. NAGLE
Institute for Nuclear Studies and Department of Physics, University of Chicago, Chicago, Illinois
(Received August 21, 1953)

GLASER has recently demonstrated that ionizing radiation can trigger violent boiling in highly superheated ether and pentane.[1] He has further shown that it is possible to photograph tracks of bubbles which mark the paths of ionizing particles passing through the liquid.

A bubble chamber using liquid hydrogen should prove useful for studying nuclear events involving protons. For example, it would provide a hydrogen target of greater density and purity than can be achieved in a cloud chamber.

In this letter we report preliminary experiments which strongly suggest that a useful liquid hydrogen bubble chamber can be

realized. We have been able to produce superheated liquid hydrogen and to trigger its boiling with minimum ionization particles.

The apparatus is shown in Fig. 1. The chamber itself was a pyrex bulb which could be observed by eye through the unsilvered nitrogen and hydrogen Dewars. The bulb communicated through a pyrex capillary with input and exhaust hydrogen lines. The pressure was controlled by means of valves on these lines. The temperature of the bulb was controlled by a resistance wire heater which opposed the conduction cooling of the pyrex capillary whose lower end was at the temperature of the liquid hydrogen bath.

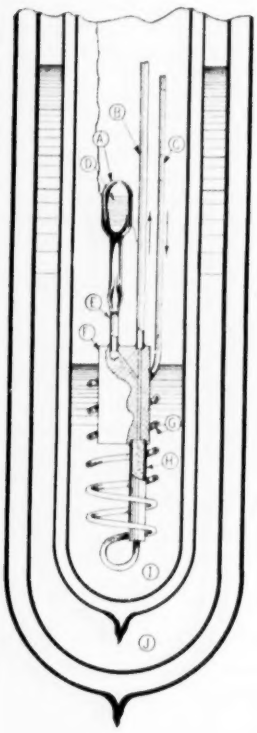

FIG. 1. Liquid hydrogen bubble chamber. *A*: Pyrex bulb. Volume 5 cm³. Inside diameter 12 mm. *B*: Exhaust tube. *C*: Input tube for purified hydrogen gas. *D*: 23-ohm heater wire wound on pyrex bulb. Operating current 80 milliamperes. *E*: Kovar tube. *F*: Copper block. *G*: Coil to condense incoming hydrogen. *H*: Glass wool trap to keep particles out of bulb. *I*: Liquid hydrogen bath. *J*: Liquid nitrogen jacket.

By controlling the temperature and pressure inside the bulb the chamber could be filled with liquid hydrogen in equilibrium with its vapor. Raising the pressure slightly would cause the vapor phase to disappear in the bulb. Thereafter, when the pressure was lowered well below the equilibrium vapor pressure the liquid could be kept in the bulb without boiling for considerable lengths of time.

The temperature was such that the liquid hydrogen was in equilibrium with its vapor at 3 atmospheres. In order to fill the bulb in a short time a filling pressure of $3\frac{3}{4}$ atmospheres was used. When the bulb was completely full the pressure was suddenly reduced from $3\frac{3}{4}$ to 1 atmosphere.

In the absence of radiation other than cosmic radiation the liquid hydrogen would remain superheated for periods up to 70 seconds before boiling. The average delay for 40 such expansions was 22 seconds. The boiling triggered immediately, however, when the bulb was exposed to a 15-millicurie Co^{60} source at a distance of 5 meters. Occasionally delays up to 2 seconds were observed but in nearly every one of 37 such expansions the delay was too short to be observed by eye.

Similar results were obtained with liquid nitrogen using higher temperatures and pressures.

The authors wish to thank Dr. Donald Glaser for his cooperation in planning this experiment. We are also much indebted to Dr. Lother Meyer for much advice and for assistance in operating the cryostat. Dr. Earl Long has been most generous in making the facilities of the Low Temperature Laboratory of the Institute for the Study of Metals available to us.

[1] Donald A. Glaser, Phys. Rev. **87**, 665 (1952); **91**, 496, 762 (1953).

Bromine Isotopes Produced by Carbon-Ion Bombardment of Copper*

JACK M. HOLLANDER
Radiation Laboratory and Department of Chemistry, University of California, Berkeley, California
(Received August 11, 1953)

IN addition to providing a novel means for the synthesis of transplutonium elements,[1] the accelerated carbon-ion beam of the Berkeley 60-inch cyclotron may also be used conveniently for the study of neutron-deficient nuclides, for it is a property of carbon-ion-induced transmutations in any but the lightest elements that the ratio of protons to neutrons added to the target nucleus is virtually always larger than unity.

The 60-inch cyclotron, which accelerates He^4 (+2) ions to ~40 Mev, should in theory produce C^{12} (+6) ions of ~120 Mev. However, unpublished experiments with G. B. Rossi and A. Ghiorso[2] have shown that the energy spread of the internal carbon ion beam is wide, a most probable energy being perhaps nearer to 90 than to 120 Mev. Beam currents measured through 1.5 mils of tantalum absorber, corresponding to the passage of ions with kinetic energies exceeding ~80 Mev, have averaged between 0.01 and 0.1 μa.

Copper foils have been bombarded in the carbon beam, and bromine chemical fractions subsequently isolated. Their decay curves showed two activities, with half-lives of 95±3 minutes and 36±2 minutes, as shown in Fig. 1. The first of these is to be identified with the 1.7-hour bromine isotope discovered by Woodward, McCown, and Pool,[3] and assigned by them to Br^{75}, on the basis

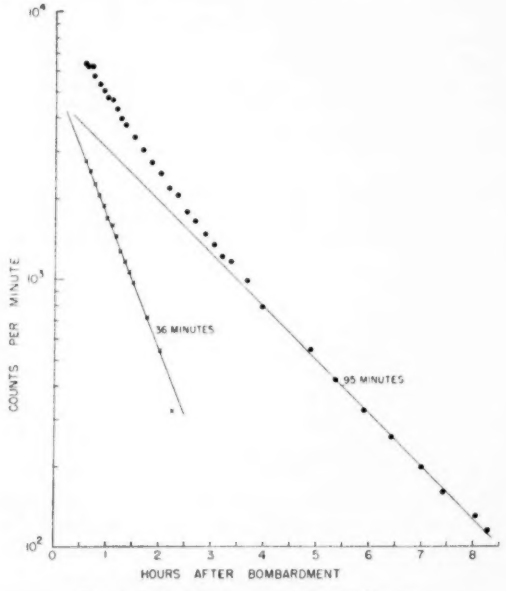

FIG. 1. Typical decay curve of bromine fraction from Cu + C^{12} bombardments.

of proton and deuteron bombardments of enriched Se^{74}. In the present experiments, the reaction producing this isotope would be $Cu^{65}(C, 2n)Br^{75}$. The 36-minute activity has not been reported previously.

The 16-hour positron emitter Br^{76} has not been observed in any carbon ion bombardments of copper. From the gross activity curves, which decay to background without tailing out into a longer component, a lower limit of ~30 can be set on the ratio of the $Cu^{65}(C, 2n)Br^{75}$ to the $Cu^{65}(C, n)Br^{76}$ reaction.

In an attempt to fix the isotopic assignment of the 36 minute bromine relative to 95 minute Br^{75}, carbon ion bombardments of isotopically enriched CuO targets[4] were made. The CuO samples carried the following analyses:

CuO I: Cu^{63}, 99.7±0.3%; Cu^{65}, 0.3%.
CuO II: Cu^{63}, 1.84±0.02%; Cu^{65}, 98.16±0.02%.

Br^{75} can be produced by carbon ions only from Cu^{65}, since a $Cu^{63}(C, \gamma)Br^{75}$ reaction would not be likely. Thus, from CuO I, any Br^{75} which is produced should have come only from the ~0.3 percent Cu^{65} remaining in that sample. One would then expect the ratio Br^{75} (from CuO II)/Br^{75} (from CuO I) to be ~300. Actually observed in two bombardments were ratios of 50 and 100, which, considering the experimental uncertainties in carbon ion beam current and chemical yields, are not inconsistent with the isotopic enrichment reported.

The cross sections for the $Cu^{65}(C, 2n)Br^{75}$ reaction and the $Cu^{65}(C, xn)$ 36 min $Br^{<75}$ reaction were roughly equal, indicating that the latter activity may be due to the $Cu^{65}(C, 3n)Br^{74}$ or $Cu^{65}(C, 4n)Br^{73}$ reaction. However, there was no appearance of the 7.1-hour Se^{73} in any of the bromine decay curves, so it is fairly certain that the 36-minute bromine does not decay through that state. In addition, the following evidence points to its assignment to Br^{74}: in spite of over a fiftyfold enrichment of Cu^{63} in CuO I as compared with CuO II, the ratio of 36 minute/95 minute activities was only slightly enhanced in CuO I, and the absolute yield of the 36-minute activity was lower by a factor of about 50 in CuO I than in CuO II, indicating that the 36-minute activity has been made in Cu^{63} by a reaction with a very low cross section, and hence may be assigned tentatively to Br^{74}, by the $Cu^{63}(C, n)Br^{74}$ reaction.

In carbon-ion bombardments of $Cu^{63}O$, but not in those of $Cu^{65}O$, a 4±1 minute bromine activity has also been observed but no further details are presently known about this activity.

I am greatly indebted to Drs. I. Perlman and M. I. Kalkstein for their helpful comments, and to G. B. Rossi and the crew of the 60-inch cyclotron for their help in making these bombardments.

* This work was performed under the auspices of the U. S. Atomic Energy Commission.
[1] Ghiorso, Thompson, Street, and Seaborg, Phys. Rev. **81**, 154 (1951).
[2] J. M. Hollander, University of California Radiation Laboratory Report UCRL-1395, June, 1951 (unpublished).
[3] Woodward, McCown, and Pool, Phys. Rev. **74**, 870 (1948).
[4] These enriched samples were kindly loaned by the Stable Isotopes Division of the Oak Ridge National Laboratory.

High-Energy (γ,d) Reactions*

J. W. DeWire, A. Silverman, and B. Wolfe
Laboratory of Nuclear Studies, Cornell University, Ithaca New York
(Received August 27, 1953)

USING a technique which electronically separates deuterons from protons,[1] we have measured $(\gamma,d):(\gamma,p)$ ratios at 90° in the laboratory system using C, Cu, and Pb targets. Figure 1 shows the experimental arrangement. The γ-ray beam from the 310-Mev Cornell synchrotron strikes a target and the product particles are analyzed in a two-crystal telescope. The energy of the particle is measured in the second crystal, 5.5 g/cm² of NaI, and dE/dx of the particle is measured in the first crystal of 0.35 g/cm² of NaI. The pulses from the two crystals are multiplied electronically; the product pulse EdE/dx being approximately proportional to $M^{0.8}Z^2E^{0.2}$. The mass dependence of the product makes possible the identification of protons and deuterons, and since the product varies slowly with energy, a large range of energies can be examined at the same time.[2]

In practice, an energy interval is set by upper and lower biases on the second crystal, for example, 27–37 Mev for most of this experiment. The experiment is now sensitive to two groups of particles. Particles of group 1 have energies between 27 and 37 Mev after going through the first crystal and stop in the second crystal. Group 2 with energies between about 70 and 90 Mev for

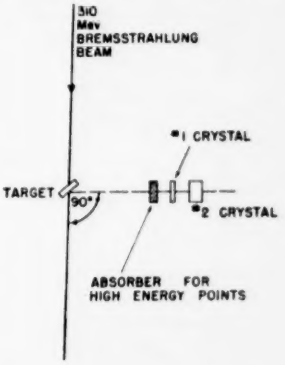

FIG. 1. Arrangement of apparatus.

protons and 115 and 145 Mev for deuterons go completely through the second crystal and lose 27–37 Mev in it. Since $dE/dx \sim M^{0.8}/E^{0.8}$, group 2 particles lose much less energy in the first crystal than do the particles of group 1. We are therefore able to discriminate against the second group by setting a lower limit to the pulses accepted from the first crystal. This technique provides a convenient method of obtaining a variable energy interval and at the same time eliminates the need for a separate anti-coincidence crystal.

The multiplication is accomplished essentially by charging a condenser at a rate proportional to the pulse height in one crystal and for a time proportional to the pulse height in the second crystal. The accumulated charge is then proportional to the product of the pulse heights. Figure 2 shows the distribution of

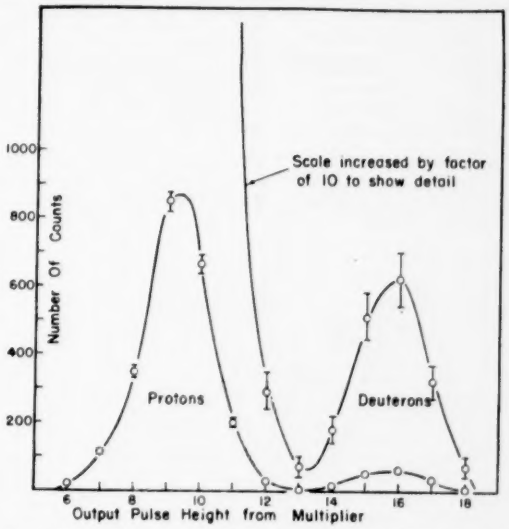

FIG. 2. Illustration of the resolution of the deuteron detector. The data above were obtained using a Cu target with the system sensitive to 43–51 Mev deuterons.

output pulses from the multiplier obtained for the case of 47-Mev deuterons from Cu, the first peak being protons, the second, deuterons.

Particles of energy greater than 45 Mev were measured by placing absorbers in front of the two-crystal telescope. With absorber in place, the protons detected are of slightly different energy than the deuterons. To obtain the ratio for protons and deuterons of the same energy, the known[3,4] proton spectrum was used.

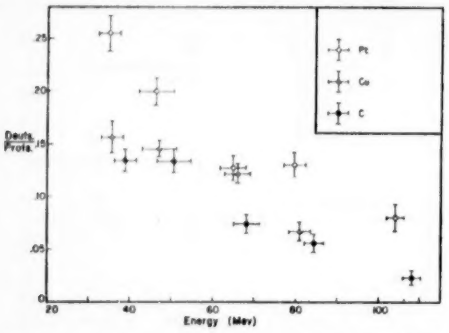

FIG. 3. The ratio of deuterons to protons produced by 310-Mev *bremsstrahlung* at 90° in the laboratory. The abscissa represents the energy of the product particles. The statistical errors are shown.

Figure 3 shows the ratio of the number of deuterons to protons per unit energy interval at various energies at 90° in the laboratory system. The A and Z dependence and the energy dependence of these ratios is suggestive of a (γ,n) or (γ,p) reaction followed by a pickup process.

* Work supported by the U. S. Office of Naval Research.

[1] Wolfe, DeWire, and Silverman, 1953 Washington meeting of the American Physical Society [Phys. Rev. **91**, 22 (1953)]. We are preparing a more detailed description of this apparatus for publication in *The Review of Scientific Instruments*.

[2] It should be pointed out that if the product $E^{0.4}dE/dx$ were used, there would be no energy dependence.

[3] C. Levinthal and A. Silverman, Phys. Rev. **82**, 822 (1951).

[4] J. C. Keck, Phys. Rev. **85**, 410 (1952).

Elastic Photoproduction of π^0's from Deuterium*

J. W. DEWIRE, A. SILVERMAN, AND B. WOLFE
Laboratory of Nuclear Studies, Cornell University, Ithaca, New York
(Received August 27, 1953)

WE have investigated the reaction $\gamma+D\rightarrow\pi^0+D$ for γ-ray energies between 250 Mev–300 Mev and π^0 mesons emitted at 90°–120° in the laboratory. Figure 1 shows the experimental arrangement. The deuteron detector is described in the previous letter.[1] The γ-ray counter detects one of the decay γ rays from the π^0. An event is recorded by a deuteron-γ-ray coincidence. Measurement of the energy and angle of the recoil deuteron determines the energy of the γ ray and the energy and angle of the π^0.

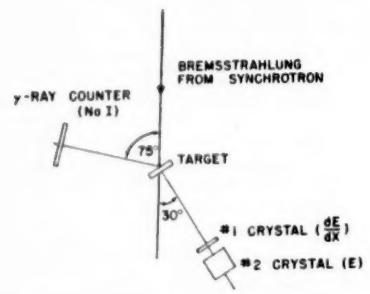

FIG. 1. Arrangement of apparatus. The γ counter is a 4-inch NaI crystal in front of which is placed a $\frac{1}{4}$-inch lead convertor and a 2-inch carbon absorber.

The experiment is performed by taking a D_2O-H_2O difference. The distribution of pulse heights from the multiplier[1] for both D_2O and H_2O are shown in Fig. 2. With the D_2O target, the distribution shows two peaks corresponding to protons and deuterons, whereas the results for H_2O show only a proton component.

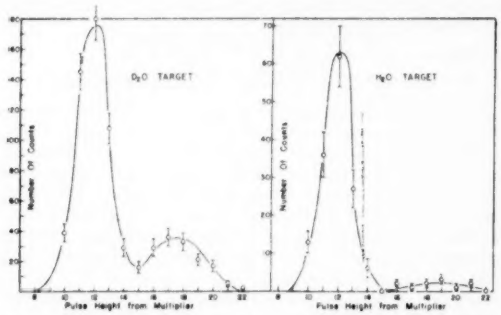

FIG. 2. Comparison of the multiplied pulse distribution for D_2O and H_2O targets, showing the large number of deuterons from D_2O. The D_2O run was for an integrated beam intensity of $7.63\times10^{10}Q$ while the H_2O run was for $3.72\times10^{11}Q$.

Several auxiliary experiments were done to check that the observed deuterons were recoils from the reaction $\gamma+D\rightarrow\pi^0+D$. (a) A 0.040-in. Cu absorber was placed in front of the deuteron detector which was just sufficient to make the detector insensitive to the highest-energy deuteron expected from the reaction; (b) the deuteron detector was moved to 70° where no recoils from the above reaction can occur; (c) the maximum energy of the synchrotron was reduced to 250 Mev so that no deuteron could have sufficient energy to be recorded. In each of these experiments, the deuteron peak disappeared and there was no detectable D_2O-H_2O difference.

This reaction is of special interest because the cross section depends rather sensitively, through interference effects, on the relative sign of the neutron and proton π^0 coupling constants, g_p and g_n. There have been several calculations of this process using the impulse approximation.[2] All of these calculations arrive at approximately the same result and may be roughly summarized as follows: Where the impulse approximation is good, the cross section for the elastic production can be written as

$$\sigma_{\text{elastic}}=|A_n+A_p|^2|I(\mathbf{k}/2)|^2. \tag{1}$$

A_n is the amplitude for π^0 production from the neutron and A_p is the same for the proton. I is an integral that depends only on the wave function of the ground state deuteron and is written as

$$I(\mathbf{k}/2)=\int|\psi_D(\mathbf{R})|^2e^{i\mathbf{k}\cdot\mathbf{R}/2}d\mathbf{R}.$$

In the same approximation, the total cross section (elastic and inelastic) can be written as

$$\sigma_{\text{total}}=A_p^2+A_n^2+2\,\text{Re}(A_p^*A_n)I(\mathbf{k}/2). \tag{2}$$

For $I(\mathbf{k}/2)\ll1$,[3] the interference term can be neglected and the total cross is just the sum of the two free cross sections:

$$\sigma_{\text{total}}=A_p^2+A_n^2.$$

Measurements at this laboratory[4] and recently confirmed at Berkeley[5] show that

$$\sigma_{\text{total}}\ (\text{deuterium})/\sigma\ (\text{hydrogen})\approx2.$$

This implies that $A_p\approx A_n$.

Returning now to the elastic cross section [Eq. (1)] and setting $A_p=A_n$, we obtain $\sigma_{\text{elastic}}\approx 0$ for destructive interference ($g_n=+g_p$) and $\sigma_{\text{elastic}}\approx 4A_p^2|I(\mathbf{k}/2)|^2$ for constructive interference ($g_p=-g_n$).[6] $I(\mathbf{k}/2)$ is evaluated by Chew and Lewis[2] using Hulthén functions for the ground state of the deuteron. Using their results and previously measured cross sections for hydrogen,[4,7] we obtain the calculated result:

$$\frac{d\sigma_{\text{elastic}}}{d\Omega}(\pi/2, E_\gamma=275 \text{ Mev})\approx 5\times 10^{-30}\frac{\text{cm}^2}{\text{sterad}}.$$

The experimental result is $d\sigma/d\Omega=3.5_{-1}^{+2}\times 10^{-30}$ cm²/sterad for γ rays between 250–300 Mev. The error shown includes estimates of what we believe to be all the uncertainties involved in measuring the absolute cross section.

This result offers rather strong evidence that the neutron and proton are oppositely coupled to the $\pi^0(g_p=-g_n)$ as required by the "symmetrical theory." The strength of this conclusion depends on the validity of the impulse approximation for this calculation. Chappalear and Brueckner[8] have recently attempted to evaluate the effect of multiple scattering. They find that the multiple scattering tends to reduce the difference between the two cases. However, the calculations are not yet complete and no quantitative information is yet available.

We are continuing this experiment in an attempt to measure the angular and energy dependence of this cross section.

* Work supported by the U. S. Office of Naval Research.
[1] DeWire, Silverman, and Wolfe, preceding Letter [Phys. Rev. **92**, 519 (1953)].
[2] G. F. Chew and H. W. Lewis, Phys. Rev. **84**, 779 (1951); N. C. Francis and R. F. Marshak, Phys. Rev. **85**, 496 (1952); Heckrotte, Henrich, and Lepore, Phys. Rev. **85**, 490 (1952); N. C. Francis, Phys. Rev. **89**, 766 (1953).
[3] $I(\mathbf{k}/2)$ is in general small. It becomes comparable to unity only near threshold or in the extreme forward direction for the π^0. None of the experimental results correspond to either of these cases.
[4] G. Cocconi and A. Silverman, Phys. Rev. **88**, 1230 (1952).
[5] W. K. H. Panofsky (private communication).
[6] More precise calculations by authors quoted in reference 2 show that the ratio of cross sections for the two cases may be of the order of 30:1 rather than ∞.
[7] A. Silverman and M. Stearns, Phys. Rev. **88**, 1225 (1952).
[8] J. Chappalear and K. A. Brueckner (private communication).

Radioactive Copper Nuclides Produced by Slow Negative Pions and Muons from Zinc*

A. Turkevich and Si Chang Fung
Institute for Nuclear Studies, University of Chicago, Chicago, Illinois
(Received September 2, 1953)

ISOTOPES of copper are made when negative pions and muons are absorbed by zinc nuclei and only neutrons are emitted. Such events correspond to the "0-prong" stars in photographic emulsions that are a good fraction (~25 percent) of all slow π^--meson interactions with complex nuclei,[1] and are the predominant mode of interaction of slow μ^- mesons with nuclei.[2] This letter reports the preliminary results of the use of radiochemical methods to get more detailed information on such events.

Zinc, in the form of kilograms of zinc chloride, was exposed to magnetically analyzed 122-Mev negative pion beam of the University of Chicago synchrocyclotron.[3] This beam is contaminated[4] with several percent of 139-Mev negative muons. The copper radioactivities formed when the beam is stopped completely in the target were determined radiochemically. Under our conditions of irradiation and chemistry, the five species listed in Table I were identified.

TABLE I. Production of copper nuclei from zinc by 122-Mev π^- beam.

Half-life	Assignment	Relative yields[a] thick target	at pion range	at muon range
10 min	Cu^{58} or Cu^{59} and Cu^{62}	1.48	1.9	1.1
25 min	Cu^{60}	0.16	0.17	0.01
3.3 hr	Cu^{61}	0.62	0.80	0.2
12.8 hr	Cu^{64}	1.00	1.0	1.0
60 hr	Cu^{67}	0.22	0.10	0.6

[a] The observed activities with an end-window proportional counter were corrected for the background activity induced when the analyzing magnet was shut off and for the fraction of electron capture in the different nuclides.

The production of three of the copper nuclides (Cu^{61}, Cu^{64}, and Cu^{67}) in a 2-in. collimated beam of pions was studied as a function of depth of penetration into a 5-in.×5-in. target of zinc chloride. Figure 1 graphs the results. The production of all three nuclides

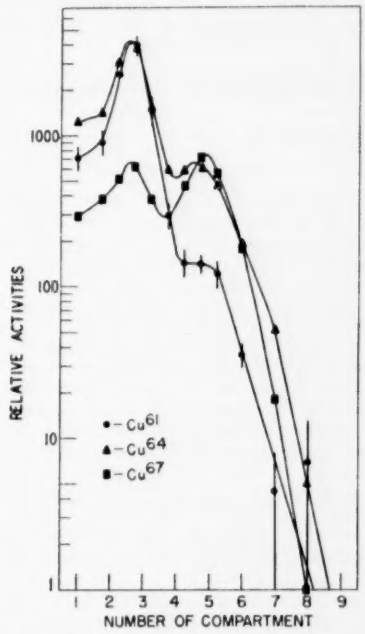

FIG. 1. Production of Cu^{61} (●), Cu^{64} (▲) and Cu^{67} (■) activities as a function of depth of penetration of a 122-Mev π^- beam (after 36.8 g/cm² of Cu initial absorber) into a $ZnCl_2$ target. Each compartment corresponds to approximately 6.2 g of $ZnCl_2$/cm².

is a maximum at the range of the pions (53 g/cm²). In addition, there is a definite second maximum in the production of Cu^{67} and Cu^{64} at approximately the range of the muons (70 g/cm²). The relative production of these three nuclides in the regions of the pion range and the muon range is also given in Table I.

On the assumption that all the stable zinc isotopes (Zn^{64}, Zn^{66}, and Zn^{68} compose 95 percent of the element) capture mesons equally and react in the same way, these data lead to the following conclusions:

1. The reaction $Zn(\mu^-; yn)Cu$ gives a different distribution of radioactive nuclides than does the corresponding reaction with pions. The data of column 5 of Table I, in particular, the very low yield of Cu^{60} and the relatively high yield of Cu^{67}, indicate a maximum probability for y a little greater than 1. This is in agreement with low neutron multiplicities observed[5] upon muon capture in elements near zinc.

2. The reaction $Zn(\pi^-; xn)Cu$ with slow pions has an apparent maximum probability at $x=2-3$. A distribution with a maximum probability at $x=5-6$ such as was found radiochemically in the reaction $(\pi^-; p, xn)$ with bromine,[6] arsenic,[7] and iodine[8] and which is implied by the average neutron multiplicity upon π^- absorption in nuclei in this region of atomic number[9] is definitely excluded. The effect of the secondary neutrons born inside the target at the death of a π^- and contributing via $(n; p, xn)$ reac-

tions has not been completely investigated yet, but targets varying in size by a factor of two give essentially the same results.

* This research was supported in part by a grant from the U. S. Atomic Energy Commission.

[1] See, e.g., Menon, Muirhead, and Rochat, Phil. Mag. **41**, 583 (1950).
[2] See, e.g., Carversin, Muirhead, Powell, and Ritson, Nature **162**, 433 (1948).
[3] The general experimental arrangement is that given by A. Turkevich and J. B. Niday, Phys. Rev. **84**, 1253 (1951).
[4] R. L. Martin (private communication).
[5] A. M. Conforto and R. D. Sard, Phys. Rev. **86**, 465 (1952); M. Widgoff, Phys. Rev. **90**, 891 (1953).
[6] T. T. Sugihara and W. F. Libby, Phys. Rev. **88**, 587 (1952).
[7] A. Turkevich and J. B. Niday, Phys. Rev. **90**, 342 (1953).
[8] L. Winsberg, Phys. Rev. **90**, 343 (1953).
[9] V. C. Tongiorgi and A. D. Edwards, Phys. Rev. **88**, 145 (1952).

Coupled-Field Green's Functions

J. G. VALATIN
Department of Mathematical Physics, University of Birmingham, Birmingham, England
(Received August 3, 1953)

ALL reference to divergent quantities can be avoided in the equations for the Green's functions of quantum electrodynamics by extending the idea of the limiting process introduced by Dirac[1] and Heisenberg.[2] The Green's functions $G_+(x_1, x_2) \sim S_{F1}'$, $\mathcal{G}(x_1, x_2) \sim D_{F1}'$ are solutions of the equations

$$(i\nabla + eA + \mu + \Sigma_c^*)G_+ = I, \quad (\Box + P_c)\mathcal{G} = I, \tag{1}$$

in which well-defined functions Σ_c^*, P_c replace the divergent functions of Schwinger's equations.[3] The definitions can be formulated without reference to the power series expansion, though the analysis of the latter was used in their derivation.

In order to illustrate the method, we consider in the lowest order approximation the contribution to Σ^* from a loop with an open end,

$$\Sigma^{*(2)}(x', x''; x_1) = -ie^2\gamma^\nu S_+(x'-x_1)\gamma_\nu D_+(x_1-x''). \tag{2a}$$

When we introduce $x = \frac{1}{2}(x'+x'')$, $\xi = x'-x''$, a straightforward calculation gives for the Fourier transform formed with $e^{ik(x_1-x)}$,

$$\Sigma^{*(2)}(k, \xi) = -ie^2(4\mu + k + 2i\nabla_\xi) \times \int_0^1 du \exp[ik(u-\tfrac{1}{2})\xi]\Delta_+^0(\xi, \mu^2 u - k^2 u(1-u)), \tag{2b}$$

where $\Delta_+^0(\xi, \mu_1^2)$ is a Hankel function of order 0, with the Fourier transform $(\mu_1^2 - p^2)^{-\frac{1}{2}}$. If we disregard the infrared problem which should be dealt with separately, (2a, b) are well-defined functions with singularities at $\xi^2 = 0$. These singularities have to be compensated by a term $\Sigma_q^{*(2)}$ before closing the loop, and Σ_c^* is defined as

$$\Sigma_c^*(x, x_1) = \int d^4\xi \delta(\xi)\{\Sigma^*(x', x''; x_1) + \Sigma_q^*(x', x''; x_1)\}, \tag{3}$$

where $\int d^4\xi \delta(\xi) \cdots$ indicates a limiting process $\xi \to 0$ to be performed from a space-like direction ξ_μ. If we write $k^2 = \mu^2$ in (2b) and form the difference of the two expressions, $\{\Delta_+^0(\xi, \mu^2 u - k^2 u(1-u)) - \Delta_+^0(\xi, \mu^2 u^2)\}$ and its first derivatives are finite for $\xi \to 0$, the finite part resulting by a kind of self-regularization. In order to exhibit a factor $(\mu + k)^2$ in the finite part, a further finite contribution is to be compensated which is obtained on writing $k \to -\mu$, after separation of a factor $(\mu + k)$. We write

$$\Sigma_q^*(k, \xi) = -[\Sigma^*(k, \xi)]_{k^2=\mu^2;\ k\to-\mu}, \tag{4}$$

which compensates, in the order considered, singularities corresponding to the divergent term $A + (k+\mu)B$ of the usual calculations and a term with $\xi\Delta_+$ corresponding to ambiguities in the latter which have to be removed there by regularization prescriptions. Further analysis of the power series expansion reveals a one-to-one correspondence of the singularities to the divergent parts as defined by Dyson,[4] with additional terms corresponding to the ambiguities. All these singularities can be duly compensated and no divergent integrals or infinite constants appear in the calculations.

One can also define Σ_c^* without reference to the power series expansion by Eq. (3). $\Sigma^*(x', x''; x_1) = \Sigma^*(x', x''; x_1, x_1)$ is conveniently obtained from $\Sigma^*(x', x''; x_1', x_1'')$ which corresponds to two open ends of the self-energy loop and can be written with an abbreviated notation as

$$\Sigma^* = ie^2(\gamma^\nu + \Lambda_q^\nu)G_+(\gamma^\kappa + \Lambda_q^\kappa + \Lambda^{*\kappa})\mathcal{G}_{\nu\kappa}. \tag{5}$$

The second term of the first factor is to compensate the singularities related to the "b" divergences of Dyson;

$$\Lambda^{*\nu}(x', x''; y; x_1) = \delta\Sigma^*(x', x''; x_1)/\delta e A_\nu(y), \tag{6}$$

and Λ_q^ν is obtained with a minus sign from $(\Lambda^{*\nu})_{A_\nu=0}$ on writing $k_1 = 0$, $k \to -\mu$ in its Fourier transform formed with $e^{ik_1(y-x_1)} \times e^{ik(x_1-x)}$. Σ_q^* in (3) is given as the sum of the expression defined by (4) for $A_\nu = 0$ and of the field-dependent term $-\int d^4y e \times A_\nu(y)\Lambda_q^\nu(x', x''; y; x_1)$.

$P_c^{\mu\nu}$ in (1) is defined by an equation analogous to (3). The first term is obtained from

$$P^{\mu\nu} = -ie^2 \operatorname{tr}(\gamma^\mu + \Lambda_q^\mu)G_+(\gamma^\nu + \Lambda^\nu)G_+, \tag{7}$$

where the detailed prescriptions for (7), which include the opening and closing of loops, will not be given here. $P^{\mu\nu}(x', x''; x_1)$ is the sum of a term $P_{[\xi]}^{\mu\nu}$ with direction-dependent ξ_μ factors (including singular contributions related to the known gauge-dependent ambiguities), and a term which in the limit $A_\nu \to 0$ has a Fourier transform $(k^\mu k^\nu - g^{\mu\nu}k^2)P_1(k, \xi)$. $P_q^{\mu\nu}$ compensates $P_{[\xi]}^{\mu\nu}$ and the contributions from $(k^\mu k^\nu - g^{\mu\nu}k^2)[P_1(k, \xi)]_{k^2=0}$.

Details will be published in due course. The quantized field equations which are still under investigation are to be defined by means of the limiting process and counter terms given by $P_q^{\mu\nu}$, Σ_q^*, Λ_q^ν.

[1] P. A. M. Dirac, Proc. Cambridge Phil. Soc. **30**, 150 (1934).
[2] W. Heisenberg, Z. Physik **90**, 209 (1934); **92**, 692 (1934).
[3] J. Schwinger, Proc. Nat. Acad. Sci. **37**, 452, 455 (1951); see also Utiyama, Sunakawa, and Imamura, Prog. Theor. Phys. **8**, 77 (1952).
[4] F. J. Dyson, Phys. Rev **75**, 1736 (1949).

The Directional Correlation and Electric Quadrupole Interaction in the γ-γ Cascade of 48.7-min Cd^{111m}†

J. J. KRAUSHAAR* AND R. V. POUND‡
Brookhaven National Laboratory, Upton, New York
(Received August 27, 1953)

THE correlation in the directions of emission of the two successive γ rays of the 48.7-min isomer Cd^{111m} has been measured using several sources differing in chemical and physical state. One purpose was to test further the hypothesis that such correlations can be disturbed through the medium of the electric quadrupole moment of the nucleus in its intermediate state.[1,2] Such effects have been observed by others[3-6] in the γ-γ correlation of the Cd^{111} following K capture in 2.8-day In^{111}. The decay schemes of these two nuclei have the same intermediate excited level, of half-life 8.5×10^{-8} sec. The use of the 48.7-min isomer allows full knowledge of the chemical and physical environments of the nucleus because no changes in electronic configuration and no important recoil energies are involved after the source has been prepared.

The directional correlations were measured using equipment and methods that have been previously described.[7] One of the counters was screened by a 0.9-mm thickness of lead and both were biased to exclude γ rays below about 0.075 Mev to eliminate coincidences due to either back-scattered γ rays or to x-rays. Samples of about 2 mg of Cd, enriched to 70.0 percent Cd^{110},[8] were bombarded in the Brookhaven reactor for 20 to 30 minute periods and data taken for about one half-life. Geometrical correction factors were determined using a collimated beam of γ rays (the 0.19-Mev γ rays of In^{114}) in a manner similar to that employed by Lawson and Frauenfelder.[9] Measurements near 180° had to be corrected by subtraction of coincidences resulting from a background of positron annihilation present in the sources.

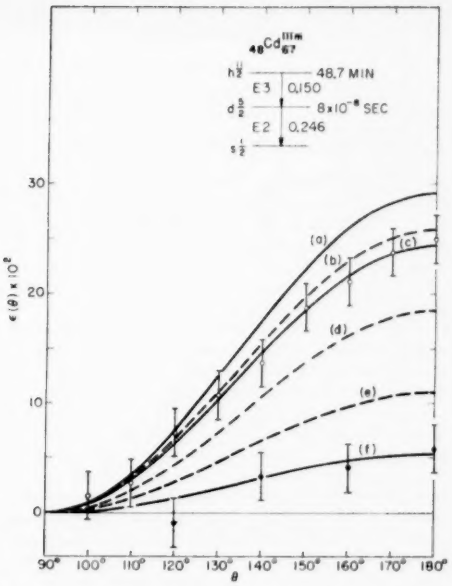

FIG. 1. Directional correlation of Cd^{111m}. (a) Theoretical curve based on pure *E3-E2* scheme; (b) $CdCl_3$ solution fitted by least squares and corrected for angular resolution; (c) $CdCl_2$ solution, least-squares fit; (d) CdO solid, fitted and corrected; (e) solid Cd metal, fitted and corrected; and (f), theoretical "hard-core" assuming axially symmetric fields. The experimental points are shown for $CdCl_2$ solution (open circles) and solid $CdCl_2$ (solid circles).

The correlations were measured in solid CdO, $CdCl_3$ in acidic aqueous solution, dry $CdCl_2$, and solid Cd metal. In addition, the anisotropy $\epsilon(150°)$ was observed with molten Cd metal. The enriched isotope was in the form of powdered CdO and this was first bombarded and used directly. The corrected least-squares fit to the CdO data, taken at 180°, 160°, 140°, and 120° is shown as curve (d) in Fig. 1.

Aqueous solutions were obtained by dissolving irradiated CdO in about 0.1 ml of dilute HCl. The experimental points using those sources are shown (open circles) in Fig. 1, to which curve (c) represents a least-squares fit and curve (b), that corrected for angular resolution.

Solid $CdCl_2$ was obtained by evaporation of solutions prepared as above to dryness. The four low-lying solid experimental points in the figure represent these data.

Metallic cadmium was prepared from the enriched CdO by electrodeposition from a cyanide solution onto a carbon cathode[10] of such purity that no activity could be detected from the carbon irradiated separately. Data collected from the resulting sources, consisting of small metal particles mixed with carbon, are represented by curve (e) which is corrected for angular resolution.

Molten metallic sources were prepared as above and, after irradiation, sealed into glass capsules containing a reducing atmosphere of hydrogen at NTP. The sources were held above the 376°C melting temperature of the metal by a heater below, and the upper part of the capsule was made hotter by a second heating coil above the source to prevent deposition of the metal on the walls. The procedure was found to produce bright droplets of liquid metal with larger pieces of ordinary cadmium.

Curve (a) represents the theoretical correlation based on the suggested decay scheme involving pure multipoles.[11] Empirically from the lifetimes, less than 0.01 percent mixture of *M4* with the *E3* upper transition would be expected, and in the second transition mixing of *M3* with the *E2* should be several orders less. The corrected measured anisotropy, $\epsilon(150°)=0.216\pm0.018$, for the molten metal is in good agreement with the value 0.2227 from the theoretical curve. The lower bound of the standard deviation allows less than 3 parts in 10^3 admixture of *M4*. Curve (a) can thus be taken as representing the undisturbed correlation.

The results for the various sources can be summarized by values of attenuation factors G_2 and G_4 such that the correlation is given as $W(\theta)=1+G_2A_2P_2(\cos\theta)+G_4A_4P_4(\cos\theta)$,[1] with $A_2=0.1786$ and $A_4=-0.0043$.[12] The smallness of $|A_4|$ makes impossible the determination of meaningful values of G_4 from the data, so the term in P_4 has been ignored. The values obtained for G_2 are listed in Table I.

Under $eQ(\partial^2V/\partial z^2)/h$ are listed approximate values for the electric quadrupole interaction necessary to explain the various attenuation factors.[1] For the aqueous solution, a correlation time

TABLE I. Attenuation coefficients and electric quadrupole interaction frequencies for the various sources of Cd^{111m}.

Source	G_2	$eQ(\partial^2V/\partial z^2)/h$ Mc/sec
Molten metal	0.97 ± 0.08	...
$CdCl_3$ solution	0.88 ± 0.05	~200
CdO solid	0.63 ± 0.08	4.1–6.6
Solid metal	0.40 ± 0.07	8.4–14.1
$CdCl_2$ solid	0.19 ± 0.06	>26

τ_c of 10^{-11} sec has been arbitrarily assumed, and the frequency given is the rms value. The molten metal would not be expected to have an rms interaction much larger than in the hexagonal solid metal and therefore, the disturbance in the molten metal should be negligible, as observed. Although CdO has a cubic crystal structure, the fine, irradiated powder may well possess average interactions of the scale suggested as the result of lattice defects.[13] The interaction in hexagonal $CdCl_2$ is sufficient to reduce the correlation to the "hard-core" for axially symmetric fields represented by curve (f) in the figure. The value of G_2 is in excellent agreement with $G_2(\lim)=\frac{1}{4}$. In contrast, results for the In^{111} scheme for $InCl_3$ fell well below the hard core.[4,6] The present results thus suggest that after-effects of the *K* capture are involved in such In^{111} correlations.

We wish to thank Drs. M. Goldhaber and A. Sunyar for helpful discussions.

† Work done under the auspices of the U. S. Atomic Energy Commission.
* Present address: Department of Physics, Stanford University, Stanford, California.
‡ Permanent address: Harvard University, Cambridge, Massachusetts.
[1] A. Abragam and R. V. Pound, Phys. Rev. **89**, 1306 (1953); **90**, 993 (1953); Phys. Rev. (to be published).
[2] Ernst Heer, Physica **18**, 1215 (1952).
[3] Albers-Schönberg, Heer, Novey, and Rüetschi, Phys. Rev. **91**, 199 (1953).
[4] R. M. Steffen, Phys. Rev. **90**, 1119 (1953).
[5] Albers-Schönberg, Hänni, Heer, Novey, and Scherrer, Phys. Rev. **90**, 322 (1953).
[6] Lawson, Frauenfelder, Jentschke, and De Pasquali (to be published).
[7] J. J. Kraushaar and M. Goldhaber, Phys. Rev. **89**, 1081 (1953).
[8] Obtained from Carbide and Carbon Chemicals Company, Oak Ridge, Tennessee.
[9] J. S. Lawson, Jr., and H. Frauenfelder, Phys. Rev. **91**, 649 (1953).
[10] We are indebted to Dr. H. Finston of Brookhaven for developing and carrying out this process.
[11] M. Goldhaber and R. D. Hill, Revs. Modern Phys. **24**, 179 (1952).
[12] S. P. Lloyd, Phys. Rev. **83**, 716 (1951).
[13] G. D. Watkins and R. V. Pound, Phys. Rev. **89**, 658 (1953).

Internal Conversion and Directional Angular Correlation of the Bi^{207} Gammas

F. K. McGOWAN AND E. C. CAMPBELL
Oak Ridge National Laboratory, Oak Ridge, Tennessee
(Received August 5, 1953)

LONG-LIVED (approximately 50 yr) Bi^{207} is known to decay by ϵ-capture to stable Pb^{207} via the 0.82-sec Pb^{207m} isomer,[1–3] which decays by the emission of 1.055-Mev and 0.555-Mev γ rays in cascade. In addition, Neumann and Perlman report[4] five

additional γ rays following the decay of Bi^{207}, but we do not observe these in the decay of the long-lived Bi^{207} source prepared at this laboratory. From lifetime and nuclear shell theory considerations these transitions are probably to be identified with $M4$ and $E2$ transitions between the levels $i_{13/2} \rightarrow f_{5/2} \rightarrow p_{1/2}$.[5]

The source of Bi^{207} was produced by bombarding Pb with 25-Mev protons in the Oak Ridge National Laboratory cyclotron. After a careful chemical separation[1] the carrier-free Bi^{207} was used in three forms: a dilute $Bi(NO_3)_3$ solution, solid $Bi(NO_3)_3 \cdot 5H_2O$, and bismuth chloride fixed on an anion exchange resin in 0.5N HCl. The differential pulse height spectrum of the γ radiation from Bi^{207} obtained with a NaI scintillation spectrometer four months after the bombardment is shown in Fig. 1. In addition to the K x-rays of Pb and the 0.555-Mev and 1.055-Mev γ rays, there are two weaker γ rays with energies 0.700 Mev and 1.76 Mev

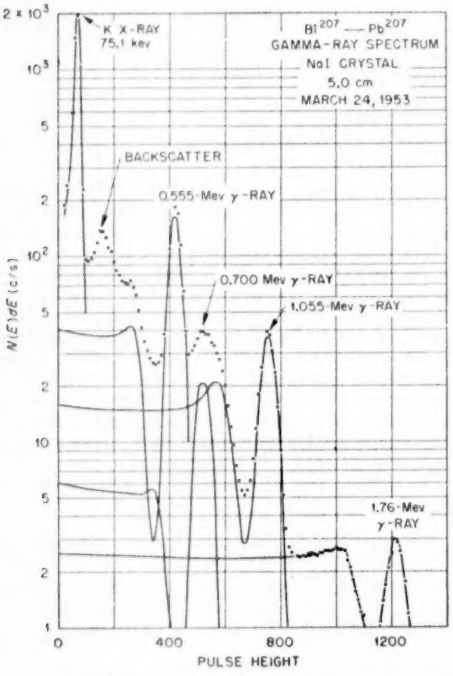

FIG. 1. Differential pulse-height spectrum of the Bi^{207} γ radiation incident on a NaI scintillation spectrometer. Each point in the spectrum contains 4096 counts.

which follow the decay of a much shorter period. The decay of the 1.76-Mev γ ray pulse spectrum with time does not appear to be a simple exponential decay. These two weaker γ rays are probably associated with the decay of bismuth but not necessarily Bi^{207}. The pulse spectrum above 1.76 Mev decreases to two decades below the peak height of the 1.76-Mev full energy peak. The K-shell internal conversion coefficients of the 0.555-Mev and 1.055-Mev γ rays were obtained from intensity measurements of the K-shell internal conversion electrons and the γ radiation with an anthracene and a NaI scintillation spectrometer, respectively. To check the method of measurement the K-shell internal conversion coefficient of the 0.661-Mev γ ray transition of Ba^{137m} was measured. The result agreed to within 6 percent of the accepted $M4$ assignment for the transition. In all experiments involving intensity measurements of the conversion electrons, the air between the source and detector was displaced with H_2 gas. The results together with the theoretical internal conversion coefficients[6] are tabulated in Table I.

TABLE I. Experimental and theoretical internal conversion coefficients.

E_γ (Mev)	$\alpha_{exp}{}^K$	Theoretical coefficients	Classification
1.055	0.096 ± 0.010	$\alpha_4{}^K = 0.0393$, $\beta_4{}^K = 0.104$, $\beta_5{}^K = 0.180$	$M4$
0.555	0.015 ± 0.002	$\alpha_1{}^K = 0.0064$, $\alpha_2{}^K = 0.017$, $\beta_1{}^K = 0.091$	$E2$

From intensity measurements of the gamma radiation it appears that Bi^{207} decays 81.5 percent to the 1.610-Mev excited state and 18.5 percent to the 0.555-Mev excited in Pb^{207}, which agrees with some recent measurements by Wapstra.[7] The half-life of the excited state at 0.555 Mev above the ground state is $T_{1/2} < 10^{-9}$ sec as measured with a delayed-coincidence scintillation spectrometer using anthracene and NaI detectors.

The directional angular correlation of the 1.055- and 0.555-Mev cascade was measured with a coincidence scintillation spectrometer using NaI detectors. The windows of the differential pulse-height analyzers were set such that one accepted only the full energy pulse spectrum from the 0.555-Mev γ ray and the other accepted only the full energy pulse spectrum from the 1.055-Mev γ ray. The resolving time 2τ of the coincidence is 1.40×10^{-8} sec. Under these conditions the true coincidence rate is of the order of one count per sec while the random rate is one percent of this. The directional angular correlation coefficients obtained from 10^6 coincidence counts collected at 90°, 135°, 180°, 225°, and 270° are summarized in Table II, together with the coefficients corrected for the finite angular resolution of the detectors.[8] There appears to be no significant change of the angular correlation with the form of the source.

TABLE II. Directional angular correlation coefficients for the Pb^{207} γ-ray cascade.

Form of the source	Experimental values α_2	Experimental values α_4	Corrected values A_2	Corrected values A_4
Bi^{207} attached to resin in 0.5 N HCl	0.1993	−0.0073	0.2168	−0.0097
	0.1943	−0.0247	0.2114	−0.0328
Dilute Bi^{207} $(NO_3)_3$ solution	0.2077	−0.0157	0.2260	−0.0209
		Mean values	0.218 ± 0.0043	−(0.0211 ± 0.0067)
		Theory	0.2208	−0.0180

These results are in good agreement with the angular distribution expected from a decay sequence 13/2($M4$)5/2($E2$)1/2 for which the theoretical angular correlation function is

$$W_{\gamma\gamma}(\theta) = 1 + 0.2208 P_2(\cos\theta) - 0.0180 P_4(\cos\theta).$$

It appears that both the internal conversion and the directional angular correlation data are consistent with the interpretation that both transitions are predominantly pure multipoles.

[1] E. C. Campbell and F. Nelson, Phys. Rev. **91**, 499 (1953).
[2] Friedlander, Wilson, Ghiorso, and Perlman, Phys. Rev. **91**, 498 (1953).
[3] M. A. Grace and J. R. Prescott, Phys. Rev. **84**, 1059 (1951).
[4] H. M. Neumann and I. Perlman, Phys. Rev. **81**, 958 (1951).
[5] M. Goldhaber and R. D. Hill, Revs. Modern Phys. **24**, 179 (1952); M. H. L. Pryce, Proc. Phys. Soc. (London) **A65**, 789 (1952).
[6] Rose, Goertzel, Spinrad, Harr, and Strong, Phys. Rev. **83**, 79 (1951).
[7] A. H. Wapstra, Dissertation, Amsterdam, 1953 (unpublished).
[8] M. E. Rose, Phys. Rev. **91**, 610 (1953).

Internal Conversion Electron-Gamma Directional Angular Correlation of Bi^{207}

F. K. MCGOWAN
Oak Ridge National Laboratory, Oak Ridge, Tennessee
(Received August 5, 1953)

SINCE the long-lived Bi^{207} provides an excellent source of monoenergetic electrons[1] from the internal conversion of the 0.555- and 1.055-Mev γ rays of Pb^{207}, the conversion electron-gamma directional angular correlation between the K-shell

internal conversion electrons of the 1.055-Mev transition and the 0.555-Mev γ ray has been measured.

A source of $Bi(NO_3)_3 \cdot 5H_2O$ 300 $\mu g/cm^2$ thick and 0.3 cm in a diameter was prepared by evaporating a drop of the liquid to dryness on a 100-$\mu g/cm^2$ Formvar film. To detect the K conversion electrons of 967 kev, one of the NaI detectors in the coincidence spectrometer was replaced with an anthracene detector 1.5 inches diameter and 0.5 cm thick. In order to diminish scattering of the conversion electrons, the air between the detector and source was displaced with H_2 gas at one atmosphere, which corresponds to 600 $\mu g/cm^2$ of scattering material for the conversion electrons to traverse. The differential pulse height spectrum of the Bi^{207} radiation incident on an anthracene scintillation spectrometer without and with a polystyrene absorber (345 mg/cm^2) to stop the conversion electrons is shown in Fig. 1. The difference between the gross pulse spectrum and the "gamma only" pulse spectrum

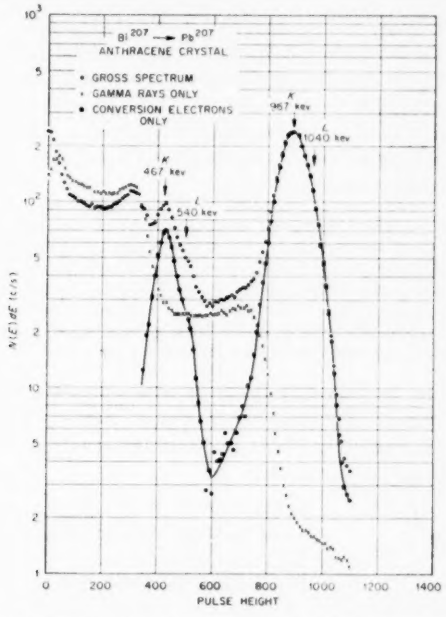

FIG. 1. Differential pulse-height spectrum of the Bi^{207} radiation incident on an anthracene scintillation spectrometer. Each point in the spectrum contains 4096 counts.

is the internal conversion electron pulse spectrum of the 0.555- and 1.055-Mev transitions. With the polystyrene in place, the Compton recoil electron spectrum is more intense than the gross spectrum at the lower energies. The additional recoil electrons being detected are some of the recoil electrons produced in the polystyrene by the γ rays.

TABLE I. Directional angular correlation coefficients for the Pb^{207} conversion electron-gamma cascade.

Experiment No.	Experimental values α_2'	Experimental values α_4'	Corrected values A_2'	Corrected values A_4'
1	0.2296	−0.0242	0.2526	−0.0335
2	0.2176	−0.0181	0.2394	−0.0250
3	0.2124	0.0000	0.2337	0.0000
4	0.2178	−0.0204	0.2396	−0.0282
		Mean values	0.2413 ± 0.0040	−(0.0216 ± 0.0075)
		Theory	0.2315	−0.0229

For the conversion electron-gamma angular correlation measurements, the window of the NaI scintillation spectrometer accepted only the full energy pulse spectrum from the 0.555-Mev γ ray and the window of the anthracene scintillation spectrometer accepted only the low energy edge of the conversion line due to 1.055-Mev transition. The true coincidence counting rate for the conversion electron-gamma correlation was of the order of two counts per sec while the random rate is one percent of this. The directional angular correlation coefficients obtained from 10^6 coincidence counts are summarized in Table I. Corrections for multiple scattering of the conversion electrons in the source, source backing, and the H_2 gas as described by Frankel[2] are very small for this high electron energy, i.e., amount to about 1 percent for the coefficient A_2' of $P_2(\cos\theta)$ and 2 percent for the coefficient A_4' of $P_4(\cos\theta)$. To check this point experimentally a 2-mg/cm^2 Al foil was inserted between the source and the detector, and no attenuation in the measured anisotropy was observed for an experimental run containing 4×10^4 coincidence counts. With the window of the analyzer set to include the L conversion electrons and part of the K conversion electrons, the measured anisotropy (uncorrected data) increased from 0.358 to 0.426.

The conversion electron-gamma angular correlation function[3] is given by

$$W_{e-\gamma}(\theta)=\sum_{\nu=0}^{\nu=m} A_\nu b_\nu P_\nu(\cos\theta),$$

where the coefficients A_ν are the γ-γ correlation coefficients and the coefficients[4] b_ν for the sequence 13/2(M4)5/2(E2)1/2 are $b_2=1.0487$ and $b_4=1.2760$. The results in Table I are in good agreement with the theoretical angular correlation function:

$$W_{e-\gamma}(\theta)=1+0.2315P_2(\cos\theta)-0.0229P_4(\cos\theta).$$

Additional measurements are in progress and more details of the present experiments will be published in a subsequent paper.

[1] F. K. McGowan and E. C. Campbell, preceding Letter [Phys. Rev. **92**, 523 (1953)].
[2] Sherman Frankel, Phys. Rev. **83**, 673 (1951).
[3] Rose, Biedenharn, and Arfken, Phys. Rev. **85**, 5 (1952).
[4] Rose, Biedenharn, and Arfken, Oak Ridge National Laboratory Report ORNL-1097 (unpublished).

Proceedings of the American Physical Society

Minutes of the Inyokern-Pasadena Meeting, December 26, 27, 29 and 30, 1952

THE 316th meeting of the American Physical Society was held on Friday and Saturday, December twenty-sixth and twenty-seventh at the U. S. Naval Ordnance Test Station, Inyokern, and on December twenty-ninth and thirteeth at the California Institute of Technology. The decision to hold part of the meeting at Inyokern turned out to be a happy one, although the difficulties encountered as a result were many. Ninety-one people not from the Station attended, and sixty-eight from the Station. The weather was excellent and the local arrangements were perfect. No attempt will be made here to thank individuals who helped in planning and in running the meeting at Inyokern, but I would like to point out that, except for its relative inaccessibility, the Naval Ordnance Test Station provides an ideal setting for a winter meeting. I wish to thank the U. S. Office of Naval Research for making possible the participation of Drs. Gaydon, Norrish, Wolfhard, and Porter, and the staff of the Station and the Pasadena Office of the U. S. Office of Naval Research for their parts in this meeting. After the sessions for invited papers on the Spectroscopy of Combustion were completed, discussions continued for another day.*

The arrangements at the California Institute of Technology were excellent, as always, and the Secretary wishes to thank Dr. R. F. Bacher, his fine staff of secretaries and especially Dr. H. V. Neher, for their untiring help.

* In addition to the invited papers listed in the Bulletin, Dr. John Laufer of the Jet Propulsion Laboratory in Pasadena gave an invited paper "Structure of a Nonhomogeneous Turbulent Field."

Those who registered at the Pasadena portion of this meeting numbered 272. The experiment of holding a popular evening lecture in connection with West Coast meetings worked out well, since the excellent lecture by Dr. Fred Hoyle of Cambridge, England was attended by approximately 1500 people. Similar lectures are to be given at future meetings.

Post-deadline papers were given by S. J. Barnett; K. Buettner; R. L. Walker, D. C. Oakley and A. V. Tollestrup; R. E. Worley; P. W. Gilles and J. L. Margrave and F. W. Warburton. The Secretary apologizes for the slight mishandling of a paper by Mary Goulks Gourley and W. D. Crozier of the New Mexico Institute of Mining and Technology. The title of this paper is "Persistent Residues From Ice Particles" and the abstract is as follows:

Ice particles, formed by cooling nuclei-free water vapor to −75°C and evaporated in an atmosphere having a prescribed ice subsaturation, leave persistent residues. These are capable of nucleating ultramicroscopically observable particles when exposed to a supersaturated atmosphere. The nucleating "activity" of these residues depends on the degree of subsaturation, the time of exposure to subsaturation, and the temperature.

Since the Secretary has received no complaints about the earlier deadline, future winter meetings will be held immediately after Christmas and the deadline will again be late in October.

J. Kaplan
Local Secretary for the Pacific Coast
University of California
Los Angeles 24, California

Errata Pertaining to Papers C5 and G4

C5, by M. Z. Krzywoblocki. In the title of this paper, "Sheet" should read "Street."

G4, by Donald R. Westervelt. In footnote 2, "J. Chem. Phys." should read "Phys. Rev."

PROGRAMME

FRIDAY MORNING AT 10:00

Station Theatre

(F. E. ROACH presiding)

Invited Papers

A1. Infrared Emission Studies of Some Equilibrium and Nonequilibrium Flame Reactions. S. SILVERMAN, *Applied Physics Laboratory, The Johns Hopkins University.* (30 min.)

A2. Absorption Spectroscopy in Stationary Flames. H. G. WOLFHARD, *London, England.* (45 min.)

A3. Comets, Carbon Stars, and Combustion Phenomena. P. SWINGS, *University of Liege.* (45 min.)

A4. Quantitative Spectroscopic Investigations of Rapid Gaseous Reactions. G. PORTER, *University of Cambridge.* (45 min.)

A5. The Study of Ignition Reactions by Flash Photolysis. R. G. W. NORRISH, *University of Cambridge.* (45 min.)

A6. Spectroscopic Studies of Flames Supported by Free Atoms. A. G. GAYDON, *Imperial College, University of London.* (45 min.)

FRIDAY AFTERNOON AT 1:00

Station Theatre

(P. SWINGS presiding)

Session B

Discussion of the Invited Papers on the Spectroscopy of Combustion

---

SATURDAY MORNING AT 9:00

Station Theatre

(F. W. BROWN presiding)

Invited Papers

C1. Water Entry Theory. E. P. COOPER, *Naval Radiological Defense Laboratory, San Francisco.* (30 min.)

C2. Cavitation and Boiling. M. S. PLESSET, *California Institute of Technology.* (30 min.)

C3. Hydroacoustic Filter Networks. C. W. HORTON, *University of Texas.* (30 min.)

C4. The Effect of Turbulence on Linear Systems. H. W. LIEPMANN, *California Institute of Technology.* (30 min.)

C5. On the Stability of Benard-Karman Vortex Sheet in Compressible Flow. M. Z. KRZYWOBLOCKI, *University of Illinois and NOTS, Inyokern.* (30 min.)

SATURDAY AFTERNOON AT 1:00

Station Theatre

(M. Z. KRZYWOBLOCKI presiding)

Session D

Discussion on Wakes and Jets

Discussion Leader: M. Z. KRZYWOBLOCKI

In addition to the invited speakers on the earlier session of the day, A. B. C. Anderson and G. V. Schliestett will join the panel.

MONDAY MORNING AT 10:00

Room 201, Bridge

(H. V. NEHER presiding)

Invited Papers

E1. Microwave Physics and the Study of Solids. C. KITTEL, *University of California, Berkeley.* (45 min.)

E2. Electronic Specific Heat in Relation to the Band Structure of Transition Metals and Alloys. J. E. GOLDMAN, *Carnegie Institute of Technology* (30 min.)

E3. Electronic X-Ray Probe for the Micro-Analysis of the Structure and Composition of Metallic Solids. ANDRE GUINIER, *University of Illinois.* (30 min.)

MONDAY AFTERNOON AT 1:30

Room 201, Bridge

(W. A. FOWLER presiding)

Contributed Papers

F1. Elastic Scattering of Protons by Li^7.* WILLIAM D. WARTERS,† *Kellogg Radiation Laboratory, California Institute of Technology.*—The elastic scattering cross section for protons in Li^7 has been measured over the proton energy range 360–1400 kev, using the variable angle 10½-inch double-focusing magnetic spectrometer. Measurements were made at scattering angles of 50, 70, 89, 110, 130, 144, and 160 degrees in the center-of-mass system. The relative stopping cross section for protons in lithium was also measured from 200–1300 kev and was found to agree with the formula of Livingston and Bethe[1] when fitted to the results of Haworth and King[2] at low energies. The maximum ratio of observed scattering cross section to Rutherford cross section for various angles near the 441.4 kev resonance in $Li^7(p\gamma)$ is:

$\theta_{c.m.}$	50°	70°	89°	110°	130°	144°	160°
$(\sigma/\sigma_R)_{max}$	1.28	1.49	1.70	1.88	2.00	2.16	2.28

Preliminary analysis, consistent with spherically symmetric γ-radiation, indicates a $J=1$ even resonance in Be^8 formed by p wave protons.

* Assisted by the joint program of the ONR and AEC.
† National Science Foundation Predoctoral Fellow.
[1] M. S. Livingston and H. A. Bethe, Revs. Modern Phys. **9**, 245 (1937).
[2] L. J. Haworth and L. D. P. King, Phys. Rev. **54**, 48 (1938).

F2. Elastic Scattering of Protons by C^{12} and C^{13}.* EDMUND A. MILNE, *Kellogg Radiation Laboratory, California Institute of Technology.*—A variable angle, double-focusing, magnetic, proton spectrometer has been used to study the elastic scattering of protons from C^{12} near the 456-kev resonance in $C^{13}(p\gamma)$ to gain information about the excited state in the compound nucleus N^{13}. Data have been taken on $C^{12}(pp)C^{12}$ from 300 kev to 550 kev at every 10° in the center-of-mass system from 30° to 160°. Analysis of the data shows the 456-kev resonance is caused by s wave protons forming a $^2S_{\frac{1}{2}}$ state[1] in N^{13} in agreement with Goldhaber and Williamson. These measurements are being extended to the 1.7 Mev resonance in $C^{12}(p\gamma)$, and in addition the elastic scattering from $C^{13}(pp)C^{13}$ is under investigation from 0.3 to 2.0 Mev.

* Assisted by the joint program of the ONR and AEC.
[1] G. Goldhaber and R. M. Williamson, Phys. Rev. **82**, 495 (1951).

F3. The Energy Loss of Low Energy Protons and Deuterons in Gases.* H. K. REYNOLDS, D. N. F. DUNBAR, W. A. WENZEL, AND W. WHALING, *Kellogg Radiation Laboratory, California Institute of Technology.*—The loss of energy of protons and deuterons passing through a gas cell has been measured over the equivalent proton energy range 25–550 kev. A monoenergetic incident beam is obtained from a Van de Graaff generator, and the energy of the transmitted particles with and without gas in the cell is measured with a magnetic spectrometer. The entrance and exit windows of the gas cell are made of thin Al of total energy loss 5–10 kev. Methods of correcting for the known variation with proton energy of the energy loss in the windows will be discussed. Changes in the window thickness under pressure, such as mechanical stretching or absorption of gas, are detected by varying the length of the gas cell. The gas pressure is measured with an oil manometer. In the pressure range of these measurements, a few mm of Hg, the energy loss in the gas has been found to be proportional to the pressure. The energy loss for protons and deuterons of the same velocity has been found to be the same within the experimental uncertainty.

* Assisted by the joint program of the ONR and AEC.

F4. The Stopping Cross Section of Several Gases for Protons and Deuterons.* D. N. F. DUNBAR, H. K. REYNOLDS, W. A. WENZEL, AND W. WHALING, *Kellogg Radiation Laboratory, California Institute of Technology.*—The stopping cross section of H_2, He, air, O_2, CO_2, and NH_3 for protons and deuterons of equivalent proton energy 25–550 kev has been measured by the method described in the previous abstract. The stopping cross sections ϵ of H_2 and He exhibit a markedly different energy dependence: $\epsilon(H_2)/\epsilon(He)$ decreases from approximately 2 at $E_p=25$ kev to 1 at $E_p=550$ kev. The stopping power of O_2 relative to air varies from 0.9 at $E_p=30$ kev to 1.1 at $E_p=550$ kev. The stopping cross sections of the gaseous compounds are discussed with particular attention to the Bragg law for the addition of stopping cross sections. Range energy curves obtained from these stopping cross sections are compared with the previous measurements of the range in cloud chambers.

* Assisted by the joint program of the ONR and AEC.

F5. Q Values of the $Ne^{21}(d,\alpha)F^{19}$ and $Ne^{21}(d,p)Ne^{22}$ Reactions.* CURT MILEIKOWSKY AND WARD WHALING, *Nobel Institute of Physics, Stockholm and Kellogg Radiation Laboratory, California Institute of Technology.*—Separated

isotopic targets of Ne^{21}, which were produced at the Nobel Institute of Physics, have been used to measure the Q values of the reactions (1) $Ne^{21}(d, \alpha)F^{19}$, and (2) $Ne^{21}(d, p)Ne^{22}$. The double-focusing magnetic spectrograph was used to compare the energy of the protons and alpha-particles from these reactions with the alpha-particles from ThC and ThC′. The angle of observation and the deuteron bombarding energy were chosen so that the particles being studied and the alpha-line used for energy calibration lay nearly side by side on the photographic plate used as a detector. The Q values measured are 6.432 ± 0.010 for reaction (1) and 8.137 ± 0.011 for reaction (2). From these Q values and the mass of F^{19} the atomic masses of Ne^{21} and Ne^{22} are obtained. Other alpha-groups from reaction (1) correspond to transitions to states in F^{19} at 0.113 ± 0.008 Mev and 0.192 ± 0.012 Mev above the ground state. Additional particle groups from N and Na contamination on the targets have been observed: the Q values measured are 8.613 ± 0.011 Mev for $N^{14}(d, p)N^{15}$ and 4.723 ± 0.008 Mev for $Na^{23}(d, p)Na^{24}$.

* Assisted by the joint program of the ONR and AEC and by the Swedish Atomic Committee.

F6. Angular Distribution of Gamma-Rays and Alpha-Particles from the Reaction $N^{15}(p, \alpha\ \gamma)C^{12}$.* ALFRED A. KRAUS, JR., A. P. FRENCH,† WILLIAM A. FOWLER, AND C. C. LAURITSEN, *Kellogg Radiation Laboratory, California Institute of Technology.*—The reaction $N^{15}(p, \alpha\gamma)C^{12}$ exhibits strong resonance[1] at 429-, 898-, and 1210-kev proton bombarding energy. We have measured the gamma-ray angular distributions at these three resonances and the alpha-particle distributions at the 898-kev and the 1210-kev resonances. The distributions at 429 kev and 898 kev are in agreement with the following spin and parity assignments: N^{15}, $\frac{1}{2}^-$; $l_p=2$; I^{16*} (12.51 Mev), 2^- or >5; O^{16*} (12.95 Mev), 2^- or >5; $l_\alpha=1$; C^{12*} (4.432 Mev), 2^+ or >4; C^{12}, O^+. The assignments for the two O^{16*} levels are identical, but the corresponding resonances do differ in the relative amounts of channel spin zero and channel spin one occurring in the proton capture. For the 429-kev resonance the fraction of channel spin zero is 0.82, while at 898 kev it is 0.58. The 1210-kev resonance shows angular distributions in agreement with $l_p=3$; O^{16*} (13.24 Mev), 4^+ or >5; $l_\alpha=2$; C^{12*} (4.432 Mev), 2^+ or >4. The assignment for the excited state of C^{12} at 4.432 Mev is obtained independently from observations at the three resonances. The ambiguities in the assignments arise only from the fact that the theoretical behavior of levels of large angular momentum has not been completely investigated.

* Assisted by the joint program of the ONR and AEC.
† Cavendish Laboratory, Cambridge, England.
[1] Schardt, Fowler, and Lauritsen, Phys. Rev. **86**, 527 (1952).

F7. Angular Anisotropy of the Gamma-Ray from $C^{13}(p, \gamma\ p')C^{13}$.* H. HUGH WOODBURY, *Kellogg Radiation Laboratory, California Institute of Technology.*—A ten-channel differential discriminator has been built and employed with a scintillation counter to investigate the gamma-ray from $C^{13}(p, \gamma p')C^{13}$ which has been previously reported.[1] In addition to confirming the reported observations made at 90° with the incident proton beam, it has been found that the radiation at 0° is considerably weaker. Excitation curves at 90° and 0° will be given and discussed.

* This work was assisted by the joint program of the ONR and AEC.
[1] Tollestrup, Day, and Woodbury, Phys. Rev. **85**, 760 (1952).

F8. Gamma-Rays from $C^{13}+D^2$.* R. J. MACKIN, JR.,† *Kellogg Radiation Laboratory, California Institute of Technology.*—Secondary electrons from γ-radiation produced by 2.4-Mev deuterons on carbon have been observed with a magnetic lens spectrometer using 1.9-percent resolution. Compton spectra from 17 mg/cm² graphite corresponding to γ-rays of 3.67 ± 0.04 and 3.83 ± 0.04 Mev have been observed. The intensity ratio is 5/4 and the combined intensity is 1/5 that of the well-known 3.1-Mev γ-ray. These lines are probably associated with the 3.68 and 3.88 levels of C^{13} indicated by proton groups[1] from $C^{12}(dp)C^{13}$. Photoelectrons from a thorium converter reveal a γ-ray of 168 ± 1 kev. It has been established that this line does not come from $C^{13}+D^2$, and its excitation curve indicates a threshold near 1.7 Mev, consistent with its interpretation as a transition between the C^{13} levels mentioned above.

* Assisted by the joint program of the ONR and AEC.
† National Science Foundation Fellow.
[1] J. Rotblat, Phys. Rev. **83**, 1271 (1951).

F9. The Beta-Decay of F^{17} and F^{20}.* CALVIN WONG, *Kellogg Radiation Laboratory, California Institute of Technology.*—The reactions $F^{17}(\beta^+)O^{17}$ and $F^{20}(\beta^-)Ne^{20}$ have been investigated using a magnetic lens spectrometer. The positron spectrum of F^{17} consists of one component of maximum energy 1.749 ± 0.006 Mev. A Fermi-Kurie plot yields a straight line from the end-point energy down to an energy of 500 kev. β-ray branching to the first excited state of O^{17} at 874 kev is estimated to be <1 percent of the ground state transition. This estimate is consistent with the failure in this experiment to observe any delayed γ-radiation other than the annihilation radiation. The ft value for the ground-state transition is 2420 seconds, while the minimum ft value for the excited state transition is $\sim2\times10^4$ seconds. The electron spectrum of F^{20} consists of one component of maximum energy 5.419 ± 0.010 Mev. The Fermi-Kurie plot is linear from the end-point energy down to an energy of 400 kev. The delayed γ-radiation spectrum also consists of one component of energy 1.627 ± 0.005 Mev. The intensity of this γ-radiation shows that the β-decay proceeds to an excited state of Ne^{20} at 1.627 ± 0.005 Mev. The ft value for the transition is 9.73×10^4 seconds.

* Assisted by the joint program of the ONR and AEC.

F10. The Coupling of Angular Momenta in Nuclear Reactions.* R. F. CHRISTY, *Kellogg Radiation Laboratory, California Institute of Technology.*—Seven nuclear reactions have been examined where the angular distribution of reaction products is not uniquely determined by knowledge of the total angular momenta of the various nuclear states involved. In these cases the result depends on the type of coupling of angular momentum vectors in the nucleus. In six of the seven, the experimental angular distribution is consistent with the assumption of Russell-Saunders coupling in the nucleus. In three of the seven, the experiments are consistent with the assumption that the bombarding particle brings a definite j in the reaction. Neither assumption is sufficient to explain the result in one reaction ($B^{11}+H^1$).

* Assisted by the joint program of the ONR and AEC.

F11. The Beta-Spectrum of S^{35} from $C_2H_5S^{35}H$ below 33 kev. G. J. PLAIN, H. L. MORRISON, P. H. PITKANEN, AND F. T. ROGERS, JR., *U. S. Naval Ordnance Test Station, Inyokern.**—The S^{35} beta-spectrum was investigated for information bearing on the low energy cutoff (abstract 13 of the 1952 Denver meeting). Approximately 1400 low energy S^{35} beta-tracks were measured out of about 35 000 beta-tracks recorded. Trace quantities of 3^{35} in labeled ethyl mercaptan[1] were used in a diffusion cloud chamber.[2] The data have been corrected for relative deficiencies at the longer ranges which arise from the finite radius of the camera field and the finite focal depth. The corrected data shows a low energy cutoff at 10 kev. To enable examination of the efficiency of the counting of short tracks, additional experiments similar to the above were carried out, using an additional small amount of tritiated water[3] in the cloud chamber. These experiments showed that our efficiency of counting for the data on S^{35} is very nearly 100 percent for energies of 10 kev and above. The published results of several other experimenters on C^{14} in $C^{14}O_2$ (gas in

counter[4]), on B^{210} in $B^{210}(CH_3)_3$ (cloud chamber[5]), on C^{14} in $BaC^{14}O_3$ and S^{35} in Na_2S^{35} (magnetic spectrometer[6]), and on B^{210} above (magnetic spectrometer[7]), all indicate the same general trend at low energies, though there is as yet no general quantitative accord.

* Post Office: China Lake, California.
[3] Obtained under Authorization No. 11695 of the USAEC.
[3] H. L. Morrison and G. J. Plain, Rev. Sci. Instr. **23**, 607 (1952).
[3] Obtained under Authorization No. 13838 of the USAEC.
[4] Angus, Cockcroft, and Curran, Phil. Mag. **40**, 522 (1949).
[5] A. Waltner and F. T. Rogers, Jr., Phys. Rev. **75**, 1445 (1949).
[6] Cook, Langer, and Price, Phys. Rev. **74**, 548 (1948).
[7] C. B. Madsen, Acta Jutlandica Aarsskrift for Aarhus Universitit **XV**, 1 (1942).

F12. Thin Target Studies of $B^{10}(\alpha, n)N^{13}$, N^{13}.* MARGUERITE ROGERS, F. K. ODENCRANTZ, AND G. J. PLAIN, *U. S., Naval Ordnance Test Station, Inyokern.**—Thin target studies have been made of the reaction $B^{10}(\alpha, n)N^{13}$, N^{13*} by means of the recoil proton tracks in Eastman NTA nuclear plates. The neutron spectrum has been measured for a number of incident alpha-particle energies between 3 and 5.3 Mev. Evidence for an excited level in the N^{13} nucleus has been obtained. Yield data will be presented, from which the existence of resonances may be inferred.

* Post Office: China Lake, California.

F13. The Effect of Cloud-Chamber Geometry on Beta-Ray Studies. PAUL H. PITKANEN, *Michelson Laboratory, U. S. Naval Ordnance Test Station, Inyokern.**—Experiments with a continuously operating cloud chamber on β-decay[1] have indicated the importance of determining the influence of chamber geometry on the observed distribution of tracks. The experimental set-up to which this analysis applies consists of a continuously operating chamber, cylindrical in shape, with a vertically mounted camera whose field of focus is also cylindrical. Formulas for the correction to the observed distribution are obtained under a number of simplifying assumptions, the most important of which are: (1) the tracks are considered to be straight; (2) the depth and area corrections are assumed to be statistically independent. The limitations imposed by these assumptions are discussed.

* Post Office: China Lake, California.
[1] Plain, Morrison, Pitkanen, and Rogers, Jr. (see abstract, this meeting).

F14. Electron Positron Scattering. H. A. HOWE AND K. R. MACKENZIE, *University of California at Los Angeles.*—The ratio of electron to positron scattering on atomic electrons was determined. A single lens beta-spectrometer was used to select positive or negative beta-particles of one energy and to focus them on a scattering foil. Beyond the foil the scattering and scattered particles were counted in coincidence by two scintillation counters located in conjugate positions for a symmetric scattering event. By changing from an electron to a positron source and reversing the current in the spectrometer, almost identical scattering conditions were obtained and the ratio of electron-electron to electron-positron scattering was found for 1.3-Mev incident particles. Using the scattering cross section as predicted by Moller for the electron-electron case, and the Bhabha formula, with exchange, for the electron-positron case, the experimental ratio was 1.87 ± 0.11 as compared with the theoretical ratio of 1.83. If the electron-positron scattering is calculated without exchange, the experimental ratio differs from the theoretical ratio by approximately 35 percent. Therefore, the experiment definitely favors the inclusion of exchange effects in the calculation.

MONDAY AFTERNOON AT 1:30

Room 155, Arms

(A. H. WARNER presiding)

Contributed Papers

G1. Annealing Effects in Irradiated Copper.* ALBERT W. OVERHAUSER, *Department of Physics, University of Illinois.*—Copper wires were bombarded with 12-Mev deuterons at a temperature of -180°C. A total flux of $1.1 \cdot 10^{17}$ deuterons/cm^2 caused an increase in electrical resistivity of $7.8 \cdot 10^{-8}$ ohm-cm. The wires were then allowed to anneal isothermally at successive temperatures from -185°C to 167°C. Recovery of the resistivity was observed at all temperatures. The annealing curves obtained for temperatures between -185°C and -60°C were of such a character that only a number of processes with varying activation energies could account for them. One-half of the increased resistivity recovered in this range, and the activation energy appropriate for processes occurring at a given temperature, was proportional to the absolute temperature. Recovery near -100°C was characterized by an activation energy of 0.44 ev. Above -60°C the annealing took on a unique behavior that could be described as a simple process with a single activation energy. The shapes of the recovery curves in this region were close to those that would be expected of a binary process, and therefore suggest that recombination of the interstitial atoms and vacancies, produced by the bombardment, occurs at these temperatures. This process accounted for 25 percent of the increased resistivity and had an activation energy of 0.68 ev. At room temperature 25 percent of the increased resistivity remained, and further anneals to temperatures as high as 167°C produced only an additional 4 percent recovery.

* This work was supported by the AEC.

G2. The Effect of Quench Temperature and Cold Work on the Ordering Rates of Cu_3Au and CuAu.* C. E. DIXON AND C. J. MEECHAN, *North American Aviation, Inc., Atomic Energy Research Department, Downey, California.*—The initial ordering rate of Cu_3Au at 200°C and the amount of ordering which occurs in one hour has been found to increase, with increasing quench temperature, and to decrease if the alloy is very slightly cold worked. Cu_3Au foils were quenched in water from temperatures above the critical temperature. The ordering rate was determined by resistivity measurements made at liquid nitrogen temperature after pulse annealing at 200°C. Specimens quenched from 600°C decreased 4.5 ohm-cm in one hour, whereas the ones quenched from 450°C decreased only 1.9 ohm-cm in the same time. Specimens which had been plastically bent to a radius of 0.3 inch after the quench decreased 1.6 and 0.5 ohm-cm for the 600°C and 450°C quenches, respectively. In CuAu the ordering rate at 150°C is also sensitive to the quench temperature but less sensitive than Cu_3Au to small amounts of cold work. CuAu will order partially at room temperature; the rate is accelerated by very severe plastic deformation and is proportional to the amount of deformation. CuAu wires cooled in air were

cold worked by twisting in liquid nitrogen and pulse annealed at room temperature. The most severely cold-worked specimen showed a decrease of 0.43 ohm-cm after 144 hours while the strain-free standard decreased 0.02 ohm-cm.

* This work is based on studies conducted for the AEC.

G3. Quenched Vacancies in AuCu and $AuCu_3$.* J. BRINKMAN, *North American Aviation, Inc., Atomic Energy Research Dept., Downey, California.*—It has been observed that the initial rate of approach to the ordered state of the disordered alloys, AuCu and $AuCu_3$ varies approximately as $\exp(-E_f/kT)$ with the temperature T, from which the alloy is quenched.[1,2] This is interpreted as an indication that the rate of ordering is proportional to the density of some lattice defect which exists in thermodynamic equilibrium at the high temperature and which can be frozen into the metal by a rapid quench. Seitz[3] has concluded that it should be possible to freeze in a non-equilibrium number of vacancies in copper. It is therefore suggested that the defects frozen into these alloys are vacancies, and that ordering occurs by their migration. If such is the case, E_f should be the energy of formation of vacancies in the alloy. Furthermore, it should be possible to measure the activation energy for migration of vacancies, E_m, by observing the dependence of the initial ordering rate on ordering temperature. An analysis of unpublished data[1,2] gives the following values for both AuCu and $AuCu_3$: $E=0.4\pm0.1$ ev; $E_m=1.2\pm0.15$ ev.

* This report is based on studies conducted for the AEC.
[1] C. E. Dixon, and C. J. Meechan (preceding abstract).
[2] P. G. Stello, North American Aviation Report: NAA-SR-171, 1952.
[3] F. Seitz, Acta Cryst. **3**, 355 (1950).

G4. Optical Effects of Radiation Damage in Alkali Halides.* DONALD R. WESTERVELT, *North American Aviation, Inc., Atomic Energy Research Dept., Downey, California.*—An absorption peak at 580 mμ has been reported in NaCl,[1] resulting from thermal treatment of electron-bombarded crystals. Similar bands have now been observed, both at room temperature and at liquid nitrogen temperature in electron-bombarded KCl, KBr, and KI, at various stages of thermal annealing. In each case after bombardment at room temperature with 1-Mev electrons, a latent absorption peak exists between the F and M bands, which develops rapidly when the damaged crystal is warmed, at the expense of the familiar electron-surplus bands. This radiation-damage band is bleached by further heating, the latter stages of the process proceeding by a first-order reaction. The case of KCl, in which the radiation-damage band can be identified with the "colloidal band" reported by Scott and Smith[2] is considered in detail.

* This report is based on studies conducted for the AEC.
[1] D. R. Westervelt, Phys. Rev. **86**, 643 (1952); see also a review by K. Przibram of recent work on crystals discolored naturally or by polonium alpha-particles, Z. Physik **130**, 269 (1951).
[2] A. B. Scott and W. A. Smith, J. Chem. Phys. **83**, 982 (1951).

G5. Annealing of Radiation Damage Effects in Copper.* R. R. EGGLESTON, *North American Aviation, Inc., Atomic Energy Research Dept., Downey, California.*—Copper specimens have been bombarded while being maintained at temperatures below -150°C with high energy alpha-particles using the University of California 60-inch cyclotron at the Crocker Laboratory in Berkeley. After the irradiation the specimens were annealed using a pulse annealing technique previously described.[1] A few specimens were given a tempering anneal at progressively higher temperatures while the others were isothermally annealed. Residual resistance was the observed physical parameter used to follow the annealing behavior in both cases. Tempering curves will be presented over the range of annealing temperature from -135°C to $+105$°C. Isothermal annealing curves at temperatures between -20°C and -65°C will also be presented. Analysis of these later curves yields an activation energy for the annealing process in this range of temperature of 14.9 kcal/mole.

* This report is based on studies conducted for the AEC.
[1] Parkins, Dienes, and Brown, J. Appl. Phys. **22**, 1012 (1951).

G6. The Influence of Cold Work and Radiation Damage on the Vibrational Spectra of Copper.* D. B. BOWEN AND G. W. RODEBACK, *North American Aviation, Inc., Atomic Energy Research Dept., Downey, California.*—The difference in Debye temperature between samples of well-annealed and cold-worked, or radiation-damaged copper wires has been measured. Simultaneous measurements of electrical resistance as a function of temperature are made on the annealed and the damaged samples. In this way the difference in the temperature dependent portion of their resistance can be observed directly and this difference fitted to a differential form of Gruneisen's equation to obtain directly the difference in Debye temperature between the samples. In each case the damaged lattice had a lower Debye temperature than the annealed one. The maximum changes are from twenty to forty degrees. The apparatus has a resolution in Debye temperature change of less than $\frac{1}{2}$ degree. There is a small variation of the change with temperature of measurement. Results on the thermal annealing of these changes will be presented. An interpretation in terms of the vibrational spectra, and the associated thermodynamic implications will be discussed.

* This report is based on studies conducted for the AEC.

G7. Radiation-Damage Energy Threshold in a Face-Centered Cubic Alloy.* J. M. DENNEY, *North American Aviation, Inc., Atomic Energy Research Dept., Downey, California.*—It has been found that suitable treatment of an alloy of iron in copper (2.4 wgt. percent iron) induces an iron precipitate whose lattice is coherent with the copper lattice. Aging at an elevated temperature insures growth of the coherent iron precipitate to near the terminal precipitate size. Since the iron is in the face-centered cubic form, it is paramagnetic, and thus the specimen is paramagnetic. Upon transforming to the stable body-centered cubic structure, the iron becomes ferromagnetic. Measurement of the saturation magnetization of the alloy is, thus, a direct measure of the mol fraction of transformed iron. The introduction of Frenkel defects by bombarding thin foils with high energy particles will initiate the transformation of the face-centered cubic iron. Foils have been bombarded with electrons from an electron accelerator at varying energies. It has been found that a threshold energy of about 0.5 Mev exists, below which the iron does not transform upon bombardment with electrons. Suitable calculations indicate that this threshold in the beam energy is associated with the energy required to form a Frenkel defect by displacing an atom from the lattice. An upper limit to the displacement energy of 25 ± 2 ev is thus obtained.

* This report is based on studies conducted for the AEC.

G8. The NAA Statitron as a Facility for Solid-State Research.* D. T. EGGEN AND H. KENWORTHY, *North American Aviation, Inc., Downey, California.*—A 2-Mev electron statitron was designed for radiation-damage experiments in solid state and radiation chemistry at the Atomic Energy Research Department of North American Aviation, Inc. In certain experiments, e.g., atomic displacement energy in crystals,[1] the energy is critical and a minimum amount of energy degradation is desired. It is necessary to irradiate the target in an extension of the accelerator tube vacuum system without passing through a window. Therefore, a high speed, large capacity vacuum system has been incorporated. In other experiments, e.g., the irradiation of alkali halide crystals for the production of F centers,[2] where the electron energy is less critical, or where a diffuse beam is required, the electrons are brought out of the accelerator tube through a window. Where

the target must be maintained in a vacuum, but where the vapor pressure is too high to be incorporated in the accelerator tube system, a window is placed between the irradiation cell attached beneath the accelerator tube, e.g., irradiation chemistry experiments on organic or liquid samples.[3] The energy of the machine has been calibrated using the Be(γ, n) at 1.667 Mev. The beam current is collected through an electronic integrating circuit and is calibrated by a calorimetric method.

* This work was performed under AEC contract.
[1] M. M. Mills, "Estimated values of electron threshold energies necessary for atomic displacements" (private communication).
[2] Westervelt, "Optical Effects of Radiation Damage on Alkali Halides," (see abstract, this meeting).
[3] Feldman, Ruebsamen, and Shon, "Radiation Chemistry of Organic Materials. I. Biphenyl," (unpublished work at North American Aviation).

G9. Treatment of the Defect Relaxation Time of Conduction Electrons in Crystals by the Tight Binding Approximation.* J. LOMONT, *North American Aviation, Inc.,† Atomic Energy Research Dept., Downey, California.*—The Bloch 1-electron approximation and the Boltzmann equation are assumed. A relaxation time $\tau(\mathbf{k})$ is defined in terms of the distribution function, and a new linear integral equation for τ is derived by letting the external field vanish. A field dependent term does not appear to vanish from the equation. If it actually does not, then the Boltzmann equation should be critically reexamined. Using the perturbation formula (in the special case of scattering by point defects) for the transition probability appearing in the equation for $\tau(\mathbf{k})$, and using the tight binding approximation form of the electronic wave function (so as to avoid the free-electron assumption), one can calculate the explicit form of the $\mathbf{k}$ dependence of the transition probability without specifying either the ionic potentials or the atomic orbitals. The result involves unspecified coefficients which depend on the type of defect considered. The $\mathbf{k}$ dependence of the relaxation time can then be found by solving the linear integral equation for it. This has been carried out for the two-dimensional model of graphite.

* J. S. Lomont, NAA-SR-205 (1952). This report is based on studies conducted for the AEC.
† Now at USNOTS, China Lake, California.

G10. Observation of Magnetic Domains by the Longitudinal Kerr Effect.* C. A. FOWLER, JR., AND E. M. FRYER, *Pomona College.*—Both the polar and the longitudinal Kerr magneto-optic effects have been recently employed with success to observe ferromagnetic domain patterns, the polar effect at normal incidence for hexagonal cobalt cut to expose free surface poles,[1] and the longitudinal effect at oblique incidence for the (100) surface of a large slab-shaped single crystal of silicon iron.[2] In the latter case at 60° incidence, the rotation of approximately 4 minutes to right or left by the adjacent antiparallel domains is enough to reveal the domains with considerable contrast when photographed through an analyzer set near extinction. A comparison of the front and back (100) faces of the demagnetized crystal shows the domain patterns to be essentially identical but oppositely directed, suggesting flux closure. A series of photographs, taken as the sample is carried through an initial magnetization curve to saturation, clearly shows the characteristic movement of domain walls. When the specimen is taken through a hysteresis cycle, the pattern of surface domains, as the sample departs from the condition of saturation, differs markedly from the pattern observed in the initial magnetization curve.

* Supported by the ONR.
[1] Williams, Foster, and Wood, Phys. Rev. **82**, 119 (1951).
[2] Fowler and Fryer, Phys. Rev. **86** 426 (1952).

G11. Flash Radiographic Studies of High Velocity Metallic Jets. LOUIS ZERNOW, *Terminal Ballistics Laboratory, Ballistic Research Laboratories, Aberdeen Proving Ground, Maryland.*—Recent improvements in the techniques of ultra high speed flash radiography will be described, including a new low voltage system for obtaining three successive radiographs of the same event. The application of this system to the study of the basic physics of high velocity jets (23,000 feet/second) from large-scale shaped charges will be illustrated with radiographs comparing the behavior of jets from a variety of metallic liners. The direct measurement of the velocity gradient along a jet by means of multiple flashes from the same x-ray tube will also be illustrated.

G12. Measurement of Heat of Dissociation of Fluorine by the Effusion Method.* HENRY WISE, *Jet Propulsion Laboratory, California Institute of Technology.*—A wide range of values have been reported[1] for the energy of dissociation of the fluorine molecule. Estimates of this fundamental physical parameter based on the long-wave limit of the continuous absorption spectrum show wide disagreement with those obtained by thermochemical considerations for the ClF molecule and the measurement of the equilibrium pressure of F_2 at elevated temperatures.[2] For a direct determination of the heat of dissociation of fluorine, the gas effusion method[3] is particularly suitable since the experimental measurements are carried out at low pressures (molecular-flow region), and, therefore, a measurable degree of dissociation is attained at relatively low temperatures. The apparatus described in this paper consisted of a nickel tube housing a thin-edged circular orifice (0.185 mm in diameter) made of the same material. From the variation in the rate of gas effusion over the temperature range from 500 to 800°K at a total pressure of 4×10^{-4} mm Hg, the heat of reaction for the process $F_2(g) = 2F(g)$ was found to be 37.6 ± 0.8 kcal/mole. The results tend to confirm the dissociation energy calculated from thermochemical data,[4] which are based on the heat of formation of ClF of 11.6 kcal/mole. They are also in good agreement with the data reported in the direct measurement of the pressure variation with temperature.[2]

* This paper presents the results of one phase of research carried out at the Jet Propulsion Laboratory under U. S. Army Ordnance Department contract.
[1] Haar and Beckett, Natl. Bur. Standards Rept. No. 1435 (Feb. 1, 1952).
[2] R. N. Doescher, J. Chem. Phys. **19**, 1070 (1951).
[3] M. Knudsen, Ann. Physik **29**, 179 (1909).
[4] Eucken and Wicke, Naturwiss. **10**, 233 (1950).

MONDAY AFTERNOON AT 1:30

Room 119, Kerchoff

(J. KAPLAN presiding)

Contributed Papers

H1. New Fine Structure in Oxygen OI.* LEE W. PARKER AND JOHN R. HOLMES, *University of Southern California.*—During a recent investigation of isotope shifts in oxygen,[1] untabulated fine structure was resolved in the triplet multiplets λ8446 ($3s\,^3S_1-3p\,^3P_{210}$), λ2884 ($3p\,^3P_{21}-3d'\,^3P_2$), and λ4368 ($3s\,^3S_1-4p\,^3P_{210}$). Interferometer patterns of these lines were analyzed to obtain splittings and relative intensities. Listed as a doublet, λ8446 has three components whose

relative intensities allowed establishment of the $3p\,^3P_{210}$ anomalous splitting as follows: $J=1$ lies 0.599 ($\pm$0.003) cm^{-1} below $J=2$, and $J=0$ lies 0.158 ($\pm$0.002) cm^{-1} above $J=2$, in close agreement with Edlén[2] and with Davis and Meissner.[3] λ2884, heretofore found single, has two components, separated by 0.558 ($\pm$0.002) cm^{-1}. Two components of λ4368, previously considered single, were resolved and have a separation of 0.300 ($\pm$0.001) cm^{-1}, the weaker component having the shorter wavelength. From the relative intensities it is deduced that $J=0$ lies above the degenerate $J=2$, 1 level of the state $4p\,^3P_{210}$, which, like $3p\,^3P_{210}$, is perturbed by an unobserved state in the displaced (^2D) system.[3]

* Supported by the ONR.
[1] Lee W. Parker and John R. Holmes, Phys. Rev. **88**, 174 (1952).
[2] Edlén, Kingle. Svenska Vetenskapsakademiens Handlingar, Ser. 3, Vol. 20, No. 10 (1943).
[3] λ8446 reported by D. O. Davis and K. W. Meissner, J. Opt. Soc. Am. **42**, 871 (1952).

H2. Preliminary Results of Direct Measurements of Photoionization in O_2.* N. WAINFAN AND W. C. WALKER, *University of Southern California* (introduced by G. L. Weissler).—By using a vacuum spectrograph as a monochromator, radiation from a constant high intensity light source was passed through an exit slit into a chamber which contains the gas at low pressures. Two low voltage ionization chambers in tandem were used to determine ion currents and thereby total absorption coefficients in the gas. In order to measure the photon flux through the exit slit, a sensitized 1P28 photomultiplier was used. The output of the 1P28 was correlated with the signal from a calibrated thermopile. In the range from 1080A to 450A the absorption coefficients were substantially the same as those reported previously.[1] Measurements of the number of ions per absorbed photon indicated that between 1080A and 850A the fraction of the total absorption which was accounted for by photo-ionization processes rose monotonically from about 0.3 to 1.0. Below 850A the absorption mechanism appears to be entirely due to photo-ionization. Work is now underway in other gases, including neon and nitrogen.

* The aid of the ONR is gratefully acknowledged.
[1] G. L. Weissler and Po Lee, J. Opt. Soc. Am. **42**, 200 (1952).

H3. The Photoelectric Yield of Platinum in the Vacuum Ultraviolet.* W. C. WALKER AND N. WAINFAN, *University of Southern California* (introduced by G. L. Weissler).—Preliminary values of the quantum yields of Pt between 1100A and 450A were obtained using a plane Pt photocathode and a Pt ring collector. A vacuum monochromator together with a photomultiplier calibrated in terms of photons per second, using the same experimental arrangement as described in a concurrent abstract by the same authors, was used in this work. The yields, expressed as the ratio of the number of photoelectrons to the number of photons, were measured for both an untreated Pt surface and the same one heated to about 1000°C. Values obtained for the untreated surface were about 20 percent larger than for the other. The results indicated a maximum yield in both cases at about 800A, with a value of 0.16 electron/photon for the heated sample at this wavelength. To either side of this maximum the ratios decreased monotonically to 0.04 at 1100A and 0.08 at 450A for the heated surface. These results agree well with those obtained by Hinteregger.[1] Data will also be presented on Ni, Ta, and other metal surfaces.

* The aid of the OOR is gratefully acknowledged.
[1] H. E. Hinteregger and K. Watanabe, Cambridge Air Force Research Center (private communication) (June, 1952).

H4. The Absorption Cross Sections of CH_4 in the Vacuum Ultraviolet. G. L. WEISSLER* AND H. SUN, *University of Southern California.*—Absolute absorption coefficients k_ν of CH_4 for extreme ultraviolet radiation were measured between 1300A and 510A for 82 wavelengths. At 1300A, $k_\nu=400$ cm^{-1}. The absorption rises to a peaked maximum of $k_\nu=1500$ cm^{-1} or $\sigma=5.6\times10^{-17}$ cm^2 at 960$\pm$20A. This wavelength corresponds to 12.9$\pm$0.2 ev and is identified as the first ionization potential of CH_4 which has been measured recently[1] to be about 13.1 ev k_ν decreases gradually to 650 cm^{-1} at 510A. The measured cross section σ at the maximum is smaller than the theoretical value of Dalgarno,[2] 9.4×10^{-17} cm^2, which was based on the method of self consistent field with exchange effects neglected. The pronounced rise of the absorption contour at 960A supports the application of a quasi-atomic model to CH. However, the existence of continuous absorption at wavelengths longer than the ionization limit perhaps points to limitations of this model. The integrated experimental cross sections between 1300A and 510A yield an f value of about 6 compared to 6.3 from theory[2] between 946A and 500A.

* The aid of the ONR is gratefully acknowledged.
[1] Lossing, Tickner, and Bryce, J. Chem. Phys. **19**, 1254 (1951).
[2] A. Dalgarno, Proc. Phys. Soc. (London) **A65**, 663 (1952).

H5. Further Results on Neon and Argon Absorption in the Extreme Ultraviolet. PO LEE AND G. L. WEISSLER,* *University of Southern California.*—Absorption of neon[1] and argon was measured between 1300A and 250A by photometric methods. Some sharp absorption edges were found corresponding to the L_1, L_2 and M_1, M_2 levels of neon and argon, respectively. For neon and ionization continuum began at 574.9A (L_3) with an absorption coefficient of $k_\nu=146\pm8$ cm^{-1} or $\sigma_\nu=5.5\pm0.3\times10^{-18}$ cm^2. The theoretical values of Seaton[2] using a dipole length and a dipole velocity approximation were $\sigma_l=5.8\times10^{-18}$ cm^2 and $\sigma_v=4.4\times10^{-18}$ cm^2, respectively. The second absorption edge (L_1) appeared at about 255A with $k_\nu=162$ cm^{-1}. The region between 575A and 380A showed results which agreed well with those calculated from the dipole length approximation.[2] Preliminary argon work showed $k_\nu=515$ cm^{-1} at 780A (M_3 edge at 786A), $k_\nu=960$ cm^{-1} at 776A (M_2 edge at 778A), and $k_\nu=270$ cm^{-1} at 418A (M_1 edge at 424A). A photo-ionization cross section at the M_2 edge was estimated to be $\sigma=3.4\pm0.3\times10^{-17}$ cm^2, compared to the theoretical one[3] of $\sigma=3\times10^{-17}$ cm^2.

* The aid of the ONR and the Cambridge Air Force Research Center is gratefully acknowledged.
[1] Improved over previous work by Po Lee and G. L. Weissler, J. Opt. Soc. Am. **42**, 214 (1952).
[2] M. J. Seaton, Proc. Rov. Soc. (London) **A208**, 408 (1951).
[3] A. Dalgarno, Proc. Phys. Soc. (London) **A65**, 663 (1952).

H6. A Multicolor Photoelectric Photometer for Study of Faint Radiations. D. R. WILLIAMS AND PIERRE ST. AMAND, *U. S. Naval Ordnance Test Station, Inyokern.**—An improved, greatly modified version of the Marlow-Pemberton night sky photometer is described. Direct current amplifiers are employed. Separate telescopes, multiplier phototubes, amplifiers and recorders are used for each wavelength region observed.

* Post Office: China Lake, California.

H7. The ν_1 Band of D_2O in the Infrared. W. S. BENEDICT, *The Johns Hopkins University*, AND NORMAN GAILAR AND EARLE K. PLYLER, *National Bureau of Standards.*—We have been measuring with higher resolution the infrared absorption of D_2O and HDO. Quite complete rotational analyses of 7 bands of D_2O and 7 bands of HDO have been achieved, permitting determination of consistent sets of vibrational and rotational constants. The present report will discuss ν_1, the symmetric stretching vibration of D_2O, previously observed only in the Raman effect, which appears with good intensity in the region 2400–2900 cm^{-1}. It is quite free of overlapping from lines of the asymmetric stretching frequency ν_3 in the region below 2600 cm^{-1}, permitting complete identification of the P branches out to $J_{K_a}=10_8$. The band origin is at 2671.7 cm^{-1}, and the inertial constants are $A=15.12$, $B=7.14$, $C=4.75$ cm^{-1}. In contrast with the corresponding bands in H_2O, where the intensity ratio $\nu_1:\nu_3$ is about 1:15, ν_1 is rather

strong, the ratio in D_2O being about 1:3. Coriolis interaction between ν_1 and ν_3 is very weak, as evidenced by only minor perturbations of the ν_1 levels with $K_a=6$ and 7, whose position coincides closely with $K_a=5$ and 6 of ν_3.

H8. Flame Zone Spectroscopy of Solid Propellants. R. G. REKERS AND D. S. VILLARS, *U. S. Naval Ordnance Test Station, Inyokern.**—The spectroscopy of burning solid propellants has been generally limited to a photographic integration of the various flame zones as the burning strand is consumed and the flame passes a spectrographic slit. A few instances have been reported in which separation of the spectral emission from the different zones of the flame has been attempted, but the results are deficient either through loss of resolution of the spectrograph system or shortness of exposure time. An automatic constant level device is reported which now permits the isolation and detailed exposure of a definite flame zone throughout the complete time of burning of a 72-inch length of strand. A discussion of the technique, illustrated with typical data on the degree of control, will be presented. Also described will be results of an exploratory spectrographic study, involving both absorption in the nonluminous regions of burning and emission in the luminous zone.

* Post Office: China Lake, California.

H9. A Possible Relationship Between the Ionosphere and the Nightglow. PIERRE ST. AMAND AND D. R. WILLIAMS, *U. S. Naval Ordnance Test Station, Inyokern.**—The nocturnal variation of the λλ6300, 6364[OI] radiation resembles that of the number of ions in the *F* region of the ionosphere. The possibility that the two phenomena may be related is discussed.

* Post Office: China Lake, California.

H10. The Height of Upper Atmosphere Emissions by the Van Rhŷn Method. F. E. ROACH, HELEN B. PETTIT, D. R. WILLIAMS, AND P. ST. AMAND, *U. S. Naval Ordnance Test Station, Inyokern.**—A critical study is made of the various problems involved in estimating the heights to nightglow emissions by the Van Rhŷn method. In particular the amount of integrated starlight and zodiacal light included as background in photometric observations is considered. A detailed analysis of several nights of observation in four colors at Cactus Peak is given.

* Post Office: China Lake, California.

H11. A Short Afterglow in Nitrogen.* W. B. KUNKEL, *University of California, Berkeley.*—A powerful rf glow discharge was used to excite intense afterglows in a large flow system at pressures ranging from 0.5 to 10 mm Hg. In addition to the well-known Lewis-Rayleigh afterglow, an extremely bright luminosity of about 0.1 second visible life was produced in pure nitrogen. Its spectrum consisted of the first positive group appearing in the same form as in the discharge itself and of the bands of molecular ions. The latter were completely suppressed when about 0.1 percent oxygen was added to the stream. Similar short glows have been observed by Kaplan[1] and by Herman[2] in pulsed systems containing electrodes. While it has been suggested[2] that the radiation may be due to electron-ion recombination it seems more likely that transitions from metastable singlet states are responsible for the population of the $\beta^3\pi_g$ state as suggested by Nicholls.[3] Moreover, strong continued selfionization of the gas by collisions between excited particles, possibly involving the $a^1\pi_g$ state, is indicated.

* Supported by the Wright Air Development Center.
[1] J. Kaplan, Phys. Rev. **42**, 807 (1932).
[2] R. Herman, Compt. rend. **220**, 593 (1945).
[3] R. W. Nicholls, Nature **162**, 231 (1948).

H12. Effects of Hydrogen Bonding on the Infrared Spectra of Alcohols. ALEXANDER VERRIJN STUART* AND G. B. B. M. SUTHERLAND, *University of Michigan.*—In order to clarify the nature of the hydrogen bond, spectra have been studied of various series of alcohols under different conditions, between 6μ and 25μ, using the well-known effect on the OH stretching vibration in the 3μ region as a guide. The results are complex, and seem to depend on the nature of the alcohol (primary or secondary) and on the position of substituents in the hydrocarbon part of the molecule. Instead of the expected two "association" bands (due to the in-plane and out-of-plane OH deformation vibrations), one finds, in general, four such bands, *viz.*, at about 7.1, 7.5, 9.0, and 15.0μ. The latter is very constant and resembles the wide association band for the OH stretching. One may identify it with the out-of-plane OH motion. In CH_3OD an association band of the same character is found at 21μ, supporting the assignment to an OH (OD) vibration. The other bands are rather irregular, and the single "monomer" band found in dilute solutions at about 8.2μ is extremely variable in position. Possible interpretations of all these results will be discussed.

* Now with Koninklijke/Shell-Laboratorium, Amsterdam, Netherlands.

H13. The Measurement of Light Scattered from a Searchlight Beam. E. V. ASHBURN, *Michelson Laboratory, U. S. Naval Ordnance Test Station, Inyokern.**—A recording photoelectric photometer has been designed which will separate the light that is scattered from a searchlight beam from the background light of the night sky, without the necessity of modulating the beam. The polarization of the scattered light is used to separate the light from the two sources. The measurement of the intensity of the light scattered from the searchlight beam is used to determine the density in the stratosphere at heights inaccessible by balloons.

* Post Office: China Lake, California.

MONDAY AFTERNOON AT 1:30

Room 22, Crellin

(L. B. LOEB presiding)

Contributed Papers

I1. Harmonic Analyses of Pulses and Spectral Analyses of Transients. S. LEROY BROWN AND JOHN M. NORWOOD, *University of Texas.*—Each quarter of a wave may be analyzed as a repeating pulse which has values of zero over the remaining three-fourths of its repetition period. This permits fifteen ordinates to be taken for each quarter-wave, or sixty ordinates for the entire wave, and thereby twenty-nine harmonics are determined. The analyses of the four quarter-wave pulses may then be combined, and thereby the wave is analyzed for fifty-eight Fourier coefficients (twenty-nine cosine terms and

twenty-nine sine terms). The approximate integration for the values of fifteen ordinates is done for each quarter-wave with a mechanical harmonic synthesizer with fifteen harmonic components. The spectral analysis of a transient is determined from thirty equispaced ordinates, the origin at the middle of the transient with fifteen equispaced ordinates on either side. The fifteen sums of pairs of ordinates symmetrical with the origin are set on the respective cosine elements of the synthesizer, and a trace is obtained which shows the distribution of the cosine components throughout the spectrum of the transient. Similarly, fifteen differences of the pairs of ordinates are set on the sine elements and the resulting trace is the spectral distribution of sine components.

I2. Variational Approach to a Theory for the Critical Stability of a Fluid. II. F. T. ROGERS, JR., *U. S. Naval Ordnance Test Station, Inyokern, California.*—We have succeeded in reformulating, and giving an approximate solution to, the problem identified in reference 1, for the case $\varphi > 0$. The reformulation incorporates Morrison's recent observations[2] as to patterns of flow when critical stability has been passed. This approximate solution is in accord with all published experimental data, to within a random factor of about 3, which probably represents experimental uncertainties. We wish to suggest that these findings may bear upon certain matters pointed out by Summerfield,[3] inasmuch as the establishment of flow (by passage beyond critical stability) involves the concommitant establishment of the three-dimensional laminar boundary layer of great extent.

[1] F. T. Rogers, Phys. Rev. **85**, 770 (1952).
[2] H. L. Morrison and F. T. Rogers, J. Appl. Phys. **23**, 1858 (1952).
[3] M. Summerfield, J. Am. Rocket Soc. 85, June 1950.

I3. Drag on a Rotating Cylinder at Low Pressures.* S. F. CHIANG AND S. A. SCHAAF, *University of California, Berkeley.*—The torque transmitted by a rarefied laminar air flow between two concentric cylinders, of which the inner one is rotating, was determined for a range of pressures extending from free molecule to continuum flow. The range covered in terms of Mach number M, Reynolds number Re and the Knudsen number K (ratio of mean free path to gap width) was $0.14 < M < 0.55$, $0.054 < Re < 50$, $0.018 < K < 3.9$. The theoretical predictions based on, respectively, (a) the Navier-Stokes equations and the first-order slip boundary condition, (b) the Burnett equations and a second-order slip flow boundary condition, and (c) the 13-moment equations and boundary conditions of H_{grad} all agree with each other and with the experimental results within ± 1 percent in that part of the slip flow range ($0.01 < K < 0.1$) covered by the experiments. The first theory agrees with the experiments over the entire range covered.

* This work was jointly supported by the ONR and OSR.

I4. Sputtering in the High Vacuum and its Relation to Radiation Damage as Described by Seitz. FRANK KEYWELL, *University of Southern California.*—The Seitz radiation damage theory[1] is introduced with reference to other experimental work which verifies the ideas involved. It is argued that radiation damage will persist to low energies; thus one should expect energetic gaseous ions striking a metal surface to produce this effect (commonly called "sputtering"). Comparison is made between the number of atoms displaced in a metallic lattice according to Seitz' theory and the number of atoms sputtered for an ion of given energy E_0 incident in a metal surface. Neutron cooling theory is applied to the process for heavier ions.[2] The effect of absorption is present, as expected, and can be roughly treated only for the heavier ions. In all cases, the number of atoms sputtered n_a is less than the number of atoms displaced N. The curves of N *vs* E_0 have the same form as n_a *vs* E_0 for the gas-metal combinations studied by use of a P.I.G. ion source. Data have been obtained for A−Ag, Ne−Ag, He−Ag, and He−Pb over a range of ~500–5000 volts. Inclusion of the effect of absorption gives close agreement between theory and observation for the A−Ag and Ne−Ag cases. Experimental sputtering thresholds agree favorably with those estimated by collision theory. An explanation is given for the nonsputtering of metals bombarded by electrons of medium energy.

[1] Frederick Seitz, Disc. Faraday Soc. **271** (1949).
[2] Frank Keywell, Phys. Rev. **87**, 160 (1952).

I5. Evaluation of Back Diffusion for Various Standard Gases as it Affects Secondary Electron Emission Coefficients.* J. K. THEOBALD, *University of California, Berkeley* (introduced by Leonard B. Loeb).—The effect of back diffusion of photoelectrons was measured in clean molecular and inert gases for two energy distributions of the electrons, and the results were applied to the analysis of the Thomson equation as an empirical formula for correcting the measurements of the secondary emission coefficients in gaseous discharges. The effect of electron attachment to oxygen molecules to form negative ions is found to be negligible at low current densities, in agreement with a theory due to Loeb and Kunkel. Back diffusion is found to depend on the ratio of field strength to pressure and the initial energy of emission, as expressed by the Loeb modification of Thomson's theory. This theory is believed to hold within a factor of 5 in the most doubtful cases, and agrees with experiment surprisingly well when the initial energy of emission and the random energy of the electrons after reaching equilibrium with the field are nearly the same. After correcting for back diffusive loss, the γ-values obtained by Lauer[1] agree satisfactorily with those of Molnar.[2]

* This work was supported by the ONR.
[1] E. J. Lauer, J. Appl. Phys. **23**, 300 (1952).
[2] J. P. Molnar, Phys. Rev. **83**, 933 (1951).

I6. The Influence of an Electric Field in Contact Charging.* JOHN W. PETERSON, *Department of Physics, University of California, Berkeley* (introduced by L. B. Loeb).—Recent experiments have indicated that the charging of nonconductors in smooth rolling contact with a metal is determined by the surface conductivity of the nonconductor, speed of rolling, equivalent of a contact potential difference between the nonconductor and the metal, pressure and nature of the atmosphere in which charging takes place, and the presence of an external electric field. Small Pyrex glass spheres rolling on nickel were used. Reduced pressures increases discharge by sparking. In the case of low surface conductivity, surface charge due to polarization of the dielectric spheres is readily measurable. Surface conductivity increases on admitting water vapor to a determined pressure, thus increasing the adsorbed water layer on the surface of the spheres. The increasing surface conductivity results in an increasing effect of the electric field, together with decreased charging in zero field. At about 55 percent relative humidity at 20°C the usual negative charge of the glass spheres can be reversed by the applied electric field, and above 60 percent relative humidity the spheres become essentially conducting.

* This study has been supported by the ONR.

I7. Vacuum Sputtering of Metallic Sodium by Inert Gas Ions.* RICHARD C. BRADLEY, *University of California, Berkeley.*—A new technique for studying the sputtering of metals by positive ion bombardment under vacuum conditions is developed. With this method metals to be sputtered are limited to the alkalis, and sputtered atoms are detected by a surface ionization detector consisting of a hot platinum foil partially surrounded by a collector plate. This yields a direct measurement of the number of atoms being sputtered into a given solid angle determined by sizes of target and detector and their relative positions. The sodium target was prepared by distilling the sodium through four stages under high

vacuum, flowing it into the target position while liquid, and allowing it to cool. Renewal of the surface is effected by reliquifying the sodium and overflowing the old target. Preliminary measurements of sputtering rates *versus* ion energy have been made, using a monochromatic beam of ions of argon, neon, and helium extracted from a Phillips Ion Gauge ion source collimated into a beam by an ion gun. The energy range covered was 25 volts to 1500 volts. The secondary electron coefficient for ion bombardment of sodium has also been measured in this same range of ion energies.

* This work was supported by the ONR.

I8. Secondary Cathode Action in N_2 with Coaxial Cylindrical Geometry.* ELSA HUBER, *Department of Physics, University of California, Berkeley.*—A study is being made of the breakdown processes in nitrogen at pressures ranging from 10- to 600-mm Hg. The discharge takes place between a platinum wire at a positive potential and a coaxial nickel cylinder and is triggered by individual α-particles sent through the gap parallel to the wire. The resulting pulses are viewed on an oscilloscope. In the purest nitrogen used to date (as indicated by mass spectrometer analysis) there is a γ_i effect, due to secondary electron liberation at the cathode by positive ions, but no observable γ_p from secondary electron liberation by photoelectrons. If the nitrogen is slightly contaminated, however, a γ_p does become apparent, and at the same time the γ_i secondary pulses become less pronounced. It is believed this change is associated with the presence of oxygen. There is some evidence that two types of nitrogen ions are involved, probably N_2^+ and N_4^+.

* This study has been supported by the ONR.

I9. Secondary Electron Emission Coefficients for Low Energy Positive Ion Bombardment of Discharge Conditioned Surfaces.* JAMES H. PARKER, *Department of Physics, University of California, Berkeley* (introduced by Leonard B. Loeb).—The vacuum secondary electron yield due to A^+ ions, i.e., γ_i, has been measured for discharge conditioned Ta, Pt, and Ni surfaces. Discharge conditioning consists of operating the surfaces at the cathode in a heavy dc glow discharge of N_2, H_2, or O_2. The range of argon ion energy over which γ_i has been determined is 3–200 ev. The spread in ion energy for this range is 2 ev. The argon ions are obtained from a Heil[1] or Finkelstein[2] ion source operating at 10^{-6} mm Hg in argon. The source and target are at the same pressure, which is low enough for large A^+ mean free paths. The targets are in the form of thin sheet (<0.001 inch) and can be outgassed by conduction current through them. The electrode assembly, which is of tantalum sheet encased in Pyrex, can be thoroughly baked and electrodes outgassed by induction heating.

* This study has been supported by the ONR.
[1] Heil, Z. Physik 120, 212 (1944).
[2] A. I. Finkelstein, Rev. Sci. Instr. 11, 44 (1940).

I10. Pre-Onset Burst Pulses in Positive Point to Plane Corona in Air.* M. R. AMIN, *Department of Physics, University of California, Berkeley.*—Mechanism of corona discharges in point to plane geometry in room air at atmospheric pressure have been investigated by the use of a photomultiplier. The correlation of the photon pulses with the induced pulses observed through a series resistor have revealed new information as to the nature of burst pulses. The burst pulse seems to consist of an initial pulse spreading over the point in less than 10^{-7} second and followed by secondary pulses each of the same duration but with smaller amplitude. The dead time just before onset is of the order of 5 to 10 microseconds and the clearing time for the whole burst is of the order of milliseconds. The number of ions in the initial pulse is of the order of 10^7 ions and in the secondary pulses of the order of 10^8 ions. These findings definitely indicate the pre-onset burst pulse corona to be a typical Geiger counter mechanism, operating at atmospheric pressure and somewhat different conditions from conventional fast counters.

* This work was supported by the ONR.

MONDAY EVENING AT 8:00

Sexson Auditorium, Pasadena City College

(R. F. BACHER presiding)

IA1. The Expanding Universe. FRED HOYLE, *Cambridge, England.*

TUESDAY MORNING AT 9:00

Room 201, Bridge

(C. C. LAURITSEN presiding)

Invited Papers

J1. The Stanford Linear Electron Accelerator. R. L. KYHL, *Stanford University.* (45 min.)

J2. The California Institute of Technology Synchrotron. R. V. LANGMUIR, *California Institute of Technology.* (30 min.)

J3. Recent Experimental Evidence Concerning Vo Particles. ROBERT B. LEIGHTON, *California Institute of Technology* (30 min.)

J4. Some Theoretical Problems Presented by the V Particles. RICHARD C. FEYNMANN, *California Institute of Technology.* (15 min.)

J5. Electron-Induced Showers. ROBERT HOFSTADTER AND ASHER KANTZ. *Stanford University.* (30 min.)

TUESDAY AFTERNOON AT 1:30

Room 201, Bridge

(R. F. CHRISTY presiding)

Contributed Papers

K1. Spectrum of Particles from Lead Bombarded by 32-Mev Protons. ROBERT M. EISBERG AND GEORGE J. IGO, *Radiation Laboratory, University of California, Berkeley.*—The inelastic and elastic particles scattered from lead when bombarded with 32-Mev protons were observed at 90° to the incident beam. Particles were detected in a telescope consisting of a proportional counter in coincidence with a sodium iodide scintillation counter. The energy of the particles was determined by pulse-height analysis on the scintillation counter pulses. The coincident proportional counter measurement of ionization insured that the particles counted in the scintillation counter were heavy and charged. The observed energy spectrum does not appear to agree with that predicted by the Weiskopf "boil off" theory in that there are too many high energy particles.

K2. The Scattering and Absorption of π^+ Mesons by Aluminum. J. F. TRACY. *Radiation Laboratory, University of California, Berkeley.*—A beam of π^+ mesons has been passed through five ¼-inch aluminum plates in an argon-filled cloud chamber in a field of 5200 gauss; 3976 tracks making 15,359 plate traversals at energies between 25 and 100 Mev (mean energy 49 Mev and average path per traversal 1.57 g/cm²) have been observed. μ^+ contamination was approximately 13 percent. Positron contamination was negligible. Twenty stops; 34 scatters $\geqslant 30°$; and 34 1-prong, 21 2-prong, one 3-prong, and one 4-prong stars were observed. All stops were reasonably accounted for by scatterers and stars hidden by the geometry. Only the faster prongs escape the aluminum without difficulty. If one assumes them to be protons, 49 prongs had more than, and 34 had less than ~30 Mev. The fast prongs were isotropic; the slow prongs, predominantly forward. One unusual event consisting of a 1-prong star and a 70-Mev electron-positron pair in coincidence may be interpreted as an inelastic charge-exchange scatter. The scattering is roughly isotropic except for a dip at 60°–90°. Cross sections (taken over all energies and corrected for geometry and beam contamination) are σ (scat), 162±28 mg; σ (star), 234±31 mb; and σ (total), 396±41 mb. All cross sections rise rapidly with energy.

K3. π^- Mesons Produced in a Cloud Chamber by High Energy Neutrons. FRANKLIN C. FORD AND WILSON M. POWELL, *Radiation Laboratory, University of California, Berkeley.*—The production of π^- mesons in oxygen by neutrons with energies around 310 Mev has been observed in the gas of a Wilson cloud-chamber filled with oxygen and water vapor. The energy and angular distribution for over one-hundred events has been obtained. The neutrons were produced by bombarding a LiD target with 340-Mev protons.

K4. The Radiofrequency Fine Structure of the Photon Beam from the Berkeley Synchrotron. RICHARD MADEY, KENNETH C. BANDTEL, AND WILSON J. FRANK, *Radiation Laboratory, University of California, Berkeley.*—The full energy spread out bremsstrahlung beam of the Berkeley synchrotron was shown to be emitted in sharp burst with the 47.7 megacycle frequency of the electrons in the doughnut. A two-counter telescope, located at about 20 inches away from a ¼-inch lead target and about 20 degrees from the photon beam direction, was used to measure an accidental coincidence counting rate as a function of the length of delay line in one input to the coincidence circuit. An estimate of the width of a single pulse of photons can be obtained from the measurement by unfolding the Gaussian resolution function of the coincidence circuit. If the time variation of the intensity of the photon beam is assumed to be a Gaussian function, then the rms value of that Gaussian is found to be less than 1.5×10^{-9} second. A calculation by E. M. McMillan[1] indicates that the full energy photon beam should exhibit fine structure if the amplitude of the azimuthal phase oscillations at full energy is less than about one radian. The experimental result is another confirmation of the theory of phase stability.

[1] E. M. McMillan (private communication).

K5. β-Decay of Cu^{67}. HARRY T. EASTERDAY, *Radiation Laboratory, University of California, Berkeley.*—The 60-hour β-activity of Cu^{67} produced by (α, p) on Ni and $(d, 2p)$ on Zn has been investigated with a thick lens spectrometer and coincidence counters. The β-spectrum is found to contain three continuous groups with maximum energies of 577, 484, and 395 kev and coversion electrons from 92- and 182-kev transitions. These results along with the fact that $\gamma-\gamma$ coincidences are absent indicate that the β-transitions are to the ground and first two excited states of Zn^{67}. Measurements of the conversion coefficients of the Ga^{67} γ-rays have also been made. Using these data and the previous results on the K capture of Ga^{67},[1,2] spin assignments for the Zn^{67} levels are suggested.

[1] A. Mukerji and P. Preiswerk, Helv. Phys. Acta **25**, 387 (1952).
[2] A. R. Brosi, Oak Ridge National Laboratory (private communication).

K6. Further Evidence for the Process $p+d\rightarrow t+\pi^+$. WILSON J. FRANK, KENNETH C. BANDTEL, RICHARD MADEY, AND BURTON J. MOYER, *Radiation Laboratory, University of California, Berkeley.*—A two-counter telescope was placed at a triton angle of 8° and another at the correlated pion angle of 110°. The four *trans*-stilbene counters were connected to a quadruple coincidence circuit having a resolution time of three millimicroseconds. The tritons are confined within a twelve-degree cone, which allows the triton telescope to be ten feet farther from the target than the pion telescope without loss of solid angle. This geometry permits the measurement of the triton velocity and the suppression of the scattered proton background by counting between the radiofrequency proton pulses from the cyclotron. The evidence for the process is as follows: (1) The CD_2-C difference obtained at the correlated angles disappeared if the telescopes and the beam axis are noncoplanar, or if one telescope is moved from its correlated angle. (2) The particles observed at the triton (or pion) telescope have the energy expected of the triton (or pion) to within ten percent. (3) The particles observed at the triton telescope have the velocity expected of the triton to within fifteen percent. The uncorrected differential cross section is 0.24±0.02 microbarn/steradian at a center-of-mass pion angle of 130° and at a laboratory proton energy of 340 Mev.

K7. A Test of the Charge Symmetry Hypothesis. H. W. WILSON AND WALTER H. BARKAS, *Radiation Laboratory, University of California, Berkeley.*—When alpha-particles bombard carbon, for every process leading to the emission of a positive meson there exists a mirror process leading to the emission of a negative meson. If the charge symmetry hypoth-

esis is valid, one would therefore predict a plus/minus ratio of unity for pion production under the conditions where the Coulomb barrier can be neglected. An experimental arrangement was employed to measure this ratio which eliminates to a large extent the known sources of systematic error. For mesons of nominal energy 15 Mev (total spread 11–21 Mev), the plus/minus ratio from carbon for mesons emitted at 90° to the 375-Mev alpha-particle beam was found to be 0.72 with a standard deviation of 0.17. Estimation of the expected depression of the ratio caused by Coulomb effects has been made.[1] It is concluded that the measured ratio agrees within its standard deviation with that anticipated on the basis of the charge symmetry hypothesis. Another experiment which attempted to utilize mesons of ≈30 Mev failed because the obtainable meson flux was too low. With the same apparatus the plus/minus ratio for pions emitted at 90° to a 330-Mev proton beam bombarding carbon was measured. A ratio of 5.4±0.8 was found.

[1] B. Fried and S. Gasiorowicz (private communication).

K8. Total Cross Sections for Positive Pions. D. Stork, *Radiation Laboratory, University of California, Berkeley.*—The total cross section for positive pions is being studied for several light nuclei as a function of energy in the neighborhood of 50 Mev. Pion beams of various energies are made by bombarding a polyethylene or carbon production target with the 340-Mev external proton beam of the Berkeley synchrocyclotron. The energy is selected by means of a 90° magnetic deflection. A coincidence from two stilbene scintillation counters placed in front of the sample triggers an oscilloscope sweep. Pulses from the front two counters and from a 14-inch diameter liquid scintillation counter placed behind the sample appear on the oscilloscope trace separated in time by means of delay lines. The traces are photographed on continuously moving film. An attenuation event is one in which the pulse from the back counter is absent. The attenuated pions are distinguished from electrons, stopped muons, and random background by means of a pulse-height analysis of the pulses from the front two counters as determined by examining the film. The cross section at 50 Mev for beryllium, carbon, and aluminum is about two-thirds the nuclear area.

K9. A Study of the Pick-Up Process in Proton-Deuteron Scattering. A. Bratenahl and B. J. Moyer, *Radiation Laboratory, University of California, Berkeley.*—To account for the unexpectedly large yield of high energy deuterons produced at small angles by high energy proton bombardment of nuclei, a mode of production has been proposed in which a nucleon is transferred from a target nucleus to the incident nucleon, the resulting pair emerging as a deuteron. This transfer or rearrangement process has been termed pick-up. According to the theory of this process, investigation of the yield of pick-up deuterons can furnish information on the wave function of nucleons in a nucleus. A reasonably direct test of the pick-up hypothesis consists in a characteristic connection between the angular distribution and the energy dependence of the yield. In the present experiment, the test is applied in the case where deuterium is the target nucleus. Observations are made of the elastic deuteron recoils in the angular range extending from 0° to 20°; the region theory shows should be dominated by pick-up. Absolute yields are obtained at these angles for incident proton energies of 95, 112, and 138 Mev. The result shows that the theory is supported by the experiment in regard to the features of the test except that the absolute yield is only 55 percent of that predicted.

K10. On the Ratio of π^+ to π^- Mesons Produced by Gamma-Rays. James Edward Carothers, *Radiation Laboratory, University of California, Berkeley.*—The minus to plus production ratio for pi-mesons produced in the 320-Mev photon beam of the Berkeley synchrotron has been measured at 60°, 90°, and 150° to the beam for beryllium and at 90° for carbon. Identification of the mesons was made by using a magnet to select a desired momentum interval and measuring the velocity of the particles delivered by the magnet. The results were as follows:

	Be	C
60°	1.93±0.12	
90°	1.96±0.10	1.27±0.06
150°	1.92±0.11	

The relative production of positive and negative mesons at 90°, per proton for positives and per neutron for negatives, from beryllium and carbon was π^+ Be/π^+ C = 1.24±0.09; π^- Be/π^- C = 1.44±0.08. The limits shown are in terms of standard deviation.

K11. Phase-Reversal Focusing in Linear Accelerators. Myron L. Good, *Radiation Laboratory, University of California, Berkeley.*—A modification, applicable to the linear accelerator, of the focusing principle discovered by Courant, Snyder, and Livingston[1] is presented. No foils, grids, magnets, or electrodes are used. One introduces, at periodic intervals along the machine, repeat lengths which are alternately greater than and less than the synchronous repeat length $l = \beta\lambda$. This causes the synchronous particle to alternately lead and lag the rf peak by the synchronous phase angle $|\phi_s|$. (This does not affect the energy gain.) It has been pointed out by McMillan[2] that in a linear accelerator without grids or foils in the path of the beam, one cannot have first-order radial focusing and phase stability at the same time. The above modification causes the beam to periodically alternate from a condition of radial defocusing (with phase stability) and one of radial focusing (with phase instability). Both the radial and phase equations of motion become, for small oscillations, the Hill-Meissner equation, and over-all stability results. The strength of focusing is comparable to that obtained by using grids. The phase acceptance angle is being investigated.

[1] Courant, Livingston, and Snyder, Phys. Rev. (to be published).
[2] E. M. McMillan, Phys. Rev. **80**, 493 (1950).

K12. Variation of Moisture Content in Nuclear Track Emulsion. Albert J. Oliver, *Radiation Laboratory, University of California, Berkeley.*—Ilford emulsions for nuclear research, both unprocessed and processed, have been brought to equilibrium with different relative humidities and then measured in thickness, volume, and weight. The variation of emulsion volume and weight with time in a vacuum, for different thicknesses of unprocessed emulsion on glass, has been followed. Moisture diffusion rates through the emulsion and the nonlinear relationship between thickness and water content have been investigated. Thicknesses were measured by a dial indicating micrometer. Volumes were measured by displacement. Humidities were maintained in some cases by salt solutions and in others by aqueous solutions of glycerine. New values have been computed for emulsion density and for the dependence of the shrinkage factor on relative humidity and processing procedure.

K13. Pion Production at 180° by Protons on Carbon. Stanley L. Leonard, *Radiation Laboratory, University of California, Berkeley.*—The pion production cross section at 180° to the beam for carbon bombarded by 340-Mev protons has been measured, using photographic emulsion techniques. Ilford C-2 emulsions imbedded in Cu or Al absorbers were exposed to magnetically separated beams of positive and negative pions emerging from graphite targets at a series of energy intervals. Mesons were identified and counted by the usual microscope techniques. The values, for $\theta = 180°$, of $d\sigma/d\Omega dE_\pi$ as a function of energy and of the integrated cross section $d\sigma/d\Omega$ have been obtained for both positive and negative

pions and the plus-minus ratios have been calculated. Corrections are made for errors resulting from pion decay in flight, the finite thickness of the target nuclear absorption in the Cu and Al, and for background pions which are probably produced in the magnet pole pieces by the fringe of the proton beam.

K14. Nuclear Scattering of "300" Mev Neutrons. W. P. BALL, BURTON J. MOYER, AND ROBERT E. RICHARDSON,* *Radiation Laboratory, University of California, Berkeley.*—Elastic and inelastic cross sections for "300" Mev neutrons on nuclei were determined. Ring type scatterers, polyethylene *n, p* converters with scintillation counters, and triple coincidence units were used. Ratios of counts in the scattered beam to those in the direct beam yielded absolute values for the cross sections. Angular distributions of neutron nuclear differential elastic scattering cross sections were obtained for carbon, aluminum, copper, and lead. The distribution for lead seems to approximate a diffraction pattern. The fit to a diffraction pattern gets progressively worse as one goes to lighter elements. Differential elastic cross sections were integrated graphically over the angles measured. The resulting integrals added to corresponding inelastic results yield total cross sections which are in agreement with those obtained by DeJuren and Moyer. Elastic and inelastic cross sections obtained in this experiment compared with lower energy results of others, show the elastic part is primarily responsible for the rapid drop in total cross sections with energy above 100 Mev found by DeJuren and Moyer.

* Now at Project Lincoln, M. I. T.

K15. Secondary Particles Induced by 375-Mev Alpha-Particles. R. W. DEUTSCH AND W. H. BARKAS, *Radiation Laboratory, University of California, Berkeley.*—Thin targets of Be, Al, Ni, Ag, Au, and U have been bombarded by an internal cyclotron beam of 375-Mev alpha-particles. Secondary particles emerging from the disintegration of the nuclei are detected in Ilford C2 nuclear track plates located beneath the median plane of the cyclotron. There are three specific positions for the nuclear plates corresponding to mean proton energies of about 5, 10, and 20 Mev. A secondary particle is identified by measurement of its radius of curvature, range, and specific ionization. The light secondaries including H^1, H^2, H^3, He^3, and He^4 fall on identifiable loci. Heavier fragments are also identified by taking into account electron pick-up.[1] Relative abundances of the secondary particles and momentum spectra are obtained.

[1] W. H. Barkas, University of California Radiation Laboratory Report No. 1937.

K16. π^+/π^- Ratios Measured with the Use of the Spiral Orbit Spectrometer.* RYOKICHI SAGANE, *Radiation Laboratory, University of California, Berkeley.*—The results of the experiment, preliminarily reported earlier,[1] are as follows: The π^+/π^- ratios for mesons produced by 345-Mev protons at 90° for energies 13±4 Mev, 18±4 Mev, and 41±2 Mev have been obtained. The ratios are Be (1.3±0.4, 5.2±1.3, 5.8±1); C (−, 5.0±1, 11.5±2.5); and Al (4±0.8, 2.5±1.2, 1.6±0.4), respectively. Plates for Cu, Ag, and Pb are now being scanned. Several developmental tests for the use of the spiral orbit spectrometer have been made. The following items will be discussed: (1) The vertical focusing is working favorably, and it is possible to adjust this effect. (2) The energy resolution of the spectrometer was usually too high compared with the energy spread caused by absorption through the targets. It is possible to reduce the resolution by adding annular ring pole pieces and increase the intensity. (3) To reduce energy spread due to absorption both for mesons and protons, thin-walled conical or tubular targets were used. (4) The projected range straggling curve of 8-Mev mesons in C2 emulsion was obtained. This enables one to calculate the absolute number of mesons arrived at the detector.

* G. Miyamoto, Proc. Phys. Math. Soc. Japan **24**, 676 (1942); **17**, 587 (1943); M. Sakai, J. Phys. Soc. Japan **5**, 178 (1950).
[1] R. Sagane and P. C. Giles, Phys. Rev. **81**, 653 (1951).

TUESDAY AFTERNOON AT 1:30

Room 155, Arms

(PAUL KIRKPATRICK presiding)

Contributed Papers

L1. Nuclear Resonance Line Broadening and Quadrupole Splitting in Metallic Beryllium.* W. D. KNIGHT, *University of California, Berkeley.*—The nuclear magnetic resonance absorption line in powdered beryllium metal is a well-resolved triplet. The observed width of the central component is 3.5 kc, and the splitting of either satellite is 12 kc. The line width increases slightly with field and temperature. The temperature dependence of the line width roughly confirms relaxation time measurements in pointing to deviations from the usually assumed inverse temperature dependence of the spin-lattice relaxation time. Beryllium is hexagonal, and its behavior will differ from that of cubic metals such as copper or sodium, in which the position of the resonance is simply shifted due to local fields generated primarily by the conduction electrons in *s* states. It is proposed that the excessive line width (about six times the calculated nuclear dipolar width) and the triplet structure arise from two mechanisms related to the noncubic crystal structure. First, the conduction electron local field will be anisotropic: in a polycrystalline material the *s* states will shift the line, while other contributions will produce broadening. Second, quadrupole coupling will spread the absorption spectrum into three peaks, corresponding to $I=3/2$. We may combine the observed splitting with Kittel's (unpublished) calculation of the contribution of the ion cores to the electric field gradient to estimate the nuclear electric quadrupole moment of Be^9 to be of the order of 0.02×10^{-24} cm².

* Supported in part by the ONR.

L2. Photoproduction of Meson Pairs.* R. D. LAWSON AND S. D. DRELL,† *Stanford University.*—For pseudoscalar mesons interacting with nucleons via pseudoscalar coupling, it follows from a perturbation calculation that the cross section for photoproduction of (π^+, π^-) pairs near threshold dominates over other possible meson pair creation cross sections by a factor of the order of $(M/\mu)^2$. This is best seen by transforming the pseudoscalar interaction Hamiltonian with the Dyson transformation.[1] The transformed Hamiltonian can be separated into one large pair term $2M(g^2/\mu^2)\int\bar{\psi}\psi\varphi^2\,d\tau$ plus other smaller terms, one of which is the usual pseudovector coupling form. This large term gives the dominant contribution to the (π^+, π^-) pair production process, but cannot contribute to the pair process in which one of the mesons is a π^0 and the other

is charged, since it cannot change the charge state of the nucleon. The (π^0, π^0) cross section is small in virtue of the fact that the γ-ray interacts only with the nucleon in this process. The total (π^+, π^-) cross section for 400-Mev incident γ-rays in the laboratory system is approximately $(g^2/4\pi)^2$ millibarns. This value is considerably larger than that given by Brueckner and Watson[2] who assume pseudovector coupling. Measurement of π^- mesons produced by γ-rays on protons may yield valuable information on the operation of the above pair term in the pseudoscalar coupling.

* Assisted by joint program of the ONR and AEC.
† Now at the Department of Physics, M. I. T.
[1] F. J. Dyson, Phys. Rev. **73**, 929 (1948).
[2] K. Brueckner and K. Watson, Phys. Rev. **87**, 621 (1952).

L3. Remark on the Second-Order Electron Self-Energy. H. P. STAPP, *University of California, Berkeley.*—The matrix formulation of perturbation theory is based on a set of unitary transformations which are designed to carry a (Hamiltonian) matrix progressively closer to diagonal form. The transformation corresponding to the second-order correction will approximately diagonalize any finite matrix provided only that the coupling parameter is sufficiently small. It is shown, however, that when this transformation is applied to the infinite matrix of the self-energy problem, the affected off-diagonal elements become infinite regardless of how small the perturbation parameter is made. Since the matrix is carried further from diagonal form by an infinite amount, even as the coupling parameter approaches zero, the (second-order) perturbation energy should not be considered a valid correction, and a different method of approximation is indicated. A modification of the usual second-order transformation can be found which exactly diagonalizes that portion of the Hamiltonian which contributes in second order. Using positron theory, this gives a finite mass correction of about one percent whose chief form is of the form $\alpha \log(1/\alpha)$, where α is the fine structure constant. No cutoff is used. The form of the solution is nonanalytic at the origin, in accordance with a recent remark by Dyson.

L4. Electro-Disintegration of Nuclei. KARL L. BROWN AND RICHARD WILSON,* *Stanford University.*—High energy electrons (24–34 Mev) from the Stanford 35-Mev linear accelerator were used to study the ratio $\bar{F}$ of the activity $A^s(\gamma, n) \times (A-1)^s$, due to the bremsstrahlung of the electrons to the activity $A^s(e, e'n)(A-1)^s$, produced by the electromagnetic field of the electrons for the isotopes Cu^{63}, Zn^{64}, Ag^{109}, and Ta^{181}. Results are compared with the theoretical calculations of Blair.[1] The Weizacker-Williams virtual photon method gives a value of $8\pi/3$ for $\bar{F}$. The experiment was the "stacked foil" type—the electron beam passed successively through a thin foil of the element being studied, a copper radiator, and a second thin foil. The resulting foil radioactivity was measured with Geiger counters. Preliminary results indicate (within experimental error) that the ratio $\bar{F}$ varies linearly with energy. $\bar{F}$ at 34 Mev is 8.5 ± 0.5, 8.7 ± 0.5, 7.5 ± 0.3, 6.2 ± 0.7; and at 33.5 Mev is 6.9 ± 0.4, 7.4 ± 0.5, 6.2 ± 0.3, 5.2 ± 0.6 for Cu, Zn, Ag, and Ta, respectively.

* Present address: Clarendon Laboratory, Oxford, England.
[1] J. S. Blair, private communication and Phys. Rev. **75**, 907 (1949).

L5. Decay Scheme of Ga^{67}. W. E. MEYERHOF, L. G. MANN, AND H. I. WEST, JR., *Stanford University.*—Using NaI(Tl) scintillation counters in coincidence (with differential discrimination) the decay scheme of Ga^{67} has been investigated. This isotope decays by K capture to excited levels of Zn^{67}. Positrons occur to less than 0.01 percent. Gamma-rays are found as follows: 0.090 Mev (4 percent), 0.092 (73.5 percent $\gamma+e^-$; $e^-/\gamma\sim0.6$), 0.182 (21.5 percent), 0.20 (2 percent), 0.30 (12.5 percent), 0.39 (4.5 percent), 0.5 (<1 percent), 0.9 ($\sim$1 percent), 1.1 (<1 percent, ?). (The percentages refer to a Ga^{67} decay probability of 100 percent.) The 0.092 gamma-ray is delayed by 8 ± 1 μs (half-life) with respect to the 0.090, 0.20, and 0.30 gamma-rays. The gamma-rays may be ordered into the following level scheme of Zn^{67} (percent K capture to each level and spin assignment given in brackets): 0 Mev ($\sim$0 percent; $f_{5/2}$), 0.092 (57 percent; $\frac{1}{2}^-$), 0.182 (23.5 percent; $\frac{3}{2}^-$), 0.39 (19 percent; $\frac{3}{2}^-$), 0.9 ($\sim$1 percent), 1.1 (<1 percent ?). The spin assignments are consistent with a preliminary analysis of gamma-gamma angular correlation experiments. The authors are very much obliged to the University of California, Berkeley, for producing the Ga^{67} in the 60-inch cyclotron by the Zn (p, n) reaction.

L6. Radiative Correction to the Collision Loss of Heavy Particles. V. Z. JANKUS, *Stanford University* (introduced by L. I. Schiff).—The usual expression for the collision loss of a heavy particle considers only the elastic collisions with atomic electrons. Recently, Jauch[1] has calculated the radiative correction due to the emission and re-absorption of virtual photons and emission of very soft, real photons. In our calculation the contribution due to the emission of hard photons is also included. The calculation, like that of Jauch, is performed in a Lorentz frame, in which the heavy particle is initially at rest. To simplify the calculation, it is assumed that the bombarding electrons in this Lorentz frame are extremely relativistic, and the Bethe-Heitler formula is used. The results show that the collision loss is increased by an amount that gets bigger as the energy increases; it is 1 percent when the incident particle energy is 100 times its rest energy. In contrast, Jauch found a decrease of 3 percent for the same energy. Since the Bethe-Heitler formula does not take into account the recoil of the scattering center, our results may be in error when the recoil velocity of the heavy particle in the center-of-mass frame is comparable with c.

[1] J. M. Jauch, Phys. Rev. **85**, 950 (1952).

L7. On the Mean Lifetime of V^0 Particles.* R. B. LEIGHTON AND W. L. ALFORD, *California Institute of Technology.*—The mean rest-lifetime of V^0 particles has been estimated, using measurements on 134 cases of V^0 decay. A case was rejected (1) if its decay point lay outside certain fiducial surfaces placed well inside the visible volume of the cloud chamber, (2) if the included angle between its two decay tracks was $\leqslant 10°$, or (3) if the V^0 path was seriously obstructed from view either above or below the decay point. The time t_i at which the ith V^0 particle decayed after crossing the upper fiducial boundary, and the time T_i that it would have remained within the fiducial volume had it not decayed, both measured in the rest system of the V^0 particle, were calculated for the remaining $N=74$ cases. The maximum-likelihood value τ of the mean life was then calculated by iteration, using the formula $\tau=\Sigma[t_i+T_i/(-1+\exp T_i/\tau)]/N$. This gave $\tau=2.5\pm0.7\times10^{-10}$ sec, where the indicated error includes both the effect of the limited sample and the effect of the finite value of the T_i. The mean value of t_i/T_i was 0.30. The mean life of 48 cases, whose apparent energy release upon decay was $\leqslant 50$ Mev was $\tau_L=3.0\pm0.8\times10^{-10}$ sec, and that of 26 cases, whose apparent energy release was >50 Mev, was $\tau_H=1.6\pm0.5\times10^{-10}$ sec. There is thus no clearly significant difference between these two groups.

* Assisted by the joint program of the ONR and AEC.

L8. Cerenkov Radiation in a Dispersive Medium. H. MOTZ AND L. I. SCHIFF, *Stanford University.*—In a recently published book on optics, Sommerfeld[1] states that the direction of propagation of Cerenkov radiation in a dispersive medium is given by the usual formula,[2] if the velocity of light in the medium is taken to be the group velocity. This is contrary to the generally accepted result, according to which the phase velocity must be used. The latter is shown to be correct,

and the role of the group velocity is discussed in a way similar to that given by Tamm.[3] In particular, a wave-packet argument is used to show that the cone of constant radiation amplitude with vertex at the electron has an angular opening that depends on the dispersion, so that the radiation does not, in general, propagate perpendicular to the planes tangent to this cone. A full account will be published in the American Journal of Physics.

[1] A. Sommerfeld, *Vorlesunger Über Theoretische Physik, Band IV, Optik* (Dieterich Verlag, Wiesbaden, 1950), p. 341.
[2] See, for example reference 3, or L. I. Schiff, *Quantum Mechanics* (McGraw-Hill Book Company, Inc., New York, 1949), p. 264.
[3] I. Tamm, J. Phys. U.S.S.R. **1**, 439 (1939); see especially Sec. 5.

L9. Agreement of Theoretical and Experimental Intensities of Soft Continuous X-Rays. R. W. HENDRICK, JR., *Stanford University.*—Calculations of the intensity of thick-target continuous x-radiation from 8 to 15A permit comparison with experimental values.[1] The theoretical intensities are obtained by integrating the emitting power of the electrons as they are stopped in the target. Emitting powers are extrapolated from calculations[2] using Sommerfeld's theory of radiation. Negligible x-ray absorption in the target results from the short range of the emitting electrons. The intensity of 10A radiation from a tungsten target can be approximated with less than 3 percent error in the region 1.25 to 3.5 kilovolts by the expression $I=C[3(V-V_0)-(V-V_0)^2+0.17(V-V_0)^3]$, if V is expressed in kilovolts. V_0 is 1.24 kilovolts, the minimum voltage for producing 10A x-radiation, and C is a determinable experimental constant. Experimental intensities measured by Stephenson and Mason (1.25 to 2 kv) deviate from the theoretical values by less than 4 percent of the 2 kv intensity if they are normalized to agree at 1.8 kv.

[1] S. T. Stephenson, and F. D. Mason, Phys. Rev. **75**, 1711 (1949).
[2] P. Kirkpatrick and L. Weidmann, Phys. Rev. **67**, 321 (1945).

L10. The Scanning X-Ray Microscope. HOWARD H. PATTEE, JR., *Stanford University.*—A proposed new type of microscope especially suitable for x-rays uses no optical elements between the specimen and image, the magnification being done electronically. The x-ray source is produced by focusing field-emission electrons onto a foil target, to the outside of which the specimen is closely affixed. This electron probe is scanned over the specimen area in synchronism with a scan on a display kinescope. The intensity of the kinescope is modulated by the output of a photomultiplier which detects the x-rays passing through the specimen. The magnification is the ratio of the kinescope sweep-length to the sweep-length of the x-ray source. Since the specimen is in direct contact with the source the diffraction effects are negligible, and the resolution does not in principle depend on the wavelength of the radiation used, but on the effective size of the source. Such a technique might therefore be used with light in order to overcome the resolution limit set by diffraction. Construction of the microscope is now in progress.

L11. Refinement and Resolution in Reconstructed Wavefront Microscopy. HUSSEIN M. A. EL-SUM AND PAUL KIRKPATRICK, *Stanford University.*—Removal of photographic noise is a double problem. Noise in the hologram is effectively smoothed out by axial rotation of all lenses and filters in the system. Noise occurs in the reconstruction, even from a clean hologram, because of actual dirt, physical defects (astigmatism, optical inhomogeneity, surface irregularities) in the optical components, and the presence of the out-of-focus conjugate image. Methods have been developed for the suppression of most of these nuisances. Disturbance arising from the conjugate image may be obviated by leaving the object to be imaged in the system along with its hologram during the reconstruction exposure. The object gives rise to a diffraction pattern which is complementary to the undesired conjugate image, and hence, they combine into a uniform photographic field. Alternatively, it is proposed to make two holograms with their background radiations differing in phase by 90°, and to reconstruct from both simultaneously, using a beam splitting and reuniting optical system. Such a process would cancel the unwanted image by interference. The resolution of a reconstructed wave-front micrograph made with a given lens may surpass that of any image directly formed by the same lens.

L12. Field Emission: Large Current Densities, Space Charge, and the Vacuum Arc. W. P. DYKE AND J. K. TROLAN, *Physics Department, Linfield College, McMinnville, Oregon.*—Field emission was obtained from a single crystal tungsten emitter under conditions of very high vacuum and clean surfaces. The geometry of the emitter was determined by electron microscopy permitting accurate calculation of both the surface electric field and an average current density. The use of pulse electronic techniques extended the observations to the upper limit of the current densities for which the normal field emission was stable. Above this limit an explosive vacuum arc occurred between electrodes. From these experiments the following conclusions were drawn: (1) The wave-mechanical, image-force, corrected theory quantitatively predicted the observed average current density up to that density for which space charge dominates the emission. (2) Space charge was effective at a current density of the order of 10^7 amperes/cm^2 where a marked deviation occurred from the usual current-voltage relationship. Space charge effects permitted the simultaneous operation of multiple emitting areas of differing geometries. (3) At a still higher critical current density in the range 10^7 to 10^8 amperes/cm^2, a field emission initiated vacuum arc occurred between electrodes resulting in a change of emitter geometry. Current density was the dominant criterion for the initiation of the vacuum arc.

L13. Electron Bunching in a Disk-Loaded Circular Wave Guide. R. B. NEAL, *Microwave Laboratory, Stanford University.*—This device has been developed to supply axially bunched electrons to the Stanford Mark III Linear Accelerator. Good initial bunching is necessary to obtain a sharp electron energy spectrum at the accelerator output. The buncher consists of a disk-loaded circular wave-guide structure 32 inches long operating in the $\pi/2$ mode. The hole diameters in the disks and the i.d. of the circular wave-guide are tapered so that the phase velocity increases from $\beta=0.5$ at the beginning to $\beta=1.0$ at the end, while the axial field strength increases by a factor of 10. Electrons are injected from an electron gun at 80 kv ($\beta_e=0.5$). About 95 percent of the electrons are bound to the traveling wave and emerge from the buncher with energies of 4 Mev. An output current of 10^{12} electrons/pulse has been obtained bunched within 20 degrees on the wave front. With this degree of bunching, all electrons at the output of the accelerator should have energies within 98 percent of maximum. The power source for the buncher is a 10.5 cm, 10 megawatt, klystron amplifier delivering 1.4 microsecond pulses at 60 cps about 2/3 of the power passes through the buncher and is used in the accelerator proper.

TUESDAY AFTERNOON AT 1:30

Room 119, Kerchoff

(R. B. BRODE presiding)

Contributed Papers

M1. Multiple-Beam Fringes of Equal Chromatic Order. W. F. KOEHLER, *Michelson Laboratory, U. S. Naval Ordnance Test Station, Inyokern.*—When the thickness or change in thickness of an air film between silvered flats is measured by means of fringes of equal chromatic order, a systematic error is introduced due to a deviation from the phase change upon reflection from that assumed by the Airy intensity distribution and due to the neglect of the thickness of the partial silver coating. A method of reducing this error will be discussed.

M2. Diffraction by an Ionized Trail. CHARLES H. PAPAS, *California Institute of Technology, Pasadena.*—In a previous paper[1] the diffraction of a plane electromagnetic wave by a perfectly conducting cylinder was examined by use of the Levine-Schwinger variational principle.[2] The incident wave was assumed to be linearly polarized parallel to the axis of the cylinder. Using the same technique Takahashi, Watanabe, and Tanimoto[3] treated the complementary case of perpendicular polarization. In this paper essentially the same method of attack is used to calculate the parallel and perpendicular scattering cross sections of an ionized column produced by a traveling meteor.[4] Mathematical difficulties, which limit the applicability of existing theories[5] to small values of a/λ (a = effective diameter of ionized trail), are removed by use of the variational principle.

[1] C. H. Papas, J. Appl. Phys. **21**, 318 (1950).
[2] Comm. Pure and Appl. Math. **3**, 355 (1950).
[3] Paper read at Annual Meeting of the Physical Society of Japan, November 2, 1950.
[4] N. Herlofson, Phys. Soc. Rep. Prog. Phys. **11**, 444 (1948).
[5] N. Herlofson, Arkiv Fysik **3**, 247 (1951).

M3. Law of Equilibrium Between Coexisting Phases. GEORGE ANTONOFF, *Fordham University.*—My law as applied to two liquid layers is $\gamma_{12} = \gamma_1 - \gamma_2$ (1), where γ_{12} is the interfacial tension, γ_1 and γ_2 surface tensions of both layers. Its theory indicates that it is a law of equilibrium and thus can have no exceptions. However, the systems often remain in false equilibrium, especially if cp and if they contain the groups OH and COOH. Thus, no measurements have significance, unless extended over a long enough period. In systems like CS_2 and H_2O equilibrium is never reached, owing to irreversible reaction; they are outside my law. Criterions of equilibrium are (1) conformity with the law (1), (2) two layers in equilibrium have the same vapor pressure, (3) the same boiling point, and (4) the same freezing point. Recently Donohue and Bartell[1] contested the above, but did not describe any experiments of long duration. Also, Rose and Seyer[2] described results equally meaningless and for the same reason. Carl Benedicks[3] attributes his results to nonvalidity of law (1) for systems with OH and COOH groups. In an earlier reference,[4] I explained why the effect cannot be the result of adsorption.

[1] Donohue and Bartell, J. Phys. Chem. **55**, 480 (1952).
[2] Rose and Seyer, J. Phys. Chem. **55**, 439 (1951).
[3] Carl Benedicks, Arkiv Fysik **3** 416 (1951).
[4] George Antonoff, J. Phys. Chem. **46**, 497 (1942).

M4. Propellant Burning Rate Calculations. G. B. SHOOK, *Michelson Laboratory, U. S. Naval Ordnance Test Station, Inyokern.*—In an extension of previous work on steady-state burning rates for solid rocket fuels,[1] a system of calculations has been devised which predicts the dependency of the rate on pressure, storage temperature, and local gas velocity. Principal parameters involved are (a) heat of explosion, (b) density, (c) specific heat, and (d) reaction rate constants for solid phase reaction. The essential variables are (a) temperature gradient at burning surface, (b) reaction rate integral, and (c) surface temperature. These are obtained by the use of an analog computer (REAC). The calculations are compared with experimental results for several laboratory batch rocket fuels.

[1] R. H. Olds and G. B. Shook, Phys. Rev. **88**, 166 (1952).

M5. The Surface Temperature of a Burning Double-Base Propellant. M. H. HUNT, C. A. HELLER, AND A. S. GORDON, *Michelson Laboratory, U. S. Naval Ordnance Test Station, Inyokern.*—The surface temperature of a burning double-base propellant has been measured in the range from one atmosphere to 1000 psi. The measuring technique has been to hold a Pt−Pt 10 percent Rh thermocouple in contact with the burning surface and to record the resulting emf. The temperatures range from 800°C at atmospheric pressure to 1700°C at 1000 psi. From this information and the known variation of burning rate with pressure, an activation energy for the surface reaction may be calculated. The validity of the measurements are discussed, and some corrections to the data are proposed.

M6. Linearized Theory of Spherical Wave Decay. L. M. TANNENWALD, *Michelson Laboratory, U. S. Naval Ordnance Test Station, Inyokern* (introduced by F. T. Rogers, Jr.).—A multiple Laplace-transform technique will be given which permits a tractable description of the motion of a spherical wave in a medium (air) having viscosity and heat conductivity (Prandtl number = 0.75).

M7. Geometrical Relations for Solid Propellant Charges for Rocket Motors. E. W. PRICE, *Michelson Laboratory, U. S. Naval Ordnance Test Station, Inyokern.*—Dependence of the gas flow field in a solid propellant rocket motor on two geometrical ballistic parameters G and J has been determined in earlier work (e.g., reference 1, where $G = qx/A_p$)[1]. Using the geometrical assumptions of reference 1, and the additional assumption that the charge burning area varies linearly with distance burned in from the initial charge surface, it is shown in the present paper that $G = lb_f f(a, R_i, w)$ and $J = (A_i/A_m)g(a, R_i, w)$, where f and g are algebraic functions. In these relations, w is the fractional distance remaining to be burned into the charge at any time during burning, and a, R_i, l, b_f, and (A_i/A_m) are dimensionless geometrical design parameters descriptive of change in charge surface area during burning, loading density of the motor, length of the charge, perimeter of the charge cross section at the end of burning, and nozzle size, respectively. Combination of these results with those of reference 1 enables one to systematically examine the variation in motor performance as a function of propellant charge geometry and to ascertain the feasible domain of motor performance.

[1] E. W. Price, J. Appl. Phys. **23**, 145 (1952).

M8. Velocity of Sound Apparatus for Liquids at 512 kc. GEORGE G. KRETSCHMAR, *Michelson Laboratory, U. S. Naval Ordnance Test Station, Inyokern.*—An ultrasonic interferometer has been constructed for measuring liquid sound velocities

in which all parts in contact with the liquid are made of stainless steel. This has the advantage that measurements may be made on corrosive liquids. The 5-mil stainless steel diaphragm is driven by a quartz crystal at 512 kc with an oscillator and tuned amplifier. The frequency is controlled by continuous monitoring with a Signal Corps Type BC 221 AH frequency meter. This permits measurements of high accuracy to be made. Test measurements were made on water. The average of three measurements was 1498.2 m/sec for the velocity of sound in distilled water at 25°C.

M9. Dependence of Jet-Tone Eigenfrequencies on Aerodynamic and Geometrical Parameters Involved. LLOYD E. SCHILBERG AND A. B. C. ANDERSON, *Michelson Laboratory, U. S. Naval Ordnance Test Station, Inyokern.*—An experimental study of the dependence of the spectrum of self-excited eigenfrequencies produced by air-jets, at relatively low Reynolds numbers, has been made. Results, expressed in non-dimensional form, indicate that $[(\Delta p/\rho)^{\frac{1}{2}}]/tf$ is a function of Reynolds number, where Δp is differential pressure across orifice; ρ, density of air; t, thickness of orifice plate; and f, eigenfrequency: In the upper range of Reynolds numbers investigated $[(\Delta p/\rho)^{\frac{1}{2}}]/tf$ is relatively independent of Reynolds number; in the lower range, it rises with decrease of Reynolds number. For any one orifice plate and jet there may be one or more eigenfrequencies rising above the turbulent background noise. Usually one of them is louder than the others. If the value $[(\Delta p/\rho)^{\frac{1}{2}}]/tf = K$ for this one is calculated, the values of $[(\Delta p/\rho)^{\frac{1}{2}}]/tf$ for the others appear to be a multiple or submultiple of K.

M10. Dependence of the Primary Pfeifenton (Pipe Tone) Frequency on Pipe-Orifice Geometry. A. B. C. ANDERSON, *Michelson Laboratory, U. S. Naval Ordnance Test Station, Inyokern.*—A derivation is presented of an expression relating the frequency of the *primary Pfeifentöne*, produced in a column of moving gas, to the geometry of the pipe-orifice combination in which the *Pfeifenton* oscillations occur. The *Pfeifentöne* appear to be initiated in and by the gas discharging continuously through the orifice. Comparison is made between results obtained with this expression and experiment. Good agreement is shown between the values of the *primary Pfeifenton* frequencies predicted by the relation and the values obtained by experiment. These results apply for a thin orifice plate and are expressed in nondimensional form. A mechanism for the excitation of these self-excited oscillations is proposed.

M11. A Wave Synthesizing Light Chopper. W. WALLIN, *Michelson Laboratory, U. S. Naval Ordnance Test Station, Inyokern.*—A means is described for modulating a light beam according to any of a class of functions describable by Fourier series.

M12. Detonation in Gases. ARTHUR L. BENNETT, *U. S. Naval Ordnance Test Station, Inyokern.*—Detonation of a stoichiometric mixture of hydrogen and oxygen in a tube 2.5 cm square and a meter long, ignited by a spark, is being studied at initial absolute pressures up to 800 mm Hg. The spectrum λ4000 to λ6500 is predominated by the *D* lines of sodium, apparently in the normal ratio of intensities. Emission of intermediate strength around λ5500 and λ6200 and a very weak emission of Ca λ4227 are the only other features seen. The intensity variation of the emission is recorded by a photomultiplier and cathode-ray scope. The intensity of the emission measured at a slit 60 cm from the spark rises in a few microseconds to a maximum and decays in about 80 microseconds for an initial pressure of one atmosphere.

M13. Nuclear Magnetic Relaxation in Viscous Liquids. ROBERT L. CONGER, *U. S. Naval Ordnance Test Station, Inyokern.**—Measurements of nuclear relaxation times of water-glycerine solutions of Cu^{++} and Mn^{++} were made over a viscosity range of from 1 to 70 centipoise. Effective magnetic moments of Cu^{++} and Mn^{++} were then calculated from these data and plotted as a function of viscosity. The resulting curve for Mn^{++} decreases gradually in a manner easily explained, while the curve for Cu^{++} shows an anomaly at about 10 centipoise.

* Post Office: China Lake, California.

TUESDAY AFTERNOON AT 1:30

Room 22, Crellin

(W. M. POWELL presiding)

Contributed Papers

N1. The Interference of Waves Generated by the Electric Field. OLEG YADOFF, *Columbia University.*—If we suspend in space, in the presence of atmospheric pressures, two needle electrodes connected with the source of an electrostatic field, we can obtain, by means of the regulation of these electrodes, a situation that creates the phenomenon of the interference of emitted waves. Such an interference can be easily observed on the surface of some not very viscous liquid. If, for instance, two needle electrodes are suspended above the surface of water placed in an open vessel, we can obtain an interference in the form of divergent waves of hyperbolic shape, greatly resembling the interfering waves obtained from the mechanically vibrating needle contacts. In the present case, the electrode is suspended in space above the surface of the liquid, while in the known case of mechanical vibration the needles touch the surface of the liquid. It is preferable to use electrodes charged with the same sign, for example, a negative sign. The enclosed photograph illustrates this phenomenon. The interference occurs not only on the surface but in the liquid itself. The penetrability increases with the increase of the degree of viscosity, but in this case there appears a convection of electrical charges through the liquid. The observed new aspect of the phenomenon of interference may have important applications in industry, for example, in different biological treatments.

N2. Some Electrical Hysteresis Properties of Ice.* FRANK K. TRUBY, *New Mexico Institute of Mining and Technology Socorro, New Mexico.*—Extensive experimentation has shown that the electrical conductivity of ice in the direction of the *C* axis is by electrons which are provided by impurity centers incorporated during the freezing process. The apparent resistance is dependent upon the sign and magnitude of the applied field. Conductivity measurements made over a continuous cycle of applied potential gradient (−4000 to +4000 volts per cm) exhibit the following characteristics: (a) The ice acts as a body rectifier along the *C* axis. (b) The front to

back conduction ratio ranges from 0 for low fields to 30,000 for higher values. The minimum electron conductivity is in the direction of the crystal's growth. (c) The conductivity is dependent upon the electrical history giving hysteresis effects with respect to the potential gradient. (d) The character of the hysteresis loop indicates a high degree of coordination in the structure suggestive of a domain regime involving the impurity centers. These results support other evidence that the number of configurations in the resonance pattern of ice is restricted greatly by high coordination within a domain or cellular structure.

* Part of the work here reported was done under contract with the ONR.

N3. The Cellular Nature of Ice Crystals. E. J. WORKMAN, *New Mexico Institute of Mining and Technology, Socorro, New Mexico.*—In an effort to explain some electrical and electromechanical effects observed in the study of ice containing minute quantities of impurities, attempts have been made to find evidence of the role of impurity centers in the crystal regime. Accordingly, a relatively large number of x-ray diffraction patterns and electron photomicrographs of ice have been made. Electron microscope studies reveal that the etched surfaces of all crystals show a fine structure pattern indicative of high binding energy around small hexagonal crystal cells. These small crystals range in size from ½ to 5 microns in width and have a depth ranging from 1 to 10 microns. The size of the unit crystals is independent of growth rate of the sample. Photographs of etched surfaces are shown in evidence that the large single crystals of ice are in fact coordinated mosaics of small hexagonal cells.

N4. A Low Power Water Boiler Type Reactor for Research Use.* M. E. REMLEY AND D. C. WOODS, *North American Aviation, Inc., Downey, California.*—A small homogeneous reactor of the water boiler type[1] has been placed in operation at the Atomic Energy Research Department of North American Aviation, Inc. The reactor core consists of a stainless steel sphere 12 inches in diameter which contains a U^{235} enriched uranyl nitrate solution. The sphere is surrounded by a cylindrical graphite reflector, which in turn is surrounded by a concrete block shield. No cooling facilities are incorporated in the design, and decomposition and fission product gases evolved during operation are collected in a stainless steel accumulator tank. With the present two feet of concrete shielding, the reactor can be operated at a maximum power of one watt and supplies a thermal flux of approximately 4×10^7 neutrons/cm²-sec in a tube through the core. Because of its small cross section, the reactor is ideally suited for cross-sectional measurements by the danger coefficient technique.[2] Data on the operating characteristics, neutron flux distributions, and experimental uses of this low power reactor will be discussed.

* This work was performed under AEC Contract AT-11-1-GEN-8.
[1] Los Alamos Scientific Laboratory, Rev. Sci. Instr. **22**, 489 (1951).
[2] Anderson, Fermi, Wattenburg, Weil, and Zinn, Phys. Rev. **72**, 16 (1947).

N5. Resonance Absorption by Conduction Electrons in Metals. A. F. KIP, T. W. GRISWOLD, AND A. M. PORTIS, *University of California, Berkeley.*—Observation of spin resonance absorption due to conduction electrons in finely divided sodium has been reported.[1] We are continuing this work and have found similar absorption in finely divided lithium. Observations were made in the 9000 mc/sec region. Since the absorption by conduction electrons is independent of temperature, in contrast to the approximate $1/T$ dependence of ordinary paramagnetism, we can rule out the possibility that the observed absorption is due to contamination by small amounts of paramagnetic materials. This is done by making observations at room temperature and at liquid nitrogen temperature with the metallic sample and a small sample of $CuSO_4\cdot5H_2O$ both in the test cavity. The relative sizes of the two signals at the two temperatures confirms the fact that the signal from the metals is essentially temperature independent, in contrast to the copper sulfate. The line width in our sample of lithium is considerably narrower than in sodium. This agrees qualitatively with the idea that metals with longer electron mean free paths give broader absorption lines, as discussed in the following abstract.

[1] Griswold, Kip, and Kittel, Phys. Rev. (to be published).

N6. Electronic Spin Resonance Line Width in Metals. ELIHU ABRAHAMS AND C. KITTEL, *University of California, Berkeley.*—The line width observed in electronic spin resonance in alkali metals[1] is attributed to the diffusion of conduction electrons. A conduction electron in the skin depth will see an rf field which is amplitude and frequency modulated, giving rise to a line width. This width is "motionally narrowed" because of the high frequency of electron-phonon collisions. The relative width $\Delta\omega/\omega$ is proportional to the square of the conductivity mean free path A. For alkali metal samples of dimensions greater than the skin depth, $\Delta\omega/\omega\approx10^{-1}$ to 10^{-2}. If the thickness t of the sample is less than the skin depth δ, there is additional narrowing by a factor $\alpha(t/\delta)^3$. Although electron-electron collisions do not contribute to the conductivity, they play a role in determining the width. We must therefore replace A^2 by AA', where $(A')^{-1}=A^{-1}+A_e^{-1}$, and A_e is the electron-electron collision mean free path. The affect of such collisions should be observable in the variation of width with temperature at temperatures low enough that $A_e<A$. Calculations of A_e will be presented.

[1] Griswold, Kip, and Kittel, Phys. Rev. (to be published).

N7. Measurement of the Transport Mean Free Path of Thermal Neutrons in Heavy Water. S. W. KASH AND D. C. WOODS, *Atomic Energy Research Department, North American Aviation, Inc.**—The transport mean free path of thermal neutrons in heavy water has been experimentally determined by a boron poisoning technique. The method involved measuring the relaxation length of thermal neutrons in a cylindrical tank containing a mixture of heavy water and boron. From the variation of the relaxation length with boron concentration, the effective value of the transport mean free path and the hydrogen impurity content were determined for the heavy water used. Correcting for the hydrogen impurity yielded a value of 2.53 ± 0.03 cm for the transport mean free path of 100 percent pure D_2O.

* Work supported by the AEC.

N8. Pulse-Height Measurements of Recoils from $B^{10}(n,\alpha)Li^7$ in Argon-CO_2 Mixtures. J. DE JUREN AND H. ROSENWASSER, *National Bureau of Standards.*—Thin films of boron deposited over a small area by vacuum evaporation have been exposed to a slow neutron flux in an ionization chamber connected to a linear amplifier. The resulting pulse-height distributions have been analyzed for a variety of pressures, field strengths, and amplifier time constants. A considerable variation in the ratio of the He^4 and Li^{7*} pulses was observed. Other authors[1,2,3] have obtained ratios from 1.84 to 1.89, whereas from conservation of momentum 1.753 is expected. These values have been cited as evidence for an increase in the average energy loss per ion pair created in argon as particle velocity is reduced. Our measurements agree with the above ratios for certain conditions but decrease to a value approaching 1.75 as pressure is reduced and field strength is increased, indicating that electron capture at the end of the Bragg curve is responsible for most of the variation.

[1] Stebler, Huber, and Bichsel, Helv. Phys. Acta **22**, 362 (1949).
[2] G. C. Hanna, Phys. Rev. **80**, 530 (1950).
[3] Rhodes, Franzen, and Stephens, Phys. Rev. **87**, 141 (1952).

N9. A Trochoidal Analyzer for Charged Particles. BERND CRASEMANN, *University of California, Berkeley.*—A magnetic analyzer has been built which makes use of the trochoidal

orbit of charged particles in a fringing magnetic field.[1] The source is placed in a vacuum chamber at the edge of a 2-cm gap between cylindrical pole pieces of 10-cm diameter. At this radius, the field, which reaches 9000 gauss at the center of the gap, has a linear gradient of 3000 gauss/cm. The particles describe approximately circular orbits that precess at right angles to the field gradient. The detector is a scintillation counter. Background is practically eliminated by dividing the light pulses from an anthracene crystal through a split Lucite light pipe and counting them with two cooled 1P21 photomultipliers in coincidence. Rough energy resolution is provided by varying the amplifier bias. Positrons and electrons can be counted with good efficiency. The apparatus has been used to study a 4-min positron activity obtained in cyclotron bombardments of Co, Ni^{60}, and Ni^{61} with alpha-particles, Ni^{61} and Ni^{62} with deuterons, Ni^{62} with protons, and Cu with neutrons.

[1] J. Thibaud, Compt. rend. **197**, 447 (1933).

SUPPLEMENTARY PROGRAMME

SP1. Characteristics of Certain Photographic Plates in the Vacuum Ultraviolet. Po Lee and G. L. Weissler,* *University of Southern California.*—The *D vs* log*t* curves of Eastman 103a-0 ultraviolet-sensitized plates have been studied in the near and the vacuum ultraviolet, respectively, together with the absorption and fluorescence spectrum of the sensitization lacquer. It was found that the ultraviolet-sensitization effect of the plate began at about 3000A, where the threshold absorption spectrum of the lacquer occurred. The absorption in the near ultraviolet did not reach total extinction for a lacquer thickness comparable to that on the commercially sensitized plates. The contrasts γ, obtained from the slopes of the *D vs* log*t* curves calibrated in the vacuum spectrograph, were constant within an experimental deviation of 4 percent throughout all observed wavelengths from 1320A to 360A and were equal to the contrast of the emulsion at the wavelength of maximum intensity of fluorescence of this lacquer, 3150A. A number of methods for the calibration of plates in air has been suggested and one of them was tested in detail. The reciprocity law and sensitivity of these ultraviolet-sensitized plates were also studied and are discussed.

* The aid of ONR and the Cambridge Air Force Research Center is gratefully acknowledged.

SP2. The Absorption Coefficients of NO and NH_3 in the Vacuum Ultraviolet. H. Sun and G. L. Weissler,* *University of Southern California.*—The NO absorption between 1300A and 370A is composed of one or more continuous regions superposed by bands. A plot of the coefficients k_ν *versus* wavelength exhibits at least two maxima, one at 920A with $k_\nu = 850$ cm^{-1} and another at 620A with $k_\nu = 920$ cm^{-1}. There are also indications of small peaks at 1300A with $k_\nu = 180$ cm^{-1} and at 760A with $k_\nu = 660$ cm^{-1}. An absorption minimum occurs near 1200A with $k_\nu \leq 50$ cm^{-1}. It has not been possible as yet to separate band absorption from continuous absorption. For this reason, the ionization continua associated with the various ionization limits of Tanaka[1] have not been correlated with these measurements. (NH_3 shows in the same region a nearly continuous absorption with a broad maximum of about $k_\nu = 1000$ cm^{-1} at 770A.) Experimental details and k_ν values for 80 wavelengths will be presented for both gases.

* The aid of ONR is gratefully acknowledged.

[1] Y. Tanaka, Sci. Pap. Inst. Phys. Chem. Res., Tokyo **39**, 456 (1942).

Author Index to Papers Presented at the Inyokern-Pasadena Meeting

Abrahams, Elihu and C. Kittel—N6
Amin, M. R.—I10
Anderson, A. B. C.—M10
Antonoff, George—M3
Ashburn, E. V.—H13
Ball, W. P., Burton J. Moyer, and Robert E. Richardson—K14
Benedict, W. S., Norman Gailar, and Earle K. Plyler—H7
Bennett, Arthur L.—M12
Bowen, D. B. and G. W. Rodeback—G6
Bradley, Richard C.—I7
Bratenahl, A. and B. J. Moyer—K9
Brinkman, J.—G3
Brown, Karl L. and Richard Wilson—L4
Brown, S. Leroy and John M. Norwood—I1
Carothers, James Edward—K10
Chiang, S. F. and S. A. Schaaf—I3
Christy, R. F.—F10
Conger, Robert L.—M13
Cooper, E. P.—C1
Crasemann, Bernd—N9
De Juren, J. and H. Rosenwasser—N8
Denney, J. M.—G7
Deutsch, R. W. and W. H. Barkas—K15
Dixon, C. E. and C. J. Meechan—G2
Dunbar, D. N. F., H. K. Reynolds, W. A. Wenzel, and W. Whaling—F4
Dyke, W. P. and J. K. Trolan—L12
Easterday, Harry T.—K5
Eggleston, R. R.—G5
Eggen, D. T. and H. Kenworthy—G8
Eisberg, Robert M. and George J. Igo—K1
El-Sum, Hussein M. A. and Paul Kirkpatrick—L11
Feynmann, Richard C.—J4
Ford, Franklin C. and Wilson M. Powell—K3
Fowler, C. A., Jr., and E. M. Fryer—G10
Frank, Wilson J., Kenneth C. Bandtel, Richard Madey, and Burton J. Moyer—K6
Gaydon, A. G.—A6
Goldman, J. E.—E2
Good, Myron L.—K11
Guinier, Andre—E3
Hendrick, R. W., Jr.—L9
Hofstadter, Robert and Asher Kantz—J5
Horton, C. W.—C3
Howe, H. A. and K. R. MacKenzie—F14
Hoyle, Fred—IA1
Huber, Elsa—I8
Hunt, M. H., C. A. Heller, and A. S. Gordon—M5
Jankus, V. Z.—L6
Kash, S. W. and D. C. Woods—N7
Keywell, Frank—I4
Kip, A. F., T. W. Griswold, and A. M. Portis—N5
Kittel, C.—E1
Knight, W. D.—L1
Koehler, W. F.—M1
Kraus, Alfred A., Jr., A. P. French, William A. Fowler, and C. C. Lauritsen—F6
Kretschmar, George G.—M8
Krzywoblocki, M. Z.—C5
Kunkel, W. B.—H11
Kyhl, R. L.—J1
Langmuir, R. V.—J2
Lawson, R. D. and S. D. Drell—L2
Lee, Po and G. L. Weissler—H5
Lee, Po and G. L. Weissler—SP1
Leighton, R. B. and W. L. Alford—L7
Leighton, Robert B.—J3
Leonard, Stanley L.—K13
Liepmann, H. W.—C4
Lomont, J.—G9
Mackin, R. J., Jr.—F8
Madey, Richard, Kenneth C. Bandtel, and Wilson J. Frank—K4
Meyerhof, W. E., L. G. Mann, and H. I. West, Jr.—L5
Mileikowsky, Curt and Ward Whaling—F5
Milne, Edmund A.—F2
Motz, H. and L. I. Schiff—L8
Neal, R. B.—L13
Norrish, R. G. W.—A5
Oliver, Albert J.—K12
Overhauser, Albert W.—G1
Papas, Charles H.—M2
Parker, James H.—I9
Parker, Lee W. and John R. Holmes—H1
Pattee, Howard H., Jr.—L10
Peterson, John W.—I6
Pitkanen, Paul H.—F13
Plain, G. J., H. L. Morrison, P. H. Pitkanen, and F. T. Rogers, Jr.—F11
Plesset, M. S.—C2
Porter, G.—A4
Price, E. W.—M7
Rekers, R. G. and D. S. Villars—H8
Remley, M. E. and D. C. Woods—N4
Reynolds, H. K., D. N. F. Dunbar, W. A. Wenzel, and W. Whaling—F3
Roach, F. E., Helen B. Pettit, D. R. Williams, and P. St. Amand—H10
Rogers, F. T., Jr.—I2
Rogers, Marguerite, F. K. Odencrantz, and G. J. Plain—F12
Sagane, Ryokichi—K16
St. Amand, Pierre and D. R. Williams—H9
Schilberg, Lloyd E. and A. B. C. Anderson—M9
Shook, G. B.—M4
Silverman, S.—A1
Stapp, H. P.—L3
Stork, D.—K8
Stuart, Alexander Verrijn and G. B. B. M. Sutherland—H12
Sun, H. and G. L. Weissler—SP2
Swings, P.—A3
Tannenwald, L. M.—M6
Theobald, J. K.—I5
Tracy, J. F.—K2
Truby, Frank K.—N2
Wainfan, N. and W. C. Walker—H2
Walker, W. C. and N. Wainfan—H3
Wallin, W.—M11
Warters, William D.—F1
Weissler, G. L. and H. Sun—H4
Westervelt, Donald R.—G4
Williams, D. R. and Pierre St. Amand—H6
Wilson, H. W. and Walter H. Barkas—K7
Wise, Henry—G12
Wolfhard, H. G.—A2
Wong, Calvin—F9
Woodbury, H. Hugh—F7
Workman, E. J.—N3
Yadoff, Oleg—N1
Zernow, Louis—G11

CONTENTS

THE PHYSICAL REVIEW SECOND SERIES, VOLUME 92, No. 2 OCTOBER 15, 1953

Sensitive Hall Measurements on NaCl and on Photoconductive PbTe . . . John L. Levy 315
Measurement of the Thermoelectric Power of Germanium at Temperatures above 75°K . . . A. F. Middleton and W. W. Scanlon 219
Theory of Thermoelectric Power in Semiconductors with Applications to Germanium . . . V. A. Johnson and K. Lark-Horovitz 226
Luminescence Studies of KI-TlI . . . Bernard Smaller and Eugene Avery 233
Superconductivity in Tin-Bismuth and Tin-Antimony Alloys . . . W. F. Love 239
Superconductivity of Titanium . . . M. C. Steele and R. A. Hein 243
Thermoelectric Power of Germanium below Room Temperature . . . H. P. R. Frederikse 248
Energy of Trapped Electrons in Ionic Solids . . . Kurt Lehovec 253
Atomic Heat of Indium below 20°K . . . J. R. Clement and E. H. Quinnell 258
Sign of the Quadrupole Interaction of Li^6 in LiCl . . . P. Kusch 260
Change in the Inversion Spectrum of ND_3 from Resonance to Nonresonance Absorption . . . G. Birnbaum and A. A. Maryott 270
One-to-Two Millimeter Wave Spectroscopy. II. H_2S . . . Charles A. Burrus, Jr., and Walter Gordy 274
Eigenfunctions of S^2 by a Spin Operator Method . . . George W. Pratt, Jr. 278
1.25-Minute Rb^{85m} Daughter of 27-Day Sr^{85} . . . L. M. Litz, S. A. Ring, and W. R. Bellwell 286
Elastic Scattering of Particles by Atomic Nuclei . . . N. C. Francis and K. M. Watson 291
Nuclear Moments of Technetium-99 . . . Karl G. Kessler and R. E. Trees 303
Hyperfine Structure Formulas for LS Coupling . . . R. E. Trees 309
Radiations of $_{64}Gd^{149}$ (18 hr) and $_{64}Gd^{145}$ (3.7 min) . . . W. C. Jordan, J. M. Cork, and S. B. Burson 315
Gamma-Gamma Directional Correlation Experiments with Mo^{99m} . . . J. J. Kraushaar 318
Theorem Concerning Angular Correlations . . . J. Wenzel and D. R. Hamilton 321
Total Neutron Cross Section of Liquid Argon . . . Janet B. Guernsey and Clark Goodman 323
Hyperfine Structure of the Spectra of Dysprosium, Cobalt, Vanadium, Manganese, and Lanthanum . . . Kiyoshi Murakawa and Tohru Kamei 325
Degradation and Range Straggling of High-Energy Radiations . . . U. Fano 328
Angular Distributions from (n,p) Nuclear Reactions . . . N. Austern, S. T. Butler, and H. McManus 350
Penetration of Gamma Radiation through Iron . . . L. A. Beach, R. B. Theus, and W. R. Faust 355
Disintegration Scheme of Br^{80} (18 min) . . . Gertrude Scharff-Goldhaber and Michael McKeown 356
Neutron Total Cross Sections at 20 Mev . . . Robert B. Day and Richard L. Henkel 358
Photoprotons from In, Co, and Bi . . . M. E. Toms and W. E. Stephens 362
Radioactive Decay of Calcium 47 . . . J. M. Cork, J. M. LeBlanc, M. K. Brice, and W. H. Nester 367
Long-Lived Activity in Neutron-Irradiated Niobium . . . David L. Douglas, Anita C. Mewherter, and Robert P. Schuman 369
Polarization of the Gamma Rays in the $F^{19}(p,\alpha\gamma)O^{16}$ Reaction . . . L. W. Fagg and S. S. Hanna 372
Neutron and Spontaneous Fission in Uranium Ores . . . W. H. Fleming and H. G. Thode 378
Study of the He^3+H^3 Reactions . . . C. D. Moak 383
Neutron Spectrum from the $O^{18}(d,n)F^{19}$ Reaction . . . Robert L. Seale 389
Production of Protons from Carbon by Monoenergetic Gamma Rays . . . John W. Weil and Boyce D. McDaniel 391
Metastable States of Ge^{77} . . . Joan P. Welker, A. W. Schardt, G. Friedlander, and J. J. Howland, Jr. 401
Search for Highly Absorbable Negative Cosmic-Ray Particles at Sea Level . . . Charles E. Miller, Joseph E. Henderson, David S. Potter, William R. Davis, Wayne M. Sandstrom, Gerald R. Garrison, and Francis M. Charbonnier 406
Polarization of Nuclei in Metals . . . Albert W. Overhauser 411
Effects of the Geomagnetic Field on Solar Cosmic Rays . . . V. Sarabhai and R. P. Kane 415
Bremsstrahlung and Electron Scattering Cross Sections in Au for 247-Mev Electrons and Positrons . . . Philip C. Fisher 420
Time Variation of Cosmic-Ray Heavy Nuclei . . . Victor H. Yngve 428
High-Energy Electron Scattering by Nuclei . . . R. W. Pidd, C. L. Hammer, and E. C. Raka 436
Properties of Heavy Unstable Particles . . . D. Lal, Yash Pal, and B. Peters 438
Distribution of Arrival Times of Air Shower Particles . . . P. Bassi, G. Clark, and B. Rossi 441
Multiple Production of Pions in Nucleon-Nucleon Collisions at Cosmotron Energies . . . E. Fermi 452
Atmospheric Effects on Cosmic-Ray Intensity Near Sea Level . . . S. Olbert 454
Multiple Cores in Air Showers . . . Omaan El-Mofty 461
Relative Ionization by Cosmic-Ray μ Mesons in a Liquid Scintillator . . . R. Reiche and J. R. Winckler 464
Strong Coupling Theory of Meson Scattering . . . Allan N. Kaufman 468
Virial Theorem for Dirac's Equation . . . N. H. March 481
Relative Correction to the Lamb Shift . . . M. Baranger, H. A. Bethe, and R. P. Feynman 482

(continued on cover three)

LANCASTER PRESS, INC., LANCASTER, PA.